SCIENTIFIC REPORTS

OPEN

Immunogenicity of Candidate MERS-CoV DNA Vaccines Based on the Spike Protein

Received: 13 September 2016
Accepted: 15 February 2017
Published: 23 March 2017

Sawsan S. Al-amri[1], Ayman T. Abbas[1,2], Loai A. Siddiq[1], Abrar Alghamdi[1], Mohammad A. Sanki[3], Muhanna K. Al-Muhanna[4], Rowa Y. Alhabbab[1,5], Esam I. Azhar[1,5], Xuguang Li[6] & Anwar M. Hashem[1,7]

MERS-coronavirus is a novel zoonotic pathogen which spread rapidly to >25 countries since 2012. Its apparent endemicity and the wide spread of its reservoir host (dromedary camels) in the Arabian Peninsula highlight the ongoing public health threat of this virus. Therefore, development of effective prophylactic vaccine needs to be urgently explored given that there are no approved prophylactics or therapeutics for humans or animals to date. Different vaccine candidates have been investigated but serious safety concerns remain over protein or full-length spike (S) protein-based vaccines. Here, we investigated the immunogenicity of naked DNA vaccines expressing different fragments of MERS-CoV S protein in mice. We found that plasmids expressing full-length (pS) or S1-subunit (pS1) could induce significant levels of S1-specific antibodies (Abs) but with distinct IgG isotype patterns. Specifically, pS1 immunization elicited a balanced Th1/Th2 response and generally higher levels of all IgG isotypes compared to pS vaccination. Interestingly, only mice immunized with pS1 demonstrated significant S1-specific cellular immune response. Importantly, both constructs induced cross-neutralizing Abs against multiple strains of human and camel origins. These results indicate that vaccines expressing S1-subunit of the MERS-CoV S protein could represent a potential vaccine candidate without the possible safety concerns associated with full-length protein-based vaccines.

Middle East respiratory syndrome coronavirus (MERS-CoV) is an emerging zoonotic pathogen recovered first from a fatal human case in Saudi Arabia in 2012[1] and continued to infect almost 1800 people in over 25 countries. Saudi Arabia has reported the largest number of cases so far with cases continuing to increase. The virus causes severe respiratory infection associated with fever, cough, acute pneumonia, shortness of breath, systemic infection and occasional multi-organ failure in infected individuals leading to death in 35–40% of the cases[2–4]. Such a severe disease usually occurs in immunocompromised patients, individuals with comorbidities and the elderly[1,4–6]. Most of the reported MERS cases are linked to hospital outbreaks and family clusters due to close contact with infected patients[4,7–10]. However, accumulating epidemiological data show high prevalence of MERS-CoV in dromedary camels from several Arabian and African countries, suggesting that dromedaries might be the reservoir hosts of this virus[4,11–15]. The continued endemicity of MERS-CoV in the Arabian Peninsula and the associated high death rate clearly represent a public health concern with potential global spread as observed in the recent outbreak in South Korea[10]. This is further complicated by the lack of prophylactic or therapeutic measures, underscoring the importance of preparedness research against this potential pandemic virus.

Several supportive therapies and antivirals were proposed and examined for the treatment of MERS-CoV infections[16–20]. However, most of these strategies were based on the experience gained during the severe acute respiratory syndrome (SARS) outbreak or from MERS-CoV *in vitro* studies and require further preclinical and

[1]Special Infectious Agents Unit, King Fahd Medical Research Center, King Abdulaziz University, Jeddah, Saudi Arabia. [2]Biotechnology Research Laboratories, Gastroenterology Surgery Center, Mansoura University, Mansoura, Egypt. [3]Hematology Laboratory, King Abdulaziz University Hospital, Jeddah, Saudi Arabia. [4]Materials Science Research Institute, National Nanotechnology Center, King Abdulaziz City for Science and Technology (KACST), Riyadh, Saudi Arabia. [5]Department of Medical Laboratory Technology, Faculty of Applied Medical Sciences, King Abdulaziz University, Jeddah, Saudi Arabia. [6]Center for Vaccine Evaluation; Biologics and Genetic Therapies Directorate; Health Canada; Ottawa, Ontario, Canada. [7]Department of Medical Microbiology and Parasitology, Faculty of Medicine, King Abdulaziz University, Jeddah, Saudi Arabia. Correspondence and requests for materials should be addressed to A.M.H. (email: amhashem@kau.edu.sa)

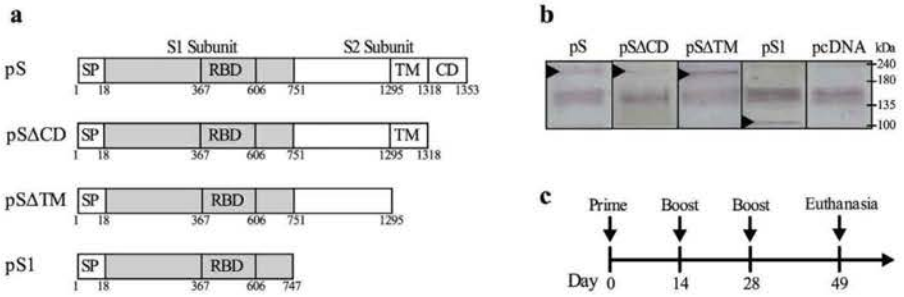

Figure 1. MERS-CoV Spike DNA vaccines. (**a**) Schematic representation of the generated DNA vaccine constructs. Four constructs were generated including one expressing full length S protein (pS) and three other constructs expressing truncated S protein with deleted cytoplasmic domain (pSΔCD), deleted transmembrane domain (pSΔTM) or deleted S2 subunit (pS1). Numbers indicate amino acids. SP: signal peptide; RBD: receptor-binding domain; TM: transmembrane domain; CD: cytoplasmic domain. (**b**) *In vitro* protein expression in cell culture. Vero E6 cells with 80–90% confluency were transfected with the DNA constructs; 48 h later, cell lysates were collected; protein expression was subsequently confirmed by western blot using anti-S1 polyclonal Abs. Arrows indicate band with expected molecular weight. (**c**) Time-line of immunization regimen.

clinical evaluation. The ideal strategy to rapidly control existing and potential outbreaks of MERS-CoV is to generate a safe and effective vaccine at least to target high-risk groups or animal hosts. The ability of more than 60% of the infected patients to recover, clear the virus and develop immunity suggest that a vaccine based on the viral components such as the spike (S) glycoprotein could be a suitable vaccine candidate. This is further supported by the isolation of several human neutralizing antibodies (nAbs) against the MERS-CoV S protein and their ability to neutralize and block viral entry and/or cell-cell spread at very low concentrations, and sometimes to confer prophylactic and therapeutic protection in animal models[21–27].

MERS-CoV S glycoprotein is composed of 2 subunits; the receptor binding domain (RBD) containing subunit (S1) and the fusion machinery subunit (S2)[28]. Several vaccines candidates based on full-length or truncated S protein were developed and investigated including DNA vaccines[29,30], viral vectored vaccines[31–35], nanoparticle-based vaccine[36], whole inactivated MERS-CoV vaccine (WIV)[37], as well as the S or RBD protein-based subunit vaccines[29,38–42]. While these experimental vaccines can induce protective response in animals, SARS-CoV vaccine development and a recent MERS-CoV report[37] suggest that there might be serious safety concerns associated with the use of full length S protein as vaccine candidate including immunopathology and disease enhancement[43–48]. These concerns were proposed to be due to inductions of Th2- skewed immune response and/or anti-S non-neutralizing Abs.

DNA vaccines represent a promising vaccine development approach due to their easy production on a large scale in a timely manner and well-established procedures for quality control. In addition, DNA vaccines can elicit Th1-biased immune response in contrast to the protein-based subunit vaccines. However, all MERS-CoV DNA vaccines reported so far were aimed at expressing full-length protein, which could induce adverse reactions. In this study, we determined the immunogenicity and potential protective effects of MERS-CoV naked DNA vaccines expressing different length of S protein.

Materials and Methods

Cell line and MERS-CoV viruses. African Green monkey kidney-derived Vero E6 cells (ATCC #1568) were grown in Dulbecco's modified Eagle's medium (DMEM) supplemented with 10% fetal bovine serum (FBS), 1% penicillin/streptomycin, and 10 mM HEPES (pH 7.2) and maintained in a humidified 5% CO_2 incubator at 37 °C. MERS-CoV strains used in this study included a human isolate (MERS-CoV/Hu/Taif/SA/2015) and two camel isolates (MERS-CoV/Camel/Taif/SA/31/2016 and MERS-CoV/Camel/Taif/SA/39/2016). MERS-CoV viruses were isolated, passaged and titrated by $TCID_{50}$ in Vero E6 cells as previously described[49]. All tested isolates were at passage no. 2. All experiments involving live virus were conducted in our Biosafety level 3 facility following the recommended safety precautions and measures.

DNA constructs. Four DNA vaccine candidates were generated as shown in Fig. 1a. Full length MERS-CoV S gene from MERS-CoV-Jeddah-human-1 isolate (GenBank accession number: KF958702) was codon optimized for efficient mammalian expression and synthesized by Bio S & T (Montreal, Canada). The coding sequence was then subcloned into the mammalian expression vector pcDNA3.1 under the control of the cytomegalovirus immediate-early promoter generating pS construct. The second construct (pS1) expressing S1 domain (aa 1–747) was produced by cloning corresponding coding region by PCR using Phusion High-Fidelity PCR Kit (Life Technologies) from pS plasmid into pcDNA3.1 vector using the following forward 5′-GATCGCGGCCGCGCCACCATGATCCAC-3′ and reverse 5′-GATCGGTACCTTACAGAATGAAAAAGACGC-3′ primers. Similarly, pSΔTM expressing truncated S protein (aa 1–1295) without the transmembrane domain and pSΔCD expressing truncated S protein (aa 1–1318) without the cytoplasmic domain were generated by PCR subcloning into pcDNA3.1 vector using the above-mentioned forward primer and the following reverse primers; 5′-GATCGGTACCTTACCACTTGTTGTAGTATG-3′ and 5′-GATCGGTACCTTACAGAATGAAAAAGACGC-3′, respectively. All constructs were cloned between *NotI*

and *KpnI* restriction sites in pcDNA3.1 vector using the T4 DNA ligase. All constructs were confirmed by restriction digestion and sequencing. Bulk endotoxin-free preparations of all four constructs as well as the empty control plasmid (pcDNA) were prepared for animal studies using a plasmid Giga purification kit (Qiagen).

***In vitro* Protein expression.** Prior to animal experiments, protein expression from all DNA constructs was confirmed *in vitro* in Vero E6 cells (Fig. 1b). Briefly, 80–90% confluent Vero E6 cells in 6-well plates were transiently transfected with 1 μg of each DNA construct (pS, pSΔCD, pSΔTM, pS1, or pcDNA) using FuGENE 6 reagent (Roche) according to manufacturer's instructions, followed by incubation at 37 °C in a 5% CO_2 incubator for 48 h. Transfected cells were then washed twice with phosphate-buffered saline (PBS) and lysed with cell lysis buffer as previously described[50], and subjected to western blot analysis for protein expression using rabbit anti-S1 Abs (Sino Biological). Western blot analysis confirmed that all gene products show bands at expected molecular weights. Notably, the large band that is observed in all blots in Fig. 1b is due to non-specific binding as it was also detected in an un-transfected cell control (data not shown).

Animal Studies. Six- to 8-week-old female BALB/c mice were obtained from the core facility in King Fahd Medical Research Center (KFMRC), King Abdulaziz University (KAU). All animal experiments were conducted in accordance with institutional guidelines and the approval of the Animal Care and Use Committee at KFMRC. Mice were divided into five experimental groups (5 mice in each group) and immunized on days 0, 14 and 28 with three doses of 100 μg of each construct dissolved in 100 μl PBS. Mice were immunized intramuscularly with two injections (50 μl each) divided between the two thighs. Three weeks after the last doses (day 49), mice were euthanized and blood as well as spleens were collected for immune response analysis.

ELISA. The end-point titers of anti-S1 total IgG Ab as well as IgG1, IgG2a and IgG2b isotypes from immunized mice were determined by ELISA as described previously[29,50] with minor modifications. Briefly, 96-well plates (EU Immulon 2 HB, Thermo Scientific) were coated with the MERS-CoV S1 protein (Sino Biological) at 2 μg/ml in PBS at 4 °C overnight. Plates were then washed 6 times with PBS containing 0.05% Tween-20 (PBS-T), followed by blocking with 5% skim milk in PBS-T for 1 h at 37 °C. After washing, plates were incubated with a 2-fold serial dilution of mouse sera starting from 1:100 and incubated for 1 h at 37 °C. Then, plates were washed and incubated with peroxidase-conjugated rabbit anti-mouse IgG, IgG1, IgG2a or IgG2b secondary Abs (Jackson Immunoresearch Laboratories) at concentrations recommended by the supplier and incubated for additional 1 h at 37 °C. After extensive washing, Tetramethylbenzidine (TMB) substrate (KPL) was added for 30 min for colorimetric development and the reaction was stopped with 0.16 M sulfuric acid. Absorbance was read spectrophotometrically at 450 nm. End-point titers were determined and expressed as the reciprocals of the final detectable dilution with a cut-off defined as the mean of pre-bleed samples plus three SD.

Viral microneutralization assay. Microneutralization (MNT) assay was performed as previously described[29,30]. Briefly, two-fold serial dilutions of heat-inactivated sera prepared in DMEM starting from a 1:5 dilution were incubated with equal volume of DMEM containing 200 $TCID_{50}$ of MERS-CoV for 1 h at 37 °C in a 5% CO_2 incubator. The virus-serum mixture was then transferred on confluent Vero E6 cell monolayers in 96-well plates (four wells were used per dilution) and incubated at 37 °C in a 5% CO_2 incubator. Cytopathic effect (CPE) was observed on days 3 to determine nAb titer. The nAb titer for each sample is reported as the reciprocal of the highest dilution that completely protected cells from CPE in 50% of the wells (MNT_{50}).

$CD8^+$ T cell intracellular cytokine staining (ICS). Memory $CD8^+$ T cell IFN-γ responses were evaluated at 3 weeks after last immunizations as previously described[50]. Briefly, single-cell suspensions of splenocytes were prepared from individual mice in each group. Spleens from mice were collected in 10 ml of RPMI 1640 supplemented with 10% FBS and smashed between frosted ends of two glass slides. Processed splenocytes were then filtered through 45-μm nylon filters and centrifuged at 800 g for 10 min. Red blood cells were then lysed by adding 5 ml of ammonium-chloride-potassium (ACK) lysis buffer (Life Technologies) for 5 min at room temperature, and equal volume of PBS was then added. Cells were centrifuged again and pellets were resuspended in RPMI 1640 at a concentration of 1×10^7 cells/ml. Splenocytes were then added to a 96-well plate (1×10^6 per well) and re-stimulated with 5 μg/ml of several synthetic S1 MHC class I–restricted peptides including S291 (KYYSIIPHSI), S319 (QPLTFLLDF), S448 (YPLSMKSDL), S498 (SYINKCSRL), S647 (NYYCLRACV), S703 (TYGPLQTPV), which were synthesized by GenScript as previously described[32]. The stimulation was conducted by incubation for 6 h at 37 °C and 5% CO_2 in the presence of Protein Transport Inhibitor Cocktail (brefeldin A) (BD Biosciences) according to the manufacturer's instructions. Stimulated cells were then washed in FACS buffer and stained with LIVE/DEAD Fixable Violet Dead Cell Stain Kit (Invitrogen) and anti-mouse CD8α –FITC antibody (clone 53–6.7; eBiosciences). The cells were then washed with FACS buffer, fixed and permeabilized with Cytofix/Cytoperm Solution (BD Biosciences) according to the manufacturer's instructions, and labeled with anti–mouse IFN-γ-APC-Cy7 antibody (clone XMG1.2; BD Biosciences). All data were acquired on a BD FACS Calibur flow cytometer and analysis was completed with Flow Jo, Version 8.8.4 (Tree Star Inc.). Results for IFN-γ producing $CD8^+$ T cells were calculated as percentage of live $CD8^+$ T cells after subtracting the values obtained from no peptide controls from each sample.

Data analysis. Statistical analysis was conducted using one-way ANOVA. Bonferroni post-test was used to adjust for multiple comparisons between the different groups. All statistical analysis was conducted using GraphPad Prism software (San Diego, CA). P values < 0.05 were considered significant.

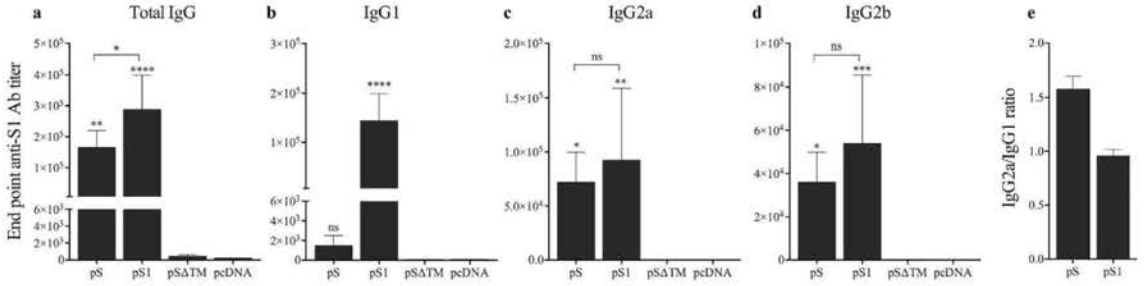

Figure 2. Humoral immune response induced by MERS-CoV Spike DNA vaccines. Circulating MERS-CoV S1-specific Abs were determined at 3 weeks post 2nd boost. End-point titers are shown for (**a**) total IgG, (**b**) IgG1, (**c**) IgG2a and (**d**) IgG2b isotypes. (**e**) IgG1/IgG2a ratio was calculated at 3 weeks after 2nd boosting to determine the type of immune response (Th2 versus Th1) induced by the various constructs. BALB/c mice were i.m. immunized with 100 μg of each construct dissolved in 100 μl PBS on days 0, 14 and 28. A control group was immunized with empty pcDNA vector. Data are shown as mean titer ± s.d. from one experiment out of two independent experiments, with n = 5 mice per treatment group in each experiment. ****$P < 0.0001$, ***$P < 0.001$, **$P < 0.01$ and *$P < 0.05$ (one-way ANOVA with Bonferroni post-test).

Results

S1-subunit DNA vaccine induces high levels of anti-S1 Abs in mice. In order to evaluate the immunogenicity of our DNA vaccine candidates, we immunized mice i.m. with three doses of the generated naked DNA constructs (Fig. 1c). To this end, evaluation of Ab levels after one or two doses of naked DNA resulted in no or barely detectable response in all groups consistent with previous report[29], and thus we only analyzed responses after the last dose. As shown in Fig. 2a, only mice immunized with pS and pS1 but not pSΔTM generated significant levels of systemic S1-specific IgG compared to control group immunized with pcDNA vector. Interestingly, pS1 elicited significantly higher levels of S1-specific total IgG compared to pS immunized mice. It is of note that DNA construct expressing truncated S protein without the cytoplasmic domain (pSΔCD) failed to induce detectable Abs in initial pilot studies; it was not tested further.

Differential induction of S1-specific IgG isotypes by Spike-based DNA vaccines. We next examined the differences in S1-specific Ab isotypes in the sera of immunized mice in order to determine the quality of the humoral response induced by the different DNA constructs. As shown in Fig. 2b–e, immunization with pS DNA vaccine mainly elicited IgG2a and IgG2b with significantly lower levels of IgG1 isotype, indicating a Th1-biased response (IgG2a/IgG1 ratio of >1.5). As expected, empty vector control (pcDNA) and pSΔTM failed to produce any anti-S1 IgG isotype. On the other hand, plasmid DNA expressing S1 subunit (pS1) induced a balanced Th1/Th2 response (IgG2a/IgG1 ratio of ~1.0) with S1-specific Abs from all isotypes. While IgG2a and IgG2b levels induced by pS1 were significantly higher compared to pSΔTM and empty vector control (pcDNA), no significant difference was observed in the levels of these two isotypes between pS and pS1-vaccinated groups. In contrast, level of S1-specific IgG1 Abs elicited by pS1 vaccine was significantly elevated compared to all groups including pS group. Collectively, compared with the full length S protein, these data suggest that S1 subunit delivered by DNA vector elicited stronger antibody responses and equal ratio of IgG2a/IgG1 whereas the full length S protein induced a Th1-skewed immune response.

S1-expressing DNA vaccine elicits significant level of IFN-γ response. Having observed the Th1-skewed response in pS-immunized mice compared to the pS1 group, we decided to evaluate S1-specific memory $CD8^+$ T cell responses by ICS. Remarkably, immunization of mice with pS vaccine did not elicit any significant levels of IFN-γ compared to control group (pcDNA) after re-stimulation with S291 peptide (Fig. 3). On the other hand, re-stimulation of $CD8^+$ T cells from pS1-vaccinated animals induced significantly higher levels of IFN-γ compared to all other groups, suggesting that immune-focusing by using S1-based vaccine could not only enhance Ab response but also cell-mediated responses. The inability of pS immunogen to induce S1-specific $CD8^+$ T cells IFN-γ was consistent with the overall weaker response compared to pS1-vaccinated group. Interestingly, re-stimulation with several other peptides within the S1 subunit as previously described[32] failed to elicit any IFN-γ from all groups (Supplementary Figure 1).

Spike-based DNA immunization elicited cross-neutralizing MERS-CoV Abs against human and camel isolates. As our DNA vaccine constructs were made using coding sequence from a 2013 isolate that directly transmitted form infected camel to a human, it was important to test their cross-neutralization activity against recent isolates. To this end, antisera from immunized mice were tested against human and camel MERS-CoV isolates from 2015 and 2016. As shown in Fig. 4, sera collected from mice immunized with DNA expressing full-length S protein or S1 subunit were found to have comparable nAb titers against the human and the camel isolates. These findings clearly show that S protein is a very promising vaccine target as it induced nAbs against human and camel MERS-CoV strains isolated in 2015 (MERS-CoV Human/1390) and 2016 (MERS-CoV Camel/31 and MERS-CoV Camel/39).

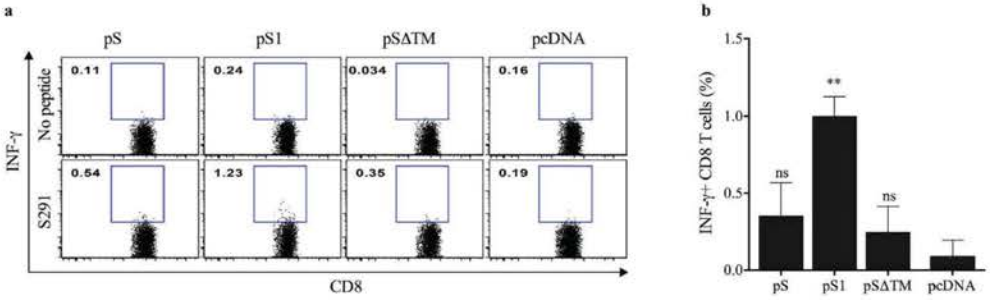

Figure 3. MERS-CoV Spike-specific memory CD8$^+$ T cell responses. Immunized BALB/c mice were sacrificed at 3 weeks after 2nd boosting and splenocytes were isolated and re-stimulated *ex vivo* with synthetic S1 peptides for IFN-γ measurement by ICS. Live CD8$^+$ T cells were stained for intracellular IFN-γ. (**a**) Flow cytometry plots are representatives from one out of two independent experiments. (**b**) Bar graph represents frequencies of IFN-γ memory CD8$^+$ T cells. Data are shown as mean ± s.d from one experiment out of two independent experiments, with n = 3 mice per treatment group in each experiment. $^{**}P < 0.01$ (one way ANOVA with Bonferroni post-test).

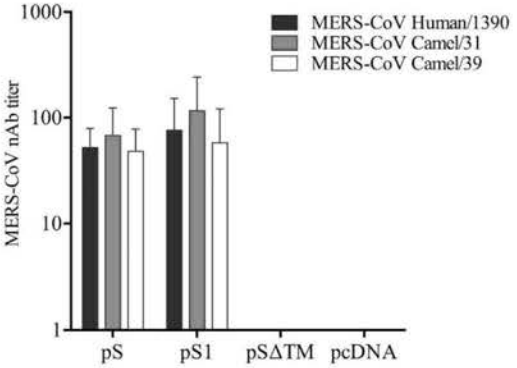

Figure 4. MERS-CoV Spike DNA vaccine induced nAbs. Neutralization titers were determined as the highest serum dilutions from each individual mouse that completely protected Vero E6 cells in at least 50% of the wells (MNT_{50}). Titers are shown as means from 5 mice per group ± s.d from one experiment out of two independent experiments.

Discussion

The rapid spread and high mortality rate of MERS-CoV infections in several countries of the Arabian Peninsula present a daunting challenge to the international community; the large zoonotic reservoir host of MERS-CoV makes it difficult to eliminate the source of transmission. While public health measures are critical to contain MERS-CoV spread and proven to be effective in limiting outbreaks, development of safe and preventive vaccine is urgently needed.

Several groups have investigated various vaccine platforms to combat MERS-CoV[29–42]. Most of these experimental vaccines were based on MERS-CoV full-length or truncated versions of the spike protein; these prototype vaccines were found to have induced high levels of nAbs and sometimes conferred protection against MERS-CoV challenge in several animal models. However, several previous SARS-CoV vaccine studies have also shown that there might be some safety concerns associated with the use of WIV[43], truncated S subunit/protein vaccines[44] or vectored vaccines expressing full-length S protein[45]. These concerns included inflammatory and immunopathological effects such as eosinophilic infiltration of the lungs as well as Ab-mediated disease enhancement (ADE) in immunized animals upon viral challenge. It is believed that induction of Th2-polarized immune response and/or non-neutralizing Abs against epitopes within the S protein (i.e. outside the neutralizing-epitope rich RBD or S1 subunit) are the reason for the observed immunopathology and disease enhancement in vaccinated animals[46–48], suggesting that use of S1 subunit over full-length S protein could be a safer option for vaccine development.

Furthermore, a recent report revealed that MERS-CoV vaccines might be associated with similar type of immunopathologies especially upon induction of Th2-skewed response or use of full-length or truncated S protein[37]. This could be a hurdle facing vaccine candidates expressing non-neutralizing epitopes such as the ones based on full-length S protein[29]. Therefore, immune focusing by using RBD or S1 subunit could represent an attractive approach for safe and effective MERS vaccine. Indeed, several versions of RBD subunit vaccine were tested[38–42] and showed very promising results even upon immunization with very low dose[51]. However, protein

subunit vaccines were found to induce skewed Th2 response. Therefore, more studies are needed to develop a safe and approved adjuvant to elicit Th1-skewed response[29,47,48].

MERS-CoV DNA vaccines can induce Th1-biased immune response even though multiple injections are usually required due to their low immunogenicity especially in large animals[29,30]. Up to date, only two studies have investigated MERS-CoV DNA vaccines by utilizing full-length S protein, which is the primary target of immune response in the host. To dissect the antigenic domains of the S protein, we examined the immunogenicity of naked DNA vaccines expressing several versions of MERS-CoV S protein in mice. We found that pS-immunized group elicited significant IgG2a and IgG2b titers (Th1-skewed response) with very subtle S1-specific $CD8^+$ IFN-γ response. On the other hand, pS1-immunization generated markedly increased levels of all IgG isotypes in a balanced Th1/Th2 response along with low but significantly elevated $CD8^+$ IFN-γ response compared to pS group. While further animal studies are required to determine whether induction of balanced Th1/Th2 or Th1-biased immune response could aid in the development of safer MERS-CoV vaccine, S1-based vaccines could be a safer option compared to the full-length S-based vaccines.

It is of note that the ELISA plates used for the measurement of binding IgG isotypes were coated with S1 recombinant protein (Fig. 2), therefore, there might be more Abs in the pS vaccinated animals targeting epitopes outside the S1 subunit (i.e. S2 subunit) that were never detected in our analysis. In addition, the observation that both pS1 and pS induced similar nAb titers (Fig. 4) suggests that full-length S protein harbors neutralizing epitopes outside the S1 region as previously reported[29]. The induction of high levels of IgG1 by pS1 vaccine and consequent balanced Th1/Th2 response could probably be explained by the secretion of S1 subunit especially that this immunogen contains the signal peptide without the cell membrane anchoring domains compared to pS vaccine. While additional studies are required to confirm this, we have previously shown that internal viral proteins such as the influenza nucleoprotein could be partially secreted and alter the immune response phenotype when fused to a secretion signal[50]. Furthermore, the weak or undetectable response in pSΔTM and pSΔCD immunized mice is noteworthy especially that Wang *et al.*, showed that MERS-CoV DNA vaccine expressing SΔTM induced limited response in mice even after electroporation[29]. Although this response could be due to misfolded protein and rapid degradation of the antigen, or low expression level of these truncated spike proteins given that expression of SΔTM gave low production yields from transfected HEK 293 as previously described[29], similar vaccines have been shown to be very effective in mice in the case of SARS-CoV[52].

The finding that immune sera from both pS and pS1 immunized mice could cross-neutralize recent human and camel field isolates is critical. Most previous studies utilized strains such as Jordan-N3 (GenBank ID: KC776174.1) and EMC/2012 (GenBank ID: JX869059.2) in live virus neutralization assay. These viruses were isolated in 2012; they may or may not be same as the currently circulating strains, given that strains used here showed 5–7 and 1–2 amino acid changes in comparison to Jordan-N3 and EMC/2012, respectively (Supplementary Figure 2). Furthermore, several other studies have used pseudovirus neutralization assay to test contemporary strains which may not replicate the actual neutralization breadth against live viruses[29,30]. It is of note that the similar levels of nAb titers in both pS and pS1 groups reported here appear to be different from the observation by others, who found significantly higher levels of nAbs induced by a DNA vaccine expressing full-length S protein compared to that expressing S1 protein[29]. However, this discrepancy in results remains to be fully understood but is likely due to the difference in experimental conditions. Specifically, Wang *et al.* utilized electroporation with DNA immunization and pseudovirus neutralization assays to determine nAbs whereas we used naked DNA vaccines and live virus neutralization assays.

Taken together, our study suggests the DNA vaccine expressing S1 subunit could represent a promising candidate vaccine against MERS-CoV while minimizing the risk of the immunopathologies associated with the use of full S protein and Th2 response. However, more studies are clearly required to enhance the immunogenicity of naked DNA vaccine and to examine the safety of this prototype vaccine.

References

1. Zaki, A. M., van Boheemen, S., Bestebroer, T. M., Osterhaus, A. D. & Fouchier, R. A. Isolation of a novel coronavirus from a man with pneumonia in Saudi Arabia. *N. Engl. J. Med.* **367,** 1814–1820, doi: 10.1056/NEJMoa1211721 (2012).
2. Bermingham, A. *et al.* Severe respiratory illness caused by a novel coronavirus, in a patient transferred to the United Kingdom from the Middle East, September 2012. *Euro. Surveill.* **17,** 20290 (2012).
3. Pebody, R. G. *et al.* The United Kingdom public health response to an imported laboratory confirmed case of a novel coronavirus in September 2012. *Euro. Surveill.* **17,** 20292 (2012).
4. Mackay, I. M. & Arden, K. E. MERS coronavirus: diagnostics, epidemiology and transmission. *Virol. J.* **12,** 222, doi: 10.1186/s12985-015-0439-5 (2015).
5. Alraddadi, B. M. *et al.* Risk Factors for Primary Middle East Respiratory Syndrome Coronavirus Illness in Humans, Saudi Arabia, 2014. *Emerg. Infect. Dis.* **22,** 49–55, doi: 10.3201/eid2201.151340 (2016).
6. Lessler, J. *et al.* Estimating the Severity and Subclinical Burden of Middle East Respiratory Syndrome Coronavirus Infection in the Kingdom of Saudi Arabia. *Am. J. Epidemiol.* **183,** 657–663, doi: 10.1093/aje/kwv452 (2016).
7. Assiri, A. *et al.* Hospital outbreak of Middle East respiratory syndrome coronavirus. *N. Engl. J. Med.* **369,** 407–416, doi: 10.1056/NEJMoa1306742 (2013).
8. Guery, B. *et al.* Clinical features and viral diagnosis of two cases of infection with Middle East Respiratory Syndrome coronavirus: a report of nosocomial transmission. *Lancet.* **381,** 2265–2272, doi: 10.1016/S0140-6736(13)60982-4 (2013).
9. Memish, Z. A., Zumla, A. I., Al-Hakeem, R. F., Al-Rabeeah, A. A. & Stephens, G. M. Family cluster of Middle East respiratory syndrome coronavirus infections. *N. Engl. J. Med.* **368,** 2487–2494, doi: 10.1056/NEJMoa1303729 (2013).
10. Park, S. H. *et al.* Outbreaks of Middle East Respiratory Syndrome in Two Hospitals Initiated by a Single Patient in Daejeon, South Korea. *Infect. Chemother.* **48,** 99–107, doi: 10.3947/ic.2016.48.2.99 (2016).
11. Hemida, M. G. *et al.* Middle East Respiratory Syndrome (MERS) coronavirus seroprevalence in domestic livestock in Saudi Arabia, 2010 to 2013. *Euro. Surveill.* **18,** 20659 (2013).
12. Alagaili, A. N. *et al.* Middle East respiratory syndrome coronavirus infection in dromedary camels in Saudi Arabia. *MBio.* **5,** e00884–14, doi: 10.1128/mBio.00884-14 (2014).
13. Azhar, E. I. *et al.* Evidence for camel-to-human transmission of MERS coronavirus. *N. Engl. J. Med.* **370,** 2499–2505, doi: 10.1056/NEJMoa1401505 (2014).

14. Müller, M. A. *et al.* MERS coronavirus neutralizing antibodies in camels, Eastern Africa, 1983-1997. *Emerg. Infect. Dis.* **20,** 2093–2095, doi: 10.3201/eid2012.141026 (2014).
15. Corman, V. M. *et al.* Antibodies against MERS coronavirus in dromedary camels, Kenya, 1992-2013. *Emerg. Infect. Dis.* **20,** 1319–1322, doi: 10.3201/eid2008.140596 (2014).
16. Falzarano, D. *et al.* Treatment with interferon-α2b and ribavirin improves outcome in MERS-CoV-infected rhesus macaques. *Nat. Med.* **19,** 1313–1317, doi: 10.1038/nm.3362 (2013).
17. Hart, B. J. *et al.* Interferon-β and mycophenolic acid are potent inhibitors of Middle East respiratory syndrome coronavirus in cell-based assays. *J. Gen. Virol.* **95,** 571–577, doi: 10.1099/vir.0.061911-0 (2014).
18. Omrani, A. S. *et al.* Ribavirin and interferon alfa-2a for severe Middle East respiratory syndrome coronavirus infection: a retrospective cohort study. *Lancet. Infect. Dis.* **14,** 1090–1095, doi: 10.1016/S1473-3099(14)70920-X (2014).
19. de Wilde, A. H. *et al.* MERS-coronavirus replication induces severe *in vitro* cytopathology and is strongly inhibited by cyclosporin A or interferon-α treatment. *J. Gen. Virol.* **94,** 1749–1760, doi: 10.1099/vir.0.052910-0 (2013).
20. Dyall, J. *et al.* Repurposing of clinically developed drugs for treatment of Middle East respiratory syndrome coronavirus infection. *Antimicrob. Agents. Chemother.* **58,** 4885–4893, doi: 10.1128/AAC.03036-14 (2014).
21. Ying, T. *et al.* Exceptionally potent neutralization of Middle East respiratory syndrome coronavirus by human monoclonal antibodies. *J. Virol.* **88,** 7796–7805, doi: 10.1128/JVI.00912-14 (2014).
22. Jiang, L. *et al.* Potent neutralization of MERS-CoV by human neutralizing monoclonal antibodies to the viral spike glycoprotein. *Sci. Transl. Med.* **6,** 234ra59, doi: 10.1126/scitranslmed.3008140 (2014).
23. Du, L. *et al.* A conformation-dependent neutralizing monoclonal antibody specifically targeting receptor-binding domain in Middle East respiratory syndrome coronavirus spike protein. *J. Virol.* **88,** 7045–7053, doi: 10.1128/JVI.00433-14 (2014).
24. Tang, X. C. *et al.* Identification of human neutralizing antibodies against MERS-CoV and their role in virus adaptive evolution. *Proc. Natl. Acad. Sci. USA* **111,** E2018–E2026, doi: 10.1073/pnas.1402074111 (2014).
25. Corti, D. *et al.* Prophylactic and postexposure efficacy of a potent human monoclonal antibody against MERS coronavirus. *Proc. Natl. Acad. Sci. USA* **112,** 10473–10478, doi: 10.1073/pnas.1510199112 (2015).
26. Pascal, K. E. *et al.* Pre- and postexposure efficacy of fully human antibodies against Spike protein in a novel humanized mouse model of MERS-CoV infection. *Proc. Natl. Acad. Sci. USA* **112,** 8738–8743, doi: 10.1073/pnas.1510830112 (2015).
27. Agrawal, A. S. *et al.* Passive Transfer of A Germline-like Neutralizing Human Monoclonal Antibody Protects Transgenic Mice Against Lethal Middle East Respiratory Syndrome Coronavirus Infection. *Sci. Rep.* **6,** 31629, doi: 10.1038/srep31629 (2016).
28. Lu, G. *et al.* Molecular basis of binding between novel human coronavirus MERS-CoV and its receptor CD26. *Nature.* **500,** 227–2231, doi: 10.1038/nature12328 (2013).
29. Wang, L. *et al.* Evaluation of candidate vaccine approaches for MERS-CoV. *Nat. Commun.* **6,** 7712, doi: 10.1038/ncomms8712 (2015).
30. Muthumani, K. *et al.* A synthetic consensus anti-spike protein DNA vaccine induces protective immunity against Middle East respiratory syndrome coronavirus in nonhuman primates. *Sci. Transl. Med.* **7,** 301ra132, doi: 10.1126/scitranslmed.aac7462 (2015).
31. Kim, E. *et al.* Immunogenicity of an adenoviral-based Middle East Respiratory Syndrome coronavirus vaccine in BALB/c mice. *Vaccine.* **32,** 5975–5982, doi: 10.1016/j.vaccine.2014.08.058 (2014).
32. Zhao, J. *et al.* Rapid generation of a mouse model for Middle East respiratory syndrome. *Proc. Natl. Acad. Sci. USA* **111,** 4970–4975, doi: 10.1073/pnas.1323279111 (2014).
33. Haagmans, B. L. *et al.* An orthopoxvirus-based vaccine reduces virus excretion after MERS-CoV infection in dromedary camels. *Science.* **351,** 77–81, doi: 10.1126/science.aad1283 (2016).
34. Guo, X. *et al.* Systemic and mucosal immunity in mice elicited by a single immunization with human adenovirus type 5 or 41 vector-based vaccines carrying the spike protein of Middle East respiratory syndrome coronavirus. *Immunology.* **145,** 476–484, doi: 10.1111/imm.12462 (2015).
35. Song, F. *et al.* Middle East respiratory syndrome coronavirus spike protein delivered by modified vaccinia virus Ankara efficiently induces virus-neutralizing antibodies. *J. Virol.* **87,** 11950–11954, doi: 10.1128/JVI.01672-13 (2013).
36. Coleman, C. M. *et al.* Purified coronavirus spike protein nanoparticles induce coronavirus neutralizing antibodies in mice. *Vaccine.* **32,** 3169–3174, doi: 10.1016/j.vaccine.2014.04.016 (2014).
37. Agrawal, A. S. *et al.* Immunization with inactivated Middle East Respiratory Syndrome coronavirus vaccine leads to lung immunopathology on challenge with live virus. *Hum. Vaccin. Immunother.* **7,** 1–6, doi: 10.1080/21645515.2016.1177688 (2016).
38. Du, L. *et al.* A truncated receptor-binding domain of MERS-CoV spike protein potently inhibits MERS-CoV infection and induces strong neutralizing antibody responses: implication for developing therapeutics and vaccines. *PLoS One* **8,** e81587, doi: 10.1371/journal.pone.0081587 (2013).
39. Yang, Y. *et al.* The amino acids 736–761 of the MERS-CoV spike protein induce neutralizing antibodies: implications for the development of vaccines and antiviral agents. *Viral. Immunol.* **27,** 543–550, doi: 10.1089/vim.2014.0080 (2014).
40. Mou, H. *et al.* The receptor binding domain of the new Middle East respiratory syndrome coronavirus maps to a 231-residue region in the spike protein that efficiently elicits neutralizing antibodies. *J. Virol.* **87,** 9379–9383, doi: 10.1128/JVI.01277-13 (2013).
41. Ma, C. *et al.* Searching for an ideal vaccine candidate among different MERS coronavirus receptor-binding fragments—the importance of immunofocusing in subunit vaccine design. *Vaccine.* **32,** 6170–6176, doi: 10.1016/j.vaccine.2014.08.086 (2014).
42. Lan, J. *et al.* Tailoring subunit vaccine immunity with adjuvant combinations and delivery routes using the Middle East respiratory coronavirus (MERS-CoV) receptor-binding domain as an antigen. *PLoS One* **9,** e112602, doi: 10.1371/journal.pone.0112602 (2014).
43. Deming, D. *et al.* Vaccine efficacy in senescent mice challenged with recombinant SARS-CoV bearing epidemic and zoonotic spike variants. *PLoS. Med.* **3,** e525, doi: 10.1371/journal.pmed.0030525 (2006).
44. Honda-Okubo, Y. *et al.* Severe acute respiratory syndrome-associated coronavirus vaccines formulated with delta inulin adjuvants provide enhanced protection while ameliorating lung eosinophilic immunopathology. *J. Virol.* **89,** 2995–3007, doi: 10.1128/JVI.02980-14 (2015).
45. Iwata-Yoshikawa, N. *et al.* Effects of Toll-like receptor stimulation on eosinophilic infiltration in lungs of BALB/c mice immunized with UV-inactivated severe acute respiratory syndrome-related coronavirus vaccine. *J. Virol.* **88,** 8597–8614, doi: 10.1128/JVI.00983-14 (2014).
46. Weingartl, H. *et al.* Immunization with modified vaccinia virus Ankara-based recombinant vaccine against severe acute respiratory syndrome is associated with enhanced hepatitis in ferrets. *J. Virol.* **78,** 12672–12676 (2004).
47. Tseng, C. T. *et al.* Immunization with SARS coronavirus vaccines leads to pulmonary immunopathology on challenge with the SARS virus. *PLoS. One.* **7,** e35421, doi: 10.1371/journal.pone.0035421 (2012).
48. Jaume, M. *et al.* SARS CoV subunit vaccine: antibody-mediated neutralisation and enhancement. *Hong. Kong. Med. J.* **18,** Suppl 2 31–6 (2012).
49. Coleman, C. M. & Frieman, M. B. Growth and Quantification of MERS-CoV Infection. *Curr. Protoc. Microbiol.* **37,** 15E.2.1–9, doi: 10.1002/9780471729259.mc15e02s37 (2015).
50. Hashem, A. M. *et al.* CD40 ligand preferentially modulates immune response and enhances protection against influenza virus. *J. Immunol.* **193,** 722–734, doi: 10.4049/jimmunol.1300093 (2014).
51. Tang, J. *et al.* Optimization of antigen dose for a receptor-binding domain-based subunit vaccine against MERS coronavirus. *Hum. Vaccin. Immunother.* **11,** 1244–1250, doi: 10.1080/21645515.2015.1021527 (2015).
52. Yang, Z. Y. *et al.* A DNA vaccine induces SARS coronavirus neutralization and protective immunity in mice. *Nature.* **428,** 561–564 (2004).

Acknowledgements

This project was funded by a research endowment fund from King Abdulaziz University Scientific Endowment (WAQF), Jeddah, Saudi Arabia under grant No. (WAQF-1435–7B) to AMH.

Author Contributions

A.T.A., M.K.A., X.L. and A.M.H. designed the study; S.S.A., A.T.A., L.A.S., A.A., M.A.S., R.Y.A. and A.M.H. conducted the experiments; A.M.H. analyzed data and prepared the figures; A.M.H., X.L. and E.I.A. wrote the manuscript. All authors read and approved the final manuscript.

Additional Information

Supplementary information accompanies this paper at http://www.nature.com/srep

Competing Interests: The authors declare no competing financial interests.

How to cite this article: Al-amri, S. S. *et al.* Immunogenicity of Candidate MERS-CoV DNA Vaccines Based on the Spike Protein. *Sci. Rep.* **7**, 44875; doi: 10.1038/srep44875 (2017).

Publisher's note: Springer Nature remains neutral with regard to jurisdictional claims in published maps and institutional affiliations.

Chapter 6

Imaging Luciferase-Expressing Viruses

Michael A. Barry, Shannon May, and Eric A. Weaver

Abstract

Optical imaging of luciferage gene expression has become a powerful tool to track cells and viruses in vivo in small animal models. Luciferase imaging has been used to study the location of infection by replication-defective and replication-competent viruses and to track changes in the distribution of viruses in mouse models. This approach has also been used in oncolytic studies as a noninvasive means to monitor the growth and killing of tumor cells modified with luciferase genes. In this chapter, we describe the techniques used for luciferase imaging as have been applied to track replication-defective and replication-competent adenoviruses in mouse and hamster models of oncolysis and virus pharmacology. Although these methods are simple, the process of obtaining accurate luciferase imaging data has many caveats that are discussed.

Key words: Luciferase, In vivo imaging, Luminescence, Luciferin, Adenovirus

1. Introduction

The technologies available to the basic scientist to track and localize viruses and tumor cells have historically been quite primitive. In most cases, virus and cell trafficking has been assessed by the use of terminal assays in which the animal must be sacrificed and the cells or viruses are tracked after the animal is "taken apart" either at the organ level or in tissue sections. These "grind and find" assays are quite laborious requiring that one actually sections the whole animal to be certain of the tissue localization of the virus to ensure that all sites are observed and unexpected localization sites are not missed. Furthermore, these terminal assays obviate the ability to perform kinetic studies in one animal over many time points.

Given these difficulties, noninvasive and nonterminal virus and cancer cell tracking was needed. One approach that partially satisfies

David H. Kirn et al. (eds.), *Oncolytic Viruses: Methods and Protocols*, Methods in Molecular Biology, vol. 797,
DOI 10.1007/978-1-61779-340-0_6,

this need is to "arm" viruses or cancer cells with reporter genes that can be detected by imaging. Reporter genes encode proteins that are easily detected in cells and in intact animals with sensitive imaging systems. The most used reporter genes include beta-galactosidase, luciferases, green fluorescent protein (GFP) and its varied color derivatives, and alkaline phosphatase. Of these, luciferase and fluorescent proteins can be used to varying degrees for optical imaging at visible wavelengths of light in small animals. One can also use reporter genes, such as thymidine kinase or the sodium iodide symporter, for high-energy PET and SPECT imaging in small animals, large animals, and in humans.

For most researchers, optical imaging is simpler and more easily obtainable in the laboratory setting than radioactive imaging for PET or SPECT. Since PET and SPECT imaging are the subject of another chapter, they are not discussed further here. One can in some cases directly image reporters, like GFP and other fluorescent proteins in living animals. In practice, high background fluorescence and scatter in the green, red, and far red wavelengths make the "noise" of imaging too high to easily detect most current fluorescent proteins in vivo (1, 2) Newer, far red fluorescent proteins to date are still difficult to image in mice (M.A. Barry et al., unpublished observations), but future near-infrared fluorophores may circumvent this difficulty.

Given these issues, luciferase imaging is arguably the best choice for noninvasive, inexpensive, and nonradioactive imaging in small animals. Given this, we have "armed" replication-defective and replication-competent adenovirus serotype 5 (Ad5) viruses with luciferase and GFP–luciferase reporter genes to track (1) sites of infection, (2) persistence of infection, (3) spread of virus, and (4) elimination of virus due to immune responses (1, 3–11) In addition, one can monitor immune responses against these proteins in immunocompetent mice (i.e., H-2^d-restricted T cells in BALB/c mice vs. GFP antibodies against luciferase (7, 8)). These virus persistence–immune response studies of course cannot be performed in immunodeficient models using human tumor xenografts.

With these applications in mind, below we provide the simple protocol for imaging codon-optimized firefly luciferase with its substrate luciferin after Ad5 infection. Similar approaches can be applied for other luciferases (e.g., Gaussia luciferase, Renilla luciferase). These other luciferases use coelenterazine rather than luciferin as a substrate, so injections of substrate and timing of imaging are different. In our hands, the coelenterazine substrate is less soluble and does not distribute as well as luciferin, so can be more difficult to use.

2. Materials

1. Dulbecco's phosphate buffered saline (DPBS) (Gibco/BRL).
2. Luciferin (Molecular Imaging Products Company) diluted to 20 mg/ml in DPBS, filter sterilize using a 0.22-μm filter. Aliquot and store at −80°C. Protect from light exposure and avoid repeated freeze–thaws.
3. Ketamine (Fort Dodge), 100 mg/ml.
4. Xylazine (Vet Tek) diluted to 20 mg/ml using sterile ddH_2O.
5. Isoflurane (Cardinal Health).

3. Methods

3.1. Animal Preparation for Luciferase Imaging

Appropriate animal protocol and biosafety approvals must be obtained before performing these experiments. Investigators should apply appropriate biosafety containment in instruments and rooms whenever imaging is performed. The following is an example of luciferase imaging after intramuscular (i.m.) injection of a replication-defective Ad5 vector (Ad-Luc).

1. Dilute Ad-Luc in DPBS to 2e11 virus particles (vp)/ml.
2. Using a 0.3-ml 29-G ½″ syringe, inject 0.025 ml of virus into each quadriceps of the mouse.
3. After 24 h, place the mouse in an isoflurane induction chamber (3–5%) (see Note 2).
4. Once the animal is under sedation, inject 0.2 ml of luciferin (20 mg/ml in sterile DPBS) intraperitoneally (i.p.). Inject the luciferin substrate 5–10 min prior to image capture.
5. Working quickly, transfer the mouse to the imaging system and maintain sedation with 1–3% isoflurane. We have found that mice can be maintained for extended lengths of time without risk to the animals at these isoflurane levels.
6. Image the mouse dorsally using a 10-min exposure with 4×4 binning or 1×1 binning depending on signal intensity.

3.2. Image Capture Using Lumazone Imager

Below is provided the steps for a Lumazone (Mag Biosystems Lumazone, in vivo imaging system; software version 2.0) (see Note 3).

1. Make sure that cap is on the white light source in the imaging cabinet.
2. Open Lumazone software. The "Lumazone Analyzer" box should display.

3. Select "Configure":
   (a) Choose "Luciferin" from Experiment Type drop down. (*This only affects how the image is titled after multichannel acquire is chosen and imaging is complete*).
   (b) Select "Chemiluminescence" box.
   (c) Select "Brightfield" box.
   (d) Select "OK."
4. Select focus/exposure:
   (a) Select on "Chemi" button (for chemiluminescence):
      - Make sure that "Adjust Exp for Binning" box is checked.
      - Choose binning setting.
      - Set "Exp Pvw" time (should show in MM:ss:mmm).
      - If "Adjust Exp for Binning" box is not checked, you also need to set the "Exp Acq" time.
   (b) Select "BF" (for brightfield).
   (c) Select "Live" to check and/or modify the focus of the image.
   (d) Select "Close."
   (e) Select "Multichannel Acquire" in the "Lumazone Analyzer" box to begin taking the image.
   (f) Once the image has been captured, select on the "Best Fit Display Range or Contrast Equalization" button to bring the picture into focus – complete for each image.
   (g) Two images display. One image is the BF/white light image. One image is the chemiluminescence image.
   (h) Save the images.

3.3. Image Display

The bright light and chemiluminescent images are captured as gray-scale images (Fig. 1) In order to create an image that is more esthetically pleasing and easier to interpret by eye, the images can be pseudocolored and overlaid onto a white light image of the animals.

1. Load the experiment. This opens up an image of the light emitted in vivo and a white light image of the animals (Fig. 1a)
2. Select the Calibrated LUT function on the analyze toolbar and select the image you want to calibrate. When prompted, select "No" in order to create a new image for calibration. This brings up an entirely new image window and does not alter the original image (Fig. 1b)

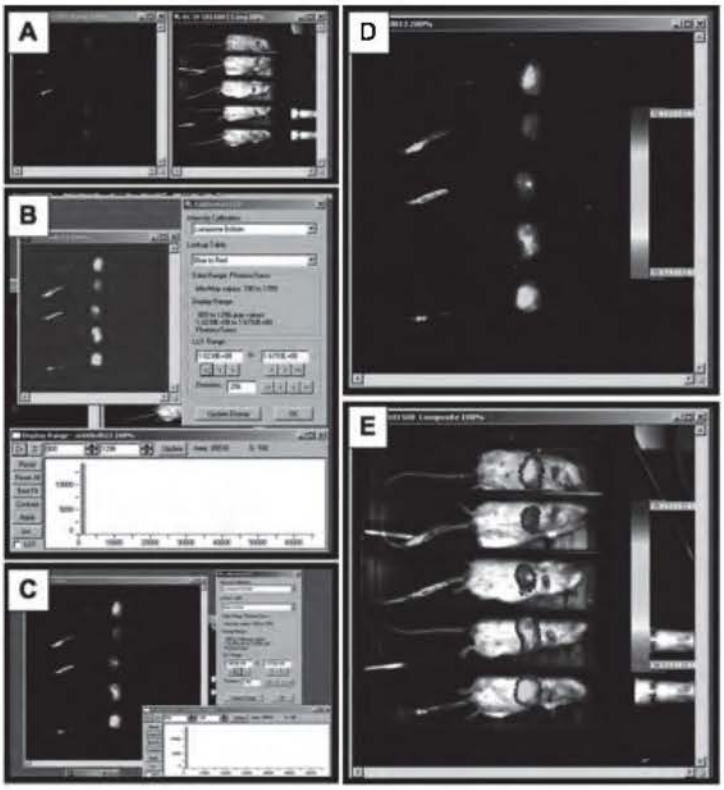

Fig. 1. Operational screens for bright light and chemiluminescent images.

3. Two windows open when the calibrated image is created. Select Best Fit in the Display Range Window and use the LUT range to adjust the image and remove low-level background signal (Fig. 1c)
4. Select OK on the Calibrated LUT window and Yes to placing a calibration bar on the image.
5. Modify the calibration bar as needed and place in an area of the image that does not show signal (Fig. 1d)
6. Make changes to the font and overall appearance of the calibration bar and select OK. This creates a pseudocolored image with a calibration bar.
7. In order to show the position of the signal relative to the animal, an overlaid image can be created.

8. Select Overlay Images and Yes and the image is calibrated. Select the calibrated image and then the white light image of the animals and an overlaid image is created (Fig. 1e)

3.4. Image Data Analysis

After capturing an image, data analysis need to be performed. There are several ways to capture and analyze the data. The primary issue of concern is light contamination, either from outside the imaging chambers from other animals or from background signal inherent to all electronics. The following is an example of image analysis performed using the Lumazone Imaging System.

1. Capture an image as previously described.
2. Load the experiment to be analyzed.
3. The first thing that needs to be done is to subtract the background signal. This can be done using gray values without intensity calibration or using photons as determined by intensity calibration.
4. Define an area of interest (AOI) in the image outside of the area, where the mice are imaged Edit > New AOI (Fig. 2a)
5. In order to define background levels, the AOI background signal levels need to be determined. Open up count/size: Measure > Count/Size. Select the range of intensity to measure. For this procedure, the range should be the full scope of the range. For the Lumazone, this range is 0 to 65,535. Select the measurements to be determined using the Count/Size function: Measure > Count/Size > Measure > Select Measurements. In this case, select the Den./Inten. (mean). Select count on the Count/Size function. To view the value, either click on the AOI or select Measure > Count/Size > Measure > View > Object Attributes. In this example, the Den./Inten. (mean) = 811.51459.
6. Once the background signal levels have been determined, they can be subtracted from the image. Open up image operations: Process > Operations. Check the following: Operation = Subtract, second operand = Number, Put result in = New Image. Enter the background signal (811.51459), deselect the AOI, and select apply (Fig. 2b) Select the Best Fit icon to view the best display range and contrast equalization.
7. Create an AOI over the area of the image to be quantitated. In the Count/Size function, select the measurements to acquire. In general, the Den./Inten. (sum) values are the most representative of the signal being measured. However, in some cases, the Den./Inten. (mean) may be more informative.
8. Depending on the values desired, gray values or converted photons/second can be reported. Select (none) in the intensity calibration if gray values are desired or select the calibration curve that was established when the unit was installed. In this

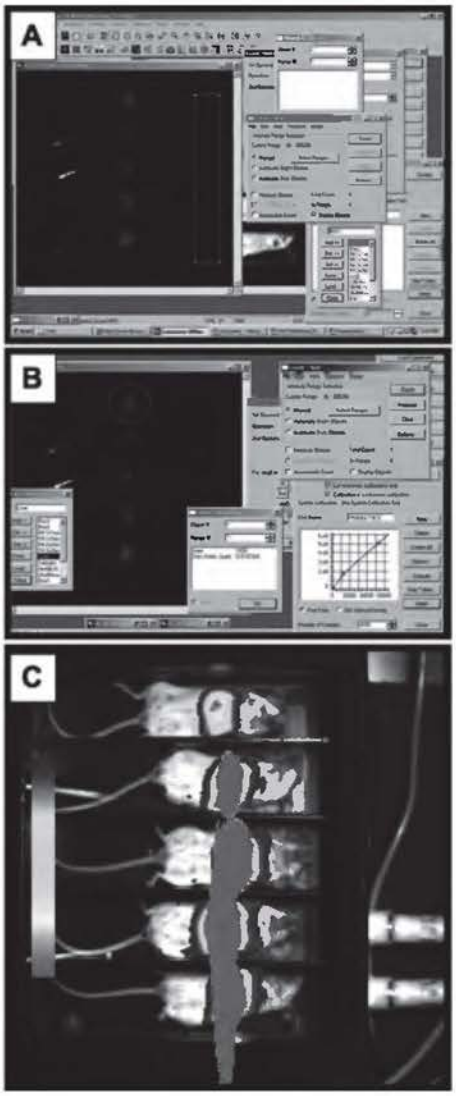

Fig. 2. Image data analysis.

case, "Lumazone Bottom" gives values reported as photons/second by converting gray values to photons using the calibration curve. Select Apply.

9. In the Count/Size function, select Count and Measure. Double click on the AOI to view the object attributes. In this example, there are 9.01972e9 photons/second emitted from the AOI (Fig. 2b) (see Note 1).

4. Notes

1. Although the basic procedure of image capture during luciferase imaging is relatively simple, luciferase imaging is a dynamic procedure. As with all catalytic reactions, the signal is constantly changing. Luciferin, for example, is being degraded by the enzyme luciferase. Therefore, the procedures should be performed in a consistent and timely manner. Also, another issue of concern is how long of an exposure is needed. This changes from experiment to experiment and is dependent upon many factors, including how much virus was administered, the route, and even the position of the animal. Overexposure as shown in Fig. 2c can lead to a loss of valuable data. In this example, the exposure time should be reduced. Another issue is that light can be reflected off other objects, but still represents signal from the animal (Fig. 2c) A chamber that has dividers to separate the animals during luciferase imaging helps eliminate this problem.
2. Alternative anesthesia (Subheading 3 1) If isoflurane is not available, the mice can be anesthetized with ketamine and xylazine. Dilute the ketamine (27.77 mg/ml) and xylazine (1.11 mg/ml) in sterile dH_2O and inject 0.1 ml i.p. into a 20- to 25-g mouse using a 1.0-ml 26-G 5/8″ syringe. The mouse is sedated for approximately 30 min.
3. Subheading 3 2: Each imaging system requires different steps in order to obtain both the chemiluminescent luciferase image as well as the bright-field white image of the animal itself.

Acknowledgments

We would like to thank all past and present Barry laboratory members for their experiences in imaging that have been distilled here. This work has been supported by the Muscular Dystrophy Association, the Ralph C. Wilson Foundation, the Propionic Acidemia Foundation, R01 AI06709, R01 AI065304, R01 CA136945-01A2, and by the NIH P50 CA91956 Prostate Cancer SPORE grant at the Mayo Clinic.

References

1. Blum, J. S., J. S. Temenoff, H. Park, J. A. Jansen, A. G. Mikos, and M. A. Barry. 2004. Development and characterization of enhanced green fluorescent protein and luciferase expressing cell line for non-destructive evaluation of tissue engineering constructs. *Biomaterials* 25:5809–5819.
2. Adams, K. E., S. Ke, S. Kwon, F. Liang, Z. Fan, Y. Lu, K. Hirschi, M. E. Mawad, M. A. Barry, and E. Sevick-Muraca. 2007. Comparison of

visible and near-infrared wavelength excitable fluorescent dyes for molecular imaging of cancer. *J Biomed Optics* 12:024017-024011-024019.

3. Mok, H., D. J. Palmer, P. Ng, and M. A. Barry. 2005. Evaluation of polyethylene glycol modification of first-generation and helper-dependent adenoviral vectors to reduce innate immune responses. *Mol Ther* 11:66–79.
4. Hofherr, S. E., S. Mok, F. C. Gushiken, J. A. Lopez, and M. A. Barry. 2007. Polyethylene Glycol Modification of Adenovirus Reduces Platelet Activation, Endothelial Cell Activation, and Thrombocytopenia. *Human Gene Therapy* 18:837–848.
5. Shashkova, E. V., K. Doronin, J. S. Senac, and M. A. Barry. 2008. Macrophage depletion combined with anticoagulant therapy increases therapeutic window of systemic treatment with oncolytic adenovirus. *Cancer research* 68:5896–5904.
6. Hofherr, S. E., E. V. Shashkova, E. A. Weaver, R. Khare, and M. A. Barry. 2008. Modification of adenoviral vectors with polyethylene glycol modulates in vivo tissue tropism and gene expression. *Mol Ther* 16:1276–1282.
7. Weaver, E. A., and M. A. Barry. 2008. Effects of Shielding Adenoviral Vectors with Polyethylene Glycol (PEG) on Vector-specific and Vaccine-mediated Immune Responses. *Hum Gene Ther* 19:1369–1382.
8. Weaver, E. A., P. N. Nehete, S. S. Buchl, J. S. Senac, D. Palmer, P. Ng, K. J. Sastry, and M. A. Barry. 2009. Comparison of replication-competent, first generation, and helper-dependent adenoviral vaccines. *PLoS ONE* 4:e5059.
9. Shashkova, E. V., S. M. May, K. Doronin, and M. A. Barry. 2009. Expanded Anticancer Therapeutic Window of Hexon-modified Oncolytic Adenovirus. *Mol Ther* Online Sept 15.
10. Doronin, K., E. V. Shashkova, S. M. May, S. E. Hofherr, and M. A. Barry. 2009. Chemical modification with high molecular weight polyethylene glycol reduces transduction of hepatocytes and increases efficacy of intravenously delivered oncolytic adenovirus. *Hum Gene Ther* 20:975–988.
11. Chen, C. Y., S. May, and M. A. Barry. 2010. Targeting Adenoviruses with Factor X-Single Chain Antibody Fusion Proteins. *Hum Gene Ther* 21(6):739–749.

Cite as: A. Baum *et al.*, *Science* 10.1126/science.abd0831 (2020).

Antibody cocktail to SARS-CoV-2 spike protein prevents rapid mutational escape seen with individual antibodies

Alina Baum, Benjamin O. Fulton, Elzbieta Wloga, Richard Copin, Kristen E. Pascal, Vincenzo Russo, Stephanie Giordano, Kathryn Lanza, Nicole Negron, Min Ni, Yi Wei, Gurinder S. Atwal, Andrew J. Murphy, Neil Stahl, George D. Yancopoulos, Christos A. Kyratsous*

Regeneron Pharmaceuticals Inc., Tarrytown, NY 10591, USA.

*Corresponding author. Email: christos.kyratsous@regeneron.com

Antibodies targeting the spike protein of SARS-CoV-2 present a promising approach to combat the COVID19 pandemic; however, concerns remain that mutations can yield antibody resistance. We investigate the development of resistance against four antibodies to the spike protein that potently neutralize SARS-CoV-2, individually as well as when combined into cocktails. These antibodies remain effective against spike variants that have arisen in the human population. However, novel spike mutants rapidly appeared following in vitro passaging in the presence of individual antibodies, resulting in loss of neutralization; such escape also occurred with combinations of antibodies binding diverse but overlapping regions of the spike protein. Importantly, escape mutants were not generated following treatment with a non-competing antibody cocktail.

A promising approach to combat the COVID19 pandemic involves development of antiviral antibodies targeting the spike protein of SARS-CoV-2. The spike protein is a key mediator of viral infectivity required for attachment and entry into target cells by binding the ACE2 receptor (*1*, *2*). A significant concern for any antiviral therapeutic is the potential for acquiring drug resistance due to the rapid mutation of viral pathogens. Such resistance becomes more obvious when selective pressure is applied in the setting of drug treatment. For example, when HIV drugs were initially used individually, such drug-selected mutations resulted in widespread resistance. The subsequent success of combination therapy for HIV demonstrated that requiring the virus to simultaneously mutate at multiple genetic positions may be the most effective way to avoid drug resistance.

We have recently described parallel efforts – utilizing genetically-humanized mice and B cells from convalescent humans – to generate a very large collection of highly-potent fully human neutralizing antibodies targeting the RBD of the spike protein of SARS-CoV-2 (*3*). The prospective goal of generating this very large collection was to select pairs of highly potent individual antibodies that could simultaneously bind the RBD spike, and thus might be ideal partners for a therapeutic antibody cocktail that could not only be an effective treatment, but might also protect against antibody resistance due to virus escape mutants that could arise in response to selective pressure from single antibody treatments.

To assess the efficacy of our recently described antiviral antibodies against the breadth of spike RBD variants represented in publicly available SARS-CoV-2 sequences identified through the end of March 2020 (representing over 7000 unique genomes), we used the VSV pseudoparticle system expressing the SARS-CoV-2 spike variants. Our top eight neutralizing antibodies maintained their potency against all tested variants (Table 1), demonstrating broad coverage against circulating SARS-CoV-2.

Next, escape mutants were selected under pressure of single antibodies, as well as of antibody combinations, by using a replicating VSV-SARS-CoV-2-S virus (Fig. 1A). We rapidly identified multiple independent escape mutants for each of the four individual antibodies within the first passage (Fig. 1, B and C, and Fig. 2). Some of these mutants became readily fixed in the population by the second passage, representing 100% of sequencing reads, and are resistant to antibody concentrations of up to 50ug/ml (~10,000-100,000 greater concentration than IC50 against parental virus). Sequencing of escape mutants (Fig. 2) revealed that single amino acid changes can ablate binding even to antibodies that were selected for breadth against all known RBD variants (Table 1), and that neutralize parental virus at low pM IC50 (*3*).

Analysis of 22,872 publicly available unique genome sequences (through the end of May 2020) demonstrated the presence of polymorphisms analogous to two of the escape amino acid residues identified in our study, albeit at an ex-

tremely low frequency of one each. Thus, although natural variants resistant to individual antiviral antibodies were not widely observed in nature, these rare escape variants could easily be selected and amplified under the pressure of ongoing antibody treatment. Although these studies were conducted with a surrogate virus in vitro, one would expect that similar escape mutations may occur with SARS-CoV-2 virus in vivo under the selective pressure of single antibody treatment. While, the differential propensity of VSV and SARS-CoV-2 viruses to acquire mutations may impact the speed at which these escape mutants may arise, the likelihood of eventual escape remains high.

Next, we evaluated escape following treatment with our previously described antibody cocktail (REGN10987+REGN10933), rationally designed to avoid escape through inclusion of two antibodies that bind distinct and non-overlapping regions of the RBD, and which can thus simultaneously bind and block RBD function. Attempts to grow VSV-SARS-CoV-2-S virus in the presence of this antibody cocktail did not result in the outgrowth of escape mutants (Table 2, Fig. 1, B and C, and Fig. 2). Thus, this selected cocktail did not rapidly select for mutants, presumably because escape would require the unlikely occurrence of simultaneous viral mutation at two distinct genetic sites, so as to ablate binding and neutralization by both antibodies in the cocktail.

In addition to the above cocktail, we also evaluated escape following treatment with additional combinations (REGN10989+REGN10934 and REGN10989+REGN10987), this time consisting of antibodies that completely or partially compete for binding to the RBD – i.e., two antibodies that bind to overlapping regions of the RBD. Under selective pressure of these combination treatments, there was rapid generation of escape mutants resistant to one combination, but not the other (Table 2, Fig. 1, B and C, and Fig. 2). For an antibody cocktail in which the components demonstrate complete competition (REGN10989+REGN10934), a single amino acid substitution was sufficient to ablate neutralization of the cocktail, demonstrating that both of these antibodies require binding to the E484 residue in order to neutralize SARS-CoV-2. Interestingly, such rapid escape did not occur for a different antibody cocktail in which the components exhibited only partial competition (REGN10989+REGN10987) (*3*); REGN10987 can weakly bind to RBD when REGN10989 is pre-bound. Thus even combination of antibodies that are not selected to simultaneously bind may occasionally resist escape because their epitopes only partially overlap, or because residues that would result in escape are not easily tolerated by the virus, and therefore not readily selected for.

To functionally confirm that the spike protein mutations detected by sequencing are responsible for the loss of SARS-CoV-2 neutralization by the antibodies, we generated VSV-SARS-CoV-2 spike pseudoparticles expressing the individual identified spike mutations. These pseudoparticles were used in neutralization assays with single and combination antibody treatments, and IC50 values were calculated (Table 2 and fig. S1). As expected, pseudoparticles with amino acid mutations that were selected by passaging the virus in the presence of the four single antibodies, as well as of the REGN10989+REGN10934 competing antibody cocktail, were sufficient to completely eliminate or greatly decrease the ability of these treatments to neutralize in these assays. Single escape mutants that were detected at low frequency in early passages in virus populations generated by two antibodies (e.g., K444Q by both REGN10934 and REGN10987), but were fixed in the later passage by only one of these antibodies (REGN10987), was able to ablate neutralization by both treatments. This suggests that antibodies can drive virus evolution and escape in different directions. However, if two antibodies have partially overlapping binding epitopes, then escape mutants fixed in the virus population by one can result in the loss of activity of the other – highlighting the risks of widespread use of single antibody treatments. Importantly, the REN10987+REGN10933 antibody cocktail – that consists of two antibodies that can simultaneously bind to two independent epitopes on the RBD – retains its ability to neutralize all identified mutants, even the ones that were selected for by single treatment with one of its components.

In our sequencing of passaged virus pools, we also identified multiple mutations outside of the RBD domain, most of which were present at various abundances within control samples, including the original inoculum and virus only passages (Fig. 2). The most abundant of these mutations (H655Y and R682Q) are near the S1'/S2' cleavage site within the spike protein and contain residues within the multibasic furin-like cleavage site. Mutations and deletions in this region have been identified with tissue culture passaged VSV-SARS-CoV-2-S as well as SARS-CoV-2 viruses and likely represent tissue culture adaptations (*4*, *5*).

As RNA viruses are well known to accumulate mutations over time, a significant concern for any antiviral therapeutic is the potential for selection of treatment-induced escape mutants. A common strategy to safeguard against escape to antibody therapeutics involves selection of antibodies binding to conserved epitopes, however this strategy may not suffice. While some informed analysis can be made regarding epitope conservation based on sequence and structural analysis (*6*), the possibility of escape still exists under strong selection pressure. Indeed, escape studies performed with anti-influenza HA stem binding antibodies have shown that escape mutants can arise despite high conservation of the stem epitope between diverse influenza sub-

types, with some escape mutations arising outside of the antibody epitope region (*7*, *8*). Antibodies that demonstrate broad neutralization across multiple species of coronaviruses, and thus may be targeting more conserved residues, have not been shown to be immune to escape upon selective pressure. In addition, their neutralization potency is orders of magnitude lower than that of the most potent neutralizing antibodies specific for SARS-CoV-2 (*6*, *9*–*11*). Neutralization is thought to be the key mechanism of action of anti-coronavirus spike antibodies and has previously been shown to correlate with efficacy in animal models (*12*), and may therefore prove to be the most important driver of initial clinical efficacy. However, as demonstrated with our single antibody escape studies, even highly potent neutralization does not protect against the rapid generation of viral escape mutants, and escape remains a major concern with individual antibody approaches.

The data described herein strongly support the notion that cocktail therapy may provide a powerful way to minimize mutational escape by SARS-CoV-2; in particular, our studies point to the potential value of antibody cocktails in which two antibodies were chosen so as to bind to distinct and non-overlapping regions of the viral target (in this case, the RBD of the spike protein), and thus require the unlikely occurrence of simultaneous mutations at two distinct genetic sites for viral escape. A clinical candidate selection criterion for broad potency that includes functional assessment against naturally circulating sequence variants, as well as inclusion of multiple antibodies with non-overlapping epitopes, may provide enhanced protection against loss of efficacy. Future in vivo animal and human clinical studies need to pay close attention to possible emergence of escape mutants and potential subsequent loss of drug efficacy.

REFERENCES AND NOTES

1. R. Yan, Y. Zhang, Y. Li, L. Xia, Y. Guo, Q. Zhou, Structural basis for the recognition of SARS-CoV-2 by full-length human ACE2. *Science* **367**, 1444–1448 (2020). doi:10.1126/science.abb2762 Medline
2. Q. Wang, Y. Zhang, L. Wu, S. Niu, C. Song, Z. Zhang, G. Lu, C. Qiao, Y. Hu, K.-Y. Yuen, Q. Wang, H. Zhou, J. Yan, J. Qi, Structural and Functional Basis of SARS-CoV-2 Entry by Using Human ACE2. *Cell* **181**, 894–904.e9 (2020). doi:10.1016/j.cell.2020.03.045 Medline
3. J. Hansen, A. Baum, K. E. Pascal, V. Russo, S. Giordano, E. Wloga, B. O. Fulton, Y. Yan, K. Koon, K. Patel, K. M. Chung, A. Herman, E. Ullman, J. Cruz, A. Rafique, T. Huang, J. Fairhurst, C. Libertiny, M. Malbec, W.-y. Lee, R. Welsh, G. Farr, S. Pennington, D. Deshpande, J. Cheng, A. Watty, P. Bouffard, R. Babb, N. Levenkova, C. Chen, B. Zhang, A. Romero Hernandez, K. Saotome, Y. Zhou, M. Franklin, S. Sivapalasingam, D. Chien Lye, S. Weston, J. Logue, R. Haupt, M. Frieman, G. Chen, W. Olson, A. J. Murphy, N. Stahl, G. D. Yancopoulos, C. A. Kyratsous, Studies in humanized mice and convalescent humans yield a SARS-CoV-2 antibody cocktail. *Science* 10.1126/science.abd0827 (2020). doi:10.1126/science.abd0827
4. S.-Y. Lau, P. Wang, B. W.-Y. Mok, A. J. Zhang, H. Chu, A. C.-Y. Lee, S. Deng, P. Chen, K.-H. Chan, W. Song, Z. Chen, K. K.-W. To, J. F.-W. Chan, K.-Y. Yuen, H. Chen, Attenuated SARS-CoV-2 variants with deletions at the S1/S2 junction. *Emerg. Microbes Infect.* **9**, 837–842 (2020). doi:10.1080/22221751.2020.1756700 Medline
5. M. E. Dieterle, D. Haslwanter, R. H. Bortz 3rd, A. S. Wirchnianski, G. Lasso, O. Vergnolle, S. A. Abbasi, J. M. Fels, E. Laudermilch, C. Florez, A. Mengotto, D. Kimmel, R. J. Malonis, G. Georgiev, J. Quiroz, J. Barnhill, L. A. Pirofski, J. P. Daily, J. M. Dye, J. R. Lai, A. S. Herbert, K. Chandran, R. K. Jangra, A replication-competent vesicular stomatitis virus for studies of SARS-CoV-2 spike-mediated cell entry and its inhibition. bioRxiv 105247 (2020).
6. D. Pinto, Y.-J. Park, M. Beltramello, A. C. Walls, M. A. Tortorici, S. Bianchi, S. Jaconi, K. Culap, F. Zatta, A. De Marco, A. Peter, B. Guarino, R. Spreafico, E. Cameroni, J. B. Case, R. E. Chen, C. Havenar-Daughton, G. Snell, A. Telenti, H. W. Virgin, A. Lanzavecchia, M. S. Diamond, K. Fink, D. Veesler, D. Corti, Cross-neutralization of SARS-CoV-2 by a human monoclonal SARS-CoV antibody. *Nature* 10.1038/s41586-020-2349-y (2020). doi:10.1038/s41586-020-2349-y Medline
7. K. Tharakaraman, V. Subramanian, D. Cain, V. Sasisekharan, R. Sasisekharan, Broadly neutralizing influenza hemagglutinin stem-specific antibody CR8020 targets residues that are prone to escape due to host selection pressure. *Cell Host Microbe* **15**, 644–651 (2014). doi:10.1016/j.chom.2014.04.009 Medline
8. K. L. Prachanronarong, A. S. Canale, P. Liu, M. Somasundaran, S. Hou, Y. P. Poh, T. Han, Q. Zhu, N. Renzette, K. B. Zeldovich, T. F. Kowalik, N. Kurt-Yilmaz, J. D. Jensen, D. N. A. Bolon, W. A. Marasco, R. W. Finberg, C. A. Schiffer, J. P. Wang, Mutations in Influenza A Virus Neuraminidase and Hemagglutinin Confer Resistance against a Broadly Neutralizing Hemagglutinin Stem Antibody. *J. Virol.* **93**, e01639-18 (2019). Medline
9. S. J. Zost, P. Gilchuk, J. B. Case, E. Binshtein, R. E. Chen, J. X. Reidy, A. Trivette, R. S. Nargi, R. E. Sutton, N. Suryadevara, L. E. Williamson, E. C. Chen, T. Jones, S. Day, L. Myers, A. O. Hassan, N. M. Kafai, E. S. Winkler, J. M. Fox, J. J. Steinhardt, K. Ren, Y. M. Loo, N. L. Kallewaard, D. R. Martinez, A. Schäfer, L. E. Gralinski, R. S. Baric, L. B. Thackray, M. S. Diamond, R. H. Carnahan, J. E. Crowe, Potently neutralizing human antibodies that block SARS-CoV-2 receptor binding and protect animals. bioRxiv 111005 (2020).
10. D. F. Robbiani, C. Gaebler, F. Muecksch, J. C. C. Lorenzi, Z. Wang, A. Cho, M. Agudelo, C. O. Barnes, A. Gazumyan, S. Finkin, T. Hagglof, T. Y. Oliveira, C. Viant, A. Hurley, H. H. Hoffmann, K. G. Millard, R. G. Kost, M. Cipolla, K. Gordon, F. Bianchini, S. T. Chen, V. Ramos, R. Patel, J. Dizon, I. Shimeliovich, P. Mendoza, H. Hartweger, L. Nogueira, M. Pack, J. Horowitz, F. Schmidt, Y. Weisblum, E. Michailidis, A. W. Ashbrook, E. Waltari, J. E. Pak, K. E. Huey-Tubman, N. Koranda, P. R. Hoffman, A. P. West Jr., C. M. Rice, T. Hatziioannou, P. J. Bjorkman, P. D. Bieniasz, M. Caskey, M. C. Nussenzweig, Convergent Antibody Responses to SARS-CoV-2 Infection in Convalescent Individuals. bioRxiv 092619 (2020).
11. Y. Cao, B. Su, X. Guo, W. Sun, Y. Deng, L. Bao, Q. Zhu, X. Zhang, Y. Zheng, C. Geng, X. Chai, R. He, X. Li, Q. Lv, H. Zhu, W. Deng, Y. Xu, Y. Wang, L. Qiao, Y. Tan, L. Song, G. Wang, X. Du, N. Gao, J. Liu, J. Xiao, X. D. Su, Z. Du, Y. Feng, C. Qin, C. Qin, R. Jin, X. S. Xie, Potent neutralizing antibodies against SARS-CoV-2 identified by high-throughput single-cell sequencing of convalescent patients' B cells. *Cell* 10.1016/j.cell.2020.05.025 (2020). doi:10.1016/j.cell.2020.05.025 Medline
12. K. E. Pascal, C. M. Coleman, A. O. Mujica, V. Kamat, A. Badithe, J. Fairhurst, C. Hunt, J. Strein, A. Berrebi, J. M. Sisk, K. L. Matthews, R. Babb, G. Chen, K.-M. V. Lai, T. T. Huang, W. Olson, G. D. Yancopoulos, N. Stahl, M. B. Frieman, C. A. Kyratsous, Pre- and postexposure efficacy of fully human antibodies against Spike protein in a novel humanized mouse model of MERS-CoV infection. *Proc. Natl. Acad. Sci. U.S.A.* **112**, 8738–8743 (2015). doi:10.1073/pnas.1510830112 Medline
13. N. C. Shaner, G. G. Lambert, A. Chammas, Y. Ni, P. J. Cranfill, M. A. Baird, B. R. Sell, J. R. Allen, R. N. Day, M. Israelsson, M. W. Davidson, J. Wang, A bright monomeric green fluorescent protein derived from Branchiostoma lanceolatum. *Nat. Methods* **10**, 407–409 (2013). doi:10.1038/nmeth.2413 Medline
14. N. D. Lawson, E. A. Stillman, M. A. Whitt, J. K. Rose, Recombinant vesicular stomatitis viruses from DNA. *Proc. Natl. Acad. Sci. U.S.A.* **92**, 4477–4481 (1995). doi:10.1073/pnas.92.10.4477 Medline

15. E. A. Stillman, J. K. Rose, M. A. Whitt, Replication and amplification of novel vesicular stomatitis virus minigenomes encoding viral structural proteins. *J. Virol.* **69**, 2946–2953 (1995). doi:10.1128/JVI.69.5.2946-2953.1995 Medline

16. M. A. Whitt, Generation of VSV pseudotypes using recombinant ΔG-VSV for studies on virus entry, identification of entry inhibitors, and immune responses to vaccines. *J. Virol. Methods* **169**, 365–374 (2010). doi:10.1016/j.jviromet.2010.08.006 Medline

17. A. Takada, C. Robison, H. Goto, A. Sanchez, K. G. Murti, M. A. Whitt, Y. Kawaoka, A system for functional analysis of Ebola virus glycoprotein. *Proc. Natl. Acad. Sci. U.S.A.* **94**, 14764–14769 (1997). doi:10.1073/pnas.94.26.14764 Medline

18. S. Fukushi, T. Mizutani, M. Saijo, S. Matsuyama, N. Miyajima, F. Taguchi, S. Itamura, I. Kurane, S. Morikawa, Vesicular stomatitis virus pseudotyped with severe acute respiratory syndrome coronavirus spike protein. *J. Gen. Virol.* **86**, 2269–2274 (2005). doi:10.1099/vir.0.80955-0 Medline

19. J. Nie, Q. Li, J. Wu, C. Zhao, H. Hao, H. Liu, L. Zhang, L. Nie, H. Qin, M. Wang, Q. Lu, X. Li, Q. Sun, J. Liu, C. Fan, W. Huang, M. Xu, Y. Wang, Establishment and validation of a pseudovirus neutralization assay for SARS-CoV-2. *Emerg. Microbes Infect.* **9**, 680–686 (2020). doi:10.1080/22221751.2020.1743767 Medline

ACKNOWLEDGMENTS

Authors would like to thank Kristen Tramaglini for program management and Johanna Hansen for help with manuscript preparation and Edward Scolnick for useful discussions. **Funding:** A portion of this project has been funded in whole or in part with Federal funds from the Department of Health and Human Services; Office of the Assistant Secretary for Preparedness and Response; Biomedical Advanced Research and Development Authority, under OT number: HHSO100201700020C. **Author contributions:** A.B.,B.O.F.,E.W., C.A.K. conceptualized and designed experiments. B.O.F., E.W., K.E.P., V.R., S.G., performed research and A.B., B.O.F., E.W., K.E.P., V.R., S.G., G.S.A., A.J.M., N.S., G.D.Y., C.A.K. analyzed data. R.C., K.L., N.N., M.N., Y.W. prepared sequencing libraries and performed bioinformatics analysis A.B., G.D.Y., C.A.K. wrote the paper. C.A.K. acquired funding. **Competing interests:** Regeneron authors own options and/or stock of the company. This work has been described in one or more pending provisional patent applications. A.J.M., N.S., G.D.Y. and C.A.K. are officers of Regeneron. **Data and materials availability:** Antibody sequences have been deposited to GenBank and are available in (*3*). Regeneron materials described in this manuscript may be made available to qualified, academic, noncommercial researchers through a material transfer agreement upon request at https://regeneron.envisionpharma.com/vt_regeneron/. For questions about how Regeneron shares materials, use the email address (preclinical.collaborations@regeneron.com).

SUPPLEMENTARY MATERIALS

science.sciencemag.org/cgi/content/full/science.abd0831/DC1
Materials and Methods
Fig. S1
References (*13–19*)

30 May 2020; accepted 11 June 2020
Published online 15 June 2020
10.1126/science.abd0831

Table 1. Anti-SARS-CoV2 spike mAbs demonstrate broad neutralization across SARS-CoV-2 spike RBD variants. Eight anti-spike antibodies were tested against sixteen SARS-CoV-2 spike protein RBD variants identified from viral sequences circulating through end of March 2020. The listed variants were encoded into pVSV-SARS-CoV-2-S (mNeon) pseudoparticles and neutralization assays were performed in Vero cells. IC50(M) values are shown for each variant. There was no observed neutralization with hIgG1 isotype control (N/A).

	Anti-SARS-CoV-2 spike monoclonal antibodies								
Variants	REGN10989	REGN10987	REGN10933	REGN10934	REGN10964	REGN10954	REGN10984	REGN10986	Isotype control
Wild-type	7.23×10^{-12}	4.06×10^{-11}	4.28×10^{-11}	5.44×10^{-11}	5.70×10^{-11}	9.22×10^{-11}	9.73×10^{-11}	9.91×10^{-11}	N/A
Q321L	1.46×10^{-11}	5.02×10^{-11}	6.85×10^{-11}	6.84×10^{-11}	5.65×10^{-11}	2.32×10^{-10}	2.75×10^{-10}	2.06×10^{-10}	N/A
V341I	1.61×10^{-11}	3.38×10^{-11}	3.37×10^{-11}	7.42×10^{-11}	1.13×10^{-10}	2.52×10^{-10}	2.49×10^{-10}	1.92×10^{-10}	N/A
A348T	7.33×10^{-12}	2.98×10^{-11}	4.13×10^{-11}	1.42×10^{-10}	3.52×10^{-11}	1.84×10^{-10}	2.01×10^{-10}	1.03×10^{-10}	N/A
N354D	1.14×10^{-11}	2.68×10^{-11}	5.89×10^{-11}	9.76×10^{-11}	1.93×10^{-10}	2.84×10^{-10}	2.64×10^{-10}	2.49×10^{-10}	N/A
S359N	4.30×10^{-12}	2.41×10^{-11}	2.12×10^{-11}	3.04×10^{-11}	6.83×10^{-11}	1.09×10^{-10}	1.23×10^{-10}	8.91×10^{-11}	N/A
V367F	1.33×10^{-11}	1.78×10^{-11}	2.40×10^{-11}	3.20×10^{-11}	8.92×10^{-11}	1.29×10^{-10}	1.53×10^{-10}	1.49×10^{-10}	N/A
K378R	1.21×10^{-11}	2.40×10^{-11}	3.52×10^{-11}	4.65×10^{-11}	6.19×10^{-11}	1.65×10^{-10}	1.88×10^{-10}	1.54×10^{-10}	N/A
R408I	1.09×10^{-11}	1.71×10^{-11}	1.98×10^{-11}	2.75×10^{-11}	4.96×10^{-11}	9.88×10^{-11}	1.35×10^{-10}	6.14×10^{-11}	N/A
Q409E	2.12×10^{-11}	4.06×10^{-11}	5.65×10^{-11}	5.94×10^{-11}	6.61×10^{-11}	2.64×10^{-10}	1.52×10^{-10}	1.95×10^{-10}	N/A
A435S	1.10×10^{-11}	3.88×10^{-11}	4.71×10^{-11}	8.07×10^{-11}	7.90×10^{-11}	2.11×10^{-10}	2.18×10^{-10}	1.51×10^{-10}	N/A
K458R	7.51×10^{-12}	1.68×10^{-11}	3.43×10^{-11}	3.46×10^{-11}	5.46×10^{-11}	1.45×10^{-10}	1.59×10^{-10}	1.00×10^{-10}	N/A
I472V	2.27×10^{-11}	4.18×10^{-11}	9.17×10^{-11}	9.40×10^{-11}	1.01×10^{-10}	3.44×10^{-10}	2.61×10^{-10}	2.24×10^{-10}	N/A
G476S	6.80×10^{-12}	1.86×10^{-11}	1.41×10^{-10}	3.51×10^{-11}	3.42×10^{-11}	1.83×10^{-10}	2.10×10^{-10}	1.13×10^{-10}	N/A
V483A	8.78×10^{-12}	2.60×10^{-11}	1.54×10^{-11}	4.43×10^{-11}	4.50×10^{-11}	1.12×10^{-10}	1.71×10^{-10}	9.70×10^{-11}	N/A
Y508H	1.71×10^{-11}	2.75×10^{-11}	4.77×10^{-11}	6.73×10^{-11}	1.02×10^{-10}	2.05×10^{-10}	2.83×10^{-10}	2.01×10^{-10}	N/A
H519P	4.51×10^{-12}	2.20×10^{-11}	3.03×10^{-11}	3.56×10^{-11}	4.45×10^{-11}	1.40×10^{-10}	1.08×10^{-10}	6.14×10^{-11}	N/A

Table 2. Neutralization potency of individual anti-spike antibodies and antibody combinations against pseudoparticles encoding individual escape mutants-IC50 summary. Escape mutations identified by RNAseq analysis within the RDB domain were cloned and expressed on pseudoparticles to assess their impact on mAb neutralization potency. Entries in boldface highlight conditions that resulted in at least 1.5 log decrease in IC50 relative to wild-type pseudoparticles or loss of neutralization. NC = IC50 could not be calculated due to poor neutralization ability. Reduction in IC50 less than 1 log can be seen in mAb combination conditions where one of the mAbs has no potency (ex: K444Q and REGN10933/10987). Refer to fig. S1 for full neutralization curves.

	Anti-SARS-CoV-2 spike monoclonal antibodies						
Escape mutants	REGN10989	REGN10987	REGN10933	REGN10934	REGN10933/ 10987	REGN10989/ 10934	REGN10989/ 10987
Wild-type	7.27×10^{-12}	3.65×10^{-11}	5.57×10^{-11}	5.99×10^{-11}	3.28×10^{-11}	8.27×10^{-12}	1.22×10^{-11}
K417E	2.49×10^{-11}	3.10×10^{-11}	**8.33×10^{-9}**	2.70×10^{-11}	4.15×10^{-11}	2.64×10^{-11}	2.72×10^{-11}
K444Q	2.47×10^{-11}	**NC**	7.81×10^{-11}	**5.38×10^{-9}**	1.23×10^{-10}	4.19×10^{-11}	4.82×10^{-11}
V445A	2.65×10^{-11}	**NC**	8.82×10^{-11}	1.42×10^{-10}	1.54×10^{-10}	4.08×10^{-11}	5.74×10^{-11}
N450D	4.10×10^{-11}	**1.20×10^{-9}**	7.60×10^{-11}	**NC**	1.88×10^{-10}	6.04×10^{-11}	5.37×10^{-11}
Y453F	2.77×10^{-11}	1.04×10^{-10}	**NC**	2.17×10^{-10}	1.15×10^{-10}	3.52×10^{-11}	2.41×10^{-11}
L455F	1.77×10^{-11}	3.87×10^{-11}	**NC**	4.34×10^{-11}	5.87×10^{-11}	1.96×10^{-11}	1.70×10^{-11}
E484K	**NC**	6.25×10^{-11}	**1.13×10^{-9}**	**NC**	6.19×10^{-11}	**NC**	1.88×10^{-10}
G485D	**NC**	2.34×10^{-11}	2.05×10^{-10}	4.47×10^{-11}	4.71×10^{-11}	1.19×10^{-10}	4.58×10^{-11}
F486V	**NC**	3.16×10^{-11}	**NC**	3.50×10^{-11}	8.8×10^{-11}	1.29×10^{-10}	6.96×10^{-11}
F490P	**6.76×10^{-10}**	3.75×10^{-11}	8.65×10^{-11}	**NC**	5.41×10^{-11}	**2.55×10^{-9}**	6.82×10^{-11}
Q493K	**NC**	4.19×10^{-11}	**NC**	3.46×10^{-11}	3.24×10^{-11}	**4.55×10^{-10}**	5.94×10^{-11}

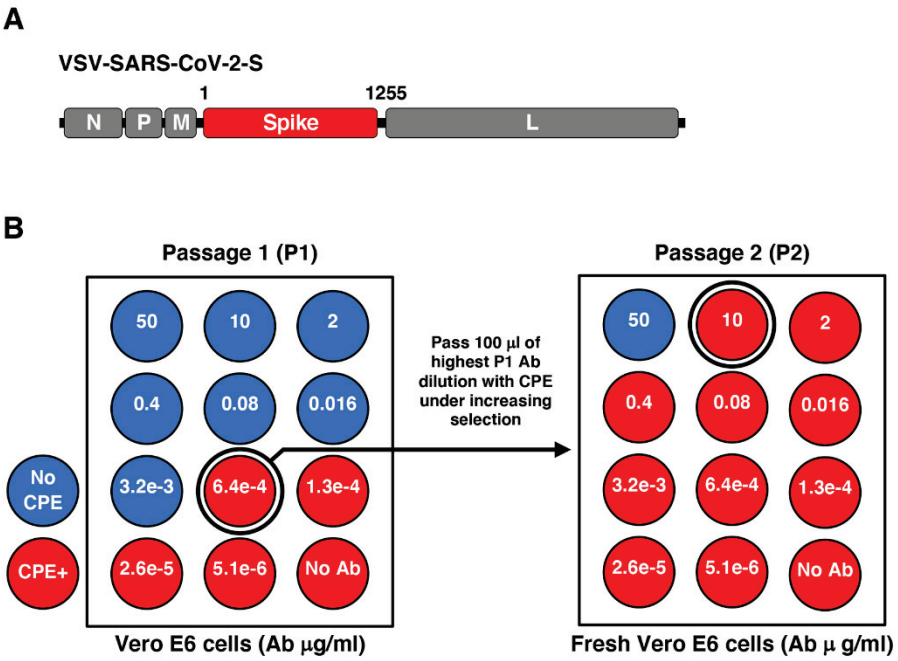

C

Passage	Antibody concentration µg/ml						
P1	50	10	2	0.4	0.08	0.016	No Ab
REGN10989	15%	30%	30%	30%	30%	≥ 90%	≥ 90%
REGN10987	0%	15%	50%	≥ 90%	≥ 90%	≥ 90%	≥ 90%
REGN10933	0%	0%	5%	20%	≥ 90%	≥ 90%	≥ 90%
REGN10934	2-5%	2-5%	30%	50%	≥ 90%	≥ 90%	≥ 90%
REGN10989 + REGN10987	0%	0%	0%	0%	20%	≥ 90%	≥ 90%
REGN10989 + REGN10934	2-5%	2-5%	20%	20%	50%	≥ 90%	≥ 90%
REGN10987 + REGN10933	0%	0%	0%	0%	60%	≥ 90%	≥ 90%
IgG Isotype Control	≥ 90%	≥ 90%	≥ 90%	≥ 90%	≥ 90%	≥ 90%	≥ 90%
P2	50	10	2	0.4	0.08	0.016	No Ab
REGN10989	≥ 90%	≥ 90%	≥ 90%	≥ 90%	≥ 90%	≥ 90%	≥ 90%
REGN10987	5%	40%	≥ 90%	≥ 90%	≥ 90%	≥ 90%	≥ 90%
REGN10933	70%	80%	≥ 90%	≥ 90%	≥ 90%	≥ 90%	≥ 90%
REGN10934	80%	≥ 90%	≥ 90%	≥ 90%	≥ 90%	≥ 90%	≥ 90%
REGN10989 + REGN10987	0%	0%	0%	0%	0%	0%	50%
REGN10989 + REGN10934	≥ 90%	≥ 90%	≥ 90%	≥ 90%	≥ 90%	≥ 90%	≥ 90%
REGN10987 + REGN10933	0%	0%	0%	0%	0%	60%	≥ 90%
IgG Isotype Control	≥ 90%	≥ 90%	≥ 90%	≥ 90%	≥ 90%	≥ 90%	≥ 90%

Fig. 1. Escape mutant screening protocol. (**A**) A schematic is displayed of the VSV-SARS-CoV-2-S virus genome encoding residues 1-1255 of the spike protein in place of the VSV glycoprotein. N, nucleoprotein, P, phosphoprotein, M, matrix, and L, large polymerase. (**B**) A total of 1.5 × 10^6 pfu of the parental VSV-SARS-CoV-2-S virus was passed in the presence of antibody dilutions for 4 days on Vero E6 cells. Cells were screened for virus replication by monitoring for virally induced cytopathic effect (CPE). Supernatants and cellular RNAs were collected from wells under the greatest antibody selection with detectable viral replication (circled wells; ≥20% CPE). For a second round of selection, 100uL of the P1 supernatant was expanded for 4 days under increasing antibody selection in fresh Vero E6 cells. RNA was collected from the well with the highest antibody concentration with detectable viral replication. The RNA was deep sequenced from both passages to determine the selection of mutations resulting in antibody escape. (**C**) The passaging results of the escape study are presented with the qualitative percentage of CPE observed in each dilution (red ≥ 20%CPE and blue < 20% CPE). Black boxes indicate dilutions that were passaged and sequenced in P1 or sequenced in P2. A no antibody control was sequenced from each passage to monitor for tissue culture adaptations.

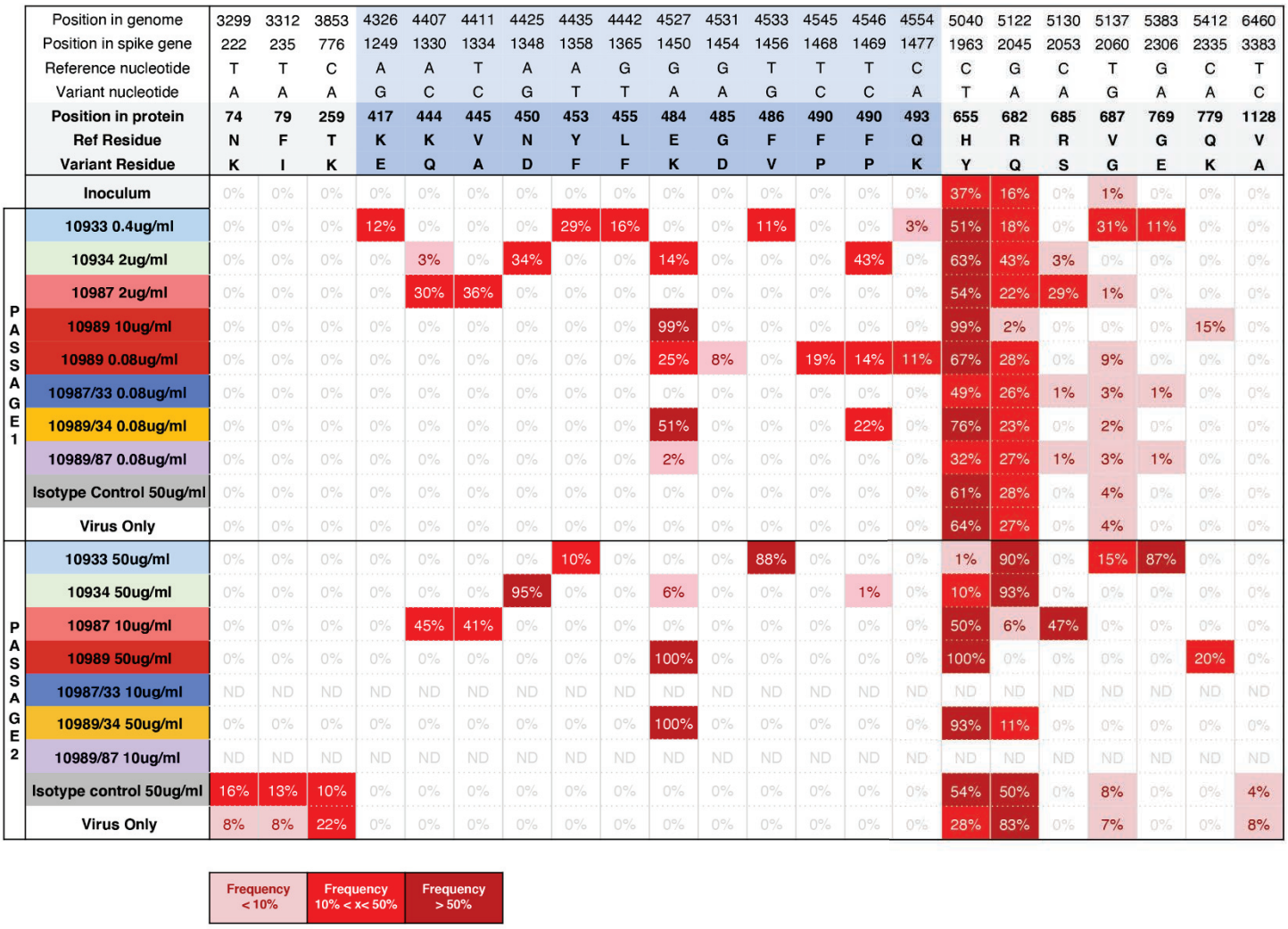

Fig. 2. Deep sequencing of passaged virus identifies escape mutations. VSV-SARS-CoV-2-S virus was mixed with either individual or combinations of anti-spike mAbs. Viral RNA from wells with the highest mAb concentration and detectable cytopathic effect (CPE) on passage 1 or 2 (collected 4 days post-infection) was isolated and RNAseq analysis was performed to identify changes in spike protein sequence relative to input virus. For passage 2, viral RNA was isolated and sequenced from wells with high mAb concentrations (>10ug/ml) with subsequently validated escape; if no validated escape was seen at these high mAb concentrations and no virus was grown, ND is shown as no virus RNA was isolated. All mutated amino acid residues within the spike protein are shown. Specific condition (concentration in ug/ml) of the well that was selected for sequencing is shown in the left-hand column (refer to Fig. 1 for outline of the experiment). Red boxes highlight residues that were mutated relative to input virus under each condition specified in the left-hand column. Percentage in each box identifies % of sequencing reads that contained the respective mutant sequence. Residues mapping to the RBD domain are highlighted in blue.

OPEN ACCESS Freely available online

PLoS one

A Vesicular Stomatitis Virus Replicon-Based Bioassay for the Rapid and Sensitive Determination of Multi-Species Type I Interferon

Marianne Berger Rentsch, Gert Zimmer*

Institut für Viruskrankheiten und Immunprophylaxe, Mittelhäusern, Switzerland

Abstract

Type I interferons (IFN) comprise a family of cytokines that signal through a common cellular receptor to induce a plethora of genes with antiviral and other activities. Recombinant IFNs are used for the treatment of hepatitis C virus infection, multiple sclerosis, and certain malignancies. The capability of type I IFN to suppress virus replication and resultant cytopathic effects is frequently used to measure their bioactivity. However, these assays are time-consuming and require appropriate biosafety containment. In this study, an improved IFN assay is presented which is based on a recombinant vesicular stomatitis virus (VSV) replicon encoding two reporter proteins, firefly luciferase and green fluorescent protein. The vector lacks the essential envelope glycoprotein (G) gene of VSV and is propagated on a G protein-expressing transgenic cell line. Several mammalian and avian cells turned out to be susceptible to infection with the complemented replicon particles. Infected cells readily expressed the reporter proteins at high levels five hours post infection. When human fibroblasts were treated with serial dilutions of human IFN-β prior to infection, reporter expression was accordingly suppressed. This method was more sensitive and faster than a classical IFN bioassay based on VSV cytopathic effects. In addition, the antiviral activity of human IFN-λ (interleukin-29), a type III IFN, was determined on Calu-3 cells. Both IFN-β and IFN-λ were acid-stable, but only IFN-β was resistant to alkaline treatment. The antiviral activities of canine, porcine, and avian type I IFN were analysed with cell lines derived from the corresponding species. This safe bioassay will be useful for the rapid and sensitive quantification of multi-species type I IFN and potentially other antiviral cytokines.

Citation: Berger Rentsch M, Zimmer G (2011) A Vesicular Stomatitis Virus Replicon-Based Bioassay for the Rapid and Sensitive Determination of Multi-Species Type I Interferon. PLoS ONE 6(10): e25858. doi:10.1371/journal.pone.0025858

Editor: Karen L. Mossman, McMaster University, Canada

Received June 7, 2011; **Accepted** September 12, 2011; **Published** October 5, 2011

Funding: This work was funded by Wilhelm Sander Foundation (www.sanst.de) (grant no. 2007.101.1); Swiss National Science Foundation (www.snf.ch), grant no. 310030_129669. The funders had no role in study design, data collection and analysis, decision to publish, or preparation of the manuscript.

Competing Interests: The authors have declared that no competing interests exist.

* E-mail: gert.zimmer@ivi.admin.ch

Introduction

IFN-α and IFN-β are structurally related cytokines of the type I interferon family which mediate an early innate immune response to viral infections. There are 13 distinct IFN-α genes present in the human genome, and a single gene encoding for IFN-β. These genes are transcriptionally activated in cells sensing a virus infection through pattern recognition receptors such as the retinoic acid inducible gene I (RIG-I) helicase. Following secretion, IFN-α and IFN-β act similarly by binding to a common, ubiquitously expressed IFN-α/β receptor resulting in the activation of the JAK/STAT signal transduction pathway and transcription of "IFN-induced genes" [1,2]. Several of these genes encode for proteins with strong antiviral activity, i.e. Mx protein, protein kinase R, and 2′-5′oligo(A) synthetase [3]. Due to their autocrine action, type I IFN may attenuate virus replication in infected cells. Probably more important is the paracrine action of type I IFN, which induces an antiviral state in previously uninfected cells, thereby blocking virus dissemination in the organism. In addition to this "classical" antiviral function, type I IFNs are known to affect cell proliferation and differentiation, to modulate the immune response, to inhibit angiogenesis, and to promote apoptosis [4,5]. Genetically engineered type I IFNs are currently in clinical use for the treatment of multiple sclerosis [6], chronic hepatitis C virus infection [7], and certain types of cancer [8,9]. An issue of increasing importance is the determination of neutralizing antibodies that are induced in some patients following recombinant IFN therapy [10].

Apart from IFN-α/β, cytokines such as IFN-γ (type II IFN) and IFN-λ (type III IFN) exhibit antiviral activities, although they bind to distinct receptors. In particular, type III IFNs induce transcriptional activation of antiviral genes similar to those activated by type I IFN. Type III IFNs act primarily on epithelial cells [11] and probably play an important role in the innate immune response of epithelial tissues to virus infections [12,13].

The accurate determination of antiviral IFN activity is a cumbersome issue. In the "classical" bioassay, serial dilutions of both a test sample with unknown IFN activity and a type I IFN standard are incubated with an appropriate cell line prior to infection with a cytolytic virus such as vesicular stomatitis virus (VSV), encephalomyocarditis virus, or Sendai virus [14,15]. The reciprocal value of the highest type I IFN dilution mediating protection of 50% of the cells from virus-induced cytopathic effects (CPE) is defined as one unit of type I IFN per volume. This classical IFN bioassay is time-consuming because the CPE normally needs 24 hours or more to develop. A faster readout

can be achieved with recombinant viruses expressing reporter proteins such as green fluorescent protein (GFP) or firefly luciferase [16,17,18,19]. However, any work with live virus requires appropriate biosafety containment. For example, a recently published IFN bioassay can only be performed in biosafety level 3 (BSL-3) facilities, because the test makes use of a recombinant Rift Valley Fever virus [19]. Viral replicon-based bioassays that take advantage of disabled propagation-incompetent viruses may provide an attractive alternative to live virus-based bioassays. A human hepatoma cell line harbouring a selectable hepatitis C virus replicon has been successfully employed for the measurement of type I IFN from patients with chronic hepatitis C virus infection [20]. However, as type I IFNs act in a species-dependent manner, this system may not be applicable to animal IFNs. Transgenic cell lines expressing a reporter gene under control of an IFN-responsive promoter may also be used to determine IFN activity under biosafe conditions [21,22]. However, it is difficult to simply relate transcriptional reporter gene activation to antiviral activity.

In this report, a novel type I IFN bioassay is presented, which is based on BSL-1-classified VSV replicon particles. The assay is highly sensitive and quantifiable due to the expression of a firefly luciferase reporter gene. In addition, the assay can be rapidly performed within 6 to 7 hours and may be used to determine the antiviral activity of IFNs from humans as well as other species. Thus, this bioassay may be of general interest for all those who want to determine the antiviral activity of cytokines such as type I IFNs.

Materials and Methods

Cells

BHK-21 cells were obtained from the German Cell Culture Collection (DSZM, Braunschweig, Germany) and grown in Earle's minimal essential medium (EMEM) supplemented with 5% fetal bovine serum (FBS). BHK-G43, a transgenic BHK-21 cell clone expressing VSV G protein in a regulated manner, was maintained as described previously [23]. The porcine kidney cell line PK-15 (ATCC, Manassas, VA) was propagated in Dulbecco's modified Eagle medium supplemented with nonessential amino acids, 1 mM Na-pyruvate and 5% horse serum. D-17 canine osteosarcoma cells (ATCC), Calu-3 human lung adenocarcinoma cells (ATCC), and NHDF normal human dermal fibroblasts (Lonza, Cologne, Germany) were maintained in EMEM with 10% FBS. The UMNSAH/DF-1 (DF-1) chicken fibroblast cell line (ATCC) was maintained in Dulbecco's Modified Eagle's Medium and 10% FBS. All cell lines were cultured at 37°C in a humidified atmosphere containing 5% CO_2, except DF-1 cells which were kept at 39°C. BALB 3T3 fibroblasts (subclone A31) were kindly provided by N. Pringle, University College, London, UK, and maintained in Dulbecco's Modified Eagle's Medium.

Interferons

Human and murine IFN-β and human IFN-λ (IL-29) were purchased from PBL InterferonSource (Piscataway, NJ). Recombinant porcine IFN-α1 [24] was kindly provided by Nicolas Ruggli (IVI, Mittelhäusern, Switzerland). Recombinant chicken IFN-α [25] was kindly provided by Peter Stäheli (University of Freiburg, Germany). Canine IFN-β [26] was kindly provided by Philippe Plattet (Department of Clinical Research and Veterinary Public Health, University of Bern).

Generation of VSV*ΔG(Luc) replicon particles

A plasmid-based rescue system [27] was used to generate a G-deleted VSV driving expression of firefly luciferase and eGFP. The previously described genomic plasmid pVSV*ΔG(HA) containing 6 distinct transcription units (N-P-M-HA-eGFP-L) [28] was modified by replacing the influenza virus HA gene in the fourth position with eGFP taking advantage of *Mlu*I and *Bst*EII endonuclease restriction sites upstream and downstream of the HA ORF, respectively. The firefly luciferase gene was amplified from the pBI-L plasmid (Clontech) by *Pfu* PCR and inserted into the fifth transcrition unit using *Xho*I and *Nhe*I endonuclease restriction sites. The resulting plasmid was designated pVSV*ΔG(Luc) and contained 6 genes in the order N-P-M-eGFP-Luc-L (Fig. 1).

For generation of VSV*ΔG(Luc) replicon particles, BHK-G43 helper cells were grown in 100-mm diameter culture dishes to 90% confluence and infected with recombinant modified vaccinia virus Ankara (5 pfu per cell) expressing T7 RNA polymerase (MVA-T7, a gift of Gerd Sutter, München, Germany). MVA-T7 has been classified by the German Central Committee for Biosafety as a BSL-1 organism (reference number 6790-10-14). Ninety minutes post infection, the medium was replaced with fresh EMEM containing 5% FBS and 10^{-9} M mifepristone (Sigma-Aldrich, Buchs, Switzerland) to induce VSV G expression [23]. Subsequently, the cells were transfected with 10 µg of pVSV*ΔG(Luc), 3 µg of pTM1-N, 5 µg of pTM1-P, and 2 µg of pTM1-L [28] using Lipofectamine™ 2000 transfection reagent (Invitrogen, Basel, Switzerland). The cells were trypsinized 24 hours post transfection and seeded into T75 flasks along with an equal number of fresh BHK-G43 cells. The cells were further incubated at 37°C for 24 hours in the presence of 10^{-9} M mifepristone. The cell culture supernatant was clarified by low-speed centrifugation and passed through a 0.20-µm-pore size filter to deplete vaccinia virus. VSV*ΔG(Luc) was further propagated on mifepristone-induced BHK-G43 cells and stored frozen at −70°C. To determine infectious virus titers, confluent BHK-21 grown in 96-well microtiter plates were inoculated in duplicate with 40 µl of serial tenfold virus dilutions for 1 h at 37°C. The wells additionally received 60 µl of EMEM and were incubated for 20 h at 37°C. The infectious titers were calculated according to the number of GFP-expressing cells/well and expressed as fluorescence-forming units per milliliter (ffu/ml).

MVA-T7 was titrated on DF-1 cells grown in 96-well microtiter plates. The cells were inoculated with tenfold serial virus dilutions for 90 min and overlayed with medium containing 0.9% methylcellulose. Following incubation for 48 h at 39°C, the cells were fixed with 3% paraformaldehyde, permeabilized with 0.25% Triton X-100, and subsequently incubated with the TW2.3 monoclonal antibody directed to the vaccinia E3L protein (kindly provided by Jonathan Yewdell, NIH, Bethesda, USA) and anti-mouse IgG conjugated to horseradish peroxidase (DAKO). Infected cell foci were visualized with the AEC peroxidase substrate and expressed as plaque-forming units per milliliter (pfu/ml). Using this assay, the final VSV replicon particle preparations proved to be free of MVA-T7.

Bioassays for determining antiviral activity

Serial twofold or fourfold dilutions of type I IFN were prepared with cell culture medium containing 5% FBS. The IFN dilutions (100 µl) were added in quadruplicates to confluent cells grown in 96-wells (5×10^4 cells/well) and incubated for either 1, 2, 4, or 20 hours at 39°C (DF-1 cells) or 37°C (all other cell lines). The cells were infected with VSV*ΔG(Luc) (m.o.i. of 5) and incubated for 5 hours at 37°C. The medium was aspirated and 30 µl of luciferase lysis buffer (Biotium Inc., Hayward, CA) was added to the cells. The cell lysates were stored at −20°C. Firefly luciferase activity was determined with a Centro LB 960 luminometer (Berthold Technologies). Luminescence was recorded for 1 s following injection of 30 µl of D-luciferin substrate (Biotium) to

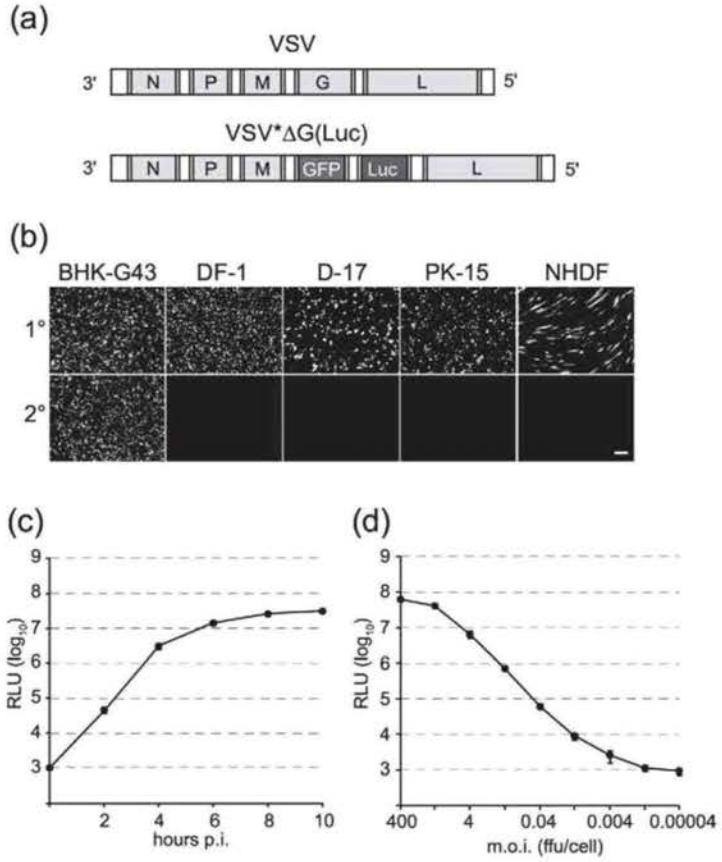

Figure 1. Expression of firefly luciferase and GFP reporter genes by a propagation-incompetent VSVΔG replicon. (a) Genome maps of authentic VSV and recombinant VSV*ΔG(Luc) vector. VSV*ΔG(Luc) lacks the glycoprotein (G) gene and drives expression of both enhanced green fluorescent protein (GFP) and firefly luciferase (Luc). (b) Cell lines derived from different species were infected with 4 ffu/cell of VSV*ΔG(Luc) (1st cycle). Sixteen hours post infection, the undiluted cell culture supernatant was passed to fresh cells (2nd cycle). GFP expression in live cells was monitored 6 h post infection using an inverse fluorescence microscope. Bar, 100 µm. (c) Firefly luciferase activity in BHK-21 cell lysates at different times post infection with 4 ffu/cell of VSV*ΔG(Luc). (d) Firefly luciferase levels in BHK-21 cell lysates 5 h post infection by VSV*ΔG(Luc) with the indicated multiplicities of infection (m.o.i.).
doi:10.1371/journal.pone.0025858.g001

white 96-well plates containing 6-µl aliquots of cell lysate. The relative antiviral activity was calculated according to the following formula: Antiviral Activity (%) = 100 - [(RLU_{+IFN} – Blank)×100/(RLU_{-IFN} - Blank)]. Mock-infected cell lysates served as blanks and relative light units (RLU) detected with these samples were subtracted from the readings taken from VSV*ΔG(Luc)-infected cell lysates. RLU_{+IFN} represents the RLU values from IFN-treated cells and RLU_{-IFN} the readings taken from reference cells, which had not received any type I IFN.

A conventional type I IFN bioassay was performed by incubating 96-well cell cultures for 20 hours with twofold dilutions of type I IFN as described above. The cells were infected with propagation-competent VSV (m.o.i. of 1 pfu/cell) and incubated until a cytopathic effect (CPE) was evident in mock-treated control cells. The cells were washed twice with PBS and stained for 1 h with 0.1% crystal violet in 10% formalin. The plates were washed with tap water to remove excess crystal violet and dried. The dye was dissolved by adding 100 µl of 70% ethanol to each well. The absorbance of crystal violet at 595 nm was determined with a microplate reader. The IFN titer was calculated as the reciprocal of the last IFN dilution causing 50% inhibition of virus-induced CPE (50 % reduction of absorbance at 595 nm compared to mock-infected cells) and was expressed as IFN units per volume. Alternatively, antiviral activity was calculated according to the following formula: Antiviral activity (%) = ($OD595_{+IFN}$ – $OD595_{-IFN}$)×100/($OD595_{Mock}$ – $OD595_{-IFN}$). $OD595_{+IFN}$ and $OD595_{-IFN}$ represent the absorbance of IFN-treated and non-treated cells following infection with VSV and staining with crystal violet, respectively. $OD595_{Mock}$ denotes the absorbance of non-infected cells.

Statistical analysis

Mean values and standard deviation were calculated. Statistical analysis was performed using the paired Student's t-test. $P<0.05$ was considered significant.

Results

Generation of the VSV*ΔG(Luc) replicon

Previously, a VSV replicon vector was generated by replacing the glycoprotein G gene of VSV with the hemagglutinin (HA) gene

of an H7N1 influenza virus and inserting an extra transcription unit into the HA-L intergenic junction to drive expression of a modified GFP gene [28]. In the present work, this vector was modified by inserting the firefly luciferase gene into the transcription unit at position 5 (thereby replacing the GFP gene) and exchanging the HA gene with the GFP gene (Fig. 1a). The resulting vector, VSV*ΔG(Luc), was propagated on BHK-G43 helper cells which express the VSV G protein in an inducible manner [23]. Up to 10^9 virus replicon particles (VRP) were released into the cell culture supernatant 24 h post infection (data not shown). Several mammalian and avian cells were found to be susceptible to infection with the VRPs in line with previous observations on the very broad cell tropism of VSV [29]. Infected cells were readily detected (5 to 6 h post infection) by means of GFP reporter expression (Fig. 1b). However, non-helper cells were unable to complement the VSV G deletion and thus could not produce infectious progeny virus. Importantly, VSV*ΔG(Luc) did not induce type I IFN in the cell lines analysed (data not shown). This can be ascribed to the host shut-off activity of the VSV matrix protein [30].

Infection of BHK-21 cells with VSV*ΔG(Luc) using a multiplicity of infection (m.o.i.) of 4 ffu/cell resulted in increasing firefly luciferase reporter activity with time (Fig. 1c). In all subsequent experiments, luciferase activity was generally recorded at 5 h post infection as the signal-to-noise ratio was sufficiently high at this time. When BHK-21 cells were infected with different virus dose rates, luciferase reporter activity increased linearly between 0.004 and 40 ffu/cell (Fig. 1d). Although 95% of the cells showed GFP fluorescence following infection with an m.o.i. of 4 ffu/cell (not shown), an m.o.i. of 40 ffu/cell caused an even tenfold higher luciferase activity suggesting that multiple infections add to the overall replication/transcription rate of the virus genome in a single cell. In all subsequent experiments an m.o.i. of 5 ffu/cell was generally used, as this guaranteed a signal-to noise ratio of about 4 $\log_{10}$.

Quantification of type I IFN antiviral activity

The luciferase reporter activity in VSV*ΔG(Luc)-infected cells depends on the replication/transcription levels of the RNA replicon. Thus, a reduction in viral genome replication as a consequence of type IFN action should lead to correspondingly lower luciferase levels. To test this hypothesis, normal human dermal fibroblasts (NHDF) were incubated for various time periods with serial dilutions of human IFN-β before infection with VSV*ΔG(Luc). A dose-dependent effect of IFN-β on firefly luciferase reporter activity was observed after 1 hour of incubation (Fig. 2a). About 1 unit of IFN-β led to 50% suppression of luciferase activity. Extending the incubation time to 2 hours did not further improve the sensitivity of the test ($p>0.05$ for the 0.08 to 1.25 IFN units range). However, if the cells were treated for 20 hours, the dose response curve was significantly shifted to lower IFN units ($p\leq0.001$ for the 0.02 to 20 units range). Approximately 0.05 units of IFN-β were now sufficient to suppress reporter activity by 50%. These results indicate that an IFNβ-induced antiviral state in NHDF cells can be detected as early as 1 hour after addition of IFN-β, although the sensitivity of the assay is higher if the cells were incubated with IFN-β for prolonged time.

VSV*ΔG(Luc) was also used to quantify the activities of porcine and chicken IFN-α. While the dose response curve of chicken IFN-α on DF-1 chicken fibroblasts (Fig. 2b) was similar to the one of human IFN-β on NHDF (Fig. 2a), porcine IFN-α showed a different kinetics on PK-15 porcine kidney cells. In these cells, a full antiviral state was accomplished only after 20 hours of treatment indicating that PK-15 cells respond rather slowly to the action of type I IFN (Fig. 2c). Thus, the assay is applicable to type I IFN from different species but may perform differentially on distinct cell types.

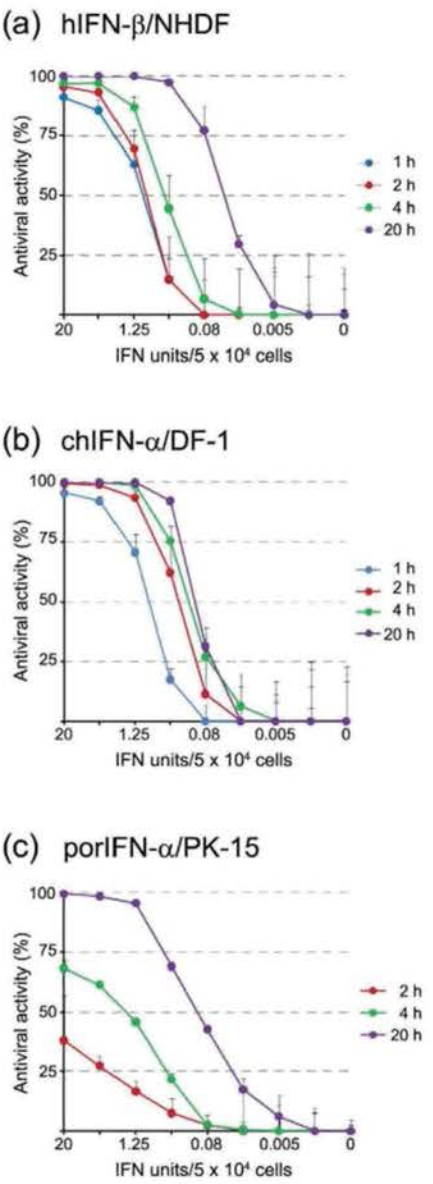

Figure 2. Determination of mammalian and avian type I IFN bioactivity. (a) NHDF (human fibroblasts), (b) DF-1 (chicken fibroblasts), and (c) PK-15 (porcine kidney) cells in 96-well plates were incubated for the indicated times with fourfold serial dilutions of type I IFN from the homologous species and subsequently infected with VSV*ΔG(Luc) (5 ffu/cell). Five hours post infection, the cells were lysed and firefly luciferase activity was recorded. Reference cells did not receive any type I IFN and demonstrated no antiviral activity. The axes of abscissas indicate the activities of the type I IFNs as determined with a conventional CPE-based IFN bioassay.
doi:10.1371/journal.pone.0025858.g002

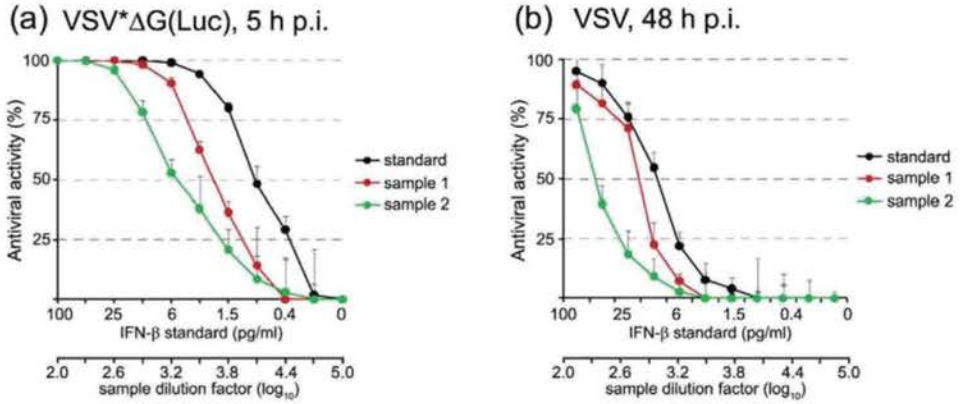

Figure 3. Validation of the VSV*ΔG(Luc) replicon bioassay. Serial twofold dilutions of IFN-β standard (starting with 100 pg/ml) and of two different test samples containing type IFN of unknown activity (starting with dilution 1/100) were prepared and incubated with NHDF for 20 h at 37°C. (a) Five hours post infection with VSV*ΔG(Luc) (m.o.i. = 5), the cells were lysed and firefly luciferase activity recorded. The antiviral activity relative to infected but non-treated cells was calculated. (b) Fourty-eight hours post infection with VSV (m.o.i. = 1), the cells were fixed with formalin containing 0.1% crystal violet, washed with water, and dried. The dye was dissolved in 70% ethanol before absorbance at 595 nm was recorded. The relative antiviral activity (%) was calculated.
doi:10.1371/journal.pone.0025858.g003

To further evaluate the bioassay, samples containing type I IFN of unknown activity were tested against a commercial IFN-β standard and the results were compared with those obtained with a conventional IFN bioassay based on VSV cytotoxicity. Human type I IFN was induced in NHDF human fibroblasts following infection with VSV*M_q [30]. This propagation-competent virus expresses a mutant matrix protein that is unable to block the nucleocytoplasmic RNA transport of the cell. Before the samples were tested for antiviral activity, VSV*M_q was inactivated for 30 min with 0.1 M HCl to avoid any interference with the bioassay (see also the section on thermal and pH stability of IFN). When the VSV*ΔG(Luc) replicon bioassay was used, about 0.8 pg/ml of a commercial IFN-β standard resulted in 50% antiviral activity. In consideration of the final dilution producing 50% antiviral activity, the type I IFN concentration of two test samples was defined as 4000 pg/ml and 1440 pg/ml, respectively (Fig. 3a). When the samples were tested with the conventional bioassay (Fig. 3b), the values were in the same range (5000 and 1500 pg/ml), indicating that both assays principally agree. Nevertheless, the replicon-based bioassay proved to be more sensitive than the conventional one as lower amounts of type I IFN were sufficient to reduce the luciferase reporter activity by 50% (compare curves shown in Fig. 3a with those in Fig. 3b).

Characterization of the species-dependent action of type I IFN

The species-dependent action of type I IFN was analysed by incubating human, canine, murine, and chicken cells for 20 hours with 5 units of type I IFN from either the homologous species or a different one. When cells were treated with the respective homologous IFN an antiviral state was induced as indicated by the lack of GFP expression 6 hours post infection with VSV*ΔG(Luc) (Fig. 4a). In contrast, untreated cells or cells that

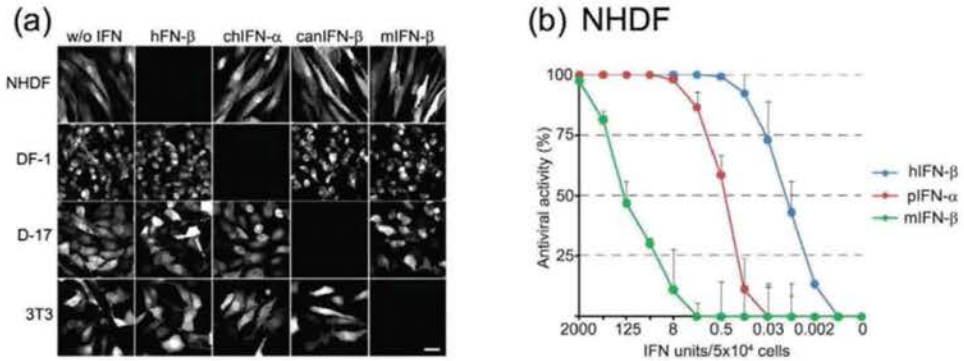

Figure 4. Type I IFNs act in a species-specific manner. (a) Cells derived from different species were treated for 20 h with the indicated type I IFNs (5 units/well) and subsequently infected with VSV*ΔG(Luc). Expression of GFP was monitored 6 h post infection by fluorescence microscopy. Bar, 30 μm. (b) NHDF were incubated for 20 h with serial fourfold dilutions of human, porcine and murine type I IFNs. The cells were subsequently infected with VSV*ΔG(Luc) for 5 h and firefly luciferase activity was recorded in the cell lysates.
doi:10.1371/journal.pone.0025858.g004

had received type I IFN from a different species were not protected and showed GFP expression accordingly. To compare the effects of different concentrations of homologous and heterologous type I IFN on human cells, we treated NHDF for 20 hours with serial dilutions of human, porcine, and murine type I IFN prior to infection with VSV*ΔG(Luc). Firefly luciferase reporter activity in infected cell lysates indicated that porcine IFN-α is active in NHDF albeit at reduced levels compared to human IFN-β (Fig. 4b; $p \leq 0.0049$ for the 0.008 to 2.0 units range). Murine IFN-β showed an even lower activity on NHDF (ED_{50} of 500 units per 5×10^4 NHDF cells; $p \leq 0.0003$ for the 0.008 to 500 units range). These results demonstrate that type I IFNs act in a species-dependent manner and accentuate the need for selecting appropriate cell lines to determine their activity.

Thermal and pH stability of type I and type III IFN

We often encounter the problem that the activity of type I IFN has to be determined in a sample containing live virus. As virus infection may interfere with the bioassay, it has to be inactivated before the assay is performed, preferentially without touching the activity of type I IFN. As many viruses can simply be inactivated by treatment with heat, we first analysed the thermal stability of human IFN-β using the VSV*ΔG(Luc) bioassay. The antiviral activity of human IFN-β was fully maintained when the cytokine was incubated for 30 min at 50°C (Fig. 5a). At 60°C, 99% of the activity was preserved ($p = 0.021$). At 70°C, the activity of human IFN-β dropped to 83% ($p = 0.0017$). Incubation at higher temperatures (80°C and 90°C) affected the activity more drastically, although some activity was still left at these temperatures. Only when human IFN-β was heated to 100°C for 30 min, activity was completely abolished. In contrast to human IFN-β, porcine IFN-α was completely inactivated at 70°C ($p < 0.0001$), whereas human IFN-λ (IL-29), a type III IFN, showed even higher residual activity at 80°C and 90°C ($p < 0.001$), suggesting that these cytokines have different physicochemical properties.

To study the sensitivity of type I and type III IFNs to conditions of extreme pH, human IFN-β and human IFN-λ were treated for 30 min with either 0.1 M HCl, 0.1 M NaOH or H_2O, adjusted to neutral pH, and assayed on NHDF and Calu-3 cells, respectively. It turned out that the antiviral activity of human IFN-β was not significantly affected by acid ($p > 0.05$) (Fig. 5b), confirming the previously noted acid-stability of type I IFNs [31]. IFN-λ showed similar properties as antiviral activity was maintained following treatment with 0.1 M HCl (Fig. 5c). In contrast, alkaline treatment significantly reduced the activity of IFN-λ ($p < 0.05$ for the 250 − 1 ng/ml range), whereas IFN-β was not affected ($p > 0.05$) (Fig. 5b). Thus, treatment with acid may be employed to inactivate virus in a test sample without affecting the activity of type I and type III IFNs. On the other hand, alkaline may be used to differentiate between type I and type III IFNs.

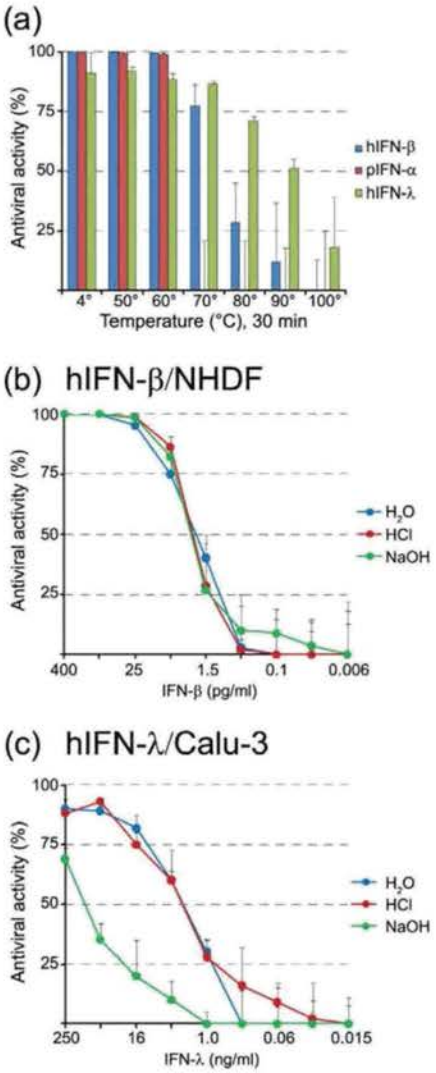

Figure 5. Analysis of type I IFN stability. (a) Human IFN-β and porcine IFN-α (each at 800 units/ml) were heated for 30 min at the indicated temperatures and thereafter diluted 1:10 with medium containing 5% FBS. The heat-treated IFN preparations were incubated for 20 h with NHDF and PK-15 cells, respectively (8 units per 5×10^4 cells). Luciferase reporter activity was determined in cell lysates 5 hours post infection with VSV*ΔG(Luc). (b) Human IFN-β and (c) human IFN-λ were incubated for 30 min at 20°C with either 0.1 M HCl, 0.1 M NaOH, or H_2O, and then adjusted to neutral pH. NHDF and Calu-3 cells were incubated for 20 h with fourfold serial dilutions of HCl/NaOH-treated IFN-β and IFN-λ, respectively, and subsequently infected with VSV*ΔG(Luc). Firefly luciferase activity was determined in cell lysates 5 h post infection.
doi:10.1371/journal.pone.0025858.g005

Discussion

Conventional bioassays take advantage of the antiviral activity of type I IFN to measure the inhibition of virus-induced cytopathic effects in cell culture [14]. In this study, we presented an improved bioassay by employing a recombinant VSV replicon equipped with two reporter proteins. This assay proved to be advantageous over the conventional assay with respect to biosafety, sensitivity, and time requirements.

The use of cytopathic viruses in conventional type I IFN bioassays makes appropriate biosafety measures necessary to reduce the risk of unwanted virus transmission and infection. In this regard, the VSV*ΔG(Luc) replicon particles can be regarded as biosafe. Since the modified VSV genome lacks the envelope glycoprotein (G) gene, VSV*ΔG(Luc) is propagated on helper cells providing the G glycoprotein *in trans* [23]. The replicon particles produced on these cells can run a single cycle of infection but

cannot produce any infectious progeny [28]. Another aspect contributing to biosafety is that the RNA replicon replicates exclusively in the cytosol and does not produce cDNA intermediates. Thus, in the case of an accidental infection any risk of recombination with or integration into host chromosomal DNA can be excluded.

Virus preparations that are used for IFN bioassays must not contain any type I IFN which may distort the results. In addition, the viruses should not induce IFN in infected reporter cells to assure that the effects measured are solely due to the exogenous IFN added. Both criteria are fulfilled for VSV*ΔG(Luc). The helper cells used to propagate the replicon particles are derived from BHK-21 cells, which are defective in the synthesis of type I IFN [32]. In addition, the VSVΔG replicon does not induce type I IFN in infected reporter cells, because the VSV matrix protein efficiently blocks the nuclear export of cellular mRNA including the IFN mRNA [30,33].

Conventional type IFN bioassays often take 24 hours or more to be completed as they rely on the inhibition of cytopathic effects. In contrast, the bioassay presented here takes advantage of the firefly luciferase reporter, which can be detected with high sensitivity long before a cytopathic effect is apparent. Although the luciferase reporter enabled us to unambiguously quantify the IFN-mediated reduction of virus replication, we frequently observed that the standard deviations for the antiviral activities increased when the cells were treated with low amounts of type I IFN. This likely reflects the high reporter gene expression at low levels of type I IFN and the inaccuracy associated with pipetting small volumes (6 µl).

The engagement of a common cellular receptor by type I IFNs leads to activation of the JAK/STAT pathway and transcriptional induction of several genes with antiviral activity [1,2]. It is common practice that cells are incubated with type I IFN for several hours to induce an antiviral state [15,19]. Our findings suggest that an antiviral state can be detected much earlier. For example, treatment of NHDF with 1 unit of human IFN-β for 1 hour and subsequent infection with VSV*ΔG(Luc) for 5 hours was sufficient to suppress firefly reporter expression by 50%, even though the effective dose was further lowered with longer incubation times. While DF-1 fibroblasts responded to chicken IFN-α with dose response kinetics similar to the one observed with human IFN-β on NHDF, PK-15 cells responded to porcine type I IFN in a much slower way. Thus, compared to conventional bioassays VSV*ΔG(Luc) may allow quantification of type I IFN in a considerably shorter time provided an appropriate cell line has been selected. The selection of a suitable cell line is also important with respect to the species it is derived from, as full activity of type I IFN was only observed with cells from the corresponding species. Since VSV is able to infect a broad spectrum of mammalian and avian cells, the new bioassay may be used to determine the bioactivity of type I IFNs from many different animals.

Although type I IFNs are the predominant cytokines with antiviral activity [34], it cannot be excluded that test samples contain other cytokines that inhibit VSV replication. Indeed, using the VSV*ΔG(Luc) replicon assay, it was possible to quantify the antiviral activity of IFN-λ (Il-29), a type III IFN. This raises the important question of how to distinguish between different antiviral cytokines? Certainly, neutralizing antibodies may be employed to specify the antiviral cytokine present in the sample. In addition, the extraordinary acid-stability of type I IFNs may be used to differentiate them from acid-labile cytokines such as type II IFNs [35]. However, acid may not be used to distinguish between type I and type III IFNs as IFN-λ proved to be acid-stable as well. Since IFN-λ but not IFN-β was sensitive to 0.1 M NaOH, treatment with alkaline may be used instead. However, the conditions of treatment still have to be optimized to guarantee the complete inactivation of type III IFNs while maintaining the activity of type I IFNs.

In addition to antiviral cytokines, test samples may also contain unknown viruses that potentially interfere with the bioassay. Treatment with heat or acid may be used to inactivate these viruses without affecting the bioactivity of type I and type III IFNs. However, as heat-inactivated influenza viruses still may be able to induce type I IFN [36], virus inactivation by acid may be more convenient.

The correct and reliable determination of type I IFN biological activity is an important issue. The new bioassay presented in this study represents an attractive alternative to conventional type I IFN bioassays that work with cytotoxic live viruses. VSV*ΔG(Luc) is easily produced and handled under BSL-1 conditions. The activity of the replicon can be easily determined and standardized taking advantage of the two reporter proteins. It may be stored for prolonged time in lyophilized form without losing its activity. Finally, the proven sensitivity, rapidity, and accurateness of the assay recommends it for the determination of type I IFN from a number of mammalian and avian species. Finally, the test may be further developed to quantify the antiviral activity of other cytokines such as type II and type III IFNs.

Acknowledgments

We thank Peter Stäheli, University of Freiburg, Philippe Plattet, University of Bern, and Nicolas Ruggli, IVI Mittelhäusern, for providing recombinant type I IFN.

Author Contributions

Conceived and designed the experiments: GZ. Performed the experiments: MBR GZ. Analyzed the data: GZ. Wrote the paper: GZ.

References

1. Der SD, Zhou A, Williams BR, Silverman RH (1998) Identification of genes differentially regulated by interferon alpha, beta, or gamma using oligonucleotide arrays. Proc Natl Acad Sci U S A 95: 15623–15628.
2. Schoggins JW, Wilson SJ, Panis M, Murphy MY, Jones CT, et al. (2011) A diverse range of gene products are effectors of the type I interferon antiviral response. Nature 472: 481–485.
3. Sadler AJ, Williams BR (2008) Interferon-inducible antiviral effectors. Nat Rev Immunol 8: 559–568.
4. Maher SG, Romero-Weaver AL, Scarzello AJ, Gamero AM (2007) Interferon: cellular executioner or white knight? Curr Med Chem 14: 1279–1289.
5. Takaoka A, Hayakawa S, Yanai H, Stoiber D, Negishi H, et al. (2003) Integration of interferon-alpha/beta signalling to p53 responses in tumour suppression and antiviral defence. Nature 424: 516–523.
6. Vosoughi R, Freedman MS (2010) Therapy of MS. Clin Neurol Neurosurg 112: 365–385.
7. Tsubota A, Fujise K, Namiki Y, Tada N (2011) Peginterferon and ribavirin treatment for hepatitis C virus infection. World J Gastroenterol 17: 419–432.
8. Ferrantini M, Capone I, Belardelli F (2007) Interferon-alpha and cancer: mechanisms of action and new perspectives of clinical use. Biochimie 89: 884–893.
9. Rizza P, Moretti F, Belardelli F (2010) Recent advances on the immunomodulatory effects of IFN-alpha: implications for cancer immunotherapy and autoimmunity. Autoimmunity 43: 204–209.
10. Malucchi S, Gilli F, Caldano M, Sala A, Capobianco M, et al. (2011) One-year evaluation of factors affecting the biological activity of interferon beta in multiple sclerosis patients. J Neurol 258: 895–903.
11. Sommereyns C, Paul S, Staeheli P, Michiels T (2008) IFN-lambda (IFN-lambda) is expressed in a tissue-dependent fashion and primarily acts on epithelial cells in vivo. PLoS Pathog 4: e1000017.
12. Mordstein M, Neugebauer E, Ditt V, Jessen B, Rieger T, et al. (2010) Lambda interferon renders epithelial cells of the respiratory and gastrointestinal tracts resistant to viral infections. J Virol 84: 5670–5677.
13. Pott J, Mahlakoiv T, Mordstein M, Duerr CU, Michiels T, et al. (2011) IFN-lambda determines the intestinal epithelial antiviral host defense. Proc Natl Acad Sci U S A 108: 7944–7949.

14. Meager A (2002) Biological assays for interferons. J Immunol Methods 261: 21–36.
15. Perler L, Pfister H, Schweizer M, Peterhans E, Jungi TW (1999) A bioassay for interferon type I based on inhibition of Sendai virus growth. J Immunol Methods 222: 189–196.
16. Park MS, Shaw ML, Munoz-Jordan J, Cros JF, Nakaya T, et al. (2003) Newcastle disease virus (NDV)-based assay demonstrates interferon-antagonist activity for the NDV V protein and the Nipah virus V, W, and C proteins. J Virol 77: 1501–1511.
17. Kopecky-Bromberg SA, Martinez-Sobrido L, Frieman M, Baric RA, Palese P (2007) Severe acute respiratory syndrome coronavirus open reading frame (ORF) 3b, ORF 6, and nucleocapsid proteins function as interferon antagonists. J Virol 81: 548–557.
18. Valmas C, Grosch MN, Schumann M, Olejnik J, Martinez O, et al. (2010) Marburg virus evades interferon responses by a mechanism distinct from ebola virus. PLoS Pathog 6: e1000721.
19. Kuri T, Habjan M, Penski N, Weber F (2010) Species-independent bioassay for sensitive quantification of antiviral type I interferons. Virol J 7: 50.
20. Vrolijk JM, Kaul A, Hansen BE, Lohmann V, Haagmans BL, et al. (2003) A replicon-based bioassay for the measurement of interferons in patients with chronic hepatitis C. J Virol Methods 110: 201–209.
21. Larocque L, Bliu A, Xu R, Diress A, Wang J, et al. (2011) Bioactivity determination of native and variant forms of therapeutic interferons. J Biomed Biotechnol 2011. 174615 p.
22. Schwarz H, Harlin O, Ohnemus A, Kaspers B, Staeheli P (2004) Synthesis of IFN-beta by virus-infected chicken embryo cells demonstrated with specific antisera and a new bioassay. J Interferon Cytokine Res 24: 179–184.
23. Hanika A, Larisch B, Steinmann E, Schwegmann-Wessels C, Herrler G, et al. (2005) Use of influenza C virus glycoprotein HEF for generation of vesicular stomatitis virus pseudotypes. J Gen Virol 86: 1455–1465.
24. Balmelli C, Vincent IE, Rau H, Guzylack-Piriou L, McCullough K, et al. (2005) Fc gamma RII-dependent sensitisation of natural interferon-producing cells for viral infection and interferon-alpha responses. Eur J Immunol 35: 2406–2415.
25. Schultz U, Rinderle C, Sekellick MJ, Marcus PI, Staeheli P (1995) Recombinant chicken interferon from Escherichia coli and transfected COS cells is biologically active. Eur J Biochem 229: 73–76.
26. Rothlisberger A, Wiener D, Schweizer M, Peterhans E, Zurbriggen A, et al. (2010) Two domains of the V protein of virulent canine distemper virus selectively inhibit STAT1 and STAT2 nuclear import. J Virol 84: 6328–6343.
27. Schnell MJ, Buonocore L, Whitt MA, Rose JK (1996) The minimal conserved transcription stop-start signal promotes stable expression of a foreign gene in vesicular stomatitis virus. J Virol 70: 2318–2323.
28. Kalhoro NH, Veits J, Rautenschlein S, Zimmer G (2009) A recombinant vesicular stomatitis virus replicon vaccine protects chickens from highly pathogenic avian influenza virus (H7N1). Vaccine 27: 1174–1183.
29. Bloor S, Maelfait J, Krumbach R, Beyaert R, Randow F (2010) Endoplasmic reticulum chaperone gp96 is essential for infection with vesicular stomatitis virus. Proc Natl Acad Sci U S A 107: 6970–6975.
30. Hoffmann M, Wu YJ, Gerber M, Berger-Rentsch M, Heimrich B, et al. (2010) Fusion-active glycoprotein G mediates the cytotoxicity of vesicular stomatitis virus M mutants lacking host shut-off activity. J Gen Virol 91: 2782–2793.
31. Jariwalla R, Grossberg SE, Sedmak JJ (1975) The influence of physicochemical factors on the thermal inactivation of murine interferon. Arch Virol 49: 261–272.
32. Taylor-Papadimitriou J, Stoker M (1971) Effect of interferon on some aspects of transformation by polyoma virus. Nat New Biol 230: 114–117.
33. Faria PA, Chakraborty P, Levay A, Barber GN, Ezelle HJ, et al. (2005) VSV disrupts the Rae1/mrnp41 mRNA nuclear export pathway. Mol Cell 17: 93–102.
34. Randall RE, Goodbourn S (2008) Interferons and viruses: an interplay between induction, signalling, antiviral responses and virus countermeasures. J Gen Virol 89: 1–47.
35. Virelizier JL, Allison AC, de Maeyer E (1977) Production by mixed lymphocyte cultures of a type II interferon able to protect macrophages against virus infection. Infect Immun 17: 282–285.
36. Isaacs A, Lindenmann J (1957) Virus interference. I. The interferon. Proc R Soc Lond B Biol Sci 147: 258–267.

Position Paper

Selection and interpretation of clinical pathology indicators of hepatic injury in preclinical studies

L. Boone, D. Meyer, P. Cusick, D. Ennulat, A. Provencher Bolliger, N. Everds, V. Meador, G. Elliott, D. Honor, D. Bounous, H. Jordan, for the Regulatory Affairs Committee of the American Society for Veterinary Clinical Pathology

Abstract: This position paper delineates the expert recommendations of the Regulatory Affairs Committee of the American Society for Veterinary Clinical Pathology for the use of preclinical, clinical pathology endpoints in assessment of the potential for drug-induced hepatic injury in animals and humans. Development of these guidelines has been based on current recommendations in the relevant preclinical and human clinical trial literature; they are intended to provide a method for consistent and rigorous interpretation of liver-specific data for the identification of hepatic injury in preclinical studies and potential liability for hepatic injury in human patients. (*Vet Clin Pathol.* 2005;34:182–188)

Key Words: ALT, hepatic injury, hepatotoxicity, liver, preclinical safety assessment

Detection of potential human hepatic injury is a major challenge in preclinical pharmaceutical research and can present a severe impediment to the development of novel, efficacious, and safe drugs. The majority of drugs that cause hepatic injury in preclinical studies do not progress to clinical trials or are developed with substantial patient monitoring.[1,2] Integrated evaluation of all study data, including the results of alanine aminotransferase (ALT) measurement and liver histology, has been shown to be crucial for the identification of hepatic injury in preclinical studies as an indicator of potential liability for hepatic injury in humans. However, a retrospective review of 548 compounds marketed between 1975 and 1999 indicated that 10.2% were withdrawn or acquired a black box warning,[3] with hepatic injury cited as a predominant reason for withdrawal or addition of a warning to the label. Growing concerns about adverse hepatic drug reactions have led to commentaries[4] concerning the adequacy of current practices for evaluating hepatic injury in preclinical studies. Similar concerns have resulted in the release of draft position papers regarding the detection of drug-induced liver injury from agencies responsible for the investigation of the safety and efficacy of human health products within the United States (Federal Drug Administration, FDA)[5] and Canada (Health Canada).[6] Recently, the agency responsible for evaluation of human health products in Europe, the European Medicines Agency (EMEA), also indicated their intent to draft a guidance paper for detection of drug-induced liver injury for human health products.[7]

The authors are Diplomates of the American College of Veterinary Pathologists in Clinical Pathology (Boone, Meyer, Cusick, Ennulat, Bolliger, Everds, Meador, Elliott, Honor, Bounous, and Jordan) and Anatomic Pathology (Cusick, Ennulat, Meador); the American College of Veterinary Internal Medicine (Meyer); and the American Board of Toxicology (Cusick). The Regulatory Affairs Committee is a standing committee of the American Society for Veterinary Clinical Pathology (ASVCP), Madison, WI, USA. An earlier but not substantively different version of this paper was submitted to the European Medicines Agency (EMEA) to provide guidance in the preparation of recommendations for the detection of drug-induced liver injury for human health products in Europe. Corresponding author: Laura I. Boone, DVM, PhD (boone_laura_I@lilly.com).

The draft documents from the FDA and Health Canada and the notice from the EMEA suggest that the introduction of novel biomarkers and assays (eg, transcript profiling, proteomics, and metabonomics) may enhance detection of hepatic injury in preclinical studies. However, before these techniques can be incorporated into the assessment of hepatic injury in a preclinical study, they must undergo a robust validation process that encompasses traditional methods of assay validation (ie, sensitivity, specificity, accuracy, and precision) as well as characterization of biologic context, variability, species relevance, and linkage to a clinical endpoint. Therefore, the best method for identification of potential drug-induced hepatic injury in preclinical studies remains the integrated evaluation of clinical pathology parameters and results of histologic evaluation with other preclinical study data. As described above, ALT is a critical parameter for the identification of potential drug-induced hepatic injury in both preclinical studies and human patients. For this reason, the measurement and interpretation of serum ALT activity is a cornerstone of these updated recommendations for the identification of hepatic injury in preclinical studies.

Objective

This position paper was prepared by members of the Regulatory Affairs Committee of the American Society for Veterinary Clinical Pathology (ASVCP) for submission to the EMEA Committee for Medicinal Products for Human Use (CHMP) for use during the preparation of their hepatotoxicity position paper. The Committee's goal was to provide expert recommendations on the use of clinical pathology data for identification of potential drug-induced hepatic injury in preclinical toxicity studies.

The Regulatory Affairs Committee is composed of veterinary clinical pathologists with expertise in interpretation of clinical pathology data from preclinical studies in the safety assessment of xenobiotics (ie, food additives, chemicals, and drugs) for domestic and international pharmaceutical, chemical, and research companies. The committee's primary charge is to respond to regulatory guidance from national and international regulatory agencies regarding the use and interpretation of clinical pathology parameters in safety assessment studies.

Included within this article are recommendations for appropriate parameters for identification of hepatic injury in multiple laboratory animal species (rat, dog, and nonhuman primate [NHP]) and guidelines for interpretation of those parameters in preclinical studies to provide the best possible detection of potential adverse effects in humans. A review of previously published recommendations of clinical pathology testing in preclinical studies, current recommended parameters, and the use and limitations of additional parameters not routinely assessed (clinical chemistry parameters, novel biomarkers, and novel bioassays) also are provided.

Previously Published Recommendations for Clinical Pathology Testing in Toxicity and Safety Studies

Minimal recommendations for the panel of clinical chemistry analytes to be measured as part of the clinical pathology evaluation of laboratory animals in toxicology and safety studies have been established and published.[8] The recommendations include the times for sample collection and a list of parameters in preclinical repeat-dose toxicology or safety studies for identification of hepatic injury. Of note, the guidelines for timing and frequency of sample collection were minimal recommendations that could be modified based on species, study objectives and duration, and the biological activity of the compound. Following is a summary of these previously published recommendations:

- For studies with either rodent or nonrodent species (ie, dogs and NHPs), clinical pathology parameters should be evaluated at study termination. If a compound-free recovery group is included in the study design, clinical pathology evaluation should also occur at termination of the recovery period.
- In rats, interim evaluation in long-duration preclinical studies is generally considered unnecessary provided the clinical pathology evaluation is conducted in studies of shorter duration using doses that meet or exceed those used in the study of longer duration. Predose clinical pathology evaluations are not recommended in rats because of genetic homogeneity within laboratory rat strains and the relatively large number of animals per group in rat studies.
- In nonrodent species, predose and ≥ 1 interim evaluation of clinical pathology parameters are recommended because of the small number of animals per group and the interanimal variability. Additionally, in studies of <6 weeks duration, evaluation of clinical pathology parameters is recommended within 7 days of the initiation of dosing.
- A minimum of 2 of the following serum parameters for the identification of hepatocellular injury should be measured in preclinical studies: ALT, aspartate aminotransferase (AST), sorbitol dehydrogenase (SDH), glutamate dehydrogenase (GDH), or total bile acids (TBA). Similarly, ≥ 2 of the following serum parameters for identification of hepatobiliary injury should be measured: alkaline phosphatase (ALP), γ-glutamyltransferase (GGT), 5′-nucleotidase (5′-NT), total bilirubin (TBILI), or TBA.

Updated Recommendations for Clinical Pathology Parameters of Hepatic Injury in Preclinical Studies

The recommendations of this committee for identification of hepatic injury in preclinical toxicology or safety studies in rats, dogs, and NHPs are presented below. All of these recommended parameters are included in the minimal recommendations for clinical pathology testing in preclinical studies that were published previously (as presented above).[8] Furthermore, these recommended parameters are included within the list of parameters recommended by a committee within the National Academy of Clinical Biochemistry (NACB) and approved by the American Association for the

Study of Liver Diseases (AASLD) for identification of hepatic injury in human beings. This list comprises ALT, AST, and ALP activities, and TBILI, direct bilirubin, total protein, and albumin concentrations.[9] The correlation of these recommended parameters with those recommended for identification of hepatic injury in humans makes them suitable and applicable parameters for the evaluation of potential hepatic injury in preclinical studies. It is important to note that this recommended list could be modified at the discretion of the veterinary clinical pathologist to include parameters that are optimized to the species of interest or to specific patterns of hepatic injury.

Indicators of hepatocellular injury: ALT and AST

The aminotransferase enzymes, ALT and AST, also termed transaminases, are recommended for the assessment of hepatocellular injury in rats, dogs, and NHPs in preclinical studies. ALT is considered a more specific and sensitive indicator of hepatocellular injury than AST in rats, dogs, and NHPs. The magnitude of ALT increase is usually greater than that of AST when both are increased due to hepatic injury, in part because of the longer half-life of ALT and the greater proportion of AST that is bound to mitochondria.[10–13] Hepatic causes of increased serum ALT activity, with or without increased AST activity, include hepatocellular necrosis, injury, or regenerative/reparative activity.[14–16] Decreases in ALT activity have been observed with concurrent hepatic microsomal enzyme induction in the rat.[17] Increases in ALT activity also have been reported with concurrent hepatic microsomal induction in the dog and rat but were not considered indicative of hepatic injury because no substantive concurrent changes in liver histology or liver weight were observed.[18,19] Increased serum ALT activity can also be affected by extrahepatic factors. Muscle injury can cause increases in serum transaminase activity, but AST is generally higher than ALT when both are concurrently increased.[16,20] Procedure-related handling and type of restraint also can cause increases in AST activity with or without increases in ALT activity in mice and NHPs.[21,22] Therefore, type of restraint and extent of handling should be considered in the evaluation of increased AST activity, with or without increased ALT activity.

ALT is considered a more specific and sensitive test of hepatocellular injury in humans, compared with other clinical pathology analytes.[9] Guidelines have been published for interpretation of ALT activity in humans in the absence of histologic data (ie, results from autopsy or liver biopsy). Specifically, >2× increases in ALT activity alone above the upper limit of normal (ULN) are considered indicative of hepatocellular injury whereas >3× increases in ALT accompanied by 2× increases above the ULN in TBILI concentration are indicative of more severe and potentially life-threatening hepatocellular injury.[14,23]

Supplemental indicators of hepatocellular injury: SDH and GDH

Serum SDH and GDH activities have been shown to be specific for liver injury.[13,24] The measurement of these supplemental enzymes is useful when additional indicators of hepatic pathology are desired or in species where ALT activity is either low or nonspecific such as swine, guinea pigs, some strains of rats, and woodchucks.[25,26] Of note, neither parameter is used routinely by physicians to evaluate human hepatic damage.

Indicators of hepatobiliary injury: ALP and TBILI

ALP and TBILI are recommended for the assessment of hepatobiliary injury in rats, dogs, and NHPs in preclinical studies. These recommended parameters are included within the group of parameters recommended for use in humans for identification of hepatic injury as listed above.[9]

In species used in preclinical studies, hepatobiliary pathology and bone growth/disease are the 2 most common causes of increased serum ALP activity. Increases in ALP activity due to hepatobiliary pathology generally precede increases in TBILI concentration in most species.[16,27,28] Increased ALP activity from the liver in the absence of cholestasis has been reported in dogs with increased endogenous or administered glucocorticoids[15,16,29] and in rats and dogs with concurrent microsomal enzyme induction.[17,19] In rats, intestinal ALP is the major circulating isoenzyme, so a transient increase in serum ALP may occur postprandially, whereas fasting can result in a decrease in serum ALP.[30,31] Decreases in ALP activity have been reported in rats with concurrent microsomal enzyme induction in the absence of changes in food consumption.[17]

In human beings, serum ALP activity increases with cholestasis but generally remains <3× the ULN.[32] Extrahepatic isoforms of ALP are present in bone, intestine, and placenta. Differentiating between hepatic and extrahepatic isoforms in human medicine is performed rarely, as the hepatic origin of the increased ALP can be confirmed with concurrent increases in other indicators of cholestasis such as GGT.[33]

Increases in the serum TBILI concentration are generally the result of bile retention subsequent to impairment of intrahepatic or extrahepatic bile flow (cholestasis), increased production associated with accelerated erythrocyte destruction, or altered bilirubin metabolism.[16,26,34,35] The unconjugated (indirect-reacting) fraction of bilirubin generated from the degradation of erythrocytes and the conjugated (direct-reacting) fraction together comprise the TBILI concentration. Bilirubin fractionation is generally only of value for exploring drug-related inhibition of the bilirubin-conjugating enzyme, uridine diphosphate glucuronosyltransferase (UGT1A1).[36–38] Concomitant bilirubinuria is supportive of an increase in the circulating conjugated bilirubin level due to cholestasis.

In human beings, consistent increases in TBILI <2× ULN or isolated increases >2× ULN are interpreted as a biochemical abnormality rather than as an indicator of hepatic injury. In contrast, repeated increases in conjugated bilirubin >2× ULN alone or with concurrent increases in AST and/or ALP activities are considered indicative of liver injury.[23]

Supplemental indicator of hepatobiliary injury: GGT

GGT is a canalicular enzyme whose serum activity is increased in cholestatic liver disease. Increases in circulating GGT activity can arise from impaired bile flow and biliary epithelial

necrosis.[15,26,39,40] An increase in circulating GGT without evidence of biliary pathology is associated with the use of some anticonvulsant medications in humans and dogs and an increase in circulating glucocorticoids in dogs and rats.[18,41–43] In both dogs and rats, GGT is a less sensitive but more specific indicator of cholestasis when compared with ALP.[31,43]

Concurrent increases in GGT and ALP activities are considered more indicative of a hepatic enzyme source but do not exclude concurrent bone disease.[9] Currently, there are no established guidelines for interpretation of GGT activity in drug-induced hepatic injury in human beings.[23]

Supplemental indicators of hepatic synthetic function

Total protein, albumin, triglycerides, cholesterol, glucose, urea, activated partial thromboplastin time, and prothrombin time are considered as supplemental indicators of hepatic synthetic function. In drug-induced hepatic injury, evaluation of these parameters may be instrumental in the identification of deleterious effects on glucose metabolism and hepatic synthesis of proteins, lipids, and coagulation factors.[16] Furthermore, with the exception of triglycerides, these parameters are included in the minimal recommendations for clinical pathology testing in preclinical studies.[8]

Hepatic parameters not routinely assessed in preclinical studies

Several additional analytes are available that, for a number of reasons, are not routinely assessed in preclinical studies. These include: ALP isoenzymes, 5′NT, α-glutathione-(*S*)-transferase (αGST), lactate dehydrogenase (LDH), and TBA. In routine preclinical safety studies, the determination of tissue-specific ALP isoforms/isoenzymes (liver, bone, intestine, and in dogs, steroid-induced) generally provide no additional information beyond that provided by the measurement of total ALP activity. 5′-NT and αGST assays are used to a limited extent in toxicity and safety studies and are not widely used by physicians to evaluate human hepatic damage. 5′NT lacks additional value beyond that offered by the measurement of ALP and GGT activity.[26] The measurement of αGST does not offer additional information beyond the measurement of ALT.[44] LDH is an enzyme present in most tissues and lacks hepatic specificity. Serum TBA concentration is measured as an indicator of hepatic function because bile acids are synthesized in the liver, transported to the intestine in bile, and absorbed via the enterohepatic circulation. However, serum TBA concentration is generally less sensitive for the evaluation of hepatocellular injury and cholestasis than are routine enzyme activities.[13,16,34]

Novel bioassays and biomarkers

Novel safety and efficacy biomarkers are needed to enhance clinical diagnostic capability as well as reduce drug development costs and late-stage attrition within the pharmaceutical industry.[45] The increased use of transcript profiling, proteomic, and metabonomic platforms in drug development will undoubtedly lead to the identification and greater implementation of novel bioassays in future preclinical and clinical studies. These biomarkers may be highly varied technologically, ranging from microarray and differential gene or protein expression "signatures" based on polymerase chain reaction (PCR) assays to measurement of serum, plasma, or urinary proteins or metabolites. Regardless of the technologic platform, validation and implementation of each candidate biomarker or bioassay requires a robust validation process that encompasses traditional methods of assay validation (ie, sensitivity, specificity, accuracy, and precision) as well as characterization of biologic context, variability, species relevance, and linkage to a clinical endpoint.[46,47]

Recommendations for the Interpretation of Clinical Pathology Data in the Identification of Hepatic Injury in Preclinical Studies in Rats, Dogs, and Non-human Primates

Expert recommendations were developed for the interpretation of clinical pathology data in the identification of potential drug-induced hepatic injury and in preclinical studies. Definitions for frequently used terms in preclinical toxicology studies are included below and, with the exception of the definition of "NOAEL," are adopted from those previously published.[48]

It is important to note that criteria used for the interpretation of clinical pathology data in preclinical studies differ from those used in the clinical evaluation of humans exposed to xenobiotics. Specifically, interpretation of clinical pathology data in human clinical trials is contingent on the magnitude (or fold) increase of the value above the upper limit of the population reference interval or the known ULN for that individual. This is not an appropriate approach to the assessment of toxicity in preclinical trials. Rather, compound-related effects on clinical pathology values in preclinical trials in rats, dogs, and NHPs are determined by comparison with mean and individual animal data from concurrent controls[8] using reference intervals developed from historic control data to place the changes in context. In dogs and NHP, comparison of interim, terminal, or reversibility data with pretreatment data is also useful for determining compound-related effects and their reversibility.

Terminology of effect level

No observed-effect level (NOEL). "The highest exposure level at which there are no effects (adverse or nonadverse) observed in the exposed population, when compared with its appropriate control."[48] Compound-related changes therefore define the NOEL.

Adverse. "A biochemical, morphological, or physiological change (in response to a stimuli) that either singly or in combination adversely affects the performance of the whole organism or reduces the organism's ability to respond to an additional environmental challenge."[48] An adverse hepatic effect identified within the confines of a study should be considered as an indicator of a potential liability for hepatic injury in humans.

No observed-adverse-effect level (NOAEL). For the purpose of identifying hepatic injury in preclinical studies, we propose the following definition of NOAEL: the level of exposure

within a preclinical study at which there are no adverse effects. Specifically, the NOAEL is the level of exposure at which there are no toxicologically relevant increases in the incidence or severity of effects between compound-treated and control populations. Compound-related findings must be identified as *adverse* to establish the NOAEL. Nonadverse changes are compound-related but of insufficient magnitude to be adverse and often consist of normal physiologic compensatory mechanisms or anticipated pharmacologic activity. The proposed definition of NOAEL has been modeled after a previous definition.[48] Importantly, this definition differs from that of Lewis et al, in that we propose that statistical significance alone does not indicate that a change in the value of a parameter is compound-related nor does it indicate toxicologic or biologic relevance.

General guidelines for clinical pathology data interpretation

Rendering an opinion regarding the classification and interpretation of the finding is the obligation of the veterinary clinical pathologist. General guidelines for interpretation of clinical pathology parameters are as follows:

- Determination of the relationship of a change in the value of a clinical pathology parameter to compound administration (ie, is it compound-related?) and interpretation of its biologic or toxicologic importance (ie, is it adverse?) are accomplished through comparison of individual animal and group mean data with concurrent controls in all preclinical studies, regardless of species. In studies using dogs and NHPs, it is essential that the determination of the relationship of the finding to the compound and interpretation of the magnitude of change also incorporate comparisons of post-treatment changes to pretreatment values.

- Statistical analyses can be a useful tool to aid in data interpretation; however, statistical significance alone does not indicate that the change in the value of a parameter is compound-related nor does it indicate toxicologic or biologic relevance.[8,15] In dogs and NHPs, statistical analysis of changes in clinical pathology data is further complicated by interindividual and intraindividual variability and by the low number of animals per dose group. For these reasons, the use of statistical analysis in the evaluation of clinical pathology data augments but does not replace comparisons of individual data with concurrent controls in all species, nor does it replace comparisons of individual data with pretreatment values in dogs and NHPs. Therefore, the role of the veterinary clinical pathologist is to identify the relationship of the finding to the compound and its biologic relevance based on individual and group mean data compared with concurrent control data and, in dogs and NHPs, to pretreatment values.

- Clinical pathology parameters cannot be evaluated in isolation. The determination of whether drug-induced clinical pathology findings are adverse is based on the magnitude of the changes in all concurrently evaluated pathology parameters, as well as in-life observations, metabolism data, and pharmacologic class effects. In-life observations and body weight and food consumption data provide additional indicators of compound-related and adverse effects on treated animals. Other compound-related information, such as potential interference, hepatic microsomal enzyme data, and previous experience with the compound or related compounds in other species may be useful in interpreting clinical pathology indicators of hepatic effects. Concurrent evaluation of clinical pathology data with absorption, distribution, metabolism, and elimination (ADME) data and the results of safety pharmacology studies can help determine the relevance of the findings to human metabolism and safety. Concurrent evaluation of toxicokinetic data is helpful for the evaluation of individual animals with incongruous changes in clinical pathology values. Determination of changes after a drug-free period provides important evidence about the potential for reversibility of compound-related findings.

- Ultimately, concurrent evaluation of all data from the study results in the determination of the number of affected animals per dose group, dose-specific and/or gender-specific responses, and the reversibility of the changes. These data then are integrated to identify compound-related changes (NOEL) and compound-related adverse changes (NOAEL). Correlation of these study-specific interpretations with data from other studies in the same or alternative preclinical species provides important information for assessment of the risk profile for the human population.

Guidelines for interpreting changes in the values of specific hepatic parameters

As mentioned previously, guidelines have been published for the interpretation of ALT activity in humans when concurrent histologic data (ie, results from autopsy or liver biopsy) are not available. In contrast, numeric guidelines for the integrated interpretation of increases in ALT activity using all preclinical data have not been established in rats, dogs, and NHPs. However, general guidelines for the integrated interpretation of ALT with concurrent histologic changes or increases in other serum indicators of hepatocellular injury have been published.[49] Specifically, those guidelines recommend that increases in ALT activity that correlate with detrimental histologic changes should be considered adverse. Additionally, concurrent increases in the activity of ≥ 2 enzymatic indicators of hepatic injury also should be considered adverse. This document, however, does not provide guidance regarding the interpretation of increases in ALT activity alone in interim clinical pathology evaluations, when histologic evaluations are not routinely conducted, or at study termination in the absence of concurrent histologic changes. Therefore, the members of the Regulatory Affairs Committee, in consultation with colleagues from domestic and international companies with expertise in preclinical safety assessment, propose the following guidelines for the integrated assessment and interpretation of indicators of

hepatic injury in preclinical studies, to augment the previously-published general guidelines.

Serum ALT activity

An increase in serum ALT activity in the range of 2–4× or higher in individual or group mean data when compared with concurrent controls should raise concern as an indicator of potential hepatic injury unless a clear alternative explanation is found. When an increase in ALT activity of this magnitude is identified, it is the role of the veterinary clinical pathologist to determine whether the increase is adverse based on the integrated evaluation of all preclinical data. The data for this integrated evaluation consist of other clinical pathology indicators of hepatocellular and hepatobiliary injury and diminished hepatic function, organ weight, macroscopic and microscopic observations in liver and other tissues, enzyme induction data, and relationship to dose, duration, gender, species, and reversibility. This recommendation for evaluation of ALT data is presented as a range based on the slight variability of the concentration gradients between hepatic tissue and serum ALT enzyme activities for preclinical animal species and human beings. The magnitude of ALT enzyme activity in the liver of humans, dogs, and rats is approximately 35 U/g, 32 U/g, and 24 U/g, respectively, whereas the respective mean serum levels are approximately 16 U/L, 23 U/L, and 38 U/L. These data suggest that increases in serum ALT levels of 2–4× in the dog and rat are of sufficient magnitude to indicate extensive hepatocellular injury and serve as a harbinger of potential hepatic injury in humans based on the similar concentration gradients. Although a value for ALT activity in the liver of NHPs was not found for this comparison, the approximate mean serum value of 40 U/L in cynomolgus and rhesus monkeys suggests that a similar concentration gradient is likely for these species.[50–52]

Serum TBILI concentration

Increases in serum TBILI concentration in individual or group mean data when compared with concurrent control values should be critically evaluated and compared with other study data to exclude other factors that can influence serum bilirubin concentrations. Causes for increased bilirubin in the absence of cholestasis consist of hemolysis (in vivo or in vitro), sepsis, and drug-related inhibition of UGT1A1.[16,36–38] Once these causes have been eliminated, concurrent evaluation of bilirubin with other hepatic parameters is necessary to determine the relationship of the changes to the compound and their toxicologic or biologic significance. In the absence of changes in other hepatic parameters or hemolysis, increases in TBILI concentration alone are unlikely to be adverse. Additionally, the pattern of concurrent increases in ALT and bilirubin values should be critically evaluated in preclinical toxicity studies given the increased number of serious outcomes associated with this pattern of changes in humans.[14,23]

Serum ALP and GGT activities

Specific guidelines for interpretation of the magnitude of changes in ALP activity in preclinical studies are not provided because of the potential contribution of extrahepatic factors. These contributing factors include increases in intestinal or bone isoenzyme activity, primary compound-related effects (ie, glucocorticoid-induced ALP production in the dog), and increases in ALP activity with concurrent hepatic microsomal enzyme induction in dogs and rodents.[16,17,19,29]

Specific guidelines for interpretation of changes in GGT activity in preclinical studies are not provided because this parameter is recommended only as a supplemental test in certain species, particularly when evaluated with changes in ALP activity.

Summary

These recommendations for the selection of clinical pathology parameters and interpretation of liver-specific clinical pathology data provide a consistent and rigorous approach to the use of preclinical, clinical pathology endpoints in the identification and assessment of drug-induced hepatic injury in animals and the potential for hepatic injury in humans. These guidelines are based on the best available knowledge in the relevant preclinical and human clinical trial literature and the consensus expertise of veterinary clinical pathologists, who are responsible for and trained in the integrated assessment of clinical pathology data.

Acknowledgments

The authors gratefully acknowledge the contributions of colleagues working in domestic and international pharmaceutical, chemical, and research companies, as well others in the ASVCP, in the preparation and review of this document.

References

1. Amacher DE. Serum transaminase elevations as indicators of hepatic injuries following the administration of drugs. *Regul Toxicol Pharmacol.* 1998;27:119–130.
2. Kaplowitz N. Drug-induced liver disorders: implication for drug development and regulation. *Drug Saf.* 2001;24:483–490.
3. Lasser KE, Allen PD, Woohandler SJ, Himmelstein DU, Wolfe SM, Bor DH. Timing of new black box warnings and withdrawals for prescription medications. *JAMA.* 2002;287:2215–2220.
4. Alden C, Lin J, Smith P. Predictive toxicology technology for avoiding idiosyncratic liver injury. *PreClinica.* 2003;May/June:27–35.
5. FDA Working Group. *Nonclinical Assessment of Potential Hepatotoxicity in Man.* Rockville, MD: Center for Drug Evaluation and Research; 2000. Available at: http://www.fda.gov/cder/livertox/preclinical.pdf. Accessed July 11, 2005.
6. Health Canada Scientific Advisory Panel on Hepatotoxicity. *Draft Recommendations from the Scientific Advisory Panel Sub-groups on Hepatotoxicity: Hepatotoxicity of Health Products.* Ottawa, Canada: Health Canada; 2004. Available at: http://www.hc-sc.gc.ca/hpfb-dgpsa/tpd-dpt/sap_h_2004-07-26_dp_v6_e.html. Accessed July 11, 2005.
7. EMEA. *Concept Paper on the Development of a Committee for Medicinal Products for Human Use (CHMP) Guideline on Detection of Early Signals for Hepatotoxicity from Non-Clinical Documentation;* 2004. London, UK: European Agency for the Evaluation of Medicinal Products. Available at: http://www.emea.eu.int/pdfs/human/swp/001004en.pdf. Accessed July 11, 2005.
8. Weingand K, Brown G, Hall R, et al. Harmonization of animal clinical pathology testing in toxicity and safety studies. *Fundam Appl Toxicol.* 1996;29:198–201.
9. Dufour DR, Lott JA, Nolte FS, Gretch DR, Koff RS, Seeff LB. Diagnosis and monitoring of hepatic injury, I: performance characteristics of laboratory tests. *Clin Chem.* 2000;46:2027–2049.

10. Carakostas MC, Gossett KA, Church GE, Cleghorn BL. Evaluating toxin-induced hepatic injury in rats by laboratory results and discriminant analysis. *Vet Pathol.* 1986;23:264–269.
11. Boyd JW. Serum enzymes in the diagnosis of disease in man and animals. *J Comp Pathol.* 1988;98:381–404.
12. Blair PC, Thompson MB, Wilson RE, Esber HH, Maronpot RR. Correlation of changes in serum analytes and hepatic histopathology in rats exposed to carbon tetrachloride. *Toxicol Lett.* 1991;55:149–159.
13. Travlos GS, Morris RW, Elwell MR, Duke A, Rosenblum S, Thompson MB. Frequency and relationship of clinical chemistry and liver and kidney histopathology findings in 13-week toxicity studies in rats. *Toxicology.* 1996;107:17–29.
14. Zimmerman HJ. *Hepatotoxicity: The Adverse Effects of Drugs and Other Chemicals on the Liver.* 2nd ed. Philadelphia, PA: Lippincott, Williams, and Wilkins; 1999.
15. Hall RL. Principles of clinical pathology for toxicology studies. In: Hayes WA, ed. *Principles and Methods of Toxicology.* 4th ed. Philadelphia, PA: Taylor and Francis; 2001:1001–1038.
16. Meyer DJ, Harvey JW. Hepatobiliary and skeletal muscle enzymes and liver function tests. In: Meyer DJ and Harvey JW, eds. *Veterinary Laboratory Medicine: Interpretation and Diagnosis.* 3rd ed. St. Louis, MO: Saunders; 2004:169–192.
17. Boone L, Vahle J, Meador V, Brown D. The effect of cytochrome P450 enzyme induction on clinical pathology parameters in F344 rats [abstract]. *Vet Pathol.* 1998;35:417.
18. Amacher DE, Schomaker SJ, Burkhardt JE. The relationship among microsomal enzyme induction, liver weight, and histological change in rat toxicology studies. *Food Chem Toxicol.* 1998;36:831–839.
19. Amacher DE, Schomaker SJ, Burkhardt JE. The relationship among enzyme induction, liver weight, and histological change in beagle toxicology studies. *Food Chem Toxicol.* 2001;39:817–825.
20. Valentine BA, Blue JT, Shelley SM, Cooper BJ. Increased serum alanine aminotransferase activity associated with muscle necrosis in the dog. *J Vet Intern Med.* 1990;4:140–143.
21. Swaim LD, Taulor HW, Jersey GC. The effect of handling on serum ALT activity in mice. *J Appl Toxicol.* 1985;5:160–162.
22. Landi MS, Kissinger JT, Campbell SA, Kenney CA, Jenkins EL Jr. The effects of four types of restraint on serum alanine aminotransferase and aspartate aminotransferase in the *Macaca fascicularis*. *J Am Coll Toxicol.* 1990;9:517–523.
23. Benichou D. Criteria of drug-induced liver disorders: report of international consensus meeting. *J Hepatol.* 1990;11:272–276.
24. O'Brien PJ, Slaughter MR, Polley SR, Kramer K. Advantages of glutamate dehydrogenase as a blood marker of acute hepatic injury in rats. *Lab Anim.* 2002;36:313–321.
25. Hornbuckle WE, Graham ES, Roth L, Baldwin BH, Wickenden C, Tennant BC. Laboratory assessment of hepatic injury in the woodchuck (*Marmota monax*). *Lab Anim Sci.* 1985;35:376–381.
26. Hoffmann WE, Solter PF, Wilson BW. Clinical enzymology. In: Loeb WF, Quimby FW, eds. *The Clinical Chemistry of Laboratory Animals.* 2nd ed. Philadelphia, PA: Taylor and Francis; 1999:399–454.
27. Tennant BC. Hepatic function. In: Kaneko JJ, Harvey JW, Bruss ML, eds. *Clinical Biochemistry of Domestic Animals.* 5th ed. San Diego, CA: Academic Press; 1997:327–352.
28. Portmann BC, Nakanuma Y. Diseases of the bile ducts. In: MacSween RNM, Burt AD, Portmann BC, Ishak KG, Scheuer PJ, Anthony PP. eds. *Pathology of the Liver.* 4th ed. Philadelphia, PA: Churchill Livingstone; 2002:435–506.
29. Wiedmeyer CE, Solter PF, Hoffmann WE. Kinetics of mRNA expression of alkaline phosphatase isoenzymes in hepatic tissues from glucocorticoid-treated dogs. *Am J Vet Res.* 2002;63:1089–1095.
30. Elialim R, Mahmood A, Alpers DH. Rat intestinal alkaline phosphatase secretion into lumen and serum is coordinately regulated. *Biochim Biophys Acta.* 1991;1091:1–8.
31. Loeb WF. The rat. In: Loeb WF, Quimby FW, eds. *The Clinical Chemistry of Laboratory Animals.* 2nd ed. Philadelphia, PA: Taylor and Francis; 1999:33–48, 643–726.
32. Dufour DR, Lott JA, Nolte FS, Gretch DR, Koff RS, Seeff LB. Diagnosis and monitoring of hepatic injury, II: recommendations for use of laboratory tests in screening, diagnosis, and monitoring. *Clin Chem.* 2000;46:2050–2068.
33. Burt AD, Day CP. Pathophysiology of the liver. In: MacSween RMN, Burt AD, Portmann BC, Ishak KG, Scheuer PJ, Anthony PP, eds. *Pathology of the Liver.* 4th ed. London, UK: Churchill Livingstone; 2002:67–106.
34. Tennant BC. Assessment of hepatic function. In: Loeb WF, Quimby FW, eds. *The Clinical Chemistry of Laboratory Animals.* 2nd ed. Philadelphia, PA: Taylor and Francis; 1999:501–518.
35. Rothuizen J, Jaundice. In: Ettinger SJ, Feldman EC, eds. *Textbook of Veterinary Internal Medicine,* 5th ed. Philadelphia, PA: WB Saunders; 2000:210–212.
36. Zucker SD, Qin X, Rouster SD, et al. Mechanism of indinavir-induced hyperbilirubinemia. *Proc Natl Acad Sci U S A.* 2001;98:12671–12676.
37. Basu NK, Kole L, Owens IS. Evidence for phosphorylation requirement for human bilirubin UDP-glucuronosyltransferase (UGT1A1) activity. *Biochem Biophys Res Commun.* 2003;303:98–104.
38. Innocenti F, Ratain MJ. Irinotecan treatment in cancer patients with UGT1A1 polymorphisms. *Oncol.* 2003;17:52–55.
39. Meyer DJ, Noonan NE. Liver tests in dogs receiving drugs (diphenylhydantoin and primidone). *J Am Anim Hosp Assoc.* 1981;17:261–264.
40. Leonard TB, Neptun DA, Popp JA. Serum gamma glutamyl transferase as a specific indicator of bile duct lesions in the rat liver. *Am J Pathol.* 1984;116:262–269.
41. Noonan NE, Meyer DJ. Use of plasma arginase and gamma-glutamyltransferase as specific indicators of hepatocellular or hepatobiliary disease in the dog. *Am J Vet Res.* 1979;40:942–947.
42. Solter PF, Hoffmann WE, Chambers MD, Schaeffer DJ, Kuhlenschmidt MS. Hepatic total 3 alpha-hydroxy bile acids concentration and enzyme activities in prednisone-treated dogs. *Am J Vet Res.* 1994;55: 1086–1092.
43. Bain PJ. Liver. In: Latimer KS, Mahaffey EA, Prasse KW, eds. *Duncan and Prasse's Veterinary Laboratory Medicine: Clinical Pathology.* 4th ed. Ames, IA: Iowa State Press; 2003:193–214.
44. Giffen PS, Pick CR, Price MA, Williams A, York MJ. Alpha-glutathione-*S*-transferase in the assessment of hepatotoxicity— its diagnostic utility in comparison with other recognized markers in the Wistar Han rat. *Toxicol Pathol.* 2002;30:365–372.
45. Lathia CD. Biomarkers and surrogate endpoints: how and when might they impact drug development? *Dis Markers.* 2002;18:83–90.
46. Lesko LJ, Atkinson AJ. Use of biomarkers and surrogate endpoints in drug development and regulatory decision-making: criteria, validation, strategies. *Annu Rev Pharmacol Toxicol.* 2001;41:347–66.
47. Manolio T. Novel risk markers and clinical practice. *N Engl J Med.* 2004;349:1587–1589.
48. Lewis RW, Billington R, Debryune E, Gamer A, Lang B, Carpanini F. Recognition of adverse and nonadverse effects in toxicity studies. *Toxicol Pathol.* 2002;30:66–74.
49. Davis DT. Enzymology in preclinical safety evaluation. *Toxicol Pathol.* 1992;20:501–505.
50. Boyd JW. The mechanisms relating to increases in plasma enzymes and isoenzymes in disease of animals. *Vet Clin Pathol.* 1983;12: 9–24.
51. Loeb, WF (1999). Appendix. In: Loeb, WF, Quimby FW, eds. *The Clinical Chemistry of Laboratory Animals.* 2nd ed., Philadelphia, PA: Taylor and Francis; 1999:643–726.
52. Henry JB. *Clinical Diagnosis and Management by Laboratory Methods,* 20th ed. Philadelphia, PA: WB Saunders Company; 2001:1431.

RESEARCH ARTICLE

CORONAVIRUS

Potent neutralizing antibodies from COVID-19 patients define multiple targets of vulnerability

Philip J. M. Brouwer[1]*, Tom G. Caniels[1]*, Karlijn van der Straten[1,2]*, Jonne L. Snitselaar[1], Yoann Aldon[1], Sandhya Bangaru[3], Jonathan L. Torres[3], Nisreen M. A. Okba[4], Mathieu Claireaux[1], Gius Kerster[1], Arthur E. H. Bentlage[5], Marlies M. van Haaren[1], Denise Guerra[1], Judith A. Burger[1], Edith E. Schermer[1], Kirsten D. Verheul[1], Niels van der Velde[6], Alex van der Kooi[6], Jelle van Schooten[1], Mariëlle J. van Breemen[1], Tom P. L. Bijl[1], Kwinten Sliepen[1], Aafke Aartse[1,7], Ronald Derking[1], Ilja Bontjer[1], Neeltje A. Kootstra[8], W. Joost Wiersinga[2], Gestur Vidarsson[5], Bart L. Haagmans[4], Andrew B. Ward[3], Godelieve J. de Bree[2]†, Rogier W. Sanders[1,9]†, Marit J. van Gils[1]†

The rapid spread of severe acute respiratory syndrome coronavirus 2 (SARS-CoV-2) has had a large impact on global health, travel, and economy. Therefore, preventative and therapeutic measures are urgently needed. Here, we isolated monoclonal antibodies from three convalescent coronavirus disease 2019 (COVID-19) patients using a SARS-CoV-2 stabilized prefusion spike protein. These antibodies had low levels of somatic hypermutation and showed a strong enrichment in VH1-69, VH3-30-3, and VH1-24 gene usage. A subset of the antibodies was able to potently inhibit authentic SARS-CoV-2 infection at a concentration as low as 0.007 micrograms per milliliter. Competition and electron microscopy studies illustrate that the SARS-CoV-2 spike protein contains multiple distinct antigenic sites, including several receptor-binding domain (RBD) epitopes as well as non-RBD epitopes. In addition to providing guidance for vaccine design, the antibodies described here are promising candidates for COVID-19 treatment and prevention.

The rapid emergence of three novel pathogenic human coronaviruses in the past two decades has caused major concerns. The latest, severe acute respiratory syndrome coronavirus 2 (SARS-CoV-2), is responsible for >3 million infections and 230,000 deaths worldwide as of 1 May 2020 (*1*). Coronavirus disease 2019 (COVID-19), caused by SARS-CoV-2, is characterized by mild, flu-like symptoms in most patients. However, severe cases can present with bilateral pneumonia that may rapidly deteriorate into acute respiratory distress syndrome (*2*). With high transmission rates and no proven curative treatment available, health care systems are severely overwhelmed, and stringent public health measures are in place to prevent infection. Safe and effective treatment and prevention measures for COVID-19 are urgently needed.

During the outbreak of the first severe acute respiratory syndrome coronavirus (SARS-CoV) and Middle Eastern respiratory syndrome coronavirus (MERS-CoV), plasma of recovered patients containing neutralizing antibodies (NAbs) was used as a safe and effective treatment option to decrease viral load and to reduce mortality in severe cases (*3*, *4*). Recently, a small number of COVID-19 patients treated with convalescent plasma showed clinical improvement and a decrease in viral load (*5*). An alternative treatment strategy would be to administer purified monoclonal antibodies (mAbs) with neutralizing capacity. mAbs can be thoroughly characterized in vitro and expressed in large quantities. In addition, because of the ability to control dosing and composition, mAb therapy has improved efficacy over convalescent plasma treatment and prevents the potential risks of antibody-dependent enhancement (ADE) from non-neutralizing or poorly neutralizing Abs present in plasma that consists of a polyclonal mixture (*6*). Recent studies with patients infected with the Ebola virus highlight the superiority of mAb treatment over convalescent plasma treatment (*7*, *8*). Moreover, mAb therapy has been proven safe and effective against influenza virus, rabies virus, and respiratory syncytial virus (RSV) (*9*–*11*).

The main target for NAbs on coronaviruses is the spike (S) protein, a homotrimeric glycoprotein that is anchored in the viral membrane. Recent studies have shown that the S protein of SARS-CoV-2 bears considerable structural homology to that of SARS-CoV, consisting of two subdomains: the N-terminal S1 domain, which contains the N-terminal domain (NTD) and the RBD for the host cell receptor angiotensin-converting enzyme-2 (ACE2), and the S2 domain, which contains the fusion peptide (*12*, *13*). Similar to other viruses containing class 1 fusion proteins (e.g., HIV-1, RSV, and Lassa virus), the S protein undergoes a conformational change and proteolytic cleavage upon host cell receptor binding from a prefusion to a postfusion state, enabling merging of viral and target cell membranes (*14*, *15*). When expressed as recombinant soluble proteins, class 1 fusion proteins generally have the propensity to switch to a postfusion state. However, most NAb epitopes present in the prefusion conformation (*16*–*18*). The recent successes of isolating potent NAbs against HIV-1 and RSV using stabilized prefusion glycoproteins reflect the importance of using the prefusion conformation for isolating and mapping mAbs against SARS-CoV-2 (*19*, *20*).

Early efforts at obtaining NAbs focused on reevaluating SARS-CoV–specific mAbs isolated after the 2003 outbreak that might cross-neutralize SARS-CoV-2 (*21*, *22*). Although two mAbs were described to cross-neutralize SARS-CoV-2, most SARS-CoV NAbs did not bind SARS-CoV-2 S protein or neutralize SARS-CoV-2 virus (*12*, *21*–*23*). More recently, the focus has shifted from cross-neutralizing SARS-CoV NAbs to the isolation of new SARS-CoV-2 NAbs from recovered COVID-19 patients (*24*–*28*). S protein fragments containing the RBD have yielded multiple NAbs that can neutralize SARS-CoV-2 by targeting different RBD epitopes (*24*–*28*). In light of the rapid emergence of escape mutants in the RBD of SARS-CoV and MERS, monoclonal NAbs targeting epitopes other than the RBD are a valuable component of any therapeutic antibody cocktail (*29*, *30*). Indeed, therapeutic antibody cocktails with a variety of specificities have been used successfully against Ebola virus disease (*7*) and are being tested widely in clinical trials for HIV-1 (*31*). NAbs targeting non-RBD epitopes have been identified for SARS-CoV and MERS, supporting the rationale for sorting mAbs using the entire ectodomain of the SARS-CoV-2 S protein (*32*). In addition, considering the high sequence identity between the S2 subdomains of SARS-CoV-2 and SARS-CoV, using the complete S protein ectodomain instead of only the RBD may allow the isolation of mAbs that cross-neutralize different β-coronaviruses (*33*). In an attempt to obtain mAbs that target both RBD and non-RBD epitopes, we set out to isolate mAbs using the complete prefusion S protein ectodomain of SARS-CoV-2.

[1]Department of Medical Microbiology, Amsterdam UMC, University of Amsterdam, Amsterdam Institute for Infection and Immunity, 1105AZ Amsterdam, Netherlands. [2]Department of Internal Medicine, Amsterdam UMC, University of Amsterdam, Amsterdam Institute for Infection and Immunity, 1105AZ Amsterdam, Netherlands. [3]Department of Integrative Structural and Computational Biology, The Scripps Research Institute, La Jolla, CA 92037, USA. [4]Department of Viroscience, Erasmus Medical Center, Rotterdam, 3015GD, Netherlands. [5]Sanquin Research, Department of Experimental Immunohematology, Amsterdam, Netherlands and Landsteiner Laboratory, Amsterdam UMC, University of Amsterdam, 1006AD Amsterdam, Netherlands. [6]IBIS Technologies BV, 7521PR Enschede, Netherlands. [7]Department of Virology, Biomedical Primate Research Centre, 2288GJ Rijswijk, Netherlands. [8]Department of Experimental Immunology, Amsterdam UMC, University of Amsterdam, Amsterdam Institute for Infection and Immunity, 1105AZ Amsterdam, Netherlands. [9]Department of Microbiology and Immunology, Weill Medical College of Cornell University, New York, NY 10021, USA.
*These authors contributed equally to this work.
†Corresponding author. Email: m.j.vangils@amsterdamumc.nl (M.J.v.G.); r.w.sanders@amsterdamumc.nl (R.W.S.); g.j.debree@amsterdamumc.nl (G.J.d.B.)

Phenotyping SARS-CoV-2–specific B cell subsets

We collected a single blood sample from three polymerase chain reaction–confirmed SARS-CoV-2–infected individuals (COSCA1, COSCA2, and COSCA3) ~4 weeks after symptom onset. COSCA1 (a 47-year-old male) and COSCA2 (a 44-year-old female) showed symptoms of an upper respiratory tract infection and mild pneumonia, respectively (Table 1). Both remained in home isolation during the course of COVID-19 symptoms. COSCA3, a 69-year-old male, developed a severe pneumonia and became respiratory insufficient 1.5 weeks after symptom onset, requiring admission to the intensive

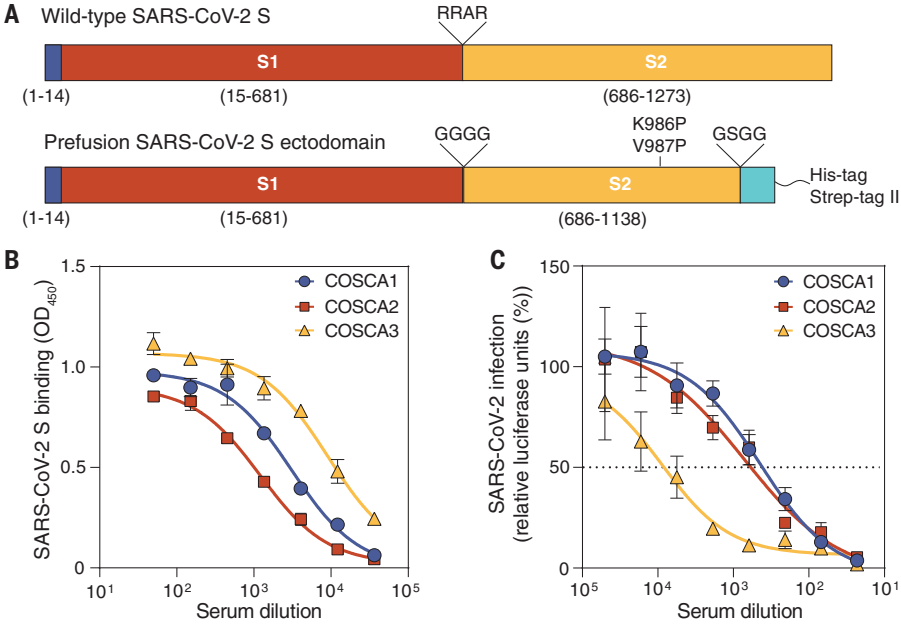

Fig. 1. Design of SARS-CoV-2 S protein and serology of COSCA1, COSCA2, and COSCA3. (**A**) (Top) Schematic overview of the authentic SARS-CoV-2 S protein with the signal peptide shown in blue and the S1 (red) and S2 (yellow) domains separated by a furin-cleavage site (RRAR; top). (Bottom) Schematic overview of the stabilized prefusion SARS-CoV-2 S ectodomain, where the furin cleavage site is replaced with a glycine linker (GGGG), two proline mutations are introduced (K986P and V987P), and a trimerization domain (cyan) preceded by a linker (GSGG) is attached. (**B**) Binding of sera from COSCA1, COSCA2, and COSCA3 to prefusion SARS-CoV-2 S protein as determined by ELISA. The mean values and SDs of two technical replicates are shown. (**C**) Neutralization of SARS-CoV-2 pseudovirus by heat-inactivated sera from COSCA1, COSCA2, and COSCA3. The mean and SEM of at least three technical replicates are shown. The dotted line indicates 50% neutralization.

Table 1. Patient characteristics, symptoms of COVID-19, treatment modalities, and sampling time points of three SARS-CoV-2–infected patients.

	COSCA1	COSCA2	COSCA3
Patient characteristics			
Age (years)	47	44	69
Gender	Male	Female	Male
Comorbidities	None	None	None
Symptoms, from onset to relief, days			
Fever (>38°C)	4–10	1–4	6–18
Coughing	2–35	3–17	1–20
Sputum production	2–35	No	1–20
Dyspnea	4–24	No	No
Sore throat	1–5	5–17	No
Rhinorrhea	2–34	5–17	No
Anosmia	No	5–17	No
Myalgia	No	1–4	6–18
Headache	No	No	1–18
Other	No	No	Delirium
Treatment modalities, treatment period, days			
Hospital admission	No	No	8–24
ICU admission	No	No	11–18
Oxygen therapy	No	No	8–24
Intubation	No	No	11–16
Dialysis	No	No	No
Drug therapy			
Antiviral	No	No	No
Antibiotic	No	No	Cefotaxime, 8–12 Ciprofloxacin, 8–11
Immunomodulatory	No	No	No
NSAIDs	No	No	No
Sampling time point, days after symptom onset	27	28	23

care unit for mechanical ventilation. To identify S protein–specific antibodies in the sera obtained from all three patients, we generated soluble, prefusion-stabilized S proteins of SARS-CoV-2 using stabilization strategies previously described for S proteins of SARS-CoV-2 and other β-coronaviruses (Fig. 1A) (*12*, *34*). As demonstrated by the size-exclusion chromatography trace, SDS–polyacrylamide gel electrophoresis (PAGE), and blue native PAGE, the resulting trimeric SARS-CoV-2 S proteins were of high purity (fig. S1, A and B). Sera from all patients showed strong binding to the S protein of SARS-CoV-2 in an enzyme-linked immunosorbent assay (ELISA), with end-point titers of 13,637, 6133, and 48,120 for COSCA1, COSCA2, and COSCA3, respectively (Fig. 1B), and showed cross-reactivity to the S protein of SARS-CoV (fig. S1C). COSCA1, COSCA2, and COSCA3 had varying neutralizing potencies against SARS-CoV-2 pseudovirus, with 50% inhibition of virus infection (ID_{50}) values of 383, 626, and 7645, respectively (Fig. 1C), and similar activities against authentic virus (fig. S1D). In addition, all sera showed cross-neutralization of SARS-CoV pseudovirus and authentic SARS-CoV virus, albeit with low potency (fig. S1, E and F). The potent S protein–binding and -neutralizing responses observed for COSCA3 are consistent with earlier findings showing that severe disease is associated with a strong humoral response (*35*). On the basis of these strong serum binding and neutralization titers, we sorted SARS-CoV-2 S protein–specific B cells for mAb isolation from COSCA1, COSCA2, and COSCA3.

Peripheral blood mononuclear cells were stained dually with fluorescently labeled prefusion SARS-CoV-2 S proteins and analyzed for the frequency and phenotype of specific B cells by flow cytometry (Fig. 2A and fig S2). The analysis revealed a frequency ranging from 0.68 to 1.74% of S protein–specific B cells ($S\text{-}AF647^+$, $S\text{-}BV421^+$) among the total pool of B cells ($CD19^+Via\text{-}CD3^-CD14^-CD16^-$), (Fig. 2B). These SARS-CoV-2 S protein–specific B cells showed a predominant memory ($CD20^+CD27^+$) and plasmablasts/plasma cells (PBs/PCs) ($CD20^-CD27^+CD38^+$) phenotype. We observed a threefold higher percentage of PBs/PCs for SARS-CoV-2 S protein–specific B cells compared with total B cells ($P = 0.034$), indicating an enrichment of specific B cells in this subpopulation (Fig. 2C). COSCA3, who experienced severe symptoms, showed the highest frequency of PBs/PCs in both total (34%) and specific (60%) B cells (Fig. 2C and fig. S2). As expected, the SARS-CoV-2 S protein–specific B cells were enriched in the immunoglobulin G–positive (IgG^+) and IgM^-/IgG^- (most likely representing IgA^+) B cell populations, although a substantial portion of the specific B cells were IgM^+, particularly for COSCA3 (Fig. 2D).

Genotypic signatures of the SARS-CoV-2–specific antibody response

SARS-CoV-2 S protein–specific B cells were subsequently single-cell sorted for sequencing and mAb isolation. In total, 409 heavy chain (HC) and light chain (LC) pairs were obtained from the sorted B cells of the three patients (137, 165, and 107 from COSCA1, COSCA2, and COSCA3, respectively), of which 323 were unique clonotypes. Clonal expansion occurred in all three patients (Fig. 3A) but was strongest in COSCA3, where it was dominated by HC variable (VH) regions VH3-7 and VH4-39 (34 and 32% of SARS-CoV-2 S protein–specific sequences, respectively). Even though substantial clonal expansion occurred in COSCA3, the median somatic hypermutation (SHM) was 1.4%, with similar SHM in COSCA1 and COSCA2 (2.1 and 1.4%, respectively) (Fig. 3B). These SHM levels are similar

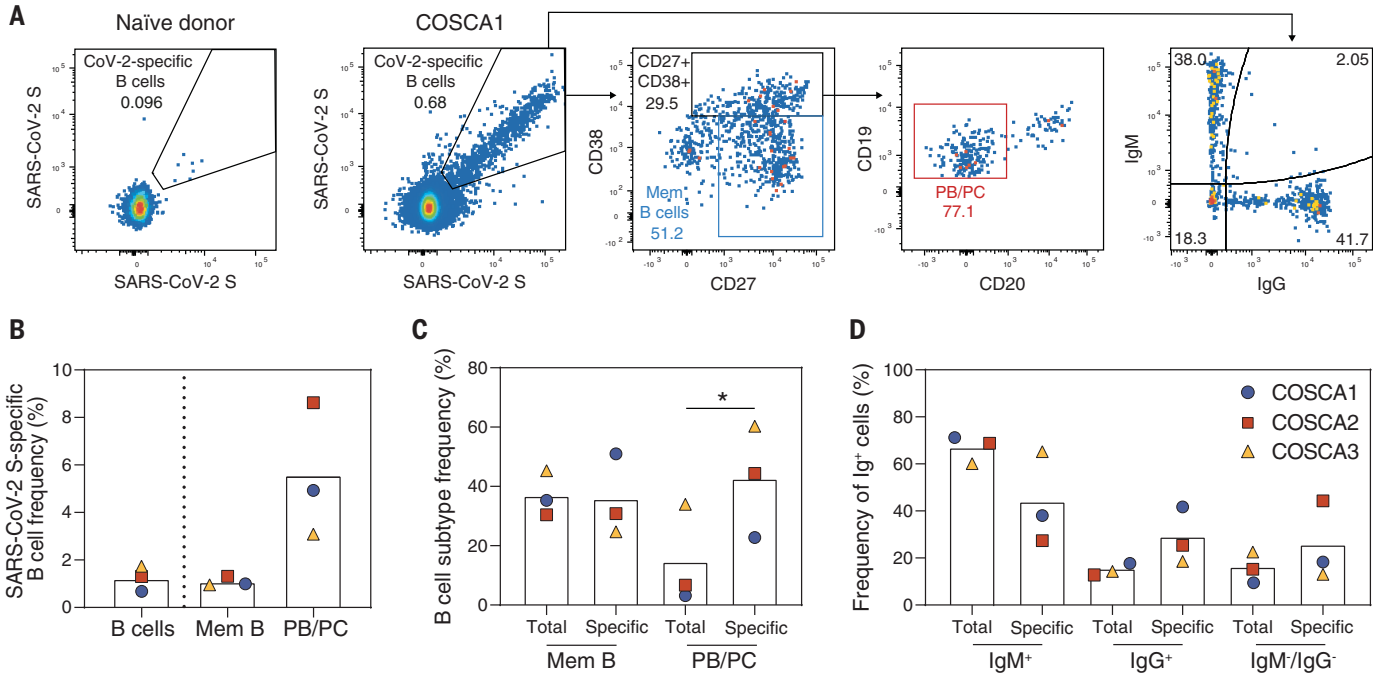

Fig. 2. Characterization of SARS-CoV-2 S protein–specific B cells derived from COSCA1, COSCA2, and COSCA3. (**A**) Representative gates of SARS-CoV-2 S protein–specific B cells shown for a naïve donor (left panel) or COSCA1 (middle left panel). Each dot represents a B cell. The gating strategy to identify B cells is shown in fig. S2. From the total pool of SARS-CoV-2 S protein–specific B cells, $CD27^+CD38^-$ memory B cells (Mem B cells; blue gate) and $CD27^+CD38^+$ B cells were identified (middle panel). From the latter gate, PBs/PCs ($CD20^-$; red gate) could be identified (middle right panel). SARS-CoV-2 S protein–specific B cells were also analyzed for their IgG or IgM isotype (right panel). (**B**) Frequency of SARS-CoV-2 S protein–specific B cells in total B cells, Mem B cells, and PBs/PCs. Symbols represent individual patients, as shown in (D). (**C**) Comparison of the frequency of Mem B cells ($CD27^+CD38^-$) and PB/PC cells ($CD27^+CD38^+CD20^-$) between the specific (SARS-CoV2 S^{++}) and nonspecific B cells (gating strategy is shown in fig. S2). Symbols represent individual patients, as shown in (D). Statistical differences between two groups were determined using paired *t* test (*$P = 0.034$). (**D**) Comparison of the frequency of IgM^+, IgG^+, and IgM^-IgG^- B cells in specific and nonspecific compartments. Bars represent means; symbols represent individual patients.

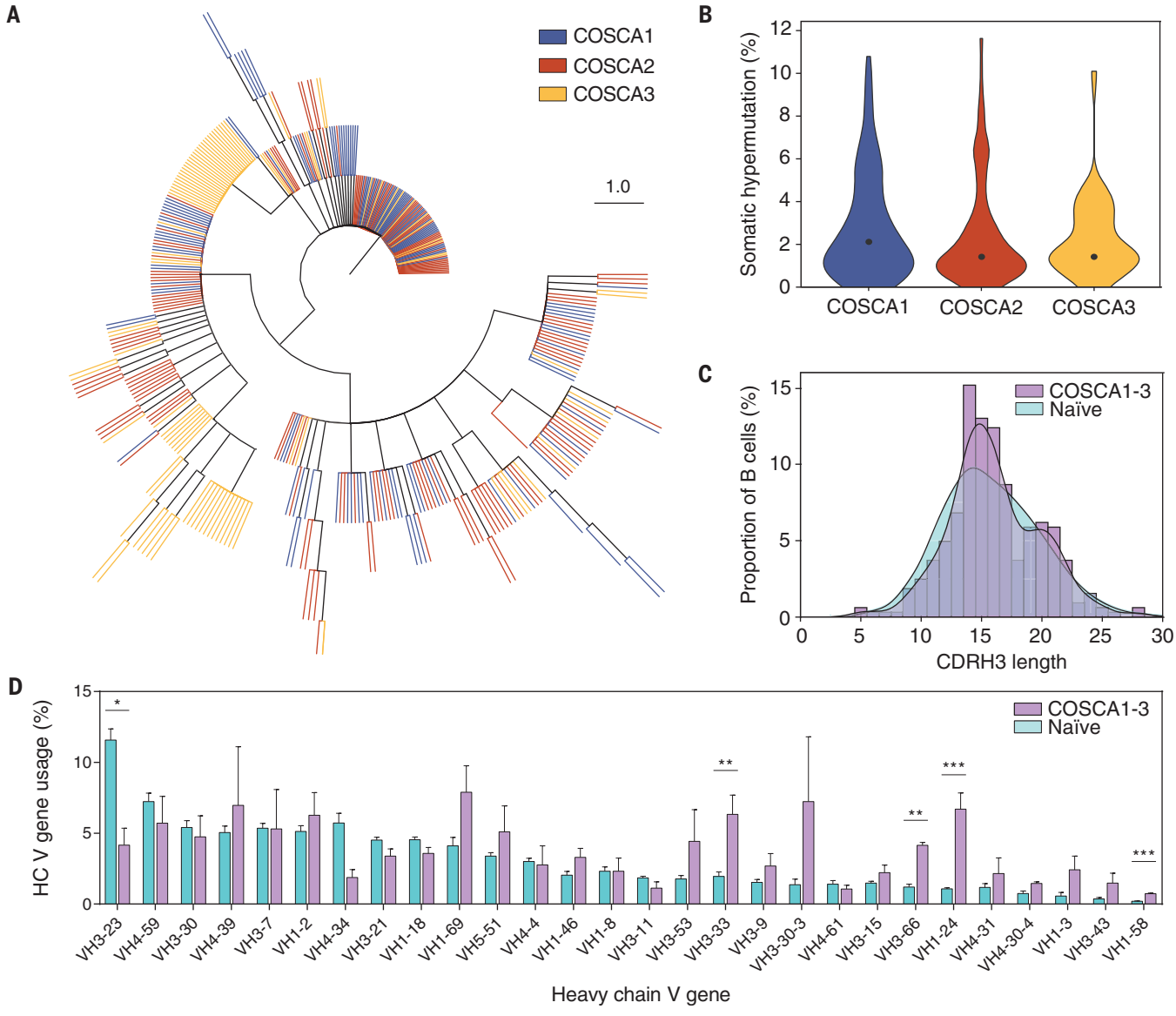

Fig. 3. Genotypic characterization of SARS-CoV-2 S protein–specific B cell receptors. (**A**) Maximum-likelihood phylogenetic tree of 409 isolated paired B cell receptor HCs. Each color represents sequences isolated from different patients (COSCA1, COSCA2, and COSCA3). (**B**) Violin plot showing SHM levels (%; nucleotides) per patient. The dot represents the median SHM percentage. (**C**) Distribution of CDRH3 lengths in B cells from COSCA1, COSCA2, and COSCA3 (purple, *n* = 323) versus a representative naïve population from three donors (cyan, *n* = 9.791.115) (*37*). (**D**) Bar graphs showing the mean (± SEM) VH gene usage (%) in COSCA1, COSCA2, and COSCA3 (purple, *n* = 323) versus a representative naïve population (cyan, *n* = 363,506,788). The error bars represent the variation between different patients (COSCA1, COSCA2, and COSCA3) or naïve donors (*37*). Statistical differences between two groups were determined using unpaired *t* tests (with Holm–Sidak correction for multiple comparisons, adjusted *P* values: *$P < 0.05$; **$P < 0.01$; ***$P < 0.001$).

to those observed in response to infection with other respiratory viruses (*36*).

A hallmark of antibody diversity is the heavy chain complementarity-determining region 3 (CDRH3). Because the CDRH3 is composed of V, D, and J gene segments, it is the most variable region of an antibody in terms of both amino acid composition and length. The average length of CDRH3 in the naïve human repertoire is 15 amino acids (*37*), but for a subset of influenza virus and HIV-1 broadly neutralizing antibodies, long CDRH3 regions of 20 to 35 amino acids are crucial for high-affinity antigen–antibody interactions (*38*, *39*). Even though the mean CDRH3 length of isolated SARS-CoV-2 S protein–specific B cells did not differ substantially from that of a naïve population (*37*), we observed a significant difference in the distribution of CDRH3 length (two-sample Kolmogorov–Smirnov test, $P = 0.006$) (Fig. 3C). This difference in CDRH3 distribution can largely be attributed to an enrichment of longer (~20 amino acid) CDRH3s, leading to a bimodal distribution as opposed to the bell-shaped distribution that was observed in the naïve repertoire (Fig. 3C and fig. S3).

Next, to determine SARS-CoV-2–specific signatures in B cell receptor repertoire usage, we compared ImmunoGenetics (IMGT) database–assigned unique germline V regions from the sorted SARS-CoV-2 S protein–specific B cells with the well-defined extensive germline repertoire in the naïve population (Fig. 3D) (*37*). Multiple VH genes were enriched in COSCA1, COSCA2, and COSCA3 compared with the naïve repertoire, including VH3-33 ($P = 0.009$) and VH1-24 ($P < 0.001$) (Fig. 3D). Even though the enrichment of VH1-69 was not significant ($P > 0.05$), it should be noted

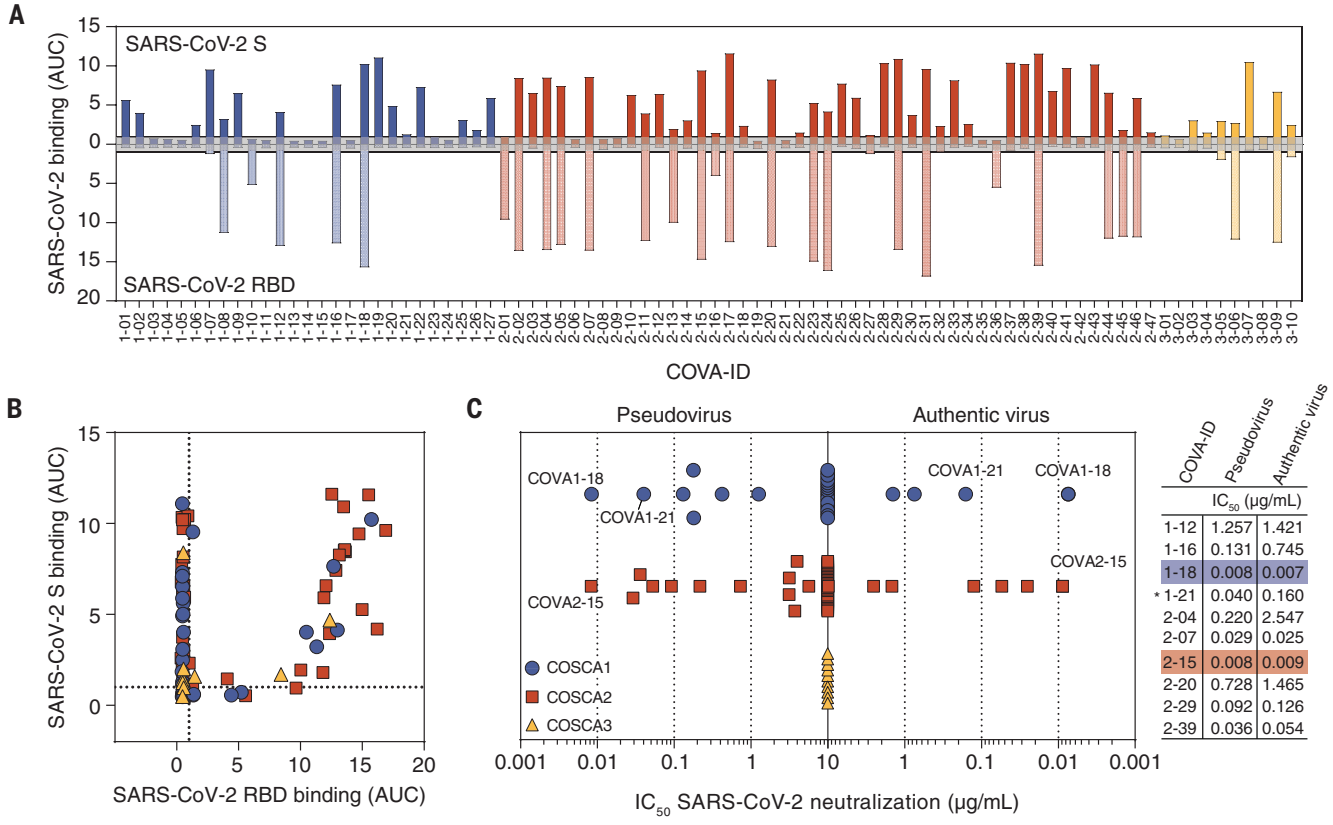

COVA-ID	Pseudovirus IC50 (μg/mL)	Authentic virus IC50 (μg/mL)
1-12	1.257	1.421
1-16	0.131	0.745
1-18	0.008	0.007
*1-21	0.040	0.160
2-04	0.220	2.547
2-07	0.029	0.025
2-15	0.008	0.009
2-20	0.728	1.465
2-29	0.092	0.126
2-39	0.036	0.054

Fig. 4. Phenotypic characterization of SARS-CoV-2 S protein–specific mAbs. (**A**) Bar graph depicting the binding of mAbs from COSCA1 (blue), COSCA2 (red), and COSCA3 (yellow) to SARS-CoV-2 S protein (dark shading) and SARS-CoV-2 RBD (light shading) as determined by ELISA. Each bar indicates the representative area under the curve (AUC) of the mAb indicated below from two experiments. The gray area represents the cutoff for binding (AUC = 1). The maximum concentration of mAb tested was 10 μg/ml. (**B**) Scatter plot depicting the binding of mAbs from COSCA1, COSCA2, and COSCA3 [see (C) for color coding] to SARS-CoV-2 S protein and SARS-CoV-2 RBD as determined by ELISA. Each dot indicates the representative AUC of a mAb from two experiments. (**C**) Midpoint neutralization concentrations (IC_{50}) of SARS-CoV-2 pseudovirus (left) or authentic SARS-CoV-2 virus (right). Each symbol represents the IC_{50} of a single mAb. For comparability, the highest concentration was set to 10 μg/ml, although the actual start concentration for the authentic virus neutralization assay was 20 μg/ml. The IC_{50}s for pseudotyped and authentic SARS-CoV-2 virus of a selection of potently neutralizing RBD and non-RBD–specific mAbs (with asterisk) are shown in the adjacent table. Colored shading indicates the most potent mAbs from COSCA1, COSCA2, and COSCA3.

that an enrichment of VH1-69 has been shown in response to a number of other viral infections, including influenza virus, hepatitis C virus, and rotavirus (*40*), and an enrichment of VH3-33 was observed in response to malaria vaccination, whereas the enrichment of VH1-24 appears to be specific for COVID-19 (Fig. 3D) (*41*). By contrast, VH4-34 ($P > 0.05$) and VH3-23 ($P = 0.018$) were substantially underrepresented in SARS-CoV-2–specific sequences compared with the naïve population. Although usage of most VH genes was consistent between COVID-19 patients, VH3-30-3 and VH4-39 in particular showed considerable variability. Thus, upon SARS-CoV-2 infection, the S protein recruits a subset of B cells from the naïve repertoire enriched in specific VH segments and CDRH3 domains.

Identification of unusually potent SARS-CoV-2–neutralizing antibodies

Subsequently, all HC and LC pairs were transiently expressed in human embryonic kidney (HEK) 293T cells and screened for binding to SARS-CoV-2 S protein by ELISA. A total of 84 mAbs that showed high-affinity binding were selected for small-scale expression in HEK 293F cells and purified (table S1). We obtained few S protein–reactive mAbs from COSCA3, possibly because most B cells from this individual were IgM^+, whereas cloning into an IgG backbone nullified avidity contributions to binding and neutralization present in the serum. To gain insight in the immunodominance of the RBD as well as its ability to cross-react with SARS-CoV, we assessed the binding capacity of these mAbs to the prefusion S proteins and the RBDs of SARS-CoV-2 and SARS-CoV using ELISA. Of the 84 mAbs tested, 32 (38%) bound to the SARS-CoV-2 RBD (Fig. 4, A and B), with seven mAbs (22%) showing cross-binding to SARS-CoV RBD (fig. S4A). We also observed 33 mAbs (39%) that bound strongly to SARS-CoV-2 S but did not bind the RBD, of which 10 mAbs (30%) also bound to the S protein of SARS-CoV (Fig. 4, A and B). Notably, some mAbs that bound very weakly to soluble SARS-CoV-2 S protein in ELISA showed strong binding to membrane-bound S protein, implying that their epitopes are presented poorly on the stabilized soluble S protein or that avidity is important for their binding (table S1). Surface plasmon resonance (SPR) assays confirmed binding of 77 mAbs to S protein and 21 mAbs to the RBD with binding affinities in the nanomolar to picomolar range (table S1).

All 84 mAbs were subsequently tested for their ability to block infection. A total of 19 mAbs (23%) inhibited SARS-CoV-2 pseudovirus infection with varying potencies (Fig. 4C) and, of these, 14 (74%) bound the RBD. Seven of the 19 mAbs could be categorized as potent neutralizers [median inhibitory concentration (IC_{50}) < 0.1 μg/ml], six as moderate neutralizers (IC_{50} = 0.1 to 1 μg/mL), and six as weak neutralizers (IC_{50} = 1 to 10 μg/ml). With an IC_{50} of 0.008 μg/ml, the RBD-targeting antibodies COVA1-18 and COVA2-15 in particular were unusually potent. However, they were

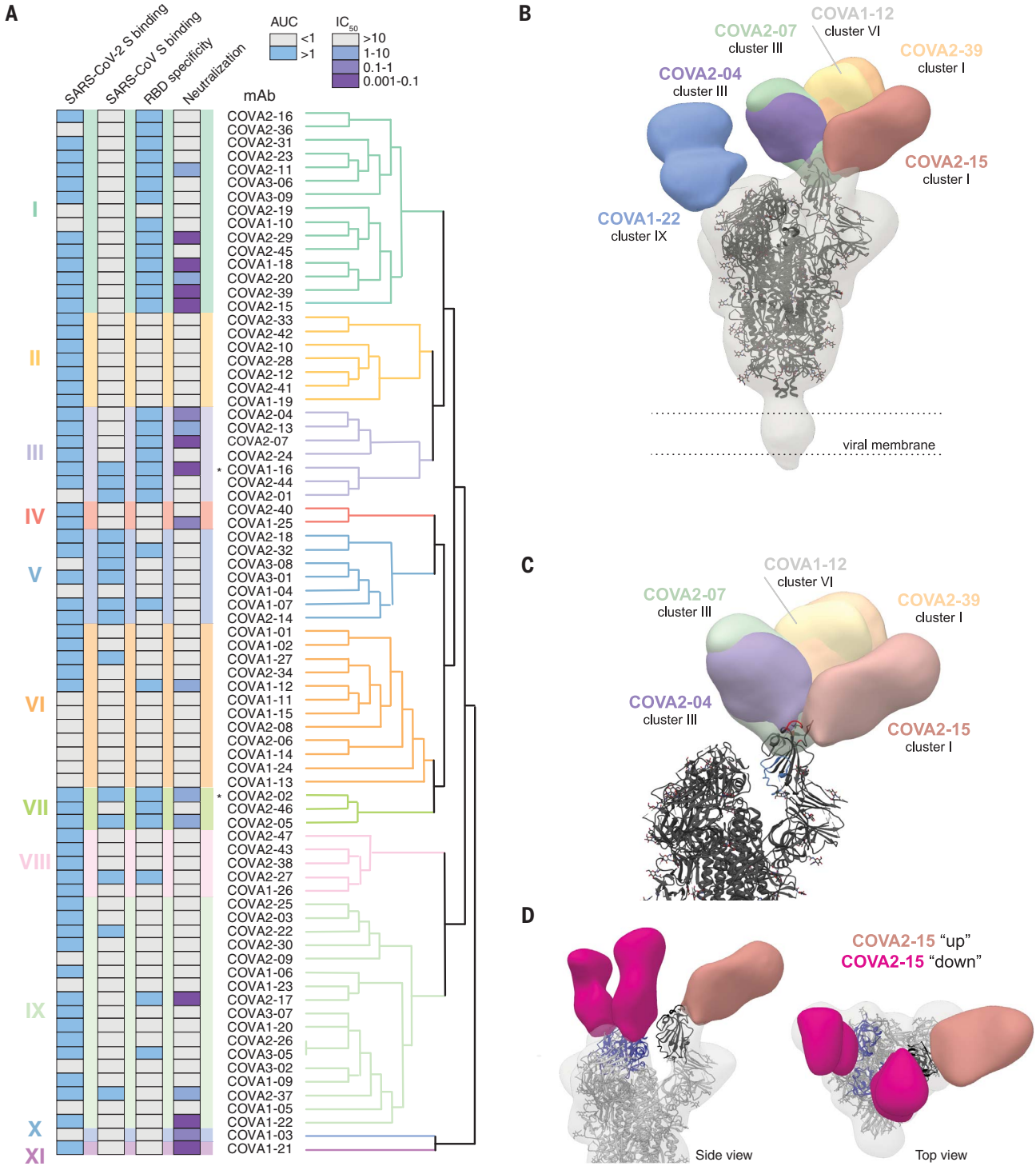

Fig. 5. Antigenic clustering of SARS-CoV-2 S protein–specific mAbs. (**A**) Dendrogram showing hierarchical clustering of the SPR-based cross-competition heat map (table S2). Clusters are numbered I to XI and are depicted with color shading. ELISA binding to SARS-CoV-2 S protein, SARS-CoV S protein, and SARS-CoV-2 RBD as presented by AUC and neutralization IC_{50} (μg/ml) of SARS-CoV-2 is shown in the columns on the left. ELISA AUCs are shown in gray (AUC < 1) or blue (AUC > 1), and neutralization IC_{50} is shown in gray (>10 μg/ml), blue (1 to 10 μg/ml), violet (0.1 to 1 μg/ml), or purple (0.001 to 0.1 μg/ml). Asterisks indicate antibodies that cross-neutralize SARS-CoV pseudovirus. (**B**) Composite figure demonstrating binding of NTD-mAb COVA1-22 (blue) and RBD mAbs COVA2-07 (green), COVA2-39 (orange), COVA1-12 (yellow), COVA2-15 (salmon), and COVA2-04 (purple) to SARS-CoV-2 spike (gray). The spike model (PDB 6VYB) is fit into the density. (**C**) Magnification of SARS-CoV-2 spike comparing epitopes of RBD mAbs with the ACE2-binding site (red) and the epitope of mAb CR3022 (blue). (**D**) Side (left) and top (right) views of the 3D reconstruction of COVA2-15 bound to SARS-CoV-2 S protein. COVA2-15 binds to both the down (magenta) and up (salmon) conformations of the RBD. The RBDs are colored blue in the down conformation and black in the up conformation. The angle of approach for COVA2-15 enables this broader recognition of the RBD while also partially overlapping with the ACE2-binding site and therefore blocking receptor engagement.

quite different in other aspects, such as their HC V gene usage (VH3-66 versus VH3-23), LC usage (VL7-46 versus VK2-30), HC sequence identity (77%), and CDRH3 length (12 versus 22 amino acids). Seventeen of the mAbs also interacted with the SARS-CoV S and RBD proteins and two of these cross-neutralized the SARS-CoV pseudovirus (IC_{50} = 2.5 μg/ml for COVA1-16 and 0.61 μg/ml for COVA2-02; fig. S4B), with COVA2-02 being more potent against SARS-CoV than against SARS-CoV-2. Next, we assessed the ability of the 19 mAbs to block infection of authentic SARS-CoV-2 virus (Fig. 4C and fig. S4C). Although previous reports suggested a decrease in neutralization sensitivity of primary SARS-CoV-2 compared with pseudovirus (*25*, *27*, *28*), we observed very similar potencies for seven of the 19 NAbs, including the most potent NAbs (IC_{50} = 0.007 and 0.009 μg/ml for COVA1-18 and COVA2-15, respectively; Fig. 4C). NAbs COVA1-18, COVA2-04, COVA2-07, COVA2-15, and COVA2-39 also showed strong competition with ACE2 binding, illustrating that blocking ACE2 binding is their likely mechanism of neutralization (fig. S4D). The RBD-targeting mAb COVA2-17, however, showed incomplete competition with ACE2. This corroborates previous observations that the RBD encompasses multiple distinct antigenic sites, some of which do not involve blocking of ACE2 binding (*23*, *25*, *26*). The non-RBD NAbs all bear substantially longer CDRH3s compared with RBD NAbs (fig. S4E), suggesting a convergent, CDRH3-dependent contact between antibody and epitope.

Multiple targets of vulnerability on the SARS-CoV-2 S protein

To identify and characterize the antigenic sites on the S protein and their interrelationships, we performed SPR-based cross-competition assays using S protein, followed by clustering analysis. We note that competition clusters do not necessarily equal epitope clusters but the analysis can provide clues as to the relationship between mAb epitopes. We identified 11 competition clusters, of which nine contained more than one mAb and two contained only one mAb (clusters X and XI; Fig. 5A and fig. S5). All nine multiple-mAb clusters included mAbs from at least two of the three patients, emphasizing that these clusters represent common epitopes targeted by the human humoral immune response during SARS-CoV-2 infection. Three clusters included predominantly RBD-binding mAbs (clusters I, III, and VII), with cluster I forming two subclusters. These three clusters were confirmed by performing cross-competition experiments with soluble RBD instead of complete S protein (fig. S5B). Four clusters (V, VI, XIII, and IX) included predominantly mAbs that did not interact with RBD, and clusters II, IV, X, and XI consisted exclusively of non-RBD mAbs. mAbs with diverse phenotypes (e.g., RBD and non-RBD–binding mAbs) merged together in multiple clusters, suggesting that these mAbs might target epitopes bridging the RBD and non-RBD sites or that they sterically interfere with each other's binding as opposed to binding to overlapping epitopes. Although clusters II, V, and VIII contained only mAbs incapable of neutralizing SARS-CoV-2, clusters I, III, IV, VI, and VII included both non-NAbs and NAbs. Cluster V was formed mostly by non-RBD–targeting mAbs that also bound to SARS-CoV. However, these mAbs were not able to neutralize either SARS-CoV-2 or SARS-CoV, suggesting that these mAbs target a conserved non-neutralizing epitope on the S protein. Finally, the two non-RBD mAbs COVA1-03 and COVA1-21 formed single-mAb competition clusters (clusters X and XI, respectively) and showed an unusual competition pattern, because binding of either mAb blocked binding by most of the other mAbs, but not vice versa (figs. S5 and S6 and table S2). We hypothesize that these two mAbs allosterically interfere with mAb binding by causing conformational changes in the S protein that shield or impair most other mAb epitopes. COVA1-21 also efficiently blocked virus infection without blocking ACE2, suggesting an alternative mechanism of neutralization than blocking ACE2 engagement (fig. S4C). The SPR-based clustering was corroborated using biolayer interferometry competition assays on a subset of NAbs (fig. S6). Overall, our data are consistent with the previous identification of multiple antigenic RBD sites for SARS-CoV-2 and additional non-RBD sites on the S protein, as described for SARS-CoV and MERS-CoV (*32*, *42*).

To visualize how selected NAbs bound to their respective epitopes, we generated Fab–SARS-CoV-2 S complexes that were imaged by single-particle negative-stain electron microscopy (EM; Fig. 5, B and C, and fig. S7). We obtained low-resolution reconstruction with six Fabs, including five RBD-binding Fabs from three different competition clusters. COVA1-12 overlapped highly with the epitope of COVA2-39, whereas COVA2-04 approached the RBD at a different angle somewhat similar to that of the cross-binding SARS-CoV–specific mAb CR3022 (*42*). The EM reconstructions confirmed the RBD as the target of these NAbs but revealed a diversity in approach angles (Fig. 5B). Furthermore, whereas four RBD NAbs interacted with a stoichiometry of one Fab per trimer, consistent with one RBD being exposed in the "up state" and two in the less accessible "down state" (*13*, *43*), COVA2-15 bound with a stoichiometry of three per trimer (fig. S7). COVA2-15 was able to bind RBD domains in both the up and down state (Fig. 5D). In either conformation, the COVA2-15 epitope partially overlapped with the ACE2-binding site, and therefore the mAb blocks receptor engagement. The higher stoichiometry of this mAb may explain its unusually strong neutralization potency. None of the epitopes of the five RBD Fabs overlapped with that of CR3022, which is unable to neutralize SARS-CoV-2 (*42*), although COVA2-04 does approach the RBD from a similar angle as CR3022. The sixth Fab for which we generated a three-dimensional (3D) reconstruction was from the non-RBD mAb COVA1-22 placed in competition cluster IX. EM demonstrated that this mAb bound to the NTD of S1. Such NTD NAbs have also been found for MERS-CoV (*44*).

Conclusions

Convalescent COVID-19 patients showed strong anti–SARS-CoV-2 S protein–specific B cell responses and developed memory and antibody-producing B cells that may have participated in the control of infection and the establishment of humoral immunity. We isolated 19 NAbs that targeted a diverse range of antigenic sites on the S protein, of which two showed picomolar neutralizing activities (IC_{50} = 0.007 and 0.009 μg/ml or 47 and 60 pM, respectively) against authentic SARS-CoV-2 virus. This illustrates that SARS-CoV-2 infection elicits high-affinity and cross-reactive mAbs targeting the RBD as well as other sites on the S protein. Several of the potent NAbs had VH segments virtually identical to their germline origin, which holds promise for the induction of similar NAbs by vaccination because extensive affinity maturation does not appear to be a requirement for potent neutralization. The most potent NAbs both targeted the RBD on the S protein and fell within the same competition cluster, but were isolated from two different individuals and bore little resemblance genotypically. Although direct comparisons are difficult, the neutralization potency of these and several other mAbs exceeds the potencies of the most advanced HIV-1 and Ebola mAbs under clinical evaluation, as well as the approved anti-RSV mAb palivizumab (*45*). Through large-scale SPR-based competition assays, we defined NAbs that targeted multiple sites of vulnerability on the RBD and the additional previously undefined non-RBD epitopes on SARS-CoV-2. This is consistent with the identification of multiple antigenic RBD sites for SARS-CoV-2 and the presence of additional non-RBD sites on the S protein of SARS-CoV and MERS-CoV (*32*). Subsequent structural characterization of these potent NAbs will guide vaccine design, and simultaneous targeting of multiple non-RBD and RBD epitopes with mAb cocktails paves the way for safe and effective COVID-19 prevention and treatment.

REFERENCES AND NOTES

1. E. Dong, H. Du, L. Gardner, *Lancet Infect. Dis.* **20**, 533–534 (2020).
2. N. Chen *et al.*, *Lancet* **395**, 507–513 (2020).
3. J. Mair-Jenkins *et al.*, *J. Infect. Dis.* **211**, 80–90 (2015).
4. J. H. Ko *et al.*, *Antivir. Ther.* **23**, 617–622 (2018).

5. C. Shen *et al*., *JAMA* **323**, 1582 (2020).
6. R. Kulkarni, in *Dynamics of Immune Activation in Viral Diseases*, P. V. Bramhachari, Ed. (Springer, 2020), pp. 9–41.
7. S. Mulangu *et al*., *N. Engl. J. Med.* **381**, 2293–2303 (2019).
8. J. van Griensven *et al*., *N. Engl. J. Med.* **374**, 33–42 (2016).
9. E. Hershberger *et al*., *EBioMedicine* **40**, 574–582 (2019).
10. N. J. Gogtay *et al*., *Clin. Infect. Dis.* **66**, 387–395 (2018).
11. T. Sandritter, *J. Pediatr. Health Care* **13**, 191–195, quiz 196–197 (1999).
12. D. Wrapp *et al*., *Science* **367**, 1260–1263 (2020).
13. A. C. Walls *et al*., *Cell* **181**, 281–292.e6 (2020).
14. F. Li, *Annu. Rev. Virol.* **3**, 237–261 (2016).
15. J. Shang *et al*., *Nature* **581**, 221–224 (2020).
16. R. W. Sanders *et al*., *PLOS Pathog.* **9**, e1003618 (2013).
17. J. E. Robinson *et al*., *Nat. Commun.* **7**, 11544 (2016).
18. S. Jiang, C. Hillyer, L. Du, *Trends Immunol.* **41**, 355–359 (2020).
19. J. S. McLellan, W. C. Ray, M. E. Peeples, *Curr. Top. Microbiol. Immunol.* **372**, 83–104 (2013).
20. D. Sok *et al*., *Proc. Natl. Acad. Sci. U.S.A.* **111**, 17624–17629 (2014).
21. X. Tian *et al*., *Emerg. Microbes Infect.* **9**, 382–385 (2020).
22. C. Wang *et al*., *Nat. Commun.* **11**, 2251 (2020).
23. D. Pinto *et al*., Structural and functional analysis of a potent Sarbecovirus neutralizing antibody. bioRxiv 2020.04.07.023903 [Preprint]. 10 April 2020); https://doi.org/10.1101/2020.04.07.023903.
24. X. Chen *et al*., *Cell. Mol. Immunol.* **17**, 647–649 (2020).
25. S. J. Zost, P. Gilchuk *et al*., Potently neutralizing human antibodies that block SARS-CoV-2 receptor binding and protect animals. bioRxiv 2020.05.22.111005 [Preprint]. 22 May 2020; https://doi.org/10.1101/2020.05.22.111005.
26. D. F. Robbiani *et al*., Convergent antibody responses to SARS-CoV-2 infection in convalescent individuals. bioRxiv 2020.05.13.092619 [Preprint]. 22 May 2020; https://doi.org/10.1101/2020.05.13.092619.
27. B. Ju *et al*., *Nature* 10.1038/s41586-020-2380-z (2020).
28. T. F. Rogers *et al*., Rapid isolation of potent SARS-CoV-2 neutralizing antibodies and protection in a small animal model. bioRxiv 2020.05.11.088674 [Preprint]. 15 May 2020; https://doi.org/10.1101/2020.05.11.088674.
29. X. C. Tang *et al*., *Proc. Natl. Acad. Sci. U.S.A.* **111**, E2018–E2026 (2014).
30. J. ter Meulen *et al*., *PLOS Med.* **3**, e237 (2006).
31. M. Grobben, R. A. Stuart, M. J. van Gils, *Curr. Opin. Virol.* **38**, 70–80 (2019).
32. B. Shanmugaraj, K. Siriwattananon, K. Wangkanont, W. Phoolcharoen, *Asian Pac. J. Allergy Immunol.* **38**, 10–18 (2020).
33. S. F. Ahmed, A. A. Quadeer, M. R. McKay, *Viruses* **12**, 254 (2020).
34. J. Pallesen *et al*., *Proc. Natl. Acad. Sci. U.S.A.* **114**, E7348–E7357 (2017).
35. J. Zhao *et al*., *Clin. Infect. Dis.* ciaa344 (2020).
36. E. Goodwin *et al*., *Immunity* **48**, 339–349.e5 (2018).
37. B. Briney, A. Inderbitzin, C. Joyce, D. R. Burton, *Nature* **566**, 393–397 (2019).
38. N. C. Wu *et al*., *Nat. Commun.* **8**, 15371 (2017).
39. L. Yu, Y. Guan, *Front. Immunol.* **5**, 250 (2014).
40. F. Chen, N. Tzarum, I. A. Wilson, M. Law, *Curr. Opin. Virol.* **34**, 149–159 (2019).
41. J. Tan *et al*., *Nat. Med.* **24**, 401–407 (2018).
42. M. Yuan *et al*., *Science* **368**, 630–633 (2020).
43. Q. Wang *et al*., *Cell* **181**, 894–904.e9 (2020).
44. N. Wang *et al*., *Cell Rep.* **28**, 3395–3405.e6 (2019).
45. K. E. Pascal *et al*., *J. Infect. Dis.* **218** (suppl. 5), S612–S626 (2018).

ACKNOWLEDGMENTS

We thank C. Russell and A. Han for helpful comments on the manuscript; J. Koopsen for help with the phylogenetic analyses; and H. Turner, B. Anderson, and C. Bowman for assistance with the EM studies. **Funding:** This work was supported by a Netherlands Organization for Scientific Research (NWO) Vici grant (to R.W.S.); by the Bill & Melinda Gates Foundation through the Collaboration for AIDS Vaccine Discovery (CAVD) grants OPP1111923, OPP1132237, and INV-002022 to R.W.S. and grant OPP1170236 to A.B.W.; by the Fondation Dormeur, Vaduz (to R.W.S. and to M.J.v.G.) and Health Holland PPS-allowance LSHM20040 (to M.J.v.G.); and by the Netherlands Organisation for Health Research and Development (ZONMW to B.L.H). M.J.v.G. is a recipient of an AMC Fellowship from Amsterdam UMC and a COVID-19 grant from the Amsterdam Institute for Infection and Immunity. R.W.S and M.J.v.G. are recipients of support from the University of Amsterdam Proof of Concept fund (contract no. 200421) as managed by Innovation Exchange Amsterdam (IXA). The funders had no role in study design, data collection, data analysis, data interpretation, or data reporting. **Author contributions:** P.J.M.B., T.G.C., K.v.d.S., G.V., B.H., A.B.W., G.J.d.B., R.W.S., and M.J.v.G. conceived and designed experiments. K.v.d.S., W.J.W., N.K., and G.d.B arranged medical ethical approval, recruitment of study participants, and collection of study material. P.J.M.B., T.G.C., J.L.S., Y.A., S.B., J.L.T., N.M.A.O., G.K., A.E.H.B., M.M.v.H., D.G., J.A.B., E.E.S., K.D.V., J.v.S., M.J.v.B., T.P.L.B., K.S., R.D., and I.B. performed the experiments. P.J.M.B., T.G.C., M.C., and A.A. set up experimental assays. P.J.M.B., T.G.C., K.v.d.S., N.v.d.V., A.v.d.K., R.W.S., and M.J.v.G. analyzed and interpreted data. P.J.M.B., T.G.C., K.v.d.S., G.J.d.B., R.W.S., and M.J.v.G. wrote the manuscript with input from all listed authors. **Competing interests:** Amsterdam UMC has filed a patent application concerning the SARS-CoV-2 mAbs described here. **Data and materials availability:** Reagents and materials presented in this study are available from the corresponding authors under a materials transfer agreement with the Amsterdam UMC. Variable domain sequences of HC and LCs are available in table S1 and were uploaded on GenBank under accession numbers MT599820 to MT599987. The coordinates of the negative stain electron microscopy reconstructions were deposited in the Electron Microscopy Data Bank under accession numbers EMD-22061 to EMD-22066.

SUPPLEMENTARY MATERIALS

science.sciencemag.org/content/369/6504/643/suppl/DC1
Materials and Methods
Figs. S1 to S5
References (*46*–*56*)
Tables S1 and S2
MDAR Reproducibility Checklist

View/request a protocol for this paper from *Bio-protocol*.

4 May 2020; accepted 10 June 2020
Published online 15 June 2020
10.1126/science.abc5902

Cite as: Y. Cai *et al.*, *Science* 10.1126/science.abd4251 (2020).

Distinct conformational states of SARS-CoV-2 spike protein

Yongfei Cai[1,2*], Jun Zhang[1,2*], Tianshu Xiao[1,2], Hanqin Peng[1], Sarah M. Sterling[3,4], Richard M. Walsh Jr.[3,4], Shaun Rawson[3,4,5], Sophia Rits-Volloch[1], Bing Chen[1,2†]

[1]Division of Molecular Medicine, Boston Children's Hospital, Boston, MA 02115, USA. [2]Department of Pediatrics, Harvard Medical School, Boston, MA 02115, USA. [3]The Harvard Cryo-EM Center for Structural Biology, Harvard Medical School, Boston, MA 02115, USA. [4]Department of Biological Chemistry and Molecular Pharmacology, Blavatnik Institute, Harvard Medical School, Boston, MA 02115, USA. [5]SBGrid Consortium, Harvard Medical School, Boston, MA 02115, USA.

*These authors contributed equally to this work.

†Corresponding author. Email: bchen@crystal.harvard.edu

Intervention strategies are urgently needed to control the SARS-CoV-2 (severe acute respiratory syndrome coronavirus 2) pandemic. The trimeric viral spike (S) protein catalyzes fusion between viral and target cell membranes to initiate infection. Here we report two cryo-EM structures, derived from a preparation of the full-length S protein, representing its prefusion (2.9Å resolution) and postfusion (3.0Å resolution) conformations, respectively. The spontaneous transition to the postfusion state is independent of target cells. The prefusion trimer has three receptor-binding domains clamped down by a segment adjacent to the fusion peptide. The postfusion structure is strategically decorated by N-linked glycans, suggesting possible protective roles against host immune responses and harsh external conditions. These findings advance our understanding of SARS-CoV-2 entry and may guide development of vaccines and therapeutics.

The current coronavirus pandemic is having devastating social and economic consequences. Coronaviruses (CoVs) are enveloped positive-stranded RNA viruses. They include severe acute respiratory syndrome (SARS) and Middle East respiratory syndrome (MERS), both with significant fatalities (*1–3*), as well as several endemic common-cold viruses (*4*). With a large number of similar viruses circulating in bats and camels (*5–8*), the possibility of additional outbreaks poses major threats to global public health. The current disease, COVID-19 (coronavirus disease 2019), caused by a new virus SARS-CoV-2 (*9*), has created urgent needs for diagnostics, therapeutics and vaccines. Meeting these needs requires a deep understanding of the structure-function relationships of viral proteins and relevant host factors.

For all enveloped viruses, membrane fusion is a key early step for entering host cells and establishing infection (*10*). Although an energetically favorable process, membrane fusion has high kinetic barriers when two membranes approach each other, mainly due to repulsive hydration forces (*11*, *12*). For viral membrane fusion, free energy to overcome these kinetic barriers comes from refolding of virus-encoded fusion proteins from a primed, metastable prefusion conformational state to a stable, postfusion state (*13–15*). The fusion protein for CoV is its spike (S) protein that decorates the virion surface as an extensive crown (hence, "corona"). The protein also induces neutralizing antibody responses and is therefore an important target for vaccine development (*16*). The S protein is a heavily glycosylated type I membrane protein anchored in the viral membrane. It is first produced as a precursor that trimerizes and is thought to be cleaved by a furin-like protease into two fragments: the receptor-binding fragment S1 and the fusion fragment S2 (Fig. 1A) (*17*). Binding through the receptor-binding domain (RBD) in S1 to a host cell receptor (e.i., angiotensin converting enzyme 2 (ACE2) for both SARS-CoV and SARS-CoV-2) and further proteolytic cleavage at a second site in S2 (S2' site), by a serine protease TMPRSS2 (*18*) or endosomal cysteine proteases cathepsins B and L (CatB/L), are believed to trigger dissociation of S1 and irreversible refolding of S2 into a postfusion conformation – a trimeric hairpin structure formed by heptad repeat 1 (HR1) and heptad repeat 2 (HR2) (*19*, *20*). These large structural rearrangements bring together the viral and cellular membranes, ultimately leading to fusion of the two bilayers.

Since the first genome sequence of SARS-CoV-2 was released (*21*), several structures have been reported for S protein complexes, including the ectodomain stabilized in the prefusion conformation (*22–24*) and RBD-ACE2 complexes (*25–28*) (fig. S1), building upon the previous success of the structural biology of S proteins from other CoVs (*20*). In the stabilized S ectodomain, S1 folds into four domains - NTD (N-terminal domain), RBD, and two CTDs (C-terminal domains) and protects the prefusion conformation of S2 in which HR1 bends back toward the viral membrane (fig. S1, A and B). The RBD samples two distinct conformations – "up" representing a receptor-accessible state and "down" representing a receptor-inaccessible state. Structures representing the postfusion state of S2 from mouse hepatitis virus (fig. S1E) and a lower-resolution one from SARS-CoV (fig. S1F), suggest how the structural rearrangements of S2 proceed to promote membrane fusion and viral entry (*29*, *30*). Comparison of the pre-

and post-fusion states reveals that HR1 undergoes a "jack-knife" transition that can insert the fusion peptide (FP) into the target cell membrane. Folding back of HR2 places the FP and transmembrane (TM) segments at the same end of the molecule, causing the membranes with which they interact to bend toward each other, effectively leading to membrane fusion. In the previous structures, the regions near the viral membrane are either not present or disordered, and yet they all appear to play critical structural and functional roles (*31–35*).

To gain further insight, we aimed to determine the pre and post fusion states of full-length wild-type S protein of SARS-CoV-2.

Results

Purification of intact S protein

To produce a functional SARS-CoV-2 S protein, we transfected HEK293 cells with an expression construct of a full-length wildtype S sequence with a C-terminal strep-tag (Fig. 1A). These cells fused efficiently with cells transfected with an intact human ACE2 construct, even without addition of any extra proteases (fig. S2), suggesting that the S protein expressed on the cell surfaces is fully functional for membrane fusion. The fusion efficiency was not affected by the C-terminal strep-tag. To purify the full-length S protein, we lysed the cells and solubilized all membrane-bound proteins in 1% detergent NP-40. The strep-tagged S protein was then captured on strep-tactin resin in 0.3% NP-40. The purified S protein eluted from a size-exclusion column as three distinct peaks in 0.02% NP-40 (Fig. 1B). Analysis by Coomassie-stained SDS-PAGE (Fig. 1C) showed that peak 1 contained both the uncleaved S precursor and the cleaved S1/S2 complex; peak 2 had primarily the cleaved but dissociated S2 fragment; and peak 3 included mainly the dissociated S1 fragment, as judged by N-terminal sequencing and Western blot (fig. S3). This was confirmed by negative stain EM (Fig. 1C). Peak 1 showed the strongest binding to soluble ACE2, comparable to that for the purified soluble S ectodomain trimer, while peak 2 showed the weakest binding, since it contained mainly the S2 fragment (fig. S4). While the cleavage at the S1/S2 (furin) site is clearly demonstrated by protein sequencing of the N terminus of the S2 fragment in peak 2, cleavage at the S2' site is not obvious. We observed in some preparations a band around 20 kDa, a size expected for the S1/S2-S2' fragment (Fig. 1C). We obtained a similar gel filtration profile when another detergent (DDM) was used to solubilize the S protein (fig. S5), suggesting that the S protein dissociation during gel filtration chromatography is not triggered by any specific detergent. We also identified a major contaminating protein in the preparation as endoplasmic reticulum chaperone BiP precursor (*36*), which may have a role in facilitating S protein folding.

Cryo-EM structure determination

Cryo-EM images were acquired with selected grids prepared from all three peaks, on a Titan Krios electron microscope operated at 300 keV and equipped with a BioQuantum energy filter and a Gatan K3 direct electron detector. We used RELION (*37*) for particle picking, two-dimensional (2D) classification, three dimensional (3D) classification and refinement. Structure determination was performed by rounds of 3D classification, refinement and masked local refinement, as described in the supplementary materials. The final resolution was 2.9Å for the prefusion S protein; 3.0Å for the S2 in the postfusion conformation (figs. S6 to S9).

Structure of the prefusion S trimer

The overall architecture of the full-length S protein in the prefusion conformation is very similar to the published structures of a soluble S trimer stabilized by a C-terminal foldon trimerization tag and two proline substitutions at the boundary between HR1 and the central helix (CH) in S2 (fig. S1) (*22, 23*). In our new structure, the N terminus, several peripheral loops and glycans that were invisible in the soluble trimer structures are ordered (Fig. 2, A and B, and fig. S10A). As described previously, the four domains of the S1 fragment, NTD, RBD, CTD1 and CTD2, wrap around the three-fold axis, covering the S2 fragment underneath. The furin cleavage site at the S1/S2 boundary is in a surface-exposed and disordered loop (Fig. 2B), so it is unclear whether this structure represents the uncleaved or cleaved trimer, although the sample clearly contains both forms (Fig. 1C). Likewise, the S2 fragment has a conformation nearly identical to that in the previous trimer structures, with most of the polypeptide chain packed around a central three-stranded coiled coil formed by CH, including the connector domain (CD), which links CH and the C-terminal HR2 through an additional linker region. A difference between our structure and the published trimer structures is that a ~25-residue segment in S2 immediately downstream of the fusion peptide is ordered. The segments, HR2, TM and CT, not observed in previous structures, are still not visible.

Several features are different between our structure and the previously described prefusion conformations. First, the N terminus in our structure is ordered and adopts a conformation similar to that in SARS-CoV, including a disulfide bond (Cys15-Cys136) and a N-linked glycan at Asn17 (Fig. 3A) (*38*). It would be important to confirm whether this region is unfolded with no disulfide bond in the stabilized soluble constructs or folded and simply poorly defined by density, despite a disulfide bond, particularly if they are widely used for vaccine studies.

Second, another disulfide containing segment (residues 828-853), immediately downstream of the fusion peptide is also absent from the structures of the soluble ectodomain,

but ordered in our structure (Fig. 3B). We designate it as the fusion-peptide proximal region (FPPR). The FPPR is disordered in both the closed and RBD-up conformations of the stabilized soluble S trimer. In our full-length structure, it packs rather tightly around an internal disulfide bond between Cys840 and Cys851, further reinforced by a salt bridge between Lys835 and Asp848, as well as by an extensive hydrogen bond network. When compared with the RBD-up conformation by superposition of the rest of S2, the FPPR clashes with CTD1, which rotates outwards with the RBD in the flipping-up transition. Thus, a structured FPPR, abutting the opposite side of CTD1 from the RBD, appears to help clamp down the RBD and stabilize the closed conformation of the S trimer. It is not obvious why the FPPR is also not visible in the published, closed S ectodomain structure with all three RBDs in the down conformation (*23*). Our structure of the full-length S protein suggests that CTD1 is a structural relay between RBD and FPPR that can sense the displacement on either side. The latter is directly connected to the fusion peptide. Lack of a structured FPPR in the stabilized, soluble S trimer may explain why the RBD-up conformation is readily detected in that preparation. In addition, a D614G mutation, identified in recent SARS-CoV-2 isolates, has been suggested to lead to more efficient entry (*39*, *40*). D614 forms a salt bridge with K854 in the FPPR (fig. S10B), supporting a functional role of the FPPR in membrane fusion. In the 3D classification of our prefusion particles from two independent data sets, only one subclass with an RBD flipped up was observed (fig. S6), suggesting that the RBD-up conformation is relatively rare in our full-length S preparation. The map for this subclass was refined to 4.7Å without C3 symmetry and we could not model the FPPR. The FPPR is ordered in all other maps that are refined to 3.5Å or higher resolution.

When we aligned our full-length structure with the soluble S trimer structure by the S2 portion, the three S1 subunits in the soluble trimer structure move outwards away from the three-fold axis, up to ~12Å in peripheral areas (Fig. 3C and fig. S11), suggesting the full length S trimer is more tightly packed among the three protomers than the mutated soluble trimer. Examining the region near the proline mutations between HR1 and CH, we found that the K986P mutation appeared to eliminate a salt bridge between Lys986 in one protomer and either Asp 427 or Asp428 in another protomer; thus, the mutation could create a net charge (three for one trimer) inside the trimer interface. This may explain why the soluble trimer with the PP mutation has a looser structure than the full-length S with wildtype sequence. Whether this loosening leads to disordered FPPRs in the closed trimer will require additional experimental evidence. However, the proline mutations, designed to destabilize the postfusion conformation and strengthen the prefusion structure, may also impact the prefusion structure.

Structure of the postfusion S2 trimer

3D reconstruction of the sample from peak 2 yielded a postfusion structure of the S2 trimer, shown in Fig. 4A. The overall architecture of the SARS-CoV-2 S2 in the postfusion conformation is nearly identical to that of the published structure derived from the S2 ectodomain of mouse hepatitis virus (MHV) produced in insect cells (fig. S1) (*29*). In the structure, HR1 and CH form an unusually long central three-stranded coiled coil (~180Å). The connector domain, together with a segment (residues 718-729) in the S1/S2-S2' fragment, form a three-stranded β sheet, which is invariant between the prefusion and postfusion structures. In the postfusion state, residues 1127-1135 join the connector β sheet to expand it into four strands, while projecting the C-terminal HR2 toward the viral membrane. Another segment (residues 737-769) in the S1/S2-S2' fragment makes up three helical regions locked by two disulfide bonds that pack against the groove of the CH part of the coiled coil to form a short six helix bundle structure (6HB-1 in Fig. 4B). It is unclear whether the S'2 site is cleaved because it is in a disordered region spanning 142 residues (Fig. 4B), as in the MHV S2 structure. Nevertheless, the S1/S2-S2' fragment is an integral part of the postfusion structure and would not dissociate, regardless of cleavage at the S2' site. The N-terminal region of HR2 adopts a one-turn helical conformation and also packs against the groove of the HR1 coiled-coil; the C-terminal region of HR2 forms a longer helix that makes up the second six-helix bundle structure with the rest of the HR1 coiled-coil (6HB-2 in Fig. 4B). Thus, the long central coiled-coil is reinforced multiple times along its long axis, making it a very rigid structure, as evident even from 2D class averages of particles in the cryo images (fig. S8).

A striking feature of the postfusion S2 is its surface decoration by N-linked glycans (Fig. 4C), also visible in the 2D class averages (fig. S8). Five glycans at residues Asn1098, Asn1134, Asn1158, Asn1173 and Asn1194 are positioned along the long axis with a regular spacing with four of them aligned on the same side of the trimer. If these glycosylation sites are fully occupied by branched sugars, they may shield most surfaces of the postfusion S2 trimer. A similar pattern has been recently described in a paper posted in ChinaXiv (http://www.chinaxiv.org/user/download.htm?id=30394) for a SARS-CoV S2 preparation derived from a soluble S ectodomain construct produced in insect cells and triggered by proteolysis and low pH. The reason for this decoration is unclear given that a postfusion structure has accomplished its mission, and should not need to be concealed from the immune system.

Peak 3 contains primarily the dissociated monomeric S1 fragment, which has the smallest size (~100 kDa) and shows the lowest contrast in cryo grids of the three particle types we describe. We carried out a preliminary 3D reconstruction

analysis (fig. S12), further confirming its identity.

Discussion

Architecture of S protein on the surface of SARS-CoV-2 virion

The fact that the cleaved S1/S2 complex dissociates in the absence of ACE2 and that the S2 fragment adopts a postfusion conformation under mild detergent conditions, suggesting that the kinetic barrier for the conformational transition relevant to viral entry is surprisingly low for this S protein. Whether or not this observation relates directly to efficient membrane fusion or infection is unclear. Nevertheless, it is noteworthy that the postfusion S2 trimer not only has a very stable and rigid structure, but also that it is strategically decorated with N-linked glycans along its long axis, as if under selective pressure for functions other than the membrane fusion process. Although some have suggested that viral fusion proteins may further oligomerize in their postfusion conformation to facilitate fusion pore formation (*41*), the protruding surface glycans of the SARS-CoV-2 S2 make this scenario unlikely. A more plausible possibility is a protective role that the S2 postfusion structure could play if it is also present on the surface of an infectious and mature virion. It may induce nonneutralizing antibody responses to evade the host immune system; it may also shield the more vulnerable prefusion S1/S2 trimers under conditions outside the host by decorating the viral surface with interspersed rigid spikes (Fig. 5A). Several recent reports have provided some evidence supporting this possibility. First, EM images of a β-propiolactone inactivated SARS-CoV-2 virus preparation, purified by a potassium tartrate-glycerol density gradient, appeared to have lost all S1 subunits, leaving only the postfusion S2 on the virion surfaces (*42*). Likewise, EM images of a β-propiolactone inactivated SARS-CoV-2 virus vaccine candidate (PiCoVacc) also showed needle-like spikes on its surfaces (*43*). Second, spontaneous shedding of SARS-CoV-2 S1 from pseudoviruses in absence of ACE2 has been reported (*39*). Third, binding antibodies against S2 are readily detectable in COVID-19 patients (*44*), suggesting S2 is more exposed to the host immune system than indicated by the unprotected surfaces on the prefusion structures (*22*, *23*) (Fig. 2). We therefore suggest that postfusion S2 trimers may have a protective function by constituting part of the crown on the surface of mature and infectious SARS-CoV-2 virion (Fig. 5). The postfusion S2 spikes are probably formed after spontaneous dissociation of S1, independent of the target cells.

Membrane fusion

We identify a structure near the fusion peptide – the fusion peptide proximal region (FPPR), which may play a critical role in the fusogenic structural rearrangements of S protein. There appears to be crosstalk between the RBD and the FPPR, mediated by CTD1, as a structured FPPR clamps down the RBD while an RBD-up conformation disorders the FPPR. Moreover, the FPPR is close to the S1/S2 boundary and the S2' cleavage site, and thus might be the center of activities relevant to conformational changes in S. One possibility is that one FPPR occasionally flips out of position due to intrinsic protein dynamics, allowing the RBDs to sample the up conformation. A fluctuation of this kind would loosen the entire S trimer, as observed in modified soluble S trimer constructs (*22*, *23*). Once an RBD is fixed in the up position by binding to ACE2 on the surface of a target cell, a flexible FPPR may enable exposure of the S2' cleavage site immediately upstream of the adjacent fusion peptide. The phenotype of the D614G mutation appears to be consistent with the notion that the FPPR is involved in membrane fusion (*39*, *40*). Cleavage at the S2' site releases the structural constraints on the fusion peptide, which may initiate a cascade of refolding events in S2, including formation of the long central three stranded coiled-coil, folding back of HR2 and ultimately membrane fusion. Cleavage at the S1/S2 site allows complete dissociation of S1, which may also facilitate S2 refolding.

Puzzles regarding membrane fusion remain, as the regions near the viral membrane are still not visible in the reconstructions. Yet these regions all play critical structural and functional roles. For example, the conserved hydrophobic region immediately preceding the TM domain, and possibly the TM itself, have been shown to be crucial for S protein trimerization and membrane fusion (*31*). The cytoplasmic tail, containing a palmitoylated cysteine-rich region, is believed to be involved in viral assembly and cell-cell fusion (*32*–*35*). Whether other viral proteins, such M protein, may help stabilize the spike by interacting with the HR2 remains an interesting question. Thus, we still need a high-resolution structure of an intact S protein in the context of the membrane and other viral components to answer the various open questions.

Considerations for vaccine development

A safe and effective vaccine is the primary medical option to reduce or eliminate the threat posed by SARS-CoV-2. The first round of vaccine candidates with various forms of the spike (S) protein of the virus are passing rapidly through preclinical studies in animal models and clinical trials in humans. Our study raises several potential concerns about the current vaccine strategies. First, vaccines using the full-length wildtype sequence of S protein may produce the various forms in vivo that we have observed here. The postfusion conformations could expose immunodominant, nonneutralizing epitopes that distract the host immune system, as documented for other viruses, such as HIV-1 and RSV (*45*, *46*). Second, the approach to stabilize the prefusion conformation by introducing proline mutations at residues 986 and 987 may not be optimal, as the K986P mutation may break a salt bridge between protomers that contributes to the trimer

stability. The resulting S trimer structure with a relaxed apex may induce antibodies that could not efficiently recognize S trimer spikes on the virus, although it may be more effective in inducing anti-RBD neutralizing responses than the closed form. Third, in light of the possibility that the postfusion S2 is present on infectious virions, vaccines using β-propiolactone inactivated viruses may require additional quality control tests. Although the PiCoVacc appears to provide protection against challenges in nonhuman primates after three immunizations (*43*), it is unclear how to minimize the number of the postfusion S2 trimers to avoid batch variations. Structure-guided immunogen design may be particularly critical if SARS-CoV-2 becomes seasonal and returns with antigenic drift, as do influenza viruses (*47*).

REFERENCES AND NOTES

1. E. de Wit, N. van Doremalen, D. Falzarano, V. J. Munster, SARS and MERS: Recent insights into emerging coronaviruses. *Nat. Rev. Microbiol.* **14**, 523–534 (2016). doi:10.1038/nrmicro.2016.81 Medline
2. N. S. Zhong, B. J. Zheng, Y. M. Li, L. L. M. Poon, Z. H. Xie, K. H. Chan, P. H. Li, S. Y. Tan, Q. Chang, J. P. Xie, X. Q. Liu, J. Xu, D. X. Li, K. Y. Yuen, J. S. M. Peiris, Y. Guan, Epidemiology and cause of severe acute respiratory syndrome (SARS) in Guangdong, People's Republic of China, in February, 2003. *Lancet* **362**, 1353–1358 (2003). doi:10.1016/S0140-6736(03)14630-2 Medline
3. B. Hijawi, M. Abdallat, A. Sayaydeh, S. Alqasrawi, A. Haddadin, N. Jaarour, S. Alsheikh, T. Alsanouri, Novel coronavirus infections in Jordan, April 2012: Epidemiological findings from a retrospective investigation. *East. Mediterr. Health J.* **19**, S12–S18 (2013). doi:10.26719/2013.19.supp1.S12 Medline
4. V. M. Corman, D. Muth, D. Niemeyer, C. Drosten, Hosts and sources of endemic human coronaviruses. *Adv. Virus Res.* **100**, 163–188 (2018). doi:10.1016/bs.aivir.2018.01.001 Medline
5. Y. Guan, B. J. Zheng, Y. Q. He, X. L. Liu, Z. X. Zhuang, C. L. Cheung, S. W. Luo, P. H. Li, L. J. Zhang, Y. J. Guan, K. M. Butt, K. L. Wong, K. W. Chan, W. Lim, K. F. Shortridge, K. Y. Yuen, J. S. Peiris, L. L. Poon, Isolation and characterization of viruses related to the SARS coronavirus from animals in southern China. *Science* **302**, 276–278 (2003). doi:10.1126/science.1087139 Medline
6. B. Hu, L.-P. Zeng, X.-L. Yang, X.-Y. Ge, W. Zhang, B. Li, J.-Z. Xie, X.-R. Shen, Y.-Z. Zhang, N. Wang, D.-S. Luo, X.-S. Zheng, M.-N. Wang, P. Daszak, L.-F. Wang, J. Cui, Z.-L. Shi, Discovery of a rich gene pool of bat SARS-related coronaviruses provides new insights into the origin of SARS coronavirus. *PLOS Pathog.* **13**, e1006698 (2017). doi:10.1371/journal.ppat.1006698 Medline
7. H. A. Mohd, J. A. Al-Tawfiq, Z. A. Memish, Middle East Respiratory Syndrome Coronavirus (MERS-CoV) origin and animal reservoir. *Virol. J.* **13**, 87 (2016). doi:10.1186/s12985-016-0544-0 Medline
8. A. Banerjee, K. Kulcsar, V. Misra, M. Frieman, K. Mossman, Bats and coronaviruses. *Viruses* **11**, 41 (2019). doi:10.3390/v11010041 Medline
9. P. Zhou, X.-L. Yang, X.-G. Wang, B. Hu, L. Zhang, W. Zhang, H.-R. Si, Y. Zhu, B. Li, C.-L. Huang, H.-D. Chen, J. Chen, Y. Luo, H. Guo, R.-D. Jiang, M.-Q. Liu, Y. Chen, X.-R. Shen, X. Wang, X.-S. Zheng, K. Zhao, Q.-J. Chen, F. Deng, L.-L. Liu, B. Yan, F.-X. Zhan, Y.-Y. Wang, G.-F. Xiao, Z.-L. Shi, A pneumonia outbreak associated with a new coronavirus of probable bat origin. *Nature* **579**, 270–273 (2020). doi:10.1038/s41586-020-2012-7 Medline
10. S. Belouzard, J. K. Millet, B. N. Licitra, G. R. Whittaker, Mechanisms of coronavirus cell entry mediated by the viral spike protein. *Viruses* **4**, 1011–1033 (2012). doi:10.3390/v4061011 Medline
11. R. P. Rand, V. A. Parsegian, Physical force considerations in model and biological membranes. *Can. J. Biochem. Cell Biol.* **62**, 752–759 (1984). doi:10.1139/o84-097 Medline
12. V. A. Parsegian, N. Fuller, R. P. Rand, Measured work of deformation and repulsion of lecithin bilayers. *Proc. Natl. Acad. Sci. U.S.A.* **76**, 2750–2754 (1979). doi:10.1073/pnas.76.6.2750 Medline
13. S. C. Harrison, Viral membrane fusion. *Virology* **479-480**, 498–507 (2015). doi:10.1016/j.virol.2015.03.043 Medline
14. M. Kielian, Mechanisms of virus membrane fusion proteins. *Annu. Rev. Virol.* **1**, 171–189 (2014). doi:10.1146/annurev-virology-031413-085521 Medline
15. W. Weissenhorn, A. Dessen, L. J. Calder, S. C. Harrison, J. J. Skehel, D. C. Wiley, Structural basis for membrane fusion by enveloped viruses. *Mol. Membr. Biol.* **16**, 3–9 (1999). doi:10.1080/096876899294706 Medline
16. L. Du, Y. He, Y. Zhou, S. Liu, B.-J. Zheng, S. Jiang, The spike protein of SARS-CoV—A target for vaccine and therapeutic development. *Nat. Rev. Microbiol.* **7**, 226–236 (2009). doi:10.1038/nrmicro2090 Medline
17. B. J. Bosch, R. van der Zee, C. A. de Haan, P. J. Rottier, The coronavirus spike protein is a class I virus fusion protein: Structural and functional characterization of the fusion core complex. *J. Virol.* **77**, 8801–8811 (2003). doi:10.1128/JVI.77.16.8801-8811.2003 Medline
18. M. Hoffmann, H. Kleine-Weber, S. Schroeder, N. Krüger, T. Herrler, S. Erichsen, T. S. Schiergens, G. Herrler, N.-H. Wu, A. Nitsche, M. A. Müller, C. Drosten, S. Pöhlmann, SARS-CoV-2 cell entry depends on ACE2 and TMPRSS2 and is blocked by a clinically proven protease inhibitor. *Cell* **181**, 271–280.e8 (2020). doi:10.1016/j.cell.2020.02.052 Medline
19. J. K. Millet, G. R. Whittaker, Host cell entry of Middle East respiratory syndrome coronavirus after two-step, furin-mediated activation of the spike protein. *Proc. Natl. Acad. Sci. U.S.A.* **111**, 15214–15219 (2014). doi:10.1073/pnas.1407087111 Medline
20. M. A. Tortorici, D. Veesler, Structural insights into coronavirus entry. *Adv. Virus Res.* **105**, 93–116 (2019). doi:10.1016/bs.aivir.2019.08.002 Medline
21. F. Wu, S. Zhao, B. Yu, Y.-M. Chen, W. Wang, Z.-G. Song, Y. Hu, Z.-W. Tao, J.-H. Tian, Y.-Y. Pei, M.-L. Yuan, Y.-L. Zhang, F.-H. Dai, Y. Liu, Q.-M. Wang, J.-J. Zheng, L. Xu, E. C. Holmes, Y.-Z. Zhang, A new coronavirus associated with human respiratory disease in China. *Nature* **579**, 265–269 (2020). doi:10.1038/s41586-020-2008-3 Medline
22. D. Wrapp, N. Wang, K. S. Corbett, J. A. Goldsmith, C.-L. Hsieh, O. Abiona, B. S. Graham, J. S. McLellan, Cryo-EM structure of the 2019-nCoV spike in the prefusion conformation. *Science* **367**, 1260–1263 (2020). doi:10.1126/science.abb2507 Medline
23. A. C. Walls, Y.-J. Park, M. A. Tortorici, A. Wall, A. T. McGuire, D. Veesler, Structure, function, and antigenicity of the SARS-CoV-2 spike glycoprotein. *Cell* **181**, 281–292.e6 (2020). doi:10.1016/j.cell.2020.02.058 Medline
24. R. Henderson, R. Henderson, R. J. Edwards, K. Mansouri, K. Janowska, V. Stalls, S. Gobeil, M. Kopp, A. Hsu, M. Borgnia, R. Parks, B. F. Haynes, P. Acharya, Controlling the SARS-CoV-2 spike glycoprotein conformation. bioRxiv 2020.05.18.102087 [Preprint]. 18 May 2020; https://doi.org/10.1101/2020.05.18.102087.
25. J. Lan, J. Ge, J. Yu, S. Shan, H. Zhou, S. Fan, Q. Zhang, X. Shi, Q. Wang, L. Zhang, X. Wang, Structure of the SARS-CoV-2 spike receptor-binding domain bound to the ACE2 receptor. *Nature* **581**, 215–220 (2020). doi:10.1038/s41586-020-2180-5 Medline
26. R. Yan, Y. Zhang, Y. Li, L. Xia, Y. Guo, Q. Zhou, Structural basis for the recognition of SARS-CoV-2 by full-length human ACE2. *Science* **367**, 1444–1448 (2020). doi:10.1126/science.abb2762 Medline
27. J. Shang, G. Ye, K. Shi, Y. Wan, C. Luo, H. Aihara, Q. Geng, A. Auerbach, F. Li, Structural basis of receptor recognition by SARS-CoV-2. *Nature* **581**, 221–224 (2020). doi:10.1038/s41586-020-2179-y Medline
28. Q. Wang, Y. Zhang, L. Wu, S. Niu, C. Song, Z. Zhang, G. Lu, C. Qiao, Y. Hu, K.-Y. Yuen, Q. Wang, H. Zhou, J. Yan, J. Qi, Structural and functional basis of SARS-CoV-2 entry by using human ACE2. *Cell* **181**, 894–904.e9 (2020). doi:10.1016/j.cell.2020.03.045 Medline
29. A. C. Walls, M. A. Tortorici, J. Snijder, X. Xiong, B.-J. Bosch, F. A. Rey, D. Veesler, Tectonic conformational changes of a coronavirus spike glycoprotein promote membrane fusion. *Proc. Natl. Acad. Sci. U.S.A.* **114**, 11157–11162 (2017). doi:10.1073/pnas.1708727114 Medline
30. W. Song, M. Gui, X. Wang, Y. Xiang, Cryo-EM structure of the SARS coronavirus spike glycoprotein in complex with its host cell receptor ACE2. *PLOS Pathog.* **14**, e1007236 (2018). doi:10.1371/journal.ppat.1007236 Medline
31. B. Schroth-Diez, K. Ludwig, B. Baljinnyam, C. Kozerski, Q. Huang, A. Herrmann, The role of the transmembrane and of the intraviral domain of glycoproteins in membrane fusion of enveloped viruses. *Biosci. Rep.* **20**, 571–595 (2000). doi:10.1023/A:1010415122234 Medline

32. B. J. Bosch, C. A. de Haan, S. L. Smits, P. J. Rottier, Spike protein assembly into the coronavirion: Exploring the limits of its sequence requirements. *Virology* **334**, 306–318 (2005). doi:10.1016/j.virol.2005.02.001 Medline
33. E. Lontok, E. Corse, C. E. Machamer, Intracellular targeting signals contribute to localization of coronavirus spike proteins near the virus assembly site. *J. Virol.* **78**, 5913–5922 (2004). doi:10.1128/JVI.78.11.5913-5922.2004 Medline
34. C. M. Petit, J. M. Melancon, V. N. Chouljenko, R. Colgrove, M. Farzan, D. M. Knipe, K. G. Kousoulas, Genetic analysis of the SARS-coronavirus spike glycoprotein functional domains involved in cell-surface expression and cell-to-cell fusion. *Virology* **341**, 215–230 (2005). doi:10.1016/j.virol.2005.06.046 Medline
35. R. Ye, C. Montalto-Morrison, P. S. Masters, Genetic analysis of determinants for spike glycoprotein assembly into murine coronavirus virions: Distinct roles for charge-rich and cysteine-rich regions of the endodomain. *J. Virol.* **78**, 9904–9917 (2004). doi:10.1128/JVI.78.18.9904-9917.2004 Medline
36. S. M. Hurtley, D. G. Bole, H. Hoover-Litty, A. Helenius, C. S. Copeland, Interactions of misfolded influenza virus hemagglutinin with binding protein (BiP). *J. Cell Biol.* **108**, 2117–2126 (1989). doi:10.1083/jcb.108.6.2117 Medline
37. S. H. Scheres, RELION: Implementation of a Bayesian approach to cryo-EM structure determination. *J. Struct. Biol.* **180**, 519–530 (2012). doi:10.1016/j.jsb.2012.09.006 Medline
38. R. N. Kirchdoerfer, N. Wang, J. Pallesen, D. Wrapp, H. L. Turner, C. A. Cottrell, K. S. Corbett, B. S. Graham, J. S. McLellan, A. B. Ward, Stabilized coronavirus spikes are resistant to conformational changes induced by receptor recognition or proteolysis. *Sci. Rep.* **8**, 15701 (2018). doi:10.1038/s41598-018-34171-7 Medline
39. L. Zhang, C. B. Jackson, H. Mou, A. Ojha, E. S. Rangarajan, T. Izard, M. Farzan, H. Choe, The D614G mutation in the SARS-CoV-2 spike protein reduces S1 shedding and increases infectivity. bioRxiv 2020.06.12.148726 [Preprint]. 12 June 2020; https://doi.org/10.1101/2020.06.12.148726.
40. Z. Daniloski, T. X. Jordan, J. K. Ilman, X. Guo, G. Bhabha, B. R. tenOever, N. E. Sanjana, The Spike D614G mutation increases SARS-CoV-2 infection of multiple human cell types. bioRxiv 10.1101/2020.06.14.151357 [Preprint]. 7 July 2020; https://doi.org/10.1101/2020.06.14.151357.
41. T. Danieli, S. L. Pelletier, Y. I. Henis, J. M. White, Membrane fusion mediated by the influenza virus hemagglutinin requires the concerted action of at least three hemagglutinin trimers. *J. Cell Biol.* **133**, 559–569 (1996). doi:10.1083/jcb.133.3.559 Medline
42. C. Liu, Y. Yang, Y. Gao, C. Shen, B. Ju, C. Liu, X. Tang, J. Wei, X. Ma, W. Liu, S. Xu, Y. Liu, J. Yuan, J. Wu, Z. Liu, Z. Zhang, P. Wang, L. Liu, Viral architecture of SARS-CoV-2 with post-fusion spike revealed by cryo-EM. bioRxiv 2020.03.02.972927 [Preprint]. 5 March 2020; https://doi.org/10.1101/2020.03.02.972927.
43. Q. Gao, L. Bao, H. Mao, L. Wang, K. Xu, M. Yang, Y. Li, L. Zhu, N. Wang, Z. Lv, H. Gao, X. Ge, B. Kan, Y. Hu, J. Liu, F. Cai, D. Jiang, Y. Yin, C. Qin, J. Li, X. Gong, X. Lou, W. Shi, D. Wu, H. Zhang, L. Zhu, W. Deng, Y. Li, J. Lu, C. Li, X. Wang, W. Yin, Y. Zhang, C. Qin, Development of an inactivated vaccine candidate for SARS-CoV-2. *Science* **369**, 77–81 (2020). doi:10.1126/science.abc1932 Medline
44. F. Wu, A. Wang, M. Liu, Q. Wang, J. Chen, S. Xia, Y. Ling, Y. Zhang, J. Xun, L. Lu, S. Jiang, H. Lu, Y. Wen, J. Huang, Neutralizing antibody responses to SARS-CoV-2 in a COVID-19 recovered patient cohort and their implications. medRxiv 2020.03.30.20047365 [Preprint]. 20 April 2020; https://doi.org/10.1101/2020.03.30.20047365.
45. J. S. McLellan, M. Chen, M. G. Joyce, M. Sastry, G. B. E. Stewart-Jones, Y. Yang, B. Zhang, L. Chen, S. Srivatsan, A. Zheng, T. Zhou, K. W. Graepel, A. Kumar, S. Moin, J. C. Boyington, G.-Y. Chuang, C. Soto, U. Baxa, A. Q. Bakker, H. Spits, T. Beaumont, Z. Zheng, N. Xia, S.-Y. Ko, J.-P. Todd, S. Rao, B. S. Graham, P. D. Kwong, Structure-based design of a fusion glycoprotein vaccine for respiratory syncytial virus. *Science* **342**, 592–598 (2013). doi:10.1126/science.1243283 Medline
46. G. Frey, J. Chen, S. Rits-Volloch, M. M. Freeman, S. Zolla-Pazner, B. Chen, Distinct conformational states of HIV-1 gp41 are recognized by neutralizing and non-neutralizing antibodies. *Nat. Struct. Mol. Biol.* **17**, 1486–1491 (2010). doi:10.1038/nsmb.1950 Medline
47. J. J. Skehel, D. C. Wiley, Receptor binding and membrane fusion in virus entry: The influenza hemagglutinin. *Annu. Rev. Biochem.* **69**, 531–569 (2000). doi:10.1146/annurev.biochem.69.1.531 Medline
48. G. Frey, H. Peng, S. Rits-Volloch, M. Morelli, Y. Cheng, B. Chen, A fusion-intermediate state of HIV-1 gp41 targeted by broadly neutralizing antibodies. *Proc. Natl. Acad. Sci. U.S.A.* **105**, 3739–3744 (2008). doi:10.1073/pnas.0800255105 Medline
49. J. M. Kovacs, J. P. Nkolola, H. Peng, A. Cheung, J. Perry, C. A. Miller, M. S. Seaman, D. H. Barouch, B. Chen, HIV-1 envelope trimer elicits more potent neutralizing antibody responses than monomeric gp120. *Proc. Natl. Acad. Sci. U.S.A.* **109**, 12111–12116 (2012). doi:10.1073/pnas.1204533109 Medline
50. J. Chen, J. M. Kovacs, H. Peng, S. Rits-Volloch, J. Lu, D. Park, E. Zablowsky, M. S. Seaman, B. Chen, Effect of the cytoplasmic domain on antigenic characteristics of HIV-1 envelope glycoprotein. *Science* **349**, 191–195 (2015). doi:10.1126/science.aaa9804 Medline
51. S. Q. Zheng, E. Palovcak, J.-P. Armache, K. A. Verba, Y. Cheng, D. A. Agard, MotionCor2: Anisotropic correction of beam-induced motion for improved cryo-electron microscopy. *Nat. Methods* **14**, 331–332 (2017). doi:10.1038/nmeth.4193 Medline
52. A. Rohou, N. Grigorieff, CTFFIND4: Fast and accurate defocus estimation from electron micrographs. *J. Struct. Biol.* **192**, 216–221 (2015). doi:10.1016/j.jsb.2015.08.008 Medline
53. T. Wagner, F. Merino, M. Stabrin, T. Moriya, C. Antoni, A. Apelbaum, P. Hagel, O. Sitsel, T. Raisch, D. Prumbaum, D. Quentin, D. Roderer, S. Tacke, B. Siebolds, E. Schubert, T. R. Shaikh, P. Lill, C. Gatsogiannis, S. Raunser, SPHIRE-crYOLO is a fast and accurate fully automated particle picker for cryo-EM. *Commun. Biol.* **2**, 218 (2019). doi:10.1038/s42003-019-0437-z Medline
54. E. F. Pettersen, T. D. Goddard, C. C. Huang, G. S. Couch, D. M. Greenblatt, E. C. Meng, T. E. Ferrin, UCSF Chimera—A visualization system for exploratory research and analysis. *J. Comput. Chem.* **25**, 1605–1612 (2004). doi:10.1002/jcc.20084 Medline
55. P. Emsley, B. Lohkamp, W. G. Scott, K. Cowtan, Features and development of Coot. *Acta Crystallogr. D Biol. Crystallogr.* **66**, 486–501 (2010). doi:10.1107/S0907444910007493 Medline
56. A. Morin, B. Eisenbraun, J. Key, P. C. Sanschagrin, M. A. Timony, M. Ottaviano, P. Sliz, Collaboration gets the most out of software. *eLife* **2**, e01456 (2013). doi:10.7554/eLife.01456 Medline
57. P. D. Adams, P. V. Afonine, G. Bunkóczi, V. B. Chen, I. W. Davis, N. Echols, J. J. Headd, L.-W. Hung, G. J. Kapral, R. W. Grosse-Kunstleve, A. J. McCoy, N. W. Moriarty, R. Oeffner, R. J. Read, D. C. Richardson, J. S. Richardson, T. C. Terwilliger, P. H. Zwart, PHENIX: A comprehensive Python-based system for macromolecular structure solution. *Acta Crystallogr. D Biol. Crystallogr.* **66**, 213–221 (2010). doi:10.1107/S0907444909052925 Medline

ACKNOWLEDGMENTS

We thank M. Liao for generous advice, SBGrid team for technical support, and S. Harrison, M. Liao, A. Carfi and D. Barouch for critical reading of the manuscript. Negative stain and cryo-EM data were collected at the Molecular Electron Microscopy Suite and the Harvard Cryo-EM Center for Structural Biology, respectively, at Harvard Medical School. **Funding:** This work was supported by NIH grants AI147884 (to B.C.), 3R01AI147884-01A1S1 (to B.C), AI141002 (to B.C.), AI127193 (to B.C. and James Chou), as well as a COVID19 Award by Massachusetts Consortium on Pathogen Readiness (MassCPR; to B.C.). **Author Contribution:** B.C. and Y.C. conceived the project. Y.C. and H.P. expressed and purified the full-length S protein. T.X. expressed and purified soluble ACE2, performed SPR and cell-cell fusion experiments. Y.C. and J.Z. performed negative stain EM analysis. J.Z. prepared cryo grids and performed EM data collection with contributions from S.S. and R.M.W.. J.Z. processed the cryo-EM data, built and refined the atomic models for the prefusion S trimer and the postfusion S2 trimer. Y.C. processed the S1 data. S.R. contributed to data processing for S1 and provided computational support. S.R.V. contributed to cell culture and protein production. All authors analyzed the data. B.C., Y.C., J.Z. and T.X. wrote the manuscript with input from all other authors. **Competing interests:** The authors declare no competing interests. **Data and materials availability:** The atomic structure coordinates are deposited in the RCSB Protein Data Bank (PDB) under the accession numbers 6XR8 and 6XRA; and the electron microscopy maps have been deposited in the Electron Microscopy Data Bank (EMDB) under the accession numbers EMD-22292 and EMD-22293. All materials generated during the current study are available from the

SUPPLEMENTARY MATERIALS

science.sciencemag.org/cgi/content/full/science.abd4251/DC1
Materials and Methods
Figs. S1 to S12
Table S1
References (*48*–*57*)
MDAR Reproducibility Checklist

20 June 2020; accepted 14 July 2020
Published online 21 July 2020
10.1126/science.abd4251

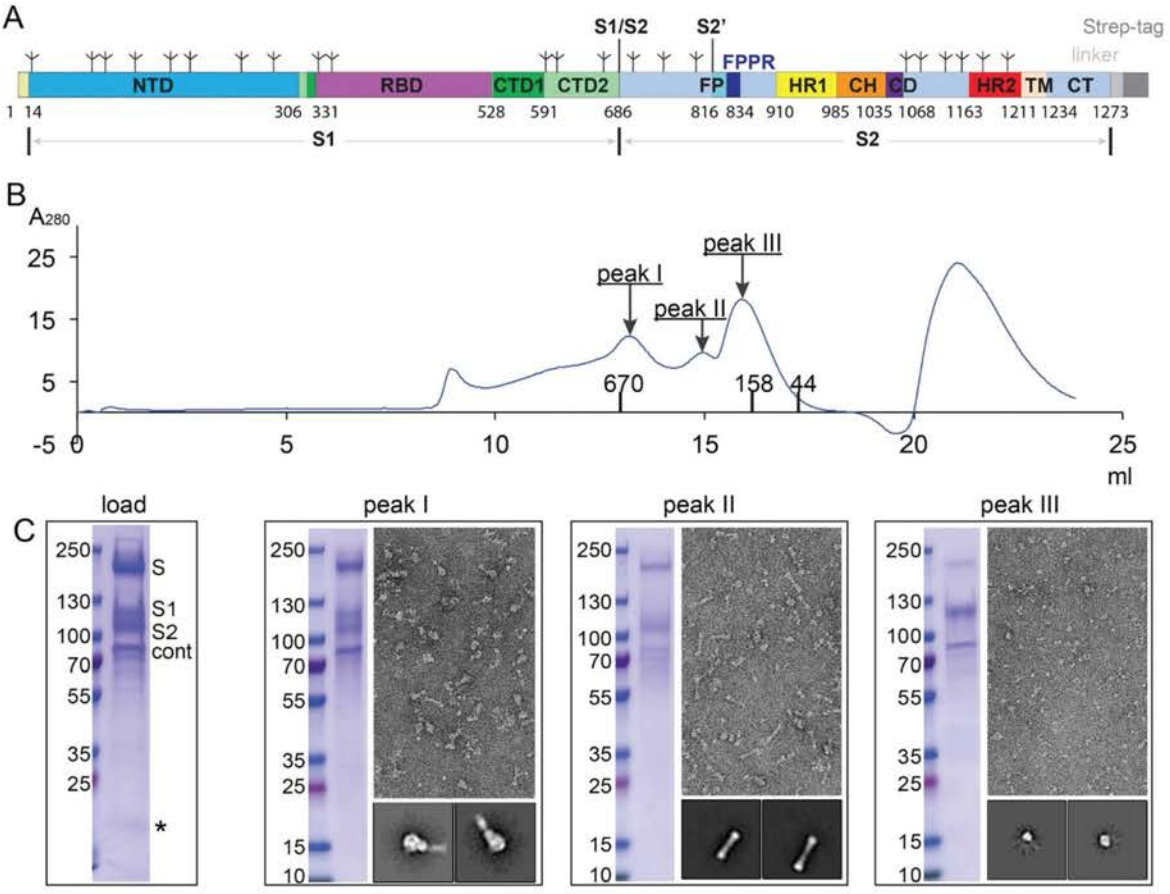

Fig. 1. Preparation of a full-length SARS-CoV-2 spike protein. (A) Schematic representation of the expression construct of full-length SARS-CoV-2 spike (S) protein. Segments of S1 and S2 include: NTD, N-terminal domain; RBD, receptor-binding domain; CTD1, C-terminal domain 1; CTD2, C-terminal domain 2; S1/S2, S1/S2 cleavage site; S2', S2' cleavage site; FP, fusion peptide; FPPR, fusion peptide proximal region; HR1, heptad repeat 1; CH, central helix region; CD, connector domain; HR2, heptad repeat 2; TM, transmembrane anchor; CT, cytoplasmic tail; and tree-like symbols for glycans. A strep-tag was fused to the C terminus of S protein by a flexible linker. (B) The purified S protein was resolved by gel-filtration chromatography on a Superose 6 column in the presence of detergent NP-40. The molecular weight standards include thyoglobulin (670 kDa), γ-globulin (158 kDa) and ovalbumin (44 kDa). Three major peaks (peak I-III) contain the S protein. (C) Load sample and peak fractions from (B) were analyzed by Coomassie stained SDS-PAGE. Labeled bands were confirmed by Western blot (S, S1 and S2) or protein sequencing (S2 and Cont; S and S1 bands did not gave any meaningful results probably due to a blocked N terminus). Cont, copurified contaminating protein, identified as endoplasmic reticulum chaperone BiP precursor by N-terminal sequencing. *, a putative S1/S2-S2' fragment. Representative images and 2D averages by negative stain EM of three peak fractions are also shown. The box size of 2D averages is ~510Å.

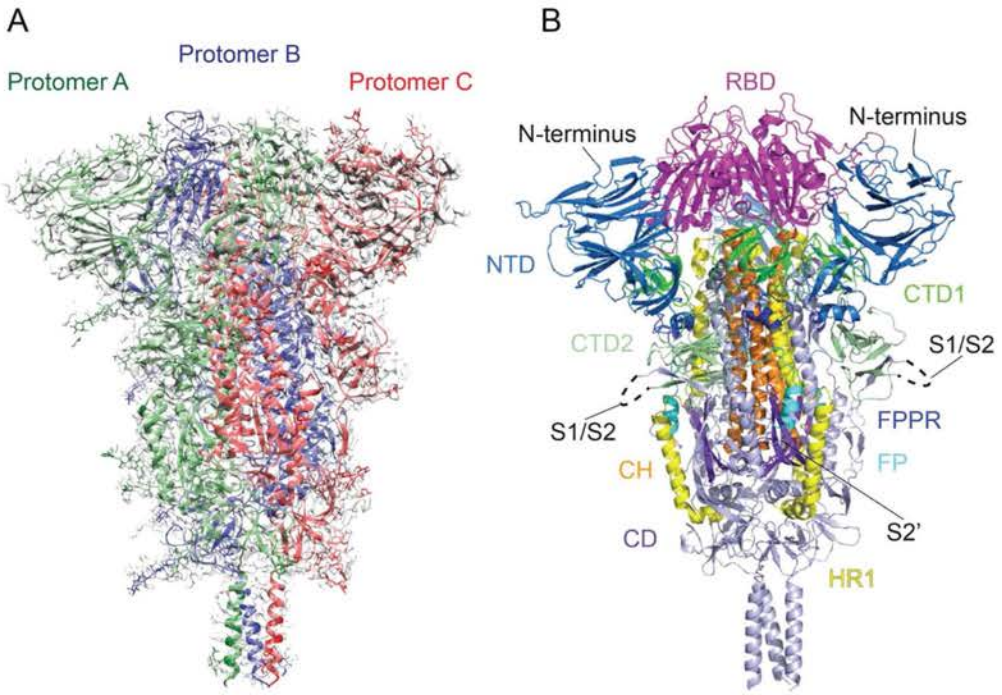

Fig. 2. Cryo-EM structure of the SARS-CoV-2 S protein in the prefusion conformation. (**A**) The structure of the S trimer was modeled based on a 2.9Å density map. Three protomers (A, B, and C) are colored in green, blue and red, respectively. (**B**) Overall structure of S protein in the prefusion conformation shown in ribbon representation. Various structural components in the color scheme shown in Fig. 1A include NTD, N-terminal domain; RBD, receptor-binding domain; CTD1, C-terminal domain 1; CTD2, C-terminal domain 2; FP, fusion peptide; FPPR, fusion peptide proximal region; HR1, heptad repeat 1; CH, central helix region; and CD, connector domain. N terminus, S1/S2 cleavage site and S2' cleavage site are indicated.

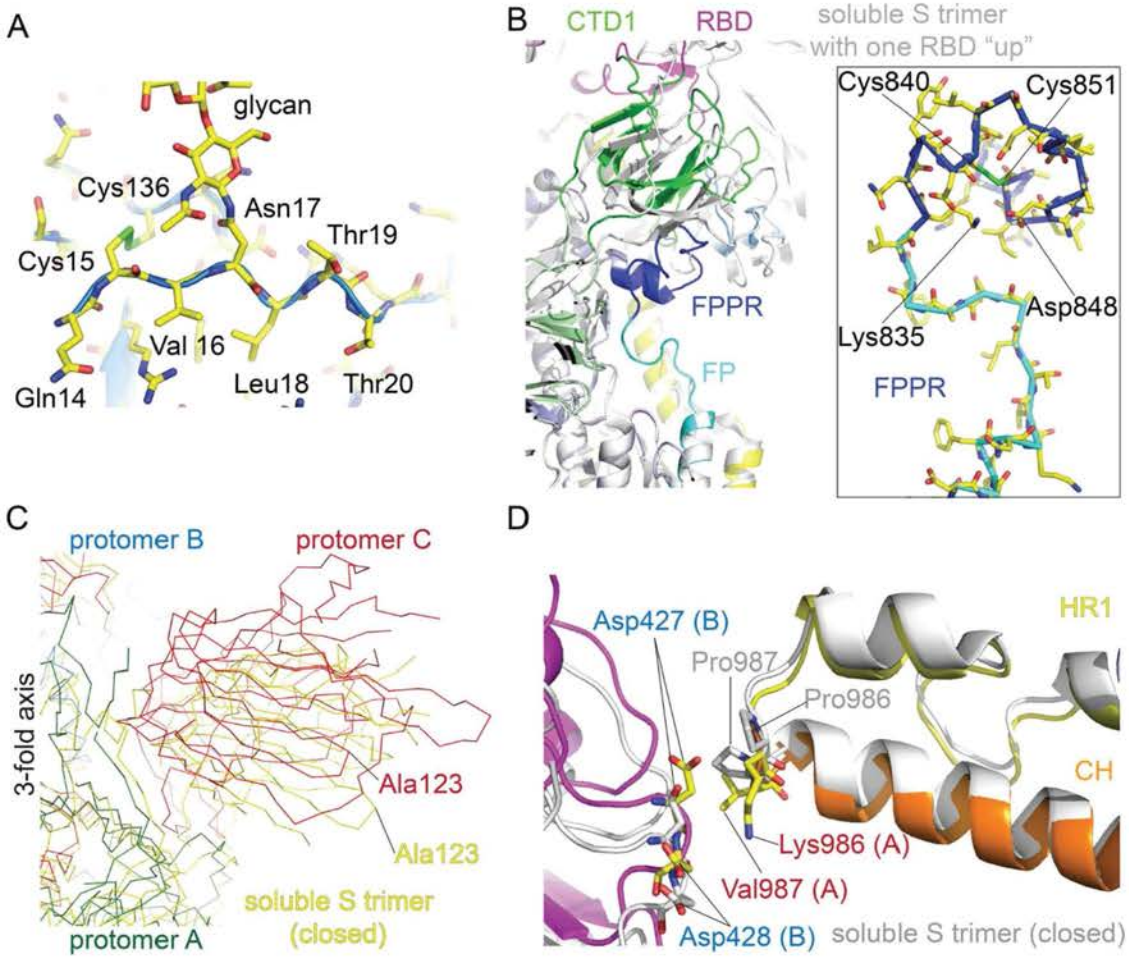

Fig. 3. Selected new features of the SARS-CoV-2 prefusion S trimer. (**A**) N-terminal segment of S protein. The N terminus is at residue Gln14 after cleavage of the signal peptide. Cys15 forms a disulfide bond with Cys136. We observed good density for the N-linked glycan at Asn17. (**B**) A segment immediately downstream of the fusion peptide, while disordered in the stabilized soluble S ectodomain trimer structure, forms a tightly packed structure, designated FPPR for the fusion peptide proximal region, abutting CTD1. The newly identified FPPR structure would clash with CTD1 in the RBD up conformation. Various domains are shown in the color scheme in Fig. 2B. The structure of the soluble S trimer with one RBD in the up conformation (PDB ID: 6vyb) is shown in gray. In the box, a close-up view of the FPPR with adjacent fusion peptide in both surface representation and stick model. (**C**) The SARS-CoV-2 prefusion S trimer, viewed along the threefold axis, is superposed on the structure of the stabilized soluble S ectodomain trimer in the closed conformation with all three RBDs in the down conformation (PDB ID: 6vxx). While the S2 region is well aligned, there is a significant shift (e.g., ~12Å between two Ala123 residues) in S1. (**D**) Impact of the proline mutations introduced at residues 986 and 987 to stabilize the prefusion conformation. K986P mutation removes a salt bridge between Lys986 of one protomer and either Asp427 or Asp428 of another protomer in the trimer interface.

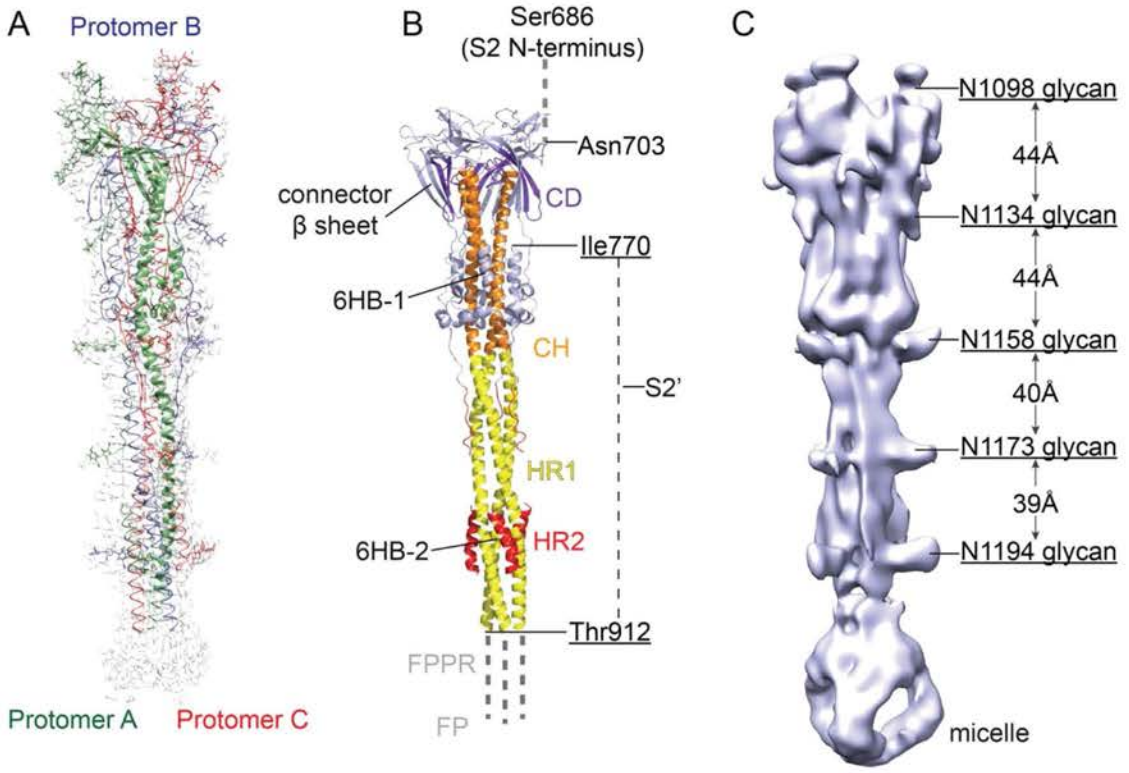

Fig. 4. Cryo-EM structure of the SARS-CoV-2 S2 in the postfusion conformation. (**A**) The structure of the S2 trimer was modeled based on a 3.3Å density map. Three protomers (A, B, and C) are colored in green, blue and red, respectively. (**B**) Overall structure of the S2 trimer in the postfusion conformation shown in ribbon diagram. Various structural components in the color scheme shown in Fig. 1A include HR1, heptad repeat 1; CH, central helix region; CD, connector domain; and HR1, heptad repeat 2. The S2' cleavage site is in a disordered loop between Ile770 and Thr912. Possible locations of the S2 N terminus (S1/S2 cleavage site), the FP and FPPR are also indicated. (**C**) A low-resolution map showing the density pattern for 5 N-linked glycans, with almost equal spacing along the long axis.

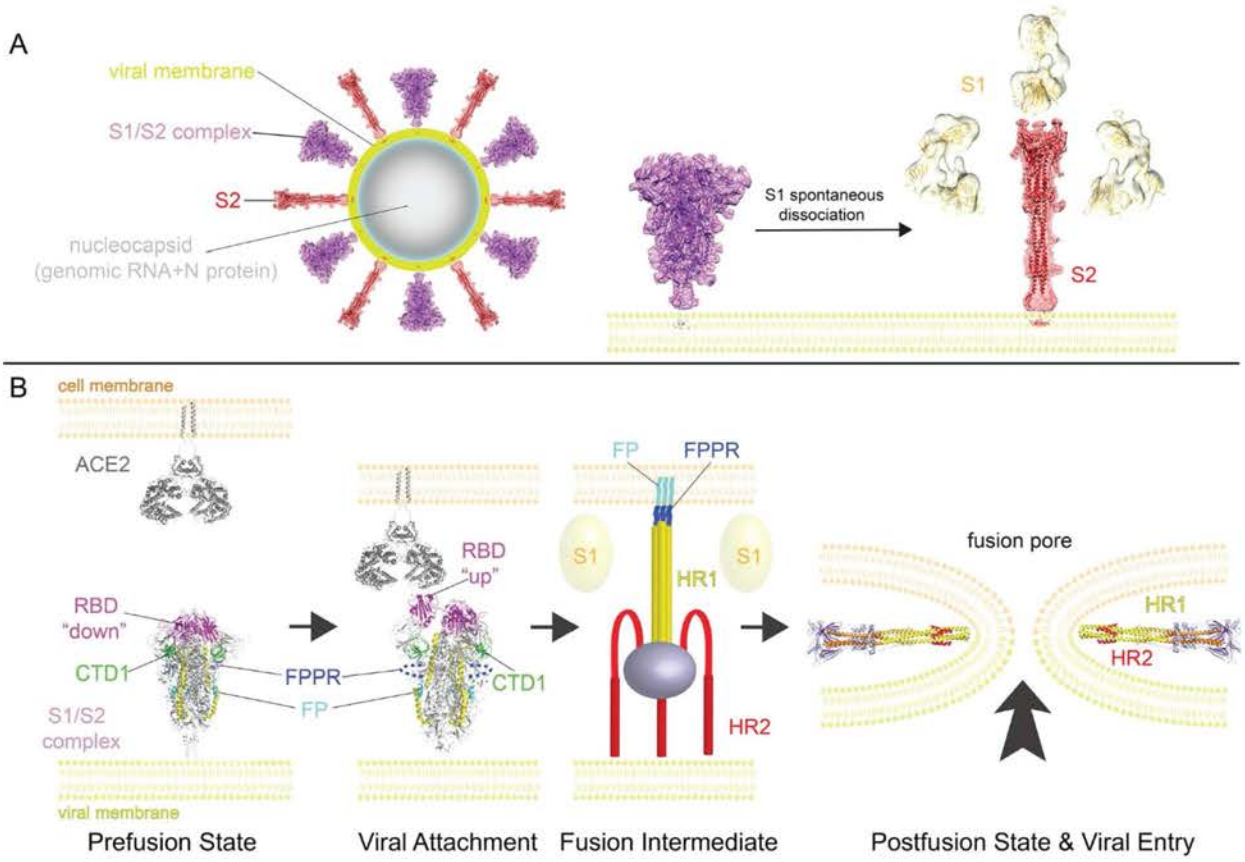

Fig. 5. A model for structural rearrangements of SARS-Cov-2 S protein. (A) Structural changes independent of a target cell. We suggest that both the prefusion and postfusion spikes are present on the surface of mature virion and the ratio between them may vary (diagram of virion). The postfusion spikes on the virion are formed by S2 after S1 dissociates in the absence of ACE2. (B) ACE2-dependent structural rearrangements. Structural transition from the prefusion to postfusion conformation inducing membrane fusion likely proceeds stepwise as follows: 1) FPPR clamps down RBD through CTD1 in the prefusion S trimer (this study), but it occasionally flips out of position and allows an RBD to sample the up conformation (PDB ID: 6vyb). 2) RBD binding to ACE2 (PBD ID: 6m17) creates a flexible FPPR that enables exposure of the S2' cleavage site immediately upstream of the adjacent fusion peptide (FP). Cleavage at the S2' site, and perhaps also the S1/S2 site, releases the structural constraints on the fusion peptide and initiates a cascade of refolding events in S2, probably accompanied by complete dissociation of S1. 3) Formation of the long central three-stranded coiled-coil and folding back of HR2. 4) Formation of the postfusion structure of S2 (this study) that brings the two membranes together, facilitating formation of a fusion pore and viral entry.

Molecular Therapy
Nucleic Acids
Original Article

Treatment of Hemophilia A Using Factor VIII Messenger RNA Lipid Nanoparticles

Chun-Yu Chen,[1] Dominic M. Tran,[1] Alex Cavedon,[2] Xiaohe Cai,[1] Raj Rajendran,[2] Meghan J. Lyle,[1] Paolo G.V. Martini,[2] and Carol H. Miao[1,3]

[1]Seattle Children's Research Institute, Seattle, WA, USA; [2]Moderna, Cambridge, MA, USA; [3]Department of Pediatrics, University of Washington, Seattle, WA, USA

Hemophilia A (HemA) patients are currently treated with costly and inconvenient replacement therapy of short-lived factor VIII (FVIII) protein. Development of lipid nanoparticle (LNP)-encapsulated mRNA encoding FVIII can change this paradigm. LNP technology constitutes a biocompatible and scalable system to efficiently package and deliver mRNA to the target site. Mice intravenously infused with the luciferase mRNA LNPs showed luminescence signals predominantly in the liver 4 h after injection. Repeated injections of LNPs did not induce elevation of liver transaminases. We next injected LNPs carrying mRNAs encoding different variants of human FVIII (F8 LNPs) into HemA mice. A single injection of B domain-deleted F8 LNPs using different dosing regimens achieved a wide range of therapeutic activities rapidly, which can be beneficial for various usages in hemophilia treatment. The expression slowly declined yet remained above therapeutic levels up to 5–7 days post-injection. Furthermore, routine repeated injections of F8 LNPs in immunodeficient mice produced consistent expression of FVIII over time. In conclusion, F8 LNP treatment produced rapid and prolonged duration of FVIII expression that could be applied to prophylactic treatment and potentially various other treatment options. Our study showed potential for a safe and effective platform of new mRNA therapies for HemA.

INTRODUCTION

Coagulation factor VIII (FVIII) is an X-linked gene that encodes a large glycoprotein and participates in the intrinsic pathway of the coagulation cascade.[1] FVIII assists formation of blood clots to prevent further blood loss after injury. The bleeding disorder resulting from insufficiency of FVIII protein level or deficiency of FVIII function is called hemophilia A (HemA). The occurrence of HemA is generally 1 in 5,000–10,000 males, and the mortality rates of patients with severe HemA increase when undergoing major surgery.[2,3] Therapy for severe HemA patients requires not only on-demand treatment to rescue patients from excessive bleeding following trauma or surgery, but also prophylactic treatment to prevent bleeding without visible signs, including joints, soft tissues, or muscle hemorrhages. Frequent infusions (three to four times per week) of costly FVIII to prevent spontaneous bleeding episodes in these patients is required due to the short half-life (8–12 h) of FVIII protein.

An alternative for protein replacement therapy is to utilize gene therapy to introduce a functional FVIII gene into patients for longer-term FVIII expression, thus reducing the treatment frequency while also reducing risk of spontaneous bleeding events. However, the method of delivery needs careful consideration. For example, using viruses carrying genetic material increases the risk of oncogenic mutagenesis due to viral integration.[4–6] In addition, FVIII transgene expression needs to be achieved and maintained at therapeutic levels, and sensitive genotoxicity detection assays remain yet to be developed for clinical gene therapy. Furthermore, immune responses to viral vectors and transgenes precluded its application to a significant portion of HemA patients. To avoid these problems encountered by DNA delivery using viral vectors, messenger RNA (mRNA)-based genetic materials can be used to rescue insufficient FVIII expression in HemA patients.

The advantages of mRNA therapy include no risk of oncogenic mutagenesis and rapid protein expression, as mRNAs do not translocate to the nucleus and are instead processed via translation in the cytoplasm. Recently, it was shown that functional protein was efficiently produced by using a 5-methoxy-U-modified codon-optimized mRNA successfully delivered into specific sites.[7] For example, intradermal injections of modified mRNA encoding vascular endothelial growth factor A (VEGF-A) led to local functional VEGF-A protein expression and transient skin blood flow enhancement in men with type 2 diabetes mellitus (T2DM), indicating the therapeutic potential for regenerative angiogenesis.[8] Furthermore, recent development of lipid nanoparticles (LNPs) enabled efficient packaging of mRNA and delivery to liver to produce a high level of protein expression.[9,10] For example, delivery of LNP-encapsulated mRNA encoding human methylmalonyl-CoA mutase (MMUT) reduced circulating metabolites and dramatically improved survival and weight gain in a mouse model with isolated methylmalonic acidemia (MMA) syndrome.[7] In addition, LNPs have been used to deliver factor IX mRNA into hemophilia B mice with good results.[11,12]

Received 13 March 2020; accepted 30 March 2020;
https://doi.org/10.1016/j.omtn.2020.03.015.

Correspondence: Carol H. Miao, PhD, Seattle Children's Research Institute, 1900 9th Avenue, Seattle, WA 98101, USA.
E-mail: carol.miao@seattlechildrens.org

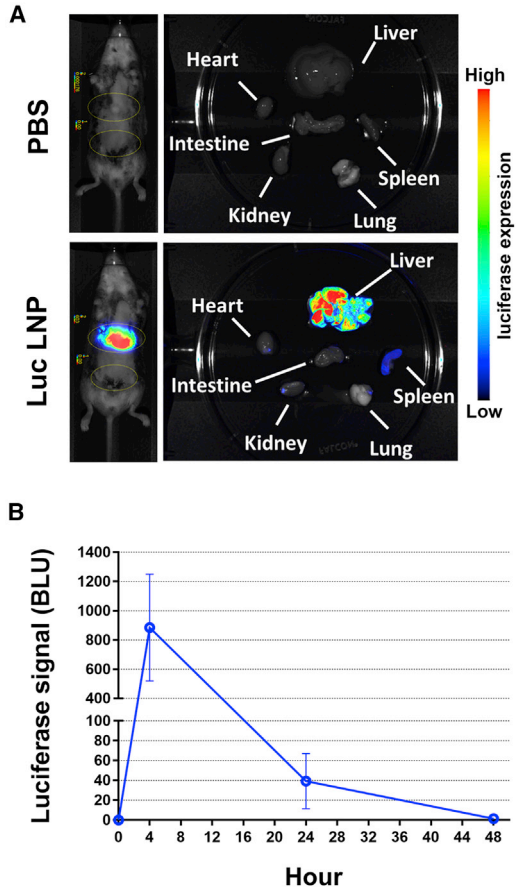

Figure 1. Luciferase mRNA Lipid Nanoparticles (Luc LNPs) Deliver mRNA Efficiently to Liver

(A and B) Localization and levels of luciferase expression in mice. 2 mg/kg Luc LNPs was intravenously administered to wild-type C57BL/6 mice (N = 6). Luc LNP-treated mice and control mice treated with PBS were anesthetized and infused with 10 μL/g luceferin at different time points. Luciferase expression was examined using a bioluminescent *in vivo* imaging system (IVIS). (A) Localization of luciferase expression in mice at 4 h post-treatment. Left panels: *In vivo* imaging was performed to examine the luciferase expression in whole animals. Right panels: The mice were sacrificed, and major organs were harvested for examination of luciferase expression. Luciferase expression in different organs is shown in color scales as indicated in the side bar, representing low to high levels of expression. (B) Luciferase expression levels in the treated mouse livers are presented as average luciferase signals ± standard deviations in bioluminescence light units (BLU).

In this study, we used a non-viral carrier made of biodegradable lipids, LNPs, to encapsulate FVIII mRNAs (F8 LNPs), which were systemically delivered via intravenous injection to HemA mice. We showed that administration of F8 LNPs can rescue biological function and continually produce therapeutic levels of FVIII protein for 5 days. We also showed rapid and consistent expression of FVIII protein after repeated injections of F8 LNPs, indicating the translational potential of mRNA-based therapy for routine prophylactic treatment.

RESULTS

LNPs Are Efficiently Delivered to the Liver

To test the delivery function of LNPs and therapeutic effect of mRNA-based treatment, we first examined the biodistribution and protein expression of luciferase mRNA carrying LNPs (Luc LNPs) *in vivo*. After injection of 2 mg/kg Luc LNPs into mice, luciferase signals were traced using a small animal live imaging method. Mice injected with Luc LNPs displayed high bioluminescence signals compared to control mice that were injected with PBS only. Images also showed that the bioluminescence signal was mainly detected in the liver, and weak or no signal was observed in spleen and other organs, suggesting that LNPs delivered mRNA to the liver efficiently (Figure 1A). The luciferase signal could be detected within 4 h, indicating highly efficient mRNA translation after Luc LNP administration (Figure 1B). Immunostaining of luciferase protein in liver of treated mice was also performed using endothelial markers and the nuclear markers. The results clearly demonstrated that Luc LNPs predominantly targeted hepatocyte cells rather than endothelial cells (Figure S1).

Biocompatibility of mRNA LNPs

Routine prophylaxis is required to prevent frequent bleeding episodes in severe HemA patients. Examination of liver toxicity after multiple injections of therapeutic mRNA LNPs is necessary prior to clinical use. To evaluate biocompatibility of mRNA LNPs, mice were repeatedly injected once daily with 2 mg/kg Luc LNPs for 5 consecutive days. All mice showed consistent expression of luciferase (Figure 2A). Alanine aminotransferase (ALT) and aspartate aminotransferase (AST) levels were monitored to assess the potential for liver inflammation after Luc LNP injection. Mice injected with nonfunctional factor IX (FIX) mRNA LNPs or PBS served as nonspecific and naive controls, respectively. No significant difference was observed in both ALT and AST values among all three groups of mice (Figure 2B). These results suggest that repeated infusions of mRNA LNPs did not induce any detectable liver injury, indicating that mRNA LNPs are suitable for therapeutic treatment.

To examine whether human F8 LNPs are suitable for treatment of HemA patients, we used HemA mice as the chosen hemophilic animal disease model. HemA mice were injected with 2 mg/kg F8 LNPs encapsulating each of several FVIII mRNA variants or control Luc LNPs (Figure 3A). The FVIII activities in treated mouse plasma were measured by an activated partial thromboplastin time (aPTT) clotting assay. HemA mice injected with F8 LNPs encapsulating full-length human FVIII mRNA (F8-FL LNPs) exhibited elevated clotting activity 6 h after injection and reached a peak activity level of 5.5% after 24 h (Figure 3B). As expected, mice treated with control Luc LNPs produced no FVIII activity.

Nascent translated FVIII proteins will translocate to the lumen of the endoplasmic reticulum (ER) and undergo post-translational modification before secretion from cells.[13,14] However, retention of FVIII protein in the ER prevents Golgi transportation and FVIII secretion, leading to delayed elevation of plasma FVIII levels.[2] To overcome

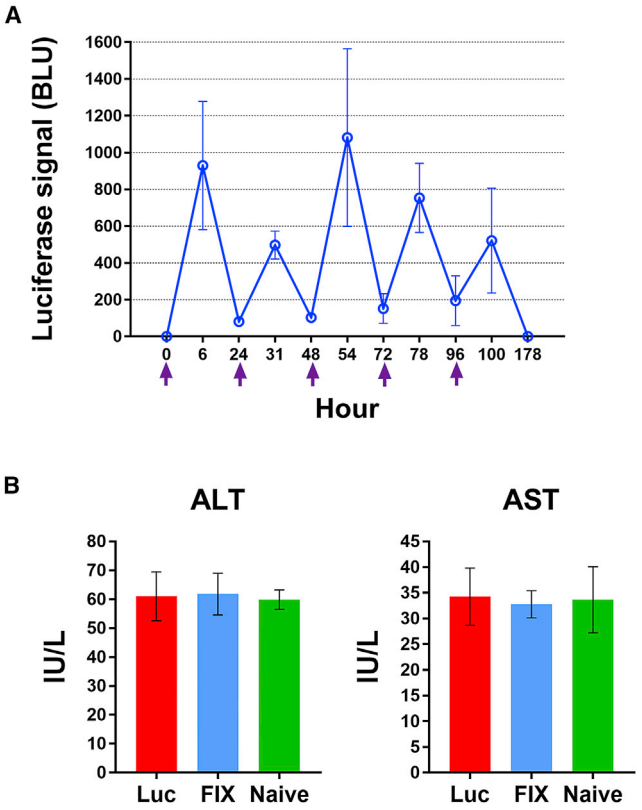

Figure 2. Biocompatibility of the LNPs Carrying mRNAs for *In Vivo* Delivery

2 mg/kg Luc LNPs was intravenously administrated to wild-type C57BL/6 mice (N = 4) for 5 consecutive days. (A) Luciferase expression in C57BL/6 mice following repeated injections of Luc LNPs examined by *in vivo* imaging. Arrows indicate injection time of Luc LNPs. Luciferase expression signals (BLU) were examined 4 h after each injection using an *in vivo* imaging system. (B) Liver enzyme tests following repeated injections of Luc LNPs in mice. ALT and AST levels in plasma were measured in treated mice. Mice injected with nonfunctional factor IX (FIX) mRNA LNPs (N = 4) or PBS (N = 2) served as the mRNA control and naive control, respectively. One-way ANOVA revealed no significant effect of LNPs on levels of ALT or AST (ALT, p = 0.9558; AST, p = 0.9040) between all groups. Data are presented as average values ± standard deviations.

delayed transportation of FVIII, a F309S mutation was introduced in the A1 domain of FVIII mRNA to decrease the retention time in the ER and increase secretion efficiency.[15] Incorporating the F309S mutation showed a similar expression pattern, but higher clotting activity in HemA mice injected with F8 LNPs encapsulating F309S-mutated full-length FVIII mRNA (F8-FL-F309S LNPs). The mice administered F8-FL-F309S LNPs showed 20.5% FVIII clotting activity, which, however, dropped below 10% rapidly within 2 days (Figure 3B).

Owing to the biochemical characteristics of FVIII, full-length human FVIII mRNA is inefficiently translated compared to other comparably sized proteins. Biogenetic modification of FVIII protein is required to elevate the yield of FVIII protein.[16] It has been reported that B domain-deleted human FVIII containing six N-linked glycosylation sites (BDD-hFVIII/N6) showed higher expression levels of FVIII compared to full-length FVIII *in vitro* and *in vivo*.[17,18] To this end, BDD-FVIII/N6 mRNA was designed and encapsulated into LNPs (Figure 3A). In addition, previous studies suggest that the carboxyl terminus of the B domain contains a furin recognition motif (R-H-Q-R), which is the predominant cleavage site to separate FVIII into its heavy chain and light chain. Metal ion-dependent heterodimer FVIII protein is composed of these chains and is the major secreted form after post-translational modification.[19] Compared to the heterodimer form of secreted human BDD-FVIII/N6, the single-chain form of BDD-canine FVIII exhibits higher activity and is more stable.[20] Mutation of the furin cleavage site is reported to contribute to the enhanced secretion level that is associated with increased circulating FVIII.[21] To further elevate the FVIII expression in HemA mice, we introduced a deletion in the furin recognition motif to partially disrupt the furin recognition motif (F8-N6Δ2-F309S) or fully delete the furin recognition motif (F8-N6Δ4-F309S) in BDD-FVIII/N6 mRNA. FVIII activity in HemA mice injected with either BDD-FVIII/N6 mRNA containing a wild-type (WT) (F8-N6-F309S) or mutated furin site (F8-N6Δ2-F309S or F8-N6Δ4-F309S) displayed significantly higher activity than did F8-FL-F309S LNPs. Among the F8 LNP variants, F8-N6Δ2-F309S LNPs produced a higher average FVIII activity than that of F8-N6-F309S and F8-N6Δ4-F309S variants (Figure 3C). After injection of 2 mg/kg LNPs carrying these three different BDD-FVIII variants, FVIII expression achieved peak expression levels higher than 1,000% FVIII activity and slowly declined during a 7-day period. In addition, we examined the kinetics of FVIII expression at multiple time points during the initial 24-h period after F8 LNP injection. The data showed that low levels of FVIII can already be detected at half an hour post-injection, and the levels continued to increase to peak levels at 24 h post-injection (Figure S2).

Immunoblotting was performed to verify FVIII proteins synthesized by F8 LNPs. The molecular size of FVIII detected from mice administrated with F8-FL-F309S LNPs was comparable to that in normal human plasma (Figure 3D). Immunoblotting analysis also showed diversity of molecular weight in furin mutant F8 LNP variants. FVIII proteins from F8-N6Δ2-F309S and F8-N6Δ4-F309S LNPs displayed high-molecular-weight single chains of BDD-FVIII/N6, whereas F8-N6-F309S LNPs without a furin site mutation showed predominantly the heavy chain form of BDD-FVIII/N6 and absence of the single chain form (Figure 3E).

Repeated Injections of Human F8 LNPs Induced FVIII Inhibitor Formation

Since F8-N6Δ2-F309S LNPs showed higher activity than other F8 LNP variants on average, we used F8-N6Δ2-F309S LNPs in the following experiments. Mice injected with 2 mg/kg F8-N6Δ2-F309S LNPs can restore FVIII activity and maintain activity more than 7 days above a trough level of 1%; however, the association between elevated FVIII activity and increased thrombotic risk still needed to be evaluated. High plasma FVIII activity may result in a dose-dependent risk of venous thromboembolism.[22] To evade thrombotic risk, different dosages of F8-N6Δ2-F309S were examined. 0.1, 0.2, and

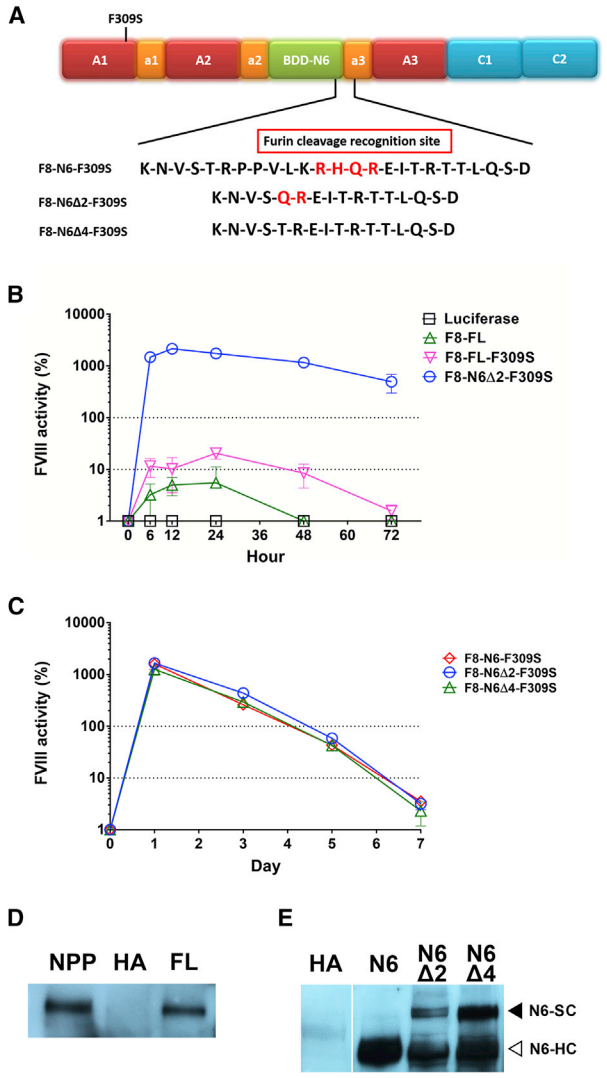

Figure 3. Injection of FVIII Variant mRNA LNPs (F8 LNPs) Restored Clotting Activity in HemA Mice

(A) Different furin cleavage site-mutated FVIII mRNAs were encapsulated into LNPs. Amino acids marked in red denote the residues contained in the furin cleavage recognition site. (B) FVIII activity of mice injected with F8-FL LNPs, F8-FL-F309S LNPs, and F8-N6Δ2-F309S LNPs were measured by an aPTT assay at different time points, respectively (N = 3/group). (C) FVIII activity of HemA mice injected with 2 mg/kg F8-N6-F309S, F8-N6Δ2-F309S, and F8-N6Δ4-F309S LNPs (N = 3–6/group), respectively. FVIII activity was measured in different time points by an aPTT assay. Data are presented as average FVIII activities ± standard deviations. (D and E) Western blot to detect plasma FVIII 1 day after LNP treatment in mice injected with 2 mg/kg F8-FL-F309S LNPs (FL) (D), and in mice injected with 2 mg/kg F8-N6-F309S (N6), F8-N6Δ2-F309S (N6Δ2), and F8-N6Δ4-F309S (N6Δ4) LNPs, respectively (E). Human normal pooled plasma (NPP) served as a positive control, and plasma from untreated HemA mice (HA) served as a negative control. Arrowheads in (E) indicate the single chain FVIII-N6 (N6-SC) and heavy chain of FVIII-N6 (N6-HC).

0.4 mg/kg F8-N6Δ2-F309S LNPs were injected into HemA mice and antigen levels and FVIII activity were measured at days 1, 3, 5, and 7. The expression profile was similar in different mouse groups injected with different dosages of F8-N6Δ2-F309S LNPs. All mouse groups showed that the highest FVIII expression levels and activities were detected at day 1 and reached trough levels at day 5 or day 7 (Figures 4A and 4B). In order to verify whether blood clotting can be corrected in 0.2 mg/kg F8-N6Δ2-F309S LNP-treated mice at day 7, we examined the coagulation activity using whole blood isolated from treated mice by a rotational thromboelastometry (ROTEM) assay (Figure 4C). We found that at 7 days after F8 LNP delivery, the treated mice still had significant correction of coagulation parameters, including clotting time (CT) and clot formation time (CFT), compared with HemA mice (Figure 4D). The average half-life of FVIII:C expressed from F8-N6Δ2-F309S mRNA can reach about 22 h. In comparison, the FVIII levels from 0.1 mg/kg F8-N6Δ2-F309S LNP-treated mice were too low (undetectable) at day 5 for prophylactic treatment, whereas those from 0.4 mg/kg F8-N6Δ2-F309S LNP-treated mice were very high (867%) at day 1 with potentially increased thrombotic risk. Compared to treatment dosages of 0.1 and 0.4 mg/kg, mice treated with 0.2 mg/kg F8-N6Δ2-F309S LNPs showed optimal performance that exhibited ~200% FVIII activity at day 1 and above 5% activity at day 7. Such levels are suitable for prophylactic treatment lasting 5–7 days.

To reduce the frequency of bleeding episodes in HemA patients, injection of FVIII protein ideally should be performed two to three times per week. To develop protocols for treating HemA patients, we monitored the FVIII expression performance in HemA mice after administration with 0.2 mg/kg F8-N6-F309S-Δ2 LNPs two to four times within 2 weeks. The results suggested that almost all treated mice can sustain FVIII activity higher than 1% within 2 weeks (Figure 5). However, FVIII expression levels decreased when the frequency of injections increased. Mice treated with two F8-N6Δ2-F309S LNP administrations within 2 weeks showed no difference in FVIII expression levels when compared between their first and second injections (Figures 5A and 5B), but mice that received three or four F8-N6Δ2-F309S LNP injections within 2 weeks displayed dramatic reduction of FVIII expression level (Figures 5C–5F). The plasma FVIII level decreased notably after the third injection and could not be detected after a fourth injection at day 11. The decreases of FVIII expression levels were found to be associated with the formation of inhibitors against FVIII, which were detected by a Bethesda assay at 2 weeks following multiple injections of F8-N6Δ2-F309S LNPs (Figure 5G). This anti-FVIII immune response is anticipated since this strain of HemA mice is prone to develop FVIII inhibitors following repeated FVIII treatment.[23]

Routine Injections of Human F8 LNPs Induced FVIII Inhibitor Formation

Severe HemA patients have a high risk of spontaneous bleeding into muscles, soft tissue, skull, or joints, leading to serious complications. To improve the quality of life, routine injection of FVIII is required to prevent asymptomatic bleeding. According to clinical data, most

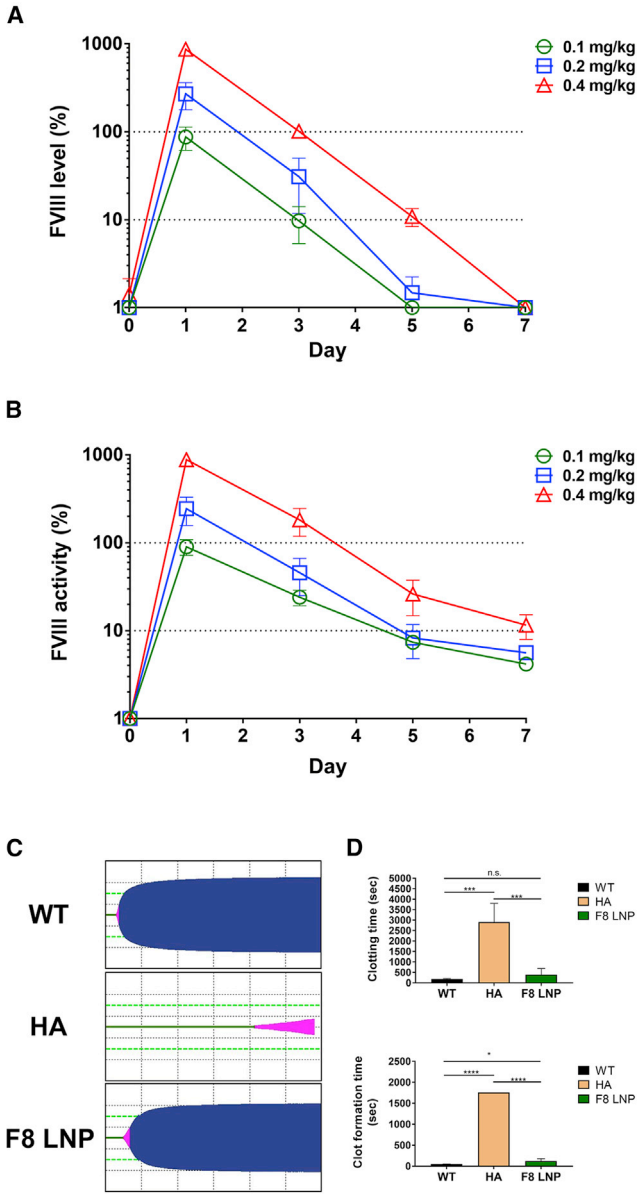

Figure 4. Dose Titration of F8 LNPs

To titrate the F8 LNP dosage best suited for treatment, HemA mice were injected with 0.1, 0.2, and 0.4 mg/kg F8-N6Δ2-F309S LNPs (N = 3/group). (A and B) FVIII antigen levels (A) and activities (B) were measured using ELISA and an aPTT assay, respectively. Coagulation activities of HemA mice were measured using a ROTEM assay 7 days after injection of 0.2 mg/kg F8-N6Δ2-F309S LNPs. Wild-type (WT) mice and HemA mice (HA) treated with Luc LNPs served as controls (N = 4–6/group). (C and D) Representative ROTEM graphs (C) and clotting times and clot formation time (D) of each group are shown. Data are presented as average experimental values ± standard deviation. Statistical comparisons were performed using one-way ANOVA. *$p < 0.05$, ***$p < 0.001$, ****$p < 0.0001$.

HemA patients (~70%) do not develop FVIII inhibitors.[24–26] To evade human FVIII inhibitor development in the HemA mouse model, we evaluated the potential of F8-N6Δ2-F309S LNPs for prophylactic treatment using immunodeficient NOD.Cg-*Prkdc*^{scid} *Il2rg*^{tm1Wjl}/SzJ (NSG) mice. First, we used NSG HemA mice to examine the FVIII antigen and activity level after F8-N6Δ2-F309S LNP injections. Two injection cycles were carried out, and the results showed similar expression patterns of FVIII as those observed in immunocompetent HemA mice (Figures 6A and 6B). Then, NSG mice were routinely injected with F8-N6Δ2-F309S LNPs every 5 days for 2 months and the FVIII protein was detected by a human FVIII-specific ELISA. The treated mice consistently expressed FVIII with peak levels around 150%–220% after each injection, suggesting that systemic delivery of F8-N6Δ2-F309S LNPs can provide a potentially superior routine prophylaxis protocol for severe HemA patients (Figure 6C).

DISCUSSION

Clinically, patients with hemophilia receive on-demand therapy with coagulation factor concentrates to prevent excessive bleeding in trauma, injury, and surgery. Patients with severe HemA require routine prophylactic infusion of FVIII to prevent spontaneous bleeding into joints or muscle. Conventional FVIII concentrates have a 12-h half-life on average. Severe HemA patients require a prophylaxis treatment regimen with three to four times per week repeated injections.[27] Recent recombinant FVIII products modified with polyethylene glycol, Fc fragment, or albumin could extend the half-life of FVIII, thereby reducing the frequency of prophylaxis treatment to two to three times per week injections.[28,29] However, individual dosing of half-life-extended recombinant FVIII differs between HemA patients to maintain levels higher than 1%. Given the process involved to produce safe and effective FVIII concentrates, current prophylactic treatment is a heavy financial burden for patients.[30]

Compared to protein replacement therapy, gene therapy can offer a change in the paradigm of hemophilia care. Gene transfer using adeno-associated virus (AAV) viral vectors carrying BDD-FVIII could achieve long-term correction of the phenotype. Clinical data suggest that HemA patients receiving gene therapy could reduce bleeding events compared to routine FVIII prophylaxis.[31,32] However, FVIII expression in treated patients did not show consistent levels across patients. FVIII expression starts to decline in some patients within 2 years, as reported in a long-term clinical trial.[33] Furthermore, the presence of anti-AAV vector antibodies reduces or abolishes the transduction efficiency of AAV and prevents repeated treatment in HemA patients.[4,34] To date, there is no standard protocol to monitor the genotoxicity resulting from potential insertional mutations caused by AAV vectors in a clinical setting. More studies are needed to access the safety and efficacy of viral gene therapy.[4,35–37]

mRNA-based therapy has recently emerged as an important alternative since mRNA has no risk of integrational mutations as opposed to viral vector-based therapies. The mRNAs delivered into cells would not translocate to the nucleus and instead undergo translation in the cytoplasm with natural post-translational modification of encoded protein. Furthermore, modifications including replacement of uridine 5′-triphosphates (UTPs) by N1-methylpseudo-UTP and

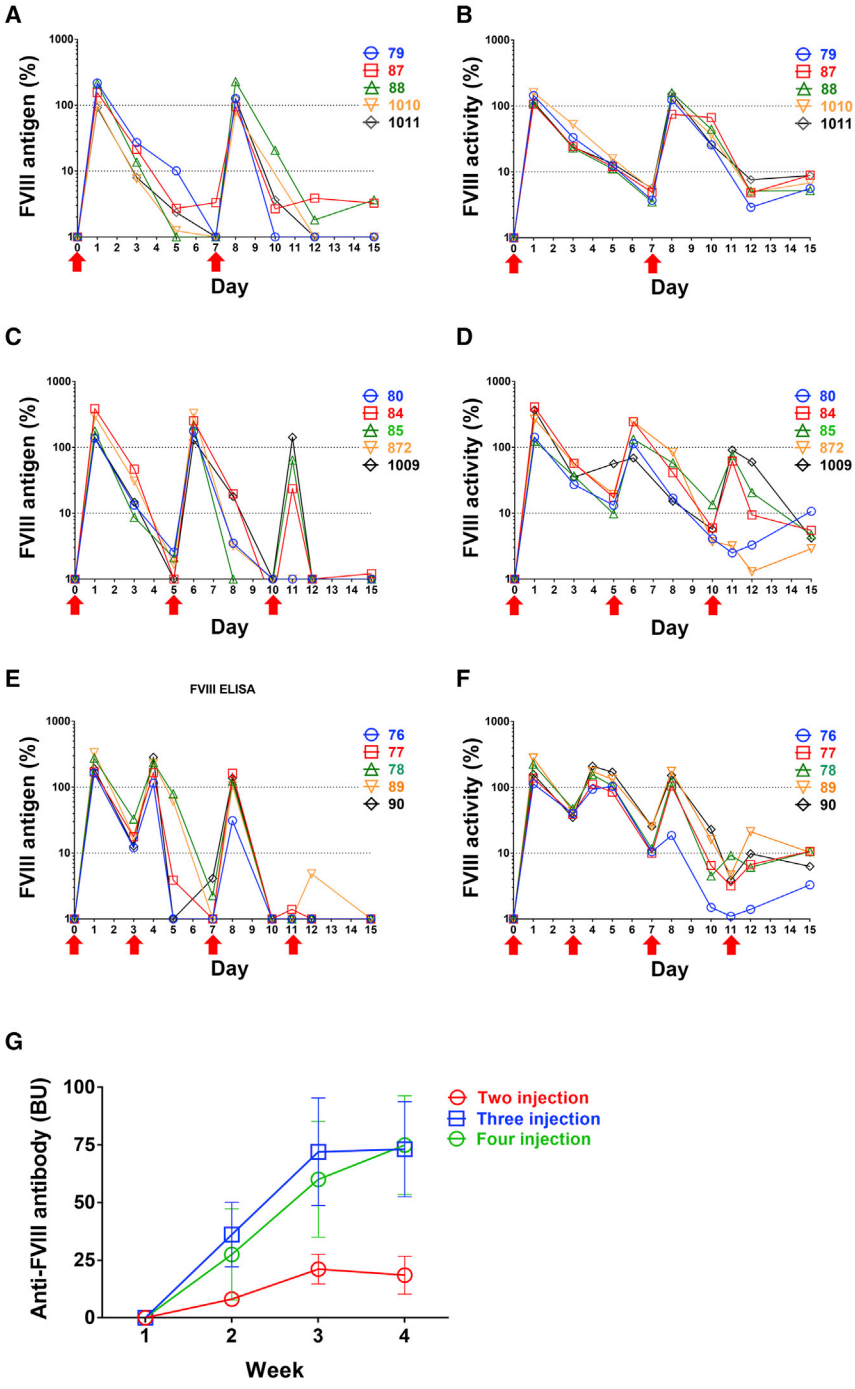

Figure 5. Repeated Injections of F8 LNPs into HemA Mice

(A–F) HemA mice were repeatedly injected with 0.2 mg/kg F8-N6Δ2-F309S LNPs (A and B) two times, (C and D) three times, and (E and F) four times within 2 weeks, respectively. FVIII antigen levels (A, C, and E) and FVIII activities (B, D, and F) were measured using ELISA and an aPTT assay. Arrows indicate the days of F8 LNP injections (N = 5/group). Each symbol represents data obtained from an individual mouse. (G) Anti-FVIII antibodies of F8 LNP repeatedly injected mice were measured by a Bethesda assay (N = 5/group). Data are presented as average experimental values ± standard deviation.

addition of cap-1 structure yielded mRNAs with increased stability and translational activity and reduced immunogenicity.[38–40] Codon optimization of mRNA further enhanced protein expression levels.[41,42] Moreover, the clinical-grade good manufacturing practice (GMP) production of clinical *in vitro*-transcribed (IVT) mRNA costs 5- to 10-fold less than that of production of recombinant protein.[43]

To improve safety, efficiency, and tissue-targeting of mRNA delivery, we developed optimized LNPs carrying hFVIII mRNA for efficient delivery into liver cells. The opsonized LNPs bound to apolipoprotein E (ApoE) and low-density lipoprotein (LDL) receptors and facilitated specific uptake of LNPs by hepatocytes.[44,45] In addition, the formulation of F8 LNPs incorporated a "diffusible" polyethylene glycol (PEG) lipid that can shed from the LNP particle to significantly improve transfection.[46] Of note, the total amount of PEG used in F8 LNP treatment was much lower than the acceptable daily intake of PEG in humans, and the use of diffusible PEG lipids reduced any potential immune responses to LNP-associated PEG.[47] Following LNP delivery, mRNA was translated, and functional FVIII protein can be detected within half an hour. The average half-life of FVIII generated by hF8 LNPs (F8-N6Δ2-F309S LNPs) is about 22 h, which is much longer than that for commercial FVIII products.[27] According to our *in vivo* data, one to two per week injections of 0.2 mg/kg hF8 LNPs are sufficient to maintain a trough level higher than 1% in HemA mice 7 days after F8 LNP delivery. Our F8 LNPs can provide a considerably higher flexible range of FVIII levels, compared to published formulated FVIII mRNA.[48] In our protocol, we have used novel FVIII mutant molecules and achieved more potent treatment efficacy with longer half-life of FVIII expression and reproducible pharmacology in multidose studies. Furthermore, it was known that the half-life of infused hFVIII is significantly shorter in mice than in humans.[49] Therefore, the frequency of F8 LNP dosing can be further reduced in clinical treatment. Compared to FVIII concentrates and recombinant FVIII protein, which require prophylaxis regimen of three to four times and two to three times weekly injections, respectively, we expect that once every 7 days or longer intervals of F8 LNP

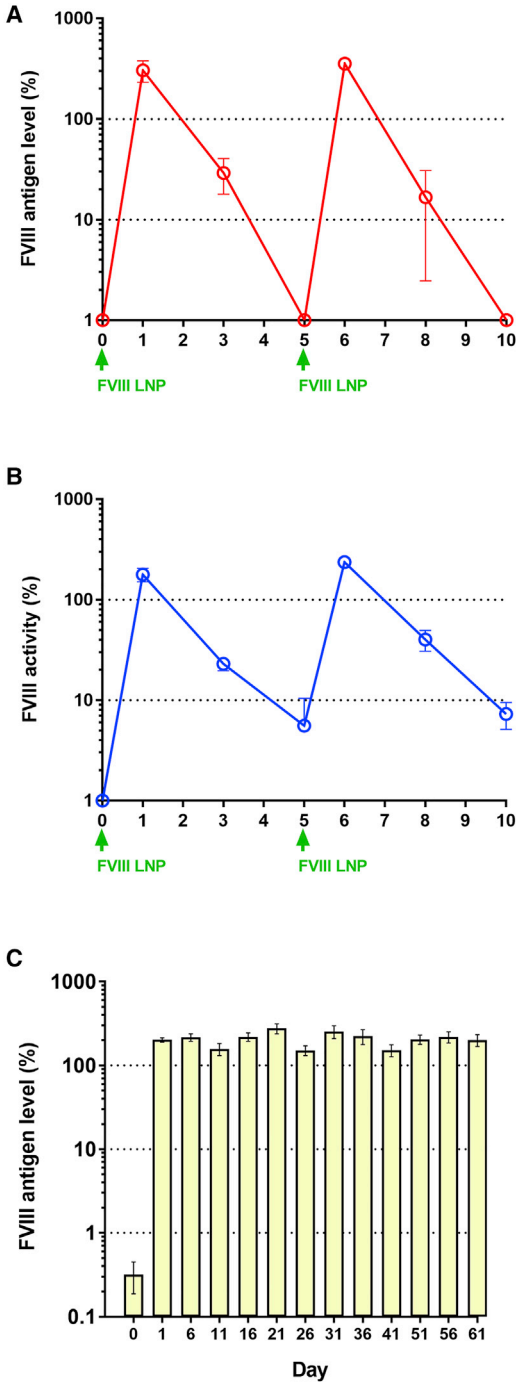

Figure 6. NSG Mice Routinely Injected with F8 LNPs Can Consistently Express FVIII Protein

(A and B) NSG HemA mice were injected with 0.4 mg/kg F8-N6Δ2-F309S LNPs. FVIII antigen (A) and activity (B) levels were detected 1 day, 3 days, and 5 days after injection by ELISA and an aPTT assay, respectively. Two repeated injection cycles were examined (N = 3). (C) NSG mice were injected with 0.4 mg/kg F8-N6Δ2-F309S LNPs every 5 days for 2 months. FVIII antigen level was detected 1 day after injection by a human FVIII-specific ELISA (N = 7). The day 0 samples were collected before injection. Arrows indicate injection time of F8 LNPs. Data are presented as average values ± standard deviations.

treatment will be sufficient for prophylactic treatment. Importantly, note that mRNA LNPs are biocompatible and lipids are rapidly degraded and eliminated after delivery and therefore can be safely administered with repeated injections.[7]

We observed FVIII gene expression, albeit at low levels, with full-length FVIII (F8-FL), indicating that FVIII mRNA can be correctly processed and expressed in liver cells following delivery of F8 LNPs. To elevate the efficiency of FVIII secretion, we introduced a F309S mutation and furin cleavage site deletion in FVIII mRNA. In accordance with those mutations, mice injected by LNPs with mutant FVIII mRNA showed higher FVIII level and clotting activity compared to WT FVIII. Most interestingly, FVIII expression levels were significantly increased up to 100- to 200-fold when mRNAs encoding B domain-deleted FVIII variants were encapsulated in LNPs. It is unclear at this point why such significant enhancement was obtained. It is potentially due to differences in delivery, translation, and secretion efficiency. As shown in the results, with higher dosages of F8-N6Δ2-F309S LNPs (0.2–2 mg/kg), 200%–1,000% activities can be achieved with a single treatment, providing a wide spectrum and flexibility for prophylactic treatment and other treatment options for hemophilia patients. As shown in our results, FVIII expression starts rapidly after F8LNP delivery. Even at half an hour after delivery, we already detected 2%–5% FVIII levels in mouse plasma, and FVIII levels continue to increase to peak levels at 24 h post-injection. With appropriate dosages, correction of blood clotting can be maintained to at least 7 days post-injection. With different dosing regimens, F8 LNPs can be used in various treatment scenarios. For example, F8 LNPs can be used for patients who are scheduled for major surgeries or had suffered from spontaneous bleeding in joints or muscle. Recently developed bispecific factor IXa and factor X antibody, Hemlibra (emicizumab-kxwh) was shown to successfully reduce the frequency of bleeding episodes in HemA patients with inhibitor. However, there are several limitations for treating hemophilia patients, and long-term toxicity and safety still need to be carefully assessed. HemA patients need to receive Hemlibra combined with other bypassing agents when undergoing major surgery;[50] however, serious thrombotic side effects have occurred in some patients.[51,52] There were also several instances when treated patients developed neutralizing antibody against the drug.[53]

Immunodeficient NSG mice were used to evaluate the routine treatment regimen of repeated injections of F8 LNPs for long-term therapeutic effect. First, we used NSG HemA mice to demonstrate their expression pattern: both antigen and activity levels were similar to those observed in 129/SV × C57BL/6 HemA mice, suggesting that different genetic background did not affect FVIII protein expression kinetics. Subsequently, we performed a long-term treatment of F8 LNPs in NSG mice. F8 LNP treatment was carried out at 5-day intervals for 2 months. NSG mice persistently express FVIII protein, suggesting that this protocol is suitable for routine prophylaxis treatment to

achieve therapeutic efficacy. According to clinical data published on inhibitor formation incidence in severe HemA patients undergoing treatment of FVIII concentrates, more than 70% of patients do not generate FVIII inhibitors and are suitable for repeated F8 LNP treatment.[24–26]

Although inhibitor development is dependent on genetics and environmental factors, several studies indicated that recombinant FVIII products showed higher immunogenicity than did plasma-derived FVIII products. One of the possible reasons is that posttranslational modifications of recombinant FVIII such as glycosylation from non-human mammalian cell lines contribute to the increase of FVIII immunogenicity.[54,55] In contrast to recombinant FVIII products, FVIII derived from F8 LNPs undergoes intrinsic post-translation modification, which potentially eliminates the increased risk of antibody formation induced against FVIII synthesized from different species. In addition, further genetic modification of FVIII mRNA can address the immunogenic issue of FVIII. For example, reducing FVIII immunogenicity may be achieved by either mutation of the FVIII sequence or fusion with specific proteins or peptides.[56–59]

In conclusion, F8 LNP treatment offers several significant advantages over current protein replacement therapy and alternative therapies. Delivery of F8 LNPs produced rapid initial expression and a wide range of FVIII levels up to 1000% by administering different dosing regimens. These unique properties can lead to prophylactic application and various other treatment scenarios. Furthermore, the prolonged intervals between repeated treatment, flexibility of construct modification, native post-transcriptional modification of FVIII protein, high efficiency of F8 LNP delivery, and relative ease and reduced cost of scaling up to human use can potentially make F8 LNP treatment a much safer and superior protocol to substitute protein replacement therapy in the clinic. In addition, a major advantage of FVIII mRNA LNP therapy is that it is easy to improve FVIII function by modification of mRNA sequence encoding newly developed FVIII protein with higher activity or longer half-life. Future investigation in formulating F8 LNPs for subcutaneous injections is also currently ongoing, which will further increase the ease of administering the therapy and improve the quality of patient life.

MATERIALS AND METHODS

Synthesis of mRNA and LNPs

Formulation of LNPs was according to previous methods.[7] Briefly, different variants of codon-optimized hFVIII mRNAs were synthesized from linearized DNA plasmids using *in vitro* transcription by T7 RNA polymerase, and ribonucleotide UTPs were replaced by 1-methylpseudo-UTP. A cap-1 structure and poly(A) tail were added to 5′ and 3′ UTRs of mRNA, respectively, to enhance mRNA translation efficiency. Lipid components (ionizable lipid:distearoylphosphatidylcholine (DSPC):cholesterol:PEG lipid, 50:10:38.5:1.5) were mixed with synthesized mRNAs at a volume ratio of 1:3 and assembled by NanoAssemblr system (Precision NanoSystems, San Francisco, CA, USA) to synthesize mRNA LNPs. All LNPs were tested for particle size, RNA encapsulation, and endotoxin to be <100 nm, >80%, and <10 endotoxin units (EU)/mL, respectively.

Animals

HemA mice generated by targeted disruption of the FVIII gene in exon 16 were used in mixed genetic background of 129/SV × C57BL/6 mice at the age of 8–12 weeks. NOD.Cg-*Prkdc*^{scid} *Il2rg*^{tm1Wjl}/SzJ mice (NSG mice, stock no. 0005557) were purchased from Jackson Laboratory (Sacramento, CA, USA). NSG HemA mice were purchased from the Gene Knockout Mouse Core Laboratory of the National Taiwan University Center of Genomic Medicine. All experimental mice were housed in a specific pathogen-free (SPF) facility in Seattle Children's Research Institute according to the animal care guidelines of the National Institutes of Health and the Seattle Children's Research Institute. The experimental protocols used in this study were approved by the Institutional Animal Care and Use Committee of the Seattle Children's Research Institute.

LNP Injection and Sample Collection

Mice were intravenously injected with mRNA LNPs through the retro-orbital plexus at different doses according to the experimental design. Blood samples from experimental mice were collected from the retro-orbital plexus at indicated time points and centrifuged immediately at 500 × *g* for 5 min to obtain sera. Samples were aliquoted and stored at −80°C for further experiments.

Live Imaging of Experimental Mice Using an Intravital Imaging System

Prior to the experiments, mice were anesthetized using isoflurane and hair was removed by hair removal cream (Nair, Ewing, NJ, USA). Mice were subcutaneously injected with 10 μL/g D-luciferin (PI88293, Fisher Scientific) in PBS 10 min before imaging. All images were monitored by Image Studio software for the Pearl Trilogy imaging system.

aPTT Assay and Bethesda Assay

Plasma hFVIII was examined using a modified clotting assay utilizing aPTT reagent and FVIII-deficient plasma.[60,61] hFVIII activity was evaluated according to a standard curve obtained from serially diluted normal human pooled plasma. FVIII inhibitor levels were quantitated using Bethesda assays.

FVIII ELISA

hFVIII antigen levels introduced by FVIII-LNPs in HemA mice and NSG mice were examined by ELISA using murine anti-FVIII antibody (GMA-8020, Green Mountain Antibody, Burlington, VT, USA) and biotin-labeled murine anti-FVIII antibody (GMA-8015, Green Mountain Antibody). This pair of anti-FVIII antibodies does not cross-react with endogenous murine FVIII in NSG mice. Serially diluted normal human plasma was used as standards to evaluate human FVIII antigen level.

AST/ALT Assays

Liver cell injury of experimental mice was evaluated using an ALT reagent set (Teco Diagnostics, Anaheim, CA, USA) and an AST commercial enzyme kit (Randox, London, UK), respectively.

Western Blot

Plasma samples were electrophoresed in 4%–15% SDS-PAGE (Bio-Rad) and electrotransferred to polyvinylidene fluoride (PVDF) membranes using an iBlot gel transfer device (Thermo Fisher Scientific, Waltham, MA, USA). Membranes were blotted with non-fat skimmed milk subsequently. Human FVIII was detected by sheep-anti-human FVIII antibody (Affinity Biologicals, Ancaster, ON, Canada) following horseradish peroxidase-conjugated anti-sheep immunoglobulin G (IgG) (Thermo Fisher Scientific). ECL signals were developed with the enhanced chemiluminescence (ECL) reagent (Thermo Fisher Scientific).

Thromboelastography

Coagulation function of mice treated with F8 LNPs was examined 7 days after treatment. WT mice and HA (HemA) mice treated with Luc LNPs (HA) served as controls. Whole blood was collected by submental bleeding, and 3.8% citric acid was used as an anticoagulant. Clotting time and clot formation time were directly measured using an INTEM (activated intrinsic pathway) kit assay by rotational thromboelastometry (ROTEM delta, Instrumentation Laboratory, Bedford, MA, USA).

Statistical Analyses

All statistical analyses were carried out utilizing GraphPad Prism 7 software. The data were compared using a two-tailed unpaired Student's t test and one-way or two-way analysis of variance (ANOVA) followed by Bonferroni's *post hoc* multiple comparison tests. A p value <0.05 was considered statistically significant.

SUPPLEMENTAL INFORMATION

Supplemental Information can be found online at https://doi.org/10.1016/j.omtn.2020.03.015.

AUTHOR CONTRIBUTIONS

C.-Y.C. developed the study design, performed experiments, analyzed data, and wrote the manuscript. D.M.T. performed experiments and reviewed the manuscript. A.C., X.C., R.R., and M.J.L. performed experiments. P.G.V.M. reviewed the manuscript. C.H.M. developed the study concept, analyzed results, and wrote and revised the manuscript.

CONFLICTS OF INTEREST

C.H.M. received funding of a Sponsored Research Administration (SRA) grant from Moderna, Inc. R.R. is a former Moderna employee. A.C., and P.G.V.M are employees of, and receive salary and stock options from, Moderna, Inc. C.H.M. and P.G.V.M are inventors of a patent on F8 LNP technology. The remaining authors declare no competing interests.

ACKNOWLEDGMENTS

The work is partly supported by a Sponsored Research Administration (SRA) grant from Moderna Therapeutics.

REFERENCES

1. Davie, E.W., Fujikawa, K., and Kisiel, W. (1991). The coagulation cascade: initiation, maintenance, and regulation. Biochemistry *30*, 10363–10370.
2. Escobar, M.A., Brewer, A., Caviglia, H., Forsyth, A., Jimenez-Yuste, V., Laudenbach, L., Lobet, S., McLaughlin, P., Oyesiku, J.O.O., Rodriguez-Merchan, E.C., et al. (2018). Recommendations on multidisciplinary management of elective surgery in people with haemophilia. Haemophilia *24*, 693–702.
3. Tong, K.M., Wang, J.D., Chang, S.T., Cheng, Y.Y., and Wang, S.S. (2018). Outcome of perioperative hemostatic management in patients with hemophilia without inhibitors undergoing 161 invasive or surgical procedures. J. Chin. Med. Assoc. *81*, 926–929.
4. Colella, P., Ronzitti, G., and Mingozzi, F. (2017). Emerging Issues in AAV-mediated *in vivo* gene therapy. Mol. Ther. Methods Clin. Dev. *8*, 87–104.
5. Biasco, L., Rothe, M., Büning, H., and Schambach, A. (2017). Analyzing the genotoxicity of retroviral vectors in hematopoietic cell gene therapy. Mol. Ther. Methods Clin. Dev. *8*, 21–30.
6. Kao, C.Y., Yang, S.J., Tao, M.H., Jeng, Y.M., Yu, I.S., and Lin, S.W. (2013). Incorporation of the factor IX Padua mutation into FIX-Triple improves clotting activity in vitro and in vivo. Thromb. Haemost. *110*, 244–256.
7. An, D., Schneller, J.L., Frassetto, A., Liang, S., Zhu, X., Park, J.S., Theisen, M., Hong, S.J., Zhou, J., Rajendran, R., et al. (2017). Systemic messenger RNA therapy as a treatment for methylmalonic acidemia. Cell Rep. *21*, 3548–3558.
8. Gan, L.M., Lagerström-Fermér, M., Carlsson, L.G., Arfvidsson, C., Egnell, A.C., Rudvik, A., Kjaer, M., Collén, A., Thompson, J.D., Joyal, J., et al. (2019). Intradermal delivery of modified mRNA encoding VEGF-A in patients with type 2 diabetes. Nat. Commun. *10*, 871.
9. Hassett, K.J., Benenato, K.E., Jacquinet, E., Lee, A., Woods, A., Yuzhakov, O., Himansu, S., Deterling, J., Geilich, B.M., Ketova, T., et al. (2019). Optimization of lipid nanoparticles for intramuscular administration of mRNA vaccines. Mol. Ther. Nucleic Acids *15*, 1–11.
10. Cao, J., An, D., Galduroz, M., Zhuo, J., Liang, S., Eybye, M., Frassetto, A., Kuroda, E., Funahashi, A., Santana, J., et al. (2019). mRNA therapy improves metabolic and behavioral abnormalities in a murine model of citrin deficiency. Mol. Ther. *27*, 1242–1251.
11. DeRosa, F., Guild, B., Karve, S., Smith, L., Love, K., Dorkin, J.R., Kauffman, K.J., Zhang, J., Yahalom, B., Anderson, D.G., and Heartlein, M.W. (2016). Therapeutic efficacy in a hemophilia B model using a biosynthetic mRNA liver depot system. Gene Ther. *23*, 699–707.
12. Ramaswamy, S., Tonnu, N., Tachikawa, K., Limphong, P., Vega, J.B., Karmali, P.P., Chivukula, P., and Verma, I.M. (2017). Systemic delivery of factor IX messenger RNA for protein replacement therapy. Proc. Natl. Acad. Sci. USA *114*, E1941–E1950.
13. Dorner, A.J., Wasley, L.C., and Kaufman, R.J. (1989). Increased synthesis of secreted proteins induces expression of glucose-regulated proteins in butyrate-treated Chinese hamster ovary cells. J. Biol. Chem. *264*, 20602–20607.
14. Tagliavacca, L., Wang, Q., and Kaufman, R.J. (2000). ATP-dependent dissociation of non-disulfide-linked aggregates of coagulation factor VIII is a rate-limiting step for secretion. Biochemistry *39*, 1973–1981.
15. Fantacini, D.M., Fontes, A.M., de Abreu Neto, M.S., Covas, D.T., and Picanço-Castro, V. (2016). The F309S mutation increases factor VIII secretion in human cell line. Rev. Bras. Hematol. Hemoter. *38*, 135–140.
16. Lynch, C.M., Israel, D.I., Kaufman, R.J., and Miller, A.D. (1993). Sequences in the coding region of clotting factor VIII act as dominant inhibitors of RNA accumulation and protein production. Hum. Gene Ther. *4*, 259–272.
17. Miao, H.Z., Sirachainan, N., Palmer, L., Kucab, P., Cunningham, M.A., Kaufman, R.J., and Pipe, S.W. (2004). Bioengineering of coagulation factor VIII for improved secretion. Blood *103*, 3412–3419.
18. Wang, X., Shin, S.C., Chiang, A.F., Khan, I., Pan, D., Rawlings, D.J., and Miao, C.H. (2015). Intraosseous delivery of lentiviral vectors targeting factor VIII expression in platelets corrects murine hemophilia A. Mol. Ther. *23*, 617–626.
19. Kaufman, R.J., Wasley, L.C., and Dorner, A.J. (1988). Synthesis, processing, and secretion of recombinant human factor VIII expressed in mammalian cells. J. Biol. Chem. *263*, 6352–6362.

20. Sabatino, D.E., Freguia, C.F., Toso, R., Santos, A., Merricks, E.P., Kazazian, H.H., Jr., Nichols, T.C., Camire, R.M., and Arruda, V.R. (2009). Recombinant canine B-domain-deleted FVIII exhibits high specific activity and is safe in the canine hemophilia A model. Blood *114*, 4562–4565.

21. Nguyen, G.N., George, L.A., Siner, J.I., Davidson, R.J., Zander, C.B., Zheng, X.L., Arruda, V.R., Camire, R.M., and Sabatino, D.E. (2017). Novel factor VIII variants with a modified furin cleavage site improve the efficacy of gene therapy for hemophilia A. J. Thromb. Haemost. *15*, 110–121.

22. Jenkins, P.V., Rawley, O., Smith, O.P., and O'Donnell, J.S. (2012). Elevated factor VIII levels and risk of venous thrombosis. Br. J. Haematol. *157*, 653–663.

23. Ye, P., Thompson, A.R., Sarkar, R., Shen, Z., Lillicrap, D.P., Kaufman, R.J., Ochs, H.D., Rawlings, D.J., and Miao, C.H. (2004). Naked DNA transfer of factor VIII induced transgene-specific, species-independent immune response in hemophilia A mice. Mol. Ther. *10*, 117–126.

24. Tuddenham, E.G. (1999). Molecular biological aspects of inhibitor development. Vox Sang. *77* (*Suppl 1*), 13–16.

25. Ehrenforth, S., Kreuz, W., Scharrer, I., Linde, R., Funk, M., Güngör, T., Krackhardt, B., and Kornhuber, B. (1992). Incidence of development of factor VIII and factor IX inhibitors in haemophiliacs. Lancet *339*, 594–598.

26. Kreuz, W., Becker, S., Lenz, E., Martinez-Saguer, I., Escuriola-Ettingshausen, C., Funk, M., Ehrenforth, S., Auerswald, G., and Kornhuber, B. (1995). Factor VIII inhibitors in patients with hemophilia A: epidemiology of inhibitor development and induction of immune tolerance for factor VIII. Semin. Thromb. Hemost. *21*, 382–389.

27. Cafuir, L.A., and Kempton, C.L. (2017). Current and emerging factor VIII replacement products for hemophilia A. Ther. Adv. Hematol. *8*, 303–313.

28. Mancuso, M.E., and Santagostino, E. (2017). Outcome of clinical trials with new extended half-life FVIII/IX concentrates. J. Clin. Med. *6*, 6.

29. Lieuw, K. (2017). Many factor VIII products available in the treatment of hemophilia A: an embarrassment of riches? J. Blood Med. *8*, 67–73.

30. Thorat, T., Neumann, P.J., and Chambers, J.D. (2018). Hemophilia burden of disease: a systematic review of the cost-utility literature for hemophilia. J. Manag. Care Spec. Pharm. *24*, 632–642.

31. George, L.A. (2017). Hemophilia gene therapy comes of age. Blood Adv. *1*, 2591–2599.

32. Rangarajan, S., Walsh, L., Lester, W., Perry, D., Madan, B., Laffan, M., Yu, H., Vettermann, C., Pierce, G.F., Wong, W.Y., and Pasi, K.J. (2017). AAV5-Factor VIII Gene Transfer in Severe Hemophilia A. N. Engl. J. Med. *377*, 2519–2530.

33. BioMarin (2019). BioMarin provides 3 years of clinical data from ongoing phase 1/2 study of valoctocogene roxaparvovec gene therapy for severe hemophilia A. PRNewswire, May 28, 2019, https://investors.biomarin.com/2019-05-28-BioMarin-Provides-3-Years-of-Clinical-Data-from-Ongoing-Phase-1-2-Study-of-Valoctocogene-Roxaparvovec-Gene-Therapy-for-Severe-Hemophilia-A.

34. Miesbach, W., O'Mahony, B., Key, N.S., and Makris, M. (2019). How to discuss gene therapy for haemophilia? A patient and physician perspective. Haemophilia *25*, 545–557.

35. Chandler, R.J., LaFave, M.C., Varshney, G.K., Trivedi, N.S., Carrillo-Carrasco, N., Senac, J.S., Wu, W., Hoffmann, V., Elkahloun, A.G., Burgess, S.M., and Venditti, C.P. (2015). Vector design influences hepatic genotoxicity after adeno-associated virus gene therapy. J. Clin. Invest. *125*, 870–880.

36. Donsante, A., Miller, D.G., Li, Y., Vogler, C., Brunt, E.M., Russell, D.W., and Sands, M.S. (2007). AAV vector integration sites in mouse hepatocellular carcinoma. Science *317*, 477.

37. Rosas, L.E., Grieves, J.L., Zaraspe, K., La Perle, K.M., Fu, H., and McCarty, D.M. (2012). Patterns of scAAV vector insertion associated with oncogenic events in a mouse model for genotoxicity. Mol. Ther. *20*, 2098–2110.

38. Kwon, H., Kim, M., Seo, Y., Moon, Y.S., Lee, H.J., Lee, K., and Lee, H. (2018). Emergence of synthetic mRNA: in vitro synthesis of mRNA and its applications in regenerative medicine. Biomaterials *156*, 172–193.

39. Karikó, K., Muramatsu, H., Welsh, F.A., Ludwig, J., Kato, H., Akira, S., and Weissman, D. (2008). Incorporation of pseudouridine into mRNA yields superior nonimmunogenic vector with increased translational capacity and biological stability. Mol. Ther. *16*, 1833–1840.

40. Vaidyanathan, S., Azizian, K.T., Haque, A.K.M.A., Henderson, J.M., Hendel, A., Shore, S., Antony, J.S., Hogrefe, R.I., Kormann, M.S.D., Porteus, M.H., and McCaffrey, A.P. (2018). Uridine depletion and chemical modification increase Cas9 mRNA activity and reduce immunogenicity without HPLC purification. Mol. Ther. Nucleic Acids *12*, 530–542.

41. Ward, N.J., Buckley, S.M., Waddington, S.N., Vandendriessche, T., Chuah, M.K., Nathwani, A.C., McIntosh, J., Tuddenham, E.G., Kinnon, C., Thrasher, A.J., and McVey, J.H. (2011). Codon optimization of human factor VIII cDNAs leads to high-level expression. Blood *117*, 798–807.

42. Mauro, V.P., and Chappell, S.A. (2014). A critical analysis of codon optimization in human therapeutics. Trends Mol. Med. *20*, 604–613.

43. Sahin, U., Karikó, K., and Türeci, Ö. (2014). mRNA-based therapeutics—developing a new class of drugs. Nat. Rev. Drug Discov. *13*, 759–780.

44. Sabnis, S., Kumarasinghe, E.S., Salerno, T., Mihai, C., Ketova, T., Senn, J.J., Lynn, A., Bulychev, A., McFadyen, I., Chan, J., et al. (2018). A novel amino lipid series for mRNA delivery: improved endosomal escape and sustained pharmacology and safety in non-human primates. Mol. Ther. *26*, 1509–1519.

45. Kulkarni, J.A., Cullis, P.R., and van der Meel, R. (2018). Lipid nanoparticles enabling gene therapies: from concepts to clinical utility. Nucleic Acid Ther. *28*, 146–157.

46. Ambegia, E., Ansell, S., Cullis, P., Heyes, J., Palmer, L., and MacLachlan, I. (2005). Stabilized plasmid-lipid particles containing PEG-diacylglycerols exhibit extended circulation lifetimes and tumor selective gene expression. Biochim. Biophys. Acta *1669*, 155–163.

47. Judge, A., McClintock, K., Phelps, J.R., and Maclachlan, I. (2006). Hypersensitivity and loss of disease site targeting caused by antibody responses to PEGylated liposomes. Mol. Ther. *13*, 328–337.

48. Russick, J., Delignat, S., Milanov, P., Christophe, O., Boros, G., Denis, C.V., Lenting, P.J., Kaveri, S.V., and Lacroix-Demazes, S. (2020). Correction of bleeding in experimental severe hemophilia A by systemic delivery of factor VIII-encoding mRNA. Haematologica *105*.

49. Dwarki, V.J., Belloni, P., Nijjar, T., Smith, J., Couto, L., Rabier, M., Clift, S., Berns, A., and Cohen, L.K. (1995). Gene therapy for hemophilia A: production of therapeutic levels of human factor VIII in vivo in mice. Proc. Natl. Acad. Sci. USA *92*, 1023–1027.

50. Kizilocak, H., Yukhtman, C.L., Marquez-Casas, E., Lee, J., Donkin, J., and Young, G. (2019). Management of perioperative hemostasis in a severe hemophilia A patient with inhibitors on emicizumab using global hemostasis assays. Ther. Adv. Hematol. *10*, 2040620719860025.

51. Langer, A.L., Etra, A., and Aledort, L. (2018). Evaluating the safety of emicizumab in patients with hemophilia A. Expert Opin. Drug Saf. *17*, 1233–1237.

52. Wada, H., Matsumoto, T., and Katayama, N. (2017). Emicizumab prophylaxis in hemophilia A with inhibitors. N. Engl. J. Med. *377*, 2193–2194.

53. Young, G., Liesner, R., Chang, T., Sidonio, R., Oldenburg, J., Jiménez-Yuste, V., Mahlangu, J., Kruse-Jarres, R., Wang, M., Uguen, M., et al. (2019). A multicenter, open-label phase 3 study of emicizumab prophylaxis in children with hemophilia A with inhibitors. Blood *134*, 2127–2138.

54. Calvez, T., Chambost, H., d'Oiron, R., Dalibard, V., Demiguel, V., Doncarli, A., Gruel, Y., Huguenin, Y., Lutz, P., Rothschild, C., et al.; for FranceCoag Collaborators (2018). Analyses of the FranceCoag cohort support differences in immunogenicity among one plasma-derived and two recombinant factor VIII brands in boys with severe hemophilia A. Haematologica *103*, 179–189.

55. Lai, J., Hough, C., Tarrant, J., and Lillicrap, D. (2017). Biological considerations of plasma-derived and recombinant factor VIII immunogenicity. Blood *129*, 3147–3154.

56. Ettinger, R.A., Liberman, J.A., Gunasekera, D., Puranik, K., James, E.A., Thompson, A.R., and Pratt, K.P. (2018). FVIII proteins with a modified immunodominant T-cell epitope exhibit reduced immunogenicity and normal FVIII activity. Blood Adv. *2*, 309–322.

57. Muczynski, V., Casari, C., Moreau, F., Aymé, G., Kawecki, C., Legendre, P., Proulle, V., Christophe, O.D., Denis, C.V., and Lenting, P.J. (2018). A factor VIII-nanobody fusion protein forming an ultrastable complex with VWF: effect on clearance and antibody formation. Blood *132*, 1193–1197.

58. Powell, J.S., Josephson, N.C., Quon, D., Ragni, M.V., Cheng, G., Li, E., Jiang, H., Li, L., Dumont, J.A., Goyal, J., et al. (2012). Safety and prolonged activity of recombinant factor VIII Fc fusion protein in hemophilia A patients. Blood *119*, 3031–3037.

59. Dumont, J.A., Liu, T., Low, S.C., Zhang, X., Kamphaus, G., Sakorafas, P., Fraley, C., Drager, D., Reidy, T., McCue, J., et al. (2012). Prolonged activity of a recombinant factor VIII-Fc fusion protein in hemophilia A mice and dogs. Blood *119*, 3024–3030.

60. Liu, C.L., Ye, P., Lin, J., Djukovic, D., and Miao, C.H. (2014). Long-term tolerance to factor VIII is achieved by administration of interleukin-2/interleukin-2 monoclonal antibody complexes and low dosages of factor VIII. J. Thromb. Haemost. *12*, 921–931.

61. Peng, B., Ye, P., Blazar, B.R., Freeman, G.J., Rawlings, D.J., Ochs, H.D., and Miao, C.H. (2008). Transient blockade of the inducible costimulator pathway generates long-term tolerance to factor VIII after nonviral gene transfer into hemophilia A mice. Blood *112*, 1662–1672.

SARS and MERS: recent insights into emerging coronaviruses

Emmie de Wit[1], Neeltje van Doremalen[1], Darryl Falzarano[2] and Vincent J. Munster[1]

Abstract | The emergence of Middle East respiratory syndrome coronavirus (MERS-CoV) in 2012 marked the second introduction of a highly pathogenic coronavirus into the human population in the twenty-first century. The continuing introductions of MERS-CoV from dromedary camels, the subsequent travel-related viral spread, the unprecedented nosocomial outbreaks and the high case-fatality rates highlight the need for prophylactic and therapeutic measures. Scientific advancements since the 2002–2003 severe acute respiratory syndrome coronavirus (SARS-CoV) pandemic allowed for rapid progress in our understanding of the epidemiology and pathogenesis of MERS-CoV and the development of therapeutics. In this Review, we detail our present understanding of the transmission and pathogenesis of SARS-CoV and MERS-CoV, and discuss the current state of development of measures to combat emerging coronaviruses.

Nosocomial transmission
Transmission of an infectious agent by staff, equipment or the environment in a health care setting.

[1]*Laboratory of Virology, Division of Intramural Research, National Institute of Allergy and Infectious Diseases, National Institutes of Health, Rocky Mountain Laboratories, Hamilton, Montana 59840, USA.*
[2]*Vaccine and Infectious Disease Organization – International Vaccine Centre and Department of Veterinary Microbiology, University of Saskatchewan, 120 Veterinary Road, Saskatoon, Saskatchewan S7N 5E3, Canada.*

Correspondence to V.J.M.
vincent.munster@nih.gov

doi:10.1038/nrmicro.2016.81
Published online 27 Jun 2016

This century has seen the global spread of two previously unknown coronaviruses. In November 2002, the first known case of severe acute respiratory syndrome (SARS) occurred in Foshan, China[1]. New cases emerged in mainland China, and by February 2003, more than 300 cases had been reported, around one-third of which were in health care workers[1]. Individuals who were infected and subsequently travelled spread the outbreak to Hong Kong[2] and from there to Vietnam, Canada and several other countries[3]. In March 2003, the WHO established a network of laboratories to determine the causative agent of SARS. A remarkable global effort led to the identification of SARS coronavirus (SARS-CoV) in early April of that year[4–6]. By July 2003 and after a total of 8,096 reported cases, including 774 deaths in 27 countries[7], no more infections were detected, and the SARS pandemic was declared to be over. Five additional SARS cases, resulting from zoonotic transmission, occurred in December 2003–January 2004 (REF. 8), but no human SARS cases have been detected since. Measures of infection control, rather than medical interventions, ended the SARS pandemic. However, certain SARS-CoV-like viruses found in bats have recently been shown to be able to infect human cells without prior adaptation[9,10], which indicates that SARS could re-emerge.

In June 2012, 10 years after the first emergence of SARS-CoV, a man in Saudi Arabia died of acute pneumonia and renal failure. A novel coronavirus, Middle East respiratory syndrome coronavirus (MERS-CoV), was isolated from his sputum[11]. A cluster of cases of severe respiratory disease had occurred in April 2012 in a hospital in Jordan and was retrospectively diagnosed as MERS[12], and a cluster of three cases of MERS in the UK was identified in September 2012 (REF. 13). MERS-CoV continued to emerge and spread to countries outside of the Arabian Peninsula as a result of travel of infected persons; often, these imported MERS cases resulted in nosocomial transmission. In May 2015, a single person returning from the Middle East started a nosocomial outbreak of MERS in South Korea that involved 16 hospitals and 186 patients[14]. As of 26 April 2016, there have been 1,728 confirmed cases of MERS, including 624 deaths in 27 countries[15].

This Review highlights the pandemic and epidemic potential of emerging coronaviruses and discusses our current knowledge of the biology of SARS-CoV and MERS-CoV, including their transmission, their pathogenesis and the development of medical countermeasures. Key features of these viruses are the dominance of nosocomial transmission, and pathogenesis that is driven by a combination of viral replication in the lower respiratory tract and an aberrant host immune response. Several potential treatments for SARS and MERS have been identified in animal and *in vitro* models, including small-molecule protease inhibitors, neutralizing antibodies and inhibitors of the host immune response. However, efficacy data from human clinical trials are lacking but are needed to move these potential countermeasures forward.

Replication of SARS-CoV and MERS-CoV

SARS-CoV and MERS-CoV belong to the Coronavirus genus in the *Coronaviridae* family and have large, positive-sense RNA genomes of 27.9 kb and 30.1 kb,

Proofreading
The correction of errors that are acquired during the replication of DNA or RNA.

respectively (FIG. 1a). Similarly to all viruses in the order *Nidovirales*, SARS-CoV and MERS-CoV have a unique coding strategy: two-thirds of the viral RNA is translated into two large polyproteins, and the remainder of the viral genome is transcribed into a nested set of subgenomic mRNAs[16,17] (FIG. 1b). The two polyproteins, pp1a and pp1ab, encode 16 non-structural proteins (nsp1–nsp16)[18] that make up the viral replicase–transcriptase complex. The polyproteins are cleaved by two proteases, papain-like protease (PLpro; corresponding to nsp3) and a main protease, 3C-like protease (3CLpro; corresponding to nsp5). The nsps rearrange membranes that are derived from the rough endoplasmic reticulum (RER) into double-membrane vesicles, in which viral replication and transcription occur[19]. One unique feature of coronaviruses is the exoribonuclease (ExoN) function of nsp14 (REF. 20), which provides the proofreading capability required to maintain a large RNA genome without the accumulation of detrimental mutations[21,22]. SARS-CoV and MERS-CoV transcribe 12 and 9 subgenomic RNAs,

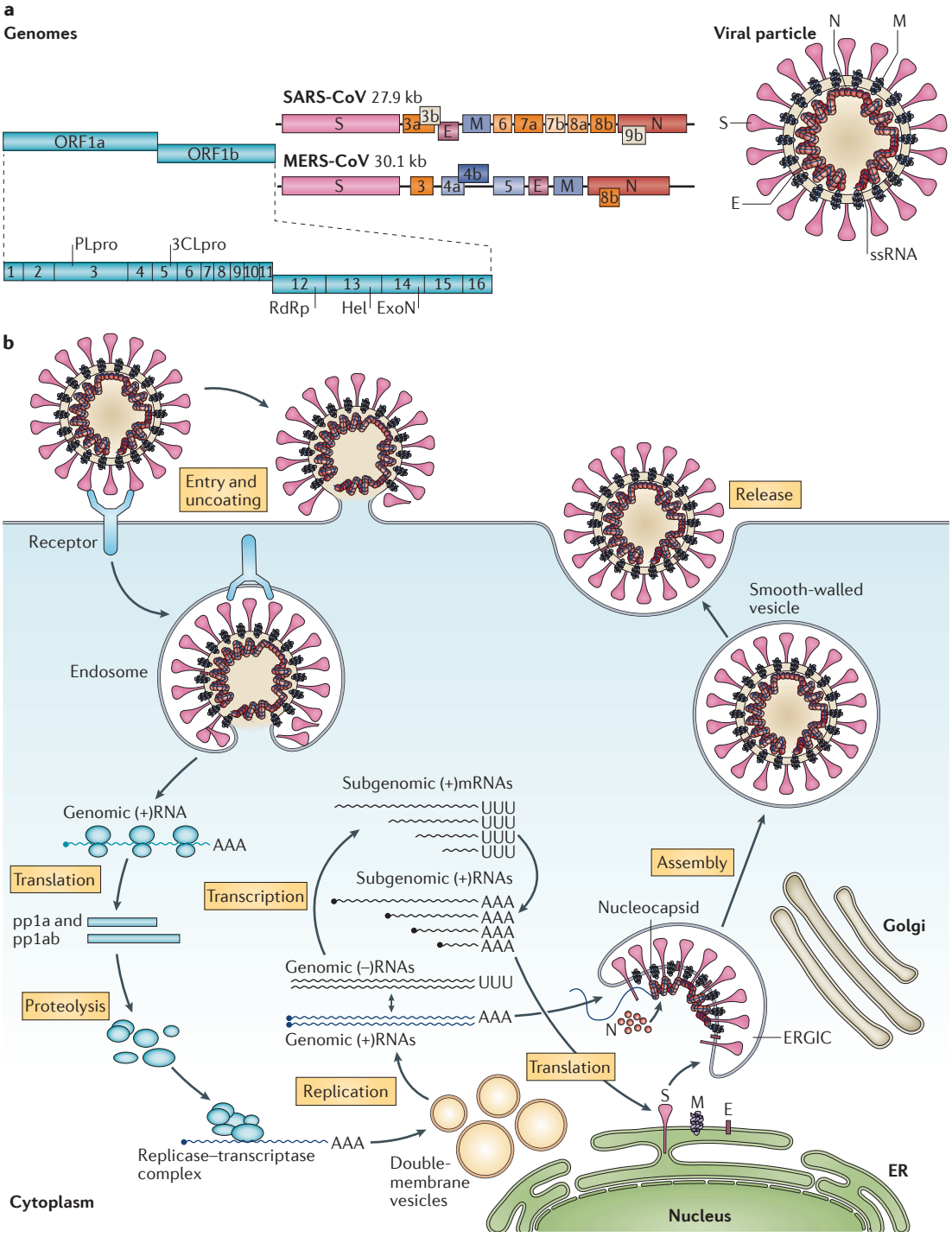

ER–Golgi intermediate compartment
(ERGIC). A cellular compartment that facilitates transport between the endoplasmic reticulum (ER) and the Golgi complex.

Super spreaders
Infected individuals who each infect a disproportionately large number of secondary cases.

respectively, and these encode the four structural proteins spike (S), envelope (E), membrane (M) and nucleocapsid (N), as well as several accessory proteins that are not involved in viral replication but interfere with the host innate immune response or are of unknown or poorly understood function.

The envelope spike glycoprotein binds to its cellular receptor, angiotensin-converting enzyme 2 (ACE2) for SARS-CoV and dipeptidyl peptidase 4 (DPP4) for MERS-CoV[23]. After membrane fusion, either directly with the host cell membrane or with the endosome membrane, the viral RNA genome is released into the cytoplasm, and the RNA is uncoated to allow translation of the two polyproteins, transcription of the subgenomic RNAs and replication of the viral genome (FIG. 1b). Newly formed envelope glycoproteins are inserted in the RER or Golgi membranes; genomic RNA and nucleocapsid proteins combine to form nucleocapsids, and the viral particles bud into the ER–Golgi intermediate compartment (ERGIC). Virion-containing vesicles subsequently fuse with the plasma membrane to release the virus[24].

Reservoirs and transmission

The first indication of the source of SARS-CoV was the detection of the virus in masked palm civets and a raccoon dog and the detection of antibodies against the virus in Chinese ferret badgers in a live-animal market in Shenzhen, China[25]. However, these animals were only incidental hosts, as there was no evidence for the circulation of SARS-CoV-like viruses in palm civets in the wild or in breeding facilities[26]. Rather, bats are the reservoir of a wide variety of coronaviruses, including SARS-CoV-like and MERS-CoV-like viruses[27] (FIG. 2).

Figure 1 | **SARS-CoV and MERS-CoV structure and replication. a** | The single-stranded RNA (ssRNA) genomes of severe acute respiratory syndrome coronavirus (SARS-CoV) and Middle East respiratory syndrome coronavirus (MERS-CoV) encode two large polyproteins, pp1a and pp1ab, which are proteolytically cleaved into 16 non-structural proteins (nsps), including papain-like protease (PLpro), 3C-like protease (3CLpro), RNA-dependent RNA polymerase (RdRp), helicase (Hel) and exonuclease (ExoN). An additional 9–12 ORFs are encoded through the transcription of a nested set of subgenomic RNAs. SARS-CoV and MERS-CoV form spherical particles that consist of four structural proteins. The envelope glycoprotein spike (S) forms a layer of glycoproteins that protrude from the envelope. Two additional transmembrane glycoproteins are incorporated in the virion: envelope (E) and membrane (M). Inside the viral envelope resides the helical nucleocapsid, which consists of the viral positive-sense RNA ((+)RNA) genome encapsidated by protein nucleocapsid (N). **b** | Following entry of the virus into the host cell, the viral RNA is uncoated in the cytoplasm. ORF1a and ORF1ab are translated to produce pp1a and pp1ab, which are cleaved by the proteases that are encoded by ORF1a to yield 16 nsps that form the RNA replicase–transcriptase complex. This complex localizes to modified intracellular membranes that are derived from the rough endoplasmic reticulum (ER) in the perinuclear region, and it drives the production of negative-sense RNAs ((–)RNAs) through both replication and transcription. During replication, full-length (–)RNA copies of the genome are produced and used as templates for full-length (+)RNA genomes. During transcription, a subset of 7–9 subgenomic RNAs, including those encoding all structural proteins, is produced through discontinuous transcription. In this process, subgenomic (–)RNAs are synthesized by combining varying lengths of the 3′end of the genome with the 5′ leader sequence necessary for translation. These subgenomic (–)RNAs are then transcribed into subgenomic (+)mRNAs. Although the different subgenomic mRNAs may contain several ORFs, only the first ORF (that closest to the 5′end) is translated. The resulting structural proteins are assembled into the nucleocapsid and viral envelope at the ER–Golgi intermediate compartment (ERGIC), followed by release of the nascent virion from the infected cell.

Thus, the search for the reservoir of MERS-CoV initially focused on bats, but a serological survey in dromedary camels from Oman and the Canary Islands showed a high prevalence of MERS-CoV-neutralizing antibodies in these animals[28]. In addition, MERS-CoV RNA was detected in swabs that were collected from dromedary camels at a farm in Qatar that was linked to two human cases of MERS, and infectious virus was isolated from dromedary camels in Saudi Arabia and Qatar[29–32]. Serological evidence for the circulation of a MERS-CoV-like virus in dromedary camels has been obtained in the Middle East, Eastern Africa and Northern Africa, dating back as far as 1983 (REF. 33). Dromedary camels in Saudi Arabia harbour several viral genetic lineages[34], including those that have caused human outbreaks. Taken together, these data strongly point to the role of dromedary camels as a reservoir for MERS-CoV. The ubiquity of infected dromedary camels close to humans and the resulting continuing zoonotic transmission may explain why MERS-CoV continues to cause infections in humans, whereas SARS-CoV, without the continuing presence of an infected intermediate host and with relatively infrequent human–bat interactions, has caused no more infections in humans.

Human-to-human transmission of SARS-CoV and MERS-CoV occurs mainly through nosocomial transmission; 43.5–100% of MERS cases in individual outbreaks were linked to hospitals, and very similar observations were made for some of the SARS clusters[35,36]. Transmission between family members occurred in only 13–21% of MERS cases and 22–39% of SARS cases. Transmission of MERS-CoV between patients was the most common route of infection (62–79% of cases), whereas for SARS-CoV, infection of health care workers by infected patients was very frequent (33–42%)[35]. The predominance of nosocomial transmission is probably due to the fact that substantial virus shedding occurs only after the onset of symptoms[37,38], when most patients are already seeking medical care[39]. An analysis of hospital surfaces after the treatment of patients with MERS showed the ubiquitous presence of viral RNA in the environment for several days after patients no longer tested positive[40]. Moreover, many patients with SARS or MERS were infected through super spreaders[14,35,37,41–43].

The pathogenesis of SARS-CoV and MERS-CoV

The clinical courses of SARS and MERS are remarkably similar, although there are subtle differences (BOX 1). Owing to the current sparsity of data on human MERS-CoV infections[44], the pathogenesis of this virus is poorly understood; however, similar mechanisms may underlie the pathogenesis of both MERS and SARS.

The binding of spike protein to ACE2 and the subsequent downregulation of this receptor contribute to lung injury during SARS[45]. Although it seems counter-intuitive that receptor downregulation would increase pathology, it has been shown that ACE2 can protect against acute lung injury. The downregulation of ACE2 results in the excessive production of angiotensin II by the related enzyme ACE, and it has been suggested that the stimulation of type 1a angiotensin II receptor

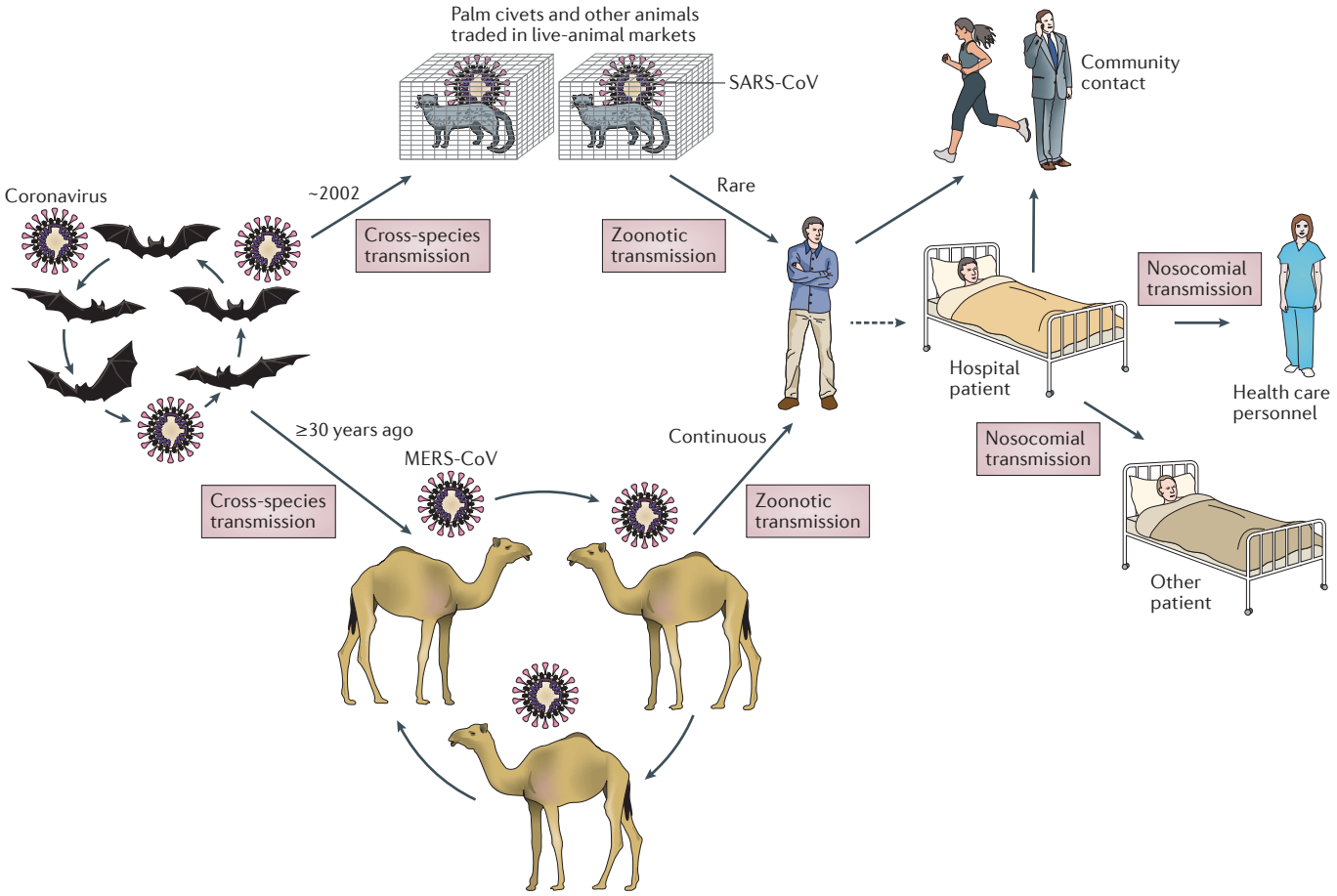

Figure 2 | **The emergence of SARS-CoV and MERS-CoV.** Bats harbour a wide range of coronaviruses, including severe acute respiratory syndrome coronavirus (SARS-CoV)-like and Middle East respiratory syndrome coronavirus (MERS-CoV)-like viruses. SARS-CoV crossed the species barrier into masked palm civets and other animals in live-animal markets in China; genetic analysis suggests that this occurred in late 2002. Several people in close proximity to palm civets became infected with SARS-CoV. A MERS-CoV ancestral virus crossed the species barrier into dromedary camels; serological evidence suggests that this happened more than 30 years ago. Abundant circulation of MERS-CoV in dromedary camels results in frequent zoonotic transmission of this virus. SARS-CoV and MERS-CoV spread between humans mainly through nosocomial transmission, which results in the infection of health care workers and patients at a higher frequency than infection of their relatives.

(AGTR1A) increases pulmonary vascular permeability, thus potentially explaining the increased lung pathology when the expression of ACE2 is decreased[46].

Immunopathology. The immune response is essential for the resolution of an infection, but it can also result in immunopathogenesis. One indication that immunopathogenesis may contribute to SARS was the observation that viral loads were found to be decreasing while disease severity increased[39,47]. It is unclear whether a similar trend applies to MERS[48,49]. Moreover, progression to acute respiratory distress syndrome (ARDS) is associated with the upregulation of pro-inflammatory cytokines and chemokines, particularly interleukin-1β (IL-1β), IL-8, IL-6, CXC-chemokine ligand 10 (CXCL10) and CC-chemokine ligand 2 (CCL2)[50,51]; increased plasma levels of these molecules have been detected in patients with SARS[52–55]. Retrospective longitudinal studies in patients who recovered from SARS versus those who succumbed to the disease have shown an early expression of interferon-α (IFNα), IFNγ, CXCL10, CCL2 and proteins that are encoded by IFN-stimulated genes (ISGs) in all patients, but only patients who survived then had gene expression profiles that are indicative of the development of an adaptive immune response. By contrast, patients who succumbed maintained high levels of CXCL10, CCL2 and ISG-encoded proteins, whereas spike-specific antibodies were present at low levels or were absent[56], which suggests that severe disease is related to the lack of a switch from an innate immune response to an adaptive immune response.

Experiments using Collaborative Cross mouse lines and mouse-adapted SARS-CoV identified one host gene, *Trim55*, as important for SARS pathogenesis. Although there was no difference in clinical signs or viral replication in *Trim55*$^{-/-}$ mice compared with wild-type mice, perivascular cuffing and the number of inflammatory cells in the lungs were reduced in the *Trim55*$^{-/-}$ mice[57].

Acute respiratory distress syndrome
(ARDS). A life-threatening condition in which the accumulation of fluid and inflammatory cells in the lungs decreases the exchange of oxygen and carbon dioxide to dangerously low levels.

Collaborative Cross mouse
One of a panel of recombinant inbred mouse strains derived from a genetically diverse set of founder strains and designed for the analysis of complex traits.

Perivascular cuffing
The aggregation of leukocytes around blood vessels.

Box 1 | **Clinical features of SARS and MERS**

Severe acute respiratory syndrome coronavirus (SARS-CoV) and Middle East respiratory syndrome coronavirus (MERS-CoV) have an incubation period of ~5 days, and 95% of patients develop disease within 13 days of exposure[14,38,144–146]. Common early symptoms are fever, chills, coughing, malaise, myalgia and headache, and less common symptoms include diarrhoea, vomiting and nausea[2,6,39,89,90,92,95,144,146–148]. Upper respiratory tract symptoms and viral shedding are rare, which explains difficulties in obtaining a laboratory diagnosis from nasal or nasopharyngeal swabs[149]. Abnormal chest X-rays are more common in patients with MERS (90–100%)[144,148] than in those with SARS (60–100%)[39,89]. Accordingly, only 20–30% of patients with SARS require intensive care and subsequent mechanical ventilation, whereas 50–89% of patients with MERS require intensive care[2,39,89,90,95,144,147,148]. The higher incidence of acute respiratory distress syndrome (ARDS) in individuals with MERS is reflected in the case fatality rate: this is ~36% for MERS compared with ~10% for SARS[15,145].

Comorbidities have an important role in both SARS and MERS. Several risk factors are associated with poor disease outcome, especially advanced age and male sex[2,14,39,144,146,148,150,151]. For MERS, additional risk factors for a poor outcome include diabetes mellitus, hypertension, cancer, renal and lung disease, and co-infections[14,144,146,148,150,151].

Health care settings seem to increase the risk of viral transmission owing to aerosol-generating procedures such as intubation and bronchoscopy. Appropriate hospital hygiene practices and awareness are crucial to limit future nosocomial outbreaks.

The involvement of the host immune response in the pathogenesis of SARS, and most likely also that of MERS, suggests that drugs which inhibit viral replication will need to be combined with treatments that control detrimental immune responses.

Immune evasion. SARS-CoV and MERS-CoV use several strategies to avoid the innate immune response. Viral pathogen-associated molecular patterns (PAMPs), such as double-stranded RNA (dsRNA) or uncapped mRNA, are detected by pattern recognition receptors (PRRs), such as retinoic acid-inducible gene I protein (RIG-I; also known as DDX58) or melanoma differentiation-associated protein 5 (MDA5; also known as IFIH1)[58]. This triggers complex signalling cascades involving MYD88 that lead to the production of type I IFNs and the activation of the transcription factor nuclear factor-κB (NF-κB). In turn, active NF-κB induces the transcription of pro-inflammatory cytokines (FIG. 3a). Type I IFNs signal through IFNα/β receptor (IFNAR) and downstream molecules such as signal transducer and activator of transcription (STAT) proteins to stimulate the production of antiviral proteins that are encoded by ISGs, such as IFN-induced protein with tetratricopeptide repeats 1 (IFIT1; FIG. 3b). Collectively, this establishes an antiviral immune response that limits viral replication in infected and in neighbouring cells (FIG. 3).

Infection of knockout mice revealed the importance of innate immunity. Infection of *Myd88*$^{-/-}$ and *Stat1*$^{-/-}$ mice, but not mice that were deficient in IFN receptors, with a mouse-adapted strain of SARS-CoV resulted in more severe disease than infection with a non-adapted SARS-CoV strain[59,60]. Moreover, MERS-CoV infection of wild-type mice that were transduced with human DPP4 caused mild disease, but symptoms were more severe in *Myd88*$^{-/-}$ mice and *Ifnar1*$^{-/-}$ mice[61].

SARS-CoV and MERS-CoV avoid host detection of their dsRNA by replicating in virus-induced double-membrane vesicles that lack PRRs[19,62,63]. Moreover, the recognition of SARS-CoV mRNAs, for example, by MDA5 and IFIT1 is prevented by capping of the viral mRNAs by nsp14 and the nsp10–nsp16 complex[64]. Recombinant SARS-CoV that lacks the methylation activity of nsp16 is attenuated and exhibits increased sensitivity to type I IFNs. This effect is dependent on IFIT1 or MDA5, as the same virus is not attenuated in mice that are deficient in either molecule[65]. Although mRNA capping has not yet been shown for MERS-CoV, structural similarity between the MERS-CoV nsp10–nsp16 complex and the SARS-CoV nsp10–nsp16 complex suggests that a similar mechanism exists to avoid host recognition of MERS-CoV mRNAs by cytosolic PRRs[66].

SARS-CoV encodes at least eight proteins that interact with the signalling cascades downstream of PRRs; in MERS-CoV, several proteins have been identified with similar functions (FIG. 3). The nucleocapsid protein of SARS-CoV has been associated with the suppression of RNAi in mammalian cells[67]. Furthermore, this protein antagonizes IFN induction, probably early in the signalling cascade, as downstream signalling molecules relieve the inhibition[68]. MERS-CoV ORF4a has a similar IFN-antagonistic function, involving the binding of dsRNA and subsequent inhibition of MDA5 activation[69], potentially through interaction with IFN-inducible dsRNA-dependent protein kinase activator A (PRKRA; also known as PACT), which interacts with MDA5 and RIG-I[70]. Moreover, MERS-CoV ORF4a, ORF4b, ORF5 and membrane protein inhibit the nuclear trafficking of IFN-regulatory factor 3 (IRF3) and activation of the *IFNB* promoter[71]. These viral proteins, except for ORF5, also inhibit the expression of genes that are under the control of an IFN-stimulated response element (ISRE), and ORF4a reduces the expression of genes that are stimulated by NF-κB[71]. Finally, MERS-CoV ORF4b interacts with TBK1 and inhibitor of NF-κB kinase-ε (IKKε), thereby suppressing the interaction between IKKε and mitochondrial antiviral-signalling protein (MAVS) and inhibiting the phosphorylation of IRF3 (REF. 72).

The membrane protein of SARS-CoV inhibits the formation of a signalling complex that contains IKKε, thus repressing the activation of IRF3 and IRF7 and their induction of type I IFN expression. The membrane protein of MERS-CoV inhibits IRF3 function and the expression of genes that are regulated by an ISRE, including IFNβ[71], but whether this occurs through a mechanism similar to that of SARS-CoV is unclear.

SARS-CoV PLpro disrupts NF-κB signalling[73] and blocks the phosphorylation of IRF3 indirectly[73,74]. Furthermore, SARS-CoV PLpro inhibits the induction of type I IFNs, potentially through the deubiquitylation of phosphorylated IRF3 (REFS 73,75). Similar functions have been described for MERS-CoV PLpro[76].

Experiments involving recombinantly expressed proteins, *in vitro* translation, protein overexpression and minireplicon systems have shown that nsp1 of SARS-CoV blocks the IFN response through the inhibition of

Type I IFNs
(Type I interferons). A group of IFNs, including IFNα and IFNβ, with immune-modulating and antiviral functions.

RNAi
A biological process in which small RNA molecules induce the degradation of specific mRNA molecules, thereby inhibiting gene expression.

Minireplicon systems
Systems in which a DNA molecule is produced that contains the viral leader and trailer sequences, with an assayable reporter replacing the viral ORFs. When combined with the expression of viral proteins in *trans*, this system can be used to model the viral life cycle without the necessity of using infectious virus.

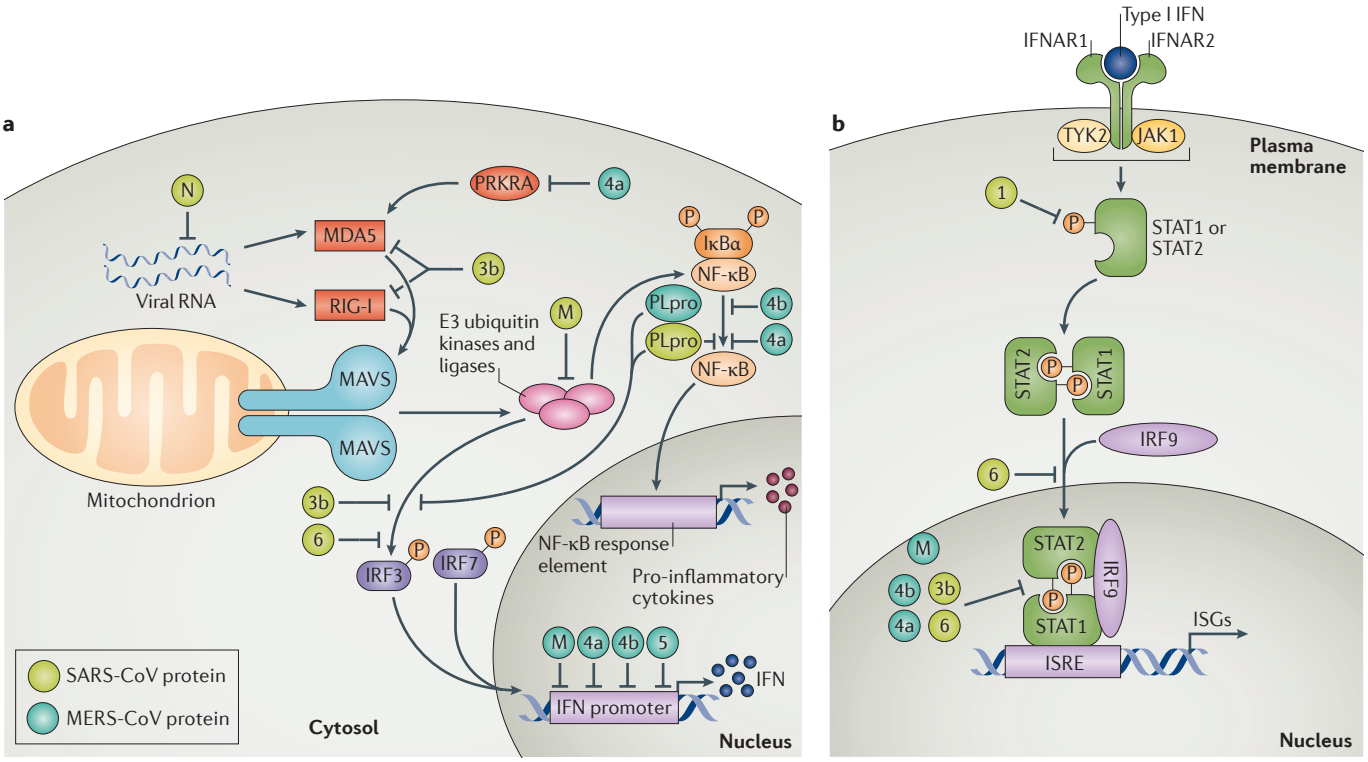

Figure 3 | **Evasion of the innate immune response by SARS-CoV and MERS-CoV. a** | The innate immune response is activated by the detection of viral pathogen-associated molecular patterns (PAMPs), such as double-stranded RNA (dsRNA) or uncapped mRNA. This occurs via host pattern recognition receptors (PRRs), such as retinoic acid-inducible gene I protein (RIG-I) and melanoma differentiation-associated protein 5 (MDA5), potentially via dsRNA-binding partners such as IFN-inducible dsRNA-dependent protein kinase activator A (PRKRA). Following PRR-mediated detection of a PAMP, the resulting interaction of PRRs with mitochondrial antiviral-signalling protein (MAVS) activates nuclear factor-κB (NF-κB) through a signalling cascade involving several kinases. Activated NF-κB translocates to the nucleus, where it induces the transcription of pro-inflammatory cytokines. The kinases also phosphorylate (P) IFN-regulatory factor 3 (IRF3) and IRF7, which form homodimers and heterodimers and enter the nucleus to initiate the transcription of type I interferons (type I IFNs). Both severe acute respiratory syndrome coronavirus (SARS-CoV) and Middle East respiratory syndrome coronavirus (MERS-CoV) have developed mechanisms to interfere with these signalling pathways, as shown; these subversion strategies involve both structural proteins (membrane (M) and nucleocapsid (N)) and non-structural proteins (nsp1, nsp3b, nsp4a, nsp4b, nsp5, nsp6 and papain-like protease (PLpro); indicated in the figure by just their nsp numbers and letters). **b** | Binding of type I IFNs to their dimeric receptor, IFNα/β receptor (IFNAR), activates the Janus kinase (JAK)–signal transducer and activator of transcription (STAT) signalling pathway, in which JAK1 and TYK2 kinases phosphorylate STAT1 and STAT2, which form complexes with IRF9. These complexes move into the nucleus to initiate the transcription of IFN-stimulated genes (ISGs) under the control of promoters that contain an IFN-stimulated response element (ISRE). Collectively, the expression of cytokines, IFNs and ISGs establishes an antiviral innate immune response that limits viral replication in infected and in neighbouring cells. Again, viral proteins have been shown to inhibit these host signalling pathways to evade this immune response. IκBα, NF-κB inhibitor-α.

STAT1, degradation of host mRNAs and inactivation of the host translational machinery through a tight association with the 40S ribosomal subunit[77–80]. Nsp1 of MERS-CoV also inhibits the translation of mRNAs and induces mRNA degradation, although the translational inhibition is achieved through a different mechanism than ribosome binding, which selectively targets the translation of nuclear mRNAs and thereby spares cytoplasmic viral mRNAs[81].

SARS-CoV ORF3b inhibits the production of type I IFN, the phosphorylation of IRF3 and gene expression from an ISRE promoter[82,83]. SARS-CoV ORF6 also blocks the nuclear translocation of STAT1 (REF. 83).

Both nsp7 and nsp15 from SARS-CoV were also suggested to be IFN antagonists, but the underlying mechanism is unknown[73]. nsp15 is an inhibitor of MAVS-induced apoptosis; however, this occurs through an IFN-independent mechanism[84]. Finally, transcriptomic and proteomic analysis of human airway cell cultures showed that MERS-CoV but not SARS-CoV induces repressive histone modifications that downregulate the expression of certain ISGs[85].

It should be noted that most of the interactions of SARS-CoV and MERS-CoV proteins with innate immune pathways were established in *in vitro* systems, which rely on the overexpression of viral and,

Table 1 | **Potential therapeutics for MERS**

Treatment	Stage of development	References
Host protease inhibitors	*In vitro* inhibition	132
Viral protease inhibitors	*In vitro* inhibition	97,99,112–114
Repurposed FDA-approved drugs	*In vitro* inhibition	62,99,113,115
Monoclonal and polyclonal antibodies	Effective in mouse, rabbit and non-human primate models	118–121, 123–128
Convalescent plasma	Effective in a mouse model; clinical trial approved	122
Interferons	Effective in non-human primate models; off-label use in patients	87,97–99, 101–105,108–111
Ribavirin	Effective in a non-human primate model; off-label use in patients	87,88,101,102, 108–111
Mycophenolic acid	Failed to protect in a non-human primate model	97,99,105,113
Lopinavir and ritonavir	Effective in a non-human primate model; off-label use in patients	105,109–111

MERS, Middle East respiratory syndrome.

sometimes, cellular proteins, and these interactions have rarely been confirmed in the context of viral replication *in vitro* or *in vivo*.

Treatment of severe coronavirus infections

Several strategies are being considered to treat infections with MERS-CoV (TABLE 1) and SARS-CoV, including the use of antibodies, IFNs, inhibitors of viral and host proteases, and host-directed therapies.

Current therapies. In the absence of a clinically proven effective antiviral therapy against SARS-CoV and MERS-CoV, patients mainly receive supportive care, which is often supplemented by different combinations of drugs. Ribavirin[86] and various types of IFN have been given to patients with MERS in Saudi Arabia[87] and China[88], typically in combination with a broad-spectrum antibiotic and oxygen. The efficacy of treatments for SARS-CoV and MERS-CoV infection currently remains unclear. In addition, treatment for MERS is typically started only in a late disease stage, when immunopathology predominates and antiviral drugs are likely to provide little benefit.

Ribavirin was used most frequently during the SARS outbreak, often in combination with corticosteroids, which have an anti-inflammatory effect[2,89–92]. IFNα was also given, usually in combination with immunoglobulins or thymosins, which stimulate the development of T cells, and in a small number of cases in combination with ribavirin[93,94]. None of these treatments was tested in a clinical trial, which makes it difficult to assess their efficacy. In fact, retrospective analysis did not yield a treatment combination that was clearly effective. Moreover, the data from patients are contradictory about whether ribavirin, when used alone, provided a benefit or was possibly even detrimental[89,90,92,95]. *In vitro* coronaviruses have a lower sensitivity to ribavirin than other viruses. Deletion of the nsp14-encoding sequence increases the sensitivity of coronaviruses to ribavirin; however, the underlying mechanism is unclear and is not related to the proofreading function of nsp14 (REF. 96). Therefore, ribavirin should be considered only in combination with other antiviral treatments.

Although IFNs are effective against MERS-CoV *in vitro*[97–99], their effect in humans has yet to be proved. The effectiveness of IFN is increased *in vitro* if ribavirin is added[98,100], and a combined use of the two drugs reduces disease severity in a rhesus macaque model of MERS[101]. The potential side effects of these treatments, such as fatigue, depression and anaemia, have inhibited their use as a first-line treatment for MERS, and they are generally administered only after a patient's condition starts to deteriorate. For example, one study of five patients who were infected with MERS-CoV indicated no survival following ribavirin and IFNα2b therapy; however, therapy was not started until 10 days after admission[87]. A separate study found an improvement in survival 14 days after MERS diagnosis and the start of treatment, but not 28 days after[102]. In a third study, a combination of IFNα2a and ribavirin or IFNβ1a and ribavirin did not improve survival; however, some of the patients were more than 50 years old and had pre-existing renal failure[103]. In a single case in which ribavirin and IFNα2b were started shortly after admission to hospital, the patient started to improve on day 6 after admission and made a complete recovery[104].

IFNβ1b is a more potent inhibitor of MERS-CoV replication *in vitro* than other types of IFN[97,99], and an improved outcome of disease was observed in common marmosets after challenge with MERS-CoV[105]. Thus, the type of IFN that is used for treatment in humans should be reconsidered (usually, IFNα is used). Furthermore, ribavirin and/or IFNs should be tested in clinical trials to determine their efficacy in MERS treatment and to establish treatment protocols.

Additional antiviral treatments. The protease inhibitors lopinavir and ritonavir, which are used in combination to treat infection with HIV, improved the outcome of patients with SARS when combined with ribavirin, compared with patients who were treated with ribavirin alone[106,107]. Lopinavir showed no clear antiviral activity against MERS-CoV *in vitro*[97], and it is thus rarely used in patients with MERS. However, lopinavir and ritonavir improve the outcome in common marmosets when treatment is initiated 6 hours after infection with MERS-CoV[105]. Thus, the testing of lopinavir and ritonavir in clinical trials in patients with MERS should be reconsidered. One patient who received pegylated IFNα, ribavirin, lopinavir and ritonavir in combination had undetectable levels of MERS-CoV in the blood 2 days after the initiation of therapy; however, this patient did not survive[108]. The combination of IFNα, ribavirin, lopinavir and ritonavir was also used for MERS treatment in South Korea, but efficacy data are not yet available. However, three case reports indicate recovery in five out of seven patients who were treated with this combination[109–111].

As 3CLpro and PLpro are essential for cleavage of the viral polyproteins and are distinct from cellular proteases, they are ideal drug targets, in particular PLpro,

Ribavirin
A broadly active antiviral nucleoside analogue with several direct and indirect mechanisms of action; mainly used for the treatment of hepatitis C, in combination with interferon.

Pegylated
Having polyethylene glycol (PEG) attached, to a drug for example; this moiety improves the solubility, decreases the immunogenicity and increases the stability, of the drug of interest, thereby allowing a reduced dosing frequency to be used.

which is involved in both viral replication and IFN antagonism. Indeed, most antiviral drug-like molecules have been developed against 3CLpro and PLpro, which was aided by the rapid report of crystal structures of these proteases[112].

PLpro was initially identified as a drugable target for SARS-CoV; recently, it has been noted that some of the compounds that target PLpro from SARS-CoV are also active against PLpro from MERS-CoV. For example, both 6-mercaptopurine and 6-thioguanine inhibit MERS-CoV and SARS-CoV *in vitro*[113]; however, the efficacy of these molecules has not yet been tested *in vivo*. Mycophenolic acid also inhibits the replication of MERS-CoV *in vitro*[97,99] through the inhibition of PLpro[113], but it had no effect in marmosets[105].

As new coronaviruses are likely to emerge from bats, protease inhibitors were designed against bat coronaviruses with the goal of developing a universal antiviral compound against emerging zoonotic coronaviruses. This approach yielded an inhibitor of Tylonycteris bat coronavirus HKU4 (HKU4-CoV), which is closely related to MERS-CoV[11]. This inhibitor, named SG85, indeed inhibits MERS-CoV replication *in vitro*[112]. Similarly, peptidomimetics that target and inhibit 3CLpro of MERS-CoV, HKU4-CoV and Pipistrellus bat coronavirus HKU5 (HKU5-CoV) have also been identified, but have not yet progressed beyond the *in vitro* stage[114].

Several other drugs that were approved for use in humans were shown to inhibit the replication of MERS-CoV *in vitro*, notably chloroquine, chlorpromazine, loperamide and cyclosporine A[62,99,113,115], although their mechanisms of action are unknown, and the benefit of cyclosporine A in patients is debatable owing to the immunosuppressive effect of the drug. Although cyclophilin inhibitors that do not result in immunosuppression are available, their activity against MERS-CoV has not yet been tested.

Antibody and plasma therapy. Plasma from convalescent patients and/or antibody therapies have been the leading proposed treatment for MERS so far[116]. There are several potential advantages to this approach. For example, as case numbers increase, the pool of survivors becomes larger; provided these individuals have sufficiently high antibody titres and are willing and able to donate plasma, this is a low-tech, reasonably safe treatment option. Furthermore, generation of monoclonal antibodies for use in humans is well established, with a fairly straightforward path to safety and efficacy testing. However, to date, there are very few reports on the use of convalescent plasma and none on the use of monoclonal antibodies as treatments for acute, severe respiratory disease in humans. A post hoc meta-analysis of 32 studies of either SARS or severe influenza found a significant reduction in the pooled odds of mortality when convalescent plasma was used[117]. However, study design was rated as low or very low quality, as there were generally a lack of control groups and a moderate-to-high risk of bias, which suggests that a properly designed clinical trial of convalescent plasma use in severe respiratory infections is needed[117]. Potent monoclonal antibodies that neutralize the MERS-COV spike protein *in vitro* have been developed[118–121]. However, with a few exceptions, *in vivo* data relating to the use of convalescent plasma or monoclonal antibodies in the treatment of MERS are currently lacking. Serum from high-titre dromedary camels decreased MERS-CoV loads in the lungs of mice that had been transduced with human DPP4 (REF. 122). Human polyclonal antibodies against the spike protein were generated by vaccinating transchromosomic bovines, and treatment with these antibodies reduced viral titres in the lungs of DPP4-transduced mice when treatment was administered 24 or 48 hours after challenge with MERS-CoV[123]. DPP4-transduced mice were also treated with humanized neutralizing monoclonal antibody 4C2h, which is directed against the receptor-binding domain of the MERS-CoV spike protein, 1 day after MERS-CoV challenge, and this treatment also decreased viral titres in the lungs[124], as did the neutralizing antibody LCA60, which was obtained from a convalescent patient and produced recombinantly[125]. Human neutralizing monoclonal antibodies REGN3048 and REGN3051 also provided a benefit in mice that expressed human DPP4 and were challenged with MERS-CoV[126]. The human neutralizing monoclonal antibody m332 reduced MERS-CoV replication in the lungs of rabbits following prophylactic, but not therapeutic, treatment[127]. Treatment of rhesus macaques with the human monoclonal antibody 311B-N1 day after challenge resulted in reduced lung pathology[128]. In all of these studies, viral replication was not completely inhibited, and there were some pathological alterations to the lungs, despite the therapy. Furthermore, none of the studies addressed the potential emergence of escape mutants *in vivo*.

Alternatively, antibodies that target the region of DPP4 that binds to the spike protein could be used to prevent entry of MERS-CoV; this approach was successful *in vitro*[129]. However, whether such a treatment would be feasible and would not have substantial adverse effects in humans remains to be determined.

Host-directed therapies. Host-directed strategies can also limit viral replication. For example, the spike protein of SARS-CoV is cleaved by cathepsin B and cathepsin L, transmembrane protease serine 2 (TMPRSS2) and possibly other host proteases[130,131]. Inhibition of host serine proteases by camostat reduced the entry of SARS-CoV and increased survival in a mouse model[132]. However, the targeting of host proteases is more likely to result in undesirable side effects than the targeting of viral proteases.

Another underappreciated strategy is attenuation of detrimental host responses. The development of such treatments would require a thorough understanding of the host responses that are involved in acute lung injury and ARDS, processes that are unfortunately poorly understood at the moment. Nonetheless, *in vitro* studies and limited studies in animal models with other respiratory viruses have shown that anaphylatoxin C5a is important for the development of acute lung injury, and blocking anaphylatoxin C5a can reduce lung pathology[133].

Peptidomimetics
Compounds that mimic biologically active peptides or proteins.

Anaphylatoxin C5a
A complement-activated molecule that is important for the recruitment to and activation of inflammatory cells in the lungs.

Subunit vaccines
Vaccines that contain immunogenic parts of a pathogen rather than the entire pathogen.

DNA vaccines
Vaccines based on the direct introduction of a plasmid encoding an antigen; following *in situ* production of this antigen, an immune response is mounted against it.

Changes in gene expression during *in vitro* MERS-CoV infection were used to predict potential effective drugs. One of the drugs with predicted efficacy, the kinase inhibitor SB203580, modestly inhibited SARS-CoV and MERS-CoV replication following the treatment of cells prior to infection, but treatment after infection inhibited replication of only SARS-CoV and not MERS-CoV[134].

Vaccines. Vaccination could be used to prevent infection or to reduce disease severity, viral shedding and thereby transmission, thus helping to control MERS outbreaks. Several vaccination strategies were developed against SARS-CoV and tested in animals, such as an inactivated virus, a live-attenuated virus, viral vectors, subunit vaccines, recombinant proteins and DNA vaccines[135,136]. Similar approaches have been used for the development of experimental MERS-CoV vaccines[137]. To date, three MERS-CoV vaccines have been evaluated in non-human primates. In one study, rhesus macaques were primed with DNA encoding the spike protein, followed by boosts with spike DNA and with recombinant protein consisting of the spike subunit containing the receptor-binding domain, or primed and boosted once with the subunit protein. Both approaches reduced pathological changes in lung function in animals that were infected with MERS-CoV 19 weeks after the last vaccination[138]. Moreover, three vaccinations with a recombinantly expressed protein that contains the receptor-binding domain of the spike protein reduced viral loads and lung pathology in rhesus macaques that were infected 2 weeks after the last vaccination[139]. Three DNA vaccinations with a construct encoding the full-length spike sequence reduced viral loads and pathology in the lungs after challenge with MERS-CoV 5 weeks after the last vaccination[140].

One concern of vaccination in humans is vaccine-mediated enhancement of disease, a process in which the disease following infection is more severe in vaccinated individuals than in unvaccinated individuals. Although this was observed in only a small subset of vaccine studies that were carried out for SARS-CoV[136] and has not yet been observed in any of the published MERS-CoV vaccine studies, it is an important concern. Moreover, it is unclear who to vaccinate against MERS-CoV, as healthy individuals seem to be at little risk of severe disease. Older patients or patients with underlying disease, who have the highest risk of severe MERS, would be important target populations. However, vaccination in such patients can be problematic owing to their poor immune responses, as has been established for influenza virus[141]. In addition, vaccination of people with a high risk of exposure to MERS-CoV, such as health care workers, slaughterhouse workers and camel herders, is advisable[142].

Outlook

As our understanding of the pathogenesis of emerging coronaviruses increases, so will the opportunities for the rational design of therapeutics that target viral replication or immunopathology. The rational design of new drugs and the repurposing of existing compounds have already resulted in the development of PLpro inhibitors and the identification of kinase inhibitors that inhibit the replication of SARS-CoV and MERS-CoV *in vitro*. However, only a few potential treatments have progressed past the identification of an effect *in vitro*, and *in vivo* studies to select the most promising treatment options are required. The development of several mouse models of MERS is thus an important step forward (BOX 2). Owing to the acute nature of MERS and the important role of immunopathology, combination therapies aimed at simultaneously inhibiting viral replication, limiting viral dissemination and dampening the host response are likely to yield the best results. Furthermore, treatment should be started as early as possible, rather than waiting until the patient has already developed extensive lung damage.

The development of therapies against SARS and MERS needs to focus on testing in humans, in properly controlled clinical trials. The current non-standardized, uncontrolled approach to treatment is not informative and may not be beneficial to the patient. The recent Ebola outbreak has demonstrated that rapid clinical trial design and approval are possible and that exceptional situations call for deviations from normal procedures (BOX 3).

While treatments are being developed and evaluated, the prevention of viral transmission is key to reducing the burden of MERS. The large proportion of nosocomial MERS-CoV infections indicates that preventive measures in hospitals are currently either not fully implemented or insufficient. Prevention of zoonotic transmission from dromedary camels is another possibility to decrease the number of MERS cases. The

Box 2 | **Animal models**

Most of our understanding of the pathogenesis of severe acute respiratory syndrome (SARS) and Middle East respiratory syndrome (MERS) comes from animal studies. Ideally, these models recapitulate all or specific aspects of human disease. Several mouse models have been established, for example by using mouse-adapted SARS coronavirus (SARS-CoV) or expressing human receptors in mice[152]. Although it has been recognized that mice might poorly mimic specific human responses to infection, the availability of knockout and transgenic mice enables the targeted study of virus–host interactions. Several non-human primate models have been developed for SARS-CoV and MERS coronavirus (MERS-CoV)[152]. The close relationship of non-human primates to humans often allows faithful recapitulation of a disease and the host response. However, these benefits are countered by the need for specialized husbandry, the sometimes limited availability of the animals and reagents, and high costs.

The pathogenesis of SARS-CoV and MERS-CoV in their respective reservoir hosts is not nearly as well studied as that in humans. Currently, only one experimental-infection study has been carried out in bats with MERS-CoV[153], and none has been carried out for other coronaviruses. Thus, data are mostly limited to the detection of coronaviruses in naturally infected bats. The detection of coronaviruses mainly in faecal samples from bats and not in oral swabs suggests that replication in bats occurs predominantly in the gastrointestinal tract[9,154,155]. By contrast, a combination of intratracheal and intranasal inoculation of masked palm civets with SARS-CoV resulted in interstitial pneumonia, with oral and rectal viral shedding[156].

The pathogenesis of MERS-CoV in dromedary camels has been studied experimentally in a limited number of animals. These animals developed transient mild disease; however, large quantities of MERS-CoV were shed from the upper respiratory tract, in line with the predominant replication of MERS-CoV in the nasal turbinates and larynx in these animals, which explains the frequent zoonotic transmission[157].

Box 3 | **Preparing for emerging viruses: lessons from SARS-CoV, MERS-CoV and Ebola virus**

When the severe acute respiratory syndrome (SARS) outbreak developed into the first pandemic of the twenty-first century, it became clear that the medical and scientific communities were not adequately prepared for the emergence of highly pathogenic viruses. Whereas several months elapsed and several thousand cases of SARS were observed before the causative agent was identified as SARS coronavirus (SARS-CoV)[4–6], subsequent advances in molecular diagnostic tools, such as next generation sequencing, meant that Middle East respiratory syndrome coronavirus (MERS-CoV) was identified before it caused a large outbreak of MERS[11]. The availability of the full-length genome of MERS-CoV enabled the rapid development and distribution of diagnostic assays. The first animal models of disease, several treatment efficacy studies and the identification of the reservoir followed soon after. Unfortunately, the SARS pandemic did not yield solid clinical data on the efficacy of treatment regimens. These data are urgently needed for the treatment of MERS, as well as to prepare for novel coronaviruses that may emerge. Several studies have used synthetic biology to study the zoonotic transmission potential of SARS-CoV-like viruses from bats[9,10,158,159].

The Ebola virus outbreak in West Africa has highlighted the need for fast-tracking of potential treatments, as several clinical trials were started only towards the end of the outbreak. The combined experiences of the outbreaks of SARS, MERS and Ebola provide a blueprint for the response to emerging pathogens: after the identification of the causative agent, diagnostic assays need to be developed and distributed rapidly, and simultaneously, awareness of the new syndrome and reporting of (suspected) cases must be increased. In addition, infection control measures in health care facilities are essential. Research needs to focus on understanding the epidemiology, including pathogen transmission and identification of the reservoir and/or intermediate hosts. Animal models need to be developed, as well as therapeutic and prophylactic measures. Finally, promising treatments need to be fast-tracked into clinical trials.

first vaccines against MERS-CoV have been tested in dromedary camels[140,143]; indeed, when camels were vaccinated with a modified vaccinia virus that expresses the MERS-CoV spike protein, subsequent challenge of these animals with MERS-CoV resulted in less viral shedding than in unvaccinated animals[143], thereby potentially limiting the transmission to naive animals or to humans. Certainly, there has been progress in the development of vaccines and therapies against emerging coronaviruses, but more research and rigorous testing is required if we are to successfully combat these novel pathogens.

1. Zhong, N. S. *et al.* Epidemiology and cause of severe acute respiratory syndrome (SARS) in Guangdong, People's Republic of China, in February, 2003. *Lancet* **362**, 1353–1358 (2003).
2. Lee, N. *et al.* A major outbreak of severe acute respiratory syndrome in Hong Kong. *N. Engl. J. Med.* **348**, 1986–1994 (2003).
3. Guan, Y. *et al.* Molecular epidemiology of the novel coronavirus that causes severe acute respiratory syndrome. *Lancet* **363**, 99–104 (2004).
4. Drosten, C. *et al.* Identification of a novel coronavirus in patients with severe acute respiratory syndrome. *N. Engl. J. Med.* **348**, 1967–1976 (2003).
5. Ksiazek, T. G. *et al.* A novel coronavirus associated with severe acute respiratory syndrome. *N. Engl. J. Med.* **348**, 1953–1966 (2003).
6. Peiris, J. S. *et al.* Coronavirus as a possible cause of severe acute respiratory syndrome. *Lancet* **361**, 1319–1325 (2003).
7. WHO. Summary of probably SARS cases with onset of illness from 1 November 2002 to 31 July 2003. *WHO*, http://www.who.int/csr/sars/country/table2004_04_21/en/ (2004).
8. Wang, M. *et al.* SARS-CoV infection in a restaurant from palm civet. *Emerg. Infect. Dis.* **11**, 1860–1865 (2005).
9. Ge, X. Y. *et al.* Isolation and characterization of a bat SARS-like coronavirus that uses the ACE2 receptor. *Nature* **503**, 535–538 (2013).
The isolation of a bat SARS-CoV-like virus that uses the human ACE2 as a receptor without prior adaptation, which suggests the potential for emergence without prior adaptation.
10. Menachery, V. D. *et al.* A SARS-like cluster of circulating bat coronaviruses shows potential for human emergence. *Nat. Med.* **21**, 1508–1513 (2015).
An assessment of the zoonotic potential of SARS-CoV-like viruses circulating in bats.
11. Zaki, A. M., van Boheemen, S., Bestebroer, T. M., Osterhaus, A. D. & Fouchier, R. A. Isolation of a novel coronavirus from a man with pneumonia in Saudi Arabia. *N. Engl. J. Med.* **367**, 1814–1820 (2012).
The first identification of MERS-CoV as the cause of severe lower respiratory disease in humans.
12. Hijawi, B. *et al.* Novel coronavirus infections in Jordan, April 2012: epidemiological findings from a retrospective investigation. *East. Mediterr. Health J.* **19** (Suppl. 1), S12–S18 (2013).
13. Wise, J. Patient with new strain of coronavirus is treated in intensive care at London hospital. *BMJ* **345**, e6455 (2012).
14. Korea Centers for Disease Control and Prevention. Middle East respiratory syndrome coronavirus outbreak in the Republic of Korea, 2015. *Osong Public Health Res. Perspect.* **6**, 269–278 (2015).
15. WHO. Coronavirus infections: disease outbreak news. *WHO*, http://www.who.int/csr/don/26-april-2016-mers-saudi-arabia/en/ (2016).
16. Pasternak, A. O., Spaan, W. J. & Snijder, E. J. Nidovirus transcription: how to make sense…? *J. Gen. Virol.* **87**, 1403–1421 (2006).
17. Perlman, S. & Netland, J. Coronaviruses post-SARS: update on replication and pathogenesis. *Nat. Rev. Microbiol.* **7**, 439–450 (2009).
18. Fehr, A. R. & Perlman, S. Coronaviruses: an overview of their replication and pathogenesis. *Methods Mol. Biol.* **1282**, 1–23 (2015).
19. Knoops, K. *et al.* SARS-coronavirus replication is supported by a reticulovesicular network of modified endoplasmic reticulum. *PLoS Biol.* **6**, e226 (2008).
20. Snijder, E. J. *et al.* Unique and conserved features of genome and proteome of SARS-coronavirus, an early split-off from the coronavirus group 2 lineage. *J. Mol. Biol.* **331**, 991–1004 (2003).
21. Eckerle, L. D. *et al.* Infidelity of SARS-CoV nsp14-exonuclease mutant virus replication is revealed by complete genome sequencing. *PLoS Pathog.* **6**, e1000896 (2010).
The finding that nsp14 has a crucial role in the proofreading ability of SARS-CoV.
22. Sevajol, M., Subissi, L., Decroly, E., Canard, B. & Imbert, I. Insights into RNA synthesis, capping, and proofreading mechanisms of SARS-coronavirus. *Virus Res.* **194**, 90–99 (2014).
23. Raj, V. S. *et al.* Dipeptidyl peptidase 4 is a functional receptor for the emerging human coronavirus-EMC. *Nature* **495**, 251–254 (2013).
The demonstration that DPP4 is the receptor for MERS-CoV.
24. Masters, P. S. & Perlman, S. in *Fields Virology* (eds Knipe, D. M. & Howley, P. M.) 825–858 (Wolters Kluwer, 2013).
25. Guan, Y. *et al.* Isolation and characterization of viruses related to the SARS coronavirus from animals in southern China. *Science* **302**, 276–278 (2003).
26. Wang, L. F. *et al.* Review of bats and SARS. *Emerg. Infect. Dis.* **12**, 1834–1840 (2006).
27. Drexler, J. F., Corman, V. M. & Drosten, C. Ecology, evolution and classification of bat coronaviruses in the aftermath of SARS. *Antiviral Res.* **101**, 45–56 (2014).
28. Reusken, C. B. *et al.* Middle East respiratory syndrome coronavirus neutralizing serum antibodies in dromedary camels: a comparative serological study. *Lancet Infect. Dis.* **13**, 859–866 (2013).
The first of several papers to provide serological evidence for the circulation of MERS-CoV among dromedary camels; this finding eventually led to the identification of dromedary camels as the main reservoir for MERS-CoV.
29. Haagmans, B. L. *et al.* Middle East respiratory syndrome coronavirus in dromedary camels: an outbreak investigation. *Lancet Infect. Dis.* **14**, 140–145 (2014).
30. Azhar, E. I. *et al.* Evidence for camel-to-human transmission of MERS coronavirus. *N. Engl. J. Med.* **370**, 2499–2505 (2014).
31. Hemida, M. G. *et al.* MERS coronavirus in dromedary camel herd, Saudi Arabia. *Emerg. Infect. Dis.* **20**, 1231–1234 (2014).
32. Raj, V. S. *et al.* Isolation of MERS coronavirus from a dromedary camel, Qatar, 2014. *Emerg. Infect. Dis.* **20**, 1339–1342 (2014).
33. Muller, M. A. *et al.* MERS coronavirus neutralizing antibodies in camels, Eastern Africa, 1983–1997. *Emerg. Infect. Dis.* **20**, 2093–2095 (2014).
34. Sabir, J. S. *et al.* Co-circulation of three camel coronavirus species and recombination of MERS-CoVs in Saudi Arabia. *Science* **351**, 81–84 (2016).
35. Chowell, G. *et al.* Transmission characteristics of MERS and SARS in the healthcare setting: a comparative study. *BMC Med.* **13**, 210 (2015).
An analysis of the predominant role for nosocomial transmission in the epidemiology of both SARS and MERS.
36. Hunter, J. C. *et al.* Transmission of Middle East respiratory syndrome coronavirus infections in healthcare settings, Abu Dhabi. *Emerg. Infect. Dis.* **22**, 647–656 (2016).
37. Anderson, R. M. *et al.* Epidemiology, transmission dynamics and control of SARS: the 2002–2003 epidemic. *Philos. Trans. R. Soc. Lond. B. Biol. Sci.* **359**, 1091–1105 (2004).

38. Cowling, B. J. *et al.* Preliminary epidemiological assessment of MERS-CoV outbreak in South Korea, May to June 2015. *Euro Surveill.* **20**, 7–13 (2015).
39. Peiris, J. S. *et al.* Clinical progression and viral load in a community outbreak of coronavirus-associated SARS pneumonia: a prospective study. *Lancet* **361**, 1767–1772 (2003).
A description of the clinical representation of SARS-CoV respiratory disease in patients from Hong Kong.
40. Bin, S. Y. *et al.* Environmental contamination and viral shedding in MERS patients during MERS-CoV outbreak in South Korea. *Clin. Infect. Dis.* **62**, 755–760 (2015).
Evidence that infectious MERS-CoV can be detected on common hospital surfaces during an outbreak, which highlights the potential for nosocomial transmission and stresses the need for infection control.
41. Kucharski, A. J. & Althaus, C. L. The role of superspreading in Middle East respiratory syndrome coronavirus (MERS-CoV) transmission. *Euro Surveill.* **20**, 14–18 (2015).
42. Oh, M. D. *et al.* Middle East respiratory syndrome coronavirus superspreading event involving 81 persons, Korea 2015. *J. Korean Med. Sci.* **30**, 1701–1705 (2015).
43. Wong, G. *et al.* MERS, SARS, and Ebola: the role of super-spreaders in infectious disease. *Cell Host Microbe* **18**, 398–401 (2015).
44. Ng, D. L. *et al.* Clinicopathologic, immunohistochemical, and ultrastructural findings of a fatal case of Middle East respiratory syndrome coronavirus infection in the United Arab Emirates, April 2014. *Am. J. Pathol.* **186**, 652–658 (2016).
45. Kuba, K. *et al.* A crucial role of angiotensin converting enzyme 2 (ACE2) in SARS coronavirus-induced lung injury. *Nat. Med.* **11**, 875–879 (2005).
46. Imai, Y. *et al.* Angiotensin-converting enzyme 2 protects from severe acute lung failure. *Nature* **436**, 112–116 (2005).
47. Wang, W. K. *et al.* Temporal relationship of viral load, ribavirin, interleukin (IL)-6, IL-8, and clinical progression in patients with severe acute respiratory syndrome. *Clin. Infect. Dis.* **39**, 1071–1075 (2004).
48. Drosten, C. *et al.* Clinical features and virological analysis of a case of Middle East respiratory syndrome coronavirus infection. *Lancet Infect. Dis.* **13**, 745–751 (2013).
49. Poissy, J. *et al.* Kinetics and pattern of viral excretion in biological specimens of two MERS-CoV cases. *J. Clin. Virol.* **61**, 275–278 (2014).
50. Binnie, A., Tsang, J. L. & dos Santos, C. C. Biomarkers in acute respiratory distress syndrome. *Curr. Opin. Crit. Care* **20**, 47–55 (2014).
51. Williams, A. E. & Chambers, R. C. The mercurial nature of neutrophils: still an enigma in ARDS? *Am. J. Physiol. Lung Cell. Mol. Physiol.* **306**, L217–L230 (2014).
52. Baas, T., Taubenberger, J. K., Chong, P. Y., Chui, P. & Katze, M. G. SARS-CoV virus–host interactions and comparative etiologies of acute respiratory distress syndrome as determined by transcriptional and cytokine profiling of formalin-fixed paraffin-embedded tissues. *J. Interferon Cytokine Res.* **26**, 309–317 (2006).
53. Faure, E. *et al.* Distinct immune response in two MERS-CoV-infected patients: can we go from bench to bedside? *PLoS ONE* **9**, e88716 (2014).
54. Kong, S. L., Chui, P., Lim, B. & Salto-Tellez, M. Elucidating the molecular physiopathology of acute respiratory distress syndrome in severe acute respiratory syndrome patients. *Virus Res.* **145**, 260–269 (2009).
55. Tang, N. L. *et al.* Early enhanced expression of interferon-inducible protein-10 (CXCL-10) and other chemokines predicts adverse outcome in severe acute respiratory syndrome. *Clin. Chem.* **51**, 2333–2340 (2005).
56. Cameron, M. J. *et al.* Interferon-mediated immunopathological events are associated with atypical innate and adaptive immune responses in patients with severe acute respiratory syndrome. *J. Virol.* **81**, 8692–8706 (2007).
57. Gralinski, L. E. *et al.* Genome wide identification of SARS-CoV susceptibility loci using the Collaborative Cross. *PLoS Genet.* **11**, e1005504 (2015).
58. Jensen, S. & Thomsen, A. R. Sensing of RNA viruses: a review of innate immune receptors involved in recognizing RNA virus invasion. *J. Virol.* **86**, 2900–2910 (2012).
59. Frieman, M. B. *et al.* SARS-CoV pathogenesis is regulated by a STAT1 dependent but a type I, II and III interferon receptor independent mechanism. *PLoS Pathog.* **6**, e1000849 (2010).
60. Sheahan, T. *et al.* MyD88 is required for protection from lethal infection with a mouse-adapted SARS-CoV. *PLoS Pathog.* **4**, e1000240 (2008).
61. Zhao, J. *et al.* Rapid generation of a mouse model for Middle East respiratory syndrome. *Proc. Natl Acad. Sci. USA* **111**, 4970–4975 (2014).
A study in which the DPP4-based host restriction is overcome in mice by expression of the human variant of DPP4, leading to the development of several transgenic mouse models.
62. de Wilde, A. H. *et al.* MERS-coronavirus replication induces severe *in vitro* cytopathology and is strongly inhibited by cyclosporin A or interferon-α treatment. *J. Gen. Virol.* **94**, 1749–1760 (2013).
63. Snijder, E. J. *et al.* Ultrastructure and origin of membrane vesicles associated with the severe acute respiratory syndrome coronavirus replication complex. *J. Virol.* **80**, 5927–5940 (2006).
64. Bouvet, M. *et al. In vitro* reconstitution of SARS-coronavirus mRNA cap methylation. *PLoS Pathog.* **6**, e1000863 (2010).
65. Menachery, V. D. *et al.* Attenuation and restoration of severe acute respiratory syndrome coronavirus mutant lacking 2′-O-methyltransferase activity. *J. Virol.* **88**, 4251–4264 (2014).
66. Menachery, V. D., Debbink, K. & Baric, R. S. Coronavirus non-structural protein 16: evasion, attenuation, and possible treatments. *Virus Res.* **194**, 191–199 (2014).
67. Cui, L. *et al.* The nucleocapsid protein of coronaviruses acts as a viral suppressor of RNA silencing in mammalian cells. *J. Virol.* **89**, 9029–9043 (2015).
68. Lu, X., Pan, J., Tao, J. & Guo, D. SARS-CoV nucleocapsid protein antagonizes IFN-β response by targeting initial step of IFN-β induction pathway, and its C-terminal region is critical for the antagonism. *Virus Genes* **42**, 37–45 (2011).
69. Niemeyer, D. *et al.* Middle East respiratory syndrome coronavirus accessory protein 4a is a type I interferon antagonist. *J. Virol.* **87**, 12489–12495 (2013).
70. Siu, K. L. *et al.* Middle east respiratory syndrome coronavirus 4a protein is a double-stranded RNA-binding protein that suppresses PACT-induced activation of RIG-I and MDA5 in the innate antiviral response. *J. Virol.* **88**, 4866–4876 (2014).
71. Yang, Y. *et al.* The structural and accessory proteins M, ORF 4a, ORF 4b, and ORF 5 of Middle East respiratory syndrome coronavirus (MERS-CoV) are potent interferon antagonists. *Protein Cell* **4**, 951–961 (2013).
72. Yang, Y. *et al.* Middle East respiratory syndrome coronavirus ORF4b protein inhibits type I interferon production through both cytoplasmic and nuclear targets. *Sci. Rep.* **5**, 17554 (2015).
73. Frieman, M., Ratia, K., Johnston, R. E., Mesecar, A. D. & Baric, R. S. Severe acute respiratory syndrome coronavirus papain-like protease ubiquitin-like domain and catalytic domain regulate antagonism of IRF3 and NF-κB signaling. *J. Virol.* **83**, 6689–6705 (2009).
74. Devaraj, S. G. *et al.* Regulation of IRF-3-dependent innate immunity by the papain-like protease domain of the severe acute respiratory syndrome coronavirus. *J. Biol. Chem.* **282**, 32208–32221 (2007).
75. Matthews, K., Schafer, A., Pham, A. & Frieman, M. The SARS coronavirus papain like protease can inhibit IRF3 at a post activation step that requires deubiquitination activity. *Virol. J.* **11**, 209 (2014).
76. Bailey-Elkin, B. A. *et al.* Crystal structure of the Middle East respiratory syndrome coronavirus (MERS-CoV) papain-like protease bound to ubiquitin facilitates targeted disruption of deubiquitinating activity to demonstrate its role in innate immune suppression. *J. Biol. Chem.* **289**, 34667–34682 (2014).
77. Huang, C. *et al.* SARS coronavirus nsp1 protein induces template-dependent endonucleolytic cleavage of mRNAs: viral mRNAs are resistant to nsp1-induced RNA cleavage. *PLoS Pathog.* **7**, e1002433 (2011).
78. Kamitani, W., Huang, C., Narayanan, K., Lokugamage, K. G. & Makino, S. A two-pronged strategy to suppress host protein synthesis by SARS coronavirus nsp1 protein. *Nat. Struct. Mol. Biol.* **16**, 1134–1140 (2009).
79. Tanaka, T., Kamitani, W., DeDiego, M. L., Enjuanes, L. & Matsuura, Y. Severe acute respiratory syndrome coronavirus nsp1 facilitates efficient propagation in cells through a specific translational shutoff of host mRNA. *J. Virol.* **86**, 11128–11137 (2012).
80. Wathelet, M. G., Orr, M., Frieman, M. B. & Baric, R. S. Severe acute respiratory syndrome coronavirus evades antiviral signaling: role of nsp1 and rational design of an attenuated strain. *J. Virol.* **81**, 11620–11633 (2007).
81. Lokugamage, K. G. *et al.* Middle East respiratory syndrome coronavirus nsp1 inhibits host gene expression by selectively targeting mRNAs transcribed in the nucleus while sparing mRNAs of cytoplasmic origin. *J. Virol.* **89**, 10970–10981 (2015).
82. Freundt, E. C., Yu, L., Park, E., Lenardo, M. J. & Xu, X. N. Molecular determinants for subcellular localization of the severe acute respiratory syndrome coronavirus open reading frame 3b protein. *J. Virol.* **83**, 6631–6640 (2009).
83. Kopecky-Bromberg, S. A., Martinez-Sobrido, L., Frieman, M., Baric, R. A. & Palese, P. Severe acute respiratory syndrome coronavirus open reading frame (ORF) 3b, ORF 6, and nucleocapsid proteins function as interferon antagonists. *J. Virol.* **81**, 548–557 (2007).
84. Lei, Y. *et al.* MAVS-mediated apoptosis and its inhibition by viral proteins. *PLoS ONE* **4**, e5466 (2009).
85. Menachery, V. D. *et al.* Pathogenic influenza viruses and coronaviruses utilize similar and contrasting approaches to control interferon-stimulated gene responses. *mBio* **5**, e01174-14 (2014).
86. Graci, J. D. & Cameron, C. E. Mechanisms of action of ribavirin against distinct viruses. *Rev. Med. Virol.* **16**, 37–48 (2006).
87. Al-Tawfiq, J. A., Momattin, H., Dib, J. & Memish, Z. A. Ribavirin and interferon therapy in patients infected with the Middle East respiratory syndrome coronavirus: an observational study. *Int. J. Infect. Dis.* **20**, 42–46 (2014).
88. Ling, Y., Qu, R. & Luo, Y. Clinical analysis of the first patient with imported Middle East respiratory syndrome in China. *Zhonghua Wei Zhong Bing Ji Jiu Yi Xue* **27**, 630–634 (in Chinese) (2015).
89. Booth, C. M. *et al.* Clinical features and short-term outcomes of 144 patients with SARS in the greater Toronto area. *JAMA* **289**, 2801–2809 (2003).
90. Poutanen, S. M. *et al.* Identification of severe acute respiratory syndrome in Canada. *N. Engl. J. Med.* **348**, 1995–2005 (2003).
91. So, L. K. *et al.* Development of a standard treatment protocol for severe acute respiratory syndrome. *Lancet* **361**, 1615–1617 (2003).
92. Tsang, K. W. *et al.* A cluster of cases of severe acute respiratory syndrome in Hong Kong. *N. Engl. J. Med.* **348**, 1977–1985 (2003).
93. Loutfy, M. R. *et al.* Interferon alfacon-1 plus corticosteroids in severe acute respiratory syndrome: a preliminary study. *JAMA* **290**, 3222–3228 (2003).
94. Zhao, Z. *et al.* Description and clinical treatment of an early outbreak of severe acute respiratory syndrome (SARS) in Guangzhou, PR China. *J. Med. Microbiol.* **52**, 715–720 (2003).
95. Hsu, L. Y. *et al.* Severe acute respiratory syndrome (SARS) in Singapore: clinical features of index patient and initial contacts. *Emerg. Infect. Dis.* **9**, 713–717 (2003).
96. Smith, E. C., Blanc, H., Surdel, M. C., Vignuzzi, M. & Denison, M. R. Coronaviruses lacking exoribonuclease activity are susceptible to lethal mutagenesis: evidence for proofreading and potential therapeutics. *PLoS Pathog.* **9**, e1003565 (2013).
97. Chan, J. F. *et al.* Broad-spectrum antivirals for the emerging Middle East respiratory syndrome coronavirus. *J. Infect.* **67**, 606–616 (2013).
98. Falzarano, D. *et al.* Inhibition of novel β coronavirus replication by a combination of interferon-α2b and ribavirin. *Sci. Rep.* **3**, 1686 (2013).
99. Hart, B. J. *et al.* Interferon-β and mycophenolic acid are potent inhibitors of Middle East respiratory syndrome coronavirus in cell-based assays. *J. Gen. Virol.* **95**, 571–577 (2014).
100. Morgenstern, B., Michaelis, M., Baer, P. C., Doerr, H. W. & Cinatl, J. Ribavirin and interferon-β synergistically inhibit SARS-associated coronavirus replication in animal and human cell lines. *Biochem. Biophys. Res. Commun.* **326**, 905–908 (2005).
101. Falzarano, D. *et al.* Treatment with interferon-α2b and ribavirin improves outcome in MERS-CoV-infected rhesus macaques. *Nat. Med.* **19**, 1313–1317 (2013).
The first application of a potential treatment option for MERS through the repurposing of IFNα2b and ribavirin in a non-human primate model.
102. Omrani, A. S. *et al.* Ribavirin and interferon alfa-2a for severe Middle East respiratory syndrome coronavirus infection: a retrospective cohort study. *Lancet Infect. Dis.* **14**, 1090–1095 (2014).

103. Shalhoub, S. *et al.* IFN-α2a or IFN-β1a in combination with ribavirin to treat Middle East respiratory syndrome coronavirus pneumonia: a retrospective study. *J. Antimicrob. Chemother.* **70**, 2129–2132 (2015).
104. Khalid, M. *et al.* Ribavirin and interferon-α2b as primary and preventive treatment for Middle East respiratory syndrome coronavirus: a preliminary report of two cases. *Antivir. Ther.* **20**, 87–91 (2015).
105. Chan, J. F. *et al.* Treatment with lopinavir/ritonavir or interferon-β1b improves outcome of MERS-CoV infection in a non-human primate model of common marmoset. *J. Infect. Dis.* **212**, 1904–1913 (2015).
106. Chan, K. S. *et al.* Treatment of severe acute respiratory syndrome with lopinavir/ritonavir: a multicentre retrospective matched cohort study. *Hong Kong Med. J.* **9**, 399–406 (2003).
107. Chu, C. M. *et al.* Role of lopinavir/ritonavir in the treatment of SARS: initial virological and clinical findings. *Thorax* **59**, 252–256 (2004).
108. Spanakis, N. *et al.* Virological and serological analysis of a recent Middle East respiratory syndrome coronavirus infection case on a triple combination antiviral regimen. *Int. J. Antimicrob. Agents* **44**, 528–532 (2014).
109. Choi, W. J., Lee, K. N., Kang, E. J. & Lee, H. Middle East respiratory syndrome-coronavirus infection: a case report of serial computed tomographic findings in a young male patient. *Korean J. Radiol* **17**, 166–170 (2016).
110. Kim, U. J., Won, E. J., Kee, S. J., Jung, S. I. & Jang, H. C. Combination therapy with lopinavir/ritonavir, ribavirin and interferon-α for Middle East respiratory syndrome: a case report. *Antivir. Ther.* http://dx.doi.org/10.3851/IMP3002 (2015).
111. Rhee, J. Y., Hong, G. & Ryu, K. M. Clinical implications of five cases of Middle East respiratory syndrome coronavirus infection in South Korea Outbreak. *Jpn J. Infect. Dis.* http://dx.doi.org/10.7883/yoken.JJID.2015.445 (2016).
112. Hilgenfeld, R. From SARS to MERS: crystallographic studies on coronaviral proteases enable antiviral drug design. *FEBS J.* **281**, 4085–4096 (2014).
113. Cheng, K. W. *et al.* Thiopurine analogs and mycophenolic acid synergistically inhibit the papain-like protease of Middle East respiratory syndrome coronavirus. *Antiviral Res.* **115**, 9–16 (2015).
114. Tomar, S. *et al.* Ligand-induced dimerization of Middle East respiratory syndrome (MERS) coronavirus nsp5 protease ($3CL^{pro}$): implications for nsp5 regulation and the development of antivirals. *J. Biol. Chem.* **290**, 19403–19422 (2015).
115. de Wilde, A. H. *et al.* Screening of an FDA-approved compound library identifies four small-molecule inhibitors of Middle East respiratory syndrome coronavirus replication in cell culture. *Antimicrob. Agents Chemother.* **58**, 4875–4884 (2014).
116. International Severe Acute Respiratory & Emerging Infection Consortium. Treatment of MERS-CoV: decision support tool. *International Severe Acute Respiratory & Emerging Infection Consortium*, https://isaric.tghn.org/site_media/media/articles/Decision_Support_Document_v1_1_20130729.pdf (updated 29 July 2013).
117. Mair-Jenkins, J. *et al.* The effectiveness of convalescent plasma and hyperimmune immunoglobulin for the treatment of severe acute respiratory infections of viral etiology: a systematic review and exploratory meta-analysis. *J. Infect. Dis.* **211**, 80–90 (2015).
118. Du, L. *et al.* A conformation-dependent neutralizing monoclonal antibody specifically targeting receptor-binding domain in Middle East respiratory syndrome coronavirus spike protein. *J. Virol.* **88**, 7045–7053 (2014).
119. Jiang, L. *et al.* Potent neutralization of MERS-CoV by human neutralizing monoclonal antibodies to the viral spike glycoprotein. *Sci. Transl Med.* **6**, 234ra59 (2014).
120. Tang, X. C. *et al.* Identification of human neutralizing antibodies against MERS-CoV and their role in virus adaptive evolution. *Proc. Natl Acad. Sci. USA* **111**, E2018–E2026 (2014).
121. Ying, T. *et al.* Exceptionally potent neutralization of Middle East respiratory syndrome coronavirus by human monoclonal antibodies. *J. Virol.* **88**, 7796–7805 (2014).
122. Zhao, J. *et al.* Passive immunotherapy with dromedary immune serum in an experimental animal model for Middle East respiratory syndrome coronavirus infection. *J. Virol.* **89**, 6117–6120 (2015).
123. Luke, T. *et al.* Human polyclonal immunoglobulin G from transchromosomic bovines inhibits MERS-CoV *in vivo*. *Sci. Transl Med.* **8**, 326ra21 (2016).
124. Li, Y. *et al.* A humanized neutralizing antibody against MERS-CoV targeting the receptor-binding domain of the spike protein. *Cell Res.* **25**, 1237–1249 (2015).
125. Corti, D. *et al.* Prophylactic and postexposure efficacy of a potent human monoclonal antibody against MERS coronavirus. *Proc. Natl Acad. Sci. USA* **112**, 10473–10478 (2015).
126. Pascal, K. E. *et al.* Pre- and postexposure efficacy of fully human antibodies against Spike protein in a novel humanized mouse model of MERS-CoV infection. *Proc. Natl Acad. Sci. USA* **112**, 8738–8743 (2015).
The first description of the prophylactic and therapeutic efficacy of monoclonal antibodies in a mouse model.
127. Houser, K. V. *et al.* Prophylaxis with a MERS-CoV-specific human monoclonal antibody protects rabbits from MERS-CoV infection. *J. Infect. Dis.* **213**, 1557–1561 (2016).
128. Johnson, R. F. *et al.* 3B11-N, a monoclonal antibody against MERS-CoV, reduces lung pathology in rhesus monkeys following intratracheal inoculation of MERS-CoV Jordan-n3/2012. *Virology* **490**, 49–58 (2016).
129. Ohnuma, K. *et al.* Inhibition of Middle East respiratory syndrome coronavirus infection by anti-CD26 monoclonal antibody. *J. Virol.* **87**, 13892–13899 (2013).
130. Elshabrawy, H. A. *et al.* Identification of a broad-spectrum antiviral small molecule against severe acute respiratory syndrome coronavirus and Ebola, Hendra, and Nipah viruses by using a novel high-throughput screening assay. *J. Virol.* **88**, 4353–4365 (2014).
131. Glowacka, I. *et al.* Evidence that TMPRSS2 activates the severe acute respiratory syndrome coronavirus spike protein for membrane fusion and reduces viral control by the humoral immune response. *J. Virol.* **85**, 4122–4134 (2011).
132. Zhou, Y. *et al.* Protease inhibitors targeting coronavirus and filovirus entry. *Antiviral Res.* **116**, 76–84 (2015).
133. Wang, R., Xiao, H., Guo, R., Li, Y. & Shen, B. The role of C5a in acute lung injury induced by highly pathogenic viral infections. *Emerg. Microbes Infect.* **4**, e28 (2015).
134. Josset, L. *et al.* Cell host response to infection with novel human coronavirus EMC predicts potential antivirals and important differences with SARS coronavirus. *mBio* **4**, e00165-13 (2013).
135. Graham, R. L., Donaldson, E. F. & Baric, R. S. A decade after SARS: strategies for controlling emerging coronaviruses. *Nat. Rev. Microbiol.* **11**, 836–848 (2013).
136. Roper, R. L. & Rehm, K. E. SARS vaccines: where are we? *Expert Rev. Vaccines* **8**, 887–898 (2009).
137. Du, L. & Jiang, S. Middle East respiratory syndrome: current status and future prospects for vaccine development. *Expert Opin. Biol. Ther.* **15**, 1647–1651 (2015).
138. Wang, L. *et al.* Evaluation of candidate vaccine approaches for MERS-CoV. *Nat. Commun.* **6**, 7712 (2015).
139. Lan, J. *et al.* Recombinant receptor binding domain protein induces partial protective immunity in rhesus macaques against Middle East respiratory syndrome coronavirus challenge. *EBioMedicine* **2**, 1438–1446 (2015).
140. Muthumani, K. *et al.* A synthetic consensus anti-spike protein DNA vaccine induces protective immunity against Middle East respiratory syndrome coronavirus in nonhuman primates. *Sci. Transl Med.* **7**, 301ra132 (2015).
141. Mastalerz-Migas, A., Bujnowska-Fedak, M. & Brydak, L. B. Immune efficacy of first and repeat trivalent influenza vaccine in healthy subjects and hemodialysis patients. *Adv. Exp. Med. Biol.* **836**, 47–54 (2015).
142. Muller, M. A. *et al.* Presence of Middle East respiratory syndrome coronavirus antibodies in Saudi Arabia: a nationwide, cross-sectional, serological study. *Lancet Infect. Dis.* **15**, 629 (2015).
143. Haagmans, B. L. *et al.* An orthopoxvirus-based vaccine reduces virus excretion after MERS-CoV infection in dromedary camels. *Science* **351**, 77–81 (2016).
The finding that vaccination of dromedary camels reduces MERS-CoV shedding on infection, which provides a proof-of-principle for the vaccination of dromedary camels to block zoonotic transmission.
144. Assiri, A. *et al.* Epidemiological, demographic, and clinical characteristics of 47 cases of Middle East respiratory syndrome coronavirus disease from Saudi Arabia: a descriptive study. *Lancet Infect. Dis.* **13**, 752–761 (2013).
A report of the clinical presentation of MERS in patients in Saudi Arabia.
145. Leung, G. M. *et al.* The epidemiology of severe acute respiratory syndrome in the 2003 Hong Kong epidemic: an analysis of all 1755 patients. *Ann. Intern. Med.* **141**, 662–673 (2004).
146. Zumla, A., Hui, D. S. & Perlman, S. Middle East respiratory syndrome. *Lancet* **386**, 995–1007 (2015).
147. Al-Abdallat, M. M. *et al.* Hospital-associated outbreak of Middle East respiratory syndrome coronavirus: a serologic, epidemiologic, and clinical description. *Clin. Infect. Dis.* **59**, 1225–1233 (2014).
148. Saad, M. *et al.* Clinical aspects and outcomes of 70 patients with Middle East respiratory syndrome coronavirus infection: a single-center experience in Saudi Arabia. *Int. J. Infect. Dis.* **29**, 301–306 (2014).
149. Memish, Z. A. *et al.* Respiratory tract samples, viral load, and genome fraction yield in patients with Middle East respiratory syndrome. *J. Infect. Dis.* **210**, 1590–1594 (2014).
150. Feikin, D. R. *et al.* Association of higher MERS-CoV virus load with severe disease and death, Saudi Arabia, 2014. *Emerg. Infect. Dis.* **21**, 2029–2035 (2015).
151. Majumder, M. S., Kluberg, S. A., Mekaru, S. R. & Brownstein, J. S. Mortality risk factors for Middle East respiratory syndrome outbreak, South Korea, 2015. *Emerg. Infect. Dis.* **21**, 2088–2090 (2015).
152. Gretebeck, L. M. & Subbarao, K. Animal models for SARS and MERS coronaviruses. *Curr. Opin. Virol.* **13**, 123–129 (2015).
153. Munster, V. J. *et al.* Replication and shedding of MERS-CoV in Jamaican fruit bats (*Artibeus jamaicensis*). *Sci. Rep.* **6**, 21878 (2016).
154. Lau, S. K. *et al.* Severe acute respiratory syndrome coronavirus-like virus in Chinese horseshoe bats. *Proc. Natl Acad. Sci. USA* **102**, 14040–14045 (2005).
155. Li, W. *et al.* Bats are natural reservoirs of SARS-like coronaviruses. *Science* **310**, 676–679 (2005).
156. Wu, D. *et al.* Civets are equally susceptible to experimental infection by two different severe acute respiratory syndrome coronavirus isolates. *J. Virol.* **79**, 2620–2625 (2005).
157. Adney, D. R. *et al.* Replication and shedding of MERS-CoV in upper respiratory tract of inoculated dromedary camels. *Emerg. Infect. Dis.* **20**, 1999–2005 (2014).
The first description of MERS-CoV replication and shedding in the respiratory tract of dromedary camels, which suggests that MERS-CoV infects the upper respiratory tract in dromedary camels.
158. Becker, M. M. *et al.* Synthetic recombinant bat SARS-like coronavirus is infectious in cultured cells and in mice. *Proc. Natl Acad. Sci. USA* **105**, 19944–19949 (2008).
159. Menachery, V. D. *et al.* SARS-like WIV1-CoV poised for human emergence. *Proc. Natl Acad. Sci. USA* **113**, 3048–3053 (2016).

Acknowledgements
The work was supported by the Intramural Research Program of the National Institute of Allergy and Infectious Diseases (NIAID), US National Institutes of Health.

Competing interests statement
The authors declare no competing interests.

Design of SARS-CoV-2 RBD mRNA Vaccine Using Novel Ionizable Lipids

Uri Elia, Srinivas Ramishetti, Niels Dammes, Erez Bar-Haim, Gonna Somu Naidu, Efi Makdasi, Ofer Cohen*, Dan Peer*

U. Elia, Dr. S. Ramishetti, Dr. N. Dammes, Dr. G. Somu Naidu, Prof. D. Peer
Laboratory of Precision NanoMedicine, School of Molecular Cell Biology and Biotechnology, George S. Wise Faculty of Life Sciences, Tel Aviv, 69978 Israel peer@tauex.tau.ac.il

U. Elia, Dr. S. Ramishetti, Dr. N. Dammes, Dr. G. Somu Naidu, Prof. D. Peer
Center for Nanoscience and Nanotechnology, Tel Aviv, 69978 Israel peer@tauex.tau.ac.il

U. Elia, Dr. S. Ramishetti, Dr. N. Dammes, Dr. G. Somu Naidu, Prof. D. Peer
Department of Materials Sciences and Engineering, Iby and Aladar Fleischman Faculty of Engineering, Tel Aviv, 69978 Israel peer@tauex.tau.ac.il

U. Elia, Dr. S. Ramishetti, Dr. N. Dammes, Dr. G. Somu Naidu, Prof. D. Peer
Cancer Biology Research Center, Tel Aviv University, Tel Aviv, 69978 Israel peer@tauex.tau.ac.il

U. Elia, Dr. E. Bar-Haim, Dr. O. Cohen
Department of Biochemistry and Molecular Genetics, Israel Institute for Biological Research, Ness-Ziona 76100 Israel oferc@iibr.goc.il

Dr. E. Makdasi
Department of Infectious Diseases, Israel Institute for Biological Research, Ness-Ziona 76100 Israel

Keywords: SARS-CoV-2, COVID-19, mRNA vaccine, Lipid nanoparticles, Ionizable lipids.

Abstract

The novel coronavirus SARS-CoV-2 has been identified as the causal agent of COVID-19 and stands at the center of the current global human pandemic, with death toll exceeding one million. The urgent need for a vaccine has led to the development of various immunization approaches. mRNA vaccines represent a cell-free, simple and rapid platform for immunization, and therefore have been employed in recent studies towards the development of a SARS-CoV-2 vaccine. In this study, we present the design of a lipid nanoparticles (LNP)-encapsulated receptor binding domain (RBD) mRNA vaccine. Several ionizable lipids have been evaluated *in vivo* in a luciferase mRNA reporter assay, and two leading LNPs formulation have been chosen for the subsequent RBD mRNA vaccine experiment. Intramuscular administration of LNP RBD mRNA elicited robust humoral response, high level of neutralizing antibodies and a Th1-biased cellular response in BALB/c mice. These novel lipids open new avenues for mRNA vaccines in general and for a COVID19 vaccine in particular.

Introduction

Severe acute respiratory syndrome coronavirus (SARS-CoV) 2, is a novel coronavirus identified as the etiological agent of coronavirus disease 19 (COVID-19). This coronavirus stands at the center of the current global human pandemic, with recent reports of more than 36 million cases and over one million deaths worldwide [1]. The urgent need for a vaccine has led to an unprecedented recruitment of academic laboratories, hospitals and pharmaceutical companies around the world, which translated into a wide array (>180) of pre-clinical and clinical studies being conducted in an effort to develop an effective vaccine against SARS-CoV-2 [2]. These vaccine candidates can be classified into several categories: inactivated/live attenuated virus, recombinant viral vector, recombinant protein, DNA vaccine and messenger RNA (mRNA) vaccine.

The mRNA vaccine platform has developed extremely rapidly in the past few years, mainly due to advances in mRNA stabilization and the introduction of efficient delivery methods that originated largely from the siRNA field. mRNA vaccines hold several advantages over traditional vaccine approaches such as inactivated/ live attenuated, subunit or DNA-based vaccines: This platform poses no potential risk of infection or genome integration, does not require entry to the nucleus, and can be developed very rapidly and easily. This last advantage has been demonstrated very clearly in the current COVID-19 pandemic, with the development of an mRNA vaccine by Moderna directed against the spike protein of SARS-CoV-2, with only 66 days from sequence selection to first human dosing [3].

One of the main challenges in mRNA therapy is efficient delivery of mRNA to target cells and tissues. High susceptibility to degradation by omnipresent ribonucleases

(RNases), together with inherent negative charge, hinder the successful delivery of mRNA to cells and subsequent translocation across the negatively charged cell membrane. Hence, successful mRNA delivery requires a carrier molecule which will protect it from degradation, and facilitate cellular uptake. Lipid nanoparticles (LNPs) are a clinically advanced, non-viral delivery system for siRNA, approved by the FDA [4]. In the past few years, LNPs have emerged as one of the most advanced and efficient mRNA delivery platforms. Recent reports demonstrate antigen-encoded mRNA encapsulated in lipid nanoparticles (mRNA-LNPs) as a potent vaccine platform for several infectious diseases including viral infections such as HIV, CMV, Rabies, influenza, Zika, and most recently SARS-CoV-2 [3,5-10]. LNPs are generally comprised of four components: 1) an ionizable lipid, which promotes self-assembly of the LNPs; 2) cholesterol as a stabilizing agent; 3) a phospholipid for support of lipid bilayer structure; and 4) a polyethylene glycol (PEG)-lipid, which increases the half-life of the molecule. Of these, the ionizable lipid is a key player for efficient intracellular delivery of the mRNA. The ionizable lipid facilitates mRNA encapsulation, promotes interaction with cell membrane, and is suggested to play a part in endosomal escape, a key step in the delivery of mRNA into the cytoplasm, and subsequent translation of the protein of interest [11].

Our lab previously demonstrated the design and synthesis of novel ionizable amino lipids for efficient siRNA delivery to leukocyte subsets [12]. Herein, we have selected several structurally different ionizable lipids and screened for *in vivo* mRNA-LNPs delivery for vaccine applications. The screen yielded two LNP formulations, which were chosen for further immunization studies using SARS-CoV-2 RBD mRNA. These experiments demonstrated the development of a specific humoral and cellular response against the

antigen, as well as neutralizing antibodies that blocked viral infection in a VSV Plaque Reduction Neutralization Test (PRNT). Additionally, we measured Th1/Th2 specific cytokine secretion in response to LNP-RBD mRNA vaccination.

Results

LNPs preparation and physicochemical characterization

The structures of the new amino lipids are shown in Figure 1A. The lipids were structurally different in their head group region, linker and lipid tails. LNPs were produced by mixing of lipids and mRNA through micro fluidic mixture device. A schematic illustration of LNP synthesis is shown in Figure 1B and described in details in the materials and methods section. The resultant mRNA-LNPs were small and uniformly distributed as evidenced by small hydrodynamic diameter and polydispersity index (PDI), measured by dynamic light scattering (DLS) (Figure 1C). Except lipid 5, the mean size of the LNPs was less than 100 nm in diameter. Transmission electron microscopy (TEM) analysis supported the DLS data, showing small and uniform size distribution of the particles (Figure 1D).

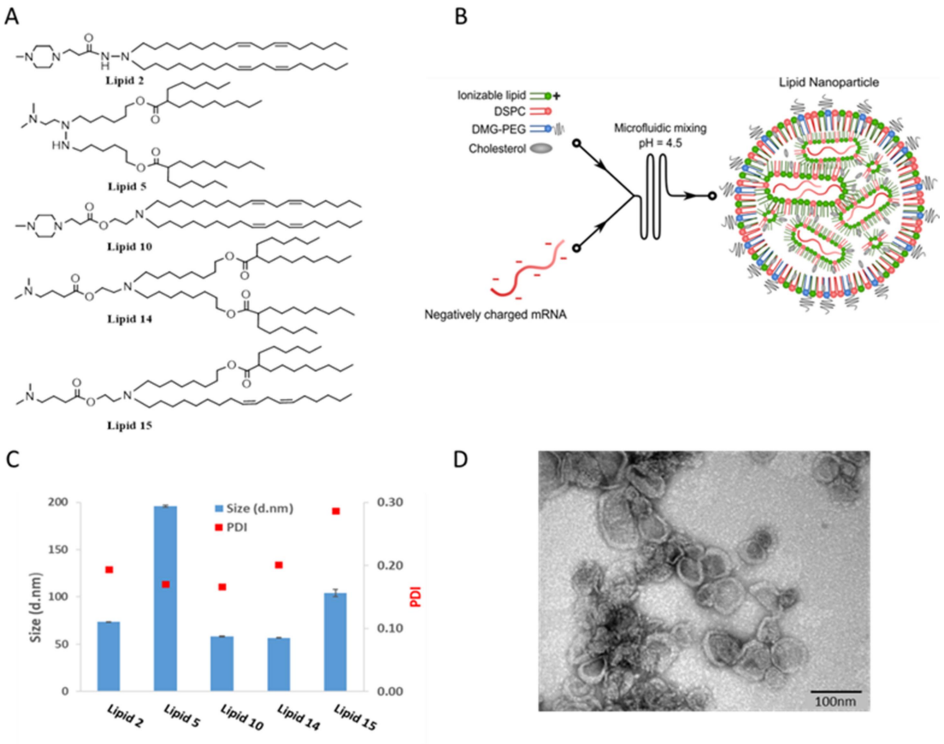

Figure 1. Chemical structures and physicochemical properties of designed LNPs Panel A: Schematic illustrations of the structures of the designed lipids. Panel B: Schematic illustration of LNP synthesis. Panel C: Representative size distribution and polydispersity index (PDI) of LNPs measured by dynamic light scattering Panel D: Representative TEM images of LNP #2. Scale bar 100 nm.

In vivo luciferase expression screen shows two distinct formulations with superior protein expression.

In order to evaluate the *in vivo* efficiency of the LNPs in terms of distribution, protein expression efficiency and kinetics, we conducted a luciferase mRNA-based *in vivo* screen. Animals were injected via the intradermal (i.d.), intramuscular (i.m.) or subcutaneous (s.c.) routes with 5ug luciferase-mRNA encapsulated with one of the five LNP-based formulations, represented herein as LNP #2, #5, #10, #14, #15, and luciferase expression was evaluated daily using IVIS. As shown in Figure 2, LNPs #14 and #15 were superior to other formulations in terms of protein expression level and its duration in all three routes of administration. Since i.d. and i.m. injections exhibited higher and more prolonged protein expression, further immunization studies were conducted using these routes of administration. We chose to proceed with LNPs #2, #14, and #15. Although not showing relative advantage in terms of protein expression *in vivo*, we chose to include LNP #2 in order to eliminate the possibility of a discrepancy between *in vivo* luciferase expression and the resulting immunologic response.

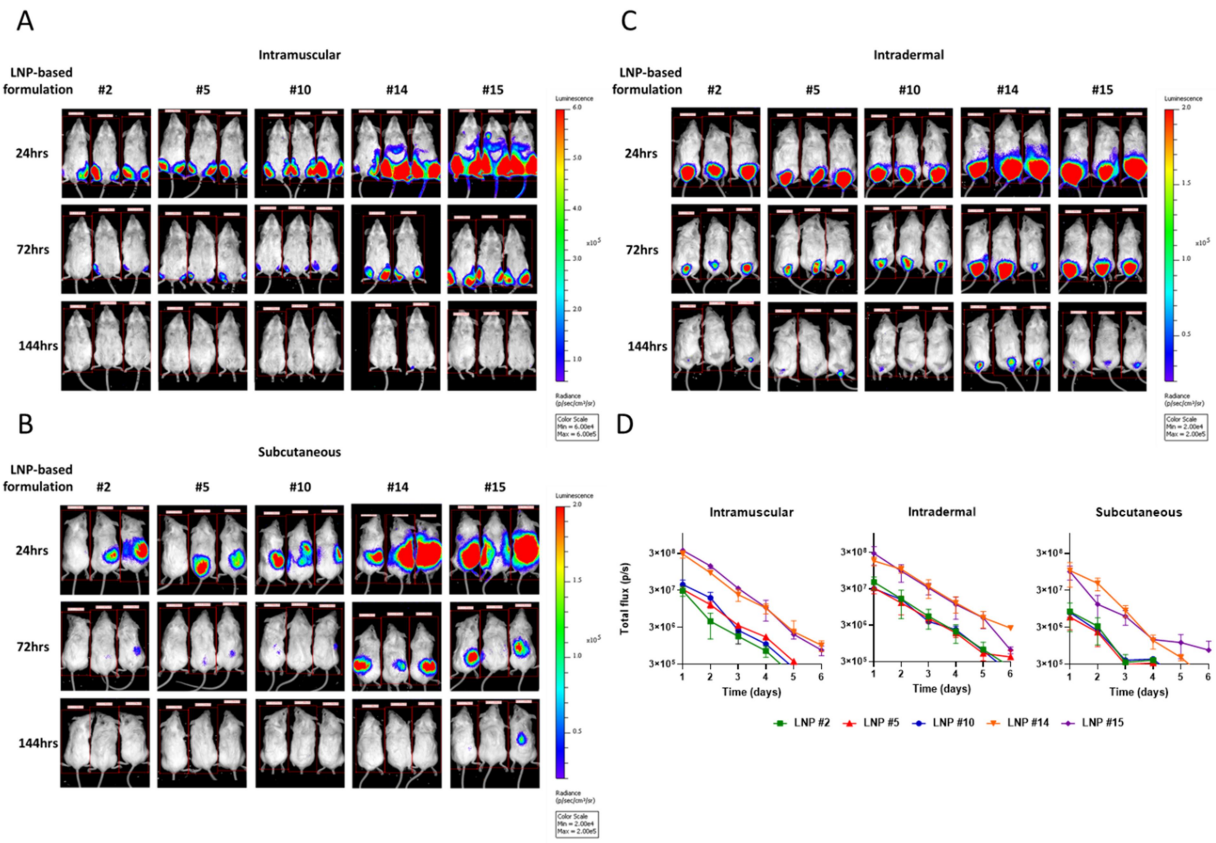

Figure 2. *In vivo* expression pattern of LNP-encapsulated luc mRNA. Representative IVIS images of groups of female BALB/c mice injected with 5 µg luc mRNA encapsulated by five LNP formulations by the intramuscular (panel A) intradermal (panel B), and subcutaneous (panel C) routes. Panel D- quantification of the bioluminescent signal detected throughout six days of monitoring.

Immune response to luciferase expression

Next, we examined the immune response that was developed against the luciferase protein. Intramuscular-immunized mice were bled and sacrificed 4 weeks after immunization with LNP-encapsulated luciferase mRNA. A panel of assays including ELISA for the detection of anti-luciferase antibodies, and ELISpot for evaluation of luciferase-specific cellular response were tested. While the humoral response was limited, with no statistically significant differences between the vaccinated animals and the

control naïve mice, as expected after a single dose administration (Figure 3A), a substantial cellular response was detected when splenocytes were stimulated with the luciferase protein. Interestingly, immunization with LNPs #2 and #14 yielded a significantly stronger (~3 fold and ~5 fold, respectively) cellular response compared to LNP #15 (Figure 3B). Based on these results, we decided to perform the following vaccinations with the two leading formulations #2 and #14.

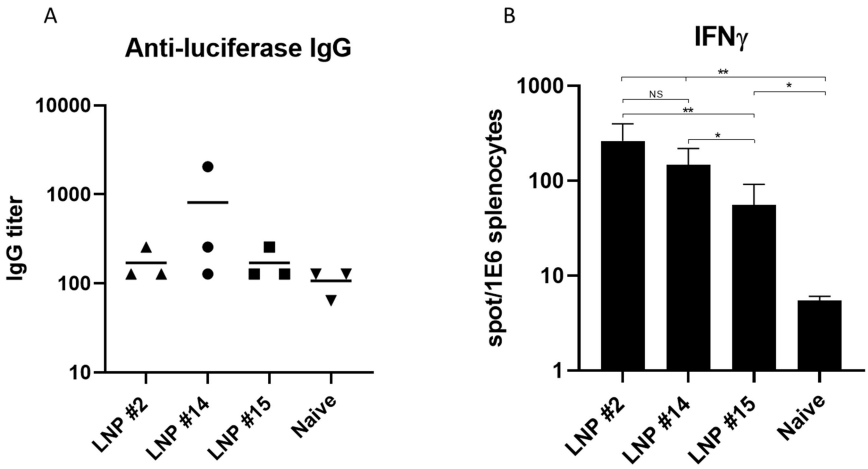

Figure 3. *In vivo* luciferase expression leads to specific cellular immune response. Female BALB/c mice were intramuscularly administered with 5μg LNPs-luc mRNA or untreated (naïve). Serum and spleens were collected 28 days post-administration for evaluation of luciferase-specific humoral (panel A) and cellular response (panel B), as described in the materials and methods section. Statistical analysis was performed using unpaired two-tailed Student's t-test (n.s., not significant; $^{*}p<0.05$, $^{**}p<0.01$).

Immune responses in RBD mRNA-vaccinated mice

Similar to SARS-CoV, SARS-CoV-2 recognizes angiotensin-converting enzyme 2 (ACE2) as receptor for host cell entry. SARS-CoV-2 spike (S) protein consists of S1,

including receptor-binding domain (RBD), and S2 subunits [13]. For our vaccine platform, we chose the RBD of SARS-CoV-2 as the target antigen for the mRNA coding sequence, as described in the materials and methods section. Mice were immunized i.m. or i.d. with either naked RBD mRNA (5μg), LNPs-encapsulated (#2 or #14) RBD mRNA (5μg), or Empty LNPs. We also included a recombinant RBD (rRBD) study group, which was immunized (s.c.) with a recombinant RBD protein (10μg) for comparison with the mRNA vaccinated groups. In all groups, a prime-boost vaccination regimen was employed, with animals being primed at day 0, and boosted 25 days later. Blood and spleens were collected at day 23 (pre-boost) and 39 (14 days post-boost) for evaluation of immune responses (see outline in Figure 4A).

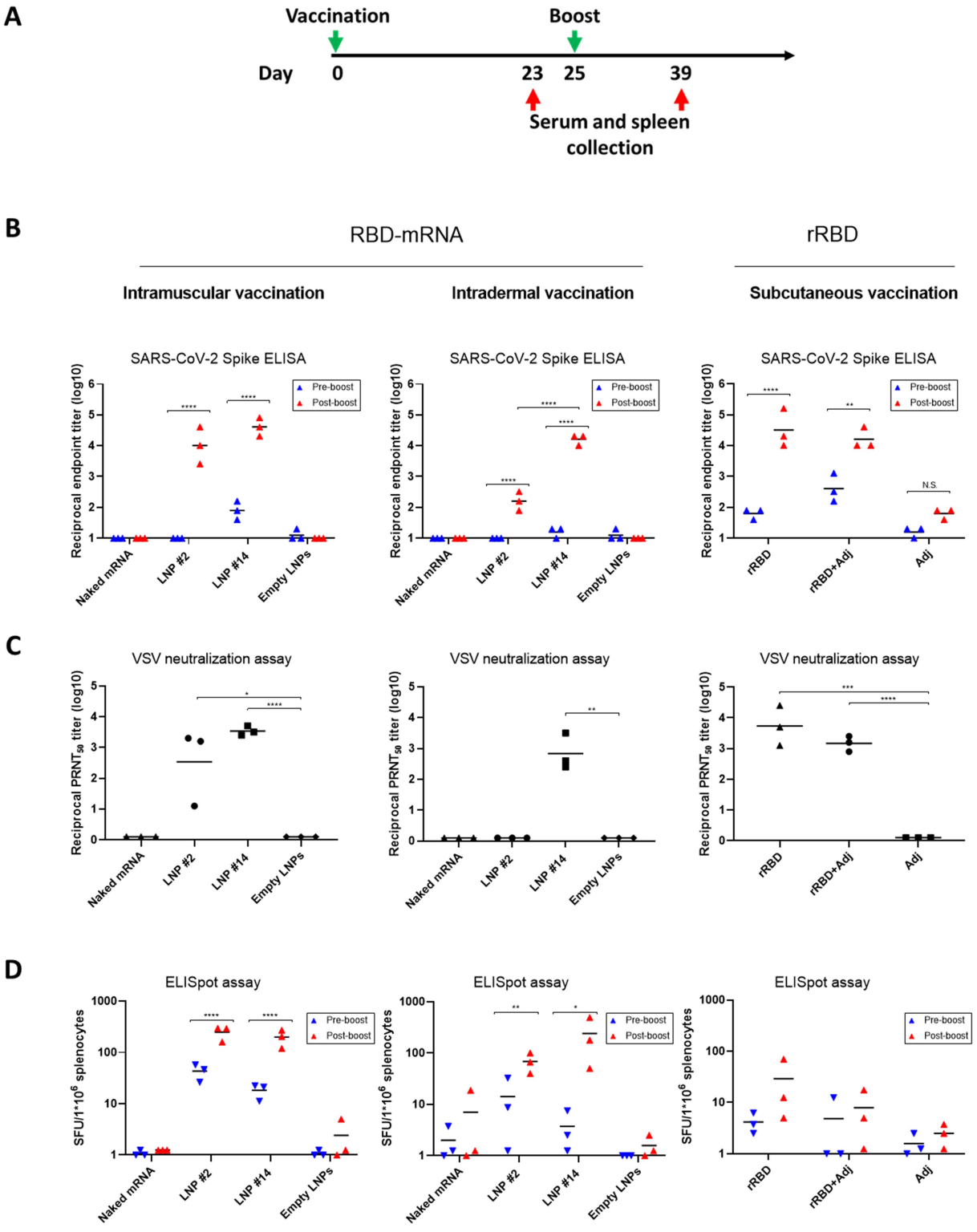

Figure 4. Immunization of mice with LNPs-RBD mRNA leads to a robust immune response. Female BALB/c mice were immunized either i.m. or i.d. with 5μg LNPs-RBD

mRNA or s.c. with 10μg rRBD, and boosted with an equivalent dose 25 days later. Serum and spleen were collected at days 23 ("pre-boost") and 39 ("post-boost") after initial vaccination. Panel A- Schematic diagram of immunization and sample collection. Panel B- SARS-CoV-2 spike-specific IgG antibody titer was determined by ELISA. Panel C- $PRNT_{50}$ titers were determined post-boost using a VSV-based pseudovirus PRNT assay. Panel D- SARS-CoV-2 spike-specific cellular response was determined by ELISpot. Statistical analysis was performed using a two-way ANOVA with Tukey's multiple comparisons test (for ELISA data) or an unpaired two-tailed Student's t-test (for $PRNT_{50}$ and ELISpot data) ($^{*}p<0.05$, $^{**}p<0.01$, $^{***}p<0.001$, $^{****}p<0.0001$).

As can be seen in Figure 4B, pre-boost humoral response against SARS-CoV-2 spike was limited, both in mRNA (naked or LNP-encapsulated) and rRBD-vaccinated mice. However, a robust antibody response could be detected 14 days after the boost in both LNP-encapsulated mRNA and recombinant protein groups, while no response was observed in the naked mRNA group. While both LNP formulations exhibited a boost effect at the i.m. route, a differential antibody response was observed at the i.d. route between LNP #2- and #14-encapsulated RBD mRNA, with only the latter yielding a substantial anti-RBD titer (>10,000) (Figure 4B). Most importantly, this differential response was also evident in the post-boost VSV neutralizing assay, where i.d. LNP #14-encapsulated RBD mRNA vaccination induced a significant neutralizing response, while no neutralizing activity was apparent in LNP #2-encapsulated RBD mRNA vaccinated mice (Figure 4C). Immunization with rRBD also led to a robust boost effect in terms of anti-spike and neutralizing antibodies. Interestingly, no significant difference was observed between vaccinations with the recombinant RBD protein alone or in the presence of the CFA/IFA adjuvant.

The cellular immune response to SARS-CoV-2 plays a crucial role in the ability of the immune system to overcome infection [14,15]. We thus evaluated the cellular response that

developed after immunization with LNP-encapsulated RBD or rRBD by using the ELISpot method for quantification of IFNγ-secreting cells. In contrast to the humoral response, which was very limited before boost administration, a clear specific cellular response was observed 23 days after priming, particularly in mice that were vaccinated via the i.m. route.

A significant increase in specific cellular response was observed after boost administration in both i.m. and i.d. routes of administration, and in both LNP formulations of the RBD mRNA. Conversely, immunization of mice with recombinant RBD did not lead to a significant cellular response, and the post-boost elevation in IFNγ secretion was not statistically significant (Figure 4D).

We next evaluated the Th1/Th2 cytokine secretion profile of LNP RBD mRNA vaccinated mice. As shown in Figure 5 (and Figure 4D of ELISpot results for IFNγ response), a specific and statistically significant secretion of IFNγ and IL-2 was observed in vaccinated mice compared to vehicle treatment, both before and after boost administration. In contrast, Th2 cytokines were either below limit of detection (IL-4) or in comparable levels in vaccinated versus vehicle-treated animals (IL-10).

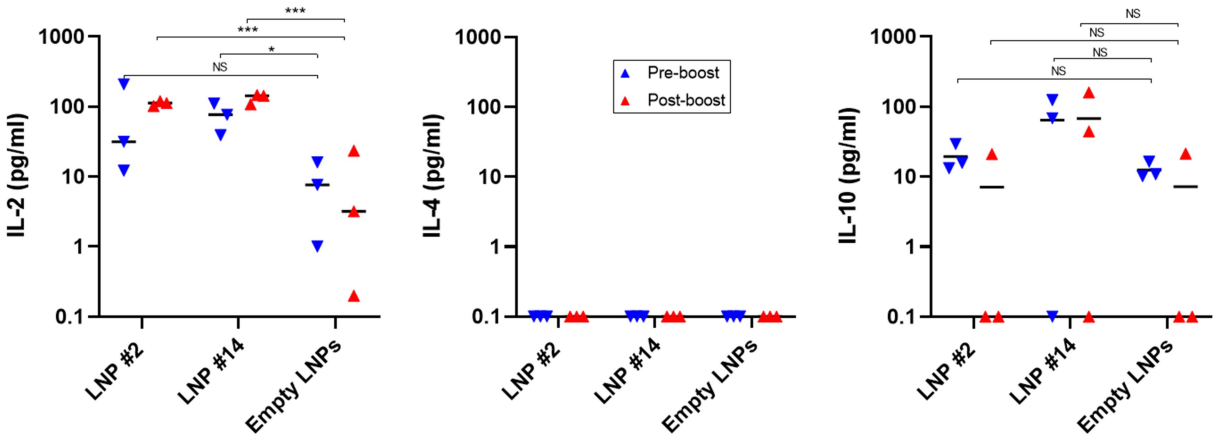

Figure 5. Cytokine profile of induced responses. Splenocytes from i.m. vaccinated mice were stimulated with SARS-CoV-2 spike and analyzed for cytokine secretion by ELISA. Statistical analysis was performed using an unpaired two-tailed Student's t-test ($^{*}p<0.05$, $^{**}p<0.01$, $^{***}p<0.001$, $^{****}p<0.0001$).

Discussion

Severe acute respiratory syndrome coronavirus 2 (SARS-CoV-2) has recently emerged as a global pandemic, risking most of the earth's population health, and leading towards a worldwide economic crisis since its outbreak. Numerous vaccination platforms have been recently employed in the quest for an effective vaccine against the virus. mRNA-based vaccines have been extensively explored in the last few years for immune therapy applications and viral infections. Due to its negative charge and stability issues, mRNA molecules need suitable agents for intracellular delivery. LNPs are one of the most clinically advanced and commonly used tool for mRNA delivery [16].

In the present study, we developed LNPs-encapsulated mRNA as a vaccine platform. Endosomal escape of LNPs is a key step for endosomal release and functional activity of

mRNA therapeutics. Towards this, several structurally-different lipids were chosen from our previous work. Lipid #2 and #5 contain hydrazine linker and lipids #10, #14 and #15 contains ethanolamine linker. However, the hydrophobic lipid tails chosen from fusogenic linoleic tails or acid sensitive mixed hydrophobic lipid tails. We compared these lipids in the form of LNPs for their ability to deliver mRNA and facilitate protein expression in mice, by employing commonly used routes of administration. First, we conducted a luciferase-based screen to evaluate protein expression efficiency and kinetics. IVIS data showed that two of these formulations, LNP #14 and #15, were more potent in terms of both level and duration of luciferase expression, as was measured by the luminescence signal after luciferin injection.

Next, we examined the immunologic response that developed against the expressed luciferase protein. The immunogenicity of the luciferase protein has been demonstrated previously [17], and we speculated that *in vivo* mRNA delivery efficiency would correlate with the resulting immunological responses. While the humoral response was rather limited, as one would expect after a single immunization, a substantial cellular response was recorded against the luciferase protein. Interestingly, immunization with LNP #2, led to a robust cellular immune response that was comparable to that of LNP #14 despite a lower and shorter-lived luminescent signal. This shows that one should take caution in making predictions regarding immunogenicity based on protein expression patterns. The elicitation of a significant immune response depends ultimately on the extent to which the delivered antigen is taken up by antigen presenting cells (APC), which migrate to lymph nodes and induce T cell activation and subsequent production of immune mediators. It is therefore possible, that in the case of LNP #2, while the IVIS data indicated a more

limited pattern of luciferase expression, the tissues and cell types in which the protein was expressed, enabled the establishment of a more robust immune response. This issue will be further addressed in future studies that will evaluate tissue and organ-specific luciferase expression.

Given the robust cellular response observed in animals injected with LNPs #2 and #14, these formulations were used for the subsequent vaccination experiment with SARS-CoV-2 RBD mRNA. The RBD protein was chosen as an antigen for immunization based on recent data demonstrating the importance of the RBD domain in SARS-CoV-2 vaccine design, by elicitation of protective immunity by an RBD-based DNA vaccine [18] and a recombinant RBD-based vaccine [19].

Mice were vaccinated in a prime-boost regimen with naked RBD mRNA, LNP-encapsulated RBD mRNA or recombinant RBD.

Firstly, naked RBD mRNA immunization was unable to elicit detectable humoral or cellular responses before or after the boost, suggesting that the mRNA was most likely degraded and was incapable of triggering an effective immune response. Conversely, mice immunized with LNP RBD mRNA developed substantial anti-spike IgG titers, a robust cellular response, and high levels of neutralizing antibodies after boost administration in both intramuscular and intradermal groups. Interestingly, while the pre-boost humoral response was largely undetected in these immunization groups, ELISpot analysis demonstrated that a cellular response could be detected at that early stage, particularly in mice immunized intramuscularly, demonstrating the importance of characterization of the cellular response in SARS-CoV-2 immunization studies. While the two LNP formulations, #2 and #14, led to comparable humoral and cellular

responses in intramuscularly-immunized mice, formulation #14 exhibited superior immunogenicity following intradermal administration of LNP RBD mRNA. This effect was most pronounced at the PRNT assay results (Figure 4C, middle panel). The observed cellular responses induced by LNP #14 may be attributed to their ability to activate APC via i.d. and i.m. administration, whereas LNP #2 is proficient via i.m. route only. This interesting observation suggests that not only LNPs structure but also route of administration needs to be considered for future clinical development of vaccines.

A large number of recombinant protein vaccines are currently in pre-clinical development, and several spike/RBD-based vaccines have entered clinical trials [2]. In order to evaluate the relative efficiency of our LNP-based mRNA vaccine, we performed a recombinant RBD immunization experiment in parallel, using a standard protein immunization protocol (a prime-boost s.c. administration of recombinant protein in the presence of an adjuvant) **[20]**. Although displaying comparable anti-RBD IgG and VSV neutralizing titers, the recombinant RBD immunization was unable to mount a significant cellular response as was recorded in the LNP RBD mRNA vaccine groups (Figure 4). These data demonstrate the inherent advantage of mRNA vaccination over recombinant protein vaccination in elicitation of immune response. While recombinant protein vaccination is dependent upon antigen uptake by APC, intracellular antigen expression following mRNA vaccination eventually leads to efficient peptide epitope MHC class I presentation which facilitates cytolytic T lymphocyte priming (in addition to helper T cell response). This combined activation of the two T cell subtypes yields a robust, long term humoral and cellular response, which may account for the apparent cellular response

we observe following LNP RBD mRNA vaccination, and not after recombinant RBD immunization.

Two major concerns in the development of a safe SARS-CoV-2 vaccine is antibody-dependent enhancement (ADE) and vaccine-associated enhanced respiratory disease (VAERD), which could worsen the clinical manifestations of infection [21]. Since these two phenomena have been linked with a T helper 2 cell-biased response [21], we evaluated Th1 (IFNγ, IL-2) and Th2 (IL-4, IL-10) cytokine secretion in response to stimulation of splenocytes from vaccinated mice with SARS-CoV-2 spike. Our data demonstrate that both mRNA LNP formulations induced a Th1-biased cellular response towards the spike protein.

In summary, we report here an LNP-based RBD mRNA vaccine which was designed using a preliminary *in vivo* screen of structurally-different ionizable lipid-based LNPs. Several groups have recently reported evidence of immunogenicity and efficacy of LNP-based RBD mRNA vaccines [22-25], but have not referred to the issue of LNP lipid composition. The physicochemical properties of the ionizable lipids may have dramatic effects on delivery and protein expression efficiency, and should be considered upon LNP-based mRNA vaccine design.

Materials and methods

Animals

Female BALB/c mice (6–8 weeks old) were obtained from Charles River and randomly assigned into cages in groups of 10 animals. The mice were allowed free access to water and rodent diet (Harlan, Israel). All animal experiments were conducted in accordance with the guideline of the Israel Institute for Biological Research (IIBR) animal experiments committee. Protocol numbers: #M-60-19, #M-30-20.

Production of SARS-CoV-2 antigens for immunization and *in vitro* assays

Recombinant SARS-CoV-2 spike glycoprotein, was expressed in pcDNA3.1^{+} plasmid, as recently described [26]. A stabilized soluble version of the spike protein (based on GenPept: QHD43416 ORF amino acids 1-1207) was designed to include proline substitutions at positions 986 and 987, and disruptive replacement of the furin cleavage site RRAR (residues at position 682-685) with GSAS. C-terminal his-tag as well as a strep-tag, were included in order to facilitate protein purification. Expression of the recombinant proteins was performed using ExpiCHO^{TM} Expression system (Thermoscientific, USA, Cat# A29133) following purification using HisTrap^{TM} (GE Healthcare, UK) and Strep-Tactin®XT (IBA, Germany). The purified protein was sterile-filtered and stored in PBS.

Human Fc-RBD fused protein was expressed using previously designed Fc-fused protein expression vector (Tal-Noy-Poral et al 2015), giving rise to a protein comprising of two RBD moieties (amino acids 331-524, see accession number of the S protein above) owing

to the homodimeric human (gamma1) Fc domain (huFc). Expression of the recombinant proteins was performed using ExpiCHO™ Expression system (Thermoscientific, USA) following purification using HiTrap Protein-A column (GE healthcare, UK). The purified protein was sterile-filtered and stored in PBS.

mRNA

CleanCap® firefly luciferase mRNA was a kind gift from BioNtech RNA Pharmaceuticals (Mainz, Germany). CleanCap®, pseudouridine-substituted Fc-conjugated RBD mRNA (331-524 aa) was purchased from TriLink Bio Technologies (San Diego, CA, USA). The Fc-conjugated RBD mRNA was designed to include the exact translated Fc-RBD protein sequence as the recombinant protein.

LNP preparation and characterization

LNPs were synthesized by mixing one volume of lipid mixture of ionizable lipid, DSPC, Cholesterol and DMG-PEG (40:10.5:47.5:2 mol ratio) in ethanol and three volumes of mRNA (1:16 w/w mRNA to lipid) in acetate buffer. Lipids and mRNA were injected in to a micro fluidic mixing device Nanoassemblr® (Precision Nanosystems, Vancouver BC) at a combined flow rate of 12 mL/min. The resultant mixture was dialyzed against phosphate buffered saline (PBS) (pH 7.4) for 16 h to remove ethanol.

Particles in PBS were analyzed for size and uniformity by dynamic light scattering (DLS). Zeta potential was determined using the Malvern zeta-sizer (Malvern Instruments Ltd., Worcestershire, UK). RNA encapsulation in LNPs was calculated according to Quant-iT RiboGreen RNA Assay Kit (Thermo Fisher, Waltham, MA, USA).

Animal vaccination experiments

For *in vivo* LNP formulations screen, groups of 6-8-week-old female BALB/c mice were administered intramuscularly (50µl in both hind legs), intradermally (100µl) or subcutaneously (100µl) with luciferase mRNA (5µg) encapsulated with five different LNP formulations (LNPs #2, #5, #10, #14, #15). Luciferase expression was monitored as described in the bioluminescence imaging studies section. 28 days post-intramuscular injection, serum and spleen were collected from mice for evaluation of the immunologic response that developed towards luciferase.

For RBD mRNA vaccination studies, groups of 6-8-week-old female BALB/c mice were administered intramuscularly (50µl in both hind legs) or intradermally (100µl) with SARS-CoV-2 mRNA (5µg) encapsulated with LNP formulations #2 or #14.

For recombinant RBD (rRBD) vaccination studies, groups of 6-8-week-old female BALB/c mice were administered subcutaneously (100µl) with hFc-rRBD (10µg), hFc-rRBD emulsified in complete/incomplete Freund's adjuvant (CFA/IFA), or adjuvant alone as control.

Both RBD mRNA- and recombinant RBD- immunized animals were boosted at day 25 with the same priming dose administered on day 0. Serum and spleens were collected on day 23 ("pre-boost") and 49 ("post-boost") for evaluation of immunologic response towards SARS-CoV-2 RBD, and measurement of cytokine secretion.

Bioluminescence Imaging Studies

Bioluminescence imaging was performed with an IVIS Spectrum imaging system (Caliper Life Sciences). Female BALB/c mice were administered D-luciferin (Regis Technologies) at a dose of 150 mg/kg intraperitoneally. Mice were anesthetized after receiving D-luciferin with a mixture of ketamine (60 mg/kg) and xylazine (10 mg/kg) and placed on the imaging platform. Mice were imaged at 5 minutes post administration of D-luciferin using an exposure time of 60 seconds. Bioluminescence values were quantified by measuring photon flux (photons/second) in the region of interest using the Living IMAGE Software provided by Caliper.

ELISA

ELISA was performed for the detection of luciferase- or SARS-CoV-2 spike-specific antibodies in immunized mouse sera. MaxiSORP ELISA plates (Nunc) were pre-coated with recombinant luciferase (0.4µg/ml, Promega, #E1701) or spike protein (2µg/ml) overnight at 4^{o}C in carbonate buffer. Plated were washed three times with PBST (PBS+0.05% Tween-20) and blocked with 2% BSA (Sigma-Aldrich, #A8022) in PBST for 1 h at 37 ^{o}C. After three washes with PBST, plates were incubated with serially diluted mouse sera for 1 h at 37 ^{o}C. Following washing, goat anti-mouse alkaline phosphatase-conjugated IgG (Jackson Immuno Research Labs, #115-055-003) was added for 1 h at 37 ^{o}C. The plates were washed with PBST and reactions were developed with p-nitrophenyl phosphate substrate (PNPP, Sigma-Aldrich, N2765). Plates were read at 405 nm absorbance and antibody titers were calculated as the highest serum dilution with an OD value above 2 times the average OD of the negative controls.

Cytokine assays

Splenocytes from immunized mice were incubated in the presence of SARS-CoV-2 spike protein (10μg/ml). Culture supernatants were harvested 48 h later and analyzed for cytokines by ELISA techniques with commercially available kits. IL-2 (DY402), IL-4 (DY404) and IL-10 (DY417) kits were obtained from R & D Systems, Minneapolis, Minn.

Murine IFNγ ELISpot Assay

Mice spleens were dissociated in GentleMACS C-tubes (Miltenyi Biotec), filtered, treated with Red Blood Cell Lysing Buffer (Sigma-Aldrich, #R7757), and washed. Pellets were resuspended in 1ml of CTL-Test™ Medium (*CTL*, *#CTLT 005*) supplemented with 1% fresh glutamine, and 1 mM Pen/Strep (Biological Industries, Israel), and single cell suspensions were seeded into 96-well, high-protein-binding, PVDF filter plates at 400,000 cells/well. Mice were tested individually in duplicates by stimulation with recombinant luciferase (13μg/ml, Promega, #E1701), SARS-CoV-2 spike protein (10μg/ml), Concanavalin A (Sigma-Aldrich, #0412) (2μg/ml) as positive control, or CTL medium as negative control (no antigen). Cells were incubated with antigens for 24 h, and the frequency of IFNγ-secreting cells was determined using Murine IFNγ Single-Color Enzymatic ELISPOT kit (CTL, #MIFNG 1M/5) with strict adherence to the manufacturer's instructions. Spot forming units (SFU) were counted using an automated ELISpot counter (Cellular Technology Limited).

Plaque Reduction Neutralization Test (PRNT)

VSV-spike [27]stocks were prepared by infection of Vero E6 cells for several days. When viral cytopathic effect (CPE) was observed, media were collected, clarified by centrifugation, aliquoted and stored at -80°C. Titer of stock was determined by plaque assay using Vero E6 cells.

For plaque reduction neutralization test (PRNT), Vero E6 cells ($0.5*10^6$ cells/well in 12-well plates) were cultured in DMEM supplemented with 10% FCS, MEM non-essential amino acids, 2nM L-Glutamine, 100 Units/ml Penicillin, 0.1 mg/ml streptomycin and 12.5 Units/ml Nystatin (Biological Industries, Israel) overnight at 37°C, 5% CO_2.

Serum samples were 3-fold serially diluted (ranging from 1:50-1:12,500) in 400 µl of MEM supplemented with 2% FCS, MEM non-essential amino acids, 2nM L-Glutamine, 100 Units/ml Penicillin, 0.1 mg/ml streptomycin and 12.5 Units/ml Nystatin. 400 µl containing 300 PFU/ml of VSV-spike were then added to the diluted serum samples and the mixture was incubated at 37 °C, 5% CO_2 for 1 h. Monolayers were then washed once with DMEM w/o FBS and 200 µl of each serum-virus mixture was added in triplicates to the cells for 1 h. Virus mixture without serum was used as control. 1 ml overlay [MEM containing 2% FBS and 0.4% tragacanth (Sigma, Israel)] was added to each well and plates were incubated at 37 °C, 5%CO_2 for 72 h. The number of plaques in each well was determined following media aspiration, cells fixation and staining with 1 ml of crystal violet (Biological Industries, Israel). NT50 was defined as serum dilution at which the plaque number was reduced by 50%, compared to plaque number of the control (in the absence of serum).

Transmission Electron Microscopy Analysis

A drop of aqueous solution containing LNPs was placed on the carbon-coated copper grid and dried. The morphology of LNPs was analyzed by a JEOL 1200 EX (Japan) transmission electron microscope

Statistical analysis

All values are presented as mean plus standard error of the mean (s.e.m). Antibody titers, neutralizing titers, ELISpot data and cytokine levels were compared using two-way ANOVAs or t-tests as depicted in the figure captions. All statistical analyses were performed using GraphPad Prism 8 statistical software.

Competing interests

D.P. declares financial interests in ART Bioscience. None of them relates to this work. The rest of the authors declare no financial interests.

Acknowledgments

This work was supported by the Lewis Trust grant to D.P.

Data availability

All relevant data are available from the authors upon reasonable request.

References

1. World Health Organization. https://www.who.int/docs/default-source/coronaviruse/situation-reports/20201012-weekly-epi-update-9.pdf Published October 12, 2020.
2. World Health Organization. https://www.who.int/publications/m/item/draft-landscape-of-covid-19-candidate-vaccines Published October 2, 2020.
3. Jackson, L. A.; Anderson, E. J.; Rouphael, N. G.; Roberts, P. C.; Makhene, M.; Coler, R. N.; McCullough, M. P.; Chappell, J. D.; Denison, M. R.; Stevens, L. J.; Pruijssers, A. J.; McDermott, A.; Flach, B.; Doria-Rose, N. A.; Corbett, K. S.; Morabito, K. M.; O'Dell, S.; Schmidt, S. D.; Swanson, P. A., 2nd; Padilla, M.; Mascola, J. R.; Neuzil, K. M.; Bennett, H.; Sun, W.; Peters, E.; Makowski, M.; Albert, J.; Cross, K.; Buchanan, W.; Pikaart-Tautges, R.; Ledgerwood, J. E.; Graham, B. S.; Beigel, J. H.; m, R. N. A. S. G. *N Engl J Med* **2020**.
4. Adams, D.; Gonzalez-Duarte, A.; O'Riordan, W. D.; Yang, C. C.; Ueda, M.; Kristen, A. V.; Tournev, I.; Schmidt, H. H.; Coelho, T.; Berk, J. L.; Lin, K. P.; Vita, G.; Attarian, S.; Plante-Bordeneuve, V.; Mezei, M. M.; Campistol, J. M.; Buades, J.; Brannagan, T. H., 3rd; Kim, B. J.; Oh, J.; Parman, Y.; Sekijima, Y.; Hawkins, P. N.; Solomon, S. D.; Polydefkis, M.; Dyck, P. J.; Gandhi, P. J.; Goyal, S.; Chen, J.; Strahs, A. L.; Nochur, S. V.; Sweetser, M. T.; Garg, P. P.; Vaishnaw, A. K.; Gollob, J. A.; Suhr, O. B. *N Engl J Med* **2018**, 379(1), 11-21.
5. Alberer, M.; Gnad-Vogt, U.; Hong, H. S.; Mehr, K. T.; Backert, L.; Finak, G.; Gottardo, R.; Bica, M. A.; Garofano, A.; Koch, S. D.; Fotin-Mleczek, M.; Hoerr, I.; Clemens, R.; von Sonnenburg, F. *Lancet* **2017**, 390(10101), 1511-1520.
6. Bahl, K.; Senn, J. J.; Yuzhakov, O.; Bulychev, A.; Brito, L. A.; Hassett, K. J.; Laska, M. E.; Smith, M.; Almarsson, O.; Thompson, J.; Ribeiro, A. M.; Watson, M.; Zaks, T.; Ciaramella, G. *Mol Ther* **2017**, 25(6), 1316-1327.

7. John, S.; Yuzhakov, O.; Woods, A.; Deterling, J.; Hassett, K.; Shaw, C. A.; Ciaramella, G. *Vaccine* **2018**, 36(12), 1689-1699.

8. Pardi, N.; Hogan, M. J.; Pelc, R. S.; Muramatsu, H.; Andersen, H.; DeMaso, C. R.; Dowd, K. A.; Sutherland, L. L.; Scearce, R. M.; Parks, R.; Wagner, W.; Granados, A.; Greenhouse, J.; Walker, M.; Willis, E.; Yu, J. S.; McGee, C. E.; Sempowski, G. D.; Mui, B. L.; Tam, Y. K.; Huang, Y. J.; Vanlandingham, D.; Holmes, V. M.; Balachandran, H.; Sahu, S.; Lifton, M.; Higgs, S.; Hensley, S. E.; Madden, T. D.; Hope, M. J.; Kariko, K.; Santra, S.; Graham, B. S.; Lewis, M. G.; Pierson, T. C.; Haynes, B. F.; Weissman, D. *Nature* **2017**, 543(7644), 248-251.

9. Pardi, N.; Secreto, A. J.; Shan, X.; Debonera, F.; Glover, J.; Yi, Y.; Muramatsu, H.; Ni, H.; Mui, B. L.; Tam, Y. K.; Shaheen, F.; Collman, R. G.; Kariko, K.; Danet-Desnoyers, G. A.; Madden, T. D.; Hope, M. J.; Weissman, D. *Nat Commun* **2017**, 8, 14630.

10. Sahin, U.; Muik, A.; Derhovanessian, E.; Vogler, I.; Kranz, L. M.; Vormehr, M.; Baum, A.; Pascal, K.; Quandt, J.; Maurus, D.; Brachtendorf, S.; Lorks, V.; Sikorski, J.; Hilker, R.; Becker, D.; Eller, A. K.; Grutzner, J.; Boesler, C.; Rosenbaum, C.; Kuhnle, M. C.; Luxemburger, U.; Kemmer-Bruck, A.; Langer, D.; Bexon, M.; Bolte, S.; Kariko, K.; Palanche, T.; Fischer, B.; Schultz, A.; Shi, P. Y.; Fontes-Garfias, C.; Perez, J. L.; Swanson, K. A.; Loschko, J.; Scully, I. L.; Cutler, M.; Kalina, W.; Kyratsous, C. A.; Cooper, D.; Dormitzer, P. R.; Jansen, K. U.; Tureci, O. *Nature* **2020**.

11. Yonezawa, S.; Koide, H.; Asai, T. *Adv Drug Deliv Rev* **2020**.

12. Ramishetti, S.; Hazan-Halevy, I.; Palakuri, R.; Chatterjee, S.; Naidu Gonna, S.; Dammes, N.; Freilich, I.; Kolik Shmuel, L.; Danino, D.; Peer, D. *Adv Mater* **2020**, 32(12), e1906128.

13. Shang, J.; Ye, G.; Shi, K.; Wan, Y.; Luo, C.; Aihara, H.; Geng, Q.; Auerbach, A.; Li, F. *Nature* **2020**, 581(7807), 221-224.

14. Grifoni, A.; Weiskopf, D.; Ramirez, S. I.; Mateus, J.; Dan, J. M.; Moderbacher, C. R.; Rawlings, S. A.; Sutherland, A.; Premkumar, L.; Jadi, R. S.; Marrama, D.; de Silva, A. M.; Frazier, A.; Carlin, A.

F.; Greenbaum, J. A.; Peters, B.; Krammer, F.; Smith, D. M.; Crotty, S.; Sette, A. *Cell* **2020**, 181(7), 1489-1501 e1415.

15. Zheng, H. Y.; Zhang, M.; Yang, C. X.; Zhang, N.; Wang, X. C.; Yang, X. P.; Dong, X. Q.; Zheng, Y. T. *Cell Mol Immunol* **2020**, 17(5), 541-543.
16. Ickenstein, L. M.; Garidel, P. *Expert Opin Drug Deliv* **2019**, 16(11), 1205-1226.
17. Petkov, S. P.; Heuts, F.; Krotova, O. A.; Kilpelainen, A.; Engstrom, G.; Starodubova, E. S.; Isaguliants, M. G. *Hum Vaccin Immunother* **2013**, 9(10), 2228-2236.
18. Lainšček, D.; Fink, T.; Forstnerič, V.; Hafner-Bratkovič, I.; Orehek, S.; Strmšek, Ž.; Manček-Keber, M.; Pečan, P.; Esih, H.; Malenšek, Š.; Aupič, J.; Dekleva, P.; Plaper, T.; Vidmar, S.; Kadunc, L.; Benčina, M.; Omersa, N.; Anderluh, G.; Pojer, F.; Lau, K.; Hacker, D.; Correia, B.; Peterhoff, D.; Wagner, R.; Jerala, R. *bioRxiv* **2020**, 2020.2008.2028.244269.
19. Yang, J.; Wang, W.; Chen, Z.; Lu, S.; Yang, F.; Bi, Z.; Bao, L.; Mo, F.; Li, X.; Huang, Y.; Hong, W.; Yang, Y.; Zhao, Y.; Ye, F.; Lin, S.; Deng, W.; Chen, H.; Lei, H.; Zhang, Z.; Luo, M.; Gao, H.; Zheng, Y.; Gong, Y.; Jiang, X.; Xu, Y.; Lv, Q.; Li, D.; Wang, M.; Li, F.; Wang, S.; Wang, G.; Yu, P.; Qu, Y.; Yang, L.; Deng, H.; Tong, A.; Li, J.; Wang, Z.; Yang, J.; Shen, G.; Zhao, Z.; Li, Y.; Luo, J.; Liu, H.; Yu, W.; Yang, M.; Xu, J.; Wang, J.; Li, H.; Wang, H.; Kuang, D.; Lin, P.; Hu, Z.; Guo, W.; Cheng, W.; He, Y.; Song, X.; Chen, C.; Xue, Z.; Yao, S.; Chen, L.; Ma, X.; Chen, S.; Gou, M.; Huang, W.; Wang, Y.; Fan, C.; Tian, Z.; Shi, M.; Wang, F. S.; Dai, L.; Wu, M.; Li, G.; Wang, G.; Peng, Y.; Qian, Z.; Huang, C.; Lau, J. Y.; Yang, Z.; Wei, Y.; Cen, X.; Peng, X.; Qin, C.; Zhang, K.; Lu, G.; Wei, X. *Nature* **2020**.
20. Du, L.; Zhao, G.; He, Y.; Guo, Y.; Zheng, B. J.; Jiang, S.; Zhou, Y. *Vaccine* **2007**, 25(15), 2832-2838.
21. Graham, B. S. *Science* **2020**, 368(6494), 945-946.

22. Laczko, D.; Hogan, M. J.; Toulmin, S. A.; Hicks, P.; Lederer, K.; Gaudette, B. T.; Castano, D.; Amanat, F.; Muramatsu, H.; Oguin, T. H., 3rd; Ojha, A.; Zhang, L.; Mu, Z.; Parks, R.; Manzoni, T. B.; Roper, B.; Strohmeier, S.; Tombacz, I.; Arwood, L.; Nachbagauer, R.; Kariko, K.; Greenhouse, J.; Pessaint, L.; Porto, M.; Putman-Taylor, T.; Strasbaugh, A.; Campbell, T. A.; Lin, P. J. C.; Tam, Y. K.; Sempowski, G. D.; Farzan, M.; Choe, H.; Saunders, K. O.; Haynes, B. F.; Andersen, H.; Eisenlohr, L. C.; Weissman, D.; Krammer, F.; Bates, P.; Allman, D.; Locci, M.; Pardi, N. *Immunity* **2020**.

23. Lu, J.; Lu, G.; Tan, S.; Xia, J.; Xiong, H.; Yu, X.; Qi, Q.; Yu, X.; Li, L.; Yu, H.; Xia, N.; Zhang, T.; Xu, Y.; Lin, J. *Cell Res* **2020**, 30(10), 936-939.

24. Tai, W.; Zhang, X.; Drelich, A.; Shi, J.; Hsu, J. C.; Luchsinger, L.; Hillyer, C. D.; Tseng, C. K.; Jiang, S.; Du, L. *Cell Res* **2020**, 30(10), 932-935.

25. Zhang, N. N.; Li, X. F.; Deng, Y. Q.; Zhao, H.; Huang, Y. J.; Yang, G.; Huang, W. J.; Gao, P.; Zhou, C.; Zhang, R. R.; Guo, Y.; Sun, S. H.; Fan, H.; Zu, S. L.; Chen, Q.; He, Q.; Cao, T. S.; Huang, X. Y.; Qiu, H. Y.; Nie, J. H.; Jiang, Y.; Yan, H. Y.; Ye, Q.; Zhong, X.; Xue, X. L.; Zha, Z. Y.; Zhou, D.; Yang, X.; Wang, Y. C.; Ying, B.; Qin, C. F. *Cell* **2020**, 182(5), 1271-1283 e1216.

26. Noy-Porat, T.; Makdasi, E.; Alcalay, R.; Mechaly, A.; Levy, Y.; Bercovich-Kinori, A.; Zauberman, A.; Tamir, H.; Yahalom-Ronen, Y.; Israeli, M.; Epstein, E.; Achdout, H.; Melamed, S.; Chitlaru, T.; Weiss, S.; Peretz, E.; Rosen, O.; Paran, N.; Yitzhaki, S.; Shapira, S. C.; Israely, T.; Mazor, O.; Rosenfeld, R. *Nat Commun* **2020**, 11(1), 4303.

27. Yahalom-Ronen, Y.; Tamir, H.; Melamed, S.; Politi, B.; Shifman, O.; Achdout, H.; Vitner, E. B.; Israeli, O.; Milrot, E.; Stein, D.; Cohen-Gihon, I.; Lazar, S.; Gutman, H.; Glinert, I.; Cherry, L.; Vagima, Y.; Lazar, S.; Weiss, S.; Ben-Shmuel, A.; Avraham, R.; Puni, R.; Lupu, E.; Bar David, E.; Sittner, A.; Erez, N.; Zichel, R.; Mamroud, E.; Mazor, O.; Levy, H.; Laskar, O.; Yitzhaki, S.; Shapira, S. C.; Zvi, A.; Beth-Din, A.; Paran, N.; Israely, T. *bioRxiv* **2020**, 2020.2006.2018.160655.

TOXICOLOGICAL SCIENCES **116(2)**, 397–412 (2010)
doi:10.1093/toxsci/kfq144
Advance Access publication May 13, 2010

Diagnostic Performance of Traditional Hepatobiliary Biomarkers of Drug-Induced Liver Injury in the Rat

Daniela Ennulat,*,[1] Michal Magid-Slav,† Sabine Rehm,* and Kay S. Tatsuoka†

*Department of Safety Assessment and †Department of Quantitative Sciences, GlaxoSmithKline, King of Prussia, Pennsylvania

[1]To whom correspondence should be addressed at Department of Safety Assessment, GlaxoSmithKline, 709 Swedeland Road, UEO462, PO Box 1539, King of Prussia, PA 19406-0939. Fax: (610) 270-7202. E-mail: daniela_2_ennulat@gsk.com.

Received March 10, 2010; accepted May 10, 2010

Nonclinical studies provide the opportunity to anchor biochemical with morphologic findings; however, liver injury is often complex and heterogeneous, confounding the ability to relate biochemical changes with specific patterns of injury. The aim of the current study was to compare diagnostic performance of hepatobiliary markers for specific manifestations of drug-induced liver injury in rat using data collected in a recent hepatic toxicogenomics initiative in which rats ($n = 3205$) were given 182 different treatments for 4 or 14 days. Diagnostic accuracy of alanine aminotransferase (ALT), aspartate aminotransferase (AST), total bilirubin (Tbili), serum bile acids (SBA), alkaline phosphatase (ALP), gamma glutamyl transferase (GGT), total cholesterol (Chol), and triglycerides (Trig) was evaluated for specific types of liver histopathology by Receiver Operating Characteristic (ROC) analysis. To assess the relationship between biochemical and morphologic changes in the absence of hepatocellular necrosis, a second ROC analysis was performed on a subset of rats ($n = 2504$) given treatments ($n = 152$) that did not cause hepatocellular necrosis. In the initial analysis, ALT, AST, Tbili, and SBA had the greatest diagnostic utility for manifestations of hepatocellular necrosis and biliary injury, with comparable magnitude of area under the ROC curve and serum hepatobiliary marker changes for both. In the absence of hepatocellular necrosis, ALT increases were observed with biochemical or morphologic evidence of cholestasis. In both analyses, diagnostic utility of ALP and GGT for biliary injury was limited; however, ALP had modest diagnostic value for peroxisome proliferation, and ALT, AST, and total Chol had moderate diagnostic utility for phospholipidosis. None of the eight markers evaluated had diagnostic value for manifestations of hypertrophy, cytoplasmic rarefaction, inflammation, or lipidosis.

Key Words: **Receiver Operating Characteristic; hepatotoxicity; clinical chemistry; histopathology; ALT; AST; bilirubin; bile acids; ALP; GGT; rats.**

Clinical chemistry data are routinely used for noninvasive monitoring of liver disease in animals and humans; yet, the relationship between biochemical and morphologic changes during liver injury is often unclear. Although alanine aminotransferase (ALT) activity is most commonly used for clinical monitoring of liver injury in humans (Dufour *et al*., 2000a,b; Prati *et al*., 2002), ALT changes may fail to identify patients with minimal to mild liver pathology, and the magnitude of change in ALT or other hepatobiliary markers can have no relationship to the severity or prognosis of liver injury (Abraham and Furth, 1995; Aithal and Day, 1999; Dufour *et al*., 2000b; Kaplowitz, 2005; Pratt and Kaplan, 2000; Sturgill and Lambert, 1997). Similarly, discrepancies between clinical chemistry findings and liver histopathology can be seen in nonclinical toxicology studies, where marked changes in plasma or serum markers of hepatobiliary injury can occur in the absence of morphologic evidence of drug-induced liver injury and vice versa (Solter, 2005; Travlos *et al*., 1996; Wang *et al*., 1997).

During liver injury, differences in the magnitude of biochemical signals and morphologic changes may arise because of differences in temporal onset of these effects. In addition, histopathology may underestimate the severity of injury when hepatobiliary markers are early indicators of injury, have short circulating half-lives, or are depleted following an initial insult (Hoffman *et al*., 1999; Wang *et al*., 1997). Likewise, changes in hepatobiliary markers may be attributed to factors other than liver injury such as restraint (Landi *et al*., 1990; Nathwani *et al*., 2005b; Valentine *et al*., 1990), pharmacologically mediated effects on transporter function (Campbell *et al*., 2004; Zucker *et al*., 2001), or metabolism (Jackson *et al*., 2008; Jin *et al*., 2004; Sapolsky *et al*., 2000). Most importantly in both animals and humans, relating biochemical changes to liver histopathology can be confounded by the complexity of drug-induced liver injury because it often manifests as multiple histopathologic findings rather than discrete or isolated changes (Travlos *et al*., 1996; Tsui, 2003). As a result, biochemical changes often have to be

This work was presented at the national meeting of the American College of Veterinary Pathologists (Boston, MA, December, 2005), and at a Pharmaceutical Research and Manufacturers of America DruSafe meeting (Bethesda, MD, June, 2006).

interpreted in the context of combined rather than discrete morphologic findings.

Recently, data collected from a large number of acute toxicity studies from a hepatic toxicogenomics initiative at GlaxoSmithKline provided an opportunity to evaluate the relationship between biochemical and morphologic findings in the rat. Rats were given a variety of treatments including classic hepatotoxicants, other compounds known to elicit liver injury, nontoxic comparator compounds, or specialized diets. Hepatotoxicity was characterized using traditional biochemical parameters and histopathology.

The objective of this analysis was to characterize the relationship between biochemical and morphologic changes during subacute liver injury in the rat. Histopathologic changes were categorized by type of morphologic change and summarized for incidence and associated biochemical changes. Diagnostic performance of biochemical parameters was evaluated using Receiver Operating Characteristic (ROC) analysis. Because of the well-defined relationship between transaminase increases and hepatocellular necrosis, a second ROC analysis was performed in which rats given treatments that caused hepatocellular necrosis or degeneration were omitted to evaluate the relationship between biochemical changes and liver histopathologic findings other than hepatocellular degeneration/necrosis. Diagnostic accuracy was assessed using ROC data in parallel with magnitude of biomarker change for all markers for each type of hepatotoxic change in the presence and absence of hepatocellular necrosis.

MATERIALS AND METHODS

Animals. Male Crl:CD(SD)IGS BR Sprague Dawley rats were obtained from Charles River Laboratories (Wilmington, MA) at 7–8 weeks of age weighing approximately 225–275 g. The rats were housed individually in suspended wire mesh cages (at 18°C–26°C, relative humidity of 50 ± 20% on a 12-h light/12-h dark cycle), fed Certified Rodent Diet #8728C *ad libitum* (Harlan Teklad, Inc., Madison, WI), and acclimated for 4 days prior to randomization to a treatment group. All animal husbandry and experimental procedures were in accordance with the Guide for the Care and Use of Laboratory Animals (NIH Publication, 25, No. 28, 16 August 1996) and were approved by the Institutional Animal Care and Use Committee of the facility in which the studies were conducted.

Test articles. Test articles ($n = 182$) were selected to create a variety of manifestations of liver injury. These compounds included classic or "tool" hepatotoxicants, drugs, and dietary treatments known to elicit specific types of hepatic injury. In addition, subsets of rats were given nontoxic comparator compounds or corresponding vehicles only (Supplementary table 1). Selection of doses known to cause liver injury without lethality was based on literature review or historical experience. Test articles were obtained from Sigma–Aldrich (St Louis, MO) or provided by the sponsor, and dietary treatments were obtained from either Dyets, Inc. (Bethlehem, PA) or Research Diets (New Brunswick, NJ). Dose formulations were prepared daily within 24 h of administration, and dose concentrations were not adjusted for purity.

General study design. Treatments (generally three dose groups per treatment) were administered to rats ($n = 5$ per dose group) once daily for 4 or 14 days by oral gavage, intravenous, or intraperitoneal injection; dietary treatments were fed *ad libitum* for the same intervals of time. Rats were sacrificed by exsanguination under isofluorane anesthesia following an overnight fast on day 5 or 15, and blood was collected for measurement of clinical pathology parameters by cardiac puncture at necropsy. Clinical chemistry parameters including serum ALT, aspartate aminotransferase (AST), total alkaline phosphatase (ALP), and gamma glutamyl transferase activities (GGT); total bilirubin (Tbili), serum bile acids (SBA), and cholesterol (Chol); and triglycerides (Trig), urea nitrogen, creatinine, albumin, calcium, inorganic phosphorus, sodium, potassium, chloride, and glucose were measured on a Hitachi 911 (Boehringer Mannheim, Indianapolis, IN). Only ALT, AST, Tbili, SBA, ALP, GGT, Trig, and Chol data are presented in the current report.

Livers were weighed, and longitudinal slices were then collected from the center of the left lateral lobe, fixed in 10% neutral buffered formalin, trimmed, processed to paraffin sections, and stained with hematoxylin and eosin. All microscopic evaluation was performed by one pathologist (D.E.) and peer reviewed by another (S.R.) using interpretive criteria and diagnoses routinely employed in nonclinical studies. Liver histopathology was assessed with knowledge of liver weights and treatment group but without knowledge of clinical chemistry data.

Transmission electron microscopy (TEM) was performed on selected livers. Samples of formalin-fixed liver were minced into ~1 mm^3 pieces, fixed with 2.5% glutaraldehyde in 0.1M cacodylate buffer, postfixed with 1% osmium, dehydrated with a graded series of ethanols, and embedded in epoxy resin. Sections approximately 90 nm thick were cut and collected on copper grids, stained with uranyl acetate and lead citrate, and examined.

Selectively, special histochemical stains were applied and included Masson's trichrome, Perl's iron, and Hall's stain for collagen, ferric iron, and bilirubin, respectively. In addition, immunohistochemistry for lysosome-associated membrane protein-2 (LAMP-2), a lysosomal outer membrane glycoprotein, was performed for qualitative evaluation of phospholipidosis on the Ventana Discovery System (Ventana Medical Systems, Tucson, AZ). Briefly, formalin-fixed paraffin-embedded sections were deparaffinized, rehydrated, blocked, and stained with a rabbit anti-LAMP-2 antibody (Zymed Laboratories, Carlsbad, CA) labeled with rabbit Ultra MAP-HRP polymer (Ventana Medical Systems). Staining was detected with 3,3′ diaminobenzidine and counterstained with hematoxylin. Isotype-matched immunoglobulin G (Southern Biotechnology, Birmingham, AL) and omission of the primary antibody were used as negative controls.

Data analysis. Clinical chemistry and histopathology data were processed prior to analysis as outlined in Figure 1. Clinical chemistry parameters, except for GGT, were normalized to the respective control mean and expressed as the fold change of each individual or group mean value relative to the concurrent control mean. Absolute rather than normalized values were used for performance evaluation of GGT as serum GGT values are inherently low in the rat (Huseby *et al.*, 1992; Lahrichi *et al.*, 1982).

Histopathologic findings were assigned by predominant process into different categories of injury (Table 1). When multiple findings related to a specific pathologic process were identified in an individual rat, only the finding of greatest severity for that process was recorded to avoid redundancy. Common spontaneous findings of periportal hepatocellular vacuolation and random multifocal or single cell hepatocellular necrosis, for which incidence in controls can be highly variable across studies, were assessed within treatments for dose response. These findings were considered treatment related when present with greater incidence and/or severity in treated rats than in concurrent controls. Only treatment-related findings were included in the data analyses. Finally, because of the strong association between hepatocellular necrosis or degeneration with changes in ALT and other markers (Abboud and Kaplowitz, 2007; Zimmerman, 2000), rats given treatments that caused hepatocellular necrosis or degeneration were excluded from a second analysis performed to evaluate the relationship between biochemical changes and other types of injury in the absence of hepatocellular necrosis. Specifically, rats with zonal or single cell hepatocellular necrosis or degeneration, or treatment-related single cell or random multifocal coagulative necrosis were identified. All rats from treatments with these findings

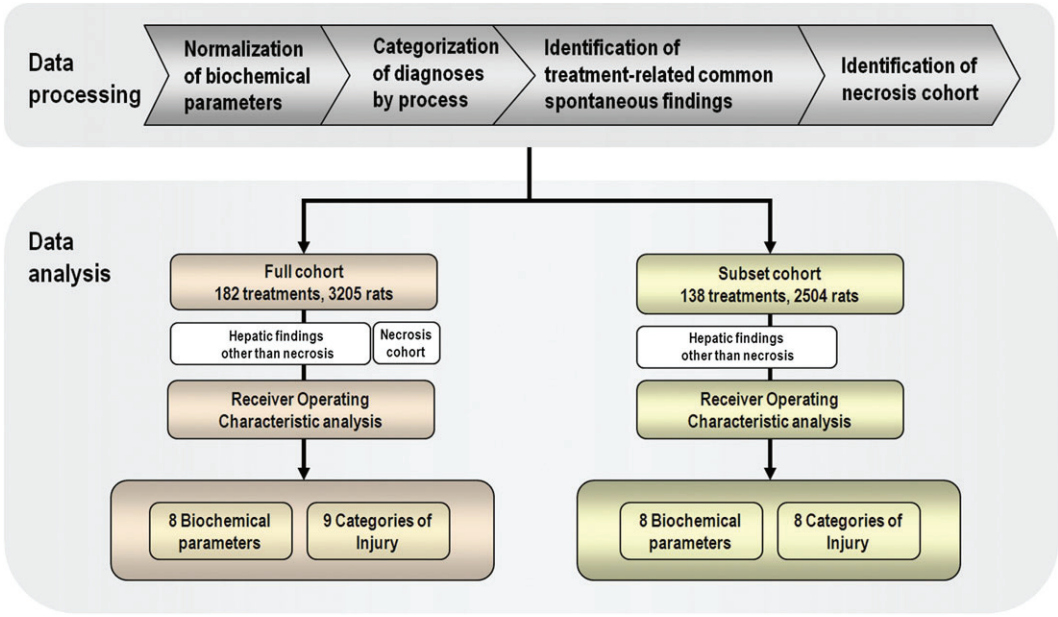

FIG. 1. Data processing and analysis. Clinical pathology data were normalized to control mean, and morphologic diagnoses were grouped by category of injury. Common spontaneous findings were considered to be associated with treatment if present with greater incidence and/or severity than concurrent control. Rats given treatments that caused hepatocellular necrosis and rats with spontaneous or non–dose-related hepatocellular necrosis were grouped into a Necrosis cohort that was omitted from the Subset cohort. In the Full or comprehensive analysis, all rats from all treatments were evaluated using ROC analysis; the Subset ROC analysis was restricted to rats remaining after removal of the necrosis cohort.

($n = 608$ from 44 treatments) and all rats with spontaneous random multifocal or single cell hepatocellular necrosis ($n = 93$ rats given 67 treatments) were included in a necrosis cohort ($n = 701$) that was omitted from the second or subset ROC analysis.

Morphologic data were compared with biochemical data for the full and subset cohorts by both categories of injury and as specific morphologic diagnoses. Data for individual morphologic diagnoses were compared with categorical data, and only summary data for morphologic diagnoses that differed from their respective categories of injury and were of sufficient prevalence (i.e., present in 25 or more rats) are detailed further. Throughout the text, categorical data are indicated by upper case and morphologic diagnoses are represented by lower case.

Diagnostic performance of clinical chemistry parameters was evaluated for all morphologic diagnoses and categories of injury by ROC analysis. ROC curves plot the true-positive fraction (sensitivity) on the *y*-axis as a function of the false-positive fraction (1-specificity) on the *x*-axis for all values of a biochemical test at all possible test decision thresholds versus a definitive reference standard. Here, clinical chemistry data were evaluated against histopathology as reference standard, and histopathology findings were used as a binary or dichotomous endpoint, indicating the presence or absence of a specific morphology. ROC analyses were performed in R (Ihaka and Gentleman, 1996; http://www.R-project.org).

The area under the ROC curve (AUC) is widely used as an estimate of the accuracy of a diagnostic test for classification of disease state (Hanley and McNeil, 1982; Pepe *et al.*, 2004; Poynard *et al.*, 2007; Zweig and Campbell, 1993). A diagnostic test with an AUC of 1 is considered to be a perfect test, whereas a test with an AUC of 0.5 indicates a random or nondiagnostic test result. In general, diagnostic tests with AUC values between 0.7 and 0.9 are considered to be of moderate diagnostic accuracy (Gardner and Greiner, 2006; Swets, 1982). Within the current data set, an AUC ≥ 0.75 was significantly different from an AUC of 0.5 based on a Bonferroni adjustment for multiplicity and was therefore considered indicative of a diagnostic test. The nonparametric method of DeLong *et al.* (1988) was used to compute AUC values and evaluate statistical significance for each of the clinical chemistry parameters as predictors of liver injury. This methodology was also used to compare AUC data between clinical chemistry parameters for each category or morphologic diagnosis of liver injury. The incremental diagnostic value for all possible combinations of all eight biochemical parameters was evaluated by ROC analysis for both the full and the subset cohort. Statistical significance was defined as $p \leq 0.05$.

RESULTS

Type and Incidence of Morphologic Findings

Diverse manifestations of liver injury covering the broad spectrum of hepatotoxicity in the rat were observed (Table 1, Fig. 2). Liver injury ranged from no or minimal evidence of liver injury in approximately half of the rats to severe hepatotoxicity involving multiple pathologic processes in smaller subsets of rats (Fig. 2B–D). In general, as the severity of hepatotoxic injury increased, complexity of injury based on number of concurrent morphologic diagnoses increased in parallel. Similarly, following removal of the necrosis cohort, complexity of injury decreased for all categories in the subset cohort where the largest impact, indicated by effect on animal number, was observed for rats with Biliary Change or Fibrosis, with lesser impact for manifestations of Hypertrophy, Peroxisome Proliferation, or Lipidosis. For specific morphologic diagnoses, no rats with macrovesicular vacuolation remained following removal of the necrosis cohort, and the incidences of mixed portal inflammation and centrilobular mononuclear

TABLE 1
Prevalence of Liver Injury by Category and Morphologic Diagnosis

Category	Full cohort	Subset cohort	Morphologic diagnosis	Full cohort	Subset cohort
Hepatocellular necrosis	**281**				
Zonal necrosis	**181**				
Centrilobular necrosis	154		Degeneration, centrilobular	41	
			Necrosis, single cell, centrilobular	35	
			Necrosis, centrilobular	78	
Periportal necrosis	27		Degeneration, ballooning, periportal	10	
			Necrosis, single cell, periportal	3	
			Necrosis, periportal	14	
Nonzonal necrosis	**100**		Necrosis, random multifocal, or single cell	82	
			Degeneration, ballooning	3	
			Hydropic change	8	
			Necrosis, subcapsular	7	
Lipidosis	**530**	**328**	Vacuolation, NOS	325	198
			Vacuolation, periportal/midzonal	257	165
			Vacuolation, panlobular	51	25
			Vacuolation, centrilobular	17	8
			Vacuolation, microvesicular, NOS	104	63
			Vacuolation, macrovesicular	30	0
			Vacuolation, mixed	58	54
			Vacuolation, Kupffer cell, NOS	13	13
Phospholipidosis	**40**	**28**	Vacuolation, microvesicular	40	28
			Biliary epithelial vacuolation/hypertrophy	15	7
			Vacuolation, Kupffer cell	11	15
Inflammation	**405**	**177**	Kupffer cell hypertrophy/hyperplasia	193	119
			Portal inflammation, mixed	100	27
			Centrilobular inflammation, mononuclear	77	5
			Capsulitis/fibrinous peritonitis	36	19
			Portal inflammation, lymphocytic	23	21
			Portal inflammation, mononuclear	23	7
Hypertrophy	**395**	**256**	Hypertrophy, panlobular, hepatocellular	253	155
			Cytoplasmic alteration, eosinophilic, homogeneous	28	8
			Hypertrophy, periportal	73	37
			Hypertrophy, centrilobular	69	64
Cytoplasmic change	**192**	**101**	Glycogen accumulation, panlobular	98	64
			Cytoplasmic alteration, basophilia	88	32
			Cytoplasmic inclusion, basophilic	6	5
Fibrosis	**141**	**20**	Fibrosis, portal	67	14
			Fibrosis, centrilobular	59	0
			Fibrosis, subcapsular	15	6
Biliary change	**126**	**19**	Biliary hyperplasia	68	9
			Biliary degeneration with regeneration	58	10
			Biliary necrosis	8	0
			Ductular bile stasis	2	0
Peroxisome proliferation	**133**	**114**	Cytoplasmic alteration, granular, eosinophilic		
Other	**364**	**210**	Increased hepatocellular mitoses	342	199
			Extramedullary hematopoiesis	27	16
			Vasculopathy, portal	10	3

Note. Summary incidence of treatment-related findings by animal number (*n*) for each category and morphologic diagnosis in the full and subset cohorts. Categories and subcategories of injury are listed in bold font, morphologic diagnoses within categories are unbolded. With exception of zonal necrosis for which diagnoses are listed in increasing order of severity, morphologic diagnoses are listed in decreasing order of prevalence and secondary morphologic diagnoses are offset right. Primary morphologic diagnoses were mutually exclusive within categories of injury other than for the inflammation or other categories, for which multiple findings could be observed within the same rat. NOS, not otherwise specified.

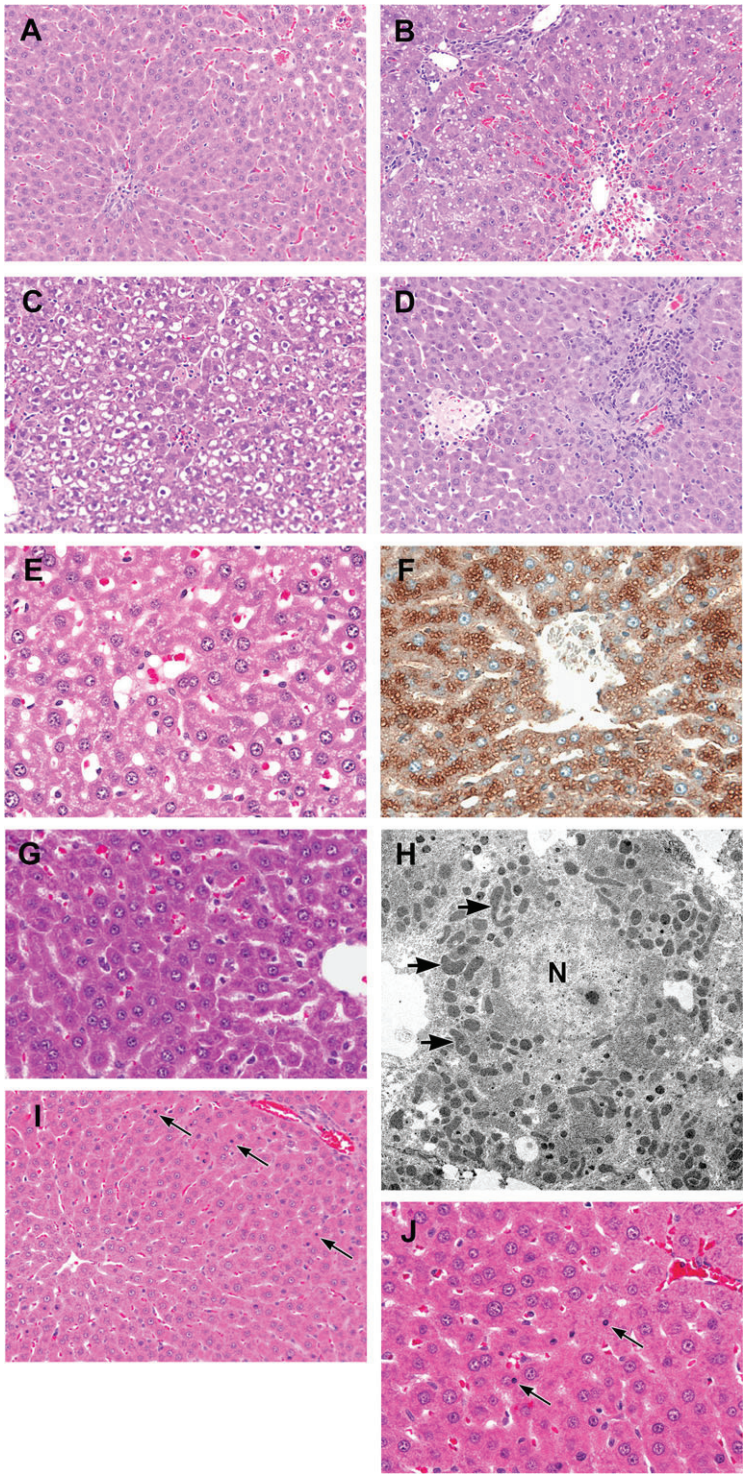

FIG. 2. Histopathology of liver. Control liver, ×20 (A). Centrilobular necrosis and hemorrhage with periportal vacuolation. Dimethylnitrosamine, 10 mg/kg, ×20 objective (B). Cytoplasmic rarefaction with single-cell necrosis. Dexamethasone, 80 mg/kg[1], ×20 objective (C). Biliary hyperplasia with portal fibrosis and inflammation with focal coagulative necrosis (bile infarct). diaminodiphenyl methane, 50 mg/kg, ×20 objective (D). Panlobular microvesicular hepatocellular vacuolation confirmed as hepatic phospholipidosis by TEM. Maprotilene, 300 mg/kg, ×20 objective (E). LAMP-2 immunoreactivity of hepatocellular vacuoles in hepatic phospholipidosis (confirmed by transmission electron microscopy). Amiodarone, 300 mg/kg for 14 days, ×10 objective (F). Basophilic cytoplasmic alteration. Piroxicam, 50 mg/kg, ×20 objective (G), Increased number and pleomorphic mitochondria (arrows, transmission electron microscopy). Piroxicam, 50 mg/kg, ×3800 (H). Basophilic cytoplasmic hepatocellular inclusions (arrows). Methylcarbamate, 1000 mg/kg, ×10 objective (i), ×40 objective (I, J). [1]Dose duration of 4 days and all slides stained with hematoxylin and eosin unless otherwise specified.

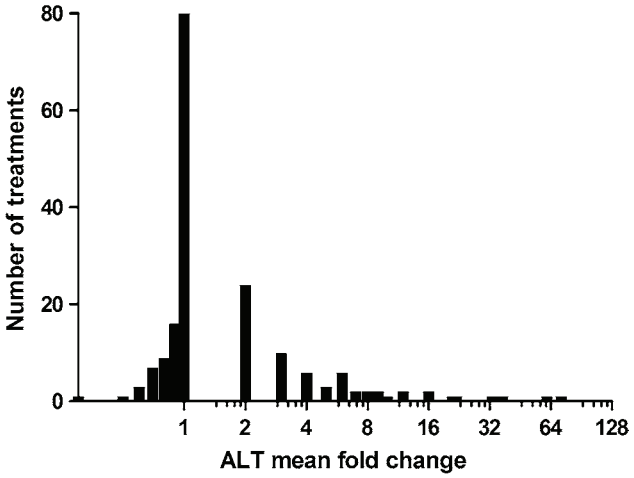

FIG. 3. Frequency distribution of mean ALT changes across treatments.

inflammation were considerably decreased in the subset cohort (Table 1). Because histopathologic evaluation was performed using diagnostic criteria and nomenclature commonly used in nonclinical safety evaluation, only findings requiring additional clarification are discussed below.

Hepatocellular necrosis or degeneration was subdivided into zonal (specifically centrilobular or periportal) and nonzonal (i.e., diffuse or random multifocal) necrosis. Zonal necrosis was the most prevalent type of hepatocellular necrosis, and centrilobular necrosis (Fig. 2B) was more common than periportal necrosis. Manifestations of nonzonal hepatocellular necrosis or degeneration included dose-responsive single cell (Fig. 2C) or focal hepatocellular necrosis (Fig. 2D), ballooning degeneration characterized by hepatocellular swelling and degeneration, hydropic degeneration, and subcapsular necrosis.

Hepatic lipidosis, identified as hepatocellular vacuolation, was subcategorized as vacuolation not otherwise specified (NOS), microvesicular, macrovesicular, or mixed. Vacuolation NOS, characterized by the presence of few small cytoplasmic vacuoles within hepatocytes, was most common. Periportal hepatocellular vacuolation NOS (Fig. 2B) was one of the most common histologic findings in this study ($n = 333$) and was especially prevalent in both control and treated rats in studies where Labrafil was used as a vehicle. However, when evaluated for relationship to treatment based on dose-responsive increase in incidence and/or severity relative to concurrent controls, treatment-related periportal vacuolation was identified in less than 20% of these rats ($n = 63$). Microvesicular vacuolation, characterized by the presence of multiple, small cytoplasmic vacuoles, was due to phospholipidosis in a subset of rats based on transmission electron microscopy, characteristic morphology, and immunoreactivity for LAMP-2 (Fig. 2E and 2F; Obert *et al*., 2007). In this subset, hepatocellular microvesicular vacuolation was often accompanied by biliary and/or Kupffer cell vacuolation. Biliary vacuolation was always associated with phospholipidosis; however, Kupffer cell vacuolation was also identified in a subset of rats with no evidence of phospholipidosis. Macrovesicular vacuolation, characterized by the presence of single large vacuoles which displaced and/or compressed hepatocellular nuclei, was observed in rats given carbon tetrachloride and chloroform, often in association with centrilobular necrosis. Mixed hepatocellular vacuolation, identified by cytoplasmic vacuolation with both multiple, small vacuoles and discrete, larger vacuoles, was primarily identified in rats given dietary treatments, particularly the Surwitt diet, and to a lesser extent the Lombardi choline–deficient and L-amino acid–defined diets.

Homogeneous eosinophilic hepatocellular cytoplasmic alteration, interpreted as hypertrophy or proliferation of smooth endoplasmic reticulum, was included within the hypertrophy category because it was, with exception of a small number of rats given rotenone or microcystin, uniformly associated with panlobular hepatocellular hypertrophy.

Glycogen accumulation, which manifested as cytoplasmic rarefaction, was the predominant finding in the Cytoplasmic Change category (Fig. 2C). Basophilic cytoplasmic hepatocellular alteration, identified as diffuse cytoplasmic basophilia by light microscopy (Fig. 2G), is typically seen in association with proliferation of rough endoplasmic reticulum but was associated with increased cytoplasmic content of enlarged and pleomorphic mitochondria in rats given piroxicam or diclofenac that were examined by transmission electron microscopy (Fig. 2H). Basophilic cytoplasmic inclusions were observed in a small number of rats given methyl carbamate (Fig. 2I and 2J). These inclusions were previously identified as Feulgen-positive nucleolar remnants (Quest *et al*., 1987).

Biliary changes were relatively infrequent. Biliary hyperplasia was often seen in the absence of evidence of biliary epithelial damage, whereas biliary degeneration or necrosis was uniformly associated with either regeneration or hyperplasia of biliary epithelia. Biliary degeneration with regeneration was characterized by loss of ductular architecture and cytoplasmic basophilia, often with mitotic activity, and either attenuation or swelling of epithelia (Fig. 2D). Overt biliary necrosis, identified as diffuse coagulative necrosis of interlobular bile ducts, was only seen in rats given α-napthylisothiocyanate or diaminodiphenyl methane. Biliary epithelial changes were variably associated with portal fibrosis and inflammation but were highly associated with hepatocellular necrosis, as indicated by the marked decrease in number of rats in the Biliary Change category following removal of the necrosis cohort. Bile stasis was rare, consistent with other reports for rat, and in contrast to other preclinical species (Cattley and Popp, 2002; Travlos *et al*., 1996).

Other findings included increased hepatocellular mitoses, most commonly associated with hepatocellular necrosis, hypertrophy, or peroxisome proliferation; increased extramedullary hematopoiesis; and vasculopathy, primarily involving vasculature of the larger or septal biliary tracts.

TABLE 2
Clinical Chemistry Changes for Hepatocellular Degeneration or Necrosis

	n	ALT	AST	Tbili	SBA	ALP	GGT	Chol	Trig
Hepatocellular necrosis	281	7.8 (15)	4.9 (7.5)	8.4 (26)	5.7 (12.2)	1.5 (1)	1.9 (4.9)	1.8 (1.1)	2.6 (12.2)
		2.9	2.5	2	2.1	1.2	0	1.5	1.3
Zonal necrosis	181	9 (18)	5.4 (8.1)	9.8 (30)	6.3 (10.6)	1.5 (0.9)	1.8 (3.5)	1.9 (1.2)	3.1 (15)
		3.5	2.8	2.9	2.9	1.3	0	1.6	1.1
Centrilobular necrosis	154	8.9 (19)	5.2 (8.4)	10 (32)	6.5 (11.2)	1.5 (0.9)	1.6 (3.6)	1.8 (1.3)	3.5 (17)
		2.9	2.6	2.5	2.6	1.3	0	1.6	1.3
Periportal necrosis	27	10 (10.5)	6.6 (5.7)	8.7 (13)	5.5 (5.3)	1.6 (0.6)	2.5 (3.3)	2.2 (0.9)	1.4 (1.1)
		7.1	5.3	3.3	3.6	1.6	2	2.3	1.1
Nonzonal necrosis	100	5.5 (8.2)	3.9 (6.2)	5.7 (16.9)	4.4 (14.7)	1.3 (1.1)	2.1 (6.7)	1.6 (0.9)	1.7 (1.7)
		2	2.1	1.7	1.7	1	0	1.4	1.3

Note. Clinical chemistry data are expressed as mean (SD) and median of the mean fold change relative to the concurrent control mean for each parameter.

Characterization of Biochemical Findings

Both incidence and severity of liver histopathologic findings were reflected in the distribution and magnitude of clinical chemistry changes observed. Serum ALT activity was used as a biochemical index of liver injury to characterize distribution of the biochemical changes, as ALT is considered to be the most sensitive and specific indicator of hepatic injury in preclinical species (Amacher, 1998; Boone *et al*., 2005). Based on the mean ALT values for each treatment, the frequency distribution of ALT changes (Fig. 3) was skewed toward the left with a long right hand tail because the majority (77%) of treatments had less than twofold increases in ALT at the highest dose (mean (SD) 1.1 (0.3), median 1.07). Nearly half of all treatments had no increase in ALT, and many treatments had overt decreases in ALT. Of these, the largest decreases in serum ALT activities were observed in rats given treatments known to interfere with pyridoxal-5′-phosphate metabolism such as hydrazine, isoniazid, or the pyridoxine-deficient diet. For the remaining treatments, approximately 9% had ALT increases between two- and fivefold (3.1 (0.8), 2.8), 8% had ALT increases of 5- to 10-fold (7.3 (1.5), 6.9), and 6% had ALT increases of more than 10-fold control mean (30.1 (14.9), 21.4).

ALT and AST Are Increased in Association with Tbili and SBA during Hepatocellular Necrosis

Increases in ALT uniformly exceeded AST increases for manifestations of hepatocellular necrosis. Transaminase increases were largest for rats with zonal necrosis, and increases for periportal necrosis were larger than for centrilobular necrosis (Table 2). For both centrilobular and periportal necrosis, ALT and AST increases were generally associated with comparable increases in both Tbili and SBA but with only minimal changes in ALP, GGT, total Chol, and/or Trig (Table 2). Concurrent biliary pathology was identified in the majority of rats with periportal necrosis (92%) and in a moderate number of rats with nonzonal necrosis (41%, Fig. 4). Biliary morphologic changes were identified in less than 14% of rats with centrilobular necrosis; however, the largest increases in Tbili and SBA generally occurred in rats with concomitant centrilobular necrosis and biliary pathology.

Hepatobiliary Marker Changes for Hepatic Injury Other Than Necrosis

In the full cohort, increases in ALT, AST, Tbili, and SBA for Biliary Change and Fibrosis and increases in ALT, AST, and Chol for Phospholipidosis were of comparable magnitude to increases seen for hepatocellular necrosis or degeneration and generally exceeded increases seen for all other categories of liver injury (Table 3). Minimal increases in ALP and GGT were observed for rats with Biliary Change or Fibrosis.

Removal of the necrosis cohort significantly decreased both magnitude and variability of hepatobiliary marker changes for all categories of liver injury. With the exception of Phospholipidosis, where increases in AST, total Chol, and to a lesser extent ALT were sustained, and Biliary Change, where modest increases in ALT, AST, Tbili, and total Chol persisted following removal of the necrosis cohort, magnitude and variability of hepatobiliary marker changes were significantly decreased and were generally comparable to control values for all other categories of injury in the subset cohort.

For individual morphologic diagnoses, hepatobiliary marker changes were generally comparable in both magnitude and variability to changes observed for each respective category of injury with few exceptions (Supplementary table 2). Most notably, although modest increases in all eight hepatobiliary markers were observed for Hypertrophy, hepatobiliary marker data for centrilobular hypertrophy were comparable to controls in both the full and subset cohorts. In contrast, for periportal hypertrophy, modest increases of considerable variability were observed for ALT and SBA in the full cohort, whereas total Chol was markedly decreased

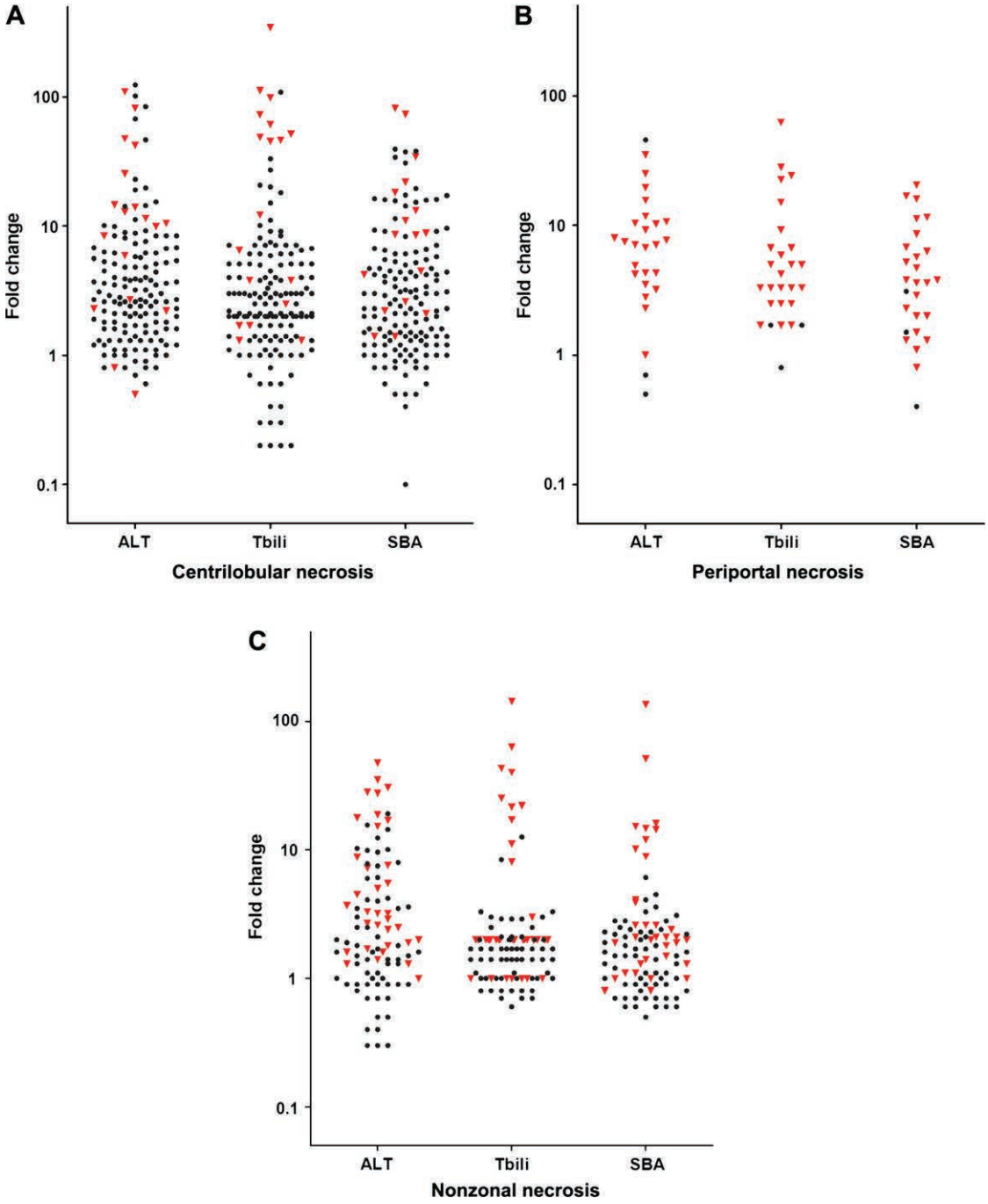

FIG. 4. Scatter plot of ALT, Tbili, and SBA values for rats with hepatocellular necrosis or degeneration. Biomarker values for rats with centrilobular (A), periportal (B), or nonzonal necrosis (C) are presented as fold change relative to control mean. For manifestations of necrosis, inverted red triangles represent rats with concurrent hepatocellular necrosis and biliary pathology.

relative to both categorical and concurrent control values in the subset cohort. For Lipidosis, increases in ALT, AST, Tbili, and SBA for rats with panlobular vacuolation NOS were larger than categorical changes for the full cohort but were comparable to categorical or control data for the subset cohort. Hepatobiliary changes for rats with periportal vacuolation NOS or mixed vacuolation in both the full and subset cohort were of lower magnitude or comparable to control data. For Inflammation, ALT, AST, Tbili, SBA, and Chol increases for mixed portal inflammation exceeded corresponding categorical changes in the full cohort but were comparable in the subset cohort. For Cytoplasmic Change, increases in ALT, AST, Tbili, SBA, and Trig for

TABLE 3
Clinical Chemistry Changes by Category of Injury

	Hepatocellular Necrosis		Biliary Change		Fibrosis		Hypertrophy		Inflammation		Cytoplasmic Change		Peroxisome Proliferation		Lipidosis		Phospholipidosis		Other	
Full (*n*)	**281**		**126**		**141**		**395**		**405**		**192**		**133**		**530**		**40**		**364**	
Subset (*n*)	n/a		19		20		256		177		101		114		328		28		210	
ALT	**7.8 (15)**	2.9	**9 (14.5)**	4.2	**7.8 (15)**	2.7	**3.3 (10)**	1.2	**3.9 (9.2)**	1.2	**3.6 (9.6)**	1.2	**1.2 (0.6)**	1	**2.2 (4.8)**	1	**6.4 (10)**	3.2	**3.4 (10.5)**	1.1
			3.4 (2.6)*	2.2	2.3 (2.2)*	1.1	1.4 (1.1)*	1.1	1.5 (2.3)*	0.9	1.1 (0.7)*	0.9	1.1 (0.4)*	1	1.2 (1.4)*	0.9	3.8 (3.4)*	3.2	1.2 (1.7)*	1
AST	**4.9 (7.5)**	2.5	**5.6 (6.7)**	3.1	**4.4 (6.1)**	2.3	**2.6 (5.3)**	1.3	**3 (5.1)**	1.3	**2.3 (3.5)**	1.4	**1.5 (2.2)**	1.1	**2 (3.2)**	1.1	**4.8 (5.1)**	3.1	**2.5 (5.4)**	1.2
			3.7 (3)*	2.2	2.3 (2.2)*	1.2	1.4 (1.2)*	1.1	1.5 (1.6)*	1	1.3 (0.7)*	1.1	1.2 (0.6)*	1.1	1.4 (1.8)*	1	4.4 (5)	2.5	1.3 (1.1)*	1
Tbili	**8.4 (26)**	2	**13 (37)**	2	**12 (36)**	2	**3.8 (19)**	1.4	**5.1 (21)**	1	**6.1 (29)**	1.2	**1.9 (4.7)**	1	**1.9 (4.9)**	1	**1.7 (1.4)**	1.1	**2.9 (7.8)**	1
			2 (1.1)*	2	1.8 (1.2)*	2	1.6 (1.1)*	1	1.2 (0.6)*	1	1.5 (1.2)*	1	1.3 (0.6)*	1	1.3 (0.9)*	1	1.8 (1.6)	1.1	1.3 (0.9)*	1
SBA	**5.7 (12)**	2.1	**7.2 (16)**	2.3	**6.2 (15)**	2.2	**2.4 (4.8)**	1.1	**3.3 (8.6)**	1.2	**3.3 (11)**	1.1	**1 (0.8)**	0.8	**1.6 (1.8)**	1	**1.2 (0.5)**	1	**3.1 (7.6)**	1.1
			2.5 (2.7)*	1.2	2.2 (2.6)*	1	1.2 (1)*	0.9	1.4 (1.9)*	0.9	1.2 (1.4)*	0.8	1 (0.8)**	0.9	1.3 (1.9)*	0.8	1.1 (0.5)	1	1.4 (1.8)*	0.9
ALP	**1.5 (1)**	1.2	**1.7 (1.3)**	1.3	**1.7 (1.3)**	1.2	**1.3 (0.6)**	1.2	**1.2 (0.9)**	1	**1.3 (1)**	1	**1.3 (0.4)**	1.2	**1.1 (0.4)**	1	**1.2 (0.5)**	1	**1.3 (0.5)**	1.1
			1.2 (0.4)*	1	1.1 (0.4)*	1	1.2 (0.5)**	1.1	1 (0.3)*	0.9	1.3 (0.6)	1.1	1.3 (0.3)*	1.2	1 (0.3)*	0.9	1.2 (0.6)	1	1.1 (0.4)*	1
GGT	**1.9 (4.9)**	0	**1.5 (3)**	0	**1.8 (3.6)**	0	**1.3 (4.4)**	0	**1.5 (6.8)**	0	**2.2 (8.7)**	0	**0.7 (8)**	0	**0.4 (1.9)**	0	**0.4 (0.6)**	0	**1.3 (6.2)**	0
			0.3 (0.6)*	0	0.4 (0.6)*	0	0.7 (2.3)*	0	1.3 (9)	0	2.7 (11)	0	0.9 (8.7)	0	0.1 (0.4)*	0	0.2 (0.4)*	0	0.8 (6.6)**	0
Chol	**1.8 (1.1)**	1.5	**2.1 (1.1)**	1.8	**2.2 (1.2)**	1.8	**1.3 (0.9)**	1.2	**1.4 (0.8)**	1.2	**1.4 (0.9)**	1.3	**0.9 (0.4)**	0.8	**1.3 (0.7)**	1.1	**1.5 (0.7)**	1.5	**1.3 (0.9)**	1.1
			1.8 (0.6)**	1.6	1.5 (0.5)*	1.4	1.1 (0.7)*	1.1	1.2 (0.5)*	1.2	1.1 (0.6)*	1.1	0.9 (0.3)	0.8	1.2 (0.5)**	1.1	1.8 (0.6)*	1.8	1 (0.5)*	1
Trig	**2.6 (12)**	1.3	**3.8 (17)**	1.1	**3.5 (17)**	1.1	**2.1 (10)**	0.9	**2.1 (10)**	1.1	**3.4 (15)**	1.6	**1.4 (2.2)**	0.9	**1.1 (1.1)**	0.9	**0.9 (0.4)**	1	**1.3 (1.4)**	1
			0.9 (0.2)*	0.8	1 (0.3)*	0.9	1.1 (0.9)*	0.9	1.1 (0.6)*	1	1.6 (1.1)*	1.5	1.1 (0.8)*	0.9	1 (0.6)*	0.9	0.9 (0.4)	1.1	1.1 (0.6)*	0.9

Note. Biochemical data are summarized by category for all rats (Full, in bold font) and rats remaining following removal of the necrosis cohort (Subset, in unbold font). All parameters with exception of GGT are expressed as the mean (SD) of the mean fold change of the concurrent control mean; GGT data are expressed as the mean of absolute or individual GGT values. Median values are provided to context variability in hepatobiliary marker data. n/a, not applicable. Statistically significant differences are indicated by $*p \leq 0.001$ and $**p \leq 0.05$ for Subset versus Full cohort.

TABLE 4
ALT and Other Hepatobiliary Marker Changes in the Absence of Hepatocellular Necrosis

	n	ALT	Tbili	SBA	ALP
Cholestasis	**33**	**6 (4)**	**3.1 (2.9)**	**2.1 (2.4)**	**1.4 (0.6)**
		5.0	**2.0**	**1.3**	**1.3**
Phospholipidosis	12	6.6 (3.5)	3.5 (2.1)	2.2 (2.2)	1.6 (0.8)
		5.9	2	1.4	1.4
Other histologic findings	13	6.1 (5.7)	2.2 (1.3)	2.9 (3.5)	1.4 (0.5)
		4.5	2	1.6	1.2
No histologic findings	8	5.3 (1.9)	6.1 (4.7)	1.6 (0.9)	1.3 (0.6)
		4.9	4.0	1.2	1.0
No cholestasis	17	**4.8 (2.3)**	**1.1 (0.4)**	**1.1 (0.4)**	**1 (0.3)**
		3.9	1	1	0.9
Phospholipidosis	5	5.2 (1.7)	1 (0)	1.2 (0.2)	1.1 (0.3)
		5.1	1.0	1.2	1.0
Other histologic findings	9	5 (2.9)	1.1 (0.5)	1.1 (0.5)	0.9 (0.3)
		4.0	1.0	1.0	0.8
No histologic findings	3	3.4 (0.4)	1.3 (0.2)	0.8 (0.2)	0.9 (0.1)
		3.4	1.3	0.8	0.9

Note. Hepatobiliary marker changes for rats with ALT increases ≥ threefold of control mean ($n = 50$) and no microscopic evidence of hepatocellular necrosis; marker changes are expressed as mean (SD) and median fold change relative to concurrent control mean. Rats are subcategorized into Cholestasis or No cholestasis cohorts based on the presence of ≥ twofold increases in Tbili, SBA and/or ALP for cholestasis ($n = 33$), or no biochemical or morphologic evidence of cholestasis in the presence or absence of other histologic findings for No cholestasis ($n = 17$). Summary data for Cholestasis and No cholestasis cohorts are listed in bold font.

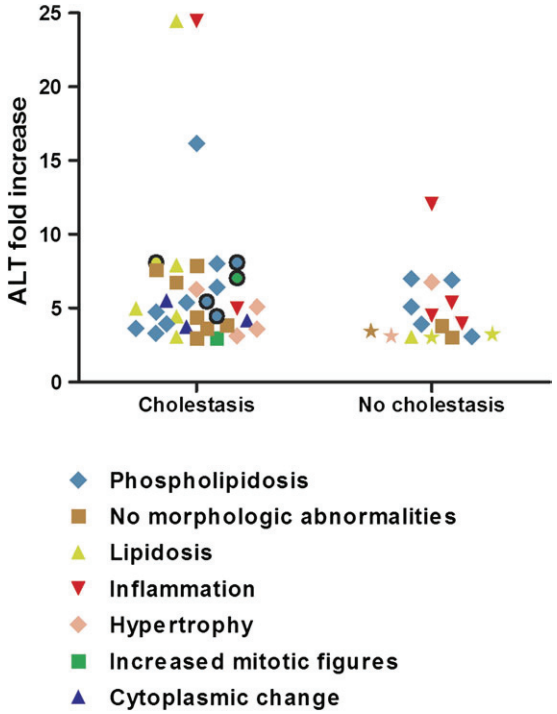

FIG. 5. ALT increases in the absence of hepatocellular necrosis. Scatter plot of ALT values for rats with ≥ threefold increases in ALT and no morphologic evidence of necrosis, which were given treatments that did not cause necrosis ($n = 50$ rats, 26 unique treatments). Rats are subdivided by predominant finding into categories of Cholestasis (based on the presence of ≥ twofold increases in Tbili, SBA and/or ALP), and No cholestasis (rats without cholestasis but with other or no morphologic findings). The predominant findings for each rat are indicated by the color of the symbol; secondary findings of biliary pathology and < twofold increases in ALP are indicated by the circular and star-shaped symbols, respectively.

cytoplasmic rarefaction/glycogen accumulation were smaller than categorical increases for the full cohort, whereas increases for rats with basophilic cytoplasmic alteration exceeded corresponding categorical changes. With exception of Trig for rats with basophilic cytoplasmic alteration in the subset cohort, values for these markers were comparable to control and categorical values in the subset cohort. Collectively, these data suggest that in the absence of hepatocellular necrosis or degeneration, manifestations of hypertrophy, lipidosis, hepatic inflammation, or hepatocellular cytoplasmic change are generally not associated with remarkable changes in these traditional hepatobiliary markers.

Cholestasis Can Occur with ALT Increases in the Absence of Hepatocellular Necrosis or Degeneration

When biochemical changes were evaluated for rats which had no morphologic evidence of hepatocellular necrosis and which were given treatments that did not cause hepatocellular necrosis, ALT increases of more than threefold of control occurred in approximately 2% of the rats (Table 4, Fig. 5). Of these, the majority (66%) had biochemical evidence of cholestasis based on the presence of more than twofold increases in Tbili, SBA, and/or ALP. Whereas increases in Tbili were greatest in rats with cholestasis and no histologic abnormalities, the largest ALT increases occurred in rats with concurrent phospholipidosis and cholestasis (data not shown). Cholestasis was primarily associated with phospholipidosis and/or biliary pathology, and less commonly with hypertrophy, lipidosis, glycogen accumulation, or parenchymal inflammation. For rats without cholestasis, ALT increases were generally of lower magnitude and primarily associated with phospholipidosis, parenchymal inflammation, or lipidosis. Several rats had mild increases in ALP (≤ 1.7-fold) that were associated with peroxisome proliferation, lipidosis, or no morphologic abnormalities. These findings suggest that in the absence of hepatocellular necrosis, ALT increases may be associated with cholestasis and can occur in the absence of histologic changes related to hepatocellular or biliary injury.

Diagnostic Performance of Hepatobiliary Markers

In the full ROC analysis, ALT, AST, Tbili, and SBA had the greatest diagnostic accuracy for Hepatocellular Necrosis,

Biliary Change and Fibrosis (Table 5, Fig. 6). For Hepatocellular Necrosis, diagnostic performance of ALT was comparable to that of AST and performance of Tbili was comparable to SBA; however, ALT and AST outperformed both Tbili and SBA ($p < 0.05$). In contrast, ALP, GGT, total Chol, and Trig had limited diagnostic utility for Hepatocellular Necrosis. For Biliary Change and Fibrosis, Chol also had moderate diagnostic accuracy; however, ALP, GGT, and Trig had limited diagnostic utility for both Biliary Change and Fibrosis. For Biliary Change, although diagnostic performance was comparable for ALT, AST, and Tbili, AST outperformed both SBA and Chol ($p < 0.05$). Following removal of the necrosis cohort, the diagnostic utility of all hepatobiliary markers for manifestations of Biliary Change and Fibrosis diminished considerably, as reflected by lower values and/or increased variability of AUC data in the subset analysis (Table 5, Fig. 7).

For other types of liver pathology, ALT had diagnostic utility for Phospholipidosis in both cohorts and Chol had diagnostic utility for Phospholipidosis in the subset cohort. ALP had modest diagnostic utility for Peroxisome Proliferation in either cohort. All of the hepatobiliary markers had limited diagnostic accuracy for the remaining categories of Hypertrophy, Inflammation, or Lipidosis in either the full or the subset analysis.

Several hepatobiliary markers had diagnostic utility for specific morphologic diagnoses that differed from that of the respective category (Supplementary table 2). These included increases in ALT and Tbili for panlobular vacuolation (full cohort), increases in ALT, AST, Tbili, SBA, and Chol in rats with mixed periportal inflammation (full cohort), decreases in Chol values for periportal hypertrophy (subset cohort), increases in ALP for cytoplasmic rarefaction/glycogen accumulation (subset cohort), and increases in Trig for basophilic cytoplasmic alteration (full and subset cohort). Analysis of incremental diagnostic value did not demonstrate any added value for any combinations of clinical chemistry parameters in either the full or the subset cohort.

DISCUSSION

Drug-induced liver injury is often complex, and liver histologic findings commonly reflect multiple rather than single pathologic processes. To address both the complexity of hepatotoxic manifestations and to evaluate the relationship between transaminase changes and liver injury other than hepatocellular necrosis, a novel analytic approach was employed in which rats were subdivided into cohorts based on the presence or absence of hepatocellular necrosis. To avoid selection bias or confounding effects of subcellular degenerative changes that would be inapparent by light microscopy, all rats with microscopic evidence of necrosis and rats that were given treatments that caused necrosis were omitted from a second or subset analysis. Observed differences in both magnitude of biomarker change or diagnostic performance between full and subset cohorts provided further evidence of the dominant influence of hepatocellular degeneration/necrosis on serum levels of these traditional hepatobiliary markers.

ROC analysis was selected for evaluation of diagnostic performance because of the ability to perform a joint assessment of sensitivity and specificity without designation of specific diagnostic thresholds, and also because of independence of marker performance from disease prevalence (Obuchowski, 2005). ROC analysis is not without limitations, however, because accuracy of tests for disease classification within the clinically or diagnostically relevant range is not always reflected by summary of test performance for an entire data set into a single measure such as an AUC. Methods such as evaluation of partial AUCs or determination of sensitivity at specific false-positive rates can be used to more specifically focus evaluation of test performance based on clinical objectives (Mulherin and Miller, 2002; Obuchowski, 2005). Because of limitations in size of subgroups for many of the different manifestations of hepatotoxicity and because the objective of this study was to provide a generalized evaluation of diagnostic utility rather than identification of specific diagnostic thresholds, these and other indices of diagnostic performance were not calculated. Whereas AUC data provide a comprehensive summary of biomarker performance, AUC values do not immediately inform clinical or preclinical decision making (Langlotz, 2003). As a result, serum marker changes normalized to concurrent control were summarized and presented in parallel with AUC data to provide a more direct representation of hepatobiliary marker changes that are associated with specific manifestations of liver injury.

In the current study, ALT, AST, Tbili, and SBA had comparable diagnostic utility and magnitude of increase for both hepatocellular necrosis and biliary pathology. In addition, cholestasis occurred in the majority of rats with ALT increases without morphologic evidence of hepatocellular necrosis. This observation is noteworthy because the close relationship between hepatocellular necrosis and biochemical or morphologic manifestations of cholestasis is less commonly recognized in preclinical species. Intrahepatic cholestasis is a common manifestation of drug-induced liver injury in humans (Levy and Lindor, 2004; Lewis and Zimmerman, 1999) and is often the earliest manifestation of injury during liver transplant rejection (Lefkowitch, 2004). Similarly, transaminase increases are common in animal models of bile duct ligation (Aksu *et al.*, 2009) and can be seen in patients with cholelithiasis and cholecystitis in which transaminase increases are in part attributed to local bile acid–mediated cytotoxicity (Chang *et al.*, 2009; Nathwani *et al.*, 2005a). Although cholestasis can exert local effects, cholestasis is also mechanistically related to hepatocellular necrosis and apoptosis through a variety of processes including but not limited to

TABLE 5
Diagnostic Performances of Hepatobiliary Markers

	Hepatocellular Necrosis	Biliary Change	Fibrosis	Hypertrophy	Inflammation	Cytoplasmic Change	Peroxisome Proliferation	Lipidosis	Phospholipidosis	Other
Full (*n*)	**275**	**129**	**140**	**390**	**402**	**191**	**133**	**517**	**40**	**363**
Subset (*n*)	n/a	19	20	255	177	101	114	315	28	210
ALT	**0.86 (0.83, 0.89)***	**0.86 (0.82, 0.9)**	**0.81 (0.77, 0.86)**	**0.66 (0.63, 0.69)**	**0.64 (0.61, 0.67)**	**0.61 (0.56, 0.66)**	**0.56 (0.52, 0.6)**	**0.55 (0.52, 0.58)**	**0.81 (0.74, 0.88)**	**0.62 (0.58, 0.65)**
		0.82 (0.69, 0.95)	0.67 (0.53, 0.82)	0.65 (0.61, 0.69)	0.5 (0.45, 0.55)	0.51 (0.45, 0.57)	0.58 (0.53, 0.62)	0.51 (0.48, 0.55)	0.86 (0.78, 0.94)	0.53 (0.49, 0.57)
AST	**0.87 (0.84, 0.89)***	**0.88 (0.85, 0.91)****	**0.82 (0.79, 0.86)**	**0.64 (0.6, 0.67)**	**0.67 (0.64, 0.7)**	**0.66 (0.62, 0.71)**	**0.56 (0.51, 0.61)**	**0.59 (0.56, 0.61)**	**0.78 (0.69, 0.86)**	**0.61 (0.58, 0.65)**
		0.83 (0.72, 0.94)	0.75 (0.65, 0.85)	0.59 (0.54, 0.63)	0.57 (0.52, 0.61)	0.6 (0.54, 0.67)	0.59 (0.54, 0.64)	0.53 (0.49, 0.56)	0.8 (0.69, 0.91)	0.53 (0.49, 0.58)
Tbili	**0.82 (0.79, 0.85)**	**0.85 (0.82, 0.88)**	**0.82 (0.78, 0.86)**	**0.68 (0.65, 0.7)**	**0.59 (0.56, 0.63)**	**0.61 (0.56, 0.65)**	**0.6 (0.55, 0.64)**	**0.6 (0.58, 0.63)**	**0.68 (0.61, 0.75)**	**0.62 (0.59, 0.65)**
		0.82 (0.72, 0.92)	0.71 (0.56, 0.86)	0.65 (0.62, 0.69)	0.51 (0.47, 0.55)	0.6 (0.55, 0.66)	0.62 (0.57, 0.67)	0.57 (0.54, 0.6)	0.69 (0.59, 0.79)	0.56 (0.52, 0.6)
SBA	**0.83 (0.8, 0.85)**	**0.82 (0.79, 0.86)**	**0.81 (0.78, 0.85)**	**0.62 (0.59, 0.65)**	**0.65 (0.62, 0.68)**	**0.6 (0.55, 0.65)**	**0.54 (0.49, 0.58)**	**0.57 (0.54, 0.6)**	**0.6 (0.52, 0.68)**	**0.65 (0.62, 0.68)**
		0.71 (0.6, 0.82)	0.67 (0.56, 0.78)	0.59 (0.55, 0.63)	0.55 (0.51, 0.6)	0.52 (0.46, 0.58)	0.51 (0.46, 0.56)	0.51 (0.48, 0.55)	0.63 (0.54, 0.73)	0.57 (0.53, 0.61)
ALP	**0.69 (0.66, 0.73)**	**0.74 (0.69, 0.79)**	**0.71 (0.66, 0.76)**	**0.63 (0.6, 0.67)**	**0.56 (0.53, 0.6)**	**0.53 (0.48, 0.59)**	**0.77 (0.73, 0.81)**	**0.53 (0.5, 0.56)**	**0.6 (0.51, 0.69)**	**0.64 (0.61, 0.68)**
		0.63 (0.5, 0.75)	0.59 (0.45, 0.72)	0.64 (0.6, 0.68)	0.56 (0.51, 0.61)	0.59 (0.51, 0.66)	0.79 (0.75, 0.83)	0.54 (0.5, 0.57)	0.59 (0.47, 0.71)	0.59 (0.55, 0.64)
GGT	**0.63 (0.6, 0.66)**	**0.67 (0.63, 0.72)**	**0.69 (0.64, 0.73)**	**0.58 (0.55, 0.6)**	**0.57 (0.54, 0.59)**	**0.59 (0.55, 0.62)**	**0.56 (0.54, 0.57)**	**0.5 (0.48, 0.52)**	**0.59 (0.52, 0.67)**	**0.57 (0.55, 0.6)**
		0.57 (0.47, 0.67)	0.62 (0.51, 0.72)	0.57 (0.54, 0.59)	0.51 (0.48, 0.53)	0.61 (0.56, 0.65)	0.54 (0.53, 0.56)	0.54 (0.52, 0.55)	0.55 (0.48, 0.63)	0.52 (0.49, 0.54)
Chol	**0.7 (0.66, 0.74)**	**0.82 (0.78, 0.86)**	**0.83 (0.79, 0.86)**	**0.55 (0.51, 0.58)**	**0.6 (0.57, 0.63)**	**0.6 (0.56, 0.65)**	**0.73 (0.69, 0.77)**	**0.54 (0.52, 0.57)**	**0.65 (0.54, 0.76)**	**0.54 (0.5, 0.57)**
		0.84 (0.74, 0.93)	0.75 (0.65, 0.85)	0.5 (0.45, 0.55)	0.58 (0.54, 0.62)	0.5 (0.43, 0.57)	0.71 (0.66, 0.76)	0.57 (0.54, 0.61)	0.86 (0.78, 0.93)	0.57 (0.52, 0.61)
Trig	0.65 (0.61, 0.69)	**0.63 (0.59, 0.68)**	**0.64 (0.59, 0.69)**	**0.53 (0.49, 0.56)**	**0.59 (0.56, 0.63)**	**0.72 (0.67, 0.77)**	**0.53 (0.47, 0.59)**	**0.5 (0.47, 0.53)**	**0.56 (0.45, 0.66)**	**0.55 (0.52, 0.59)**
		0.51 (0.43, 0.58)	0.54 (0.45, 0.63)	0.54 (0.49, 0.59)	0.57 (0.52, 0.61)	0.65 (0.56, 0.73)	0.51 (0.45, 0.57)	0.51 (0.47, 0.55)	0.54 (0.41, 0.67)	0.53 (0.48, 0.57)

Note. AUC data are presented as mean (95% confidence interval). Full cohort data are presented in bold font and subset cohort data are listed below unbolded. n/a, not applicable. Statistically significant differences between markers with AUC $\geq$ 0.75 within categories for either cohort are indicated by *$p \leq 0.05$ versus Tbili and SBA, and **$p \leq 0.05$ versus SBA and cholesterol.

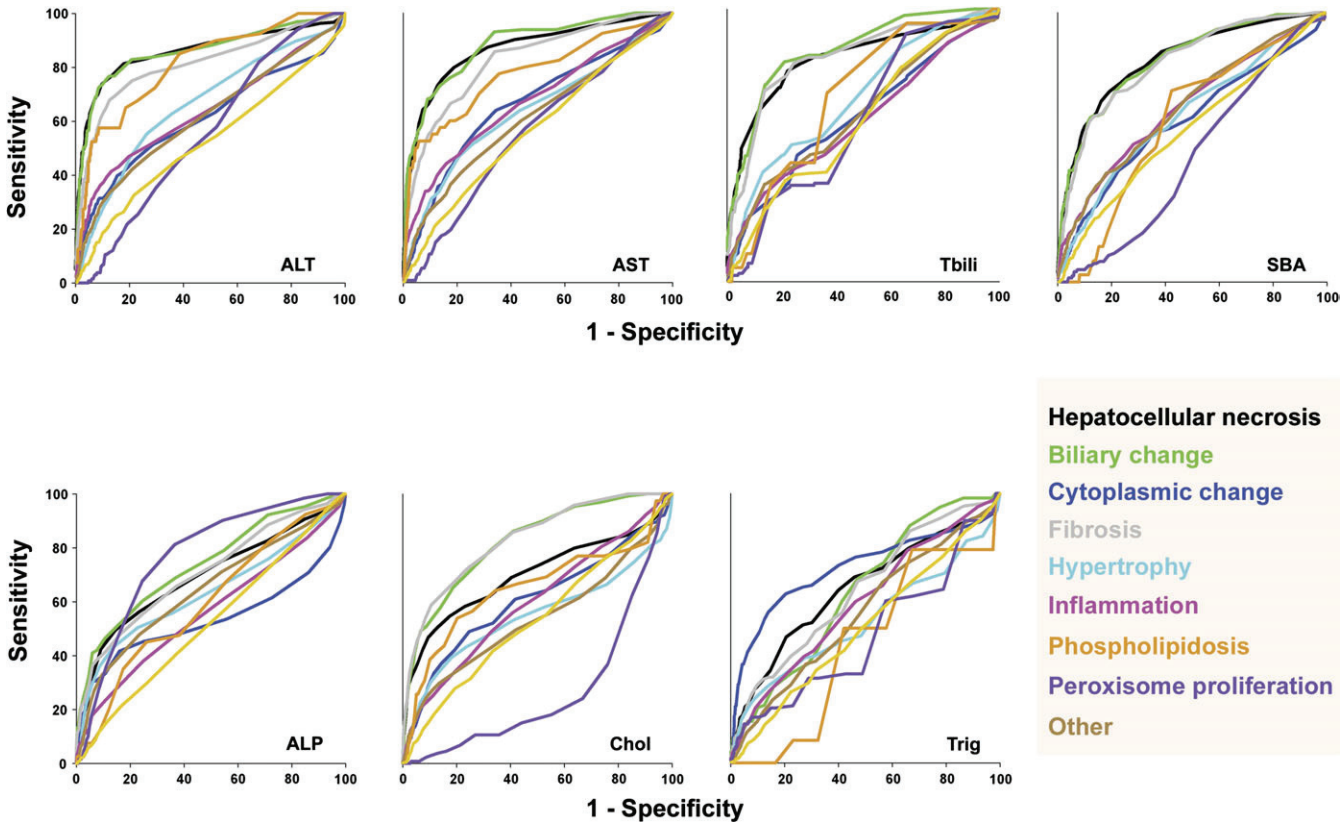

FIG. 6. ROC curves by parameter and category of injury for the Full cohort.

Fas- and tumor necrosis factor-related apoptosis-inducing ligand (TRAIL)-mediated activation of hepatocyte death receptors, bile acid–mediated activation of mitochondrial pro-apoptotic pathways, and oxidative stress (Malhi *et al.*, 2006). Therefore, concomitant increases in biliary markers may provide added perspective or mechanistic insight on transaminase activity increases in the absence of relevant histopathologic changes in preclinical studies.

Although commonly used as markers of biliary pathology, ALP and GGT were of limited diagnostic utility in this study, whereas Tbili and SBA were excellent markers of both hepatocellular injury and biliary pathology or cholestasis. In rats, the major circulating form of ALP is the intestinal rather than the liver isoenzyme (Hoffman *et al.*, 1999); however, total serum ALP activity is commonly measured. Total serum ALP activity is generally minimally increased in association with intrahepatic cholestasis in rat (Travlos *et al.*, 1996) but can be markedly increased in rat bile duct ligation models (Hoffman *et al.*, 1999). In this study, diagnostic performance of ALP across categories of injury in either cohort was poor, and ALP changes for all categories of injury were either of low magnitude (full cohort) or comparable to controls (subset cohort); therefore, ALP measured as total serum activity is a poor marker of hepatobiliary injury in the rat. Similarly, GGT activity was often not quantifiable in either treated or control rats and had poor diagnostic utility across all categories of injury in both cohorts. The diagnostic utility of GGT should not be discounted in chronic preclinical toxicology studies where progressive increases in GGT activity can correlate quantitatively with an increase in biliary epithelial mass as reflected in the rat chronic α-napthylisothiocyanate model of cholangiodestructive cholestasis (Leonard *et al.*, 1984).

Marker performance for specific morphologic diagnoses generally paralleled that for categorical changes; however, some exceptions were observed. In the current study, although diagnostic performance of ALT and AST was comparable for centrilobular and periportal necrosis, transaminase increases were lower or even absent for rats with centrilobular necrosis. This finding is similar to the minimal or absent transaminase changes reported in rats with hepatic centrilobular necrosis (O'Brien *et al.*, 2002; Wang *et al.*, 1997). The absence of prominent increases in ALT with centrilobular hepatic necrosis may be related to the primarily periportal localization of ALT (Jungermann and Katz, 1989), combined effects of rapid clearance of ALT from serum, and timing of sample collection relative to onset of injury, as ALT has an extremely short circulating half-life of less than 8 h in rat relative to 45–60 h in dog or human (Boyd, 1983; Hoffman *et al.*, 1999). Determination of serum transaminase activity is the current standard for measurement of ALT across species; however,

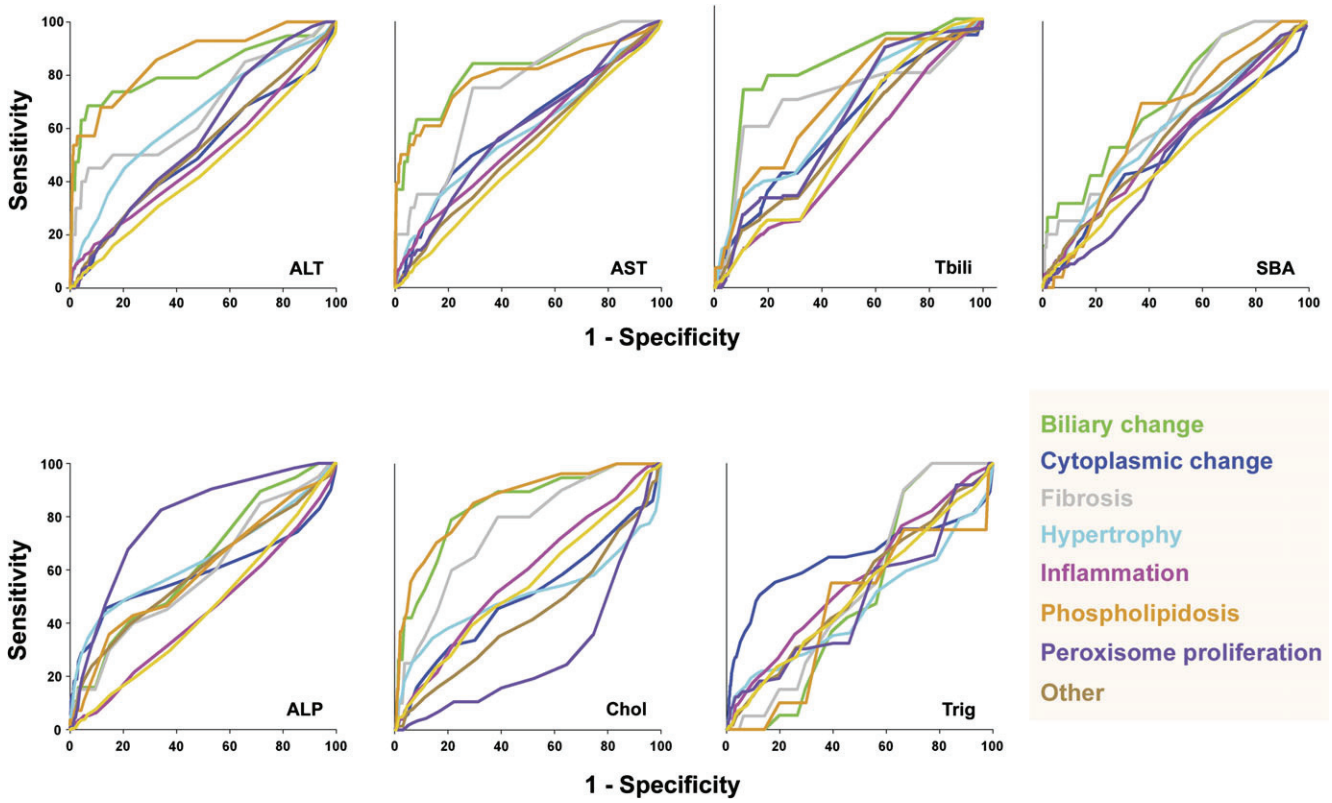

FIG. 7. ROC curves by parameter and category of injury for the Subset cohort.

immunoassays for ALT isoenzymes (Lindblom *et al*., 2007) or addition of other markers such as glutamate dehydrogenase (O'Brien *et al*., 2002) may improve biochemical characterization of hepatocellular injury in the rat and other species.

Although transaminase increases are classically associated with hepatocellular necrosis/degeneration or increased membrane permeability (Solter, 2005), serum transaminase activities can be also be influenced by extrahepatic tissues. Therefore, one limitation of this study was that histologic evaluation was limited to liver. Although well-characterized hepatotoxicants with known toxicities and mechanisms of action were used and, with exception of rats with Phospholipidosis, serum ALT activities consistently exceeded increases in serum AST activity as expected for hepatic injury, extrahepatic effects on traditional hepatobiliary markers cannot be excluded. Other findings including hypertrophy or lipid accumulation are also often linked with transaminase changes. Centrilobular hypertrophy is a common sequela to hepatic drug-metabolizing enzyme induction, and concurrent ALT, ALP, and GGT increases, when noted, are often incorrectly attributed to induction of hepatic activity of these hepatobiliary marker enzymes (Ennulat *et al*., Forthcoming). In the current study, ALT and other hepatobiliary markers had no diagnostic utility and were comparable to control values for centrilobular hypertrophy in both cohorts, indicating the lack of an effect of centrilobular hypertrophy on hepatobiliary marker values. Similarly, Chol and Trig changes are often related to hepatic lipidosis, however, neither had diagnostic utility nor remarkable serum increases for manifestations of hepatic lipidosis in the current study. This study clearly demonstrates that in the absence of hepatocellular necrosis or degeneration, morphologic changes such as hepatocellular hypertrophy or lipidosis are typically not associated with clinical chemistry changes.

In conclusion, the evaluation of the diagnostic utility of eight conventional serum biomarkers of hepatobiliary injury for prediction of drug-induced liver injury in rat demonstrated the specificity and comparable diagnostic utility of ALT, AST, Tbili, and SBA for prediction of manifestations of hepatocellular necrosis/degeneration and biliary pathology. However, all eight conventional hepatobiliary markers evaluated had comparatively low diagnostic utility for manifestations of hepatocellular hypertrophy, lipidosis, cytoplasmic change, or inflammation.

SUPPLEMENTARY DATA

Supplementary data are available online at http://toxsci.oxfordjournals.org/.

ACKNOWLEDGMENTS

The authors would like to thank Dr Patrick Wier for his sponsorship and intellectual contributions on this initiative and Kimberly Roland for her oversight of the studies. We also are grateful to Drs Stephen Newsholme, Frances Clemo, Holly Jordan, and Terry Sellers for their critical review of the manuscript and Rosanna Mirabile, Tracy Gales, and Beverly Maleeff for their excellent technical assistance.

REFERENCES

Abboud, G., and Kaplowitz, N. (2007). Drug-induced liver injury. *Drug Saf.* **30,** 277–294.

Abraham, S. C., and Furth, E. E. (1995). Receiver operating characteristic analysis of serum chemical parameters as tests of liver transplant rejection and correlation with histology. *Transplantation* **59,** 740–746.

Aithal, P. G., and Day, C. P. (1999). The natural history of histologically proved drug induced liver disease. *Gut* **44,** 731–735.

Aksu, B., Umit, H., Kanter, M., Guzel, A., Inan, M., Civelek, S., Aktas, C., and Uzun, H. (2009). Effects of sphingosylphosphorylcholine against cholestatic oxidative stress and liver damage in the common bile duct ligated rats. *J. Pediat. Surg.* **44,** 702–710.

Amacher, D. E. (1998). Serum transaminase elevations as indicators of hepatic injury following the administration of drugs. *Regul. Toxicol. Pharmacol.* **27,** 119–130.

Boone, L. I., Meyer, D. J., Cusick, P., Ennulat, D., Provencher Bollinger, A., Everds, N. E., Meador, V., Elliott, G., Honor, D., Bounous, D., *et al*. (2005). Selection and interpretation of clinical pathology indicators of hepatic injury in preclinical studies. *Vet. Clin. Pathol.* **34,** 182–188.

Boyd, J. W. (1983). The mechanisms relating to increases in plasma enzymes and isoenzymes in diseases of animals. *Vet. Clin. Pathol.* **12,** 9–24.

Campbell, S. D., de Morais, S. M., and Xu, J. J. (2004). Inhibition of human organic anion transporting polypeptide OATP1B1 as a mechanism of drug-induced hyperbilirubinemia. *Chem. Biol. Interact.* **150,** 179–187.

Cattley, R. C., and Popp, J. A. (2002). Liver. In *Handbook of Toxicological Pathology*, 2nd ed. (W. M. Haschek, C. G. Rousseaux, and M. A. Wallig, Eds.), pp. 187–225. Academic Press, San Diego, CA.

Chang, C.-W., Chang, W.-H., Lin, C.-C., Chu, C.-H., Wang, T.-E., and Shih, S.-C. (2009). Acute transient hepatocellular injury in cholelithiasis and cholecystitis without evidence of choledocholithiasis. *World J. Gastroenterol.* **15,** 3788–3792.

DeLong, E. R., DeLong, D. M., and Clarke-Pearson, D. L. (1988). Comparing the areas under two or more correlated receiver operating characteristic curves: a nonparametric approach. *Biometrics* **44,** 837–845.

Dufour, D., Lott, J., Nolte, F., Gretch, D., Koff, R., and Seeff, L. (2000a). Diagnosis and monitoring of hepatic injury. I. Performance characteristics of laboratory tests. *Clin. Chem.* **46,** 2027–2049.

Dufour, D., Lott, J., Nolte, F., Gretch, D., Koff, R., and Seeff, L. (2000b). Diagnosis and monitoring of hepatic injury. II. Recommendations for use of laboratory tests in screening, diagnosis, and monitoring. *Clin. Chem.* **46,** 2050–2068.

Ennulat, D., Walker, D., Clemo, F., Magid-Slav, M., Ledieu, D., Graham, M., Botts, S., and Boone, L. (2010). Effects of hepatic drug metabolizing enzyme induction on clinical pathology parameters in animals and man. *Toxicol. Pathol.* Advance Access published on June 28, 2010; doi:10.1177/0192623310374332.

Gardner, I. A., and Greiner, M. (2006). Receiver-operating characteristic curves and likelihood ratios: improvements over traditional methods for the evaluation and application of veterinary clinical pathology tests. *Vet. Clin. Pathol.* **35,** 8–17.

Hanley, J. A., and McNeil, B. J. (1982). The meaning and use of the area under a receiver operating characteristic (ROC) curve. *Radiology* **143,** 29–36.

Hoffman, W. E., Solter, P. E., and Wilson, B. W. (1999). Clinical enzymology. In *The Clinical Chemistry of Laboratory Animals*, 2nd ed. (W. F. Loeb and F. W. Quimby, Eds.), pp. 399–444. Taylor and Francis, Philadelphia, PA.

Huseby, N. E., Kindberg, G. M., Grøstad, M., and Berg, T. (1992). Clearance of purified human liver gamma-glutamyltransferase after intravenous injection in the rat. *Clin. Chim. Acta* **205,** 197–203.

Ihaka, R., and Gentleman, R. (1996). R: a language for data analysis and graphics. *J. Comput. Graph. Stat.* **5,** 299–314.

Jackson, E. R., Kilroy, C., Joslin, D. L., Schomaker, S. J., Pruimboom-Brees, I., and Amacher, D. E. (2008). The early effects of short-term dexamethasone administration on hepatic and serum alanine aminotransferase in the rat. *Drug Chem. Toxicol.* **31,** 427–445.

Jin, J. Y., DuBois, D. C., Almon, R. R., and Jusko, W. J. (2004). Receptor/gene-mediated pharmacodynamic effects of methylprednisolone on phosphoenolpyruvate carboxykinase regulation in rat liver. *J. Pharmacol. Exp. Ther.* **309,** 328–339.

Jungermann, K., and Katz, N. (1989). Functional specialization of different hepatocyte populations. *Physiol. Rev.* **69,** 708–764.

Kaplowitz, N. (2005). Idiosyncratic drug hepatotoxicity. *Nat. Rev. Drug Discov.* **4,** 489–499.

Lahrichi, M., Ratanasavanh, D., Galteau, M. M., and Siest, G. (1982). Effect of chronic ethanol administration on gamma-glutamyltransferase activities in plasma and in hepatic plasma membranes of male and female rats. *Enzyme* **28,** 251–257.

Landi, M., Kissinger, J. T., Campbell, S. A., Kenney, C. A., and Jenkins, E. L. (1990). The effects of four types of restraint on serum alanine aminotransferase and aspartate aminotransferase in the *Macaca fascicularis*. *J. Am. Coll. Toxicol.* **9,** 517–523.

Langlotz, C. P. (2003). Fundamental measures of diagnostic examination performance: usefulness for clinical decision making and research. *Radiology* **228,** 3–9.

Lefkowitch, J. H. (2004). Histological assessment of cholestasis. *Clin. Liver Dis.* **8,** 27–40.

Leonard, T. B., Neptun, D. A., and Popp, J. A. (1984). Serum gamma glutamyl transferase as a specific indicator of bile duct lesions in the rat liver. *Am. J. Pathol.* **116,** 262–269.

Levy, C., and Lindor, K. D. (2004). Drug-induced cholestasis. *Clin. Liver Dis.* **7,** 311–320.

Lewis, J. H., and Zimmerman, H. J. (1999). Drug- and chemical-induced cholestasis. *Clin. Liver Dis.* **3,** 433–464.

Lindblom, P., Rafter, I., Copley, C., Andersson, U., Hedberg, J. J., Berg, A. L., Samuelsson, A., Hellmold, H., Cotgreave, I., and Glinghammar, B. (2007). Isoforms of alanine aminotransferases in human tissues and serum-differential tissue expression using novel antibodies. *Arch. Biochem. Biophys.* **466,** 66–77.

Malhi, H., Gores, G. J., and Lemasters, J. J. (2006). Apoptosis and necrosis in the liver: a tale of two deaths? *Hepatology* **43,** S31–S44.

Mulherin, S. A., and Miller, W. C. (2002). Spectrum bias or spectrum effect? Subgroup variation in diagnostic test evaluation. *Ann. Intern. Med.* **137,** 598–602.

Nathwani, R. A., Kumar, R., Reynolds, T. B., and Kaplowitz, N. (2005). Marked elevation in serum transaminases: an atypical presentation of choledocholithiasis. *Am. J. Gastroenterol.* **100,** 295–298.

Nathwani, R. A., Pais, S., Reynolds, T. B., and Kaplowitz, N. (2005). Serum alanine transferase in skeletal muscle diseases. *Hepatology* **41,** 380–382.

Obert, L. A., Sobocynski, G. C., Brobowski, W. F., Metz, A. L., Rolsma, M. D., Altrogge, D. M., and Dunstan, R. W. (2007). An immunohistochemical approach to differentiate hepatic lipidosis from hepatic phospholipidosis in rats. *Toxicol. Pathol.* **35,** 728–734.

O'Brien, P. J., Slaughter, M. R., Polley, S. R., and Kramer, K. (2002). Advantages of glutamate dehydrogenase as a blood biomarker of acute hepatic injury in rats. *Lab. Anim.* **36,** 313–321.

Obuchowski, N. A. (2005). Fundamentals of clinical research for radiologists. *AJR Am. J. Roentgenol.* **184,** 364–372.

Pepe, M. S., Janes, H., Longton, G., Leisenring, W., and Newcomb, P. (2004). Limitations of the odds ratio in gauging the performance of a diagnostic, prognostic, or screening marker. *Am. J. Epidemiol.* **159,** 882–890.

Poynard, T., Halfon, P., Castera, L., Munteanu, M., Imbert-Bismut, F., Ratziu, V., Benhamou, V., Bourliere, M., and De Ledinghen, V. (2007). FibroPaca Group. (2007). Standardization of ROC curve areas for diagnostic evaluation of liver fibrosis markers based on prevalences of fibrosis stages. *Clin. Chem.* **53,** 1615–1622.

Prati, D., Taioli, E., Zanella, A., Della Torre, E., Butelli, S., Del Vecchio, E., Vianello, L., Zanuso, F., Mozzi, F., Milani, S., *et al.* (2002). Updated definitions of healthy ranges for serum alanine aminotransferase levels. *Ann. Intern. Med.* **137,** 1–10.

Pratt, D. S., and Kaplan, M. M. (2000). Evaluation of abnormal liver-enzyme results in asymptomatic patients. *N. Engl. J. Med.* **342,** 1266–1271.

Quest, J. A., Chan, P. C., Crawford, D., Kanagalingam, K. K., and Hall, W. C. (1987). Thirteen-week oral toxicity study of methyl carbamate in rats and mice. *Fundam. Appl. Toxicol.* **8,** 389–399.

Sapolsky, R. M., Romero, L. M., and Munck, A. U. (2000). How do glucocorticoids influence stress responses? Integrating permissive, suppressive, stimulatory, and preparative actions. *Endocr. Rev.* **21,** 55–89.

Solter, P. F. (2005). Clinical pathology approaches to hepatic injury. *Toxicol. Pathol.* **33,** 9–16.

Sturgill, M. G., and Lambert, G. H. (1997). Xenobiotic-induced hepatotoxicity: mechanisms of liver injury and methods of monitoring hepatic function. *Clin. Chem.* **43,** 11512–11526.

Swets, J. A. (1982). Sensitivities and specificities of diagnostic tests. *JAMA* **248,** 548–550.

Travlos, G. S., Morris, R. W., Elwell, M. R., Duke, A., Rosenblum, S., and Thompson, M. B. (1996). Frequency and relationships of clinical chemistry and liver and kidney histopathology findings in 13-week toxicity studies in rats. *Toxicology* **107,** 17–29.

Tsui, W. M. S. (2003). Drug-associated changes in the liver. *Curr. Diagn. Pathol.* **9,** 96–104.

Valentine, B. A., Blue, J. T., Shelley, S. M., and Cooper, B. J. (1990). Increased alanine aminotransferase activity associated with muscle necrosis in the dog. *J. Vet. Intern. Med.* **4,** 140–143.

Wang, P.-Y., Kaneko, T., Tsukada, H., Nakano, M., Nakajima, T., and Sato, A. (1997). Time courses of hepatic injuries induced by chloroform and by carbon tetrachloride: comparison of biochemical and histopathological changes. *Arch. Toxicol.* **71,** 638–645.

Zimmerman, H. J. (2000). Drug-induced liver disease. *Clin. Liver Dis.* **4,** 73–96.

Zucker, S. D., Qin, X., Rouster, S. D., Yu, F., Green, R. M., Keshavan, P., Feinberg, J., and Sherman, K. E. (2001). Mechanism of indinavir-induced hyperbilirubinemia. *Proc. Natl. Acad. Sci. USA* **98,** 12671–12676.

Zweig, M. H., and Campbell, G. (1993). Receiver-operating characteristic (ROC) plots: a fundamental evaluation tool in clinical medicine. *Clin. Chem.* **39,** 561–577.

Fukuchi et al. Molecular Brain (2020) 13:122
https://doi.org/10.1186/s13041-020-00665-7

Molecular Brain

RESEARCH Open Access

Visualization of activity-regulated BDNF expression in the living mouse brain using non-invasive near-infrared bioluminescence imaging

Mamoru Fukuchi[1*], Ryohei Saito[2,3], Shojiro Maki[2], Nami Hagiwara[1], Yumena Nakajima[1], Satoru Mitazaki[1], Hironori Izumi[4] and Hisashi Mori[4]

Abstract

Altered levels of brain-derived neurotrophic factor (BDNF) have been reported in neurologically diseased human brains. Therefore, it is important to understand how the expression of BDNF is controlled under pathophysiological as well as physiological conditions. Here, we report a method to visualize changes in BDNF expression in the living mouse brain using bioluminescence imaging (BLI). We previously generated a novel transgenic mouse strain, *Bdnf-Luciferase* (*Luc*), to monitor changes in *Bdnf* expression; however, it was difficult to detect brain-derived signals in the strain using BLI with D-luciferin, probably because of incomplete substrate distribution and light penetration. We demonstrate that TokeOni, which uniformly distributes throughout the whole mouse body after systematic injection and produces a near-infrared bioluminescence light, was suitable for detecting signals from the brain of the *Bdnf-Luc* mouse. We clearly detected brain-derived bioluminescence signals that crossed the skin and skull after intraperitoneal injection of TokeOni. However, repeated BLI using TokeOni should be limited, because repeated injection of TokeOni on the same day reduced the bioluminescence signal, presumably by product inhibition. We successfully visualized kainic acid-induced *Bdnf* expression in the hippocampus and sensory stimulation-induced *Bdnf* expression in the visual cortex. Taken together, non-invasive near-infrared BLI using *Bdnf-Luc* mice with TokeOni allowed us to evaluate alterations in BDNF levels in the living mouse brain. This will enable better understanding of the involvement of BDNF expression in the pathogenesis and pathophysiology of neurological diseases.

Keywords: Bioluminescence, Brain-derived neurotrophic factor, In vivo imaging, Near-infrared

Introduction

Brain-derived neurotrophic factor (BDNF), a member of the neurotrophin family, is fundamentally involved in a variety of functions in the developing and mature brain [1]. Consistent with the crucial roles of BDNF in the central nervous system (CNS), alterations in BDNF levels have been found in the brains of patients with neurodegenerative or neuropsychiatric diseases [2–4]. Abnormal expression levels of BDNF have been reported in the postmortem brains of Alzheimer's disease [5], Parkinson's disease [6], Huntington's disease [7], depression [8], and schizophrenia [9]. Higher expression levels of BDNF in the brain (dorsolateral prefrontal cortex) correlate with slower cognitive decline [10]. Furthermore, lower levels of BDNF in cerebrospinal fluids are

* Correspondence: fukuchi@takasaki-u.ac.jp
[1]Laboratory of Molecular Neuroscience, Faculty of Pharmacy, Takasaki University of Health and Welfare, 60 Nakaorui-machi, Takasaki, Gunma 370-0033, Japan
Full list of author information is available at the end of the article

associated with the progression of mild cognitive impairment to Alzheimer's disease [11]. These findings indicate that a reduction of BDNF levels in the brain may trigger CNS dysfunction, resulting in neurological diseases. However, because neuronal *Bdnf* expression is regulated by neuronal activity [12], it is also plausible that neuronal dysfunction in neurological diseases can result in a reduction of BDNF levels in the brain. Despite numerous studies reporting reduced levels of BDNF in neurologically diseased brains, there is no evidence showing whether reduced BDNF levels in the brain are the cause or result of a disease.

Bioluminescence imaging (BLI) is a popular technique for monitoring changes in expression levels of target molecules. Compared to fluorescence imaging using fluorescent molecules, such as green fluorescent protein, signal intensity obtained by BLI is relatively low, and the addition of a substrate is necessary to obtain signals. However, excitation lights, which can be toxic, are not required, and the signals can be obtained non-invasively with high signal to noise ratio [13, 14]. We previously generated a novel transgenic mouse strain termed *Bdnf-Luciferase* (*Luc*) to monitor changes in *Bdnf* expression in vivo as well as in vitro, using a firefly Luc as an imaging probe [15, 16]. In this mouse strain, expression levels of Luc reflect endogenous *Bdnf* expression. Because levels of Luc can be evaluated by measuring bioluminescence produced by reaction with a substrate, such as D-luciferin, the most popular and commonly used substrate for in vitro and in vivo BLI, changes in *Bdnf* expression can be evaluated by detecting bioluminescence signals. The induction of *Bdnf* expression can be visualized in living neuronal cell cultures [15, 16]. In addition, bioluminescence signals from living *Bdnf-Luc* mice can be detected after intraperitoneal administration of D-luciferin [16]. However, despite endogenous *Bdnf* being highly expressed in the brain, signals from the brain were poorly detected in the mice [16]. The emission maximum of bioluminescence light produced by firefly Luc with D-luciferin is 578 nm at 25 °C and 612 nm at 37 °C [17] and, therefore, does not penetrate biological tissues well, because of light absorption by hemoglobin and melanin in the tissues [18, 19]. In addition, a heterogeneous biodistribution of D-luciferin has been reported [20, 21]. Furthermore, D-luciferin is a specific substrate for an ATP-binding cassette (ABC) transporter G2 (ABCG2) [22] and, therefore, it may limit an ability of D-luciferin to cross blood-brain-barrier (BBB). To improve BLI, novel substrates for Luc have been developed. For example, CycLuc1, a synthetic luciferin, has been shown to greatly improve the sensitivity of BLI, although the emission maximum is 612 nm [23]. Previously, Cao et al., (2018) reported in vivo imaging of myelination events using myelin basic protein promoter-driven Luc transgenic mice and CycLuc1 [24]. In addition, CycLuc1 amide nicely improved to detect bioluminescence signals from the brain in particular [25]. Furthermore, firefly Luc has been mutated to optimize the detection of bioluminescence from the brain using synthetic luciferins CycLuc1, CycLuc2, and their respective amides [26]. Iwano et al., (2013) developed a series of firefly Luc analogues to improve light penetration [27]. AkaLumine hydrochloride (also called TokeOni) is a novel Luc substrate that produces near-infrared light with a wavelength of approximately 680 nm and enables visualization of signals from deep tissues [28]. Furthermore, firefly Luc has been optimized for TokeOni, and an engineered BLI systems, termed AkaBLI, enables visualization of bioluminescence signals from the brain of a freely moving animal [29]. We previously detected signals from brain regions after the systematic injection of TokeOni into *Bdnf-Luc* mice; however, the signals were detected by an invasive method (we removed the skin to expose the skull before in vivo imaging) [16], and it is still unclear whether changes in *Bdnf* expression under physiological conditions can be visualized by non-invasive in vivo BLI.

In the present study, we examined the properties of two Luc substrates, seMpai and TokeOni, both of which produce near-infrared light, using *Bdnf-Luc* mice, and found that TokeOni to be the most suitable substrate for detecting bioluminescence signals from mouse brain regions non-invasively. We successfully visualized drug-induced and sensory stimulation-induced *Bdnf* expression in the living *Bdnf-Luc* mouse brain, although repeated BLI using TokeOni should be limited, presumably because of product inhibition. This report shows that induction of *Bdnf* expression in the mouse brain can be visualized under physiological conditions, and this non-invasive in vivo BLI method will facilitate further investigation of the roles of BDNF in neurological disease. In addition, this report provides instructive information for the in vivo use of TokeOni with other Luc mice line.

Methods

Animals

All animal care procedures and experiments were approved by the Animal Experiment Committee of the University of Toyama (Authorization No. S-2010 MED-51, A2011PHA-18, and A2014PHA-1) and Takasaki University of Health and Welfare (Authorization No. 1733, 1809, 1913, and 2008), and were performed in accordance with the Guidelines for the Care and Use of Laboratory Animals of the University of Toyama and Takasaki University of Health and Welfare. Mice were housed under standard laboratory conditions (12 h–12 h/light-dark cycle at 22 ± 2 °C) and had free access to

food and water. The generation of *Bdnf-Luc* mice has been described previously [15, 16] and 8–14 week-old *Bdnf-Luc* mice were used.

In vivo BLI

One day before in vivo BLI, the black fur was shaved from the top of the head of *Bdnf-Luc* mice under inhalation anesthesia with 2.0% isoflurane. D-luciferin (Promega, Madison, WI, USA), TokeOni, and seMpai were dissolved in saline at the concentration of 10 mg/ml. *Bdnf-Luc* mice were anesthetized by inhalation of 2.0% isoflurane, and then Luc substrate solution was administered intraperitoneally [0.1 ml substrate solution/10 g body weight (dose of each substrate: 100 mg/kg)]. In our previous report, TokeOni was used at 150 mg/kg or 75 mg/kg, and the signals from the brain region were successfully detected [16]. Therefore, in the current study, we determined the dose of TokeOni at 100 mg/kg. To compare the bioluminescence signals in the same conditions, the dose of the other substrates was also determined at 100 mg/kg. Five minutes after substrate administration, BLI was performed using an IVIS in vivo imaging system [PerkinElmer, Boston, MA, USA (Exposure time: 2 min, Binning: Medium, F/Stop: 1)]. Pseudocolored bioluminescent images representing the spatial distribution of emitted photons were overlaid on photographs of the mouse taken in the chamber. The results shown in Supplementary Figure 2 were generated by in vivo BLI performed according to our previous report [16].

KA administration and analysis of endogenous BDNF expression

Kainic acid [KA (Sigma-Aldrich, St. Louis, MO, USA)] was dissolved in saline at 2.5 mg/ml. Saline or KA solution was administered intraperitoneally to *Bdnf-Luc* mice [0.1 ml substrate solution/10 g body weight (dose of KA: 25 mg/kg)]. Six hours after the administration of saline or KA, in vivo BLI was performed using TokeOni. After BLI, the mice were decapitated while still anesthetized and cerebral cortex and hippocampus were isolated to examine changes in endogenous *Bdnf* mRNA and BDNF protein levels.

Total RNA was purified from the cerebral cortex and hippocampus using ISOGEN (Nippongene, Tokyo, Japan), according to the manufacturer's instructions. One microgram of purified total RNA was reverse-transcribed into cDNA using a PrimeScript 1st Strand cDNA Synthesis Kit (TaKaRa Bio, Kusatsu, Japan), according to the manufacturer's instructions. Real-time PCR was performed using SYBR Select Master Mix (Thermo Fisher Scientific, Waltham, MA, USA), according to the manufacturer's instructions. Fold-change values were calculated by the $^{\Delta\Delta}$Ct method to determine relative gene expression. Primer sequences of *Bdnf* and *Gapdh* were as described previously [16]. The levels of *Bdnf* mRNA were normalized to those of *Gapdh* mRNA.

Protein extraction was performed using T-PER Protein Extraction Reagent (Thermo Fisher Scientific) supplemented with Halt Protease Inhibitor Cocktail (Thermo Fisher Scientific), according to the manufacturer's instructions. Protein concentrations were determined using a BCA Protein Assay Kit (Thermo Fisher Scientific). After heat denaturation of samples in Laemmli Sample Buffer (BioRad, Hercules, CA, USA) supplemented with 2-mercaptoethanol, 10 μg of protein was separated by SDS-PAGE (for BDNF: 15% polyacrylamide gel, for α-Tubulin: 10% polyacrylamide gel). Separated proteins were transferred to a PVDF membrane. The membrane was washed, blocked with 5% skimmed milk, and then treated with a primary antibody {anti-BDNF antibody [Abcam, Cambridge, UK (ab108319, 1:1000)] or anti-α-Tubulin antibody [Wako, Osaka, Japan (1:1000)]} diluted in Can Get Signal Solution 1 (TOYOBO, Osaka, Japan) overnight at 4 °C with shaking. The membrane was washed, treated with a secondary antibody {anti-rabbit IgG HRP-conjugated [GE Healthcare, Buckinghamshire, England (1:5000)] or anti-mouse IgG HRP-conjugated [GE Healthcare, (1:5000)]} diluted in Can Get Signal Solution 2 (TOYOBO) for 1 h at room temperature with shaking, and then washed. Each band was detected using ImmunoStar Zeta (Wako). Intensity of each band was measured using Image J. The levels of BDNF were normalized to those of α-Tubulin.

Sensory stimulation

The black fur was shaved from the top of the head of *Bdnf-Luc* mice under inhalation anesthesia with 2.0% isoflurane, and then the mice were housed in the dark for 6.5 days. We then performed in vivo BLI using TokeOni without lighting. After BLI, the mice were housed in the dark for a further 2 days, and then the mice were exposed to light for 1 h. After light exposure, the mice were housed in the dark for 5 h, and then in vivo BLI was performed again. Region of interest (ROI) analysis was performed according to previous reports [30, 31] with modifications. Briefly, the region of the cerebral cortex was estimated by the bioluminescence signal image (Supplementary Fig. 3a, the region surrounded by a red line), and the region was covered with 16 × 24 ROIs (Supplementary Fig. 3a, 16 × 24 boxes shown in white line). ROIs containing visual cortex (ROI V1 and V2) or somatosensory cortex (ROI S1 and S2) were estimated by mouse brain atlas.

Statistics

All data are presented as the mean ± the standard error of the mean (SEM). Statistical analyses were performed using Prism 7 software (GraphPad). Detailed information

regarding statistical analysis of each result is shown in each figure legend.

Results

Detection of bioluminescence signals from the living *Bdnf-Luc* mouse brain

We first tried to identify a suitable substrate of firefly Luc to enable visualization of changes in *Bdnf* expression in living *Bdnf-Luc* mouse brains using non-invasive in vivo BLI. We used D-luciferin, TokeOni, and seMpai, as Luc substrates (Fig. 1a). TokeOni and seMpai are synthetic luciferins and produce near-infrared light [27, 28, 32]. TokeOni barely dissolves in a neutral pH buffer; a solution with an acidic pH is required, which may be unsuitable for certain experiments. In contrast, seMpai can be dissolved in neutral pH solvents.

To compare the detection of bioluminescence signals produced by each substrate, we administered each substrate to *Bdnf-Luc* mice under inhalation anesthesia and then measured bioluminescence signals (Fig. 1b). Endogenous BDNF is highly abundant in the brain; therefore, strong bioluminescence signals were expected from the brain. However, we could not identify the region of cerebral cortex after intraperitoneal injection of D-luciferin (Fig. 1c). On the other hand, we detected signals from the brain after intracerebroventricular injection of D-luciferin (Supplementary Fig. 1). The signal intensity from the head region obtained using seMpai as a Luc substrate was lower compared with that obtained using D-luciferin (Fig. 1c). In contrast, we clearly detected signals from brain regions, probable the region of cerebral cortex in particular, after injection of TokeOni (Fig. 1c). Both ROI analysis (Fig. 1d) and line profiles (Fig. 1e)

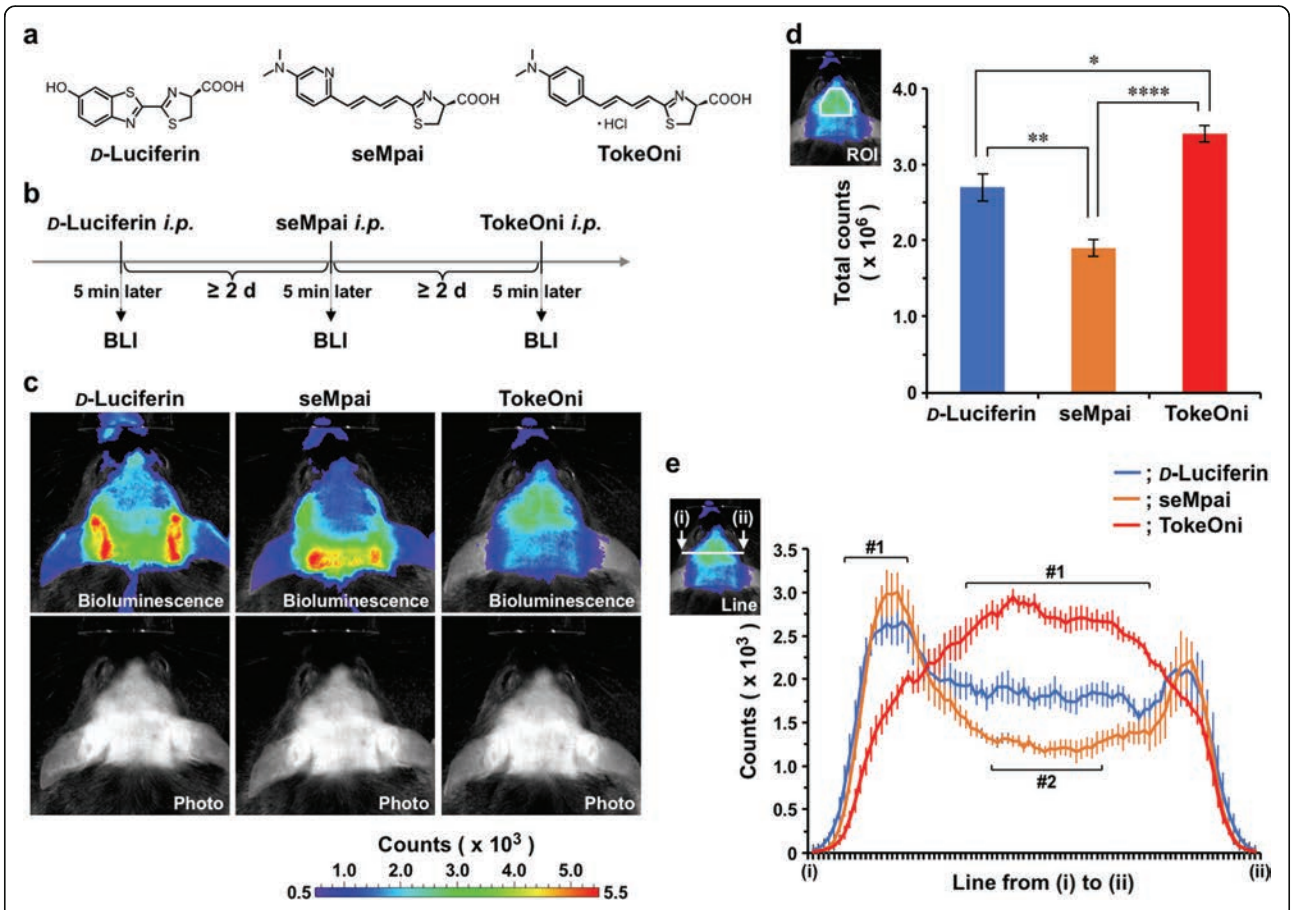

Fig. 1 Comparison of luciferase substrates for in vivo BLI using *Bdnf-Luc* mice. **a.** Structure of D-luciferin, seMpai, and TokeOni. **b.** Schedule of experiments. D-luciferin, seMpai, and TokeOni were administered intraperitoneally to *Bdnf-Luc* mice, and in vivo BLI was performed 5 min after each administration. Each substrate was injected into mice with at least 2 d intervals. **c.** Representative images of in vivo BLI using D-luciferin, seMpai, or TokeOni as a luciferase substrate. Bioluminescence; counts indicated by pseudocolored images. Photo; photographs corresponding to bioluminescence images. **d.** ROI analysis. Data represent the mean ± SEM of four independent experiments using one-way ANOVA with Tukey's multiple comparisons test (*$p < 0.05$, **$p < 0.01$, and ****$p < 0.0001$). **e.** Line profiles [counts from (i) to (ii)]. Data represent the mean ± SEM of four independent experiments using two-way ANOVA with Dunnett's multiple comparisons test [#1; significant difference between D-Luciferin versus TokeOni ($p < 0.05$), #2; significant difference between D-Luciferin versus seMpai ($p < 0.05$)]

showed that higher signal intensities from brain regions were detected using TokeOni compared with using D-luciferin and seMpai. Furthermore, in previous experiments we removed the skin to expose the skull before in vivo BLI [16]; however, bioluminescence signals were clearly detected from the brain of *Bdnf-Luc* mice using TokeOni (Fig. 1c–e), indicating that it is not necessary to expose the skull before in vivo BLI. Thus, TokeOni was the most suitable substrate tested for the non-invasive visualization of BDNF expression levels in the living *Bdnf-Luc* mouse brain.

Visualization of kainic acid-induced *Bdnf* expression in living mouse hippocampus

In our previous study, we successfully visualized the induction of *Bdnf* expression after intracerebroventricular injection of pituitary adenylate cyclase-activating polypeptide [16], which increases *Bdnf* expression in the cerebral cortex [15]. In this study, we examined whether the induction of *Bdnf* expression could be visualized non-invasively in *Bdnf-Luc* mice by in vivo BLI using TokeOni. Kainic acid (KA) increases *Bdnf* expression in the rodent brain [33, 34]; however, we could not detect significant changes in bioluminescence signals after KA administration to *Bdnf-Luc* mice when we use D-luciferin as a Luc substrate (Supplementary Fig. 2). Here, we administered saline or KA to *Bdnf-Luc* mice and then measured bioluminescence signals using TokeOni as a Luc substrate. Compared with signals from saline-administered mice, the signals from the brain were clearly increased after KA administration (Fig. 2a). ROI analysis revealed that the signals from the brain were significantly increased by KA administration (Fig. 2b). In addition, the signals seemed to be strongly increased in the hippocampus (Fig. 2a). To confirm this, we investigated the expression levels of endogenous BDNF in the hippocampus and cerebral cortex after in vivo BLI. Both *Bdnf* mRNA (Fig. 2c) and BDNF protein (Fig. 2d, e) levels were significantly increased by KA administration in the hippocampus but not in the cerebral cortex of *Bdnf-Luc* mice. These results strongly indicated that changes in endogenous *Bdnf* expression could be visualized in the living *Bdnf-Luc* mouse brain by in vivo BLI with TokeOni.

Limitation of using TokeOni for repeated in vivo BLI

One of the advantages of non-invasive BLI to evaluate changes in target gene expression is repeated measurements in the same individual. However, it is necessary to administer a Luc substrate at each measurement. Therefore, we next examined whether TokeOni could be repeatedly administered to *Bdnf-Luc* mice. Five minutes after the administration of D-luciferin to mice, we could detect bioluminescence signals (Fig. 3a, b). The signals were barely detectable 6 h after the administration but could be detected again by re-administration of D-

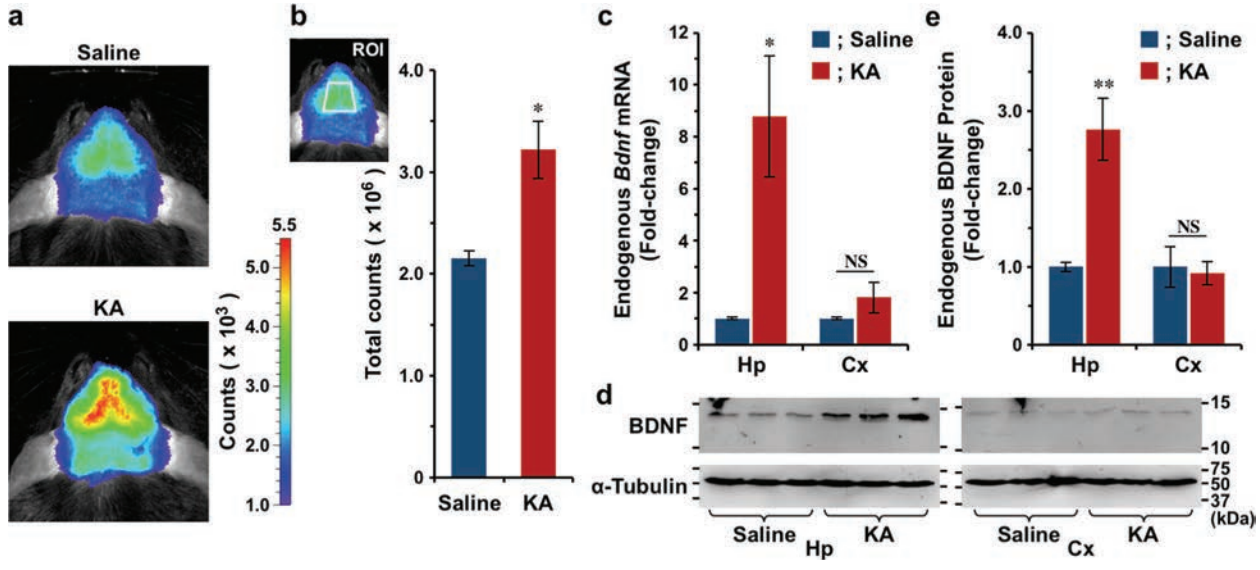

Fig. 2 Visualization of KA-induced *Bdnf* expression. **a.** Representative images of in vivo BLI 6 h after administration of saline or KA. **b.** ROI analysis. Data represent the mean ± SEM of three independent experiments using the unpaired *t* test (*$p < 0.05$). **c.** RT-PCR analysis. After in vivo BLI, total RNA was prepared from the hippocampus (Hp) and cerebral cortex (Cx) of *Bdnf-Luc* mice to examine changes in endogenous *Bdnf* mRNA levels. Data represent the mean ± SEM of three independent experiments using the unpaired *t* test (*$p < 0.05$, NS; not significant). **d.** Immunoblot analysis. After in vivo BLI, proteins were extracted from the hippocampus and cerebral cortex of *Bdnf-Luc* mice to examine changes in endogenous BDNF protein levels. **e.** The intensities of bands shown in Fig. 2d were quantified using Image J. Data represent the mean ± SEM of three independent experiments using the unpaired *t* test (**$p < 0.01$, NS; not significant)

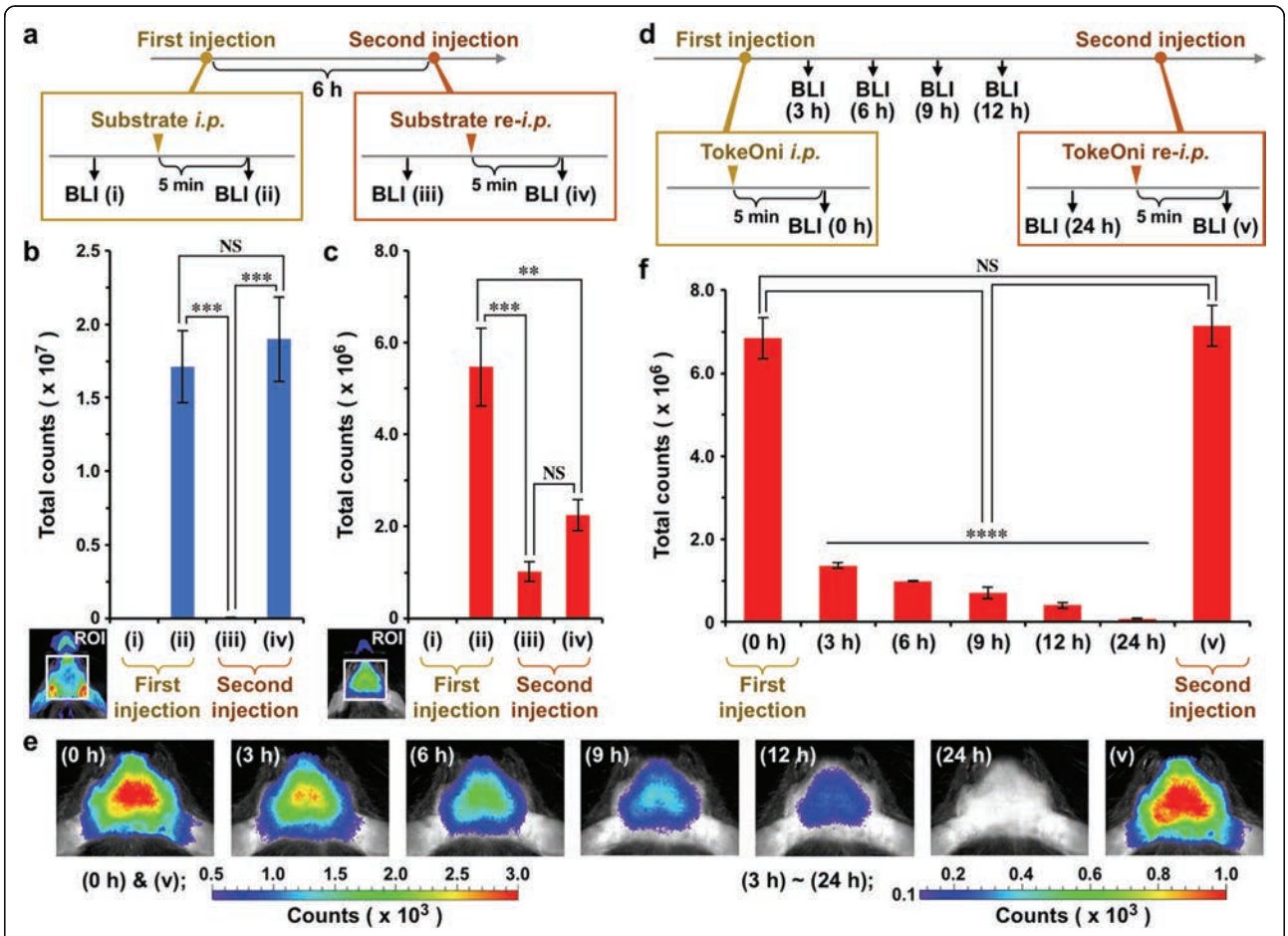

Fig. 3 Limitation of using TokeOni for repeated in vivo BLI. **a.** Schedule of experiments. In vivo BLI was performed before (i) and after (ii) the intraperitoneal administration of each substrate to *Bdnf-Luc* mice (First injection). Six hours after the first injection, in vivo BLI was performed before (iii) and after (iv) substrate administration again (Second injection). **b.** ROI analysis to measure counts at each step. D-luciferin was administered according to the schedule shown in Fig. 3a. Data represent the mean ± SEM of three independent experiments using one-way ANOVA with Tukey's multiple comparisons test (***$p < 0.001$, NS; not significant). **c.** ROI analysis. TokeOni administration and in vivo BLI were performed according to the schedule shown in Fig. 3a. Data represent the mean ± SEM of four independent experiments using one-way ANOVA with Tukey's multiple comparisons test (**$p < 0.01$, ***$p < 0.001$, NS; not significant). **d.** Schedule of experiments. In vivo BLI was performed 5 min after the intraperitoneal administration of TokeOni to *Bdnf-Luc* mice (0 h). Then, in vivo BLI was repeatedly performed at 3, 6, 9, 12, and 24 h without further TokeOni administration. Twenty-four hours after in vivo BLI, TokeOni was re-injected into the mice, and in vivo BLI was performed again (v). **e.** Representative images of in vivo BLI. The pseudocolored range shown to the left (from 0.5×10^3 to 3.0×10^3) corresponds to the images at (0 h) and (v), and the range shown to the right (from 0.2×10^3 to 1.0×10^3) corresponds to the other images. **f.** ROI analysis. TokeOni administration and in vivo BLI were performed according to the schedule shown in Fig. 3d. Data represent the mean ± SEM of four independent experiments using one-way ANOVA with Tukey's multiple comparisons test (****$p < 0.0001$, NS; not significant)

luciferin (Fig. 3a, b). The signal intensity after the second injection was almost the same as the intensity after the first injection (Fig. 3b), indicating that D-luciferin can be repeatedly used for in vivo BLI. Compared with signals detected 5 min after the administration of TokeOni to mice, the signal strength was decreased but still detectable 6 h after the administration (Fig. 3a, c). However, the signal intensity after the second injection was significantly lower than the intensity after the first injection (Fig. 3c). To examine this response further, we administered TokeOni to *Bdnf-Luc* mice once and then performed in vivo BLI at 0, 3, 6, 9, 12, and 24 h after the administration (Fig. 3d). Compared to signals at 0 h, the signals were reduced but detectable 3 h after the administration (Fig. 3e, f). The signals were still detectable at 12 h, but very weak at 24 h after the administration (Fig. 3e, f). Twenty-four hours after the first injection, we re-administered TokeOni to the mice and could detect signals at comparable levels to those after the first injection (Fig. 3e, f). Thus, although TokeOni is a beneficial substrate for detecting bioluminescence signals from living mouse brains non-invasively, the substrate should be administered to mice at appropriate intervals, such as once a day.

Visualization of sensory-driven *Bdnf* expression in the living mouse visual cortex

We next tried to visualize the induction of *Bdnf* expression in the living *Bdnf-Luc* mouse brain under physiological conditions. Light exposure increases BDNF expression in the visual cortex [35, 36]. We, therefore, housed *Bdnf-Luc* mice in the dark for 6.5 days and then performed BLI [Fig. 4a, Light (–)]. After BLI, the mice were again housed in the dark. Two days after the first BLI, the mice were exposed to light for 1 h, housed in the dark for 5 h, and BLI signals measured again [Fig. 4a, Light (+)]. Compared with the signals from the brain of *Bdnf-Luc* mice housed in the dark, light exposure for 1 h increased the signal intensity (Fig. 4b). The signals were likely to be higher in the visual cortex; therefore, we performed ROI analysis (Supplementary Fig. 3). The signals in ROI V1 and V2, the region containing the visual cortex, were significantly increased after light exposure (Fig. 4c). In contrast, the signals in ROI S1 and S2, the region containing the somatosensory cortex, did not change in response to light (Fig. 4c). Thus, we successfully visualized the induction of *Bdnf* expression in the visual cortex of living *Bdnf-Luc* mice in response to sensory stimulation.

Discussion

We previously generated a transgenic mouse strain, *Bdnf-Luc*, to visualize changes in *Bdnf* expression in living cells and mice [15, 16]. However, D-luciferin was not suitable for visualizing changes in *Bdnf* expression in the living mouse brain. One of the problems regarding the detection of bioluminescence signals produced by D-luciferin in *Bdnf-Luc* mouse brain was the poor ability of the substrate to cross the BBB [20, 21]. The ability of D-luciferin to cross the BBB may be limited by ACBG2 [22]. This is also supported the detection of signals from the brain when D-luciferin was injected directly into the brain ventricles of *Bdnf-Luc* mice. Furthermore, the signals obtained from the head region using seMpai were lower than those produced by D-luciferin, suggesting that seMpai may be less able to cross the BBB compared with D-luciferin. The signals produced by D-luciferin, as well as seMpai, were also detected in the regions without black fur. These signals were probably derived from surface tissues such as skin, as previously reported [16]. We confirmed that endogenous *Bdnf* mRNA was expressed in the skin of the head region [16]. However, the signals were strongly detected in the base of the ears in

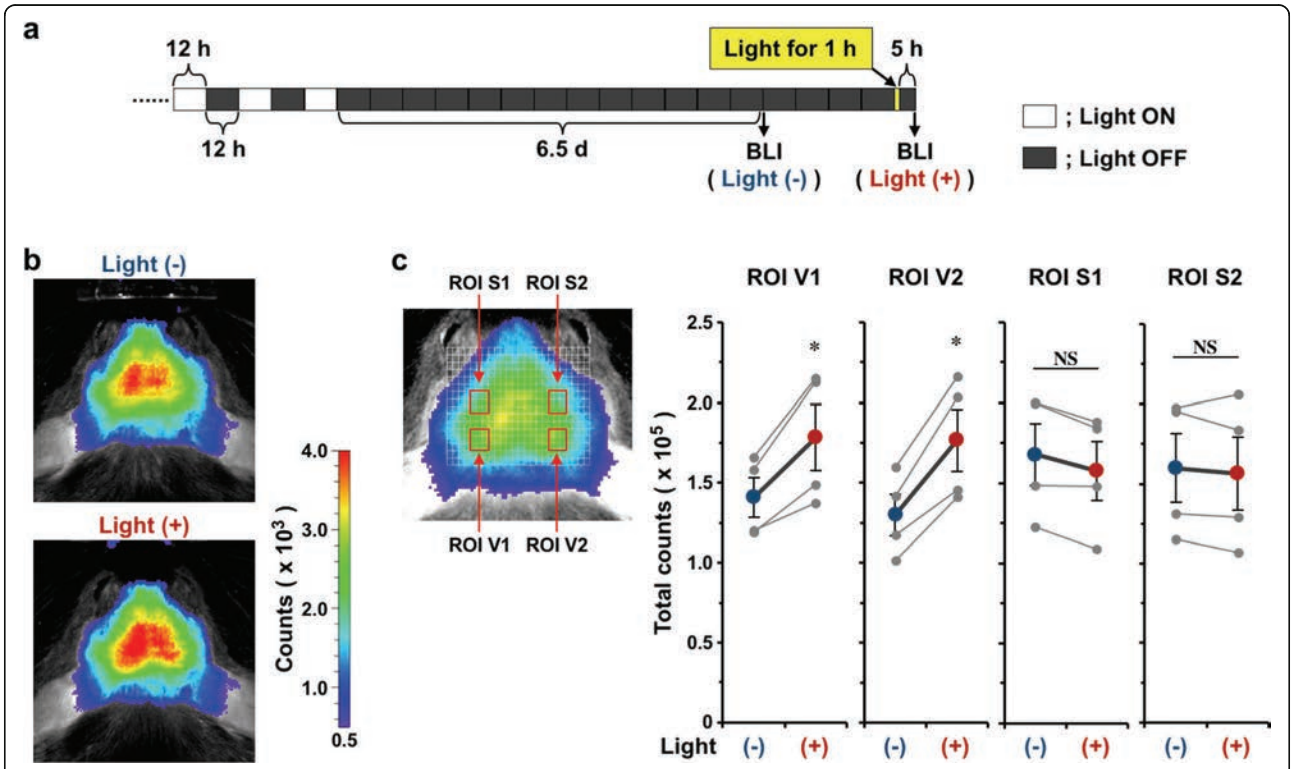

Fig. 4 Visualization of sensory stimulation-induced *Bdnf* expression. **a.** Schedule of experiments (also refer to the Materials and methods). **b.** Representative images of in vivo BLI. In vivo BLI was performed 6.5 d after houseing *Bdnf-Luc* mice in the dark [Light (–)]. The mice were housed in the dark for an additional 2 d, and were then exposed to light for 1 h. After light exposure for 1 h, the mice were again housed in the dark for 5 h, and then in vivo BLI was performed [Light (+)]. **c.** ROI analysis. ROI V1 and V2 contains the visual cortex, and ROI S1 and S2 contains the somatosensory cortex (also refer to Supplementary Fig. 3 in detail). Data represent the mean ± SEM of four independent experiments using the paired *t* test (*$p < 0.05$, NS; not significant)

particular, when we injected D-luciferin to the mice. Further investigations are necessary to identify the bioluminescence signals from peripheral tissues. A hairless mouse strain [31] would help us further examine peripheral *Bdnf* expression by in vivo BLI. In contrast, TokeOni produced signals in the brain, reflecting the high expression levels of endogenous BDNF in the brain.

The other problem of bioluminescence tissue penetration was also solved by using TokeOni, because it produces near-infrared bioluminescence. In our previous study, we removed the skin from the top of the skull of *Bdnf-Luc* mice before in vivo BLI, even if TokeOni was used [16]. However, in this study, we found that the signals were detectable after crossing the skull and skin. In addition, our current results regarding KA-induced *Bdnf* expression demonstrated that the signals in the hippocampus could be detected. Because previous reports suggest that KA disrupts the BBB [37], it might be possible that KA-induced increase in the bioluminescence signals is due to the BBB dysfunction. If so, the KA-induced signals would be also observed using D-luciferin. However, we could not observe the significant changes in the signals after KA administration when we used D-luciferin as a substrate for Luc. On the other hand, it has been shown that the signals obtained by TokeOni have also been detected from the striatum [29]. Thus, we suggest that TokeOni will enable non-invasive in vivo BLI and also bioluminescence signals from deeper brain regions to be detected. In the previous report, bioluminescence signals were successfully detected in freely moving animals using AkaBLI [29]. Therefore, it would be possible to visualize changes in *Bdnf* expression, if the firefly Luc in *Bdnf-Luc* mice is replaced by Akaluc, which is an optimized firefly Luc for TokeOni.

Our current results may reflect differences in the pharmacokinetics of D-luciferin and TokeOni in mice. The in vitro *K*m value of TokeOni is lower than that of D-Luciferin [28], suggesting that the affinity of TokeOni to Luc is higher than that of D-luciferin, which would result in the long-lasting detection of signals produced by TokeOni in vivo. Furthermore, the second signals were significantly reduced when TokeOni was administered to *Bdnf-Luc* mice at 6 h intervals. This reduction is probably caused by product inhibition [38, 39]; enzymatic reaction products of TokeOni may inhibit the Luc-TokeOni enzymatic reaction. In any case, the first and second signal intensities were comparable when TokeOni was administered to mice at 24 h intervals. Therefore, an appropriate interval of administration should be examined before TokeOni is applied to each Luc mouse line. In addition, we previously reported that luciferase activity was stably detected in primary neuronal cells prepared from *Bdnf-Luc* mice after pharmacological inhibition of de novo transcription, despite *Luc* and endogenous *Bdnf* mRNA levels being similarly decreased under the same conditions [40]. Therefore, it should be noted that rapid decreases in *Bdnf* expression and oscillatory changes in *Bdnf* expression are difficult to visualize by in vivo BLI using *Bdnf-Luc* mice.

A number of reports show lower BDNF levels in brains with neurological diseases [2–4, 10, 11]. Non-invasive near-infrared in vivo BLI using *Bdnf-Luc* mice and TokeOni will allow changes in *Bdnf* expression in the brain under physiological and pathophysiological conditions to be examined. Therefore, this method will facilitate further understanding of the relationship between alterations in BDNF levels in the brain and pathophysiology of neurological diseases, assuming that disease model mice can be generated using *Bdnf-Luc* mice. In addition, near-infrared BLI enable the detection of bioluminescence from deep tissue regions, including those of the brain. TokeOni is now commercially available; therefore, our findings also provide instructive information for the application of this substrate to other Luc mouse line.

Supplementary information

Supplementary information accompanies this paper at https://doi.org/10.1186/s13041-020-00665-7.

Additional file 1: Figure S1. In vivo BLI after intracerebroventricular injection of *D*-luciferin into *Bdnf-Luc* mice. **Figure S2.** Detection of bioluminescence signals using *D*-luciferin 6 h after administration of saline or KA to *Bdnf-Luc* mice. **Figure S3.** Visualization of sensory stimulation-induced *Bdnf* expression (ROI analysis).

Abbreviations

ABCG2: ATP-binding cassette (ABC) transporter G2; BBB: Blood-brain-barrier; BDNF: Brain-derived neurotrophic factor; BLI: Bioluminescence imaging; CNS: Central nervous system; KA: Kainic acid; Luc: Luciferase; ROI: Region of interest

Acknowledgements

We are grateful to Kuroganekasei Co. Ltd. (Nagoya, Japan) for donating TokeOni and seMpai. We thank Jeremy Allen, PhD, from Edanz Group (www.edanzediting.com/ac) for editing a draft of this manuscript. This work was supported by the Japan Society for the promotion of Science (JSPS) KAKENHI Grant Nos. 25870256 [Grant-in-Aid for Young Scientists (B) to MF], 16 K12894 (Grant-in-Aid for Challenging Exploratory Research to MF), 16H05275 [Grant-in-Aid for Scientific Research (B) to MF], and 19 K22817 [Grant-in-Aid for Challenging Research (Exploratory) to MF], the Takeda Science Foundation (to MF), and the Mochida Memorial Foundation for Medical and Pharmaceutical Research (to MF).

Authors' contributions

MF designed and supervised the study, performed experiments, analyzed data, and wrote the manuscript. RS and SMak developed luciferin analogues. NH, YN, and SMit performed experiments. HI and HM generated *Bdnf-Luc* mice. All authors contributed to manuscript writing and editing. The author(s) read and approved the final manuscript.

Funding

JSPS KAKENHI Grant Nos. 25870256 [Grant-in-Aid for Young Scientists (B) to MF], 16 K12894 (Grant-in-Aid for Challenging Exploratory Research to MF), 16H05275 [Grant-in-Aid for Scientific Research (B) to MF], and 19 K22817 [Grant-in-Aid for Challenging Research (Exploratory) to MF], the Takeda Science Foundation (to MF), and the Mochida Memorial Foundation for Medical and Pharmaceutical Research (to MF).

Availability of data and materials
All data needed to evaluate the conclusions in the paper are present in the paper.

Ethics approval and consent to participate
Not applicable.

Consent for publication
Not applicable.

Competing interests
The authors declare that they have no competing interests.

Author details
[1]Laboratory of Molecular Neuroscience, Faculty of Pharmacy, Takasaki University of Health and Welfare, 60 Nakaorui-machi, Takasaki, Gunma 370-0033, Japan. [2]Department of Engineering Science, Graduate School of Informatics and Engineering, The University of Electro-Communications, 1-5-1 Chofugaoka, Chofu, Tokyo 182-8585, Japan. [3]School of Pharmacy, Tokyo University of Pharmacy and Life Science, 1432-1 Horinouchi, Hachioji, Tokyo 192-0392, Japan. [4]Department of Molecular Neuroscience, Graduate School of Medicine and Pharmaceutical Sciences, University of Toyama, 2630 Sugitani, Toyama, Toyama 930-0194, Japan.

Received: 2 July 2020 Accepted: 2 September 2020
Published online: 07 September 2020

References

1. Park H, Poo MM. Neurotrophin regulation of neural circuit development and function. Nat Rev Neurosci. 2013;14(1):7–23.
2. Angoa-Pérez M, Anneken JH, Kuhn DM. The role of brain-derived neurotrophic factor in the pathophysiology of psychiatric and neurological disorders. J Psychiatry Psychiatric Disord. 2017;1(5):252–69.
3. Numakawa T, Odaka H, Adachi N. Actions of brain-derived neurotrophic factor in the neurogenesis and neuronal function, and its involvement in the pathophysiology of brain diseases. Int J Mol Sci. 2018;19(11):3650.
4. Lima Giacobbo B, Doorduin J, Klein HC, Dierckx RAJO, Bromberg E, de Vries EFJ. Brain-derived neurotrophic factor in brain disorders: focus on neuroinflammation. Mol Neurobiol. 2019;56(5):3295–312.
5. Ferrer I, Marín C, Rey MJ, Ribalta T, Goutan E, Blanco R, et al. BDNF and full-length and truncated TrkB expression in Alzheimer disease. Implications in therapeutic strategies. J Neuropathol Exp Neurol. 1999;58(7):729–39.
6. Mogi M, Togari A, Kondo T, Mizuno Y, Komure O, Kuno S, et al. Brain-derived growth factor and nerve growth factor concentrations are decreased in the substantia nigra in Parkinson's disease. Neurosci Lett. 1999; 270(1):45–8.
7. Zuccato C, Ciammola A, Rigamonti D, Leavitt BR, Goffredo D, Conti L, et al. Loss of huntingtin-mediated BDNF gene transcription in Huntington's disease. Science. 2001;293(5529):493–8.
8. Dwivedi Y, Rizavi HS, Conley RR, Roberts RC, Tamminga CA, Pandey GN. Altered gene expression of brain-derived neurotrophic factor and receptor tyrosine kinase B in postmortem brain of suicide subjects. Arch Gen Psychiatry. 2003;60(8):804–15.
9. Weickert CS, Hyde TM, Lipska BK, Herman MM, Weinberger DR, Kleinman JE. Reduced brain-derived neurotrophic factor in prefrontal cortex of patients with schizophrenia. Mol Psychiatry. 2003;8(6):592–610.
10. Buchman AS, Yu L, Boyle PA, Schneider JA, De Jager PL, Bennett DA. Higher brain BDNF gene expression is associated with slower cognitive decline in older adults. Neurology. 2016;86(8):735–41.
11. Forlenza OV, Diniz BS, Teixeira AL, Radanovic M, Talib LL, Rocha NP, et al. Lower cerebrospinal fluid concentration of brain-derived neurotrophic factor predicts progression from mild cognitive impairment to Alzheimer's disease. NeuroMolecular Med. 2015;17(3):326–32.
12. Lyons MR, West AE. Mechanisms of specificity in neuronal activity-regulated gene transcription. Prog Neurobiol. 2011;94(3):259–95.
13. Troy T, Jekic-McMullen D, Sambucetti L, Rice B. Quantitative comparison of the sensitivity of detection of fluorescent and bioluminescent reporters in animal models. Mol Imaging. 2004;3(1):9–23.
14. Prescher JA, Contag CH. Guided by the light: visualizing biomolecular processes in living animals with bioluminescence. Curr Opin Chem Biol. 2010;14(1):80–9.
15. Fukuchi M, Tabuchi A, Kuwana Y, Watanabe S, Inoue M, Takasaki I, et al. Neuromodulatory effect of Gαs- or Gαq-coupled G-protein-coupled receptor on NMDA receptor selectively activates the NMDA receptor/Ca^{2+}/calcineurin/cAMP response element-binding protein-regulated transcriptional coactivator 1 pathway to effectively induce brain-derived neurotrophic factor expression in neurons. J Neurosci. 2015;35(14):5606–24.
16. Fukuchi M, Izumi H, Mori H, Kiyama M, Otsuka S, Maki S, et al. Visualizing changes in brain-derived neurotrophic factor (BDNF) expression using bioluminescence imaging in living mice. Sci Rep. 2017;7(1):4949.
17. Zhao H, Doyle TC, Coquoz O, Kalish F, Rice BW, Contag CH. Emission spectra of bioluminescent reporters and interaction with mammalian tissue determine the sensitivity of detection *in vivo*. J Biomed Opt. 2005;10(4): 41210.
18. Dawson JB, Barker DJ, Ellis DJ, Grassam E, Cotterill JA, Fisher GW, et al. A theoretical and experimental study of light absorption and scattering by *in vivo* skin. Phys Med Biol. 1980;25(4):695–709.
19. Weissleder R, Ntziachristos V. Shedding light onto live molecular targets. Nat Med. 2003;9(1):123–8.
20. Lee K-H, Byun SS, Paik J-Y, Lee SY, Song SH, Choe YS, et al. Cell uptake and tissue distribution of radioiodine labelled *D*-luciferin: implications for luciferase based gene imaging. Nucl Med Commun. 2003;24(9):1003–9.
21. Berger F, Paulmurugan R, Bhaumik S, Gambhir SS. Uptake kinetics and biodistribution of ^{14}C-D-luciferin–a radiolabeled substrate for the firefly luciferase catalyzed bioluminescence reaction: impact on bioluminescence based reporter gene imaging. Eur J Nucl Med Mol Imaging. 2008;35(12): 2275–85.
22. Bakhsheshian J, Wei BR, Chang KE, Shukla S, Ambudkar SV, Simpson RM, et al. Bioluminescent imaging of drug efflux at the blood-brain barrier mediated by the transporter ABCG2. Proc Natl Acad Sci U S A. 2013;110(51): 20801–6.
23. Evans MS, Chaurette JP, Adams ST Jr, Reddy GR, Paley MA, Aronin N, et al. A synthetic luciferin improves bioluminescence imaging in live mice. Nat Methods. 2014;11(4):393–5.
24. Cao J, Hu Y, Shazeeb MS, Pedraza CE, Pande N, Weinstock D, et al. In vivo optical imaging of myelination events in a myelin basic protein promoter-driven luciferase transgenic mouse model. ASN Neuro. 2018;10: 1759091418777329.
25. Mofford DM, Adams ST Jr, Reddy GS, Reddy GR, Miller SC. Luciferin amides enable *in vivo* bioluminescence detection of endogenous fatty acid amide hydrolase activity. J Am Chem Soc. 2015;137(27):8684–7.
26. Adams ST Jr, Mofford DM, Reddy GS, Miller SC. Firefly luciferase mutants allow substrate-selective bioluminescence imaging in the mouse brain. Angew Chem Int Ed Eng. 2016;55(16):4943–6.
27. Iwano S, Obata R, Miura C, Kiyama M, Hama K, Nakamura M, et al. Development of simple firefly luciferin analogs emitting blue, green, red, and near-infrared biological window light. Tetrahedron. 2013;69(19):3847–56.
28. Kuchimaru T, Iwano S, Kiyama M, Mitsumata S, Kadonosono T, Niwa H, et al. A luciferin analogue generating near-infrared bioluminescence achieves highly sensitive deep-tissue imaging. Nat Commun. 2016;7:11856.
29. Iwano S, Sugiyama M, Hama H, Watakabe A, Hasegawa N, Kuchimaru T, et al. Single-cell bioluminescence imaging of deep tissue in freely moving animals. Science. 2018;359(6378):935–9.
30. Izumi H, Ishimoto T, Yamamoto H, Nishijo H, Mori H. Bioluminescence imaging of arc expression enables detection of activity-dependent and plastic changes in the visual cortex of adult mice. Brain Struct Funct. 2011; 216(2):91–104.
31. Izumi H, Ishimoto T, Yamamoto H, Mori H. Application of hairless mouse strain to bioluminescence imaging of arc expression in mouse brain. BMC Neurosci. 2017;18(1):18.
32. Saito R, Kuchimaru T, Higashi S, Lu SW, Kiyama M, Iwano S, et al. Synthesis and luminescence properties of near-infrared N-heterocyclic luciferin analogues for *in vivo* optical imaging. Bull Chem Soc Jpn. 2019;92(3):608–18.
33. Gall CN. Seizure-induced changes in neurotrophin expression: implications for epilepsy. Exp Neurol. 1993;124(1):150–66.
34. Koppel I, Aid-Pavlidis T, Jaanson K, Sepp M, Pruunsild P, Palm K, et al. Tissue-specific and neural activity-regulated expression of human BDNF gene in BAC transgenic mice. BMC Neurosci. 2009;10:68.
35. Castrén E, Zafra F, Thoenen H, Lindholm D. (1992) light regulates expression of brain-derived neurotrophic factor mRNA in rat visual cortex. Proc Natl Acad Sci U S A. 1992;89(20):9444–8.

36. Lyons MR, Chen LF, Deng JV, Finn C, Pfenning AR, Sabhlok A, et al. The transcription factor calcium-response factor limits NMDA receptor-dependent transcription in the developing brain. J Neurochem. 2016;137(2):164–76.
37. Han JY, Ahn SY, Yoo JH, Nam SY, Hong JT, Oh KW. Alleviation of kainic acid-induced brain barrier dysfunction by 4-O-methylhonokiol in *in vitro* and *in vivo* models. Biomed Res Int. 2015;2015:893163.
38. Fontes R, Dukhovich A, Sillero A, Sillero MA. Synthesis of dehyroluciferin by firefly luciferase: effect of dehyroluciferin, coenzyme a and nucleoside riphosphates on the luminescent reaction. Biochem Biophys Res Commun. 1997;237(2):445–50.
39. Ribeiro C, Esteves da Silva JC. Kinetics of inhibiton of firefly luciferase by oxyluciferin and dehyroluciferyl-adenylate. Photochem Photobiol Sci. 2008;7(9):1085–90.
40. Fukuchi M, Okuno Y, Nakayama H, Nakano A, Mori H, Mitazaki S, et al. Screening inducers of neuronal BDNF gene transcription using primary cortical cell cultures from BDNF-luciferase transgenic mice. Sci Rep. 2019;9(1):11833.

Publisher's Note

Molecular Therapy
Nucleic Acids
Original Article

Optimization of Lipid Nanoparticles for Intramuscular Administration of mRNA Vaccines

Kimberly J. Hassett,[1] Kerry E. Benenato,[1] Eric Jacquinet,[1] Aisha Lee,[1] Angela Woods,[1] Olga Yuzhakov,[1] Sunny Himansu,[1] Jessica Deterling,[1] Benjamin M. Geilich,[1] Tatiana Ketova,[1] Cosmin Mihai,[1] Andy Lynn,[1] Iain McFadyen,[1] Melissa J. Moore,[1] Joseph J. Senn,[1] Matthew G. Stanton,[1,2] Örn Almarsson,[1] Giuseppe Ciaramella,[1,3] and Luis A. Brito[1]

[1]Moderna Therapeutics, 200 Technology Square, Cambridge, MA 02139, USA

mRNA vaccines have the potential to tackle many unmet medical needs that are unable to be addressed with conventional vaccine technologies. A potent and well-tolerated delivery technology is integral to fully realizing the potential of mRNA vaccines. Pre-clinical and clinical studies have demonstrated that mRNA delivered intramuscularly (IM) with first-generation lipid nanoparticles (LNPs) generates robust immune responses. Despite progress made over the past several years, there remains significant opportunity for improvement, as the most advanced LNPs were designed for intravenous (IV) delivery of siRNA to the liver. Here, we screened a panel of proprietary biodegradable ionizable lipids for both expression and immunogenicity in a rodent model when administered IM. A subset of compounds was selected and further evaluated for tolerability, immunogenicity, and expression in rodents and non-human primates (NHPs). A lead formulation was identified that yielded a robust immune response with improved tolerability. More importantly for vaccines, increased innate immune stimulation driven by LNPs does not equate to increased immunogenicity, illustrating that mRNA vaccine tolerability can be improved without affecting potency.

INTRODUCTION

Since the first active immunization, vaccines have provided increased life expectancy and improved public health, saving countless lives.[1,2] Today, a variety of technologies exist for vaccine development, including live and attenuated viruses, recombinant proteins, synthetic peptides, glycoconjugates, and nucleic acids.[1] Nucleic-acid (DNA and mRNA)-based vaccines offer several advantages over other technologies. They can be rapidly produced with reduced development time and costs by using a common manufacturing platform and purification methods regardless of the antigen. Unlike manufacturing for other vaccines, these methods would not include propagation of viruses or purification of a recombinant protein. The antigen would be expressed *in situ*, allowing for transmembrane domains to be present, if needed, and multimeric complexes to be formed.[3] Additionally, nucleic acids do not suffer from anti-vector immunity like viral vectored vaccines do. Lastly, proteins produced by nucleic-acid-based vaccines can provide a more natural presentation to the immune system, yielding better T cell responses.[4] Even so, more than two decades after the first proof-of-concept report,[5] no nucleic-acid-based vaccine has been approved for use in humans.

A key factor hampering both DNA and mRNA vaccine development is the lack of a potent, well-tolerated delivery system. Because DNA requires delivery to the nucleus, an inherently inefficient process, high doses (1–2 mg) and an electroporation device are required to generate robust immune responses. Although recent advances in DNA electroporation have shown promise, the broad adoption of the technology will likely be limited due to the necessity of a specialized device and the pain associated with electroporation.[6–8] An advantage of mRNA over DNA is that mRNA only requires cytosolic delivery. In rodents, early studies showed that intramuscular administration of buffer-formulated mRNA can lead to measurable levels of immunogenicity.[9] However, a recent phase I trial of a rabies mRNA vaccine administered in Ringer's buffer yielded no immunogenicity unless delivered with a high-pressure intra-dermal injection device.[10]

Although promising, these results highlight the need for more potent intracellular delivery technologies for mRNA vaccines. One such technology is lipid nanoparticles (LNPs). LNPs are typically composed of an ionizable lipid, cholesterol, PEGylated lipid, and a helper lipid such as distearoylphosphatidylcholine (DSPC). Early work with small interfering RNA (siRNA) identified the ionizable lipid as the primary driver of potency.[11–13] The most clinically

Received 28 September 2018; accepted 26 January 2019;
https://doi.org/10.1016/j.omtn.2019.01.013.

[2]Present address: Generation Bio, 215 First Street, Suite 150, Cambridge, MA 02142, USA

[3]Present address: Beam Therapeutics, 325 Vassar Street, Cambridge, MA 02139, USA

Correspondence: Luis A. Brito, Moderna Therapeutics, 200 Technology Square, Cambridge, MA 02139, USA.
E-mail: luis.brito@modernatx.com

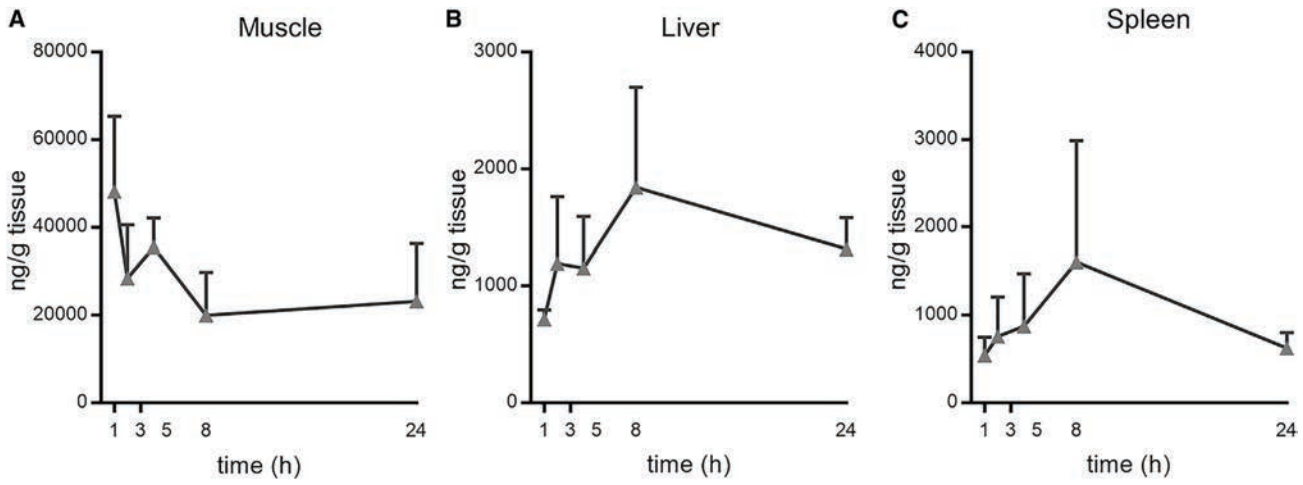

Figure 1. Pharmacokinetics of LNPs containing MC3 after IM administration in mice

Lipid concentration (nanograms per gram) after IM administration of modified mRNA encoding luciferase formulated in LNPs containing MC3 (gray triangles) in muscle, liver, and spleen up to 24 h post-injection (n = 3 per group per time point).

advanced LNP contains the ionizable lipid MC3 and has been shown to be safe in humans after intravenous (IV) administration of siRNA.[14] Our own vaccine trials with MC3-based LNPs for influenza gave 100% seroconversion with a 100-μg dose of modified mRNA. However, consistent with other vaccines,[15,16] we did observe mild to moderate local and systemic adverse events.[17] As healthy individuals ranging from day-old newborns to the elderly receive vaccines, critical features for broad vaccine adoption are minimal injection site reactivity and high tolerability. To date, the only LNPs evaluated for intramuscular (IM) mRNA vaccine delivery were originally optimized for IV delivery of siRNA to the liver.[18,19] Although there are preclinical reports of novel LNPs being evaluated for vaccines, no rationale has been provided regarding formulation composition or selection.[20–22]

Here, we describe rational evolution and selection of an improved formulation for IM administration of mRNA, focusing on the impact of the ionizable lipid component as the primary driver of expression and tolerability. Our previous experience with IV administration of the proprietary ionizable lipids showed rapid clearance compared to MC3,[23] resulting in improved systemic tolerability. Our work here illustrates that the ideal formulation for IV expression is not necessarily ideal for IM expression. Additionally, we also show that increased innate immune stimulation driven by the LNP is not necessary for increased immunogenicity, illustrating that we have an opportunity to improve vaccine tolerability without affecting vaccine potency.

RESULTS

Observations of mild to moderate adverse events in our clinical work with MC3[17] and data showing slow MC3 clearance after IV administration[23] fueled a hypothesis that the adverse events might be related to the extended presence of MC3 at the injection site. Mass spectrometry analysis of muscle tissue revealed that, 24 h after IM injection, the MC3 concentration only decreased by 50% compared to C_{max} (Figure 1A). Further, MC3 was also detectable in liver and spleen 24 h post-IM injection (Figures 1B and 1C). Thus, IM administration of MC3-formulated mRNA LNPs resulted in extended local and systemic lipid exposure.

The goal of the work described here was to identify a new ionizable lipid with improved tolerability and a potency equal or better than that of MC3. To do so, we screened 30 novel LNPs, each containing a different ionizable lipid in place of MC3. Each LNP formulation maintained the same lipid-nitrogen-to-phosphate ratio (N:P) and molar composition of lipid components (ionizable lipid, cholesterol, phospholipid, and polytheylene glycol [PEG] lipid). Co-formulation of mRNAs encoding firefly luciferase and the H10N8 influenza hemagglutinin (HA) antigen allowed both protein expression and immunogenicity to be evaluated in the same study. Luciferase activity was measured by whole-body imaging 6 h post-IM injection of the first dose. Immunogenicity was evaluated by quantifying α-H10 immunoglobulin (Ig)G titers 2 weeks after the second dose, which was administered 3 weeks after the first. The ionizable lipids screened here all contain a tertiary amine with ester-containing lipid tails to enable rapid *in vivo* metabolism.[23] In addition, we also tested the quaternary ammonium containing lipid N-[1-(2,3-Dioleoyloxy)propyl]-N,N,N-trimethylammonium (DOTAP).

Consistent with our previous publications, MC3-formulated mRNA yielded robust titers and protein expression at a low dose (0.001 mg per kg).[17,24] In contrast, we observed no detectable protein expression or immunogenicity for DOTAP-containing LNPs (Figure 2A). Many of our novel biodegradable lipids proved superior to MC3 for both protein expression and immunogenicity upon IM administration. However, there was no strong relationship between protein

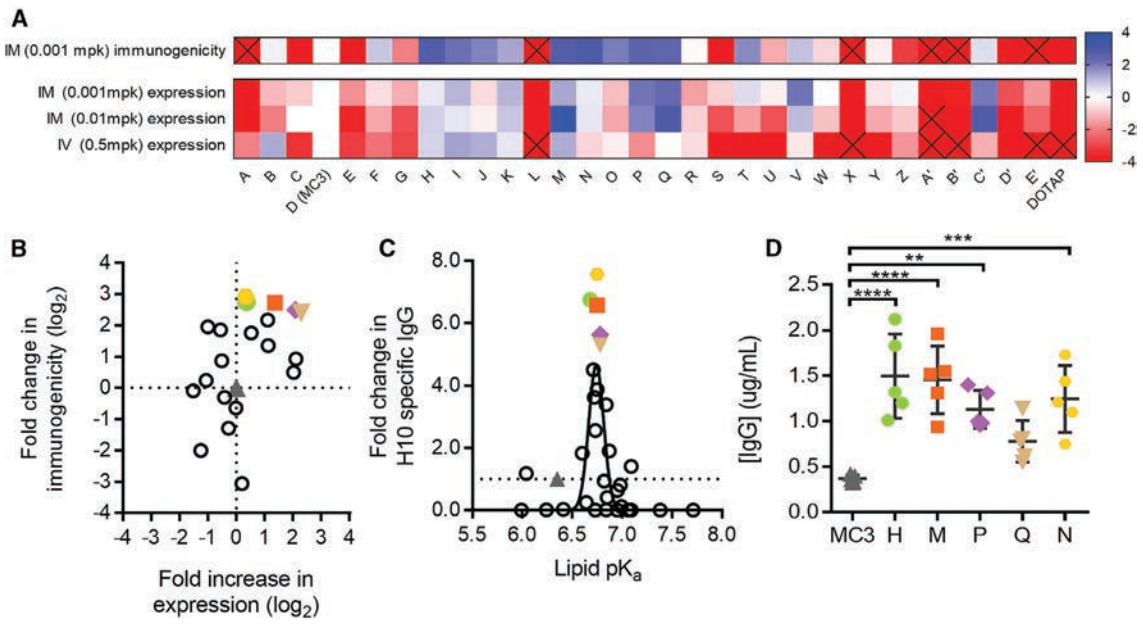

Figure 2. Expression and Immunogenicity from LNPs Containing Novel Ionizable Lipids in Mice

(A) Thirty novel lipid LNPs, A through E′ were compared to a D (MC3) LNP control for expression and immunogenicity. Lipids are arranged left to right in order of pKa from low (A) to high (DOTAP). Expression measured by luminescence in flux (photons per second) 6 h after administration of modified mRNA encoding luciferase delivered at 0.5 mg/kg IV in CD-1 mice, 0.01 mg/kg IM or 0.001 mg/kg IM in BALB/c mice (n = 5 per group). Immunogenicity measured by H10-specific IgG titers measured 2 weeks after two doses administered 3 weeks apart delivered IM at 0.001 mg/kg IM in BALB/c mice (n = 5 per group). Data are represented as $\log_2$ fold change compared to MC3. Squares containing an X indicate >4-fold change ($\log_2$) lower than for MC3. (B) Log_2 fold increase in expression was compared to the $\log_2$ fold change in immunogenicity at the low dose level administered IM (0.001 mg/kg). The five lead novel lipids and MC3 LNPs are labeled accordingly: MC3 (gray triangles), lipid H (green circles), lipid M (orange squares), lipid P (purple diamonds), lipid Q (tan inverted triangles), and lipid N (yellow hexagons). (C) Lipid pK_a versus fold increase in immunogenicity at 0.001 mg/kg IM for lipids A through E′. (D) Circulating IgG antibody (micrograms per milliliter of serum) 6 h after administration of 0.2 mg/kg modified mRNAs encoding the heavy chain and light chain of an influenza monoclonal antibody formulated at a 2:1 mass ratio in LNPs containing MC3 or novel lipids (n = 5 per group). *p < 0.05; **p < 0.01; ***p < 0.001; ****p < 0.0001, ordinary one-way ANOVA with Dunnett's multiple comparisons test of each novel lipid versus MC3.

expression and immunogenicity (r = 0.54). Of the 14 lipids yielding higher α-H10 IgG titers than MC3, four lipids yielded significantly less luciferase expression relative to MC3, whereas four lipids yielded significantly greater luciferase activity (Figure 2B). The two lipids with the highest α-H10 IgG titers were only 1.3-fold better than MC3 with regard to protein expression, illustrating that protein expression upon IM administration was a poor predictor of immunogenicity.

We also found little correspondence in rank between the LNPs with regard to IM versus IV expression (Figure 2A), illustrating that formulations can behave differently when administered locally versus systemically. A possible explanation for the lack of correlation between IM and IV performance could be that the optimal physical or chemical properties differ between the two routes. One strong determinant of immunogenicity was the lipid pKa, with a range of 6.6–6.9 being optimal for IM immunogenicity (Figure 2C). This differs from the optimal pKa range for IV delivery of siRNAs and mRNAs, which has been reported as 6.2–6.6.[11,23] mRNA encapsulation efficiencies and LNP sizes ranged from 69% to 100% and from 50 to 142 nm, respectively. While there was no relationship between encapsulation efficiency and either IM protein expression or immunogenicity, there was a relationship between both readouts and LNP size, with the best performing formulations being 75–95 nm (Figures S1A and S1B).

For further study, we picked the five ionizable lipids exhibiting the greatest increase in α-H10 IgG titers compared to MC3 (colored symbols in Figure 2; structures in Figure 3A). Notably, the pKa for all five lipids was very close to 6.75 (Figure 2C). As an additional measure of potency, we compared the ability of each lead LNP to drive the expression of a secreted IgG antibody after IM administration in mice (Figure 2D). With the exception of lipid Q, the other four lipids yielded higher IgG serum concentrations than MC3 ($p < 0.05$).

To understand the biodegradability of these lipids, we measured lipid levels after IM administration. As expected, IM delivery of these LNPs in CD-1 mice was followed by rapid clearance (Figures 3B–3D). All lead lipids degraded faster than MC3 in muscle (Figure 3B), spleen (Figure 3C), and liver (Figure 3D). 24 h post-injection, the amount of lipid present in muscle dropped considerably from peak levels for all formulations tested, though lipids H and Q did not return to baseline levels by 48 h. Liver and spleen lipid levels closely followed

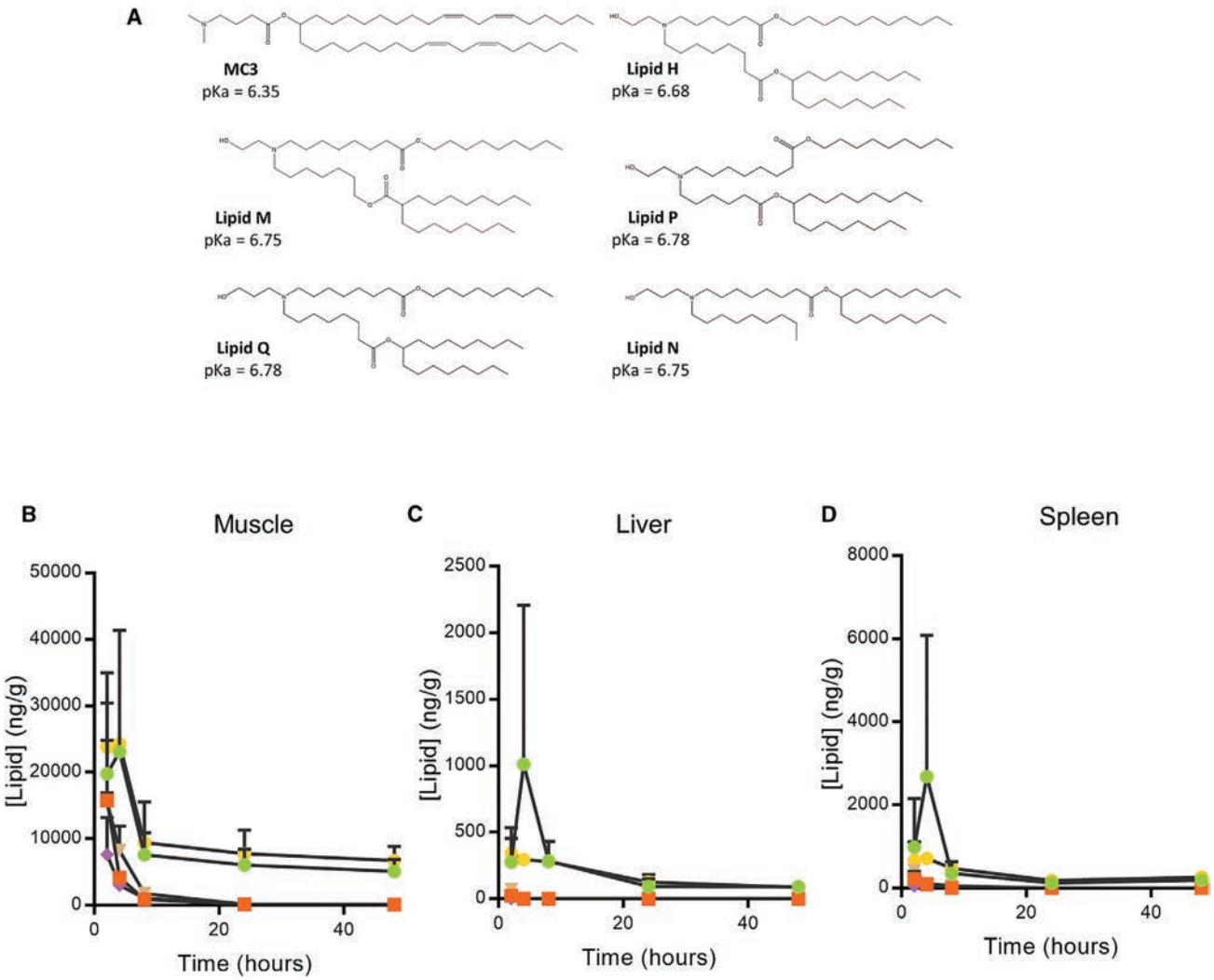

Figure 3. Chemical Structure and Pharmacokinetics of Lead Lipids

(A) Chemical structures and pK_a of MC3 and novel lipids. (B–D) Lipid concentration (nanograms per gram) after IM administration of modified mRNA encoding luciferase formulated in LNPs containing lipid H (green circles), lipid M (orange squares), lipid P (purple diamonds), lipid Q (tan inverted triangles), and lipid N (yellow hexagons) in (B) muscle, (C) liver, and (D) spleen up to 48 h post-injection (n = 3 per group per time point).

IM lipid levels, though lipid H showed a peak at 6 h that dropped by 24 h in the spleen and liver.

Immunogenicity in non-human primates (NHPs) was evaluated after IM injections of H10N8 mRNA formulated with the five lead lipids as LNPs. ELISA antibody titers (Figure 4A) and HAI titers (Figure 4B) were not statistically different for any group (one-way ANOVA, $p > 0.05$), except lipid P was significantly lower than MC3 after the first dose (one-way ANOVA, $p < 0.01$) by ELISA and after the second dose (one-way ANOVA, $p < 0.001$) by HAI titer. Immune responses were measurable after a single dose by ELISA. After a second dose, both HAI and ELISA titers boosted considerably, indicating strong immune priming.

We also tested protein expression of the five lead lipids in NHPs. 500 μg IgG mRNA formulated in LNPs was injected IM, and serum antibody expression levels were monitored for 2 weeks. While three out of the five selected lipids yielded expression comparable to that of MC3-based LNPs, lipid H ($p < 0.001$) and lipid M ($p = 0.05$) showed significantly more expression over time then MC3 (Figure 4C). For lipid H, the maximum antibody concentration measured 24 h post-injection was three times the antibody concentration measured with MC3-formulated material.

To assess tolerability in NHPs, the site of injection was monitored for edema (Figure 4D) and erythema (Figure 4E) 1 and 3 days after injection and was rated based on severity. Despite enhanced protein

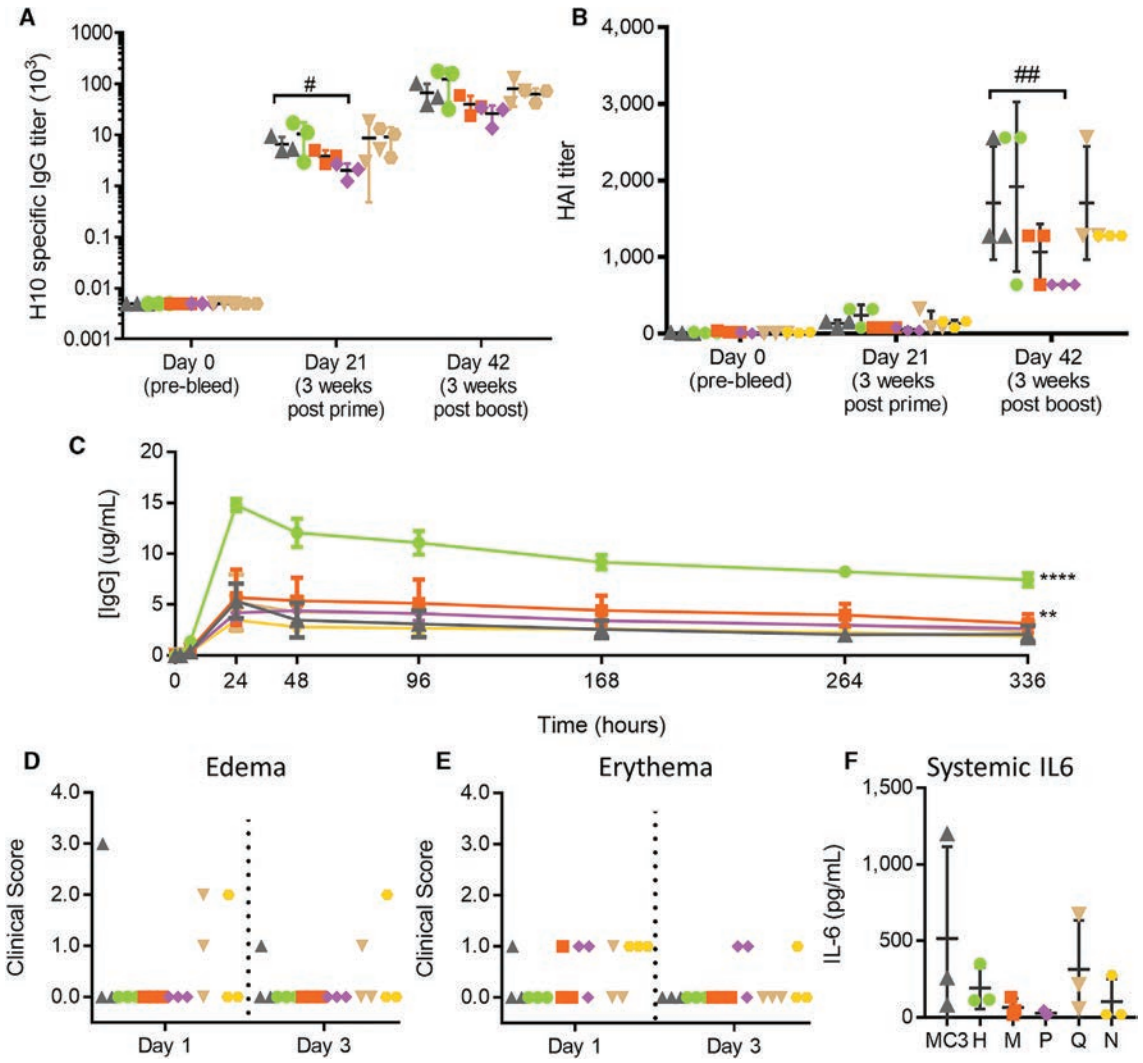

Figure 4. Expression and Immunogenicity in Non-human Primates

(A and B) Immunogenicity measured by H10-specific (A) ELISA or (B) HAI at days 0, 21 (3 weeks after the first dose), and 42 (3 weeks after the second dose). Each dose in cynomolgus monkeys contained 5 μg modified mRNA encoding H10N8 formulated in LNPs containing either MC3 (gray triangles), lipid H (green circles), lipid M (orange squares), lipid P (purple diamonds), lipid Q (tan inverted triangles), or lipid N (yellow hexagons) (n = 3 per group). (C) Circulating IgG levels (in micrograms per milliliter) after a 500-μg IM administration in cynomolgus monkeys of modified mRNA encoding heavy- and light-chain antibodies in a 2:1 weight ratio formulated in LNPs containing MC3 or novel lipids (n = 3 per group). (D and E) Site of injection was monitored for (D) edema and (E) erythema 1 and 3 days after injection. (F) Circulating IL-6 levels (in picograms per milliliter) 6 h after administration. $^{\#}p > 0.05$; $^{\#\#}p > 0.001$, two-way ANOVA with Dunnett's multiple comparison test of each lipid versus MC3 at each time point. $^{**}p > 0.01$; $^{****}p > 0.0001$, z test of areas under the curve (AUCs) for each novel lipid versus MC3.

expression, NHPs injected with lipid-H-based LNPs exhibited no signs of swelling or redness 1 or 3 days post-injection, with all NHPs receiving a score of 0 for both edema and erythema. All other novel lipids evaluated elicited mild to moderate scores for edema and erythema in at least 1 animal dosed. The MC3 group had one NHP receive a score of 3 for edema on day 1 post-injection, resolving to a score of 1 on day 3 post-injection. All lipids tested, except for lipid H, elicited an erythema score of 1 in at least one NHP. Serum interleukin (IL)-6 levels were comparable for all lipids based on one-way ANOVA (Figure 4F). The NHPs in the MC3 group with the highest level of IL-6 also showed the highest level of edema, indicating a strong innate immune response in that individual animal.

To assess and compare the local tolerability of the different ionizable lipid LNPs, we administered 0.01 mg or 0.1 mg mRNA expressing prM-E from the Zika virus formulated in either MC3, lipid H, lipid M, lipid P, lipid Q, or lipid N in Sprague-Dawley rats IM. Serum cytokines in rats receiving both the high and low doses were measured 6 h after administration, using a 22-plex Luminex panel. Changes were observed in eotaxin, GRO-alpha,

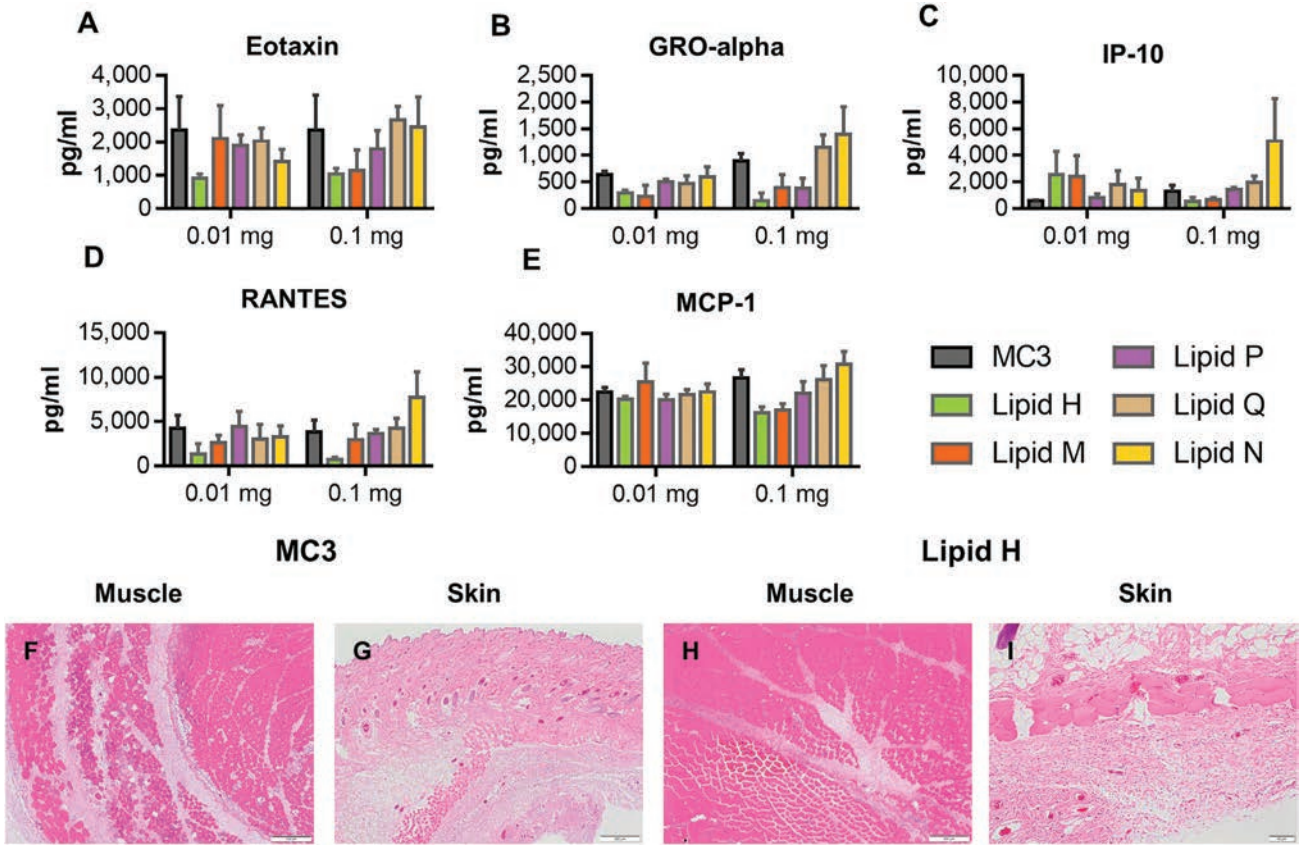

Figure 5. Tolerability in Rats

Serum concentrations (in picograms per milliliter) of cytokines (A) eotaxin, (B) GRO-alpha, (C) IP-10, (D) RANTES, and (E) MCP-1 were measured 6 h after a single IM administration of 0.01 mg or 0.1 mg modified mRNA encoding prM-E from Zika virus formulated in LNPs containing MC3 (gray), lipid H (green), lipid M (orange), lipid P (purple), lipid Q (tan), or lipid N (yellow) (n = 3 per group). (F–I) Representative histology sections stained with H&E 2 days after a single IM administration of 0.1 mg of modified mRNA encoding prM-E from Zika virus formulated in LNPs containing MC3 or lipid H in the (F and H) muscle and (G and I) skin. (F) MC3 muscle; (G) MC3 skin; (H) lipid H muscle; (I) lipid H skin.

IP-10, RANTES, and MCP-1 (Figures 5A–5E). With the exception of IP-10 at the 0.01 mg dose, lipid H induced the lowest systemic cytokine production.

Forty-eight hours after administration, animals were sacrificed, and the injection sites were collected, paraffin embedded, sectioned, H&E stained, and blindly reviewed by a pathologist (Table 1). To evaluate, compare, and rank the local tolerability of each LNP, various endpoints were evaluated and graded, including mixed-cell inflammation at the injection site and in the dermis, myofiber necrosis, and relative number of degenerated neutrophils. MC3-formulated mRNA was the worst tolerated lipid tested, whereas lipid H was the best tolerated lipid tested (Figures 5F–5I).

Rats dosed with MC3 formulations at both the high and low doses displayed a dose-dependent mixed-cell inflammation characterized by edema; numerous intact and degenerate neutrophils; macrophages; and a few lymphocytes distending endomysium, epimysium, and adjacent connective tissue of the muscle and compressing myofibers at the injection site (Figures 5F and S3A). A dose-dependent multifocal degeneration and/or necrosis of individual myofibers, infiltrated by inflammatory cells at times, was also observed. The mixed inflammation observed in the muscle extended into the subcutaneous portion of the skin (Figures 5G and S3B). The subcutaneous tissue was expanded by edema and numerous intact and degenerate neutrophils, macrophages, and a few lymphocytes.

The dose-related mixed-cell inflammation observed in rats administered lipid H was lower in magnitude and severity when compared to the rats given MC3 (Figure 5H). The relative amount of degenerate neutrophils was also lower, and it is worth noticing that there was less degeneration and/or regeneration and/or necrosis in the myofibers. The extension and spillage of the inflammation from the muscular injection site into the subcutaneous tissue was also less severe and with much less edema than in animals given MC3 (Figure 5I).

Table 1. Pathology Summary

Formulation and Dose	Muscle Fiber Necrosis	Mixed-Cell Inflammation	Degenerate Neutrophils	Mixed-Cell Inflammation	Degenerate Neutrophils
MC3					
0.01 mg	2.3	2.4	1.7	2	0
0.1 mg	2.3	2.7	3.3	2	1
Lipid H					
0.01 mg	1	1.8	1	0	0
0.1 mg	1.3	2.9	2.3	1.3	0
Lipid M					
0.01 mg	2	2	1.3	1.7	0
0.1 mg	1.7	2.7	2	2	0
Lipid P					
0.01 mg	2.3	2.2	1.7	1.3	0
0.1 mg	2.3	2.8	2.3	2.3	0.7
Lipid Q					
0.01 mg	2.3	2.2	2	0.7	0
0.1 mg	2	2.9	3	2.5	1
Lipid N					
0.01 mg	0.7	1.4	2	0	0
0.1 mg	1.3	2	2.3	0	0

Rats (n = 3 per group) were injected IM with 0.01 or 0.1 mg modified mRNA encoding prM-E from the Zika virus formulated in LNPs containing MC3 or lipid H. Average histopathology scores on a 0–4 scale were recorded for events occurring in the muscle and skin.

DISCUSSION

mRNA vaccines delivered with LNPs have the potential to address numerous unmet medical needs not accessible with current vaccine technologies. Multiple reports from the siRNA field have shown that the ionizable lipid is the primary driver of LNP potency.[11–13] In this work, we observed the impact of ionizable lipid identity on expression, immunogenicity, and tolerability when delivered IM. Our working hypothesis was that the inclusion of a biodegradable lipid within an LNP would lead to vaccines with improved tolerability, as the lipid would be cleared quickly from the site of injection following mRNA delivery, and other tissues would also have minimal exposure to the lipid due to metabolic breakdown and clearance. Interestingly, throughout our initial screening, we noticed little correlation between expression and vaccine immunogenicity, indicating that expression alone is insufficient to identify improved mRNA vaccine formulations. We also observed a divergence in the best expressing formulations between the IV and IM routes of administration.

Ionizable lipid pK_a is thought to affect the protein opsonization of the particles, cellular uptake, and endosomal escape efficiency. The optimal lipid pK_a for siRNA-mediated knockdown in the liver has been reported to be between 6.2 and 6.5, in line with our finding of the optimal pK_a for mRNA delivery to and expression in the liver as between 6.2 and 6.8.[11,13,23] However, the best lipids with respect to protein expression after IV administration generally had lower pK_as than the best lipids for protein expression after IM administration. Lipids such as V (pK_a = 6.87) and AC (pK_a = 7.09) show little to no expression after IV administration yet were some of the highest expressing lipids after IM administration, indicating a yet-to-be-elucidated difference between these two routes of administration. Different cell types have shown variations in endosome acidification, demonstrating the need for additional work to better understand the performance of LNPs in the context of mRNA delivery across multiple tissues.[25,26] We also found that optimal lipid pK_a for immunogenicity was between 6.6 and 6.8. Independent of cytosolic mRNA delivery, lipid pK_a may also play a role in formulation interactions with the immune system. Although this research area has not been thoroughly explored, a recent report illustrates how ionizable lipids can drive uptake and transfection in immune cells, demonstrating potential areas of research for LNP-mediated delivery of mRNA vaccines.[27] Although lipid pK_a was found to be an important factor for driving immunogenicity, it was not the only factor, as many lipids fell within that pK_a range and were no better than the MC3 control. In addition to differences in pK_a, lipid H also showed an improvement in endosomal escape efficiency, consistent with our previously published report on this class of lipids (Figure S4).[23]

Multiple previous reports speak to the need for a balance between expression and immune stimulation for optimal mRNA vaccine potency.[28,29] Pollard et al. documented the negative impact of interferon signaling on the magnitude of mRNA expression.[29] The mRNAs we used all contained a base modification on uridine to minimize innate immune activation.[24,30] As the mRNA is immune silent compared with canonical uridine-containing mRNA, both antigen selection

and delivery system are important to generate potent immune responses. LNPs have been shown to be effective adjuvants for protein subunit vaccines, but it is unclear how important that adjuvant mechanism is for inducing immune responses from an mRNA vaccine. We previously showed that MC3-based LNPs generated innate immune activation and a potent cellular infiltrate.[31] The histopathology presented here for lipid H, compared to that for MC3, is consistent with improved tolerability and reduced innate immune stimulation. The reduction in inflammatory cell infiltrate, myofiber damage, and systemic cytokines support the hypothesis that mRNA vaccines may not require a strong adjuvant response for potent immune responses.

The improved tolerability and safety mediated by the inclusion of biodegradable lipids within LNPs correlate well with lipid half-life after IV delivery.[23,32] The lead ionizable lipids in this study showed improved biodegradability while maintaining immune titers compared to MC3. The tolerability data suggest that this increased biodegradability leads to a reduction in injection site inflammation. Our data also show that extended residence time of the ionizable lipid post-transfection is not required for a robust immune response. Indeed, clearance is preferred to extended residence, which results in undesirable inflammation at the site of injection beyond when the protein antigen is cleared. Interestingly, the data also indicate that biodegradability is not the only factor in tolerability—lipid H was the best tolerated lipid yet showed a biodegradability similar to that of the other lead lipids tested. Degradation and tolerability of the lipid metabolites likely contribute to the tolerability of any formulation.

Other components, such as PEG, may play a role in vaccine potency due to the impact of anti-PEG responses that have been well described for IV-administered liposomal therapeutics. To date, there is no published information on the impact of anti-PEG responses across other routes of administration. The field of viral vector delivery has described how anti-vector immunity can substantially reduce immune response and can even completely prevent vaccine boosting when a homologous vector is used for both priming and boosting.[33] Given that we see a substantial increase in immune titers after a second dose, we do not believe that a neutralizing anti-PEG response affects the LNP-based vaccines we describe here.

The tolerability of any new vaccine is a key performance criterion, as vaccines are given to healthy individuals throughout different stages of life, from 1-day-old neonates to the elderly. Here, we have described the identification, performance, and tolerability assessment of novel ionizable lipids for inclusion in mRNA vaccine formulations. We focused on the ionizable lipid component of the LNP, as it has been previously demonstrated to be the primary driver of LNP potency and tolerability. Given their improved tolerability and increased antigen expression, the formulations we identified have the potential for both active and passive immunization applications.

MATERIALS AND METHODS

mRNA Synthesis and Formulation

UTR sequences and mRNA production processes were performed as previously described.[19] Briefly, mRNA was synthesized *in vitro* by T7 RNA polymerase-mediated transcription from a linearized DNA template, which incorporates the 5′ and 3′ UTRs and a poly(A) tail. The final mRNA utilizes Cap1 and full replacement of uridine with N1-methyl-pseudouridine. mRNA encoding influenza HA genes originated from the H10N8 strain[34], and the mRNA encoding prM-E from Zika utilized the signal sequences from human IgE (MDWTWILFLVAAATRVHS) and the prM and E genes from an Asian ZIKV strain (Micronesia 2007; GenBank: EU545988), which is >99% identical to circulating American strains.[35] All coding sequences were generated using a proprietary algorithm.

LNP formulations were prepared using a modified procedure of a method previously described.[17] Briefly, lipids were dissolved in ethanol at molar ratios of 50:10:38.5:1.5 (ionizable lipid:DSPC:cholesterol:PEG lipid). LNPs formulated with the ionizable lipid MC3 were used as a control throughout these studies and were produced as previously described.[11] Novel ionizable lipids were synthesized as described elsewhere.[36] The lipid mixture was combined with an acidification buffer of 50 mM sodium citrate (pH 4.0) or 25 mM sodium acetate (pH 5.0) containing mRNA at a volume ratio of 3:1 (aqueous:ethanol) using a microfluidic mixer (Precision Nanosystems, Vancouver, BC, Canada). The ratio of nitrogen present on the ionizable N:P ratio was set to 5.67 for each formulation. Formulations were dialyzed against PBS (pH 7.2) or 20 mM Tris (pH 7.4) with 8% sucrose in Slide-A-Lyzer dialysis cassettes (Thermo Scientific, Rockford, IL, USA) for at least 18 h. Formulations were concentrated using Amicon ultra-centrifugal filters (EMD Millipore, Billerica, MA, USA), if needed, and then passed through a 0.22-μm filter and stored at 4°C (PBS) or −20°C (20 mM Tris-8% sucrose) until use. Formulations were tested for particle size, RNA encapsulation, and endotoxin. All LNPs were found to be between 50 and 142 nm in size by dynamic light scattering and with greater than 69% encapsulation and <3 EU/mL endotoxin. Lead lipids selected for further evaluation were between 66 and 107 nm, with greater than 72% encapsulation.

pK_a Analysis

Assay buffers (buffers containing 150 mM sodium chloride, 10 mM sodium phosphate, 10 mM sodium borate, and 10 mM sodium citrate) were pH adjusted with sodium hydroxide or hydrochloric acid to create buffers with pH ranges from pH 3 to pH 11.5. In a black-bottom, 96-well plate, 300 μM 6-(*p*-toluidino)-2-naphthalenesulfonic acid sodium salt in DMSO (TNS reagent) (Sigma-Aldrich, St. Louis, MO, USA), LNP, and assay buffer were combined. Each pH unit of buffer was repeated in triplicate with TNS reagents and LNPs. Fluorescent measurements were taken using a Synergy H1 microplate reader (BioTek Instruments, Winooski, VT, USA), with excitation set to 325 nm and emission collected at 435 nm. Fluorescence intensity was plotted against the pH of the assay buffer. The log of the inflection point was assigned the apparent pK_a of the LNP.

Expression and Immunogenicity Screening Studies in a Murine Model

All animal experiments and husbandry followed guidelines from NIH (NIH publication #8023, eighth edition) and the U.S. National Research Council. Female BALB/c mice 5–8 weeks old were purchased from Charles River Laboratories (Wilmington, MA, USA) and housed at Moderna Therapeutics (Cambridge, MA, USA). Mice were acclimated for at least 3 days before the initiation of a study. Initial murine screening studies evaluated expression and immunogenicity in the same study, as previous work showed that co-formulation of the two mRNAs did not affect individual results (data not shown). On days 1 and 22, mice were injected in the quadriceps with 50 μL lipid nanoparticle formulations encapsulating an equal amount of luciferase and H10N8 mRNAs. 6 h post-dose, animals received an intraperitoneal injection of 3 mg luciferin and were imaged on an *in vivo* imaging system (IVIS Spectrum, PerkinElmer, Waltham, MA, USA). On days 21 and 36, mice were bled through the submandibular cavity. Serum was separated from the blood by centrifugation and then used to evaluate immunogenicity by ELISA. Group geometric means were calculated for each LNP evaluated and compared to the geometric mean of the MC3 group in the same study (expression) or of all MC3 groups tested (immunogenicity).

Lipid Clearance in a Murine Model

Female CD-1 mice were purchased from and housed at Charles River Laboratories. Mice were acclimated for at least 3 days before the initiation of a study. Mice were injected IM with 50 μL containing 2 μg of luciferase mRNA formulated in LNPs. At 1, 2, 4, 8, and 24 h post-injection, 3 mice were sacrificed and the plasma, spleen, liver, site of injection muscle, and draining lymph nodes were harvested. Tissues were frozen and sent to Agilux (Worcester, MA, USA) for evaluation of the remaining lipid by mass spectroscopy.

Quantification of Lipid by LC-MS/MS

Tissue samples were homogenized by Omni probe following the addition of 19 equivalents (w/v) of water. Lipid and proteins were precipitated and analyzed against calibration standards prepared in a matching blank. Chromatographic separation and quantification was accomplished with a liquid chromatography-tandem mass spectroscopy (LC-MS/MS) system. Samples were separated on a Clipeus C8 column (Higgins Analytical, Mountain View, CA, USA) equilibrated with 35% solvent A containing 5 mM formic acid in 50% methanol (H_2O:MeOH:FA, 50:50:1) and 65% solvent B containing 5 mM formic acid in methanol (MeOH:FA, 100:1; Thermo Fisher Scientific). A triple-quadrupole MS/MS system (Applied Biosystems, API 5500) operated in positive ion mode was used for signal detection.

Tolerability in a Rat Model

Female Sprague-Dawley rats were purchased from Charles River Laboratories and housed at Moderna Therapeutics, Cambridge MA, USA. Rats were injected with 100 μL containing either 10 or 100 μg of mRNA formulated in LNPs. 6 h post-injection, blood was drawn, and serum was used for Luminex cytokine analysis (Austin, TX, USA). 48 h post-injection, rats were sacrificed, and the liver, site of injection, muscle, and skin were collected. Tissues were sectioned, stained with H&E, evaluated by a blinded board-certified pathologist, and graded on a scale from 0 to 5 based on severity for myofiber necrosis, mixed-cell infiltration within muscle and skin, and degenerate neutrophils in muscle and skin.

Expression and Immunogenicity in NHPs

NHP studies were conducted at Charles River Laboratories (Sherbrooke, QC, Canada) using naive cynomolgus monkeys, 2–5 years old and weighing 2–3 kg. Animals were housed in stainless steel, perforated-floor cages, in a temperature- and humidity-controlled environment (21–26°C and 30–70%, respectively), with an automatic 12-h/12-h dark/light cycle. Animals were fed PMI Nutrition Certified Primate Chow No. 5048 twice daily. Tuberculin tests were carried out on arrival at the test facility. The study plan and procedures were approved by pre-clinical services Sherbrook (PCS-SHB) IACUC. Animal experiments and husbandry followed NIH (Publication no. 8023, eighth edition), U.S. National Research Council, and Canadian Council on Animal Care (CCAC) guidelines.

To evaluate expression, cynomolgus NHPs were injected IM with 300 μL containing a total of 500 μg mRNA (heavy chain and light chain in a 2:1 weight:weight ratio) encoding an antibody formulated in LNPs. The site of injection was monitored for erythema and edema and graded for severity from 0 (no reaction) to 4 (severe reaction). Blood was collected 6 h before dosing and then 2, 6, 24, 48, 96, 168, 264, and 336 h post-injection to measure antibody levels. Blood from −6, 48, and 336 h was used to measure hematology, coagulation, D-dimer, and clinical chemistry markers.

To evaluate immunogenicity, cynomolgus monkeys received IM injections of 5 μg H10N8 mRNA-formulated LNP in 100 μL on days 1 and 22. 0.5 mL blood was collected on day 22 and day 43 post-dosing from a peripheral vein and centrifuged at 1200 × *g* for 10 min at 4°C for separation of serum. Serum was stored at −80°C until analysis by hemagglutination inhibition assay (HAI) and ELISA.

HAI Assay

The HAI titers of serum samples were determined using a protocol described previously.[17] Sera were first treated with receptor-destroying enzyme (RDE) to inactivate nonspecific inhibitors. The RDE was inactivated by incubation at 56°C for 30 min. Treated sera were serially diluted in 96-well plates, mixed with a standardized amount of recombinant HA (8 HA units of H10N8; Medigen, Frederick, MD, USA), and incubated for 30 min at room temperature. Turkey red blood cells (RBCs) (Lampire Biological Laboratories, Everett, PA, USA) were then added to the wells of the 96-well plates, mixed, and incubated at room temperature for 45 min. The most dilute serum sample that completely inhibited HA was the reported titer for that replicate. Each serum sample was analyzed in triplicate, and the results are reported as the geometric mean of the 3 results.

Anti-H10N8 ELISA

Nunc MaxiSorp 96-well plates (Thermo Fisher, Rochester, NY, USA) were coated at 100 µL per well with 1 µg/mL H10 protein in PBS overnight at 4°C. Plates were washed three times with PBS containing 0.1% Tween 20 (wash buffer). 200 µL Superblock (Pierce, Rockford, IL, USA) was added to each well and incubated at 37°C for at least 1.5 h and then washed three times with wash buffer. In each well, 100 µL PBS containing 5% goat serum (GIBCO, Gaithersburg, MD, USA) with 0.1% Tween 20 was added, and serum was serially diluted and incubated for 2 h at 37°C. Plates were washed three times, and 100 µL horseradish peroxidase (HRP)-conjugated goat anti-mouse IgG antibody (Southern Biotech, Birmingham, AL, USA) diluted 1:20,000 in PBS containing 5% goat serum with 0.1% Tween 20 was added and incubated for 1 h at 37°C. Plates were washed three times, and 100 µL SureBlue TMB Microwell Peroxidase substrate (Kirkegaard & Perry Labs, Milford, MA, USA) was added to each well and incubated for 15 min. 100 µL TMB Stop Solution (Kirkegaard & Perry Labs, Milford, MA, USA) was added to each well, and the plates were read at 450 nm. The average blank value was subtracted from each sample. Titers were defined as the reciprocal serum dilution at approximately $OD_{450\ nm}$ (optical density 450 nm) = 0.6 (normalized to a standard included on every plate).

Monoclonal Antibody Detection

QUICKPLEX 96-well plates (MSD) were coated with 100 µg of 1 µg/mL capture protein in PBS per well and incubated overnight at 4°C. Plates were washed with PBS with 0.5% Tween 20 three times. Serial dilutions for a reference standard and samples were performed into a 100-µL final volume in the plate and then were incubated at room temperature for 1.5 h, with shaking at 120 rpm. Plates were washed with PBS with 0.5% Tween 20 three times. 50 µL affinity-purified goat anti-human IgG (sulfo-tagged) at 0.5 µg/mL was added to each well and incubated for 1 h at room temperature, with shaking at 120 rpm. After incubation, plates were washed six times, and 150 µL MSD Read Buffer T was added to each well. The plates were read on an MSD instrument (Meso Scale Diagnostics, Rockville, MD, USA).

SUPPLEMENTAL INFORMATION

Supplemental Information includes Supplemental Methods and four figures and can be found with this article online at https://doi.org/10.1016/j.omtn.2019.01.013.

AUTHOR CONTRIBUTIONS

Conceptualization, G.C. and L.A.B.; Methodology, K.J.H., K.E.B., E.J., and L.A.B.; Formal analysis, K.J.H. and I.M.; Investigation, K.J.H., E.J., A. Lee, A.W., O.Y., S.H., J.D., B.M.G., T.K., and A. Lynn; Writing – Original Draft, K.J.H., and L.A.B.; Writing – Review and Editing, K.J.H., M.J.M., and L.A.B.; Visualization, K.J.H., I.M., and L.A.B.; Supervision, K.E.B., C.M., J.J.S., M.G.S., O.A., and G.C.

CONFLICTS OF INTEREST

All authors are either current or previous employees of Moderna Therapeutics and own stock options and/or shares in the company.

ACKNOWLEDGMENTS

We would like to thank Moderna's Preclinical Production group for production of mRNA and Moderna's Nonclinical Sciences group for *in vivo* experiments. This work was funded by Moderna Therapeutics.

REFERENCES

1. Rappuoli, R., Mandl, C.W., Black, S., and De Gregorio, E. (2011). Vaccines for the twenty-first century society. Nat. Rev. Immunol. *11*, 865–872.
2. Riedel, S. (2005). Edward Jenner and the history of smallpox and vaccination. Proc. (Bayl. Univ. Med. Cent.) *18*, 21–25.
3. John, S., Yuzhakov, O., Woods, A., Deterling, J., Hassett, K., Shaw, C.A., and Ciaramella, G. (2018). Multi-antigenic human cytomegalovirus mRNA vaccines that elicit potent humoral and cell-mediated immunity. Vaccine *36*, 1689–1699.
4. Deering, R.P., Kommareddy, S., Ulmer, J.B., Brito, L.A., and Geall, A.J. (2014). Nucleic acid vaccines: prospects for non-viral delivery of mRNA vaccines. Expert Opin. Drug Deliv. *11*, 885–899.
5. Ulmer, J.B., Donnelly, J.J., Parker, S.E., Rhodes, G.H., Felgner, P.L., Dwarki, V.J., Gromkowski, S.H., Deck, R.R., DeWitt, C.M., Friedman, A., et al. (1993). Heterologous protection against influenza by injection of DNA encoding a viral protein. Science *259*, 1745–1749.
6. Ferraro, B., Morrow, M.P., Hutnick, N.A., Shin, T.H., Lucke, C.E., and Weiner, D.B. (2011). Clinical applications of DNA vaccines: current progress. Clin. Infect. Dis. *53*, 296–302.
7. Roos, A.K., Eriksson, F., Walters, D.C., Pisa, P., and King, A.D. (2009). Optimization of skin electroporation in mice to increase tolerability of DNA vaccine delivery to patients. Mol. Ther. *17*, 1637–1642.
8. Tebas, P., Roberts, C.C., Muthumani, K., Reuschel, E.L., Kudchodkar, S.B., Zaidi, F.I., White, S., Khan, A.S., Racine, T., Choi, H., et al. (2017). Safety and immunogenicity of an anti-Zika virus DNA vaccine - preliminary report. N. Engl. J. Med. Published online October 4, 2017. https://doi.org/10.1056/NEJMoa1708120.
9. Carralot, J.P., Probst, J., Hoerr, I., Scheel, B., Teufel, R., Jung, G., Rammensee, H.G., and Pascolo, S. (2004). Polarization of immunity induced by direct injection of naked sequence-stabilized mRNA vaccines. Cell. Mol. Life Sci. *61*, 2418–2424.
10. Alberer, M., Gnad-Vogt, U., Hong, H.S., Mehr, K.T., Backert, L., Finak, G., Gottardo, R., Bica, M.A., Garofano, A., Koch, S.D., et al. (2017). Safety and immunogenicity of a mRNA rabies vaccine in healthy adults: an open-label, non-randomised, prospective, first-in-human phase 1 clinical trial. Lancet *390*, 1511–1520.
11. Jayaraman, M., Ansell, S.M., Mui, B.L., Tam, Y.K., Chen, J., Du, X., Butler, D., Eltepu, L., Matsuda, S., Narayanannair, J.K., et al. (2012). Maximizing the potency of siRNA lipid nanoparticles for hepatic gene silencing in vivo. Angew. Chem. Int. Ed. Engl. *51*, 8529–8533.
12. Love, K.T., Mahon, K.P., Levins, C.G., Whitehead, K.A., Querbes, W., Dorkin, J.R., Qin, J., Cantley, W., Qin, L.L., Racie, T., et al. (2010). Lipid-like materials for low-dose, in vivo gene silencing. Proc. Natl. Acad. Sci. USA *107*, 1864–1869.
13. Semple, S.C., Akinc, A., Chen, J., Sandhu, A.P., Mui, B.L., Cho, C.K., Sah, D.W., Stebbing, D., Crosley, E.J., Yaworski, E., et al. (2010). Rational design of cationic lipids for siRNA delivery. Nat. Biotechnol. *28*, 172–176.
14. Coelho, T., Adams, D., Silva, A., Lozeron, P., Hawkins, P.N., Mant, T., Perez, J., Chiesa, J., Warrington, S., Tranter, E., et al. (2013). Safety and efficacy of RNAi therapy for transthyretin amyloidosis. N. Engl. J. Med. *369*, 819–829.
15. Roman, F., Vaman, T., Kafeja, F., Hanon, E., and Van Damme, P. (2010). AS03(A)-adjuvanted influenza A (H1N1) 2009 vaccine for adults up to 85 years of age. Clin. Infect. Dis. *51*, 668–677.
16. Reisinger, K.S., Baxter, R., Block, S.L., Shah, J., Bedell, L., and Dull, P.M. (2009). Quadrivalent meningococcal vaccination of adults: phase III comparison of an investigational conjugate vaccine, MenACWY-CRM, with the licensed vaccine, Menactra. Clin. Vaccine Immunol. *16*, 1810–1815.
17. Bahl, K., Senn, J.J., Yuzhakov, O., Bulychev, A., Brito, L.A., Hassett, K.J., Laska, M.E., Smith, M., Almarsson, Ö., Thompson, J., et al. (2017). Preclinical and clinical

demonstration of immunogenicity by mRNA vaccines against H10N8 and H7N9 influenza viruses. Mol. Ther. *25*, 1316–1327.

18. Geall, A.J., Verma, A., Otten, G.R., Shaw, C.A., Hekele, A., Banerjee, K., Cu, Y., Beard, C.W., Brito, L.A., Krucker, T., et al. (2012). Nonviral delivery of self-amplifying RNA vaccines. Proc. Natl. Acad. Sci. USA *109*, 14604–14609.
19. Richner, J.M., Himansu, S., Dowd, K.A., Butler, S.L., Salazar, V., Fox, J.M., Julander, J.G., Tang, W.W., Shresta, S., Pierson, T.C., et al. (2017). Modified mRNA vaccines protect against Zika virus infection. Cell *168*, 1114–1125.e10.
20. Pardi, N., Hogan, M.J., Pelc, R.S., Muramatsu, H., Andersen, H., DeMaso, C.R., Dowd, K.A., Sutherland, L.L., Scearce, R.M., Parks, R., et al. (2017). Zika virus protection by a single low-dose nucleoside-modified mRNA vaccination. Nature *543*, 248–251.
21. Lutz, J., Lazzaro, S., Habbeddine, M., Schmidt, K.E., Baumhof, P., Mui, B.L., Tam, Y.K., Madden, T.D., Hope, M.J., Heidenreich, R., and Fotin-Mleczek, M. (2017). Unmodified mRNA in LNPs constitutes a competitive technology for prophylactic vaccines. NPJ Vaccines *2*, 29.
22. Oberli, M.A., Reichmuth, A.M., Dorkin, J.R., Mitchell, M.J., Fenton, O.S., Jaklenec, A., Anderson, D.G., Langer, R., and Blankschtein, D. (2017). Lipid nanoparticle assisted mRNA delivery for potent cancer immunotherapy. Nano Lett. *17*, 1326–1335.
23. Sabnis, S., Kumarasinghe, E.S., Salerno, T., Mihai, C., Ketova, T., Senn, J.J., Lynn, A., Bulychev, A., McFadyen, I., Chan, J., et al. (2018). A novel amino lipid series for mRNA delivery: improved endosomal escape and sustained pharmacology and safety in non-human primates. Mol. Ther. *26*, 1509–1519.
24. Richner, J.M., Himansu, S., Dowd, K.A., Butler, S.L., Salazar, V., Fox, J.M., Julander, J.G., Tang, W.W., Shresta, S., Pierson, T.C., et al. (2017). Modified mRNA vaccines protect against Zika virus infection. Cell *169*, 176.
25. Kou, L., Sun, J., Zhai, Y., and He, Z. (2013). The endocytosis and intracellular fate of nanomedicines: Implication for rational design. Asian Journal of Pharmaceutical Sciences *8*, 1–10.
26. Rybak, S.L., and Murphy, R.F. (1998). Primary cell cultures from murine kidney and heart differ in endosomal pH. J. Cell. Physiol. *176*, 216–222.
27. Fenton, O.S., Kauffman, K.J., Kaczmarek, J.C., McClellan, R.L., Jhunjhunwala, S., Tibbitt, M.W., Zeng, M.D., Appel, E.A., Dorkin, J.R., Mir, F.F., et al. (2017). Synthesis and biological evaluation of ionizable lipid materials for the in vivo delivery of messenger RNA to B lymphocytes. Adv. Mater. *29*, 1606944.
28. Brito, L.A., Chan, M., Shaw, C.A., Hekele, A., Carsillo, T., Schaefer, M., Archer, J., Seubert, A., Otten, G.R., Beard, C.W., et al. (2014). A cationic nanoemulsion for the delivery of next-generation RNA vaccines. Mol. Ther. *22*, 2118–2129.
29. Pollard, C., Rejman, J., De Haes, W., Verrier, B., Van Gulck, E., Naessens, T., De Smedt, S., Bogaert, P., Grooten, J., Vanham, G., and De Koker, S. (2013). Type I IFN counteracts the induction of antigen-specific immune responses by lipid-based delivery of mRNA vaccines. Mol. Ther. *21*, 251–259.
30. Karikó, K., Buckstein, M., Ni, H., and Weissman, D. (2005). Suppression of RNA recognition by Toll-like receptors: the impact of nucleoside modification and the evolutionary origin of RNA. Immunity *23*, 165–175.
31. Liang, F., Lindgren, G., Lin, A., Thompson, E.A., Ols, S., Röhss, J., John, S., Hassett, K., Yuzhakov, O., Bahl, K., et al. (2017). Efficient targeting and activation of antigen-presenting cells in vivo after modified mRNA vaccine administration in rhesus macaques. Mol. Ther. *25*, 2635–2647.
32. Maier, M.A., Jayaraman, M., Matsuda, S., Liu, J., Barros, S., Querbes, W., Tam, Y.K., Ansell, S.M., Kumar, V., Qin, J., et al. (2013). Biodegradable lipids enabling rapidly eliminated lipid nanoparticles for systemic delivery of RNAi therapeutics. Mol. Ther. *21*, 1570–1578.
33. Liu, J., Ewald, B.A., Lynch, D.M., Denholtz, M., Abbink, P., Lemckert, A.A., Carville, A., Mansfield, K.G., Havenga, M.J., Goudsmit, J., and Barouch, D.H. (2008). Magnitude and phenotype of cellular immune responses elicited by recombinant adenovirus vectors and heterologous prime-boost regimens in rhesus monkeys. J. Virol. *82*, 4844–4852.
34. Chen, H., Yuan, H., Gao, R., Zhang, J., Wang, D., Xiong, Y., Fan, G., Yang, F., Li, X., Zhou, J., et al. (2014). Clinical and epidemiological characteristics of a fatal case of avian influenza A H10N8 virus infection: a descriptive study. Lancet *383*, 714–721.
35. Lanciotti, R.S., Kosoy, O.L., Laven, J.J., Velez, J.O., Lambert, A.J., Johnson, A.J., Stanfield, S.M., and Duffy, M.R. (2008). Genetic and serologic properties of Zika virus associated with an epidemic, Yap State, Micronesia, 2007. Emerg. Infect. Dis. *14*, 1232–1239.
36. Benenato, K.E., Kumarasinghe, E.S., and Cornebise, M. (2017). Compounds and compositions for intracellular delivery of therapeutic agents. US patent application publication 20170210697 A1, filed March 31, 2017, and published July 27, 2017.

nature structural & molecular biology

ARTICLES

https://doi.org/10.1038/s41594-020-0479-4

Controlling the SARS-CoV-2 spike glycoprotein conformation

Rory Henderson[1,2]✉, Robert J. Edwards[1,2], Katayoun Mansouri[1], Katarzyna Janowska[1], Victoria Stalls[1], Sophie M. C. Gobeil[1], Megan Kopp[1], Dapeng Li[1], Rob Parks[1], Allen L. Hsu[3], Mario J. Borgnia[3], Barton F. Haynes[1,2,4] and Priyamvada Acharya[1,5]✉

The coronavirus (CoV) spike (S) protein, involved in viral–host cell fusion, is the primary immunogenic target for virus neutralization and the current focus of many vaccine design efforts. The highly flexible S-protein, with its mobile domains, presents a moving target to the immune system. Here, to better understand S-protein mobility, we implemented a structure-based vector analysis of available β-CoV S-protein structures. Despite an overall similarity in domain organization, we found that S-proteins from different β-CoVs display distinct configurations. Based on this analysis, we developed two soluble ectodomain constructs for the SARS-CoV-2 S-protein, in which the highly immunogenic and mobile receptor binding domain (RBD) is either locked in the all-RBDs 'down' position or adopts 'up' state conformations more readily than the wild-type S-protein. These results demonstrate that the conformation of the S-protein can be controlled via rational design and can provide a framework for the development of engineered CoV S-proteins for vaccine applications.

The ongoing global pandemic of the novel SARS-CoV-2 coronavirus presents an urgent need for the development of effective preventative and treatment therapies. The viral spike (S)-protein is a prime target for such therapies because of its critical role in the virus life cycle. The transmembrane CoV S-protein spike trimer is composed of interwoven protomers that include an N-terminal receptor-binding S1 subunit and a C-terminal S2 subunit that contains the fusion elements (Fig. 1a,b)[1]. The S1 subunit is subdivided into the N-terminal domain (NTD) followed by the receptor-binding domain (RBD) and two structurally conserved subdomains (SD1 and SD2). Together, these domains cap the S2 subunit, protecting the conserved fusion machinery. Binding to the host receptor via the RBD in S1 is followed by proteolytic cleavage of the spike by host proteases[2]. Large conformational changes in the S-protein result in S1 shedding and exposure of the fusion machinery in S2. Class I fusion proteins, such as the CoV-2 S-protein, undergo large conformational changes during the fusion process and must, by necessity, be highly flexible and dynamic. Indeed, cryo-EM structures of the SARS-CoV-2 spike reveal considerable flexibility and dynamics in the S1 subunit[1,2], especially around the RBD, which exhibits two discrete conformational states—a 'down' state that is shielded from receptor binding and an 'up' state that is receptor-accessible.

The wealth of structural information for β-CoV S-proteins, including the recently determined cryo-EM structures of the SARS-CoV-2 spike[1–11], has provided a rich source of detailed geometric information from which to begin precise examination of the macromolecular transitions underlying triggering of this fusion machine. Several structures of soluble ectodomain constructs that retain the complete S1 subunit and the surface-exposed S2 subunit have been determined. These include SARS-CoV-2[1,3], SARS[4–8], MERS[4,9] and other human[1,10] and murine[11] β-CoV S-proteins. These structures revealed remarkable conformational heterogeneity in the S-protein spikes, especially in the RBD region. Within a single protomer, the RBD could adopt a closed down state in which the RBD covers the apical region of the S2 protein near the C terminus of the first heptad repeat (HR1), or an open up state in which the RBD is dissociated from the apical central axis of S2 and the NTD (Fig. 1a). Furthermore, the cryo-EM structures strongly suggest a large degree of domain flexibility in both the down and up states in the NTD and RBD. Although these structures have provided essential information to identify the relative arrangement of these domains, the degree to which conformational heterogeneity may be altered via mutation during the natural evolution of the virus and in a vaccine immunogen design context remains to be determined.

In this study we quantify the variability in the S1 and S2 geometric arrangements to reveal important regions of flexibility to consider and to target for structure-based immunogen design. Based on these analyses, we design mutations that alter the conformational distribution of the domains in the S-protein. We visualize the effect of our designs using a structural determination pipeline relying first on single-particle analysis by negative-stain electron microscopy (NSEM) for rapid and low-cost assessment of the spike ectodomains at low resolution, followed by cryo-EM for high-resolution information on the changes introduced by these mutations. Our results reveal a heterogeneous conformational landscape of the SARS-CoV-2 spike that is highly susceptible to modification by the introduction of mutations at sites of contact between the S1 and S2 subunits. We also present data on modified SARS-CoV-2 ectodomain constructs stabilized in conformations that have not yet been seen in the current available structures, with great interest and direct application in vaccine design.

Results

Defining domain geometry and arrangements in SARS-CoV-2 spike. To characterize the unique arrangement of distinct domains

[1]Duke Human Vaccine Institute, Durham, NC, USA. [2]Duke University, Department of Medicine, Durham, NC, USA. [3]Genome Integrity and Structural Biology Laboratory, NIEHS, NIH, Department of Health and Human Services, Durham, NC, USA. [4]Duke University, Department of Immunology, Durham, NC, USA. [5]Duke University, Department of Surgery, Durham, NC, USA. ✉e-mail: rory.henderson@duke.edu; priyamvada.acharya@duke.edu

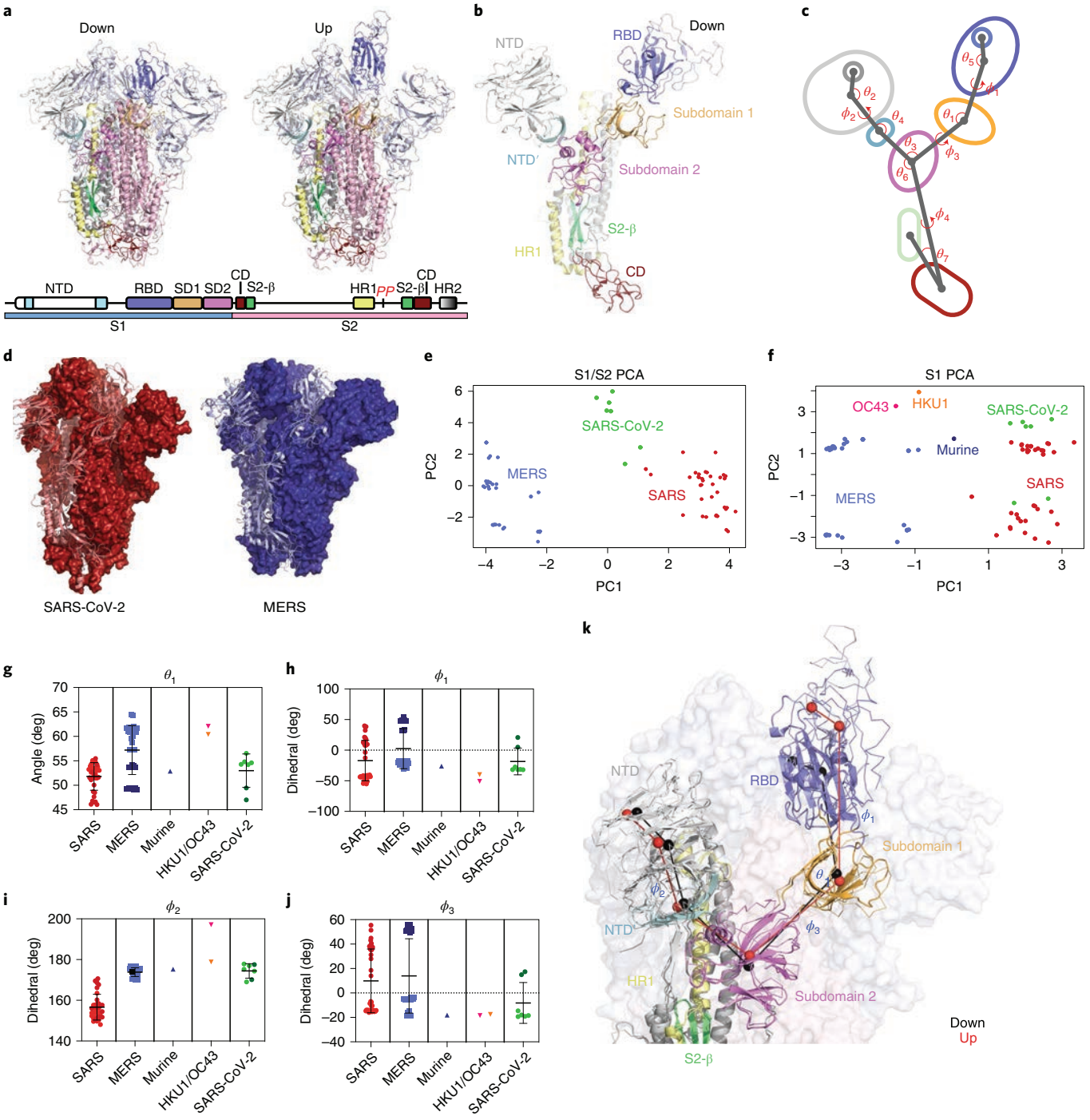

Fig. 1 | Vector-based analysis of the CoV S-protein demonstrates remarkable variability in the S-protein conformation within 'up' and 'down' states between CoV strains. a, Cartoon representations of the down (top left) and up (top right) state SARS-2 structures (PDB 6VXX and 6VYB, respectively), colored according to the specified domains (bottom). **b**, A single down-state protomer of the CoV S-protein with labeled domains (PDB 6VXX). The RBD is in its down conformation. **c**, A simplified diagram of the CoV S-protein depicting the centroids and vectors connecting them, with the determined angles (θ) and dihedrals (ϕ) labeled. **d**, The SARS-2 (left, PDB 6VXX) and MERS (right, PDB 6Q04) structures, each with a single protomer depicted in cartoon representation and the remaining two in surface representation. The structures were aligned with the images captured from the same angle for visualization. **e**, Principal components analysis (PCA) of the SARS and MERS protomers showing measures between the S1 and S2 domains. **f**, PCA of the SARS, MERS, HKU1 and murine CoV protomers showing measures only between the S1 domains. **g**, Angle between the SD2-to-SD1 vector and the SD1-to-RBD vector. **h**, Dihedral about the SD1-to-RBD vector. **i**, Dihedral about the NTD-to-NTD′ vector. The OC43 value of −162° has been adjusted to 197° (+360°) for visualization. **j**, Dihedral about the SD2-to-SD1 vector. Data points for SARS, MERS and SARS-2 in **g**–**j** are colored according to the up (dark) and down (light) states and the color code in the PCA analysis in **e** and **f**. Lines show mean and s.d. The PDB IDs for all structures represented in the PCA and angle/dihedral plots are listed in Supplementary Table 1. **k**, Structural representation of the **g**–**j** angles and dihedrals overlaid on an alignment between a SARS-2 down (cartoon structure with black centroids and lines; PDB 6VXX) and an up (ribbon structure with red centroids and lines; PDB 6VYB) state protomer. Adjacent protomers are depicted as a transparent surface with S1 (light blue) and S2 (light pink). Source data for graphs are provided in Supplementary Data 1.

in the different β-CoV spikes, we first developed a quantitative definition of their relative positions (Fig. 1). Examination of available SARS and MERS S-protein structures revealed the following: (1) domains in the S1 subunit (NTD, RBD and subdomains) and in the S2 subunit (connector domain (CD)) move as rigid bodies and (2) these domains display a pronounced array of relative shifts between those in the S1 subunit and the S2 subunit β-sheet motif and CD. To quantify these movements, we analyzed the relevant regions of motion and their structural disposition in available β-CoV ectodomain spike structures, including 15 for SARS[4,5,7,8], 16 for MERS[4,8,9,12], one each for HKU1[1,10], OC43[1,10] and a murine β-CoV, and three SARS-CoV-2[3,13] structures (Fig. 1e–j and Extended Data Fig. 1). Each protomer in these structures displaying asymmetric up/down RBD states was examined independently, yielding a dataset of 83 structural states. Structures lacking the RBD were not analyzed. Only the S1 subunits were analyzed for the HKU1, OC43 and murine β-CoV S-protein structures. Information regarding whether the constructs are cleaved, mutated and/or liganded is provided in Supplementary Table 1.

The NTD was split into a primary N-terminal section and a secondary C-terminal section based on visual inspection of this region in the various β-CoV structures. Vectors connecting each region's Cα centroids were generated and used to define the relative dispositions of the domains (Fig. 1b,c). The vector magnitudes and select angles and dihedrals were used to identify the breadth of differences in domain positioning and compare between β-CoV viruses (Fig. 1e–j). Projecting the S1 and S2 subunit vector data for SARS-CoV-1, MERS and SARS-CoV-2 using the principal components analysis method revealed that each virus's S-protein structures resided in distinct clusters (Fig. 1e). A similar analysis of the S1 subunit vectors with the addition of data from the murine β-CoV, HKU1 and OC43 generally retained these clusters, with the three additional structures lying in relatively unique positions (Fig. 1f). The SARS-CoV-1 structures split into two distinct clusters, separated largely by differences in the up/down states, with SARS-CoV-2 structures splitting with it. The distinct clustering of SARS-CoV-1 compared to SARS-CoV-2 in the PCA results, which include the S2 subunit data, suggests that there are key differences in the S1 disposition relative to S2 between SARS-CoV-1 and SARS-CoV-2.

Consistent with the PCA analysis, examination of specific angles and dihedrals indicated that β-CoV S-proteins in various viruses differ markedly from one another (Fig. 1g–j). This is in addition to considerable variability in the domain arrangements within different virus S-proteins, demonstrating its wide structural lability (Fig. 1e–j). In particular, both ϕ_1 and ϕ_3 (Fig. 1h,j), describing the dihedrals about the vector connecting SD2 to SD1 and the vector connecting SD1 to the RBD (Fig. 1b,c), respectively, effectively reported on the up and down configurations and indicated substantial differences between SARS-CoV-1 and MERS in both the up and down states. Differences in the angular disposition of the NTD elements of SARS-CoV-1 and MERS as measured by ϕ_1, θ_2 and θ_4 were also observed (Fig. 1i and Extended Data Fig. 1a,c). Additional S1 and S1/S2 subunit differences between viruses were observed for vectors involving SD2. This includes the SD2 to CD ϕ_4 dihedral, which differs markedly between MERS/SARS-CoV-2 and SARS-CoV-1, and the angle between the vectors connecting the NTD′ to SD2 and SD2 to the CD, demonstrating a shift in SARS-CoV-2 (Extended Data Fig. 1e,g). Finally, the disposition of the CD to the inner portion of S2 measured as an angle between a vector connected to an interior S2 β-sheet motif and the vector connecting the CD to SD2 indicates SARS-CoV-1 differs from both MERS and SARS-CoV-2 (Extended Data Fig. 1f). The MERS disposition appears to respond to RBD triggering in some structures, displaying a bimodal distribution (Extended Data Fig. 1f).

These results demonstrate that, although the individual domain architectures and overall arrangements are conserved, important differences between these domains exist between viruses, suggesting that subtle differences in interdomain contacts could play a major role in determining these distributions and thereby alter surface antigenicity and the propensity of the domains to access up and down RBD states.

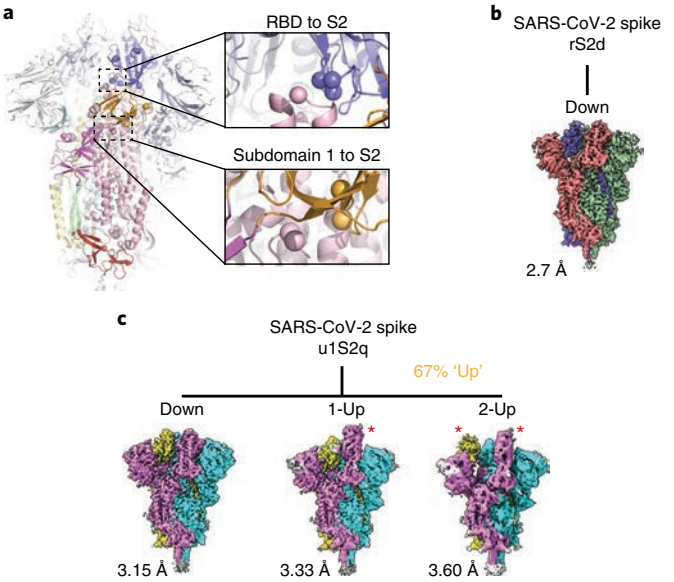

Fig. 2 | Cryo-EM structures reveal differential stabilization of the S-protein in the mutant ectodomain constructs. a, The S-protein spike, highlighting the two regions of interest for structure and computation-based design (PDB 6VXX). **b**, The rS2d RBD-to-S2 locked structure displaying only the all-RBD-down state map. **c**, The u1S2q SD1-to-S2 mutated structure displaying the all-RBD-down state, the 1-RBD up state and the 2-RBD up state. The percentage shown in orange is the sum of particles found in either the 1- or 2-RBD up state. Each protomer in each map is colored differently, with resolutions for these listed below. Red asterisks indicate up-state RBDs.

Differential stabilization of SARS-CoV-2 spike ectodomain RBD orientation. Based on the observed variability in the analysis of β-CoV spikes, we asked whether the propensity for the RBD to display the down and up states could be modified via mutations, without altering the exposed antigenic surfaces. We focused on domain pairs that moved relative to each other (Fig. 1) and identified interaction sites that could alter the S-protein conformational distribution. That is, modification of the up/down equilibrium could be achieved by modifying either the RBD or subdomain contact surfaces. To this end, we selected contact regions between the RBD and S2, the RBD and NTD, SD1 and S2, and SD2 and S2. Mutations at these sites were selected based on in silico mutagenesis using the Schrödinger Biologics suite[14–16]. To eliminate exposure of the receptor binding site of the RBD, we examined the potential for disulfide linkages between the RBD and its contact with S2 near the C terminus of HR1 to prevent RBD exposure.

We identified a double cysteine mutant, S383C D985C (RBD to S2 double mutant (rS2d), Extended Data Fig. 2), as a candidate. The transition from the down state to the up state involves shifts in the RBD to NTD contacts. Therefore, to prevent these shifts, we identified a site in an RBD groove adjacent to the NTD, and prepared a triple mutant, D398L S514L E516L (RBD to NTD triple mutant (rNt), Extended Data Fig. 2). As SD1 acts as a hinge point for the RBD up/down transitions (Figs. 1a–c and 2i,j), we hypothesized that enhanced hydrophobicity at the SD1 to S2 interface might shift the position of SD1, thus influencing the hinge and potentially the

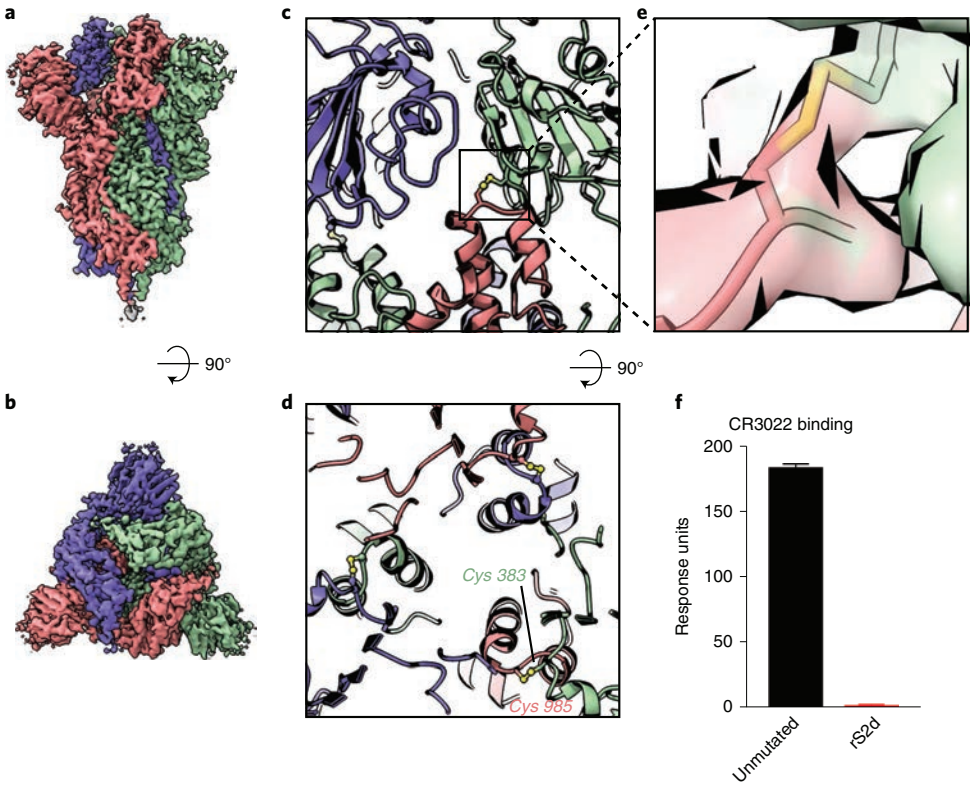

Fig. 3 | Cryo-EM structure of the rS2d construct locked in the down state. a, Cryo-EM reconstruction of rS2d, colored by chain. **b**, Rotated view (by ~90°) of **a**. **c**, Magnified view showing the engineered disulfide linking the RBD of one protomer and the S2 domain of the adjacent protomer. The disulfide bridge is shown as spheres and colored by elements. **d**, Rotated view (by ~90°) of **c**. **e**, Magnified view of the engineered interchain disulfide showing the cryo-EM density as a transparent surface and the underlying model in stick representation. **f**, Binding of antibody CR3022 to the unmutated structure (black bar) and rS2d (red bar). The spike was captured on a streptavidin chip and binding to CR3022 immunoglobulin-G (IgG) was measured by surface plasmon resonance (SPR). Data shown are means and s.d. of three technical repeats and are representative of five independent experiments.

propensity for RBD triggering. A double mutant, N866I A570L (subdomain 1 to S2 double mutant (u1S2d)), and a quadruple mutant, A570L T572I F855Y N856I (subdomain 1 to S2 quadruple mutant (u1S2q)), were identified for this purpose (Extended Data Fig. 2). Finally, we identified a double cysteine mutant, G669C and T866C, to link SD2 to S2 (subdomain 2 to S2 double mutant (u2S2d), Extended Data Fig. 2).

NSEM analysis of SARS-CoV-2 spike ectodomain proteins. The mutants were prepared in the context of a previously published SARS-CoV-2 ectodomain construct[3] (Extended Data Fig. 3). To assess the quality of the purified proteins, we performed NSEM analysis (Extended Data Fig. 4). The micrographs show a reasonably uniform distribution of particles consistent with the size and shape of the SARS-CoV-2 spike ectodomain. Two-dimensional (2D) class averages showed spike populations with well-resolved domain features.

Following 3D classification then homogeneous refinement, the unmutated spike resolved into two classes of roughly equal proportions that differed in the position of their RBD domains. One class displayed all three RBDs in their down positions, whereas the other class displayed one RBD in the up position. This was consistent with published cryo-EM results[13] that describe a 1:1 ratio between the down and 1-up states of the SARS-CoV-2 spike ectodomain.

The mutant spikes, analyzed using a similar workflow, showed different conformation distributions compared to the unmutated spike. The most pronounced changes were observed in the rS2d and u1S2q constructs (Extended Data Fig. 4c,e). For the rS2d construct, we observed only the down conformation (Extended Data Fig. 4c); the 1-RBD up state was not found in this dataset. In the u1S2q data, we observed an S-protein population with 2 RBDs in the up position, which has been reported before for the SARS-CoV-1 and MERS CoV spike ectodomains[7,9]. These two constructs were selected for downstream, high-resolution characterization by cryo-EM.

Cryo-EM and properties of the SARS-CoV-2 spike constructs. We collected cryo-EM datasets for the rS2d and u1S2q constructs (Figs. 2–6, Table 1 and Extended Data Figs. 5–9). Consistent with the NSEM analysis, following multiple rounds of 2D and 3D classification, we found a population of down state spike in the rS2d dataset (Fig. 3 and Extended Data Fig. 6). We then implemented additional exhaustive ab initio classifications, as well as heterogeneous classifications using low-pass filtered maps of known open conformations of CoV spikes to search for open state spikes in the dataset. We were unable to find any such states, suggesting that the disulfide bond between the RBD and the S2 subunit effectively locked the SARS-CoV-2 spike in its down conformation. The rS2d cryo-EM reconstruction had an overall resolution of 2.7 Å, but the local resolution varied widely (Extended Data Fig. 6g), with the highest resolutions in the S2 subunit (Extended Data Fig. 6h) and higher disorder and lower local resolutions in the S1 subunit; this is consistent with previous structures of the SARS-CoV-2 spike[3,13]. We observed connecting density at the site of the engineered disulfide link in rS2d, thus confirming disulfide formation (Fig. 3c–e). Alignment of this structure with that of the unmutated down closed state structure (PDB 6VXX)[13] indicated that the overall protein structure was otherwise unperturbed (root-mean-square deviation (r.m.s.d.) of 0.5 Å).

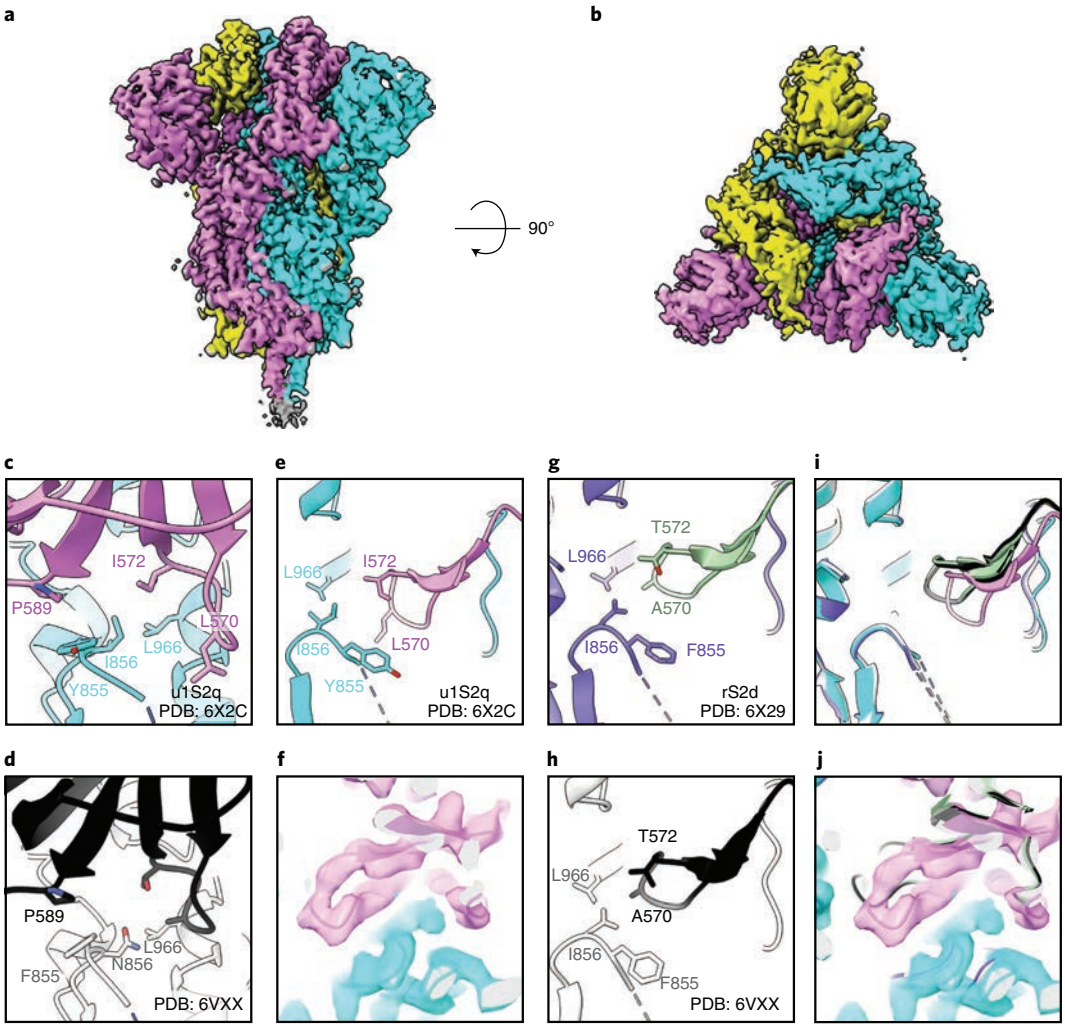

Fig. 4 | Cryo-EM structures of RBD-down S-proteins reveal differential stabilization of domain positions. a, Cryo-EM reconstruction of u1S2q colored by chain. **b**, Rotated view (by ~90°) of **a**. **c**, Magnified view of the region containing the mutations, showing the proximity of the F855Y and N856I residue loop to the S2 residue L966 and S1 residue P589. **d**, Similar region to that shown in **c** but for the unmutated structure (PDB 6VXX). **e**, Magnified view of the region containing the mutations at a different angle than the one shown in **c**. **f**, The loop containing the A570L and T572I mutations, with the cryo-EM map shown as a transparent surface and fitted model shown in cartoon representation. **g**,**h**, Similar region to that shown in **e** but for the rS2d structure (PDB 6X29) (**g**) and the unmutated structure (PDB 6VXX) (**h**). **i**,**j**, Overlay of the three down state structures (**i**) and with the cryo-EM reconstruction for the down state for the u1S2q construct (**j**).

We next tested the binding of rS2d to antibody CR3022 (Fig. 3f and Extended Data Fig. 7a)[17,18]. CR3022 binds an epitope on the RBD of the SARS-CoV-1 and SARS-CoV-2 spikes that is occluded in the down RBD conformation. Although we observed robust binding for the unmutated spike to CR3022, no measurable binding was observed for rS2d, confirming that the RBD in the rS2d construct is locked in a down conformation. Also, as expected, the rS2d mutant showed reduced binding to angiotensin-converting enzyme 2 (ACE-2) compared to the unmutated spike (Extended Data Fig. 7b,c), and such activity could be abrogated using an ACE-2 or a CR3022 IgG-immobilized column for purification (Extended Data Fig. 7c–h).

In contrast to rS2d, the u1S2q spike displayed widespread rearrangement of the S1 subunits (Extended Data Figs. 8 and 9). In the down state structure, the mutated S2 position remained in the configuration observed in the unmutated construct, with the F855Y and N856I residue loop in close proximity to S2 residue L966 and S1 residue P589 (Fig. 4c,d), suggesting that these mutations had little impact on the observed shifts. However, the S2-interactive SD1 displayed a rigid body movement relative to both the rS2d and unmutated constructs, with θ_1 and ϕ_3 displacements of 3.7° and 2.4°, respectively (Fig. 4e–j and Extended Data Fig. 10). This resulted in displacement of the A570L + T572I-containing loop from the unmutated position near the S2 L966 residue (Fig. 4i,j). The S2 contact disruption is accompanied by an angular shift of the NTD away from the primary trimer axis due to SD1 to NTD′ contacts, yielding θ_3 and ϕ_2 shifts of 6.0° each, respectively (Extended Data Fig. 10). The subdomain rearrangement impacts the positioning of the RBD with only a minor shift in the ϕ_1 dihedral of 0.1° indicating that the RBD moved with SD1, indicated in the θ_1/ϕ_3 shifts. The newly acquired arrangement in both the RBD and NTD was further accompanied by an apparent increase in their flexibility, suggesting conformational heterogeneity. These down state shifts were observed in both the single RBD up structure and the two RBD up structures (Figs. 5 and 6 and Extended Data Fig. 10). The extent to which the SD1 shift differed from that observed in the unmutated construct was context-dependent in the 1-RBD up state (Fig. 5c–h). Although the down state RBD in contact with the up state RBD displayed the large shift in position observed in the all down state (Fig. 5d,g), the down state RBD with its terminal position free displayed an

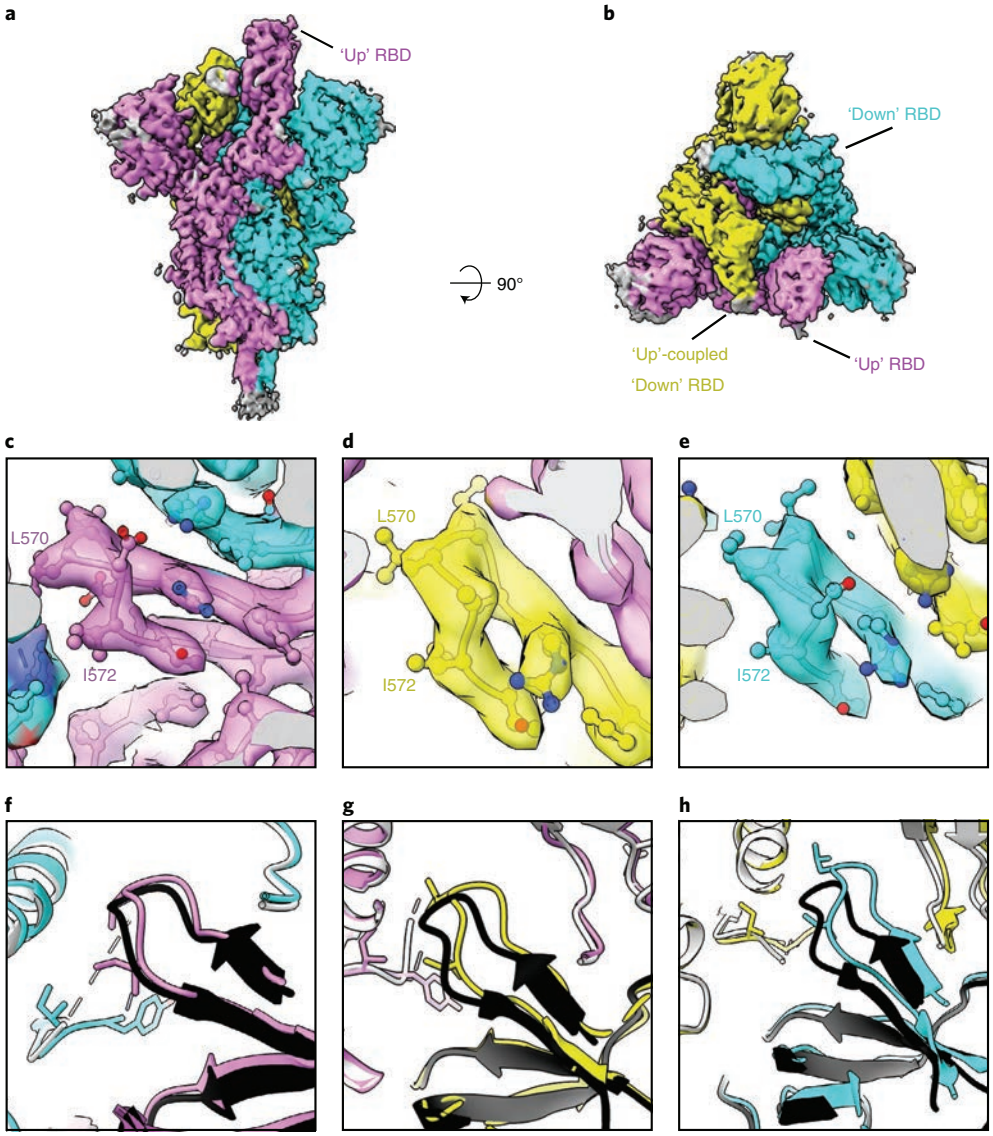

Fig. 5 | Cryo-EM structure of the u1S2q 1-RBD up state reveals increasing relaxation of the triggered RBD toward the unmutated structure. a, Cryo-EM reconstruction of the u1S2q 1-RBD up state colored by chain. **b**, Rotated view (by ~90°) of **a**. **c**–**e**, Magnified views of the region containing the A570L and T572I mutations in the 'up' RBD protomer (**c**), the 'up'-coupled 'down' RBD protomer (**d**) and the 'down' RBD protomer (**e**) of the asymmetric 1-RBD up spike. The cryo-EM reconstruction is shown as a transparent surface with the underlying fitted model in cartoon representation and residues as balls and sticks. **f**–**h**, The 1-RBD up structure of the unmutated spike (PDB 6VYB) (shown in black and gray) superimposed on the u1S2q 1-RBD up structure (PDB 6X2B, this study), colored according to the coloring scheme in **a**. Overlays are shown for the 'up' RBD protomer (**f**), the 'up'-coupled 'down' RBD protomer (**g**) and the 'down' RBD protomer (**h**).

intermediate SD1 configuration (Fig. 5e,h). The up state RBD in the u1S2q construct resided largely in the position occupied in the unmutated construct (Fig. 5c,f). This indicated that the effect of the mutations was primarily isolated to the down state and suggested these mutations act to destabilize the down state rather than to stabilize the up state. These features were largely recapitulated in the u1S2q 2-RBD up state conformation, with subdomain 1 retaining the shift in the down state RBD (Supplementary Table 1). The structural details presented here indicate that, while locking the down state RBD into its unmutated position had little impact on the overall configuration of S1, altering the disposition of SD1 had wide-ranging impacts, consistent with the observed virus-to-virus differences in the geometric analysis described in Fig. 1.

We measured the binding of u1S2q with antibody CR3022 and ACE-2 (Fig. 6c and Extended Data Fig. 7a–c) and observed a modest but reproducible increase in ACE-2 binding for u1S2q compared to the unmutated spike, consistent with the higher propensity of u1S2q to adopt RBD-up conformations (Extended Data Fig. 7b,c). The affinities of the CR3022 antibody to the unmutated spike or u1S2q were similar and also consistent with the previously published affinity of CR3022 for an RBD-only construct[17] (Fig. 6c). On docking of the crystal structure of the CR3022 Fab in complex with the RBD (PDB 6YLA)[17] onto the 1-up and 2-up structures of u1S2q, we found that the CR3022 constant domain clashed with the NTD and the adjacent RBD in both the 1-up conformation and the 2-up conformations (Fig. 6d,e). As previously suggested[17], CR3022 binding is therefore likely to require a conformational change that rotates the RBD away from the central axis of the spike. In summary, none of the structures of the structural states of the spike determined thus far are compatible with CR3022 binding and our data show that CR3022 must induce or capture this potentially transient state in both the unmutated and u1S2q spikes.

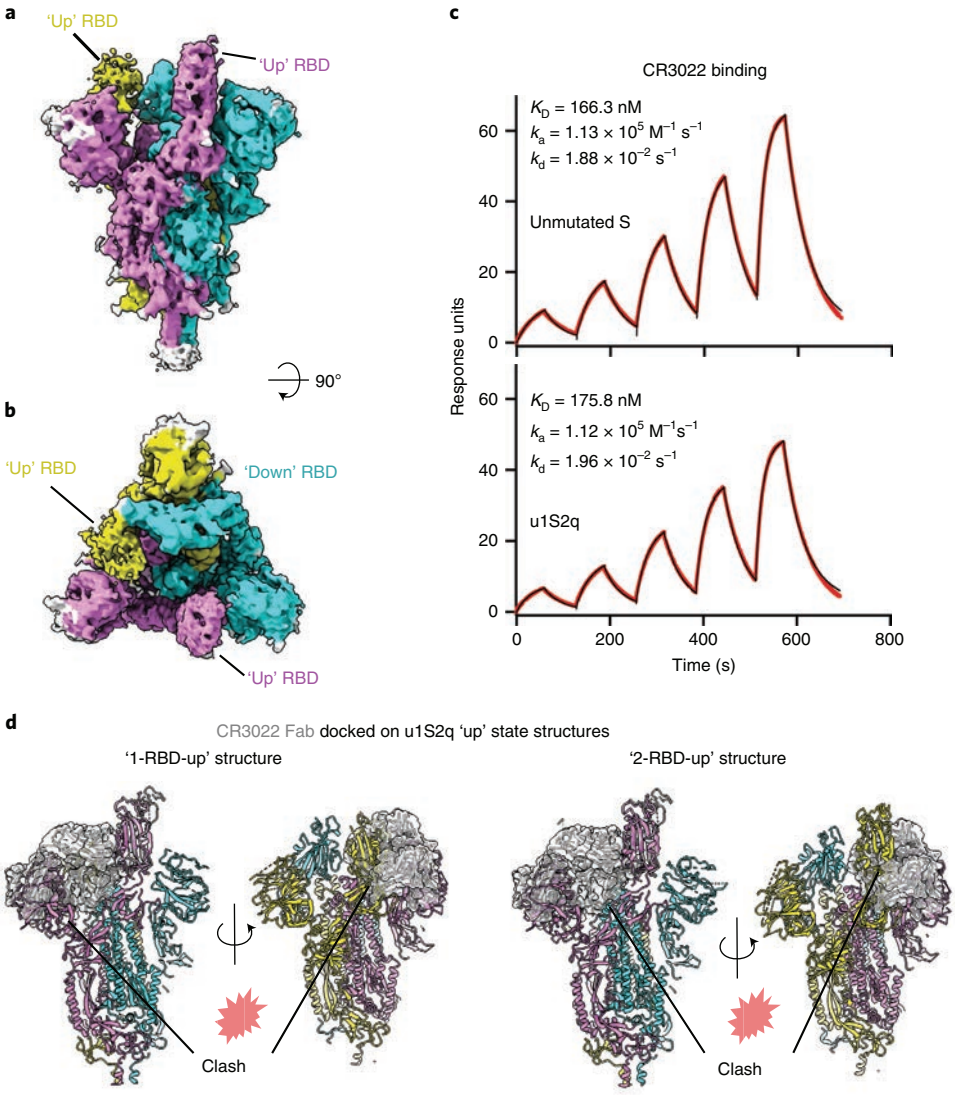

Fig. 6 | Structure of the u1S2q 2-RBD up state. a, Cryo-EM reconstruction of u1S2q, colored by chain. **b**, Rotated view (by ~90°) of **a**. **c**, Binding of antibody CR3022 to the unmutated construct (top) and u1s2q (bottom). Binding of CR3022 Fab to the S-proteins was measured by SPR using single-cycle kinetics. The black lines are the binding sensorgrams and the red lines show fits of the data to a 1:1 Langmuir binding model. **d**, CR3022 (shown as a semi-transparent, gray surface) modeled on the 1-up u1S2q structure (left) and the 2-up u1S2q structure (right) using RBD in the crystal structure of the CR3022-RBD complex (PDB 6W41) to superimpose on the up RBD of the u1S2q structures. Locations of potential clashes are indicated in each model.

Discussion

Conformational plasticity is a hallmark of the enveloped-virus fusion-protein structure due to the necessity of protecting the conserved viral fusion elements from host immune responses while retaining a sufficiently steep free-energy gradient to enable host cell fusion[19]. Exposed elements are generally well conditioned to be permissive and responsive to mutations through genetic drift and host immune adaptation. Conformational plasticity, however, presents an important difficulty in the context of vaccine and drug design. Indeed, lessons learned in the continued effort to produce a broadly protective HIV-1 vaccine have demonstrated the importance of a detailed understanding and control of fusion protein dynamics[20–31]. SARS-CoV-2 is probably no exception in this regard and, indeed, the conformational plasticity of the SARS-CoV-2 S-protein appears greater than that of the HIV-1 Env.

We aimed to develop a quantitative understanding of β-CoV structural states between viruses and within each RBD down and up state configuration. The wide breadth of domain arrangements and the relatively small contact area between the S1 and S2 subunits suggest that large changes in S-protein structure may occur from few mutations. A recent report indicated that the D614G mutation (located in the SD2 region and contacting S2) causes a potential fitness gain[32]. Based on our results showing that a disulfide linkage between SD2 and S2 in u2S2d decreased the population of up state RBDs (Extended Data Fig. 4b), the D614G mutation may indeed alter the conformational landscape of the SARS-CoV-2 S-protein. It was previously noted that the RBD up states observed in MERS and SARS-CoV-1 were not observed in the OC43, MHV or HKU1 S-protein structures[10]. We note that the SD1 u1S2q mutation sites are all asparagine in those other CoV S-proteins, and each displays a marked difference in SD1 positioning relative to the u1S2q structure. Thus, sequence differences at interdomain contact sites are not uncommon, and our observations suggest that the β-coronaviruses can quickly evade conformationally selective antibody responses.

Table 1 | Cryo-EM data collection, refinement and validation statistics

	rS2d (EMD-21997, PDB 6X29)	u1S2q all down (EMD-22001, PDB 6X2C)	u1S2q 1-up (EMD-21999, PDB 6X2A)	u1S2q 2-up (EMD-22000, PDB 6X2B)
Data collection and processing				
Magnification	81,000	81,000	81,000	81,000
Voltage (kV)	300	300	300	300
Electron exposure ($e^-/Å^2$)	65.18	66.82	66.82	66.82
Defocus range (μm)	0.63–2.368	0.55–2.94	0.55–2.94	0.55–2.94
Pixel size (Å)	1.06	1.058	1.058	1.058
Symmetry imposed	*C*3	*C*3	*C*1	*C*1
Initial particle images (no.)	631,937	906,517	906,517	906,517
Final particle images (no.)	367,259	192,430	255,013	133,957
Map resolution (Å)	2.7	3.2	3.3	3.6
FSC threshold	0.143	0.143	0.143	0.143
Map resolution range (Å)	2.4–4.4	2.7–6.4	2.8–7.1	3.2–9.3
Refinement				
Initial model used	PDB 6VXX	PDB 6VXX	PDB 6VYB	PDB 6VYB
Model resolution (Å)	2.8	3.2	3.3	3.6
FSC threshold	0.143	0.143	0.143	0.143
Map sharpening *B* factor ($Å^2$)	−113.3	−124.3	−113.7	−107.7
Model composition				
Nonhydrogen atoms	22,806	22,800	21,562	21,144
Protein residues	2,916	2,913	2,875	2,864
R.m.s. deviations				
Bond lengths (Å)	0.009	0.012	0.012	0.011
Bond angles (°)	1.2	1.906	1.839	1.814
Validation				
MolProbity score	1.23	1.34	1.15	1.31
Clashscore	0.33	0.20	0.14	0.32
Poor rotamers (%)	1.96	3.17	1.64	2.08
Ramachandran plot				
Favored (%)	94.37	94.37	93.31	92.88
Allowed (%)	5.52	5.32	6.29	6.69
Disallowed (%)	0.11	0.32	0.39	0.43

However, the degree to which this evasion mechanism is effectively utilized by the virus is uncertain, as such mutations may simultaneously incur a fitness penalty.

From the perspective of immunogen development, the constructs developed here present an opportunity to examine the ability of differentially stabilized S-protein particles to induce two different, yet important antibody responses. First, the u1S2q construct developed here displayed a prominent two-RBD up state distribution, demonstrating that interdomain contact modifications can lead to higher exposure of the immunogenic receptor-binding regions. Because RBD-directed responses that target the ACE-2 binding site form a dominant proportion of neutralizing immune responses in infected patients[33], constructs that increase exposure and access to these sites could be useful candidates for vaccination regimens aimed at eliciting such responses. Indeed, full-length SARS-CoV-2 spike structures, either detergent-solubilized[34] or virion-associated[35], suggest that the down state is the predominant state that, in a vaccination context, may limit RBD-directed responses. The u1S2q mutations may therefore provide a means to enhance the induction of RBD responses in full-length S-protein immunogens. Furthermore, this design could also be used to identify receptor-binding-site-directed antibodies from patient sera, including potential new antibodies that may target sites that require a two-RBD up conformation. Second, the disulfide-linked down state locked double mutant (rS2d) would presumably not elicit antibodies targeting the receptor binding site (these make up the majority of observed responses in convalescent patients[36,37]), but it would still be capable of eliciting antibodies such as S309 that are able to bind the down state RBD[38]. Indeed, a study of MERS responses suggests non-RBD responses (particularly NTD and S2 epitopes) will play an important role in vaccine-induced protection[39]. From a theoretical perspective, the wide control over the RBD up/down distribution available to the virus suggests that, by analogy to HIV-1 viruses, which are notoriously difficult to neutralize, conformational blocking of antibody responses would not be unusual. Although there might be a fitness cost to the virus, it would not necessarily render the virion non-infectious. Using the double mutant rS2d as an immunogen provides a platform for inducing non-RBD responses that may be needed to protect against such evasion. Although the low expression yields of rS2d are a potential hindrance to its utility, introduction of other mutations, such as the

recently described mutations designed to stabilize the S2 region[40], may provide a way to further stabilize rS2d and increase its utility as an immunogen.

Complicating factors, such as a potential for antibody-induced enhancement, may favor the use of truncated, single-domain constructs with fewer potentially weak or non-neutralizing epitopes. Nevertheless, the designs presented here will allow for a detailed characterization of vaccine immunogenicity and antigenicity, paving the way for the development of vaccines for the novel SARS-CoV-2 and eventually a broadly protective β-CoV vaccine. Thus, although the previous generation of stabilizing mutations ensured well-folded spike trimers, the rational design approach developed here provides a means to controlling the RBD orientation distribution and should allow us to explore the impact of conformational dynamics from the perspective of vaccine and drug development.

Online content

Any methods, additional references, Nature Research reporting summaries, source data, extended data, supplementary information, acknowledgements, peer review information; details of author contributions and competing interests; and statements of data and code availability are available at https://doi.org/10.1038/s41594-020-0479-4.

Received: 18 May 2020; Accepted: 7 July 2020;
Published online: 22 July 2020

References

1. Kirchdoerfer, R. N. et al. Pre-fusion structure of a human coronavirus spike protein. *Nature* **531**, 118–121 (2016).
2. Hoffmann, M. et al. SARS-CoV-2 cell entry depends on ACE2 and TMPRSS2 and is blocked by a clinically proven protease inhibitor. *Cell* **181**, 271–280 (2020).
3. Wrapp, D. et al. Cryo-EM structure of the 2019-nCoV spike in the prefusion conformation. *Science* **367**, 1260–1263 (2020).
4. Yuan, Y. et al. Cryo-EM structures of MERS-CoV and SARS-CoV spike glycoproteins reveal the dynamic receptor binding domains. *Nat. Commun.* **8**, 15092 (2017).
5. Gui, M. et al. Cryo-electron microscopy structures of the SARS-CoV spike glycoprotein reveal a prerequisite conformational state for receptor binding. *Cell Res.* **27**, 119–129 (2017).
6. Song, W., Gui, M., Wang, X. & Xiang, Y. Cryo-EM structure of the SARS coronavirus spike glycoprotein in complex with its host cell receptor ACE2. *PLoS Pathog.* **14**, e1007236 (2018).
7. Kirchdoerfer, R. N. et al. Stabilized coronavirus spikes are resistant to conformational changes induced by receptor recognition or proteolysis. *Sci. Rep.* **8**, 15701 (2018).
8. Walls, A. C. et al. Unexpected receptor functional mimicry elucidates activation of coronavirus fusion. *Cell* **176**, 1026–1039 (2019).
9. Pallesen, J. et al. Immunogenicity and structures of a rationally designed prefusion MERS-CoV spike antigen. *Proc. Natl Acad. Sci. USA* **114**, E7348–E7357 (2017).
10. Tortorici, M. A. et al. Structural basis for human coronavirus attachment to sialic acid receptors. *Nat. Struct. Mol. Biol.* **26**, 481–489 (2019).
11. Walls, A. C. et al. Cryo-electron microscopy structure of a coronavirus spike glycoprotein trimer. *Nature* **531**, 114–117 (2016).
12. Park, Y.-J. et al. Structures of MERS-CoV spike glycoprotein in complex with sialoside attachment receptors. *Nat. Struct. Mol. Biol.* **26**, 1151–1157 (2019).
13. Walls, A. C. et al. Structure, function and antigenicity of the SARS-CoV-2 spike glycoprotein. *Cell* **180**, 281–292 (2020).
14. Madhavi Sastry, G., Adzhigirey, M., Day, T., Annabhimoju, R. & Sherman, W. Protein and ligand preparation: parameters, protocols and influence on virtual screening enrichments. *J. Comput. Aided Mol. Des.* **27**, 221–234 (2013).
15. Salam, N. K., Adzhigirey, M., Sherman, W. & Pearlman, D. A. Structure-based approach to the prediction of disulfide bonds in proteins. *Protein Eng. Des. Sel.* **27**, 365–374 (2014).
16. Beard, H., Cholleti, A., Pearlman, D., Sherman, W. & Loving, K. A. Applying physics-based scoring to calculate free energies of binding for single amino acid mutations in protein–protein complexes. *PLoS ONE* **8**, e82849 (2013).
17. Yuan, M. et al. A highly conserved cryptic epitope in the receptor binding domains of SARS-CoV-2 and SARS-CoV. *Science* **368**, 630–633 (2020).
18. ter Meulen, J. et al. Human monoclonal antibody combination against SARS coronavirus: synergy and coverage of escape mutants. *PLoS Med.* **3**, e237 (2006).
19. Rey, F. A. & Lok, S.-M. Common features of enveloped viruses and implications for immunogen design for next-generation vaccines. *Cell* **172**, 1319–1334 (2018).
20. de Taeye, S. W. et al. Immunogenicity of stabilized HIV-1 envelope trimers with reduced exposure of non-neutralizing epitopes. *Cell* **163**, 1702–1715 (2015).
21. He, L. et al. HIV-1 vaccine design through minimizing envelope metastability. *Sci. Adv.* **4**, eaau6769 (2018).
22. Zhang, P. et al. Interdomain stabilization impairs CD4 binding and improves immunogenicity of the HIV-1 envelope trimer. *Cell Host Microbe* **23**, 832–844 (2018).
23. Chuang, G.-Y. et al. Structure-based design of a soluble prefusion-closed HIV-1 Env trimer with reduced CD4 affinity and improved immunogenicity. *J. Virol.* **91**, e02268-16 (2017).
24. Torrents de la Peña, A. et al. Improving the immunogenicity of native-like HIV-1 envelope trimers by hyperstabilization. *Cell Rep.* **20**, 1805–1817 (2017).
25. Medina-Ramírez, M. et al. Design and crystal structure of a native-like HIV-1 envelope trimer that engages multiple broadly neutralizing antibody precursors in vivo. *J. Exp. Med.* **214**, 2573–2590 (2017).
26. Steichen, J. M. et al. HIV vaccine design to target germline precursors of glycan-dependent broadly neutralizing antibodies. *Immunity* **45**, 483–496 (2016).
27. Kulp, D. W. et al. Structure-based design of native-like HIV-1 envelope trimers to silence non-neutralizing epitopes and eliminate CD4 binding. *Nat. Commun.* **8**, 1655 (2017).
28. Yang, L. et al. Structure-guided redesign improves NFL HIV Env trimer integrity and identifies an inter-protomer disulfide permitting post-expression cleavage. *Front. Immunol.* **9**, 1631 (2018).
29. Sharma, S. K. et al. Cleavage-independent HIV-1 Env trimers engineered as soluble native spike mimetics for vaccine design. *Cell Rep.* **11**, 539–550 (2015).
30. Guenaga, J. et al. Structure-guided redesign increases the propensity of HIV Env to generate highly stable soluble trimers. *J. Virol.* **90**, 2806–2817 (2016).
31. Sliepen, K. et al. Structure and immunogenicity of a stabilized HIV-1 envelope trimer based on a group-M consensus sequence. *Nat. Commun.* **10**, 2355 (2019).
32. Korber, B. et al. Tracking changes in SARS-CoV-2 Spike: evidence that D614G increases infectivity of the COVID-19 virus. *Cell* https://doi.org/10.1016/j.cell.2020.06.043 (2020).
33. Barnes, C. O. et al. Structures of human antibodies bound to SARS-CoV-2 spike reveal common epitopes and recurrent features of antibodies. *Cell* **182**, 1–15 (2020).
34. Cai, Y. et al. Distinct conformational states of SARS-CoV-2 spike protein. Preprint at *bioRxiv* https://doi.org/10.1101/2020.05.16.099317 (2020).
35. Turoňová, B. et al. In situ structural analysis of SARS-CoV-2 spike reveals flexibility mediated by three hinges. Preprint at *bioRxiv* https://doi.org/10.1101/2020.06.26.173476 (2020).
36. Zost, S. J. et al. Rapid isolation and profiling of a diverse panel of human monoclonal antibodies targeting the SARS-CoV-2 spike protein. *Nat. Med.* https://doi.org/10.1038/s41591-020-0998-x (2020).
37. Brouwer, P. J. M. et al. Potent neutralizing antibodies from COVID-19 patients define multiple targets of vulnerability. *Science* https://doi.org/10.1126/science.abc5902 (2020).
38. Pinto, D. et al. Cross-neutralization of SARS-CoV-2 by a human monoclonal SARS-CoV antibody. *Nature* **583**, 290–295 (2020).
39. Wang, L. et al. Importance of neutralizing monoclonal antibodies targeting multiple antigenic sites on the Middle East Respiratory Syndrome coronavirus spike glycoprotein to avoid neutralization escape. *J. Virol.* **92**, e02002–e02017 (2018).
40. Hsieh, C.-L. et al. Structure-based design of prefusion-stabilized SARS-CoV-2 spikes. Preprint at *bioRxiv* https://doi.org/10.1101/2020.05.30.125484 (2020).

Methods

Vector-based analysis. Vector analysis was performed using available cryo-EM structures for SARS-CoV-2[3,13], SARS[4,5,7,8], MERS[4,9] and other human[1,10] and murine[11] β-CoV spike proteins. Domains for the vector analysis were selected based on visual inspection of alignments between SARS, MERS and SARS-CoV-2 structures. Specifically, Cα centroids were determined for the S1 NTD, RBD, SD1 and SD2 (SARS-CoV-2 residues 27–43 and 54–271, 330–443 and 503–528, 323–329 and 529–590, 294–322 and 591–696, respectively; equivalent SARS/MERS/murine/HKU1/OC43 residues selected based on structural alignment with SARS-CoV-2), as well as a β-sheet motif in the NTD (residues 116–129 and 169–172) and a helix motif in the RBD (residues 403–410). The NTD was split into two regions with the SD1-contacting, SD2-adjacent portion referred to here as NTD′ (residues 44–53 and 272–293). Cα centroids in the S2 subunit were obtained for a β-sheet motif (residues 717–727 and 1047–1071) and the CD domain (711–716 and 1072–1122). Vector magnitudes, angles and dihedrals between these centroids were determined and used in the subsequent analysis. Vector analysis was performed using the VMD[41] Tcl interface. PCA was performed in R with the vector data centered and scaled[42].

Rational structure-based design. Structures for SARS-COV-1 (PDB 5X58[4]), MERS (PDB 6Q04[12]) and SARS-CoV-2 (PDB 6VXX[13]) were prepared in Maestro[43] using the protein preparation wizard[14] followed by in silico mutagenesis using Schrödinger's cysteine mutation[15] and residue scanning[16] tools. Residue scanning was first performed for individual selected sites allowing mutations to Leu, Ile, Trp, Tyr and Val, followed by scanning of combinations for those that yielded a negative overall score. Scores and visual inspection were used in the selection of the prepared constructs.

Protein expression and purification. The SARS-CoV-2 ectodomain constructs were produced and purified as described previously[3]. Briefly, a gene encoding residues 1−1208 of the SARS-CoV-2 S (GenBank MN908947) with proline substitutions at residues 986 and 987, a 'GSAS' substitution at the furin cleavage site (residues 682–685), a C-terminal T4 fibritin trimerization motif, an HRV3C protease cleavage site, a TwinStrepTag and an 8XHisTag was synthesized and cloned into the mammalian expression vector pαH. All mutants were introduced in this background. Expression plasmids encoding the ectodomain sequence were used to transiently transfect FreeStyle293F cells using Turbo293 (SpeedBiosystems). Protein was purified on the sixth day post-transfection from the filtered supernatant using StrepTactin resin (IBA).

Antibody CR3022 was produced in Expi293 cells and purified by Protein A affinity. To express the ACE-2 constructs, the ACE-2 gene was cloned as a fusion protein with either the human or mouse Fc region attached to the C-terminal end of ACE-2. A 6X His-tag was added to the C-terminal end of the Fc domain of each construct. ACE-2 with human Fc tag was purified by Protein A affinity chromatography, and ACE-2 with mouse Fc tag was purified by Ni-NTA chromatography.

Thermal shift assay. The thermal shift assay was performed using Tycho NT.6 (NanoTemper Technologies). Spike variants were diluted (0.15 mg ml^{-1}) in nCoV buffer (2 mM Tris, pH 8.0, 200 mM NaCl, 0.02% sodium azide) and run in duplicates in capillary tubes. Intrinsic fluorescence was recorded at 330 nm and 350 nm while heating the sample from 35 to 95 °C at a rate of 3 °C min^{-1}. The ratio of fluorescence (350/330 nm) and the inflection temperatures (Ti) were calculated by Tycho NT.6.

Negative-stain electron microscopy. A 100 µg ml^{-1} final concentration of the spike was made in 5% glycerol in HBS pH 7.4 (20 mM HEPES, 150 mM NaCl) with 7.5 mM gluteraldehyde at room temperature. After 5-min incubation, gluteraldehyde was quenched by adding sufficient 1 M Tris stock, pH 7.4 to give a final concentration of 75 mM Tris and incubated for 5 min. The carbon-coated grids (CF300-cu, EMS) were glow-discharged for 20 s at 15 mA. A 5-µl sample incubated on grid for 10–15 s was blotted and then stained with 2% uranyl formate. Images were obtained with a Philips EM420 electron microscope operated at 120 kV, at ×82,000 magnification and with a pixel size of 4.02 Å. The RELION[44] program was used to perform class averaging of the single-particle images.

Cryo-electron microscopy sample preparation, data collection and processing. Purified SARS-CoV-2 spike preparations were diluted to a concentration of ~1 mg ml^{-1} in 2 mM Tris pH 8.0, 200 mM NaCl and 0.02% NaN_3, then 2.5 µl of protein was deposited on a CF-1.2/1.3 grid that had been glow-discharged for 30 s in a PELCO easiGlow glow discharge cleaning system. After 30-s incubation in >95% humidity, excess protein was blotted away for 2.5 s before being plunge-frozen into liquid ethane using a Leica EM GP2 plunge freezer (Leica Microsystems). Frozen grids were imaged in a Titan Krios system (Thermo Fisher) equipped with a K3 detector (Gatan). Data were acquired using the Leginon system[45]. The dose was fractionated over 50 raw frames and collected at a 50-ms frame rate. This dataset was energy-filtered with a slit width of 30 eV. Individual frames were aligned and dose-weighted[46]. CTF estimation, particle picking, 2D classifications, ab initio model generation, heterogeneous refinements, homogeneous 3D refinements and local resolution calculations were carried out in cryoSPARC[47].

Cryo-electron microscopy structure fitting and analysis. Structures of the all down state (PDB 6VXX) and single RBD up state (PDB 6VYB) from the previously published SARS-CoV-2 ectodomain were used to fit the cryo-EM maps in Chimera[48]. The 2-RBD up state was generated in PyMol using the single RBD up state structure. Mutations were made in PyMol[49]. Coordinates were then fitted manually in Coot[50] followed by iterative refinement using Phenix[51] real space refinement and subsequent manual coordinate fitting in Coot. Structure and map analysis were performed using PyMol, Chimera[48] and ChimeraX[52].

Surface plasmon resonance. The binding of antibody CR3022 and ACE-2 to the SARS-CoV-2 spike constructs was assessed by SPR, in two experimental formats, on a Biacore T-200 system (GE Healthcare) at 25 °C using HBS-EP+ (10 mM HEPES, pH 7.4, 150 mM NaCl, 3 mM EDTA and 0.05% surfactant P-20) as the running buffer. In the first format, the spike constructs were captured on an SA chip and were assayed by flowing over CR3022 IgG or ACE-2-Fc. The surface was regenerated between injections by flowing over SA regeneration buffer (1 M NaCl, 50 mM NaOH) solution for 10 s with a flow rate of 100 µl min^{-1}. Blank sensorgrams were obtained by injection of the same volume of HBS-EP+ buffer in place of IgGs and Fab solutions. Sensorgrams were corrected with corresponding blank curves. In the second format, CR3022 IgG or ACE-2-human Fc was captured on CM5 chip immobilized with human Anti-Fc (8,000 RU), and binding was measured by flowing over each of the spike constructs at 200 nM in running buffer. The surface was regenerated between injections by flowing over 3 M $MgCl_2$ solution for 10 s with a flow rate of 100 µl min^{-1}. To assess the affinity of CR3022 to the unmutated and u1S2q spikes, the spikes were captured on an SA chip as described above, and five concentrations of CR3022 were injected in a single-cycle kinetics format. Sensorgram data were analyzed using the BiaEvaluation software (GE Healthcare).

Reporting Summary. Further information on research design is available in the Nature Research Reporting Summary linked to this Article.

Data availability

Cryo-EM reconstructions and atomic models have been deposited in the EMDB and wwPDB with accession codes EMD-21997, EMD-21999, EMD-22000 and EMD-22001 and PDB 6X29, 6X2A, 6X2B and 6X2C. Source data for graphs are available in Supplementary Data 1.

Code availability

The code developed to determine vector magnitudes, angles and dihedrals for this study is available from the corresponding authors upon reasonable request.

References

41. Humphrey, W., Dalke, A. & Schulten, K. VMD: visual molecular dynamics. *J. Mol. Graph.* **14**, 33–38 (1996).
42. R Core Team *R: A Language and Environment for Statistical Computing* (R Foundation for Statistical Computing, 2017).
43. Maestro (Schrödinger, 2020).
44. Scheres, S. H. W. in *Methods in Enzymology* Vol. 579 (ed. Crowther, R. A.) 125–157 (Academic Press, 2016).
45. Suloway, C. et al. Automated molecular microscopy: the new Leginon system. *J. Struct. Biol.* **151**, 41–60 (2005).
46. Zheng, S. Q. et al. MotionCor2: anisotropic correction of beam-induced motion for improved cryo-electron microscopy. *Nat. Methods* **14**, 331–332 (2017).
47. Punjani, A., Rubinstein, J. L., Fleet, D. J. & Brubaker, M. A. cryoSPARC: algorithms for rapid unsupervised cryo-EM structure determination. *Nat. Methods* **14**, 290–296 (2017).
48. Pettersen, E. F. et al. UCSF Chimera—a visualization system for exploratory research and analysis. *J. Comput. Chem.* **25**, 1605–1612 (2004).
49. The PyMOL Molecular Graphics System (Schrödinger, 2015).
50. Emsley, P., Lohkamp, B., Scott, W. G. & Cowtan, K. Features and development of *Coot*. *Acta Crystallogr. D Biol. Crystallogr.* **66**, 486–501 (2010).
51. Afonine, P. V. et al. Real-space refinement in *PHENIX* for cryo-EM and crystallography. *Acta Crystallogr. D Struct. Biol.* **74**, 531–544 (2018).
52. Goddard, T. D. et al. UCSF ChimeraX: meeting modern challenges in visualization and analysis. *Protein Sci.* **27**, 14–25 (2018).

Acknowledgements

Initial cryo-EM data were collected on the Titan Krios system at the Shared Materials and Instrumentation Facility in Duke University. Data collection for high-resolution structure determination was performed at the National Center for Cryo-EM Access and Training (NCCAT) and the Simons Electron Microscopy Center located at the New York Structural Biology Center, supported by the NIH Common Fund Transformative High Resolution Cryo-Electron Microscopy program (U24 GM129539) and by grants

from the Simons Foundation (SF349247) and NY State. We thank E. Eng, D. Bobe, M. Walters and H. Leddy for microscope alignments and assistance with cryo-EM data collection as well as J. McLellan for providing the plasmid for the unmutated construct and K. Manne for preparing the CR3022 Fab. This work was supported by U19 AI142596 (B.F.H.), Integrated Preclinical/Clinical AIDS Vaccine Development Program, NIAID, NIH; Duke University Center for AIDS Research (CFAR); an administrative supplement to NIH R01 AI145687 for coronavirus research and Translating Duke Health Initiative (P.A. and R.C.H.), the Intramural Research Program of the NIH; National Institute of Environmental Health Sciences (ZIC ES103326 to M.J.B.), and a contract from the State of North Carolina Pandemic Recovery Office through funds from the Coronavirus Aid, Relief and Economic Security (CARES) Act. This study utilized the computational resources offered by Duke Research Computing (http://rc.duke.edu; NIH 1S10OD018164-01) at Duke University. We thank M. DeLong, C. Kneifel, M. Newton, V. Orlikowski, T. Milledge and D. Lane from the Duke Office of Information Technology and Research Computing for providing assistance with setting up and maintaining the computing environment.

Author contributions

R.H. and P.A. conceived the study, determined cryo-EM structures and analyzed data. R.H. led computational studies. P.A. led structural studies. R.J.E. led NSEM studies and analyzed data. K.M. collected NSEM data and performed initial data analysis. K.J., V.S., S.G. and D.L. produced, purified and analyzed proteins. M.K. and A.L.H. optimized cryo-EM specimens. K.J. and R.P. performed binding studies to optimize spike preparations. R.J.E., M.J.B., B.F.H. and P.A. supervised studies. R.H. and P.A. wrote the manuscript with help from all authors.

Competing interests

The authors declare no competing interests.

Additional information

Extended data is available for this paper at https://doi.org/10.1038/s41594-020-0479-4.

Supplementary information is available for this paper at https://doi.org/10.1038/s41594-020-0479-4.

Correspondence and requests for materials should be addressed to R.H. or P.A.

Peer review information Inês Chen was the primary editor on this article and managed its editorial process and peer review in collaboration with the rest of the editorial team.

Reprints and permissions information is available at www.nature.com/reprints.

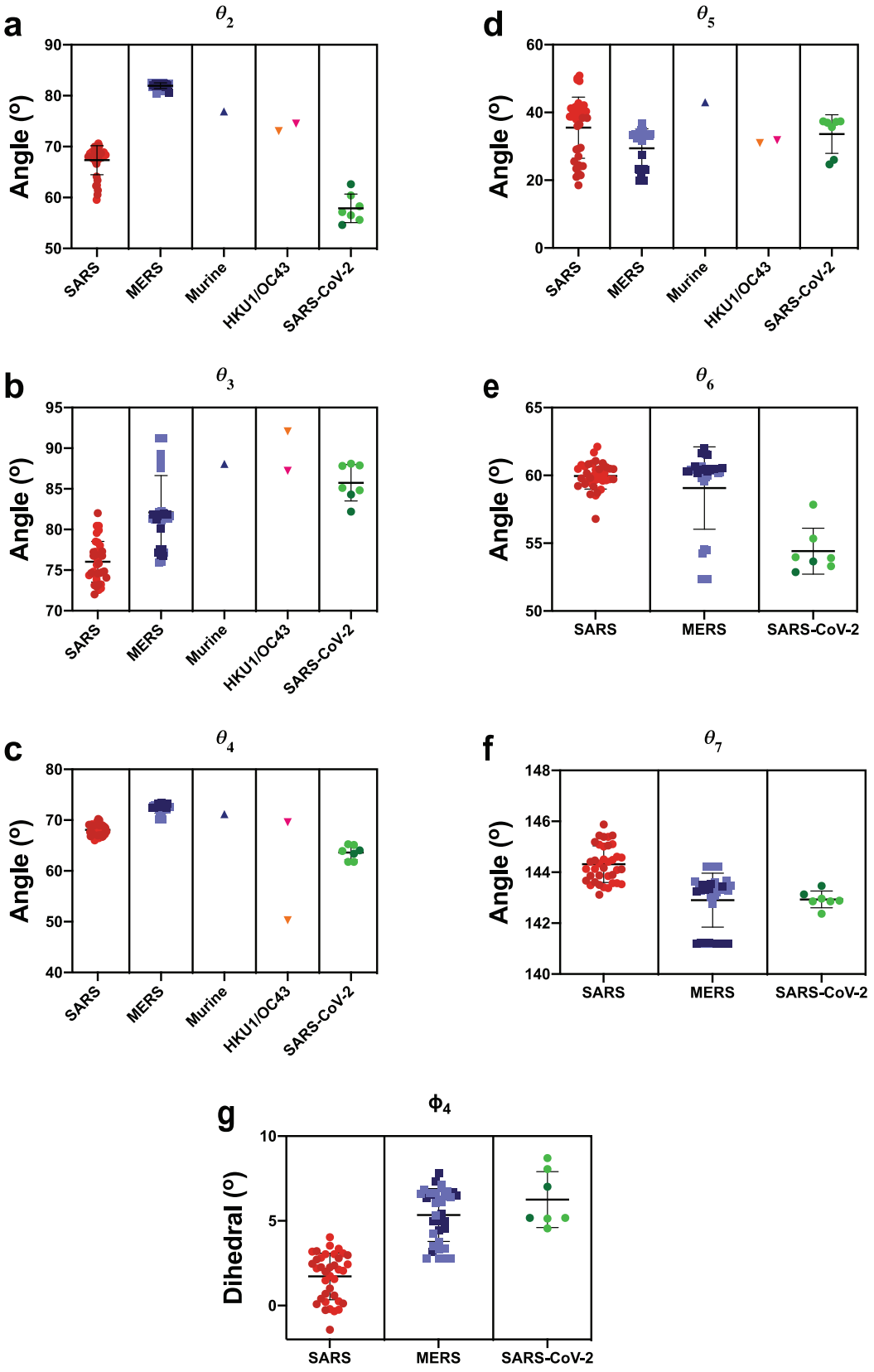

Extended Data Fig. 1 | See next page for caption.

Extended Data Fig. 1 | β-CoV Vector Analysis. a, The angle between the vectors connecting the NTD sheet motif centroid and the NTD centroid and the vector connecting the the NTD centroid to the NTD' centroid. **b**, The angle between the vectors connecting the NTD' centroid and the SD2 centroid and the vector connecting the the SD2 centroid to the SD1 centroid. **c**, The angle between the vectors connecting the NTD centroid and the NTD' centroid and the vector connecting the the NTD' centroid to the SD2 centroid. **d**, The angle between the vectors connecting the SD1 centroid and the RBD centroid and the vector connecting the the RBD centroid to the RBD helix motif centroid. **e**, The angle between the vectors connecting the NTD' centroid and the SD2 centroid and the vector connecting the the SD2 centroid to the CD centroid. **f**, The angle between the vectors connecting the SD2 centroid and the CD centroid and the vector connecting the the CD centroid to the β-sheet motif centroid. **g**, The dihedral about the SD2 centroid and the CD centroid. Points for SARS, MERS, and SARS-2 in Fig. 1 (**g**)–(**j**) colored according to 'up' (dark) and 'down' (light) states according to the color code in the PCA analysis, panels (**e**) and (**f**). Individual data points shown as symbols; lines denote mean and s.d. The source data are available in Supplementary Data 1.

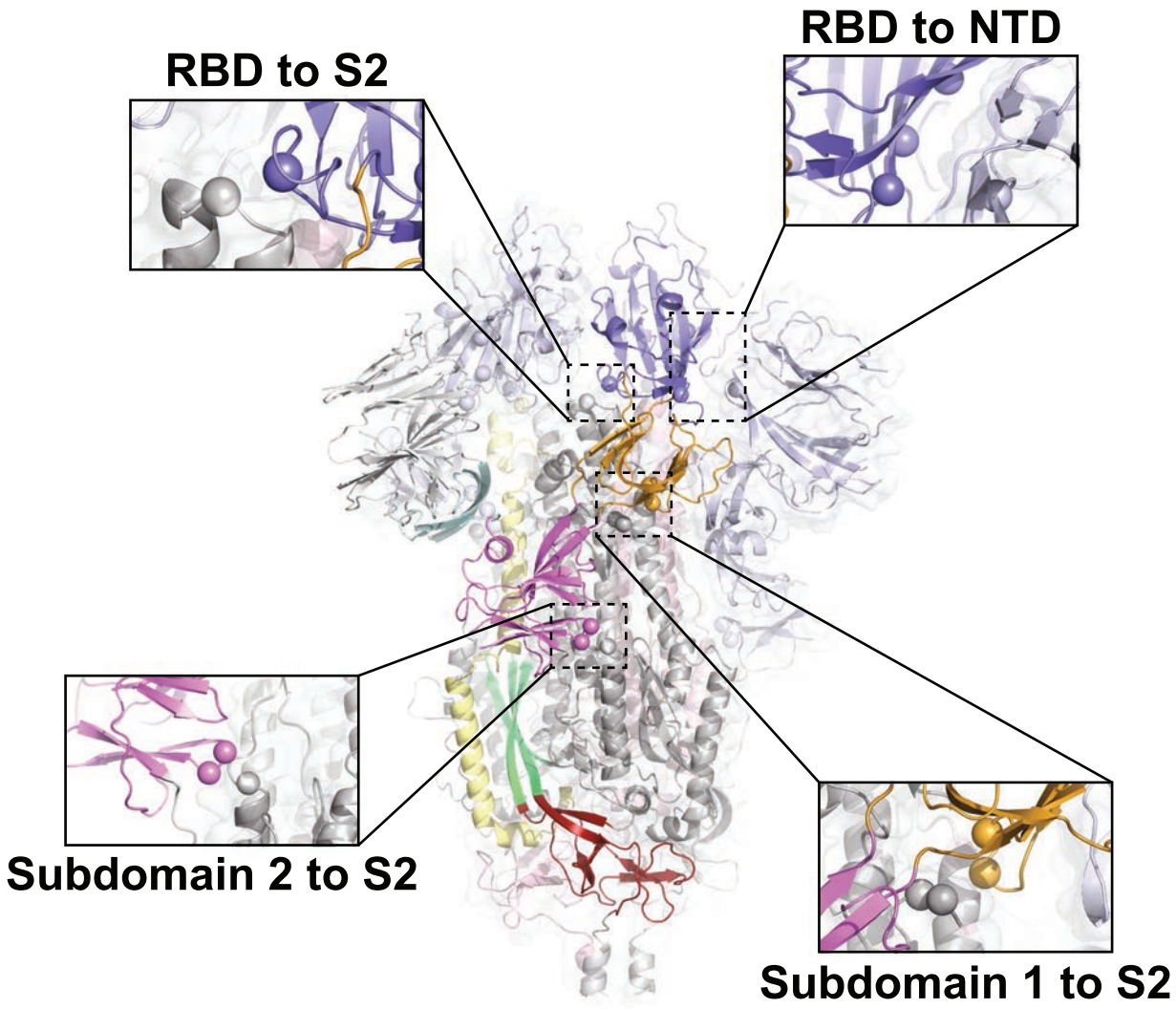

Extended Data Fig. 2 | Sites identified for differential stabilization of the SARS-CoV-2 S-protein. Single protomer colored according to Fig. 1 with remaining two protomers color according to S1 (light blue) and S2 (gray). Spheres indicate candidate mutation sites.

a

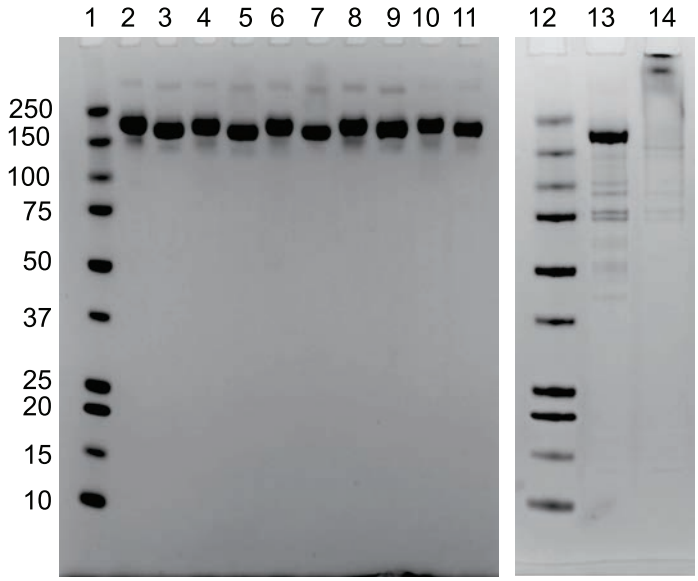

Legend:
1. Marker
2. Reduced Unmutated S
3. Non-Reduced Unmutated S
4. Reduced u2S2d
5. Non-Reduced u2S2d
6. Reduced rNt
7. Non-Reduced rNt
8. Reduced u1S2q
9. Non-Reduced u1S2q
10. Reduced u2S2d
11. Non-Reduced u1S2d
12. Marker
13. Reduced rS2d
14. Non-reduced rS2d

b

Spike construct	Yield (mg)
Unmutated	3-5
u1S2q	2.15
rs2d	0.168
u1S2d	0.65
u2S2d	0.3
rNt	0.26

Extended Data Fig. 3 | SDS-PAGE and yields of purified S protein constructs. a, SDS-PAGE gels of the S protein constructs. **b**, Yields/L of the S protein constructs.

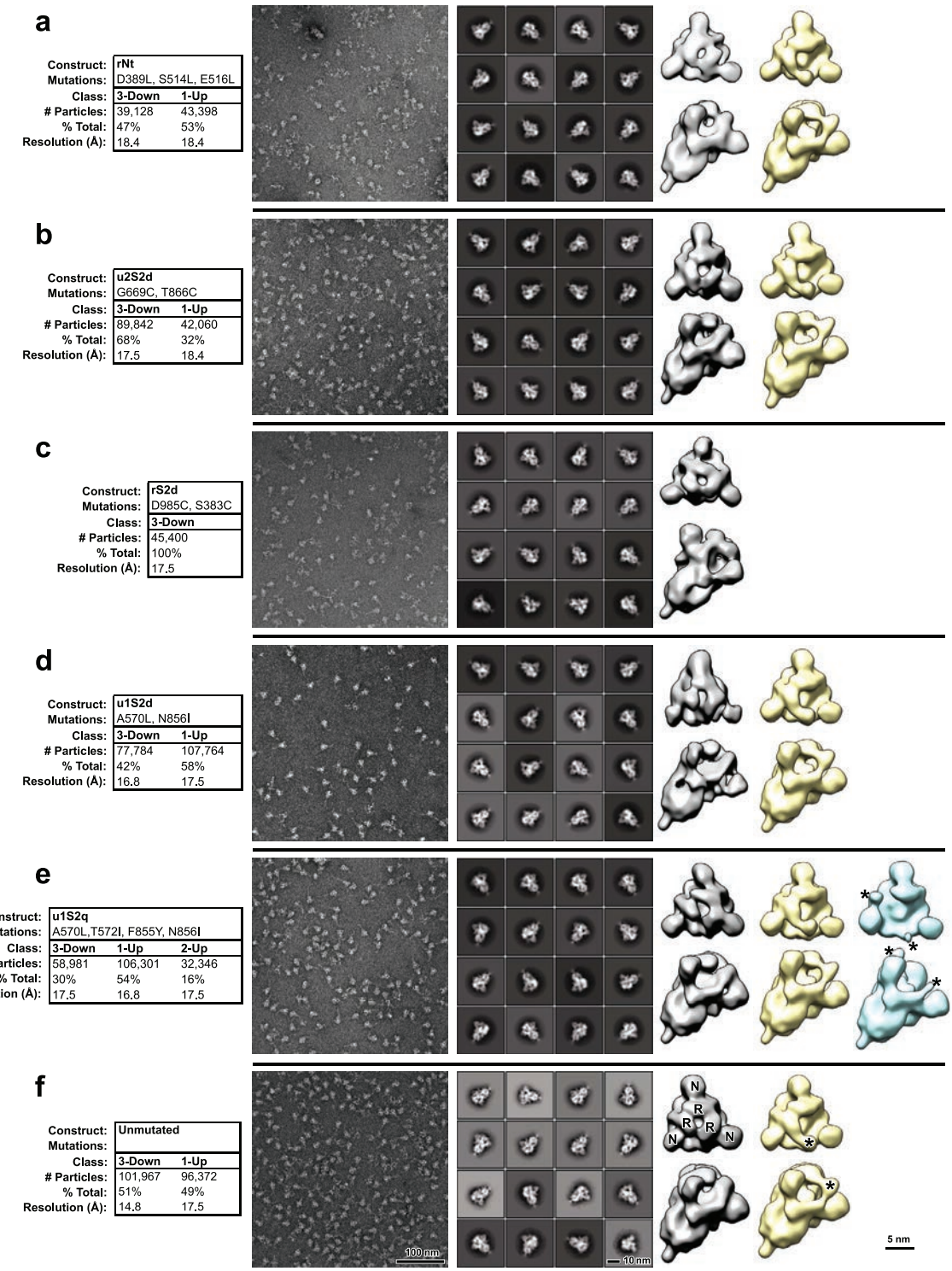

Extended Data Fig. 4 | Negative stain electron microscopy analysis of S-protein constructs. a, Data tables, indicating construct names, mutations, observed classes, number and percent of particles per class and final resolution (gold-standard Fourier-shell correlation, 0.143 level). **b**, Raw micrographs. **c**, Representative 2D class averages. **d**, 3D reconstructions of 3-RBD-down classes, shown in top view, looking down the S-protein 3-fold axis on the left and tilted view on the right. Receptor binding domains and N-terminal domains of first structure marked with R and N, respectively. **e**, 3D reconstructions of 1-RBD-up classes. Up-RBD is marked with an asterisk. **f**, 3D reconstruction of 2-RBD-up class. Density for up-RBDs is weak, indicated by asterisks.

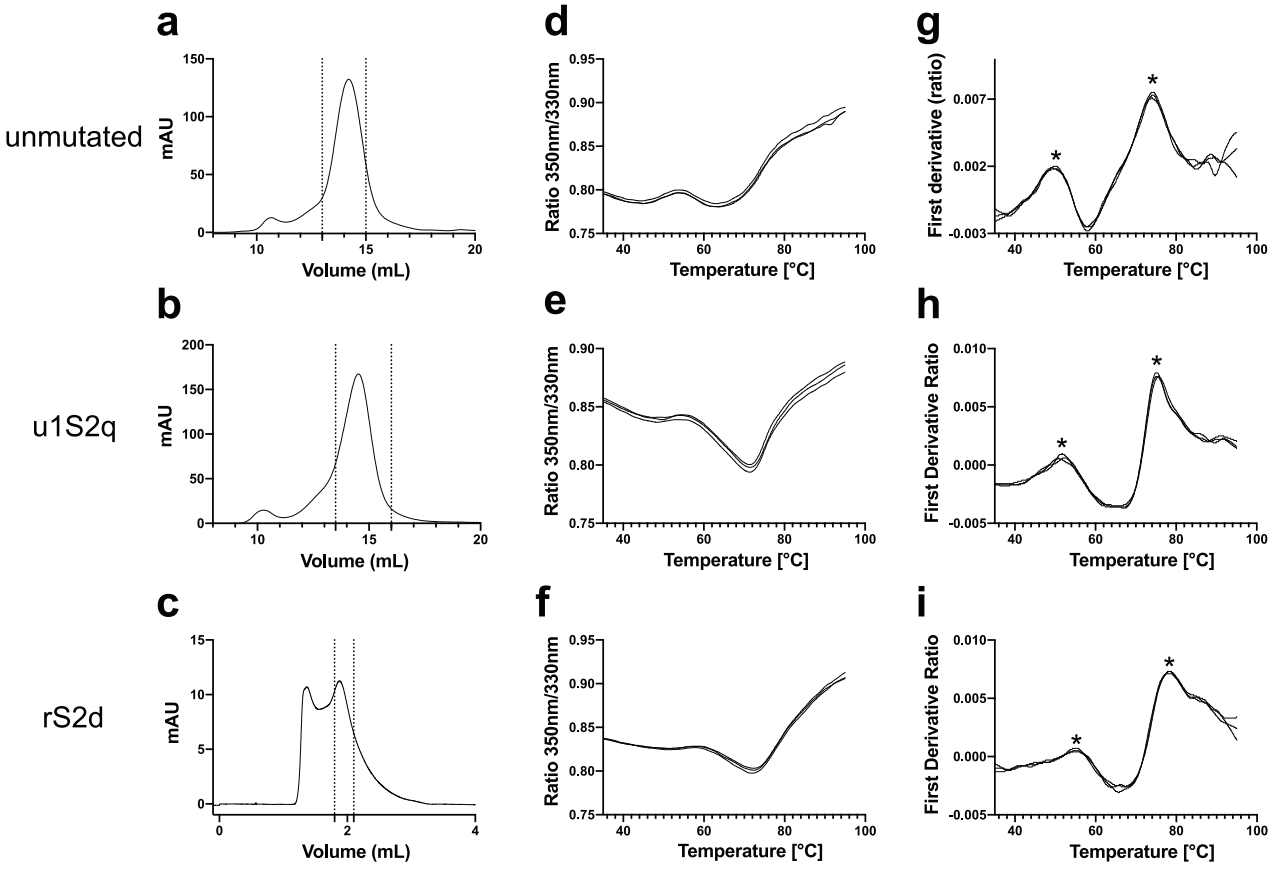

j

	Ti value (°C)	Ti value (°C)
Unmutated	50.1	74.3
u1S2q	51.7	75.2
rS2d	55.2	78.3

Ti, inflection temperature determined in the nCoV buffer (2 mM Tris, pH 8.0, 200 mM NaCl, 0.02% sodium azide).

Extended Data Fig. 5 | Thermostability of the S protein constructs. a–c, SEC profile of the S-proteins. The dotted lines indicate the portion of the peak that was collected for further studies. The unmutated and u1S2q spikes were run on a Superose 6 Increase 10/300 column, and the rS2d spike was run on an analytical Superose 6 Increase 5/150 column. **d–i**, Unfolding profile curves obtained by intrinsic fluorescence measurements using Tycho NT. 6. **d–f**, show ratio between fluorescence at 350 nm and 330 nm. **g-i**, plot the first derivative of this ratio. **j**, Inflection temperatures for the S-proteins. Asterisk mark the inflection temperatures in (**g**).

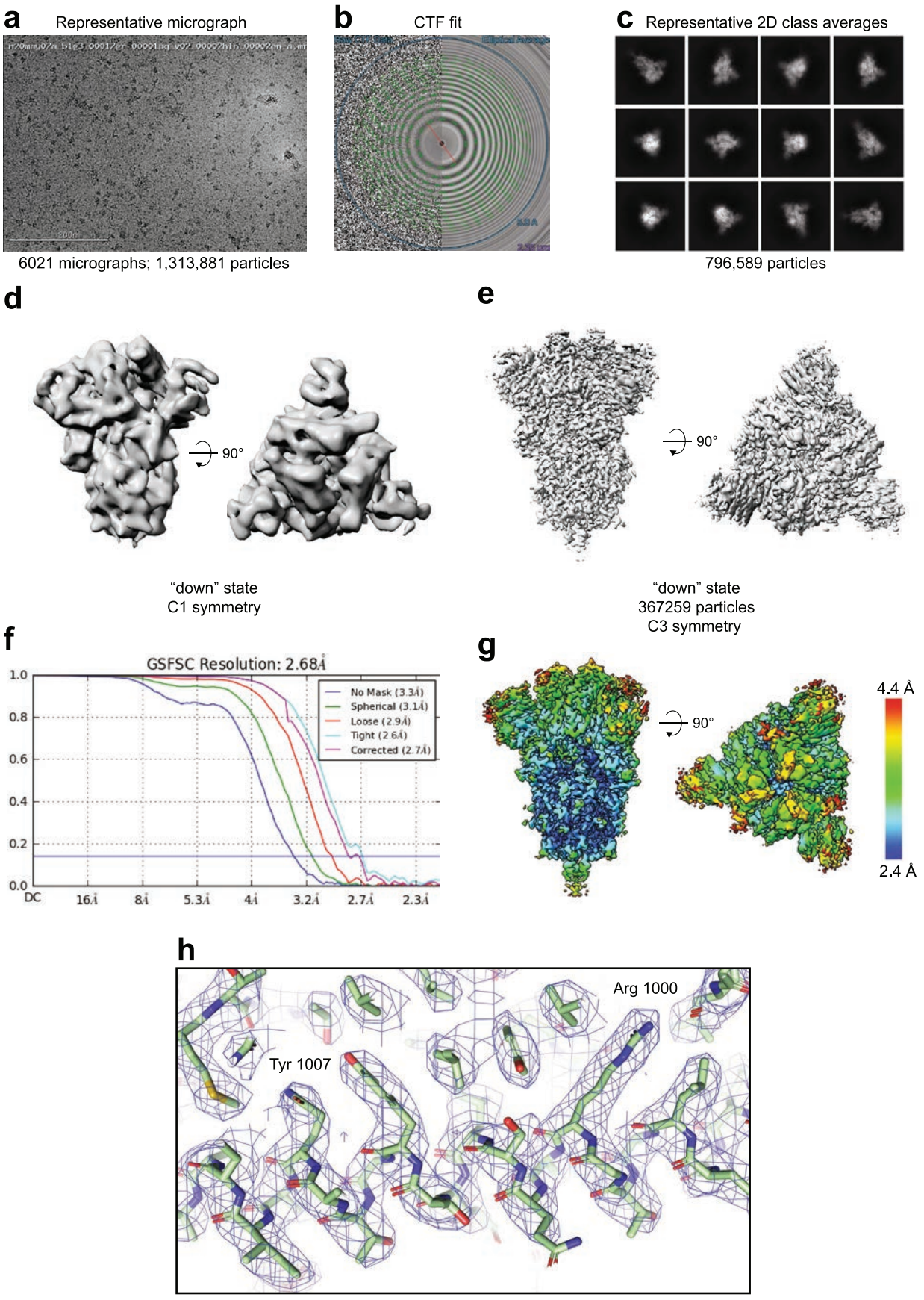

Extended Data Fig. 6 | Cryo-EM data processing details for rS2d. a, Representative micrograph. **b**, CTF fit **c**, Representative 2D class averages. **d**, *Ab initio* reconstruction. **e**, Refined map **f**, Fourier shell correlation curves **g**, Refined map colored by local resolution. **h**, Zoomed-in view of the S2 region showing cryo-EM reconstruction as a transparent grey surface, the underlying fitted model in cartoon representation, and residues in ball-and-stick representation.

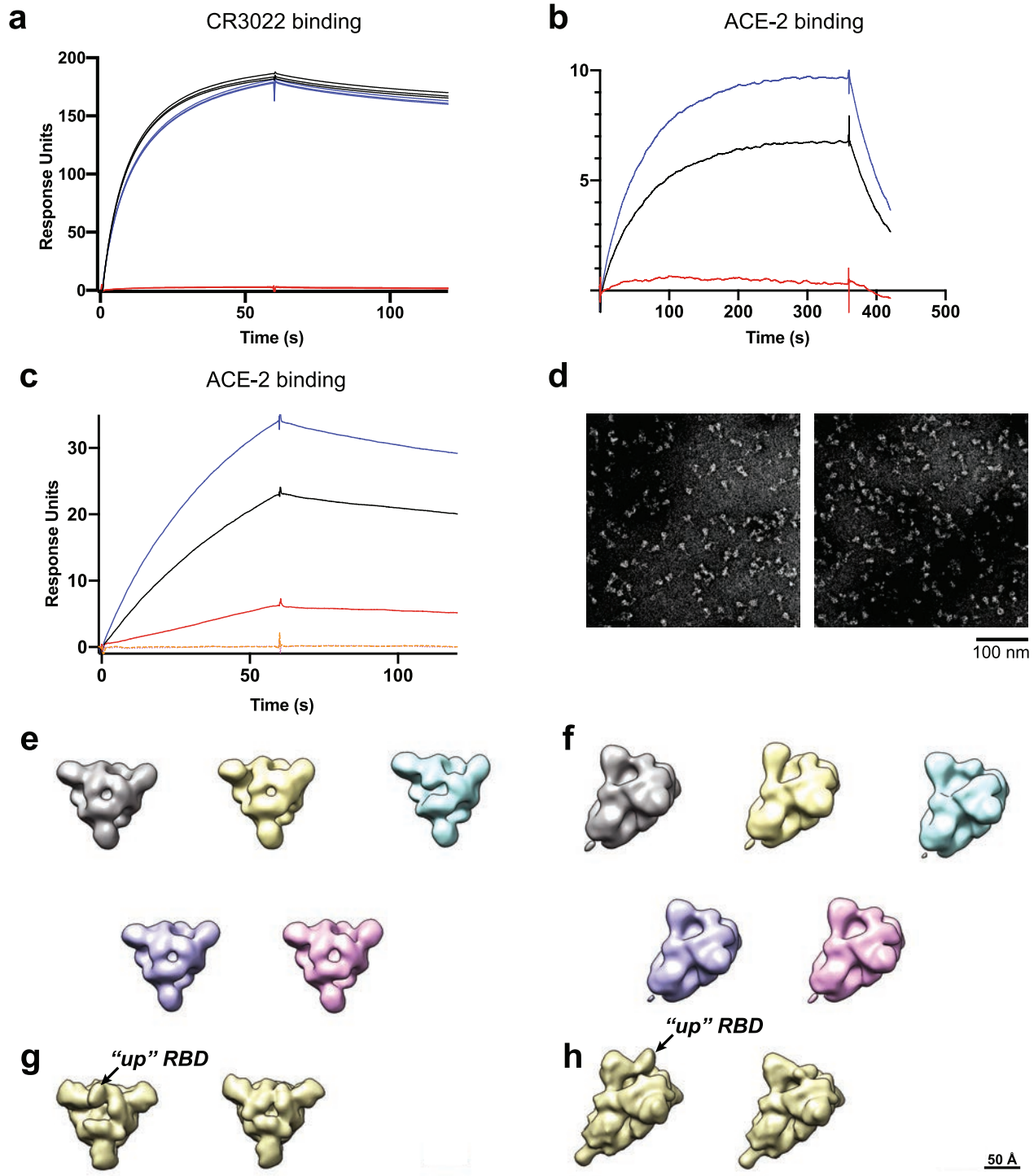

Extended Data Fig. 7 | Binding of spike constructs to ACE-2 and RBD-binding antibody CR3022. a, SPR sensorgrams of CR3022 antibody binding to unmutated (black line), u1S2q (blue line) or rS2d (red line) spike captured on a strepdavidin chip. **b**, SPR sensorgrams of ACE-2 (with C-terminal human Fc tag) to unmutated (black line), u1S2q (blue line) or rS2d (red line) spike captured on a strepdavidin chip. **c**, SPR sensorgrams of binding of unmutated (black line), u1S2q (blue line) or rS2d (red line) spike to ACE-2 (with C-terminal human Fc tag) captured on an anti-mouse Fc surface. The orange and magenta dotted lines are binding curves for rS2d following negative selection over a CR3022 or ACE-2 column, respectively. **d**, Representative NSEM micrographs of the flow-through after negative selection of the rS2d sample through an ACE-2 column (left) and CR3022 column (right). **e**, Top views and **f**, side views of 3D classes of particles from the dataset from the CR3022 column-eluted sample. C1 symmetry was used during classification. For comparison, images from cryo-EM maps low-pass filtered to 20 Å of the 1-RBD 'up' state (EMD-21457) and 3-RBD 'down' state (EMD-21452) are shown in figures **g**, top view and **h**, side view.

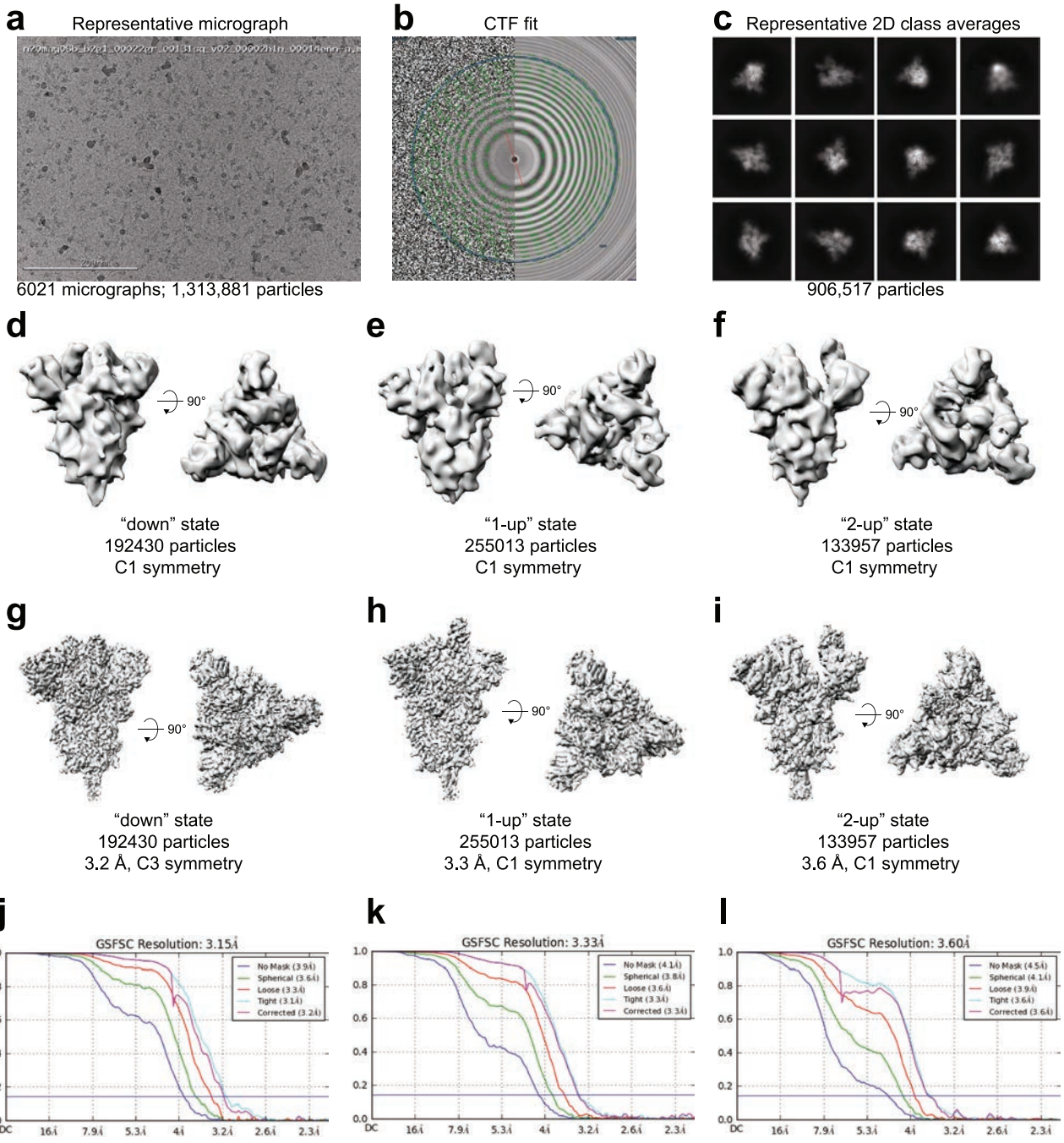

Extended Data Fig. 8 | Cryo-EM data processing details for u1s2q. a, Representative micrograph. **b**, CTF fit **c**, Representative 2D class averages. **d**–**f**, *Ab initio* reconstructions for the (**d**) 'down' state, (**e**) '1-up' state and (**f**) '2-up' state. **g**–**i**, Refined maps for the (**g**) 'down' state, (**h**) '1-up' state and (**i**) '2-up' state. **j**–**l**, Fourier shell correlation curves for the (**j**) 'down' state, (**e**) '1-up' state and (**f**) '2-up' state.

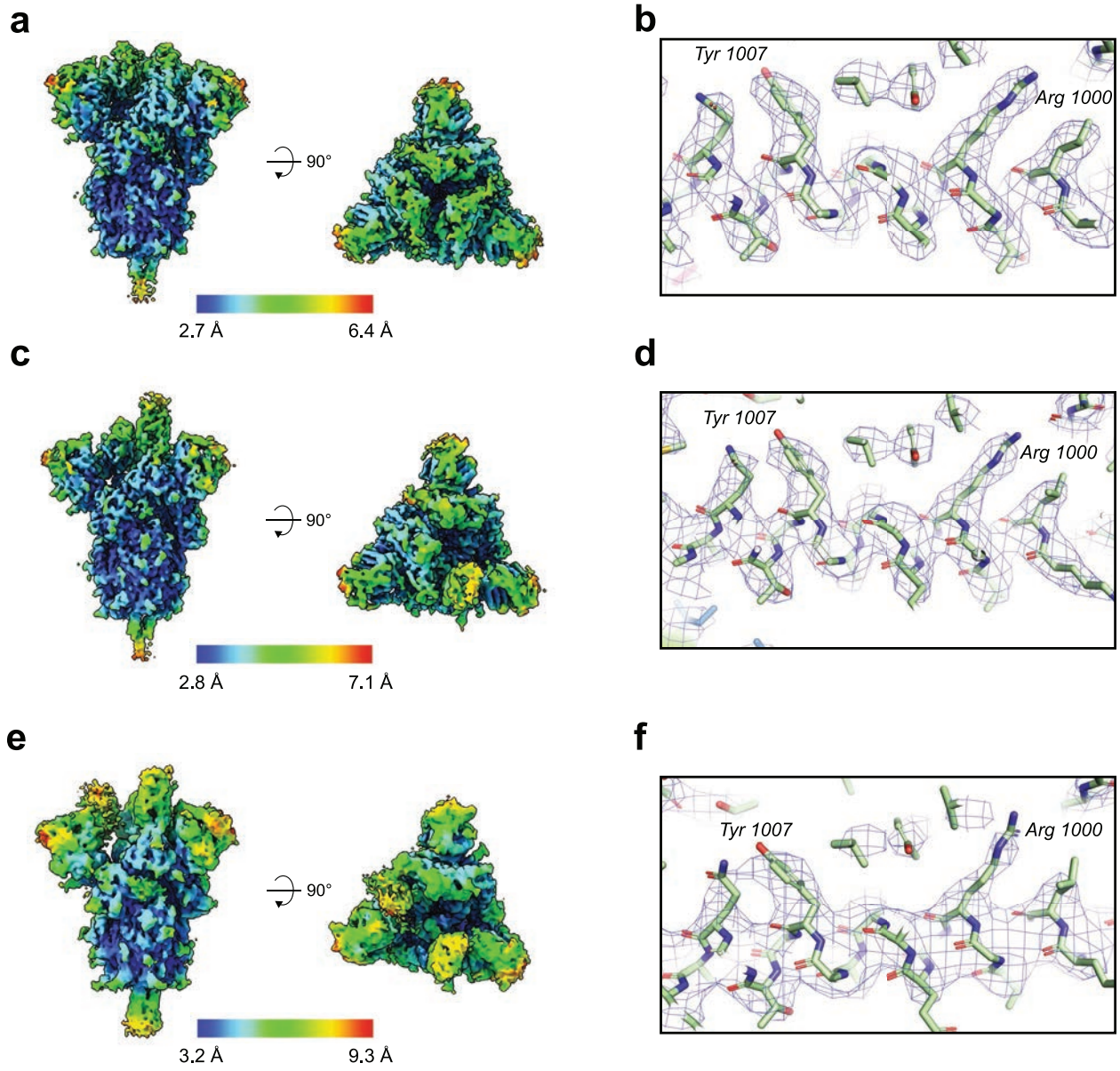

Extended Data Fig. 9 | Local map resolution for u1s2q. a, Refined cryo-EM maps colored by local resolution and **b**, Zoom-in image showing region in the S2 domain with the cryo-EM map shown as a transparent surface and underlying fitted model in cartoon representation, with residues shown as balls and sticks. **c**, and **d**, Same information as presented in panels (**a**) and (**b**) but for the 1-RBD 'up' state. (**e**) and (**f**) Same information as presented in panels (**a**) and (**b**) but for the 2-RBD 'up' state.

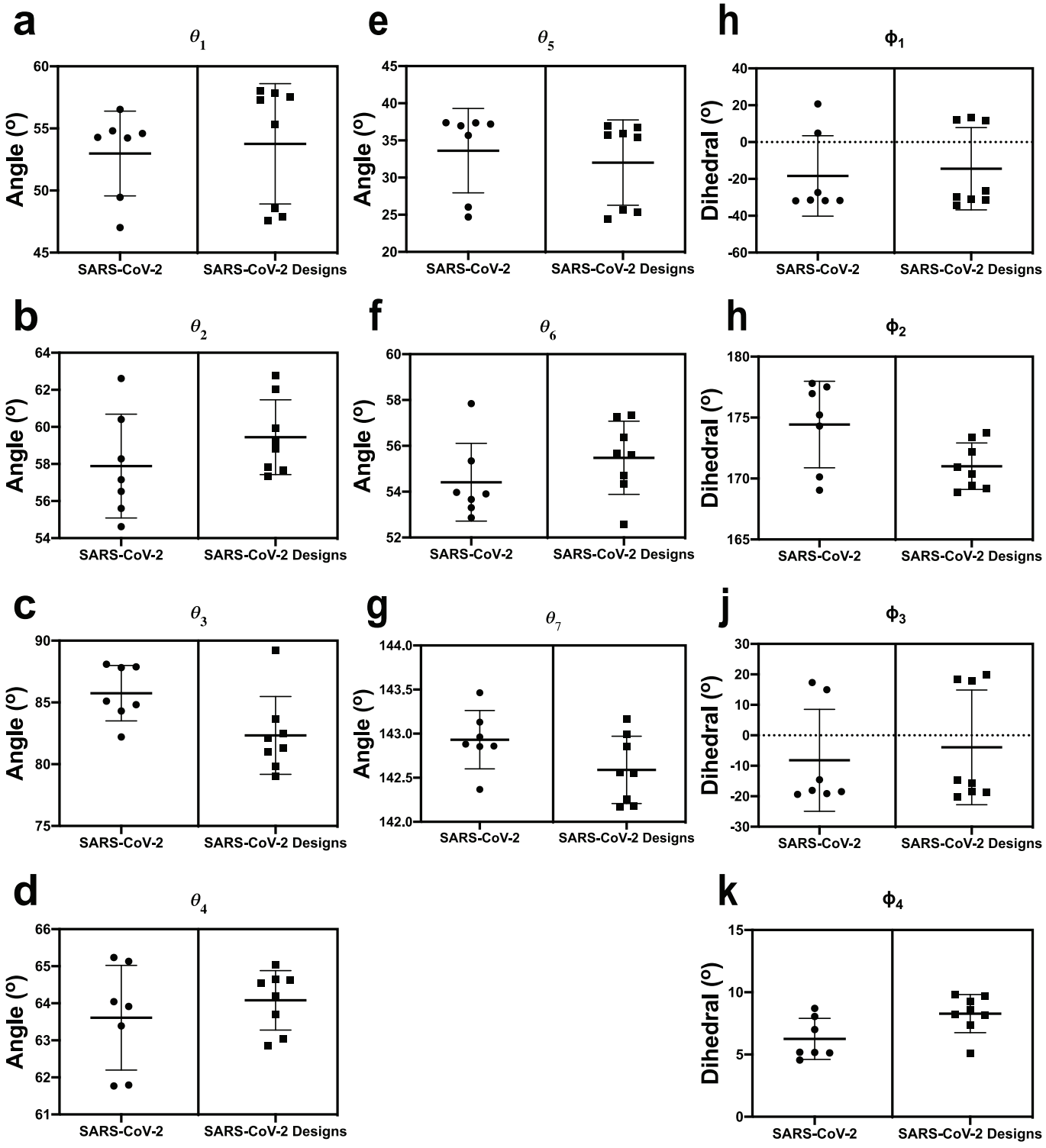

Extended Data Fig. 10 | β-CoV Vector Analysis of SARS-2 and SARS-2 Designs. a–k, Angles and dihedrals for SARS-2 structures and SARS-2 designs depicted in Fig. 1c. Individual data points are shown as circles or squares; lines denote mean and s.d.

Article

Cell

SARS-CoV-2 Cell Entry Depends on ACE2 and TMPRSS2 and Is Blocked by a Clinically Proven Protease Inhibitor

Markus Hoffmann,[1,13,*] Hannah Kleine-Weber,[1,2,13] Simon Schroeder,[3,4] Nadine Krüger,[5,6] Tanja Herrler,[7] Sandra Erichsen,[8,9] Tobias S. Schiergens,[10] Georg Herrler,[5] Nai-Huei Wu,[5] Andreas Nitsche,[11] Marcel A. Müller,[3,4,12] Christian Drosten,[3,4] and Stefan Pöhlmann[1,2,14,*]

[1]Infection Biology Unit, German Primate Center – Leibniz Institute for Primate Research, Göttingen, Germany
[2]Faculty of Biology and Psychology, University Göttingen, Göttingen, Germany
[3]Charité-Universitätsmedizin Berlin, corporate member of Freie Universität Berlin, Humboldt-Universität zu Berlin, and Berlin Institute of Health, Institute of Virology, Berlin, Germany
[4]German Centre for Infection Research, associated partner Charité, Berlin, Germany
[5]Institute of Virology, University of Veterinary Medicine Hannover, Hannover, Germany
[6]Research Center for Emerging Infections and Zoonoses, University of Veterinary Medicine Hannover, Hannover, Germany
[7]BG Unfallklinik Murnau, Murnau, Germany
[8]Institute for Biomechanics, BG Unfallklinik Murnau, Murnau, Germany
[9]Institute for Biomechanics, Paracelsus Medical University Salzburg, Salzburg, Austria
[10]Biobank of the Department of General, Visceral, and Transplant Surgery, Ludwig-Maximilians-University Munich, Munich, Germany
[11]Robert Koch Institute, ZBS 1 Highly Pathogenic Viruses, WHO Collaborating Centre for Emerging Infections and Biological Threats, Berlin, Germany
[12]Martsinovsky Institute of Medical Parasitology, Tropical and Vector Borne Diseases, Sechenov University, Moscow, Russia
[13]These authors contributed equally
[14]Lead Contact
*Correspondence: mhoffmann@dpz.eu (M.H.), spoehlmann@dpz.eu (S.P.)
https://doi.org/10.1016/j.cell.2020.02.052

SUMMARY

The recent emergence of the novel, pathogenic SARS-coronavirus 2 (SARS-CoV-2) in China and its rapid national and international spread pose a global health emergency. Cell entry of coronaviruses depends on binding of the viral spike (S) proteins to cellular receptors and on S protein priming by host cell proteases. Unravelling which cellular factors are used by SARS-CoV-2 for entry might provide insights into viral transmission and reveal therapeutic targets. Here, we demonstrate that SARS-CoV-2 uses the SARS-CoV receptor ACE2 for entry and the serine protease TMPRSS2 for S protein priming. A TMPRSS2 inhibitor approved for clinical use blocked entry and might constitute a treatment option. Finally, we show that the sera from convalescent SARS patients cross-neutralized SARS-2-S-driven entry. Our results reveal important commonalities between SARS-CoV-2 and SARS-CoV infection and identify a potential target for antiviral intervention.

INTRODUCTION

Several members of the family *Coronaviridae* constantly circulate in the human population and usually cause mild respiratory disease (Corman et al., 2019). In contrast, the severe acute respiratory syndrome coronavirus (SARS-CoV) and the Middle East respiratory syndrome coronavirus (MERS-CoV) are transmitted from animals to humans and cause severe respiratory diseases in afflicted individuals, SARS and MERS, respectively (Fehr et al., 2017). SARS emerged in 2002 in Guangdong province, China, and its subsequent global spread was associated with 8,096 cases and 774 deaths (de Wit et al., 2016; WHO, 2004). Chinese horseshoe bats serve as natural reservoir hosts for SARS-CoV (Lau et al., 2005; Li et al., 2005a). Human transmission was facilitated by intermediate hosts like civet cats and raccoon dogs, which are frequently sold as food sources in Chinese wet markets (Guan et al., 2003). At present, no specific antivirals or approved vaccines are available to combat SARS, and the SARS pandemic in 2002 and 2003 was finally stopped by conventional control measures, including travel restrictions and patient isolation.

In December 2019, a new infectious respiratory disease emerged in Wuhan, Hubei province, China (Huang et al., 2020; Wang et al., 2020; Zhu et al., 2020). An initial cluster of infections was linked to Huanan seafood market, potentially due to animal contact. Subsequently, human-to-human transmission occurred (Chan et al., 2020) and the disease, now termed coronavirus disease 19 (COVID-19) rapidly spread within China. A novel coronavirus, SARS-coronavirus 2 (SARS-CoV-2), which is closely related to SARS-CoV, was detected in patients and is believed to be the etiologic agent of the new lung disease (Zhu et al., 2020). On February 12, 2020, a total of 44,730 laboratory-confirmed infections were reported in China, including 8,204

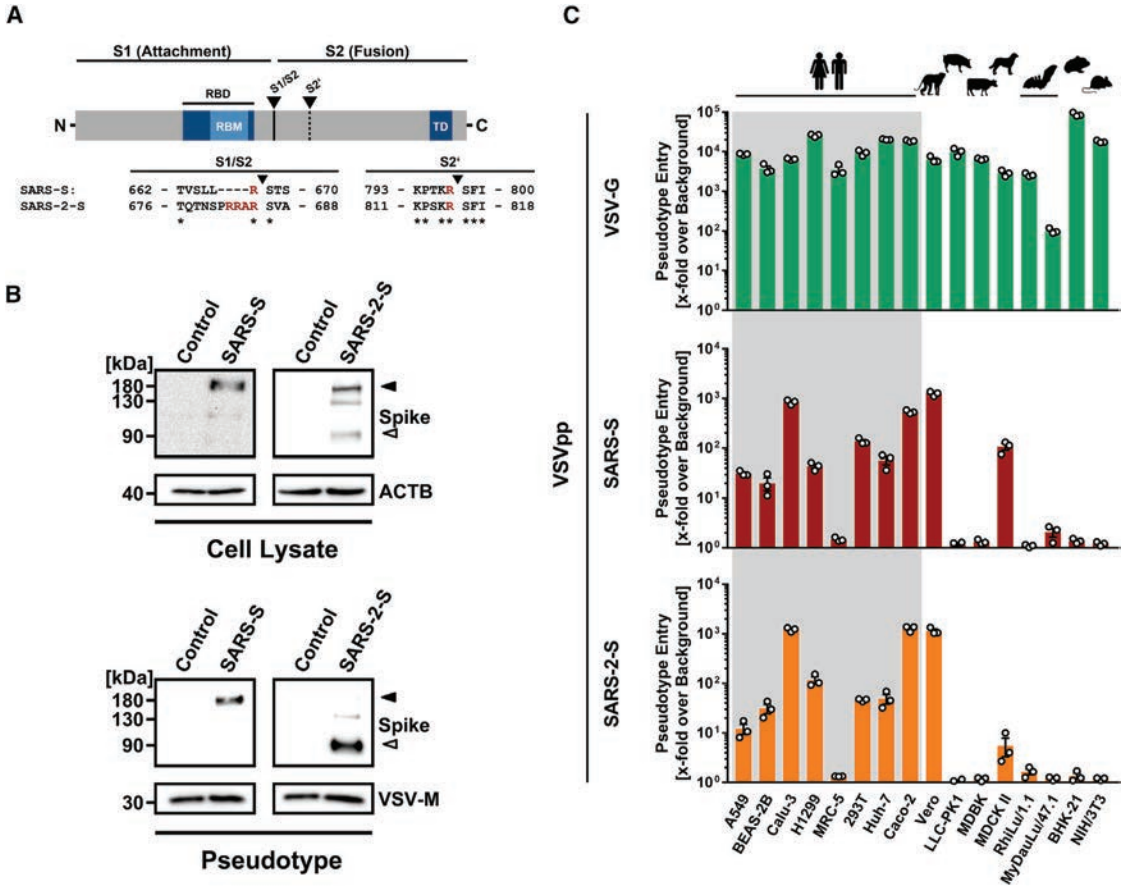

Figure 1. SARS-2-S and SARS-S Facilitate Entry into a Similar Panel of Mammalian Cell Lines

(A) Schematic illustration of SARS-S including functional domains (RBD, receptor binding domain; RBM, receptor binding motif; TD, transmembrane domain) and proteolytic cleavage sites (S1/S2, S2′). Amino acid sequences around the two protease recognition sites (red) are indicated for SARS-S and SARS-2-S (asterisks indicate conserved residues). Arrow heads indicate the cleavage site.

(B) Analysis of SARS-2-S expression (upper panel) and pseudotype incorporation (lower panel) by western blot using an antibody directed against the C-terminal hemagglutinin (HA) tag added to the viral S proteins analyzed. Shown are representative blots from three experiments. β-Actin (cell lysates) and VSV-M (particles) served as loading controls (M, matrix protein). Black arrow heads indicate bands corresponding to uncleaved S proteins (S0) whereas gray arrow heads indicate bands corresponding to the S2 subunit.

(C) Cell lines of human and animal origin were inoculated with pseudotyped VSV harboring VSV-G, SARS-S, or SARS-2-S. At 16 h postinoculation, pseudotype entry was analyzed by determining luciferase activity in cell lysates. Signals obtained for particles bearing no envelope protein were used for normalization. The average of three independent experiments is shown. Error bars indicate SEM. Unprocessed data from a single experiment are presented in Figure S1.

severe cases and 1,114 deaths (WHO, 2020). Infections were also detected in 24 countries outside China and were associated with international travel. At present, it is unknown whether the sequence similarities between SARS-CoV-2 and SARS-CoV translate into similar biological properties, including pandemic potential (Munster et al., 2020).

The spike (S) protein of coronaviruses facilitates viral entry into target cells. Entry depends on binding of the surface unit, S1, of the S protein to a cellular receptor, which facilitates viral attachment to the surface of target cells. In addition, entry requires S protein priming by cellular proteases, which entails S protein cleavage at the S1/S2 and the S2' site and allows fusion of viral and cellular membranes, a process driven by the S2 subunit (Figure 1A). SARS-S engages angiotensin-converting enzyme 2 (ACE2) as the entry receptor (Li et al., 2003) and employs the cellular serine protease TMPRSS2 for S protein priming (Glowacka et al., 2011; Matsuyama et al., 2010; Shulla et al., 2011). The SARS-S/ACE2 interface has been elucidated at the atomic level, and the efficiency of ACE2 usage was found to be a key determinant of SARS-CoV transmissibility (Li et al., 2005a, 2005b). SARS-S und SARS-2-S share ~76% amino acid identity. However, it is unknown whether SARS-2-S like SARS-S employs ACE2 and TMPRSS2 for host cell entry.

RESULTS

Evidence for Efficient Proteolytic Processing of SARS-2-S

The goal of our study was to obtain insights into how SARS-2-S facilitates viral entry into target cells and how this process can be

blocked. For this, we first asked whether SARS-2-S is robustly expressed in a human cell line, 293T, commonly used for experimentation because of its high transfectability. Moreover, we analyzed whether there is evidence for proteolytic processing of the S protein because certain coronavirus S proteins are cleaved by host cell proteases at the S1/S2 cleavage site in infected cells (Figure 1A). Immunoblot analysis of 293T cells expressing SARS-2-S protein with a C-terminal antigenic tag revealed a band with a molecular weight expected for unprocessed S protein (S0) (Figure 1B). A band with a size expected for the S2 subunit of the S protein was also observed in cells and, more prominently, in vesicular stomatitis virus (VSV) particles bearing SARS-2-S (Figure 1B). In contrast, an S2 signal was largely absent in cells and particles expressing SARS-S (Figure 1B), as previously documented (Glowacka et al., 2011; Hofmann et al., 2004b). These results suggest efficient proteolytic processing of SARS-2-S in human cells, in keeping with the presence of several arginine residues at the S1/S2 cleavage site of SARS-2-S but not SARS-S (Figure 1A). In contrast, the S2′ cleavage site of SARS-2-S was similar to that of SARS-S.

SARS-2-S and SARS-S Mediate Entry into a Similar Spectrum of Cell Lines

Replication-defective VSV particles bearing coronavirus S proteins faithfully reflect key aspects of coronavirus host cell entry (Kleine-Weber et al., 2019). We employed VSV pseudotypes bearing SARS-2-S to study cell entry of SARS-CoV-2. Both SARS-2-S and SARS-S were robustly incorporated into VSV particles (Figure 1B), allowing a meaningful side-by-side comparison; although, formally, comparable particle incorporation of the S1 subunit remains to be demonstrated. We first asked which cell lines were susceptible to SARS-2-S-driven entry, using a panel of well-characterized cell lines of human and animal origin, respectively. All cell lines were readily susceptible to entry driven by the glycoprotein of the pantropic VSV (VSV-G) (Figure 1C; Figure S1), as expected. Most human cell lines and the animal cell lines Vero and MDCKII were also susceptible to entry driven by SARS-S (Figure 1C). Moreover, SARS-2-S facilitated entry into an identical spectrum of cell lines as SARS-S (Figure 1C), suggesting similarities in choice of entry receptors.

SARS-CoV-2 Employs the SARS-CoV Receptor for Host Cell Entry

In order to elucidate why SARS-S and SARS-2-S mediated entry into the same cell lines, we next determined whether SARS-2-S harbors amino acid residues required for interaction with the SARS-S entry receptor ACE2. Sequence analysis revealed that SARS-CoV-2 clusters with SARS-CoV-related viruses from bats (SARSr-CoV), of which some but not all can use ACE2 for host cell entry (Figure 2A; Figure S2). Analysis of the receptor binding motif (RBM), a portion of the receptor binding domain (RBD) that makes contact with ACE2 (Li et al., 2005a), revealed that most amino acid residues essential for ACE2 binding by SARS-S were conserved in SARS-2-S (Figure 2B). In contrast, most of these residues were absent from S proteins of SARSr-CoV previously found not to use ACE2 for entry (Figure 2B) (Ge et al., 2013; Hoffmann et al., 2013; Menachery et al., 2020). In agreement with these findings, directed expression of human and bat (*Rhinolophus alcyone*) ACE2 but not human DPP4, the entry receptor used by MERS-CoV (Raj et al., 2013), or human APN, the entry receptor used by HCoV-229E (Yeager et al., 1992), allowed SARS-2-S- and SARS-S-driven entry into otherwise non-susceptible BHK-21 cells (Figure 3A). Moreover, antiserum raised against human ACE2 blocked SARS-S- and SARS-2-S- but not VSV-G- or MERS-S-driven entry (Figure 3B). Finally, authentic SARS-CoV-2 infected BHK-21 cells transfected to express ACE2 cells but not parental BHK-21 cells with high efficiency (Figure 3C), indicating that SARS-2-S, like SARS-S, uses ACE2 for cellular entry.

The Cellular Serine Protease TMPRSS2 Primes SARS-2-S for Entry, and a Serine Protease Inhibitor Blocks SARS-CoV-2 Infection of Lung Cells

We next investigated protease dependence of SARS-CoV-2 entry. SARS-CoV can use the endosomal cysteine proteases cathepsin B and L (CatB/L) (Simmons et al., 2005) and the serine protease TMPRSS2 (Glowacka et al., 2011; Matsuyama et al., 2010; Shulla et al., 2011) for S protein priming in cell lines, and inhibition of both proteases is required for robust blockade of viral entry (Kawase et al., 2012). However, only TMPRSS2 activity is essential for viral spread and pathogenesis in the infected host whereas CatB/L activity is dispensable (Iwata-Yoshikawa et al., 2019; Shirato et al., 2016; Shirato et al., 2018; Zhou et al., 2015).

In order to determine whether SARS-CoV-2 can use CatB/L for cell entry, we initially employed ammonium chloride, which elevates endosomal pH and thereby blocks CatB/L activity. 293T cells (TMPRSS2^{-}, transfected to express ACE2 for robust S protein-driven entry) and Caco-2 cells (TMPRSS2^{+}) were used as targets. Ammonium chloride blocked VSV-G-dependent entry into both cell lines whereas entry driven by Nipah virus F and G proteins was not affected (Figure S3A; data not shown), consistent with Nipah virus but not VSV being able to fuse directly with the plasma membrane (Bossart et al., 2002). Ammonium chloride treatment strongly inhibited SARS-2-S- and SARS-S-driven entry into TMPRSS2^{-} 293T cells (Figure S3 A), suggesting CatB/L dependence. Inhibition of entry into TMPRSS2^{+} Caco-2 cells was less efficient compared to 293T cells (Figure S3 A), which would be compatible with SARS-2-S priming by TMPRSS2 in Caco-2 cells. Indeed, the clinically proven serine protease inhibitor camostat mesylate, which is active against TMPRSS2 (Kawase et al., 2012), partially blocked SARS-2-S-driven entry into Caco-2 (Figure S3 B) and Vero-TMPRSS2 cells (Figure 4A). Full inhibition was attained when camostat mesylate and E-64d, an inhibitor of CatB/L, were added (Figure 4A; Figure S3B), indicating that SARS-2-S can use both CatB/L as well as TMPRSS2 for priming in these cell lines. In contrast, camostat mesylate did not interfere with SARS-2-S-driven entry into the TMPRSS2^{-} cell lines 293T (Figure S3B) and Vero (Figure 4A), which was efficiently blocked by E-64d and therefore is CatB/L dependent. Moreover, directed expression of TMPRSS2 rescued SARS-2-S-driven entry from inhibition by E-64d (Figure 4B), confirming that SARS-2-S can employ TMPRSS2 for S protein priming.

We next analyzed whether TMPRSS2 usage is required for SARS-CoV-2 infection of lung cells. Indeed, camostat mesylate significantly reduced MERS-S-, SARS-S-, and SARS-2-S- but

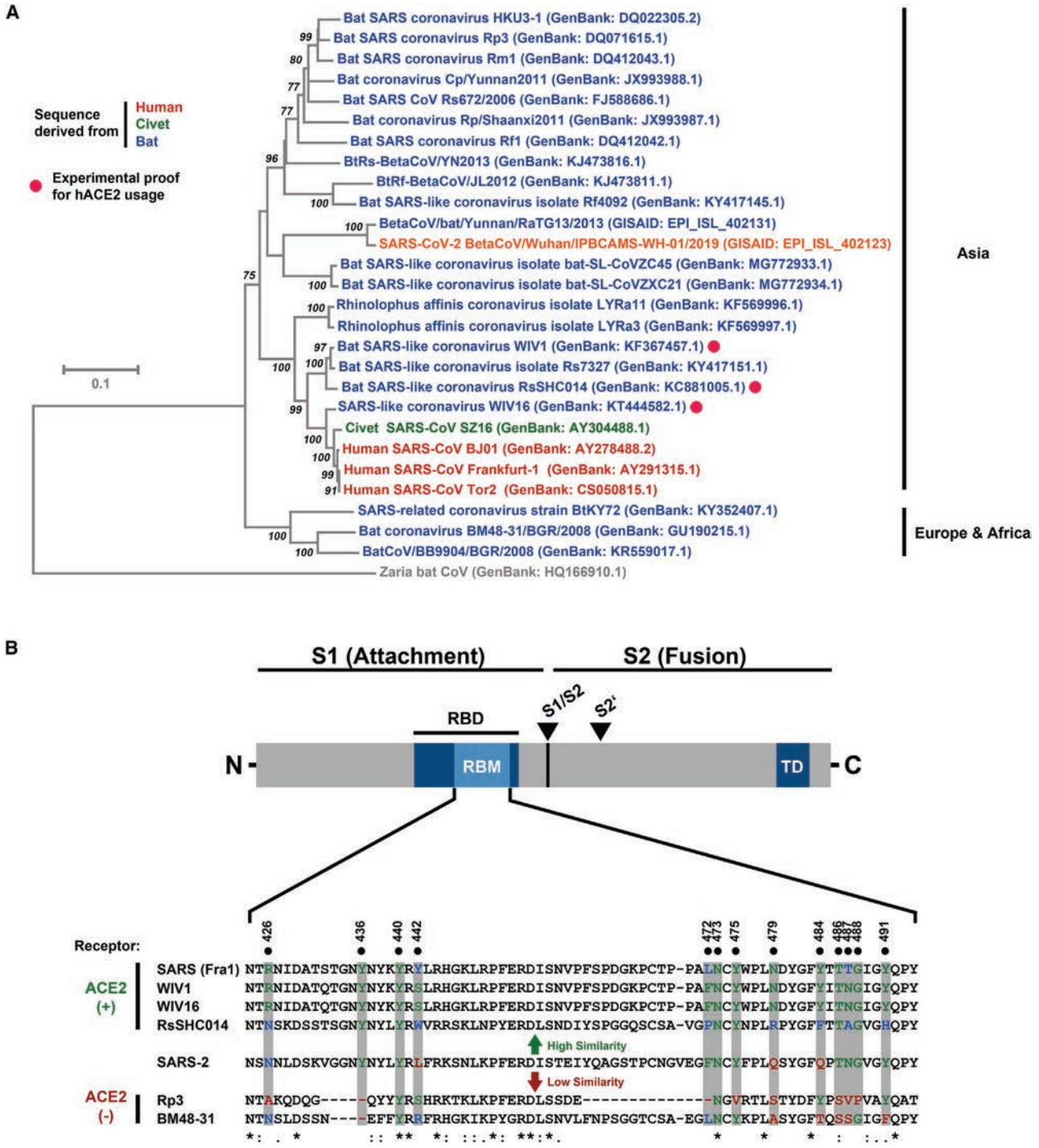

Figure 2. SARS-2-S Harbors Amino Acid Residues Critical for ACE2 Binding

(A) The S protein of SARS-CoV-2 clusters phylogenetically with S proteins of known bat-associated betacoronaviruses (see Figure S2 for more details).

(B) Alignment of the receptor binding motif of SARS-S with corresponding sequences of bat-associated betacoronavirus S proteins, which are able or unable to use ACE2 as cellular receptor, reveals that SARS-CoV-2 possesses crucial amino acid residues for ACE2 binding.

not VSV-G-driven entry into the lung cell line Calu-3 (Figure 4C) and exerted no unwanted cytotoxic effects (Figure S3 C). Similarly, camostat mesylate treatment significantly reduced Calu-3 infection with authentic SARS-CoV-2 (Figure 4D). Finally, camostat mesylate treatment inhibited SARS-S- and SARS-2-S- but not VSV-G-driven entry into primary human lung cells (Figure 4E).

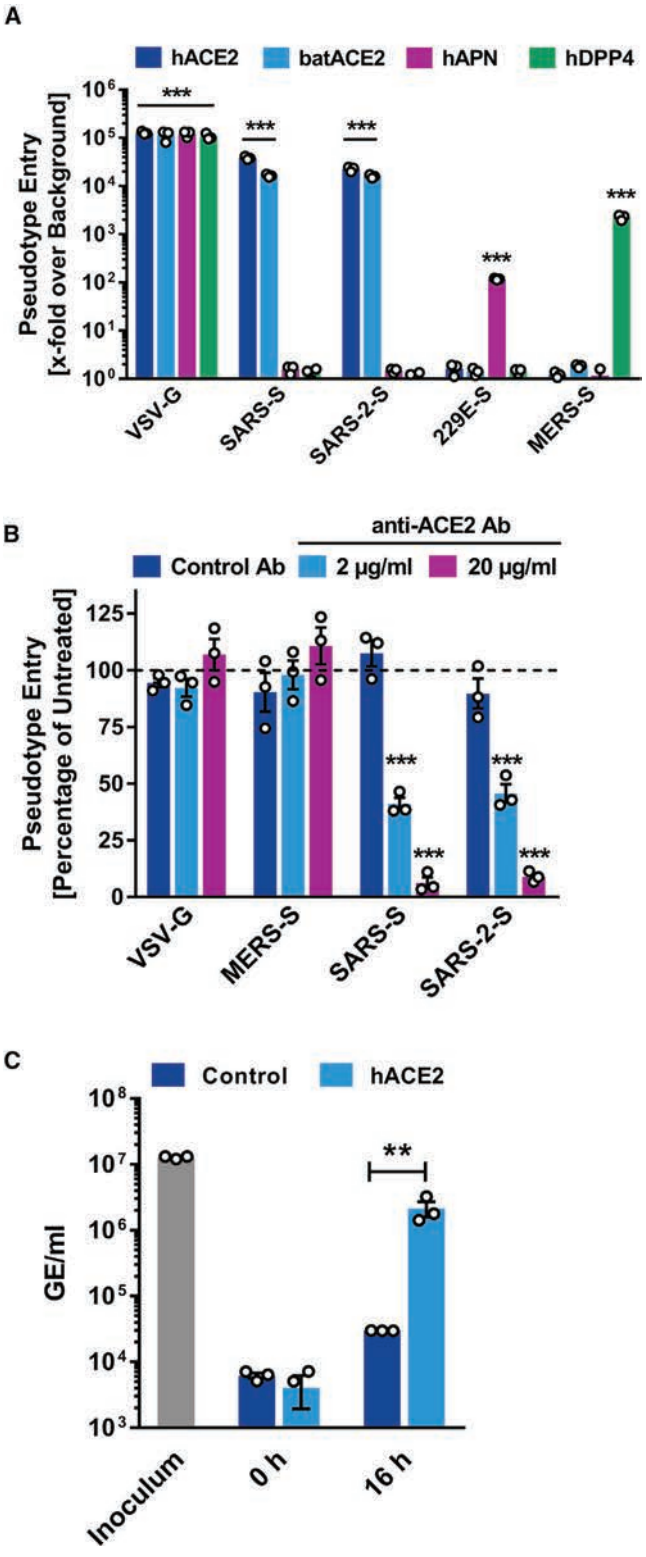

Figure 3. SARS-2-S Utilizes ACE2 as Cellular Receptor

(A) BHK-21 cells transiently expressing ACE2 of human or bat origin, human APN, or human DPP4 were inoculated with pseudotyped VSV harboring VSV-G, SARS-S, SARS-2-S, MERS-S, or 229E-S. At 16 h postinoculation, pseudotype entry was analyzed (normalization against particles without viral envelope protein).

(B) Untreated Vero cells as well as Vero cells pre-incubated with 2 or 20 µg/mL of anti-ACE2 antibody or unrelated control antibody (anti-DC-SIGN, 20 µg/mL) were inoculated with pseudotyped VSV harboring VSV-G, SARS-S, SARS-2-S, or MERS-S. At 16 h postinoculation, pseudotype entry was analyzed (normalization against untreated cells).

(C) BHK-21 cells transfected with ACE2-encoding plasmid or control transfected with DsRed-encoding plasmid were infected with SARS-CoV-2 and washed, and genome equivalents in culture supernatants were determined by quantitative RT-PCR.

The average of three independent experiments conducted with triplicate samples is shown in (A–C). Error bars indicate SEM. Statistical significance was tested by two-way ANOVA with Dunnett posttest. Cells transfected with empty vector served as reference in (A) whereas cells that were not treated with antibody served as reference in (B).

Collectively, SARS-CoV-2 can use TMPRSS2 for S protein priming and camostat mesylate, an inhibitor of TMPRSS2, blocks SARS-CoV-2 infection of lung cells.

Evidence that Antibodies Raised against SARS-CoV Will Cross-Neutralize SARS-CoV-2

Convalescent SARS patients exhibit a neutralizing antibody response directed against the viral S protein (Liu et al., 2006). We investigated whether such antibodies block SARS-2-S-driven entry. Four sera obtained from three convalescent SARS patients inhibited SARS-S- but not VSV-G-driven entry in a concentration-dependent manner (Figure 5). In addition, these sera also reduced SARS-2-S-driven entry, although with lower efficiency compared to SARS-S (Figure 5). Similarly, rabbit sera raised against the S1 subunit of SARS-S reduced both SARS-S- and SARS-2-S-driven entry with high efficiency, and again inhibition of SARS-S-driven entry was more efficient. Thus, antibody responses raised against SARS-S during infection or vaccination might offer some level of protection against SARS-CoV-2 infection.

DISCUSSION

The present study provides evidence that host cell entry of SARS-CoV-2 depends on the SARS-CoV receptor ACE2 and can be blocked by a clinically proven inhibitor of the cellular serine protease TMPRSS2, which is employed by SARS-CoV-2 for S protein priming. Moreover, it suggests that antibody responses raised against SARS-CoV could at least partially protect against SARS-CoV-2 infection. These results have important implications for our understanding of SARS-CoV-2 transmissibility and pathogenesis and reveal a target for therapeutic intervention.

The finding that SARS-2-S exploits ACE2 for entry, which was also reported by Zhou and colleagues (Zhou et al., 2020) while the present manuscript was in revision, suggests that the virus might target a similar spectrum of cells as SARS-CoV. In the lung, SARS-CoV infects mainly pneumocytes and macrophages (Shieh et al., 2005). However, ACE2 expression is not limited to the lung, and extrapulmonary spread of SARS-CoV in ACE2$^+$ tissues was observed (Ding et al., 2004; Gu et al., 2005; Hamming et al., 2004). The same can be expected for SARS-CoV-2, although affinity of SARS-S and SARS-2-S for ACE2 remains

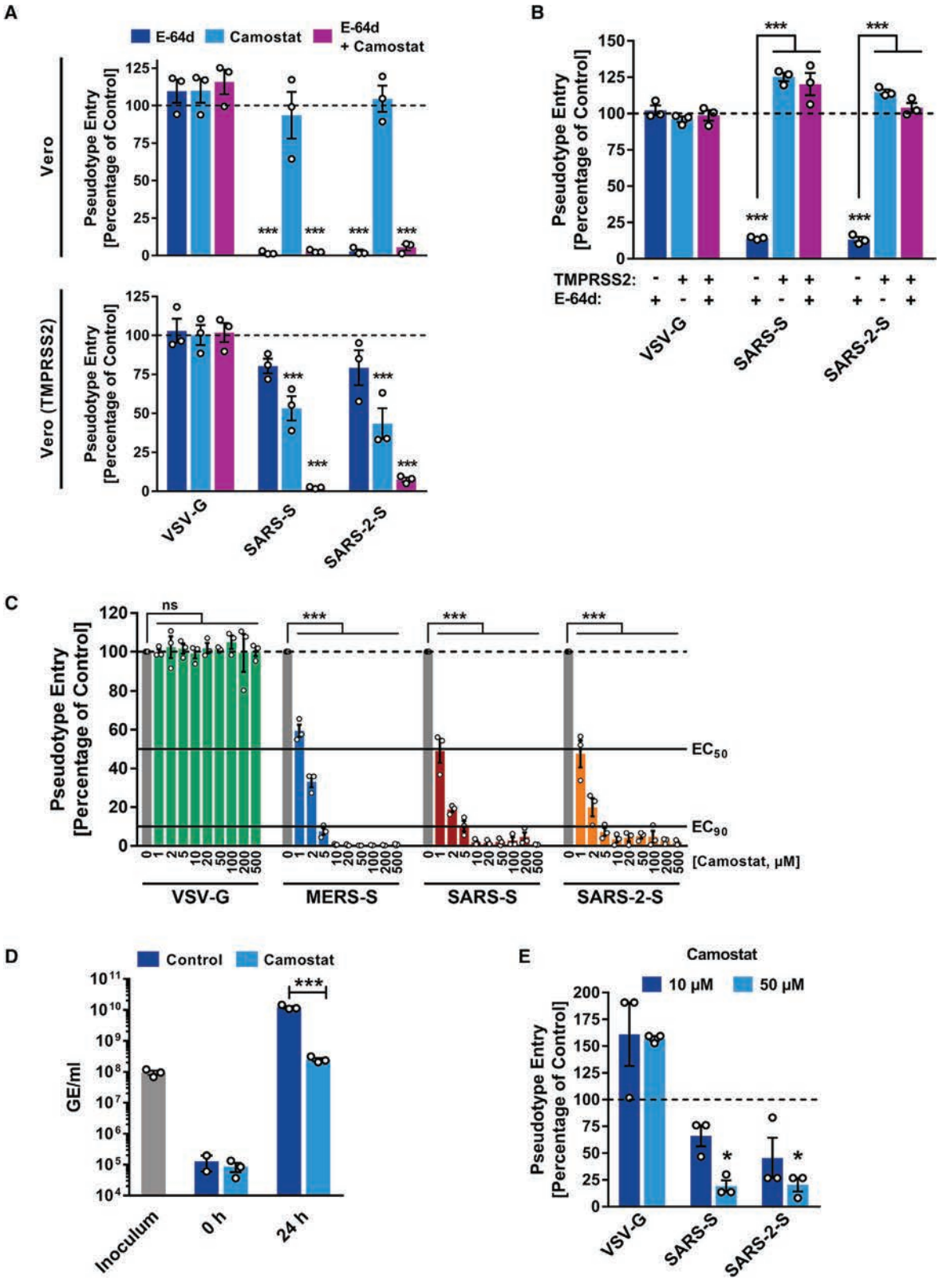

(legend on next page)

to be compared. It has been suggested that the modest ACE2 expression in the upper respiratory tract (Bertram et al., 2012; Hamming et al., 2004) might limit SARS-CoV transmissibility. In light of the potentially increased transmissibility of SARS-CoV-2 relative to SARS-CoV, one may speculate that the new virus might exploit cellular attachment-promoting factors with higher efficiency than SARS-CoV to ensure robust infection of $ACE2^{+}$ cells in the upper respiratory tract. This could comprise binding to cellular glycans, a function ascribed to the S1 domain of certain coronaviruses (Li et al., 2017; Park et al., 2019). Finally, it should be noted that ACE2 expression protects from lung injury and is downregulated by SARS-S (Haga et al., 2008; Imai et al., 2005; Kuba et al., 2005), which might promote SARS. It will thus be interesting to determine whether SARS-CoV-2 also interferes with ACE2 expression.

Priming of coronavirus S proteins by host cell proteases is essential for viral entry into cells and encompasses S protein cleavage at the S1/S2 and the S2′ sites. The S1/S2 cleavage site of SARS-2-S harbors several arginine residues (multibasic), which indicates high cleavability. Indeed, SARS-2-S was efficiently cleaved in cells, and cleaved S protein was incorporated into VSV particles. Notably, the cleavage site sequence can determine the zoonotic potential of coronaviruses (Menachery et al., 2020; Yang et al., 2014, 2015), and a multibasic cleavage site was not present in RaTG13, the coronavirus most closely related to SARS-CoV-2. It will thus be interesting to determine whether the presence of a multibasic cleavage site is required for SARS-CoV-2 entry into human cells and how this cleavage site was acquired.

The S proteins of SARS-CoV can use the endosomal cysteine proteases CatB/L for S protein priming in $TMPRSS2^{-}$ cells (Simmons et al., 2005). However, S protein priming by TMPRSS2 but not CatB/L is essential for viral entry into primary target cells and for viral spread in the infected host (Iwata-Yoshikawa et al., 2019; Kawase et al., 2012; Zhou et al., 2015). The present study indicates that SARS-CoV-2 spread also depends on TMPRSS2 activity, although we note that SARS-CoV-2 infection of Calu-3 cells was inhibited but not abrogated by camostat mesylate, likely reflecting residual S protein priming by CatB/L. One can speculate that furin-mediated precleavage at the S1/S2 site in infected cells might promote subsequent TMPRSS2-dependent entry into target cells, as reported for MERS-CoV (Kleine-Weber et al., 2018; Park et al., 2016). Collectively, our present findings and previous work highlight TMPRSS2 as a host cell factor that is critical for spread of several clinically relevant viruses, including influenza A viruses and coronaviruses (Gierer et al., 2013; Glowacka et al., 2011; Iwata-Yoshikawa et al., 2019; Kawase et al., 2012; Matsuyama et al., 2010; Shulla et al., 2011; Zhou et al., 2015). In contrast, TMPRSS2 is dispensable for development and homeostasis (Kim et al., 2006) and thus constitutes an attractive drug target. In this context, it is noteworthy that the serine protease inhibitor camostat mesylate, which blocks TMPRSS2 activity (Kawase et al., 2012; Zhou et al., 2015), has been approved in Japan for human use, but for an unrelated indication. This compound or related ones with potentially increased antiviral activity (Yamamoto et al., 2016) could thus be considered for off-label treatment of SARS-CoV-2-infected patients.

Convalescent SARS patients exhibit a neutralizing antibody response that can be detected even 24 months after infection (Liu et al., 2006) and that is largely directed against the S protein. Moreover, experimental SARS vaccines, including recombinant S protein (He et al., 2006) and inactivated virus (Lin et al., 2007), induce neutralizing antibody responses. Although confirmation with infectious virus is pending, our results indicate that neutralizing antibody responses raised against SARS-S could offer some protection against SARS-CoV-2 infection, which may have implications for outbreak control.

In sum, this study provided key insights into the first step of SARS-CoV-2 infection, viral entry into cells, and defined potential targets for antiviral intervention.

STAR★METHODS

Detailed methods are provided in the online version of this paper and include the following:

- KEY RESOURCES TABLE
- LEAD CONTACT AND MATERIALS AVAILABILITY
- EXPERIMANTAL MODEL AND SUBJECT DETAILS
  - Cell cultures, primary cells, viral strains
- METHOD DETAILS
  - Plasmids
  - Pseudotyping of VSV and transduction experiments
  - Quantification of cell viability

Figure 4. SARS-2-S Employs TMPRSS2 for S Protein Priming in Human Lung Cells

(A) Importance of activity of CatB/L or TMPRSS2 for host cell entry of SARS-CoV-2 was evaluated by adding inhibitors to target cells prior to transduction. E-64d and camostat mesylate block the activity of CatB/L and TMPRSS2, respectively (additional data for 293T cells transiently expressing ACE2 and Caco-2 cells are shown in Figure S3).

(B) To analyze whether TMPRSS2 can rescue SARS-2-S-driven entry into cells that have low CatB/L activity, 293T cells transiently expressing ACE2 alone or in combination with TMPRSS2 were incubated with CatB/L inhibitor E-64d or DMSO as control and inoculated with pseudotypes bearing the indicated viral surface proteins.

(C) Calu-3 cells were pre-incubated with the indicated concentrations of camostat mesylate and subsequently inoculated with pseudoparticles harboring the indicated viral glycoproteins.

(D) Calu-3 cells were pre-incubated with camostat mesylate and infected with SARS-CoV-2. Subsequently, the cells were washed and genome equivalents in culture supernatants were determined by quantitative RT-PCR.

(E) In order to investigate whether serine protease activity is required for SARS-2-S-driven entry into human lung cells, primary human airway epithelial cells were incubated with camostat mesylate prior to transduction.

The average of three independent experiments conducted with triplicate or quadruplicate samples is shown in (A–E). Error bars indicate SEM. Statistical significance was tested by two-way ANOVA with Dunnett posttest. Cells that did not receive inhibitor served as reference in (A), (C), (D), and (E) whereas cells transfected with empty vector and not treated with inhibitor served as reference in (B).

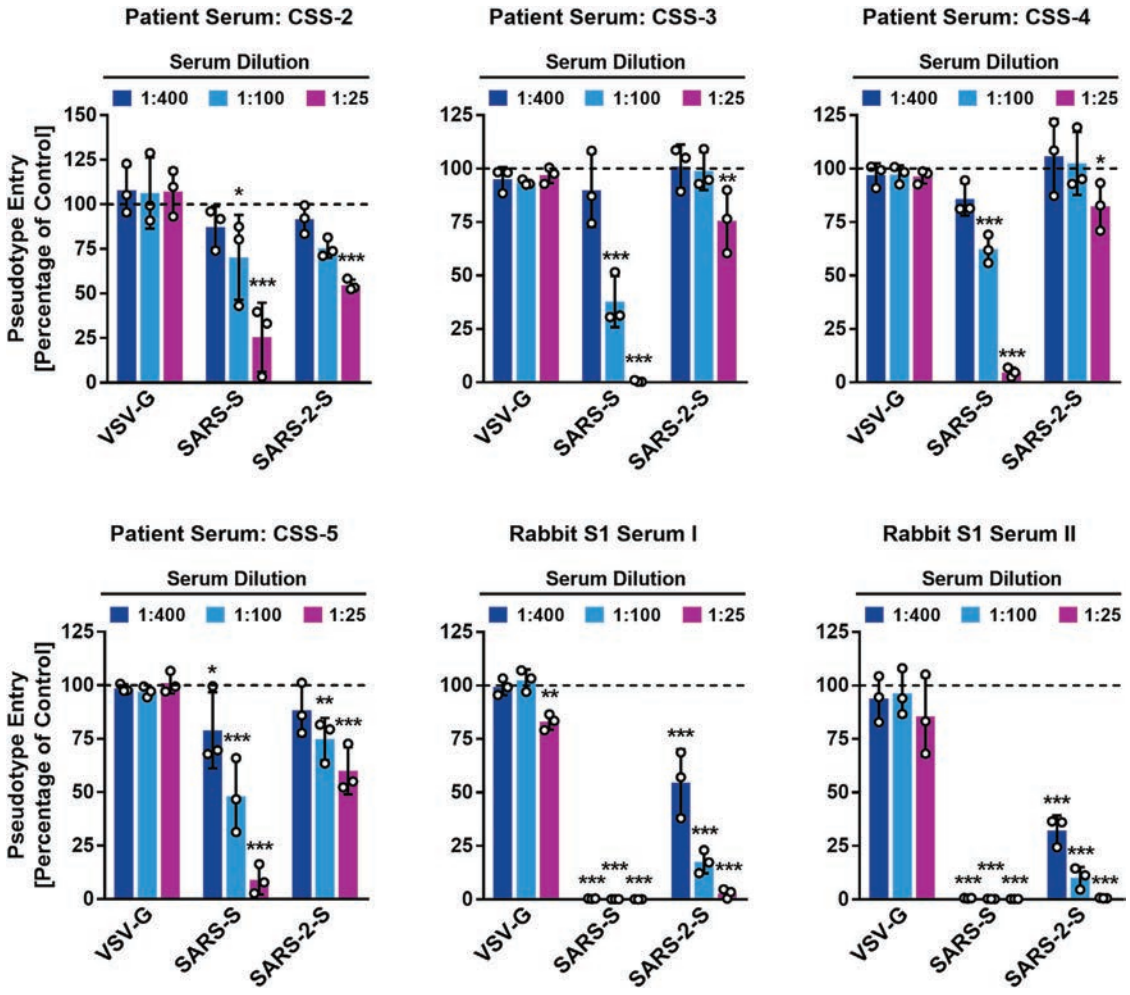

Figure 5. Sera from Convalescent SARS Patients Cross-Neutralize SARS-2-S-Driven Entry

Pseudotypes harboring the indicated viral surface proteins were incubated with different dilutions of sera from three convalescent SARS patients or sera from rabbits immunized with the S1 subunit of SARS-S and subsequently inoculated onto Vero cells in order to evaluate cross-neutralization potential. The average of three independent experiments performed with triplicate samples is shown. Error bars indicate SEM. Statistical significance was tested by two-way ANOVA with Dunnett posttest.

ACKNOWLEDGMENTS

We thank Heike Hofmann-Winkler for discussion, Andrea Maisner for Nipah F and G expression plasmids, Anette Teichmann for technical assistance, and Roberto Cattaneo for plasmid pCG1. We acknowledge the support of the non-profit foundation HTCR, which holds human tissue on trust, making it broadly available for research on an ethical and legal basis. We gratefully acknowledge the authors and the originating and submitting laboratories for their sequence and metadata shared through GISAID, on which this research is based. This work was supported by BMBF (RAPID Consortium, 01KI1723D and 01KI1723A to C.D. and S.P.) and German Research Foundation (DFG) (WU 929/1-1 to N.-H.W.).

AUTHOR CONTRIBUTIONS

Conceptualization, M.H. and S.P.; Formal analysis, M.H., H.K.-W., M.A.M., and S.P.; Investigation, M.H., H.K.-W., S.S., N.K., T.H., N.-H.W., and M.A.M.; Resources, T.H., S.E., T.S.S., G.H., A.N., M.A.M., and C.D.; Writing – Original Draft, M.H. and S.P.; Writing – Review & Editing, all authors; Funding acquisition, S.P., N.-H.W., and C.D.

DECLARATION OF INTERESTS

The authors declare no competing interests.

Received: February 6, 2020
Revised: February 13, 2020
Accepted: February 25, 2020
Published: March 5, 2020

REFERENCES

Berger Rentsch, M., and Zimmer, G. (2011). A vesicular stomatitis virus replicon-based bioassay for the rapid and sensitive determination of multi-species type I interferon. PLoS ONE *6*, e25858.

Bertram, S., Glowacka, I., Blazejewska, P., Soilleux, E., Allen, P., Danisch, S., Steffen, I., Choi, S.Y., Park, Y., Schneider, H., et al. (2010). TMPRSS2 and TMPRSS4 facilitate trypsin-independent spread of influenza virus in Caco-2 cells. J. Virol. *84*, 10016–10025.

Bertram, S., Heurich, A., Lavender, H., Gierer, S., Danisch, S., Perin, P., Lucas, J.M., Nelson, P.S., Pöhlmann, S., and Soilleux, E.J. (2012). Influenza and SARS-coronavirus activating proteases TMPRSS2 and HAT are expressed at multiple sites in human respiratory and gastrointestinal tracts. PLoS ONE *7*, e35876.

Bossart, K.N., Wang, L.F., Flora, M.N., Chua, K.B., Lam, S.K., Eaton, B.T., and Broder, C.C. (2002). Membrane fusion tropism and heterotypic functional activities of the Nipah virus and Hendra virus envelope glycoproteins. J. Virol. *76*, 11186–11198.

Brinkmann, C., Hoffmann, M., Lübke, A., Nehlmeier, I., Krämer-Kühl, A., Winkler, M., and Pöhlmann, S. (2017). The glycoprotein of vesicular stomatitis virus promotes release of virus-like particles from tetherin-positive cells. PLoS ONE *12*, e0189073.

Buchholz, U., Müller, M.A., Nitsche, A., Sanewski, A., Wevering, N., Bauer-Balci, T., Bonin, F., Drosten, C., Schweiger, B., Wolff, T., et al. (2013). Contact investigation of a case of human novel coronavirus infection treated in a German hospital, October-November 2012. Euro Surveill. *18*, 20406.

Chan, J.F., Yuan, S., Kok, K.H., To, K.K., Chu, H., Yang, J., Xing, F., Liu, J., Yip, C.C., Poon, R.W., et al. (2020). A familial cluster of pneumonia associated with the 2019 novel coronavirus indicating person-to-person transmission: a study of a family cluster. Lancet *395*, 514–523.

Corman, V.M., Lienau, J., and Witzenrath, M. (2019). [Coronaviruses as the cause of respiratory infections]. Internist (Berl.) *60*, 1136–1145.

Corman, V.M., Landt, O., Kaiser, M., Molenkamp, R., Meijer, A., Chu, D.K., Bleicker, T., Brünink, S., Schneider, J., Schmidt, M.L., et al. (2020). Detection of 2019 novel coronavirus (2019-nCoV) by real-time RT-PCR. Euro Surveill. *25* https://doi.org/10.2807/1560-7917.ES.2020.25.3.2000045.

de Wit, E., van Doremalen, N., Falzarano, D., and Munster, V.J. (2016). SARS and MERS: recent insights into emerging coronaviruses. Nat. Rev. Microbiol. *14*, 523–534.

Ding, Y., He, L., Zhang, Q., Huang, Z., Che, X., Hou, J., Wang, H., Shen, H., Qiu, L., Li, Z., et al. (2004). Organ distribution of severe acute respiratory syndrome (SARS) associated coronavirus (SARS-CoV) in SARS patients: implications for pathogenesis and virus transmission pathways. J. Pathol. *203*, 622–630.

Fehr, A.R., Channappanavar, R., and Perlman, S. (2017). Middle East Respiratory Syndrome: Emergence of a Pathogenic Human Coronavirus. Annu. Rev. Med. *68*, 387–399.

Ge, X.Y., Li, J.L., Yang, X.L., Chmura, A.A., Zhu, G., Epstein, J.H., Mazet, J.K., Hu, B., Zhang, W., Peng, C., et al. (2013). Isolation and characterization of a bat SARS-like coronavirus that uses the ACE2 receptor. Nature *503*, 535–538.

Gierer, S., Bertram, S., Kaup, F., Wrensch, F., Heurich, A., Krämer-Kühl, A., Welsch, K., Winkler, M., Meyer, B., Drosten, C., et al. (2013). The spike protein of the emerging betacoronavirus EMC uses a novel coronavirus receptor for entry, can be activated by TMPRSS2, and is targeted by neutralizing antibodies. J. Virol. *87*, 5502–5511.

Glowacka, I., Bertram, S., Müller, M.A., Allen, P., Soilleux, E., Pfefferle, S., Steffen, I., Tsegaye, T.S., He, Y., Gnirss, K., et al. (2011). Evidence that TMPRSS2 activates the severe acute respiratory syndrome coronavirus spike protein for membrane fusion and reduces viral control by the humoral immune response. J. Virol. *85*, 4122–4134.

Gu, J., Gong, E., Zhang, B., Zheng, J., Gao, Z., Zhong, Y., Zou, W., Zhan, J., Wang, S., Xie, Z., et al. (2005). Multiple organ infection and the pathogenesis of SARS. J. Exp. Med. *202*, 415–424.

Guan, Y., Zheng, B.J., He, Y.Q., Liu, X.L., Zhuang, Z.X., Cheung, C.L., Luo, S.W., Li, P.H., Zhang, L.J., Guan, Y.J., et al. (2003). Isolation and characterization of viruses related to the SARS coronavirus from animals in southern China. Science *302*, 276–278.

Haga, S., Yamamoto, N., Nakai-Murakami, C., Osawa, Y., Tokunaga, K., Sata, T., Yamamoto, N., Sasazuki, T., and Ishizaka, Y. (2008). Modulation of TNF-alpha-converting enzyme by the spike protein of SARS-CoV and ACE2 induces TNF-alpha production and facilitates viral entry. Proc. Natl. Acad. Sci. USA *105*, 7809–7814.

Hamming, I., Timens, W., Bulthuis, M.L., Lely, A.T., Navis, G., and van Goor, H. (2004). Tissue distribution of ACE2 protein, the functional receptor for SARS coronavirus. A first step in understanding SARS pathogenesis. J. Pathol. *203*, 631–637.

He, Y., Li, J., Heck, S., Lustigman, S., and Jiang, S. (2006). Antigenic and immunogenic characterization of recombinant baculovirus-expressed severe acute respiratory syndrome coronavirus spike protein: implication for vaccine design. J. Virol. *80*, 5757–5767.

Hoffmann, M., Müller, M.A., Drexler, J.F., Glende, J., Erdt, M., Gützkow, T., Losemann, C., Binger, T., Deng, H., Schwegmann-Weßels, C., et al. (2013). Differential sensitivity of bat cells to infection by enveloped RNA viruses: coronaviruses, paramyxoviruses, filoviruses, and influenza viruses. PLoS ONE *8*, e72942.

Hofmann, H., Geier, M., Marzi, A., Krumbiegel, M., Peipp, M., Fey, G.H., Gramberg, T., and Pöhlmann, S. (2004a). Susceptibility to SARS coronavirus S protein-driven infection correlates with expression of angiotensin converting enzyme 2 and infection can be blocked by soluble receptor. Biochem. Biophys. Res. Commun. *319*, 1216–1221.

Hofmann, H., Hattermann, K., Marzi, A., Gramberg, T., Geier, M., Krumbiegel, M., Kuate, S., Uberla, K., Niedrig, M., and Pöhlmann, S. (2004b). S protein of severe acute respiratory syndrome-associated coronavirus mediates entry into hepatoma cell lines and is targeted by neutralizing antibodies in infected patients. J. Virol. *78*, 6134–6142.

Hofmann, H., Pyrc, K., van der Hoek, L., Geier, M., Berkhout, B., and Pöhlmann, S. (2005). Human coronavirus NL63 employs the severe acute respiratory syndrome coronavirus receptor for cellular entry. Proc. Natl. Acad. Sci. USA *102*, 7988–7993.

Huang, C., Wang, Y., Li, X., Ren, L., Zhao, J., Hu, Y., Zhang, L., Fan, G., Xu, J., Gu, X., et al. (2020). Clinical features of patients infected with 2019 novel coronavirus in Wuhan (China: Lancet).

Imai, Y., Kuba, K., Rao, S., Huan, Y., Guo, F., Guan, B., Yang, P., Sarao, R., Wada, T., Leong-Poi, H., et al. (2005). Angiotensin-converting enzyme 2 protects from severe acute lung failure. Nature *436*, 112–116.

Iwata-Yoshikawa, N., Okamura, T., Shimizu, Y., Hasegawa, H., Takeda, M., and Nagata, N. (2019). TMPRSS2 Contributes to Virus Spread and Immunopathology in the Airways of Murine Models after Coronavirus Infection. J. Virol. *93* https://doi.org/10.1128/JVI.01815-18.

Kawase, M., Shirato, K., van der Hoek, L., Taguchi, F., and Matsuyama, S. (2012). Simultaneous treatment of human bronchial epithelial cells with serine and cysteine protease inhibitors prevents severe acute respiratory syndrome coronavirus entry. J. Virol. *86*, 6537–6545.

Kim, T.S., Heinlein, C., Hackman, R.C., and Nelson, P.S. (2006). Phenotypic analysis of mice lacking the Tmprss2-encoded protease. Mol. Cell. Biol. *26*, 965–975.

Kleine-Weber, H., Elzayat, M.T., Hoffmann, M., and Pöhlmann, S. (2018). Functional analysis of potential cleavage sites in the MERS-coronavirus spike protein. Sci. Rep. *8*, 16597.

Kleine-Weber, H., Elzayat, M.T., Wang, L., Graham, B.S., Müller, M.A., Drosten, C., Pöhlmann, S., and Hoffmann, M. (2019). Mutations in the Spike Protein of Middle East Respiratory Syndrome Coronavirus Transmitted in Korea Increase Resistance to Antibody-Mediated Neutralization. J. Virol. *93* https://doi.org/10.1128/JVI.01381-18.

Kuba, K., Imai, Y., Rao, S., Gao, H., Guo, F., Guan, B., Huan, Y., Yang, P., Zhang, Y., Deng, W., et al. (2005). A crucial role of angiotensin converting

enzyme 2 (ACE2) in SARS coronavirus-induced lung injury. Nat. Med. *11*, 875–879.

Kumar, S., Stecher, G., Li, M., Knyaz, C., and Tamura, K. (2018). MEGA X: Molecular Evolutionary Genetics Analysis across Computing Platforms. Mol Biol Evol *35*, 1547–1549.

Lau, S.K., Woo, P.C., Li, K.S., Huang, Y., Tsoi, H.W., Wong, B.H., Wong, S.S., Leung, S.Y., Chan, K.H., and Yuen, K.Y. (2005). Severe acute respiratory syndrome coronavirus-like virus in Chinese horseshoe bats. Proc. Natl. Acad. Sci. USA *102*, 14040–14045.

Li, W., Moore, M.J., Vasilieva, N., Sui, J., Wong, S.K., Berne, M.A., Somasundaran, M., Sullivan, J.L., Luzuriaga, K., Greenough, T.C., et al. (2003). Angiotensin-converting enzyme 2 is a functional receptor for the SARS coronavirus. Nature *426*, 450–454.

Li, F., Li, W., Farzan, M., and Harrison, S.C. (2005a). Structure of SARS coronavirus spike receptor-binding domain complexed with receptor. Science *309*, 1864–1868.

Li, W., Zhang, C., Sui, J., Kuhn, J.H., Moore, M.J., Luo, S., Wong, S.K., Huang, I.C., Xu, K., Vasilieva, N., et al. (2005b). Receptor and viral determinants of SARS-coronavirus adaptation to human ACE2. EMBO J. *24*, 1634–1643.

Li, W., Hulswit, R.J.G., Widjaja, I., Raj, V.S., McBride, R., Peng, W., Widagdo, W., Tortorici, M.A., van Dieren, B., Lang, Y., et al. (2017). Identification of sialic acid-binding function for the Middle East respiratory syndrome coronavirus spike glycoprotein. Proc. Natl. Acad. Sci. USA *114*, E8508–E8517.

Lin, J.T., Zhang, J.S., Su, N., Xu, J.G., Wang, N., Chen, J.T., Chen, X., Liu, Y.X., Gao, H., Jia, Y.P., et al. (2007). Safety and immunogenicity from a phase I trial of inactivated severe acute respiratory syndrome coronavirus vaccine. Antivir. Ther. (Lond.) *12*, 1107–1113.

Liu, W., Fontanet, A., Zhang, P.H., Zhan, L., Xin, Z.T., Baril, L., Tang, F., Lv, H., and Cao, W.C. (2006). Two-year prospective study of the humoral immune response of patients with severe acute respiratory syndrome. J. Infect. Dis. *193*, 792–795.

Matsuyama, S., Nagata, N., Shirato, K., Kawase, M., Takeda, M., and Taguchi, F. (2010). Efficient activation of the severe acute respiratory syndrome coronavirus spike protein by the transmembrane protease TMPRSS2. J. Virol. *84*, 12658–12664.

Menachery, V.D., Dinnon, K.H., III, Yount, B.L., Jr., McAnarney, E.T., Gralinski, L.E., Hale, A., Graham, R.L., Scobey, T., Anthony, S.J., Wang, L., et al. (2020). Trypsin treatment unlocks barrier for zoonotic bat coronaviruses infection. J. Virol. *94* https://doi.org/10.1128/JVI.01774-19.

Munster, V.J., Koopmans, M., van Doremalen, N., van Riel, D., and de Wit, E. (2020). A Novel Coronavirus Emerging in China - Key Questions for Impact Assessment. N. Engl. J. Med. *382*, 692–694.

Park, J.E., Li, K., Barlan, A., Fehr, A.R., Perlman, S., McCray, P.B., Jr., and Gallagher, T. (2016). Proteolytic processing of Middle East respiratory syndrome coronavirus spikes expands virus tropism. Proc. Natl. Acad. Sci. USA *113*, 12262–12267.

Park, Y.J., Walls, A.C., Wang, Z., Sauer, M.M., Li, W., Tortorici, M.A., Bosch, B.J., DiMaio, F., and Veesler, D. (2019). Structures of MERS-CoV spike glycoprotein in complex with sialoside attachment receptors. Nat. Struct. Mol. Biol. *26*, 1151–1157.

Raj, V.S., Mou, H., Smits, S.L., Dekkers, D.H., Müller, M.A., Dijkman, R., Muth, D., Demmers, J.A., Zaki, A., Fouchier, R.A., et al. (2013). Dipeptidyl peptidase 4 is a functional receptor for the emerging human coronavirus-EMC. Nature *495*, 251–254.

Shieh, W.J., Hsiao, C.H., Paddock, C.D., Guarner, J., Goldsmith, C.S., Tatti, K., Packard, M., Mueller, L., Wu, M.Z., Rollin, P., et al. (2005). Immunohistochemical, in situ hybridization, and ultrastructural localization of SARS-associated coronavirus in lung of a fatal case of severe acute respiratory syndrome in Taiwan. Hum. Pathol. *36*, 303–309.

Shirato, K., Kanou, K., Kawase, M., and Matsuyama, S. (2016). Clinical Isolates of Human Coronavirus 229E Bypass the Endosome for Cell Entry. J. Virol. *91* https://doi.org/10.1128/JVI.01387-16.

Shirato, K., Kawase, M., and Matsuyama, S. (2018). Wild-type human coronaviruses prefer cell-surface TMPRSS2 to endosomal cathepsins for cell entry. Virology *517*, 9–15.

Shulla, A., Heald-Sargent, T., Subramanya, G., Zhao, J., Perlman, S., and Gallagher, T. (2011). A transmembrane serine protease is linked to the severe acute respiratory syndrome coronavirus receptor and activates virus entry. J. Virol. *85*, 873–882.

Simmons, G., Gosalia, D.N., Rennekamp, A.J., Reeves, J.D., Diamond, S.L., and Bates, P. (2005). Inhibitors of cathepsin L prevent severe acute respiratory syndrome coronavirus entry. Proc. Natl. Acad. Sci. USA *102*, 11876–11881.

Wang, C., Horby, P.W., Hayden, F.G., and Gao, G.F. (2020). A novel coronavirus outbreak of global health concern. Lancet *395*, 470–473.

WHO (2004). Summary of probable SARS cases with onset of illness from 1 November 2002 to 31 July 2003. https://www.who.int/csr/sars/country/table2004_04_21/en/.

WHO (2020). Novel Coronavirus(2019-nCoV) Situation Report 23. https://www.who.int/docs/default-source/coronaviruse/situation-reports/20200212-sitrep-23-ncov.pdf?sfvrsn=41e9fb78_4.

Wu, N.H., Yang, W., Beineke, A., Dijkman, R., Matrosovich, M., Baumgärtner, W., Thiel, V., Valentin-Weigand, P., Meng, F., and Herrler, G. (2016). The differentiated airway epithelium infected by influenza viruses maintains the barrier function despite a dramatic loss of ciliated cells. Sci. Rep. *6*, 39668.

Yamamoto, M., Matsuyama, S., Li, X., Takeda, M., Kawaguchi, Y., Inoue, J.I., and Matsuda, Z. (2016). Identification of Nafamostat as a Potent Inhibitor of Middle East Respiratory Syndrome Coronavirus S Protein-Mediated Membrane Fusion Using the Split-Protein-Based Cell-Cell Fusion Assay. Antimicrob. Agents Chemother. *60*, 6532–6539.

Yang, Y., Du, L., Liu, C., Wang, L., Ma, C., Tang, J., Baric, R.S., Jiang, S., and Li, F. (2014). Receptor usage and cell entry of bat coronavirus HKU4 provide insight into bat-to-human transmission of MERS coronavirus. Proc. Natl. Acad. Sci. USA *111*, 12516–12521.

Yang, Y., Liu, C., Du, L., Jiang, S., Shi, Z., Baric, R.S., and Li, F. (2015). Two Mutations Were Critical for Bat-to-Human Transmission of Middle East Respiratory Syndrome Coronavirus. J. Virol. *89*, 9119–9123.

Yeager, C.L., Ashmun, R.A., Williams, R.K., Cardellichio, C.B., Shapiro, L.H., Look, A.T., and Holmes, K.V. (1992). Human aminopeptidase N is a receptor for human coronavirus 229E. Nature *357*, 420–422.

Zhou, Y., Vedantham, P., Lu, K., Agudelo, J., Carrion, R., Jr., Nunneley, J.W., Barnard, D., Pöhlmann, S., McKerrow, J.H., Renslo, A.R., and Simmons, G. (2015). Protease inhibitors targeting coronavirus and filovirus entry. Antiviral Res. *116*, 76–84.

Zhou, P., Yang, X.L., Wang, X.G., Hu, B., Zhang, L., Zhang, W., Si, H.R., Zhu, Y., Li, B., Huang, C.L., et al. (2020). A pneumonia outbreak associated with a new coronavirus of probable bat origin. Nature. https://doi.org/10.1038/s41586-020-2012-7.

Zhu, N., Zhang, D., Wang, W., Li, X., Yang, B., Song, J., Zhao, X., Huang, B., Shi, W., Lu, R., et al. (2020). A Novel Coronavirus from Patients with Pneumonia in China, 2019. N Engl J Med. *382*, 727–733.

STAR★METHODS

KEY RESOURCES TABLE

REAGENT or RESOURCE	SOURCE	IDENTIFIER
Antibodies		
Monoclonal anti-HA antibody produced in mouse	Sigma-Aldrich	Cat.#: H3663; RRID: AB_262051
Monoclonal anti-β-actin antibody produced in mouse	Sigma-Aldrich	Cat.#: A5441; RRID: AB_476744
Monoclonal anti-VSV-M (23H12) antibody	KeraFast	Cat.#: EB0011; RRID: AB_2734773
Polyclonal anti-ACE2 antibody	R&D Systems	Cat.#: AF933; RRID: AB_355722
Polyclonal anti-DC-SIGN antibody	Santa Cruz	Cat.#: sc-11038; RRID:AB_639038
Monoclonal anti-mouse, peroxidase-coupled	Dianova	Cat.#: 115-035-003; RRID:AB_10015289
Anti-VSV-G antibody (I1, produced from CRL-2700 mouse hybridoma cells)	ATCC	Cat.# CRL-2700; RRID:CVCL_G654
Bacterial and Virus Strains		
VSV*ΔG-FLuc	(Berger Rentsch and Zimmer, 2011)	N/A
SARS-CoV-2 isolate Munich 929	Laboratory of Christian Drosten	N/A
One Shot™ OmniMAX™ 2 T1R Chemically Competent *E. coli*	ThermoFisher Scientific	Cat.#: C854003
Biological Samples		
Patient serum, CSS-2	Laboratory of Christian Drosten	N/A
Patient serum, CSS-3	Laboratory of Andreas Nitsche	N/A
Patient serum, CSS-4	Laboratory of Andreas Nitsche	N/A
Patient serum, CSS-5	Laboratory of Andreas Nitsche	N/A
Rabbit serum, anti-SARS-S1 rabbit I	Laboratory of Stefan Pöhlmann	N/A
Rabbit serum, anti-SARS-S1 rabbit II	Laboratory of Stefan Pöhlmann	N/A
Chemicals, Peptides, and Recombinant Proteins		
Camostat mesylate	Sigma-Aldrich	SML0057
E-64d	Sigma-Aldrich	E8640
Ammonium chloride	Carl Roth	Cat.#: 5050.2
Critical Commercial Assays		
Beetle-Juice Kit	PJK	Cat.#: 102511
CellTiter-Glo® Luminescent Cell Viability Assay	Promega	Cat.#: G7570
Experimental Models: Cell Lines		
A549	Laboratory of Georg Herrler	ATCC Cat# CRM-CCL-185; RRID:CVCL_0023
BEAS-2B	Laboratory of Stefan Pöhlmann	ATCC Cat# CRL-9609; RRID:CVCL_0168
Calu-3	Laboratory of Stephan Ludwig	ATCC Cat# HTB-55; RRID:CVCL_0609
NCI-H1299	Laboratory of Stefan Pöhlmann	ATCC Cat# CRL-5803; RRID:CVCL_0060
Huh-7	Laboratory of Thomas Pietschmann	JCRB Cat# JCRB0403; RRID:CVCL_0336
Caco-2	Laboratory of Stefan Pöhlmann	ATCC Cat# HTB-37; RRID:CVCL_0025

(*Continued on next page*)

Continued

REAGENT or RESOURCE	SOURCE	IDENTIFIER
Vero	Laboratory of Andrea Maisner	ATCC Cat# CRL-1586; RRID:CVCL_0574
Vero-TMPRSS2	This paper	N/A
LLC-PK1	Laboratory of Georg Herrler	ATCC Cat# CRL-1392; RRID:CVCL_0391
MDBK	Laboratory of Georg Herrler	ATCC Cat# CCL-22; RRID:CVCL_0421
MDCKII	Laboratory of Georg Herrler	ATCC Cat# CRL-2936; RRID:CVCL_B034
RhiLu/1.1	Laboratory of Christian Drosten, Laboratory of Marcel A. Müller	N/A; RRID: CVCL_RX22
MyDauLu/47.1	Laboratory of Christian Drosten, Laboratory of Marcel A. Müller	N/A; RRID: CVCL_RX18
BHK-21	Laboratory of Georg Herrler	ATCC Cat# CCL-10; RRID:CVCL_1915
NIH/3T3	Laboratory of Stefan Pöhlmann	ATCC Cat# CRL-1658; RRID:CVCL_0594
HAE	HTCR Foundation (Human Tissue and Cell Research)	N/A
293T	DSMZ	Cat.#: ACC-635; RRID: CVCL_0063
Oligonucleotides		
SARS-2-S (BamHI) F AAGGCCGGATCCGCCACCATGTTTCT GCTGACCACCAAGC	Sigma-Aldrich	N/A
SARS-2-S (Xbal) R AAGGCCTCTAGATTAGGTGTAGTGCAG TTTCACG	Sigma-Aldrich	N/A
SARS-2-S-HA (Xbal) R AAGGCCTCTAGATTACGCATAATCC GGCACATCATACGGATAGGTGTAGTGCAGTTTCACG	Sigma-Aldrich	N/A
WH-Ssyn 651F CAAGATCTACAGCAAGCACACC	Sigma-Aldrich	N/A
WH-Ssyn 1380F GTCGGCGGCAACTACAATTAC	Sigma-Aldrich	N/A
WH-Ssyn 1992F CTGTCTGATCGGAGCCGAGCAC	Sigma-Aldrich	N/A
WH-Ssyn 2648F TGAGATGATCGCCCAGTACAC	Sigma-Aldrich	N/A
WH-Ssyn 3286F GCCATCTGCCACGACGGCAAAG	Sigma-Aldrich	N/A
Recombinant DNA		
Synthetic, codon-optimized (humanized) SARS-2-S	ThermoFisher Scientific (GeneArt)	N/A
Plasmid: pCG1-SARS-S	(Hoffmann et al., 2013)	N/A
Plasmid:pCG1-SARS-S-HA	This paper	N/A
Plasmid: pCG1-SARS-2-S	This paper	N/A
Plasmid: pCG1-SARS-2-S-HA	This paper	N/A
Plasmid: pCAGGS-229E-S	(Hofmann et al., 2005)	N/A
Plasmid: pCAGGS-MERS-S	(Gierer et al., 2013)	N/A
Plasmid: pCAGGS-VSV-G	(Brinkmann et al., 2017)	N/A
Plasmid: pCAGGS-NiV-F	Laboratory of Andrea Maisner	N/A
Plasmid: pCAGGS-NiV-G	Laboratory of Andrea Maisner	N/A
Plasmid: pCG1-hACE2	(Hoffmann et al., 2013)	N/A
Plasmid: pCG1-batACE2	(Hoffmann et al., 2013)	N/A
Plasmid: pCG1-hAPN	(Hofmann et al., 2004a)	N/A
Plasmid: pQCXIP-DsRed-hDPP4	(Kleine-Weber et al., 2018)	N/A
Plasmid: pQCXIBL-hTMPRSS2	(Kleine-Weber et al., 2018)	N/A
Plasmid: pCG1	Laboratory of Roberto Cattaneo	N/A
Plasmid: pCAGGS-DsRed	Laboratory of Stefan Pöhlmann	N/A

(*Continued on next page*)

Continued

REAGENT or RESOURCE	SOURCE	IDENTIFIER
Plasmid: pCAGGS-eGFP	Laboratory of Stefan Pöhlmann	N/A
Software and Algorithms		
Hidex Sense Microplate Reader Software	Hidex Deutschland Vertrieb GmbH	https://www.hidex.de/
ChemoStar Imager Software (version v.0.3.23)	Intas Science Imaging Instruments GmbH	https://www.intas.de/
MEGA 7.0.26	Kumar et al., 2018	https://www.megasoftware.net
Adobe Photoshop CS5 Extended (version 12.0 × 32)	Adobe	https://www.adobe.com/
GraphPad Prism (version 8.3.0(538))	GraphPad Software	https://www.graphpad.com/
Microsoft Office Standard 2010 (version 14.0.7232.5000)	Microsoft Corporation	https://products.office.com/

LEAD CONTACT AND MATERIALS AVAILABILITY

Requests for material can be directed to Markus Hoffmann (mhoffmann@dpz.eu) and the lead contact, Stefan Pöhlmann (spoehlmann@dpz.eu). All materials and reagents will be made available upon installment of a material transfer agreement (MTA).

EXPERIMANTAL MODEL AND SUBJECT DETAILS

Cell cultures, primary cells, viral strains

All cell lines were incubated at 37°C and 5% CO_2 in a humidified atmosphere. 293T (human, kidney), BHK-21 (Syrian hamster, kidney cells), Huh-7 (human, liver), LLC-PK1 (pig, kidney), MRC-5 (human, lung), MyDauLu/47.1 (Daubenton's bat [*Myotis daubentonii*], lung), NIH/3T3 (Mouse, embryo), RhiLu/1.1 (Halcyon horseshoe bat [*Rhinolophus alcyone*], lung) and Vero (African green monkey, kidney) cells were incubated in Dulbecco's' modified Eagle medium (PAN-Biotech). Calu-3 (human, lung), Caco-2 (human, colon), MDBK (cattle, kidney) and MDCKII (Dog, kidney) cells were incubated in Minimum Essential Medium (ThermoFisher Scientific). A549 (human, lung), BEAS-2B (human, bronchus) and NCI-H1299 (human, lung) cells were incubated in DMEM/F-12 Medium with Nutrient Mix (ThermoFisher Scientific). Vero cells stably expressing human TMPRSS2 were generated by retroviral transduction and blasticidin-based selection. All media were supplemented with 10% fetal bovine serum (Biochrom), 100 U/mL of penicillin and 0.1 mg/mL of streptomycin (PAN-Biotech), 1x non-essential amino acid solution (10x stock, PAA) and 10 mM sodium pyruvate (ThermoFisher Scientific). For seeding and subcultivation, cells were first washed with phosphate buffered saline (PBS) and then incubated in the presence of trypsin/EDTA solution (PAN-Biotech) until cells detached. Transfection was carried out by calcium-phosphate precipitation. Lung tissue samples were obtained and experimental procedures were performed within the framework of the non-profit foundation HTCR, including the informed patient's consent.

For preparation of human airway epithelial cells, bronchus tissue was derived from patients undergoing pulmonary resection and was provided by the Biobank of the Department of General, Visceral, and Transplant Surgery, Ludwig-Maximilians- University Munich. Primary human airway epithelial cells were subsequently isolated as described (Wu et al., 2016). In brief, tissue with a length of approximately 10 mm and a diameter of 8mm was collected and incubated for 24 h at 4°C with DMEM (GIBCO) containing 1 mg/mL protease type XIV and 10 μg/mL DNase I, 100 units/mL penicillin and 100 μg/mL streptomycin, 2.5 μg/mL amphotericin B, and 50 μg/mL gentamicin (GIBCO). The epithelial cells were then harvested from the mucosal surface using the scalpel and were resuspended in growth medium. After incubation at 37°C, 5% CO_2 for 2 h to remove adherent fibroblast cells, non-adherent cells were seeded on a collagen I coated flask and maintained at 37°C, 5% CO_2. The growth medium was refreshed every 2 days and consisted of a 1:1 mixture of DMEM (GIBCO) and Airway Epithelial Cell basal medium (Promocell, Heidelberg, Germany) supplemented with 52 μg/mL bovine pituitary extract, 15 ng/mL retinoic acid, 5μg/mL insulin, 0.5 μg/mL hydrocortisone, 0.5 μg/mL epinephrine, 10 μg/mL transferrin, 1 ng/mL human epidermal growth factor (Corning), 1.5 ng/mL bovine serum albumin, 100 units/mL penicillin and 100 μg/mL streptomycin, with or without 5 μM Rho-associated protein kinase inhibitor (Y-27632), as previously described (Wu et al., 2016). If not stated otherwise all materials were purchased from Sigma-Aldrich.

For infection experiments with SARS-CoV-2, the SARS-CoV-2 isolate Munich 929 was propagated in VeroE6 cells (passage 1) after primary isolation from patient material on Vero-TMPRSS2 cells (passage 0).

METHOD DETAILS

Plasmids

Expression plasmids for vesicular stomatitis virus (VSV, serotype Indiana) glycoprotein (VSV-G), Nipah virus (NiV) fusion (F) and attachment glycoprotein (G), SARS-S (derived from the Frankfurt-1 isolate) with or without a C-terminal HA epitope tag, HCoV-229E-S, MERS-S, human and bat angiotensin converting enzyme 2 (ACE2), human aminopeptidase N (APN), human

dipeptidyl-peptidase 4 (DPP4) and human TMPRSS2 have been described elsewhere (Bertram et al., 2010; Brinkmann et al., 2017; Gierer et al., 2013; Hoffmann et al., 2013; Hofmann et al., 2005; Kleine-Weber et al., 2019). For generation of the expression plasmids for SARS-2-S with or without a C-terminal HA epitope tag we PCR-amplified the coding sequence of a synthetic, codon-optimized (for human cells) SARS-2-S DNA (GeneArt Gene Synthesis, ThermoFisher Scientific) based on the publicly available protein sequence in the National Center for Biotechnology Information database (NCBI Reference Sequence: YP_009724390.1) and cloned in into the pCG1 expression vector via BamHI and XbaI restriction sites.

Pseudotyping of VSV and transduction experiments

For pseudotyping, VSV pseudotypes were generated according to a published protocol (Berger Rentsch and Zimmer, 2011). In brief, 293T transfected to express the viral surface glycoprotein under study were inoculated with a replication-deficient VSV vector that contains expression cassettes for eGFP (enhanced green fluorescent protein) and firefly luciferase instead of the VSV-G open reading frame, VSV*ΔG-fLuc (kindly provided by Gert Zimmer, Institute of Virology and Immunology, Mittelhäusern/Switzerland). After an incubation period of 1 h at 37°C, the inoculum was removed and cells were washed with PBS before medium supplemented with anti-VSV-G antibody (I1, mouse hybridoma supernatant from CRL-2700; ATCC) was added in order to neutralize residual input virus (no antibody was added to cells expressing VSV-G). Pseudotyped particles were harvested 16 h postinoculation, clarified from cellular debris by centrifugation and used for experimentation.

For transduction, target cells were grown in 96-well plates until they reached 50%–75% confluency before they were inoculated with respective pseudotyped VSV. For experiments addressing receptor usage, cells were transfected with expression plasmids 24 h before transduction. In order to block ACE2 on the cell surface, cells were pretreated with 2 or 20 μg/mL anti-ACE2 antibody (R&D Systems, goat, AF933). As control, an unrelated anti-DC-SIGN antibody (Serotec, goat, 20 μg/mL) was used. For experiments involving ammonium chloride (final concentration 50 mM) and protease inhibitors (E-64d, 25 μM; camostat mesylate, 1-500 μM), target cells were treated with the respective chemical 2 h before transduction. For neutralization experiments, pseudotypes were pre-incubated for 30 min at 37°C with different serum dilutions. Transduction efficiency was quantified 16 h posttransduction by measuring the activity of firefly luciferase in cell lysates using a commercial substrate (Beetle-Juice, PJK) and a Hidex Sense plate luminometer (Hidex).

Quantification of cell viability

Cell viability following treatment of Calu-3 cells with camostat mesylate was analyzed using the CellTiter-Glo® Luminescent Cell Viability Assay (Promega). In brief, Calu-3 cells grown to 50% confluency in 96-well plates were incubated for 24 h in the absence or presence of different concentrations (1-500 μM) of camostat mesylate. Next, the culture medium was aspirated and 100 μl of fresh culture medium was added before an identical volume of the assay substrate was added. Wells containing only culture medium served as a control to determine the assay background. After 2 min of incubation on a rocking platform and additional 10 min without movement, samples were transferred into white opaque-walled 96-well plates and luminescent signal were recorded using a Hidex Sense plate luminometer (Hidex).

Analysis of SARS-2-S expression and particle incorporation

To analyze S protein expression in cells, 293T cells were transfected with expression vectors for HA-tagged SARS-2-S or SARS-S or empty expression vector (negative control). The culture medium was replaced at 16 h posttransfection and the cells were incubated for an additional 24 h. Then, the culture medium was removed and cells were washed once with PBS before 2x SDS-sample buffer (0.03 M Tris-HCl, 10% glycerol, 2% SDS, 0.2% bromophenol blue, 1 mM EDTA) was added and cells were incubated for 10 min at room temperature. Next, the samples were heated for 15 min at 96°C and subjected to SDS-PAGE and immunoblotting.

For analysis of S protein incorporation into pseudotyped particles, 1 mL of the respective VSV pseudotypes were loaded onto a 20% (w/v) sucrose cushion (volume 50 μl) and subjected to high-speed centrifugation (25.000 g for 120 min at 4°C). Thereafter, 1 mL of supernatant was removed and the residual volume was mixed with 50 μl of 2x SDS-sample buffer, heated for 15 min at 96°C and subjected to SDS-PAGE and immunoblotting. After protein transfer, nitrocellulose membranes were blocked in 5% skim milk solution (5% skim milk dissolved in PBS containing 0.05% Tween-20, PBS-T) for 1 h at room temperature and then incubated over night at 4°C with the primary antibody (diluted in in skim milk solution)). Following three washing intervals of 10 min in PBS-T the membranes were incubated for 1 h at room temperature with the secondary antibody (diluted in in skim milk solution), before the membranes were washed and imaged using an in in house-prepared enhanced chemiluminescent solution (0.1 M Tris-HCl [pH 8.6], 250 μg/mL luminol, 1 mg/mL para-hydroxycoumaric acid, 0.3% H_2O^2) and the ChemoCam imaging system along with the ChemoStar Professional software (Intas Science Imaging Instruments GmbH). The following primary antibodies were used: Mouse anti-HA tag (Sigma-Aldrich, H3663, 1:2,500), mouse anti-β-actin (Sigma-Aldrich, A5441, 1:2,000), mouse anti-VSV matrix protein (Kerafast, EB0011, 1:2,500). As secondary antibody we used a peroxidase-coupled goat anti-mouse antibody (Dianova, 115-035-003, 1:10000).

Infection with authentic SARS-CoV-2

BHK-21 cells (1.6 x10^5 cells/mL) were transfected with ACE2 and DsRed as a negative control. After 24 h, cells were washed with PBS and infected with 8x10^7 genome equivalents (GE) per 24-well of SARS-CoV-2 isolate Munich 929 for 1 h at 37°C. Calu-3 cells (5 x10^5 cells/mL) were mock treated or treated with 100 μM camostat mesylate (Sigma Aldrich) 2 h prior to infection with SARS-CoV-2

isolate Munich 929 at a multiplicity of infection (MOI) of 0.001 for 1 h at 37°C. After infection, cells were washed three times with PBS before 500 μl of DMEM medium was added. At 16 or 24 h post infection, 50 μl culture supernatant was subjected to viral RNA extraction using a viral RNA kit (Macherey-Nagel) according to the manufacturer's instructions. GE per ml were detected by real time RT-PCR using a previously reported protocol (Corman et al., 2020).

Sera

The convalescent human anti-SARS-CoV sera (CSS-2 to CSS-5) stemmed from the serum collection of the national consiliary laboratory for coronavirus diagnostics at Charité, Berlin, Germany or the Robert Koch Institute, Berlin, Germany. All sera were previously tested positive using a recombinant S-based immunofluorescence test (Buchholz et al., 2013). CSS-2 was taken from a SARS patient 3.5 years post onset of disease. CSS-3 and CSS-4 originated from a second SARS patient 24 and 36 days post onset of disease. CSS-5 was collected from a third SARS patient 10 days post onset of disease. Rabbit sera were obtained by immunizing rabbits with purified SARS-S1 protein fused to the Fc portion of human immunoglobulin.

Phylogenetic analysis

Phylogenetic analysis (neighbor-joining tree, bootstrap method with 5,000 iterations, Poisson substitution model, uniform rates among sites, complete deletion of gaps/missing data) was performed using the MEGA7.0.26 software. Reference sequences were obtained from the National Center for Biotechnology Information and GISAID (Global Initiative on Sharing All Influenza Data) databases. Reference numbers are indicated in the figures.

QUANTIFICATION AND STATISTICAL ANALYSIS

One-way or two-way analysis of variance (ANOVA) with Dunnett posttest was used to test for statistical significance. Only p values of 0.05 or lower were considered statistically significant ($p > 0.05$ [ns, not significant], $p \leq 0.05$ [*], $p \leq 0.01$ [**], $p \leq 0.001$ [***]). For all statistical analyses, the GraphPad Prism 7 software package was used (GraphPad Software).

DATA AND CODE AVAILABILITY

The study did not generate unique datasets or code.

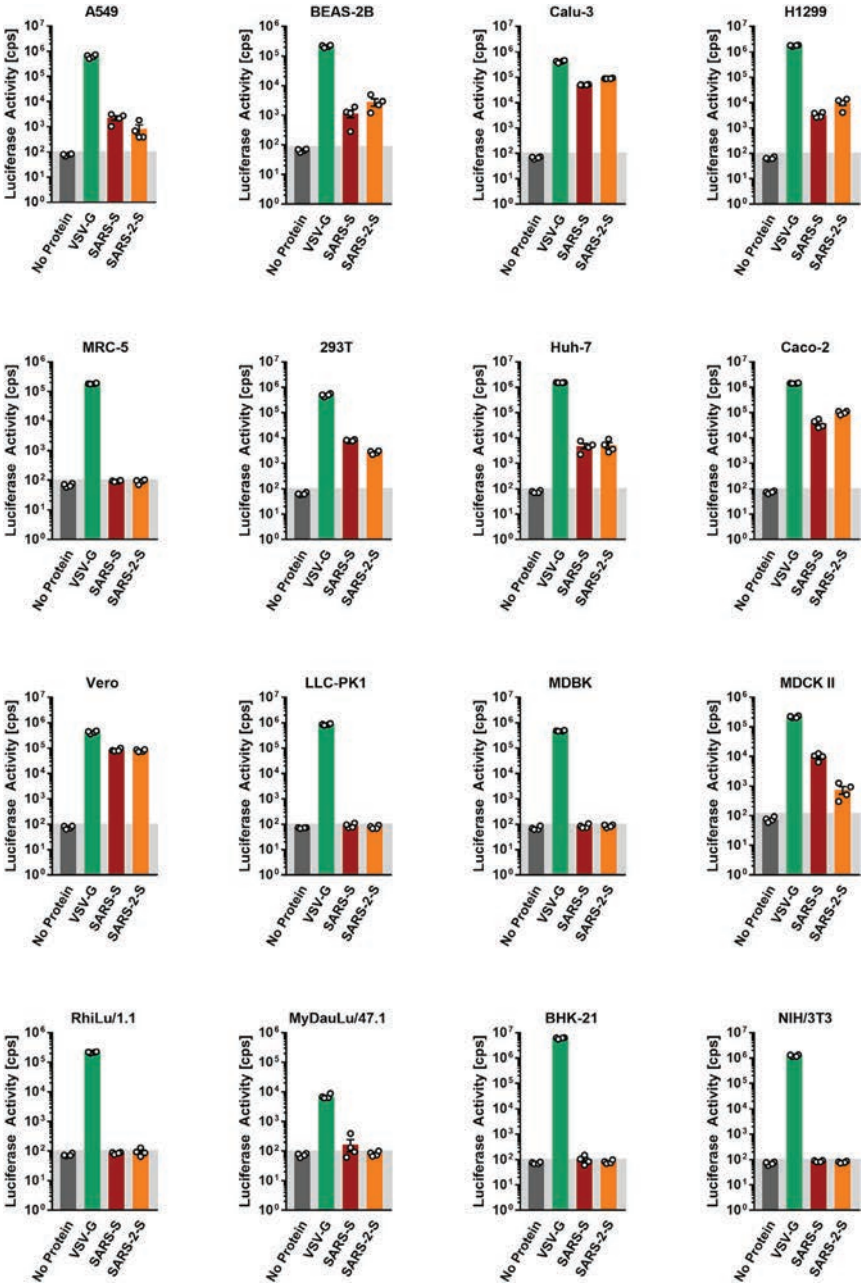

Figure S1. Representative Experiment Included in the Average, Related to Figure 1C

The indicated cells lines were inoculated with pseudoparticles harboring the indicated viral glycoprotein or harboring no glycoprotein (no protein) and luciferase activities in cell lysates were determined at 16 h posttransduction. The experiment was performed with quadruplicate samples, the average ± SD is shown.

Figure S2. Extended Version of the Phylogenetic Tree, Related to Figure 2B

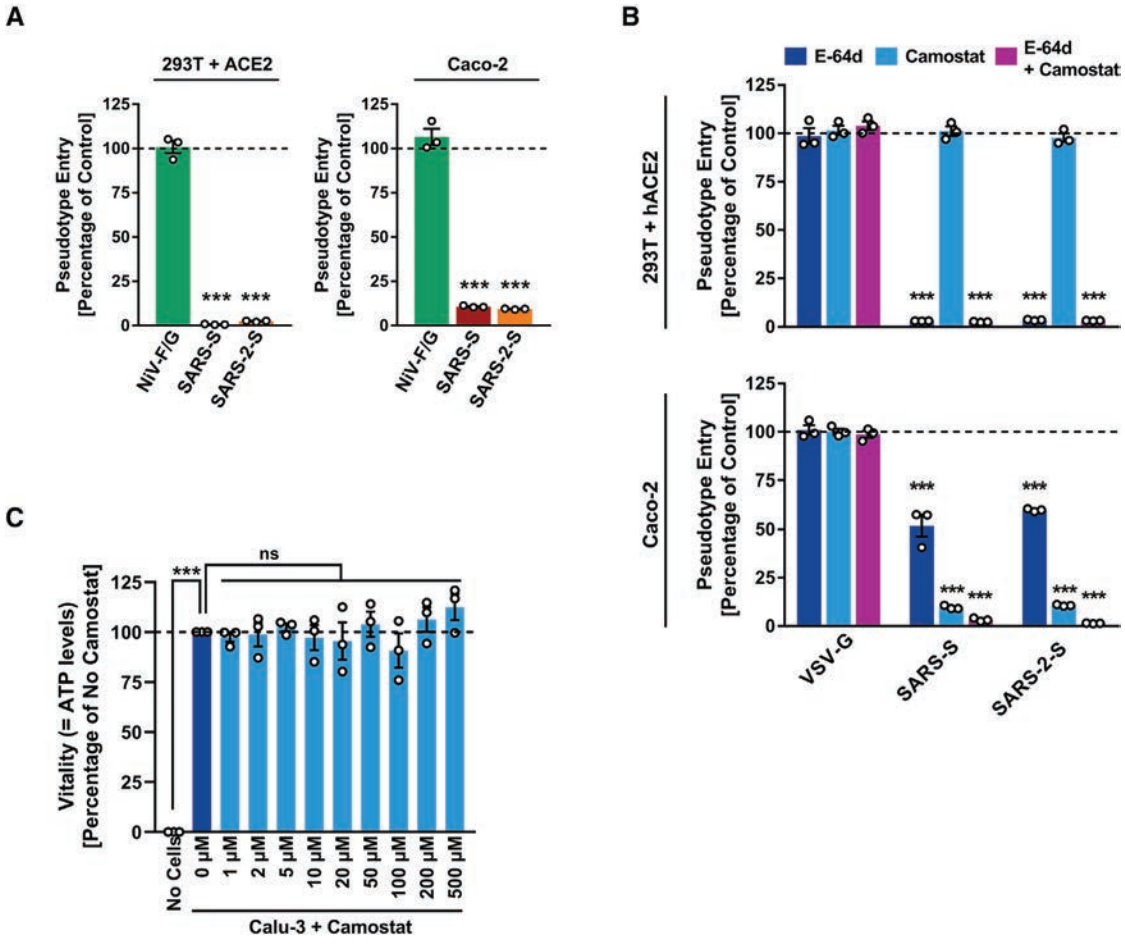

Figure S3. Protease Requirement for SARS-2-S-Driven Entry and Absence of Unwanted Cytotoxicity of Camostat Mesylate, Related to Figure 4

(A and B) Importance of endosomal low pH (A) and activity of CatB/L or TMPRSS2 (B) for host cell entry of SARS-CoV-2 was evaluated by adding inhibitors to target cells prior to transduction. Ammonium chloride (A) blocks endosomal acidification while E-64d and camostat mesylate (B) block the activity of CatB/L and TMPRSS2, respectively. Entry into cells not treated with inhibitor was set as 100%.

(C) Absence of cytotoxic effects of camostat mesylate. Calu-3 cells were treated with camostat mesylate identically as for infection experiments and cell viability was measured using a commercially available assay (CellTiter-Glo, Promega).

CHAPTER TWO

Coronavirus Spike Protein and Tropism Changes

R.J.G. Hulswit, C.A.M. de Haan[1], B.-J. Bosch[1]
Faculty of Veterinary Medicine, Utrecht University, Utrecht, The Netherlands
[1]Corresponding authors: e-mail address: c.a.m.dehaan@uu.nl; b.j.bosch@uu.nl

Contents

Abstract

Coronaviruses (CoVs) have a remarkable potential to change tropism. This is particularly illustrated over the last 15 years by the emergence of two zoonotic CoVs, the severe acute respiratory syndrome (SARS)- and Middle East respiratory syndrome (MERS)-CoV. Due to their inherent genetic variability, it is inevitable that new cross-species transmission events of these enveloped, positive-stranded RNA viruses will occur. Research into these medical and veterinary important pathogens—sparked by the SARS and MERS outbreaks—revealed important principles of inter- and intraspecies tropism changes. The primary determinant of CoV tropism is the viral spike (S) entry protein. Trimers of the S glycoproteins on the virion surface accommodate binding to a cell surface receptor and fusion of the viral and cellular membrane. Recently, high-resolution structures of two CoV S proteins have been elucidated by single-particle cryo-electron microscopy. Using this new structural insight, we review the changes in the S protein that relate to changes in virus tropism. Different concepts underlie these tropism changes at the cellular, tissue, and host species level, including the promiscuity or

Advances in Virus Research, Volume 96
ISSN 0065-3527
http://dx.doi.org/10.1016/bs.aivir.2016.08.004

adaptability of S proteins to orthologous receptors, alterations in the proteolytic cleavage activation as well as changes in the S protein metastability. A thorough understanding of the key role of the S protein in CoV entry is critical to further our understanding of virus cross-species transmission and pathogenesis and for development of intervention strategies.

1. INTRODUCTION

Coronaviruses (CoVs) (order *Nidovirales*, family *Coronaviridae*, subfamily *Coronavirinae*) are enveloped, positive-sense RNA viruses that contain the largest known RNA genomes with a length of up to 32 kb. The subfamily *Coronavirinae*, which contains viruses of both medical and veterinary importance, can be divided into the four genera *alpha-*, *beta-*, *gamma-* and *deltacoronavirus* (α-, β-, γ- and δ-*CoV*). The coronavirus particle comprises at least the four canonical structural proteins E (envelope protein), M (membrane protein), N (nucleocapsid protein), and S (spike protein). In addition, viruses belonging to lineage A of the *betacoronaviruses* express the membrane-anchored HE (hemagglutinin–esterase) protein. The S glycoprotein contains both the receptor-binding domain (RBD) and the domains involved in fusion, rendering it the pivotal protein in the CoV entry process.

Coronaviruses primarily infect the respiratory and gastrointestinal tract of a wide range of animal species including many mammals and birds. Although individual virus species mostly appear to be restricted to a narrow host range comprising a single animal species, genome sequencing and phylogenetic analyses testify that CoVs have crossed the host species barrier frequently (Chan et al., 2013; Woo et al., 2012). In fact most if not all human coronaviruses seem to originate from bat CoVs (BtCoVs) that transmitted to humans directly or indirectly through an intermediate host. It therefore appears inevitable that similar zoonotic infections will occur in the future.

In the past 15 years, the world witnessed two such zoonotic events. In 2002–2003 cross-species transmissions from bats and civet cats were at the base of the SARS (severe acute respiratory syndrome)-CoV epidemic that found its origin in the Chinese Guangdong province (Li et al., 2006; Song et al., 2005). The SARS-CoV nearly became a pandemic and led to over 700 deaths, before it disappeared when the appropriate hygiene and quarantine precautions were taken. In 2012, the MERS (Middle East respiratory syndrome)-CoV emerged in the human population on the Arabian

Peninsula and currently continues to make a serious impact on the local but also global health system with 1800 laboratory confirmed cases and 640 deaths as of September 1, 2016 (WHO | Middle East respiratory syndrome coronavirus (MERS-CoV) – Saudi Arabia, 2016). The natural reservoir of MERS-CoV is presumed to be in dromedary camels from which zoonotic transmissions repeatedly give rise to infections of the lower respiratory tract in humans (Alagaili et al., 2014; Azhar et al., 2014; Briese et al., 2014; Reusken et al., 2013; Widagdo et al., 2016). Besides these two novel CoVs, four other CoVs were previously identified in humans which are found in either the *alphacoronavirus* (HCoV-NL63 and HCoV-229E) or the *betacoronavirus* genera (HCoV-OC43 and HCoV-HKU1). Phylogenetic analysis has shown that the bovine CoV (BCoV) has been the origin for HCoV-OC43 following a relatively recent cross-species transmission event (Vijgen et al., 2006). Moreover, HCoV-NL63, HCoV-229E, SARS-CoV, and MERS-CoV also have been predicted to originate from bats (Annan et al., 2013; Bolles et al., 2011; Corman et al., 2015; Hu et al., 2015; Huynh et al., 2012).

In general, four major criteria determine cross-species transmission of a particular virus (Racaniello et al., 2015). The cellular tropism of a virus is determined by the susceptibility of host cells (i.e., presence of the receptor needed for entry) as well as by the permissiveness of these host cells to allow the virus to replicate and to complete its life cycle. A third determinant consists of the accessibility of susceptible and permissive cells in the host. Finally, the innate immune response may restrict viral replication in a host species-specific manner. The above-mentioned criteria may play a critical role in the success of a cross-species transmission event. However, for CoVs, it seems that host tropism and changes therein are particularly determined by the susceptibility of host cells to infection. While CoV accessory genes, including the HE proteins, are thought to play a role in host tropism and adaptation to a new host, the S glycoprotein appears to be the main determinant for the success of initial cross-species infection events. In this review, we focus on the molecular changes in the S protein that underlie tropism changes at the cellular, tissue, and host species level and put these in perspective of the recently published cryo-EM structures.

2. STRUCTURE OF THE CORONAVIRUS S PROTEIN

The CoV S protein is a class I viral fusion protein (Bosch et al., 2003) similar to the fusion proteins of influenza, retro-, filo-, and paramyxoviruses

(Baker et al., 1999; Bartesaghi et al., 2013; Lee et al., 2008; Lin et al., 2014). Like other class I viral fusion proteins, the S protein folds into a metastable prefusion conformation following translation. The size of the abundantly N-glycosylated S protein varies greatly between CoV species ranging from approximately 1100 to 1600 residues in length, with an estimated molecular mass of up to 220 kDa. Trimers of the S protein form the 18–23-nm long, club-shaped spikes that decorate the membrane surface of the CoV particle. Besides being the primary determinant in CoV host tropism and pathogenesis, the S protein is also the main target for neutralizing antibodies elicited by the immune system of the infected host (Hofmann et al., 2004).

The S protein can be divided into two functionally distinct subunits: the globular S_1 subunit is involved in receptor recognition, whereas the S_2 subunit facilitates membrane fusion and anchors S into the viral membrane (Fig. 1A). The S_1 and S_2 domains may be separated by a cleavage site that is recognized by furin-like proteases during S protein biogenesis in the infected cell. X-ray crystal structures of several S domains have furthered our understanding of the S protein in the past. In addition, recent elucidation of the high-resolution structures of the spike ectodomain of two betacoronaviruses—MHV and HCoV-HKU1—by single-particle cryo-electron microscopy (Kirchdoerfer et al., 2016; Walls et al., 2016) has provided novel insights into the architecture of the S trimer in its prefusion state (Fig. 1B and C).

2.1 Structure of the S_1 Subunit

The S_1 subunit of the betacoronavirus spike proteins displays a multidomain architecture and is structurally organized in four distinct domains A–D of which domains A and B may serve as a RBD (Fig. 1C). The core structure of domain A displays a galectin-like β-sandwich fold, whereas domain B contains a structurally conserved core subdomain of antiparallel β-sheets (Kirchdoerfer et al., 2016; Li et al., 2005a; Walls et al., 2016; Wang et al., 2013). Importantly, domain B is decorated with an extended loop on the viral membrane-distal side. This loop may differ greatly in size and structure between virus species of the betacoronavirus genus and is therefore also referred to as hypervariable region (HVR). The cryo-EM structures of the MHV-A59 and HCoV-HKU1 S trimers show an intricate interlocking of the three S_1 subunits (Fig. 1B). Oligomerization of the S protomers results in a closely clustered trimer of the individual B domains close to the three-fold axis of the spike on top of the S_2 trimer, whereas the three A domains are

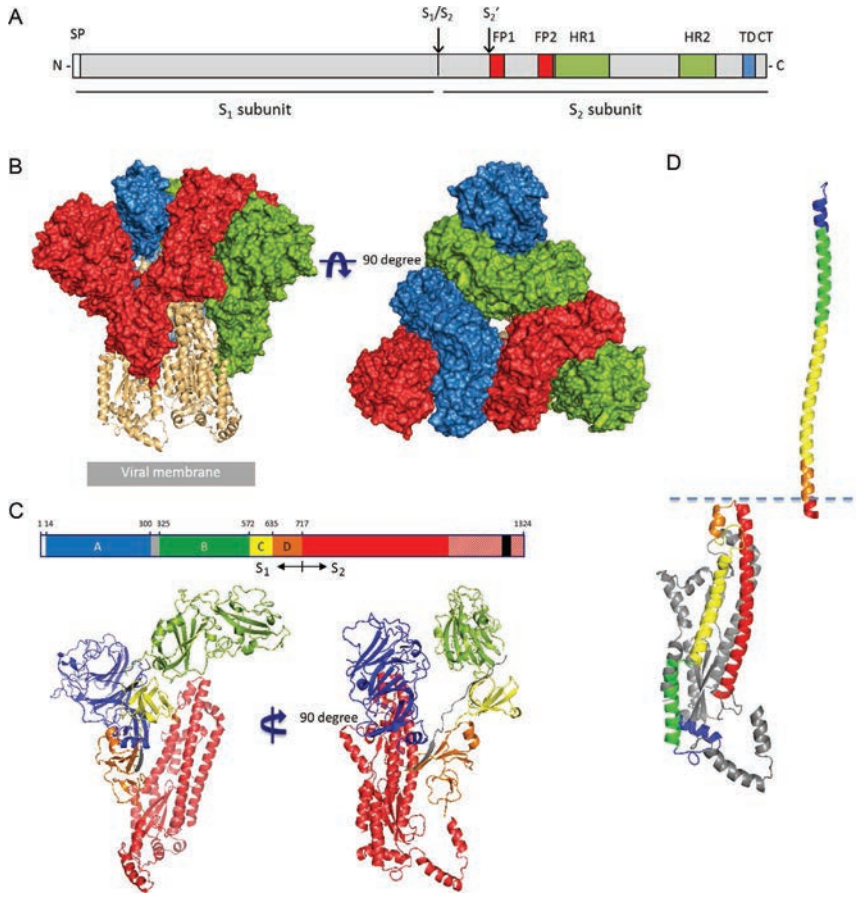

Fig. 1 Spike protein features and structure of the mouse hepatitis coronavirus spike glycoprotein trimer. (A) Schematic linear representation of the coronavirus S protein with relevant domains/sites indicated: signal peptide (SP), two proteolytic cleavage sites (S_1/S_2 and S_2'), two proposed fusion peptides (FP1 and FP2), two heptad repeat regions (HR1 and HR2), transmembrane domain (TD), and cytoplasmic tail (CT). (B) *Front* and *top view* of the trimeric mouse hepatitis coronavirus (strain A59) spike glycoprotein ectodomain obtained by cryo-electron microscopy analysis (Walls et al., 2016; PDB: 3JCL). Three S_1 protomers (surface presentation) are colored in *red*, *blue*, and *green*. The S_2 trimer (cartoon presentation) is colored in *light orange*. (C) Schematic representation of MHV spike protein sequence (drawn to scale), the S_1 domains A, B, C, and D are colored in *blue*, *green*, *yellow*, and *orange*, respectively, and the linker region connecting domains A and B in *gray*, the S_2 region is colored in *red*, and the TM region is indicated as a *black box*. *Red-shaded* region indicates spike region that was

(Continued)

ordered more distally of the center. In contrast to domains A and B, the S_1 C-terminal domains C and D are made up of discontinuous parts of the primary protein sequence and form β-sheet-rich structures directly adjacent to the S_2 stalk core, while the separate S_1 domains are interconnected by loops covering the S_2 surface. Compared to the S_2 subunit, the S_1 subunit displays low level of sequence conversation among species of different CoV genera. Moreover, S_1 subunits vary considerably in sequence length ranging from 544 (infectious bronchitis virus (IBV) S) to 944 (229-related bat coronavirus S) residues in length (Fig. 2), indicating differences in architecture of the spikes of species from different CoV genera. Structural information from the spikes of *gamma-* and *deltacoronavirus* species is currently lacking. Two independently folding domains have been assigned in the S_1 subunit of alphacoronavirus spikes, that can interact with host cell surface molecules, an N-terminal domain (in transmissible gastroenteritis virus (TGEV) S residues 1–245) and a more C-terminal domain (in TGEV S residues 506–655). Contrary to betacoronaviruses, these two receptor-interacting domains in alphacoronavirus spikes are separated in sequence by some 275 residues, which may fold into one or more separate domains. Structural information is only available for the C-terminal S_1 RBD of two α-CoV S proteins, which differs notably from that of betacoronaviruses. The RBD in the S_1 CTR of alphacoronaviruses displays a β-sandwich core structure, whereas a β-sheet core structure is seen for betacoronaviruses (Reguera et al., 2012; Wu et al., 2009).

2.2 Structure of the S_2 Subunit

The highly conserved S_2 subunit contains the key protein segments that facilitate virus-cell fusion. These include the fusion peptide, two heptad

Fig. 1—Cont'd not resolved in the cryo-EM structure. (*Lower panel*) Two views on the structure of the mouse hepatitis virus spike glycoprotein protomer (cartoon representation); domains are colored as depicted earlier. (D) Comparison of the S_2 HR1 region in its pre- and postfusion conformation. (*Lower left*) Structure of the MHV S_2 protomer (cartoon presentation) with four helices of the HR1 region (and consecutive linker region) and the downstream central helix colored in *blue*, *green*, *yellow*, *orange*, and *red*, respectively. (*Upper right*) The structure of a single SARS-CoV S HR1 helix of the postfusion six-helix bundle structure (PDB: 1WYY) is colored according to the homologous HR1 region in the MHV S_2 prefusion structure shown in the *lower left panel*. Structures are aligned based on the N-terminal segment of the central helix (in *red*). Figures were generated with PyMOL.

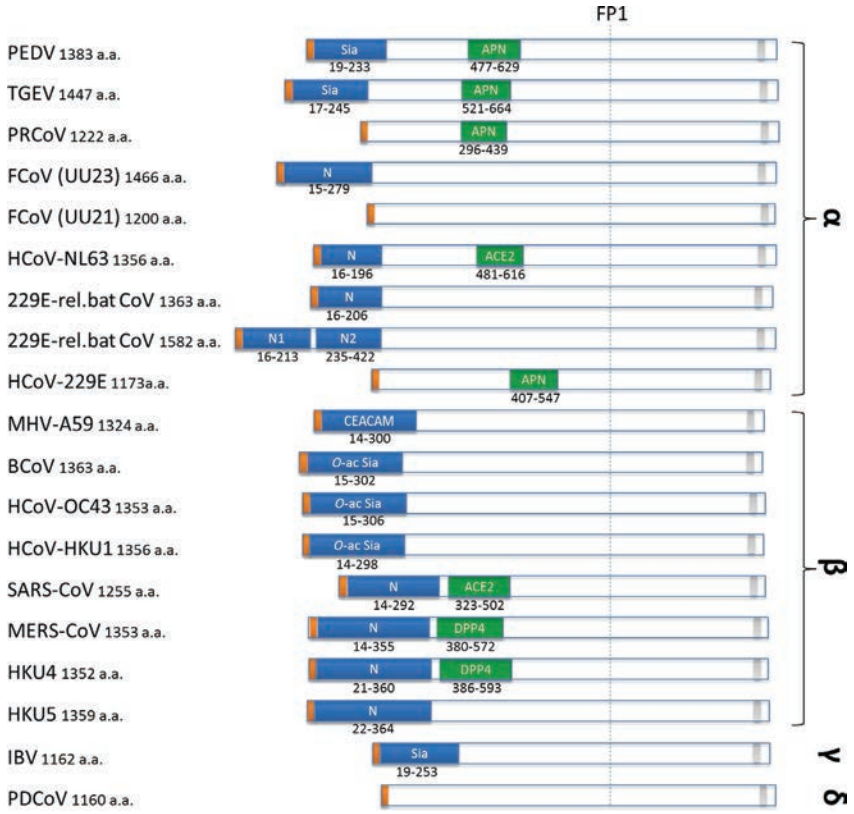

Fig. 2 Overview of currently known receptors and their binding domains within S_1. Schematic representation of coronavirus spike proteins drawn to scale. *Yellow boxes* indicate signal peptides. *Blue boxes* indicate the N-terminal regions in alpha- and betacoronavirus spike proteins, which were mapped based on sequence homology between viruses within the same genus. *Green boxes* indicate known receptor-binding domains in the C-terminal region of S_1. Known receptors are indicated in the *boxes*: *APN*, aminopeptidase N; *ACE2*, angiotensin-converting enzyme 2; *CEACAM*, carcinoembryonic antigen-related cell adhesion molecule 1; *Sia*, sialic acid; *O-ac Sia*, *O*-acetylated sialic acid; *DPP4*, dipeptidyl peptidase-4. *Gray boxes* indicate transmembrane domains. Spikes proteins are shown of PEDV strain CV777 (GB: AAK38656.1), TGEV strain Purdue P115 (GB: ABG89325.1), PRCoV strain ISU-1 (GB: ABG89317.1), Feline CoV strain UU23 (GB: ADC35472.1), Feline CoV strain UU21 (GB: ADL71466.1), Human CoV NL63 (GB: YP_003767.1), 229E-related bat CoV with one N domains (GB: ALK28775.1), 229E-related bat CoV with two N domains (GB: ALK28765.1), Human CoV 229E strain inf-1 (GB: NP_073551.1), MHV strain A59 (GB: ACO72893), BCoV strain KWD1 (GB: AAX38489), HCoV-OC43 strain Paris (GB: AAT84362), HCoV-HKU1 (GB: AAT98580), SARS-CoV strain Urbani (GB: AAP13441), MERS-CoV strain EMC/2012 (GB: YP_009047204), HKU4 (GB: AGP04928), HKU5 (GB: AGP04943), IBV strain Beaudette (GB: ADP06471), and PDCoV

(Continued)

repeat regions (HR1 and HR2) and the transmembrane domains which are well conserved among CoV species across different genera. In the MHV and HKU1 S prefusion structures, the S_2 domain consists of multiple α-helical segments and a three-stranded antiparallel β-sheet at the viral membrane-proximal end. A 75 Å long central helix located immediately downstream of the HR1 region stretches along the threefold axis over the entire length of the S_2 trimer. The HR1 motif itself folds as four individual α-helices along the length of the S_2 subunit, in contrast to the 120 Å long α-helix formed by this region in postfusion structures (Duquerroy et al., 2005; Gao et al., 2013; Xu et al., 2004). A 55 Å long helix upstream of the S_2' cleavage site runs parallel to and is packed against the central helix via hydrophobic interactions (Fig. 1C). The fusion peptide forms a short helix of which the strictly conserved hydrophobic residues are buried in an interface with other elements of S_2. Unlike other class I fusion proteins, this conserved fusion peptide (FP1) is not directly upstream of HR1 but located some 65 residues upstream of this region (Fig. 1A). Intriguingly, a recent published report provided experimental evidence for the existence of another fusion peptide (FP2) immediately upstream of the HR1 region (Ou et al., 2016), that had been predicted earlier based on the position, hydrophobicity profile and amino acid composition canonical for class I viral fusion peptides (Bosch and Rottier, 2008; Bosch et al., 2004; Chambers et al., 1990). The HR2 region locates closely to the C-terminal end of the S ectodomain, but it appeared to be disordered in both cryo-EM structures and therefore its prefusion conformation remains unknown.

The metastable prefusion conformation of S_2 is locked by the cap formed by the intertwined S_1 protomers. The distal tip of the S_2 trimer connects via hydrophobic interactions with domains B. This distal tip of the S_2 trimer consists of the C-terminal region of HR1 in the prefusion conformation, while the entire HR1 rearranges to form a central three-helix coiled coil in the postfusion structure (Duquerroy et al., 2005; Lu et al., 2014; Supekar et al., 2004). Interactions between this region of the S_2 trimer and domain B may therefore prevent premature conformational changes resulting in the conversion of the prefusion S protein into the very stable

Fig. 2—Cont'd strain USA/Ohio137/2014 (GB: AIB07807). PSI-BLAST analysis using the NTR of the HCoV-NL63 S protein (residues 16–196) as a query detected two homologous regions in the first 425 residues of the 229E-related bat coronavirus spike protein (GB: ALK28765.1)—designated N1 (residues 32–213) and N2 (residues 246–422) with 32% and 35% amino acid sequence identity, respectively, suggesting a duplication of the NTR. Spike proteins are drawn to scale and aligned at the position of the conserved fusion peptide (FP1).

postfusion structure. Also domains C and D of the betacoronavirus S_1 subunit and the linker region connecting domain A and B interact with the surface of the adjacent S_2 protomer and may hence play a role in stabilizing the prefusion S_2 trimer. Domain A appears to play a minor role in this respect in view of its relatively small a surface area that interacts with the S_2 trimer.

3. SPIKE–RECEPTOR INTERACTIONS

3.1 Different Domains Within S_1 May Act as RBD

Over the past decades, molecular studies on the CoV S glycoprotein have shown that both the N-terminal region (NTR, domain A in β-CoV) and the C-terminal region of S_1 (CTR, comprising domain B, C, and D in β-CoV) can bind host receptors and hence function as RBDs (Fig. 2) (Li, 2015). The CTR of alpha- and betacoronaviruses appears to bind proteinaceous receptors exclusively. The α-CoV HCoV-229E, serotype II feline CoV (FCoV), TGEV, and porcine respiratory coronavirus use the human aminopeptidase N (APN) of their respective hosts as receptors (Bonavia et al., 2003; Delmas et al., 1992; Reguera et al., 2012). The HCoV-NL63 (α-CoV) and SARS-CoV (β-CoV) both utilize angiotensin-converting enzyme 2 (ACE2) as a functional receptor (Li et al., 2005b; Wu et al., 2009), whereas the β-CoVs MERS-CoV and BtCoV-HKU4 recruit dipeptidyl peptidase-4 (DPP4) as a functional receptor (Lu et al., 2013; Mou et al., 2013; Raj et al., 2013; Wang et al., 2014; Yang et al., 2014).

The receptor-binding motifs (RBMs) in the S_1 CTRs of alpha- and betacoronavirus spike proteins are presented on one or more loops extending from the β-sheet core structure. Within *alpha-* and *betacoronavirus* genera the RBD core is structurally conserved yet the RBM(s) that determine receptor specificity may vary extensively. For instance, the CTR of the α-CoVs PRCoV and HCoV-NL63 has a similar core structure suggesting common evolutionary origin but diverged in their RBMs recruiting different receptors (APN and ACE2, respectively). A similar situation is seen for the CTRs of β-CoVs SARS-CoV and MERS-CoV that bind ACE2 and DPP4, respectively (Li, 2015). Conversely, the CTRs of the α-CoV HCoV-NL63 and β-CoV SARS-CoV both recognize ACE2, yet via distinct molecular interactions (ACE2 recognition via three vs one RBM, respectively), which suggested a convergent evolution pathway for these viruses in recruiting the ACE2 receptor (Li, 2015). The core

structures of the CTRs in α- and β-CoVs provide a scaffold to present RBMs from extending loop(s), which may accommodate facile receptor switching by subtle alterations in or exchange of the RBMs via mutation/recombination.

Contrary to the CTR, the NTR appears to mainly bind glycans. The NTR of the α-CoV TGEV and of the γ-CoV IBV S proteins binds to sialic acids (Promkuntod et al., 2014; Schultze et al., 1996), while the NTR of betacoronaviruses including BCoV and HCoV-OC43 was shown to bind to *O*-acetylated sialic acids (Künkel and Herrler, 1993; Peng et al., 2012; Schultze et al., 1991; Vlasak et al., 1988). Only the NTR of MHV (domain A) is known to interact with a protein receptor, being mCEACAM1a (Peng et al., 2011), while lacking any detectable sialic acid-binding activity (Langereis et al., 2010). However, as the NTR of MHV displays the β-sandwich fold of the galectins, a family of sugar-binding proteins, it probably has evolved from a sugar-binding domain (Li, 2012).

The presence of RBDs in different domains of the S protein that can bind either proteinaceous or glycan receptors illustrates a functional modularity of this glycoprotein in which different domains may fulfill the role of binding to cellular attachment or entry receptors. The CoV S protein is thought to have evolved from a more basic structure in which receptor recognition was confined to the CTR within S_1 (Li, 2015). The observed deletions of the NTR in some CoV species in nature are indicative of a less stringent requirement and integration of this domain with other regions of the spike trimer compared to the more C-terminally located domains of S_1 and support a scenario in which the NTR has been acquired at a later time point in CoV evolutionary history. For example, the NTR of MHV, which displays a human galectin-like fold, was suggested to originate from a cellular lectin acquired early on in CoV evolution (Peng et al., 2011). Acquisition of glycan-binding domains and fusion thereof to the ancestral S protein may have resulted in a great extension of CoV host range and may have caused an increase in CoV diversity. The general preference of the NTR and CTR to bind to, respectively, glycan or protein receptors may be related to their arrangement in the S protein trimer. In contrast to the CTR, which is located in the center of the S trimer, the NTR is more distally oriented (Fig. 1B). As protein–glycan interactions are often of low affinity, the more distal orientation of domain A may allow multivalent receptor interactions, thereby increasing avidity. Interestingly, some CoVs appear to have a dual receptor usage as they may bind via their NTR and CTR to glycan and protein receptors, respectively (Fig. 2).

3.2 CoV Protein Receptor Preference

Although the number of currently known CoV receptors is limited, receptor usage does not appear to be necessarily conserved between closely related virus species such as HCoV-229E (APN) and HCoV-NL63 (ACE2), whereas identical receptors (ACE2) can be targeted by virus species from different genera such as HCoV-NL63 and SARS-CoV. It seems that CoVs prefer certain types of host proteins as their entry receptor, with three out of four of the so far identified proteinaceous receptors being ectopeptidases (APN, ACE2, and DPP4), although enzymatic activity of these proteins was shown not to be required for infection by their respective viruses (Bosch et al., 2014). Possibly, the localization to certain membrane microdomains and efficient internalization of two of these proteins in polarized cells (APN and DPP4) may contribute to their suitability to function as entry receptors (Aït-Slimane et al., 2009). In the case of MERS-CoV, the region of DPP4 that is bound by the S protein coincides with the binding site for its physiological ligand adenosine deaminase (Raj et al., 2014). Employment of conserved epitopes such as these may also contribute to the cross-species transmission potential of viruses (Bosch et al., 2014), as is exemplified by MERS-CoV being able to use goat, camelid, cow, sheep, horse, pig, monkey, marmoset, and human DPP4 as entry receptor (Barlan et al., 2014; Eckerle et al., 2014; Falzarano et al., 2014; Müller et al., 2012; van Doremalen et al., 2014). Similarly, this may apply for the ability of feline, canine, porcine, and human CoVs to use fAPN as entry receptor, at least in vitro (Tresnan et al., 1996).

4. S PROTEIN PROTEOLYTIC CLEAVAGE AND CONFORMATIONAL CHANGES

Coronavirus entry is a tightly regulated process that appears to be orchestrated by multiple triggers that include receptor binding and proteolytic processing of the S protein and that ultimately results in virus-cell fusion. It is initiated by virion attachment mediated through interaction of either the NTR or CTR (or both) in the S_1 subunit of the spike protein with host receptors. Upon attachment, the virus is taken up via receptor-mediated endocytosis by clathrin- or caveolin-dependent pathways (Burkard et al., 2014; Eifart et al., 2007; Inoue et al., 2007; Nomura et al., 2004) although other entry routes have also been reported (Wang et al., 2008). Prior to and/or during endocytic uptake the CoV S protein

is proteolytically processed. The spike protein may contain two proteolytic cleavage sites. One of the cleavage sites is located at the boundary between the S_1 and S_2 subunits (S_1/S_2 cleavage site), while the other cleavage site is located immediately upstream of the first fusion peptide (S_2' cleavage site). Although not irrevocably proven, it is expected that all CoVs depend on proteolytic cleavage on or close to S_2' for fusion to occur. Virus-cell fusion thus not only critically depends on the conformational changes following spike–receptor engagement, and perhaps on acidification of endosomal vesicles (Eifart et al., 2007; Matsuyama and Taguchi, 2009; Zelus et al., 2003), but also on proteolytic activation of the S protein by proteases along the endocytic route (Burkard et al., 2014; Simmons et al., 2005). Indeed, inhibition of intracellular proteases has been shown to block virus entry and virus-cell fusion (Burkard et al., 2014; Frana et al., 1985; Simmons et al., 2005; Yamada and Liu, 2009). The specific proteolytic cleavage requirements of the S protein at the S_1/S_2 boundary and particularly at the S_2' site may furthermore determine the intracellular site of fusion (Burkard et al., 2014). In agreement herewith, it has become evident that the protease expression profile of host cells may form an additional determinant of the host cell tropism of coronaviruses (Millet and Whittaker, 2015).

Analysis of the CoV S prefusion conformation suggests that relocation (or shedding) of the S_1 subunits that cap the S_2 subunit is a prerequisite for the conformational changes in S_2 that ultimately result in fusion. Shedding of S_1 probably requires receptor binding as well as proteolytic processing at S_1/S_2. The cryo-EM structure indicates that the S_1/S_2 proteolytic cleavage site is accessible to proteases prior to spike–receptor interaction, and depending on the particular cleavage site present may already be processed in the cell in which the virions are produced. As indicated earlier, the conformational changes in the S protein that result in virus-cell fusion most likely also require cleavage at the S_2' site immediately upstream of the fusion peptide. Interestingly, the S_2' cleavage site is located within an α-helix exposed on the prefusion S structure which prevents efficient proteolytic cleavage (Robertson et al., 2016). This indicates the necessity for preceding conformational changes induced by receptor binding and subsequent shedding of S_1, upon which the secondary structure of the S_2' site transforms into a cleavable flexible loop. Following proteolytic cleavage activation at the S_2' site, hydrophobic interactions between the fusion peptide and the adjacent S_2 helices are disturbed which allows the four α-helices and the connecting regions that make up the HR1 region in the prefusion S protein to refold into a long trimeric coiled coil (Fig. 1D). This coiled coil

forms an N-terminal extension of the central helix projecting the fusion peptide(s) toward the target membrane. Successively, the fusion peptide(s) will be inserted into the limiting membrane of the host cell endocytic compartment. Next, as a consequence of S_2 rearrangements, the two HR regions will interact to form an antiparallel energetically stable six-helix bundle (Bosch et al., 2003, 2004), enabling the close apposition and subsequent fusion of the viral and host lipid bilayers.

5. TROPISM CHANGES ASSOCIATED WITH S PROTEIN MUTATIONS

Changes in the S protein may result in an altered host, tissue, or cellular tropism of the virus. This is clearly exemplified by genomic recombination events that result in exchange of (part of) the S protein and in a concomitant change in tropism. The propensity of CoVs to undergo homologous genomic recombination has been exploited for the genetic manipulation of these viruses (de Haan et al., 2008; Haijema et al., 2003; Kuo et al., 2000). To this end, interspecies chimeric coronaviruses were generated, which carried the spike ectodomain of another CoV and which could be selected based on their altered requirement for an entry receptor. Exchange of S protein genes may also occur in vivo, resulting in altered tropism as is illustrated by the occurrence of serotype II feline infectious peritonitis virus (FIPV). This virus results from a naturally occurring recombination event between feline and canine CoVs (CCoVs) in which the feline virus acquires a CCoV spike gene (Herrewegh et al., 1995; Terada et al., 2014). As a result of the acquisition of this new S protein, the rather harmless enteric feline CoV (FECV) turns into a systemically replicating and deadly FIPV. As FECV has a strict feline tropism (Myrrha et al., 2011), while CCoV has been shown to infect feline cells (Levis et al., 1995), it is likely that serotype II FIPVs arise in cats coinfected with serotype I FECV and CCoV. Furthermore, as different recombination sites have been observed for each serotype II FIPV, while serotype II FECVs have not been observed, it appears that serotype II FIPVs exclusively result of reoccurring recombination events (Terada et al., 2014). In addition to these feline–CCoV recombinants, a chimeric porcine coronavirus with a TGEV backbone and a spike of the porcine epidemic diarrhea virus (PEDV) was recently isolated from swine fecal samples in Italy and Germany, likely also resulting from a recombination event (Akimkin et al., 2016; Boniotti et al., 2016). Moreover, the α-CoV HKU2 BtCoV probably resulted from genomic recombination as it encodes

an S protein that resembles a betacoronavirus S protein except for its N-terminal region that is similar to that of alphacoronaviruses (Lau et al., 2007). Thus, such genomic recombination events are not necessarily restricted to occur between viruses of the same genus.

5.1 S_1 Receptor Interactions Determining Tropism

5.1.1 S_1 NTR Changes

Several changes in the amino-terminal domain of S_1 have been associated with changes in the tropism of the virus. For example, for several α-CoVs, loss of NTR of the S protein appears to be accompanied with a loss of enteric tropism. While the porcine CoV TGEV displays a tropism for both the gastrointestinal and respiratory tract, the closely related PRCoV, which lacks the sialic acid-binding N-terminal region (Krempl et al., 1997), only replicates in the respiratory tract. The loss of sialic acid-binding activity by four-amino acid changes in the NTR of its S protein resulted in an almost complete loss of enteric tropism (Krempl et al., 1997). Similar to TGEV, enteric serotype I FCoVs also have been reported to bind to sialic acids (Desmarets et al., 2014). Large deletions within the S_1 subunit corresponding to the N-terminal region have been found in variants of the systemically replicating FIPV (strains UU16, UU21, and C3663) after intrahost emergence from enteric FECV (Chang et al., 2012; Terada et al., 2012). Also FIPVs seem to have lost the ability to replicate in the enteric tract (Pedersen, 2014). Clinical isolates of human coronavirus 229E as well as of the related alpaca coronavirus, both of which cause respiratory infections, encode relatively short spike proteins that lack the NTR (Crossley et al., 2012; Farsani et al., 2012). In contrast, closely related bat coronaviruses with intestinal tropism contain S proteins with a NTR or sometimes even two copies of the NTR (Corman et al., 2015) (Fig. 2). Overall, these observations suggest that the alphacoronavirus spike NTR—in particular its sialic acid-binding activity—may contribute to the enteric tropism of these alphacoronaviruses, while it is not required for replication in the respiratory tract or in other extraintestinal organs. It has been hypothesized that the sialic acid-binding activity of the spike protein can allow virus binding to (i) soluble sialoglycoconjugates that may protect the virus from hostile conditions in the stomach or (ii) to mucins that may prevent the loss of viruses by intestinal peristalsis and allow the virus to pass the thick mucus barrier, thereby gaining access to the intestinal cells to initiate infection (Schwegmann-Wessels et al., 2003).

Besides deletions of entire domains of the S protein, more subtle changes consisting of amino acid substitutions in S_1 NTR may also suffice to alter the virus' tropism. For example, MHV variants have been observed that acquired the ability to use the human homologue of their murine CEACAM1a receptor to enter cells as a result of mutations in their RBD that is located in S_1 NTR (Baric et al., 1999).

5.1.2 S_1 CTR Changes

As the CTR of the S_1 subunit contains the protein RBD for most CoVs, also mutations in this part of S have been associated with changes in the virus' tropism. Perhaps the most well-known example of viral cross-species transmission involves the SARS-CoV. Studies support a transmission model in which a SARS-like CoV was transmitted from *Rhinolophus* bats to palm civets, which subsequently transmitted the palm civet-adapted virus to humans at local food markets in southern China (Li et al., 2006). According to this model, SARS-like viruses adapted to both the palm civet and human host, which was reflected in the rapid viral evolution observed for these viruses within these species (Song et al., 2005). Two-amino acid substitutions within the RBD were elucidated that are of relevance for binding to the ACE2 proteins of palm civets and humans (Li et al., 2005b, 2006; Qu et al., 2005). From these studies it appears that due to strong conservation of ACE2 between mammalian species only a few amino acid alterations within the RBD are needed to change coronavirus host species tropism. Indeed serial passage of SARS-CoVs in vitro or in vivo can rapidly lead to adaptation to new host species (Roberts et al., 2007). SARS-like viruses isolated from bats displayed major differences including a deletion in the ACE2 RBM compared to human SARS-CoV (Drexler et al., 2010; Ren et al., 2008) and as a consequence were unable of using human ACE2 as an entry receptor (Becker et al., 2008). However, recently a novel SARS-like BtCoV was identified, which could use ACE2 of *Rhinolophus* bats, palm civets as well as of humans as a functional receptor (Ge et al., 2013). These findings not only provide further evidence that bats are indeed the natural reservoir for SARS-like CoVs, but also that these bat coronaviruses can directly include human ACE2 in their receptor repertoire. The detection of sequences of SARS-CoV-like viruses in palm civets and raccoon dogs (Guan et al., 2003; Tu et al., 2004) therefore probably reflects the unusually wide host range of these viruses. A similar promiscuous receptor usage is also observed for MERS-CoV which binds to DPP4 of many species (Barlan

et al., 2014; Eckerle et al., 2014; Falzarano et al., 2014; Müller et al., 2012; van Doremalen et al., 2014) as indicated earlier.

Just as SARS like and MERS-CoVs are able to use entry receptors of different host species, also several α-CoVs display promiscuity to orthologous receptors. For example, the feline APN molecule can be used as a receptor by feline (serotype II FIPV), canine (CCoV), porcine (TGEV), and human (HCoV-229E) α-CoVs in cell culture (Tresnan and Holmes, 1998; Tresnan et al., 1996). Conversely, serotype II FIPV can only enter cells expressing feline APN (Tresnan and Holmes, 1998). The ability of TGEV and CCoV to use feline APN as a receptor probably results from strong conservation of the viral-binding motif (VBM) among APN orthologs in combination with the RBDs recognizing APN in a similar fashion (Reguera et al., 2012). Though recruiting the same receptor, HCoV-229E binds another domain within APN, which apparently is also conserved in feline APN (Kolb et al., 1997; Tusell et al., 2007). Conservation of the VBM obviates the need for large adaptations within the RBD of these viruses to orthologous receptors allowing more facile cross-species transmission.

Other mutations in the S_1 CTR associated with altered tropism have been described for the β-CoV MHV. Similar to the humanized CEACAM1a-recognizing MHV variant, serial passaging of virus-infected cells resulted in the selection of viruses with an extended host range, which were subsequently shown to be able to enter cells in a heparan sulfate-dependent and CEACAM1a-independent manner (de Haan et al., 2005; Schickli et al., 1997). Two sets of mutations in the S protein were shown to be critically required for this phenotype, both of which resulted in the occurrence of multibasic heparan sulfate-binding sites. While one heparan sulfate-binding site was located in the S_2 subunit immediately upstream of the fusion peptide, the other was located in the S_1 CTR. The presence of this latter, but not of the former, domain resulted in MHV that depended on both heparan sulfate and CEACAM1a for entry. Additional introduction of the second heparan sulfate-binding site enabled the virus to become mCEACAM1a independent (de Haan et al., 2006). In addition, a mutation of the HVR of S_1 may affect CoV tropism as was demonstrated for the MHV strain JHM (MHV-JHM). The spike protein of MHV-JHM may induce receptor-independent fusion (Gallagher et al., 1992, 1993). However, deletion of residues in HVR of MHV-JHM resulted in the spike protein being entirely dependent on CEACAM1a binding for fusion (Dalziel et al., 1986; Gallagher and Buchmeier, 2001; Phillips and Weiss, 2001).

5.2 Changes in Proteolytic Cleavage Site and Other S_2 Mutations Associated with Altered Tropism

5.2.1 Changes in Proteolytic Cleavage Sites

Although the S_2 subunit does not appear to contain any RBDs, several mutations in this subunit have been associated with changes in the virus' tropism. Some of these changes affect the cleavage sites in the S protein that are located at the S_1/S_2 boundary or immediately upstream of the fusion peptide (S_2' cleavage site). As these cleavages appear to be essential for virus-cell fusion, the availability of host proteases to process the S protein is of critical importance for the virus' tropism. The importance of S protein cleavage at the S_1/S_2 boundary for the tropism of the virus is exemplified by the BtCoV HKU4, which is closely related to the MERS-CoV. Although domain B of the HKU4 S protein can interact with both bat and human DPP4, it is only in the context of bat cells, but not human cells, that the virus can utilize these molecules as entry receptors (Yang et al., 2014). In contrast, MERS-CoV can enter cells of human and bat origin via both DPP4 orthologues. This difference results from host restriction factors at the level of proteolytic cleavage activation. Two-amino acid substitutions (S746R and N762A) in the S_1/S_2 boundary of the S protein were shown to be crucial for the adaptation of bat MERS-like CoV to the proteolytic environment of the human cells (Yang et al., 2015).

Although probably not directly responsible for the tropism change associated with the enterically replicating FECV evolving into the systemically replicating FIPV, loss of a furin cleavage site at S_1/S_2 junction is observed in the majority of the FIPVs, whereas this furin cleavage site is strictly conserved in the parental FECV strains (Licitra et al., 2013). Apparently, conservation of this furin cleavage site is not required for efficient systemic replication. However, as FIPV is generally not found in the feces of cats, it may well be that loss of the furin cleavage site at S_1/S_2—as well as mutations in other parts of the genome, such as the accessory genes—may prevent efficient replication of FIPV in the enteric tracts.

Besides the influence of the S_1/S_2 cleavage site, virus tropism may also depend on the S_2' cleavage site upstream of FP1. In contrast to wild-type MHV strain A59, a recombinant MHV carrying a furin cleavage site at this position was shown to no longer depend on lysosomal proteases for efficient entry to occur (Burkard et al., 2014). As a consequence, this virus was able to infect cells in which trafficking to lysosomes was inhibited. Cleavage at the S_2' site may also be important for the tropism of PEDV, which causes major damage to the biofood industry in Asia and the Americas (Lee, 2015;

Song et al., 2015). PEDV replication in cell culture is strictly dependent on trypsin-like proteases, a requirement which is expected to limit its tropism in vivo to the enteric tract. The trypsin dependency of PEDV entry was shown, however, to be lifted after introduction of a furin cleavage site at the S_2' cleavage site by a single-amino acid substitution. Such mutations may potentially affect the spread of this virus in the pig by allowing it to replicate in nonenteric tissues in the absence of trypsin-like proteases (Li et al., 2015).

5.2.2 Other S_2 Mutations Associated with Altered Tropism

Mutations in other parts of the S_2 subunit than those affecting the proteolytic cleavage sites may also influence the tropism of different CoVs. Several studies report a correlation between mutations in the HR1 region of FCoVs and the conversion of FECV into FIPV (Bank-Wolf et al., 2014; Desmarets et al., 2016; Lewis et al., 2015). Such a correlation appeared even more convincing for mutations found in the recently identified FP2 (Chang et al., 2012; Ou et al., 2016). While these correlations suggest an important role for the S protein in the transition of FECV into FIPV, the causal relationship between these mutations in S and FIP remains to be determined. It is plausible, however, that such mutations may play a role in the acquired ability of FIPVs to infect macrophages. Indeed, for serotype II FCoV, the ability to replicate in macrophages was shown to be determined by residues located in the C-terminal part of the S_2 subunit, although the responsible residues were not identified (Rottier et al., 2005).

Also for other CoVs, mutations in the S_2 subunit have been linked to changes in the virus' tropism. A serially passaged MHV-A59 virus was shown to obtain mutations (M936V, P939L, F948L, and S949I) in and adjacent to the HR1 region which conveyed host range expansion of the mutant virus to normally nonpermissive mammalian cell types in vitro (Baric et al., 1999; McRoy and Baric, 2008). Contrary, Krueger et al. reported three mutations in the S_2 subunit of MHV-JHM (V870A located upstream of the S_2' cleavage site and A994V and A1046V located in the HR1 region) all of which reduced the CEACAM1a-independent fusogenicity of this virus (Krueger et al., 2001). Many studies on MHV-JHM point to a crucial role of a leucine at amino acid position 1114 in S protein fusogenicity. The MHV S cryo-EM structure demonstrates that the L1114 residue is located in the central helix and contributes to interprotomer interactions. A L1114F substitution in the MHV-JHM S protein

was observed in a mutant strain of JHM and correlated with an increased S_1–S_2 stability and the loss of the ability to induce CEACAM1a-independent fusion (Taguchi and Matsuyama, 2002), while a substitution of the same residue to an Arg (L1114R) reduced the neurotropism of this virus (Tsai et al., 2003). Mutants resistant to a monoclonal antibody (Wang et al., 1992) and soluble receptor (Saeki et al., 1997) also correlate with substitutions at this specific residue, illustrating the importance of this residue in S fusogenicity. For the MERS-CoV, mutations in HR1 have been identified that are thought to be associated with its adaptive evolution (Forni et al., 2015). Among these sites, position 1060 is particularly interesting, as it appears to correspond to substitutions found in MHV and IBV that modify the tropism of these viruses (MHV: E1035D; IBV: L857F; Navas-Martin et al., 2005; Yamada et al., 2009). Substitution E1035D in HR1 of MHV was shown to restore the hepatotropism of an otherwise non-hepatotropic MHV, the latter resulting from mutations in the S_1 NTR and the S_1/S_2 cleavage site. These studies collectively indicate that mutations in and close to the HR regions may affect CoV tropism, possibly by affecting the metastability and consequently fusogenicity of the S protein and/or the formation of the postfusion six-helix bundle.

6. CONCLUDING REMARKS

It appears that changes in the S protein associated with altered tropism can be found in several regions of the spike protein. These regions obviously include the NTR and CTR of S_1 that are involved in the interaction with attachment and/or entry receptors. Substitutions within the S_1 RBDs may convey an altered viral tropism by adaptation of the virus to new or orthologous entry receptors. In addition, the S protein cleavage sites are important for host tropism as the processing of these sites by host proteases will critically affect the removal of the S_1-mediated locking of the S_2 prefusion conformation by shedding of S_1 (S_1/S_2 cleavage site) and the release of the fusion peptide(s) (S_2' cleavage site). Finally, changes in S_2 (particularly in the HR regions) may compensate for yet suboptimal spike binding to orthologous receptors by which low relative affinity interactions suffice to induce the required conformational changes of the S protein that ultimately result in the formation of the postfusion six-helix bundle and virus-cell fusion.

The observation that the different domains of the S protein all contribute to the tropism of CoVs is indicative of a coordinated interplay between these

domains. This interplay has also been inferred from several studies, which reported changes in one S protein subunit often to be accompanied by adaptations in the other subunit (Saeki et al., 1997; Wang et al., 1992). In addition, the interplay between S_1 and S_2 has also been shown to be important for changes in the tropism of the virus as indicated earlier (de Haan et al., 2006; Navas-Martin et al., 2005). The recently published cryo-EM structures of CoV spike proteins (Kirchdoerfer et al., 2016; Walls et al., 2016) now provide structural evidence for the complex interplay between the subunits and domains of the S protein.

From all these studies, a picture arises in which the S protein is progressively destabilized through receptor engagement and proteolytic activation. In this process the S_1 subunits serve as a safety pin that stabilizes the fusogenic S_2 trimer. The safety pin is discharged upon interaction with a specific receptor and processing by host cell proteases and thereby gives way to conformational changes of the instable S_2 subunit. Subsequent release of the fusion peptide may resemble the pulling of the trigger which inevitably results in fusion of viral and host membranes through interaction of the heptad repeats regions.

Based on the presented data we propose a model in which the ability of a CoV to cross the host species barrier is critically dependent on the interplay between the different regions of the S proteins. In this model, the probable low affinity of the S_1 RBD for a novel receptor must be compensated by sufficiently low S_2 metastability, which depends on both proteolytic cleavage of the S protein and the S_2 interprotomer interactions. These required S protein characteristics may be generated during naturally occurring quasispecies variation and may result in the ability of the virus to replicate in and adapt to a new host.

ACKNOWLEDGMENTS

This study is supported by TOP Project Grant (91213066) funded by ZonMW and as part of the Zoonotic Anticipation and Preparedness Initiative (ZAPI project; IMI Grant Agreement No. 115760), with the assistance and financial support of IMI and the European Commission. We thank Mark Bakkers for his help in preparing figures.

REFERENCES

Aït-Slimane, T., Galmes, R., Trugnan, G., Maurice, M., 2009. Basolateral internalization of GPI-anchored proteins occurs via a clathrin-independent flotillin-dependent pathway in polarized hepatic cells. Mol. Biol. Cell 20 (17), 3792–3800. http://dx.doi.org/10.1091/mbc.E09-04-0275.

Akimkin, V., Beer, M., Blome, S., Hanke, D., Höper, D., Jenckel, M., Pohlmann, A., 2016. New chimeric porcine coronavirus in swine feces, Germany, 2012. Emerg. Infect. Dis. 22 (7), 1314–1315. http://dx.doi.org/10.3201/eid2207.160179.

Alagaili, A.N., Briese, T., Mishra, N., Kapoor, V., Sameroff, S.C., Burbelo, P.D., et al., 2014. Middle East respiratory syndrome coronavirus infection in dromedary camels in Saudi Arabia. mBio 5 (2). http://dx.doi.org/10.1128/mBio.00884-14. e00884-14.

Annan, A., Baldwin, H.J., Corman, V.M., Klose, S.M., Owusu, M., Nkrumah, E.E., et al., 2013. Human betacoronavirus 2c EMC/2012-related viruses in bats, Ghana and Europe. Emerg. Infect. Dis. 19 (3), 456–459. http://dx.doi.org/10.3201/eid1903.121503.

Azhar, E.I., El-Kafrawy, S.A., Farraj, S.A., Hassan, A.M., Al-Saeed, M.S., Hashem, A.M., Madani, T.A., 2014. Evidence for camel-to-human transmission of MERS coronavirus. N. Engl. J. Med. 26 (26), 2499–2505. http://dx.doi.org/10.1056/NEJMoa1401505.

Baker, K.A., Dutch, R.E., Lamb, R.A., Jardetzky, T.S., 1999. Structural basis for paramyxovirus-mediated membrane fusion. Mol. Cell 3 (3), 309–319. http://dx.doi.org/10.1016/S1097-2765(00)80458-X.

Bank-Wolf, B.R., Stallkamp, I., Wiese, S., Moritz, A., Tekes, G., Thiel, H.J., 2014. Mutations of 3c and spike protein genes correlate with the occurrence of feline infectious peritonitis. Vet. Microbiol. 173 (3–4), 177–188. http://dx.doi.org/10.1016/j.vetmic.2014.07.020.

Baric, R.S., Sullivan, E., Hensley, L., Yount, B., Chen, W., 1999. Persistent infection promotes cross-species transmissibility of mouse hepatitis virus. J. Virol. 73 (1), 638–649.

Barlan, A., Zhao, J., Sarkar, M.K., Li, K., McCray, P.B., Perlman, S., Gallagher, T., 2014. Receptor variation and susceptibility to Middle East respiratory syndrome coronavirus infection. J. Virol. 88 (9), 4953–4961. http://dx.doi.org/10.1128/JVI.00161-14.

Bartesaghi, A., Merk, A., Borgnia, M.J., Milne, J.L.S., Subramaniam, S., 2013. Prefusion structure of trimeric HIV-1 envelope glycoprotein determined by cryo-electron microscopy. Nat. Struct. Mol. Biol. 20 (12), 1352–1357. http://dx.doi.org/10.1038/nsmb.2711.

Becker, M.M., Graham, R.L., Donaldson, E.F., Rockx, B., Sims, A.C., Sheahan, T., et al., 2008. Synthetic recombinant bat SARS-like coronavirus is infectious in cultured cells and in mice. Proc. Natl. Acad. Sci. U.S.A. 105 (50), 19944–19949. http://dx.doi.org/10.1073/pnas.0808116105.

Bolles, M., Donaldson, E., Baric, R., 2011. SARS-CoV and emergent coronaviruses: viral determinants of interspecies transmission. Curr. Opin. Virol. 1 (6), 624–634. http://dx.doi.org/10.1016/j.coviro.2011.10.012.

Bonavia, A., Zelus, B.D., Wentworth, D.E., Talbot, P.J., Holmes, K.V., 2003. Identification of a receptor-binding domain of the spike glycoprotein of human coronavirus HCoV-229E. J. Virol. 77 (4), 2530–2538. http://dx.doi.org/10.1128/JVI.77.4.2530-2538.2003.

Boniotti, M.B., Papetti, A., Lavazza, A., Alborali, G., Sozzi, E., Chiapponi, C., et al., 2016. Porcine epidemic diarrhea virus and discovery of a recombinant swine enteric coronavirus, Italy. Emerg. Infect. Dis. 22 (1), 83–87. http://dx.doi.org/10.3201/eid2201.

Bosch, B.J., Rottier, P.J.M., 2008. Nidovirus entry into cells. In: Perlman, S., Gallagher, T., Snijder, E. (Eds.), Nidoviruses. American Society of Microbiology, Washington, DC, pp. 157–178. http://dx.doi.org/10.1128/9781555815790.ch11.

Bosch, B.J., Van Der Zee, R., de Haan, C.A.M., Rottier, P.J.M., 2003. The coronavirus spike protein is a class I virus fusion protein: structural and functional characterization of the fusion core complex. J. Virol. 77 (16), 8801–8811. http://dx.doi.org/10.1128/JVI.77.16.8801.

Bosch, B.J., Martina, B.E.E., Van Der Zee, R., Lepault, J., Haijema, B.J., Versluis, C., et al., 2004. Severe acute respiratory syndrome coronavirus (SARS-CoV) infection inhibition using spike protein heptad repeat-derived peptides. Proc. Natl. Acad. Sci. U.S.A. 101 (22), 8455–8460. http://dx.doi.org/10.1073/pnas.0400576101.

Bosch, B.J., Smits, S.L., Haagmans, B.L., 2014. Membrane ectopeptidases targeted by human coronaviruses. Curr. Opin. Virol. 6 (1), 55–60. http://dx.doi.org/10.1016/j.coviro.2014.03.011.

Briese, T., Mishra, N., Jain, K., East, M., Syndrome, R., Quasispecies, C., et al., 2014. Dromedary camels in Saudi Arabia include homologues of human isolates revealed through whole-genome analysis etc. mBio 5 (3), 1–5. http://dx.doi.org/10.1128/mBio.01146-14. Editor.

Burkard, C., Verheije, M.H., Wicht, O., van Kasteren, S.I., van Kuppeveld, F.J., Haagmans, B.L., et al., 2014. Coronavirus cell entry occurs through the endo-/lysosomal pathway in a proteolysis-dependent manner. PLoS Pathog. 10 (11), e1004502. http://dx.doi.org/10.1371/journal.ppat.1004502.

Chambers, P., Pringle, C.R., Easton, A.J., 1990. Heptad repeat sequences are located adjacent to hydrophobic regions in several types of virus fusion glycoproteins. J. Gen. Virol. 71 (12), 3075–3080. http://dx.doi.org/10.1099/0022-1317-71-12-3075.

Chan, F.J., To, K.K., Tse, H., Jin, D.-Y., Yuen, K.-Y., 2013. Interspecies transmission and emergence of novel viruses: lessons from bats and birds. Trends Microbiol. 21 (10), 544–555. http://dx.doi.org/10.1016/j.tim.2013.05.005.

Chang, H.W., Egberink, H.F., Halpin, R., Spiro, D.J., Rottier, P.J.M., 2012. Spike protein fusion peptide and feline coronavirus virulence. Emerg. Infect. Dis. 18 (7), 1089–1095. http://dx.doi.org/10.3201/eid1807.120143.

Corman, V.M., Baldwin, H.J., Tateno, A.F., Zerbinati, R.M., Annan, A., Owusu, M., et al., 2015. Evidence for an ancestral association of human coronavirus 229E with bats. J. Virol. 89 (23), 11858–11870. http://dx.doi.org/10.1128/JVI.01755-15.

Crossley, B.M., Mock, R.E., Callison, S.A., Hietala, S.K., 2012. Identification and characterization of a novel alpaca respiratory coronavirus most closely related to the human coronavirus 229E. Viruses 4 (12), 3689–3700. http://dx.doi.org/10.3390/v4123689.

Dalziel, R.G., Lampert, P.W., Talbot, P.J., Buchmeier, M.J., 1986. Site-specific alteration of murine hepatitis virus type 4 peplomer glycoprotein E2 results in reduced neurovirulence. J. Virol. 59 (2), 463–471. Retrieved from, http://www.ncbi.nlm.nih.gov/entrez/query.fcgi?cmd=Retrieve&db=PubMed&dopt=Citation&list_uids=3016306.

de Haan, C.A.M., Li, Z., te Lintelo, E., Bosch, B.J., Haijema, B.J., Rottier, P.J.M., 2005. Murine coronavirus with an extended host range uses heparan sulfate as an entry receptor. J. Virol. 79 (22), 14451–14456. http://dx.doi.org/10.1128/JVI.79.22.14451-14456.2005.

de Haan, C.A.M., te Lintelo, E., Li, Z., Raaben, M., Wurdinger, T., Bosch, B.J., Rottier, P.J.M., 2006. Cooperative involvement of the S1 and S2 subunits of the murine coronavirus spike protein in receptor binding and extended host range. J. Virol. 80 (22), 10909–10918. http://dx.doi.org/10.1128/JVI.00950-06.

de Haan, C.A.M., Haijema, B.J., Masters, P.S., Rottier, P.J.M., 2008. Manipulation of the coronavirus genome using targeted RNA recombination with interspecies chimeric coronaviruses. Methods Mol. Biol. 454, 229–236. http://dx.doi.org/10.1007/978-1-59745-181-9_17.

Delmas, B., Gelfi, J., L'Haridon, R., Vogel, L.K., Sjöström, H., Norén, O., Laude, H., 1992. Aminopeptidase N is a major receptor for the entero-pathogenic coronavirus TGEV. Nature 357 (6377), 417–420. http://dx.doi.org/10.1038/357417a0.

Desmarets, L.M.B., Theuns, S., Roukaerts, I.D.M., Acar, D.D., Nauwynck, H.J., 2014. Role of sialic acids in feline enteric coronavirus infections. J. Gen. Virol. 95 (9), 1911–1918. http://dx.doi.org/10.1099/vir.0.064717-0.

Desmarets, L.M.B., Vermeulen, B.L., Theuns, S., Conceição-Neto, N., Zeller, M., Roukaerts, I.D.M., et al., 2016. Experimental feline enteric coronavirus infection reveals an aberrant infection pattern and shedding of mutants with impaired infectivity in enterocyte cultures. Sci. Rep. 6, 20022. http://dx.doi.org/10.1038/srep20022.

Drexler, J.F., Gloza-Rausch, F., Glende, J., Corman, V.M., Muth, D., Goettsche, M., et al., 2010. Genomic characterization of severe acute respiratory syndrome-related coronavirus in European bats and classification of coronaviruses based on partial RNA-dependent RNA polymerase gene sequences. J. Virol. 84 (21), 11336–11349. http://dx.doi.org/10.1128/JVI.00650-10.

Duquerroy, B.S., Vigouroux, A., Rottier, P.J.M., Rey, F.A., Berend, T., Bosch, J., 2005. Central ions and lateral asparagine/glutamine zippers stabilize the post-fusion hairpin conformation of the SARS coronavirus spike glycoprotein. Virology 335 (2), 276–285. http://dx.doi.org/10.1016/j.virol.2005.02.022.

Eckerle, I., Corman, V.M., Müller, M.A., Lenk, M., Ulrich, R.G., Drosten, C., 2014. Replicative capacity of MERS coronavirus in livestock cell lines. Emerg. Infect. Dis. 20 (2), 276–279. http://dx.doi.org/10.3201/eid2002.131182.

Eifart, P., Ludwig, K., Böttcher, C., de Haan, C.A.M., Rottier, P.J.M., Korte, T., Herrmann, A., 2007. Role of endocytosis and low pH in murine hepatitis virus strain A59 cell entry. J. Virol. 81 (19), 10758–10768. http://dx.doi.org/10.1128/JVI.00725-07.

Falzarano, D., de Wit, E., Feldmann, F., Rasmussen, A.L., Okumura, A., Peng, X., et al., 2014. Infection with MERS-CoV causes lethal pneumonia in the common marmoset. PLoS Pathog. 10 (8), e1004250. http://dx.doi.org/10.1371/journal.ppat.1004250.

Farsani, S.M.J., Dijkman, R., Jebbink, M.F., Goossens, H., Ieven, M., Deijs, M., et al., 2012. The first complete genome sequences of clinical isolates of human coronavirus 229E. Virus Genes 45 (3), 433–439. http://dx.doi.org/10.1007/s11262-012-0807-9.

Forni, D., Filippi, G., Cagliani, R., De Gioia, L., Pozzoli, U., Al-Daghri, N., et al., 2015. The heptad repeat region is a major selection target in MERS-CoV and related coronaviruses. Sci. Rep. 5, 14480. http://dx.doi.org/10.1038/srep14480.

Frana, M.F., Behnke, J.N., Sturman, L.S., Holmes, K.V., 1985. Proteolytic cleavage of the E2 glycoprotein of murine coronavirus: host-dependent differences in proteolytic cleavage and cell fusion. J. Virol. 56 (3), 912–920. Retrieved from, http://www.pubmedcentral.nih.gov/articlerender.fcgi?artid=252664&tool=pmcentrez&rendertype=abstract.

Gallagher, T.M., Buchmeier, M.J., 2001. Coronavirus spike proteins in viral entry and pathogenesis. Virology 279 (2), 371–374. http://dx.doi.org/10.1006/viro.2000.0757.

Gallagher, T.M., Buchmeier, M.J., Perlman, S., 1992. Cell receptor-independent infection by a neurotropic murine coronavirus. Virology 19 (1), 517–522. Retrieved from, http://www.ncbi.nlm.nih.gov/pubmed/1413526.

Gallagher, T.M., Buchmeier, M.J., Perlman, S., 1993. Dissemination of MHV4 (strain JHM) infection does not require specific coronavirus receptors. Adv. Exp. Med. Biol. 342, 279–284. Retrieved from, http://www.ncbi.nlm.nih.gov/pubmed/8209743.

Gao, J., Lu, G., Qi, J., Li, Y., Wu, Y., Deng, Y., et al., 2013. Structure of the fusion core and inhibition of fusion by a heptad repeat peptide derived from the S protein of Middle East respiratory syndrome coronavirus. J. Virol. 87 (24), 13134–13140. http://dx.doi.org/10.1128/JVI.02433-13.

Ge, X.Y., Li, J.L., Yang, X.L., Chmura, A.A., Zhu, G., Epstein, J.H., et al., 2013. Isolation and characterization of a bat SARS-like coronavirus that uses the ACE2 receptor. Nature 503 (7477), 535–538. http://dx.doi.org/10.1038/nature12711.

Guan, Y., Zheng, B.J., He, Y.Q., Liu, X.L., Zhuang, Z.X., Cheung, C.L., et al., 2003. Isolation and characterization of viruses related to the SARS coronavirus from animals in southern China. Science 302 (5643), 276–278. http://dx.doi.org/10.1126/science.1087139.

Haijema, B.J., Volders, H., Rottier, P.J.M., 2003. Switching species tropism: an effective way to manipulate the feline coronavirus genome. J. Virol. 77 (8), 4528–4538. http://dx.doi.org/10.1128/JVI.77.8.4528-4538.2003.

Herrewegh, A.A.P.M., Vennema, H., Horzinek, M.C., Rottier, P.J.M., de Groot, R.J., 1995. The molecular genetics of feline coronaviruses: comparative sequence analysis of the ORF7a/7b transcription unit of different biotypes. Virology 212 (2), 622–631.

Hofmann, H., Hattermann, K., Marzi, A., Gramberg, T., Geier, M., Krumbiegel, M., et al., 2004. S protein of severe acute respiratory syndrome-associated coronavirus mediates entry into hepatoma cell lines and is targeted by neutralizing antibodies in infected patients. J. Virol. 78 (12), 6134–6142. http://dx.doi.org/10.1128/JVI.78.12.6134-6142.2004.

Hu, B., Ge, X., Wang, L.-F., Shi, Z., 2015. Bat origin of human coronaviruses. Virol. J. 12 (1), 221. http://dx.doi.org/10.1186/s12985-015-0422-1.

Huynh, J., Li, S., Yount, B., Smith, A., Sturges, L., Olsen, J.C., et al., 2012. Evidence supporting a zoonotic origin of human coronavirus strain NL63. J. Virol. 86 (23), 12816–12825. http://dx.doi.org/10.1128/JVI.00906-12.

Inoue, Y., Tanaka, N., Tanaka, Y., Inoue, S., Morita, K., Zhuang, M., et al., 2007. Clathrin-dependent entry of severe acute respiratory syndrome coronavirus into target cells expressing ACE2 with the cytoplasmic tail deleted. J. Virol. 81 (16), 8722–8729. http://dx.doi.org/10.1128/JVI.00253-07.

Kirchdoerfer, R.N., Cottrell, C.A., Wang, N., Pallesen, J., Yassine, H.M., Turner, H.L., et al., 2016. Pre-fusion structure of a human coronavirus spike protein. Nature 531 (7592), 118–121. http://dx.doi.org/10.1038/nature17200.

Kolb, A.F., Hegyi, A., Siddell, S.G., 1997. Identification of residues critical for the human coronavirus 229E receptor function of human aminopeptidase N. J. Gen. Virol. 78 (11), 2795–2802.

Krempl, C., Schultze, B., Laude, H., 1997. Point mutations in the S protein connect the sialic acid binding activity with the enteropathogenicity of transmissible gastroenteritis coronavirus. J. Virol. 71 (4), 3285–3287.

Krueger, D.K., Kelly, S.M., Lewicki, D.N., Ruffolo, R., Gallagher, T.M., 2001. Variations in disparate regions of the murine coronavirus spike protein impact the initiation of membrane fusion. J. Virol. 75 (6), 2792–2802. http://dx.doi.org/10.1128/JVI.75.6.2792-2802.2001.

Künkel, F., Herrler, G., 1993. Structural and functional analysis of the surface protein of human coronavirus OC43. Virology 195 (1), 195–202.

Kuo, L., Godeke, G.J., Raamsman, M.J., Masters, P.S., Rottier, P.J., 2000. Retargeting of coronavirus by substitution of the spike glycoprotein ectodomain: crossing the host cell species barrier. J. Virol. 74 (3), 1393–1406. http://dx.doi.org/10.1128/JVI.74.3.1393-1406.2000.

Langereis, M.A., van Vliet, A.L.W., Boot, W., de Groot, R.J., 2010. Attachment of mouse hepatitis virus to *O*-acetylated sialic acid is mediated by hemagglutinin-esterase and not by the spike protein. J. Virol. 84 (17), 8970–8974. http://dx.doi.org/10.1128/JVI.00566-10.

Lau, S.K.P., Woo, P.C.Y., Li, K.S.M., Huang, Y., Wang, M., Lam, C.S.F., et al., 2007. Complete genome sequence of bat coronavirus HKU2 from Chinese horseshoe bats revealed a much smaller spike gene with a different evolutionary lineage from the rest of the genome. Virology 367 (2), 428–439. http://dx.doi.org/10.1016/j.virol.2007.06.009.

Lee, C., 2015. Porcine epidemic diarrhea virus: an emerging and re-emerging epizootic swine virus. Virol. J. 12 (1), 193. http://dx.doi.org/10.1186/s12985-015-0421-2.

Lee, J.E., Fusco, M.L., Hessell, A.J., Oswald, W.B., Burton, D.R., Saphire, E.O., 2008. Structure of the ebola virus glycoprotein bound to an antibody from a human survivor. Nature 454 (7201), 177–182. http://dx.doi.org/10.1038/nature07082.

Levis, R., Cardellichio, C.B., Scanga, C.A., Compton, S.R., Holmes, K.V., 1995. Multiple receptor-dependent steps determine the species specificity of HCV-229E infection. Adv. Exp. Med. Biol. 380, 337–343. Retrieved from, http://www.ncbi.nlm.nih.gov/pubmed/8830504.

Lewis, C.S., Porter, E., Matthews, D., Kipar, A., Tasker, S., Helps, C.R., Siddell, S.G., 2015. Genotyping coronaviruses associated with feline infectious peritonitis. J. Gen. Virol. 96 (Pt. 6), 1358–1368. http://dx.doi.org/10.1099/vir.0.000084.

Li, F., 2012. Evidence for a common evolutionary origin of coronavirus spike protein receptor-binding subunits. J. Virol. 86 (5), 2856–2858. http://dx.doi.org/10.1128/JVI.06882-11.

Li, F., 2015. Receptor recognition mechanisms of coronaviruses: a decade of structural studies. J. Virol. 89 (4), 1954–1964. http://dx.doi.org/10.1128/JVI.02615-14.

Li, F., Li, W., Farzan, M., Harrison, S.C., 2005a. Structure of SARS coronavirus spike receptor-binding domain complexed with receptor. Science 309 (5742), 1864–1868. http://dx.doi.org/10.1126/science.1116480.

Li, W., Zhang, C., Sui, J., Kuhn, J.H., Moore, M.J., Luo, S., et al., 2005b. Receptor and viral determinants of SARS-coronavirus adaptation to human ACE2. EMBO J. 24 (8), 1634–1643. http://dx.doi.org/10.1038/sj.emboj.7600640.

Li, W., Wong, S.-K., Li, F., Kuhn, J.H., Huang, I.-C., Choe, H., Farzan, M., 2006. Animal origins of the severe acute respiratory syndrome coronavirus: insight from ACE2-S-protein interactions. J. Virol. 80 (9), 4211–4219. http://dx.doi.org/10.1128/JVI.80.9.4211-4219.2006.

Li, W., Wicht, O., van Kuppeveld, F.J.M., He, Q., Rottier, P.J.M., Bosch, B.-J., 2015. A single point mutation creating a furin cleavage site in the spike protein renders porcine epidemic diarrhea coronavirus trypsin-independent for cell entry and fusion. J. Virol. 89 (15), 8077–8081. http://dx.doi.org/10.1128/JVI.00356-15.

Licitra, B.N., Millet, J.K., Regan, A.D., Hamilton, B.S., Rinaldi, V.D., Duhamel, G.E., Whittaker, G.R., 2013. Mutation in spike protein cleavage site and pathogenesis of feline coronavirus. Emerg. Infect. Dis. 19 (7), 1066–1073. http://dx.doi.org/10.3201/eid1907.121094.

Lin, X., Eddy, N.R., Noel, J.K., Whitford, P.C., Wang, Q., Ma, J., Onuchic, J.N., 2014. Order and disorder control the functional rearrangement of influenza hemagglutinin. Proc. Natl. Acad. Sci. U.S.A. 111, 12049–12054. http://dx.doi.org/10.1073/pnas.1412849111.

Lu, G., Hu, Y., Wang, Q., Qi, J., Gao, F., Li, Y., et al., 2013. Molecular basis of binding between novel human coronavirus MERS-CoV and its receptor CD26. Nature 500 (7461), 227–231. http://dx.doi.org/10.1038/nature12328.

Lu, L., Liu, Q., Zhu, Y., Chan, K.-H., Qin, L., Li, Y., et al., 2014. Structure-based discovery of Middle East respiratory syndrome coronavirus fusion inhibitor. Nat. Commun. 5, 3067. http://dx.doi.org/10.1038/ncomms4067.

Matsuyama, S., Taguchi, F., 2009. Two-step conformational changes in a coronavirus envelope glycoprotein mediated by receptor binding and proteolysis. J. Virol. 83 (21), 11133–11141. http://dx.doi.org/10.1128/JVI.00959-09.

McRoy, W.C., Baric, R.S., 2008. Amino acid substitutions in the S2 subunit of mouse hepatitis virus variant V51 encode determinants of host range expansion. J. Virol. 82 (3), 1414–1424. http://dx.doi.org/10.1128/JVI.01674-07.

Millet, J.K., Whittaker, G.R., 2015. Host cell proteases: critical determinants of coronavirus tropism and pathogenesis. Virus Res. 202, 120–134. http://dx.doi.org/10.1016/j.virusres.2014.11.021.

Mou, H., Raj, V.S., van Kuppeveld, F.J.M., Rottier, P.J.M., Haagmans, B.L., Bosch, B.J., 2013. The receptor binding domain of the new Middle East respiratory syndrome coronavirus maps to a 231-residue region in the spike protein that efficiently elicits neutralizing antibodies. J. Virol. 87 (16), 9379–9383. http://dx.doi.org/10.1128/JVI.01277-13.

Müller, M.A., Raj, V.S., Muth, D., Meyer, B., Kallies, S., Smits, S.L., et al., 2012. Human coronavirus EMC does not require the SARS-coronavirus receptor and maintains broad replicative capability in mammalian cell lines. mBio 3 (6). http://dx.doi.org/10.1128/mBio.00515-12. e00515-12.

Myrrha, L.W., Silva, F.M.F., de Oliveira Peternelli, E.F., Junior, A.S., Resende, M., de Almeida, M.R., 2011. The paradox of feline coronavirus pathogenesis: a review. Adv. Virol. 2011, 109849. http://dx.doi.org/10.1155/2011/109849.

Navas-Martin, S., Hingley, S.T., Weiss, S.R., 2005. Murine coronavirus evolution in vivo: functional compensation of a detrimental amino acid substitution in the receptor binding domain of the spike glycoprotein. J. Virol. 79 (12), 7629–7640. http://dx.doi.org/10.1128/JVI.79.12.7629-7640.2005.

Nomura, R., Kiyota, A., Suzaki, E., Kataoka, K., Ohe, Y., Miyamoto, K., et al., 2004. Human coronavirus 229E binds to CD13 in rafts and enters the cell through caveolae. J. Virol. 78 (16), 8701–8708. http://dx.doi.org/10.1128/JVI.78.16.8701-8708.2004.78/16/8701 [pii].

Ou, X., Zheng, W., Shan, Y., Mu, Z., Dominguez, S.R., Holmes, K.V., Qian, Z., 2016. Identification of the fusion peptide-containing region in betacoronavirus spike glycoproteins. J. Virol. 90 (12), 5586–5600. http://dx.doi.org/10.1128/JVI.00015-16. JVI.00015–16.

Pedersen, N.C., 2014. An update on feline infectious peritonitis: virology and immunopathogenesis. Vet. J. 201 (2), 123–132. http://dx.doi.org/10.1016/j.tvjl.2014.04.017.

Peng, G., Sun, D., Rajashankar, K.R., Qian, Z., Holmes, K.V., Li, F., 2011. Crystal structure of mouse coronavirus receptor-binding domain complexed with its murine receptor. Proc. Natl. Acad. Sci. U.S.A. 108 (26), 10696–10701. http://dx.doi.org/10.1073/pnas.1104306108.

Peng, G., Xu, L., Lin, Y.L., Chen, L., Pasquarella, J.R., Holmes, K.V., Li, F., 2012. Crystal structure of bovine coronavirus spike protein lectin domain. J. Biol. Chem. 287 (50), 41931–41938. http://dx.doi.org/10.1074/jbc.M112.418210.

Phillips, J.J., Weiss, S.R., 2001. MHV neuropathogenesis: the study of chimeric S genes and mutations in the hypervariable region. Adv. Exp. Med. Biol. 494, 115–119. Retrieved from, http://www.ncbi.nlm.nih.gov/pubmed/11774454.

Promkuntod, N., van Eijndhoven, R., de Vrieze, G., Gröne, A., Verheije, M., 2014. Mapping of the receptor-binding domain and amino acids critical for attachment in the spike protein of avian coronavirus infectious bronchitis virus. Virology 448, 26–32. http://dx.doi.org/10.1016/j.virol.2013.09.018.

Qu, X.X., Hao, P., Song, X.J., Jiang, S.M., Liu, Y.X., Wang, P.G., et al., 2005. Identification of two critical amino acid residues of the severe acute respiratory syndrome coronavirus spike protein for its variation in zoonotic tropism transition via a double substitution strategy. J. Biol. Chem. 280 (33), 29588–29595. http://dx.doi.org/10.1074/jbc.M500662200.

Racaniello, V.R., Skalka, A.M., Flint, J., Rall, G.F., 2015. Principles of Virology, Bundle. American Society of Microbiology, Washington, DC. http://dx.doi.org/10.1128/9781555819521.

Raj, V.S., Mou, H., Smits, S.L., Dekkers, D.H.W., Müller, M.A., Dijkman, R., et al., 2013. Dipeptidyl peptidase 4 is a functional receptor for the emerging human coronavirus-EMC. Nature 495, 251–254. http://dx.doi.org/10.1038/nature12005.

Raj, V.S., Smits, S.L., Provacia, L.B., van den Brand, J.M.A., Wiersma, L., Ouwendijk, W.J.D., et al., 2014. Adenosine deaminase acts as a natural antagonist for dipeptidyl peptidase 4-mediated entry of the Middle East respiratory syndrome coronavirus. J. Virol. 88 (3), 1834–1838. http://dx.doi.org/10.1128/JVI.02935-13.

Reguera, J., Santiago, C., Mudgal, G., Ordoño, D., Enjuanes, L., Casasnovas, J.M., 2012. Structural bases of coronavirus attachment to host aminopeptidase N and its inhibition by neutralizing antibodies. PLoS Pathog. 8 (8), e1002859. http://dx.doi.org/10.1371/journal.ppat.1002859.

Ren, W., Qu, X., Li, W., Han, Z., Yu, M., Zhou, P., et al., 2008. Difference in receptor usage between severe acute respiratory syndrome (SARS) coronavirus and SARS-like coronavirus of bat origin. J. Virol. 82 (4), 1899–1907. http://dx.doi.org/10.1128/JVI.01085-07.

Reusken, C.B., Haagmans, B.L., Müller, M.A., Gutierrez, C., Godeke, G.-J., Meyer, B., et al., 2013. Middle East respiratory syndrome coronavirus neutralising serum antibodies in dromedary camels: a comparative serological study. Lancet Infect. Dis. 13 (10), 859–866. http://dx.doi.org/10.1016/S1473-3099(13)70164-6.

Roberts, A., Deming, D., Paddock, C.D., Cheng, A., Yount, B., Vogel, L., et al., 2007. A mouse-adapted SARS-coronavirus causes disease and mortality in BALB/c mice. PLoS Pathog. 3 (1), e5. http://dx.doi.org/10.1371/journal.ppat.0030005.

Robertson, A.L., Headey, S.J., Ng, N.M., Wijeyewickrema, L.C., Scanlon, M.J., Pike, R.N., Bottomley, S.P., 2016. Protein unfolding is essential for cleavage within the α-helix of a model protein substrate by the serine protease, thrombin. Biochimie 122, 227–234. http://dx.doi.org/10.1016/j.biochi.2015.09.021.

Rottier, P.J.M., Nakamura, K., Schellen, P., Volders, H., Haijema, B.J., 2005. Acquisition of macrophage tropism during the pathogenesis of feline infectious peritonitis is determined by mutations in the feline coronavirus spike protein. J. Virol. 79 (22), 14122–14130. http://dx.doi.org/10.1128/JVI.79.22.14122-14130.2005.

Saeki, K., Ohtsuka, N., Taguchi, F., 1997. Identification of spike protein residues of murine coronavirus responsible for receptor-binding activity by use of soluble receptor-resistant mutants. J. Virol. 71 (12), 9024–9031. Retrieved from, http://www.ncbi.nlm.nih.gov/pubmed/9371559.

Schickli, J.H., Zelus, B.D., Wentworth, D.E., Sawicki, S.G., Holmes, K.V., 1997. The murine coronavirus mouse hepatitis virus strain A59 from persistently infected murine cells exhibits an extended host range. J. Virol. 71 (12), 9499–9507. Retrieved from, http://www.ncbi.nlm.nih.gov/pubmed/9371612.

Schultze, B., Gross, H.-J., Brossmer, R., Herrler, G., 1991. The S protein of bovine coronavirus is a hemagglutinin recognizing 9-0-acetylated sialic acid as a receptor determinant. J. Virol. 65 (11), 6232–6237.

Schultze, B., Krempl, C., Ballesteros, M.L., Shaw, L., Schauer, R., Enjuanes, L., Herrler, G., 1996. Transmissible gastroenteritis coronavirus, but not the related porcine respiratory coronavirus, has a sialic acid (N-glycolylneuraminic acid) binding activity. J. Virol. 70 (8), 5634–5637. Retrieved from, http://www.ncbi.nlm.nih.gov/pubmed/8764078.

Schwegmann-Wessels, C., Zimmer, G., Schroder, B., Breves, G., Herrler, G., 2003. Binding of transmissible gastroenteritis coronavirus to brush border membrane sialoglycoproteins. J. Virol. 77 (21), 11846–11848. http://dx.doi.org/10.1128/JVI.77.21.11846.

Simmons, G., Gosalia, D.N., Rennekamp, A.J., Reeves, J.D., Diamond, S.L., Bates, P., 2005. Inhibitors of cathepsin L prevent severe acute respiratory syndrome coronavirus entry. Proc. Natl. Acad. Sci. U.S.A. 102 (33), 11876–11881.

Song, H.-D., Tu, C.-C., Zhang, G.-W., Wang, S.-Y., Zheng, K., Lei, L.-C., et al., 2005. Cross-host evolution of severe acute respiratory syndrome coronavirus in palm civet and human. Proc. Natl. Acad. Sci. U.S.A. 102 (7), 2430–2435. http://dx.doi.org/10.1073/pnas.0409608102.

Song, D., Moon, H., Kang, B., 2015. Porcine epidemic diarrhea: a review of current epidemiology and available vaccines. Clin. Exp. Vaccine Res. 4 (2), 166–176. http://dx.doi.org/10.7774/cevr.2015.4.2.166.

Supekar, V.M., Bruckmann, C., Ingallinella, P., Bianchi, E., Pessi, A., Carfi, A., 2004. Structure of a proteolytically resistant core from the severe acute respiratory syndrome coronavirus S2 fusion protein. Proc. Natl. Acad. Sci. U.S.A. 101 (52), 17958–17963. http://dx.doi.org/10.1073/pnas.0406128102.

Taguchi, F., Matsuyama, S., 2002. Soluble receptor potentiates receptor-independent infection by murine coronavirus. J. Virol. 76 (3), 950–958. Retrieved from, http://www.ncbi.nlm.nih.gov/pubmed/11773370.

Terada, Y., Shiozaki, Y., Shimoda, H., Mahmoud, H.Y.A.H., Noguchi, K., Nagao, Y., et al., 2012. Feline infectious peritonitis virus with a large deletion in the 5′-terminal region of the spike gene retains its virulence for cats. J. Gen. Virol. 93 (Pt. 9), 1930–1934. http://dx.doi.org/10.1099/vir.0.043992-0.

Terada, Y., Matsui, N., Noguchi, K., Kuwata, R., Shimoda, H., Soma, T., et al., 2014. Emergence of pathogenic coronaviruses in cats by homologous recombination between feline and canine coronaviruses. PLoS One 9 (9), e106534. http://dx.doi.org/10.1371/journal.pone.0106534.

Tresnan, D.B., Holmes, K.V., 1998. Feline aminopeptidase N is a receptor for all group I coronaviruses. Adv. Exp. Med. Biol. 440, 69–75. Retrieved from, http://www.ncbi.nlm.nih.gov/pubmed/9782266.

Tresnan, D.B., Levis, R., Holmes, K.V., 1996. Feline aminopeptidase N serves as a receptor for feline, canine, porcine, and human coronaviruses in serogroup I. J. Virol. 70 (12), 8669–8674. Retrieved from, http://www.pubmedcentral.nih.gov/articlerender.fcgi?artid=190961&tool=pmcentrez&rendertype=abstract.

Tsai, J.C., De Groot, L., Pinon, J.D., Iacono, K.T., Phillips, J.J., Seo, S.H., et al., 2003. Amino acid substitutions within the heptad repeat domain 1 of murine coronavirus spike protein restrict viral antigen spread in the central nervous system. Virology 312 (2), 369–380. http://dx.doi.org/10.1016/S0042-6822(03)00248-4.

Tu, C., Crameri, G., Kong, X., Chen, J., Sun, Y., Yu, M., et al., 2004. Antibodies to SARS coronavirus in civets. Emerg. Infect. Dis. 10 (12), 2244–2248. http://dx.doi.org/10.3201/eid1012.040520.

Tusell, S.M., Schittone, S.A., Holmes, K.V., 2007. Mutational analysis of aminopeptidase N, a receptor for several group 1 coronaviruses, identifies key determinants of viral host range. J. Virol. 81 (3), 1261–1273. http://dx.doi.org/10.1128/JVI.01510-06.

van Doremalen, N., Miazgowicz, K.L., Milne-Price, S., Bushmaker, T., Robertson, S., Scott, D., et al., 2014. Host species restriction of Middle East respiratory syndrome coronavirus through its receptor, dipeptidyl peptidase 4. J. Virol. 88 (16), 9220–9232. http://dx.doi.org/10.1128/JVI.00676-14.

Vijgen, L., Keyaerts, E., Lemey, P., Maes, P., Van Reeth, K., Nauwynck, H., et al., 2006. Evolutionary history of the closely related group 2 coronaviruses: porcine hemagglutinating encephalomyelitis virus, bovine coronavirus, and human coronavirus OC43. J. Virol. 80 (14), 7270–7274. http://dx.doi.org/10.1128/JVI.02675-05.

Vlasak, R., Luytjes, W., Spaan, W., Palese, P., 1988. Human and bovine coronaviruses recognize sialic acid-containing receptors similar to those of influenza C viruses. Proc. Natl. Acad. Sci. U.S.A. 85 (12), 4526–4529. http://dx.doi.org/10.1073/pnas.85.12.4526.

Walls, A.C., Tortorici, M.A., Bosch, B.-J., Frenz, B., Rottier, P.J.M., DiMaio, F., et al., 2016. Cryo-electron microscopy structure of a coronavirus spike glycoprotein trimer. Nature 531 (7592), 114–117. http://dx.doi.org/10.1038/nature16988.

Wang, F.I., Fleming, J.O., Lai, M.M., 1992. Sequence analysis of the spike protein gene of murine coronavirus variants: study of genetic sites affecting neuropathogenicity. Virology 186 (2), 742–749. Retrieved from, http://www.ncbi.nlm.nih.gov/pubmed/1310195.

Wang, H., Yang, P., Liu, K., Guo, F., Zhang, Y., Zhang, G., Jiang, C., 2008. SARS coronavirus entry into host cells through a novel clathrin- and caveolae-independent endocytic pathway. Cell Res. 18 (2), 290–301. http://dx.doi.org/10.1038/cr.2008.15.

Wang, N., Shi, X., Jiang, L., Zhang, S., Wang, D., Tong, P., et al., 2013. Structure of MERS-CoV spike receptor-binding domain complexed with human receptor DPP4. Cell Res. 23 (8), 986–993. http://dx.doi.org/10.1038/cr.2013.92.

Wang, Q., Qi, J., Yuan, Y., Xuan, Y., Han, P., Wan, Y., et al., 2014. Bat origins of MERS-CoV supported by bat coronavirus HKU4 usage of human receptor CD26. Cell Host Microbe 16 (3), 328–337. http://dx.doi.org/10.1016/j.chom.2014.08.009.

WHO | Middle East respiratory syndrome coronavirus (MERS-CoV) – Saudi Arabia, 2016. WHO.

Widagdo, W., Raj, V.S., Schipper, D., Kolijn, K., van Leenders, G.J.L.H., Bosch, B.J., Bensaid, A., 2016. Differential expression of the Middle East respiratory syndrome coronavirus receptor in the upper respiratory tracts of humans and dromedary camels. J. Virol. 90 (9), 4838–4842. http://dx.doi.org/10.1128/JVI.02994-15. Editor.

Woo, P.C.Y., Lau, S.K.P., Lam, C.S.F., Lau, C.C.Y., Tsang, A.K.L., Lau, J.H.N., et al., 2012. Discovery of seven novel mammalian and avian coronaviruses in the genus deltacoronavirus supports bat coronaviruses as the gene source of alphacoronavirus and betacoronavirus and avian coronaviruses as the gene source of gammacoronavirus and deltacoronavirus. J. Virol. 86 (7), 3995–4008. http://dx.doi.org/10.1128/JVI.06540-11.

Wu, K., Li, W., Peng, G., Li, F., 2009. Crystal structure of NL63 respiratory coronavirus receptor-binding domain complexed with its human receptor. Proc. Natl. Acad. Sci. U.S.A. 106 (47), 19970–19974. http://dx.doi.org/10.1073/pnas.0908837106.

Xu, Y., Lou, Z., Liu, Y., Pang, H., Tien, P., Gao, G.F., Rao, Z., 2004. Crystal structure of severe acute respiratory syndrome coronavirus spike protein fusion core. J. Biol. Chem. 279 (47), 49414–49419. http://dx.doi.org/10.1074/jbc.M408782200.

Yamada, Y., Liu, D.X., 2009. Proteolytic activation of the spike protein at a novel RRRR/S motif is implicated in furin-dependent entry, syncytium formation, and infectivity of coronavirus infectious bronchitis virus in cultured cells. J. Virol. 83 (17), 8744–8758. http://dx.doi.org/10.1128/JVI.00613-09.

Yamada, Y., Liu, X.B., Fang, S.G., Tay, F.P.L., Liu, D.X., 2009. Acquisition of cell-cell fusion activity by amino acid substitutions in spike protein determines the infectivity of a coronavirus in cultured cells. PLoS One 4 (7), e6130. http://dx.doi.org/10.1371/journal.pone.0006130.

Yang, Y., Du, L., Liu, C., Wang, L., Ma, C., Tang, J., et al., 2014. Receptor usage and cell entry of bat coronavirus HKU4 provide insight into bat-to-human transmission of MERS coronavirus. Proc. Natl. Acad. Sci. U.S.A. 111 (34), 12516–12521. http://dx.doi.org/10.1073/pnas.1405889111.

Yang, Y., Liu, C., Du, L., Jiang, S., Shi, Z., Baric, R.S., Li, F., 2015. Two mutations were critical for bat-to-human transmission of Middle East respiratory syndrome coronavirus. J. Virol. 89 (17), 9119–9123. http://dx.doi.org/10.1128/JVI.01279-15.

Zelus, B.D., Schickli, J.H., Blau, D.M., Weiss, S.R., Holmes, K.V., 2003. Conformational changes in the spike glycoprotein of murine coronavirus are induced at 37 degrees C either by soluble murine CEACAM1 receptors or by pH 8. J. Virol. 77 (2), 830–840. http://dx.doi.org/10.1128/JVI.77.2.830-840.2003.

Editorial

Regulation of T follicular helper cells by ICOS

Andreas Hutloff

T follicular helper (TFH) cells are gatekeepers of the humoral immune response. Without help from this $CD4^+$ T cell subset, B cells cannot differentiate into high-affinity memory B cells and antibody-producing long-lived plasma cells which are the basis of protective immune responses. At the same time, dysregulated TFH cell responses are causative for many autoimmune disorders (reviewed in [1]). The inducible T cell costimulator ICOS, which is structurally and functionally related to CD28, has been known for many years as an important regulator of TFH cells. ICOS knock-out mice as well as ICOS-deficient patients have only few TFH cells and very small germinal centers upon immunization, which results in severely compromised antigen-specific immunoglobulin levels and the phenotype of common variable immunodeficiency in humans (reviewed in [2]). However, the molecular mechanisms responsible for this defect were unknown until recently. Now, within the last few months a series of independent publications unraveled the complete signaling pathway of how ICOS regulates TFH cells [3-6].

ICOS exerts its costimulatory function via activation of the phosphatidylinositol-3- (PI3-) kinase which results in activation of Akt, also known as protein kinase B (Figure 1). Akt phosphorylates the transcription factor Foxo1, which is thereby retained in the cytoplasm [5, 6]. Among the many Foxo1 downstream targets, the transcription factor Klf2 turned out to be of special importance for TFH cells [4, 6]. Knock-out of Klf2 results in strongly enhanced number of TFH cells [4]. Klf2 directly binds to the promotor regions of the chemokine receptors Cxcr5 and Ccr7, the cell homing receptors Sell (encoding CD62L) and Selplg (encoding PSGL-1), and the sphingosine-1-phosphate receptor (S1pr1) [6]. Klf2 has to be expressed at low levels to maintain the typical expression pattern of homing receptors which keep TFH cells in the B cell follicle. This means that ICOS costimulation does not directly regulate any of the lineage-defining transcription factors for TFH cells like Bcl-6 and Ascl-2, but is important for the correct localization of TFH cells within secondary lymphoid organs. In addition, Klf2 promotes expression of the transcription factors T-bet and Gata3, which promote differentiation of Th1 and Th2 cells, respectively [4, 6].

Beside the ICOS - Klf2 axis, a second independent pathway exists. Although the cytoplasmic tail of ICOS preferentially recruits the p50α/p110δ isoform of PI3 kinase [2], activation of p85α is also possible. This PI3 kinase subunit can bind intracellular osteopontin (OPN-i), which facilitates nuclear translocation [3]. In the nucleus, OPN-i dimerizes with Bcl-6 and protects it from proteasomal degradation. However, this OPN-i and the above Klf2 pathway do act at different times. Upon ICOS signaling blockade, Klf2 is upregulated within a few hours and TFH cells lose their typical homing receptor pattern in less than 24 hours [6]. In contrast, complete degradation of Bcl-6 takes several days [3, 6]. Therefore, the ICOS - Klf2 axis first leads to emigration of TFH cells out of the B cell follicle (and thereby to a loss of function), whereas the osteopontin pathway acts as a second strike pathway eliminating the lineage-defining transcription factor Bcl-6.

Another important finding especially for potential therapeutic applications is that ICOS and the structurally related CD28 molecule act in different phases of TFH cell differentiation [6]. Blockade of the CD28 pathway using a soluble CTLA-4-Ig chimera (Abatacept) is already in clinical use for treatment of autoimmune disorders, whereas blockade of the ICOS pathway is under clinical evaluation. Unlike CD28, ICOS does not regulate any of the early differentiation steps of naive T cells into TFH

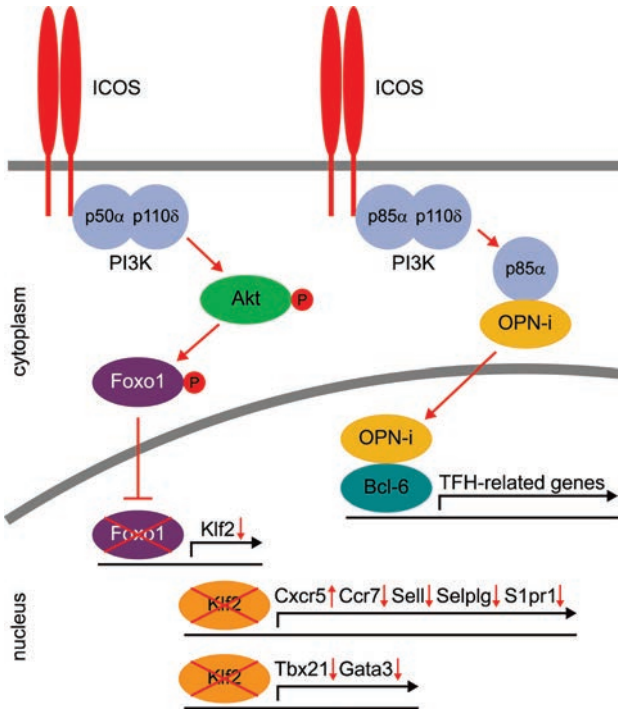

Figure 1: Signaling pathway for ICOS costimulation in TFH cells.

cells, such as upregulation of Bcl-6. Instead, ICOS - but no longer CD28 - is important to maintain the phenotype of already differentiated TFH cells [6]. This unique role of ICOS for later phases of the immune reaction makes this costimulatory molecule very attractive for therapeutic intervention. For vaccination purposes, persistence of TFH cells and thereby prolongation of the germinal center reaction would be advantageous, whereas for the treatment of autoimmune diseases it is desired to remove already existing autoreactive TFH cells.

In this context, it will be important to see whether TFH cell irretrievable lose their phenotype upon ICOS costimulation blockade. This loss of TFH cell markers resembles the phenotype of TFH memory cells, which also strongly downregulate CXCR5 and Bcl-6 in the absence of antigen [7]. However, TFH memory cells are able to rapidly regain their phenotype upon secondary antigen contact. Therefore, following-up the fate of converted TFH cells upon ICOS costimulation blockade will be an important area of future research.

Andreas Hutloff: Chronic Immune Reactions, German Rheumatism Research Centre (DRFZ), a Leibniz Institute, Berlin, Germany

***Correspondence to**: Andreas Hutloff, **email** hutloff@drfz.de*

Keywords: Immunology and Microbiology Section, Immune response, Immunity

***Received**: June 29, 2015*

***Published**: July 09, 2015*

REFERENCES

1. Ueno H et al. Nat Immunol. 2015; 16: 142-152.
2. Simpson TR et al. Curr Opin Immunol. 2010; 22: 326-332.
3. Leavenworth JW et al. Nat Immunol. 2015; 16: 96-106.
4. Lee JY et al. Immunity. 2015; 42: 252-264.
5. Stone EL et al. Immunity. 2015; 42: 239-251.
6. Weber JP et al. J Exp Med. 2015; 212: 217-233.
7. Weber JP et al. Eur J Immunol. 2012; 42: 1981-1988.

Available online at www.sciencedirect.com
SCIENCE DIRECT
Vaccine 24 (2006) 3057–3062
Vaccine
www.elsevier.com/locate/vaccine

Short communication

In vivo monitoring of DNA vaccine gene expression using firefly luciferase as a naked DNA

Yong Hyun Jeon [a,c,d], Yun Choi [b,c], Joo Hyun Kang [a,d,*], June-Key Chung [a,c,d], Yong Jin Lee [a,c,d], Chul Woo Kim [b,c], Jae Min Jeong [a,c,d], Dong Soo Lee [a,d], Myung Chul Lee [a]

[a] *Department of Nuclear Medicine, Seoul National University College of Medicine, Seoul, Korea*
[b] *Department of Pathology, Seoul National University College of Medicine, Seoul, Korea*
[c] *Department of Tumor Biology, Seoul National University College of Medicine, Seoul, Korea*
[d] *Laboratory of Molecular Imaging and Therapy of Cancer Research Institute, Seoul National University College of Medicine, Seoul, Korea*

Received 25 November 2005; received in revised form 6 January 2006; accepted 10 January 2006
Available online 30 January 2006

Abstract

The administration of naked DNA into animals is increasing as a research tool to develop DNA vaccine. To monitor the distribution and duration of gene expression of a DNA vaccine in living organisms, we used the naked DNA encoding firefly luciferase (F*luc*) as an imaging reporter gene, and evaluated in vivo bioluminescent images in a murine model. We observed bioluminescence at the injection site and at inguinal lymph node from 10 h to 24 h post-injection when DNA vaccine encoding F*luc* (pcDNA3.1-F*luc*) was injected into the bilateral posterior flanks in mice. F*luc* gene expressions at injection sites and unilateral posterior flank inguinal lymph node were also confirmed by RT-PCR. However, when pcDNA3.1-F*luc* was injected into the mid-dorsum bioluminescent signals were observed at the injection site for up to 14 days post-injection, but no bioluminescent signals were detected in inguinal lymph nodes. Concurrent mRNA expressions of F*luc* gene at injection sites but not at inguinal lymph nodes were confirmed by RT-PCR. These findings suggest that optical imaging using F*luc* could be useful for monitoring the location, intensity and duration of gene expression of naked DNA vaccines in living animals non-invasively and repetitively.

Keywords: Firefly luciferase; In vivo visualization; DNA vaccine gene expression

1. Introduction

DNA vaccines comprised of a bacterial plasmid encoding a variety of viral, bacterial and parasitic antigens have emerged as an immunotherapy modality for small animals or human. Immunization with DNA vaccine results in effective humoral and cellular immune responses that protect against disease in pre-clinical models of infectious diseases, cancer, and autoimmunity [1–3]. As compared with radiotherapy and chemotherapy, DNA vaccines have few side effects, and therapy can be conducted in parallel with conventional therapies.

Various methods such as the gene gun, skin patch, direct injection, and electroporation techniques via intramuscular, intradermal, or intra-pinna routes have been examined to deliver DNA vaccines into living organisms [4]. These methods and routes aim to increase host immune response. When DNA vaccine is injected into a target site and transfected into antigen presenting cells (APCs) without being degraded, a strong immune response may ensue in the host. However, if injected DNA does not migrate to an immune-related organ or is degraded by other factors, an effective immune response may be ineffective. Moreover, the fate of DNA vaccines may be evaluated by determining their effective distribution or expression in the host following vaccination [5].

Some researchers have reported on the distributions and expressional durations of DNA vaccine using β-galactosidase

Abbreviation: F*luc*, firefly luciferase

* Corresponding author. Tel.: +82 2 3668 7067; fax: +82 2 745 7690.
E-mail address: kang2325@snu.ac.kr (J.H. Kang).

0264-410X/$ – see front matter © 2006 Elsevier Ltd. All rights reserved.
doi:10.1016/j.vaccine.2006.01.033

administered via various injection routes [6–8]. It has been well shown that gene expression is detectable at the injection site and in other organs by invasive methods, such as, in situ hybridization, immunohistochemistry, and RT-PCR. These invasive techniques require that experimental animals must be sacrificed and organs extracted to confirm the gene expressions of such vaccines.

However, to obtain the data on consistent DNA vaccine gene expression in living animals, in vivo real-time monitoring of DNA vaccine gene expression might be required. Therefore, we investigated the use of an in vivo imaging method based on an optical imaging reporter gene, firefly luciferase (F*luc*). Luciferase emits light when it catalyzes its substrate, D-luciferin, in the presence of ATP, and this makes it possible to obtain bioluminescent images of animals using a hypersensitive cooled charge-coupled device camera [9]. Several groups have reported on the in vivo imaging of F*luc* in living animals during tumor metastasis, gene therapy, and stem cell trafficking [10–17].

In this study, we undertook this study to monitor the distribution and duration of gene expression of a naked DNA vaccine administered intradermally in the posterior flank and in the mid dorsum using F*luc* and an in vivo imaging system.

2. Materials and methods

2.1. Animals

Specific pathogen-free 6-week-old female BALB/c mice were obtained from SLC Inc. (Japan). All experimental animals were housed under specific pathogen-free conditions and handled in accord with the guidelines of the Seoul National University Animal Research Committee.

2.2. Expression vector and plasmid preparation

F*luc* cDNA was amplified from plasmid pIRES-F*Luc* using forward primer 5′-CCCAAGCTTATGGAAGACGCCAAAAACAT and reverse primer 5′-CCCCTCGAGTTACAATTTGGACTTTCCGC. Amplification products were treated with *Hin*dIII and *Xho*I restriction enzymes and subcloned downstream of the internal CMV promoter between corresponding sites of pcDNA3.1 (+) (Invitrogen, Grand Island, NY) to produce pcDNA3.1-F*luc*. Plasmid DNA was amplified in *E. coli* DH5α and purified by large-scale plasmid preparations using endotoxin-free Giga Prep columns (QIAGEN, Chatsworth, CA). DNA was dissolved in endotoxin-free TE buffer for storage.

2.3. Immunization with pcDNA3.1-Fluc for monitoring Fluc gene expression

To monitor F*luc* gene expression in vivo, pcDNA3.1-F*luc* (100 μg/100 μl) were intradermally injected into bilateral posterior flanks and in the mid dorsum.

2.4. Imaging in living mice

The IVIS200 imaging system (Xenogen Corp., Alameda, CA, USA), which included an optical CCD camera mounted on a light-tight specimen chamber, was used for data acquisition and analysis. Firefly D-luciferin potassium salt, the F*luc* substrate, was purchased from Xenogen, and diluted to 3 mg/100 μl in PBS before use. Mice were intraperitoneally injected with 100 μl of this D-luciferin solution. A mouse was placed in a specimen chamber with the CCD camera mounted and cooled to −105 °C, with a field of view (FOV) set at 26 cm above the sample shelf. Light emitted by luciferase in mice was then measured. Gray scale photographic images and bioluminescent color images were superimposed using LIVINGIMAGE V. 2.12 software overlay (Xenogen Corp., Alameda, CA, USA) and IGOR image analysis software. Bioluminescence signals are expressed in units of photons per cubic centimeter per second per steradian ($P/cm^2\ s^{-1}\ sr^{-1}$). For the monitoring of pcDNA3.1-F*luc* gene expression, mice were repeatedly imaged at 4, 10, 16, and 24 h, and at 3, 7, 11, and 14 days after DNA injection at two sites (bilateral posterior flank and mid-dorsum) by using the CCD camera to acquire photons 20 min after the intraperitoneal injection of 3 mg of D-luciferin dissolved in 100 μl of PBS. Subsequently, at 24 h or 14 days after acquiring bioluminescent images, mice were sacrificed, skinned and bioluminescent images were obtained.

2.5. RNA extraction and RT-PCR

Various organs (skin at the injection site, inguinal lymph nodes, spleen, and muscle) were removed from immunized mice and pulverized using a homogenizer. Total RNA was extracted from lysates in the presence of RNase inhibitors using the TRIzol reagent protocol (Molecular Research Center, Cincinnati, Ohio). To remove contaminating plasmid DNA, RNA samples were incubated with 10 U/ml of RNase-free DNase (Boehringer, Mannheim, Roche Diagnostics GmbH, Mannheim, Germany) for 2 h at 37 °C. RNA with a 260:280 ratio between 1.8 and 2.0, was dissolved in DEPC-treated water, and cDNA was generated from the mRNA template using a Primer random $p(dN)_6$ (Boehringer, Mannheim, Roche Diagnostics GmbH, Mannheim, Germany) and M-MLV reverse transcriptase (Invitrogen, Grand Island, NY). F*luc* PCR was performed in a total volume of 20 μl containing 1 μl of cDNA, 2 μl of 10× reaction buffer, forward primer 5′-GGCCTTTATGAGGATCTCTCT and reverse primer 5′-CGCCTTGATTGACAAGGATCC, 2 μl of 2.5 mM dNTP mix, and 1.5 U of TaKaRa EX Taq (TaKaRa). Samples were subjected to 5 min of denaturation at 94 °C followed by 30 cycles of 30 s at 94 °C, 30 s at 53 °C and 90 s at 72 °C, and a final extension for 7 min at 72 °C. β-Actin was amplified as a control using the same reaction solution but with forward primer 5′-TGACGGGGTCACCCACACTGTGCCCATCTA and reverse primer 5′-CTAGAAGCATTTGCGGTGGACGATGGAGGG. Samples were sub-

jected to 10 min of denaturation at 94 °C followed by 30 cycles of 30 s at 95 °C, 1 min at 51 °C and 1 min 72 °C, and a final extension for 5 min at 72 °C. PCR products were separated in 2% agarose gel and visualized using ethidium bromide.

3. Results

3.1. In vivo visualization of Fluc gene expression following the intradermal injection of pcDNA3.1-Fluc in the bilateral posterior flank

At 4 h after administration of naked DNA vaccine containing F*luc*, no significant bioluminescence was observed at injection sites or inguinal lymph node (Fig. 1B). However, bioluminescent signals were detected at injection sites 10 h after injection. At 24 h, intense bioluminescent signals were observed at the intradermal injection site (arrowheads), and at the unilateral posterior flank inguinal lymph node close to injection sites (arrows). When skins were removed to confirm the locations of bioluminescent signals (Fig. 1C), bioluminescent signals was observed at unilateral inguinal lymph node (arrows). But gene expression of pcDNA3.1-F*luc* was not observed in peripheral lymph nodes (data not shown).

3.2. In vivo visualization of Fluc gene expression following the intradermal injection of pcDNA3.1-Fluc in the mid dorsum

We injected pcDNA3.1-F*luc* in the mid-dorsum as an injection site to investigate whether different injection sites affect the location, intensity and duration of naked DNA vaccine gene expression. At 4 h after injecting pcDNA3.1-F*luc* into the mid-dorsum, no bioluminescent signals were observed at any sites, including the injection site (Fig. 2B).

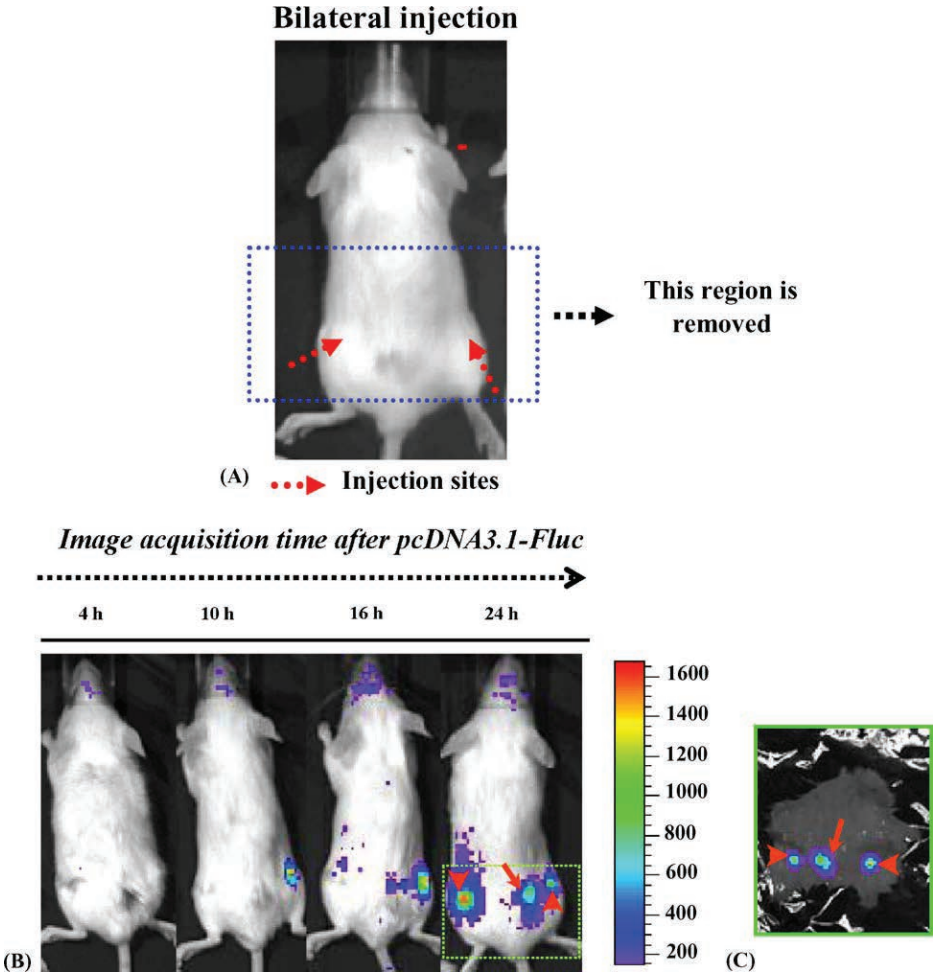

Fig. 1. In vivo visualization of pcDNA3.1-F*luc* gene expression in the skin after an intradermal injection of naked DNA vaccine in bilateral posterior flanks. (A) The diagram of pcDNA3.1-F*luc* injection site in bilateral posterior flanks. The red arrows indicate injection sites. The blue dotted square box indicates removed intact skin site. (B) The pcDNA3.1-F*luc* (100 μg/100 μl) was intradermally injected in bilateral posterior flanks. Following an i.p. injection 3 mg/100 μl D-luciferin, the bioluminescent images of seven mice were serially obtained using the IVIS200 system at 4, 10, 16, and 24 h after DNA injection. (C) Twenty-four hours after acquiring bioluminescent images, mice were sacrificed, skinned and a new set of bioluminescent images were obtained. The above is representative of five results. Arrow heads indicate injection site of pcDNA3.1-F*luc*. Arrow indicates inguinal lymph node. Experiments were performed in duplicate.

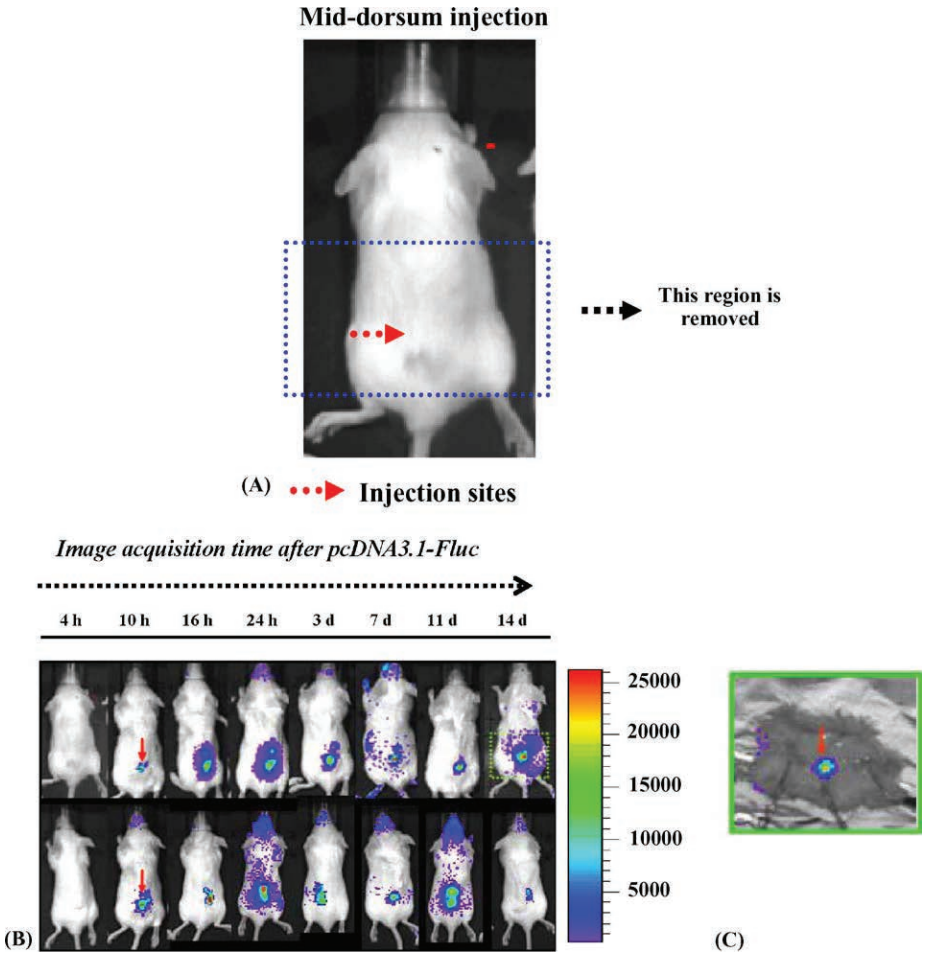

Fig. 2. In vivo visualization of the gene expression of pcDNA3.1-F*luc* in the skin after an intradermal injection of naked DNA vaccine in the mid-dorsum. (A) The diagram of pcDNA3.1-F*luc* injection site of mid-dorsum. The red arrows indicate injection site. The blue dotted square box indicates removed intact skin site. (B) The pcDNA3.1-F*luc* (100 μg/100 μl) was intradermally injected in the mid-dorsum. Following the i.p. injection 3 mg/100 μl D-luciferin, bioluminescent images of seven mice were serially obtained using the IVIS system at designated times (4, 10, 16, 24 h and 3, 7, 11, 14 days) after DNA injection. (C) Fourteen days after the acquisition of bioluminescent images mice were sacrificed, skinned and bioluminescent images were obtained. At 24 h after pcDNA3.1-F*luc* injection, we also monitored bioluminescent signals at injection sites in removed skin (data not shown). Arrow indicates injection site of pcDNA3.1-F*luc*. The above is representative of five results, and experiments were performed in duplicate.

However, at 10 h after injection bioluminescent signals were detected at injection sites (Fig. 2B, arrows), and these signals were maintained for up to 14 days after injection.

However, we were unable to detect bioluminescent signals in inguinal lymph nodes close to injection sites. Subsequently, bioluminescent signals were only observed at the removed injection site in the skin (Fig. 2C, arrows).

3.3. Analysis of RT-PCR

When total RNAs from each organ (skin, inguinal lymph nodes, spleen and muscle) were measured by RT-PCR, F*luc* gene expression was observed at the injection site and at inguinal lymph nodes when the injection was administered in the bilateral posterior flanks (Fig. 3). However, when an injection was administered in the mid-dorsum, gene expression was observed at the injection site only, not at inguinal lymph nodes. There was no gene expression in the spleen and muscle in both groups.

4. Discussion

DNA vaccines induce strong humoral and cellular immune responses and have been shown to be effective against infectious, cancer and viral diseases in organism. A variety of injection methods and other routes for improving immune response to DNA vaccine have been reported in the literature [4,6,18], and it is evident that the therapeutic efficacies of DNA vaccines are dependent on administration methods and routes. Thus, effective methods are required to monitor the expression kinetics of DNA vaccine in living organisms in real-time, but few studies have evaluated the kinetics of DNA vaccine gene expressions with respect to the delivery meth-

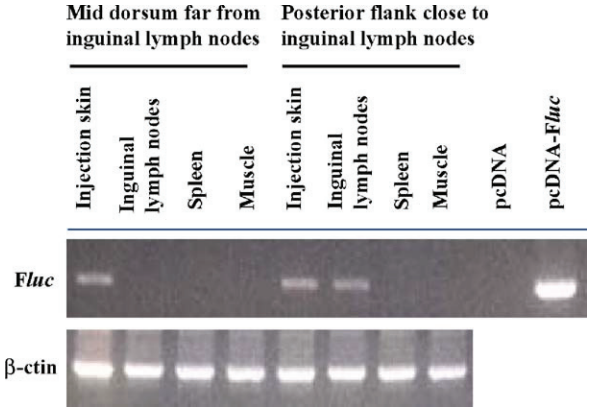

Fig. 3. Detection of transgene expression by RT-PCR following pcDNA3.1-F*luc* vaccination in the bilateral posterior flanks and in the mid dorsum. Various organs (skin at the injection site, inguinal lymph nodes, spleen, and muscle) were examined for pcDNA3.1-F*luc* gene expression at 24 h after injection in the mid-dorsum and bilateral posterior flanks, and RT-PCR analysis was performed. All RNA samples were treated with RNase-free DNase.

ods used in living organisms. Moreover, the majority of the techniques that use reporter genes, such as β-galactosidase, are invasive in nature.

In this study, we observed the gene expression of a DNA vaccine injected into bilateral posterior flanks by in vivo imaging. The bioluminescent signals were detected at 10 h after pcDNA3.1-F*luc* administration and were maintained until 24 h post-injection. Furthermore, we found that pcDNA3.1-F*luc* was expressed in inguinal lymph nodes by bioluminescent imaging (Fig. 1B), and this was confirmed by RT-PCR (Fig. 3). These findings agree with previous reports, which found that DNA vaccines injected intradermally, are taken up and transiently expressed in skin, lymph nodes, and muscle [5–8,19].

We also monitored the gene expression following injection into the mid dorsum. In this case, bioluminescent signals were detected at the injection site as early as 10 h after pcDNA3.1-F*luc* treatment, peaked at 24 h and persisted for 14 days. This data suggests that DNA vaccine was expressed from 10 h after administration and that this was maintained for 14 days. In fact, we detected pcDNA3.1-F*luc* gene expression more than a month after treatment (data not shown). However, in contrast to treatment to posterior flank, no signals were observed at inguinal lymph node closest to injection sites at 24 h or 14 days by imaging or by RT-PCR (Figs. 2 and 3). The reasons for this were not yet determined and this work continues. However, the above result agrees with a previous report on this topic, specifically, that the gene expression of naked DNA vaccine encoding β-gal was maintained up to 15 days after intradermal adminstration [6]. But optical imaging system has some limitations compared with invasive procedures. The emitted light could not penetrate to deep tissue because of light-scattering and absorbing properties. Thus, strong signals are required to monitor the gene expression in living organisms. Other group could effectively monitor the small amounts of target protein by using invasive procedures with in vitro luciferase assay from early time points (10 s or 10 min) in the post-mortem [20]. These facts show that invasive procedures are more sensitive than optical imaging to monitor gene expression. If two methods (optical imaging and invasive methods) are applied to study for gene expression of naked DNA, we could obtain reliable results and analysis the data more precisely.

In summary, optical imaging using F*luc* could provide a useful means of monitoring gene expressions by naked DNA vaccines non-invasively, repetitively. In addition, F*luc* could be useful candidate for the development of a DNA vaccine protocol. Moreover, the described technique and optical reporter gene (F*luc*) could be used to determine optimal injection sites for DNA vaccines, and to decide on the type and frequency of adjuvant supplementations.

Acknowledgements

This work was supported in part by grants from The Cancer Research Center, the Korean Science & Engineering Foundation (KOSEF) through the Tumor Immunity Medical Research Center at Seoul National University College of Medicine, Korea. Y.H. Jeon, J.H. Kang, Y.J. Lee, and Y. Choi were supported by the BK21 Project for Medicine, Dentistry, and Pharmacy in Korea (2004).

References

[1] Manthorpe M, Cornefert-Jensen F, Hartikka J, Felgner J, Rundell A, Margalith M, et al. Gene therapy by intramuscular injection of plasmid DNA: studies on firefly luciferase gene expression in mice. Hum Gene Ther 1993;4(4):419–31.
[2] Ulmer JB, Donnelly JJ, Parker SE, Rhodes GH, Felgner PL, Dwarki VJ, et al. Heterologous protection against influenza by injection of DNA encoding a viral protein. Science 1993;259(5102):1745–9.
[3] Wolff JA, Malone RW, Williams P, Chong W, Acsadi Q, Jani A, et al. Direct gene transfer into mouse muscle in vivo. Science 1990;247(4949 Pt 1):1465–8.
[4] Peachman KK, Rao M, Alving CR. Immunization with DNA through the skin. Methods 2003;31(3):232–42.
[5] Dupuis M, Denis-Mize K, Woo C, Goldbeck C, Selby MJ, Chen M, et al. Distribution of DNA vaccines determines their immunogenicity after intramuscular injection in mice. J Immunol 2000;165(5):2850–8.
[6] Forg P, von Hoegen P, Dalemans W, Schirrmacher V. Superiority of the ear pinna over muscle tissue as site for DNA vaccination. Gene Ther 1998;5(6):789–97.
[7] Hengge UR, Walker PS, Vogel JC. Expression of naked DNA in human, pig, and mouse skin. J Clin Invest 1996;97(12):2911–6.
[8] Maeda S, Ohmori K, Kurata K, Sakaguchi M, Masuda K, Ohno K, et al. Expression of LacZ gene in canine muscle by intramuscular inoculation of a plasmid DNA. J Vet Med Sci 2004;66(3):337–9.
[9] Wilson T, Hastings JW. Bioluminescence Annu Rev Cell Dev Biol 1998;14:197–230.
[10] Honigman A, Zeira E, Ohana P, Abramovitz R, Tavor E, Bar I, et al. Imaging transgene expression in live animals. Mol Ther 2001;4(3):239–49.

[11] De A, Lewis XZ, Gambhir SS. Noninvasive imaging of lentiviral-mediated reporter gene expression in living mice. Mol Ther 2003;7(5 Pt 1):681–91.
[12] Ray P, Bauer E, Iyer M, Barrio JR, Satyamurthy N, Phelps ME, et al. Monitoring gene therapy with reporter gene imaging. Semin Nucl Med 2001;31(4):312–20.
[13] Ray P, De A, Min JJ, Tsien RY, Gambhir SS. Imaging tri-fusion multimodality reporter gene expression in living subjects. Cancer Res 2004;64(4):1323–30.
[14] Contag CH, Jenkins D, Contag PR, Negrin RS. Use of reporter genes for optical measurements of neoplastic disease in vivo. Neoplasia 2000;2(1–2):41–52.
[15] Jenkins DE, Hornig YS, Oei Y, Dusich J, Purchio T. Bioluminescent human breast cancer cell lines that permit rapid and sensitive in vivo detection of mammary tumors and multiple metastases in immune deficient mice. Breast Cancer Res 2005;7(4):R444–54.
[16] Scatena CD, Hepner MA, Oei YA, Dusich JM, Yu SF, Purchio T, et al. Imaging of bioluminescent LNCaP-luc-M6 tumors: a new animal model for the study of metastatic human prostate cancer. Prostate 2004;59(3):292–303.
[17] Jenkins DE, Yu SF, Hornig YS, Purchio T, Contag PR. In vivo monitoring of tumor relapse and metastasis using bioluminescent PC-3M-luc-C6 cells in murine models of human prostate cancer. Clin Exp Metastasis 2003;20(8):745–56.
[18] Trimble C, Lin CT, Hung CF, Pai S, Juang J, He L, et al. Comparison of the CD8+ T cell responses and antitumor effects generated by DNA vaccine administered through gene gun, biojector, and syringe. Vaccine 2003;21(25–26):4036–42.
[19] Hengge UR, Dexling B, Mirmohammadsadegh A. Safety and pharmacokinetics of naked plasmid DNA in the skin: studies on dissemination and ectopic expression. J Invest Dermatol 2001;116(6):979–82.
[20] Satkauskas S, Bureau MF, Mahfoudi A, Mir LM. Slow accumulation of plasmid in muscle cells: supporting evidence for a mechanism of DNA uptake by receptor-mediated endocytosis. Mol Ther 2001;4(4):317–23.

CellPress
REVIEWS

Science & Society

Neutralizing Antibodies against SARS-CoV-2 and Other Human Coronaviruses

Shibo Jiang,[1,2] Christopher Hillyer,[1] and Lanying Du[1,*]

Coronavirus (CoV) disease 2019 (COVID-19) caused by severe acute respiratory syndrome (SARS)-CoV-2 (also known as 2019-nCoV) is threatening global public health, social stability, and economic development. To meet this challenge, this article discusses advances in the research and development of neutralizing antibodies (nAbs) for the prevention and treatment of infection by SARS-CoV-2 and other human CoVs.

Current Situation with SARS-CoV-2 and Other Human CoVs

Three emerging, highly pathogenic human CoVs are SARS-CoV, Middle East respiratory syndrome (MERS)-CoV, and COVID-19 virus, which was previously named 2019-nCoV by the World Health Organization (WHO), and is also known as hCoV-19 or SARS-CoV-2 [1]. Atypical pneumonia (SARS) was first reported from Guangdong Province, China in late 2002. SARS caused a global pandemic in 2003 with approximately 10% (774/8098) case fatality rate (CFR) [2]. SARS-CoV has not circulated in humans since 2004. MERS-CoV was first reported from Saudi Arabia in 2012 and has continued to infect humans with limited human-to-human transmission, leading to a CFR of approximately 34.4% (858/2494) in 27 countries, according to the most recent WHO report[i]. Both SARS-CoV and MERS-CoV are zoonotic viruses. They use bats as their natural reservoirs and transmit from bats to intermediate hosts (e.g., palm civets for SARS-CoV, dromedary camels for MERS-CoV), leading to infection in humans [2,3].

Different from SARS-CoV and MERS-CoV, SARS-CoV-2 was first reported in Wuhan, China in December 2019 and is characterized by its rapid spread and virulent human-to-human transmission [4], resulting in 125 048 confirmed cases including 4613 deaths (CFR 3.7%), particularly in Wuhan, China and in at least 117 other countries, territories, or areas as of March 12, 2020. With no vaccines or treatments on the horizon, researchers are exploring various medical interventions, including nAbs, to control the continuous spread of SARS-CoV-2 and the global COVID-19 pandemic [5]. SARS-CoV-2 is also a zoonotic virus with bats as its natural reservoir [4], but its intermediate hosts have not been identified.

Pathogenesis and Key Proteins of SARS-CoV-2 and Other Human CoVs

SARS-CoV-2 infection mainly results in pneumonia and upper/lower respiratory tract infection. Fever and cough are two major clinical symptoms, but others include shortness of breath, muscle pain (myalgias)/fatigue, confusion, headache, sore throat, and even acute respiratory distress syndrome, leading to respiratory or multiorgan failure [6]. For elderly people with underlying comorbidities such as diabetes, hypertension, or cardiovascular disease, SARS-CoV-2 infection may result in severe and fatal respiratory diseases. So far, its effects on children have been generally mild. The virus can be transmitted through respiratory droplets or close contact with infected surfaces or objects and is detectable in multiple samples, including saliva, stool, and blood [7]. To develop vaccines and therapeutics, we must understand the behavior of key proteins in SARS-CoV-2.

Similar to SARS-CoV and MERS-CoV, SARS-CoV-2 is an enveloped, single-stranded, and positive (+)-sense RNA virus, belonging to the beta-CoV genera in the family *Coronaviridae* [4]. The genome of this and other emerging pathogenic human CoVs encodes four major structural proteins [spike (S), envelope (E), membrane (M), and nucleocapsid (N)], approximately 16 nonstructural proteins (nsp1–16), and five to eight accessory proteins. Among them, the S protein plays an essential role in viral attachment, fusion, entry, and transmission. It comprises an N-terminal S1 subunit responsible for virus–receptor binding and a C-terminal S2 subunit responsible for virus–cell membrane fusion [2,3]. S1 is further divided into an N-terminal domain (NTD) and a receptor-binding domain (RBD). SARS-CoV-2 and SARS-CoV bind angiotensin-converting enzyme 2 (ACE2) while MERS-CoV binds dipeptidyl peptidase 4 (DPP4), as receptors on the host cell expressing ACE2 (e.g., pneumocytes, enterocytes) or DPP4 (e.g., liver or lung cells including Huh-7, MRC-5, and Calu-3) [2,3,8]. Phylogenetically, SARS-CoV-2 is closely related to SARS-CoV, sharing approximately 79.6% genomic sequence identity [4]. During infection, CoV first binds the host cell through interaction between its S1-RBD and the cell membrane receptor, triggering conformational changes in the S2 subunit that result in virus fusion and entry into the target cell (see human CoV life cycle in Figure 1A) [2,3].

nAbs against SARS-CoV, MERS-CoV, and SARS-CoV-2

Virus nAbs induced by vaccines or infected virus play crucial roles in controlling viral infection. Currently developed SARS-CoV- and MERS-CoV-specific nAbs include monoclonal antibodies (mAbs), their functional antigen-binding fragment (Fab), the single-chain variable region fragment (scFv), or single-domain antibodies [nanobodies (Nbs)] [8]. They target S1-RBD, S1-NTD, or the S2 region, blocking

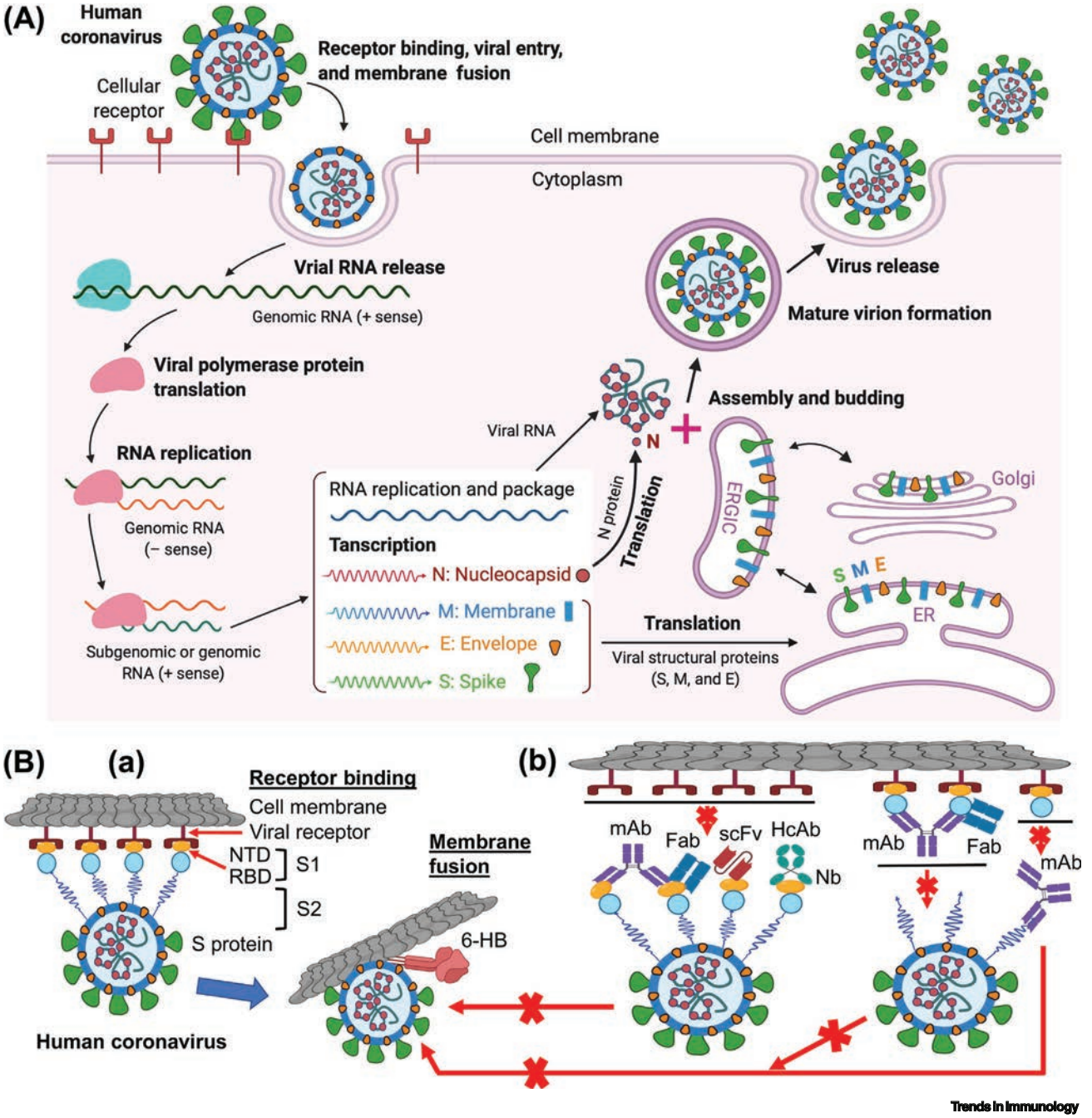

Figure 1. Life Cycle of Highly Pathogenic Human Coronaviruses (CoVs) and Specific Neutralizing Antibodies (nAbs) against These Coronaviruses. (A) Life cycle of highly pathogenic human CoVs. These CoVs enter host cells by first binding to their respective cellular receptors [angiotensin-converting enzyme 2 (ACE2) for severe acute respiratory syndrome (SARS)-CoV-2 or SARS-CoV and dipeptidyl peptidase 4 (DPP4) for Middle East respiratory syndrome (MERS)-CoV] on the membranes of host cells expressing ACE2 (e.g., pneumocytes, enterocytes) or DPP4 (e.g., liver or lung cells including Huh-7, MRC-5, and Calu-3) via the surface spike (S) protein, which mediates virus–cell membrane fusion and viral entry. Viral genomic RNA is released and translated into viral polymerase proteins. The negative (–)-sense genomic RNA is synthesized and used as a template to form subgenomic or genomic positive (+)-sense RNA. Viral RNA and nucleocapsid (N) structural protein are replicated, transcribed, or synthesized in the cytoplasm, whereas other viral structural proteins, including S, membrane (M), and envelope (E), are transcribed then translated in the endoplasmic reticulum (ER) and transported to the Golgi. The viral RNA–N complex and S, M, and E proteins are further assembled in the ER–Golgi intermediate compartment (ERGIC) to form a mature virion, then released from host cells. (B) Potential targets of nAbs against SARS-CoV-2 and other pathogenic human

(Figure legend continued at the bottom of the next page.)

the binding of RBDs to their respective receptors and interfering with S2-mediated membrane fusion or entry into the host cell, thus inhibiting viral infections [2,5]. The putative targets and mechanisms of these SARS-CoV and MERS-CoV nAbs are shown in Figure 1B. Representative SARS-CoV and MERS-CoV RBD-specific nAbs are summarized in Table 1. No SARS-CoV-2-specific nAbs have been reported, but we herein introduce SARS-CoV- and MERS-CoV-specific nAbs in the context of their potential cross-neutralizing activity against SARS-CoV-2 infection.

SARS-CoV nAbs

All currently developed anti-SARS-CoV nAbs target the viral S protein. Most target the RBD, while a few target regions in the S2 subunit or the S1/S2 proteolytic cleavage site. For example, the human neutralizing mAbs S230.15 and m396 were isolated from SARS-CoV-infected individuals. They neutralize human and palm civet SARS-CoV infection by interacting with the RBD, thus blocking binding between the viral RBD and the cellular ACE2 receptor [9]. Other human mAbs, such as S109.8 and S227.14, have cross-neutralizing activity against multiple human, palm civet, and raccoon dog SARS-CoV infectious clones, protecting mice against four different homologous and heterologous SARS-CoV strains [10]. Human nAb 80R (scFv or mAb) neutralizes SARS-CoV infection by blocking the RBD–ACE2 interaction, although its protective efficacy has not yet been reported [11]. A variety of SARS-CoV RBD-specific mouse neutralizing mAbs are sufficiently potent to block RBD–ACE2 binding, thus neutralizing viral infection in ACE2-transfected HEK293T cells [12]. Despite their strong neutralizing activity and/or protection in cells or animal models, none of these SARS-CoV nAbs has ever been evaluated in clinical studies. Thus, to determine potential cross-neutralizing activity against SARS-CoV-2 infection, such studies should be vigorously undertaken.

MERS-CoV nAbs

A number of MERS-CoV-specific nAbs have been reported, most of which target the RBD in the S protein [3,8]. A few recognize epitopes on the S1-NTD and regions of the S2 subunit [3]. Among these nAbs, human mAbs or Fabs (MERS-27, m336, MERS-GD27, or MCA1 isolated from humans), humanized mAbs (hMS-1, 4C2 h), mouse mAbs (Mersmab1, 4C2, or D12 isolated from mice), and Nbs (HCAb-83 or NbMS10-Fc isolated from dromedary camels or llamas) recognize epitopes on the RBD and have been demonstrated to neutralize pseudotyped and/or live MERS-CoVs [3,8]. Several human/humanized mAbs and Nbs can protect mice, rabbits, or common marmosets from MERS-CoV infection [3,8]. So far, only one MERS-CoV nAb isolated from transchromosomic cattle has been evaluated in Phase I trials (SAB-301)[ii] [8]. No other nAbs have gone to clinical trials, again suggesting the urgency of developing nAbs with potential cross-neutralizing activity against SARS-CoV-2 infection.

SARS-CoV-2 nAbs

Currently, polyclonal antibodies from recovered SARS-CoV-2-infected patients have been used to treat SARS-CoV-2 infection, but no SARS-CoV-2-specific neutralizing mAbs have been reported. Researchers are working hard to develop such mAbs and/or their functional fragments as putative prophylactic or therapeutic agents to prevent or treat COVID-19. Once such antibodies are produced, the next steps will involve *in vitro* testing for neutralizing and/or cross-neutralizing activity, *in vivo* evaluation in available COVID-19 animal models for protective efficacy, preclinical studies, and clinical trials testing the safety and efficacy before they are approved for clinical application. Therefore, it may take one to several years for such SARS-CoV-2 neutralizing mAbs or their fragments to be ready for human use.

However, since SARS-CoV-2 is closely related to SARS-CoV and since their S proteins have high sequence identity [4], researchers have attempted to discover SARS-CoV nAbs with potential cross-reactivity and/or cross-neutralizing activity against SARS-CoV-2 infection. Notably, a SARS-CoV RBD-specific human neutralizing mAb, CR3022, could bind SARS-CoV-2 RBD with high affinity and recognize an epitope on the RBD that does not overlap with the ACE2-binding site [13]. In addition, sera from convalescent SARS patients or from animals specific for SARS-CoV S1 may cross-neutralize SARS-CoV-2 infection by reducing S protein-mediated SARS-CoV-2 entry [14]. Moreover, SARS-CoV RBD-specific polyclonal antibodies have cross-reacted with the SARS-CoV-2 RBD protein and cross-neutralized SARS-CoV-2 infection in HEK293T cells stably expressing the human ACE2 receptor, opening avenues for the potential development of SARS-

CoVs. (a) Human CoV receptor binding and membrane fusion process. The CoV first binds a viral receptor (ACE2 or DPP4) through the receptor-binding domain (RBD) in the S protein, followed by fusion of the virus with cell membranes via the formation of a six-helix bundle (6-HB) fusion core. NTD, N-terminal domain. (b) Potential targets of nAbs on the S protein of human CoVs. Monoclonal antibody (mAb), antigen-binding fragment (Fab), single-chain variable region fragment (scFv), or single-domain antibody [nanobody (Nb) or VHH derived from camelid heavy chain antibody (HcAb)] binds to the RBD, S1 subunit (non-RBD, including NTD), or S2 of the viral S protein, blocking binding between the RBD and the respective receptor (for RBD-targeting nAbs), interfering with the conformational change of S (for S1-targeting nAbs), or hindering S2-mediated membrane fusion (for S2-targeting nAbs), leading to the inhibition of infection with pathogenic human CoVs in the host cells. This figure was created using BioRender (https://biorender.com/).

Table 1. Representative SARS-CoV RBD- and MERS-CoV RBD-Targeting nAbs[a]

Ab name	Source	Neutralizing activity	Neutralizing mechanism	Protective efficacy	Refs[b]
S230.15 m396 mAbs	Human	Neutralize human (strains GD03, Urbani, Tor2) and palm civet (strains SZ3, SZ16) SARS-CoV infection	Recognize epitopes (residues 408, 442, 443, 460, 475) on SARS-CoV S1 protein, interfering with RBD–ACE2 receptor interaction	Protect mice against challenge of SARS-CoV (strains Urbani, rGD03, or rSZ16)	[9]
S109.8 S227.14 S230.15 mAbs	Human	Neutralize human (Urbani, GZ02, CUHK-W1), palm civet (HC/SZ/61/03), and raccoon dog (A031G) SARS-CoV infectious clones containing S variants	Inhibit the binding of SARS-CoV RBD–ACE2 receptor	Protect mice against challenge of SARS-CoV infectious clones (Urbani, GZ02, HC/SZ/61/03) or mouse-adapted strain (MA15)	[10]
80R scFv, mAb	Human	Neutralize live SARS-CoV (strain Urbani) infection	Recognize epitopes on SARS-CoV S1 (residues 261–672), blocking RBD–ACE2 binding and inhibiting syncytium formation	NA	[11]
CR3022 CR3014 scFv, mAb	Human	Neutralize live SARS-CoV (strain HKU-39849) infection; CR3022 could neutralize CR3014 escape variants	Recognize epitopes on SARS-CoV RBD (residues 318–510); CR3022 binds SARS-CoV-2 RBD with high affinity	CR3014 protects ferrets against SARS-CoV (strain HKU-39849) infection	[13]
33G4 35B5 30F9 mAbs	Mouse	Neutralize human (strains GD03, Tor2) and palm civet (SZ3) pseudotyped SARS-CoV infection	Recognize epitopes on SARS-CoV RBD, blocking RBD–ACE2 receptor binding	NA	[12]
MERS-27 m336 MERS-GD27 MCA1 mAbs, Fabs	Human	Neutralize divergent strains of pseudotyped and live (strain EMC2012) MERS-CoV infection	Recognize a number of key epitopes on MERS-CoV RBD protein, blocking RBD–DPP4 receptor binding	Prophylactically and therapeutically prevent and treat MERS-CoV (strain EMC2012) challenge in hDPP4-Tg mice, rabbits, or common marmosets	[3,8]
4C2 h hMS-1 mAbs	Humanized	Neutralize divergent strains of pseudotyped and live (strain EMC2012) MERS-CoV infection	Recognize epitopes (residues 510, 511, 553) on MERS-CoV RBD protein, blocking RBD–DPP4 receptor binding	Prevent MERS-CoV (strain EMC2012) challenge in Ad5/hDPP4-transduced or hDPP4-Tg mice	[3]
Mersmab1 4C2 D12 mAbs	Mouse	Neutralize pseudotyped and live (strain EMC2012) MERS-CoV infection	Recognize a number of key epitopes on MERS-CoV RBD protein, blocking RBD–DPP4 receptor binding	NA	[3]
HCAb-83 Nb	Dromedary camel	Neutralizes live MERS-CoV (strain EMC2012) infection	Recognizes epitope (residue 539) on MERS-CoV RBD protein	Prophylactically prevents MERS-CoV (strain EMC2012) challenge in hDPP4-Tg mice	[8]
NbMS10-Fc Nb	Llama	Neutralizes multiple strains of pseudotyped and live (strain EMC2012) MERS-CoV infection	Recognizes epitope (residue 539) on MERS-CoV RBD protein	Prophylactically and therapeutically prevents and treats MERS-CoV (strain EMC2012) challenge in hDPP4-Tg mice	[8]

[a]Abbreviations: Ab, antibody; Ad5/hDPP4-transduced mice, adenovirus serotype 5-hDPP4-transduced mice; hDPP4-Tg mice, human DPP4-transgenic mice; NA, not applicable; rGD03 or rSZ16, recombinant SARS-CoVs bearing the S protein of GD03 or SZ16; S, spike.
[b]Note: Due to space limitations, some review articles, rather than original research papers reporting the antibodies, are cited.

CoV RBD-based vaccines that might eventually prevent SARS-CoV-2 and SARS-CoV infection [15]. It is also possible that SARS-CoV RBD-targeting nAbs might be applied for prophylaxis and treatment of SARS-CoV-2 infection in the current absence of SARS-CoV-2-specific vaccines and antibodies. However, robust testing lies ahead.

Concluding Remarks and Future Perspectives

SARS-CoV-2 continues to infect people globally with the concomitant urgency to develop effective nAbs as prophylactic and therapeutic agents to prevent and treat its infection and control its spread. Studies from SARS-CoV and MERS-CoV have demonstrated that many fragments (S1-NTD, RBD, S2) in S proteins can be used as targets to develop nAbs. Still,

RBD-specific antibodies have greater potency to neutralize infection with divergent virus strains, suggesting that the RBD of SARS-CoV-2 can also serve as an important target for the development of potent and specific nAbs. Cocktails comprising antibodies specific for RBD and other regions in the S protein may further improve the breadth and potency of nAbs against SARS-CoV-2 and its escape-mutant strains. Human sera from convalescent patients have been used to treat COVID-19, but lessons learned from SARS show that some non-nAbs targeting the non-RBD regions in the S protein may cause an antibody-dependent enhancement (ADE) effect on viral infectivity and disease, as well as other harmful immune responses [2]. On a positive note, some anti-SARS-CoV nAbs have shown cross-reactivity or cross-neutralizing activity against SARS-CoV-2 infection *in vitro*. Thus, overall, research on SARS-CoV- and MERS-CoV-specific nAbs should provide important guidelines for the rapid design and development of SARS-CoV-2-specific nAbs.

Acknowledgments

This study was supported by National Institutes of Health (NIH) grants R01AI137472 and R01AI139092.

Resources

[i]www.who.int/emergencies/mers-cov/en/

[ii]https://clinicaltrials.gov/ct2/show/NCT02788188

[1]Lindsley F. Kimball Research Institute, New York Blood Center, New York, NY, USA
[2]Key Laboratory of Medical Molecular Virology (MOE/NHC/CAMS), School of Basic Medical Sciences, Fudan University, Shanghai, China

*Correspondence:
ldu@nybc.org (L. Du).

https://doi.org/10.1016/j.it.2020.03.007

References

1. Coronaviridae Study Group of the International Committee on Taxonomy of Viruses (2020) The species *Severe acute respiratory syndrome-related coronavirus*: classifying 2019-nCoV and naming it SARS-CoV-2. *Nat. Microbiol.* Published online March 2, 2020. https://doi.org/10.1038/s41564-020-0695-z
2. Du, L. *et al.* (2009) The spike protein of SARS-CoV – a target for vaccine and therapeutic development. *Nat. Rev. Microbiol.* 7, 226–236
3. Du, L. *et al.* (2017) MERS-CoV spike protein: a key target for antivirals. *Expert Opin. Ther. Targets* 21, 131–143
4. Zhou, P. *et al.* (2020) A pneumonia outbreak associated with a new coronavirus of probable bat origin. *Nature* 579, 270–273
5. Jiang, S. *et al.* (2020) An emerging coronavirus causing pneumonia outbreak in Wuhan, China: calling for developing therapeutic and prophylactic strategies. *Emerg. Microbes Infect.* 9, 275–277
6. Huang, C. *et al.* (2020) Clinical features of patients infected with 2019 novel coronavirus in Wuhan, China. *Lancet* 395, 497–506
7. Young, B.E. *et al.* (2020) Epidemiologic features and clinical course of patients infected with SARS-CoV-2 in Singapore. *JAMA.* Published online March 3, 2020. https://doi.org/10.1001/jama.2020.3204
8. Zhou, Y. *et al.* (2019) Advances in MERS-CoV vaccines and therapeutics based on the receptor-binding domain. *Viruses* 11, E60
9. Zhu, Z. *et al.* (2007) Potent cross-reactive neutralization of SARS coronavirus isolates by human monoclonal antibodies. *Proc. Natl. Acad. Sci. U. S. A.* 104, 12123–12128
10. Rockx, B. *et al.* (2008) Structural basis for potent cross-neutralizing human monoclonal antibody protection against lethal human and zoonotic severe acute respiratory syndrome coronavirus challenge. *J. Virol.* 82, 3220–3235
11. Sui, J. *et al.* (2004) Potent neutralization of severe acute respiratory syndrome (SARS) coronavirus by a human mAb to S1 protein that blocks receptor association. *Proc. Natl. Acad. Sci. U. S. A.* 101, 2536–2541
12. He, Y. *et al.* (2006) Cross-neutralization of human and palm civet severe acute respiratory syndrome coronaviruses by antibodies targeting the receptor-binding domain of spike protein. *J. Immunol.* 176, 6085–6092
13. Tian, X. *et al.* (2020) Potent binding of 2019 novel coronavirus spike protein by a SARS coronavirus-specific human monoclonal antibody. *Emerg. Microbes Infect.* 9, 382–385
14. Hoffmann, M. *et al.* (2020) SARS-CoV-2 cell entry depends on ACE2 and TMPRSS2 and is blocked by a clinically proven protease inhibitor. *Cell.* Published online March 4, 2020. https://doi.org/10.1016/j.cell.2020.02.052
15. Tai, W. *et al.* (2020) Characterization of the receptor-binding domain (RBD) of 2019 novel coronavirus: implication for development of RBD protein as a viral attachment inhibitor and vaccine. *Cell. Mol. Immunol.* Published online March 19, 2020. https://doi.org/10.1038/s41423-020-0400-4

Spotlight

'Nervous' Immunity: Walking the Tightrope

Subhash Kulkarni,[1,*] Sravya Kurapati,[2,3] and Milena Bogunovic[2,*]

There is a major gap in our understanding of how the intestinal immune and nervous systems are integrated to regulate protective adaptations to enteric infections while maintaining tissue homeostasis. Three recent complementary reports published in *Cell* (2020) provide new mechanistic insights into how this enteric neuro-immune crosstalk may occur.

The gastrointestinal (GI) tract is a portal through which toxins and pathogens, along with nutrients, can gain entrance into the body. The intestine acts as a guard to sift through ingested material so that beneficial nutrients are absorbed, while toxins and pathogens are neutralized and expelled. Some of these protective functions are achieved through primary physiologic responses, such as vomiting and diarrhea, which are regulated by the neuro-epithelial sensory system and underlying neural circuits. A second line of response to danger requires the immune system, whose diverse cell types can provide both sensory signals and effector responses. Analysis of evolution, embryonic development, and functional interactions between the nervous and immune systems suggests that the two systems are integrated in gut protection. In mammals, this integration occurs through crosstalk between immune cells and gut-innervating neurons that are either extrinsic to the gut wall or reside inside the gut as a part of the enteric nervous system (ENS) [1,2]. Three recent complementary reports provide new mechanistic insights into how this enteric neuro-immune crosstalk maintains GI health and how it is impacted in response to enteric infection [3–5] (see Figure 1).

Infections by entero-invasive bacteria, including *Salmonella enterica* serovars, pose a major threat to human health, especially in light of rising antibiotic resistance. Despite our understanding of early immunological events in response to *Salmonella* evasion, the neuro-immune circuits that regulate resistance to

Immunity, Vol. 23, 165–175, August, 2005, Copyright ©2005 by Elsevier Inc. DOI 10.1016/j.immuni.2005.06.008

Suppression of RNA Recognition by Toll-like Receptors: The Impact of Nucleoside Modification and the Evolutionary Origin of RNA

Katalin Karikó,[1,*] Michael Buckstein,[2] Houping Ni,[2] and Drew Weissman[2]
[1]Department of Neurosurgery
[2]Department of Medicine
University of Pennsylvania School of Medicine
Philadelphia, Pennsylvania 19104

Summary

DNA and RNA stimulate the mammalian innate immune system through activation of Toll-like receptors (TLRs). DNA containing methylated CpG motifs, however, is not stimulatory. Selected nucleosides in naturally occurring RNA are also methylated or otherwise modified, but the immunomodulatory effects of these alterations remain untested. We show that RNA signals through human TLR3, TLR7, and TLR8, but incorporation of modified nucleosides m5C, m6A, m5U, s2U, or pseudouridine ablates activity. Dendritic cells (DCs) exposed to such modified RNA express significantly less cytokines and activation markers than those treated with unmodified RNA. DCs and TLR-expressing cells are potently activated by bacterial and mitochondrial RNA, but not by mammalian total RNA, which is abundant in modified nucleosides. We conclude that nucleoside modifications suppress the potential of RNA to activate DCs. The innate immune system may therefore detect RNA lacking nucleoside modification as a means of selectively responding to bacteria or necrotic tissue.

Introduction

The innate immune system is the first line of defense against invading pathogens (Medzhitov, 2001). This system utilizes TLRs to recognize conserved pathogen-associated molecular patterns and orchestrate the initiation of immune responses. TLRs are germ line-encoded signaling receptors with extracellular leucine-rich repeats and intracellular signaling domains. In humans, ten distinct TLR family members have been identified, and corresponding microbial ligands for most have been identified. Several TLRs recognize and respond to nucleic acids. DNA containing unmethylated CpG motifs, characteristic of bacterial and viral DNA, activate TLR9 (Hemmi et al., 2000). Double-stranded (ds)RNA, a frequent viral constituent, has been shown to activate TLR3 (Alexopoulou et al., 2001; Wang et al., 2004), single-stranded (ss)RNA activates mouse TLR7 (Diebold et al., 2004), and RNA oligonucleotides with phosphorothioate internucleotide linkages are ligands of human TLR8 (Heil et al., 2004). Based on structural and sequence similarities, TLR7, TLR8, and TLR9 form a subfamily. Activation of these receptors depends upon endosomal acidification and leads to interferon production. Human TLR7 and TLR8 are stimulated by the synthetic antiviral compound R-848 (Jurk et al., 2002), but a natural ligand has not been identified.

It has been known for decades that selected DNA and RNA molecules have the unique property to activate the immune system. It was discovered only recently that secretion of interferon in response to DNA is mediated by unmethylated CpG motifs acting upon TLR9 present on immune cells (Hemmi et al., 2000). For years, bacterial and mammalian DNA were portrayed as having the same chemical structure, which hampered the understanding of why only bacterial, but not mammalian, DNA is immunogenic. Recently, however, the sequence and structural microheterogeneity of DNA has come to be appreciated. For example, methylated cytidine in CpG motifs of DNA has proven to be the structural basis of recognition for the innate immune system. In light of this finding and given that multiple TLRs respond to RNA, a question emerges as to whether the immunogenicity of RNA is under the control of similar types of modification. This possibility is not unreasonable given that RNA undergoes nearly one hundred different nucleoside modifications (Rozenski et al., 1999). Importantly, the extent and quality of RNA modifications depend on the RNA subtype and correlate directly with the evolutionary level of the organism from which the RNA is isolated. Ribosomal RNA, the major constituent (~80%) of cellular RNA, contains significantly more nucleoside modifications when obtained from mammalian cells versus bacteria. Human rRNA, for example, has ten times more pseudouridine (Ψ) and 25 times more 2′-O-methylated nucleosides than bacterial rRNA, whereas rRNA from mitochondria, an organelle that is a remnant of eubacteria (Margulis and Chapman, 1998), has very few modifications (Bachellerie and Cavaille, 1998). Transfer RNA is the most heavily modified subgroup of RNA. In mammalian tRNAs, up to 25% of the nucleosides are modified, whereas there are significantly less modifications in prokaryotic tRNAs. Bacterial mRNA contains no nucleoside modifications, whereas mammalian mRNAs have modified nucleosides such as 5-methylcytidine (m5C), N6-methyladenosine (m6A), inosine and many 2′-O-methylated nucleosides in addition to N7-methylguanosine (m7G), which is part of the 5′-terminal cap (Bokar and Rottman, 1998). The presence of modified nucleosides was also demonstrated in the internal regions of many viral RNAs including influenza, adeno, and herpes simplex; surprisingly, modified nucleosides were more frequent in viral than in cellular mRNAs (Bokar and Rottman, 1998). A substantial number of nucleoside modifications are uniquely present in either bacterial or mammalian RNA, thus providing an additional molecular feature for immune cells to discriminate between microbial and host RNA. Considering that cells usually contain five to ten times more RNA than DNA, presence of such distinctive characteristics on RNA could make them a rich molecular source for sampling by the immune system, a notion becoming evident by the identification of multiple TLRs signaling in response to RNA. The role

*Correspondence: kariko@mail.med.upenn.edu

of nucleoside modifications on the immunostimulatory potential of RNA, however, is not known.

In recent years, we have investigated the immunomodulatory effect of RNA on human DCs. These studies demonstrated that in vitro-transcribed RNA activates/matures DCs (Weissman et al., 2000) partially by a mechanism in which double-stranded regions of the RNA signal through TLR3 (Kariko et al., 2004). Recently, it was noted that in vitro transcripts, or total RNA derived from bacteria, but not from eukaryotic cells, can prime DCs for high-level IL-12 secretion (Koski et al., 2004). The molecular basis for the discrimination between these various RNAs is not fully understood. In this report, we sought to determine whether naturally occurring nucleoside modifications modulate the immunostimulatory potential of RNA and the role TLRs might play in this process.

Results

Naturally Occurring RNAs Are Not Equally Potent Activators of DCs

We recently demonstrated that RNA transcribed in vitro or released from necrotic mammalian cells activates human DCs (Kariko et al., 2004). In an independent study, we also determined that although in vitro-transcribed RNAs are effective, eukaryotic mRNA and tRNA did not stimulate cultured human DCs (Koski et al., 2004). This finding prompted us to investigate the immunostimulatory potential of different cellular RNA subtypes. The objective was to identify the likely RNA components from necrotic cells that activated DCs in the original experimental setting. We first isolated RNA from different subcellular compartments (cytoplasm, nucleus, and mitochondria). These RNA isolates as well as total RNA, tRNA, and polyA-tail-selected mRNA, all from mammalian sources, were complexed to lipofectin and added to monocyte-derived DCs (MDDCs) generated with GM-CSF and IL-4. We determined that mammalian total, nuclear, and cytoplasmic RNA and mRNA all induced TNF-α secretion, although at very low levels relative to RNA synthesized in vitro by T7 RNA polymerase (RNAP) (Figure 1). Interestingly, mammalian tRNA did not induce any detectable level of TNF-α, whereas mitochondrial (mt)RNA was the most potent RNA type to stimulate MDDCs. Considering that mtRNA shares more characteristics with bacterial RNA than with other mammalian RNA types, it was not surprising to find that bacterial total RNA was also a very potent activator of MDDCs (Figure 1). Bacterial tRNA, which is modified but to a lesser extent than mammalian tRNA, induced a low level of TNF-α, whereas tRNAs from other sources (yeast, wheat germ, and bovine) were nonstimulatory (Figure 1 and data not shown). Similar results were observed when RNAs from other mammalian sources were tested as well as when the RNA repertoires were analyzed by using GM-CSF + IFN-α-generated MDDCs (data not shown). When RNA samples were digested with Benzonase, capable of cleaving both ssRNA and dsRNA, RNA signaling was abolished in MDDCs, verifying that RNA is the active component that triggers TNF-α secretion (Figure 1). These findings demonstrate that from the view of immunostimulation not all naturally occurring RNAs are equal. The activation potentials of RNAs seem to have an inverse correlation with the extent of their nucleoside modification, because bacterial RNA and mtRNA that contain only a few modifications are the most potent activators of DCs, whereas extremely modified tRNAs have little to no activity.

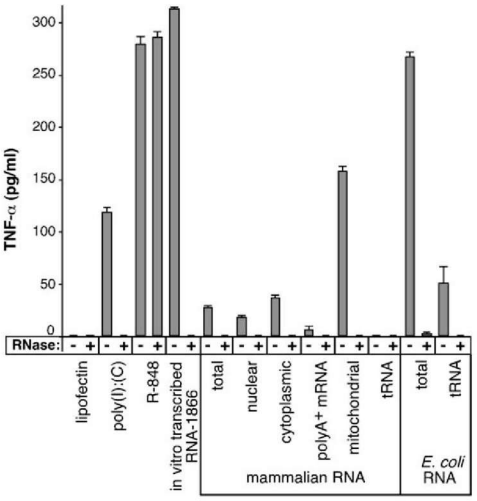

Figure 1. Production of TNF-α by MDDCs Transfected with Natural RNA

Human MDDCs were incubated with lipofectin alone, or complexed with R-848 (1 μg/ml), or RNA (5 μg/ml) from 293 cells (total, nuclear, and cytoplasmic RNAs), mouse heart (polyA$^+$ mRNA), human platelet mitochondrial RNA, bovine tRNA, bacterial tRNA, and total RNA (*E. coli*) with or without RNase digestion. After 8 hr, TNF-α was measured in the supernatants by ELISA. Mean values ± SEM are shown. The results are representative of three independent experiments.

In Vitro-Transcribed RNA Stimulates Human TLR3, TLR7, and TLR8, but Most of the Nucleoside-Modified RNAs Are Not Stimulatory

Naturally, all RNA is synthesized from four basic ribonucleotides, ATP, CTP, UTP and GTP, but some of the incorporated nucleosides are modified posttranscriptionally in almost all types of RNA. The extent and nature of modifications vary and depend on the RNA type as well as the evolutionary level of the organism from where the RNA is derived. Because findings with natural RNA suggested that nucleoside modifications might influence the ability of RNA to activate DCs, we set out to further investigate this possibility. First, to obtain RNA with selected modifications, we performed in vitro transcription reactions in which one or two of the four nucleotide triphosphates (NTPs) were substituted with a corresponding nucleoside-modified NTP. Several sets of RNA with different primary sequences ranging in length between 0.7 and 1.9 kb and containing either none, one, or two types of modified nucleosides were

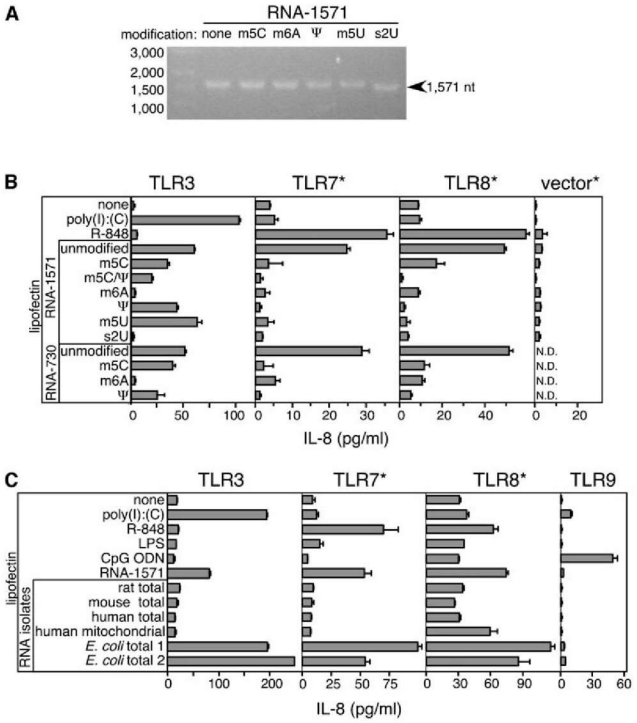

Figure 2. TLR-Dependent Activation by RNA

(A) Aliquots (1 μg) of in vitro-transcribed RNA-1571 without (none) or with m5C, m6A, Ψ, m5U, or s2U nucleoside modifications were analyzed on denaturing agarose gel followed by ethidium bromide-staining and UV illumination.

(B) 293 cells stably expressing human TLR3, TLR7, TLR8, and control vectors were treated with lipofectin alone or complexed with R-848 (1 μg/ml) or the indicated RNA (5 μg/ml). Modified nucleosides present in RNA-730 and RNA-1571 are noted. 293-ELAM-luc cells were used as control cells, but other controls gave similar results.

(C) CpG ODN-2006 (5 μg/ml), LPS (1.0 μg/ml), and RNA isolates were obtained from rat liver, mouse cell line (TUBO) and human spleen (total), or human platelet mitochondrial RNA, or from two different *E. coli* sources. 293-hTLR9 cells served as control. After 8 hr, IL-8 was measured in the supernatants by ELISA.

Mean values ± SEM are shown. Cell lines transformed to express hTLR3-targeted siRNA are indicated with an asterisk. The results are representative of four independent experiments. N.D., not determined.

transcribed. Modified RNAs analyzed by denaturing gel electrophoresis were indistinguishable from their nonmodified counterparts in such that all were intact and migrated as expected based on their sizes (Figure 2A).

We and others recently demonstrated that in vitro-transcribed RNA activates human TLR3 (Kariko et al., 2004) and murine TLR7 (Diebold et al., 2004), whereas chemically synthesized oligoribonucleotides (ORNs) stimulate murine TLR7 and human TLR8 (Heil et al., 2004). Therefore, to determine whether modification of nucleosides influences the RNA-mediated activation of TLRs, we utilized human 293 cell lines stably transformed to express human TLR3, TLR7, or TLR8 and monitored TLR activation through IL-8 release. First, TLR3-transformed cells were treated with lipofectin-complexed RNA (RNA-1571, RNA-730, or RNA-1866) and, as expected based on previous studies (Kariko et al., 2004), high levels of IL-8 secretion were measured. RNA containing m6A or s2U modifications did not induce detectable levels of IL-8 (Figure 2B and data not shown). The presence of other nucleoside modifications such as m5C, m5U, Ψ, or m5C/Ψ in the RNA had a less remarkable suppression or no effect at all on the potential of RNA to activate TLR3 (Figure 2B).

We previously noted that the parental 293 cells express a low level of endogenous TLR3 (Kariko et al., 2004). Therefore, the unwanted expression of endogenous TLR3 was eliminated by stably transfecting the 293-hTLR8 cell line with a plasmid expressing TLR3-specific short hairpin (sh)RNA. This newly generated cell line, which did not respond to poly(I):(C), was used for further study (Figure 2B). When the 293-hTLR8 cells expressing TLR3-targeted shRNA were transfected with in vitro-transcribed RNAs, they secreted large amounts of IL-8; however, transfecting RNA containing any of the nucleoside modifications did not stimulate these cells (Figure 2B). In some experiments, we observed that m6A modification in the RNA permitted a limited amount of IL-8 release. Control cells (293, 293-pUNO null, 293-TLR3-sh, and 293-hTLR9) did not respond to RNA transfection. (Figures 2B and 2C and data not shown). To rule out that clonal artifacts were responsible for RNA-induced stimulation, at least three separate clones for each TLR-expressing cell line were analyzed and gave similar results.

In a previous study, human TLR8, but not human TLR7, was shown to signal in response to guanosine- and uridine-rich ssRNA oligomers with phosphorothioate internucleotide linkages (Heil et al., 2004). Given that TLR7 and TLR8 share R-848 as a ligand, we sought to determine whether long RNA with natural phosphodiester internucleotide linkages was also a shared ligand for these human TLRs. All of the in vitro-transcribed RNAs induced IL-8 at levels comparable to R-848 when transfected into 293-hTLR7 cells expressing TLR3-targeted shRNA. However, transfection of RNA containing modified nucleosides resulted in no induction of IL-8 (Figure 2B). Experiments performed on

cell lines expressing hTLR7 from different constructs gave similar results. Overall, these experiments demonstrate that RNA activates human TLR3, TLR7, and TLR8 and that nucleoside modifications limit the capacity of RNA to stimulate these TLRs. Specifically, m6A and s2U modifications suppress the ability of RNA to stimulate TLR3, whereas m6A, m5C, m5U, s2U, and Ψ modifications block stimulation of TLR7 and TLR8.

In the next set of experiments, RNAs isolated from natural sources were tested. First, RNA from different mammalian species were transfected into 293 cells stably expressing human TLR3, TLR7, or TLR8 (TLR7 and TLR8 cell lines also expressed TLR3-targeted shRNA). None of these RNAs induced substantial IL-8 secretion. However, bacterial total RNA, obtained from two different *E. coli* sources, induced robust IL-8 secretion (Figure 2C). These results and additional experimental evidence, first that bacterial RNA transfected to 293-hTLR9 did not induce IL-8 secretion (Figure 2C) and second that LPS and unmethylated DNA (CpG ODN), the potential contaminants in bacterial RNA isolates, did not activate the tested TLRs (Figure 2C), together indicate that bacterial RNA is an activator of TLR3, TLR7, and TLR8. Mitochondrial RNA isolated from human platelets also stimulated human TLR8, but not TLR3 or TLR7 (Figure 2C). Collectively, these data directly demonstrate that RNA that is scarce in modified nucleosides, such as those isolated from bacteria or mitochondria, stimulate selected human TLRs, whereas total mammalian RNA abundant in nucleoside modifications are non- or minimally stimulatory.

Modified Nucleosides Reduce the Capacity of RNA to Induce Cytokine Secretion and Activation Marker Expression by DCs

RNAs containing modified or unmodified nucleosides were tested on DCs. A representative data set obtained with MDDCs and IFN-α-generated MDDCs (Figures 3A and 3B) demonstrates that nucleoside modifications diminish the ability of RNA to induce TNF-α and IL-12 secretion. Results were similar (data not shown) when other sets of RNA with the same base modifications but different primary sequences and lengths were tested or when the RNAs were further modified by adding 5′ cap structure and/or 3′ end polyA-tail or by removing the 5′ triphosphate moiety, which was previously reported to promote interferon production (Kim et al., 2004). RNAs of different length and sequence induced varying amounts of TNF-α from DCs, typically less than a 2-fold difference (Figure 3C). However, we detected more variability when MDDCs from different donors were used. In most of the experiments, MDDCs responded to RNA treatment as presented in Figure 3A, but ~25% of the time, the presence of m6A reduced the RNA-mediated MDDC activation more potently than m5C or Ψ did. Under those circumstances, the relative sensitivity of MDDCs to poly(I):(C) and R-848 treatments also differed. (Figure S1 available in the Supplemental Data with this article online). This variability was not observed for primary DCs described below. By using Northern analysis we also confirmed that cellular uptake and stability of the transfected RNAs were not influenced by the nucleoside modifications (data not shown).

To determine whether primary blood DCs responded to RNA in a manner similar to cytokine-generated DCs, we purified primary monocytoid (DC1, BDCA-1$^+$) and plasmacytoid (DC2, BDCA-4$^+$) DCs from peripheral blood. Both cell types produced TNF-α when exposed to R-848, but only DC1 responded to poly(I):(C), though at a very low level, demonstrating absence of TLR3 activity in DC2. Transfection of in vitro transcripts induced TNF-α secretion in both DC1 and DC2 (Figure 3D). Data with modified RNA revealed that only transcripts in which uridine was replaced with m5U, Ψ, or s2U were not stimulatory, whereas RNAs containing m5C and m6A were almost as potent inducers of cytokines as the corresponding unmodified RNAs. This was unexpected because DC2s do not express TLR3 or TLR8 and as such should resemble the response observed in 293-hTLR7 cells. To determine whether m5C and m6A exert a dominant stimulatory effect, transcripts with m6A/Ψ double modification were tested and found to be nonstimulatory, whereas the mixture of RNA with single type of modification (m6A + Ψ) was a potent cytokine inducer. This suggested that primary DCs likely have an additional RNA signaling entity that recognizes m5C- and m6A-modified RNA and whose signaling is inhibited by modification of U residues.

FACS analysis of MDDCs treated with RNA-1571 and its modified versions revealed that modified nucleosides such as m5C, m6A, Ψ, s2U, and m6A/Ψ decrease the ability of RNAs to induce cell surface expression of CD80, CD83, CD86, and MHC class II (Figure 4). Collectively, these results demonstrate that the capacity of RNA to induce DCs to mature and secrete cytokines depends on the subtype of DC as well as on the characteristics of nucleoside modification present in the RNA with the general tendency of modifications blocking stimulation.

Suppression of RNA-Mediated Immune Stimulation Is Proportional to the Number of Modified Nucleosides Present in RNA

To ideally define the importance of nucleoside modifications that are components of natural RNA would require the construction of RNAs in vitro that accurately model the extent and diversity of nucleoside modifications of native RNAs and the ability to selectively remove modifications present in natural RNA isolates, both of which are beyond current technology. Most of the nucleoside-modified RNA utilized in the present study contained one type of modification amassing ~25% of the total nucleotides in the RNA. Because the ratio of any one particular modified nucleoside, though variable, is much lower than 25% in native RNAs, we asked what is the minimal frequency of any one particular modified nucleoside that is sufficient to limit the immunostimulatory potential of RNA. To answer this question, two approaches were used to generate RNA with limited numbers of modified nucleosides. First, we transcribed RNA in vitro in the presence of decreasing amounts of m6A, Ψ, or m5C and increasing amounts of the corresponding unmodified NTPs. We expected the incorporation of modified nucleoside phosphates into RNA to be proportional to the ratio contained in the transcription reaction, because prior RNA yields ob-

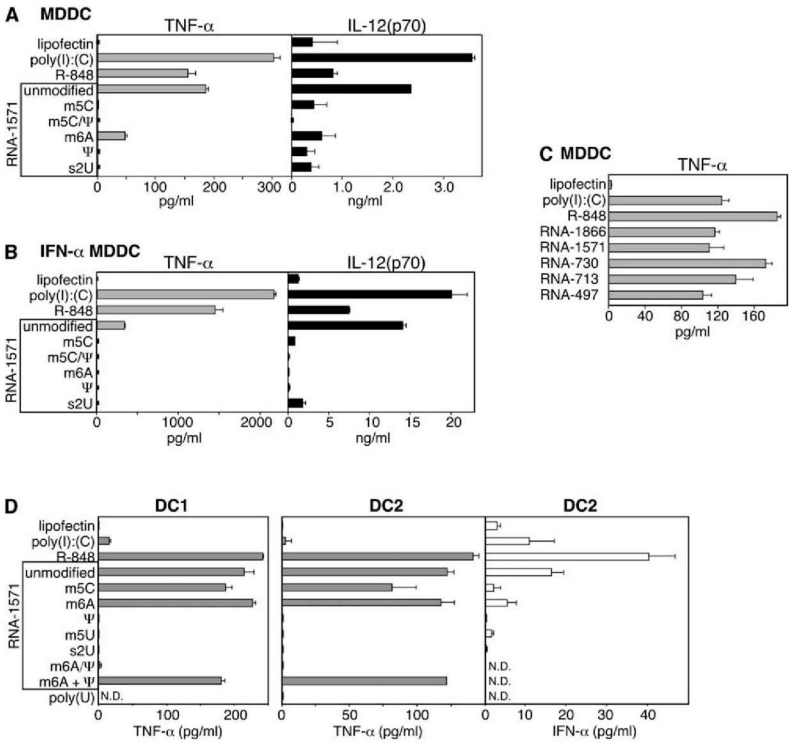

Figure 3. Cytokine Production by RNA-Transfected DCs

MDDC (A and C), IFN-α MDDCs (B), and primary DC1 and DC2 (D) were treated for 8–16 hr with lipofectin alone or complexed with R-848 (1 μg/ml) or the indicated RNA (5 μg/ml). Modified nucleosides present in RNA-1571 are noted. TNF-α, IL-12(p70), and IFN-α were measured in the supernatant by ELISA. Mean values ± SEM are shown. The results are representative of ten (A and C), four (B), and six (D) independent experiments. N.D., not determined.

tained with T7 RNAP suggested the enzyme utilizes NTPs of m6A, Ψ, or m5C almost as efficiently as the basic NTPs. HPLC analysis confirmed this notion, showing for example, that after digestion of RNA transcribed in the presence of UTP:ΨTP in a 50:50 ratio, nearly equal amounts of incorporated UMP and ΨMP were released (Figure 5A). When RNA-1571 with increasing amounts of modified nucleoside content were transfected into MDDCs, we detected that the presence of an increasing amount of modified nucleosides proportionally inhibited the capacity of RNA to induce TNF-α (Figure 5B). The presence of 0.2%–0.4% m6A, Ψ, or m5C in the RNA, which corresponds to approximately three to six modified nucleosides per one molecule of the 1571 nt-long RNA, was sufficient to cause detectable inhibition of cytokine secretion (Figure 5B). When RNAs with modified nucleoside levels of 1.7%–3.2%, which correspond to 14–29 modifications per molecule, were tested, the RNA could maintain only half of its capacity to induce expression of TNF-α. When similar transfection experiments were performed on TLR-expressing 293 cells, usually a higher percent (~2.5%) of modified nucleoside content was required to inhibit RNA-mediated signaling events (data not shown).

In the second approach, we utilized chemically synthesized 21-mer ORNs with phosphodiester internucleotide linkages and 5′ monophosphate and identical primary sequences but with modified nucleosides such as m5C, Ψ, or 2′-O-methyl-U (Um) in a single position (Figure 6A). Results obtained after transfection of MDDCs with the synthetic ORNs demonstrated that short unmodified ORNs were capable of inducing significant TNF-α secretion, but the presence of a single nucleoside modification was sufficient to abolish this effect (Figure 6B). Repeating the experiments on TLR-transformed 293 cells expressing TLR3-targeted siRNA, we found that control ORN induced 293-hTLR8 cells to secrete IL-8, whereas those containing modified nucleosides did not. When testing ORNs on hTLR3- or hTLR7-expressing cell lines, however, we saw no IL-8 secretion under any conditions (data not shown). Finally, by using Northern assay, we tested the 21-mer chemically synthesized ORNs along with 31-mer in vitro transcripts for their ability to induce TNF-α mRNA in MDDCs. ORN5

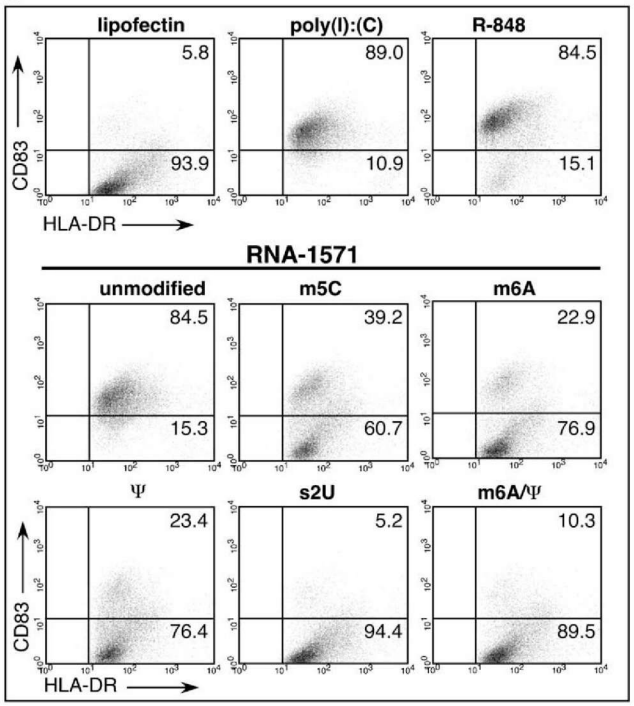

Figure 4. Activation of DCs by RNA

MDDCs were treated for 20 hr with lipofectin alone or complexed with R-848 (1 μg/ml) or the indicated RNA (5 μg/ml). Modified nucleosides present in RNA-1571 are indicated.
(A) CD83 and HLA-DR staining is shown.
(B) TNF-α was measured in the supernatants by ELISA (the asterisk represents cells that were cultured in 30-fold larger than usual volume of medium for flow cytometry). Mean fluorescence of CD80 and CD86 was determined by flow cytometry. Data are representative of four independent experiments.

B

	TNF-α*	CD80	CD86
	pg/ml	mean fluorescence	
lipofectin	0	7.6	55.3
poly(I):(C)	45.6	59.4	257.4
R848	48.3	55.2	235.4
RNA-1866			
unmodified	26.7	52.7	246.4
m5C	0	16.4	108.6
m6A	0	12.4	78.4
Ψ	0	12.0	87.5
s2U	0	8.0	62.7
m6A/Ψ	0	8.6	68.4

and ORN6 (31-mers) caused robust induction, whereas the 21-mer ORN1 control induced less TNF-α mRNA, although still well detectable, particularly in cells exposed to the protein synthesis inhibitor cycloheximide, which is also known to block degradation of selected mRNAs. More importantly, ORNs containing a single modified nucleoside induced less TNF-α mRNA, and consistently, ORN2-Um, the 2′-O-methylated ORN, was the least stimulatory (Figure 6C). Taken together, these results demonstrate that RNA-mediated immune stimulation is suppressed proportionally by the number of modified nucleosides present in RNA. Modification, when present in a single or very few positions, depending on the length of RNA, was sufficient to inhibit the stimulatory effect of RNA on MDDC and 293 cells expressing individual TLRs.

Discussion

We demonstrate here that a variety of natural RNAs had different capacities to activate immune cells. The most potent RNAs were those that had the least number of modified nucleosides; therefore, we hypothesize that nucleoside modification suppresses the immune-stimulatory effect of RNA. In a quest to prove this, several novel lines of evidence were discovered about RNA-mediated immune activation. Initially, we established that RNA is a ligand for human TLR7. Next, by using

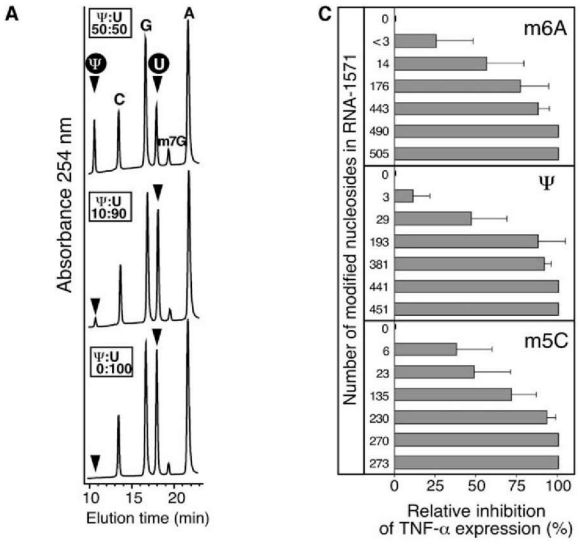

B

Modified nucleoside in reaction[a] (%)	m6A						Ψ						m5C					
	0	1	10	50	90	99	100	1	10	50	90	99	100	1	10	50	90	99	100
in RNA[b]																			
expected (%)	0	0.3	3.2	16	29	32	32	0.3	2.9	14	26	28	29	0.2	1.7	9	16	17	17
measured (%)	0	<0.2	0.9	11	28	31	32	0.2	1.9	12	24	28	29	0.4	1.4	9	15	17	17
measured (number)	0	<3	14	176	443	490	505	3	29	193	381	441	451	6	23	135	230	270	273

Figure 5. Analyzing RNA Containing Different Amounts of Modified Nucleosides

Capped RNA-1571 containing m6A, Ψ, or m5C was transcribed under conditions in which the relative ratio of m6ATP, ΨTP, or m5CTP to the corresponding unmodified NTP was 0%, 1%, 10%, 50%, 90%, 99%, and 100%.

(A) All transcripts were digested to monophosphates and analyzed by reversed-phase HPLC to determine the relative amount of modified nucleoside incorporation. For simplicity, only symbols for the nucleosides are shown. Representative absorbance profiles obtained by RNA transcribed in the presence of pseudouridine- and uridine-triphosphates (Ψ:U) at the indicated ratios are shown. Elution times are noted for 3′-monophosphates of pseudouridine (Ψ), cytidine (C), guanosine (G), uridine (U), 7-methylguanosine (m7G), and adenoside (A).

(B) Modified nucleoside content of RNA-1571. The expected percentage of m6A, Ψ, or m5C in RNA-1571 was calculated based on the relative amount of modified NTP in the transcription reaction and the nucleoside composition of RNA-1571 (expected percentage). The values for measured modified nucleoside content (in percentage) were determined based on relative values obtained after quantitation of the HPLC chromatograms. Based on these measured values and on the nucleoside content of RNA-1571 (A: 505, U: 451, C: 273, and G: 342), the number of m6A, Ψ ,or m5C per molecule of RNA-1571 was calculated. "a" represents values (%) for m6ATP, ΨTP, and m5CTP relative to ATP UTP and CTP, respectively. "b" represents values for m6A, Ψ, and m5C monophosphates relative to all NMPs.

(C) MDDCs were transfected with lipofectin-complexed capped RNA-1571 (5 μg/ml) containing the indicated amount of m6A, Ψ, or m5C. After 8 hr, TNF-α was measured in the supernatants by ELISA. Data are expressed as relative inhibition of TNF-α. Mean values ± SEM obtained in three independent experiments are shown. The number of m6A, Ψ, or m5C per molecule of RNA-1571 was calculated as indicated in (B).

RNA bearing modified nucleosides such as m5C, m5U, s2U, m6A, Ψ, or 2′-O-methyl-U, all constituents of natural RNA, we showed that modifying U, A, and C nucleosides, in general, suppresses the capacity of RNA to activate cytokine-generated DCs, as measured by secretion of TNF-α and IL-12 and by expression of CD80, CD83, CD86, and HLA-DR. Interestingly, only uridine modifications, such as m5U, s2U, or Ψ, but not m5C or m6A, could abolish the capacity of RNA to activate primary, blood-derived DCs. Distinct TLRs responded differently to RNA containing different modified nucleosides. RNA with m6A and s2U modifications did not activate TLR3, and those with m5C, m5U, s2U, m6A, or Ψ did not activate TLR7 or TLR8, whereas unmodified RNA could activate all these human TLRs. Finally, we show that RNA-mediated immune stimulation is suppressed proportionally with the number of modified nucleosides present in RNA and that even a few modifications are sufficient to exert a suppressive effect.

Nucleoside modification is the foundation of the most ancient "immune" mechanism. Bacteria methylate selected nucleosides in their own genome, which enables them to distinguish and destroy an invader's unmodified DNA with restriction enzymes. During evolution, the discrimination between host and pathogen based on characteristics of DNA methylation remains an important component of the immune system. In mammalian DNA, cytosines in CpG motifs are mostly methylated, but the lack of such modification in the genomes of microbial pathogens is recognized by TLR9, which then mediates the induction of the mammalian innate immune response (Hemmi et al., 2000).

Despite the fact that the immune stimulatory activity of RNA was discovered decades before such was identified for DNA and that RNA contains numerous modified nucleosides (Rozenski et al., 1999), the effect of nucleoside modifications on RNA immunity has not been explored. From the standpoint of immune activation, RNA and DNA share many characteristics. We have shown that RNA, similarly to DNA, is more immunogenic when derived from bacteria than from mammalian cells (Figures 1 and 2C) (Koski et al., 2004). Similar to mammalian DNA, mammalian RNA also exerts a limited but detectable level of immune activation (Figure 1). Others have reported that mammalian RNA induces IFN-α when delivered to immune cells (Diebold et al., 2004). To explain why mammalian RNAs are immunogenic, it was reasoned that in those experiments transfected RNA entered the endosomal compartments of immune cells, therefore the immune system might

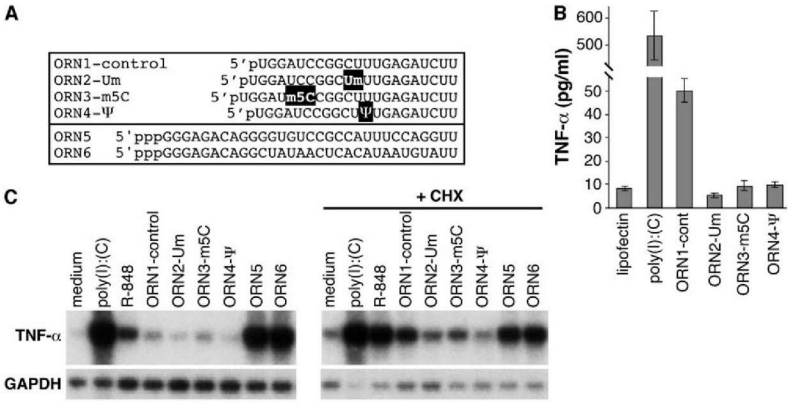

Figure 6. TNF-α Expression by RNA-Transfected DCs

(A) Sequences of oligoribonucleotides (ORNs) synthesized chemically (ORN1-4) or transcribed in vitro (ORN5-6) are shown. Positions of modified nucleosides Um (2′-O-methyluridine), m5C, and Ψ are highlighted. Human MDDCs were transfected with lipofectin alone (medium), R-848 (1 μg/ml), or with the indicated RNA (5 μg/ml) complexed with lipofectin. Where noted, cells were treated with 2.5 μg/ml cycloheximide (CHX). After 8 hr incubation, TNF-α was measured in the supernatant by ELISA (B). Mean values ± SEM are shown. The results are representative of three independent experiments. RNA isolated from the cells were analyzed by Northern blot (C).

discriminate between self and nonself RNA based on cellular location rather than some unique pathogen-associated molecular pattern (Crozat and Beutler, 2004). It has been shown, however, that the human innate immune system can also discriminate between molecular features of eukaryotic and bacterial mRNA and recognize mRNA devoid of polyA-tail as stimulatory (Koski et al., 2004). In this report, we observed potent immune stimulation with bacterial, but not with mammalian, total RNA and concluded that this was due to the difference in their modified nucleoside content. This is supported by the observation that the major mass of total RNA is rRNA, and modified nucleosides are abundant in mammalian, but not in bacterial, rRNA: 3% versus 0.8% (Bachellerie and Cavaille, 1998). We also observed that suppression of RNA-mediated immune stimulation correlated with the level of this difference in modified nucleoside content (Figure 5C). The present study now identifies nucleoside modification as a novel feature of RNA recognized by the innate immune system, specifically by TLR3, TLR7, and TLR8 (Figure 2). We observed earlier that RNA from necrotic cells activated DCs, whereas RNA from apoptotic cells did not (Kariko et al., 2004). Based on the results presented in this report, we now propose that mammalian RNA, especially the least-modified mtRNA, likely contributed to the observed effect. The immune potential of mammalian RNA might also explain why degradation of RNA during apoptosis is so critical. Fragmentation of genomic DNA is a well-established process and used consistently as a technique to define apoptosis itself. Although less described, a well-orchestrated degradation of cellular RNA also occurs in apoptotic, but not necrotic, cells. Interestingly, the most immunogenic mtRNA degrades at a very early stage of apoptosis (Crawford et al., 1997), hours before the breakdown of cytoplasmic RNA, DNA laddering (Houge et al., 1995), or morphological changes associated with apoptosis could be detected.

Both RNA and DNA are central immunogenic determinants in the autoimmune disease of systemic lupus erythematosus (SLE), which is characterized by production of autoantibodies directed against DNA, RNA, and proteins associated with nucleic acids (Ronnblom et al., 2003). In the development of SLE, studies now have established the involvement of TLR9 activation by mammalian DNA that bears hypomethylated CpG motifs (Boule et al., 2004). Another prominent target molecule in SLE is U1 small nuclear RNA, which has been recently shown to activate TLR3 (Hoffman et al., 2004), suggesting the potential involvement of an RNA-sensitive TLR in the disease process.

Nucleosides in native RNA become modified post-transcriptionally as part of their maturation process. Almost one hundred different types of modified nucleosides have been identified in RNA, but the physiological significance of these alterations is not well understood. Most of the modifications occur nonrandomly at positions conserved across diverse species, implying that they are important. Surprisingly, however, even the extensively modified tRNA could function without any modification (Sampson and Uhlenbeck, 1988), thus leaving the role of nucleoside modification very puzzling.

Pseudouridine is the most abundant modified nucleoside in RNA. It is generated by isomerization of uridines. We have demonstrated here that pseudouridine along with the other uridine modifications m5U and s2U uniquely suppress the capacity of RNA to activate primary DCs (Figure 3D). This finding implies that unmodified uridine probably contributes to the immune stimulatory action of RNA. Indeed, several points of evidence support this suggestion. In an earlier study, poly(U) was identified as the only homopolymer capable of inducing IL-12 in primed DCs (Koski et al., 2004). By using DCs

from TLR7 null mice, Diebold et al. identified TLR7 as the responding receptor for poly(U) treatment (Diebold et al., 2004). Others have shown that even nucleoside mixtures with uridine are sufficient to stimulate PBMCs to secrete TNF-α (Heil et al., 2004). Of interest, we did not find that poly(U) or any other RNA homopolymer activated primary DCs or human TLR3, TLR7, or TLR8 when transformed 293 cells expressing these receptors were used for testing. Presence of Ψ in RNA promotes base stacking, thereby stabilizing RNA duplex regions (Charette and Gray, 2000), which might explain why Ψ-modified RNA could potently activate TLR3 (Figure 2B).

N6-methyladenosine (m6A) is the only base-modified nucleoside that is present in all RNA types, including rRNA, tRNA, and snRNA, as well as in mRNAs of cellular and viral origins. The methylation in m6A interferes with Watson-Crick base pairing, thus, its presence destabilizes RNA duplexes (Kierzek and Kierzek, 2003). This characteristic of m6A might explain why RNA containing m6A did not stimulate TLR3 (Figure 2B). m6A is present in mRNA of mammalian cells and RNA of viruses that replicate in the nucleus such as influenza, adenovirus, HSV, SV40, and RSV (Bokar and Rottman, 1998). In general, m6A modifications were found internally, mostly in coding sequences, and viral mRNA usually contained significantly more m6A than cellular mRNA (Bokar and Rottman, 1998). Interestingly, Rous sarcoma virus replicated similarly with and without m6A when tested in cell culture (Kane and Beemon, 1987), therefore no function could be assigned to m6A in this viral mRNA. It is tempting to speculate that the presence of m6A in viral RNA might serve the virus by allowing it to avoid immune activation. This suggestion is strengthened by considering that the frequency of m6A modifications found in viral mRNAs, up to eight per a 1.8 kb-long segment of influenza RNA (Narayan et al., 1987), is sufficient to suppress the capacity of RNA to activate DCs (Figure 5). Because those early studies with viruses were performed in cell culture and not in animals, the immune suppressive effect of m6A might have been missed.

RNA containing either m6A or m5C stimulated primary DC1 and DC2 as potently as the corresponding nonmodified RNA (Figure 3D). This was an unexpected finding, because DC2 express only TLR7 (Ito et al., 2002; Matsumoto et al., 2003) and thus resemble 293-hTLR7 cells that did not respond to any of the modified RNA (Figure 2B). Because all tested RNA were delivered by transfection to the cells, where they could interact with many different RNA binding proteins, it is possible an RNA receptor is uniquely present in primary DCs, but not in 293 cells or MDDCs. Such an RNA sensor could likely recognize U-rich RNA patterns even in the presence of the m6A and m5C nucleoside residues, but not when the U residues are masked by modifications. Support for this hypothesis was provided by the observations that RNA containing both m6A and Ψ modifications on the same strand did not activate DC1 or DC2, whereas mixtures of RNA containing either m6A or Ψ modification on separate strands potently activated these cells (Figure 3D). In this regard, there are already examples for single- and double-stranded RNA-responsive cytoplasmic receptors such as FADD, RIG-1, and PKR that function in the innate immune system independently from TLRs (Sen and Sarkar, 2005).

By using TLR7-expressing cell lines, we demonstrate (Figure 2) that in vitro-transcribed RNA and bacterial RNA, but not dsRNA, are ligands for human TLR7. This finding is in discordance with results obtained by Heil et al. (2004), who showed that human TLR7 was nonresponsive to RNA oligomers with phosphorothioate linkage. Differences in the stimulating RNA, such as long RNA versus short ORNs with phosphorothioate linkage, likely account for the conflicting result. We observed that all in vitro-transcribed RNAs, regardless of their primary sequence, as well as bacterial RNA activated TLR7 expressing 293 cells, demonstrating that natural RNA is a ligand for this receptor.

In summary, we demonstrate that selected natural RNA isolated from mammalian and bacterial cells and RNA transcribed in vitro or synthesized chemically activate human DCs and stably transformed 293 cells expressing human TLR3, TLR7, or TLR8. Such activation was reduced or completely eliminated with RNA containing naturally occurring modified nucleosides, such as m5C, m6A, m5U, pseudouridine, or 2′-O-methyl-U. Insights gained from this study could advance our understanding of autoimmune diseases where nucleic acids play a prominent role in the pathogenesis, determine a role for nucleoside modifications in viral RNA, and give future directions into the design of therapeutic RNAs.

Experimental Procedures

Plasmids and Reagents

Plasmids pTEVluc (D. Gallie, UC Riverside), pT7T3D-MART-1 (ATCC, Manassas, VA), pUNO-hTLR3 (InvivoGen, San Diego, CA), and pSVren (Kariko et al., 2004) were obtained. Human TLR3-specific siRNA, pTLR3-sh was constructed by inserting synthetic ODN-encoding shRNA with 20 nt-long homology to human TLR3 (nt 703–722, accession: NM_003265) into plasmid pSilencer 4.1-CMV-neo (Ambion, Austin, TX). pCMV-hTLR3 was obtained by first cloning hTLR3-specific PCR product (nt 80–2887; accession NM_003265) into pCRII-TOPO (Invitrogen, Carlsbad, CA), then released with NheI-HindIII cutting and subcloning to the corresponding sites of pcDNA3.1 (Invitrogen). Cells were treated with the following reagents: LPS (*E. coli* 055:B5) (Sigma Chemical Co, St. Louis, MO), CpG ODN-2006, and R-848 (InvivoGen).

Cells and Cell Culture

Human embryonic kidney 293 cells (ATCC) were propagated in DMEM supplemented with glutamine (Invitrogen) and 10% FCS (Hyclone, Ogden, UT) (complete medium). 293-hTLR3 and 293 pUNO null cell lines were generated by transforming 293 cells with pUNO-hTLR3 and pUNO null. Cell lines 293-hTLR7, 293-hTLR8, and 293-hTLR9 (InvivoGen) were grown in complete medium supplemented with blasticidin (10 μg/ml) (Invivogen). Cell lines 293-ELAM-luc and TLR7-293 (M. Lamphier, Eisai Research Institute, Andover MA) and TLR3-293 cells were cultured as described (Kariko et al., 2004). Cell lines 293, 293-hTLR7, and 293-hTLR8 were stably transfected with pTLR3-sh and selected with G-418 (400 μg/ml) (Invitrogen). Neo-resistant colonies were screened, and only those that did not express TLR3, determined as lack of IL-8 secretion in response to poly(I):(C), were used. Cell lines were used as soon as possible, because shRNA-mediated suppression of TLR3 became leaky over time. Leukopheresis samples were obtained from HIV-uninfected volunteers through an IRB-approved protocol. DCs were produced as described previously and treated with GM-CSF (50 ng/ml) + IL-4 (100 ng/ml) (Weissman et al., 2000) or IFN-α (1000 U/ml) (Santini et al., 2000) (R&D Systems, Minneapolis, MN) in AIM

V medium (Invitrogen). Primary myeloid and plasmacytoid DCs (DC1 and DC2) were obtained from peripheral blood by using BDCA-1 and BDCA-4 cell isolation kits (Miltenyi Biotec Auburn, CA), respectively.

RNA

In Vitro-Transcribed RNA

By using in vitro transcription assays (MessageMachine and MegaScript kits; Ambion), the following long RNAs were generated by T7 RNAP as described (Kariko et al., 1998) (note: the names of templates are in parentheses), the number in the name of the RNA specifies the length: RNA-1866 (NdeI-linearized pTEVluc) encodes firefly luciferase and a 50 nt-long polyA-tail, RNA-1571 (SspI-linearized pSVren) encodes *Renilla* luciferase, RNA-730 (HindIII-linearized pT7T3D-MART-1) encodes the human melanoma antigen MART-1, RNA-713 (EcoRI-linearized pT7T3D-MART-1) corresponds to antisense sequence of MART-1, and RNA-497 (BglII-linearized pCMV-hTLR3) encodes a partial 5′ fragment of hTLR3. To obtain RNA bearing nucleoside modification, the transcription reaction was assembled with the replacement of one (or two) of the basic NTPs with the corresponding triphosphate-derivative(s) of the modified nucleotide 5-methylcytidine, 5-methyluridine, 2-thiouridine, N6-methyladenosine, or pseudouridine (TriLink, San Diego, CA). In each transcription reaction, all four nucleotides or their derivatives were present in equimolar (7.5 mM) concentration. In selected experiments, 6 mM m7GpppG cap analog (New England BioLabs, Beverly, MA) was also included to obtain capped RNA. To obtain RNA containing increasing amounts of m6A, Ψ, or m5C, the transcription reaction was performed in a reaction mix in which the ratio of one particular modified NTP relative to the corresponding unmodified NTP was 0%, 1%, 10%, 50%, 90%, 99%, and 100%. By using DNA oligodeoxynucleotide templates and T7 RNAP (Silencer siRNA construction kit, Ambion), ORN5 and ORN6 were generated.

Natural and Synthetic RNA

Mitochondria were isolated from outdated platelets (obtained from the University of Pennsylvania Blood Bank under an IRB approved protocol) by using a fractionation lyses procedure as described by the manufacturer (Mitochondria Isolation Kit; Pierce, Rockford, IL). RNA was isolated from the purified mitochondria, cytoplasmic and nuclear fractions of 293 cells, unfractioned 293 cells, rat liver, mouse cell line TUBO, and DH5α strain of *E. coli* by Master Blaster (Bio-Rad, Hercules, CA). Bovine tRNA, wheat tRNA, yeast tRNA, *E. coli* tRNA, poly(A)$^+$ mRNA from mouse heart, and poly(I):(C) were purchased from Sigma; total RNA from human spleen and *E. coli* RNA were purchased from Ambion. Oligoribonucleotide 5′-monophosphates were synthesized chemically (Dharmacon, Lafayette, CO).

Aliquots of RNA samples were incubated in the presence of Benzonase nuclease (1 U per 5 μl of RNA at 1 μg/μl for 1 hr) (Novagen, Madison, WI). Aliquots of RNA-730 were digested with alkaline phosphatase (New England Biolab). Generally, RNA samples were analyzed by denaturing agarose or polyacrylamide gel electrophoresis for quality assurance. Assays for LPS in RNA preparations using the Limulus Amebocyte Lysate gel clot assay were negative with a sensitivity of 3 pg/ml (University of Pennsylvania, Core Facility).

HPLC Analysis

Nucleoside monophosphates were separated and visualized via HPLC (Greenwood and Gentry, 2002). Briefly, first to release free nucleoside 3′-monophosphates, 5 μg aliquots of RNA were digested with 0.1 U RNase T2 (Invitrogen) in 10 μl of 50 mM NaOAc and 2 mM EDTA buffer (pH 4.5) overnight, then the samples were injected into an Agilent 1100 HPLC by using a Waters Symmetry C18 column (Waters, Milford, MA). Buffer A consisted of 30 mM KH_2PO_4 and 10 mM tetraethylammonium phosphate (PicA reagent, Waters), pH 6.0. Buffer B was acetonitrile. At a flow rate of 1 mL/min, a gradient from 100% buffer A to 30% buffer B was run over 60 min. Nucleotides were detected by using a photodiode array at 254 nm. Identities were verified by retention times and spectra. Relative percentage of modified versus the corresponding unmodified nucleosides in RNA was determined for each transcript.

Treatment of Cells

Parental 293, 293-hTLR7, and 293-hTLR8 cells, all expressing TLR3-specific siRNA, and 293-hTLR9, TLR3-293 were seeded into 96-well plates (5 × 10^4 cells/well) and cultured without antibiotics. On the subsequent day, the cells were exposed to R-848 or RNA with prior complexing to lipofectin (Invitrogen) as previously described (Kariko et al., 1998). The RNA was removed after 1 hr, and the cells were further incubated in complete medium for 7 hr. Supernatants were collected for IL-8 measurement.

DCs in 96-well plates (~1.1 × 10^5 cells/well) were treated with R-848, lipofectin alone, or complexed with RNA for 1 hr when the medium was replaced by fresh medium. Cells and medium were harvested at the end of an 8–20 hr incubation; cells were harvested for either RNA isolation or flow cytometry, whereas the collected culture medium was subjected to cytokine ELISA. The levels of IL-12 (p70) (BD Biosciences Pharmingen, San Diego, CA), IFN-α, TNF-α, and IL-8 (Biosource International, Camarillo, CA) were measured in supernatants by ELISA. Cultures were performed in triplicate to quadruplicate and measured in duplicate.

Analysis of DC Activation

DCs treated as described above were analyzed by flow cytometry after 20 hr. DCs were stained with CD83-phycoerythrin mAb (Research Diagnostics Inc, Flanders, NJ), HLA-DR-Cy5PE, and CD80 or CD86-fluorescein isothiocyanate mAb and analyzed on a FACScalibur flow cytometer by using CellQuest software (BD Biosciences).

Northern Blot Analysis

RNA was isolated from MDDCs after an 8 hr incubation following treatment as described above. Where noted, cells were treated with 2.5 μg/ml cycloheximide (Sigma) 30 min prior to the stimulation and throughout the entire length of incubation. RNA samples were processed and analyzed on Northern blots as described (Kariko et al., 2004) by using human TNF-α and GAPDH probes derived from plasmids (pE4 and pHcGAP, respectively) obtained from ATCC.

Supplemental Data

Supplemental Data include one figure and are available with this article online at http://www.immunity.com/cgi/content/full/23/2/165/DC1/.

Acknowledgments

This work was supported by National Institutes of Health grants AI060505, AI50484, and DE14825.

Received: January 14, 2005
Revised: May 26, 2005
Accepted: June 15, 2005
Published: August 23, 2005

References

Alexopoulou, L., Holt, A.C., Medzhitov, R., and Flavell, R.A. (2001). Recognition of double-stranded RNA and activation of NF-kB by Toll-like receptor 3. Nature *413*, 732–738.

Bachellerie, J.-P., and Cavaille, J. (1998). Small nucleolar RNAs guide the ribose methylations of eukaryotic rRNAs. In Modification and Editing of RNA, H. Grosjean and R. Benne, eds. (Washington D.C.: ASM Press), pp. 255–272.

Bokar, J.A., and Rottman, F.M. (1998). Biosynthesis and functions of modified nucleosides in eukaryotic mRNA. In Modification and Editing of RNA, H. Grosjean and R. Benne, eds. (Washington D.C.: ASM Press), pp. 183–200.

Boule, M.W., Broughton, C., Mackay, F., Akira, S., Marshak-Rothstein, A., and Rifkin, I.R. (2004). Toll-like receptor 9-dependent and -independent dendritic cell activation by chromatin-immunoglobulin G complexes. J. Exp. Med. *199*, 1631–1640.

Charette, M., and Gray, M.W. (2000). Pseudouridine in RNA: what, where, how, and why. IUBMB Life *49*, 341–351.

Crawford, D.R., Lauzon, R.J., Wang, Y., Mazurkiewicz, J.E., Schools, G.P., and Davies, K.J. (1997). 16S mitochondrial ribosomal

RNA degradation is associated with apoptosis. Free Radic. Biol. Med. *22*, 1295–1300.

Crozat, K., and Beutler, B. (2004). TLR7: a new sensor of viral infection. Proc. Natl. Acad. Sci. USA *101*, 6835–6836.

Diebold, S.S., Kaisho, T., Hemmi, H., Akira, S., and Reis e Sousa, C. (2004). Innate antiviral responses by means of TLR7-mediated recognition of single-stranded RNA. Science *303*, 1529–1531.

Greenwood, R.C., and Gentry, D.R. (2002). The effect of antibiotic treatment on the intracellular nucleotide pools of Staphylococcus aureus. FEMS Microbiol. Lett. *208*, 203–206.

Heil, F., Hemmi, H., Hochrein, H., Ampenberger, F., Kirschning, C., Akira, S., Lipford, G., Wagner, H., and Bauer, S. (2004). Species-specific recognition of single-stranded RNA via Toll-like receptor 7 and 8. Science *303*, 1526–1529.

Hemmi, H., Takeuchi, O., Kawai, T., Kaisho, T., Sato, S., Sanjo, H., Matsumoto, M., Hoshino, K., Wagner, H., Takeda, K., and Akira, S. (2000). A Toll-like receptor recognizes bacterial DNA. Nature *408*, 740–745.

Hoffman, R.W., Gazitt, T., Foecking, M.F., Ortmann, R.A., Misfeldt, M., Jorgenson, R., Young, S.L., and Greidinger, E.L. (2004). U1 RNA induces innate immunity signaling. Arthritis Rheum. *50*, 2891–2896.

Houge, G., Robaye, B., Eikhom, T., Golstein, J., Mellgren, G., Gjertsen, B., Lanotte, M., and Doskeland, S. (1995). Fine mapping of 28S rRNA sites specifically cleaved in cells undergoing apoptosis. Mol. Cell. Biol. *15*, 2051–2062.

Ito, T., Amakawa, R., Kaisho, T., Hemmi, H., Tajima, K., Uehira, K., Ozaki, Y., Tomizawa, H., Akira, S., and Fukuhara, S. (2002). Interferon-a and Interleukin-12 are induced differentially by Toll-like receptor 7 ligands in human blood dendritic cell subsets. J. Exp. Med. *195*, 1507–1512.

Jurk, M., Heil, F., Vollmer, J., Schetter, C., Krieg, A.M., Wagner, H., Lipford, G., and Bauer, S. (2002). Human TLR7 or TLR8 independently confer responsiveness to the antiviral compound R-848. Nat. Immunol. *3*, 499.

Kane, S., and Beemon, K. (1987). Inhibition of methylation at two internal N6-methyladenosine sites caused by GAC to GAU mutations. J. Biol. Chem. *262*, 3422–3427.

Kariko, K., Kuo, A., Barnathan, E.S., and Langer, D.J. (1998). Phosphate-enhanced transfection of cationic lipid-complexed mRNA and plasmid DNA. Biochim. Biophys. Acta *1369*, 320–334.

Kariko, K., Ni, H., Capodici, J., Lamphier, M., and Weissman, D. (2004). mRNA is an endogenous ligand for Toll-like receptor 3. J. Biol. Chem. *279*, 12542–12550.

Kierzek, E., and Kierzek, R. (2003). The thermodynamic stability of RNA duplexes and hairpins containing N6-alkyladenosines and 2-methylthio-N6-alkyladenosines. Nucleic Acids Res. *31*, 4472–4480.

Kim, D.H., Longo, M., Han, Y., Lundberg, P., Cantin, E., and Rossi, J.J. (2004). Interferon induction by siRNAs and ssRNAs synthesized by phage polymerase. Nat. Biotechnol. *22*, 321–325. Published online: February 8, 2004. 10.1038/nbt940.

Koski, G.K., Kariko, K., Xu, S., Weissman, D., Cohen, P.A., and Czerniecki, B.J. (2004). Cutting edge: innate immune system discriminates between RNA containing bacterial versus eukaryotic structural features that prime for high-level IL-12 secretion by dendritic cells. J. Immunol. *172*, 3989–3993.

Margulis, L., and Chapman, M.J. (1998). Endosymbioses: cyclical and permanent in evolution. Trends Microbiol. *6*, 342–345.

Matsumoto, M., Funami, K., Tanabe, M., Oshiumi, H., Shingai, M., Seto, Y., Yamamoto, A., and Seya, T. (2003). Subcellular localization of Toll-like receptor 3 in human dendritic cells. J. Immunol. *171*, 3154–3162.

Medzhitov, R. (2001). Toll-like receptors and innate immunity. Nat. Rev. Immunol. *1*, 135–145.

Narayan, P., Ayers, D.F., Rottman, F.M., Maroney, P.A., and Nilsen, T.W. (1987). Unequal distribution of N6-methyladenosine in influenza virus mRNAs. Mol. Cell. Biol. *7*, 1572–1575.

Ronnblom, L., Eloranta, M.L., and Alm, G.V. (2003). Role of natural interferon-alpha producing cells (plasmacytoid dendritic cells) in autoimmunity. Autoimmunity *36*, 463–472.

Rozenski, J., Crain, P., and McCloskey, J. (1999). The RNA Modification Database: 1999 update. Nucleic Acids Res. *27*, 196–197.

Sampson, J.R., and Uhlenbeck, O.C. (1988). Biochemical and physical characterization of an unmodified yeast phenylalanine transfer RNA transcribed in vitro. Proc. Natl. Acad. Sci. USA *85*, 1033–1037.

Santini, S.M., Lapenta, C., Logozzi, M., Parlato, S., Spada, M., Di Pucchio, T., and Belardelli, F. (2000). Type I interferon as a powerful adjuvant for monocyte-derived dendritic cell development and activity in vitro and in Hu-PBL-SCID mice. J. Exp. Med. *191*, 1777–1788.

Sen, G.C., and Sarkar, S.N. (2005). Transcriptional signaling by double-stranded RNA: role of TLR3. Cytokine Growth Factor Rev. *16*, 1–14.

Wang, T., Town, T., Alexopoulou, L., Anderson, J.F., Fikrig, E., and Flavell, R.A. (2004). Toll-like receptor 3 mediates West Nile virus entry into the brain causing lethal encephalitis. Nat. Med. *10*, 1366–1373.

Weissman, D., Ni, H., Scales, D., Dude, A., Capodici, J., McGibney, K., Abdool, A., Isaacs, S.N., Cannon, G., and Kariko, K. (2000). HIV gag mRNA transfection of dendritic cells (DC) delivers encoded antigen to MHC class I and II molecules, causes DC maturation, and induces a potent human in vitro primary immune response. J. Immunol. *165*, 4710–4717.

nature COMMUNICATIONS

ARTICLE

Received 17 Mar 2015 | Accepted 2 Sep 2015 | Published 13 Oct 2015

DOI: 10.1038/ncomms9533 OPEN

Mucosal vaccination with attenuated *Mycobacterium tuberculosis* induces strong central memory responses and protects against tuberculosis

Deepak Kaushal[1,2,*], Taylor W. Foreman[1,3,*], Uma S. Gautam[1], Xavier Alvarez[1], Toidi Adekambi[4,5], Javier Rangel-Moreno[6], Nadia A. Golden[1], Ann-Marie F. Johnson[1], Bonnie L. Phillips[1,3], Muhammad H. Ahsan[1], Kasi E. Russell-Lodrigue[1], Lara A. Doyle[1], Chad J. Roy[1], Peter J. Didier[1], James L. Blanchard[1], Jyothi Rengarajan[4,5], Andrew A. Lackner[1,2,7], Shabaana A. Khader[8] & Smriti Mehra[1,9,10]

Tuberculosis (TB) is a global pandaemic, partially due to the failure of vaccination approaches. Novel anti-TB vaccines are therefore urgently required. Here we show that aerosol immunization of macaques with the *Mtb* mutant in SigH (MtbΔ*sigH*) results in significant recruitment of inducible bronchus-associated lymphoid tissue (iBALT) as well as $CD4^+$ and $CD8^+$ T cells expressing activation and proliferation markers to the lungs. Further, the findings indicate that pulmonary vaccination with MtbΔ*sigH* elicited strong central memory $CD4^+$ and $CD8^+$ T-cell responses in the lung. Vaccination with MtbΔ*sigH* results in significant protection against a lethal TB challenge, as evidenced by an approximately three log reduction in bacterial burdens, significantly diminished clinical manifestations and granulomatous pathology and characterized by the presence of profound iBALT. This highly protective response is virtually absent in unvaccinated and BCG-vaccinated animals after challenge. These results suggest that future TB vaccine candidates can be developed on the basis of MtbΔ*sigH*.

[1] Tulane National Primate Research Center, Covington, Louisiana 70433, USA. [2] Department of Microbiology and Immunology, Tulane Health Sciences Center, New Orleans, Louisiana 70112, USA. [3] Biomedical Sciences Graduate Program, Tulane Health Sciences Center, New Orleans, Louisiana 70112, USA. [4] Yerkes National Primate Research Center, Atlanta, Georgia 30329, USA. [5] Emory Vaccine Center, Atlanta, Georgia 30329, USA. [6] University of Rochester Medical Center, Rochester, New York 14642, USA. [7] Department of Pathology, Tulane Health Sciences Center, New Orleans, Louisiana 70112, USA. [8] Department of Molecular Microbiology, Washington University at St Louis, St Louis, Missouri 63110, USA. [9] Center for Biomedical Research Excellence, Louisiana State University School of Veterinary Medicine, Baton Rouge, Louisiana 70803, USA. [10] Department of Pathobiological Sciences, Louisiana State University School of Veterinary Medicine, Baton Rouge, Louisiana 70803, USA. * These authors contributed equally to this work. Correspondence and requests for materials should be addressed to D.K. (email: dkaushal@tulane.edu) or to S.M. (email: smehra@lsu.edu).

Despite widespread use of the bacille Calmette-Guérin (BCG) vaccine, *Mycobacterium tuberculosis* (*Mtb*) infection and the resulting incidence of tuberculosis (TB) remains a major global concern. The BCG vaccine, to a large extent and with some exceptions, mitigates only the most severe aspects of infection and exhibits a highly variable efficacy, especially in high-burden areas[1]. The majority of *Mtb*-infected individuals, including BCG-vaccinated ones, develop persistent but asymptomatic TB infection following *Mtb* exposure, rather than sterilizing immunity[2]. These individuals retain a finite risk of reactivation because of comorbidities such as HIV or diabetes. Developing new and efficacious TB vaccines is clearly the most effective intervention for containing the TB pandaemic[3–5]. To this end, a number of novel candidates are currently being evaluated either as potential replacements for BCG or to boost BCG-generated responses using a variety of approaches[6]. However, a frontline candidate that attempted to boost existing BCG responses failed to protect a target population against TB in a high-burden setting[7]. These results provide further impetus to the objective of replacing BCG with a new live attenuated vaccine.

The failure to generate an effective TB vaccine is attributed to a lack of specific immune correlates of protection from *Mtb* infection and TB disease. Of interest are adaptive responses, particularly pathogen-specific memory $CD4^+$ and $CD8^+$ T-cell-mediated responses essential for successful bacterial control during LTBI. BCG is generally considered to be inefficient in generating central memory $CD4^+$ and $CD8^+$ T-cell responses[8], although long-term immunity following BCG administration is possible in some settings[9]. This contributes to the widely perceived inability of the vaccine to confer long-term protection against TB[10]. Thus, understanding related immune parameters and how perturbation by comorbidities leads to TB may be useful for effective TB vaccine design.

Aerosol delivery of BCG to the lung enhances protective efficacy[11], including in macaques[12]. Further, aerosol TB vaccination might allow co-delivery of vaccine and adjuvants[13]. Aerosol–BCG resulted in significantly improved protection in guinea pigs against *Mtb* challenge compared with conventional vaccination[11]. Besides, an adenoviral vector expressing *Mtb* antigens elicited robust responses following aerosol delivery[14].

Attenuated mycobacteria have evoked interest as potential BCG-replacement vaccines[15]. The *Mtb* antigen repertoire counterintuitively evokes strong immunity, suggesting that such responses work in the pathogen's favour[16]. Immune-evasive pathways of *Mtb* are therefore the key to understand mechanisms of *Mtb* persistence[17]. SigH orchestrates a key stress-response pathway in *Mtb* that mitigates oxidative stress through induction of antioxidant production[18]. The *Mtb* mutant in *sigE*, which is part of the SigH regulon, elicited protection from *Mtb* infection[19]. Further, the *M. avium paratuberculosis sigH* mutant is being evaluated as a candidate vaccine for protecting cattle (US20140271719A1 (Pending US Patent, Adel Talaat)). Besides, aerosol immunization of macaques with the Mtb*Δsig*H mutant failed to cause disease[20]. This was in direct contrast to the phenotype of this mutant in C57Bl/6 mice, in which the *sigH*-null strain replicated to levels comparable to those of parental *Mtb*[18]. While the Mtb*Δsig*H mutant in H37Rv did not have a phenotype in monocytes[21], the mutant in the CDC1551 strain exhibited growth restriction in bone marrow-derived macrophages (BMDMs)[22]. These results suggest that Mtb*Δsig*H fails to neutralize host-generated oxidants *in vivo* and is controlled in an elite manner by the primate innate immune system. Macaques accurately model several aspects of the human TB syndrome including partial protection from BCG vaccination[23,24], different outcomes[25] and the full spectrum of pathology[26,27], and have the unique capacity to model *Mtb*/HIV co-infection[28,29]. A World Health Organization working group strongly recommended validation of candidate live TB vaccines in this model[30].

In the current study, aerosol vaccination with Mtb*Δsig*H elicited strong $CD4^+$ and $CD8^+$ central memory T-cell responses as well as a robust T-helper 1 (Th1) response correlating with significantly greater protection from lethal *Mtb* challenge in rhesus macaques. Furthermore, protection from lethal TB in Mtb*Δsig*H-vaccinated animals was characterized by the presence of highly organized bronchus-associated lymphoid tissue (iBALT) associated with granulomas, following *Mtb* challenge.

Results

Mtb*Δsig*H infection and increased iBALT. We have previously established a correlation between the levels of ectopic lymphoid structures known as iBALT and the control of *Mtb* infection in a latent state. Experimentally infected macaques had significantly greater levels of iBALT in their lungs during LTBI, and this response was markedly reduced during TB disease[31]. iBALT was characterized by the presence of $CD20^+$ B and $CXCR5^+$ T cells. The expression of CXCR5 on T cells within iBALT follicles governed correct orientation and localization of T cells and macrophage activation[31]. Since aerosol infection of macaque lungs with Mtb*Δsig*H resulted in the virtually complete clearance of infection, we used samples from this previous study[20] to assess whether the lungs of Mtb*Δsig*H-infected macaques harboured increased iBALT. Lung sections from six macaques, each exposed to high doses of *Mtb* CDC1551 strain or the isogenic Mtb*Δsig*H mutant, were co-stained for expression of CD3 and CD45R (B220)[31]. Immunofluorescence revealed that lung lesions from animals infected with the mutant contained significantly greater iBALT signal (Fig. 1a), relative to those infected with *Mtb*

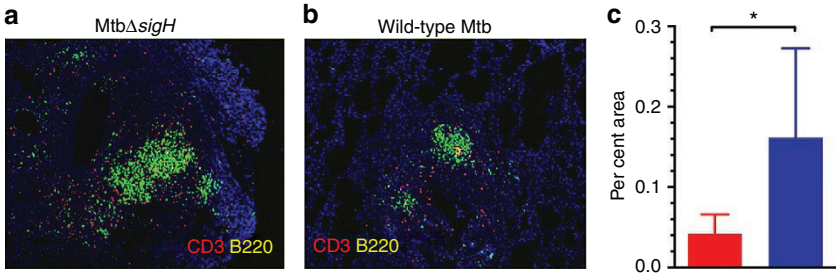

Figure 1 | iBALT formation induced by Mtb*Δsig*H vaccination. Co-staining with CD3 and B220 revealed that lung granulomas following infection with Mtb*Δsig*H (**a**) exhibited a significantly increased iBALT response relative to infection with *Mtb* (**b**). White scale bar, 500 μm. Data from multiple lesions from six different animals were used in the analyses. (**c**) The percentage of area occupied by iBALT follicles relative to total lung area was analysed in animals challenged with *Mtb* (red) and Mtb*Δsig*H (dark blue). $^*P<0.05$ (Student's *t*-test). Data are means ± s.d. Samples from four to five animals in each group were used for analysis.

(Fig. 1b). The percentage of area occupied by iBALT was significantly greater in samples from MtbΔ*sigH*-infected than *Mtb*-infected animals ($P<0.05$; Fig. 1c). In addition, the total lung area involved in iBALT follicles (μm^2; $P<0.01$) and the average size of these iBALT follicles (μm^2; $P<0.0001$, Student's *t*-test) was also significantly greater in sections derived from MtbΔ*sigH*-infected, relative to *Mtb*-infected animals (Supplementary Fig. 1a,b). These results further support our previous observations that protection from *Mtb* infection directly correlates with the presence of granuloma-associated iBALT and suggested that the lungs of MtbΔ*sigH*-infected macaques could exemplify an environment conducive to protection from TB.

Analysis of aerosol-MtbΔ*sigH* as an anti-TB vaccine candidate. Encouraged by the magnitude of iBALT induction in macaques infected with MtbΔ*sigH*, we conceived a vaccine study to assess both the immunogenicity as well as the efficacy of this mutant as a potential vaccine against pulmonary TB. The design of the macaque study is outlined in Fig. 2a. Since enhanced iBALT responses were observed in the lungs of animals infected with the mutant strain via the aerosol route, we postulated that vaccination via the same route would have a greater chance of eliciting protection. Furthermore, BCG vaccination is more effective via the pulmonary route, indicating that local responses, elicited by matching the route of the vaccination to that of infection, may be critical to protect against TB[11,12]. Before and following single aerosol vaccination with MtbΔ*sigH* at a dose that elicited strong iBALT response[20], both peripheral blood and lung compartments were repeatedly sampled to obtain cells for immune studies and transcriptomics. Eight weeks post vaccination, animals were challenged via aerosol, with a highly lethal dose of *Mtb*. Unvaccinated and BCG (aerosol)-vaccinated groups were included as appropriate controls (Fig. 2a). All animals that received aerosol–BCG or MtbΔ*sigH* vaccination became tuberculin skin test (TST) positive (Supplementary Table 1).

Absence of disease on vaccination with MtbΔ*sigH* or BCG. Aerosolization of broth-cultured, log-phase BCG and MtbΔ*sigH* was performed as described in the Methods section[20,25,29,32,33]. Microbial efficiency of BCG and MtbΔ*sigH* was highly equivalent during aerosolization. Aerosol vaccination of macaques with MtbΔ*sigH* and BCG deposited ~1,000 colony-forming unit (CFU) bacilli into the deep lung. Aerosol vaccination with either strain resulted in a positive TST (Supplementary Table 1) but did not induce dyspnoea, anorexia or significant changes in body temperatures relative to pre-infection values (Fig. 2b). The body weights of all vaccinated animals also remained relatively normal during the post-vaccination/pre-challenge phase with the exception of a slight decline (<3%) in the body weights of BCG-vaccinated animals 3–4 weeks post vaccination (Fig. 2c). None of the vaccinated animals exhibited an increase in serum C-reactive protein (CRP) levels relative to unvaccinated animals at any time post vaccination (Fig. 2d). Further, thoracic radiographs acquired post vaccination on all 14 vaccinated animals were normal (Fig. 2e).

Differential persistence of MtbΔ*sigH* and BCG in BAL. The persistence of live mycobacteria was evaluated in bronchoalveolar lavage (BAL) from both MtbΔ*sigH*- and BCG-vaccinated macaques. Three weeks after vaccination, greater levels of MtbΔ*sigH* were recovered from BAL compared with BCG (Fig. 3a). At week 5 post vaccination, BCG could not be recovered from BAL, while detectable levels of MtbΔ*sigH* were still recovered (Fig. 3a), indicating that this strain might persist longer

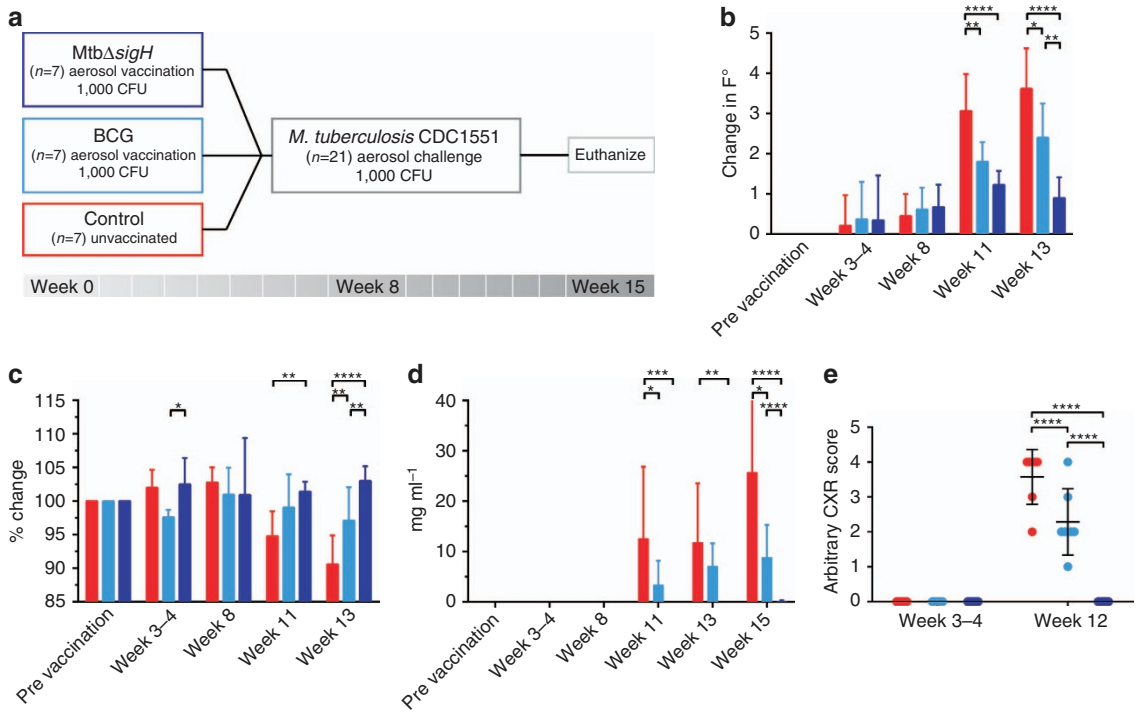

Figure 2 | Study outline and clinical correlates of vaccination and infection. (**a**) Three groups of seven macaques were used: unvaccinated (red); vaccinated with BCG (light blue) and vaccinated with MtbΔ*sigH* (dark blue). (**b**) Changes (Δ°F) in body temperature; (**c**) changes in percentage of body weight; (**d**) changes in serum CRP ($\mu g\,ml^{-1}$) levels; and (**e**) changes in relative thoracic radiograph (CXR) scores, over the course of the vaccination and infection phases. CXRs were scored in a blinded manner by categorizing between zero and four based on increasing involvement in the granulomatous pathology. *$P<0.05$, **$P<0.01$, ***$P<0.001$, ****$P<0.0001$ using two-way ANOVA with Tukey's correction for multiple comparisons. Data are means ± s.d. Samples from all seven animals in each group were used for analysis at each time point.

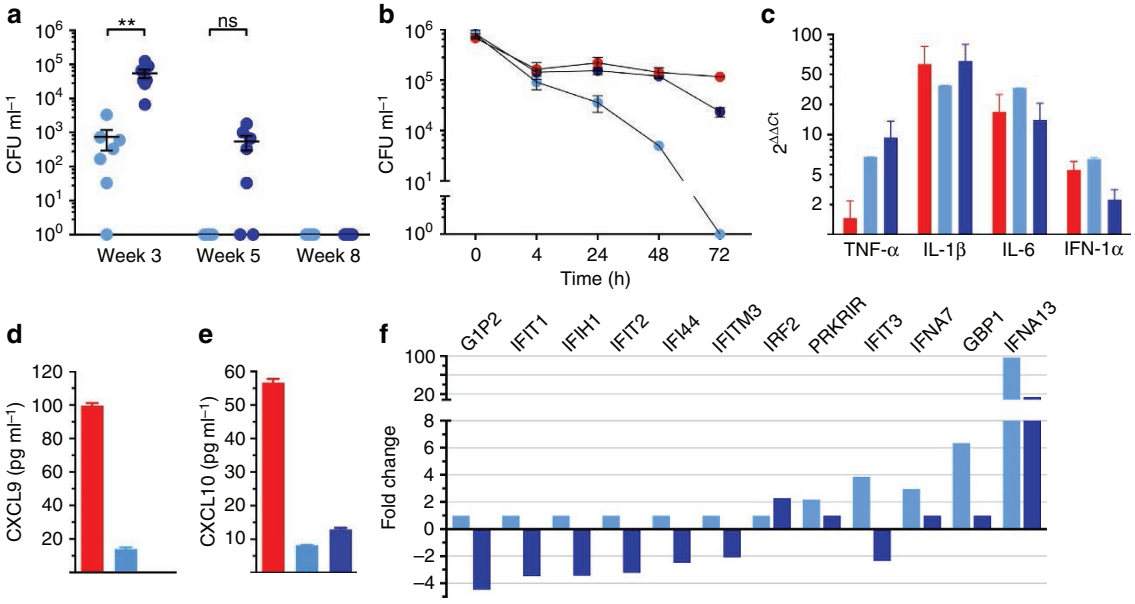

Figure 3 | Comparative measures of bacterial burden in BAL following aerosol vaccination and restriction during intraphagosomal culturing *in vitro*. (**a**) BCG (light blue) and MtbΔ*sigH* (dark blue) CFU levels in total BAL samples at weeks 3, 5 and 8 after vaccination. (**b**) Rhesus macaque BMDM *in vitro* killing assay in CFU ml^{-1} with *Mtb* (red), BCG and MtbΔ*sigH*. $^{**}P<0.01$ using two-way ANOVA with Tukey's correction for multiple comparisons. Data are means ± s.d. (**c**) Relative expression ($2^{\Delta\Delta Ct}$) of TNF-α, IL-1β, IL-6 and IFN-1α in BMDMs infected with *Mtb*, BCG and MtbΔ*sigH* using real-time RT–PCR. (**d**,**e**) Absolute expression of CXCL9 (**d**) and CXCL10 (**e**; pg ml^{-1}) in supernatants derived from BMDMs infected with *Mtb*, BCG and MtbΔ*sigH* using cytokine analysis assay. (**f**) Microarray-derived fold changes of gene expression of 12 Type I interferon genes in the BAL of BCG- and MtbΔ*sigH*-vaccinated animals. For analysis involving BAL, samples from all seven animals in each group were used for analysis at each time point (**a**). For CFU analysis *in vitro*, the experiment was performed twice, with four biological replicates in each instance (**b**). Transcript and cytokine analyses were performed on biological replicates (**c**–**f**). ns, not significant.

than BCG in human lungs. Eight weeks after vaccination, CFU for neither strain was recovered from the BAL of vaccinated macaques. Furthermore, macaque BMDMs were able to kill BCG at a faster rate than both *Mtb* and MtbΔ*sigH* *in vitro* (Fig. 3b). BMDMs infected with MtbΔ*sigH* expressed greater levels of tumour-necrosis factor-α (TNF-α) and interleukin (IL)-1β but not IL-6 transcripts relative to BCG (Fig. 3c). In addition, BMDMs infected with MtbΔ*sigH* also secreted significantly lower levels of inflammatory chemokines CXCL9 (Fig. 3d) and CXCL10 (Fig. 3e) in supernatants, relative to the BCG-vaccinated or the unvaccinated groups. Both the expression and anti-*Mtb* activity of TNF-α is strongly enhanced by IL-1β via direct augmentation of caspase-dependent apoptosis[34]. Infection of BMDMs with MtbΔ*sigH* results in both higher TNF-α expression and greater apoptosis relative to *Mtb*[22]. The activity of IL-1β is itself regulated by Type I interferons, whose expression is positively controlled by IRF1 and negatively by IRF2. Elicitation of Type I interferon response inhibits IL-1β and TNF-α activity, and promotes the progression of active TB, as is the case during infection with hypervirulent *Mtb* strains[35]. Abrogation of Type I responses reverses this trend and is being considered as a host-directed therapy for TB[36]. Accordingly, the expression of Type I genes was significantly higher in BAL samples obtained 3 weeks after vaccination from animals that received BCG, and significantly lower in animals that received MtbΔ*sigH* (Fig. 3f). The IRF2 gene expression level was lower in the BAL of BCG-vaccinated and more than twofold higher in the BAL of MtbΔ*sigH*-vaccinated animals (Fig. 3f). The expression of prototypical Type I molecule IFN-γ was also higher in BMDMs infected with BCG and *Mtb*, relative to those infected with MtbΔ*sigH* (Fig. 3c).

MtbΔ*sigH* induces protective immune signatures in the lung. Global immune responses to vaccination with MtbΔ*sigH* or BCG were analysed by transcriptome profiling of BAL samples collected before vaccination and 3 weeks post vaccination. The genes significantly induced in BAL after BCG vaccination were involved in cellular transport, DNA binding by regulatory protein, RNA processing or were part of the lumen, non-membrane-bound organelle or macromolecular complex assembly (Fig. 4). The only major category of genes induced following BCG vaccination was that categorized as pertaining to immune system development (Fig. 4). Conversely, the expression of genes involved in NK cell signalling, MAPK signalling and JAK/STAT signalling, cytokine signalling, T-cell signalling, calcium signalling, neuroactive/growth receptors and lipid biosynthesis were induced to higher levels in the BAL from MtbΔ*sigH*-vaccinated macaques (Fig. 4). Further, a large majority of these genes were either not expressed or were expressed to significantly lower levels in the BAL of animals vaccinated with BCG (Fig. 4). Thus, vaccination with MtbΔ*sigH* appeared to result in the induction of a markedly stronger innate immune response, as indicated by the differential induction of NK cell, MAPK and JAK/STAT signalling pathways as well as genes from the cytokine, T-cell receptor and calcium signalling pathways (Fig. 4), although the differential persistence of the two mycobacterial strains could have played a role in this differential response. In addition, enhanced immune cell differentiation, proliferation, activation and processing, as well as macromolecular synthesis, which are associated with heightened cytokine and T-cell responses, were evidenced by the increased expression levels of neuroactive/growth factor receptor signalling, potentiation and lipid biosynthesis pathways in BAL samples derived from animals vaccinated with MtbΔ*sigH* (Fig. 4).

Local increases in T cells due to MtbΔ*sigH* vaccination. Local and systemic immune responses were compared following vaccination by analysis of BAL and blood, respectively. Marked

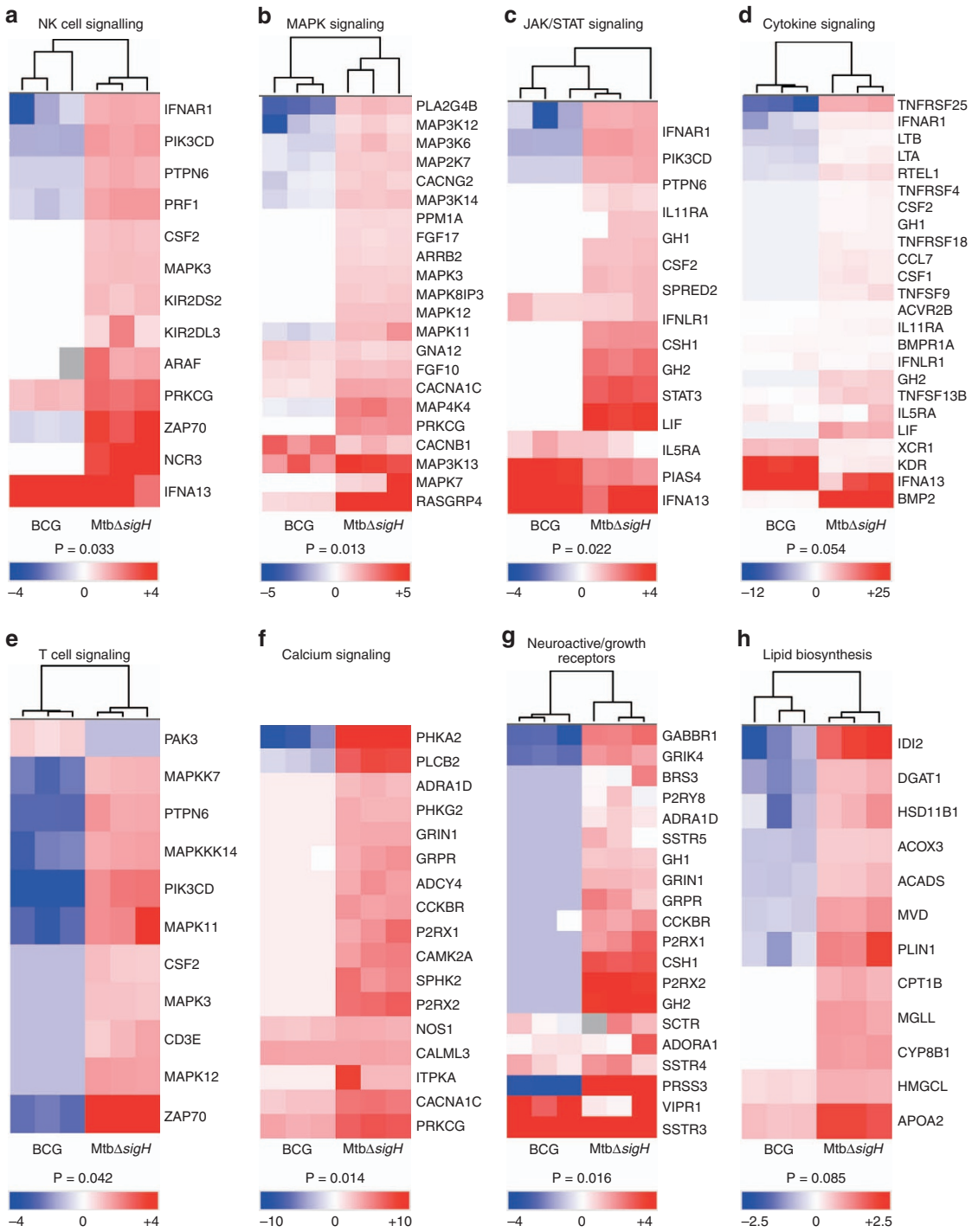

Figure 4 | Transcriptomics from BAL 3 weeks after immunization. Total RNA isolated from BAL samples of three animals vaccinated with BCG and another three with Mtb*ΔsigH*, obtained 3 weeks after vaccination, was subjected to amplification and macaque-specific DNA microarray analysis. The expression of genes belonging to natural killer cells (**a**), MAP Kinase (**b**), JAK/STAT (**c**), cytokine (**d**), T cells (**e**), calcium signalling (**f**), neuroactive/growth receptors (**g**) and lipid biosynthesis (**h**) pathways were induced to significantly higher levels in the BAL of animals vaccinated with Mtb*ΔsigH*, relative to those vaccinated with BCG. *P* values shown are derived from the analysis of significant terms in DAVID with Bonferroni correction for multiple comparisons. BAL samples from three animals in each group were used for microarray experiments.

increases in $CD4^+$ and $CD8^+$ T-cell numbers were found in BAL immediately post vaccination ($P<0.001$; two-way analysis of variance analysis of variance (ANOVA) with Tukey's correction; Fig. 5a,b); however, no differences in the frequency of $CD4^+$ and $CD8^+$ T cells were observed in the periphery post vaccination (Supplementary Fig. 2). In addition, no differences in the chemokine receptors CXCR3, CXCR4, CCR7 or activation marker CD69 were detected systemically, which indicated no significant variation in the functional phenotype of T cells in the blood (Supplementary Fig. 3). However, a significant increase in the number of circulating $CD4^+CCR5^+$ T cells was discovered in the Mtb*ΔsigH* group between weeks 2 and 3 ($P<0.05$; two-way ANOVA with Tukey's correction; Supplementary Fig. 3). No differences were observed in the memory status of circulating

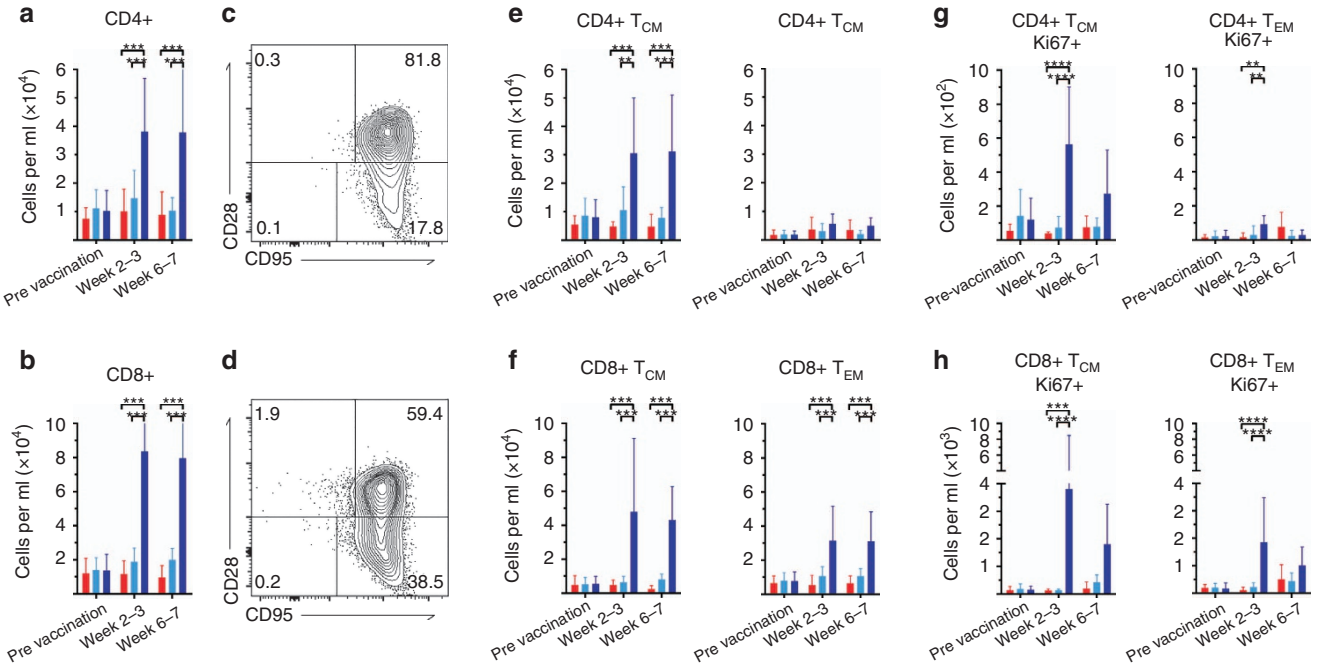

Figure 5 | T-cell response to immunization in BAL. Vaccination with MtbΔ*sigH* (dark blue) induced a significantly higher central memory immune response relative to BCG vaccination (light blue), or no vaccination (red). Quantification of $CD4^+$ (**a**) and $CD8^+$ (**b**) T cells migrating to the lung after vaccination. Representative plots of central memory ($CD28^+CD95^+$), effector memory ($CD28^-CD95^+$) and naive ($CD28^+CD95^-$) $CD4^+$ (**c**,**e**) and $CD8^+$ (**d**,**f**) T cells in BAL. Quantification of $CD4^+$ (**e**) T_{CM} and T_{EM} cells, $CD8^+$ T_{CM} and T_{EM} cells (**f**) in BAL, and the proliferative capability of these cells (**g**,**h**). $^*P<0.05$; $^{**}P<0.01$; $^{***}P<0.001$; $^{****}P<0.0001$ using two-way ANOVA with Tukey's correction for multiple comparisons. Data are means ± s.d. BAL samples from all 21 animals ($n=7$, three groups) were included in the flow cytometry experiments and analyses. Samples from all seven animals in each group were used for analysis at each time point.

T cells, including central (T_{CM} – $CD28^+CD95^+$) and effector memory (T_{EM} – $CD28^-CD95^+$) cells or naïve T cells ($CD28^+CD95^-$; Supplementary Fig. 2)[37].

While no significant changes were discovered in T-cell frequencies in the peripheral blood, a strong lung-specific central and effector memory response was initiated post vaccination with MtbΔ*sigH*. This response was apparent immediately after vaccination by significant increases in the number of $CD4^+$ central memory (T_{CM}) ($P<0.01$–0.001; two-way ANOVA with Tukey's correction) as well as $CD8^+$ T_{CM} and effector memory (T_{EM}; $P<0.001$) in the BAL (Fig. 5c–f), with a marked increase in proliferation as measured by Ki67 positivity ($P<0.01$–0.0001; Fig. 5g,h). A significant increase in the number of $CD69^+$ T cells ($P<0.001$ for MtbΔ*sigH* versus BCG and $P<0.01$–0.001 for MtbΔ*sigH* versus unvaccinated groups; Fig. 6a,b) indicated that T cells in BAL were antigen-stimulated via the T-cell receptor. The polarity of the T-cell response was examined using the markers CCR5 and CXCR3, which are preferentially expressed by Th1 cells, as well as CXCR4, which is preferentially expressed by T-helper 2 (Th2) cells. The results revealed that T cells in BAL immediately post-MtbΔ*sigH* vaccination preferentially expressed high levels of CCR5 and CXCR3 compared with T cells recruited following vaccination with BCG ($P<0.01$–0.001; Fig. 6c,d). Thus, aerosol vaccination with MtbΔ*sigH* induced transcriptomic and cellular signatures indicative of a strong Th1 response that resulted in accumulation of memory T cells.

Vaccination with MtbΔ*sigH* protects from lethal *Mtb* challenge. To evaluate the potential of the attenuated mycobacterium to serve as a TB vaccine, all animals were challenged with a high dose of *Mtb* CDC1551, which has historically produced lethal TB in rhesus macaques within 10 weeks[20,32]. Unvaccinated animals rapidly developed pulmonary granulomatous pathology with rapid increases in body temperatures ($P<0.01$ for MtbΔ*sigH* relative to BCG and $P<0.0001$ for MtbΔ*sigH* versus unvaccinated groups; two-way ANOVA with Tukey's correction) and serum CRP levels ($P<0.0001$ for MtbΔ*sigH* versus both other groups; Fig. 2b,d), as well as a swift decline in body weights $P<0.01$ for MtbΔ*sigH* relative to BCG and $P<0.0001$ for MtbΔ*sigH* versus unvaccinated groups; Fig. 2c). Control animals also exhibited high levels of pulmonary granulomatous involvement by radiology (Fig. 2e). The same clinical measure also increased, albeit to a lesser degree, in animals that were aerosol-vaccinated with BCG, while animals vaccinated with MtbΔ*sigH* exhibited virtually no evidence of disease ($P<0.0001$ for MtbΔ*sigH* versus unvaccinated as well as versus BCG; Fig. 2b–e). Three weeks post-*Mtb* challenge (week 11), the increase in body temperatures in unvaccinated animals was significant relative to BCG-vaccinated ($P<0.01$) and highly significant relative to MtbΔ*sigH*-vaccinated animals ($P<0.0001$; two-way ANOVA with Tukey's correction; Fig. 2b). Five weeks post challenge (week 13), the differences in body temperature between the unvaccinated and BCG-vaccinated groups were significant ($P<0.05$); the differences between the BCG and MtbΔ*sigH*-vaccinated groups were very significant ($P<0.01$); and the differences between the unvaccinated and MtbΔ*sigH*-vaccinated groups were highly significant ($P<0.0001$; Fig. 2b). The differences in body weight between the unvaccinated and MtbΔ*sigH*-vaccinated groups and the BCG and MtbΔ*sigH*-vaccinated groups were very significant at week 11 ($P<0.01$; Fig. 2c) and while by week 13, these differences had become highly significant ($P<0.0001$; two-way ANOVA with Tukey's correction). Profoundly lower serum CRP levels were detected in the macaques vaccinated with MtbΔ*sigH* relative to macaques that were not vaccinated at weeks 11 and 13 and at time of euthanasia ($P<0.0001$). At both week 11 ($P<0.05$) and

while euthanasia ($P<0.0001$; two-way ANOVA with Tukey's correction), the serum CRP levels detected in the macaques vaccinated with MtbΔ*sigH* were also significantly lower than levels measured in the BCG-vaccinated group (Fig. 2d). Similarly, animals vaccinated with MtbΔ*sigH* exhibited significantly lower chest X-ray (CXR) scores, consistent with lack of disease following lethal challenge, in this group, relative to either BCG-vaccinated or unvaccinated macaques ($P<0.0001$ in both cases).

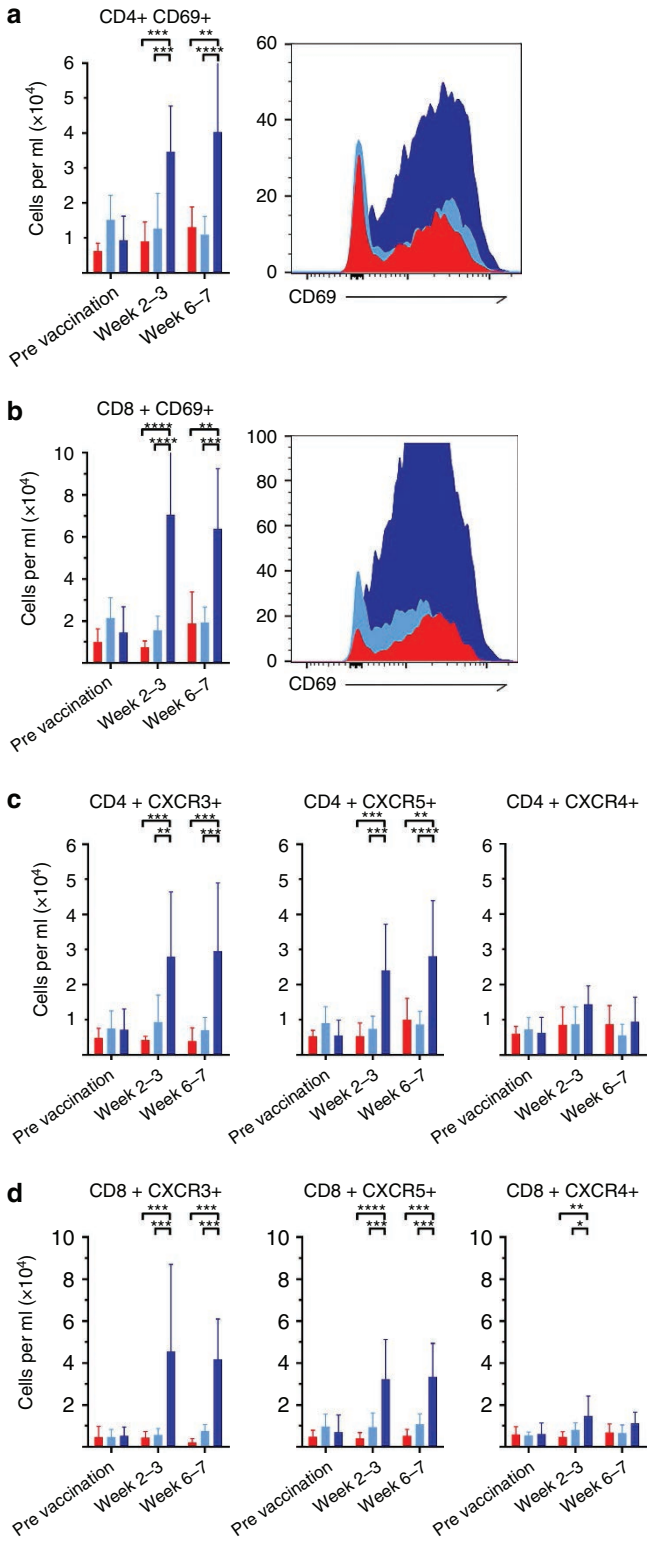

While extensive pathology was not discernable in the lungs of macaques vaccinated with the mutant, a majority of those vaccinated with BCG exhibited moderate CXR scores, again significantly lower than those in the unvaccinated group, where pathology consistent with military TB could be observed in a majority of animals.

Vaccination with MtbΔ*sigH* reduces *in vivo* bacterial burdens. The protection conferred by MtbΔ*sigH* was also evident following evaluation of bacterial burdens. Significantly lower Mtb was recovered from BAL from MtbΔ*sigH*-vaccinated animals relative to those vaccinated with BCG at 3 and 5 weeks after challenge (weeks 11 and 13; Fig. 7a). At the time of euthanasia, the total lung burden in animals vaccinated with MtbΔ*sigH* was three logs lower than burdens in unvaccinated ($P<0.01$) and two logs lower than burdens in BCG-vaccinated ($P<0.01$) animals, while bacterial loads in animals vaccinated with BCG were only 0.5–1 logs lower than in the control group ($P<0.05$; one-way ANOVA with Tukey's correction; Fig. 7b). We were unable to culture *Mtb* from >42% of all lung sections obtained from macaques vaccinated with MtbΔ*sigH*. In contrast, every section obtained from either unvaccinated animals or those vaccinated with BCG was positive for *Mtb*. Thus, the *Mtb* burden was significantly lower in the lungs of MtbΔ*sigH*-vaccinated animals following lethal challenge compared with those vaccinated with BCG. Similar results were obtained when bronchial lymph node bacterial burdens were analysed at necropsy (Fig. 7c). Using a combination of hygromycin resistance/sensitivity and PCR, we verified that the obtained CFUs were *Mtb* and not residual MtbΔ*sigH* or BCG.

Vaccination with MtbΔ*sigH* leads to reduced lung pathology. The results of the pulmonary pathology analyses mirrored those obtained following analysis of bacterial burdens. Animals vaccinated with MtbΔ*sigH* exhibited significantly fewer pulmonary lesions on challenge, as determined by both gross and histopathological examination (Fig. 8a–f and Supplementary Fig. 4) and morphometric quantitation (Fig. 8g). Thus, the animals vaccinated with MtbΔ*sigH* had fewer granulomas (the extent of lung affected by TB lesions following *Mtb* infection encompassed an average of 4%), and less TB-related pathology (for example, oedema, pneumonia and generalized foci of inflammation) than animals in the other two groups (where ~40% of the lung was affected; $P<0.0001$ in both cases; one-way ANOVA with Tukey's correction; Fig. 8g). The clinical and microbiological differences also correlated with significant differences in overall survival rates following challenge (Fig. 8h). All seven unvaccinated animals succumbed to massive pulmonary TB following a lethal aerosol *Mtb* challenge within a median of 36 days. Five out of seven BCG-vaccinated animals also succumbed to TB, within a median of 48 days. None of the MtbΔ*sigH*-vaccinated animals exhibited any overt signs of disease or required euthanasia (Fig. 8h).

Figure 6 | Local T-cell phenotype to immunization in BAL. Vaccination with MtbΔ*sigH* (dark blue) induced a significantly stronger T_H1 cell response relative to BCG vaccination (light blue), or no vaccination (red). Quantification of and representative histograms of $CD4^+CD69^+$ (**a**) and $CD8^+CD69^+$ (**b**) T cells migrating to the lung after vaccination. Absolute cell counts of phenotypic markers CXCR3, CCR5 and CXCR4 in $CD4^+$ (**c**) and $CD8^+$ (**d**) T cells in BAL at different stages of infection. $^*P<0.05$, $^{**}P<0.01$, $^{***}P<0.001$, $^{****}P<0.0001$ using two-way ANOVA with Tukey's correction for multiple comparisons. Data are means ± s.d. BAL samples from all 21 animals ($n=7$, three groups) were included in the flow cytometry experiments and analyses. Samples from all seven animals in each group were used for analysis at each time point.

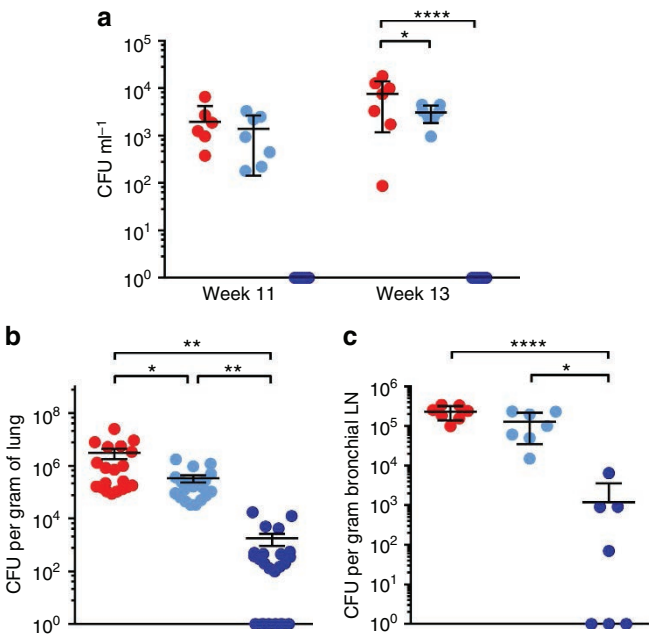

Figure 7 | Bacterial burden following lethal *Mtb* challenge. (**a**) *Mtb* CFU levels in total BAL samples at week 11 (3 weeks after challenge) and week 13 (5 weeks after challenge; (**b**). *Mtb* levels per gram of lung tissue at necropsy (**c**). *Mtb* burdens per gram of bronchial lymph node tissue at $^{*}P<0.05$; $^{**}P<0.01$; $^{***}P<0.001$; $^{****}P<0.0001$, (**a**) two-way ANOVA and (**b**,**c**) one-way ANOVA with Tukey's multiple testing correction. Data are means ± s.d. Samples from all seven animals in each group were used for analysis at each time point. For analysis of lung burdens, four pooled samples (two each from left and right lung) from each macaque, each representing five distinct lung sections were used (**b**). For analysis of bronchial lymph node burdens, one section from each animal was analysed.

Differential T-cell responses in animals post challenge. To assess an immunologic basis for protection induced by MtbΔ*sigH*, the functional phenotype of circulating $CD4^+$ and $CD8^+$ T cells was analysed by employing the same markers used for evaluating pulmonary responses following vaccination. No significant differences in the percentages of $CD4^+$ and $CD8^+$ central or effector memory cells were observed in peripheral blood immediately following challenge (Supplementary Fig. 2). However, a significant increase in $CD4^+$ $CCR5^+$ T cells was identified 7 weeks after *Mtb* challenge, as well as a significant decrease in $CD8^+$ $CXCR3^+$ T cells in peripheral blood at weeks 3 and 7 following challenge in unvaccinated animals (Supplementary Fig. 3).

Consistent with overall lung involvement and chest radiograph scores, a significantly greater number of $CD4^+$ and $CD8^+$ T cells including T_{CM} and T_{EM} were present in BAL in the unvaccinated animals compared with both BCG and MtbΔ*sigH*-vaccinated animals (Fig. 9a–d). The increased numbers of T cells in BAL in unvaccinated animals were also evident from representative histograms of $CD69^+$ T cells (Supplementary Fig. 5a,b). While no significant differences were observed in CXCR3, CCR5 and CXCR4 expression by $CD4^+$ or $CD8^+$ T cells between the two vaccinated groups (Supplementary Fig. 5c,d), a significant decrease in the number of $CD8^+$ $CXCR4^+$ was noted at weeks 11 and 15 in the MtbΔ*sigH*-vaccinated group compared with the other two groups (Supplementary Fig. 5d).

Comparison of polyfunctional *Mtb*-specific T-cell responses. To examine antigen-specific responses to *Mtb*, isolated peripheral blood mononuclear cells (PBMCs) collected 5 weeks post challenge were stimulated with whole *Mtb* cell wall and cell filtrate protein, and responses were analysed using intracellular cytokine staining for IFN-γ, IL-2 and TNF-α. The results indicated that vaccination with MtbΔ*sigH* and BCG correlated with significant increases in the percentage of polyfunctional, IFN-γ^+, IL-2^+, TNF-α^+ $CD4^+$ T cells, whereas unvaccinated animals displayed a significantly greater number percentage of monofunctional $CD4^+$ T cells (Fig. 9e,f). Unfortunately, samples from other time points were not available for analysis.

Profound iBALT post challenge in MtbΔ*sigH*-vaccinated animals. Lung samples collected after lethal *Mtb* challenge from unvaccinated (Fig. 10a,d), BCG-vaccinated (Fig. 10b,e) and MtbΔ*sigH*-vaccinated (Fig. 10c,f) macaques at the time of necropsy were assayed for iBALT by histopathology and immunofluorescence with CD3 and CD20 followed by confocal microscopy and image analysis. We observed that protection in each of these groups of macaques was strongly associated with levels of iBALT. Thus, the few, small granulomas in the lungs of animals vaccinated with MtbΔ*sigH* and challenged with *Mtb* were characterized by the presence of multiple well-organized iBALT per lesion (Fig. 10c). The presence of the follicles was also apparent in the cognate haematoxylin and eosin stains (Fig. 10 c,f). These follicles were, in general, associated with granulomas and appeared to be an outgrowth of the outer lymphocyte-rich layer (Fig. 10 c,f). While B cells constituted the majority in these follicles, $CD3^+$ cells were also present (Fig. 10c). In contrast to the multiple well-developed iBALT associated with granulomas in MtbΔ*sigH*-immunized animal, animals from the other groups (Fig. 10a,b,d,e) had fewer iBALT that were less well organized. The total area of iBALT in MtbΔ*sigH*-vaccinated macaques was significantly greater after *Mtb* challenge (Fig. 10g) than in either of the other groups, despite the fact that the area occupied by granulomas in the MtbΔ*sigH*-vaccinated group was significantly less compared with the other two groups after *Mtb* challenge (Fig. 10h). This further emphasizes the difference in BALT induction and the correlation between iBALT and latent control of *Mtb* infection.

Discussion

Previously, we showed that aerosolization of a high dose of MtbΔ*sigH* into the lungs of rhesus macaques resulted in nonpathogenic infection[20]. Here we demonstrate that pulmonary vaccination with this mutant protected against lethal challenge in macaques via the induction of a potent memory T-cell response. Further, we establish a strong correlation between the latent control of infection and iBALT, suggesting that these lymphoid structures facilitate control of TB by maintaining LTBI or sterilizing infection. Induction of BALT in response to respiratory infections is known to not only result in protection, but such responses are also less pathologic[38]. Secondary T_{FH} cells, which constitute the great majority of lymphoid follicle (including iBALT) T cells, expand from memory T cells in a B-cell-aided manner[39]. Our results therefore suggest that the interplay between B and T cells is critical for the proper development of granulomatous-protective responses to TB. This study substantiates previous work using the macaque model of TB, which showed that B cells produced antibody and were important for control of TB[40]. Our results suggest that future studies should unravel the function of B cells recruited to the lung to understand immunity from TB.

While the correlates of vaccine-induced protective immunity against TB are not completely understood, T lymphocytes expressing markers of central memory response (dual positivity for CD28 and CD95)[37]are critical for protection. A model of

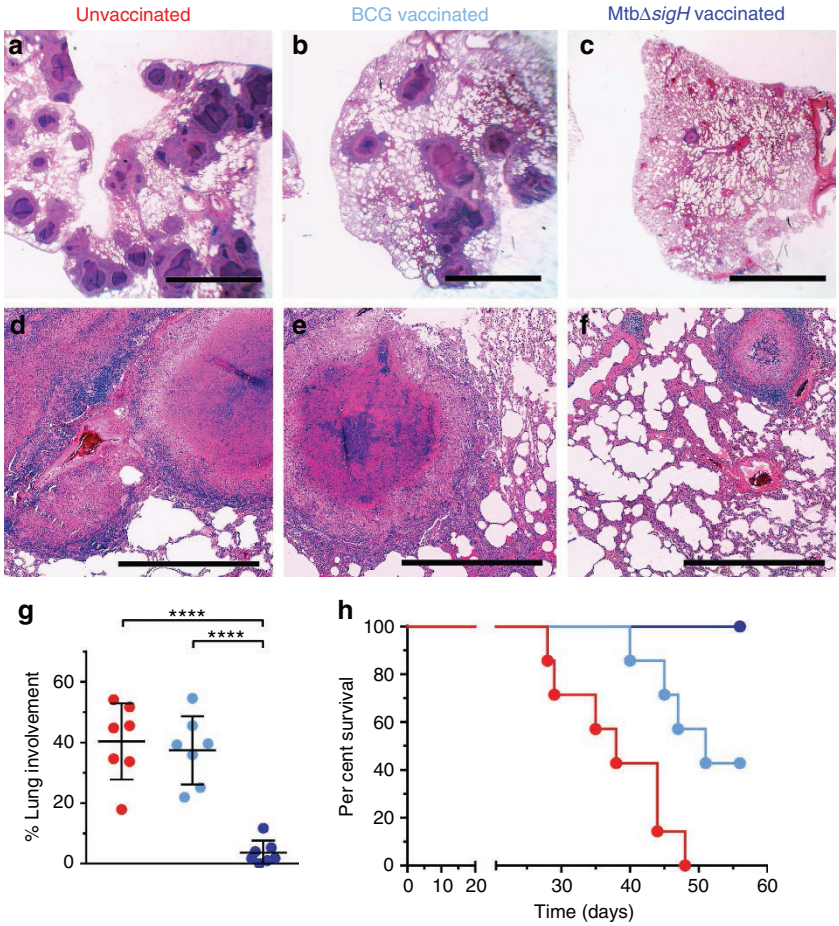

Figure 8 | Histopathological and survival analysis of lungs of *Mtb*-infected animals. Haematoxylin and eosin (H&E) staining from representative animals in each of the three groups. (**a**,**d**) Vaccine-naive group with miliary, white 2–4 mm granulomas and scattered lobular multicoloured areas of consolidation. (**b**,**e**) BCG-vaccinated with localized dark red lobar pneumonia and (**c**,**f**) MtbΔ*sigH*-vaccinated with no apparent gross lesions. Black scale bars in (**a**–**c**), 5 mm and (**d**–**f**), 500 μm. (**g**) Morphometric measures of pulmonary pathology in the different groups of unvaccinated (red), BCG-vaccinated (light blue) and MtbΔ*sigH*-vaccinated (dark blue) animals. ****$P<0.0001$ with (**g**) one-way ANOVA using Tukey's multiple testing correction. Data are means ± s.d. (**h**) Survival proportion Kaplan–Meier curves for the three groups of animals, using Mantel–Cox (log-rank) survival analysis. At least three systematic random microscopic fields from each lung, representing most lung lobes, from each of the animals in every group were used for morphometric analysis (**g**). Data from each of the seven animals per group was used for survival proportions analysis (**h**).

protective immunity that is currently gaining credence suggests that initial vaccination(s) resulting in a spike in effector response can result in the establishment of a central memory response, which is likely to result in long-term protection[41]. T_{CM} are extremely proliferative and can rapidly evolve into large numbers of effector cells expressing high levels of pro-inflammatory cytokines (for example, IFN − γ). Consequently, the finding that pulmonary vaccination with MtbΔ*sigH* resulted in potent T_{CM} (as well as T_{EM}, particularly $CD8^+$) responses during the post-vaccination phase that corresponded to a strong T_{EM} response in the challenge phase merits further evaluation. The role of chemokine receptors, including CXCR3, is critical to the recruitment of $CD8^+$ T cells, and CXCR3 expression on T_{CM} is strongly correlated with effective anti-pathogen memory responses[42]. BAL transcriptome profiling results indicated that animals vaccinated with MtbΔ*sigH* developed a highly productive pulmonary immune response, both in terms of magnitude and breadth. Prior studies have established that $CD4^+$ T cells with specificity for mycobacterial antigens are critical for the control of *Mtb* infection[43], and that $CD8^+$ T cells play an increasingly important role in this process[41,44]. SigH induces pathogen antioxidant responses during stress[45,46]. MtbΔ*sigH* is unable to induce expression of the transcriptionally linked thioredoxins and thiol peroxidases[45] that act as antioxidant buffers against the host oxidative burst[47]. Consequently, the *antioxidant* response of the MtbΔ*sigH* mutant was strongly crippled[47], and the resulting production of oxidants likely enhanced antigen-specific $CD8^+$ T-cell responses through the cross-priming of antigen presentation[48]. In addition, the ability of MtbΔ*sigH* to persist longer than BCG allowed for increased stimulation and antigen presentation, inducing a stronger, more robust, T-cell repertoire[49]. Further characterization of this T_{CM} response is however necessary to substantiate that these cells are not long-lived T_{EM} cells, since MtbΔ*sigH* antigens persist longer than BCG.

The ability of aerosol MtbΔ*sigH* vaccination to elicit highly protective responses in macaques could have roots in the fundamental processes that govern *Mtb*–macrophage interactions. *In vitro*, macrophages infected with this mutant elicited greater expression of Th1 pro-inflammatory cytokines TNF-α and IL-1β, and lower Type I interferon, relative to those infected with *Mtb* and BCG (this study and ref. 22). Together, these results indicate that the interaction of MtbΔ*sigH* with host phagocytes is critically altered by the loss of the bacillus's ability to induce SigH-mediated antioxidant functions, relative to BCG. TNF can restrict macrophage-contained *Mtb* by several mechanisms, including by potently inducing early inflammatory responses[50],

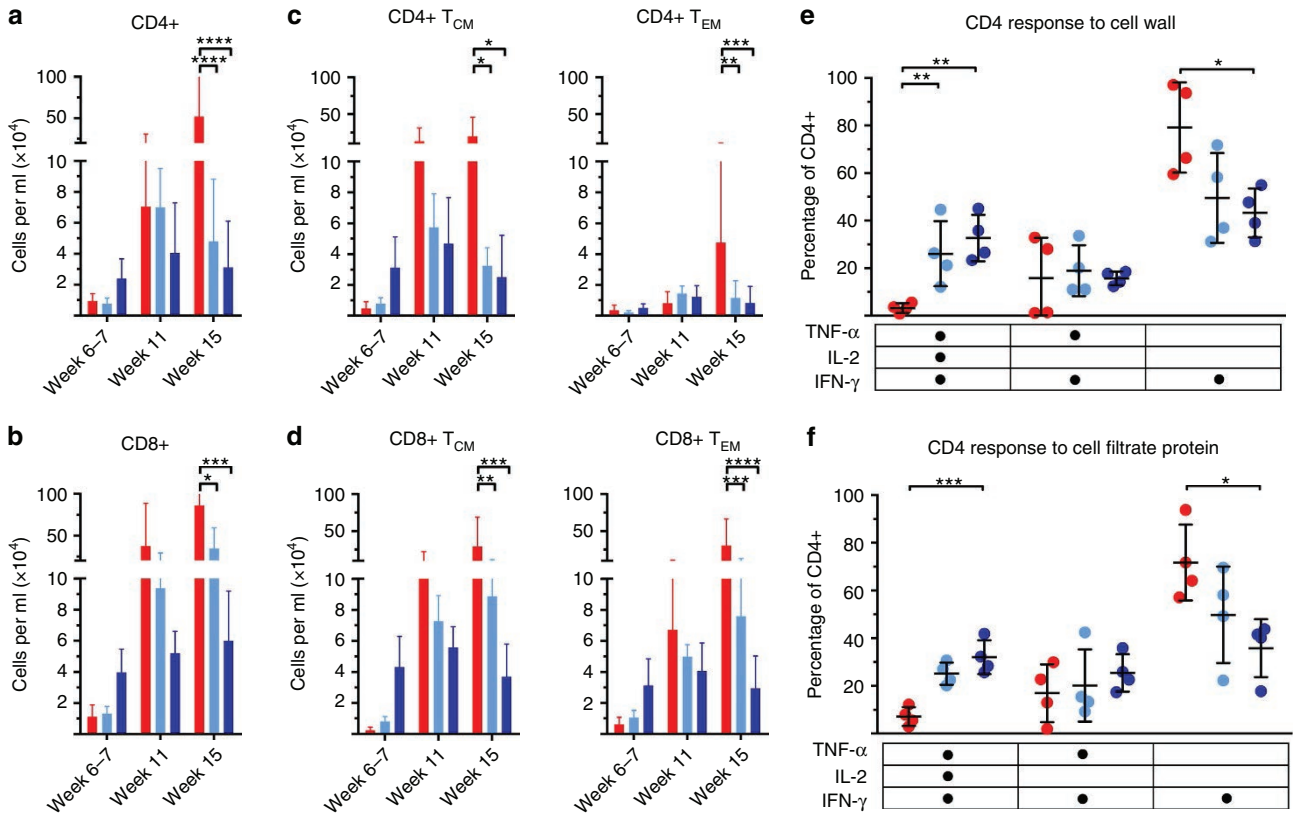

Figure 9 | Immune responses in the lung post-*Mtb* challenge. (**a**,**b**) Quantification of cells per ml of BAL of (**a**) $CD4^+$ and (**b**) $CD8^+$ T cells and of (**c**) $CD4^+$ T_{CM} and T_{EM} cells and of (**d**) $CD8^+$ T_{CM} and T_{EM} cells migrating to the lung after challenge in groups of unvaccinated (red), BCG-vaccinated (light blue) and MtbΔ*sigH*-vaccinated (dark blue) animals. (**e**,**f**) Percentage of CD4 T cells from PBMCs prepared from whole blood, producing gamma interferon, interleukin 2 and tumour necrosis factor alpha in response to (**e**) the *Mtb* cell wall and to (**f**) *Mtb* cell filtrate protein. $^*P<0.05$, $^{**}P<0.01$, $^{***}P<0.001$, $^{****}P<0.0001$ using two-way ANOVA with Tukey's correction for multiple comparisons. Data are means ± s.d. BAL samples from all 21 animals ($n=7$, three groups) were included in the flow cytometry experiments and analyses (**a**–**d**). For antigen-specific studies, samples from four animals per group were employed (**e**–**d**).

transducing apoptotic signals through activation of caspase 8 (ref. 51) activating CD8 cells[52] and potentiating IFN-γ-induced killing of *Mtb*[53,54]. On the other hand, BCG induces strong expression of the SigH regulon (including antioxidants) and is therefore unable to alter these interactions. In fact most BCG strains exhibit duplication of *sigH*, likely rendering it even less susceptible to phagocyte oxidative mechanisms[55]. *In vitro* results thus hint at the mechanism by which pulmonary vaccination with MtbΔ*sigH* could generate protective responses. Unable to counter the host oxidative burst, the mutant elicited greater IL-1β and TNF-α expression leading to significantly greater antimicrobial response, apoptosis and antigen presentation. That *Mtb* uses Type I signalling to modulate IL-1β expression is well established[56].

$CD4^+$ T cells play a key role in the control of *Mtb* infection, and polyfunctional cytokine production of antigen-specific Th1 cells is associated with this control[57]. Animals vaccinated with MtbΔ*sigH* displayed higher frequencies of *Mtb* cell wall- and culture filtrate protein-responsive polyfunctional $CD4^+$ T cells compared with unvaccinated animals. Recent data have shown that markers of T-cell immune activation in human TB are associated with smear and culture conversion during anti-TB treatment[58]. Nonetheless, the current study had some limitations; for example, protection was only demonstrated in a homologous strain. Thus, future experiments should test the efficacy of the current and related mutants against high-virulence heterologous strains of the same clade as CDC1551, as well as of a different lineage. Second, a lethal challenge at 8 weeks post vaccination may not sufficiently model protection arising from long-term antigen-specific memory T-cell responses. A prior report suggested that BCG failed to induce long-term central memory responses to *Mtb* infection, which may account for its failure to protect adults against TB[10]. Successful vaccination against TB will require elicitation of both a stable and broad repertoire of memory responses to ensure effective protection against the pathogen during a subsequent infection[41]. While the current results did not establish long-term immunity based on effective elicitation of T_{CM} responses, the findings did demonstrate that prior pulmonary vaccination with MtbΔ*sigH* resulted in a markedly superior elicitation of both $CD4^+$ and $CD8^+$ T_{CM} responses relative to BCG vaccination. An abundance of data has indicated that T_{CM} lymphocytes retain a potent proliferative capacity and can differentiate into the T_{EM} phenotype when re-exposed to the cognate antigen[59]. The current data demonstrated that MtbΔ*sigH* elicited a more efficient post-vaccination T_{CM} response, a greater T_{EM} response following challenge and conferred stronger protection. In this study, vaccines were delivered via aerosol, although BCG is given to recipients intradermally. It is impossible to directly compare the results from the aerosol–BCG group to the effectiveness of intradermal BCG vaccination. There have been recent attempts, however, to deliver vaccines, directly to the lung[11], driven by the pioneering work of Barclay *et al.*[12], who showed that macaques could be protected against TB by aerosolized BCG. While a direct

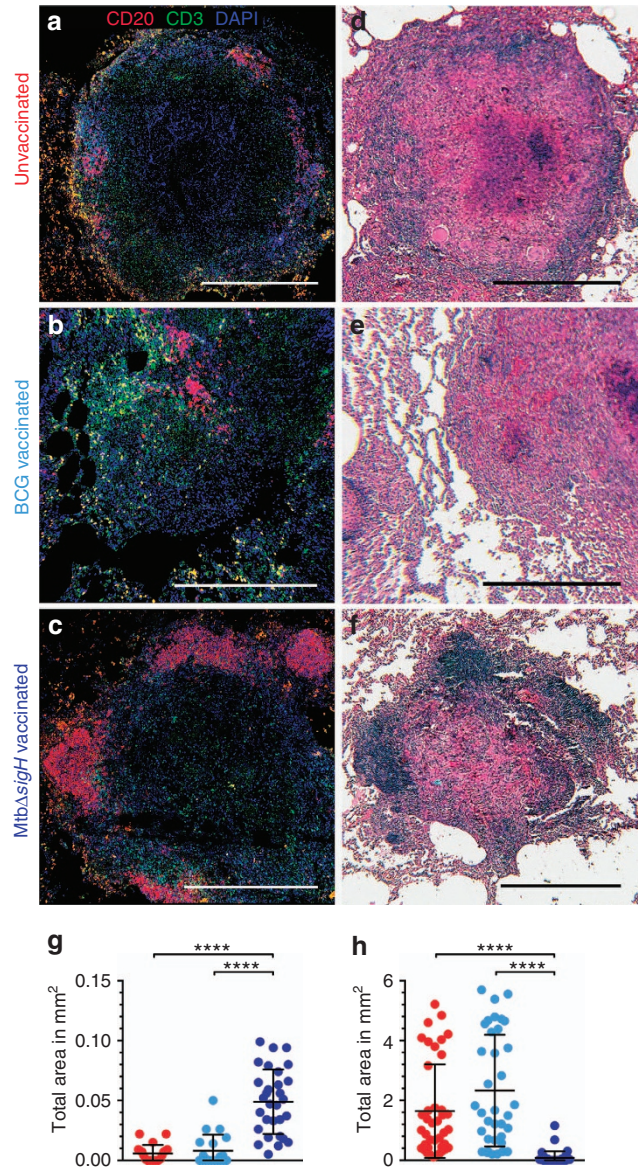

Figure 10 | Induction of BALT after lethal *Mtb* challenge correlates with protection from pulmonary granulomatous TB. (**a**–**c**) Co-staining of lung sections with CD3 (green) and CD20 (red) and staining of corresponding sections (**d**–**f**) with H&E revealed that (**a**,**d**) vaccine-naive animals and (**b**,**e**) BCG-vaccinated animals had significantly reduced iBALT follicle formation in comparison with (**c**,**f**) MtbΔ*sigH*-vaccinated animals, at necropsy, after lethal *Mtb* challenge. White and black scale bars, 500 μm. Quantification of multiple lesions in six different animals were used the analysis. (**g**) Total area (mm^2) of iBALT follicles and (**h**) granulomatous pathology in unvaccinated (red), BCG-vaccinated (light blue) and MtbΔ*sigH*-vaccinated (dark blue) animals. $^{****}P<0.0001$ using Student's *t*-test. Data are means ± s.d. At least 10 sections from each slide derived from a lung block from multiple animals in each group were used for statistical analysis (**g**–**h**).

comparison of the effectiveness of aerosol-to-intradermal-administered BCG was beyond the scope of this study, preliminary data and prior reports of intradermal BCG vaccination[14,24,60] suggest that aerosol–BCG outperformed intradermal vaccination in macaques.

Although BCG induces potent cellular responses in infants and protects them, neither the responses nor the efficacy are generally considered to be long lasting[61], although some reports strongly suggest that this is possible[9]. Furthermore, BCG does not completely protect against pulmonary TB including reactivation and reinfection[61]. New vaccines against TB are therefore urgently needed. It has therefore been hypothesized that rationally attenuated strains of *Mtb* are likely better at serving as vaccine platforms against TB, since these strains are human-adapted, in contrast to bovine-adapted BCG[61]. There are other issues that limit the effectiveness of BCG. It is only able to induce cytokines associated with long-lasting control of *Mtb* infection several months post vaccination, meanwhile enabling a window of dissemination[62]. Furthermore, *Mtb*, unlike BCG, retains known immunodominant epitopes for humans. Finally, it has been argued that *Mtb* expresses genes important for the evasion of host immune responses. SigH is one such gene allowing the pathogen to significantly induce the expression of thioredoxins, which attenuate phagocyte oxidative burst[20,22,47]. Thus, MtbΔ*sigH*, a human-adapted strain with a significant immune-evasion impairment, is exceedingly safe even after direct high-dose delivery into primate lungs.

In summary, our results provide a roadmap for identifying correlates of protection from TB in a highly human-like model. While it remains to be seen whether such responses can also be elicited following intradermal vaccination, there is considerable renewal of interest in matching the route of vaccination with that of infection in generating protection against TB[13].

Methods

Nonhuman primates. All animal procedures were approved by the Institutional Animal Care and Use Committee and were performed in strict accordance with the NIH guidelines. Twenty-one specific-pathogen-free, retrovirus-free, mycobacteria-naive, adult rhesus macaques, bred and housed at the Tulane National Primate Research Centre (TNPRC), between the ages of 3 and 12 years were assigned to three groups of seven on the basis of power calculations, which suggested that statistical significance could be detected with sufficient power in these group sizes if addressing a reduction in the average lung bacterial burden by 1log. One group of macaques ($n=7$) remained unvaccinated, a second group ($n=7$) was vaccinated with a target dose of 1,000 CFU of *M. bovis* BCG (Danish) while the third group ($n=7$) was vaccinated with an equivalent dose of the MtbΔ*sigH* isogenic mutant in the CDC1551 background. Aerosol vaccination was conducted using the same equipment and procedural configuration as the *Mtb* challenge component of the study (see below). The average ages of the animals within each group were 7.42 ± 4.26 years for the unvaccinated group, 7.38 ± 4.50 years for the BCG-vaccinated group and 6.75 ± 4.02 years for the MtbΔ*sigH* group, and these were not statistically significant differences (Supplementary Fig. 6).

Aerosol procedures for both vaccination and *Mtb* challenge. Animals were both aerosol-vaccinated and challenged with *Mtb* using the same methodology and equipment configuration. A custom head-only dynamic inhalation system housed within a class III biological safety cabinet was used for this purpose[63]. The use of this inhalation system for aerosol delivery to non human primate (NHP)[63] has been described for numerous studies involving *Mtb*[20,25,29,32] as well as other agents[64]. Initially, the respective microbial efficiencies of MtbΔ*sigH* gene mutant and the parental *Mtb* CDC1551 strains were determined through a series of aerosol-only studies. The microbial efficiencies were used to estimate achievable aerosol doses that could be delivered to each animal using mathematical formula catered to this purpose[65] for both the aerosol vaccination and subsequent challenge experiments. The animal vaccinations (and challenge exposures) were performed singly, and a 'target' dose is reported for the group based on prevailing experimental conditions, including individual animal respiratory rate, during each exposure event. Actual individual dose is based on *post hoc* analysis of active aerosol sampling of the inhalation chamber during the time of each vaccination and bacterial challenge. All aerosol infections were performed in a single day.

Clinical procedures including sampling and euthanasia. Vaccines were delivered directly to the deep lung via the aerosol route in a manner similar to how the *Mtb* challenge is administered. Eight weeks post vaccination, each of the three groups was infected via the inhalation route with a target dose of 1,000 CFU of *Mtb* CDC1551. Samples were collected before vaccination, post vaccination and post infection. For the sake of clarity, results from vaccinated and infected NHPs are reported in two phases: post vaccination, which means after aerosol vaccination with either BCG or MtbΔ*sigH*, put before challenge with *Mtb* and post infection (or post challenge), that is, after challenge with *Mtb*.

A tuberculin skin test was performed before vaccination (−2 weeks), post vaccination (3 weeks) and post infection (11 weeks) as previously described by

administration of mammalian tuberculin into the right eyelid[20,24,25,29,32,33]. Thoracic radiographs (CXRs) were acquired 2 weeks before vaccination and at 3, 7, 11 and 14 weeks post vaccination as previously described[20,24,25,29,32,66]. Briefly, the CXRs were scored by veterinary clinicians in a blinded manner on a subjective scale of 0–4, with a score of 0 denoting normal lung and a score of 4 denoting severe tuberculous pneumonia and pathology. Before vaccination/infection, all 21 animals received a score of 0, as their lungs were perfectly normal at this time. The following subjective scoring system was used: 0 (no pathological involvement); 1 (mild pathological involvement); 2 (moderate pathological involvement); 3 (extensive pathological involvement) and 4 (severe pathological involvement).

Blood was drawn before vaccination (− 2 weeks) and then weekly thereafter for the performance of complete blood count and serum chemistry[20,24,25,29,32]. Blood collected in EDTA tubes (Sarstedt AG & co.) was used for whole-blood flow cytometry using panels described previously[67]. Blood collected in Cell Preparation tubes (Sarstedt AG & co.) was used to isolate PBMC for antigen-specific assays. BAL samples were obtained as previously described, using two washes of 40-ml sterile saline 2 weeks before vaccination and at 3, 7, 11 and 14 weeks[20,24,25,29,32] and analysed for CFUs.

Necropsy to collect tissues was performed during euthanasia. There were two different reasons for euthanasia. In all 100% (7/7) unvaccinated control animals, as well as ∼57% (4/7) of BCG-vaccinated animals, disease progressed to an extent that humane euthanasia was deemed necessary by clinical veterinarians on this team (Fig. 8h and Supplementary Table 1). These humane end points were pre-defined in the animal-use protocol and applied as a measure of reduction of discomfort. The TNPRC Institutional Animal Care and Use Committee approved all animal-related procedures and activities. BCG-vaccinated (43% (3/7)) and Mtb*Δsig*H-vaccinated (100%) animals were either disease-free or had not progressed to an extent that required humane euthanasia till day 60. Such animals were euthanized for tissue collection via necropsy at that point (between days 60 and 62). At necropsy, lung, spleen and liver tissues were collected and processed as previously described, and CFUs were determined per gram of tissue, using four pooled lung samples per animal, each of which comprised five sections each, thus representing every lung lobe with at least one sample[20,24,25,29,32]. A subset of colonies obtained post-challenge necropsy was assayed for resistance to hygromycin to classify them as residual Mtb*ΔsigH*, and subjected to PCR for *sigH* and *esat*6 to classify them as residual Mtb*ΔsigH* and BCG, respectively. No evidence of residual Mtb*ΔsigH* or BCG was found. End point criteria for euthanasia were previously described. Briefly, animals were euthanized if they exhibited four or more of the following: (I) a 2 °F increase in body temperature relative to pre-infection values that persisted for three or more consecutive weeks; (II) a 15% or greater loss in body weight; (III) serum CRP values greater than 10 mg ml^{-1} for two or more consecutive readings; (IV) CXR values higher than 2; (V) respiratory discomfort resulting in vocalization; (VI) significant-to-complete loss of appetite; and (VII) detectable bacilli in BAL samples. CRP values were included as criteria for euthanasia because CRP is a marker for systemic inflammation that exhibits a high degree of correlation with active TB in macaques[20,24,25,29,32,33]. Lung pathology at necropsy was determined as described earlier[21,26,29,30,38] using stereological principles described by Sharpe *et al.*[27]. Briefly, lung involvement was quantified by point counting using an overlaid grid with 18.5-mm point spacing. Towards this end, digital images of three systematic random microscopic fields with an original magnification of ×2.5 per slide were employed. At least one sample from each of the four lobes of each lung was used. Intersections representing normal lung included interstitium and air space, while lesions comprised intersections with massive areas of inflammatory cells, haemorrhage, oedema, necrosis or individual to multifocal to lobar granulomas. Differences between completely normal and somewhat inflammed airspace containing localized, small zones of subacute inflammation sans fibrous or cellular encapsulation were not differentiated.

Transcriptomics. BAL samples were obtained from animals before vaccination (− 2 weeks), post vaccination (weeks 3 and 7) and post infection (weeks 11 and 14) as previously described[20,24,25,29,32,33,68]. For stabilization, 8 ml of 100% fetal bovine serum (Invitrogen, Life Sciences) was immediately added to 80 ml of the BAL sample. The sample was centrifuged at 400 r.p.m. for 10 min at 4 °C in an Allegra benchtop centrifuge. The pelleted cells were washed with cold RPMI media (Invitrogen, Life Sciences) and stored at − 80 °C until analysis. For transcriptomics, total macaque RNA was isolated from total BAL obtained at the pre-vaccination and the 3 week post-vaccination time points as previously described[30] using an RNAEasy kit (Qiagen), followed by RNA amplification (Ambion MessageAmp). The cDNA derived from the amplified RNA samples from pre-vaccination time points were labelled with Cy3, and samples from the 3-week post-vaccination time point were labelled with Cy5 (Agilent Technologies). Microarray analyses were performed as previously described by assessing the relative expression of transcripts in the Cy5 (experimental)-labelled samples relative to the Cy3(control)-labelled samples, using Agilent 4 × 44 k Rhesus Monkey microarrays[20,24,25,68]. Global impact of expression profiles was analysed using Database for Annotation, Visualization and Integrated Discovery (DAVID)[30].

iBALT. Immunofluorescence confocal microscopy was used to measure iBALT as previously described using formalin-fixed, paraffin-embedded tissue[31,69].

Flow cytometry. Flow cytometry was performed on whole-blood and BAL samples obtained from all 21 animals as previously described[25,33]. For T-cell phenotyping, the following antibodies were used: CD3 V500 (1:50, clone SP34-2), CD4 PerCP-Cy5.5 (1:10, clone L200), CD8 PE-TxRed (1:30, clone RPA-T8), CD28 APC (1:5, clone CD28.2), CD69 APC-Cy7 (1:20, clone FN50), CD95 PE-Cy5 (1:5, clone DX2), CD183 AL488 (1:10, clone 1C6/CXCR3), CD184 PE-Cy5 (1:5, clone 12G5), CD195 APC (1:5, clone 3A9), CD197 PE-Cy7 (1:20, clone 3D12), HLA-DR APC-Cy7 (1:75, clone L243) and Ki67 PE-Cy7 (1:50, clone B56) all purchased from BD Biosciences (San Jose, CA, USA). Flow cytometry analyses were conducted by gating first on lymphocytes followed by the elimination of B cells by gating for CD20. The remaining cells were gated for the selection of T cells using CD3, followed by gating into $CD3^+CD4^+$ and $CD3^+CD8^+$ subpopulations. The frequencies of $CD4^+$ and $CD8^+$ T cells expressing activation and homing markers were compared using Ki67, CXCR3, CCR5 and CCR7 (ref. 70). The levels of $Foxp3^+$ were determined as a measure of the T_{reg} response. Finally, the extent of $CD4^+$ and $CD8^+$ cells belonging to either T_{CM} or T_{EM} relative to the naive T-cell population were measured using a combination of CD28 and CD95 markers[37].

Antigen-specific immune response. PBMCs isolated from whole blood collected from unvaccinated, vaccinated and infected NHPs were stimulated with *Mtb* cell wall extract (BEI Resources) for the performance of intracellular cytokine staining as previously described, using *Mtb* cell filtrate protein and cell wall extract for stimulation[57].

***In vitro* infection of rhesus macaque BMDMs.** Rh-BMDMs were generated and infected with *Mtb* CDC1551, the isogenic Mtb*ΔsigH* mutant in this strain, and BCG at an multiplicity of infection of 1:10 as previously described, for 4 h (refs 22,46). CFUs were measured as described at different time points including 4, 24, 48, 72, 96 and 120 h. CXCL13 expression was measured using DNA microarray[25] and quantitative RT–PCR[22]. The expression of pro-inflammatory mediators TNF-α, IL-1β and IL-6 was measured using real-time RT–PCR as described earlier[22]. The expression of specific chemokines, for example, CXCL9 and CXCL10, was measured using the Cytokine Monkey Magnetic 29-Plex Panel kit from Life-Tech, essentially as described earlier[22].

Statistical analyses. Statistical comparisons were performed using one-way or two-way ANOVA in GraphPad Prism with Sidak's correction for multiple hypotheses. Analysis of transcriptome data was performed using Spotfire DecisionSite[24,25,68] LOWESS scripts, Ingenuity Pathways Analysis and DAVID as previously described[25]. Specifically, genes with twofold or greater induction in triplicate samples from either vaccination were uploaded to DAVID, and statistically significant accumulation of terms calculated.

References

1. Zumla, A. *et al.* The WHO 2014 global tuberculosis report-further to go. *Lancet Glob Health* **3,** e10–12 (2015).
2. Kaufmann, S. H. *et al.* Progress in tuberculosis vaccine development and host-directed therapies--a state of the art review. *Lancet Respir. Med.* **2,** 301–320 (2014).
3. Orme, I. M. Prospects for new vaccines against tuberculosis. *Trends Microbiol.* **3,** 401–404 (1995).
4. Hingley-Wilson, S. M., Sambandamurthy, V. K. & Jacobs, Jr. W. R. Survival perspectives from the world's most successful pathogen, *Mycobacterium tuberculosis*. *Nat. Immunol.* **4,** 949–955 (2003).
5. Kaufmann, S. H. *et al.* Progress in tuberculosis vaccine development and host-directed therapies-a state of the art review. *Lancet Respir. Med.* **2,** 301–320 (2014).
6. Wilkie, M. E. & McShane, H. TB vaccine development: where are we and why is it so difficult? *Thorax* **70,** 299–301 (2015).
7. Tameris, M. D. *et al.* Safety and efficacy of MVA85A, a new tuberculosis vaccine, in infants previously vaccinated with BCG: a randomised, placebo-controlled phase 2b trial. *Lancet* **381,** 1021–1028 (2013).
8. McShane, H. *et al.* BCG: myths, realities, and the need for alternative vaccine strategies. *Tuberculosis (Edinb)* **92,** 283–288 (2012).
9. Aronson, N. E. *et al.* Long-term efficacy of BCG vaccine in American Indians and Alaska Natives: A 60-year follow-up study. *JAMA* **291,** 2086–2091 (2004).
10. Henao-Tamayo, M., Ordway, D. J. & Orme, I. M. Memory T cell subsets in tuberculosis: what should we be targeting? *Tuberculosis (Edinb)* **94,** 455–461 (2014).
11. Garcia-Contreras, L. *et al.* Immunization by a bacterial aerosol. *Proc. Natl Acad. Sci. USA* **105,** 4656–4660 (2008).
12. Barclay, W. R. *et al.* Protection of monkeys against airborne tuberculosis by aerosol vaccination with bacillus Calmette-Guerin. *Am. Rev. Respir. Dis.* **107,** 351–358 (1973).
13. Manjaly Thomas, Z. R. & McShane, H. Aerosol immunisation for TB: matching route of vaccination to route of infection. *Trans. R Soc. Trop. Med. Hyg.* **109,** 175–181 (2015).

14. Darrah, P. A. *et al.* Aerosol vaccination with AERAS-402 elicits robust cellular immune responses in the lungs of rhesus macaques but fails to protect against high-dose *Mycobacterium tuberculosis* challenge. *J. Immunol.* **193,** 1799–1811 (2014).
15. Larsen, M. H. *et al.* Efficacy and safety of live attenuated persistent and rapidly cleared *Mycobacterium tuberculosis* vaccine candidates in non-human primates. *Vaccine* **27,** 4709–4717 (2009).
16. Russell, D. G. The evolutionary pressures that have molded *Mycobacterium tuberculosis* into an infectious adjuvant. *Curr. Opin. Microbiol.* **16,** 78–84 (2013).
17. Hmama, Z., Pena-Diaz, S., Joseph, S. & Av-Gay, Y. Immunoevasion and immunosuppression of the macrophage by *Mycobacterium tuberculosis*. *Immunol. Rev.* **264,** 220–232 (2015).
18. Kaushal, D. *et al.* Reduced immunopathology and mortality despite tissue persistence in a *Mycobacterium tuberculosis* mutant lacking alternative sigma factor, SigH. *Proc. Natl Acad. Sci. USA* **99,** 8330–8335 (2002).
19. Hernandez Pando, R., Aguilar, L. D., Smith, I. & Manganelli, R. Immunogenicity and protection induced by a *Mycobacterium tuberculosis* sigE mutant in a BALB/c mouse model of progressive pulmonary tuberculosis. *Infect. Immun.* **78,** 3168–3176 (2010).
20. Mehra, S. *et al.* The *Mycobacterium tuberculosis* stress response factor SigH is required for bacterial burden as well as immunopathology in primate lungs. *J. Infect. Dis.* **205,** 1203–1213 (2012).
21. Manganelli, R. *et al.* Role of the extracytoplasmic-function sigma factor sigma(H) in *Mycobacterium tuberculosis* global gene expression. *Mol. Microbiol.* **45,** 365–374 (2002).
22. Dutta, N. K. *et al.* The stress-response factor SigH modulates the interaction between *Mycobacterium tuberculosis* and host phagocytes. *PLoS ONE* **7,** e28958 (2012).
23. Barclay, W. R., Anacker, R. L., Brehmer, W., Leif, W. & Ribi, E. Aerosol-induced tuberculosis in subhuman primates and the course of the disease after intravenous BCG vaccination. *Infect. Immun.* **2,** 574–582 (1970).
24. Mehra, S. *et al.* Granuloma correlates of protection against tuberculosis and mechanisms of immune modulation by *Mycobacterium tuberculosis*. *J. Infect. Dis.* **207,** 1115–1127 (2013).
25. Mehra, S. *et al.* The DosR regulon modulates adaptive immunity and is essential for *M. tuberculosis* persistence. *Am. J. Respir. Crit. Care Med.* **191,** 1185–1196 (2015).
26. Kaushal, D., Mehra, S., Didier, P. J. & Lackner, A. A. The non-human primate model of tuberculosis. *J. Med. Primatol.* **41,** 191–201 (2012).
27. Sharpe, S. A. *et al.* Determination of lesion volume by MRI and stereology in a macaque model of tuberculosis. *Tuberculosis (Edinb)* **89,** 405–416 (2009).
28. Diedrich, C. R. *et al.* Reactivation of latent tuberculosis in cynomolgus macaques infected with SIV is associated with early peripheral T cell depletion and not virus load. *PLoS ONE* **5,** e9611 (2010).
29. Mehra, S. *et al.* Reactivation of latent tuberculosis in rhesus macaques by coinfection with simian immunodeficiency virus. *J. Med. Primatol.* **40,** 233–243 (2011).
30. Kamath, A. T. *et al.* New live mycobacterial vaccines: the Geneva consensus on essential steps towards clinical development. *Vaccine* **23,** 3753–3761 (2005).
31. Slight, S. R. *et al.* CXCR5(+) T helper cells mediate protective immunity against tuberculosis. *J. Clin. Invest.* **123,** 712–726 (2013).
32. Dutta, N. K. *et al.* Genetic requirements for the survival of tubercle bacilli in primates. *J. Infect. Dis.* **201,** 1743–1752 (2010).
33. Phillips, B. L. *et al.* LAG3 expression in active *Mycobacterium tuberculosis* infections. *Am. J. Pathol.* **185,** 820–833 (2015).
34. Jayaraman, P. *et al.* IL-1beta promotes antimicrobial immunity in macrophages by regulating TNFR signaling and caspase-3 activation. *J. Immunol.* **190,** 4196–4204 (2013).
35. Manca, C. *et al.* Hypervirulent *M. tuberculosis* W/Beijing strains upregulate type I IFNs and increase expression of negative regulators of the Jak-Stat pathway. *J. Interferon Cytokine Res.* **25,** 694–701 (2005).
36. Mayer-Barber, K. D. *et al.* Host-directed therapy of tuberculosis based on interleukin-1 and type I interferon crosstalk. *Nature* **511,** 99–103 (2014).
37. Pitcher, C. J. *et al.* Development and homeostasis of T cell memory in rhesus macaque. *J. Immunol.* **168,** 29–43 (2002).
38. Moyron-Quiroz, J. E. *et al.* Role of inducible bronchus associated lymphoid tissue (iBALT) in respiratory immunity. *Nat. Med.* **10,** 927–934 (2004).
39. Fairfax, K. C. *et al.* IL-4-secreting secondary T follicular helper (Tfh) cells arise from memory T cells, not persisting Tfh cells, through a B cell-dependent mechanism. *J. Immunol.* **194,** 2999–3010 (2015).
40. Phuah, J. Y., Mattila, J. T., Lin, P. L. & Flynn, J. L. Activated B cells in the granulomas of nonhuman primates infected with *Mycobacterium tuberculosis*. *Am. J. Pathol.* **181,** 508–514 (2012).
41. Nunes-Alves, C. *et al.* In search of a new paradigm for protective immunity to TB. *Nat. Rev. Microbiol.* **12,** 289–299 (2014).
42. Kohlmeier, J. E. *et al.* Inflammatory chemokine receptors regulate CD8(+) T cell contraction and memory generation following infection. *J. Exp. Med.* **208,** 1621–1634 (2011).
43. Caruso, A. M. *et al.* Mice deficient in CD4 T cells have only transiently diminished levels of IFN-gamma, yet succumb to tuberculosis. *J. Immunol.* **162,** 5407–5416 (1999).
44. Chen, C. Y. *et al.* A critical role for CD8 T cells in a nonhuman primate model of tuberculosis. *PLoS Pathog.* **5,** e1000392 (2009).
45. Mehra, S. & Kaushal, D. Functional genomics reveals extended roles of the *Mycobacterium tuberculosis* stress response factor sigmaH. *J. Bacteriol.* **191,** 3965–3980 (2009).
46. Mehra, S., Dutta, N. K., Mollenkopf, H. J. & Kaushal, D. *Mycobacterium tuberculosis* MT2816 encodes a key stress-response regulator. *J. Infect. Dis.* **202,** 943–953 (2010).
47. Kernodle, D. S. SigH, antioxidants, and the pathogenesis of pulmonary tuberculosis. *J. Infect. Dis.* **205,** 1186–1188 (2012).
48. Winau, F., Hegasy, G., Kaufmann, S. H. & Schaible, U. E. No life without death--apoptosis as prerequisite for T cell activation. *Apoptosis* **10,** 707–715 (2005).
49. Obst, R. *et al.* Sustained antigen presentation can promote an immunogenic T cell response, like dendritic cell activation. *Proc. Natl Acad. Sci. USA* **104,** 15460–15465 (2007).
50. Harris, J. & Keane, J. How tumour necrosis factor blockers interfere with tuberculosis immunity. *Clin. Exp. Immunol.* **161,** 1–9 (2010).
51. Wajant, H., Pfizenmaier, K. & Scheurich, P. Tumor necrosis factor signaling. *Cell. Death Differ.* **10,** 45–65 (2003).
52. Bruns, H. *et al.* Anti-TNF immunotherapy reduces CD8+ T cell-mediated antimicrobial activity against *Mycobacterium tuberculosis* in humans. *J. Clin. Invest.* **119,** 1167–1177 (2009).
53. Harris, J., Hope, J. C. & Keane, J. Tumor necrosis factor blockers influence macrophage responses to *Mycobacterium tuberculosis*. *J. Infect. Dis.* **198,** 1842–1850 (2008).
54. Schaible, U. E., Sturgill-Koszycki, S., Schlesinger, P. H. & Russell, D. G. Cytokine activation leads to acidification and increases maturation of *Mycobacterium avium*-containing phagosomes in murine macrophages. *J. Immunol.* **160,** 1290–1296 (1998).
55. Kernodle, D. S. Decrease in the effectiveness of Bacille Calmette-Guerin vaccine against pulmonary tuberculosis: a consequence of increased immune suppression by microbial antioxidants, not overattenuation. *Clin. Infect. Dis.* **51,** 177–184 (2010).
56. Novikov, A. *et al. Mycobacterium tuberculosis* triggers host type I IFN signaling to regulate IL-1beta production in human macrophages. *J. Immunol.* **187,** 2540–2547 (2011).
57. Adekambi, T. *et al.* Distinct effector memory CD4+ T cell signatures in latent *Mycobacterium tuberculosis* infection, BCG vaccination and clinically resolved tuberculosis. *PLoS ONE* **7,** e36046 (2012).
58. Riou, C. *et al.* A subset of circulating blood mycobacteria-specific CD4 T cells can predict the time to *Mycobacterium tuberculosis* sputum culture conversion. *PLoS ONE* **9,** e102178 (2014).
59. Hamilton, S. E. & Jameson, S. C. CD8 T cell memory: it takes all kinds. *Front. Immunol.* **3,** 353 (2012).
60. Lin, P. L. *et al.* The multistage vaccine H56 boosts the effects of BCG to protect cynomolgus macaques against active tuberculosis and reactivation of latent *Mycobacterium tuberculosis* infection. *J. Clin. Invest.* **122,** 303–314 (2012).
61. Ottenhoff, T. H. & Kaufmann, S. H. Vaccines against tuberculosis: where are we and where do we need to go? *PLoS Pathog.* **8,** e1002607 (2012).
62. Cruz, A. *et al.* BCG vaccination-induced long-lasting control of *Mycobacterium tuberculosis* correlates with the accumulation of a novel population of CD4(+)IL-17(+)TNF(+)IL-2(+) T cells. *Vaccine* **33,** 85–91 (2015).
63. Hartings, J. M. & Roy, C. J. The automated bioaerosol exposure system: preclinical platform development and a respiratory dosimetry application with nonhuman primates. *J. Pharmacol. Toxicol. Methods* **49,** 39–55 (2004).
64. Roy, C. J. *et al.* Thermostable ricin vaccine protects rhesus macaques against aerosolized ricin: epitope-specific neutralizing antibodies correlate with protection. *Proc. Natl Acad. Sci. USA* **112,** 3782–3787 (2015).
65. Swearengen, J. R. *Biodefense: Research Methodology and Animal Models* 2nd edn (Taylor & Francis, 2012).
66. Darrah, P. A. *et al.* Aerosol vaccination with AERAS-402 elicits robust cellular immune responses in the lungs of rhesus macaques but fails to protect against high-dose *Mycobacterium tuberculosis* challenge. *J. Immunol.* **193,** 1799–1811 (2014).
67. Dutta, N. K., McLachlan, J., Mehra, S. & Kaushal, D. Humoral and lung immune responses to *Mycobacterium tuberculosis* infection in a primate model of protection. *Trials Vaccinol.* **3,** 47–51 (2014).
68. Mehra, S. *et al.* Transcriptional reprogramming in nonhuman primate (rhesus macaque) tuberculosis granulomas. *PLoS ONE* **5,** e12266 (2010).
69. Gopal, R. *et al.* S100A8/A9 proteins mediate neutrophilic inflammation and lung pathology during tuberculosis. *Am. J. Respir. Crit. Care Med.* **188,** 1137–1146 (2013).
70. Veazey, R. S. *et al.* Dynamics of CCR5 expression by CD4(+) T cells in lymphoid tissues during simian immunodeficiency virus infection. *J. Virol.* **74,** 11001–11007 (2000).

Acknowledgements

This research was supported by startup funds and a Center for Biomedical Research Excellence (COBRE) award to S.M. (P30GM110760), awards to D.K. (AI089323, HL106790, HL106790-S1, AI111943 and RR026006), S.A.K. and D.K. (AI111914) and the TNPRC (OD011104 and AI058609), including its pilot programme, the Emory Center for AIDS Research (CFAR; AI050409), the Louisiana Board of Regents and the Tulane Office of the Vice-President for Research.

Author contributions

D.K. provided funding, advised on the experimental design, carried out the experiments, analysed the results and participated in the manuscript preparation; T.W.F. carried out the experiments, analysed the results and participated in the manuscript preparation; U.S.G. carried out the experiments and analysed results; X.A. carried out the experiments and analysed results; T.A. carried out the experiments and analysed results; J.R.-M. carried out the experiments; N.A.G. carried out the experiments; A.-M.F.J. carried out the experiments; B.L.P. carried out the experiments; M.H.A. carried out the experiments; K.E.R.-L. provided veterinary assistance; L.A.D. provided veterinary assistance; C.J.R. carried out experiments; P.J.D. performed veterinary pathology; J.L.B. provided veterinary assistance; J.R. analysed the results; A.A.L. performed veterinary pathology and assisted in data interpretation and the manuscript preparation; S.A.K. provided funding and assisted in data interpretation and manuscript preparation; S.M. provided funding, advised on the experimental design, analysed the results and participated in the manuscript preparation. All authors reviewed the manuscript before submission.

Additional information

Accession codes: DNA microarray data have been deposited in the Gene Expression Omnibus under the Accession number GPL10183.

Supplementary Information accompanies this paper at http://www.nature.com/naturecommunications

Competing financial interests: The authors declare no competing financial interests.

Reprints and permission information is available online at http://npg.nature.com/reprintsandpermissions/

How to cite this article: Kaushal, D. *et al.* Mucosal vaccination with attenuated *Mycobacterium tuberculosis* induces strong central memory responses and protects against tuberculosis. *Nat. Commun.* 6:8533 doi: 10.1038/ncomms9533 (2015).

nature

https://doi.org/10.1038/s41586-020-2665-2

Accelerated Article Preview

Structures and distributions of SARS-CoV-2 spike proteins on intact virions

Received: 2 July 2020

Accepted: 10 August 2020

Accelerated Article Preview Published online 17 August 2020

Cite this article as: Ke, Z. et al. Structures and distributions of SARS-CoV-2 spike proteins on intact virions. *Nature* https://doi.org/10.1038/s41586-020-2665-2 (2020).

Zunlong Ke, Joaquin Oton, Kun Qu, Mirko Cortese, Vojtech Zila, Lesley McKeane, Takanori Nakane, Jasenko Zivanov, Christopher J. Neufeldt, Berati Cerikan, John M. Lu, Julia Peukes, Xiaoli Xiong, Hans-Georg Kräusslich, Sjors H. W. Scheres, Ralf Bartenschlager & John A. G. Briggs

Structures and distributions of SARS-CoV-2 spike proteins on intact virions

https://doi.org/10.1038/s41586-020-2665-2

Received: 2 July 2020

Accepted: 10 August 2020

Published online: 17 August 2020

Zunlong Ke[1,6], Joaquin Oton[1,6], Kun Qu[1,6], Mirko Cortese[2], Vojtech Zila[3], Lesley McKeane[4], Takanori Nakane[1], Jasenko Zivanov[1], Christopher J. Neufeldt[2], Berati Cerikan[2], John M. Lu[1], Julia Peukes[1], Xiaoli Xiong[1], Hans-Georg Kräusslich[3,5], Sjors H. W. Scheres[1], Ralf Bartenschlager[2,5] & John A. G. Briggs[1]✉

Severe acute respiratory syndrome coronavirus 2 (SARS-CoV-2) virions are surrounded by a lipid bilayer from which spike (S) protein trimers protrude[1]. Heavily glycosylated S trimers bind the ACE2 receptor and mediate entry of virions into target cells[2–6]. S exhibits extensive conformational flexibility: it modulates exposure of its receptor binding site and later undergoes complete structural rearrangement to drive fusion of viral and cellular membranes[2,7,8]. The structures and conformations of soluble, overexpressed, purified S proteins have been studied in detail using cryo-electron microscopy[2,7,9–12]. The structure and distribution of S on the virion surface, however, has not been characterized. Here we applied cryo-electron microscopy and tomography to image intact SARS-CoV-2 virions, determining the high-resolution structure, conformational flexibility and distribution of S trimers in situ on the virion surface. These results reveal the conformations of S present on the virion, and provide a basis from which to understand interactions between S and neutralizing antibodies during infection or vaccination.

Severe acute respiratory syndrome coronavirus 2 (SARS-CoV-2) is a betacoronavirus[13,14], an enveloped virus containing a large nucleoprotein (N)-encapsidated positive sense RNA genome[15]. Three transmembrane proteins are incorporated into the viral lipid envelope: spike protein (S) and two smaller proteins, membrane protein (M) and envelope protein (E)[1,15]. When imaged by cryo-electron microscopy (cryo-EM), betacoronaviruses appear as approximately spherical particles, with variable diameters centred around 100 nm, containing a dense viroplasm, and bounded by a lipid bilayer from which prominent S trimers protrude[16,17]. S trimers of SARS-CoV-2 bind to the receptor, ACE2, on the surface of target cells and mediate subsequent viral uptake and fusion[2–5,7]. In doing so S undergoes a dramatic structural rearrangement from the prefusion form to the postfusion form[8]. The overall architectures of both pre and postfusion forms are well conserved among coronaviruses[8,18,19].

During infection, coronaviruses extensively remodel the internal membrane organization of the cell, generating viral replication organelles in which replication takes place[20–22]. The S protein, together with the other membrane protein M, and E, are inserted into membranes of the endoplasmic reticulum (ER), and traffic to the ER Golgi intermediate compartment (ERGIC). The encapsidated genome buds into the ERGIC to form virions which are then trafficked to the plasma membrane and released[20–22]. S is primed for membrane fusion by proteolytic cleavage at the S1/S2 site, and subsequently the S2′ site[23].

The prefusion structure of S from coronaviruses including SARS-CoV-2 has been extensively studied using ectopic expression of soluble, secreted forms of S, followed by purification and cryo-EM[2,7,9–11]. In the prefusion form, the receptor binding domain (RBD) sits at the top of a broad, trimeric spike, above the fusion core. Three copies of the RBD are surrounded by three copies of the N-terminal domain (NTD) which show some mobility[2,7–9]. In the closed prefusion conformation all three copies of the RBD lay flat on the spike surface, largely occluding the receptor binding site, while in the open prefusion conformation one or multiple RBDs lift up to expose the receptor binding site[2,7,9,10]. The surface of the trimer is extensively glycosylated with 22 potential N-linked glycosylation sites per monomer[2,6,7]. After receptor binding, structural transition of the prefusion to the postfusion form brings the fusion peptide and the transmembrane domain together at one end of a long, needle-like structure centred around a three-helix bundle[8]. Five N-linked glycans are spaced along the length of the postfusion spike[8].

Fully understanding how S proteins function and how they interact with the immune system, requires knowledge of the structures, conformations and distributions of S trimers within virions. Here we have applied cryo-EM methods to study the structure, conformations and distributions of S trimers in situ on the virion surface.

To avoid artefacts associated with virus concentration or purification, we aimed to image SARS-CoV-2 virions from the supernatant of infected cells without virus concentration or purification. VeroE6 cells were infected with SARS-CoV-2 (isolate Germany/BavPat1/2020)[24]. At 48 h post-infection, supernatant was clarified, inactivated by fixation with formaldehyde and stored at -80 °C. Western blot revealed that approximately 45% of total S protein monomers on virions has been cleaved at the multibasic cleavage site into S1 and S2 (Fig. 1a). Fixed supernatant was vitrified by plunge freezing and imaged by cryo-EM. Fixation

[1]Structural Studies Division, Medical Research Council Laboratory of Molecular Biology, Cambridge, CB2 0QH, United Kingdom. [2]Department of Infectious Diseases, Molecular Virology, Heidelberg University, 69120, Heidelberg, Germany. [3]Department of Infectious Diseases, Virology, Heidelberg University, 69120, Heidelberg, Germany. [4]Visual Aids Department, Medical Research Council Laboratory of Molecular Biology, Cambridge, CB2 0QH, United Kingdom. [5]German Center for Infection Research, Heidelberg partner site, 69120, Heidelberg, Germany. [6]These authors contributed equally: Zunlong Ke, Joaquin Oton, Kun Qu. ✉e-mail: jbriggs@mrc-lmb.cam.ac.uk

may help to stabilize some protein conformations by crosslinking, but is not expected to give rise to any new conformations. As expected, given the concentration of virus in cellular supernatants (around 10^7 plaque forming units/ml), small numbers of individual virions were found scattered around the grid – these were imaged by cryo-electron tomography (cryo-ET) (Fig. 1b).

Virions were approximately spherical with a diameter to the outside of the lipid bilayer of 91 ± 11 nm (n = 179) (Extended Data Fig. 1a). They contain granular densities corresponding to N, and are studded with S trimers (Fig. 1b,c). These features are generally consistent with those of other coronaviruses imaged by cryo-EM[1,16,17]. S trimers protruding from the viral surface had two morphologies – a minority were extended thin structures reminiscent of the postfusion form, while the majority are wider structures reminiscent of the prefusion form. This observation contrasts with a recent preprint showing cryo-EM images of purified SARS-CoV-2 virions inactivated with the nucleic acid modifier β-propiolactone in which only thin protrusions were seen on the viral surface[25], and is consistent with in situ observations of virus assembly[21].

We also collected tomograms of SARS-CoV-2 virions produced by infection of Calu-3 cells, a human lung carcinoma cell line that supports virus production to a titre comparable to Vero cells. The morphology of the virions and the appearance of the S trimers on the surface was consistent with that seen for virions produced from VeroE6 cells (Extended Data Fig. 2a-c). Western blot analysis showed that approximately 73% of S was in the cleaved form (Extended Data Fig. 2d).

Individual virions contained 24 ± 9 S trimers (Extended Data Fig. 1b). This value is lower than previously estimated assuming an equidistant distribution of S[21], because S is not uniformly distributed over the virus surface. A small sub-population of virions contained only few S trimers while larger virions contained more S trimers (Extended Data Fig. 1b). We identified 4,104 wide S trimers and 116 thin S trimers from 179 virions and subjected them to subtomogram averaging. The averaged structures, at 7.7 and 22 Å resolution, respectively, correspond very well to published structures of purified S trimers in the pre- and postfusion forms[2,7,8] (Fig. 2a). Overall, approximately 97% of S trimers are in the prefusion form, and 3% in the postfusion form. Pre- and postfusion forms appear to be distributed evenly among virions.

Prefusion S trimers on the virus surface may be predominantly closed, with the open conformation induced or stabilized by ACE2 binding, or the open form may also be present. Open or closed forms may induce different ranges of antibodies when used as immunogens and there are ongoing efforts to generate S protein constructs stabilized in one or other conformation[9,11,12]. To assess whether S trimers are present in open and/or closed conformations, we subjected the RBD regions of individual monomers within the trimers to classification. Three kinds of classes were found, those with the RBD in the closed position, those with the RBD in the open position, and those where the RBD was predominantly in the closed position, but with some weakening of the density, suggesting the presence of more mobile conformations (Extended Data Fig. 3). Considering the classes to which each monomer was assigned, we derived structures of fully closed trimers, and of trimers where one RBD is open, which represent ~31% and ~55% of 3,854 prefusion trimers) (Fig. 2b, Extended Data Fig. 4). We also identified a small number of trimers (~14% of 3,854 prefusion trimers) in which two RBDs are in the open conformation (Fig. 2b). These observations confirm that the opening of the RBD observed in recombinant S trimers also takes place on the virus surface, and that artificial S protein constructs stabilized in the closed and open conformations both represent structures present in situ. The receptor binding site is therefore stochastically exposed in situ, and available to interact with ACE2 and with antibodies.

The trimers do not all protrude straight from the viral surface. They can tilt by up to 90° towards the membrane, though tilts over 50° are decreasingly favoured (Extended Data Fig. 1c,d). We grouped trimers according to their orientation relative to the membrane, and averaged these groups independently. The averaged structures reveal that the membrane-proximal stalk region acts as a hinge with sufficient flexibility to allow tilting in all directions (Fig. 2c).

We generated models of individual virus particles, with S trimers located at the position, orientation and conformation that were determined by subtomogram averaging (Fig. 2d). S trimers appear to be distributed randomly on the viral surface, with no obvious clustering or relationship between location, orientation, and conformation. There is approximately one trimer per 1,000 nm^2 of membrane surface compared to approximately one per 100 nm^2 for influenza A virus[26]. The sparse distribution of S, together with the predominantly closed state, suggest that receptor binding may be less dependent on avidity effects than is the case for pandemic influenza viruses[27]. This is consistent with the higher affinity between S and ACE2 (in the nM range[2,7]) than between haemaglutinin and sialic acid (mM range[27]).

The low concentration of particles in supernatant makes high-resolution structure determination difficult. We therefore concentrated the virus by pelleting through a sucrose cushion. Concentrated virions deviate from spherical morphology (Extended Data Fig. 5), but overall features are preserved. We performed cryo-ET and subtomogram averaging on the particles, and saw predominantly prefusion S trimers, with occasional postfusion S trimers. Upon classification of the prefusion S we were only able to identify the RBD in the closed position, and monomers in which a weak RBD density is observed (Extended Data Fig. 3c).

Virions in the supernatant from infected cells show primarily prefusion S trimers which are in either closed or open prefusion conformations. Virions concentrated through a sucrose cushion continue to show prefusion conformations, but the open conformation is no longer observed. Other studies have shown that virions inactivated with β-propiolactone, rather than formaldehyde, are primarily in a postfusion state[25]. S trimers purified from membranes are found only in the closed prefusion and postfusion conformations[8], while other studies have suggested that the open RBD in soluble S trimers is found in a continuum of different positions[28]. These observations suggest that the open prefusion conformations of the spike protein we observe before, but not after concentration, are fragile (despite the fixation applied here) and may be affected by purification procedures.

Our data imply that inactivation and purification methods can alter the ratio of pre and postfusion forms, and the ratio of open and closed forms. It has been speculated that substantial amounts of postfusion S on the virus surface may protect the virus by shielding the prefusion form or may shift the host response towards non-neutralizing antibodies[8]. Given the small fraction of postfusion spikes we observed on intact virions we consider it unlikely that this is an important defence mechanism for the virus during infection, but it may be an important consideration for vaccination. Candidate vaccines based on inactivated virus particles are under development. These may present different S protein epitopes to the immune system depending on how they are prepared and therefore differ in their ability to induce a neutralizing response. For example, β-propiolactone is frequently used in vaccine production (such as for influenza virus subunit vaccines[29]), but if postfusion S induces non-neutralizing responses, β-propiolactone may not be optimal for inactivation during SARS-CoV-2 S vaccine formulation.

We next imaged the concentrated virus in 2D by cryo-EM and performed single-particle analysis on those prefusion S trimers that protruded from the sides of the virus particles, generating a consensus structure of the prefusion trimer at 3.4 Å resolution. Focused classification with partial signal subtraction on individual RBD monomers led to two classes (Extended Data Fig. 5). Consistent with the absence of open conformations in this sample by cryo-ET, we observed 81% of the monomers in which the RBD is in the closed conformation and 19% of the monomers in which density for the RBD is weaker, but predominantly in the closed position. We refined the structures of S trimers in which all three RBDs are in the closed conformation (53% of the data), and those in which at least one RBD is weak (47% of the data), to resolutions

of 3.5 Å and 4.1 Å, respectively (Fig. 3a, Extended Data Fig. 6). The two structures are highly similar, differing only in the density levels for one RBD. We used the structure with three closed RBDs to build and refine an atomic model of the S protein trimer in situ on the viral surface.

The positions of glycans on the surface of S are well resolved in our structure with density at 17 of the 22 predicted N-glycosylation sites (Fig. 3b). The other 5 glycosylation sites are in disordered NTD loops or in the stalk region and are not resolved at high resolution. At the base of the trimer a clear ring of glycans forms a collar above the stalk region. The density for the stalk region extends by 2 helical turns compared to published structures of soluble ectodomain and further at lower resolution before fading out due to stalk flexibility (Fig. 3c). SARS-CoV-2 S trimers are sparsely distributed and can be highly tilted towards the membrane. This implies that epitopes at the base of the head domain and in the stalk region, would be accessible to antibodies where they are not protected by the extensive glycan shell.

We compared the in situ structure of the S trimer to structures previously obtained using exogenously expressed purified protein. A recent study of full-length trimeric S solubilized in detergent micelles[8], identified two features that are not seen in most structures of soluble S ectodomain trimers: well-defined density for residues 14-26 of S; and a folded loop between residues 833 and 853. This loop is folded in the structure of the "locked" conformation of the ectodomain[9], and may become folded in the low-pH conditions in the endosome[30]. We observe only weak density for residues 14-26, and we do not observe folded structure for the 833-853 region. The SARS-CoV-2 strain we have imaged contains the widely circulating D614G substitution[31], this mutation abolishes a salt bridge to K854 (Fig. 3d) and may reduce folding of the 833-854 loop[9,30]. We did not observe additional density that would correspond to bound lipids such as those described in a recent preprint[10], or other bound co-factors. These may be present sub-stoichiometrically or in rare conformations but are not a general feature of the S trimer in situ. Overall, our structure is very similar to that of the soluble trimeric ectodomain in the closed prefusion form stabilized by a double proline mutation (Extended Data Fig. 7)[2,7]. This provides an important validation of the ongoing use of recombinant, purified S trimers for research, diagnostics and vaccination – they indeed represent the in situ structure of S. By demonstrating structure determination of S trimers to 3.4 Å resolution on the virion surface (Fig. 3), our data make us optimistic that cryo-EM can be used to study antibody binding to S in the context of the viral surface. Such studies could provide insights into how neutralizing antibodies block virus infection, particularly for antibodies against membrane-proximal regions of S, and thus can inform design of immunogens for vaccination.

Online content

Any methods, additional references, Nature Research reporting summaries, source data, extended data, supplementary information, acknowledgements, peer review information; details of author contributions and competing interests; and statements of data and code availability are available at https://doi.org/10.1038/s41586-020-2665-2.

1. Neuman, B. W. & Buchmeier, M. J. Supramolecular Architecture of the Coronavirus Particle. *Adv. Virus Res.* **96**, 1–27 (2016).
2. Walls, A. C. et al. Structure, Function, and Antigenicity of the SARS-CoV-2 Spike Glycoprotein. *Cell* **181**, 281–292.e6 (2020).
3. Hoffmann, M. et al. SARS-CoV-2 Cell Entry Depends on ACE2 and TMPRSS2 and Is Blocked by a Clinically Proven Protease Inhibitor. *Cell* **181**, 271–280.e8 (2020).
4. Shang, J. et al. Structural basis of receptor recognition by SARS-CoV-2. *Nature* **581**, 221–224 (2020).
5. Wang, Q. et al. Structural and Functional Basis of SARS-CoV-2 Entry by Using Human ACE2. *Cell* **181**, 894–904.e9 (2020).
6. Watanabe, Y., Allen, J. D., Wrapp, D., McLellan, J. S. & Crispin, M. Site-specific glycan analysis of the SARS-CoV-2 spike. *Science* **369**, 330–333 (2020). https://doi.org/10.1126/science.abb9983.
7. Wrapp, D. et al. Cryo-EM structure of the 2019-nCoV spike in the prefusion conformation. *Science* **367**, 1260–1263 (2020).
8. Cai, Y. et al. Distinct conformational states of SARS-CoV-2 spike protein. *Scienceeabd4251* (2020). https://doi.org/10.1126/science.abd4251
9. Xiong, X. *et al*. A thermostable, closed SARS-CoV-2 spike protein trimer. *Nat. Struct. Mol. Biol*. 2020.06.15.152835 (2020) https://doi.org/10.1038/s41594-020-0478-5.
10. Toelzer, C. *et al*. Unexpected free fatty acid binding pocket in the cryo-EM structure of SARS-CoV-2 spike protein. *bioRxiv* 2020.06.18.158584 (2020) https://doi.org/10.1101/2020.06.18.158584.
11. Henderson, R. et al. Controlling the SARS-CoV-2 spike glycoprotein conformation. *Nat. Struct. Mol. Biol*. (2020). https://doi.org/10.1038/s41594-020-0479-4
12. McCallum, M., Walls, A. C., Bowen, J. E., Corti, D. & Veesler, D. Structure-guided covalent stabilization of coronavirus spike glycoprotein trimers in the closed conformation. *Nat. Struct. Mol. Biol*. 2020.06.03.129817 (2020) https://doi.org/10.1038/s41594-020-0483-8.
13. Zhu, N. et al. A novel coronavirus from patients with pneumonia in China, 2019. *N. Engl. J. Med*. **382**, 727–733 (2020).
14. Zhou, P. et al. A pneumonia outbreak associated with a new coronavirus of probable bat origin. *Nature* **579**, 270–273 (2020).
15. Masters, P. S. & Perlman, S. CHAPTER 28 – Coronaviridae. in *Fields Virology, 6th Edition* vol. 1 826–858 (Elsevier, 2013).
16. Neuman, B. W. et al. Supramolecular architecture of severe acute respiratory syndrome coronavirus revealed by electron cryomicroscopy. *J. Virol*. **80**, 7918–7928 (2006).
17. Bárcena, M. et al. Cryo-electron tomography of mouse hepatitis virus: Insights into the structure of the coronavirion. *Proc. Natl Acad. Sci. USA* **106**, 582–587 (2009).
18. Walls, A. C. et al. Tectonic conformational changes of a coronavirus spike glycoprotein promote membrane fusion. *Proc. Natl Acad. Sci. USA* **114**, 11157–11162 (2017).
19. Yuan, Y. et al. Cryo-EM structures of MERS-CoV and SARS-CoV spike glycoproteins reveal the dynamic receptor binding domains. *Nat. Commun*. **8**, 15092 (2017).
20. Fehr, A. R. & Perlman, S. Coronaviruses: an overview of their replication and pathogenesis. *Methods Mol. Biol*. **1282**, 1–23 (2015).
21. Klein, S. *et al*. SARS-CoV-2 structure and replication characterized by in situ cryo-electron tomography. *bioRxiv* 2020.06.23.167064 (2020) https://doi.org/10.1101/2020.06.23.167064.
22. Snijder, E. J. et al. A unifying structural and functional model of the coronavirus replication organelle: Tracking down RNA synthesis. *PLoS Biol*. **18**, e3000715 (2020). https://doi.org/10.1371/journal.pbio.3000715.
23. Hoffmann, M., Hofmann-Winkler, H. & Pöhlmann, S. Priming time: How cellular proteases arm coronavirus spike proteins. in *Activation of Viruses by Host Proteases* (2018). https://doi.org/10.1007/978-3-319-75474-1_4.
24. Rothe, C. et al. Transmission of 2019-NCOV infection from an asymptomatic contact in Germany. *N. Engl. J. Med*. **382**, 970–971 (2020).
25. Liu, C. et al. Viral Architecture of SARS-CoV-2 with Post-Fusion Spike Revealed by Cryo-EM. *bioRxiv*, 1–17 (2020). https://doi.org/10.1101/2020.03.02.972927
26. Chlanda, P. et al. The hemifusion structure induced by influenza virus haemagglutinin is determined by physical properties of the target membranes. *Nat. Microbiol*. **1**, 16050 (2016).
27. Xiong, X. et al. Receptor binding by a ferret-transmissible H5 avian influenza virus. *Nature* **497**, 392–396 (2013).
28. Gui, M. et al. Cryo-electron microscopy structures of the SARS-CoV spike glycoprotein reveal a prerequisite conformational state for receptor binding. *Cell Res*. **27**, 119–129 (2017).
29. Bonnafous, P. et al. Treatment of influenza virus with beta-propiolactone alters viral membrane fusion. *Biochim. Biophys. Acta Biomembr*. **1838** (1 Pt B), 355–363 (2014).
30. Zhou, T. *et al*. A pH-dependent switch mediates conformational masking of SARS-CoV-2 spike. *bioRxiv* 2020.07.04.187989 (2020) https://doi.org/10.1101/2020.07.04.187989.
31. Korber, B. et al. Tracking changes in SARS-CoV-2 Spike: evidence that D614G increases infectivity of the COVID-19 virus. *Cell*S0092-8674(20)30820-5 (2020). https://doi.org/10.1016/j.cell.2020.06.043

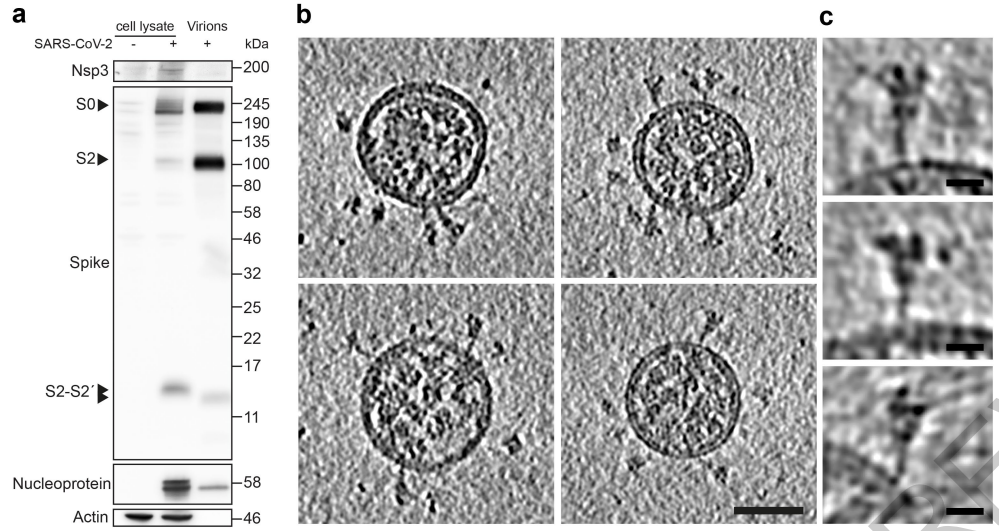

Fig. 1 | Characterization of virus production and images of SARS-CoV-2 virions. (**a**) western blot analysis of SARS-CoV-2 nsp3, S and N in lysates of VeroE6 cells and in virus preparations, representative of 3 experiments. In released virions, S is present in both cleaved and uncleaved forms. The positions of S0, S2 and the S2-S2′ cleavage product are marked. (**b**) Four representative tomographic slices of SARS-CoV-2 virions from the supernatant of infected cells. Virions are approximately spherical, contain granular density corresponding to N-packaged genome, and have S trimers protruding at variable angles from their surfaces. Scale bar 50 nm. (**c**) Three example S trimers from the data set shown as projections through the trimer to illustrate variable tilt towards the membrane. Scale bar 10 nm.

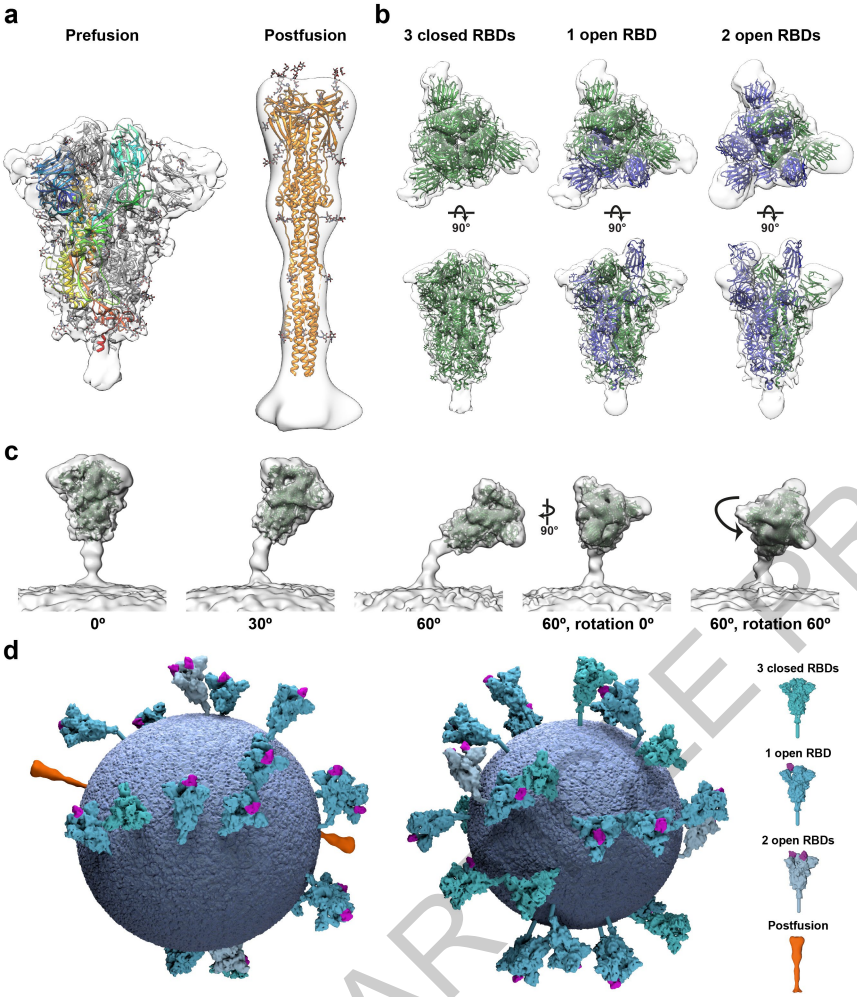

Fig. 2 | Structural analysis of SARS-CoV-2 S trimers on intact virions. (**a**) Structures of the prefusion (left) and postfusion (right) trimer from intact virions determined by subtomogram averaging. Structures are shown as transparent grey isosurfaces fitted with structures of the closed, prefusion trimer (PDB 6VXX) and the postfusion trimer (PDB 6XRA). One prefusion monomer is colored from blue (N terminus) to red (C terminus). The N-terminal domain is blue, the RBD appears cyan. The NTD does not fully occupy the EM density because some loops are not resolved or built in PDB 6VXX. (**b**) Three conformations of the prefusion trimer observed on intact virions: all RBDs in the closed position (left, fitted with PDB 6VXX); one RBD in the open position (centre, fitted with PDB 6VYB); two RBDs in the open position (right, fitted with PDB 6X2B which lacks modelled glycans). The two-open conformation has only been observed in vitro after inserting multiple stabilizing mutations. S monomers with closed RBDs are green, and with open RBDs are blue. (**c**) Averaging of subsets of trimers grouped according to their orientation relative to the membrane shows flexibility in the stalk region. Examples are shown for pools centred at 0°, 30° and 60° from the perpendicular, and for two rotations of the trimer relative to the tilt direction. (**d**) 3D models of two individual SARS-CoV-2 virions with a membrane (blue) of the measured radius, and all spike proteins shown in the conformations, positions and orientations determined by subtomogram averaging. Different S conformations are distributed over the virion surface and can be tilted by up to ~90° relative to the membrane (Extended Data Fig. 1c,d).

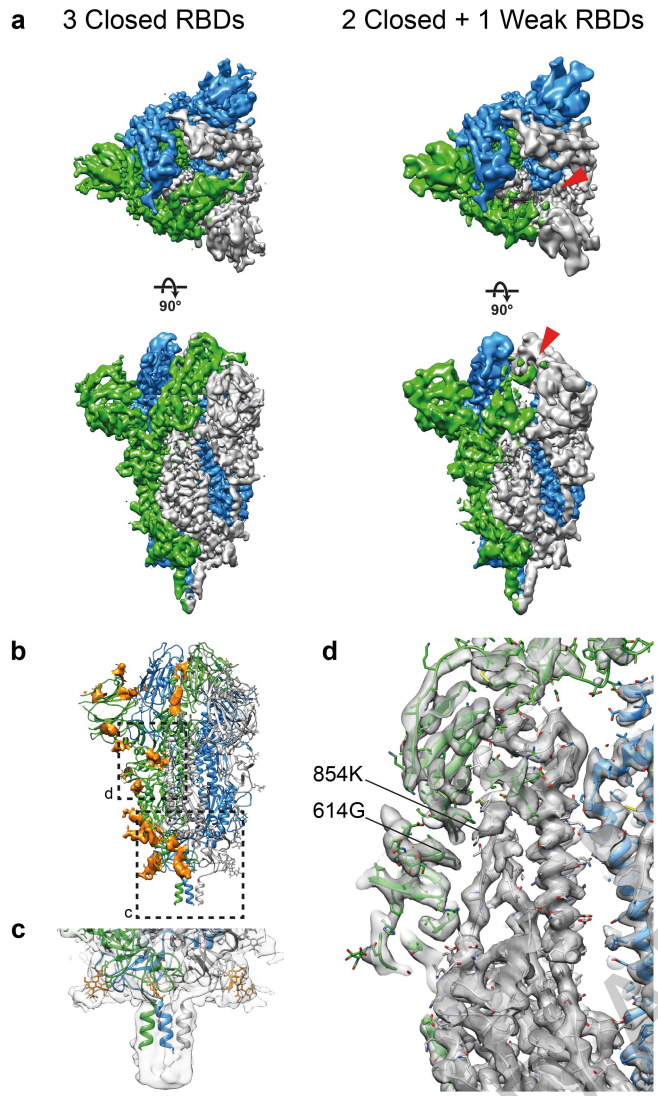

Fig. 3 | Structures of SARS-CoV-2 S trimers on intact virions by single particle reconstruction. (**a**) Top and side views of trimers with three closed RBDs (left, 3.5 Å resolution) and one weaker RBD (right, 4.1 Å resolution). Compare the left and right panels to see the weaker density for the RBD from the green monomer in the region indicated by the red arrowheads. Individual monomers are coloured white, blue and green. ((**B**)) Glycosylation profile of the S protein. Colour scheme as in (a), glycans are shown in orange. Boxes indicates the regions shown in c and d. (**c**) Close up of the base of the trimer at lower isosurface threshold to highlight the glycan ring and the extended C-terminal density. (**d**) Close up of the region of the spike where the D614G variation abolishes a salt bridge to 854K.

Methods

Cells and Virus

VeroE6 cells were obtained from ATCC and were cultured in Dulbecco's modified Eagle medium (DMEM, Life Technologies) containing 10% fetal bovine serum, 100 U/mL penicillin, 100 µg/mL streptomycin and 1% non-essential amino acids (complete medium). The Germany/BavPat1/2020 SARS-CoV-2 was isolated by Prof. Christian Drosten, Charité, Berlin, and distributed by the European Virology Archive (Ref-SKU: 026V-03883) at passage 2 (P2). A stock of SARS-CoV-2 was obtained by passaging the virus once in VeroE6 cells (P3). To produce SARS-CoV-2 virions, VeroE6 cells grown on 75 cm^2 side-bottom tissue culture flasks were infected with SARS-CoV-2 (P3) at MOI of 0.5. Culture media from infected cells were harvested at 48 h postinfection, clarified by centrifugation at 1,000 × g for 10 min, cleared through a 0.45-µm nitrocellulose filter and fixed with 4% formaldehyde for 30 min at RT. Culture medium was supplemented with 10 mM HEPES (pH 7.2) before fixation. Virus-containing medium was subsequently aliquoted and stored at −80 °C. Infectious supernatants containing SARS-CoV-2 virions were obtained from Calu-3 cells infected with P3 virus at an MOI = 5 for 48 h and processed as described above.

To obtain SARS-CoV-2 virions at high concentration, infection and harvest of VeroE6 culture medium were performed as above, followed by concentration of fixation-inactivated virions from media by ultracentrifugation through a 20% (wt/wt) sucrose cushion (120 min at 27,000 rpm in a Beckman SW32 rotor; Beckman Coulter Life Sciences). Pelleted particles were resuspended in PBS and stored in aliquots at −80 °C.

Western blot

VeroE6 or Calu-3 cells mock infected or infected for 48 h with SARS-CoV-2 (MOI = 5) were washed twice in PBS, scraped, pelleted at 700 × g for 5 min and lysed in PBS pH 7.4, containing 1% Triton-X 100 and protease inhibitors (Merck) for 30 min at 4 °C. Samples were centrifuged at 4 °C for 30 min and supernatants were collected. Total protein concentration was calculated using the Bio-Rad Protein Assay kit (Biorad). Purified viruses were prepared for western blot by centrifugation of 32 ml of virus containing supernatants on a 10% sucrose cushion in a Beckmann J25 centrifuge. Centrifugation was performed at 10,000 × g for 4 h at 4 °C. Supernatants were discarded and purified virus pellet were resuspended in 500 µl of PBS. For western blotting, 10 µg of total cell lysates and 5 µl of purified viruses were diluted in Laemmli buffer and loaded on a pre-casted Criterion XT 4–12% gradient gel (Biorad). Gels were transfered to PVDF membrane using a wet-electroblotting chamber system (Biorad) in Towbin buffer containing 10% methanol. Transfer was performed overnight at 4 °C. Membranes were washed in PBS and blocked with 10% milk in PBS containing 0.2% tween-20 (PBS-T) for 1 h. Membranes were incubated for 1 h at RT with primary antibodies specific for an epitope in the C-terminal region of S (Abcam, cat# ab252690, diluted 1:1,000 in PBS-T), for N-protein (Sino Biological, cat# 40143-MM05, diluted 1:1,000 in PBS-T), or non-structural protein 3 (nsp3) (abcam, cat# ab181620, diluted 1:500 in PBS-T). Next, the membranes were washed 3 times in PBS-T, incubated with HRP conjugated anti-mouse or anti-rabbit antibodies at 1:10,000 dilution for 1 h, washed again 3 times in PBS-T, incubated with western Lightning Plus-ECL reagent (Perkin Elmer; Waltham, MA) and imaged using an Intas ChemoCam Imager 3.2 (Intas, Göttingen). Densitometric analysis of western blot assays was performed using LabImage 1D L340 software version 4.1 (Intas, Göttingen). The blot shown is representative of three independent experiments. Uncropped, unprocessed blots are in the Source Data file.

RT–PCR and spike sequencing

Total RNA was isolated from infected VeroE6 cells 48 h after infection with Germany/BavPat1/2020 SARS-CoV-2 (P2). Spike cDNA was produced from the total RNA using superscript iii (ThermoFisher) with specific RT-primers (CAATTGTGAAGATTCTCATA). The cDNA was amplified by PCR using specific primers (Fwrd – ATGTTTGTTTTTCTTGTTTTATT; rev – TTATGTGTAATGTAATTTGA) and the resulting amplicon was sent for Sanger sequencing. Sequences were compared to the Germany/BavPat1/2020 SARS-CoV-2 reference sequence (Ref-SKU: 026V-03883) and found to be identical. Specific sequencing primers: Fwrd1 - ATGTTTGTTTTTCTTGTTTTATT;Fwrd2 – GGTTGGACAGCTGGTGCT;Fwrd3 – CCAACCATACAGAGTAGTAGTA; Rev1 – GTAGCAGCAAGATTAGCAGAA; Rev2 – TTATGTGTAATGTAATTTGA.

Cryo-ET sample preparation

Fixed virus samples from the supernatant of infected cells without any concentration step (unconc) or concentrated by pelleting through a sucrose cushion (conc) were prepared, imaged, and processed in parallel. The virus suspension was mixed with 10-nm colloidal gold (in PBS solution) in 10:1 ratio. Then 3 µl of the solution was added to a glow-discharged copper grid (C-Flat 2/2, Protochips). Grids were plunge frozen into liquid ethane by back-side blotting using a LeicaGP cryo plunger (Leica) and stored in liquid nitrogen until imaging.

Cryo-ET data collection

Cryo-ET data collection was performed essentially as described previously[32]. Cryo-grids were loaded into an FEI Titan Krios transmission electron microscope operated at 300 kV and images were recorded on a Gatan K2 Summit direct detection camera in counting mode with a 20 eV energy slit in zero-loss mode. Tomographic tilt series between −60° and +60° were collected using SerialEM 3.8.0 software[33] in a dose-symmetric scheme[34] with a 3° angular increment. A total dose of 120 e^-/A^2 per tilt series was distributed evenly among 41 tilt images. The nominal magnification was 81,000 X, giving a pixel size of 1.532 Å on the specimen. The defocus range was between -2 µm and -6 µm and 10 frames were saved for each tilt angle. All data acquisition parameters are listed in Extended Data Table 1.

Frames were motion-corrected in IMOD 4.10.30[35] and images were dose-filtered using the *alignframes* function in IMOD. Exposure filtering was implemented according to the cumulative dose per tilt as described elsewhere[36]. The contrast transfer function (CTF) was measured using non-dose-filtered images using the ctfplotter package within IMOD[37]. Tilt series stacks were sorted using IMOD *newstack* function and fiducial-alignment of all tilt series was performed in IMOD/etomo. Tomograms with less than three trackable gold fiducials were discarded. Motion-corrected and dose-filtered tilt stacks were CTF-corrected by CTF multiplication and tomograms were reconstructed by weighted back-projected in novaCTF[38]. Tomograms were low-pass filtered to 50 Å for better visualization in EMAN2.2[39] and tomographic slices were visualized with IMOD.

Extraction of S trimers from tomograms

The initial steps of subtomogram alignment and averaging were implemented using MATLAB (MathWorks) scripts which were derived from the TOM[40] and AV3[41] packages as described previously[32]. The missing wedge was modelled as the summed amplitude spectrum of background subtomograms for each tomogram, and was applied during alignment and averaging.

To generate an initial template model of the spike protein from the viral surface, 68 spikes were manually picked from four virions of tomograms that were down-scaled by 4x binning of the voxels. The 68 spikes' initial Euler angles (2 out of 3) were determined based on the vector between two points, one on the head of the spike and one on the membrane where the spike anchors, respectively. The 68 spikes were iteratively aligned to one another for four iterations applying threefold symmetry to generate a low-resolution template that resembled a prefusion conformation of the spike. This template was used as an alignment reference for all virions (below). All postfusion spikes were manually identified and picked and initial Euler angles were assigned in the same manner.

The centre of each virion was then marked manually using the Volume Tracer function in UCSF Chimera (version 1.13.1)[42] and the radius of the virion was determined centred at the membrane using the Pick Particle Chimera Plugin[43]. An oversampled spherical grid of points was generated on the virion surface with ~9 nm spacing, and subtomograms were extracted for all grid points with a box size of 96 pixels (approximately 60 nm) centred at a radius 14 nm above these grid positions (approximately the radius of the expected centre of the spike). Initial Euler angles were assigned to each subtomogram based on the orientation of the normal vectors relative to the sphere surface.

Subtomograms were aligned against the low resolution template (from the above average of 68 spikes). During this alignment, subtomogram positions converged onto clusters at the true spike positions. One subtomogram position was kept for each cluster, excluding particles within a distance of ~15 Å (10 pixels) and removing particles with cross-correlation coefficients (CCC) below 0.11. Subtomograms that had tilted by more than 90° relative to their perpendicular positions were excluded. Visual inspection of the tomograms using the Place Object Chimera Plugin[43] confirmed that subtomograms selected in this manner corresponded to S trimers on the viral surface (see below). Subtomograms were divided into two halves based on virion number. From this point on the two halves were processed independently.

Subtomogram averaging

Subsequent processing was performed in RELION[44]. For this purpose, subtomograms were reconstructed from the original tilt series images after motion correction using *relion_reconstruct*. Using dedicated python scripts, the S trimer positions in the 3D tomograms from the procedure outlined above were converted into 2D positions and defocus values in the corresponding tilt series images, as well as Euler angles in the RELION convention. Individual sub-tomograms were reconstructed at a 2x down-scaled pixel size of 3.064 Å, by 3D insertion of Fourier slices of the cropped regions of the tilt series images, each multiplied by their corresponding CTF, which included the dose filter. Similarly, 3D-CTF volumes were generated by 3D insertion of the corresponding CTF^2 slices. Subtomograms were reconstructed in a box size of 128 voxels for prefusion trimers and a box size of 192 voxels for averages of tilted spikes and for postfusion trimers.

In order to deal with the CTF pre-multiplied sub-tomograms, as well as the multiplicity of each 3D voxel in the tilt series, a modified version of RELION was used for subtomogram refinement and classification (details to be described elsewhere). Standard 3D auto-refinement was performed with C3 symmetry and a soft-edged mask around the trimers, using a 30 Å low-pass filtered map as an initial reference. Using 3,854 of the 4,104 subtomograms (excluding those that had tilted by more than 90° relative to the perpendicular position (Extended Data Fig. 1c)), a 7.7 Å consensus map was calculated for the prefusion trimers; 116 postfusion trimers led to a 22 Å map.

Angular density (Extended Data Fig. 1c) was illustrated by dividing the number of spikes per histogram bin by the sine of the tilt angle. From this histogram, the noise level in the distribution due to incorrectly aligned spikes was estimated assuming they are uniformly distributed (red dashed line in Extended Data Fig. 1c), and based on averaging over the range 140-180°. Such angles must be incorrectly alignments because they orient the spike towards the inside of the virus.

Based on the subtomograms that contributed to the consensus map we estimated that there are 23 ± 9 prefusion S trimers per virion. For a subset of 28 virions, we visually compared the trimers identified by subtomogram averaging with the tomograms to identify false positives or false negatives, finding that the number of S trimers identified by subtomogram averaging is an underestimate of the number of observed S trimers by 0.9 trimers per virion. On this basis we estimate there are 24 ± 9 prefusion S trimers per virion.

Next, we performed symmetry expansion[45], followed by focused classification without alignment and with partial signal subtraction, while keeping the orientations from the consensus refinement fixed. The mask used for focused classification was generated manually and enclosed the RBD of one monomer (Extended Data Fig. 3a), including the closest NTD of the neighbouring monomer. Classification of the primary data set (unconc1) led to three different RBD states: closed (45% of the monomers); open (28%) and with weak density (27%) (Extended Data Fig. 3a). Classification of a second, smaller data set of virus particles in supernatant (unconc2), comprising 1,224 trimers yielded 39% closed RBD, 22% open RBD and 39% weak RBD, in general agreement with the unconc1 results (Extended Data Fig. 3b). Classification of a data set of virus particles after concentration through a sucrose cushion (conc), comprising 3,788 trimers, yielded 67% of the monomers corresponding to closed RBDs and 33% to RBDs with weak density. For this data set, no RBDs in the open conformation were identified (Extended Data Fig. 3c).

The classification of the RBDs as closed, open or with weaker density was used to divide the unconc1 data set into three subsets: 31% (1,175 trimers) have no open RBDs; 55% (2,121 trimers) have one RBD in the open state; and 14% (525 trimers) have two open RBDs. The remaining 33 trimers have three RBDs in the open state and not further processed. In the class with weaker density, the RBD appears to be predominantly in the closed state and was treated as closed for this assignment. For each of the three subsets, reconstruction of the two independently refined half sets was performed using the orientations from the consensus refinement that gave the 7.7 Å consensus map described above. Subsequent standard post-processing procedures for resolution estimation, map sharpening and local-resolution filtering in RELION led to three final maps. The subset with no open RBDs gave a reconstruction with C3 symmetry in which all three RBDs were closed at 8.6 Å resolution. The other two subsets yielded structures with C1 symmetry and either one or two open RBDs, with resolutions of 8.6 Å and 9.9 Å, respectively (Extended Data Figs. 3 and 4). Note, that while fixation is not expected to give rise to any new conformations, we cannot rule out that it differentially stabilizes different conformations, and the position of the equilibrium between open and closed conformations in unfixed samples may differ from those estimated from fixed samples.

Averages of tilted spikes were generated by grouping according to the tilt and rotation of the subtomogram away from the normal vector to the membrane. Subtomograms were included in a group for averaging if they were within 15° of the displayed tilt (0°, 30° and 60°) and rotation (0°, 60°). The pools illustrated in Fig. 2c contain 14.5, 14.1, 12.0 and 10.0% of the subtomograms.

Cryo-EM sample preparation and data collection

Virus solution concentrated through a 20% (wt/wt) sucrose cushion was frozen on C-Flat 2/2 3C grids (Protochips) following the same procedure as for cryo-ET, but without adding gold fiducials. Grids were imaged on a Thermo Fisher Scientific Titan Krios transmission electron microscope that was operated at 300 kV, using a Gatan K3 direct electron detector and a Gatan BioQuantum energy filter with a 20 eV energy slit. Movies with 48 frames and an accumulated dose of 50 $e^-/Å^2$ were acquired in counting mode using SerialEM-3.8.0[33] at a nominal magnification of 81,000 X, corresponding to a calibrated pixel size of 1.061 Å/pixel. Detailed data acquisition parameters are summarized in Extended Data Table 2.

Cryo-EM image processing

The Scheduler functionality in RELION-3.1 was used for fully automated real-time processing during data collection[9,46]. Movies were motion-corrected and dose-weighted using RELION's implementation of the MotionCor2 algorithm[47]. Subsequently, non-dose-weighted sums were used to estimate the contrast transfer function (CTF) in CTFFIND-4.1.13[48]. S trimers that were extending from the sides of virus particles were picked manually (973 particles from the first 100 micrographs) and then used as a training set for optimisation of the convolutional neural network in the automated particle picking software Topaz[49]. Extracted particles were subjected to 3D classification using

a previously determined structure of the S trimer[9], lowpass-filtered to 30 Å, as initial 3D reference. The selected 286,407 particles that contributed to 3D classes corresponding to S trimers were submitted to Bayesian polishing to correct for per-particle beam-induced motions and a second round of 3D classification to select the 55,159 particles that contributed to the best class. This final consensus set of particles was subjected to CTF refinement of per-particle defocus, per-micrograph astigmatism and beam tilt, followed by a second round of Bayesian polishing. 3D auto-refinements were performed with the selected particles after each round of 3D classification, CTF refinement or Bayesian polishing. The consensus structure had a resolution of 3.4 Å.

Subsequently, symmetry expansion[45], followed by focused 3D classification with partial signal subtraction[50] was performed. Using a mask on a single RBD to focus classification into six classes, while keeping the orientations of the last consensus refinement fixed, resulted in the identification of two RBD states: closed or with weak density. S trimers with all three RBDs in the closed state were refined separately from S trimers with one RBD with weak density, resulting in two final maps with resolutions. Standard RELION post-processing was used for resolution estimation, map sharpening and local-resolution filtering. The C3 symmetric map with three closed RBD had an estimated overall resolution of 3.5 Å; the C1 map with one weaker RBD extended to 4.1 Å resolution (Extended Data Fig. 6b).

Model building and refinement

The SARS-CoV-2 S trimer structure (PDBID: 6ZP0[9]) was used as an initial model for building into the model with three closed RBDs (Extended Data Fig. 6a, middle). Residues were adjusted manually in Coot 0.9[51]. Steric clash and sidechain rotamer conformations were improved using the Namdinator web server[52]. After further iterations of manual adjustment, the structure was refined in PHENIX-1.18.2[53]. The geometry and statistics are given in Extended Data Table 2. The unmasked model-to-map FSC was calculated in PHENIX for the refined model against the full reconstruction.

3D model of spikes on authentic virions

In order to visualize the spike protein on the authentic SARS-CoV-2 virions, the coordinates, orientations and conformational classes determined by subtomogram averaging were converted into a format compatible with Maxon Cinema 4D (version S22.116), and imported together with the 3D models of the different conformational states determined by subtomogram averaging. To generate representative virion images in Fig. 2d we removed the 3 false positives from one virion and positioned the 3 false negatives on each virion which had been identified by visual inspection of the data (see above). The HR2 region was modelled as a cylinder. Images of individual virions from the data set were rendered into Adobe Photoshop to generate images for presentation.

Reporting summary

Further information on research design is available in the Nature Research Reporting Summary linked to this paper.

Data availability

Published structures for comparison or initial model building were obtained from the protein data bank (PDB) with accession codes 6VXX[2], 6VYB[2], 6X2B[11], 6XRA[8] and 6ZP0[9]. The cryo-EM and cryo-ET structures determined here, and representative tomograms are deposited in the Electron Microscopy Data Bank (EMDB) under accession codes EMD-11493 (prefusion consensus structure), EMD-11494 (3 closed RBDs from subtomogram averaging), EMD-11495 (1 open RBD), EMD-11496 (2 open RBDs), EMD-11497 (3 closed RBDs from cryo-EM), and EMD-11498 (2 open and 1 weak RBDs). The associated molecular models are deposited in the PDB under accession codes 6ZWV (3 closed RBDs from cryo-EM).

32. Wan, W. et al. Structure and assembly of the Ebola virus nucleocapsid. *Nature* **551**, 394–397 (2017).
33. Mastronarde, D. N. Automated electron microscope tomography using robust prediction of specimen movements. *J. Struct. Biol.* **152**, 36–51 (2005).
34. Hagen, W. J. H., Wan, W. & Briggs, J. A. G. Implementation of a cryo-electron tomography tilt-scheme optimized for high resolution subtomogram averaging. *J. Struct. Biol.* **197**, 191–198 (2017).
35. Kremer, J. R., Mastronarde, D. N. & McIntosh, J. R. Computer visualization of three-dimensional image data using IMOD. *J. Struct. Biol.* **116**, 71–76 (1996).
36. Grant, T. & Grigorieff, N. Measuring the optimal exposure for single particle cryo-EM using a 2.6 Å reconstruction of rotavirus VP6. *eLife* **4**, e06980 (2015).
37. Xiong, Q., Morphew, M. K., Schwartz, C. L., Hoenger, A. H. & Mastronarde, D. N. CTF determination and correction for low dose tomographic tilt series. *J. Struct. Biol.* **168**, 378–387 (2009).
38. Turoňová, B., Schur, F. K. M., Wan, W. & Briggs, J. A. G. Efficient 3D-CTF correction for cryo-electron tomography using NovaCTF improves subtomogram averaging resolution to 3.4Å. *J. Struct. Biol.* **199**, 187–195 (2017).
39. Galaz-Montoya, J. G., Flanagan, J., Schmid, M. F. & Ludtke, S. J. Single particle tomography in EMAN2. *J. Struct. Biol.* **190**, 279–290 (2015).
40. Nickell, S. et al. TOM software toolbox: acquisition and analysis for electron tomography. *J. Struct. Biol.* **149**, 227–234 (2005).
41. Förster, F., Medalia, O., Zauberman, N., Baumeister, W. & Fass, D. Retrovirus envelope protein complex structure in situ studied by cryo-electron tomography. *Proc. Natl Acad. Sci. USA* **102**, 4729–4734 (2005).
42. Pettersen, E. F. et al. UCSF Chimera--a visualization system for exploratory research and analysis. *J. Comput. Chem.* **25**, 1605–1612 (2004).
43. Qu, K. et al. Structure and architecture of immature and mature murine leukemia virus capsids. *Proc. Natl Acad. Sci. USA* **115**, E11751–E11760 (2018).
44. Bharat, T. A. M., Russo, C. J., Löwe, J., Passmore, L. A. & Scheres, S. H. W. Advances in Single-Particle Electron Cryomicroscopy Structure Determination applied to Sub-tomogram Averaging. *Structure* **23**, 1743–1753 (2015).
45. Scheres, S. H. W. Processing of Structurally Heterogeneous Cryo-EM Data in RELION. *Methods Enzymol.* **579**, 125–157 (2016).
46. Zivanov, J. et al. New tools for automated high-resolution cryo-EM structure determination in RELION-3. *eLife* **7**, (2018).
47. Zheng, S. Q. et al. MotionCor2: anisotropic correction of beam-induced motion for improved cryo-electron microscopy. *Nat. Methods* **14**, 331–332 (2017).
48. Rohou, A. & Grigorieff, N. CTFFIND4: Fast and accurate defocus estimation from electron micrographs. *J. Struct. Biol.* **192**, 216–221 (2015).
49. Bepler, T. et al. Positive-unlabeled convolutional neural networks for particle picking in cryo-electron micrographs. *Nat. Methods* **16**, 1153–1160 (2019).
50. Bai, X. C., Rajendra, E., Yang, G., Shi, Y. & Scheres, S. H. W. Sampling the conformational space of the catalytic subunit of human γ-secretase. *eLife* **4**, (2015).
51. Emsley, P. & Cowtan, K. Coot: model-building tools for molecular graphics. *Acta Crystallogr. D Biol. Crystallogr.* **60**, 2126–2132 (2004).
52. Kidmose, R. T. et al. *Namdinator* - automatic molecular dynamics flexible fitting of structural models into cryo-EM and crystallography experimental maps. *IUCrJ* **6**, 526–531 (2019). https://doi.org/10.1107/S2052252519007619.
53. Afonine, P. V. et al. Real-space refinement in PHENIX for cryo-EM and crystallography. *Acta Crystallogr. D Struct. Biol.* **74**, 531–544 (2018).

Acknowledgements We thank the staff of the MRC-LMB for generous support during the COVID-19 pandemic lockdown. We thank all the staff of the MRC-LMB EM Facility, in particular Anna Yeates, Grigory Sharov and Giuseppe Cannone, for supporting the EM experiments and Jake Grimmett and Toby Darling for supporting scientific computing. We are grateful to C. Drosten and EVAg for provision of the SARS-CoV-2 strain used here, to Manfred Frey for the Calu-3 cell line, and we acknowledge microscopy support from the Infectious Diseases Imaging Platform (IDIP) at the Center for Integrative Infectious Disease Research Heidelberg. This study was supported by funding from the European Research Council (ERC) under the European Union's Horizon 2020 research and innovation programme (ERC-CoG-648432 MEMBRANEFUSION to JAGB), the Medical Research Council as part of United Kingdom Research and Innovation (MC_UP_A025_1013 to SHWS; MC_UP_1201/16 to JAGB), the Deutsche Forschungsgemeinschaft (240245660 – SFB 1129 project 5 to HGK and project 11 to RB) and the Japan Society for the Promotion of Science (overseas research fellowship to TN).

Author contributions ZK and JAGB conceived the study, ZK, JO, KQ, MC, VZ, HGK, RB and JAGB designed the study. MC, VZ, CJN and BC prepared and characterized virus samples with supervision from HGK and RB. ZK and KQ collected cryo-EM data. ZK, JO and KQ processed cryo-EM data with assistance from TN, JZ, JML and JP, supervised by SHWS and JAGB. ZK, JO, KQ, MC and LM made figures. ZK, JO, KQ, MC, XX and JAGB interpreted data. JAGB prepared the initial draft and managed the project. ZK, JO, KQ, MC and JAGB wrote the manuscript with input from all authors. SHWS, HGK, RB and JAGB obtained funding.

Competing interests The authors declare no competing interests.

Additional information

Supplementary information is available for this paper at https://doi.org/10.1038/s41586-020-2665-2.

Correspondence and requests for materials should be addressed to J.A.G.B.

Peer review information *Nature* thanks Jason McLellan and the other, anonymous, reviewer(s) for their contribution to the peer review of this work. Peer reviewer reports are available.

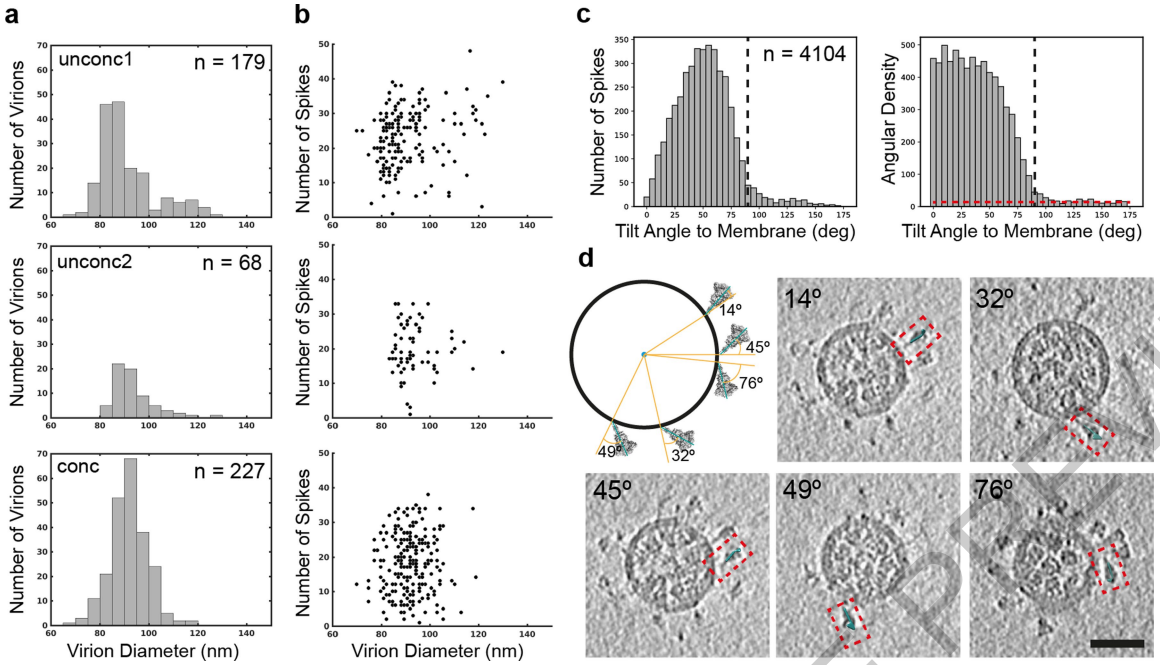

Extended Data Fig. 1 | Characterization of SARS-CoV-2 virion morphology. (**a**) Histogram of virion diameters for unconcentrated extracellular virions in the supernatant of two independent preparations (top and middle), and for extracellular virions after concentration through a sucrose cushion (bottom). After concentration the virions become less spherical. Mean and standard deviation for diameters are 91 ± 11 nm (n = 179), 94 ± 9 nm (n = 68) and 92 ± 8 nm (n = 227) for the three preparations. (**b**) Scatter plot of number of spikes identified per virion during subtomogram averaging against virion diameter for the same virions shown in panel (**a**). Visual inspection indicates that almost all spikes were identified for virions in the supernatant, but that not all spikes are identified in the concentrated preparation leading to an underestimate of the number of spikes. (**c**) Histogram of spike tilt angle towards the membrane for the larger supernatant virus data set (unconc1). The vertical black dashed line indicates 90°. 97% of particles have tilts below 90°; particles with tilts above 90° were not included in image analysis. The angular density (right) is calculated by dividing the number of spikes by the sine of the determined angle. If spikes were unconstrained in tilt, this distribution would be uniform. The angular density decreases from ~50°, indicating that higher tilts are disfavoured. The horizontal red dashed line indicates the angular distribution of noise (spikes which have failed to align), estimated based on the angular density between 140° and 180°. (**d**) Schematic diagram and examples of individual tilted spikes on virions. The schematic indicates the angle that was measured. Five examples of individual tilted spikes are marked on tomographic slices through an intact virion, with their associated angle. Scale bar 50 nm.

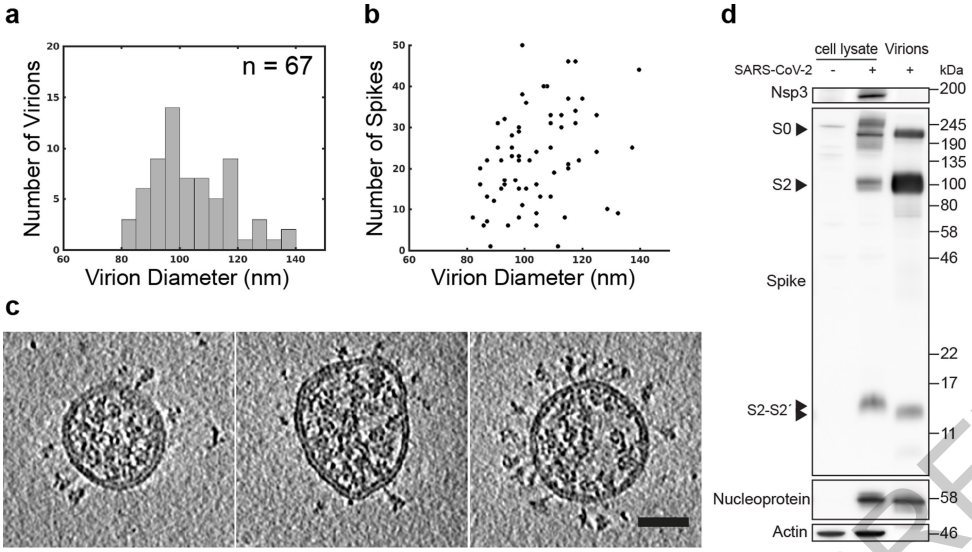

Extended Data Fig. 2 | Morphology of SARS-CoV-2 virions released from infected Calu-3 cells. As in Extended Data Fig. 1, (**a**) Histogram of virion diameters. Mean and standard deviation for diameters are 104 ± 13 nm ($n = 67$). (**b**) Scatter plot of number of spikes identified per virion during subtomogram averaging against virion diameter for the same virions shown in panel a. (**c**) central slices through three representative viruses from 67 imaged in one experiment. Virions from Calu-3 cells had a slightly broader diameter distribution than those from VeroE6 cells. Scale bar 50 nm. (**d**) western blot analysis of SARS-CoV-2 nsp3, S and N in cell lysates and in virus preparations. In released virions, S is present in both cleaved (S2, 73%) and uncleaved forms (S0, 27%).

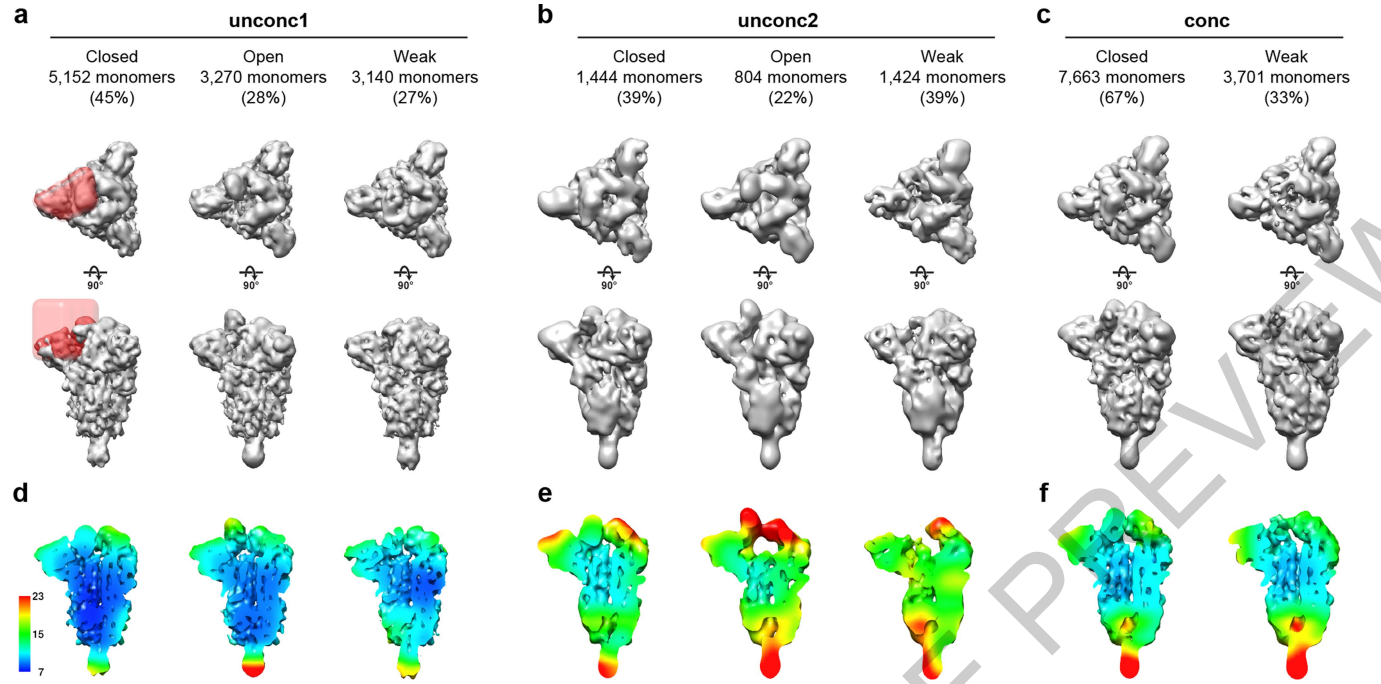

Extended Data Fig. 3 | Classification of SARS-CoV-2 spike RBDs. (**a**) Class averages obtained after focused classification on the RBD of the left monomer after symmetry expansion of the unconc1 data set. Top views and side views are shown for closed, open and weak classes. The region subjected to classification is indicated by a transparent red mask surface in the left hand panel. (**b**) Equivalent analysis for a smaller, independent data set (unconc2). (**c**) Equivalent analysis for a data set obtained after concentrating virus through a sucrose cushion (conc). Only closed and weak classes were obtained. (**d-f**) Cut-open local resolution maps for structures shown in (a-c).

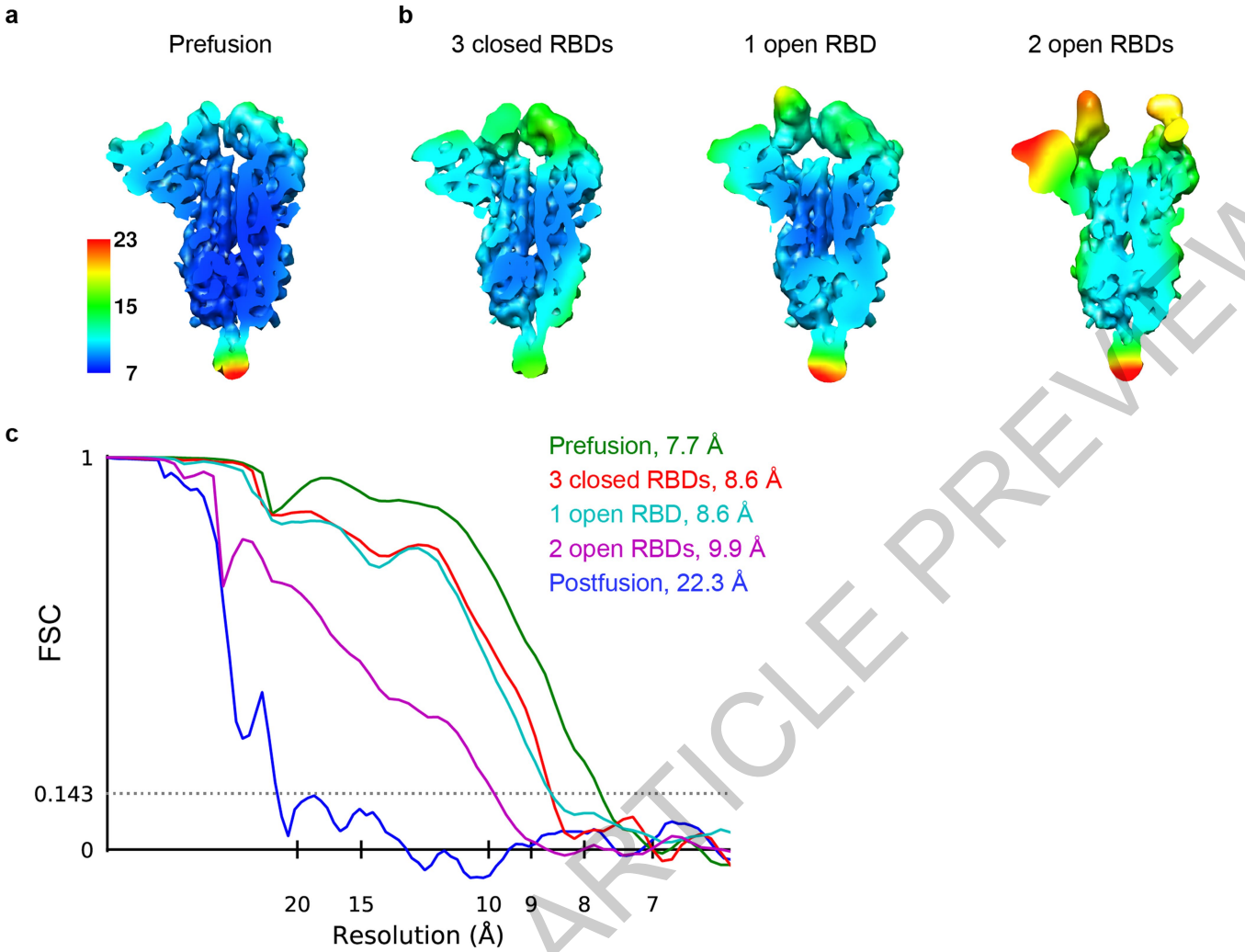

Extended Data Fig. 4 | Resolution assessment of subtomogram averaging structures. (**a**) Local resolution map for the consensus structure obtained for the prefusion S trimers. (**b**) Local resolution maps for the prefusion S trimer in three different conformations. (**c**) Global resolution assessment by Fourier shell correlation (FSC) at the 0.143 criterion for the four structures shown in a and b, as well as the postfusion S trimer.

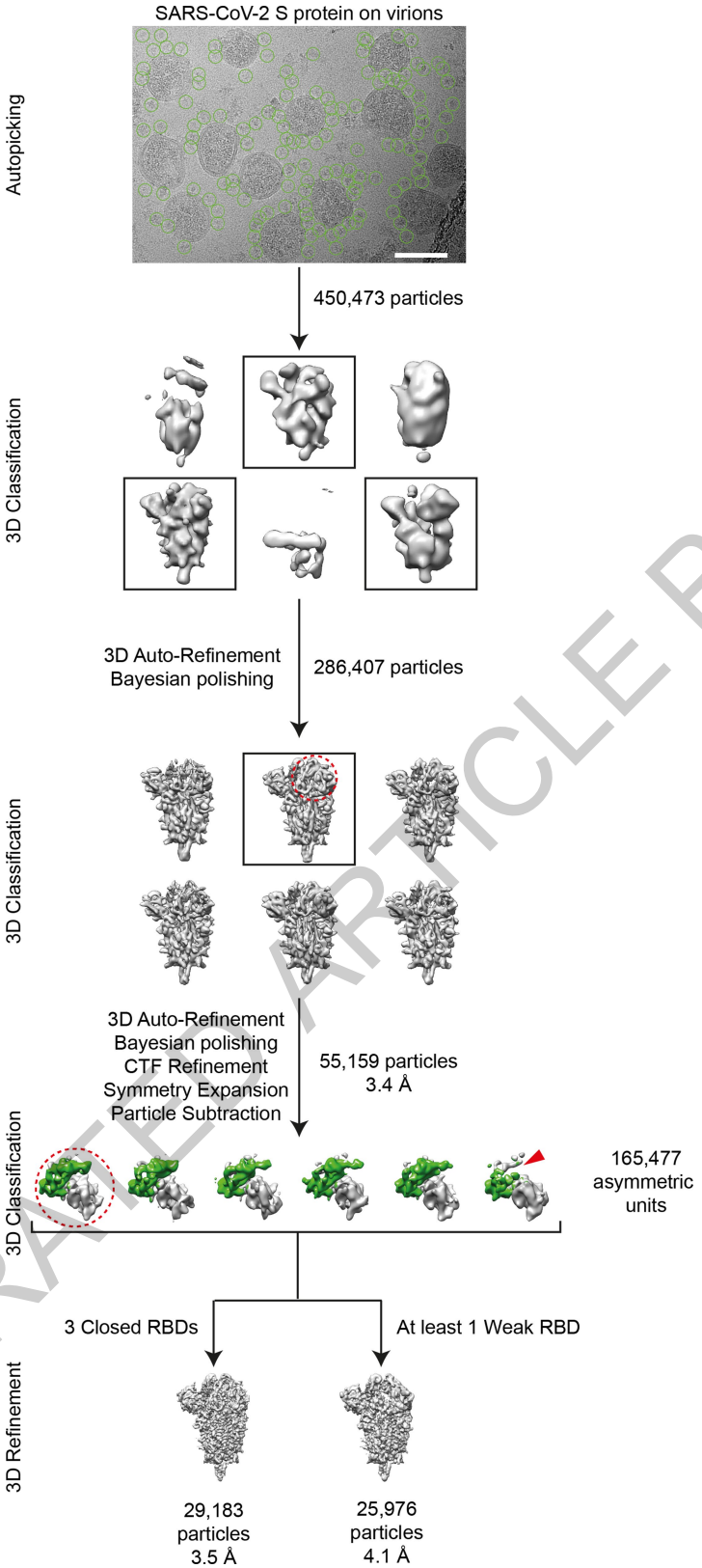

Extended Data Fig. 5 | Single particle cryo-EM image processing workflow. Automatically picked particles (green circles) were subjected to 3D classification. Scale bar 100 nm. Selected 3D classes are indicated by black boxes. RBDs from individual asymmetric units from the S trimer (red dashed circles) were locally classified to sort different conformations of RBD. The asymmetric unit subjected to local classification is shown in a top view, the RDB of the green monomer is weak in the right-hand class (red arrowhead). S trimers with all three RBDs in the closed state were further refined with C3 symmetry. S trimers where one RBD had weak density were refined with C1 symmetry. For further details see materials and methods.

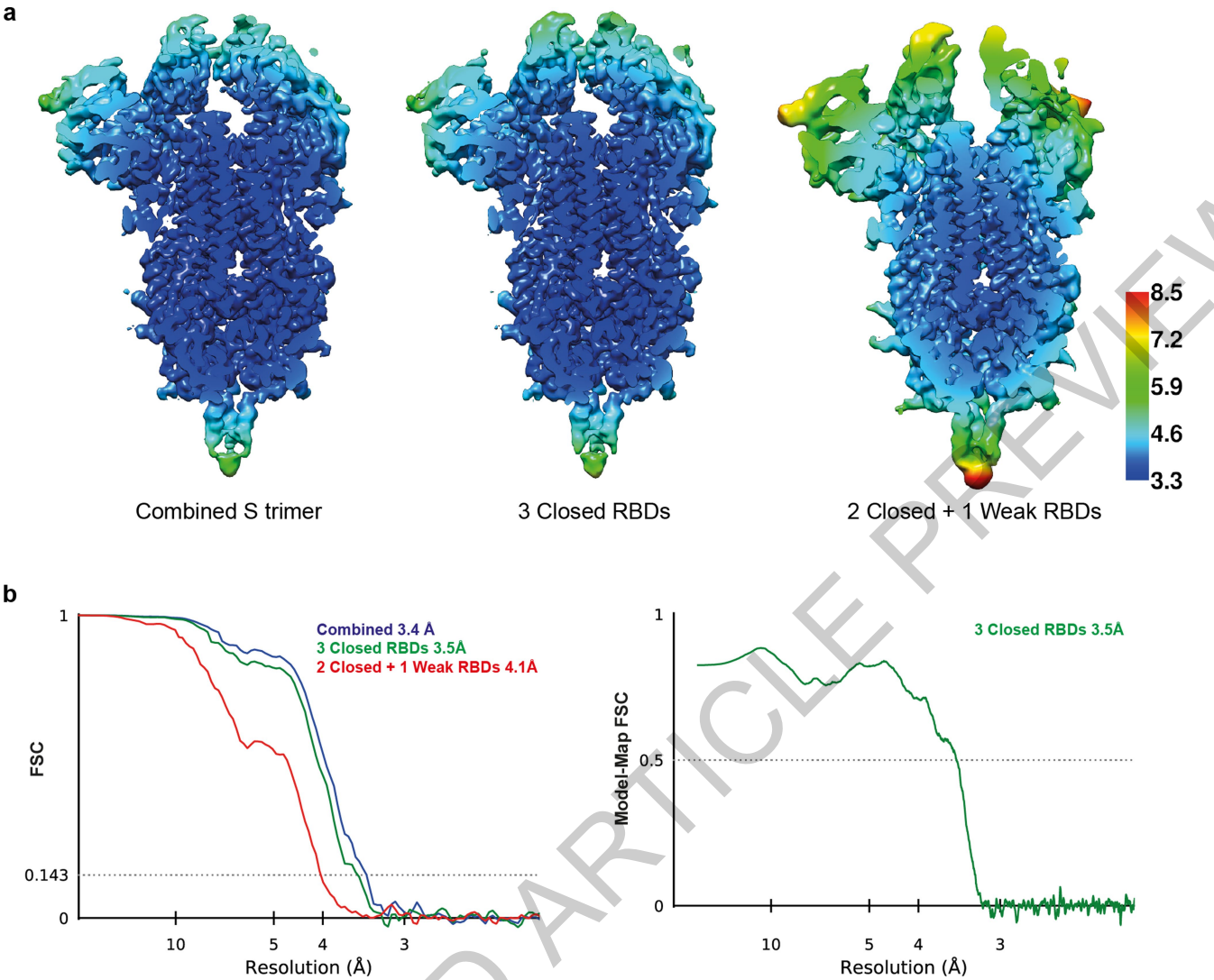

Extended Data Fig. 6 | Single particle Cryo-EM structure validation. (**a**) Cut-open cryo-EM maps obtained using all prefusion S trimers, S trimers with 3 closed RBDs or S trimers with 2 closed and 1 weak RBDs, coloured according to the local resolution. (**b**) FSC curves for the three structures in (a), and for the atomic model against the map.

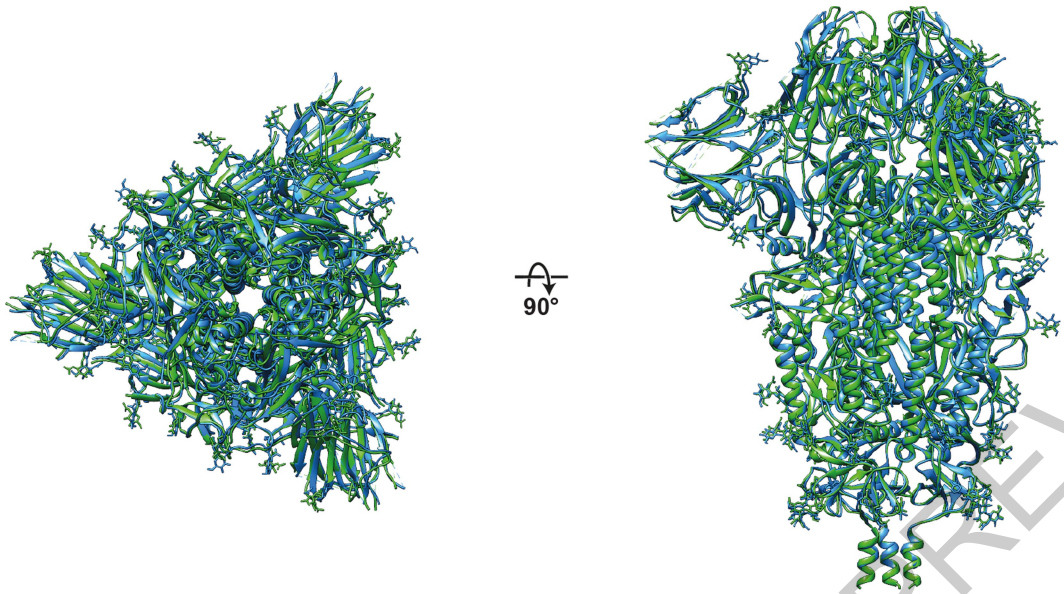

Extended Data Fig. 7 | Structural comparison of in situ structure with recombinant soluble structure. Structural superposition of S trimer modelled into the structure of the trimer with three closed RBDs (green, this study) with the published structure of recombinant, soluble closed trimer (blue, PDB 6VXX). Top and side views are shown. The structures are very similar.

Extended Data Table 1 | Cryo-ET data acquisition and image processing

Sample	VeroE6 unconc 1	VeroE6 unconc 2	VeroE6 conc	Calu-3 unconc
Data Collection				
Microscope	FEI Titan Krios	FEI Titan Krios	FEI Titan Krios	FEI Titan Krios
Voltage (keV)	300	300	300	300
Energy-filter (eV)	20	20	20	20
Detector	Gatan K2 Summit	Gatan K2 Summit	Gatan K2 Summit	Gatan K2 Summit
Recording Mode	Counting	Counting	Counting	Counting
Pixel size (Å)	1.532	1.532	1.532	1.532
Defocus range (μm)	-2 to -6	-2 to -6	-2 to -6	-2 to -6
Acquisition scheme	-60/60˚, 3˚	-60/60˚, 3˚	-60/60˚, 3˚	-60/60˚, 3˚
Total Dose (electrons/Å^2)	~120	~120	~120	~120
Frame number	10	10	10	10
Tomograms	156	65	30	57
Image processing				
Virus particles	179	68	227	NA
Subtomograms	4,104	1,335	4,136	NA
Symmetry	C3	C3	C3	NA
Resolution at 0.143 FSC (Å)	7.7	9.9	9.1	NA
EMDB ID	EMD-11493	NA	NA	

Spike trimer conformation classification

Trimer Classification	**3 closed RBDs**	**1 open RBD**	**2 open RBDs**
Trimer particles	1,175	2,121	525
Symmetry	C3	C1	C1
Resolution at 0.143 FSC (Å)	8.6	8.6	9.9
EMDB ID	EMD-11494	EMD-11495	EMD-11496

Extended Data Table 2 | Cryo-EM data collection, refinement and validation statistics

	3 Closed RBDs (EMD-11497, PDB 6ZWV)	2 Closed + 1 Weak RBDs (EMD-11498)
Data collection and processing		
Magnification	81,000	81,000
Voltage (kV)	300	300
Electron exposure (e^{-}/Å^2)	50	50
Defocus range (μm)	1.0-3.0	1.0-3.0
Pixel size (Å)	1.061	1.061
Movies (no.)	7,982	7,982
Symmetry imposed	*C3*	*C1*
Initial particle images (no.)	450,473	450,473
Final particle images (no.)	29,183	25,976
Map resolution (Å)	3.5	4.1
FSC threshold	0.143	0.143
Map resolution range (Å)	3.35-27.16	3.67-45.27
Refinement		
Initial model used	PDB 6ZP0	
Model resolution (Å)	3.5	
FSC threshold	0.5	
Map sharpening *B* factor (Å^2)	-50	
Model composition		
Non-hydrogen atoms	24036	
Protein residues	2955	
Ligands	63	
B factors (Å^2)		
Protein	130.57	
Ligand	142.74	
R.m.s. deviations		
Bond lengths (Å)	0.009	
Bond angles (°)	1.346	
Validation		
MolProbity score	1.62	
Clashscore	2.97	
Poor rotamers (%)	1.74	
Ramachandran plot		
Favored (%)	94.97	
Allowed (%)	5.03	
Disallowed (%)	0.00	

nature research

Corresponding author(s): John Briggs

Last updated by author(s): Jul 28, 2020

Reporting Summary

Nature Research wishes to improve the reproducibility of the work that we publish. This form provides structure for consistency and transparency in reporting. For further information on Nature Research policies, see our Editorial Policies and the Editorial Policy Checklist.

Statistics

For all statistical analyses, confirm that the following items are present in the figure legend, table legend, main text, or Methods section.

n/a	Confirmed	
☐	☒	The exact sample size (*n*) for each experimental group/condition, given as a discrete number and unit of measurement
☐	☒	A statement on whether measurements were taken from distinct samples or whether the same sample was measured repeatedly
☒	☐	The statistical test(s) used AND whether they are one- or two-sided *Only common tests should be described solely by name; describe more complex techniques in the Methods section.*
☒	☐	A description of all covariates tested
☒	☐	A description of any assumptions or corrections, such as tests of normality and adjustment for multiple comparisons
☐	☒	A full description of the statistical parameters including central tendency (e.g. means) or other basic estimates (e.g. regression coefficient) AND variation (e.g. standard deviation) or associated estimates of uncertainty (e.g. confidence intervals)
☒	☐	For null hypothesis testing, the test statistic (e.g. *F*, *t*, *r*) with confidence intervals, effect sizes, degrees of freedom and *P* value noted *Give P values as exact values whenever suitable.*
☒	☐	For Bayesian analysis, information on the choice of priors and Markov chain Monte Carlo settings
☒	☐	For hierarchical and complex designs, identification of the appropriate level for tests and full reporting of outcomes
☒	☐	Estimates of effect sizes (e.g. Cohen's *d*, Pearson's *r*), indicating how they were calculated

Our web collection on statistics for biologists contains articles on many of the points above.

Software and code

Policy information about availability of computer code

Data collection	SerialEM 3.8.0 for operation of electron microscope (available and referenced in the Methods section)
Data analysis	CryoET data processing (all commercial or available and referenced in methods): CTFFIND4; IMOD 4.10; NovaCTF 1.0.0, EMAN2.2; Matlab R2016b; TOM (no version number); AV3 (no version number); Python 3.7; RELION 3.1. CryoEM data processing (all available and referenced in methods): CTFFIND4.1.13; RELION 3.1. Modelling/structure refinement/visualization (all available and referenced in methods): Coot 0.9; Namdinator (no version numbering); PHENIX 1.18.2; Chimera 1.13.1; Maxon Cinema 4D version S22.116 Western blot quantification: LabImage 1D L340 software version 4.1 (Intas, Göttingen)

For manuscripts utilizing custom algorithms or software that are central to the research but not yet described in published literature, software must be made available to editors and reviewers. We strongly encourage code deposition in a community repository (e.g. GitHub). See the Nature Research guidelines for submitting code & software for further information.

Data

Policy information about availability of data

All manuscripts must include a data availability statement. This statement should provide the following information, where applicable:

- Accession codes, unique identifiers, or web links for publicly available datasets
- A list of figures that have associated raw data
- A description of any restrictions on data availability

Published structures for comparison or initial model building were obtained from the protein data bank (PDB) with accession codes 6VXX, 6VYB, 6X2B, 6XRA and 6ZP0. The cryo-EM and cryo-ET structures determined here, and representative tomograms are deposited in the Electron Microscopy Data Bank (EMDB) under accession codes EMD-11493 (prefusion consensus structure), EMD-11494 (3 closed RBDs from subtomogram averaging), EMD-11495 (1 open RBD), EMD-11496 (2 open RBDs), EMD-11497 (3 closed RBDs from cryo-EM), and EMD-11498 (2 open and 1 weak RBDs). The associated molecular models are deposited in the PDB under accession codes 6ZWV (3 closed RBDs from cryo-EM).

Field-specific reporting

Please select the one below that is the best fit for your research. If you are not sure, read the appropriate sections before making your selection.

☒ Life sciences ☐ Behavioural & social sciences ☐ Ecological, evolutionary & environmental sciences

For a reference copy of the document with all sections, see nature.com/documents/nr-reporting-summary-flat.pdf

Life sciences study design

All studies must disclose on these points even when the disclosure is negative.

Sample size	Sample sizes were determined by available electron microscopy time and the number of virus particles on electron microscopy grids. The sample size is sufficient to obtain a structure at the reported resolution, as assessed by Fourier shell correlation.
Data exclusions	For all cryo-ET experiments, tomograms which could not be used due to objects (contamination, ice, grid bars etc) obscuring the virus particle were discarded.
Replication	For cryoET and cryoEM, structures were determined from independent half datasets, which were compared to assess the resolution of the reconstruction, as described in the methods section. Two independent preparations of virus in supernatant were analysed as described in the methods section. Western blots are representative of three independent experiments.
Randomization	For CryoET, division of dataset into two random halves was done based on virus number. For CryoEM, division of datasets into two random halves was done based on standard approach in RELION 3. Other experiments did not involve randomization.
Blinding	Blinding was not applicable to this study because this type of study does not use group allocation.

Reporting for specific materials, systems and methods

We require information from authors about some types of materials, experimental systems and methods used in many studies. Here, indicate whether each material, system or method listed is relevant to your study. If you are not sure if a list item applies to your research, read the appropriate section before selecting a response.

Materials & experimental systems

n/a	Involved in the study
☐	☒ Antibodies
☐	☒ Eukaryotic cell lines
☒	☐ Palaeontology and archaeology
☒	☐ Animals and other organisms
☒	☐ Human research participants
☒	☐ Clinical data
☒	☐ Dual use research of concern

Methods

n/a	Involved in the study
☒	☐ ChIP-seq
☒	☐ Flow cytometry
☒	☐ MRI-based neuroimaging

Antibodies

Antibodies used	Anti-mouse HRP Sigma A4416 Anti-rabbit HRP Sigma A6154 Beta actin Sigma A5441 Spike Abcam Ab252690

	Nsp3 abcam ab181620 Nucleocapsid Sino Biological 40143-MM05
Validation	Commercial antibodies validated as per manufacturers website: Beta actin Sigma A5441 Immunoblot on chicken fibroblast cell extracts Spike Abcam Ab252690 Validated by ELISA on free peptide from SARS-CoV-1 Nsp3 abcam ab181620 Validated by western blot on SARS-CoV-1 infected cells Nucleocapsid Sino Biological 40143-MM05 Validated by western blot with corresponding viruses

Eukaryotic cell lines

Policy information about cell lines

Cell line source(s)	VeroE6 cells were obtained from ATCC, Calu-3 cells were obtained from Manfred Frey, originally from ATCC.
Authentication	Cells were not further authenticated
Mycoplasma contamination	Cells have been tested and are free of mycoplasma.
Commonly misidentified lines (See ICLAC register)	none

J Korean Med Sci. 2020 Feb 24;35(7):e86
https://doi.org/10.3346/jkms.2020.35.e86
eISSN 1598-6357·pISSN 1011-8934

JKMS

Brief Communication
Infectious Diseases, Microbiology & Parasitology

Viral Load Kinetics of SARS-CoV-2 Infection in First Two Patients in Korea

Jin Yong Kim [1*] **Jae-Hoon Ko** [2*] **Yeonjae Kim** [3] **Yae-Jean Kim** [4] **Jeong-Min Kim** [5] **Yoon-Seok Chung** [5] **Heui Man Kim** [5] **Myung-Guk Han** [5] **So Yeon Kim** [6] **and Bum Sik Chin** [3]

[1]Division of Infectious Diseases, Department of Internal Medicine, Incheon Medical Center, Incheon, Korea
[2]Division of Infectious Diseases, Department of Medicine, Samsung Medical Center, Sungkyunkwan University School of Medicine, Seoul, Korea
[3]Department of Internal Medicine, National Medical Center, Seoul, Korea
[4]Department of Pediatrics, Samsung Medical Center, Sungkyunkwan University School of Medicine, Seoul, Korea
[5]Division of Viral Diseases, Center for Laboratory Control of Infectious Diseases, Korea Centers for Disease Control & Prevention, Cheongju, Korea
[6]Department of Laboratory Medicine, National Medical Center, Seoul, Korea

Received: Feb 14, 2020
Accepted: Feb 19, 2020

Address for Correspondence:
Bum Sik Chin, MD, PhD
Department of Internal Medicine, National Medical Center, 245 Eulji-ro, Jung-gu, Seoul 04564, Korea.
E-mail: moberrer@nmc.or.kr

*Jin Yong Kim and Jae-Hoon Ko contributed equally to this work.

ORCID iDs
Jin Yong Kim
https://orcid.org/0000-0002-4306-1597
Jae-Hoon Ko
https://orcid.org/0000-0002-9490-6609
Yeonjae Kim
https://orcid.org/0000-0003-4144-9077
Yae-Jean Kim
https://orcid.org/0000-0002-8367-3424
Jeong-Min Kim
https://orcid.org/0000-0002-8240-0395
Yoon-Seok Chung
https://orcid.org/0000-0003-4562-5533

ABSTRACT

As of February 2020, severe acute respiratory syndrome coronavirus 2 (SARS-CoV-2) outbreak started in China in December 2019 has been spreading in many countries in the world. With the numbers of confirmed cases are increasing, information on the epidemiologic investigation and clinical manifestation have been accumulated. However, data on viral load kinetics in confirmed cases are lacking. Here, we present the viral load kinetics of the first two confirmed patients with mild to moderate illnesses in Korea in whom distinct viral load kinetics are shown. This report suggests that viral load kinetics of SARS-CoV-2 may be different from that of previously reported other coronavirus infections such as SARS-CoV.

Keywords: Coronavirus; SARS-CoV-2; 2019-nCoV; COVID-19; Viral Load Kinetics

As of February 2020, the novel coronavirus disease (COVID-19) outbreak caused by severe acute respiratory syndrome coronavirus 2 (SARS-CoV-2) started in China in December 2019 has been spreading in many countries over the world.[1-3] The numbers of confirmed cases are increasing over 70,000 including 31 Korean patients as of third week of February 2020. The World Health Organization declared the SARS-CoV-2 outbreak a public health emergency of international concern on January 30, 2020.[4] While the information on epidemiologic investigation and clinical manifestation are being accumulated, viral kinetics of the novel virus have not been systematically evaluated yet. To understand the behavior of the virus in human body, we present the viral load kinetics of the first two patients in Korea.

Upper respiratory tract (URT) and lower respiratory specimen (LRT) specimens were collected from confirmed patients every day after the diagnosis of SARS-CoV-2 infection and sent to Korea Center for Disease Control for follow-up tests and culture. Nasopharyngeal and oropharyngeal swabs were collected and placed in the same tube as URT specimen, and sputum was used as LRT specimen.[5] Serum, plasma, urine, and stool samples were also collected sequentially during the illness. Real-time reverse transcriptase polymerase chain reaction (rRT-PCR) was used to detect SARS-CoV-2 using the published sequences.[6] The cycle threshold (Ct)

Heui Man Kim
https://orcid.org/0000-0003-2908-6437
Myung-Guk Han
https://orcid.org/0000-0002-3543-1826
So Yeon Kim
https://orcid.org/0000-0003-1774-0382
Bum Sik Chin
https://orcid.org/0000-0003-3021-1434

Disclosure

The authors have no potential conflicts of interest to disclose.

Author Contributions

Conceptualization: Kim JY, Chin BS, Kim YJ. Data curation: Kim JY, Chin BS, Han MG, Kim SY, Ko JH. Formal analysis: Kim JY, Chin BS, Han MG, Kim SY, Ko JH. Methodology: Kim JM, Chung YS, Kim HM, Kim SY, Han MG. Writing – original draft: Kim YJ, Kim JY, Chin BS, Han MG, Ko JH. Writing - review & editing: Kim JY, Ko JH, Kim Y, Kim YJ, Kim JM, Chung YS, Kim HM, Han MG, Kim SY, Chin BS.

values of rRT-PCR was converted into RNA copy number of SARS-CoV-2. The detection limit of quantitative PCR reaction was 2,690 copies/mL. Detailed methods and values for the tests are presented in the **Supplementary Data 1** and **Supplementary Tables 1** to **3**.

A 35-year-old Chinese woman from Wuhan, China was confirmed to be first SARS-CoV-2 infected case in Korea. The detailed exposure history and a clinical course of this patient is described in previous report.[7] Viral load kinetics of Patient 1 is shown in **Fig. 1A** (viral RNA copies) and **Supplementary Fig. 1** (reverse Ct value). Briefly, she was quarantined at the airport due to fever (38.3°C) at the entry inspection on January 19, 2020. She had no significant exposure history and developed fever, chills, and myalgia one day before the entry to Korea (January 18, 2020, day 1 of symptom onset). The virus was detected from URT specimens on day 2 of symptom onset. As she did not have significant respiratory symptoms, LRT specimen (spontaneous sputum) was obtained with airway clearance techniques of percussion on day 3. Although any infiltration was not noticed on her chest X-ray (CXR) on the same day, LRT specimen was positive for SARS-CoV-2. On day 4, high resolution computed tomography (HRCT) was taken and multiple ground-glass opacities were observed in both sub-pleural spaces.[7] On day 5, the viral load was increased from day 3 in LRT specimen and she required oxygen supplement via nasal cannula (3 L/min). She eventually developed cough on day 7, and infiltration was observed on CXR from the next day. However, it appeared that the viral loads already started to decrease from around day 7 in both URT and LRT specimens. rRT-PCR continued to be positive at low level until day 13 (LRT specimens) and 14 (URT specimens). On day 12, her CXR was worsened with increase in oxygen requirement up to 10 L/min, while the viral loads dropped significantly from the initial values. Therefore, by the time when the significant infiltration was visible on a plain chest radiography, the viral load might be already on its lower end of detection. From day 14 (LRT specimen) and day 15 (URT specimen), rRT-PCR became undetectable for two consecutive days, respectively. She had mild loose stool from day 4 to day 19. Although RdRp and/or E gene were detected occasionally from urine and stool specimens collected from day 5 to 12, none of specimen satisfied conditions for positivity. Only one serum sample collected on day 8 showed positive rRT-PCR result, but the Ct value was adjacent to the cut-off value for positivity. Her symptoms, oxygen requirement, and CXR findings significantly improved from day 17 and she was discharged on day 20 of symptom onset (February 6, 2019).

Patient 2 was a 55-year-old Korean man, who had been working at Wuhan, China, arrived in Korea via Shanghai on January 22, 2020. The detailed exposure history and a clinical course of this patient is described in **Supplementary Data 1**. Briefly, he did not have any significant exposure history and developed sore throat and intermittent myalgia since January 10 which was controlled by nonsteroidal anti-inflammatory agent. He was tested on January 23, 2020, confirmed with SARS-CoV-2 infection next day and hospitalized on the same day. Therefore, his admission day (January 24) was considered to be the day 15 of symptom onset. His CXR on day 15 showed infiltration and chest HRCT on day 16 showed bilateral ground-glass opacity (**Supplementary Fig. 3A**). The viral load kinetics are shown in **Fig. 1B** (viral RNA copies) and **Supplementary Fig. 2** (reverse Ct value). In this patient, the initial test was performed on day 14 of symptom onset and SARS-CoV-2 was detected in both URT and LRT specimens. However, the initial viral loads were relatively lower (49,047 copies/mL for URT and 391,243 copies/mL for LRT) than those of Patient 1 (46,971,053 copies/mL for URT and 9,171,220 copies/mL for LRT) in whom the test was performed on day 2 of symptom onset. SARS-CoV-2 was detected a few more times during hospitalization from both URT and LRT specimens at low levels. As he had just mild cough with little or no sputum, LRT specimens

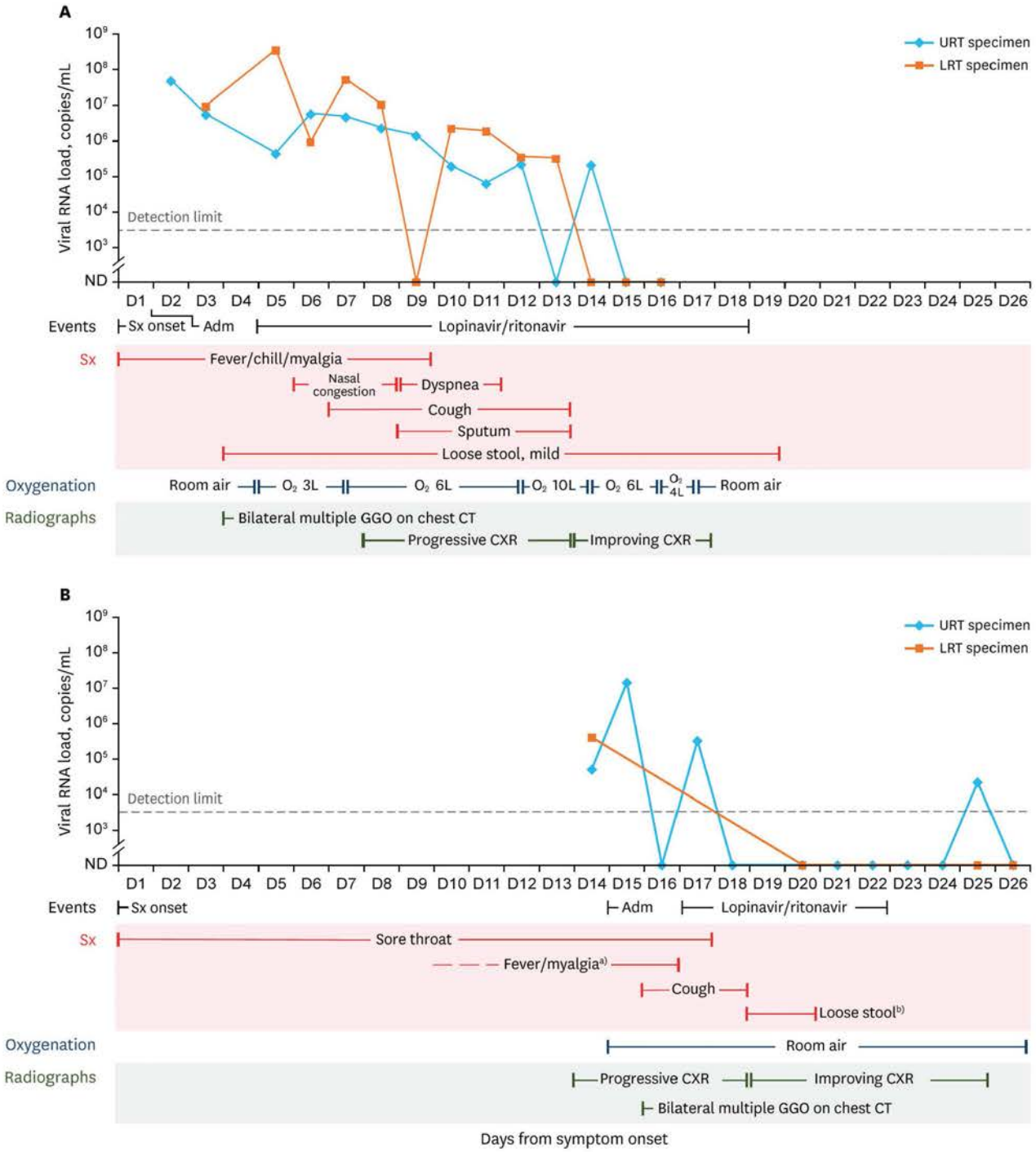

Fig. 1. Viral load kinetics according to the clinical course of the first two SARS-CoV-2 infected patients in Korea. (**A**) Viral load kinetics and clinical course of Patient 1. (**B**) Viral load kinetics and clinical course of Patient 2.
URT = upper respiratory tract, LRT = lower respiratory tract, ND = not detected, CXR = chest X-ray, GGO = ground glass opacity, CT = computed tomography, SARS-CoV-2 = severe acute respiratory syndrome coronavirus 2.
[a]In Patient 2, the exact fever duration could not be estimated because he had taken non-steroidal anti-inflammatory agent to control his myalgia and sore throat before hospitalization. When his physician discontinued the medication, the fever was observed; [b]Patient 2 experienced loose stool after taking Lopinavir/ritonavir.

https://doi.org/10.3346/jkms.2020.35.e86

were available only a few times. From D18 (URT specimen) and D20 (LRT specimen), rRT-PCR became undetectable for two consecutive days, respectively. On day 25, RdRp (Ct value of 36.69) and E (Ct value of 33.18) genes was detected again from the URT sample of day 25, it was interpreted as negative due to high Ct value of RdRp gene. From his plasma and stool specimens, only E genes were once detected on day 17 and it was also interpreted as negative result. His CXR improved from day 19 and he was discharged on day 27 (February 5, 2020).

This study presents the viral load kinetics of the first two confirmed patients in Korea in whom distinct viral load kinetics are shown. Although the viral load and CXR findings in these two patients may not represent the whole spectrum of SARS-CoV-2 illness, our report will provide many important findings and opportunity to understand this newly discovered virus infection in human. In Patient 1, we observed one example of moderate disease (shortness of breath and oxygen requirement up to 10 L/min) with corresponding radiograph findings and viral loads. We could observe her clinical presentation from day 2 of symptom onset and the whole clinical picture was captured with viral loads. There are several important implications from this observation. First, unlike SARS-CoV infection,[8] we found that viral load was highest during the early phase of the illness (3–5 days from first symptom onset, fever and myalgia were the only symptoms in Patient 1) and continued to decrease until the end of the second week. While she developed cough as well as shortness of breath and infiltration appeared on CXR at the end of first week of illness, the viral load already started to decrease at this phase. This may have a very important implication to determine the optimal time point for antiviral treatment intervention to prevent progression to severe disease. Second, the virus was detected from LRT specimens even before the development of LRT symptoms (cough, shortness of breath, and oxygen requirement) or visible infiltration on CXR. This may suggest that although the patient does not complain of any LRT symptoms, the virus is already there and causing insidious pathology, ultimately leading to LRT symptoms and chest infiltration later. However, the viral load starts to decrease in both URT and LRT specimens at the same time, which may puzzle the clinicians. Third, unlike in MERS-CoV revealing higher concentration of virus in LRT specimens,[9] viral loads were similar in both URT and LRT specimens. Fourth, low concentration of genetic materials, especially E gene, was detected in urine and stool from the end of the first week until the patient recovered from the infection. However, rRT-PCR results did not meet the criteria for SARS-CoV-2 positivity. Further studies need to be performed in non-respiratory specimens such as urine and stool samples.

In Patient 2, we observed one example of mild disease with corresponding radiograph findings and viral loads. This may represent many real-world mild cases who may present to medical facility late in their disease course. Therefore, this patient's information has also some important implications. First, even in a patient with mild disease (sore throat only), visible infiltration on CXR was observed at the end of second week. Second, even in a patient with mild disease, if visible infiltration on CXR is observed, virus is still detected in both URT and LRT specimens even at the end of second week after symptom onset. Viral loads of URT were similar with and sometimes higher than LRT specimens, and virus was detectable for longer period in URT specimen. This could be also probably because the patient did not have significant cough and had little amount of spontaneous sputum insufficient for testing.

There are also limitations in our report. Since we only presented two patients (mild and moderate), the information from these patients may not be generalizable to many other cases, especially severe cases. Second, Lopinavir/ritonavir was used in both patients on day

5 and day 17 from symptom onset, but its role cannot be determined in viral load reduction or clinical improvement. In addition, since they received Lopinavir/ritonavir which can also cause diarrhea, how much of gastrointestinal tract symptom was in fact related to SARS-CoV-2 or drug side effect. Third, we cannot estimate the time point when these patients were exposed to virus and when they started to shed the virus from their respiratory secretions. These data are also urgently needed to understand this virus better and to implement the control strategies as early as possible. Finally, the virus has not been readily cultured from these specimens, yet, although we are still trying. It is not clear whether there was not viable virus (possibly infectious) or we were not successful to culture this newly discovered virus in the beginning. Therefore, knowing the virus load that can give a positive culture result is important in the future. There is scarce information on viral load kinetics in SARS-CoV-2 infected patients throughout the illness. Therefore, although our report is based on observation from only two patients, this will provide valuable insight to understand the nature of this virus.

In conclusion, we report a unique pattern of SARS-CoV-2 viral kinetics in URT and LRT specimens from first two patients diagnosed in Korea. While two cases were different in disease course, these data will provide valuable insight to understand the nature of this virus.

ETHICS STATEMENT

The clinical data and images are presented under agreement of the patients.

ACKNOWLEDGMENTS

We greatly appreciate the efforts of all the hospital employees and their families at the Incheon Medical Center and National Medical Center, who are working tirelessly during this outbreak. We thank to Yoonju Oh, Sung Hee Kim, Yoon Soog Kang, and Kwang Sil Kim (Incheon Medical Center) for collecting and preserving clinical specimens. We thank Hyun Mee Park (Department of Radiology, National Medical Center) for the obtainment of excellent radiologic study result safely. We also thank to Yunyoung Jang, and Eunhee Kim for the dedication to protect healthcare workers of National Medical Center by infection control. We sincerely appreciate the discussion and critical feedback from Dr. Janet A Englund (Seattle Children's Hospital, Seattle, WA, USA). Lastly, we thank all the members of the Korean Society of Infectious Diseases (KSID), the groups of Korean Emerging Infectious Diseases (KoEID) application, and Korea National Clinical Management Network (KNCMN) for COVID-19, who are coping with the current global outbreak situation together.

SUPPLEMENTARY MATERIALS

Supplementary Data 1

Laboratory procedures and detailed clinical course of Patient 2

Click here to view

https://doi.org/10.3346/jkms.2020.35.e86

Supplementary Table 1

Clinical course and viral loads of Patient 1 according to the timeline from symptom onset

Click here to view

Supplementary Table 2

Clinical course and viral loads of Patient 2 according to the timeline from symptom onset

Click here to view

Supplementary Table 3

Estimated number of viral copy of respiratory specimens

Click here to view

Supplementary Fig. 1

Viral load kinetics according to the clinical course of Patient 1, presented by reverse Ct value. (**A**) Viral load kinetics of respiratory specimen, (**B**) Viral load kinetics of blood specimen, (**C**) Viral load kinetics of urine and stool specimen.

Click here to view

Supplementary Fig. 2

Viral load kinetics according to the clinical course of Patient 2, presented by reverse Ct value. (**A**) Viral load kinetics of respiratory specimen, (**B**) Viral load kinetics of blood specimen, (**C**) Viral load kinetics of urine and stool specimen.

Click here to view

Supplementary Fig. 3

Images of Patient 2. (**A**) Chest X-ray taken on admission, January 24, 2010 (day 15 from symptom onset). (**B**) High resolution computed tomography taken on January 25, 2010 (day 16 from symptom onset).

Click here to view

REFERENCES

1. Gorbalenya AE, Baker SC, Baric RS, de Groot RJ, Drosten C, Gulyaeva AA, et al. Severe acute respiratory syndrome-related coronavirus: the species and its viruses – a statement of the Coronavirus Study Group. *bioRxiv*. Forthcoming 2020.
CROSSREF
2. Li Q, Guan X, Wu P, Wang X, Zhou L, Tong Y, et al. Early Transmission Dynamics in Wuhan, China, of novel coronavirus-infected pneumonia. *N Engl J Med* 2020;NEJMoa2001316.
PUBMED | CROSSREF
3. Zhu N, Zhang D, Wang W, Li X, Yang B, Song J, et al. A novel coronavirus from patients with pneumonia in China, 2019. *N Engl J Med*. Forthcoming 2020.
PUBMED | CROSSREF

4. World Health Organization. Statement on the second meeting of the International Health Regulations (2005) Emergency Committee regarding the outbreak of novel coronavirus (2019-nCoV). https://www.who.int/news-room/detail/30-01-2020-statement-on-the-second-meeting-of-the-international-health-regulations-(2005)-emergency-committee-regarding-the-outbreak-of-novel-coronavirus-(2019-ncov). Updated 2020. Accessed February 13, 2020.
5. World Health Organization. Laboratory testing for 2019 novel coronavirus (2019-nCoV) in suspected human cases. https://www.who.int/publications-detail/laboratory-testing-for-2019-novel-coronavirus-in-suspected-human-cases-20200117. Updated 2020. Accessed February 13, 2020.
6. Corman VM, Landt O, Kaiser M, Molenkamp R, Meijer A, Chu DK, et al. Detection of 2019 novel coronavirus (2019-nCoV) by real-time RT-PCR. *Euro Surveill* 2020;25(3):2000045.
PUBMED | CROSSREF
7. Kim JY, Choe PG, Oh Y, Oh KJ, Kim J, Park SJ, et al. the first case of 2019 novel coronavirus pneumonia imported into Korea from Wuhan, China: implication for infection prevention and control measures. *J Korean Med Sci* 2020;35(5):e61.
PUBMED | CROSSREF
8. Peiris JS, Chu CM, Cheng VC, Chan KS, Hung IF, Poon LL, et al. Clinical progression and viral load in a community outbreak of coronavirus-associated SARS pneumonia: a prospective study. *Lancet* 2003;361(9371):1767-72.
PUBMED | CROSSREF
9. Huh HJ, Ko JH, Kim YE, Park CH, Hong G, Choi R, et al. Importance of specimen type and quality in diagnosing middle east respiratory syndrome. *Ann Lab Med* 2017;37(1):81-3.
PUBMED | CROSSREF

Potent neutralizing antibodies against multiple epitopes on SARS-CoV-2 spike

https://doi.org/10.1038/s41586-020-2571-7

Received: 15 June 2020

Accepted: 15 July 2020

Published online: 22 July 2020

Check for updates

Lihong Liu[1,12], Pengfei Wang[1,12], Manoj S. Nair[1,12], Jian Yu[1,12], Micah Rapp[2,12], Qian Wang[3,12], Yang Luo[1], Jasper F.-W. Chan[4,5], Vincent Sahi[1], Amir Figueroa[6], Xinzheng V. Guo[7], Gabriele Cerutti[2], Jude Bimela[2], Jason Gorman[8], Tongqing Zhou[8], Zhiwei Chen[4,5,9], Kwok-Yung Yuen[4,5], Peter D. Kwong[8,10], Joseph G. Sodroski[3], Michael T. Yin[11], Zizhang Sheng[1,2], Yaoxing Huang[1]✉, Lawrence Shapiro[1,2,10]✉ & David D. Ho[1]✉

The severe acute respiratory syndrome coronavirus-2 (SARS-CoV-2) pandemic continues, with devasting consequences for human lives and the global economy[1,2]. The discovery and development of virus-neutralizing monoclonal antibodies could be one approach to treat or prevent infection by this coronavirus. Here we report the isolation of sixty-one SARS-CoV-2-neutralizing monoclonal antibodies from five patients infected with SARS-CoV-2 and admitted to hospital with severe coronavirus disease 2019 (COVID-19). Among these are nineteen antibodies that potently neutralized authentic SARS-CoV-2 in vitro, nine of which exhibited very high potency, with 50% virus-inhibitory concentrations of 0.7 to 9 ng ml^{-1}. Epitope mapping showed that this collection of nineteen antibodies was about equally divided between those directed against the receptor-binding domain (RBD) and those directed against the N-terminal domain (NTD), indicating that both of these regions at the top of the viral spike are immunogenic. In addition, two other powerful neutralizing antibodies recognized quaternary epitopes that overlap with the domains at the top of the spike. Cryo-electron microscopy reconstructions of one antibody that targets the RBD, a second that targets the NTD, and a third that bridges two separate RBDs showed that the antibodies recognize the closed, 'all RBD-down' conformation of the spike. Several of these monoclonal antibodies are promising candidates for clinical development as potential therapeutic and/or prophylactic agents against SARS-CoV-2.

The novel coronavirus SARS-CoV-2[1,2] has caused more than 14 million confirmed infections globally, and has caused more than 600,000 deaths. This pandemic has also put much of the world on pause, with unprecedented disruption of lives and unparalleled damage to the economy. A return to some semblance of normality will depend on the ability of science to deliver an effective solution, and the scientific community has responded admirably. Drug development is well underway, and vaccine candidates have entered clinical trials. Another promising approach is the isolation of SARS-CoV-2-neutralizing monoclonal antibodies (mAbs) that could be used as therapeutic or prophylactic agents. The primary target for such antibodies is the viral spike, a trimeric protein[3,4] that is responsible for binding of the virus to the ACE2 receptor on the host cell[1,3,5,6]. The spike protein is comprised of two subunits. The S1 subunit has two major structural elements, RBD and NTD; the S2 subunit mediates virus–cell membrane fusion after the RBD has engaged ACE2. Reports of the discovery of neutralizing mAbs that target the RBD have been published recently[7–11]. We now describe our efforts in isolating and characterizing a collection of mAbs that not only target multiple epitopes on the viral spike but also show very high potency in neutralizing SARS-CoV-2.

Patient selection

Forty patients with PCR-confirmed SARS-CoV-2 infection were enrolled in a cohort study on virus-neutralizing antibodies. Plasma samples from all participants were first tested for neutralizing activity against SARS-CoV-2 pseudovirus (Wuhan-Hu-1 spike pseudotyped with vesicular stomatitis virus). Neutralizing titres varied widely, with half-maximal inhibitory concentrations (IC_{50}s) ranging from a reciprocal plasma dilution of less than 100 to roughly 13,000 (Fig. 1a). We selected five patients for isolation of mAbs because their plasma virus-neutralizing titres were

[1]Aaron Diamond AIDS Research Center, Columbia University Vagelos College of Physicians and Surgeons, New York, NY, USA. [2]Zuckerman Mind Brain Behavior Institute, Columbia University, New York, NY, USA. [3]Dana-Farber Cancer Institute, Harvard Medical School, Boston, MA, USA. [4]State Key Laboratory of Emerging Infectious Diseases, Carol Yu Centre for Infection, Department of Microbiology, Li Ka Shing Faculty of Medicine, The University of Hong Kong, Hong Kong Special Administrative Region, Hong Kong, China. [5]Centre for Virology, Vaccinology and Therapeutics, Health@InnoHK, The University of Hong Kong, Hong Kong Special Administrative Region, Hong Kong, China. [6]Department of Microbiology & Immunology Flow Cytometry Core, Columbia University Vagelos College of Physicians and Surgeons, New York, NY, USA. [7]Human Immune Monitoring Core, Columbia University Vagelos College of Physicians and Surgeons, New York, NY, USA. [8]Vaccine Research Center, National Institutes of Health, Bethesda, MD, USA. [9]AIDS Institute, Li Ka Shing Faculty of Medicine, The University of Hong Kong, Hong Kong Special Administrative Region, Hong Kong, China. [10]Department of Biochemistry, Columbia University, New York, NY, USA. [11]Division of Infectious Diseases, Department of Internal Medicine, Columbia University Vagelos College of Physicians and Surgeons, New York, NY, USA. [12]These authors contributed equally: Lihong Liu, Pengfei Wang, Manoj S. Nair, Jian Yu, Micah Rapp, Qian Wang. ✉e-mail: yh3253@cumc.columbia.edu; lss8@columbia.edu; dh2994@cumc.columbia.edu

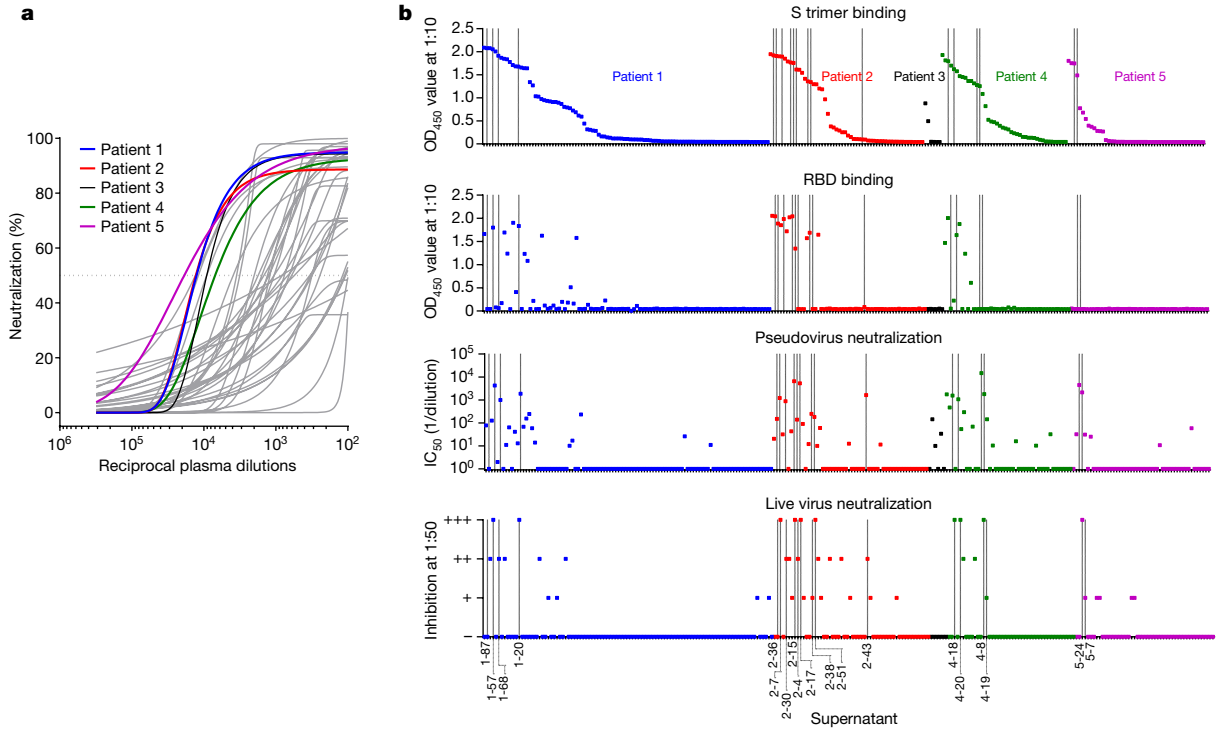

Fig. 1 | Isolation of SARS-CoV-2 mAbs from infected patients with severe disease. a, Plasma neutralization profile of 40 patients against SARS-CoV-2 pseudovirus (highlighted are five top neutralizers chosen for further study). **b**, All 252 transfection supernatants were screened for binding to the S trimer and RBD, as well as for neutralization against SARS-CoV-2 pseudovirus and live virus. For pseudovirus neutralization, the 50% inhibitory dilutions (IC_{50}) of each supernatant are plotted. For live virus, semiquantitative representation of the inhibition at a dilution of 1:50, with neutralization levels ranging from (–) for none to (+++) for complete neutralization, is plotted. Potent antibodies later identified are marked by vertical lines and labelled at the bottom. The antibodies from each patient are coloured as in **a**.

among the highest. The clinical characteristics of these five patients are summarized in Extended Data Table 1. All were severely ill with acute respiratory distress syndrome requiring mechanical ventilation.

Isolation and construction of mAbs

Peripheral blood mononuclear cells from each patient were processed as shown in Extended Data Fig. 1a, starting with cell sorting by flow cytometry. The sorting strategy focused on live memory B lymphocytes that were $CD3^-$, $CD19^+$, and $CD27^+$ (Extended Data Fig. 1b). The final step focused on those cells that bound the SARS-CoV-2 spike trimer (S trimer)[4]. A total of 602, 325, 14, 147, and 145 such B cells from patients 1, 2, 3, 4, and 5, respectively, were labelled with unique hashtags (Extended Data Fig. 1c). The cells were then placed into the 10X Chromium (10X Genomics) for single-cell 5′-mRNA and V(D)J sequencing to obtain paired heavy (H) and light (L) chain sequences. A careful bioinformatic analysis was carried out on 1,145 paired sequences to downselect 'high-confidence' antigen-specific mAbs. We recovered 331 mAb sequences, representing 252 individual clones. Only six mAbs were from patient 3, whereas 44 to 100 mAbs were identified from each of the other patients (Extended Data Fig. 2a). The VH and VL sequences of 252 antibodies (one per clone) were codon-optimized and synthesized, and each VH and VL gene was then cloned into an expression plasmid with corresponding constant regions of H chain and L chain of human IgG1. Monoclonal antibodies were then expressed by co-transfection of paired full-length H chain and L chain genes into Expi293 cells.

Monoclonal antibody screening

All 252 transfection supernatants were screened for binding to the S trimer and RBD by enzyme-linked immunosorbent assays (ELISAs), as well as for their ability to neutralize SARS-CoV-2 pseudovirus and live virus (Fig. 1b, Extended Data Fig. 2). A substantial percentage of the mAbs in the supernatants bound S trimer, and a subset of those bound RBD. Specifically, 121 supernatants were scored as positive for S trimer binding, yielding an overall hit rate of 48%. Of these, 38 were positive for RBD binding while the remaining 83 were negative. None of the 13 trimer-specific mAbs from patient 5 recognized RBD. In the pseudovirus neutralization screen, 61 supernatants were scored as positive, indicating that half of the trimer-specific mAbs were virus-neutralizing. In the screen for neutralization against SARS-CoV-2 (strain USA-WA1/2020), 41 supernatants were scored as positive. Overall, this screening strategy was quite effective in identifying neutralizing mAbs (vertical lines and labelled antibodies at the bottom of Fig. 1b) that were later identified as potent.

Sequence analysis of S trimer-specific mAbs

Of the 121 mAbs that bound the S trimer, 88% were IgG isotype, with IgG1 being predominant (Extended Data Fig. 3a). Comparison to the IgG repertoires of three healthy human donors[12] revealed a statistically significant over-representation of IGHV3-30, IGKV3-20, and IGHJ6 genes for this collection of SARS-CoV-2 mAbs (Extended Data Figs. 3b, c). In addition, the average CDRH3 length was also longer (Extended Data Fig. 3d). Notably, the average percentages of somatic hypermutation in VH and VL were 2.1 and 2.5, respectively, which were significantly lower than those found in healthy individuals (Extended Data Fig. 3e) and remarkably close to those of germline sequences.

Antigen binding and virus neutralization

Since the screening for pseudovirus neutralization was performed quantitatively with serial dilutions of the transfection supernatants,

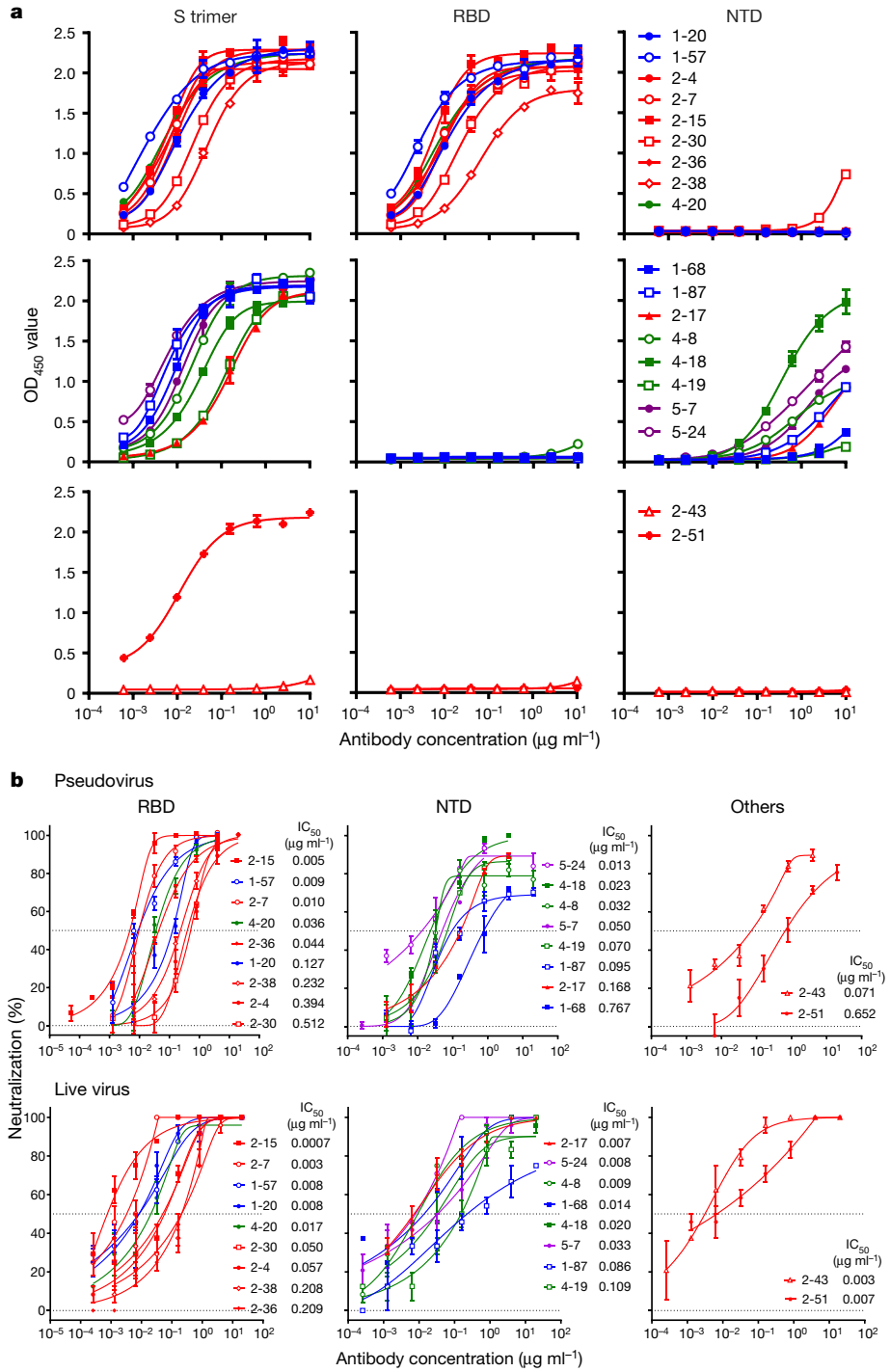

Fig. 2 | Characterization of potent neutralizing mAbs against SARS-CoV-2. **a**, Binding profiles of 19 purified potent neutralizing mAbs against the S trimer (left), RBD (middle), and NTD (right) of SARS-CoV-2. Note that mAb 2-30 bound multiple proteins at high concentrations. **b**, Neutralization profiles of the pseudovirus (top) and live virus (bottom) for the 19 purified mAbs. Epitope classifications are listed above plots. A single replicate of the binding experiment and triplicates of neutralization are presented as mean ± s.e.m.

we plotted in Extended Data Fig. 2b the best-fit neutralization curves for 130 samples that were positive in at least one of the screens shown in Fig. 1b. Most were non-neutralizing or weakly neutralizing, but 18 showed better potency. One additional supernatant was initially missed in the pseudovirus screen (patient 1 in Extended Data Fig. 2b) but was later found to be a potent neutralizing mAb. Together, these 19 mAbs were purified from transfection supernatants and further characterized for their binding and neutralization properties. As shown in Fig. 2a, quantitative ELISA showed that all but one (2-43) of the mAbs bound the S trimer. Nine of the antibodies clearly bound RBD, with little or no binding to NTD. Eight antibodies bound NTD to varying degrees, with no binding to RBD. Two mAbs bound neither RBD nor NTD, and were therefore categorized as 'other'.

The pseudovirus neutralization profiles for these purified 19 mAbs are shown in Fig. 2b (top). The RBD-directed antibodies neutralized the pseudovirus with IC_{50} values of 0.005 to 0.512 μg ml^{-1}; the NTD-directed

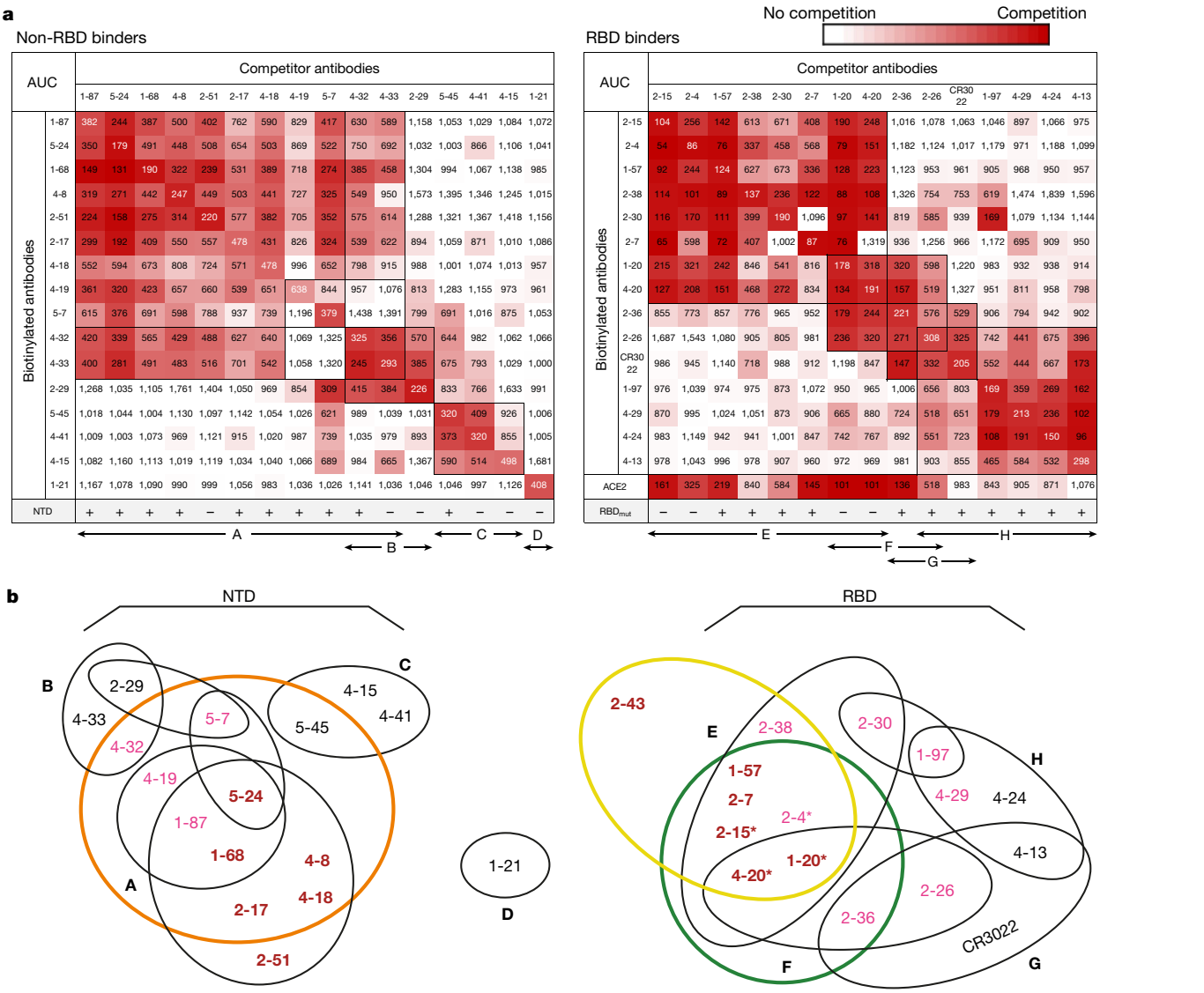

Fig. 3 | Epitope mapping of select neutralizing and non-neutralizing mAbs. **a**, Competition results of non-RBD binders (left) and RBD binders (right) in blocking binding of ACE2 or biotinylated mAb to the S trimer. In addition, the ability of each mAb to bind NTD and RBD_{mut} is shown. The numbers in each box show the area under each competition curve (AUC) as tested by ELISA. Plus and minus signs indicate binding and no binding, respectively, of the mAb to the protein. The letters A to H at the bottom denote clusters of antibody epitopes defined by the competition experiments. **b**, Venn diagram interpretation of results from **a** and Extended Data Fig. 6b.

antibodies were slightly less potent, with IC_{50} values ranging from 0.013 to 0.767 μg ml^{-1}. A common feature of the NTD mAbs was the plateauing of virus neutralization at levels short of 100%. Two antibodies, categorized as 'other', neutralized with IC_{50} values of 0.071 and 0.652 μg ml^{-1}. Antibody neutralization of the authentic or live SARS-CoV-2 (strain USA-WA1/2020) was carried out using Vero cells inoculated with a multiplicity of infection of 0.1. As shown in the bottom portion of Fig. 2b, the RBD-directed antibodies again neutralized the virus but with IC_{50} values of 0.0007 to 0.209 μg ml^{-1}; the NTD-directed antibodies showed similar potency, with IC_{50} values ranging from 0.007 to 0.109 μg ml^{-1}. Here, the plateauing effect seen in the pseudovirus neutralization assay was less apparent. Antibodies 2-43 and 2-51 neutralized the live virus with IC_{50} values of 0.003 and 0.007 μg ml^{-1}, respectively. Overall, nine mAbs exhibited high potency in neutralizing authentic SARS-CoV-2 in vitro with IC_{50} values of 0.009 μg ml^{-1} or less, including four against RBD (2-15, 2-7, 1-57, and 1-20), three against NTD (2-17, 5-24, and 4-8), and two against undetermined regions on the S trimer (2-43 and 2-51). Patient 2 alone contributed five of the top nine SARS-CoV-2 neutralizing mAbs. A correlation of the results of the two virus-neutralizing assays is shown in Extended Data Fig. 4.

Epitope mapping

All 19 potent neutralizing mAbs (Fig. 2) were further studied in antibody competition experiments to gain insight into their epitopes. We also chose 12 mAbs that bound the S trimer strongly during the initial supernatant screen, including 5 that bound RBD (1-97, 2-26, 4-13, 4-24, and 4-29) and 7 that did not bind RBD (1-21, 2-29, 4-15, 4-32, 4-33, 4-41, and 5-45). Four of these mAbs were weak in neutralizing SARS-CoV-2 pseudovirus, and the remaining eight were non-neutralizing (Extended Data

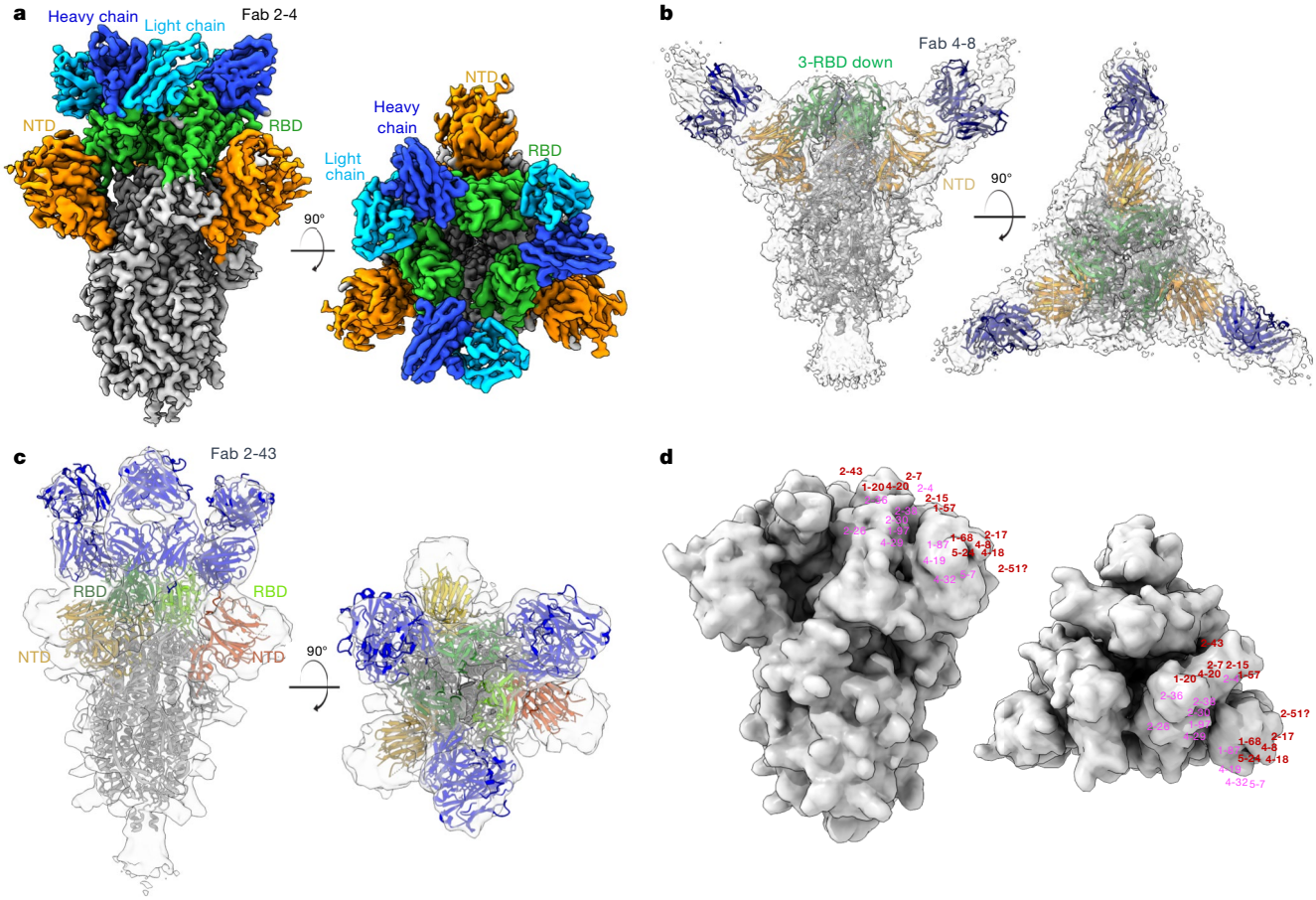

Fig. 4 | Cryo-EM reconstructions of Fab–spike complexes and visualization of neutralizing epitopes on the spike surface. a, Cryo-EM reconstruction of 2-4 Fab in complex with the S trimer at 3.2 Å overall resolution. Density is coloured with RBD in green, NTD in orange, and other regions in grey. **b**, Cryo-EM reconstruction of 4-8 Fab in complex with the S trimer (ribbon diagram, coloured as in **a**) at 3.9 Å overall resolution, with RBDs in the 'all-down' configuration. **c**, Cryo-EM reconstruction of the 2-43 Fab in complex with the S trimer at 5.8 Å resolution reveals a quaternary epitope involving RBD from one subunit and another RBD from the next. **d**, Mapping of the Venn diagrams from Fig. 3b onto the surface of the viral spike.

Fig. 5). We used ELISA to evaluate 16 non-RBD mAbs for competition in binding to the S trimer in a 'checkerboard' experiment. The extent of the antibody competition is reflected by the intensity of the heatmap in Fig. 3a. There is one large cluster (A) of mAbs that competed with one another, which partially overlaps with a small cluster (B). A third cluster (C) does not overlap at all. Note that all but one of the antibodies in cluster A recognized NTD. Antibody 2-51 is clearly directed against the NTD region even though it could not bind NTD. Moreover, one mAb from each of clusters B and C also recognized NTD, thereby indicating that all three clusters are within or near the NTD. One mAb, 1-21, appears to have a unique non-overlapping epitope (epitope region D).

We carried out a similar 'checkerboard' competition experiment by ELISA for 14 of our RBD-directed mAbs plus CR3022[13,14]. Here, the heatmap shows four epitope clusters that are serially overlapping (Fig. 3a). There is one large cluster (E) that contains mAbs that can largely block ACE2 binding. Furthermore, four antibodies in this cluster lost the ability to bind to a mutant RBD (L455R, A475R, G502R) that could no longer bind ACE2 (unpublished data). Together, these results suggest that most of the mAbs in cluster E are directed against the ACE2-binding interface of RBD. The next cluster (F) connects to both cluster E and cluster G, the location of which is defined by its member CR3022[15]. Last, cluster G overlaps another cluster (H), which includes 1-97, which strongly inhibited the binding of 2-30 to the S trimer. This finding suggests that cluster H may be proximal to one edge of cluster E.

One potent neutralizing mAb, 2-43, did not bind the S trimer in ELISA (Fig. 2a) and thus could not be tested in the above competition experiments. However, 2-43 did strongly bind the S trimer when expressed on the cell surface, as determined by flow cytometry (Extended Data Fig. 6a), and this binding was competed out by itself but not by RBD, NTD, ACE2, or the soluble S trimer[4] (Extended Data Fig. 6b). NTD-directed mAbs had only a modest effect on its binding to cell-surface S trimer, but numerous RBD-directed mAbs in cluster E potently blocked the binding of 2-43, demonstrating that this antibody is likely to target a quaternary epitope on the top of RBD.

These mapping results could be represented by two sets of Venn diagrams shown in Fig. 3b. In the non-RBD region, the potent neutralizing mAbs reside exclusively in cluster A and bind a patch on the NTD. Weaker neutralizing mAbs recognize a region at the interface between clusters A and B. In the RBD region, the most potent neutralizing mAbs also group together within one cluster (E). Given that all block ACE2 binding, it is likely they recognize the top of RBD and neutralize the virus by competitive inhibition of receptor binding. Cluster G contains CR3022, a mAb known to be directed against an epitope on a cryptic site on the side of RBD when it is in the 'up' position[15]. Cluster F is therefore likely situated between the top and this 'cryptic' site. The Venn diagram also suggests that cluster H may occupy a different side surface of RBD, perhaps in the region recognized by S309, a mAb isolated from a patient with SARS-CoV-1[8].

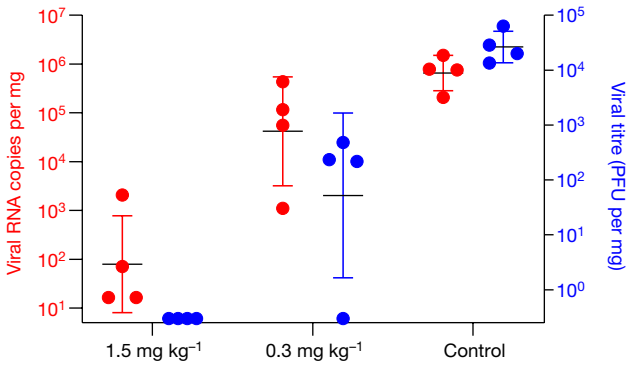

Fig. 5 | Efficacy of mAb 2-15 in protecting against SARS-CoV-2 infection in lung tissues of hamsters. One day before intranasal challenge with SARS-CoV-2, each group of hamsters was given a single intraperitoneal dose of 1.5 mg kg^{-1} of mAb 2-15 (n = 4), 0.3 mg kg^{-1} of mAb 2-15 (n = 4), or saline as control (n = 4). The viral loads in the lung tissues on day 4 after viral challenge were determined by quantitative PCR with reverse transcription (qRT–PCR; red), as well as by an assay to quantify PFUs of infectious SARS-CoV-2 (blue). All data points are shown, along with the mean ± s.d. The differences between the 1.5 mg kg^{-1} group and the control group are statistically significant at $P < 0.05$.

Cryo-electron microscopy

We produced cryo-electron microscopy (cryo-EM) reconstructions of antigen-binding fragments (Fabs) from three mAbs in complex with the S trimer[4]. First, single-particle analysis of the complex with the Fab of mAb 2-4 (RBD-directed) yielded maps of high quality (Fig. 4a; Extended Data Table 2; Extended Data Fig. 7a–d), with the most abundant particle class representing a 3-Fab-per-trimer complex, refined to an overall resolution of 3.2 Å. While density for the constant portion of the Fabs was visible, it was blurred as a result of molecular motion, and thus only the variable domains were included in the molecular model. Fab 2-4 bound the spike protein near the apex, with all RBDs in the 'down' orientation, and the structure of the antibody-bound spike protein was highly similar to previously published unliganded spike structures in the 'all-down' conformation[3,4]. Detailed interactions between mAb 2-4 and RBD are shown in Extended Data Fig. 7e–i. Overall, the structure of the 2-4 Fab–spike complex shows that neutralization of SARS-CoV-2 by this mAb is likely to result from locking the RBD in the down conformation while also occluding access to ACE2.

We also produced 3D cryo-EM reconstructions of 4-8 Fab (NTD-directed) in complex with the S trimer (Extended Data Table 2, Extended Data Fig. 8a–f). Two main particle classes were observed—one for a 3-Fab-bound complex with all RBDs 'down' at 3.9 Å resolution (Fig. 4b), and another a 3-Fab-bound complex with one RBD 'up' at 4.0 Å resolution (Extended Data Fig. 8g). However, molecular motion prevented visualization of the interaction at high resolution. Nevertheless, the density in the 4-8 map reveals the overall positions of the antibody chains that target the NTD. It is unclear how binding to the tip of the NTD results in neutralization of SARS-CoV-2.

Third, a 5.8 Å resolution reconstruction of 2-43 Fab in complex with the S trimer (Extended Data Table 2, Extended Data Fig. 8h–k) revealed three bound Fabs, each targeting a quaternary epitope on the top of the spike that included elements of the RBDs from two adjacent S1 protomers (Fig. 4c), consistent with the epitope mapping results (Fig. 3b, Extended Data Fig. 6b), including the lack of binding to isolated RBD (Fig. 2a). Given these findings, the inability of 2-43 to bind the S trimer in ELISA studies is likely to be an artefact of the assay format, as this mAb did bind the spike expressed on the cell surface and in the cryo-EM study.

Armed with these three cryo-EM reconstructions, we used the Venn diagrams from Fig. 3b to map the epitopes of many of our SARS-CoV-2-neutralizing mAbs onto the surface of the spike (Fig. 4d). This is obviously a rough approximation because antibody footprints are much larger than the area occupied by the mAb number. However, the spatial relationship of the antibody epitopes should be reasonably represented by Fig. 4d.

mAb 2-15 protects hamsters against SARS-CoV-2

To assess the in vivo potency of mAb 2-15, we performed a protection experiment in a golden Syrian hamster model of SARS-CoV-2 infection. The hamsters were first given an intraperitoneal injection of the antibody at a dose of 1.5 mg kg^{-1} or 0.3 mg kg^{-1}, or PBS alone. Intranasal inoculations of 10^5 plaque-forming units (PFU) of the HKU-001a strain of SARS-CoV-2 were carried out 24 h later. Four days after virus challenge, lung tissues were removed to quantify the viral load. As shown in Fig. 5, both viral RNA copy numbers and infectious virus titres were reduced by 4 logs or more in hamsters given 1.5 mg kg^{-1} of mAb 2-15. The protection at 0.3 mg kg^{-1} was borderline, as we had estimated. This pilot animal study demonstrates that the potency of mAb 2-15 in vitro is reflected in vivo, with complete elimination of infectious SARS-CoV-2 at a relatively modest antibody dose.

Discussion

We have identified a collection of SARS-CoV-2-neutralizing mAbs that are not only potent but also diverse. Nine of these antibodies can neutralize the authentic virus in vitro at concentrations of 9 ng ml^{-1} or less (Fig. 2b), including four directed against the RBD, three directed against the NTD, and two directed against nearby quaternary epitopes. Unexpectedly, many of the these mAbs have V(D)J sequences close to germline sequences, without extensive somatic hypermutations (Extended Data Fig. 3e), a finding that bodes well for vaccine development. Our most potent RBD-specific mAbs (for example, 2-15, 2-7, 1-57, and 1-20) compare favourably with such antibodies recently reported[7,8,10,16–20], including those with high potency[9,11,21,22]. The in vitro potency of 2-15 is well reflected in vivo in the hamster protection experiment (Fig. 5). It appears from the epitope-mapping studies that mAbs directed against the top of the RBD compete strongly with ACE2 binding and potently neutralize the virus, whereas those directed against the side surfaces of the RBD do not compete with ACE2 and neutralize less potently (Figs. 3b, 4d). Our collection of non-RBD neutralizing mAbs is unprecedented, to our knowledge, in that such antibodies have been reported only sporadically and only with substantially lower potencies[22–24]. The most potent of these mAbs are directed against (for example, 2-17, 5-24, and 4-8) or overlapping with (2-51) a patch on the NTD (Figs. 3b, 4d). It is unclear how NTD-directed mAbs block SARS-CoV-2 infection and why their neutralization profiles are different from those of RBD-directed antibodies (Fig. 2b). Nevertheless, vaccine strategies that do not include the NTD will be unable to induce an important class of virus-neutralizing antibodies.

The isolation of two mAbs (2-43 and 2-51) directed against epitopes that do not map to the RBD or NTD is also unprecedented, to our knowledge. Cryo-EM of 2-43 Fab bound to the S trimer has confirmed its epitope as quaternary in nature, crossing from the top of one RBD to the top of another RBD (Fig. 4c). It will be equally informative to understand the epitope of 2-51. We have also shown cryo-EM evidence for a neutralizing mAb (4-8) bound to the NTD of the viral spike (Fig. 4b), as well as another high-resolution structure of an mAb (2-4) bound to the RBD (Fig. 4a).

The potency and diversity of our SARS-CoV-2-neutralizing mAbs are probably attributable to patient selection. Infected individuals with severe disease develop a more robust virus-neutralizing antibody response[25]. If patient 2 had not been included, five of the top neutralizing mAbs would have been lost. The diversity of our antibodies is also attributable, in part, to the choice of using the S trimer to sort from

memory B cells, while most groups have used the RBD[7,9–11,16–19,21]. The characterization of this diverse collection of mAbs has allowed us to observe that all potent SARS-CoV-2-neutralizing antibodies described to date are directed against the top of the viral spike. RBD and NTD are, undoubtedly, quite immunogenic. Neutralizing antibodies to the stem region of the S trimer remain to be discovered. In conclusion, we believe that several of our monoclonal antibodies with strong virus-neutralizing activity are promising candidates for development as modalities to treat or prevent SARS-CoV-2 infection.

Online content

Any methods, additional references, Nature Research reporting summaries, source data, extended data, supplementary information, acknowledgements, peer review information; details of author contributions and competing interests; and statements of data and code availability are available at https://doi.org/10.1038/s41586-020-2571-7.

1. Zhou, P. et al. A pneumonia outbreak associated with a new coronavirus of probable bat origin. *Nature* **579**, 270–273 (2020).
2. Wang, C., Horby, P. W., Hayden, F. G. & Gao, G. F. A novel coronavirus outbreak of global health concern. *Lancet* **395**, 470–473 (2020).
3. Walls, A. C. et al. Structure, function, and antigenicity of the SARS-CoV-2 spike glycoprotein. *Cell* **181**, 281–292.e286 (2020).
4. Wrapp, D. et al. Cryo-EM structure of the 2019-nCoV spike in the prefusion conformation. *Science* **367**, 1260–1263 (2020).
5. Hoffmann, M. et al. SARS-CoV-2 cell entry depends on ACE2 and TMPRSS2 and is blocked by a clinically proven protease inhibitor. *Cell* **181**, 271–280.e278 (2020).
6. Wang, Q. et al. Structural and functional basis of SARS-CoV-2 entry by using human ACE2. *Cell* **181**, 894–904.e899 (2020).
7. Ju, B. et al. Human neutralizing antibodies elicited by SARS-CoV-2 infection. *Nature* https://doi.org/10.1038/s41586-020-2380-z (2020).
8. Pinto, D. et al. Cross-neutralization of SARS-CoV-2 by a human monoclonal SARS-CoV antibody. *Nature* **583**, 290–295 (2020).
9. Cao, Y. et al. Potent neutralizing antibodies against SARS-CoV-2 identified by high-throughput single-cell sequencing of convalescent patients' B cells. *Cell* **182**, 73–84.e16 (2020).
10. Wu, Y. et al. A noncompeting pair of human neutralizing antibodies block COVID-19 virus binding to its receptor ACE2. *Science* **368**, 1274–1278 (2020).
11. Hansen, J. et al. Studies in humanized mice and convalescent humans yield a SARS-CoV-2 antibody cocktail. *Science* https://doi.org/10.1126/science.abd0827 (2020).
12. Sheng, Z. et al. Gene-specific substitution profiles describe the types and frequencies of amino acid changes during antibody somatic hypermutation. *Front. Immunol.* **8**, 537 (2017).
13. ter Meulen, J. et al. Human monoclonal antibody combination against SARS coronavirus: synergy and coverage of escape mutants. *PLoS Med.* **3**, e237 (2006).
14. Tian, X. et al. Potent binding of 2019 novel coronavirus spike protein by a SARS coronavirus-specific human monoclonal antibody. *Emerg. Microbes Infect.* **9**, 382–385 (2020).
15. Yuan, M. et al. A highly conserved cryptic epitope in the receptor binding domains of SARS-CoV-2 and SARS-CoV. *Science* **368**, 630–633 (2020).
16. Rogers, T. F. et al. Isolation of potent SARS-CoV-2 neutralizing antibodies and protection from disease in a small animal model. *Science* https://doi.org/10.1126/science.abc7520 (2020).
17. Chen, X. et al. Human monoclonal antibodies block the binding of SARS-CoV-2 spike protein to angiotensin converting enzyme 2 receptor. *Cell. Mol. Immunol.* **17**, 647–649 (2020).
18. Zeng, X. et al. Isolation of a human monoclonal antibody specific for the receptor binding domain of SARS-CoV-2 using a competitive phage biopanning strategy. *Antib. Ther.* **3**, 95–100 (2020).
19. Liu, X. et al. Neutralizing antibodies isolated by a site-directed screening have potent protection on SARS-CoV-2 infection. Preprint at https://doi.org/10.1101/2020.05.03.074914 (2020).
20. Zost, S. J. et al. Rapid isolation and profiling of a diverse panel of human monoclonal antibodies targeting the SARS-CoV-2 spike protein. *Nat. Med.* https://doi.org/10.1038/s41591-020-0998-x (2020).
21. Robbiani, D. F. et al. Convergent antibody responses to SARS-CoV-2 infection in convalescent individuals. *Nature* https://doi.org/10.1038/s41586-020-2456-9 (2020).
22. Brouwer, P. J. M. et al. Potent neutralizing antibodies from COVID-19 patients define multiple targets of vulnerability. *Science* https://doi.org/10.1126/science.abc5902 (2020).
23. Chi, X. et al. A neutralizing human antibody binds to the N-terminal domain of the Spike protein of SARS-CoV-2. *Science* https://doi.org/10.1126/science.abc6952 (2020).
24. Wang, C. et al. A human monoclonal antibody blocking SARS-CoV-2 infection. *Nat. Commun.* **11**, 2251 (2020).
25. Wang, P. et al. SARS-CoV-2 neutralizing antibody responses are more robust in patients with severe disease. Preprint at https://doi.org/10.1101/2020.06.13.150250 (2020).

Methods

No statistical methods were used to predetermine sample size. The experiments were not randomized and the investigators were not blinded to allocation during experiments and outcome assessment, except where stated.

Expression and purification of SARS-CoV-2 proteins

The mammalian expression vector that encodes the ectodomain of the SARS-CoV-2 S trimer and the vector encoding RBD fused with SD1 at the N terminus and an HRV-3C protease cleavage site followed by a mFc tag and an 8 × His tag at the C terminus were kindly provided by Jason McLellan[4]. SARS-CoV-2 NTD (aa1-290) with an HRV-3C protease cleavage site, a mFc tag, and an 8 × His tag at the C terminus was also cloned into mammalian expression vector pCAGGS. Each expression vector was transiently transfected into Expi293 cells using 1 mg/ml polyethylenimine (Polysciences). Five days after transfection, the S trimer was purified using Strep-Tactin XT Resin (Zymo Research), and the RBD-mFc and NTD-mFc were purified using protein A agarose (ThermoFisher Scientific). In order to obtain RBD-SD1 and NTD, the mFc and 8 × His tags at the C terminus were removed by HRV-3C protease (Millipore-Sigma) and then purified using Ni-NTA resin (Invitrogen) followed by protein A agarose.

Sorting for S trimer-specific B cells and single-cell B cell receptor sequencing

Peripheral blood mononuclear cells from five patients and one healthy donor were stained with LIVE/DEAD Fixable Yellow Dead Cell Stain Kit (Invitrogen) at ambient temperature for 20 min, followed by washing with RPMI-1640 complete medium and incubation with 10 μg/ml S trimer at 4 °C for 45 min. Afterwards, the cells were washed again and incubated with a cocktail of flow cytometry and hashtag antibodies, containing CD3 PE-CF594 (BD Biosciences), CD19 PE-Cy7 (Biolegend), CD20 APC-Cy7 (Biolegend), IgM V450 (BD Biosciences), CD27 PerCP-Cy5.5 (BD Biosciences), anti-His PE (Biolegend), and human Hashtag 3 (Biolegend) at 4 °C for 1 h. Stained cells were then washed, resuspended in RPMI-1640 complete medium and sorted for S trimer-specific memory B cells ($CD3^-CD19^+CD27^+$S trimer$^+$ live single lymphocytes). The sorted cells were mixed with mononuclear cells from the same donor, labelled with Hashtag 1, and loaded into the 10X Chromium chip of the 5′ Single Cell Immune Profiling Assay (10X Genomics) at the Columbia University Human Immune Monitoring Core (HIMC; RRID:SCR_016740). The library preparation and quality control were performed according to the manufacturer's protocol and sequenced on a NextSeq 500 sequencer (Illumina).

Identification of S trimer-specific antibody transcripts

For each sample, full-length antibody transcripts were assembled using the VDJ module in Cell Ranger (version 3.1.0, 10X Genomics) with default parameters and the GRCh38 genome as reference. To identify cells from the antigen sort, we first used the count module in Cell Ranger to calculate copies of all hashtags in each cell from the Illumina NGS raw reads. High-confidence antigen-specific cells were identified as follows. In brief, based on the copy numbers of the hashtags observed, a cell must contain more than 100 copies of the antigen sort-specific hashtag to qualify as an antigen-specific cell. Because hashtags can fall off cells and bind to cells from a different population in the sample mixture, each cell usually has both sorted and spiked-in-specific hashtags. To enrich for true antigen-specific cells, the copy number of the specific hashtag has to be at least 1.5× higher than that of the non-specific hashtag. Low-quality cells were identified and removed using the cell-calling algorithm in Cell Ranger. Cells that did not have productive H and L chain pairs were excluded. If a cell contained more than two H or/and L chain transcripts, the transcripts with fewer than three unique molecular identifiers were removed. Cells with identical H and L chain sequences, which may have resulted from mRNA leakage, were merged into one cell. Additional filters were applied to remove low-quality cells and/or transcripts in the antibody gene annotation process.

Antibody transcript annotation and selection criteria

Antigen-specific antibody transcripts were processed using our bioinformatics pipeline SONAR for quality control and annotation[26]. In brief, V(D)J genes were assigned for each transcript using BLAST[27] with customized parameters against a germline gene database obtained from the international ImMunoGeneTics information system (IMGT) database[26,28]. On the basis of BLAST alignments of V and J regions, CDR3 was identified using the conserved second cysteine in the V region and WGXG (H chain) or FGXG (L chain) motifs in the J region (X represents any amino acid). For H chain transcripts, the constant domain 1 (CH1) sequences were used to assign isotype using BLAST with default parameters against a database of human CH1 genes obtained from IMGT. A BLAST *E*-value threshold of 10^{-6} was used to find significant isotype assignments, and the CH1 allele with the lowest *E*-value was used. Sequences other than the V(D)J region were removed and transcripts containing incomplete V(D)J or/and frame shift were excluded. We then aligned each of the remaining transcripts to the assigned germline V gene using CLUSTALO[29] and calculated the somatic hypermutation level.

To select representative antibodies for functional characterization, we first clustered all antibodies using USEARCH[30] with the following criteria: identical heavy chain V and J gene assignments, the same length of CDRH3, and CDRH3 identity higher than 0.9. For each cluster, cells with the same light chain V and J gene assignments were grouped into a clone. All clone assignments were manually checked. We then calculated the clonal size for each clone, and one H and L chain pair per clone was chosen for antibody synthesis. For clones with multiple members, the member with the highest somatic hypermutation level was chosen for synthesis. For cells having multiple high quality H or L chains, which may be from doublets, we synthesized all H and L chain combinations.

Analysis of S trimer-specific antibody repertoire

Because 88% of the S trimer-specific antibodies were IgG isotype, we compared the repertoire features to IgG repertoires from three healthy donors[12] (17,243 H chains, 27,575 kappa L chains, 20,889 lambda L chains). The repertoire data from the three healthy donors were combined and annotated using SONAR with the same process as above.

Antibody expression and purification

For each antibody, variable genes were optimized for human cell expression and synthesized by GenScript. VH and VL were inserted separately into plasmids (gWiz or pcDNA3.4) that encode the constant region for H chain and L chain. Monoclonal antibodies were expressed in Expi293 (ThermoFisher, A14527) by co-transfection of H chain and L chain expressing plasmids using polyethylenimine and culture at 37 °C with shaking at 125 rpm and 8% CO_2. On day 3 after transfection, 400 μl supernatant were collected for screening for binding to the S trimer and RBD by ELISA, and for neutralization of SARS-CoV-2 pseudovirus and authentic virus. Supernatants were also collected on day 5 for antibody purification using rProtein A Sepharose (GE, 17-1279-01) affinity chromatography.

Production of pseudoviruses

Recombinant Indiana vesicular stomatitis virus (rVSV) expressing the SARS-CoV-2 spike was generated as previously described[31,32]. HEK293T cells were grown to 80% confluency before transfection with pCMV3-SARS-CoV-2-spike (Sino Biological) using FuGENE 6 (Promega). Cells were cultured overnight at 37 °C with 5% CO_2. The next day, medium was removed and VSV-G pseudotyped ΔG-luciferase (G*ΔG-luciferase, Kerafast) was used to infect the cells in DMEM at a

MOI of 3 for 1 h before the cells were washed three times with 1× DPBS. DMEM supplemented with 2% fetal bovine serum, 100 IU/ml of penicillin and 100 μg/ml of streptomycin were added to the inoculated cells, which were cultured overnight as described above. The supernatant was removed the following day and clarified by centrifugation at 300*g* for 10 min before aliquoting and storing at −80 °C.

Pseudovirus neutralization

Neutralization assays were performed by incubating pseudoviruses with serial dilutions of heat-inactivated plasma together with supernatant or purified antibodies, and scored by the reduction in luciferase gene expression. In brief, Vero E6 cells (ATCC) were seeded in a 96-well plate at a concentration of 2×10^4 cells per well. Pseudoviruses were incubated the next day with serial dilutions of the test samples in duplicate or triplicate for 30 min at 37 °C. The mixture was added to cultured cells and incubated for an additional 24 h. The luminescence was measured using a Britelite plus Reporter Gene Assay System (PerkinElmer). IC_{50} was defined as the dilution at which the relative light units were reduced by 50% compared with the virus control wells (virus + cells) after subtraction of the background in the control groups with cells only. The IC_{50} values were calculated using nonlinear regression in GraphPad Prism 8.0.

Authentic SARS-CoV-2 neutralization

Supernatants containing expressed mAbs were diluted 1:10 and 1:50 in EMEM with 7.5% inactivated fetal calf serum and incubated with authentic SARS-CoV-2 (strain USA-WA1/2020; MOI 0.1) for 1 h at 37 °C. After incubation, the mixture was transferred onto a monolayer of Vero-E6 cells that was cultured overnight. After incubation of the cells with the mixture for 70 h at 37 °C, cytopathic effects (CPEs) caused by the infection were scored for each well from 0 to 4 to indicate the degree of virus inhibition. Semi-quantitative representation of the inhibition for each antibody-containing supernatant at a dilution of 1:50 is shown in the lowest panel of Fig. 1b with neutralization levels ranging from (−) for none to (+++) for complete neutralization.

An end-point dilution assay in a 96-well plate format was performed to measure the neutralization activity of select purified mAbs. In brief, each antibody was serially diluted (fivefold dilutions) starting at 20 μg/ml. Triplicates of each mAb dilution were incubated with SARS-CoV-2 at a MOI of 0.1 in EMEM with 7.5% inactivated fetal calf serum for 1 h at 37 °C. After incubation, the virus–antibody mixture was transferred onto a monolayer of Vero-E6 cells grown overnight. The cells were incubated with the mixture for 70 h. CPEs were visually scored for each well in a blinded fashion by two independent observers. The results were then converted into percentage neutralization at a given mAb concentration, and the averages ± s.e.m. were plotted using a five-parameter dose–response curve in GraphPad Prism 8.0.

Epitope mapping by ELISA

We coated 50 ng per well of S trimer, 50 ng per well of RBD, and 100 ng per well of NTD onto ELISA plates at 4 °C overnight. The ELISA plates were then blocked with 300 μl blocking buffer (1% BSA and 10% bovine calf serum (BCS) (Sigma)) in PBS at 37 °C for 2 h. Afterwards, supernatants from the antibody transfection or purified antibodies were serially diluted using dilution buffer (1% BSA and 20% BCS in PBS), incubated at 37 °C for 1 h. Next, 100 μl of 10,000-fold diluted Peroxidase AffiniPure goat anti-human IgG (H+L) antibody (Jackson ImmunoResearch) was added into each well and incubated for 1 h at 37 °C. The plates were washed between each step with PBST (0.5% Tween-20 in PBS). Finally, the TMB substrate (Sigma) was added and incubated before the reaction was stopped using 1 M sulfuric acid. Absorbance was measured at 450 nm.

For the competition ELISA, purified mAbs were biotin-labelled using One-Step Antibody Biotinylation Kit (Miltenyi Biotec) following the manufacturer's recommendations and purified using 40K MWCO Desalting Column (ThermoFisher Scientific). Serially diluted competitor antibodies (50 μl) were added into S trimer-precoated ELISA plates, followed by 50 μl of biotinylated antibodies at a concentration that achieves an OD_{450} reading of 1.5 in the absence of competitor antibodies. Plates were incubated at 37 °C for 1 h, and 100 μl of 500-fold diluted Avidin-HRP (ThermoFisher Scientific) was added into each well and incubated for another 1 h at 37 °C. The plates were washed with PBST between each of the previous steps. The plates were developed afterwards with TMB and absorbance was read at 450 nm after the reaction was stopped.

For the ACE2 competition ELISA, 100 ng of ACE2 protein (Abcam) was immobilized on the plates at 4 °C overnight. The unbound ACE2 was washed away by PBST and then the plates were blocked. After washing, 100 ng of S trimer in 50 μl dilution buffer was added into each well, followed by addition of another 50 μl of serially diluted competitor antibodies and then incubation at 37 °C for 1 h. The ELISA plates were washed four times with PBST and then 100 μl of 2,000-fold diluted anti-strep-HRP (Millipore Sigma) was added into each well for another 1 h at 37 °C. The plates were then washed and developed with TMB, and absorbance was read at 450 nm after the reaction was stopped.

For all the competition ELISA experiments, the relative binding of biotinylated antibodies or ACE2 to the S trimer in the presence of competitors was normalized by comparing to competitor-free controls. Relative binding curve and the area under curve (AUC) were generated by fitting the nonlinear five-parameter dose–response curve in GraphPad Prism 8.0.

Cell-surface competition binding assay

Expi293 cells were co-transfected with vectors encoding pRRL-cPPT-PGK-GFP (Addgene) and pCMV3-SARS-CoV-2 (2019-nCoV) Spike (Sino Biological) at a ratio of 1:1. Two days after transfection, cells were incubated with a mixture of biotinylated mAb 2-43 (0.25 μg/ml) and serially diluted competitor antibodies at 4 °C for 1 h. Then 100 μl of diluted APC-streptavidin (Biolegend) was added to the cells and incubated at 4 °C for 45 min. Cells were washed three times with FACS buffer before each step. Finally, cells were resuspended and binding of 2-43 to cell-surface S trimer was quantified on an LSRII flow cytometer (BD Biosciences). The mean fluorescence intensity of APC in GFP-positive cells was analysed using FlowJo and the relative binding of 2-43 to the S trimer in the presence of competitors was calculated as the percentage of the mean fluorescence intensity compared to that of the competitor-free controls.

Cryo-EM data collection and processing

SARS-CoV-2 S trimer at a final concentration of 2 mg/ml was incubated with sixfold molar excess per spike monomer of the antibody Fab fragments for 30 min in 10 mM sodium acetate pH 5.5, 150 mM NaCl, and 0.005% *n*-dodecyl-β-D-maltoside (DDM). Sample (2 μl) was incubated on C-flat 1.2/1.3 carbon grids for 30 s and vitrified using a Leica EM GP Plunge Freezer. Data were collected on a Titan Krios electron microscope operating at 300 kV equipped with a Gatan K3 direct detector and energy filter using the Leginon software package[33]. A total electron fluence of 51.3 e/Å^2 was fractionated over 40 frames, with a total exposure time of 2 s. A magnification of 81,000× resulted in a pixel size of 1.058 Å, and a defocus range of −0.4 to −3.5 μm was used. All processing was done using cryoSPARC v2.14.2[34]. Raw movies were aligned and dose-weighted using patch motion correction, and the CTF was estimated using patch CTF estimation. A small subset of approximately 200 micrographs were picked using blob picker, followed by 2D classification and manual curation of particle picks, and used to train a Topaz neural network[35]. This network was then used to pick particles from the remaining micrographs, which were extracted with a box size of 384 pixels.

For the 2-4 Fab dataset, 2D classification followed by ab initio modelling and 3D heterogeneous refinement revealed 83,927 particles

with three 2-4 Fabs bound, one to each RBD. A reconstruction of these particles using non-uniform refinement with imposed C3 symmetry resulted in a 3.6 Å map, as determined by the gold standard Fourier shell correlation (FSC). Given the relatively low resolution of the RBD–Fab interface, masked local refinement was used to obtain a 3.5 Å map with improved density. A masked local refinement of the remainder of the S trimer resulted in a 3.5 Å reconstruction. These two local refinements were aligned and combined using the vop maximum function in UCSF Chimera[36]. This was repeated for the half maps, which were used, along with the refinement mask from the global non-uniform refinement, to calculate the 3D FSC[37] and obtain an estimated resolution of 3.2 Å. All maps have been submitted to the EMDB with the ID EMD-22156.

For the 4-8 Fab dataset, image preprocessing and particle picking were performed as above. 2D classification, ab initio modelling, and 3D heterogeneous classification revealed 47,555 particles with 3 Fabs bound, one to each NTD and with all 3 RBDs in the down conformation. While this particle stack was refined to 3.9 Å using non-uniform refinement with imposed C3 symmetry, substantial molecular motion prevented the visualization of the Fab epitope at high resolution (EMD-22159). In addition, 105,278 particles were shown to have 3 Fabs bound, but with 1 RBD in the up conformation. These particles were refined to 4.0 Å using non-uniform refinement with C1 symmetry (EMD-22158), and suffered from the same conformational flexibility as the all-RBD-down particles. This flexibility was visualized using 3D variability analysis in cryoSPARC.

For the 2-43 Fab dataset, which was collected at an electron fluence of 51.69 e/Å^2, image preprocessing was performed as above, and particle picking was performed using blob picker. 2D classification, ab initio modelling, and 3D heterogeneous classification revealed 10,068 particles with 3 Fabs bound, which was refined to 5.8 Å resolution (EMD-22157).

Cryo-EM model fitting

An initial homology model of the 2-4 Fab was built using Schrodinger Release 2020-2: BioLuminate[38]. The RBD was initially modelled using the coordinates from PDB ID 6W41. The remainder of the S trimer was modelled using the coordinates from PDB ID 6VSB. These models were docked into the consensus map using Chimera. The model was then fitted interactively using ISOLDE 1.0b5[39] and COOT 0.8.9.2[40], and using real space refinement in Phenix 1.18[41]. In cases where side chains were not visible in the experimental data, they were truncated to alanine. Validation was performed using Molprobity[42] and EMRinger[43]. The model was submitted to the PDB with the ID 6XEY. Figures were prepared using ChimeraX[44].

Hamster protection experiment

In vivo evaluation of mAb 2-15 in an established golden Syrian hamster model of SARS-CoV-2 infection was performed as described previously with slight modifications[45]. Approval was obtained from the University of Hong Kong (HKU) Committee on the Use of Live Animals in Teaching and Research. In brief, 6–8-week-old male and female hamsters were obtained from the Chinese University of Hong Kong Laboratory Animal Service Centre through the HKU Laboratory Animal Unit and kept in biosafety level-2 (BSL-2) housing with access to standard pellet feed and water ad libitum until virus challenge in the BSL-3 animal facility. Each hamster ($n = 4$ per group) was intraperitoneally administered one dose of 1.5 mg/kg of mAb 2-15 in phosphate-buffered saline (PBS), 0.3 mg/kg of mAb 2-15 in PBS, or PBS alone as control. Twenty-four hours later, each hamster was intranasally inoculated with a challenge dose of 100 µl Dulbecco's modified Eagle medium containing 10^5 PFU of SARS-CoV-2 (HKU-001a strain, GenBank accession no: MT230904.1) under intraperitoneal ketamine (200 mg/kg) and xylazine (10 mg/kg) anaesthesia. The hamsters were monitored twice daily for clinical signs of disease and killed on the fourth day after the challenge. Half of each hamster's lung tissue was used for viral load determination by a quantitative SARS-CoV-2 RdRp/Hel RT–PCR assay[46] and an infectious virus titration using a plaque assay described previously[45]. Student's *t*-test was used to determine significant differences among the groups, and $P < 0.05$ was considered statistically significant.

Ethics statement

The acquisition of samples from recovering patients for isolation and identification of potent monoclonal antibodies against COVID-19 (AAAS9517) was approved by the Columbia University Institutional Review Board. Informed consent was obtained from all participants or surrogates.

Reporting summary

Further information on research design is available in the Nature Research Reporting Summary linked to this paper.

Data availability

The 19 neutralizing antibodies have been deposited in GenBank (https://www.ncbi.nlm.nih.gov/genbank/) with accession numbers from MT712278 to MT712315. Coordinates for the antibody 2-4 complex have been deposited in the Protein Data Bank as PDB 6XEY. Cryo-EM maps and data have been deposited in EMDB with deposition codes EMDB-22156 for antibody 2-4, EMDB-22158 and EMDB-22159 for antibody 4-8, and EMDB-22275 for antibody 2-43. These data are used in Fig. 4 and Extended Data Figs. 7, 8.

Code availability

Next-generation sequencing data of antibody repertoires were processed using Cell ranger v3.1.0, SONAR V1, BLAST v2.2.25, CLUSTALO1.2.3, and USEARCH v9.2.64. Cryo-EM data was collected using Leginon 3.4.beta. Cryo-EM data was processed using cryoSPARC v2.14.2, MotionCor2, Topaz v0.2.4, 3DFSC v3.0, UCSF Chimera v1.13.1, ChimeraX v0.93, ISOLDE v1.0b5, Phenix v1.18, and COOT v0.8.9.2.

26. Schramm, C. A. et al. SONAR: a high-throughput pipeline for inferring antibody ontogenies from longitudinal sequencing of B cell transcripts. *Front. Immunol.* **7**, 372 (2016).
27. Altschul, S. F. et al. Gapped BLAST and PSI-BLAST: a new generation of protein database search programs. *Nucleic Acids Res.* **25**, 3389–3402 (1997).
28. Lefranc, M. P. et al. IMGT, the international ImMunoGeneTics information system. *Nucleic Acids Res.* **37**, D1006–D1012 (2009).
29. Sievers, F. & Higgins, D. G. Clustal Omega, accurate alignment of very large numbers of sequences. *Methods Mol. Biol.* **1079**, 105–116 (2014).
30. Edgar, R. C. Search and clustering orders of magnitude faster than BLAST. *Bioinformatics* **26**, 2460–2461 (2010).
31. Nie, J. et al. Establishment and validation of a pseudovirus neutralization assay for SARS-CoV-2. *Emerg. Microbes Infect.* **9**, 680–686 (2020).
32. Whitt, M. A. Generation of VSV pseudotypes using recombinant ΔG-VSV for studies on virus entry, identification of entry inhibitors, and immune responses to vaccines. *J. Virol. Methods* **169**, 365–374 (2010).
33. Suloway, C. et al. Automated molecular microscopy: the new Leginon system. *J. Struct. Biol.* **151**, 41–60 (2005).
34. Punjani, A., Rubinstein, J. L., Fleet, D. J. & Brubaker, M. A. cryoSPARC: algorithms for rapid unsupervised cryo-EM structure determination. *Nat. Methods* **14**, 290–296 (2017).
35. Bepler, T. et al. Positive-unlabeled convolutional neural networks for particle picking in cryo-electron micrographs. *Nat. Methods* **16**, 1153–1160 (2019).
36. Pettersen, E. F. et al. UCSF Chimera—a visualization system for exploratory research and analysis. *J. Comput. Chem.* **25**, 1605–1612 (2004).
37. Tan, Y. Z. et al. Addressing preferred specimen orientation in single-particle cryo-EM through tilting. *Nat. Methods* **14**, 793–796 (2017).
38. Zhu, K. et al. Antibody structure determination using a combination of homology modeling, energy-based refinement, and loop prediction. *Proteins* **82**, 1646–1655 (2014).
39. Croll, T. I. ISOLDE: a physically realistic environment for model building into low-resolution electron-density maps. *Acta Crystallogr. D Struct. Biol.* **74**, 519–530 (2018).
40. Emsley, P. & Cowtan, K. Coot: model-building tools for molecular graphics. *Acta Crystallogr. D Biol. Crystallogr.* **60**, 2126–2132 (2004).
41. Adams, P. D. et al. Recent developments in the PHENIX software for automated crystallographic structure determination. *J. Synchrotron Radiat.* **11**, 53–55 (2004).
42. Davis, I. W., Murray, L. W., Richardson, J. S. & Richardson, D. C. MOLPROBITY: structure validation and all-atom contact analysis for nucleic acids and their complexes. *Nucleic Acids Res.* **32**, W615–W619 (2004).
43. Barad, B. A. et al. EMRinger: side chain-directed model and map validation for 3D cryo-electron microscopy. *Nat. Methods* **12**, 943–946 (2015).

44. Goddard, T. D. et al. UCSF ChimeraX: meeting modern challenges in visualization and analysis. *Protein Sci*. **27**, 14–25 (2018).
45. Chan, J. F. et al. Simulation of the clinical and pathological manifestations of Coronavirus Disease 2019 (COVID-19) in golden Syrian hamster model: implications for disease pathogenesis and transmissibility. *Clin. Infect. Dis.* https://doi.org/10.1093/cid/ciaa325 (2020).
46. Chan, J. F. et al. Improved molecular diagnosis of COVID-19 by the novel, highly sensitive and specific COVID-19-RdRp/Hel real-time reverse transcription-PCR assay validated *in vitro* and with clinical specimens. *J. Clin. Microbiol*. **58**, e00310-20 (2020).

Acknowledgements We thank N. Wang and J. McLellan for providing reagents for generating the SARS-CoV-2 S trimer and RBD-SD1 with mFc tag; W. Chen for assistance with generating the Venn diagrams; and B. DeKosky and X. Wu for helpful input. This study was supported by funding to D.D.H. from the Jack Ma Foundation, the JPB Foundation, Samuel Yin, Brii Biosciences, Tencent Charity Foundation, Roger Wu, Carol Ludwig, and Peggy and Andrew Cherng. Cryo-EM data collection was performed at the National Center for CryoEM Access and Training and the Simons Electron Microscopy Center located at the New York Structural Biology Center, supported by the NIH Common Fund Transformative High Resolution Cryo-Electron Microscopy program (U24 GM129539) and by grants from the Simons Foundation (SF349247) and NY State Assembly. Data analysis was performed at the National Resource for Automated Molecular Microscopy (NRAMM), supported by the NIH National Institute of General Medical Sciences (GM103310). Hamster experiments were conducted with support from the Health@InnoHK (Centre for Virology, Vaccinology and Therapeutics), Innovation and Technology Commission, The Government of the Hong Kong Special Administrative Region.

Author contributions D.D.H. conceived the project. L.L., P.W., M.S.N, J.Y., Q.W. and Y.H. performed many of the experiments. M.T.Y. was responsible for recruiting patients, obtaining clinical specimens, and summarizing clinical data. L.L., V.S., A.F. and X.V.G. performed and analysed the B cell sorting, 10X Genomics, sequencing and analysis of the clones. Z.S. performed bioinformatic analyses on 10X next-generation sequencing data and antibody repertoire. J.Y. cloned, expressed, and purified the mAbs. L.L. and Q.W. performed the epitope mapping and binding experiments. P.W. conducted the pseudovirus neutralization assays and M.S.N and Y.H.performed infectious SARS-CoV-2 neutralization assays. M.R., G.C., J.B., J.G., and L.S. carried out the cryo-EM studies. J.F.-W.C., Z.C., and K.-Y.Y. were responsible for the hamster experiment. Y.L. helped with project management. T.Z. and P.D.K. provided key reagents for the study, and P.D.K. contributed to the analysis and discussion of the data. L.L., P.W., M.S.N., J.Y., Y.H., Z.S., M.R., Q.W., L.S., and D.D.H. analysed the results, and D.D.H. wrote the manuscript, with contributions from each author. J.G.S. provided valuable suggestions.

Competing interests A provisional patent application has been filed for the monoclonal antibodies described in the manuscript. L.L. and D.D.H. are inventors.

Additional information

Supplementary information is available for this paper at https://doi.org/10.1038/s41586-020-2571-7.

Correspondence and requests for materials should be addressed to Y.H., L.S. or D.D.H.

Peer review information *Nature* thanks Antonio Lanzavecchia and the other, anonymous, reviewer(s) for their contribution to the peer review of this work. Peer reviewer reports are available.

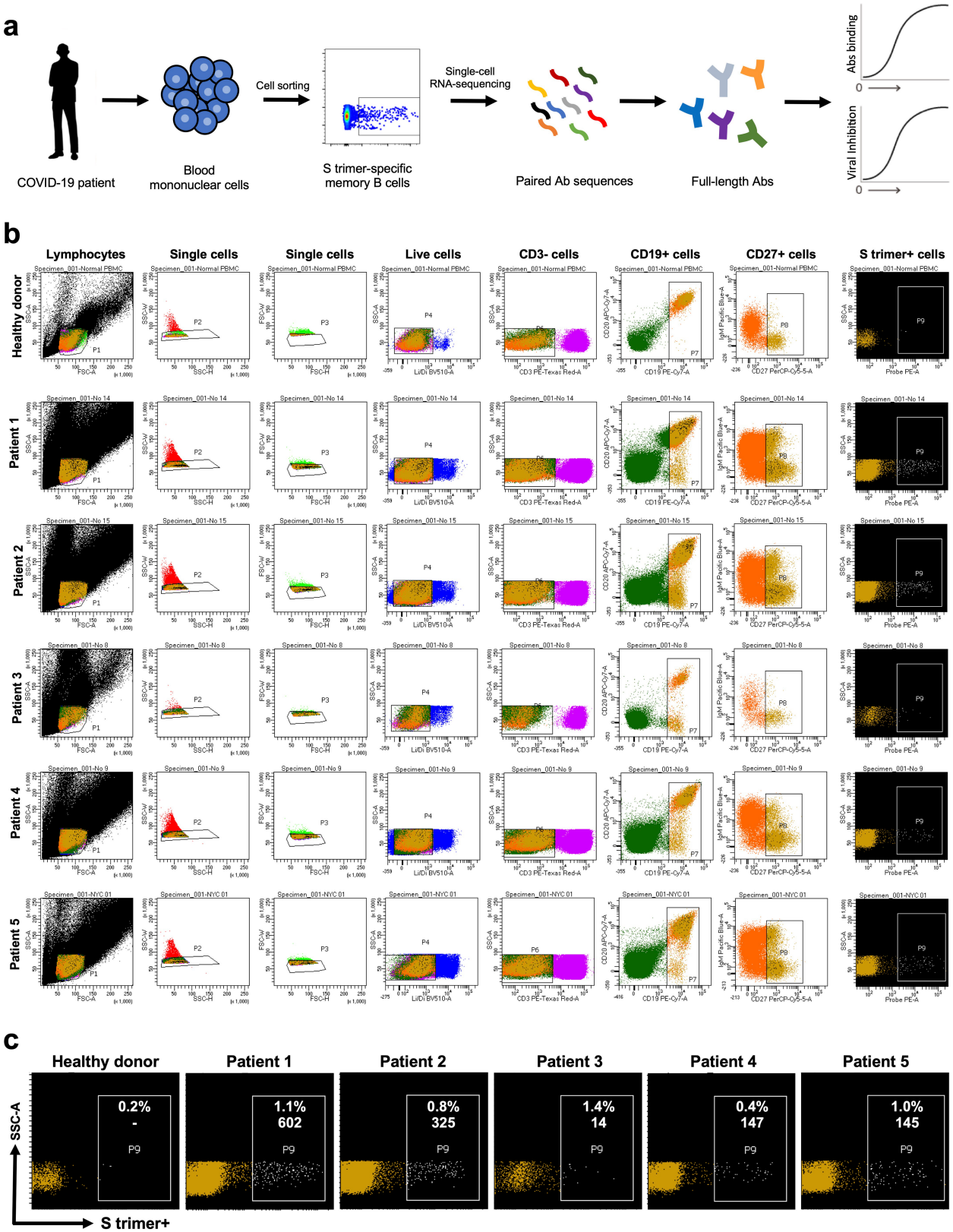

Extended Data Fig. 1 | SARS-CoV-2 S trimer-specific antibody isolation strategy. a, Schema for isolating of S trimer-specific mAbs from memory B cells in the blood of infected patients. **b**, Sorting results on the isolation of S trimer-specific memory B cells using flow cytometry. **c**, Magnified representation of the panel of S trimer-positive memory B cells for each patient. Inset numbers indicate the absolute number and the percentage of S trimer-specific memory B cells isolated from each case.

a

	Abs tested	Binding Abs			Neutralizing Abs	Neutralizing Abs
		S trimer	RBD	Non-RBD	Pseudovirus	Live virus
Total	252	121	38	83	61	41
Patient 1	100	45	19	26	19	11
Patient 2	54	29	12	17	18	18
Patient 3	6	2	0	2	3	0
Patient 4	44	32	7	25	14	6
Patient 5	48	13	0	13	7	6

b

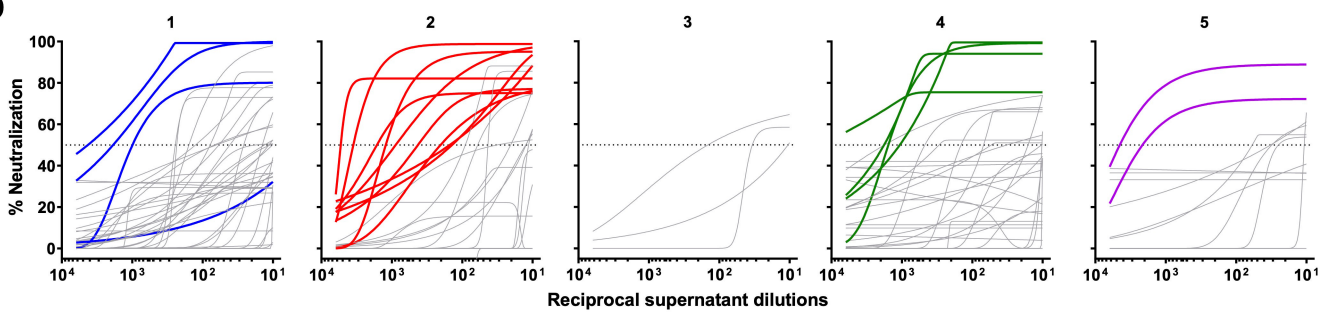

Extended Data Fig. 2 | Summary of mAb screening of transfection supernatants. a, Numbers of binding and neutralizing antibodies from patients 1 to 5. **b**, The best-fit pseudovirus neutralization curves for 130 samples that were positive in at least one of the screens shown in Fig. 1b. The 18 transfection supernatants that showed evidently better potency are highlighted in colours, while others with non-neutralizing or weakly neutralizing activities are shown in grey. One additional supernatant (Patient 1) that was initially missed in the pseudovirus screen but later found to be a potent neutralizing mAb (1-87) is also highlighted.

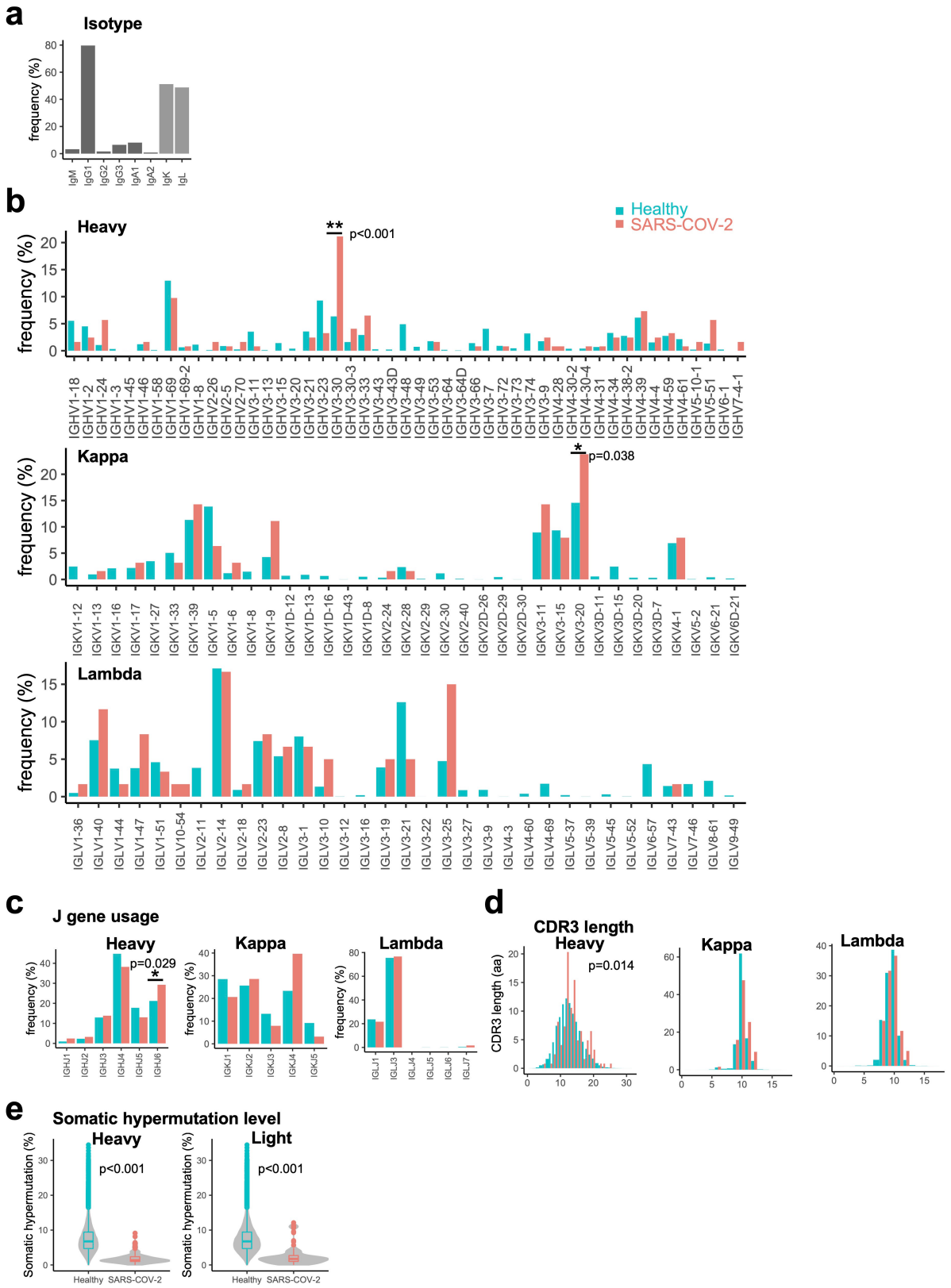

Extended Data Fig. 3 | See next page for caption.

Extended Data Fig. 3 | Genetic features of SARS-CoV-2-specific antibody repertoire. a, 108 of the 123 antigen-specific antibodies are from IgG isotype. The kappa and lambda light chains are comparably used. **b**, Compared to IgG repertoires of healthy human donors (17,243, 27,575, and 20,889 transcripts for heavy, kappa, and lambda chains respectively), IGHV3-30 (antigen-specific $n = 26$ and healthy donor $n = 1117$) and IGKV3-20 genes (antigen-specific $n = 15$ and healthy donor $n = 4,071$) are over-represented in heavy and light chain repertoires respectively (P values are 6.415×10^{-11} and 0.04332 respectively, χ^2-test with 1 degree of freedom). We did not test the enrichment of other genes because the numbers of antigen-specific antibodies are less than 15. **c**, The usage of IGHJ6 gene (antigen-specific $n = 36$ and healthy donor $n = 3646$) was significantly higher in antigen-specific antibodies (χ^2-test with 1 degree of freedom, $P = 0.02807$). **d**, The CDRH3 length of antigen-specific antibodies is significantly longer than in healthy donors (two-sided Kolmogorov–Smirnov test, $P = 0.014$). **e**, For both heavy and light chains, the V region nucleotide somatic hypermutation levels are significantly lower than in antibodies of healthy donors (two-sided Kolmogorov–Smirnov test, $P < 2.2 \times 10^{-16}$ for both heavy and light chains). For the boxplots, the middle lines are medians. The lower and upper hinges correspond to the first and third quartiles respectively. The upper whisker extends to values no larger than 1.5× IQR (the interquartile range or distance between the first and third quartiles) from the hinge. The lower whisker extends to values no smaller than 1.5× IQR from the hinge. Data points beyond the whiskers were plotted as outliers using dots.

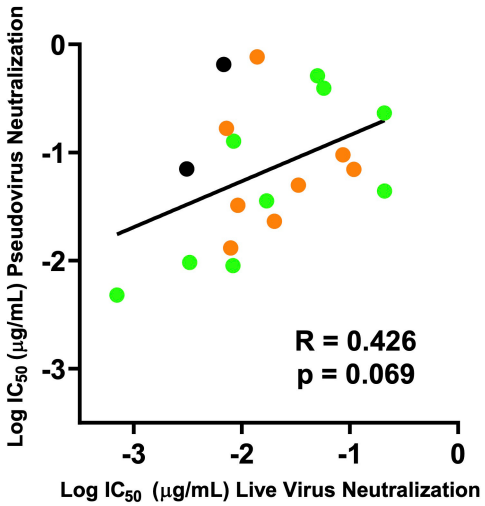

Extended Data Fig. 4 | Correlation of neutralizing antibody titres of the top 19 mAbs in the live SARS-CoV-2 assay versus the pseudovirus assay. Green circles represent RBD-directed antibodies; orange circles represent NTD-directed antibodies; and black circles represent antibodies in the 'Others' category. The Pearson correlation coefficient (*R*) and the *p* value were calculated using GraphPad Prism. Experiments were performed in triplicates for all mAbs tested.

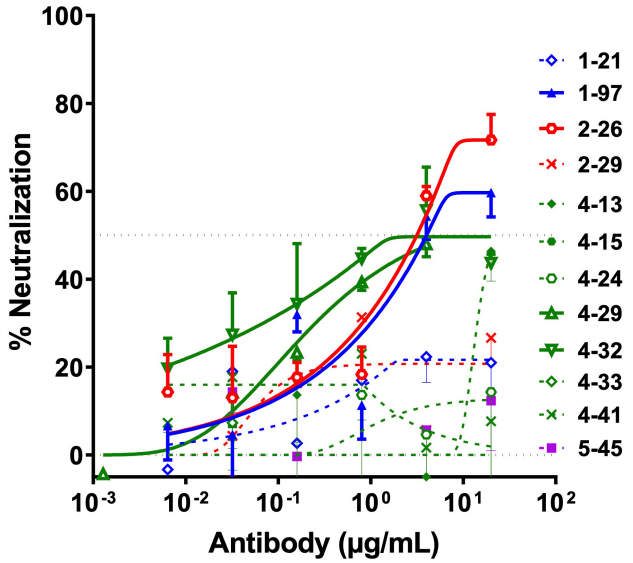

Extended Data Fig. 5 | The pseudovirus neutralization profiles for 12 purified mAbs that strongly bound the S trimer but with weak or no virus-neutralizing activities. The four mAbs with weak neutralizing activities against SARS-CoV-2 pseudovirus are shown in sold lines, and the remaining 8 non-neutralizing mAbs are shown in dashed lines.

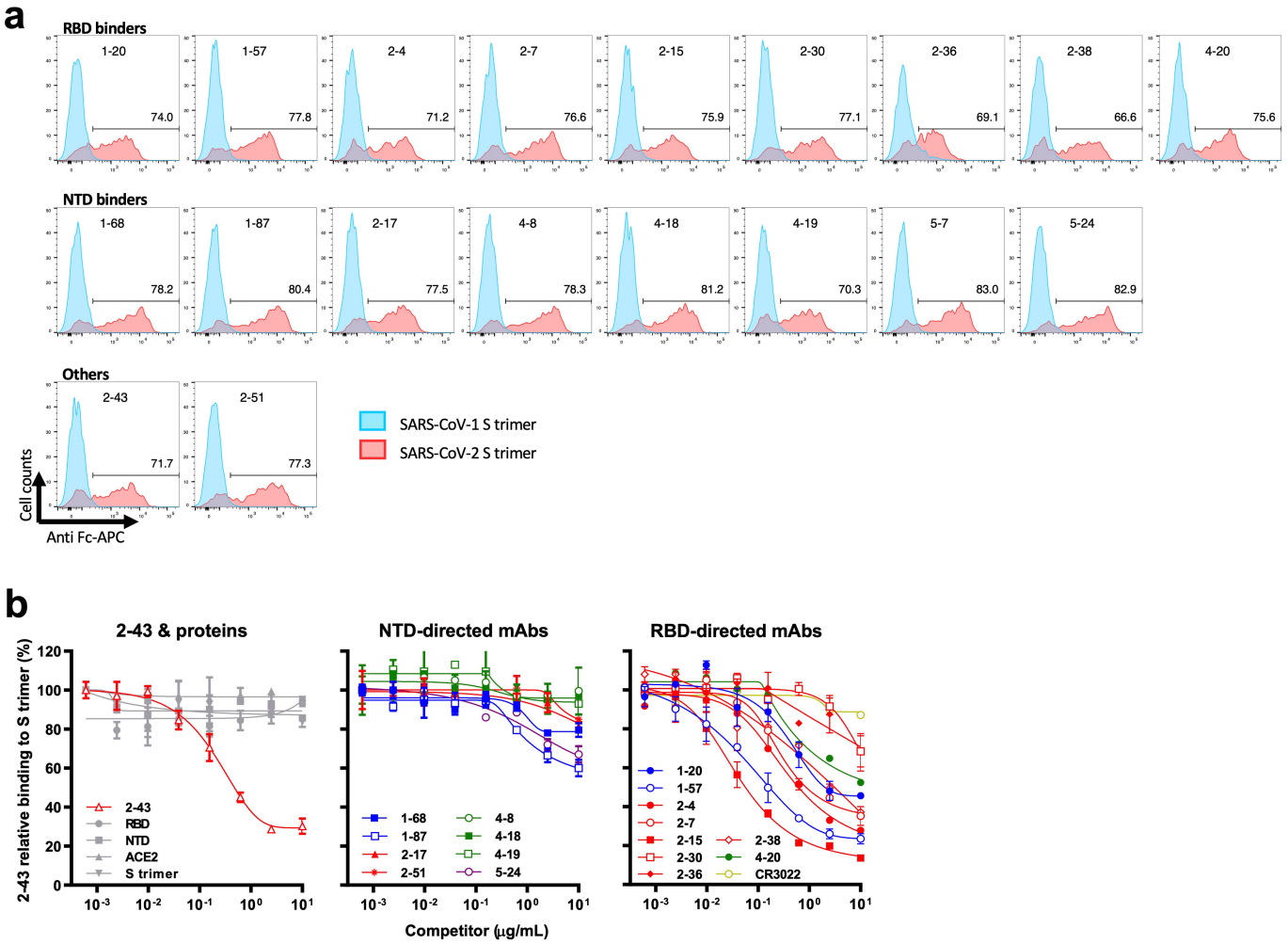

Extended Data Fig. 6 | Cell-surface staining with antibodies. a, Antibody binding to the SARS-CoV-1 (blue) and SARS-CoV-2 (red) spike proteins expressed on the cell surface. Expi293 cells were co-transfected with GFP and full-length SARS-CoV-1 or SARS-CoV-2 spike genes. After 48 h, antibody binding to spike protein in the GFP-positive cells was detected by flow cytometer. The data show all antibodies tested were able to recognize the wildtype SARS-CoV-2 spike protein but not SARS-CoV-1 spike protein. **b**, Monoclonal Ab 2-43 bound to S trimer expressed on Expi293 cell surface can be competed out by mAbs directed against RBD but only minimally by mAbs to the NTD region. Shown are representative data from three independent experiments.

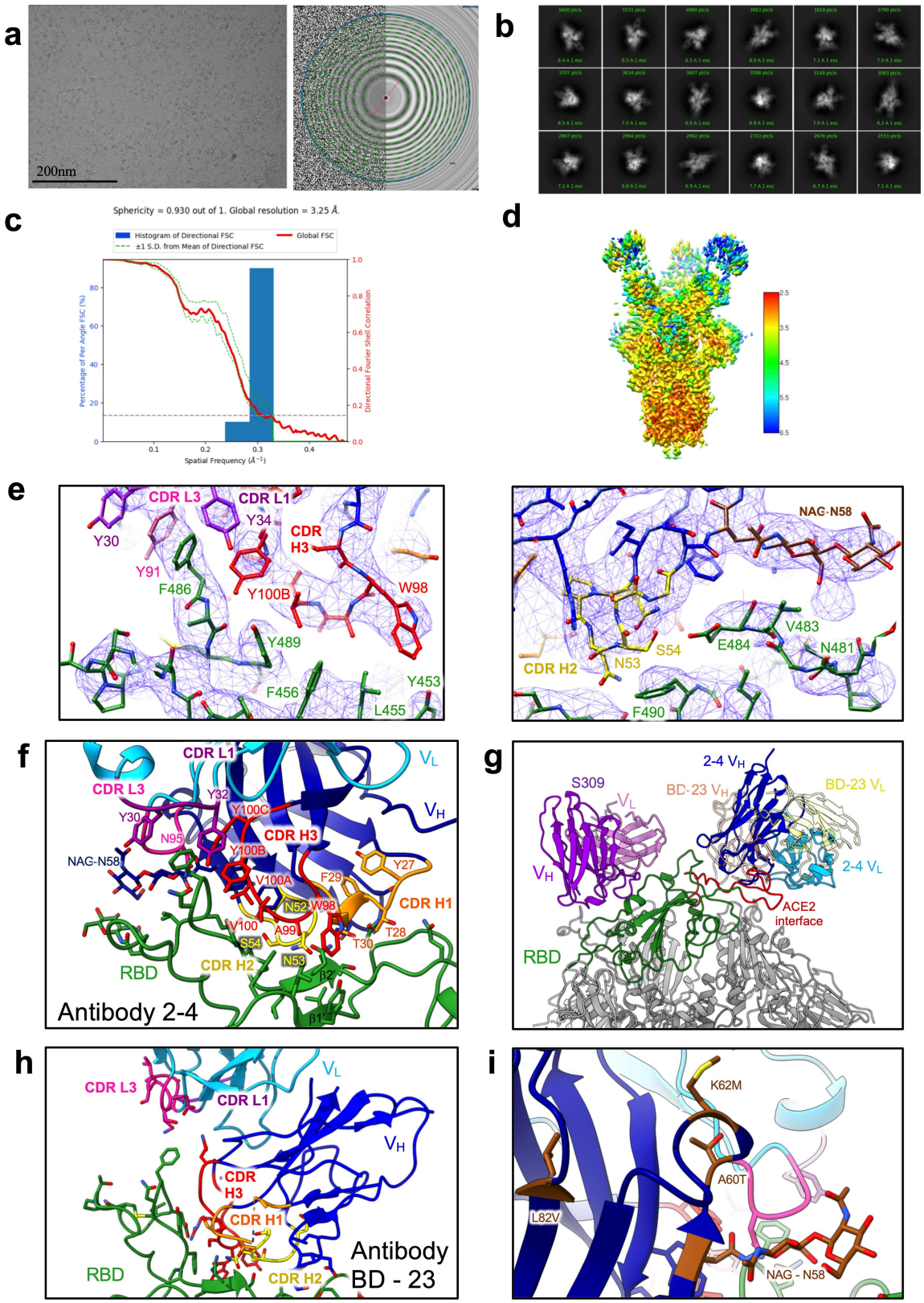

Extended Data Fig. 7 | Cryo-EM analysis of antibody 2-4 in complex with the S trimer. a, Representative micrograph and CTF of the micrograph. 8,324 micrographs were collected in total. **b**, Representative 2D class averages. **c**, Resolution of the consensus map with C3 symmetry as calculated by 3DFSC. **d**, The local resolution of the full map as calculated by cryoSPARC at an FSC cutoff of 0.5. **e**, Representative density of the Fab 2-4 (blue) and RBD (green) interface, showing interactions of CDR H3 in red, L1 in magenta, and L3 in light magenta (left), along with CDR H2 and the N-linked glycosylation added by SHM at ASN58 (right). **f**, Fab 2-4 binding interface with RBD. V_H is shown in blue, V_L in light blue, with CDRs H1 in orange, H2 in yellow, H3 in red, L1 in magenta, and L3 in light magenta. **g**, Positions of antibodies 2-4, S309[8], and BD-23[9] on the trimeric CoV-2 spike. **h**, Antibody BD-23[9] in complex with S trimer. **i**, Somatic hypermutations found only in the antibody 2-4 heavy chain, shown in brown. The mutation A60T creates an NxT sequence leading to N58 glycosylation.

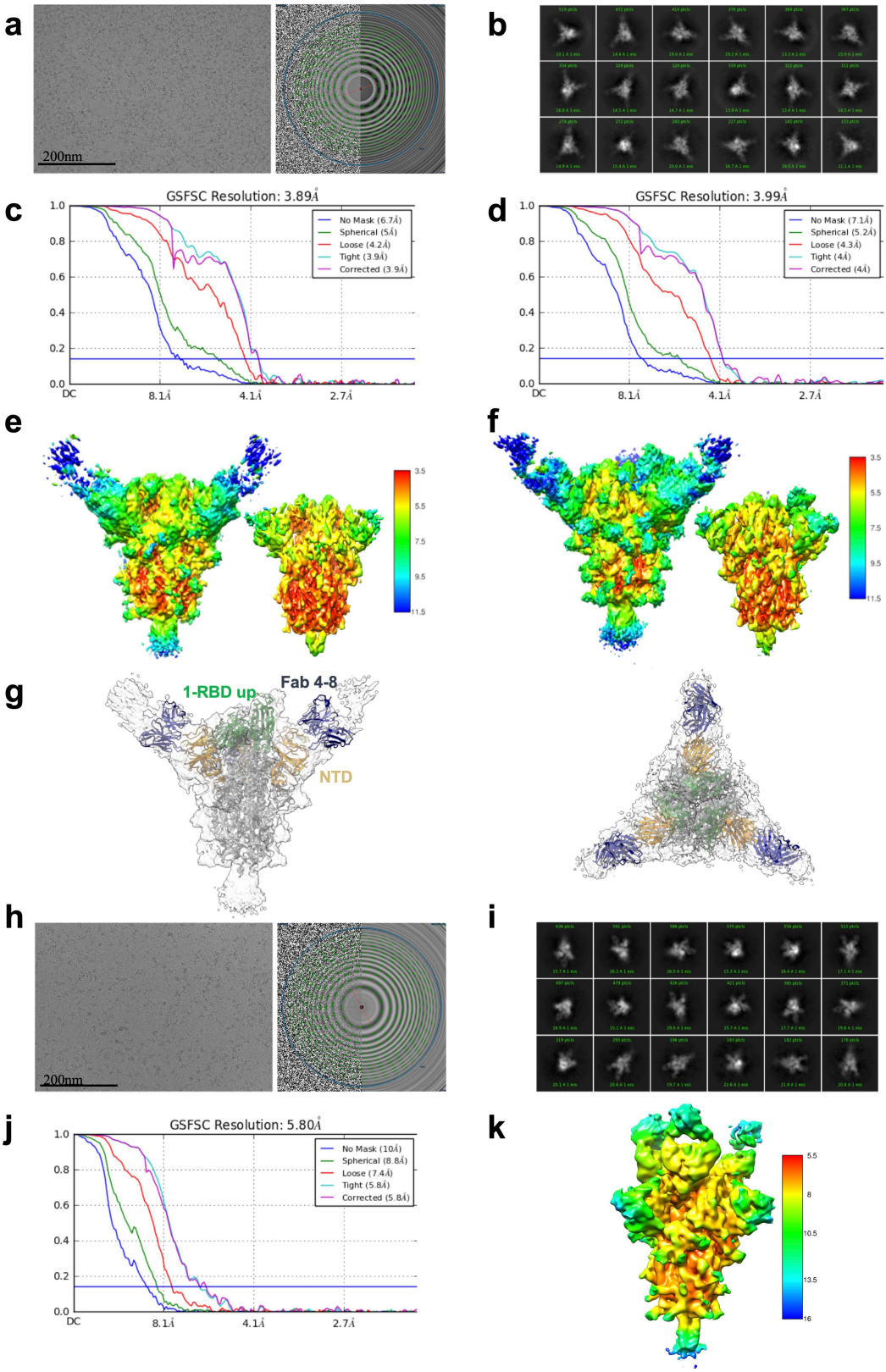

Extended Data Fig. 8 | Cryo-EM data processing for antibodies 4-8 and 2-43 in complex with S trimer. a, Representative 4-8 micrograph and CTF of the micrograph. 3,153 micrographs were collected in total. **b**, Representative 2D class averages. **c**, Resolution of the spike in the RBD down conformation in complex with Fab 4-8. **d**, Resolution of the spike in the RBD up conformation in complex with Fab 4-8. **e**, Local resolution of the spike in the RBD down conformation in complex with Fab 4-8 at an FSC cutoff of 0.5, with two thresholds shown. **f**, Local resolution of the spike in the RBD up conformation in complex with Fab 4-8 at an FSC cutoff of 0.5, with two thresholds shown. **g**, Although the map was reconstructed at 4.0Å resolution, density for 4-8 Fab is poor due to molecular motion. A rigid body fit with SARS-CoV-2 spike and an antibody variable domain model is shown. **h**–**k**, Cryo-EM data processing for antibody 2-43 in complex with the S trimer. **h**, Representative 2-43 micrograph and CTF of the micrograph. **i**, Representative 2D class averages. **j**, Resolution of Fab 2-43 in complex with S trimer. **k**, The local resolution of the full map as calculated by cryoSPARC at an FSC cutoff of 0.5.

Extended Data Table 1 | Patient information

Patient	Age	Sex & Race	Days from symptom onset to:	Biomarker	Complications	Outcome
1	57	Female, Hispanic	Admission: 7 MV: 12 Ab isolation: 18	hsCRP = 208 mg/L ESR = 58 mm/hr IL-6 = 23 pg/mL Ferritin = 766 ng/mL D-dimer = 3.4 μg/mL FEU	ARDS	Discharged on day 30
2	71	Female, Hispanic	Admission: 20 MV: 20 Ab isolation: 29	hsCRP = 33 mg/L ESR > 130 mm/hr IL-6 = 13 pg/mL Ferritin = 425 ng/mL D-dimer = 5.7 μg/mL FEU	ARDS Ventilator associated pneumonia	Discharged on day 45
3	61	Male, White	Admission: 10 MV: 10 Ab isolation: 21	hsCRP = 51 mg/L ESR = 57 mm/hr IL-6 > 315 pg/mL Ferritin = 3,238 ng/mL D-dimer = 7.4 μg/mL FEU	ARDS Acute kidney injury (hemodialysis) Sepsis	Death on day 28
4	51	Male, Black	Admission: 7 MV: 10 Ab isolation: 25	hsCRP = 88 mg/L ESR = 110 mm/hr IL-6 = 77 pg/mL Ferritin = 510 ng/mL D-dimer = 13.4 μg/mL FEU	ARDS Acute kidney injury (no hemodialysis) Ventilator associated pneumonia	Discharged on day 51
5	50	Male, White	Admission: 5 MV: 7 Ab isolation: 32	hsCRP = 2 mg/L ESR = 63 mm/hr	ARDS Neuropathy	Discharged on day 27

ARDS, acute respiratory distress syndrome; MV, mechanical ventilation; hsCRP, high sensitivity C-reactive protein, ULN >10 mg/l; ESR, erythrocyte sedimentation rate, ULN = 20 mm/h; Interleukin 6, ULN = 5 pg/ml; Ferritin, ULN = 150 ng/ml; D-dimer quantitative ULN = 0.8 ug/ml FEU.

Extended Data Table 2 | Cryo-EM data collection, refinement, and validation statistics

	SARS-CoV-2 spike with Fab 2-4 (EMDB-22156) (PDB 6XEY)	SARS-CoV-2 spike RBD up with Fab 4-8 (EMDB-22158)	SARS-CoV-2 spike RBD down with Fab 4-8 (EMDB-22159)	SARS-CoV-2 spike with Fab 2-43 (EMDB-22275)
Data collection and processing				
Magnification	81,000	81,000	81,000	81,000
Voltage (kV)	300	300	300	300
Electron exposure (e–/Å^2)	51.30	51.30	51.30	51.69
Defocus range (μm)	-0.4 to -3.5	-0.4 to -3.5	-0.4 to -3.5	-0.4 to -3.5
Pixel size (Å)	1.058	1.058	1.058	1.058
Symmetry imposed	C3	C1	C3	C1
Initial particle images (no.)	556,983	256,848	256,848	55,161
Final particle images (no.)	83,927	105,278	47,555	10,068
Map resolution (Å)	3.25	4.0	3.9	5.8
FSC threshold	0.143	0.143	0.143	0.143
Map resolution range (Å)	406.3-3.25	406.3-4.0	406.3-3.9	406.3-5.8
Refinement				
Initial model used (PDB code)	6VSB			
Model resolution (Å)	3.7			
FSC threshold	0.5			
Model resolution range (Å)	406.3-3.25			
Map sharpening *B* factor (Å^2)	-97.5			
Model composition				
Non-hydrogen atoms	28,482			
Protein residues	3788			
Ligands	63			
B factors (Å^2)				
Protein	54.35			
Ligand	73.91			
R.m.s. deviations				
Bond lengths (Å)	0.005			
Bond angles (°)	0.810			
Validation				
MolProbity score	1.51			
Clashscore	3.59			
Poor rotamers (%)	0.22			
Ramachandran plot				
Favored (%)	94.75			
Allowed (%)	5.17			
Disallowed (%)	0.08			

nature research

Corresponding author(s): David D. Ho

Last updated by author(s): Jul 6, 2020

Reporting Summary

Nature Research wishes to improve the reproducibility of the work that we publish. This form provides structure for consistency and transparency in reporting. For further information on Nature Research policies, see our Editorial Policies and the Editorial Policy Checklist.

Statistics

For all statistical analyses, confirm that the following items are present in the figure legend, table legend, main text, or Methods section.

n/a	Confirmed	
☐	☒	The exact sample size (*n*) for each experimental group/condition, given as a discrete number and unit of measurement
☐	☒	A statement on whether measurements were taken from distinct samples or whether the same sample was measured repeatedly
☐	☒	The statistical test(s) used AND whether they are one- or two-sided *Only common tests should be described solely by name; describe more complex techniques in the Methods section.*
☒	☐	A description of all covariates tested
☒	☐	A description of any assumptions or corrections, such as tests of normality and adjustment for multiple comparisons
☐	☒	A full description of the statistical parameters including central tendency (e.g. means) or other basic estimates (e.g. regression coefficient) AND variation (e.g. standard deviation) or associated estimates of uncertainty (e.g. confidence intervals)
☐	☒	For null hypothesis testing, the test statistic (e.g. *F*, *t*, *r*) with confidence intervals, effect sizes, degrees of freedom and *P* value noted *Give P values as exact values whenever suitable.*
☐	☐	For Bayesian analysis, information on the choice of priors and Markov chain Monte Carlo settings
☐	☐	For hierarchical and complex designs, identification of the appropriate level for tests and full reporting of outcomes
☒	☐	Estimates of effect sizes (e.g. Cohen's *d*, Pearson's *r*), indicating how they were calculated

Our web collection on statistics for biologists contains articles on many of the points above.

Software and code

Policy information about availability of computer code

Data collection	Cryo-EM data was collected using Leginon 3.4.beta. Sequencing of memory B cell clones done using Illumina NextSeq 500. Cell sorting was performed on FACSDiva version 8.0.1.
Data analysis	Cryo-EM data was processed using cryoSPARC v2.14.2, MotionCor2, Topaz v0.2.4, 3DFSC v3.0, UCSF Chimera v1.13.1, ChimeraX v0.93, ISOLDE v1.0b5, Phenix v1.18, and COOT v0.8.9.2. Next-generation sequencing data of antibody repertoires were processed using Cell ranger v3.1.0, SONAR V1, BLAST v2.2.25, CLUSTALO1.2.3, and USEARCH v9.2.64. FlowJo 10.4 was used for analyzing FACS data. For 10X Genomics; cellranger 3.1.0 for BCL to FASTQ conversion, and gene counting was used. GraphPad Prism 8 was used for plotting data.

For manuscripts utilizing custom algorithms or software that are central to the research but not yet described in published literature, software must be made available to editors and reviewers. We strongly encourage code deposition in a community repository (e.g. GitHub). See the Nature Research guidelines for submitting code & software for further information.

Data

Policy information about availability of data

All manuscripts must include a data availability statement. This statement should provide the following information, where applicable:

- Accession codes, unique identifiers, or web links for publicly available datasets
- A list of figures that have associated raw data
- A description of any restrictions on data availability

We confirm we have deposited the sequencing dataset into Genbank and they will become available publicly within two business day. Once the accession numbers are assigned, we will add the data availability statement in the manuscript and here. Healthy donor antibody repertoires were from previous study with SRA ID PRJNA336331. The following data availability statement will be included in the final version of the manuscript: "The 19 neutralizing antibodies were deposited to Genbank with accession numbers: ACXXXXXXXX. Coordinates for the antibody 2-4 complex are deposited in the Protein Data Bank as PDB 6XEY. Cryo-EM maps and

data are deposited in EMDB with deposition codes EMDB-22156 for antibody 2-4, EMDB-22158 and EMDB-22159 for antibody 4-8, and EMDB-22275 for antibody 2-43. These data are used in Fig. 4 and Extended Data Figs. 7, 8, 9, 10, and 11."

Field-specific reporting

Please select the one below that is the best fit for your research. If you are not sure, read the appropriate sections before making your selection.

☒ Life sciences ☐ Behavioural & social sciences ☐ Ecological, evolutionary & environmental sciences

For a reference copy of the document with all sections, see nature.com/documents/nr-reporting-summary-flat.pdf

Life sciences study design

All studies must disclose on these points even when the disclosure is negative.

Sample size	40 patients detected positive for SARS-CoV-2 using diagnostic RT-PCR tests were used for screening of neutralization abilities of their plasma samples. Based on the neutralization profile of the plasma, patients with most potent plasma were downselected for sorting of the memory B-cells and antibody isolation and cloning. The sample size is appropriate within technical capability to downselect multiple patients with potent neutralizing plasma.
Data exclusions	None
Replication	All experiments were performed and verified in multiple replicates as indicated in their methods/figure legends of the manuscript.
Randomization	All samples were selected for their ability to produce neutralization antibodies and all PBMCs were randomly processed from the 5 patients with potent neutralization of the plasma using baits specific for their ability to measure neutralization (SARS-CoV-2 S trimer). The screens for the binding and neutralization assays were also performed without any bias for selection and efficacy determined solely by the potency of the individual clones/antibodies.
Blinding	Blinded scoring of the neutralization of SARS-CoV-2 virus associated cytopathic effects were performed and average of the scores was converted to percentage of the neutralization. The results were plotted as mean +/- SEM. All other experiments in the study were predesigned with the hypothesis and strategies were laid out so as to use instruments that were calibrated to report the data. This feature led to the non-relevance of blinding for any of those experiments. Experiments were validated using technical and/or biological replicates in all cases.

Reporting for specific materials, systems and methods

We require information from authors about some types of materials, experimental systems and methods used in many studies. Here, indicate whether each material, system or method listed is relevant to your study. If you are not sure if a list item applies to your research, read the appropriate section before selecting a response.

Materials & experimental systems

n/a	Involved in the study
☐	☒ Antibodies
☐	☒ Eukaryotic cell lines
☒	☐ Palaeontology and archaeology
☒	☐ Animals and other organisms
☐	☒ Human research participants
☐	☒ Clinical data
☒	☐ Dual use research of concern

Methods

n/a	Involved in the study
☒	☐ ChIP-seq
☐	☒ Flow cytometry
☒	☐ MRI-based neuroimaging

Antibodies

Antibodies used	For S trimer-specific B cells sorting and single-cell BCR sequencing, anti-human CD3 PE-CF594 (BD Biosciences, Cat.562406, Clone SP34-2, Lot.9325656, 1:20 dilution), anti-human CD19 397 PE-Cy7 (Biolegend, Cat.302216, Clone HIB19, Lot.B276834, 1:20 dilution), anti-human CD20 APC-Cy7 (Biolegend, Cat.302314, Clone 2H7, Lot.B288789, 1:20 dilution), anti-human IgM V450 (BD Biosciences, Cat.561286, Clone G20-127, Lot.9003910, 1:20 dilution), anti-human CD27 PerCP-Cy5.5 (BD Biosciences, Cat.560612, Clone M-T271, Lot.9283016, 1:20 dilution), anti-His PE (Biolegend, Cat.362603, Clone J095G46, Lot.B269138, 1:20 dilution), Human Hashtag 3 (Biolegend, Cat.394665, Clone LNH-94,Lot.B282244, 1:20 dilution). For epitope mapping by ELISA, anti-human IgG (Jackson ImmunoResearch, Cat. 109-035-003, Polyclonal, Lot.146269, 1: 10,000 dilution), Streptavidin-APC (Biolegend, Cat.405243, Lot.B266052, 1: 2,000 dilution), Avidin-HRP (Invitrogen, Cat.18-4100-51, Lot.2197902, 1: 500 dilutions), anti-Strep-HRP (Strep-TagII - HRP, EMD Millipore, Cat.71591, Lot.3393843, 1: 2,000 dilution).
Validation	All validations are available from the commercial website under the validation sheet link for the catalogued item. 1. Anti-human CD3 PE-CF594 (BD Biosciences, Cat # 562406), https://www.bdbiosciences.com/eu/reagents/research/antibodies-buffers/immunology-reagents/anti-non-human-primate-antibodies/cell-surface-antigens/pe-cf594-mouse-anti-human-cd3-sp34-2/

p/562406
2. Anti-human CD19 397 PE-Cy7 (Biolegend, Cat# 302216), https://www.biolegend.com/en-us/products/pe-cyanine7-anti-human-cd19-antibody-1911
3. Anti-human CD20 APC-Cy7 (Biolegend, Cat# 302314), https://www.biolegend.com/en-us/products/apc-cyanine7-anti-human-cd20-antibody-1901
4. Anti-human IgM V450 (BD Biosciences, Cat # 561286), https://www.bdbiosciences.com/eu/applications/research/b-cell-research/immunoglobulins/human/v450-mouse-anti-human-igm-g20-127/p/561286
5. Anti-human CD27 PerCP-Cy5.5 (BD Biosciences, Cat# 560612), https://www.bdbiosciences.com/eu/applications/research/b-cell-research/surface-markers/human/percp-cy55-mouse-anti-human-cd27-m-t271/p/560612
6. Human Hashtag 3 (Biolegend, Cat # 394665), https://www.biolegend.com/en-us/products/totalseq-c0253-anti-human-hashtag-3-antibody-17164
7. Anti-His PE (Biolegend, Cat# 362603), https://www.biolegend.com/en-us/products/pe-anti-his-tag-antibody-9861
8. Anti-human IgG (Jackson ImmunoResearch, Cat# 109-035-003), https://www.jacksonimmuno.com/catalog/products/109-035-003
9. Streptavidin-APC (Biolegend, Cat# 405243), https://www.biolegend.com/en-us/products/apc-streptavidin-high-concentration-10081
10. Avidin-HRP (Invitrogen, Cat# 18-4100-51), https://www.thermofisher.com/order/catalog/product/18-4100-51#/18-4100-5
11. Anti-Strep-HRP (Strep-TagII –HRP, EMD Millipore, Cat# 71591), https://www.emdmillipore.com/US/en/product/StrepTag-II-Antibody-HRP-Conjugate,EMD_BIO-71591

Eukaryotic cell lines

Policy information about cell lines

Cell line source(s)	Vero-E6 (ATCC), Expi293 (Thermofisher), 293T (ATCC)
Authentication	Obtained from authenticated vendors. Cells were recovered as healthy logarithmically growing cells within 4 to 7 days after thawing. Viability was measured and found to be >90%.
Mycoplasma contamination	Mycoplasma is negative (Detected mycoplasma contamination using Mycoplasma PCR ELISA ,Sigma,catalog number is 11663925910)
Commonly misidentified lines (See ICLAC register)	No commonly misidentified lines were used in the study.

Human research participants

Policy information about studies involving human research participants

Population characteristics	Eligibility criteria include: (1) greater than age 18 (inclusive) (2) confirmed COVID-19 infection by a FDA- approved molecular based assay (including those under emergency use authorization) of respiratory or blood specimens; (3) If symptomatic with COVID-19, must have evidence of improvement of symptoms and a duration of at least 4 weeks from the onset of symptoms to day of enrollment; (4) If asymptomatic, must have a duration of at least 4 weeks from first positive molecular based COVID-19 assay to day of enrollment. Among the 40 participants enrolled in this study, the mean age was 50 (20-84) and 53% were male. Among those with race/ethnicity information, 21% were Black/African American, 38% Latinx, 3% Asian, and 38% non-Hispanic white.
Recruitment	This is a prospective study to enroll participants who have recovered from coronavirus disease (COVID-19) for the purpose of obtaining blood specimens to isolate monoclonal antibodies against SARS-CoV2 that can be developed into preventive or therapeutic agents. Potential participants were referred by health care providers from within the Columbia University Irving Medical Center/New York Presbyterian Hospital system and from outside institutions. Potential participants were contacted by study staff and informed consent signed prior to performance of study procedures. All participants with severe COVID-19 were recruited during or after prolonged hospitalization at a single medical center in New York City, while participants with mild COVID-19 were self-referred through online recruitment. All participants were recruited in March and April, 2020 during the early stages of the epidemic in New York. These factors may impact the generalizability of our findings.
Ethics oversight	This protocol, “Acquiring convalescent specimens to isolate and identify potent monoclonal antibodies against COVID-19” (AAAS9517) was approved by the Columbia University Institutional Review Board. Informed consent was obtained from all participants or surrogates. This statement is added to the manuscript.

Note that full information on the approval of the study protocol must also be provided in the manuscript.

Clinical data

Policy information about clinical studies

All manuscripts should comply with the ICMJE guidelines for publication of clinical research and a completed CONSORT checklist must be included with all submissions.

Clinical trial registration	NCT04342195
Study protocol	The protocol "Acquiring convalescent specimens to isolate and identify potent monoclonal antibodies against COVID-19" is accessible by sending request to Dr. Michael Yin <mty4@cumc.columbia.edu>.

Data collection	The study protocol was approved on 3/13/2020 and the last participant enrolled for this analysis was on 4/7/2020. All data were collected at Columbia University Irving Medical Center, New York NY. Recruitment and data collection occurred between 3/25/2020 and 4/7/2020.
Outcomes	The primary outcome for the clinical study was the SARS-CoV-2 antibody response as measured by the S-trimer and nucleocapsid ELISA and pseudovirus assays.

Flow Cytometry

Plots

Confirm that:

☒ The axis labels state the marker and fluorochrome used (e.g. CD4-FITC).

☒ The axis scales are clearly visible. Include numbers along axes only for bottom left plot of group (a 'group' is an analysis of identical markers).

☒ All plots are contour plots with outliers or pseudocolor plots.

☒ A numerical value for number of cells or percentage (with statistics) is provided.

Methodology

Sample preparation	Peripheral blood mononuclear cells from five patients and one healthy donor were stained with LIVE/DEAD™ Fixable Yellow Dead Cell Stain Kit (Invitrogen) at ambient temperature for 20 mins, followed by washing with RPMI-1640 complete medium and incubation with 10 µg/mL of S trimer at 4°C for 45 mins. Afterwards, the cells were washed again and incubated with a cocktail of flow cytometry and hashtag antibodies, containing CD3 PE-CF594 (BD Biosciences), CD19 PE-Cy7 (Biolegend), CD20 APC-Cy7 (Biolegend), IgM V450 (BD Biosciences), CD27 PerCP Cy5.5 (BD Biosciences), anti-His PE (Biolegend), and human Hashtag 3 (Biolegend) at 4°C for 1hr. Stained cells were then washed, resuspended in RPMI-1640 complete medium and sorted for S trimer-specific memory B cells (CD3-CD19+CD27+S trimer+ live single lymphocytes).
Instrument	BD FACSAriaII (P69500149)
Software	FACSDiva version 8.0.1
Cell population abundance	S trimer bait positive cells were purified from the PBMCs of the 5 patients using the gating strategy used below. Purified trimer positive memory B cells were obtained from 5 patients and compared to healthy donor (negative control) as shown in extended data figure 1.
Gating strategy	As shown in Supplementary Figure 1b, sorting of the PBMC was performed in identical manner for all the samples including healthy donor. The summary of the gating is provided herewith: All PBMCs were initially gated using FSC-A and SSC-A gates for lymphocyte populations. The lymphocytes were gated using SSC-H and SSC-W initially followed by FSC-H and FSC-W to isolate the singlets in the population. The singlets was gated based on the fluorescence from the LIVE/DEAD™ Fixable Yellow Dead Cell Stain Kit for live cells. This step was followed by selecting for CD3- population by gating the SSC-A versus CD3-PE-CF594 stained population on the Texas Red channel. The negative population was gated for B-cells by first selecting for CD19 + cells followed by CD27+ cells on the respective fluorescent channels. The subsets of CD19+ cells were then selected for S-trimer bait positive by selecting for the cells bound to anti-Histag-PE on the trimer.

☒ Tick this box to confirm that a figure exemplifying the gating strategy is provided in the Supplementary Information.

nature

https://doi.org/10.1038/s41586-020-2324-7

Accelerated Article Preview

Respiratory disease in rhesus macaques inoculated with SARS-CoV-2

Received: 22 March 2020

Accepted: 1 May 2020

Accelerated Article Preview Published online 12 May 2020

Cite this article as: Munster, V. J. et al. Respiratory disease in rhesus macaques inoculated with SARS-CoV-2. *Nature* https://doi.org/10.1038/s41586-020-2324-7 (2020).

Vincent J. Munster, Friederike Feldmann, Brandi N. Williamson, Neeltje van Doremalen, Lizzette Pérez-Pérez, Jonathan Schulz, Kimberly Meade-White, Atsushi Okumura, Julie Callison, Beniah Brumbaugh, Victoria A. Avanzato, Rebecca Rosenke, Patrick W. Hanley, Greg Saturday, Dana Scott, Elizabeth R. Fischer & Emmie de Wit

Article

Respiratory disease in rhesus macaques inoculated with SARS-CoV-2

https://doi.org/10.1038/s41586-020-2324-7

Received: 22 March 2020

Accepted: 1 May 2020

Published online: 12 May 2020

Vincent J. Munster[1], Friederike Feldmann[2], Brandi N. Williamson[1], Neeltje van Doremalen[1], Lizzette Pérez-Pérez[1], Jonathan Schulz[1], Kimberly Meade-White[1], Atsushi Okumura[1], Julie Callison[1], Beniah Brumbaugh[3], Victoria A. Avanzato[1], Rebecca Rosenke[2], Patrick W. Hanley[2], Greg Saturday[2], Dana Scott[2], Elizabeth R. Fischer[3] & Emmie de Wit[1]✉

An outbreak of a novel coronavirus, named SARS-CoV-2, causing respiratory disease and a ~2% case fatality rate started in Wuhan, China in December 2019[1,2]. Following unprecedented global spread[3], the World Health Organization declared COVID-19 a pandemic on March 11, 2020. Although data on disease in humans are emerging at a steady pace, certain aspects of the pathogenesis of SARS-CoV-2 can only be studied in detail in animal models, where repeated sampling and tissue collection is possible. Here, we show that SARS-CoV-2 causes respiratory disease in infected rhesus macaques, with disease lasting 8-16 days. Pulmonary infiltrates, a hallmark of human disease, were visible in lung radiographs. High viral loads were detected in swabs from the nose and throat of all animals as well as in bronchoalveolar lavages; in one animal we observed prolonged rectal shedding. Taken together, the rhesus macaque recapitulates moderate disease observed in the majority of human cases. The establishment of the rhesus macaque as a model of COVID-19 will increase our understanding of the pathogenesis of this disease and will aid development and testing of medical countermeasures.

SARS-CoV-2 infection in humans can be asymptomatic or result in mild to fatal Coronavirus Disease 2019 (COVID-19)[4–6]. Patients with COVID-19 pneumonia presented mainly with fever, fatigue, dyspnea and cough[7–9]. Rapidly progressing pneumonia, with bilateral opacities on x-ray or patchy shadows and ground glass opacities by CT scan were observed in COVID-19 patients[2,6,10]. Older patients with comorbidities are at highest risk for adverse outcome of COVID-19[5,7]. SARS-CoV-2 has been detected in upper and lower respiratory tract samples from patients, as well as feces and blood, but not in urine[5,11–13].

Non-human primate models that recapitulate aspects of human disease are essential for our understanding of the pathogenic processes involved in severe respiratory disease and the development of medical countermeasures such as vaccines and antivirals.

Clinical, respiratory disease

Eight adult rhesus macaques were inoculated with SARS-CoV-2 isolate nCoV-WA1-2020[14]. On day 1 post inoculation (dpi), all animals showed changes in respiratory pattern and piloerection, as reflected in their clinical scores (Fig. 1a). Other observed signs of disease included reduced appetite, hunched posture, pale appearance and dehydration (Extended Data Table 1). Coughing was occasionally heard in the room where animals were housed but could not be pinpointed to individual animals. Disease signs persisted for more than a week, with all animals completely recovered between 9 and 17 dpi (Fig. 1a and Table S1). Weight loss was observed in all animals (Fig. 1b); body temperatures spiked on 1 dpi but returned to normal levels thereafter (Fig. 1c). Under anesthesia, the animals did not show increased respiration; however, all animals showed irregular respiration patterns (Fig. 1d). Radiographs showed pulmonary infiltrates in all animals starting on 1 dpi with mild pulmonary infiltration primarily in the lower lung lobes. By 3 dpi, progression of mild pulmonary infiltration was noted into other lung lobes although still primarily in the caudal lung lobes (Fig. 1e). In one animal, pulmonary infiltrates were observed from 1-12 dpi (Extended Data Fig. 1).

Hematologic analysis of blood collected during clinical exams showed evidence of a stress leukogram[15] by 1 dpi in the majority of animals (Extended Data Fig. 2). Lymphocytes and monocytes returned to baseline after 1 dpi. Neutrophils decreased in all animals by 3 dpi and continued to decline through 5 dpi; neutropenia was observed in 2 of 4 animals. On 1 dpi, decreased hematocrit, red blood cell counts and hemoglobin were observed in all animals (Extended Data Fig. 2). In addition, reticulocyte percentages and counts decreased. At 5 dpi, two of four animals had a normocytic, normochromic non-regenerative anemia consistent with anemia of critical illness; animals did not return to their original baselines by 21 dpi. Blood chemistry analysis revealed no values outside normal range (Supplementary Information Table S2).

Serum was analyzed for changes in cytokine and chemokine levels at different time points after inoculation. Statistically significant changes were only observed on 1 dpi, with increases in IL1ra, IL6, IL10, IL15, MCP-1, MIP-1b, and on 3 dpi a small but statistically significant decrease in TGFα was observed (Extended Data Fig. 3). Although changes occurred

[1]Laboratory of Virology, National Institute of Allergy and Infectious Diseases, National Institutes of Health, Hamilton, MT, USA. [2]Rocky Mountain Veterinary Branch, National Institute of Allergy and Infectious Diseases, National Institutes of Health, Hamilton, MT, USA. [3]Research Technologies Branch, National Institute of Allergy and Infectious Diseases, National Institutes of Health, Hamilton, MT, USA. ✉e-mail: emmie.dewit@nih.gov

in the levels of some of these cytokines later after inoculation, these were not statistically significant (Extended Data Fig. 3).

High viral loads in respiratory samples

Virus shedding was highest from the nose (Fig. 2a); virus could be isolated from swabs collected on 1 and 3 dpi, but not thereafter. Viral loads were high in throat swabs immediately after inoculation but were less consistent than nose swabs thereafter; in one animal throat swabs were positive on 1 and 10 dpi but not in between (Fig. 2a). One animal showed prolonged shedding of viral RNA in rectal swabs; infectious virus could not be isolated from these swabs (Fig. 2a) and intestinal tract disease (e.g. diarrhea) was not observed. Urogenital swabs remained negative in all animals throughout the study. On 1, 3 and 5 dpi bronchoalveolar lavages (BAL) were performed on the 4 animals in the group euthanized on 21 dpi. High viral loads were detected in BAL fluid in all animals on all three time points; infectious virus could only be isolated in BAL fluid collected on 1 and 3 dpi (Fig. 2b). No viral RNA could be detected in blood (Fig. 2c) or urine (Fig. 2d).

Interstitial pneumonia

On 3 and 21 dpi, one group of 4 animals was euthanized and necropsies were performed.

On 3 dpi, varying degrees of gross lung lesions were observed in all animals (Fig. 3a and c). By 21 dpi, gross lesions were still visible in the lungs of 2 of 4 animals (Fig. 3b and c). Additionally, all animals had an increased lung weight:body weight ratio (Fig. 3d) as compared to healthy rhesus macaques, indicative of pulmonary edema. Histologically, 3 of the 4 animals euthanized on 3 dpi developed some degree of pulmonary pathology. Lesions were multifocal (Extended Data Fig. 4a), mild to moderate, interstitial pneumonia that frequently centered on terminal bronchioles. The pneumonia was characterized by thickening of alveolar septae by edema fluid and fibrin and small to moderate numbers of macrophages and fewer neutrophils. Lungs with moderate changes also had alveolar edema and fibrin with formation of hyaline membranes. There was minimal type II pneumocyte hyperplasia. Occasionally, bronchioles showed necrosis, loss and attenuation of the epithelium with infiltrates of neutrophils, macrophages and eosinophils. Multifocally, there were perivascular infiltrates of small numbers of lymphocytes forming perivascular cuffs (Extended Data Figure 4b) and minimal to mild, multifocal hyperplasia of bronchiolar associated lymphoid tissue. Three of 4 animals on 3 dpi had fibrous adhesions of the lung to the pleura. Histologic evaluation showed these to be composed of mature collagen interspersed with small blood vessels; therefore, this is most likely a chronic change rather than related to SARS-CoV-2 infection. Minimal to mild inflammation was observed in the upper airways with multifocal squamous metaplasia of the respiratory epithelium with infiltration of small numbers of neutrophils (Extended Data Figure 5).

Immunohistochemistry using a mAb against SARS-CoV demonstrated viral antigen in small numbers of type I and II pneumocytes, as well as alveolar macrophages. Antigen-positive macrophages were detected in mediastinal lymph nodes of 3 of 4 animals (Fig. 3k). Interestingly, small numbers of antigen-positive lymphocytes and macrophages were also detected in the lamina propria of the intestinal tract of all 4 animals. In one animal, all collected tissues of the gastrointestinal tract showed these antigen-positive mononuclear cells (Extended Data Figure 6).

Ultrastructural analysis of lung tissue by transmission electron microscopy confirmed the histologic diagnosis of interstitial pneumonia. The alveolar interstitial space was greatly expanded by edema, fibrin, macrophages and neutrophils (Extended Data Figure 7a). The subepithelial basement membrane was unaffected and maintained a consistent thickness and electron density. Occasionally, type I pneumocytes are separated from the basement membrane by edema; the resulting space may contain virions. Affected type I pneumocytes are lined by small to moderate numbers of virions 90-160 nm in diameter with an electron dense core bound by a less dense capsid (Extended Data Figure 7b-e). Alveolar spaces adjacent to affected pneumocytes are filled with a granular, moderately electron dense material that is consistent with edema fluid.

Replication in the respiratory tract

All tissues (n=37) collected at necropsy were analyzed for the presence of viral RNA. On 3 dpi, high viral loads were detected in the lungs of all animals (Extended Data Fig. 8a); virus could be isolated from the lungs of all 4 animals at this time. Additionally, viral RNA could be detected in other samples throughout the respiratory tract (Extended Data Fig. 8), as well as in lymphoid and gastrointestinal tissues. Viral RNA could not be detected in major organs including the central nervous system. To distinguish viral RNA derived from respiratory secretions from active virus replication, all samples with presence of viral RNA were also tested for the presence of viral mRNA (Extended Data Fig. 8). Viral mRNA was detected in all respiratory tissues but could not in any but one of the gastrointestinal tissues, indicating that virus replication in these tissues seems unlikely, although we can't exclude it due to limited sample size. By 21 dpi, viral RNA, but not mRNA, could still be detected in tissues from all 4 animals (Extended Data Fig. 8g).

Serology

Serum was analyzed for the development of IgG against SARS-CoV spike in ELISA. By 10 dpi, all four animals had seroconverted to SARS-CoV-2 spike; neutralizing responses also started to appear at 10 dpi (Extended Data Figure 9). Interestingly, the animal with the lowest and latest neutralizing antibody response was the animal with prolonged viral shedding from the intestinal tract.

Discussion

COVID-19 clinical manifestations range from asymptomatic to mild to severe[5,6,8,9,13,16]. Patients present with influenza-like symptoms such as fever and shortness of breath and may develop pneumonia requiring mechanical ventilation and support in an intensive care unit[9]. Similar to SARS-CoV and MERS-CoV, comorbidities such as hypertension and diabetes play an important role in adverse outcome of COVID-19[8,17,18]. Advanced age and chronic conditions in particular are indicators of a negative outcome[5,7–9,16], conditions that were absent in our healthy rhesus macaques. An analysis of 1099 COVID-19 cases from China showed that approximately 5% of diagnosed patients developed severe pneumonia requiring ICU attendance, 2.3% required mechanical ventilation and 1.4% died[9]. The transient, moderate disease observed here in rhesus macaques is thus in line with the majority of human COVID-19 cases. Pulmonary infiltrates on radiographs, a hallmark of human infection[2,4,6,7,9,10,16], were observed in all macaques. The shedding pattern observed in rhesus macaques is strikingly similar to that observed in humans[11,12]. In humans, consistent high SARS-CoV-2 shedding was observed from the upper and lower respiratory tract, frequent intermediate shedding from the intestinal tract and sporadic detection in blood[5]. Similar to humans, shedding of SARS-CoV-2 continued after resolution of clinical symptoms and radiologic abnormalities[19]. Limited histopathology is available from COVID-19 patients[20,21]. Our analysis of the histopathological changes observed in the lungs of rhesus macaques, suggests that they resemble those observed with SARS-CoV and MERS-CoV[21–24], with regard to lesion type and cell tropism.

Serological responses in humans are not typically detectable before 6 days after symptom onset, with IgG titers between 100 and 10,000 observed after 12 to 21 days[25,26]. Neutralizing titers were generally between 20 – 160. This corresponds to the results in our rhesus

macaque model, where IgG responses were detected around 7-10 dpi. Seroconversion was not directly followed by a decline in viral loads, as observed in COVID-19 patients[25,26].

Taken together, the rhesus macaque model recapitulates COVID-19, with regard to virus replication and shedding, the presence of pulmonary infiltrates, histological lesions and seroconversion. This extensive dataset allows us to bridge between the rhesus macaques model and the disease observed in humans and to utilize this animal model to assess the efficacy of medical countermeasures.

Online content

Any methods, additional references, Nature Research reporting summaries, source data, extended data, supplementary information, acknowledgements, peer review information; details of author contributions and competing interests; and statements of data and code availability are available at https://doi.org/10.1038/s41586-020-2324-7.

1. Wu, F. *et al*. A new coronavirus associated with human respiratory disease in China. *Nature*, https://doi.org/10.1038/s41586-020-2008-3 (2020).
2. Zhu, N. *et al*. A Novel Coronavirus from Patients with Pneumonia in China, 2019. *N Engl J Med* **382**, 727-733, https://doi.org/10.1056/NEJMoa2001017 (2020).
3. Organization, W. H. *Coronavirus disease (COVID-2019) situation reports*, https://www.who.int/emergencies/diseases/novel-coronavirus-2019/situation-reports/ (2020).
4. Yang, W. *et al*. Clinical characteristics and imaging manifestations of the 2019 novel coronavirus disease (COVID-19):A multi-center study in Wenzhou city, Zhejiang, China. *J Infect*, https://doi.org/10.1016/j.jinf.2020.02.016 (2020).
5. Yang, X. *et al*. Clinical course and outcomes of critically ill patients with SARS-CoV-2 pneumonia in Wuhan, China: a single-centered, retrospective, observational study. *Lancet Respir Med*, https://doi.org/10.1016/S2213-2600(20)30079-5 (2020).
6. Silverstein, W. K., Stroud, L., Cleghorn, G. E. & Leis, J. A. First imported case of 2019 novel coronavirus in Canada, presenting as mild pneumonia. *Lancet* **395**, 734, https://doi.org/10.1016/S0140-6736(20)30370-6 (2020).
7. Arentz, M. *et al*. Characteristics and Outcomes of 21 Critically Ill Patients With COVID-19 in Washington State. *JAMA*, https://doi.org/10.1001/jama.2020.4326 (2020).
8. Zhou, F. *et al*. Clinical course and risk factors for mortality of adult inpatients with COVID-19 in Wuhan, China: a retrospective cohort study. *Lancet*, https://doi.org/10.1016/S0140-6736(20)30566-3 (2020).
9. Guan, W. J. *et al*. Clinical Characteristics of Coronavirus Disease 2019 in China. *N Engl J Med*, https://doi.org/10.1056/NEJMoa2002032 (2020).
10. Shi, H. *et al*. Radiological findings from 81 patients with COVID-19 pneumonia in Wuhan, China: a descriptive study. *Lancet Infect Dis*, https://doi.org/10.1016/S1473-3099(20)30086-4 (2020).
11. Zou, L. *et al*. SARS-CoV-2 Viral Load in Upper Respiratory Specimens of Infected Patients. *N Engl J Med*, https://doi.org/10.1056/NEJMc2001737 (2020).
12. Kim, J. Y. *et al*. Viral Load Kinetics of SARS-CoV-2 Infection in First Two Patients in Korea. *J Korean Med Sci* **35**, e86, https://doi.org/10.3346/jkms.2020.35.e86 (2020).
13. Tang, A. *et al*. Detection of Novel Coronavirus by RT-PCR in Stool Specimen from Asymptomatic Child, China. *Emerg Infect Dis* **26**, https://doi.org/10.3201/eid2606.200301 (2020).
14. Harcourt, J. *et al*. Severe Acute Respiratory Syndrome Coronavirus 2 from Patient with 2019 Novel Coronavirus Disease, United States. *Emerg Infect Dis* **26**, https://doi.org/10.3201/eid2606.200516 (2020).
15. Everds, N. E. *et al*. Interpreting stress responses during routine toxicity studies: a review of the biology, impact, and assessment. *Toxicol Pathol* **41**, 560-614, https://doi.org/10.1177/0192623312466452 (2013).
16. Wang, D. *et al*. Clinical Characteristics of 138 Hospitalized Patients With 2019 Novel Coronavirus-Infected Pneumonia in Wuhan, China. *JAMA*, https://doi.org/10.1001/jama.2020.1585 (2020).
17. Assiri, A. *et al*. Epidemiological, demographic, and clinical characteristics of 47 cases of Middle East respiratory syndrome coronavirus disease from Saudi Arabia: a descriptive study. *Lancet Infect Dis* **13**, 752-761, https://doi.org/10.1016/S1473-3099(13)70204-4 (2013).
18. Booth, C. M. *et al*. Clinical features and short-term outcomes of 144 patients with SARS in the greater Toronto area. *JAMA* **289**, 2801-2809, https://doi.org/10.1001/jama.289.21.JOC30885 (2003).
19. Lan, L. *et al*. Positive RT-PCR Test Results in Patients Recovered From COVID-19. *JAMA*, https://doi.org/10.1001/jama.2020.2783 (2020).
20. Tian, S. *et al*. Pulmonary Pathology of Early-Phase 2019 Novel Coronavirus (COVID-19) Pneumonia in Two Patients With Lung Cancer. *J Thorac Oncol*, https://doi.org/10.1016/j.jtho.2020.02.010 (2020).
21. Xu, Z. *et al*. Pathological findings of COVID-19 associated with acute respiratory distress syndrome. *Lancet Respir Med*, https://doi.org/10.1016/S2213-2600(20)30076-X (2020).
22. Ng, D. L. *et al*. Clinicopathologic, Immunohistochemical, and Ultrastructural Findings of a Fatal Case of Middle East Respiratory Syndrome Coronavirus Infection in the United Arab Emirates, April 2014. *Am J Pathol* **186**, 652-658, https://doi.org/10.1016/j.ajpath.2015.10.024 (2016).
23. Nicholls, J. M. *et al*. Lung pathology of fatal severe acute respiratory syndrome. *Lancet* **361**, 1773-1778, https://doi.org/10.1016/s0140-6736(03)13413-7 (2003).
24. Ding, Y. *et al*. The clinical pathology of severe acute respiratory syndrome (SARS): a report from China. *J Pathol* **200**, 282-289, https://doi.org/10.1002/path.1440 (2003).
25. Roman Wölfel*, Victor M. Corman, W. G., Michael Seilmaier, Sabine Zange, Marcel A. Müller, Daniela Niemeyer, Terence C. Jones Kelly, Patrick Vollmar, Camilla Rothe, Michael Hoelscher, Tobias Bleicker, Sebastian Brünink, Julia Schneider, Rosina Ehmann, Katrin Zwirglmaier, Christian Drosten, Clemens Wendtner. Virological assessment of hospitalized cases of coronavirus disease 2019. *MEDRXIV* (2020).
26. Zhao, Y., Wang, Liu, Liao, Su, Wang, Yuan, Li, Li, Qian, Hong, Wang, Liu, Wang, He, Li, He, Zhang, Ge, Liu, Zhang, Xia, Zhang. Antibody responses to SARS-CoV-2 in patients of novel coronavirus disease 2019. *medRxiv* (2020).

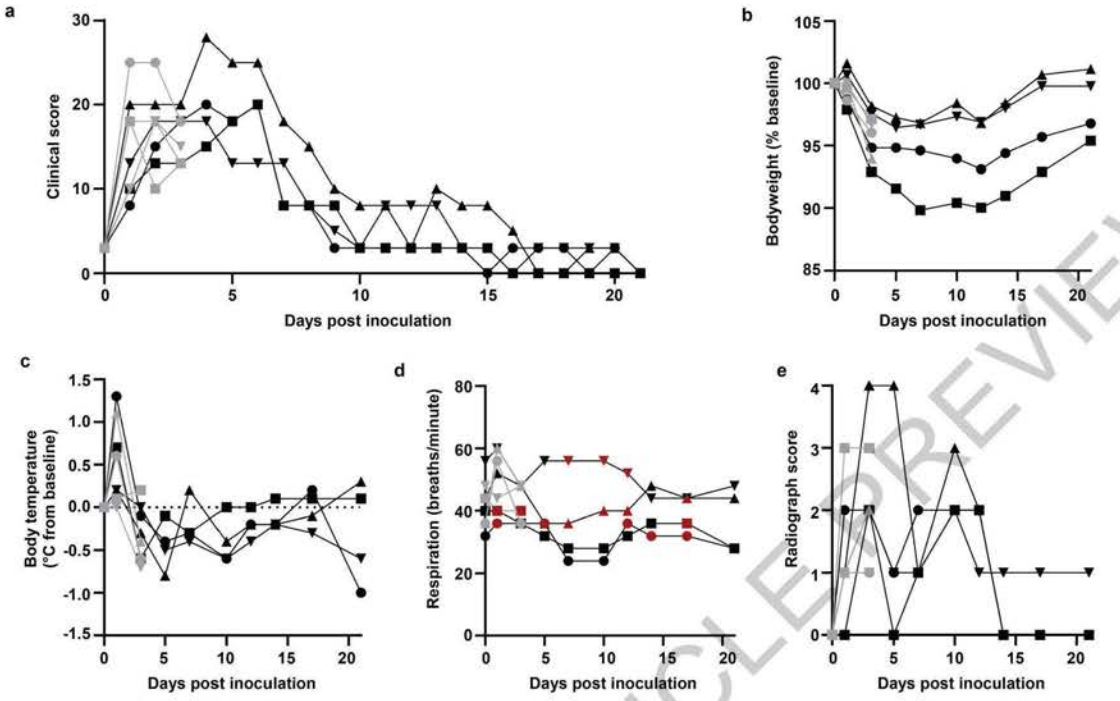

Fig. 1 | Rhesus macaques infected with SARS-CoV-2 develop respiratory disease. After inoculation with SARS-CoV-2, animals were observed for disease signs and scored according to a pre-established clinical scoring sheet (a). On clinical exams, body weight (b), and body temperature (c) were measured. Respiration rate was measured, and breathing pattern was recorded, with irregular respiration patterns indicated in red (d). Ventro-dorsal and lateral radiographs were taken on clinical exam days and scored for the presence of pulmonary infiltrates (0: normal; 1: mild interstitial pulmonary infiltrates; 2: moderate pulmonary infiltrates perhaps with partial cardiac border effacement and small areas of pulmonary consolidation; 3: severe interstitial infiltrates, large areas of pulmonary consolidation, alveolar patterns and air bronchograms). Individual lobes were scored and scores per animal per day totaled (e). Grey: animals euthanized 3 dpi; black: animals euthanized 21 dpi. Identical symbols have been used to denote identical animals throughout this manuscript.

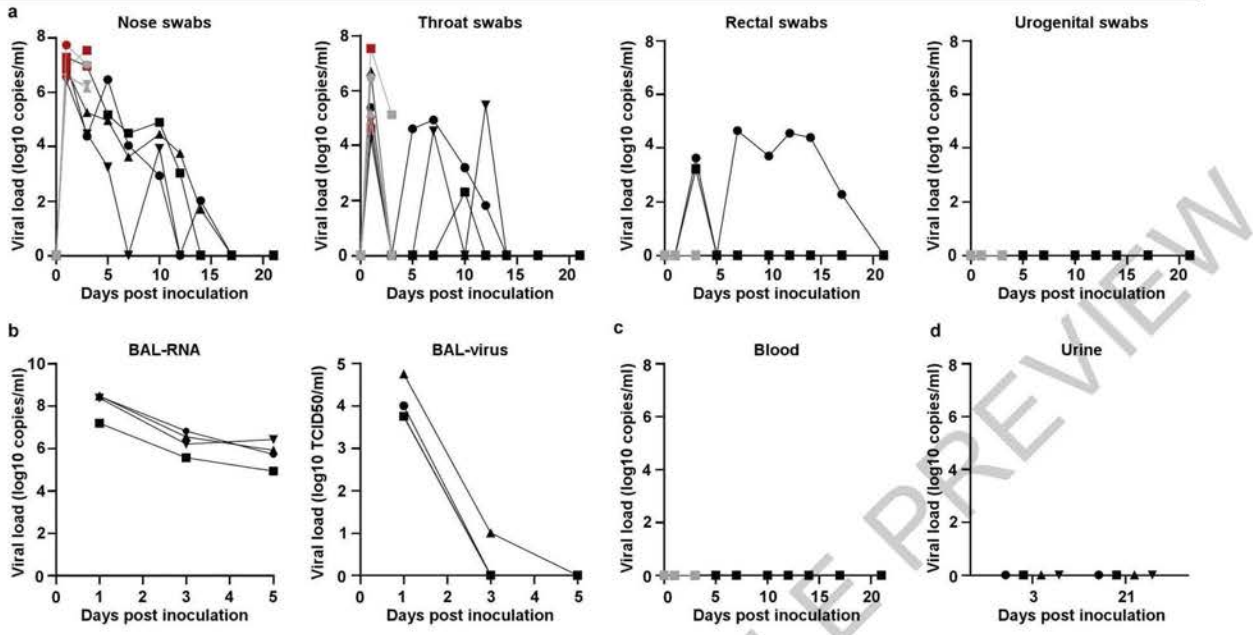

Fig. 2 | Viral loads in respiratory samples and bodily fluids. After inoculation, nose, throat, rectal and urogenital swabs were collected; viral loads in these samples were determined by qRT-PCR (a). On 1, 3, and 5 dpi, bronchoalveolar lavages were performed on the 4 animals remaining in the study through 21 dpi; viral loads and virus titers were determined in these samples. Viral loads were determined in blood collected during clinical exams (c) and urine collected at necropsy on 3 and 21 (d). Grey: animals euthanized 3 dpi; black: animals euthanized 21 dpi; red: virus was isolated from these samples. Identical symbols have been used to denote identical animals this manuscript.

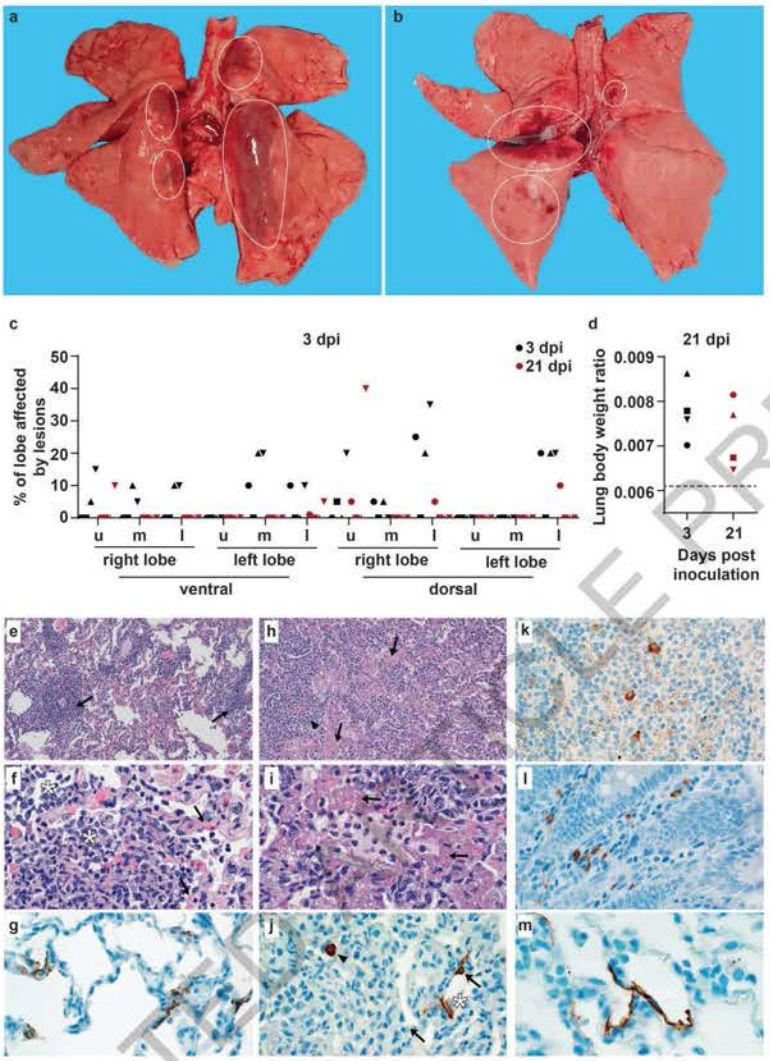

Fig. 3 | Pathological changes in rhesus macaques infected with SARS-CoV-2. Four rhesus macaques were euthanized on 3 and 21 dpi. Grossly, lungs showed focal areas of hilar consolidation and hyperemia (circles) on 3 dpi (a) and multifocal, random consolidation and hyperemia (circles) on 21 dpi (b). The percentage of the area of the lungs affected by gross lesions was estimated (c), and lung weight to body weight ratio was calculated. (d). The dotted line represents baseline ratio calculated from an in-house collection of rhesus macaque lung and bodyweights from animals with grossly normal lungs. Histological analysis was performed on tissues collected at 3 dpi (e-i). Tissue sections were collected from the same anatomical location for each animal; three tissue sections were prepared from each of the 6 lung lobes. In total, 18 lung sections were evaluated for each animal; representative images are displayed. (e) Pulmonary vessels surrounded by moderate numbers of lymphocytes and fewer macrophages (arrows). (f) Alveoli filled with small to moderate numbers of macrophages and neutrophils (asterisks). Adjacent alveolar interstitium (arrows) is thickened by edema, fibrin, neutrophils, lymphocytes and macrophages. (g) SARS-CoV-2 antigen detected by immunohistochemistry in type I pneumocytes. (h) Pulmonary vessels bounded by lymphocytes (arrowhead) and hyaline membranes (arrows) line alveolar spaces. (i) Hyaline membranes line alveoli (arrows). (j) SARS-CoV-2 antigen detected by immunohistochemistry in type I pneumocytes (asterisk) and type II pneumocytes (arrow) as well as alveolar macrophages (arrowheads). (k) SARS-CoV-2 antigen detected by immunohistochemistry in macrophages in a mediastinal lymph node. (l) SARS-CoV-2 antigen detected by immunohistochemistry in macrophages and lymphocytes in the lamina propria of the cecum. (m) SARS-CoV-2 detected by immunohistochemistry in type I pneumocytes. Magnification: e, h 100x; f, g, I, j, k, l 400x; m: 1000x. u: upper; m: middle; l: lower.

Methods

Ethics and biosafety statement

All animal experiments were approved by the Institutional Animal Care and Use Committee of Rocky Mountain Laboratories, NIH and carried out by certified staff in an Association for Assessment and Accreditation of Laboratory Animal Care (AAALAC) International accredited facility, according to the institution's guidelines for animal use, following the guidelines and basic principles in the NIH Guide for the Care and Use of Laboratory Animals, the Animal Welfare Act, United States Department of Agriculture and the United States Public Health Service Policy on Humane Care and Use of Laboratory Animals. Rhesus macaques were housed in adjacent individual primate cages allowing social interactions, in a climate-controlled room with a fixed light-dark cycle (12-hr light/12-hr dark). Animals were monitored at least twice daily throughout the experiment. Commercial monkey chow, treats, and fruit were provided twice daily by trained personnel. Water was available ad libitum. Environmental enrichment consisted of a variety of human interaction, manipulanda, commercial toys, videos, and music. The Institutional Biosafety Committee (IBC) approved work with infectious SARS-CoV-2 strains under BSL3 conditions. Sample inactivation was performed according to IBC-approved standard operating procedures for removal of specimens from high containment.

Study design

To evaluate the use of rhesus macaques as a model for SARS-CoV-2, eight adult rhesus macaques (4 males, and4 females, age 4-6 years) were inoculated via a combination of intranasal (0.5ml per nostril), intratracheal (4ml), oral (1ml) and ocular (0.25ml per eye) of a $4x10^5$ TCID50/ml ($3x10^8$ genome copies/ml) virus dilution in sterile DMEM. The animals were observed twice daily for clinical signs of disease using a standardized scoring sheet (Supplementary Information Table S1); the same person assessed the animals throughout the study. The predetermined endpoint for this experiment was 3 days post inoculation (dpi) for one group of 4 animals, and 21 dpi for the remaining 4 animals. Animals were randomly assigned to a group for necropsy prior to the start of the experiment. Blinding was not used in this study since all animals were subjected to the same treatment. Clinical exams were performed on 0, 1, 3, 5, 7, 10, 12, 14, 17 and 21 dpi on anaesthetized animals. On exam days, clinical parameters such as bodyweight, body temperature and respiration rate were collected, as well as ventro-dorsal and lateral chest radiographs. Chest radiographs were interpreted by a board-certified clinical veterinarian. The following samples were collected at all clinical exams: nasal, throat, urogenital and rectal swabs, blood. The total white blood cell count, lymphocyte, neutrophil, platelet, reticulocyte and red blood cell counts, hemoglobin, and hematocrit values were determined from EDTA blood with the IDEXX ProCyte DX analyzer (IDEXX Laboratories). Serum biochemistry (albumin, AST, ALT, GGT, BUN, creatinine) was analyzed using the Piccolo Xpress Chemistry Analyzer and Piccolo General Chemistry 13 Panel discs (Abaxis). During clinical exams on 1, 3, and 5 dpi bronchoalveolar lavages were performed using 10ml sterile saline. Of note, repeated bronchoalveolar lavages do not induce lung damage when space 48 hrs apart[27,28]. After euthanasia, necropsies were performed. The percentage of gross lung lesions was scored by a board-certified veterinary pathologist and samples of the following tissues were collected: inguinal lymph node, axillary lymph node, cervical lymph node, salivary gland, conjunctiva, nasal mucosa, oropharynx, tonsil, trachea, all six lung lobes, mediastinal lymph node, right and left bronchus, heart, liver, spleen, pancreas, adrenal gland, kidney, mesenteric lymph node, stomach, duodenum, jejunum, ileum, cecum, colon, urinary bladder, reproductive tract (testes or ovaries depending on sex of the animal), bone marrow, frontal brain, cerebellum and brainstem. Histopathological analysis of tissue slides was performed by a board-certified veterinary pathologist blinded to the group assignment of the animals.

Virus and cells

SARS-CoV-2 isolate nCoV-WA1-2020 (MN985325.1)[14] (Vero passage 3) was kindly provided by CDC and propagated once in VeroE6 cells in DMEM (Sigma) supplemented with 2% fetal bovine serum (Gibco), 1 mM L-glutamine (Gibco), 50 U/ml penicillin and 50 µg/ml streptomycin (Gibco) (virus isolation medium). The used virus stock was 100% identical to the initial deposited genbank sequence (MN985325.1) and no contaminants were detected. VeroE6 cells were maintained in DMEM supplemented with 10% fetal calf serum, 1 mM L-glutamine, 50 U/ml penicillin and 50 µg/ml streptomycin. VeroE6 cells were provided by Dr. Ralph Baric and were not authenticated in-house; mycoplasma testing is performed at regular intervals and no mycoplasma has been detected.

Quantitative PCR

RNA was extracted from swabs and BAL using the QiaAmp Viral RNA kit (Qiagen) according to the manufacturer's instructions. Tissues (30 mg) were homogenized in RLT buffer and RNA was extracted using the RNeasy kit (Qiagen) according to the manufacturer's instructions. For detection of viral RNA, 5 µl RNA was used in a one-step real-time RT-PCR E assay[29] using the Rotor-Gene probe kit (Qiagen) according to instructions of the manufacturer. In each run, standard dilutions of counted RNA standards were run in parallel, to calculate copy numbers in the samples. For detection of SARS-CoV-2 mRNA, primers targeting open reading frame 7 (ORF7) were designed as follows: forward primer 5'-TCCCAGGTAACAAACCAACC-3', reverse primer 5'-GCTCACAAGTAGCGAGTGTTAT-3', and probe FAM-ZEN-CTTGTAGATCTGTTCTCTAAACGAAC-IBFQ. 5 µl RNA was used in a one-step real-time RT-PCR using the Rotor-Gene probe kit (Qiagen) according to instructions of the manufacturer. In each run, standard dilutions of counted RNA standards were run in parallel, to calculate copy numbers in the samples.

Histopathology and immunohistochemistry

Histopathology and immunohistochemistry were performed on rhesus macaque tissues. After fixation for a minimum of 7 days in 10% neutral-buffered formalin and embedding in paraffin, tissue sections were stained with hematoxylin and eosin (HE). To detect SARS-CoV-2 antigen, immunohistochemistry was performed using an anti-SARS nucleocapsid protein antibody (Novus Biologicals) at a 1:250 dilution. This antibody was first tested on SARS-CoV-2 infected and uninfected Vero E6 cell pellets, showing specific staining with infected cells and no staining with uninfected cells. The antibody showed specific staining with infected experimental tissue and no staining with uninfected tissue from rhesus macaques. Infected tissue and cell pellet specimens showed no staining when run with Rabbit IgG controls (non-specific rabbit IgG substituted for primary antibody). Stained slides were analyzed by a board-certified veterinary pathologist.

Transmission electron microscopy. After fixation for 7 days with Karnovsky's fixative at 4 °C, excised tissues were post-fixed for 1 hour with 0.5% osmium tetroxide/0.8% potassium ferricyanide in 0.1 M sodium cacodylate, washed 3 x 5 minutes with 0.1M sodium cacodylate buffer, stained 1 hour with 1% tannic acid, washed with buffer and then further stained with2% osmium tetroxide in 0.1M sodium cacodylate and overnight with 1% uranyl acetate at 4 °C. Specimens were dehydrated with a graded ethanol series with two final exchanges in 100% propylene oxide before infiltration and final embedding in Embed-812/Araldite resin. Thin sections were cut with a Leica EM UC6 ultramicrotome (Leica, Vienna, Austria), prior to viewing at 120 kV on a Tecnai BT Spirit transmission electron microscope (Thermo fisher/FEI, Hillsboro, OR). Digital images were acquired with a Gatan Rio bottom mount digital camera system (Gatan Inc., Pleasanton, CA

and processed using Adobe Photoshop v. CC 2019 (Adobe Systems Inc, San Jose, CA).

Serum cytokine and chemokine analysis. Serum samples for analysis of cytokine/chemokine levels were inactivated with γ-radiation (2 MRad) according to standard operating procedures. Concentrations of granulocyte colony-stimulating factor, granulocyte-macrophage colony-stimulating factor, interferon (IFN)−γ, interleukin (IL)−1β, IL-1 receptor antagonist, IL-2, IL-4, IL-5, IL-6, IL-8, IL-10, IL-12/23 (p40), IL-13, IL-15, IL-17, MCP-1 and macrophage inflammatory protein (MIP)−1α, MIP-1β, soluble CD40-ligand (sCD40L), transforming growth factor-α, tumor necrosis factor (TNF)−α, vascular endothelial growth factor (VEGF) and IL-18 were measured on a Bio-Plex 200 instrument (Bio-Rad) using the Non-Human Primate Cytokine MILLIPLEX map 23-plex kit (Millipore) according to the manufacturer's instructions.

Serology

Sera were analyzed by SARS-CoV-2 spike protein (S) enzyme-linked immunosorbent assay (ELISA) as done previously for MERS-CoV[30]. Briefly, maxisorp (Nunc) plates were coated overnight with 100 ng/well S protein diluted in PBS[31] (a kind gift of Barney Graham, Vaccine Research Center, NIH) and blocked with blocker casein in PBS (Life Technologies). Sera were serially diluted in duplicate. SARS-CoV-2-specific antibodies were detected using anti-monkey IgG polyclonal antibody HRP-conjugated antibody (KPL), peroxidase-substrate reagent (KPL) and stop reagent (KPL). Optical density (OD) was measured at 405 nm. The threshold of positivity was calculated by taking the average of the day 0 values multiplied by 3.

For neutralization, sera were heat-inactivated (30 min, 56 °C) and two-fold serial dilutions were prepared in 2% DMEM. Hereafter, 100 $TCID_{50}$ of SARS-CoV-2 was added. After 60 min incubation at 37 °C, virus:serum mixture was added to VeroE6 cells and incubated at 37 °C and 5% CO2. At 5 dpi, cytopathic effect was scored. The virus neutralization titer is expressed as the reciprocal value of the highest dilution of the serum which still inhibited virus replication. All sera were analyzed in duplicate.

Reporting summary

Further information on research design is available in the Nature Research Reporting Summary linked to this paper.

Data availability

Data have been deposited in Figshare: https://doi.org/10.35092/yhjc.12026910.

27. Haley, P. J., Muggenburg, B. A., Rebar, A. H., Shopp, G. M. & Bice, D. E. Bronchoalveolar lavage cytology in cynomolgus monkeys and identification of cytologic alterations following sequential saline lavage. *Vet Pathol* **26**, 265-273, https://doi.org/10.1177/030098588902600312 (1989).
28. Krombach, F. *et al*. Short-term and long-term effects of serial bronchoalveolar lavages in a nonhuman primate model. *Am J Respir Crit Care Med* **150**, 153-158, https://doi.org/10.1164/ajrccm.150.1.8025742 (1994).
29. Corman, V. M. *et al*. Detection of 2019 novel coronavirus (2019-nCoV) by real-time RT-PCR. *Euro Surveill* **25**, https://doi.org/10.2807/1560-7917.ES.2020.25.3.2000045 (2020).
30. van Doremalen, N. *et al*. High Prevalence of Middle East Respiratory Coronavirus in Young Dromedary Camels in Jordan. *Vector Borne Zoonotic Dis* **17**, 155-159, https://doi.org/10.1089/vbz.2016.2062 (2017).
31. Wrapp, D. *et al*. Cryo-EM structure of the 2019-nCoV spike in the prefusion conformation. *Science* **367**, 1260-1263, https://doi.org/10.1126/science.abb2507 (2020).

Acknowledgements The authors would like to thank Susan Gerber and Natalie Thornburg (CDC) for providing the SARS-CoV-2 isolate used in this study; Barney Graham, Kizzmekia Corbett and Olubukola Abiona at the Vaccine Research Center (NIAID, NIH) for providing spike protein for serology; Anita Mora (NIAID, NIH) for help with figure design and staff of the Rocky Mountain Veterinary Branch (NIAID, NIH) for animal care. This study was supported by the Intramural Research Program, NIAID, NIH.

Author contributions VJM and EdW designed the study; VJM, FF, BW, NvD, LPP, JS, KMW, AO, JC, BB, VAA, RR, PH, GS, EF, DS and EdW acquired, analyzed and interpreted the data; VJM, PH, EF, DS and EdW wrote the manuscript. All authors have approved the submitted version.

Competing interests The authors declare no competing interests.

Additional information

Supplementary information is available for this paper at https://doi.org/10.1038/s41586-020-2324-7.

Correspondence and requests for materials should be addressed to E.d.W.

Peer review information *Nature* thanks Wolfgang Baumgärtner, Menno D. de Jong and Patricia Pesavento for their contribution to the peer review of this work.

Reprints and permissions information is available at http://www.nature.com/reprints.

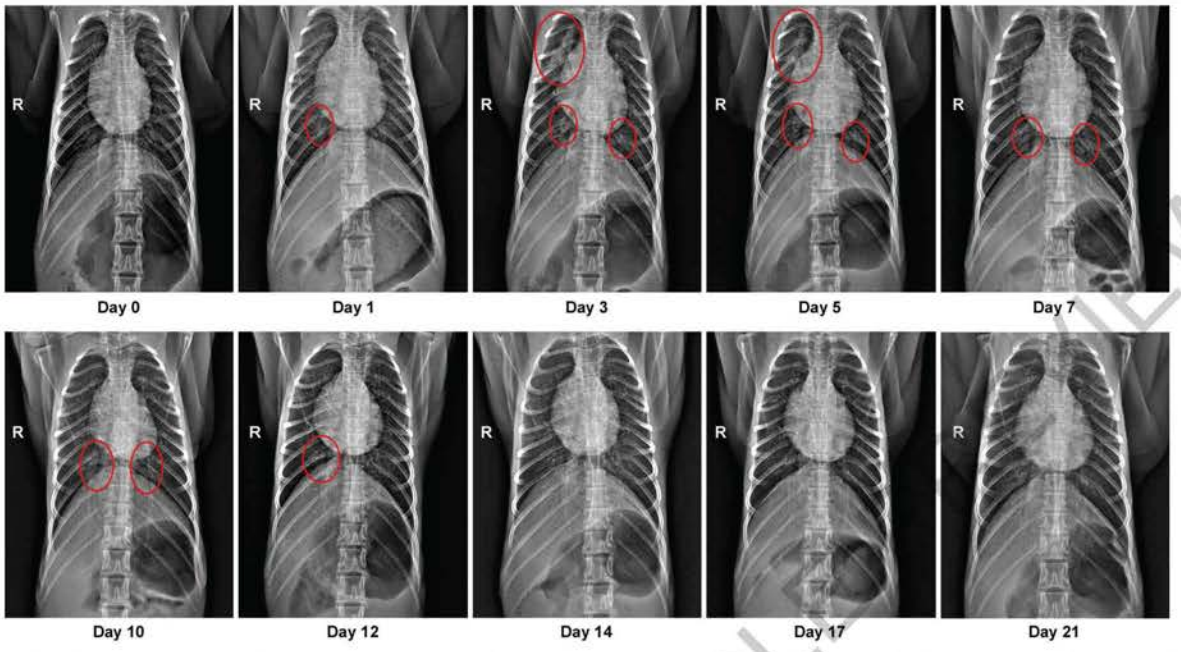

Extended Data Fig. 1 | Pulmonary infiltrates in a rhesus macaque after inoculation. Radiographs show the progression of pulmonary infiltrates throughout the study in a single animal. Of note, this animal is denoted with a black triangle throughout the manuscript. Circles indicate areas of mild to moderate pulmonary infiltrates. A marker 'R' indicates right side of the animal. Three chest radiographs were taken at each timepoint: right-lateral, left-lateral and ventro-dorsal; only the ventro-dorsal radiograph is shown.

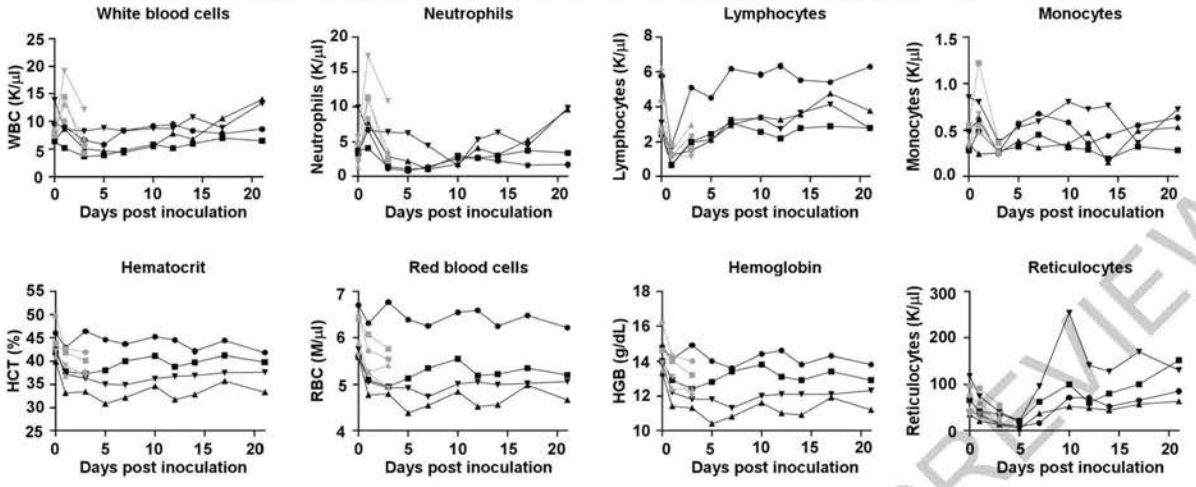

Extended Data Fig. 2 | Hematological changes in rhesus macaques infected with SARS-CoV-2. Identical symbols have been used to denote identical animals throughout the figures in this manuscript. n= 8 animals on 0, 1, and 3 dpi and n=4 animals thereafter.

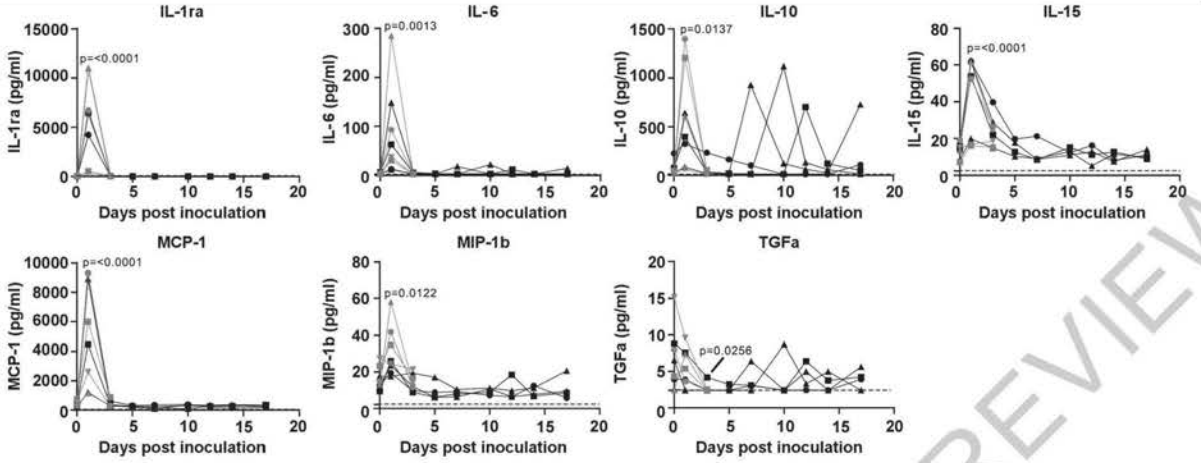

Extended Data Fig. 3 | Cytokine and chemokine levels in serum of rhesus macaques infected with SARS-CoV-2. The levels of 23 cytokines and chemokines were determined in serum at different timepoints after inoculation. Levels are displayed only for those cytokines and chemokines where statistically significant (1-way ANOVA) were observed compared to levels on day of inoculation. Identical symbols have been used to denote identical animals throughout the figures in this manuscript. The lower limit of detection is indicated with a dotted line. Serum samples were analyzed in duplicate from each animal for each timepoint; n= 8 animals on 0, 1, and 3 dpi and n=4 animals thereafter.

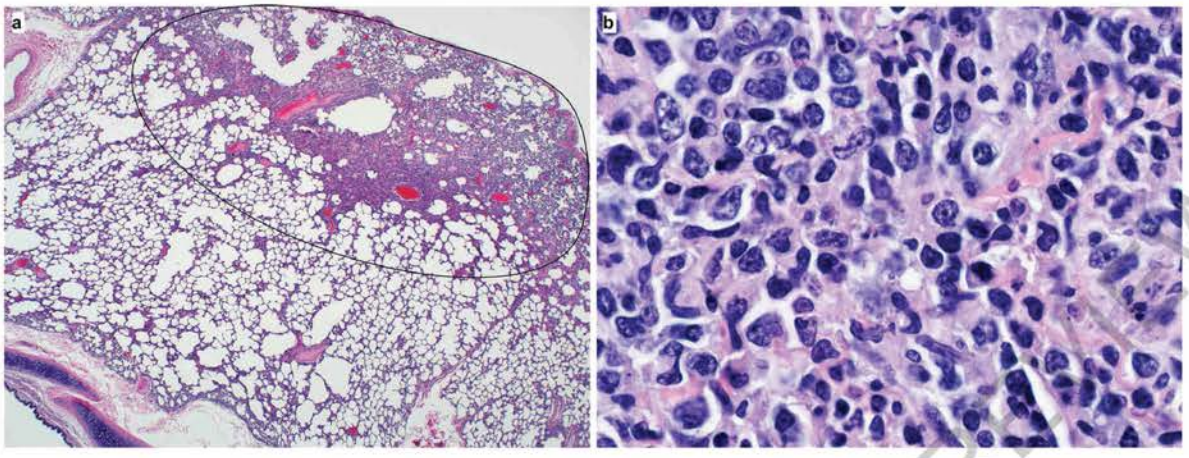

Extended Data Fig. 4 | Histological lesions in lungs of a rhesus macaque infected with SARS-CoV-2. (a) This low magnification figure displays the focal nature of SARS-CoV-2 lesions in the lungs of animals euthanized on 3 dpi. The circle indicates the lung affected by lesion; the remaining lung tissue is healthy. (b) Lymphocytes surround pulmonary vessels. Magnification 500x. Tissue sections were collected from the same anatomical location for each animal; three tissue sections were prepared from each of the 6 lung lobes. In total, 18 lung sections were evaluated for each animal (n=4); representative images are displayed.

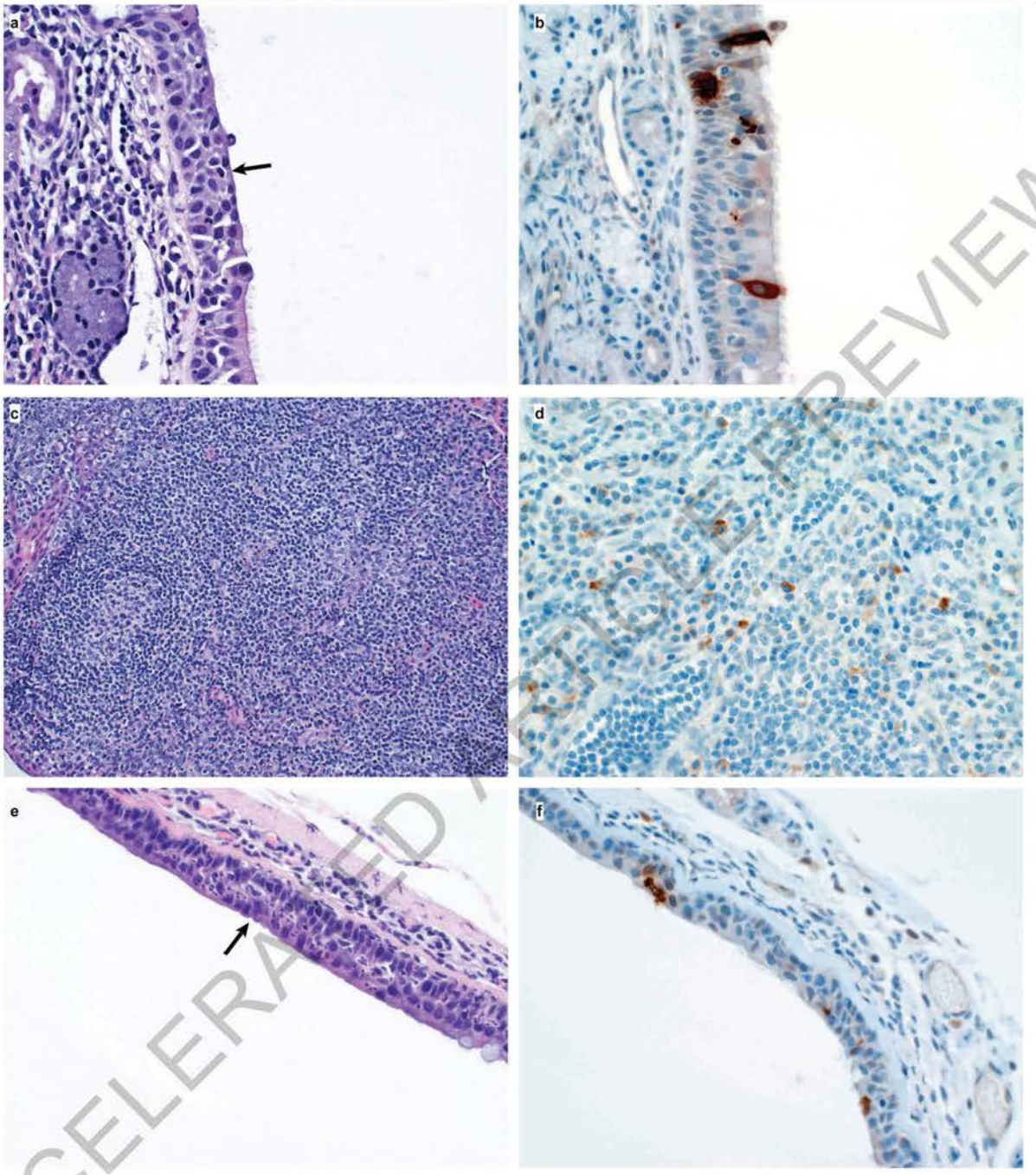

Extended Data Fig. 5 | Histological changes in the respiratory tract of rhesus macaques infected with SARS-CoV-2. (a) Squamous metaplasia of nasal turbinate respiratory epithelium (arrow). Magnification 400x. (b) SARS-CoV-2 antigen is detected by immunohistochemistry in respiratory epithelium of the nasal turbinate. Magnification 400x. (c) Essentially normal tonsil. Magnification 400x. (d) SARS-CoV-2 antigen is detected by immunohistochemistry in tonsillar macrophages. Magnification 400x. (e) Squamous metaplasia of tracheal columnar epithelium (arrow). Magnification 400x. (f) SARS-CoV-2 antigen is detected by immunohistochemistry in tracheal columnar epithelium. Magnification 400x. Tissue sections were collected from the same anatomical location for each animal (n=4) and organ; one tissue section was evaluated of the nasal turbinates of each animal; three tissue sections were evaluated from tonsil and trachea.

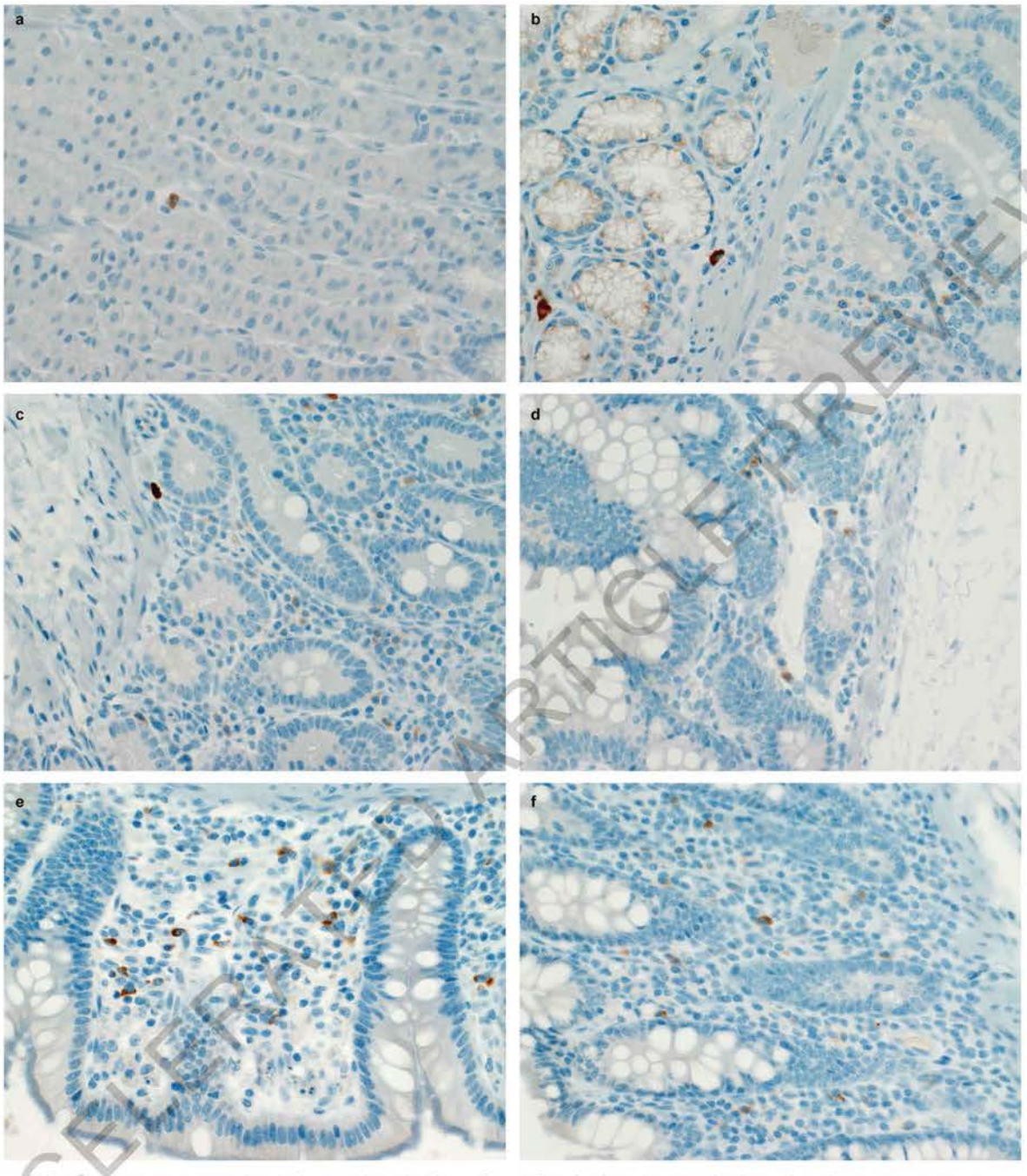

Extended Data Fig. 6 | SARS-CoV-2 antigen in the gastrointestinal tract of a rhesus macaque infected with SARS-CoV-2. Mononuclear cells staining positive for SARS-CoV-2 antigen in the lamina propria of stomach (a), duodenum (b), jejunum (c), ileum (d), cecum (e) and colon (f) of an animal infected with SARS-CoV-2 and euthanized on 3 dpi. Tissue sections were collected from the same anatomical location for each animal (n=4) and organ; three tissue sections were evaluated from each animal and organ.

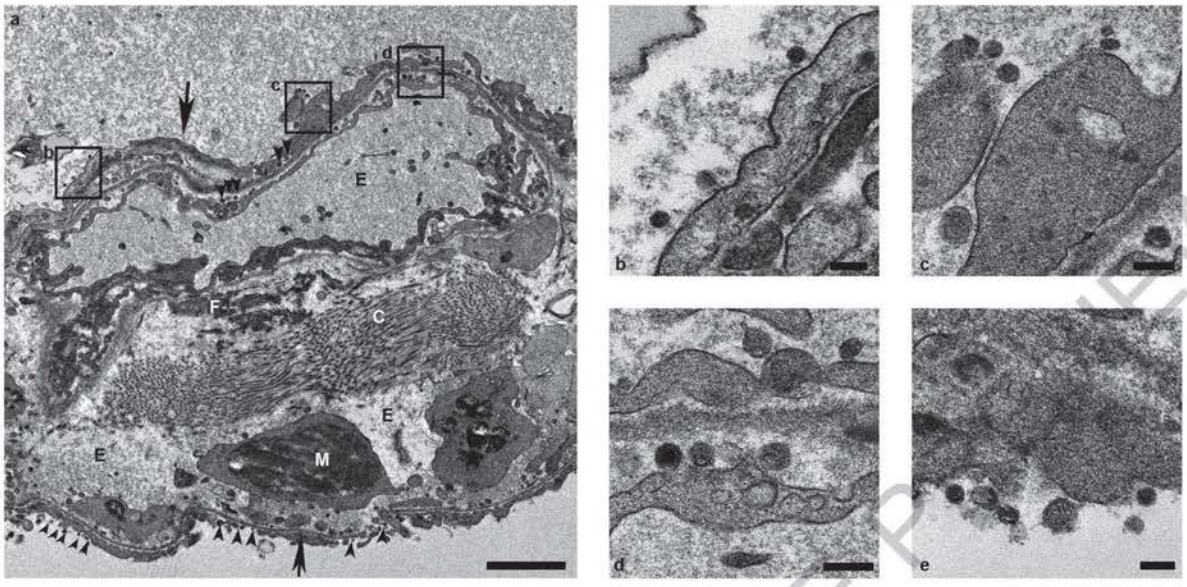

Extended Data Fig. 7 | Ultrastructural analysis of lungs of rhesus macaques infected with SARS-CoV-2. Lung tissue collected on 3 dpi was analyzed by transmission electron microscopy. The alveolar interstitium is expanded by edema (E), fibrin (F) and mononuclear (M) inflammatory cells (a). Normal collagen fibers (c) and multiple virions (arrowheads) line type I pneumocytes (arrows). Boxes in (a) indicate areas enlarged in (b-d). Scale bar in (a) represents 2µm, scale bars in (b-e) represent 0.2 µm. Three tissue samples were collected from each animal (n=4) and cut into 6 samples for analysis; a minimum of 2 samples were analyzed per animal (n=4).

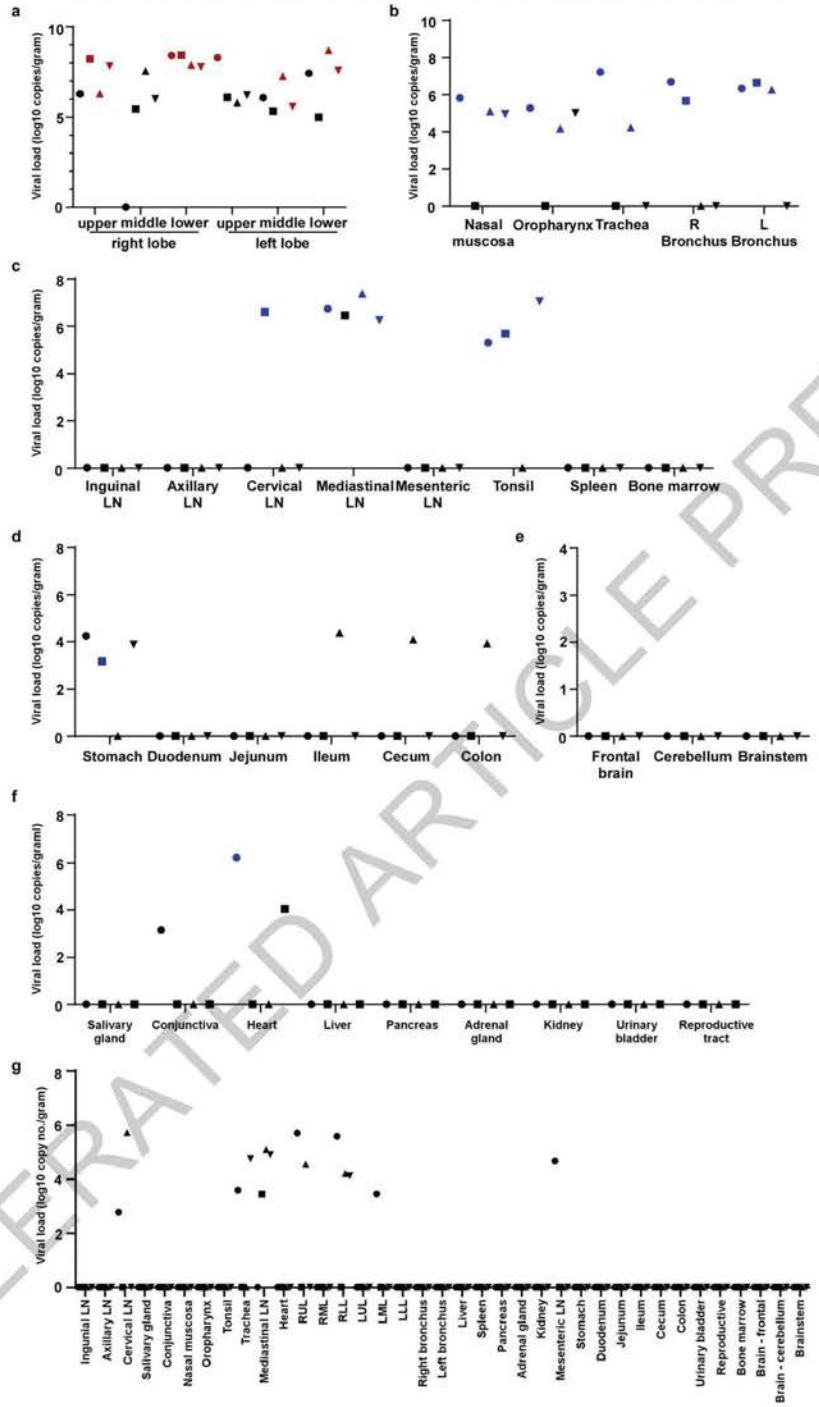

Extended Data Fig. 8 | Viral loads in tissues collected from rhesus macaques infected with SARS-CoV-2. Eight adult rhesus macaques were inoculated with SARS-CoV-2 isolate nCoV-WA1-2020 and euthanized on 3 (n=4) and 21 (n=4) dpi. Thirty-seven tissues were collected at necropsy and analyzed for the presence of viral RNA by qRT-PCR. Tissues are grouped by lung lobes collected on 3 dpi (a), with red symbols indicating tissues from which virus could be isolated in Vero E6 cells; other tissues from the respiratory tract on 3dpi (b); lymphoid tissues on 3 dpi (c); gastrointestinal tissueson 3 dpi (d); the central nervous system on 3 dpi (e); remaining tissues on 3 dpi (f); and all tissues collected on 21 dpi (g). Blue symbols in b-g indicate that viral mRNA was also detected in these tissues. Identical symbols have been used to denote identical animals throughout the figures in this manuscript. LN: lymph node; RUL: right upper lung lobe; RML: right middle lung lobe; RLL: right lower lung lobe; LUL: left upper lung lobe; LML: left middle lung lobe; LLL: left lower lung lobe; R: right; L: left.

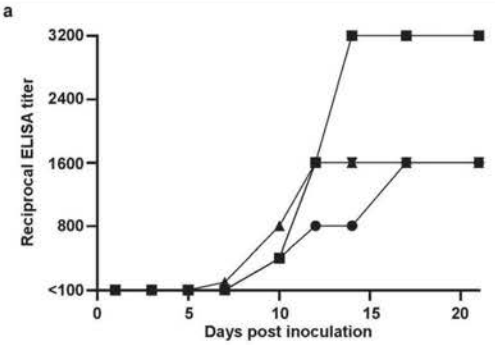

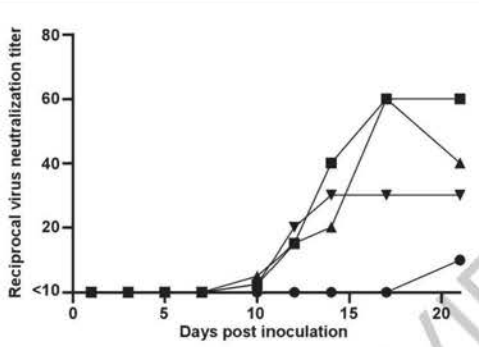

Extended Data Fig. 9 | Antibody response in rhesus macaques infected with SARS-CoV-2. Sera collected after inoculation were tested for the presence of IgG against SARS-CoV-2 spike in ELISA (a) and for the presence of neutralizing antibodies in a microneutralization assay (b). All sera were analyzed in duplicate. Identical symbols have been used to denote identical animals throughout the figures in this manuscript.

Extended Data Table 1 | Clinical signs observed in rhesus macaques inoculated with SARS-CoV-2

Animal	Clinical signs observed 1-6 dpi	Clinical signs observed 7-21 dpi	Observations at necropsy*
RM1	Hunched posture; piloerection; tachypnea; flushed appearance; red eyes; very agitated; reduced appetite; mildly dehydrated. Euthanized 3 dpi.	N/A	Gross lung lesions. Enlarged tonsils and mediastinal lymph nodes. Fluid-filled stomach, small and large intestine.
RM2	Piloerection; dyspnea; reduced appetite. Euthanized 3 dpi.	N/A	Fluid-filled stomach, small and large intestine.
RM3	Piloerection; tachypnea; flushed appearance; reduced appetite; mildly dehydrated. Euthanized 3 dpi.	N/A	Epistaxis. Gross lung lesions. Enlarged mediastinal lymph nodes. Fluid-filled stomach, small and large intestine.
RM4	Hunched posture; piloerection; tachypnea; dyspnea; reduced appetite. Euthanized 3 dpi.	N/A	Gross lung lesions. Foamy exudate from trachea. Enlarged mediastinal lymph nodes. Fluid-filled stomach, small and large intestine.
RM5	Hunched posture; piloerection; tachypnea; dyspnea; reduced appetite.	Tachypnea; dyspnea; reduced appetite; mildly dehydrated. Recovered on 9 dpi.	Gross lung lesions. Enlarged mesenteric lymph nodes.
RM6	Hunched posture; piloerection; tachypnea; dyspnea; reduced appetite; serous nasal discharge.	Piloerection; bradypnea; mildly dehydrated; crusty nasal discharge. Recovered on 10 dpi.	None.
RM7	Hunched posture; piloerection; pale appearance; tachypnea; dyspnea; irregular; labored respirations; anorexia; mildly dehydrated; serous nasal discharge.	Hunched posture; piloerection; pale appearance; tachypnea; dyspnea; reduced appetite; mildly dehydrated; crusty nasal discharge. Recovered on 17 dpi.	None.
RM8	Hunched posture; piloerection; pale appearance; increased, dyspnea; reduced appetite; serous nasal discharge.	Hunched posture; piloerection; pale appearance; increased, dyspnea; nasal discharge; reduced appetite; mildly dehydrated; serous nasal discharge. Recovered on 13 dpi.	Gross lung lesions.

* Incidental observations not related to coronavirus infection were omitted from this table.

nature COMMUNICATIONS

ARTICLE

https://doi.org/10.1038/s41467-020-17892-0 OPEN

A high-throughput neutralizing antibody assay for COVID-19 diagnosis and vaccine evaluation

Antonio E. Muruato[1,2,10], Camila R. Fontes-Garfias[1,10], Ping Ren[3,10], Mariano A. Garcia-Blanco[1,4,5], Vineet D. Menachery[2,3,6], Xuping Xie[1✉] & Pei-Yong Shi[1,6,7,8,9✉]

Virus neutralization remains the gold standard for determining antibody efficacy. Therefore, a high-throughput assay to measure SARS-CoV-2 neutralizing antibodies is urgently needed for COVID-19 serodiagnosis, convalescent plasma therapy, and vaccine development. Here, we report on a fluorescence-based SARS-CoV-2 neutralization assay that detects SARS-CoV-2 neutralizing antibodies in COVID-19 patient specimens and yields comparable results to plaque reduction neutralizing assay, the gold standard of serological testing. The fluorescence-based neutralization assay is specific to measure COVID-19 neutralizing antibodies without cross reacting with patient specimens with other viral, bacterial, or parasitic infections. Collectively, our approach offers a rapid platform that can be scaled to screen people for antibody protection from COVID-19, a key parameter necessary to safely reopen local communities.

[1] Department of Biochemistry and Molecular Biology, University of Texas Medical Branch, Galveston, TX, USA. [2] Department of Microbiology and Immunology, University of Texas Medical Branch, Galveston, TX, USA. [3] Department of Pathology, University of Texas Medical Branch, Galveston, TX, USA. [4] Programme in Emerging Infectious Diseases, Duke-NUS Medical School, Singapore, Singapore. [5] Department of Internal Medicine, University of Texas Medical Branch, Galveston, TX, USA. [6] Institute for Human Infections and Immunity, University of Texas Medical Branch, Galveston, TX, USA. [7] Sealy Institute for Vaccine Sciences, University of Texas Medical Branch, Galveston, TX, USA. [8] Sealy Center for Structural Biology & Molecular Biophysics, University of Texas Medical Branch, Galveston, TX, USA. [9] Institute for Translational Science, University of Texas Medical Branch, Galveston, TX, USA. [10] These authors contributed equally: Antonio E. Muruato, Camila R. Fontes-Garfias, Ping Ren. ✉email: xuxie@UTMB.edu; peshi@UTMB.edu

The ongoing coronavirus disease 2019 (COVID-19) pandemic is caused by severe acute respiratory syndrome coronavirus 2 (SARS-CoV-2), first reported in Wuhan, China in late 2019[1,2]. As of June 28, 2020, COVID-19 has caused 10.3 million confirmed infections and over 505,741 deaths worldwide (https://www.worldometers.info/coronavirus/). Many areas of the world have been in lockdown mode to curb the viral transmission, but the reality is that COVID-19 is here to stay until a safe and efficacious vaccine becomes available. The pandemic's catastrophic economic impact is pushing governments to reopen their economies, and this creates a public health quandary. At this time, our only option is to minimize viral transmission through social distancing and contact tracing, which relies on the diagnosis of viral RNA through reverse transcription polymerase chain reaction (RT-PCR) (https://www.fda.gov/media/134922/download). Proper public health policy would be greatly enhanced if we had a reliable and facile assay to measure the immune protection among COVID-19 recovered patients.

Coronavirus infections typically induce neutralizing antibody responses[3]. The seroconversion rates in COVID-19 patients are 50% and 100% on day 7 and 14 post symptom onset, respectively[4]. Given the unknown scale of asymptomatic infections, there is a pressing need for serological diagnosis to determine the real number of infections. Such information is essential for defining the case-fatality rate and for making the policy on the scale and duration of social lockdowns. The serological assays are also required to identify donors with high-neutralizing titers for convalescent plasma for therapy, and to define correlates of protection from SARS-CoV-2. While viral RNA-based testing for acute infection is the current standard, surveying antibody protection is a necessary part of any return to social normality.

For serodiagnosis, several COVID-19 assay platforms have achieved FDA emergency use authorizations (EUA), including ELISA[5] (https://www.fda.gov/media/137029/download), lateral flow immunoassay (https://www.fda.gov/media/136625/download), and Microsphere Immunoassay (https://www.fda.gov/media/137541/download). These assays measure antibody binding to SARS-CoV-2 spike protein. Since not all spike-binding antibodies can block viral infection, these platforms do not functionally measure antibody inhibition of SARS-CoV-2 infection. An ideal serological assay should measure neutralizing antibody levels, which should predict protection from reinfection. Conventionally, neutralizing antibodies are measured by plaque reduction neutralization test (PRNT). Although PRNT and ELISA results generally corelate with each other, particularly when the receptor-binding domain of SARS-CoV-2 spike protein is used as an ELISA antigen (https://www.genscript.com/cpass-sars-cov-2-neutralization-antibody-detection-Kit.html)[6,7], PRNT remains the gold standard for serological testing and determining immune protection[8,9]. However, due to its low throughput, PRNT is not practical for large scale serodiagnosis and vaccine evaluation. This is a major gap for COVID-19 surveillance and vaccine development.

Here, we report a fluorescence-based high-throughput neutralization assay that detects SARS-CoV-2 neutralizing antibodies in patient specimens and yields equivalent results to the gold standard plaque reduction neutralizing assay.

Results

A high-throughput fluorescence-based neutralization assay. To fill in the gap for COVID-19 serodiagnosis and vaccine evaluation, we developed a fluorescence-based assay that rapidly and reliably measures neutralization of a reporter SARS-CoV-2 by antibodies from patient specimens. The assay was built on a stable mNeonGreen (mNG) SARS-CoV-2 where the mNG gene was engineered at the ORF7 of the viral genome (Fig. 1a)[10]. The complete sequence of mNG SARS-CoV-2 is described in Supplementary Fig. 1. Figure 1b depicts the flowchart of the reporter neutralization assay in a 96-well format. The assay protocol is detailed in Supplementary Methods. Briefly, patient sera were serially diluted and incubated with the reporter virus. After incubation at 37°C for 1 h, Vero CC-81 cells (pre-seeded in a 96-well plate) were infected with the virus/serum mixtures at a multiplicity of infection (MOI) of 0.5. At 16 h post-infection, the mNG-positive cells were quantitated using a high-content imaging reader (Fig. 1b). It should be noted that Vero CC-81 cells, not Vero E6 cells, were chosen for the mNG assay to enable accurate quantification of fluorescent cells. Sixty COVID-19 serum specimens from RT-PCR-confirmed patients and 60 non-COVID-19 serum samples (archived before COVID-19 emergence) were analyzed using the reporter virus. For some COVID-19-positive specimens, the sample collection days post viral RT-PCR positive were available and are indicated in Table 1. After reporter viral infection, the cells turned green in the absence of serum (Fig. 1c, bottom panel); in contrast, incubation of the reporter virus with COVID-19 patient serum decreased the number of fluorescent cells (top panel). A dose–response curve was obtained between the number of fluorescent cells and the fold of serum dilution (Fig. 1d and Supplementary Fig. 2), which allowed for determination of the dilution fold that neutralized 50% of fluorescent cells (NT_{50}). The reporter assay rapidly diagnosed 120 specimens within 24 h: all 60 COVID-19 sera (specimens 1–60) showed positive NT_{50} of 35 to 5711, and all 60 non-COVID-19 sera (specimens 61–120) showed negative NT_{50} of <20 (Table 1).

Assay validation by plaque reduction test. To validate the reporter virus neutralization results, we performed the conventional PRNT on the same set of patient specimens. All 60 negative sera (specimens 61–120) exhibited $PRNT_{50}$ of <20 (Table 1). Among the 60 positive specimens, 57 sera (specimens 4–60) showed $PRNT_{50}$ of 40 to 3200, whereas 3 sera (specimens 1–3) exhibited $PRNT_{50}$ of <20 (Table 1). The discrepancy between the $PRNT_{50}$ and NT_{50} values for specimens 1–3 is likely due to the early infection time (within 5 days post RT-PCR positive) when neutralizing antibodies just began to develop; this discrepancy suggests that the mNG SARS-CoV-2 assay has a higher sensitivity than the conventional PRNT assay. Nevertheless, a strong correlation was observed between the reporter virus and PRNT results, with a correlation efficiency R^2 of 0.85 (Fig. 1e). The results demonstrate that when diagnosing patient specimens, the reporter virus assay delivers neutralization results comparable to the PRNT assay, the gold standard of serological testing.

Assay specificity. We evaluated the specificity of reporter neutralization assay using potentially cross-reactive sera and interfering substances (Table 2). Two groups of specimens were tested for cross reactivity. Group I included 150 clinical sera from patients with antigens or antibodies against different viruses, bacteria, and parasites. These human specimens were obtained according to two types of diagnostic results: some samples were tested positive for antibodies against specific pathogens (e.g., anti-Chikungunya virus; this group of samples are indicated by prefix "anti" in Table 2); other specimens were collected within 1 to 6 months after the patients were tested positive on pathogen antigens or nucleic acids (e.g., adenovirus antigen; this group of samples are not indicated by prefix in Table 2). Group II consisted of 19 samples with albumin, elevated bilirubin, cholesterol, rheumatoid factor, and autoimmune nuclear antibodies. None of these specimens cross-neutralized mNG SARS-CoV-2 (Table 2), including the four common cold coronaviruses (NL63, 229E,

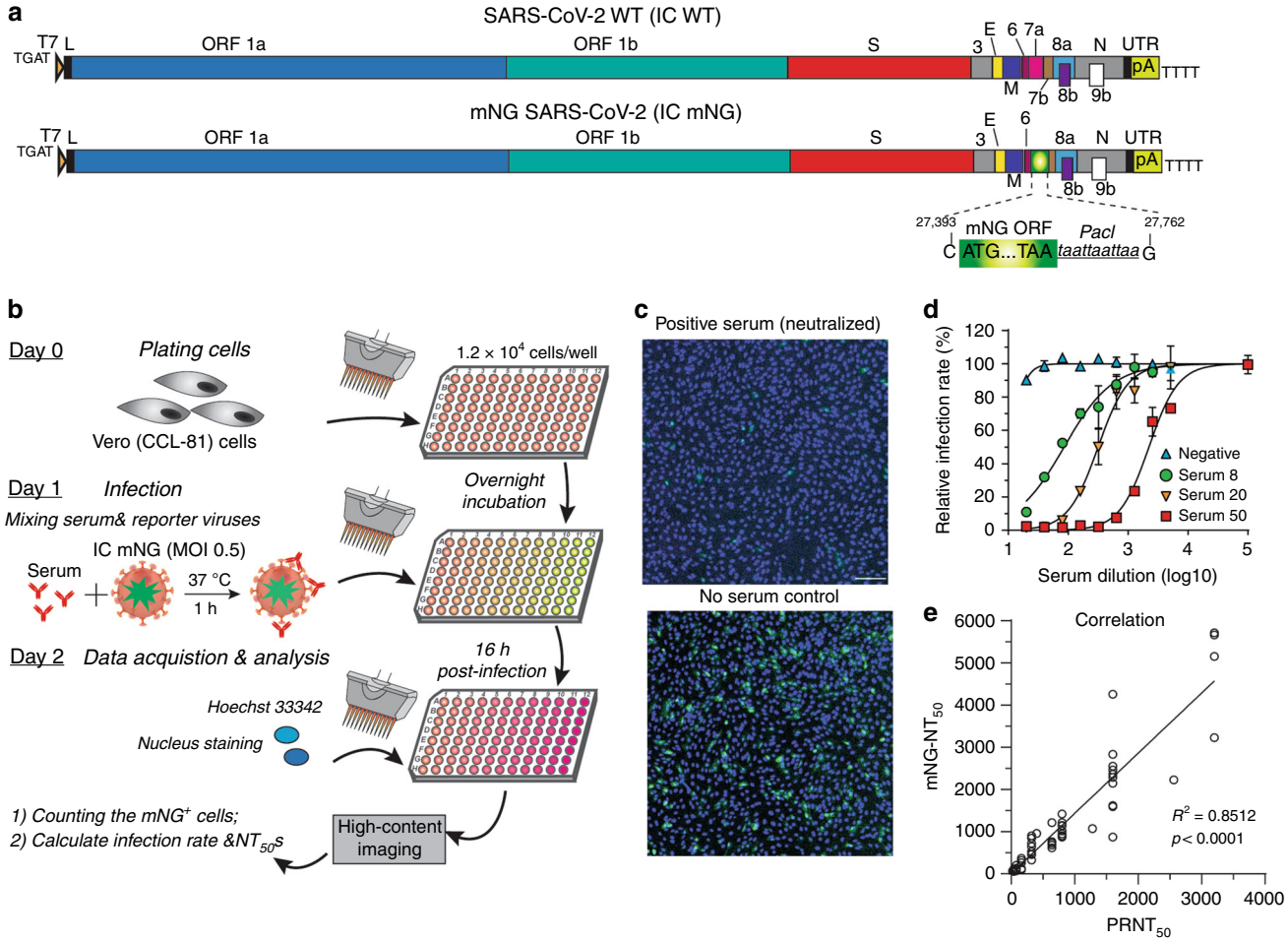

Fig. 1 A high-throughput neutralizing antibody assay for COVID-19 diagnosis. a Diagram of the cDNA constructs of wild-type (WT) SARS-CoV-2 (top panel) and mNG SARS-CoV-2 (bottom panel). The nucleotide positions of viral genome where mNG is engineered are indicated. **b** Assay flowchart. mNG SARS-CoV-2 was neutralized with COVID-19 patient sera. Vero CCL-81 cells were infected with the reporter virus/serum mixture with an MOI of 0.5. The fluorescence of infected cells was quantified to estimate the NT_{50} value for each serum. **c** Representative images of reporter virus-infected Vero CCL-81 cells. Images for a positive neutralizing serum (top panel) and no serum control (bottom panel) are presented. Scale bar, 100 μm. **d** Neutralization curves. Representative neutralization curves are presented for three positive sera and one negative sera. The means and standard deviations from two independent experiments are presented. **e** Correlation analysis of NT_{50} values between the reporter virus and PRNT assays. The Pearson correlation efficiency R^2 and *p*-value (two-tailed) are indicated.

OC43, and HUK1). Despite the low number of common cold coronavirus serum specimens, our result is consistent with the recent reports that sera from common cold coronavirus patients did not cross react with SARS-CoV-2[5,11]. More specimens are required to further validate the cross reactivity, particularly between SARS-CoV-2 and other human coronaviruses, including SARS-CoV-1 and MERS-CoV.

Discussion

In this study, we developed a rapid fluorescence-based high-throughput assay for COVID-19 serodiagnosis. The reporter virus assay is superior to many antigen/antibody binding assays because it measures functional SARS-CoV-2 neutralizing activity in the specimens. When diagnosing patient sera, the reporter virus assay generated NT_{50} values comparable to the conventional PRNT assay. Compared with the PRNT assay, our reporter neutralization test has shortened the assay turnaround time by several days and increased the testing capacity to high throughput. Toward the same direction, VSV and lentivirus pseudotyped with SARS-CoV-2 spike protein have been reported for COVID-19 neutralization assays at biosafety level 2 (BSL-2) lab[12].

Since mNG SARS-CoV-2 is stable and replicates like wild-type virus, our reporter neutralization assay provides an ideal model for high-throughput serological testing. As the mNG SARS-CoV-2 grows to >10^7 PFU/ml in cell culture[10], the reporter virus can be easily scaled up for testing large sample volumes. Besides mNG, we have begun to develop other reporter SARS-CoV-2 (e.g., luciferase or mCherry) that can also be used for such serological testing[13]. Although the current study performed the assay in a 96-well format, the assay can be readily adapted to 384- and 1536-well formats. Despite the strengths of high throughput and reliability, the current reporter neutralization assay must be performed in BSL-3 containment. Efforts are ongoing to engineer an attenuated version of SARS-CoV-2 so that the assay could be performed at a BSL-2 facility. Despite the BSL-3 limitation, the mNG reporter assay offers a rapid, high-throughput platform to test COVID-19 patient sera not previously available. Indeed, the mNG SARS-CoV-2 assay is currently being used to support clinical trials for COVID-19 vaccine candidates[14].

As neutralizing titer is a key parameter to predict immunity, the reporter neutralization assay should be useful for high-throughput evaluation of COVID-19 vaccines and for

Table 1 Comparison of neutralization titers of patient sera analyzed by reporter assay and plaque reduction assay.

[a]Serum ID[b]	[c]$PRNT_{50}$	[c]mNG-NT_{50}	[a]Serum ID[b]	[c]$PRNT_{50}$	[c]mNG-NT_{50}
1 (d1)	<20	35	32 (d9)	640	762
2 (d5)	<20	38	33 (d8)	320	846
3 (d4)	<20	50	34 (d14)	800	873
4 (d5)	40	58	35 (d16)	1600	874
5 (d5)	20	66	36 (d17)	320	900
6 (d6)	80	74	37 (d9)	800	902
7 (d8)	80	77	38 (d15)	800	949
8 (d4)	80	85	39 (d15)	400	958
9 (d5)	80	85	40 (d18)	800	1016
10 (d1)	80	95	41 (d28)	1280	1072
11 (d6)	80	96	42 (d12)	800	1139
12 (NA)	160	96	43 (d13)	800	1145
13 (d6)	40	111	44 (d14)	800	1210
14 (d6)	40	114	45 (d31)	640	1213
15 (d1)	80	115	46 (d8)	800	1419
16 (d9)	160	120	47 (d14)	1600	1590
17 (d11)	80	132	48 (d21)	1600	1617
18 (d8)	80	200	49 (d12)	1600	2148
19 (NA)	160	261	50 (NA)	2560	2225
20 (d5)	160	318	51 (d20)	1600	2287
21 (d32)	320	329	52 (d8)	1600	2362
22 (d14)	160	365	53 (d12)	1600	2463
23 (d12)	160	366	54 (d18)	1600	2554
24 (d37)	320	456	55 (d16)	1600	2832
25 (NA)	320	474	56 (d15)	3200	3228
26 (d47)	320	525	57 (d31)	3200	4257
27 (d12)	640	617	58 (NA)	3200	5152
28 (d9)	320	649	59 (d8)	3200	5662
29 (d10)	640	681	60 (NA)	3200	5711
30 (d27)	320	721	61–120	<20	<20
31 (d9)	640	727			

[a]A total of 120 patient sera were analyzed, including 60 specimens from RT-PCR-confirmed patients (specimens 1–60) and 60 negative specimens (specimens 61–120) that were collected before COVID-19 pandemic (prepandemic).
[b]Sample collection days post after RT-PCR positive test are indicated in parentheses. For some COVID-19-positive specimens, the sample collection days post after RT-PCR positive test are not available (NA).
[c]The NT_{50} and $PRNT_{50}$ values were derived from the reporter virus assay and conventional PRNT assay, respectively.

Table 2 Cross reactivity of mNG SARS-CoV-2 neutralization assay.

[a]Immune sera and [b]interfering substances	Sample number	Number of mNG tested positive
Adenovirus	1	0
Anti-Chikungunya virus	4	0
Cryptococcus neoformans antigen	2	0
Anti-Cytomegalovirus	8	0
Anti-Dengue virus	5	0
Anti-Epstein Barr Virus: capsid or nuclear antigen	8	0
Anti-Hepatitis A virus	5	0
Anti-Hepatitis B virus: surface antigen	15	0
Anti-Hepatitis C virus	3	0
Anti-Herpes simplex virus 1	7	0
Anti-Herpes simplex virus 2	5	0
Human coronavirus 229E	1	0
Human coronavirus HKU1	5	0
Human coronavirus NL63	1	0
Human coronavirus OC43	4	0
Anti-Human immunodeficiency virus 1	10	0
Human rhinovirus	3	0
Influenza B virus	2	0
Anti-Measles virus	7	0
Anti-Mumps virus	5	0
Parainfluenza virus 2	1	0
Parainfluenza virus 4	1	0
Anti-Parvovirus B19	4	0
Respiratory syncitial virus	1	0
Anti-Rubella virus	12	0
Anti-Syphilis	5	0
Anti-Toxoplasma	2	0
Anti-Typhus Fever	1	0
Anti-Varicella zoster virus	13	0
Anti-West Nile Virus	3	0
Anti-Yellow fever virus: vaccination	2	0
Anti-Zika virus	4	0
[b]Albumin (4.5 g/dl)	3	0
[b]Elevated bilirubin conjugated (>0.4 mg/dl)	3	0
[b]Elevated bilirubin unconjugated (>0.8 mg/dl)	3	0
[b]Elevated cholesterol (>200 mg/dl)	3	0
[b]Elevated rheumatoid factor (>100 IU/ml)	3	0
[b]Anti-nuclear antibodies	4	0

[a]A total of 150 sera with antigens or antibodies against different infections (or immunizations) were tested against mNG SARS-CoV-2 neutralization assay. The immune sera are listed in alphabetical order. Samples tested positive for antibodies against specific pathogens are indicated with prefix "anti", whereas samples tested positive on antigens or pathogen nucleic acids are not indicated with prefix. For the latter group, the specimens were collected within 1 to 6 months after the antigen or PCR tested positive.
[b]A total of 19 samples tested for interfering substances and autoimmune disease nuclear antibodies.

identification of high-neutralizing convalescent plasma for therapy. Treatment of severe COVID-19 patients with convalescent plasma shows clinical benefits[15]. For vaccine development, a standardized neutralizing assay will facilitate down selection of various candidates for clinical development. Furthermore, the reporter assay could be used over time to monitor the waning of protective neutralizing titers in COVID-19 patients and vaccinated individuals, to study the correlates of protection from SARS-CoV-2, and to monitor high-risk populations (such as healthcare workers) for infection prevention. Thus, the ability to rapidly measure neutralizing antibody levels in populations is essential for guiding policymakers to reopen the economy and society, deploy healthcare workers, and prepare for SARS-CoV-2 reemergence.

Methods

Cells. Vero (ATCC®CCL-81) and Vero E6 (ATCC® CRL-1586) were purchased from the American Type Culture Collection (ATCC, Bethesda, MD), and maintained in a high-glucose Dulbecco's modified Eagle's medium (DMEM) supplemented with 10% fetal bovine serum (FBS; HyClone Laboratories, South Logan, UT) and 1% penicillin/streptomycin at 37°C with 5% CO_2. All culture medium and antibiotics were purchased from ThermoFisher Scientific (Waltham, MA). All cell lines were tested negative for mycoplasma.

mNG SARS-CoV-2. The virus stock of mNG SARS-CoV-2 was produced using an infectious complementary DNA (cDNA) clone of SARS-CoV-2 in which the ORF7 of the viral genome was replaced with reporter mNG gene[10]. After rescued from the genome-length viral RNA-electroporated cells, the viral stock was prepared by amplifying the mNG SARS-CoV-2 on Vero E6 cells for one or two rounds. The titer of the virus stock was determined by a standard plaque assay.

Human sera and interfering substances. The research protocol regarding the use of human serum specimens was reviewed and approved by the University of Texas Medical Branch (UTMB) Institutional Review Board. The approved IRB protocol

number is 20-0070. All human serum specimens were obtained at the UTMB. All specimens were de-identified from patient information. A total of 60 de-identified convalescent sera from COVID-19 patients (confirmed with viral RT-PCR positive) were tested in this study. Sixty non-COVID-19 sera, collected before COVID-19 emergence[16,17], were also tested in the reporter virus and PRNT assays. For testing cross reactivity, a total of 150 de-identified specimens from patients with antigens or antibodies against different viruses, bacteria, and parasites were tested in the mNG SARS-COV-2 neutralization assay (Table 2). For testing interfering substances, 19 de-identified serum specimens with albumin, elevated bilirubin, cholesterol, rheumatoid factor, and autoimmune nuclear antibodies were tested in the reporter neutralization assay. All human sera were heat-inactivated at 56°C for 30 min before testing.

mNG SARS-CoV-2 reporter neutralization assay. Vero CCL-81 cells (1.2×10^4) in 50 µl of DMEM (Gibco) containing 2% FBS (Hyclone) and 100 U/ml Penicillium–Streptomycin (P/S; Gibco) were seeded in each well of black µCLEAR flat-bottom 96-well plate (Greiner Bio-one™). Vero CCL-81 cells, not Vero E6 cells, were selected for the mNG SARS-COV-2 assay to facilitate accurate quantification of fluorescent cells by high-content imaging. The cells were incubated overnight at 37°C with 5% CO_2. On the following day, each serum was twofold serially diluted in 2% FBS and 100 U/ml P/S DMEM, and incubated with mNG SARS-CoV-2 at 37°C for 1 h. The virus-serum mixture was transferred to the Vero CCL-81 cell plate with the final multiplicity of infection (MOI) of 0.5. For each serum, the starting dilution was 1/20 with nine two-fold dilutions to the final dilution of 1/5120. After incubating the infected cells at 37°C for 16 h, 25 µl of Hoechst 33342 Solution (400-fold diluted in Hank's Balanced Salt Solution; Gibco) were added to each well to stain cell nucleus. The plate was sealed with Breath-Easy sealing membrane (Diversified Biotech), incubated at 37°C for 20 min, and quantified for mNG fluorescence on Cytation™ 7 (BioTek). The raw images (2 × 2 montage) were acquired using 4× objective, processed, and stitched using the default setting. The total cells (indicated by nucleus staining) and mNG-positive cells were quantified for each well. Infection rates were determined by dividing the mNG-positive cell number to total cell number. Relative infection rates were obtained by normalizing the infection rates of serum-treated groups to those of non-serum-treated controls. The curves of the relative infection rates versus the serum dilutions (log10 values) were plotted using Prism 8 (GraphPad). A nonlinear regression method was used to determine the dilution fold that neutralized 50% of mNG fluorescence (NT_{50}). Each serum was tested in duplicates. All mNG SARS-CoV-2 reporter neutralization assay was performed at the BSL-3 facility at UTMB.

Plaque reduction neutralization test (PRNT). Vero E6 cells (1.2×10^6 per well) were seeded to six-well plates. On the following day, 100 PFU of infectious clone-derived wild-type SARS-CoV-2 was incubated with serially diluted serum (total volume of 200 µl) at 37°C for 1 h. The virus-serum mixture was added to the pre-seeded Vero E6 cells. After 1 h 37°C incubation, 2 ml of 2% high gel temperature agar (SeaKem) in DMEM containing 5% FBS and 1% P/S was added to the infected cells. After 2 days of incubation, 2 ml neutral red (1 g/l in PBS; Sigma) was added to the agar-covered cells. After another 5-h incubation, neutral red was removed. Plaques were counted for NT_{50} calculation. Each serum was tested in duplicates. The PRNT assay was performed at the BSL-3 facility at UTMB.

Statistical analysis. The correlation of the NT_{50} values from mNG reporter SARS-CoV-2 assay and the $PRNT_{50}$ values from plaque neutralization assay was analyzed using a linear regression model in the software Prism 8 (GraphPad). Pearson correlation coefficient and two-tailed *p*-value are calculated using the default settings in the software Prism 8.

Reporting summary. Further information on research design is available in the Nature Research Reporting Summary linked to this article.

Data availability

Source data are provided with this paper. The assay protocol and sequence of mNG reporter SARS-CoV-2 are provided in the Supplementary Information. The mNG reporter SARS-CoV-2 has been deposited to the World Reference Center for Emerging Viruses and Arboviruses (https://www.utmb.edu/wrceva) at UTMB for distribution.

Received: 20 May 2020; Accepted: 19 July 2020;
Published online: 13 August 2020

References

1. Zhou, P. et al. A pneumonia outbreak associated with a new coronavirus of probable bat origin. *Nature* **579**, 270–273 (2020).
2. Zhu, N. et al. A novel coronavirus from patients with pneumonia in China, 2019. *N. Engl. J. Med.* **382**, 727–733 (2020).
3. Huang, A. T. et al. A systematic review of antibody mediated immunity to coronaviruses: antibody kinetics, correlates of protection, and association of antibody responses with severity of disease. *medRxiv* https://doi.org/10.1101/2020.04.14.20065771 (2020).
4. Wolfel, R. et al. Virological assessment of hospitalized patients with COVID-2019. *Nature* https://doi.org/10.1038/s41586-020-2196-x (2020).
5. Amanat, F. et al. A serological assay to detect SARS-CoV-2 seroconversion in humans. *Nat. Med.* https://doi.org/10.1038/s41591-020-0913-5 (2020).
6. GeurtsvanKessel, C. H. et al. Towards the next phase: evaluation of serological assays for diagnostics and exposure assessment. *medRxiv* https://doi.org/10.1101/2020.04.23.20077156 (2020).
7. Harvala, H. et al. Convalescent plasma therapy for the treatment of patients with COVID-19: Assessment of methods available for antibody detection and their correlation with neutralising antibody levels. *medRxiv* https://doi.org/10.1101/2020.05.20.20091694 (2020).
8. Perera, R. A. et al. Serological assays for severe acute respiratory syndrome coronavirus 2 (SARS-CoV-2), March 2020. *Euro Surveill.* **25**, https://doi.org/10.2807/1560-7917.ES.2020.25.16.2000421 (2020).
9. Okba, N. M. A. et al. Severe acute respiratory syndrome coronavirus 2-specific antibody responses in coronavirus disease 2019 patients. *Emerg. Infect. Dis.* **26**, https://doi.org/10.3201/eid2607.200841 (2020).
10. Xie, X. et al. An infectious cDNA clone of SARS-CoV-2. *Cell Host Microbe* https://doi.org/10.1016/j.chom.2020.04.004 (2020).
11. Khan, S. et al. Analysis of serologic cross-reactivity between common human coronaviruses and SARS-CoV-2 using coronavirus antigen microarray. *bioRxiv* https://doi.org/10.1101/2020.03.24.006544 (2020).
12. Nie, J. et al. Establishment and validation of a pseudovirus neutralization assay for SARS-CoV-2. *Emerg. Microbes Infect.* **9**, 680–686 (2020).
13. Xie, X. et al. A nanoluciferase SARS-CoV-2 for rapid neutralization testing and screening of anti-infective drugs for COVID-19. *bioRxiv* https://doi.org/10.1101/2020.06.22.165712 (2020).
14. Mulligan, M. J. et al. Phase 1/2 study of a COVID-19 RNA vaccine candidate (BNT162b1) in adults. *Nature* (2020). *In press.*
15. Shen, C. et al. Treatment of 5 critically ill patients with COVID-19 with convalescent plasma. *JAMA* https://doi.org/10.1001/jama.2020.4783 (2020).
16. Shan, C. et al. Evaluation of a novel reporter virus neutralization test for serological diagnosis of Zika and Dengue virus infection. *J. Clin. Microbiol.* **55**, 3028–3036 (2017).
17. Shan, C. et al. A rapid Zika diagnostic assay to measure neutralizing antibodies in patients. *EBioMedicine* **17**, 157–162 (2017).

Acknowledgements

We thank colleagues at UTMB for helpful discussion during the course of this project. P.-Y.S. was supported by NIH grants AI142759, AI134907, AI145617, and UL1TR001439, and awards from the Sealy & Smith Foundation, Kleberg Foundation, John S. Dunn Foundation, Amon G. Carter Foundation, Gilson Longenbaugh Foundation, and Summerfield Robert Foundation. M.A.G.-B. was supported by NIH grant CA204806 and the Vacek Distinguished Chair. V.D.M. was supported by NIH grants U19AI100625, R00AG049092, R24AI120942, and STARs Award from the University of Texas System. A.E.M. is supported by a Clinical and Translational Science Award NRSA (TL1) Training Core (TL1TR001440) from NIH. C.R.F.-G. is supported by the predoctoral fellowship from the McLaughlin Fellowship Endowment at UTMB.

Author contributions

P.R., M.A.G.-B., V.D.M., X.X., and P.-Y.S. conceived the study. A.E.M. and C.R.F.-G. performed the experiments and analyzed the results. P.R. prepared the serum specimens. M.A.G.-B., V.D.M., X.X., and P.-Y.S. wrote the manuscript.

Competing interests

X.X., V.D.M., and P.-Y.S. have filed a patent on the reverse genetic system and reporter SARS-CoV-2. Other authors declare no competing interests.

Additional information

Supplementary information is available for this paper at https://doi.org/10.1038/s41467-020-17892-0.

Correspondence and requests for materials should be addressed to X.X. or P.-Y.S.

Peer review information *Nature Communications* thanks the anonymous reviewers for their contribution to the peer review of this work. Peer reviewer reports are available.

Reprints and permission information is available at http://www.nature.com/reprints

Publisher's note Springer Nature remains neutral with regard to jurisdictional claims in published maps and institutional affiliations.

Immunogenicity and structures of a rationally designed prefusion MERS-CoV spike antigen

Jesper Pallesen[a,1], Nianshuang Wang[b,1,2], Kizzmekia S. Corbett[c,1], Daniel Wrapp[b], Robert N. Kirchdoerfer[a], Hannah L. Turner[a], Christopher A. Cottrell[a], Michelle M. Becker[d], Lingshu Wang[e], Wei Shi[e], Wing-Pui Kong[e], Erica L. Andres[d], Arminja N. Kettenbach[b,f], Mark R. Denison[d,g], James D. Chappell[d], Barney S. Graham[c], Andrew B. Ward[a,2], and Jason S. McLellan[b,2]

[a]Department of Integrative Structural and Computational Biology, The Scripps Research Institute, La Jolla, CA 92037; [b]Department of Biochemistry and Cell Biology, Geisel School of Medicine at Dartmouth, Hanover, NH 03755; [c]Viral Pathogenesis Laboratory, Vaccine Research Center, National Institute of Allergy and Infectious Diseases, Bethesda, MD 20892; [d]Department of Pediatrics, Vanderbilt University Medical Center, Nashville, TN 37232; [e]Virology Core, Vaccine Research Center, National Institute of Allergy and Infectious Diseases, Bethesda, MD 20892; [f]Norris Cotton Cancer Center, Geisel School of Medicine at Dartmouth, Lebanon, NH 03756; and [g]Department of Pathology, Microbiology, and Immunology, Vanderbilt University School of Medicine, Nashville, TN 37232

Edited by Pamela J. Bjorkman, California Institute of Technology, Pasadena, CA, and approved July 11, 2017 (received for review May 2, 2017)

Middle East respiratory syndrome coronavirus (MERS-CoV) is a lineage C betacoronavirus that since its emergence in 2012 has caused outbreaks in human populations with case-fatality rates of ∼36%. As in other coronaviruses, the spike (S) glycoprotein of MERS-CoV mediates receptor recognition and membrane fusion and is the primary target of the humoral immune response during infection. Here we use structure-based design to develop a generalizable strategy for retaining coronavirus S proteins in the antigenically optimal prefusion conformation and demonstrate that our engineered immunogen is able to elicit high neutralizing antibody titers against MERS-CoV. We also determined high-resolution structures of the trimeric MERS-CoV S ectodomain in complex with G4, a stem-directed neutralizing antibody. The structures reveal that G4 recognizes a glycosylated loop that is variable among coronaviruses and they define four conformational states of the trimer wherein each receptor-binding domain is either tightly packed at the membrane-distal apex or rotated into a receptor-accessible conformation. Our studies suggest a potential mechanism for fusion initiation through sequential receptor-binding events and provide a foundation for the structure-based design of coronavirus vaccines.

coronavirus | neutralizing antibody | cryo-EM | X-ray crystallography | peplomer

Coronaviruses are enveloped, positive-sense, single-stranded RNA viruses. They have the largest genomes (26–32 kb) among known RNA viruses and are phylogenetically divided into four genera (α, β, γ, and δ), with betacoronaviruses further subdivided into four lineages (A, B, C, and D). Coronaviruses infect a wide range of avian and mammalian species, including humans (1). Of the six known human coronaviruses, four of them (HCoV-OC43, HCoV-229E, HCoV-HKU1, and HCoV-NL63) circulate annually in humans and generally cause mild respiratory diseases, although severity can be greater in infants, the elderly, and the immunocompromised. In contrast, the Middle East respiratory syndrome coronavirus (MERS-CoV) and the severe acute respiratory syndrome coronavirus (SARS-CoV), belonging to betacoronavirus lineages C and B, respectively, are highly pathogenic. Both viruses emerged into the human population from animal reservoirs within the last 15 y and caused outbreaks with high case-fatality rates (2, 3).

MERS-CoV was isolated in 2012 from a patient in Saudi Arabia and is still circulating across the Arabian Peninsula (3, 4). Primary transmission, most likely from camels, is now considered to be the most common route of transmission (5–7), and camels are thought to be a secondary or intermediate reservoir for MERS-CoV, with bats serving as the primary reservoir (8). Human-to-human transmission, especially as a result of close contact between patients and hospital workers within health-care settings, is another important route of transmission (9) and was responsible for an outbreak of MERS-CoV in South Korea (10). The high pathogenicity and airborne transmissibility of SARS-CoV and MERS-CoV have raised concern about the potential for another coronavirus pandemic. Unfortunately, vaccines against individual coronaviruses are not available, much less one that broadly protects against multiple coronaviruses.

Like all coronaviruses, MERS-CoV uses a large surface spike (S) glycoprotein for receptor recognition and entry into target cells (11, 12). The MERS-CoV S protein is synthesized as a single-chain inactive precursor that is cleaved by furin-like host proteases in the producing cell into two noncovalently associated

Significance

Coronaviruses such as Middle East respiratory syndrome coronavirus (MERS-CoV) cause severe respiratory distress with high fatality rates. The spike (S) glycoprotein is a determinant of host range and is the target of neutralizing antibodies and subunit vaccine development. We describe an engineering strategy for stabilization of soluble S proteins in the prefusion conformation, which results in greatly increased expression, conformational homogeneity, and elicitation of potent antibody responses. Cryo-EM structures of the stabilized MERS-CoV S protein in complex with a stem-directed neutralizing antibody provide a molecular basis for host-cell protease requirements and identify a site of immune pressure. We also defined four conformational states of the trimer wherein each receptor-binding domain is either packed together at the membrane-distal apex or rotated into a receptor-accessible conformation.

Author contributions: J.P., N.W., K.S.C., D.W., R.N.K., A.N.K., M.R.D., J.D.C., B.S.G., A.B.W., and J.S.M. designed research; J.P., N.W., K.S.C., D.W., R.N.K., H.L.T., C.A.C., M.M.B., E.L.A., A.N.K., J.D.C., and J.S.M. performed research; L.W., W.S., and W.-P.K. contributed new reagents/analytic tools; J.P., N.W., K.S.C., D.W., R.N.K., A.N.K., M.R.D., J.D.C., B.S.G., A.B.W., and J.S.M. analyzed data; and J.P., N.W., D.W., A.B.W., and J.S.M. wrote the paper.

Conflict of interest statement: J.P., N.W., K.S.C., R.N.K., H.L.T., C.A.C., B.S.G., A.B.W., and J.S.M. are inventors on US patent application no. 62/412,703, entitled "Prefusion Coronavirus Spike Proteins and Their Use." L.W., W.S., W.-P.K., and B.S.G. are inventors on US patent application no. PCT/US2016/019395, entitled "Middle East Respiratory Syndrome Coronavirus Immunogens, Antibodies and Their Use."

This article is a PNAS Direct Submission.

Freely available online through the PNAS open access option.

Data deposition: Cryo-EM reconstructions have been deposited in the Electron Microscopy Data Bank (EMDB) (accession codes EMD-8783–EMD-8793). Atomic models have been deposited in the Protein Data Bank (PDB ID codes 5W9H–5W9P). Atomic models and structure factors for the crystal structures of MERS-CoV NTD and G4 Fab have also been deposited in the Protein Data Bank (PDB ID codes 5VYH and 5VZR, respectively).

[1]J.P., N.W., and K.S.C. contributed equally to this work.

[2]To whom correspondence may be addressed. Email: Nianshuang.Wang@dartmouth.edu, andrew@scripps.edu, or Jason.S.McLellan@Dartmouth.edu.

This article contains supporting information online at www.pnas.org/lookup/suppl/doi:10.1073/pnas.1707304114/-/DCSupplemental.

www.pnas.org/cgi/doi/10.1073/pnas.1707304114

subunits, S1 and S2 (13). The S1 subunit contains the receptor-binding domain (RBD), which recognizes the host-cell receptor DPP4 (CD26) (14–16). The S2 subunit contains the fusion peptide, two heptad repeats, and a transmembrane domain, all of which are required to mediate fusion of the viral and host-cell membranes by undergoing a large conformational rearrangement. The S1 and S2 subunits trimerize to form a large prefusion spike (~600 kDa) with ~25 *N*-linked glycans per monomer. Recent cryo-EM structures of trimeric prefusion S protein ectodomains from murine hepatitis virus (MHV), HCoV-HKU1, and HCoV-NL63 have revealed an overall mushroom-like architecture, with three identical S1 subunits forming an interwoven cap that rests atop the spring-loaded S2 stem (17–19). Interestingly, in this conformation the RBDs at the C terminus of S1 are not accessible for receptor binding, suggesting that a conformational change is required to expose the RBDs. Recently, a partial cryo-EM structure of the SARS-CoV S protein ectodomain was obtained that contained one of the three RBDs rotated into a receptor-accessible conformation (20). This configuration of the trimer may represent an initial intermediate state, although many questions remain unanswered, such as why only one of the RBDs is rotated.

As the primary glycoprotein on the surface of the viral envelope, S proteins are the major target of neutralizing antibodies elicited by natural infection and are key antigens in experimental vaccine candidates (11, 21, 22). However, the S protein ectodomain from MERS-CoV is less stable and more difficult to produce than other S proteins, and soluble constructs of the RBD have been the main focus of structural studies (14, 16), antibody isolation efforts (21, 23–25), and subunit vaccine development (26). A drawback of this approach is that coronaviruses can readily generate antibody-escape mutations in the RBD (23, 27, 28). Thus, the use of a mixture of antibodies, including some directed against non-RBD epitopes, is a preferred strategy (29) and has been used successfully for the treatment of Ebola virus disease (30). However, due to the difficulty in producing prefusion-stabilized MERS-CoV S proteins, few non-RBD antibodies have been described, and less is known about their epitopes. Antibodies against the prefusion conformation of the S2 stem are particularly attractive because the stem is more conserved than the S1 cap. Therefore, the ability to produce prefusion-stabilized S protein ectodomains from highly pathogenic coronaviruses, combined with the structural characterization of non-RBD epitopes that are recognized by potent neutralizing antibodies (31), would greatly facilitate the development of broadly protective interventions for current and emerging coronaviruses. Similar approaches are currently being developed for HIV-1 and influenza (32–34). Notably, the identification of stem-directed antibodies against influenza HA (35) represented a paradigm shift in the approach to develop a universal influenza vaccine, with recent studies demonstrating substantial promise (33, 34).

In this study, we rationally designed a general strategy to retain betacoronavirus S proteins in the prefusion conformation. The prefusion-stabilized MERS-CoV S protein (MERS S-2P) retained high-affinity binding to its dimeric receptor DPP4 and a panel of neutralizing antibodies, and elicited high titers of neutralizing antibodies in mice. The MERS S-2P construct also facilitated single-particle cryo-EM studies on a complex with G4, the first identified MERS-CoV S2-directed antibody (31). G4 was isolated from immunized mice and shown to be neutralizing, yet its epitope on S2 was unknown. The structures revealed that G4 recognizes the membrane-proximal surface of a variable, glycosylated loop in the S2 connector domain and avoids the glycosylation via its angle of approach, which is directed up from the viral membrane. The structures also defined four configurations of the trimer apex that represent the receptor-inaccessible ground state and three receptor-accessible intermediates. Collectively, these results advance our understanding of MERS-CoV entry and antibody-mediated neutralization and provide a foundation for the structure-based design of vaccine antigens for highly pathogenic coronaviruses, including those expected to emerge in the future.

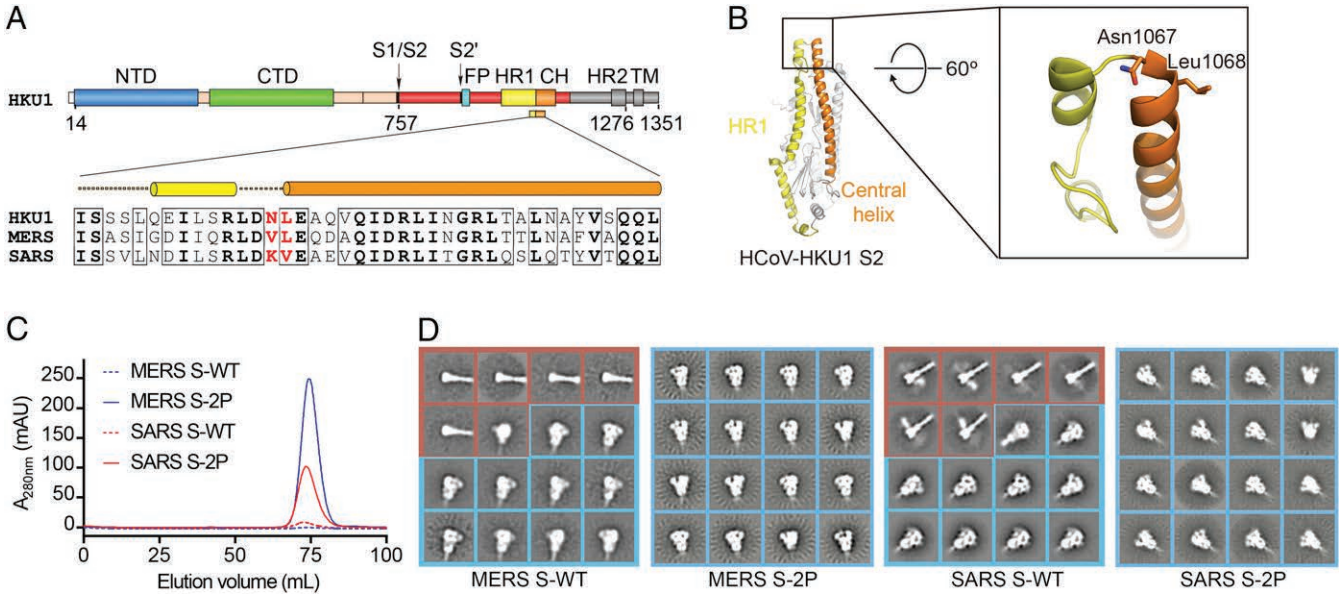

Fig. 1. Structure-based engineering of MERS-CoV and SARS-CoV S proteins. (*A*) Domain architecture of the HCoV-HKU1 S protein and sequence alignment of the helix-turn-helix between heptad repeat 1 (HR1) and the central helix (CH). The two residues colored red are those mutated to proline to retain S2 in the prefusion conformation. FP, fusion peptide; HR2, heptad repeat 2; TM, transmembrane domain. (*B*) Structure of HCoV-HKU1 S2. Residues shown in sticks in magnified region are those mutated to proline in the 2P variants. (*C*) Gel-filtration profiles of WT (dashed lines) and 2P-engineered (solid lines) S protein ectodomains from MERS-CoV (blue) and SARS-CoV (red). Each protein was produced from a 1-L transient transfection. All four proteins were expressed with a C-terminal T4 fibritin trimerization domain. The S1/S2 furin site was mutated in MERS S-WT and MERS S-2P. (*D*) Two-dimensional class averages of negative stained MERS S-WT, MERS S-2P, SARS S-WT, and SARS S-2P. All particles are included. For WT constructs both the prefusion (blue boxes) and postfusion (red boxes) conformations are visible, whereas for the 2P mutants only the prefusion conformation is observed.

Results

Engineering of Coronavirus S Proteins That Retain the Prefusion Conformation. To improve the expression and conformational homogeneity of the prefusion MERS-CoV S protein ectodomain we engineered variants based upon our previously determined structure of the trimeric S protein from the lineage A betacoronavirus HCoV-HKU1 (18) (Fig. 1 *A* and *B*). Recent work on the fusion proteins from HIV-1 and respiratory syncytial virus (RSV) (32, 36, 37) has demonstrated that proline substitutions in the loop between the first heptad repeat (HR1) and the central helix restrict premature triggering of the fusion protein and often increase expression yields of prefusion ectodomains. Introduction of single proline substitutions into a similar region in the MERS-CoV S2 subunit dramatically increased expression levels of the ectodomains, and two consecutive proline substitutions at residues V1060 and L1061 (hereafter referred to as "2P") resulted in a >50-fold improvement in yield (Fig. 1*C* and Fig. S1*A*). As evidenced by negative-stain EM, the 2P variant maintained prototypic prefusion morphology (Fig. 1*D*). Homologous substitutions in the S proteins from SARS-CoV (Fig. 1 *C* and *D* and Fig. S1*B*) and HCoV-HKU1 (Fig. S1 *B* and *C*) also increased the expression levels of the ectodomains and improved conformational homogeneity. Thus, the introduction of two consecutive proline residues at the beginning of the central helix seems to be a general strategy for retaining betacoronavirus S proteins in the prototypical prefusion conformation.

To investigate the effect of the 2P substitutions on S protein function, MERS-CoV pseudoviruses were generated with WT or 2P-containing S proteins. In contrast to WT pseudoviruses, which were highly infectious in DPP4-expressing Huh7.5 cells, pseudoviruses containing the 2P substitutions in the S protein were essentially noninfectious (Fig. 2*A*). This lack of infectivity is likely due to the ability of the introduced prolines to prevent conformational rearrangements, which presumably increases the activation energy required for fusion. However, to rule out the possibility of local misfolding as a result of the 2P substitutions, full-length WT and 2P-containing S proteins were expressed on 293T cells, and the reactivity of polyclonal sera and conformation-dependent antibodies was assessed by flow cytometry (Fig. 2*B*). The polyclonal sera, as well as neutralizing antibodies against the N-terminal domain (NTD) (mAb G2), RBD (mAb D12), and S2 subunit (mAb G4), reacted equally well to cells expressing WT or 2P-containing S proteins. Control cells expressing the RBD fused to a transmembrane domain only reacted with the polyclonal sera and D12 antibody, as expected. All three antibodies also bound to the recombinant MERS-CoV S protein ectodomains containing the 2P substitutions (MERS S-2P) via pull-down (Fig. 2*C*). We also determined that MERS S-2P bound to a soluble version of its receptor, DPP4, with a K_d of 9.4 nM (Fig. 2*D*), which is similar to reported values for the binding of DPP4 to the isolated RBD (14). Collectively, these data demonstrate that the 2P substitutions prevent fusion from occurring but do not alter the conformation of the S protein.

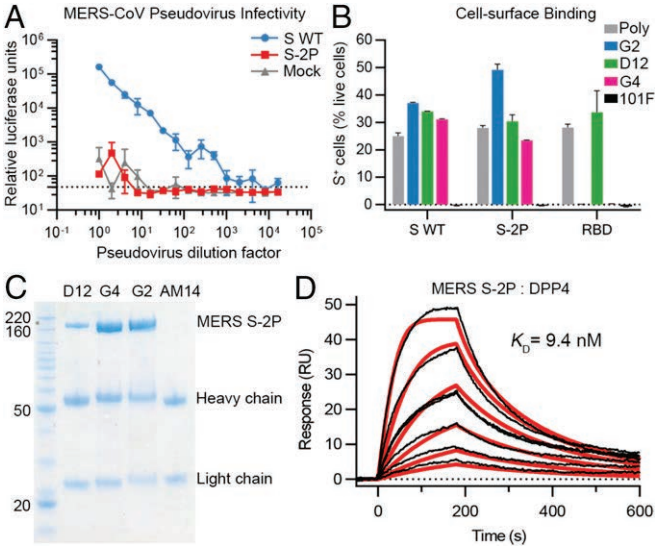

Fig. 2. Characterization of MERS S-2P. (*A*) MERS-CoV pseudoviruses encoding a luciferase reporter gene were generated with WT (S WT, blue) or 2P (S-2P, red) S proteins. Mock pseudoviruses (gray), expressing no S protein, served as a control. Infectivity in Huh7.5 cells was determined by measuring RLU. The dotted line represents background RLU. (*B*) Binding of cell-surface expressed MERS-CoV WT and 2P S proteins, as well as membrane-tethered RBD, to polyclonal sera (Poly) and monoclonal antibodies measured by flow cytometry; 101F is an RSV F-specific antibody. (*C*) SDS/PAGE analysis of copurified complexes of untagged MERS S-2P and monoclonal antibodies. AM14 is an RSV F-specific antibody. (*D*) Binding of soluble DPP4 to immobilized MERS S-2P measured by surface plasmon resonance. Best fit of the data to a 1:1 binding model is shown in red.

Immunogenicity of MERS S-2P. To determine the immunogenicity of the MERS S-2P trimer we vaccinated mice and compared the responses to those generated by monomeric S1 protein and WT S trimer (31). Each of the immunogens elicited neutralizing antibodies to the autologous England1 strain of MERS-CoV in a dose-dependent manner. S1 monomers and S WT trimers had a steeper dose effect than the S-2P trimer, which reached a plateau of neutralizing activity at a lower dose (Fig. 3*A*). At the 0.1-μg dose, MERS S-2P elicited significantly more robust neutralizing activity than S1 against four of the six homologous MERS-CoV pseudoviruses tested. The S-2P vaccination also elicited greater neutralization than S WT against three of the six homologous MERS-CoV pseudoviruses tested (Fig. 3*B*). These data demonstrate that retaining MERS-CoV S in its prefusion conformation increases the breadth and potency of the neutralizing activity elicited by vaccination.

Structure of MERS S-2P Bound to Antibody G4. We combined MERS S-2P with the S2-directed G4 Fab and conducted single-particle cryo-EM of the resulting complexes to structurally characterize our immunogen and provide atomic-level information needed for future engineering efforts (Fig. 4*A*, Fig. S2, and Tables S1 and S2). We observed several distinct subpopulations of S proteins that differed in the arrangement of the S1 apex, and these subpopulations were processed separately as described in more detail below. In addition, the cryo-EM density maps were less well-resolved in regions of the S1 NTD, as was the case in the recently determined structure of the SARS-CoV S protein (20). We consequently crystallized this domain and determined its structure to 2.0 Å using a portion of the cryo-EM map as a "search model" for molecular replacement (Fig. S3 and Table S3). We also crystallized and determined the structure of the unbound G4 Fab to 1.57 Å (Table S3), and both of these X-ray structures were used in further refinement of the cryo-EM–derived models.

Overall, the structure of the MERS S-2P protein is similar to the previously determined prefusion structures of alpha- and betacoronavirus S proteins (17–20). Our models consist of residues 18–1223 and like other structures are missing the second heptad repeat in S2, which may be flexible in the absence of a lipid bilayer. The MERS-CoV S2 subunit is arranged similarly to other coronavirus S2 subunits, with rmsd values of ∼1.5 Å for a shared core of ∼260 Cα atoms. For efficient infection of target cells, the MERS-CoV S protein requires a two-step, protease-mediated activation to facilitate membrane fusion. Furin cleavage at the S1/S2 junction occurs in the virus-producing cell, whereas cleavage at the S2′ site, upstream of the fusion peptide, occurs during viral entry at the cell surface or in endosomes

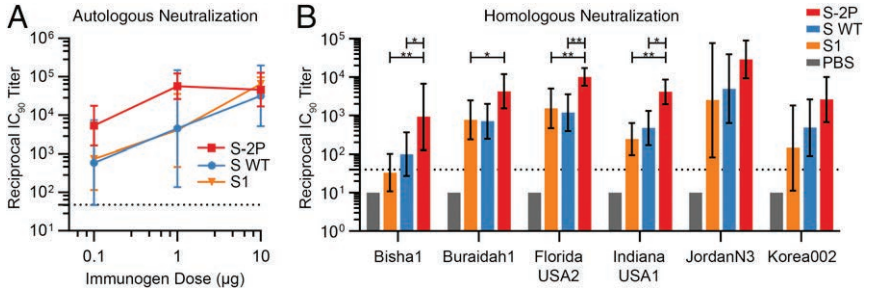

Fig. 3. Immunogenicity of MERS S-2P in mice. (*A*) Reciprocal serum IC_{90} neutralizing activity against autologous MERS England1 pseudotyped lentivirus reporter plotted against vaccine dose. (*B*) Reciprocal serum IC_{90} neutralizing activity against multiple homologous MERS-CoV pseudoviruses of sera from mice immunized with 0.1 μg of protein. For both panels, the geometric mean IC_{90} titer (GMT) of each group is represented by (*A*) symbols or (*B*) bars. Error bars represent geometric SDs. *P* values denoted as $*P < 0.05$ and $**P < 0.01$. The limit of detection for the assay is represented by dotted lines; for sera below the limit of detection a reciprocal IC_{90} titer of 10 was assigned.

and can be mediated by several proteases, including furin, TMPRSS2, and cathepsin L (11, 13, 38). However, it has not been understood why furin can access the S1/S2 site but not the S2′ site during protein biosynthesis. The S1/S2 furin site (RSVR), which remains uncleaved in our construct due to mutagenesis (ASVG), is located on an accessible solvent-exposed loop that is disordered in our structures (Fig. 4*B*). In contrast, the S2′ site (RSAR) is less exposed, particularly Arg887 at the P1 position, which interacts with Asp892 and Phe895 in the fusion peptide (Fig. 4*C*). In our structure, the peptide bond between Arg887 and Ser888 remains inaccessible to proteases, suggesting that S2′ cannot be efficiently cleaved until a conformational change occurs in S2 during the fusion process. Refolding of HR1 following DPP4 binding and S1 shedding would cause such a change and link the final proteolytic activation step to host-cell attachment, thus ensuring that irreversible refolding of S2 occurs at the proper time and place. Indeed, incubation of MERS-CoV virions with soluble DPP4 receptor increases the efficiency of furin cleavage at the S2′ site (13).

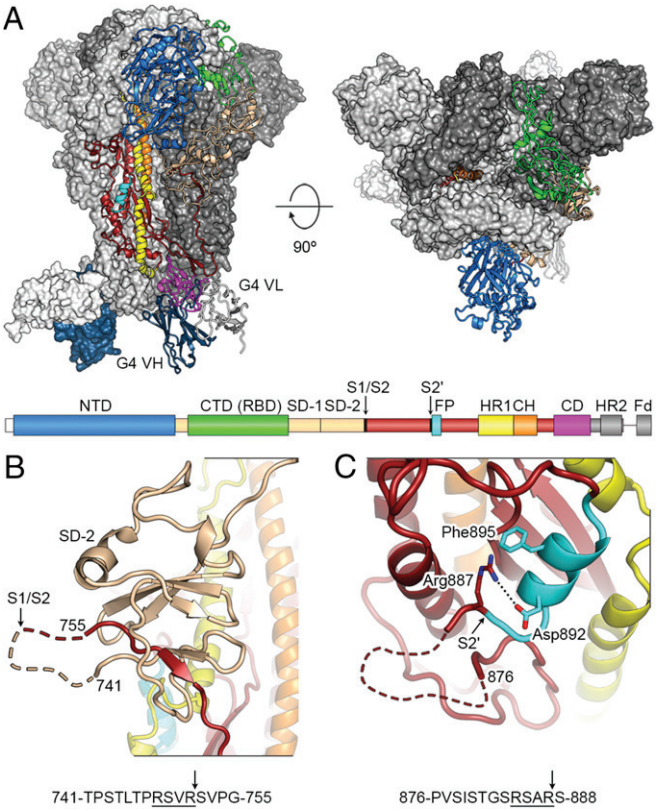

Fig. 4. Structure of MERS-CoV S-2P in complex with G4 Fab. (*A*) Structure of MERS S-2P ectodomain in complex with G4 Fab as viewed along (*Left*) and above (*Right*) the viral membrane. A single protomer of the trimeric S protein is shown in ribbon representation and colored as in the primary structure diagram. The two remaining protomers are shown as molecular surfaces and colored white and gray. CD, connector domain; CH, central helix; Fd, Foldon trimerization domain; SD-1, subdomain 1; SD-2, subdomain 2. (*B* and *C*) Magnified view of the S1/S2 (*B*) and S2′ (*C*) protease sites. Dashed lines represent disordered residues. Arrows indicate position of protease cleavage.

The MERS-CoV S2 structures also contain a well-resolved domain (residues 1152–1223) residing between HR1 and HR2 that was not completely resolved in the related betacoronavirus HCoV-HKU1, MHV, and SARS-CoV S protein structures but was observed in the alphacoronavirus HCoV-NL63 S protein structure (17–20). This connector domain contains the epitope for G4, which is the first reported S2-specific antibody that neutralizes MERS-CoV (31). The local resolution of the maps used for analysis of the antibody interface with S2 exceeds 3.7 Å. The majority of the G4 epitope (710 $Å^2$ of 880 $Å^2$ total buried surface area) consists of a glycosylated, solvent-exposed loop that extends out from two β-strands and is enshrouded by the complementarity-determining regions (CDRs) of G4 (Fig. 5*A*). The binding of G4 was substoichiometric, allowing comparison of the bound and unbound G4 epitope. In unbound protomers the loop was poorly ordered, suggesting that it is flexible in solution (Fig. S4). Arg1179 is critical for G4 binding, as it forms a cation–π interaction with HCDR2 Tyr53 as well as a salt bridge with HCDR1 Asp31 (Fig. 5*B*). In addition, G4 binding results in the formation of two hydrophobic cores that include S2 residues outside of the extended loop. These interactions may stabilize the connector domain, which is likely flexible given the poorly resolved density observed in other betacoronavirus S protein structures.

Although the epitope of G4 is contained within the relatively conserved S2 subunit, the exposed loop to which it primarily binds is variable in both sequence and length, even among lineage C betacoronaviruses (Fig. 5 *C* and *D*). The variability in this loop is reminiscent of the variable loops found in HIV-1 gp120, which arise as a result of pressure exerted by the host antibody response. Indeed, we were able to isolate MERS-CoV escape variants by growing the virus in the presence of G4, and the escape mutations (T1175I/P, R1179G/M/T, and S1185L) accumulated within and around this variable loop (Fig. 5*B* and Table S4). In addition to the sequence and length variability, this loop always contains at least one potential *N*-linked glycosylation site (Fig. 5*C*), which, like the HIV-1 gp120 variable loops, helps to shield the exposed loop from antibody recognition. G4 circumvents the glycan mask via its angle of approach, which is directed up from the viral membrane (Fig. 4*A*). This allows G4 to recognize the membrane-proximal face of the loop and avoid the glycan moieties attached to Asn1176. The requirement

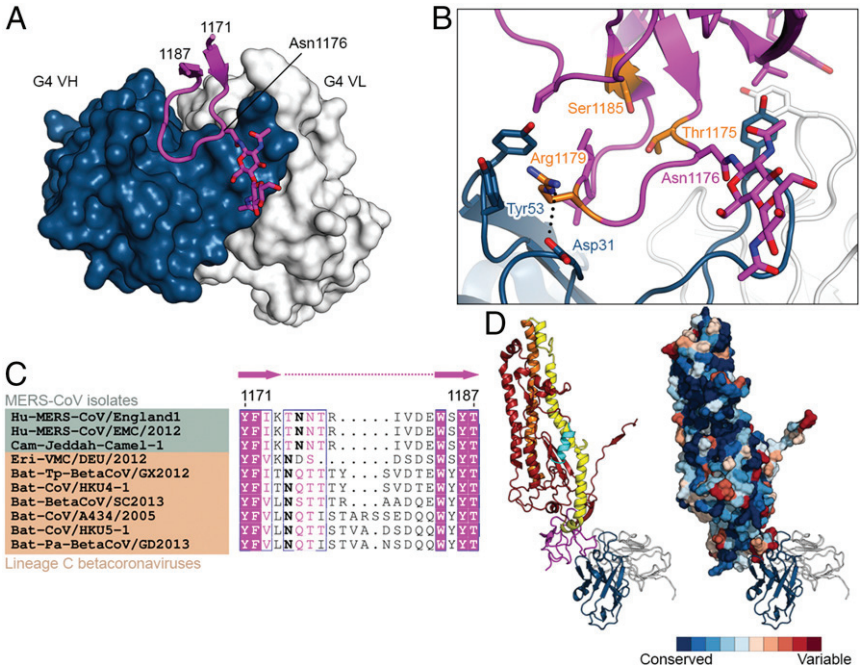

Fig. 5. G4 recognizes a variable loop in the S2 connector domain. (*A*) Structure of G4 Fab bound to a variable loop contained within the S2 subunit. Residues 1171–1187 of MERS S-2P are shown as a ribbon, with the side chain of Asn1176 and two attached *N*-acetylglucosamine moieties shown as sticks. The variable domains of G4 are shown as a molecular surface. (*B*) G4 binding interface. Side chains of interacting residues are shown as sticks, with residues substituted in G4-escape variants colored orange. Black dotted line indicates a salt bridge. (*C*) Sequence alignment of MERS-CoV isolates (green) and other lineage C betacoronaviruses (tan). Bold font indicates *N*-linked glycosylation sites. (*D*) Side views of one S2 protomer bound to G4 Fab. On the right, S2 is shown as a molecular surface and colored according to sequence conservation as determined by the ConSurf server using 66 diverse coronavirus sequences (85).

for this constrained approach likely comes at a cost to the binding affinity, as G4 has a higher affinity to deglycosylated MERS S-2P (Fig. S5). Because this loop is variable among betacoronaviruses, it should likely be eliminated in vaccine antigens designed to elicit a broadly neutralizing response against S2. As a proof of concept, we expressed a MERS S-2P variant wherein this loop was replaced with a Gly–Ser linker. This variant expressed at comparable levels to the MERS S-2P protein but had greatly reduced binding to G4 (Fig. S5). Addition of one or more *N*-linked glycosylation sites in the truncated loop would further help to shield this region from antibody recognition. Collectively, these data identify a variable loop in S2 that is likely under immune pressure and can be removed to potentially avoid virus-specific antibody responses in a vaccine antigen designed to elicit protection against multiple coronaviruses.

Receptor-Accessible S Protein Conformations. As mentioned above, during our cryo-EM studies we observed distinct subpopulations of S proteins that differed in the arrangement of the S1 apex, and processing these subpopulations separately revealed four distinct S1 crown configurations (Fig. 6*A*, Fig. S6, and Movies S1 and S2). We identified a small subpopulation of cryo-EM data (5.4%) in the tightly packed "closed" conformation, indicating that neither the 2P substitutions nor G4 binding prevent sampling of this conformation. Indeed, the 2P substitutions do not interact with the RBD and allow Arg1057 in HR1 to maintain its interaction with Tyr577 in the RBD (Fig. 6*B*). In the remaining three subpopulations of our cryo-EM data (totaling 94.6%), "open" trimers are observed with one, two, or three RBDs in an "out" conformation that extends away from the spike and does not interact with S2 or the glycosylated surface of the neighboring NTD (Fig. 6 *A* and *C*). In this extended configuration, the receptor-binding determinants are exposed at the apex of the complex and are fully accessible for interaction with DPP4 (Fig. 6*D*).

The four trimer configurations observed in our data suggest a potential mechanism for receptor-induced triggering that involves sequential activation of protomers. In this model, we speculate that DPP4 binding to transiently exposed RBDs functions as a molecular ratchet that drives the trimer to the three-RBD-out, open conformation (Fig. 7). This conformation is likely intrinsically unstable because the RBDs no longer help mediate trimerization of S1 or sterically inhibit refolding of S2 by sitting atop the central helix. In support of this model, we note that the three-RBD-out conformation is only observed in 0.3% of our cryo-EM data. Further experiments will be required to test this proposed model of receptor-induced triggering, but sequential activation of protomers in a class-I fusion protein has recently been demonstrated for Moloney murine leukemia virus (39).

Discussion

Approximately one-third of MERS-CoV infections have been fatal, making it the most lethal coronavirus described to date (40). The MERS-CoV S protein, which mediates receptor binding and membrane fusion, is the primary antigenic target for development of coronavirus vaccines (22). The introduction of two consecutive proline substitutions at the beginning of the central helix—our 2P design—presents a general approach to produce soluble prefusion coronavirus S ectodomains and overcomes the first hurdle in subunit vaccine development. Due to restricted backbone torsion angles, proline substitution can disfavor the refolding of the linker between the central helix and HR1, which for class I fusion proteins is a key step in the transition to the postfusion conformation (41). The rigidity of the helix–loop–helix afforded by the prolines impairs or abolishes the membrane fusion activity of the S protein, as evidenced in Fig. 2*A*. Similar results were obtained when prolines were substituted into influenza HA (42), and because class I fusion proteins have similar membrane fusion machinery, proline substitution has found broad use in subunit vaccine development. For HIV-1 Env, the I559P substitution in gp41 helped to produce a stable ectodomain trimer designated "SOSIP" (32), which facilitated

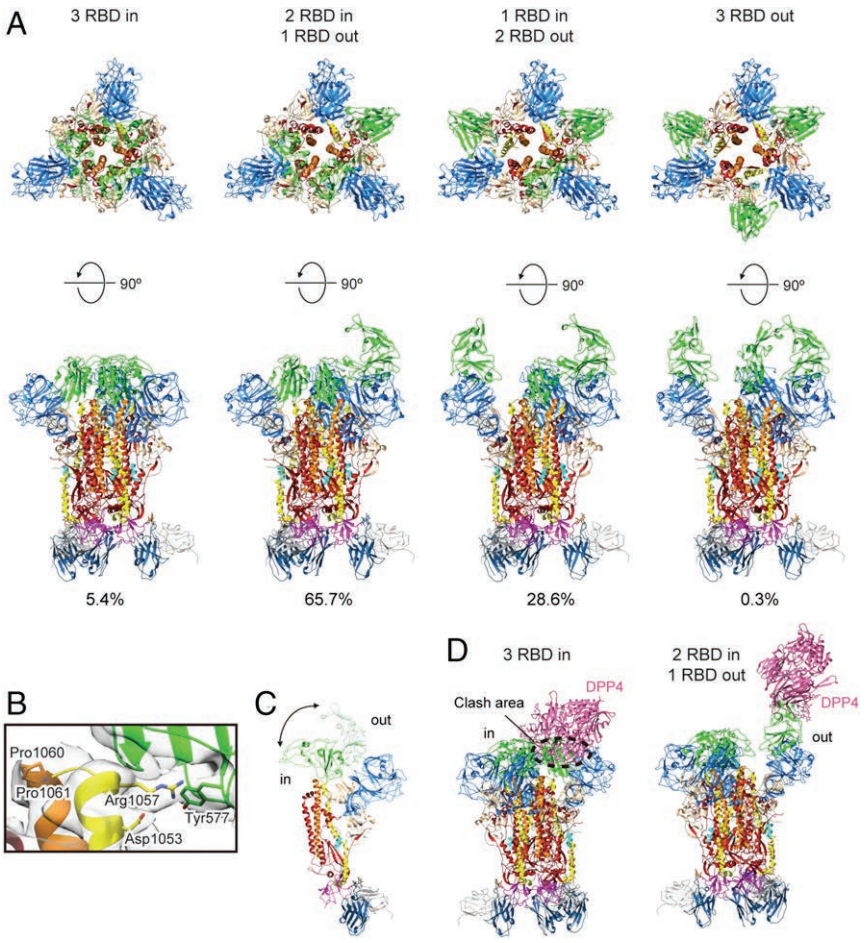

Fig. 6. RBD conformations observed in the MERS-CoV S protein. (*A*) Top and side views of the four MERS S-2P structures determined by single particle cryo-EM. Each has a unique arrangement of the three RBDs (green). The percentage of particles in the dataset belonging to each of the four structures is shown below the structures. (*B*) Interaction between an RBD (green) and the S2 helix–loop–helix spanning the central helix (orange) and HR1 (yellow). The two prolines introduced into S2 are shown as sticks, as are the side chains of interacting residues in the RBD and HR1. Electron density is shown as a transparent surface. (*C*) Superposition of one protomer with the RBD "in" and another protomer with the RBD "out." (*D*) Superposition of the RBD-DPP4 crystal structure (PDB ID code 4KR0) onto trimers with three RBDs in (*Left*) or two RBDs in and one RBD out (*Right*). Substantial clashes prevent DPP4 from binding until the RBD rotates outward.

the high-resolution structural analysis of this critical vaccine target (43–45). For RSV, an S215P substitution in the fusion (F) glycoprotein greatly increased the yield and stability of prefusion ectodomain trimers (36). This is consistent with our findings for the MERS-CoV S protein, where the 2P design resulted in a >50-fold increase in the yield of trimeric S protein in its antigenically native prefusion conformation (Fig. 1*C*). Unlike other structure-based engineering methods, such as the introduction of disulfide bonds or cavity-filling mutations (46), atomic-level information is not as critical for proline-based engineering, and the structure of a homologous protein with low sequence identity can serve as the template (Fig. 1 *A* and *B*). Thus, the proline-based strategy should be advantageous for the development of vaccine candidates against emerging coronaviruses for which structures have not yet been determined.

Our studies also characterized the interaction of a first-in-class neutralizing antibody (G4) directed against the S2 subunit, which is more conserved than the S1 cap (31). Prior mapping of neutralizing sites on coronavirus S proteins have focused on the RBD. However, neutralization escape has been described for RBD-specific mAbs, and it has been suggested that having broader epitope coverage outside of the RBD can improve protection from MERS-CoV challenge (31). The G4 epitope is largely conserved between different MERS-CoV isolates and thus G4-like antibodies present an attractive class of MERS-CoV cross-reactive antibodies for therapeutic use. The G4 epitope is, however, variable among the larger family of betacoronaviruses (Fig. 5*C*), suggesting that it is subject to immune pressure. For other coronaviruses, such as MHV and SARS-CoV, S2-directed antibodies have been isolated that recognize epitopes containing the fusion peptide (47, 48), which is relatively conserved among coronaviruses. An antibody that recognizes this region of the S2 stem, in a way that avoids most of the surrounding sequence variability, may broadly neutralize diverse coronaviruses. Potent antibodies directed against the fusion peptide of HIV-1 Env have recently been described (49, 50), providing hope that similar antibodies for coronaviruses may also be obtained through antigen-specific antibody-isolation efforts. Use of our engineered prefusion S proteins as probes to sort B cells from infected donors should greatly facilitate these efforts and lead to the development of a broadly protective immunotherapeutic.

In our structures of the trimeric prefusion MERS-CoV S protein we observe zero, one, two, or three RBDs rotated to a receptor-accessible "out" position (Fig. 6). We hypothesize that this flexibility in RBD exposure plays a role in the controlled timing of receptor engagement that ultimately leads to triggering of S toward the lower-energy postfusion state (Fig. 7). In addition, transient exposure of the RBDs, which are highly immunogenic,

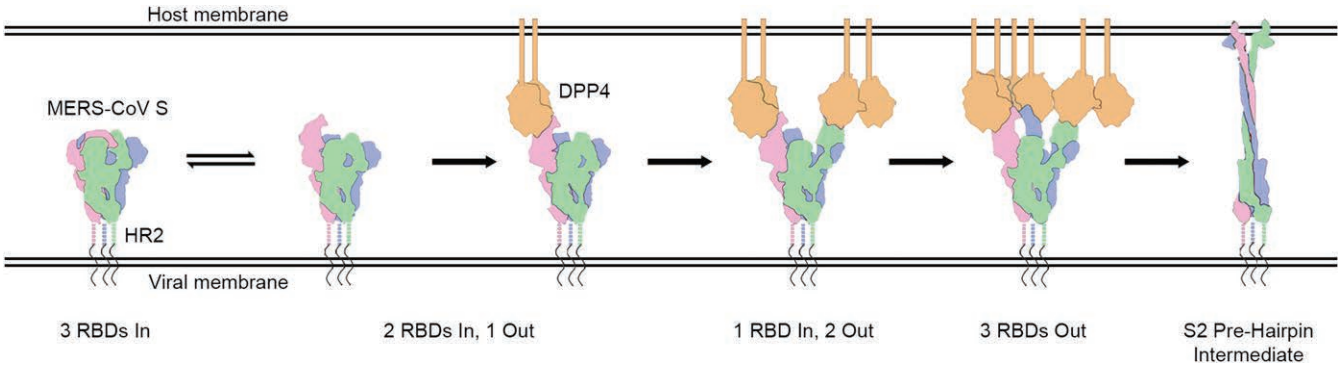

Fig. 7. Simplified model of DPP4 binding leading to MERS-CoV S triggering. The model posits that all three RBDs are in a state of equilibrium between the receptor-accessible "out" conformation and the tightly packed, receptor-inaccessible "in" conformation. DPP4 binding acts as a molecular ratchet that locks the RBD in the "out" conformation until all three RBDs are bound. This open conformation of the trimer is unstable and the S1 subunits ultimately dissociate from S2. Once the S2 subunits are no longer constrained by S1, membrane fusion can proceed by way of a prehairpin intermediate. MERS-CoV S protomers are colored pink, blue, and green and the unresolved HR2 region is depicted as a dashed line. Dimeric DPP4 is colored orange.

would help hide neutralizing epitopes from the humoral immune system. This "conformational masking" of neutralizing epitopes has also been described for HIV-1 Env (51), which like the coronavirus S proteins exists in several distinct conformations: closed ground state, CD4-accessible, and CCR5-accessible (52). For coronaviruses, this phenomenon was hinted at in the partially resolved structure of the SARS-CoV S protein, wherein a single RBD was observed in the receptor-accessible "out" conformation (20). In the structures of the S proteins from MHV and HCoV-HKU1 all three RBDs were shown to be in a tightly packed, closed configuration (17, 18). The MHV spike may not need to transiently expose the RBDs since it binds to its protein receptor CEACAM1 via the S1 NTD (53–55), and this interaction is thought to be sufficient for entry (56). For HCoV-HKU1, a protein receptor has not yet been identified, but the S1 subunit has been shown to bind *O*-acetylated sialic acids (57). Additional structural and virological studies are therefore needed to elucidate the molecular mechanisms of S protein-mediated cell entry.

Engineering class-I viral fusion proteins in the prefusion conformation can significantly improve immunogenicity through preservation of neutralization-sensitive conformational and quaternary epitopes. This is exemplified by the failure of postfusion RSV F glycoprotein vaccine antigens and the promise of prefusion-stabilized RSV F glycoproteins (36, 46, 58). Recently, the MERS-CoV S1 monomer has been shown to elicit RBD-specific neutralizing antibodies in mice and protect rhesus macaques from MERS-CoV–induced pneumonia, but protection was improved in animals primed with full-length S antigens that induced neutralizing antibodies directed to non-RBD sites (31). These data, together with the observation that the RBD has positional variability, suggest that the virus has evolved multiple mechanisms to evade neutralization by RBD-specific antibodies. The RBD sequence variability is compounded by the positional variability that allows conformational masking and transient exposure of quaternary surfaces and neutralization-sensitive sites. Our demonstration here that the prefusion-stabilized MERS-CoV S trimer (S-2P) elicits more robust neutralizing antibody responses in mice than S1 monomer or S WT suggests that MERS S-2P is a preferred antigen for vaccine development and is made more attractive due to inclusion of non-RBD epitopes and favorable manufacturing characteristics.

In summary, our 2P design, structures of the MERS-CoV S ectodomain in complex with G4, and demonstration of improved expression and immunogenicity of prefusion S proteins will serve as a basis for further engineering of MERS-CoV vaccine immunogens and provide an important step in the development of broadly protective coronavirus vaccines.

Methods

Production of S Protein Ectodomains. A mammalian-codon-optimized gene encoding MERS-CoV S (England1 strain) residues 1–1291 with a C-terminal T4 fibritin trimerization domain, an HRV3C cleavage site, an 8xHis-tag and a Twin-Strep-tag was synthesized and subcloned into the eukaryotic-expression vector pαH. The S1/S2 furin-recognition site 748-RSVR-751 was mutated to ASVG to produce a single-chain S0 protein.

A series of proline-substituted variants was generated based on this construct and the resulting plasmids were transfected into 40 mL FreeStyle 293-F cells (Invitrogen). Three hours after transfection, kifunensine was added to a final concentration of 5 μM. Cultures were harvested 6 d later, and secreted protein was purified from the supernatant using 0.5 mL Strep-Tactin resin (IBA). Protein expression levels were then assessed by SDS/PAGE (10 μL of protein-bound resin was boiled and loaded per lane). Similar strategies were used to generate and test proline-substituted variants of SARS-CoV S (Tor2 strain, residues 1–1190) and HCoV-HKU1 S (N5 strain, residues 1–1276).

For large-scale expression, 0.5–1 L FreeStyle 293-F cells were transfected. Three hours after transfection, kifunensine was added to a final concentration of 5 μM. Cultures were harvested after 6 d, and protein was purified from the supernatant using Strep-Tactin resin (IBA). HRV3C protease (1% wt/wt) was added to the protein and the reaction was incubated overnight at 4 °C. The digested protein was further purified using a Superose 6 16/70 column (GE Healthcare Biosciences).

Production of G4 Fab. The Fab region of the G4 heavy chain was fused with the HRV3C cleavage site and human IgG1 Fc fragment and subcloned into the eukaryotic expression vector pVRC8400. This plasmid was cotransfected with the G4 light chain into Expi293 cells (Invitrogen), and the secreted antibody was purified using Protein A agarose (Fisher). HRV3C protease (1% wt/wt) was added to the protein and the reaction was incubated for 2 h at room temperature. The digested antibody was passed back over Protein A agarose to remove the Fc fragment, and the unbound Fab was additionally purified using a Superdex 75 column (GE Healthcare Biosciences).

Production of MERS S-2P in Complex with G4 Fab. Purified MERS S-2P was mixed with a 1.5-fold molar excess of G4 Fab. After incubation on ice for 1 h, the complex was separated from excess Fab by size-exclusion chromatography.

Negative-Stain EM. MERS-CoV and SARS-CoV S-2P proteins were diluted with Tris-buffered saline as necessary and then spotted onto 400-mesh copper grids and stained with 1% uranyl acetate. Grids were imaged in a Tecnai T12 Spirit with a high tension of 120 kV and a Tietz TemCam-F416 complementary metal-oxide semiconductor camera at 52,000× magnification yielding a pixel size of 2.05 Å per pixel at 1.5 μm under focus. Images were collected using Leginon (59) and processed within the Appion workflow (60). Projection images were picked from the raw micrographs using a difference-of-Gaussians approach (61). Images were binned by two and then aligned using reference-free 2D classification with iterative multivariate statistical analysis/multi-reference alignment (62) to identify and remove amorphous projection images

from the image stacks. The image stacks were then realigned into 16 classes representing the entire cleaned stack.

Cryo-EM Data Collection. Approximately 3 μL of MERS S-2P/G4 Fab complex was mixed with 1 μL of a 0.04% A8-35 amphipol solution (Anatrace) immediately before sample deposition on a CF-2/2-4C C-Flat grid (Protochips; Electron Microscopy Sciences) that had been plasma-cleaned for 5 s using a mixture of Ar/O_2 (Gatan Solarus 950 Plasma system). The grid was then blotted and plunged into liquid ethane using a manual freeze plunger. Eight hundred thirteen movie micrographs were collected in one session through the Leginon software solution on an FEI Titan Krios operating at 300 kV and mounted with a Gatan K2 direct electron detector (59). Each micrograph was collected in counting mode at 29,000× nominal magnification resulting in a calibrated pixel size of 1.02 Å at the object level. A dose rate of ∼10 e^- per (camera pixel) per s was used and each movie frame was captured from an exposure time of 200 ms. Total dose for each movie micrograph was 66 $e^-/Å^2$. The nominal defocus range used was −0.7 to −2.5 μm.

Cryo-EM Data Processing. Frames in each movie micrograph were aligned and summed using MotionCorr (63). CTF estimation was then performed using CTFFind3 (64), and candidate MERS S-2P/G4 projection images were identified using a difference-of-Gaussians approach (61). Reference-free 2D classification was then performed in RELION version 1.4 (65). After 2D classification, 37,180 good projection images were refined asymmetrically (resolution 4.0 Å) as well as under C3 restraint (resolution 3.6 Å) against a negative-stain reference map rendered at 60-Å resolution. Projection images and the asymmetrically refined map were entered into RELION 3D classification, resulting in three classes each with two copies of G4 Fabs bound but with differing S1 crown configurations (resolutions 4.7 Å, 4.8 Å, and 5.0 Å). A fourth data class was characterized by having three copies of G4 Fabs bound (resolution 4.5 Å). This latter data class was further refined under C3 symmetry constraint (resolution 4.0 Å). As density corresponding to the S1 crown still exhibited more disorder than the otherwise well-ordered data classes, a local classification procedure was pursued (Fig. S2). Here, three masks each encompassing both the "in" and the "out" RBD configuration at respective RBD positions were created. By applying each of these masks in separate parallel classification protocols, separation of a homogeneous density region from a heterogeneous density region was obtained in each case. Subtraction of the homogeneous density from raw projection images was then obtained by projecting the homogeneous density map according to the projection image Euler directions already obtained from refinement. The resulting local RBD density projection images were then subjected to RELION 3D classification using the homogeneous density map (no density in the RBD area that is to be classified) as seed. In each of the three cases this resulted in two data classes corresponding to the RBD "in" or the "out" position. The original raw projection images were then recompiled into four conformationally clean data classes corresponding to three RBD "in", two RBD "in" and one RBD "out", one RBD "in" and two RBD "out," and three RBD "out." Projection images of the asymmetric classes were rotated into correct alignment (0°, 120°, or 240° Euler rotation) before further refinement. Each of the four classes was individually refined against a reference map at 60 Å simulated from our MERS S-2P coordinate build but without any RBD coordinates included (resulting map resolutions 4.0 Å, 4.6 Å, 4.8 Å, and 11.5 Å). Symmetric classes (three RBD "in" or three RBD "out") were initially refined asymmetrically to confirm correct classification of "in" and "out" positions before further refinement imposing C3 restraint. All resolutions were estimated by the FSC 0.143 criterion in RELION using a soft-edged mask with a Gaussian fall-off, encompassing entire structures and corrected for mask correlations.

Cryo-EM Model Building and Refinement. An initial model of MERS S-2P was obtained from the MODELLER homology modeling tool (66) in UCSF Chimera (67) using HCoV-HKU1 S (PDB ID code 5I08) as a template. Significant manual remodeling as well as de novo building of the S2 domain that connects the central helix with HR2 was performed in Coot (68). X-ray structures for MERS S1 NTD and MERS S1 RBD (PDB ID code 4KR0) were used to substitute the respective regions (RBD added only to models where appropriate) and the resulting homology model was combined with X-ray structures of the G4 Fab. The resulting models were then iteratively refined and manually rebuilt against their respective density maps (not remodeling S1 NTD or RBD domains) using Rosetta density-guided iterative local refinement (69) and Coot. Rosetta all-atom refinement was then performed in a modular fashion wherein well-resolved regions were refined under little restraint and gradually higher B-factor regions were refined under gradually stricter restraints. Addition of ligands and further refinements were conducted in Rosetta using the respective density maps as constraints (70) and end-refined in PHENIX (71). Models were evaluated using MolProbity (oneline-analysis command line implementation) (72) and EMRinger (command line implementation) (73) and Privateer (command line implementation) (74) and CARP (web server) (75) where appropriate.

Production of MERS-CoV S1 NTD. A gene encoding MERS-CoV S1 NTD (residues 1–353) with a C-terminal HRV3C cleavage site and human IgG1 Fc fragment was inserted into the eukaryotic expression vector pαH. Three hours after transient transfection of the plasmid into FreeStyle 293-F cells, kifunensine was added to a final concentration of 5 μM. After 6 d, the supernatant was passed over a Protein A agarose column, and deglycosylation was conducted on-column by adding EndoH (10% wt/wt) at room temperature. After 12 h, the column was washed with PBS and the NTD was eluted by incubating the resin with HRV3C (1% wt/wt). The NTD was further purified using a Superdex 75 column (GE Healthcare Biosciences).

Crystallization and X-Ray Data Collection. Purified G4 Fab was concentrated to 9.5 mg/mL in TBS (2 mM Tris, pH 8.0, and 50 mM NaCl) for crystallization. Crystals were produced at room temperature using the sitting-drop vapor-diffusion method by mixing 0.1 μL of protein with 0.1 μL of reservoir solution containing 0.1 M MES, pH 6.5, 0.2 M magnesium chloride, and 10% (wt/wt) PEG 4000. Crystals were soaked in reservoir solution supplemented with 20% (vol/vol) glycerol and flash-frozen in liquid nitrogen. X-ray diffraction data were collected at the SBC beamline 19-ID (Advanced Photon Source, Argonne National Laboratory).

Purified MERS-CoV S1 NTD was concentrated to 11.7 mg/mL in TBS for crystallization. Initial hits were obtained in the Wizard Precipitant Synergy screen (76). Crystals were obtained at room temperature using the sitting-drop vapor-diffusion method by mixing 0.1 μL of protein with 0.1 μL of reservoir solution containing 0.1 M imidazole HCl, pH 6.5, 6.6% (wt/wt) PEG 8000, and 1% (vol/vol) 2-methyl-2,4-pentanediol. Crystals were soaked in reservoir solution supplemented with 20% (vol/vol) glycerol and frozen in liquid nitrogen. X-ray diffraction data were collected at the SSRL beamline BL14-1 (Stanford Synchrotron Radiation Lightsource, SLAC National Accelerator Laboratory).

Crystal Structure Determination and Refinement. Diffraction data were processed using the CCP4 software suite: data were indexed and integrated in iMOSFLM (77) and scaled and merged with AIMLESS (78). A molecular replacement solution for the G4 Fab data was obtained using PHASER (79) and PDB ID 3QQ9 as the search model. The structure was built manually in Coot (68) and refined using PHENIX (71). Data collection and refinement statistics are presented in Table S3.

For the MERS-CoV S1 NTD dataset, molecular replacement using NTD structures from MHV and bovine coronavirus (BCoV) failed to find a solution. Therefore, a portion of the EM map corresponding to the NTD was extracted and used as the search model for molecular replacement using PHASER-MR in the PHENIX GUI following a recently published protocol (80). The solution contained only one molecule in the asymmetric unit, so noncrystallographic symmetry could not be used to improve the phases. Consequently, the core β-sheet of the BCoV NTD was manually fit into the electron density, and iterative rounds of manual building with Coot and refinement with PHENIX produced a model containing 184 residues. Using this structure as input, MR-ROSETTA (81) was able to produce a model containing 282 residues. This model was then used as input for Buccaneer (82), which produced a model containing all 341 residues. After manually adding *N*-linked glycans with Coot, additional electron density was observed that did not correspond to any chemicals in the crystallization buffer or cryosolution. We identified the chemical as folic acid using mass spectrometry, and placed the molecule into the density (Fig. S3). The folic acid is thought to have copurified with the NTD from the mammalian expression medium, but whether folic acid, or a closely related chemical analog, has a physiological role in the MERS-CoV infection cycle remains unknown. The final structure was refined using PHENIX, and the data collection and refinement statistics are presented in Table S3. Software used to determine X-ray crystal structures was curated by SBGrid (83).

Protein A Pull-Down Experiments. MERS S-2P was coexpressed with each antibody by cotransfecting 10 μg of MERS S-2P plasmid with 5 μg of heavy-chain plasmid and 5 μg of light-chain plasmid into 40 mL of FreeStyle 293-F cells (Invitrogen). Three hours after transfection, kifunensine was added to a final concentration of 5 μM. Cultures were harvested after 6 d, and protein was purified from the supernatant using 0.5 mL of Protein A resin (Thermo Fisher). After an extensive wash with PBS, 10 μL of protein-bound resin was boiled and analyzed by SDS/PAGE.

Surface Plasmon Resonance Experiments. The 8xHis-tagged MERS S-2P protein was captured on an NTA sensor chip to ∼660 response units each cycle using a

Biacore X100 (GE Healthcare). The chip was regenerated twice after each cycle using 350 mM EDTA followed by 0.5 mM $NiCl_2$. After three injections of running buffer over both the ligand-bound and reference flow cells, increasing concentrations of soluble DPP4 ectodomain were injected (1.6 nM to 50 nM with a final replicate of 12.5 nM). Data were double-reference subtracted and fit to a 1:1 binding model using Scrubber2 software.

Mouse Immunizations. Animal experiments were carried out in compliance with all pertinent US National Institutes of Health regulations and policies. The National Institutes of Health, National Institute of Allergy and Infectious Diseases, Vaccine Research Center Animal Care and Use Committee reviewed and approved all animal experiments. Female BALB/cJ mice aged 6–8 wk (Jackson Laboratory) were immunized with MERS S1, MERS S WT, or MERS S-2P protein at 0 and 3 wk. Protein (0.1 μg, 1 μg, or 10 μg) diluted in PBS was mixed 1:1 with 2× Sigma Adjuvant System. Mice were inoculated with 100 μL intramuscularly (50 μL into each hind leg). Two weeks after the final immunization, sera were collected for measurement of antibody responses.

Pseudovirus Production. Pseudovirus production, infectivity, and neutralization experiments were completed as previously described with minor adaptations (31). We synthesized cDNAs encoding spike protein using the QuikChange XL kit (Stratagene) and introduced divergent amino acids into the parental spike gene (strain England1) predicted from translated sequences of other strains: Bisha1 (GenBank accession no. KF600620), Buraidah1 (GenBank accession no. KF600630), Florida USA2 (GenBank accession no. AIZ48760), Indiana USA1 (GenBank accession no. AHZ58501), JordanN3 (GenBank accession no. KC776174), and Korea002 (GenBank accession no. AKL59401). All constructs were confirmed using sequencing. HEK293T cells were obtained from ATCC and cultured in DMEM supplemented with 10% FBS, 2 mM glutamine, and 1% penicillin/streptomycin at 37 °C and 5% CO_2. To produce MERS-CoV pseudoviruses, CMV/R-MERS-CoV spike plasmids were cotransfected into HEK293T cells with packaging plasmid pCMVDR8.2 and transducing plasmid pHR′ CMV-Luc, using Fugene 6 transfection reagent (Promega). Mock pseudoviruses were produced by omitting the MERS-CoV S plasmid. Seventy-two hours posttransfection, supernatants were collected, filtered, and frozen at −80 °C.

Pseudovirus Infectivity and Neutralization Experiments. Huh7.5 cells were provided by Deborah R. Taylor, US Food and Drug Administration, Silver Spring, MD, and cultured in DMEM supplemented with 10% FBS, 2 mM glutamine, and 1% penicillin/streptomycin at 37 °C and 5% CO_2. Pseudovirus infectivity was assessed in Huh7.5 cells plated overnight in 96-well black/white isoplates (PerkinElmer). Twofold serial dilutions of pseudoviruses were added to resting Huh7.5 cells, in triplicate. After a 2-h incubation, fresh medium was added. Cells were lysed at 72 h, and luciferase substrate (Promega) was added. Luciferase activity was measured as relative luciferase units (RLU) at 570 nm on a SpectramaxL (Molecular Devices). For neutralization experiments, serial dilutions of mouse sera (1:40, fourfold, eight dilutions) were mixed with various pseudovirus strains, which were previously titered to target 50,000 RLU. Sigmoidal curves, taking averages of triplicates at each dilution, were generated from RLU readings; 90% neutralization (IC_{90}) titers were calculated considering uninfected cells as 100% neutralization and cells transduced with only virus as 0% neutralization.

Cell-Surface Binding Assay. Cell-surface binding assays were performed as previously described with minor adaptations (31). HEK 293T cells were plated and maintained overnight to reach 80% confluence. Cells were transfected with plasmids expressing MERS-CoV S-WT, S-2P, or RBD engineered with an influenza HA transmembrane domain, using Fugene 6 transfection reagent (Promega). After 24 h, cells were detached with 4 mM EDTA in PBS, stained with ViViD viability dye (Invitrogen), and then stained with mAbs (10 μg/mL) or polyclonal sera (1:200) obtained from mice vaccinated with MERS-CoV S. Cells were subsequently stained with goat anti-mouse IgG, Alexa-488 (Invitrogen). Cells were sorted with an LSR (BD Biosciences). Data were analyzed with FlowJo software (Tree Star Inc.), using the following gating strategy: size & granularity > single cells > live cells (ViViD negative) > $Spike^+$ (Ab positive). Fluorescence background was calculated using untransfected cells stained with each respective mAb and subtracted from the data.

Isothermal Titration Calorimetry Experiments. Calorimetric titrations of G4 Fab into MERS S-2P, deglycosylated MERS S-2P, or variable-loop-deleted MERS S-2P were performed using a PEAQ isothermal titration calorimeter (ITC) (Malvern) at 25 °C. All proteins were dialyzed into PBS. Protein concentrations in the sample cell were 3.0–3.7 μM, whereas the concentration of G4 Fab in the injection syringe was 57.5 μM. Titrations consisted of 15 injections. Data were processed with the MicroCal PEAQ-ITC Analysis Software (Malvern) and fit to an independent-binding model.

Viral Resistance to Antibody-Mediated Inhibition of Infectivity. MERS-CoV variants escaping G4-mediated neutralization of infectivity were selected by serial passage of recombinant MERS-CoV strain EMC/2012 in Vero 81 cell cultures (84) supplemented with progressively escalating concentrations of antibody, eventually reaching 3.6 μg/mL at the terminal passage level, P5. The starting amount of G4, 0.4 μg/mL, corresponded to the antibody concentration required to reduce ∼40 MERS-CoV plaque-forming units by ∼70% in a plaque-reduction neutralization assay using Vero 81 cell monolayers. Culture supernatants were passed onto fresh cells 48 h postinfection and a total of 13 G4-resistant MERS-CoV isolates representing three parallel passage series were plaque-cloned from P5 cultures on Vero 81 cell monolayers in the presence of 1 μg/mL G4. Plaque isolates were expanded in antibody-free cultures of Vero cells in 25-cm^2 flasks, followed by total RNA isolation from virally infected cell monolayers using TRIzol reagent (Invitrogen). Two overlapping cDNA amplicons encompassing the entire S gene were generated by RT-PCR using SuperScript III RT (Invitrogen) and Easy-A high-fidelity thermostable DNA polymerase (Agilent Technologies) (40 cycles of RT product amplification). Resultant S-gene PCR products were subjected to dideoxy sequencing using S gene-based primers, and reads were aligned to the native EMC/2012 S-gene sequence (GenBank accession no. JX869059.2) using MacVector to identify mutations associated with neutralization-escape from G4. Cell culture-adaptive mutations in spike identified in antibody-free P10 and P20 cultures of EMC/2012 were excluded from analyses of changes arising under G4 selection.

ACKNOWLEDGMENTS. We thank members of the J.S.M. and A.B.W. laboratories for critical reading of the manuscript, E. Shipman for assistance with protein expression, Benjamin Cabrera and members of the Vaccine Research Center (VRC) Translational Research Program for technical assistance with immunogenicity experiments, J. Adolf-Bryfogle and S. Rämisch for assistance with Rosetta ligand modeling, and the beamline scientists for X-ray data collection support at SBC 19-ID (Argonne National Laboratory) and BL14-1 SLAC National Accelerator Laboratory. This work was supported by Grants P20GM113132 (to J.S.M.) and R01AI127521 (to J.S.M. and A.B.W.), NIH Contract HHSN261200800001E Agreement 6x142 (to M.R.D. and J.D.C.), and intramural funding from National Institute of Allergy and Infectious Diseases to support work at the VRC (B.S.G.). Argonne is operated by UChicago Argonne, LLC, for the US Department of Energy (DOE), Office of Biological and Environmental Research under Contract DE-AC02-06CH11357. Use of the Stanford Synchrotron Radiation Lightsource (SSRL), SLAC National Accelerator Laboratory, is supported by the DOE, Office of Science, Office of Basic Energy Sciences under Contract DE-AC02-76SF00515. The SSRL Structural Molecular Biology Program is supported by the DOE Office of Biological and Environmental Research and by the NIH, National Institute of General Medical Sciences (including P41GM103393).

1. Woo PC, Lau SK, Huang Y, Yuen KY (2009) Coronavirus diversity, phylogeny and interspecies jumping. *Exp Biol Med (Maywood)* 234:1117–1127.
2. Peiris JS, et al. (2003) Coronavirus as a possible cause of severe acute respiratory syndrome. *Lancet* 361:1319–1325.
3. Zaki AM, van Boheemen S, Bestebroer TM, Osterhaus AD, Fouchier RA (2012) Isolation of a novel coronavirus from a man with pneumonia in Saudi Arabia. *N Engl J Med* 367: 1814–1820.
4. van Boheemen S, et al. (2012) Genomic characterization of a newly discovered coronavirus associated with acute respiratory distress syndrome in humans. *MBio* 3:e00473–12.
5. Azhar EI, et al. (2014) Evidence for camel-to-human transmission of MERS coronavirus. *N Engl J Med* 370:2499–2505.
6. Alraddadi BM, et al. (2016) Risk factors for primary Middle East respiratory syndrome coronavirus illness in humans, Saudi Arabia, 2014. *Emerg Infect Dis* 22: 49–55.
7. Fehr AR, Channappanavar R, Perlman S (2017) Middle East respiratory syndrome: Emergence of a pathogenic human coronavirus. *Annu Rev Med* 68:387–399.
8. Mohd HA, Al-Tawfiq JA, Memish ZA (2016) Middle East respiratory syndrome coronavirus (MERS-CoV) origin and animal reservoir. *Virol J* 13:87.
9. Oboho IK, et al. (2015) 2014 MERS-CoV outbreak in Jeddah—A link to health care facilities. *N Engl J Med* 372:846–854.
10. Ki M (2015) 2015 MERS outbreak in Korea: Hospital-to-hospital transmission. *Epidemiol Health* 37:e2015033.
11. Gierer S, et al. (2013) The spike protein of the emerging betacoronavirus EMC uses a novel coronavirus receptor for entry, can be activated by TMPRSS2, and is targeted by neutralizing antibodies. *J Virol* 87:5502–5511.
12. Li F (2016) Structure, function, and evolution of coronavirus spike proteins. *Annu Rev Virol* 3:237–261.
13. Millet JK, Whittaker GR (2014) Host cell entry of Middle East respiratory syndrome coronavirus after two-step, furin-mediated activation of the spike protein. *Proc Natl Acad Sci USA* 111:15214–15219.
14. Lu G, et al. (2013) Molecular basis of binding between novel human coronavirus MERS-CoV and its receptor CD26. *Nature* 500:227–231.

15. Raj VS, et al. (2013) Dipeptidyl peptidase 4 is a functional receptor for the emerging human coronavirus-EMC. *Nature* 495:251–254.
16. Wang N, et al. (2013) Structure of MERS-CoV spike receptor-binding domain complexed with human receptor DPP4. *Cell Res* 23:986–993.
17. Walls AC, et al. (2016) Cryo-electron microscopy structure of a coronavirus spike glycoprotein trimer. *Nature* 531:114–117.
18. Kirchdoerfer RN, et al. (2016) Pre-fusion structure of a human coronavirus spike protein. *Nature* 531:118–121.
19. Walls AC, et al. (2016) Glycan shield and epitope masking of a coronavirus spike protein observed by cryo-electron microscopy. *Nat Struct Mol Biol*, 10.1038/nsmb.3293.
20. Gui M, et al. (2017) Cryo-electron microscopy structures of the SARS-CoV spike glycoprotein reveal a prerequisite conformational state for receptor binding. *Cell Res* 27:119–129.
21. Corti D, et al. (2015) Prophylactic and postexposure efficacy of a potent human monoclonal antibody against MERS coronavirus. *Proc Natl Acad Sci USA* 112:10473–10478.
22. Modjarrad K, et al. (2016) A roadmap for MERS-CoV research and product development: Report from a World Health Organization consultation. *Nat Med* 22:701–705.
23. Tang XC, et al. (2014) Identification of human neutralizing antibodies against MERS-CoV and their role in virus adaptive evolution. *Proc Natl Acad Sci USA* 111:E2018–E2026.
24. Jiang L, et al. (2014) Potent neutralization of MERS-CoV by human neutralizing monoclonal antibodies to the viral spike glycoprotein. *Sci Transl Med* 6:234ra259.
25. Li Y, et al. (2015) A humanized neutralizing antibody against MERS-CoV targeting the receptor-binding domain of the spike protein. *Cell Res* 25:1237–1249.
26. Zhang N, Tang J, Lu L, Jiang S, Du L (2015) Receptor-binding domain-based subunit vaccines against MERS-CoV. *Virus Res* 202:151–159.
27. Sui J, et al. (2008) Broadening of neutralization activity to directly block a dominant antibody-driven SARS-coronavirus evolution pathway. *PLoS Pathog* 4:e1000197.
28. ter Meulen J, et al. (2006) Human monoclonal antibody combination against SARS coronavirus: Synergy and coverage of escape mutants. *PLoS Med* 3:e237.
29. Mitsuki YY, et al. (2008) A single amino acid substitution in the S1 and S2 Spike protein domains determines the neutralization escape phenotype of SARS-CoV. *Microbes Infect* 10:908–915.
30. Qiu X, et al. (2014) Reversion of advanced Ebola virus disease in nonhuman primates with ZMapp. *Nature* 514:47–53.
31. Wang L, et al. (2015) Evaluation of candidate vaccine approaches for MERS-CoV. *Nat Commun* 6:7712.
32. Sanders RW, et al. (2002) Stabilization of the soluble, cleaved, trimeric form of the envelope glycoprotein complex of human immunodeficiency virus type 1. *J Virol* 76:8875–8889.
33. Impagliazzo A, et al. (2015) A stable trimeric influenza hemagglutinin stem as a broadly protective immunogen. *Science* 349:1301–1306.
34. Yassine HM, et al. (2015) Hemagglutinin-stem nanoparticles generate heterosubtypic influenza protection. *Nat Med* 21:1065–1070.
35. Ekiert DC, et al. (2009) Antibody recognition of a highly conserved influenza virus epitope. *Science* 324:246–251.
36. Krarup A, et al. (2015) A highly stable prefusion RSV F vaccine derived from structural analysis of the fusion mechanism. *Nat Commun* 6:8143.
37. Kong L, et al. (2016) Uncleaved prefusion-optimized gp140 trimers derived from analysis of HIV-1 envelope metastability. *Nat Commun* 7:12040.
38. Shirato K, Kawase M, Matsuyama S (2013) Middle East respiratory syndrome coronavirus infection mediated by the transmembrane serine protease TMPRSS2. *J Virol* 87:12552–12561.
39. Sjoberg M, Loving R, Lindqvist B, Garoff H (2017) Sequential activation of the three protomers in the Moloney murine leukemia virus Env. *Proc Natl Acad Sci USA* 114:2723–2728.
40. Arabi YM, et al. (2017) Middle East respiratory syndrome. *N Engl J Med* 376:584–594.
41. Carr CM, Kim PS (1993) A spring-loaded mechanism for the conformational change of influenza hemagglutinin. *Cell* 73:823–832.
42. Qiao H, et al. (1998) Specific single or double proline substitutions in the "spring-loaded" coiled-coil region of the influenza hemagglutinin impair or abolish membrane fusion activity. *J Cell Biol* 141:1335–1347.
43. Pancera M, et al. (2014) Structure and immune recognition of trimeric pre-fusion HIV-1 Env. *Nature* 514:455–461.
44. Lyumkis D, et al. (2013) Cryo-EM structure of a fully glycosylated soluble cleaved HIV-1 envelope trimer. *Science* 342:1484–1490.
45. Julien JP, et al. (2013) Crystal structure of a soluble cleaved HIV-1 envelope trimer. *Science* 342:1477–1483.
46. McLellan JS, et al. (2013) Structure-based design of a fusion glycoprotein vaccine for respiratory syncytial virus. *Science* 342:592–598.
47. Daniel C, et al. (1993) Identification of an immunodominant linear neutralization domain on the S2 portion of the murine coronavirus spike glycoprotein and evidence that it forms part of complex tridimensional structure. *J Virol* 67:1185–1194.
48. Zhang H, et al. (2004) Identification of an antigenic determinant on the S2 domain of the severe acute respiratory syndrome coronavirus spike glycoprotein capable of inducing neutralizing antibodies. *J Virol* 78:6938–6945.
49. Lee JH, Ozorowski G, Ward AB (2016) Cryo-EM structure of a native, fully glycosylated, cleaved HIV-1 envelope trimer. *Science* 351:1043–1048.
50. Kong R, et al. (2016) Fusion peptide of HIV-1 as a site of vulnerability to neutralizing antibody. *Science* 352:828–833.
51. Kwong PD, et al. (2002) HIV-1 evades antibody-mediated neutralization through conformational masking of receptor-binding sites. *Nature* 420:678–682.
52. Munro JB, et al. (2014) Conformational dynamics of single HIV-1 envelope trimers on the surface of native virions. *Science* 346:759–763.
53. Dveksler GS, et al. (1991) Cloning of the mouse hepatitis virus (MHV) receptor: Expression in human and hamster cell lines confers susceptibility to MHV. *J Virol* 65:6881–6891.
54. Peng G, et al. (2011) Crystal structure of mouse coronavirus receptor-binding domain complexed with its murine receptor. *Proc Natl Acad Sci USA* 108:10696–10701.
55. Kubo H, Yamada YK, Taguchi F (1994) Localization of neutralizing epitopes and the receptor-binding site within the amino-terminal 330 amino-acids of the murine coronavirus spike protein. *J Virol* 68:5403–5410.
56. Matsuyama S, Taguchi F (2009) Two-step conformational changes in a coronavirus envelope glycoprotein mediated by receptor binding and proteolysis. *J Virol* 83:11133–11141.
57. Huang X, et al. (2015) Human coronavirus HKU1 spike protein uses O-acetylated sialic acid as an attachment receptor determinant and employs hemagglutinin-esterase protein as a receptor-destroying enzyme. *J Virol* 89:7202–7213.
58. Graham BS (2016) Vaccines against respiratory syncytial virus: The time has finally come. *Vaccine* 34:3535–3541.
59. Suloway C, et al. (2005) Automated molecular microscopy: The new Leginon system. *J Struct Biol* 151:41–60.
60. Lander GC, et al. (2009) Appion: An integrated, database-driven pipeline to facilitate EM image processing. *J Struct Biol* 166:95–102.
61. Voss NR, Yoshioka CK, Radermacher M, Potter CS, Carragher B (2009) DoG Picker and TiltPicker: Software tools to facilitate particle selection in single particle electron microscopy. *J Struct Biol* 166:205–213.
62. Ogura T, Iwasaki K, Sato C (2003) Topology representing network enables highly accurate classification of protein images taken by cryo electron-microscope without masking. *J Struct Biol* 143:185–200.
63. Li X, et al. (2013) Electron counting and beam-induced motion correction enable near-atomic-resolution single-particle cryo-EM. *Nat Methods* 10:584–590.
64. Mindell JA, Grigorieff N (2003) Accurate determination of local defocus and specimen tilt in electron microscopy. *J Struct Biol* 142:334–347.
65. Scheres SH (2012) RELION: Implementation of a Bayesian approach to cryo-EM structure determination. *J Struct Biol* 180:519–530.
66. Webb B, Sali A (2016) Comparative protein structure modeling using MODELLER. *Curr Protoc Protein Sci* 86:2 9 1–2 9 37.
67. Pettersen EF, et al. (2004) UCSF Chimera—A visualization system for exploratory research and analysis. *J Comput Chem* 25:1605–1612.
68. Emsley P, Cowtan K (2004) Coot: Model-building tools for molecular graphics. *Acta Crystallogr D Biol Crystallogr* 60:2126–2132.
69. DiMaio F, et al. (2015) Atomic-accuracy models from 4.5-A cryo-electron microscopy data with density-guided iterative local refinement. *Nat Methods* 12:361–365.
70. DiMaio F, Tyka MD, Baker ML, Chiu W, Baker D (2009) Refinement of protein structures into low-resolution density maps using rosetta. *J Mol Biol* 392:181–190.
71. Adams PD, et al. (2002) PHENIX: Building new software for automated crystallographic structure determination. *Acta Crystallogr D Biol Crystallogr* 58:1948–1954.
72. Chen VB, et al. (2010) MolProbity: All-atom structure validation for macromolecular crystallography. *Acta Crystallogr D Biol Crystallogr* 66:12–21.
73. Barad BA, et al. (2015) EMRinger: Side chain-directed model and map validation for 3D cryo-electron microscopy. *Nat Methods* 12:943–946.
74. Agirre J, et al. (2015) Privateer: Software for the conformational validation of carbohydrate structures. *Nat Struct Mol Biol* 22:833–834.
75. Lutteke T, Frank M, von der Lieth CW (2005) Carbohydrate Structure Suite (CSS): Analysis of carbohydrate 3D structures derived from the PDB. *Nucleic Acids Res* 33:D242–D246.
76. Majeed S, et al. (2003) Enhancing protein crystallization through precipitant synergy. *Structure* 11:1061–1070.
77. Battye TG, Kontogiannis L, Johnson O, Powell HR, Leslie AG (2011) iMOSFLM: A new graphical interface for diffraction-image processing with MOSFLM. *Acta Crystallogr D Biol Crystallogr* 67:271–281.
78. Evans PR, Murshudov GN (2013) How good are my data and what is the resolution? *Acta Crystallogr D Biol Crystallogr* 69:1204–1214.
79. McCoy AJ, et al. (2007) Phaser crystallographic software. *J Appl Cryst* 40:658–674.
80. Jackson RN, McCoy AJ, Terwilliger TC, Read RJ, Wiedenheft B (2015) X-ray structure determination using low-resolution electron microscopy maps for molecular replacement. *Nat Protoc* 10:1275–1284.
81. DiMaio F, et al. (2011) Improved molecular replacement by density- and energy-guided protein structure optimization. *Nature* 473:540–543.
82. Cowtan K (2006) The Buccaneer software for automated model building. 1. Tracing protein chains. *Acta Crystallogr D Biol Crystallogr* 62:1002–1011.
83. Morin A, et al. (2013) Collaboration gets the most out of software. *eLife* 2:e01456.
84. Scobey T, et al. (2013) Reverse genetics with a full-length infectious cDNA of the Middle East respiratory syndrome coronavirus. *Proc Natl Acad Sci USA* 110:16157–16162.
85. Ashkenazy H, et al. (2016) ConSurf 2016: An improved methodology to estimate and visualize evolutionary conservation in macromolecules. *Nucleic Acids Res* 44:W344–W350.
86. Peng G, et al. (2012) Crystal structure of bovine coronavirus spike protein lectin domain. *J Biol Chem* 287:41931–41938.
87. Rusin SF, Schlosser KA, Adamo ME, Kettenbach AN (2015) Quantitative phosphoproteomics reveals new roles for the protein phosphatase PP6 in mitotic cells. *Sci Signal* 8:rs12.

LETTER

doi:10.1038/nature21428

Zika virus protection by a single low-dose nucleoside-modified mRNA vaccination

Norbert Pardi[1]*, Michael J. Hogan[1]*, Rebecca S. Pelc[2], Hiromi Muramatsu[1], Hanne Andersen[3], Christina R. DeMaso[2], Kimberly A. Dowd[2], Laura L. Sutherland[4], Richard M. Scearce[4], Robert Parks[4], Wendeline Wagner[3], Alex Granados[3], Jack Greenhouse[3], Michelle Walker[3], Elinor Willis[5], Jae-Sung Yu[4], Charles E. McGee[4], Gregory D. Sempowski[4], Barbara L. Mui[6], Ying K. Tam[6], Yan-Jang Huang[7], Dana Vanlandingham[7], Veronica M. Holmes[1], Harikrishnan Balachandran[8], Sujata Sahu[8], Michelle Lifton[8], Stephen Higgs[7], Scott E. Hensley[5], Thomas D. Madden[6], Michael J. Hope[6], Katalin Karikó[9], Sampa Santra[8], Barney S. Graham[10], Mark G. Lewis[3], Theodore C. Pierson[2], Barton F. Haynes[4] & Drew Weissman[1]

Zika virus (ZIKV) has recently emerged as a pandemic associated with severe neuropathology in newborns and adults[1]. There are no ZIKV-specific treatments or preventatives. Therefore, the development of a safe and effective vaccine is a high priority. Messenger RNA (mRNA) has emerged as a versatile and highly effective platform to deliver vaccine antigens and therapeutic proteins[2,3]. Here we demonstrate that a single low-dose intradermal immunization with lipid-nanoparticle-encapsulated nucleoside-modified mRNA (mRNA–LNP) encoding the pre-membrane and envelope glycoproteins of a strain from the ZIKV outbreak in 2013 elicited potent and durable neutralizing antibody responses in mice and non-human primates. Immunization with 30 μg of nucleoside-modified ZIKV mRNA–LNP protected mice against ZIKV challenges at 2 weeks or 5 months after vaccination, and a single dose of 50 μg was sufficient to protect non-human primates against a challenge at 5 weeks after vaccination. These data demonstrate that nucleoside-modified mRNA–LNP elicits rapid and durable protective immunity and therefore represents a new and promising vaccine candidate for the global fight against ZIKV.

ZIKV, first identified in 1947 (ref. 4), is a mosquito-borne and sexually transmitted flavivirus that has recently been associated with microcephaly and other birth defects in newborns and Guillain–Barré syndrome in adults[1]. Effective vaccines have been approved for other closely related flaviviruses[5–7], but vaccine candidates for ZIKV have only recently been developed[8–12]. Multiple vaccine formats have been shown to protect mice or non-human primates against ZIKV infection, including plasmid DNA[9–12], purified inactivated virus[10,11], protein subunit[8] and adenovirus vectors[8,10]. The ideal vaccine is safe and induces protective immunity after a single immunization, regardless of prior serologic history. Of the candidate Zika vaccines described to date, only a rhesus adenovirus platform (RhAd52) has been shown to confer protection after a single immunization in non-human primates; however, the efficacy of the RhAd52 vector in humans is currently unknown. Additionally, pre-existing immunity to adenovirus serotypes can limit the efficacy of such vectors[13,14], and low neutralizing titres to rhesus adenoviruses, including RhAd52, have been detected in humans[15].

mRNA has emerged as a promising vaccine modality that can elicit potent immune responses (reviewed in refs 2, 3), while avoiding the safety risks and anti-vector immunity associated with some live virus vaccines (reviewed in ref. 16). Vaccination with mRNA offers several advantages over other vaccine platforms: (i) it is a non-integrating, non-infectious gene vector that can be readily designed to express any protein with high efficiency; (ii) it has the potential for cost-effective and highly scalable manufacturing; and (iii) small doses are sufficient to induce protective immune responses.

Here, we designed a potent anti-ZIKV vaccine in which the pre-membrane and envelope (prM–E) glycoproteins of ZIKV H/PF/2013 (ref. 17) are encoded by mRNA (Extended Data Fig. 1a) containing the modified nucleoside 1-methylpseudouridine (m1Ψ), which prevents innate immune sensing and increases mRNA translation *in vivo*[18]. Nucleoside-modified ZIKV prM–E mRNA was prepared for vaccination by encapsulation in lipid nanoparticles (LNPs), which have been shown to mediate efficient and prolonged protein expression by mRNA *in vivo*[19]. Studies of ZIKV and other flaviviruses have demonstrated that co-expression of pre-membrane and envelope proteins is sufficient to assemble and secrete subviral particles[12,20]. ZIKV prM–E-encoding mRNA was first characterized by transfecting HEK293T cells and human and mouse dendritic cells. ZIKV envelope (E) protein was produced by all cell types and was secreted into the supernatant of HEK293T cells (Extended Data Fig. 1b). We hypothesize that dendritic cells also secrete E protein and that it is rapidly internalized by endocytosis, as has been proposed for HIV gag[21]. E protein in the supernatant of HEK293T cells was pelleted by ultracentrifugation when incubated with PBS, but not with 0.5% Triton X-100, consistent with subviral particle production from prM–E mRNA[20] (Extended Data Fig. 1c).

The immune response induced by the nucleoside-modified ZIKV prM–E mRNA–LNP vaccine was first analysed in C57BL/6 mice. Animals were immunized by intradermal injection of 30 μg of ZIKV prM–E mRNA–LNP or polycytidylic acid (poly(C)) RNA–LNP as a negative control. No inflammation or other adverse events were observed at the sites of injection. Polyfunctional E-protein-specific $CD4^+$ T cell responses were detected on the basis of intracellular IFNγ, TNF (also known as TNFα) and IL-2 production by splenocytes stimulated with ZIKV E protein at week 2 after vaccination (Fig. 1a and Extended Data Fig. 2). ZIKV E-protein-specific immunoglobulin G (IgG) in the serum developed quickly in vaccinated mice and stabilized at an endpoint titre of 180,000 (90 μg ml^{-1}) at weeks 8–12 (Fig. 1b and Extended Data Fig. 3a). Anti-ZIKV neutralizing antibodies (nAb) were measured using two independent assays: a standard

[1]Department of Medicine, Perelman School of Medicine, University of Pennsylvania, Philadelphia, Pennsylvania 19104, USA. [2]Viral Pathogenesis Section, National Institute of Allergy and Infectious Disease, National Institutes of Health, Bethesda, Maryland 20892, USA. [3]Bioqual Inc., Rockville, Maryland 20850-3220, USA. [4]Duke Human Vaccine Institute, Duke University School of Medicine, Durham, North Carolina 27710, USA. [5]Department of Microbiology, Perelman School of Medicine, University of Pennsylvania, Philadelphia, Pennsylvania 19104, USA. [6]Acuitas Therapeutics, Vancouver, British Columbia V6T 1Z3, Canada. [7]Diagnostic Medicine and Pathobiology, College of Veterinary Medicine and the Biosecurity Research Institute, Kansas State University, Manhattan, Kansas 66506, USA. [8]Center for Virology and Vaccine Research, Beth Israel Deaconess Medical Center, Harvard Medical School, Boston, Massachusetts 02215 USA. [9]BioNTech RNA Pharmaceuticals, An der Goldgrube 12, 55131 Mainz, Germany. [10]Vaccine Research Center, National Institute of Allergy and Infectious Disease, National Institutes of Health, Bethesda, Maryland 20892, USA.
*These authors contributed equally to this work.

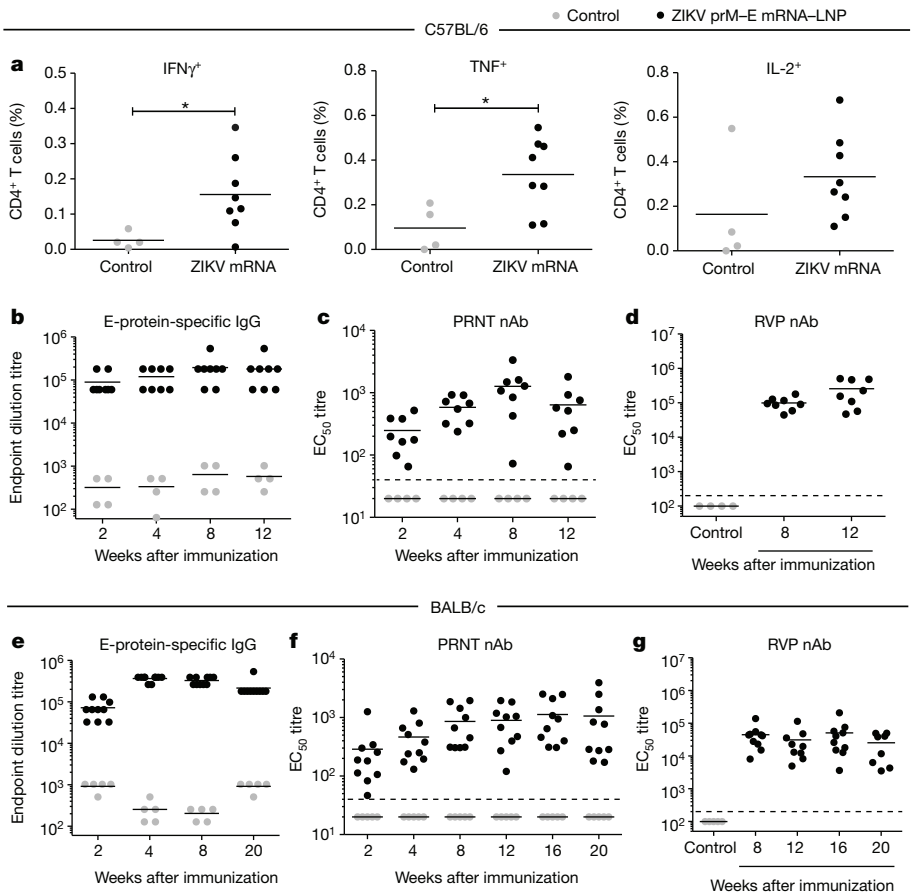

Figure 1 | Nucleoside-modified ZIKV mRNA–LNP immunization elicits ZIKV-specific T helper cell and neutralizing antibody responses. **a**–**d**, C57BL/6 mice were immunized by intradermal injection of 30 μg of nucleoside-modified ZIKV prM–E mRNA–LNP ($n = 8$) or control poly(C) RNA–LNP ($n = 4$). **a**, At week 2, splenic antigen-specific $CD4^+$ T cells were detected by intracellular cytokine staining. **b**–**d**, The antibody response was analysed by ELISA (**b**), PRNT using ZIKV MR-766 (**c**) and RVP using ZIKV H/PF/2013 (**d**). **e**–**g**, BALB/c mice were immunized similarly with ZIKV mRNA–LNP ($n = 10$) or poly(C) RNA–LNP ($n = 5$) and immune responses were analysed by ELISA (**e**), PRNT using MR-766 (**f**) and RVP using H/PF/2013 (**g**). Points represent individual mice; horizontal lines show the mean; dotted lines indicate the limit of detection. The controls in **d** and **g** are from the week 8 time point. $^*P < 0.05$ (unpaired t-test) in **a**; antibody responses in vaccine and control groups were compared at each time point by Mann–Whitney test, $P < 0.01$ for all comparisons (**b**–**g**).

plaque-reduction neutralization test (PRNT) and a ZIKV reporter viral particle (RVP) assay[12]. The mean $PRNT_{50}$ titre against ZIKV MR-766 peaked at around 1,300 at week 8 (Fig. 1c) and was relatively stable until week 12. The mean RVP nAb titre (EC_{50}) against ZIKV H/PF/2013 reached approximately 10^5 at weeks 8–12 (Fig. 1d). The detection of higher nAb titres in the RVP assay compared to other assay formats similar to PRNT has previously been reported[12]. In addition, we noted that the ratio of RVP to PRNT titres was not fixed and varied with the animal model and viral isolate.

Immunogenicity of the nucleoside-modified ZIKV prM–E mRNA–LNP vaccine was next evaluated in BALB/c mice. E-protein-specific IgG in the serum peaked at week 8 and remained stable between weeks 8 and 20 (endpoint titres around 200,000; 90–130 μg ml^{-1}) (Fig. 1e and Extended Data Fig. 3b). $PRNT_{50}$ nAb increased to a maximum of about 1,100 at week 16 and remained stable until week 20 (Fig. 1f). The RVP nAb titre rose to 50,000 at week 8 and remained above 20,000 until week 20 (Fig. 1g).

A challenge study was conducted in BALB/c mice immunized by intradermal injection of 30 μg of nucleoside-modified ZIKV prM–E mRNA–LNP or poly(C) RNA–LNP. Mice were challenged by intravenous injection at week 2 (short term) or week 20 (long term) after immunization with 200 plaque-forming units (PFU) of ZIKV PRVABC59. In the short-term protection study, 8 out of 9 control mice showed the presence of viral RNA in the blood (viraemia) by day 3, with a median peak of around 14,000 copies per ml. All ZIKV mRNA-immunized mice ($n = 9$) were protected against detectable viraemia (Fig. 2a). In the long-term study, all control mice ($n = 5$) showed viraemia on day 3, with a median peak of 1,200 copies per

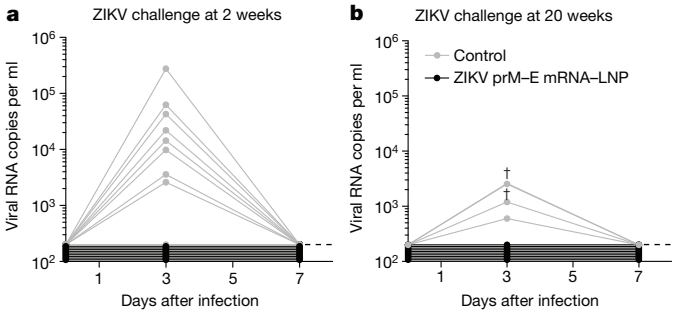

Figure 2 | A single immunization of nucleoside-modified ZIKV prM–E mRNA–LNP provides rapid and durable protection against ZIKV challenge in mice. **a**, **b**, BALB/c mice immunized by intradermal injection of 30 μg of ZIKV prM–E mRNA–LNP or control poly(C) RNA–LNP were challenged by intravenous injection of 200 PFU ZIKV PRVABC59 at 2 weeks (**a**; $n = 9$ per group) or 20 weeks (**b**; $n = 5$ control mice; $n = 10$ ZIKV mRNA–LNP mice) after vaccination and plasma viral loads were measured by qRT–PCR for ZIKV capsid RNA. Two overlapping curves are indicated by a dagger symbol. Dotted lines indicate the limit of detection (200 copies per ml), with undetectable curves staggered to show individual mice. Day 3 viraemia in vaccine and control groups was compared by Mann–Whitney test, $P < 0.001$ for both challenges.

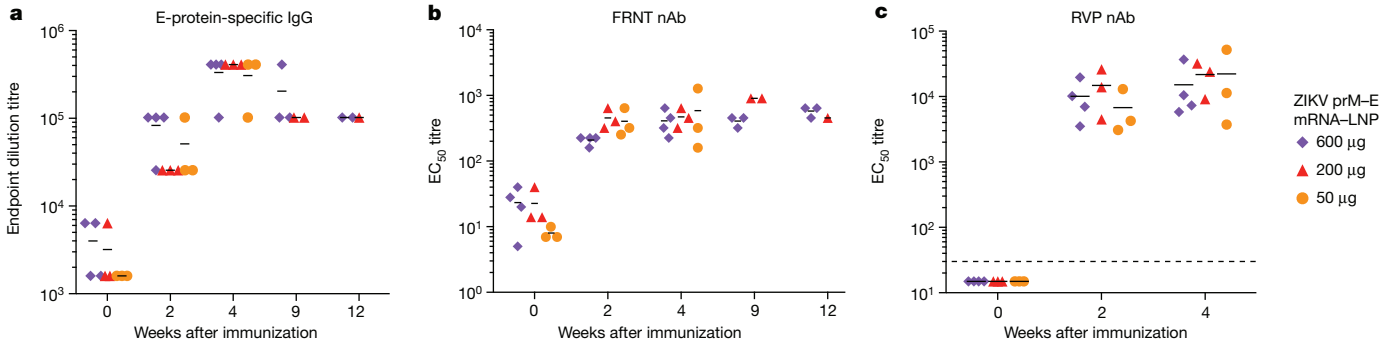

Figure 3 | Nucleoside-modified ZIKV mRNA–LNP immunization elicits potent ZIKV-specific neutralizing antibody responses in non-human primates. a–c, Rhesus macaques were immunized with 600 μg ($n = 4$), 200 μg ($n = 3$) or 50 μg ($n = 3$) of ZIKV prM–E mRNA–LNP and the antibody response was quantified by ELISA (**a**), FRNT using ZIKV MEX I-44 (**b**) and RVP using ZIKV H/PF/2013 (**c**). Data from pre-challenge (weeks 0–4 in **a**–**c**) and unchallenged (weeks 9–12 in **a**, **b**) animals are shown. Points represent individual monkeys; dotted lines indicate the limit of detection; horizontal lines indicate the mean. Immune responses in dose groups were compared by Kruskal–Wallis test, $P > 0.05$ for all comparisons.

ml, whereas none of the ZIKV mRNA-immunized mice ($n = 10$) had detectable viraemia at days 3 or 7 (Fig. 2b). These data demonstrate that a single immunization with nucleoside-modified ZIKV prM–E mRNA–LNP rapidly elicits durable protection against detectable viraemia with a heterologous ZIKV strain in mice.

We next evaluated the efficacy of the nucleoside-modified ZIKV mRNA–LNP vaccine in rhesus macaques (*Macaca mulatta*), a non-human primate species that shows several features of ZIKV infection in humans[22]. Macaques were immunized by intradermal injection with doses of 600 μg, 200 μg or 50 μg of nucleoside-modified ZIKV prM–E mRNA–LNP. Similar to mice, no inflammation or other adverse events were observed. E-protein-specific IgG and nAb were efficiently induced by all three vaccine doses, with no statistically significant differences between groups. Endpoint IgG titres rose to >300,000 in all groups at week 4 and were maintained at ≥100,000 until week 12 (Fig. 3a). $PRNT_{50}$ nAb titres against MR-766 peaked at about 400 at week 2 (Extended Data Fig. 4a). To facilitate comparison of nAb titres across laboratories, the neutralization curve is shown for a human ZIKV-neutralizing monoclonal antibody, A3594, in the PRNT assay (Extended Data Fig. 5). nAb titres obtained with a focus-reduction neutralization test (FRNT), which has a format similar to PRNT, were stable around 400 against ZIKV MEX I-44 at weeks 2–12 (Fig. 3b). The RVP assay showed nAb titres against H/PF/2013 of around 10,000 at week 2 and around 17,000 at week 4 (Fig. 3c), and a titre of around 3,000 against MR-766 at week 4 (Extended Data Fig. 4b). The neutralization of viruses from both Asian and African lineages is consistent with a previous report demonstrating the existence of only one serotype of ZIKV[23]. The absence of a significant dose-dependent effect in the antibody response in any assay (Kruskal–Wallis test, $P > 0.05$) suggests that a low dose of 50 μg (approximately 0.02 mg kg^{-1}) was sufficient, or possibly more than sufficient, to induce robust anti-ZIKV immunity in macaques.

Rhesus macaques were challenged at week 5 by subcutaneous injection of 10^4 $TCID_{50}$ of ZIKV PRVABC59 in five vaccinated animals and six control animals (Extended Data Table 1). All control animals became infected, with median peak plasma viraemia of 7,000 ZIKV RNA copies per ml (Fig. 4). By contrast, vaccinated macaques were highly protected against ZIKV infection. Four out of five animals—including three that received the lowest dose of 50 μg and one that received the medium dose of 200 μg—had no detectable viraemia (<50 copies per ml) at all time points. We detected a low and transient viral blip of 100 copies per ml at day 3 after challenge in one animal that received the highest dose of 600 μg of ZIKV prM–E mRNA–LNP, representing a 99% reduction in peak viraemia compared to the control animals. This animal exhibited among the lowest nAb titres in multiple assays at week 4 after vaccination: $PRNT_{50}$ of 36 to MR-766, $FRNT_{50}$ of 226 to MEX I-44 and RVP titres of 986 to MR-766 and 5,812 to H/PF/2013 (Fig. 3 and Extended Data Fig. 4). The significance of a low-level viral blip in one animal, including implications for a correlate of protection, are as yet uncertain and warrant further study with a greater number of animals.

In this report, we demonstrate that a single, low-dose intradermal immunization with nucleoside-modified ZIKV prM–E mRNA–LNP is protective in both mice and rhesus macaques and elicits higher nAb responses than a single immunization of multiple ZIKV vaccine candidates that have recently been reported, including purified inactivated virus (PIV) and plasmid DNA vaccines encoding prM–E or M–E[10–12]. In mice, $PRNT_{50}$ nAb increased steadily over several months, rising to levels 50–100 times higher than those induced by a single immunization with PIV or DNA vaccines[11,12]. The ZIKV mRNA–LNP vaccine conferred complete, rapid and durable protection in mice that was maintained for at least 5 months, and probably much longer, since nAb titres were stable. The challenge studies in mice also showed that ZIKV PRVABC59 replicated more efficiently ($P = 0.02$, Mann–Whitney test) in 8-week-old BALB/c mice compared to 25-week-old mice, when two identical aliquots and doses of challenge virus stock were used. A previous report has shown

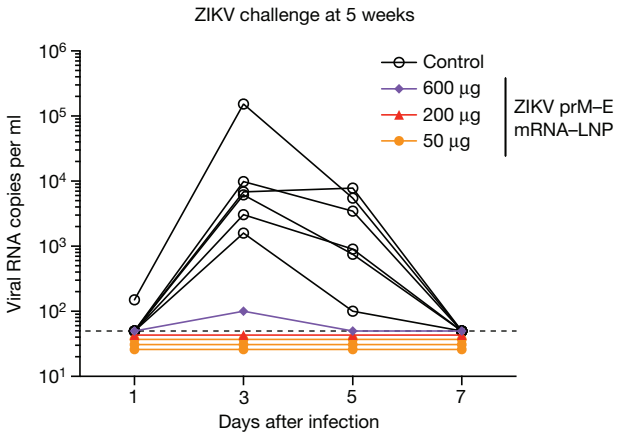

Figure 4 | A single immunization of nucleoside-modified ZIKV prM–E mRNA–LNP protects rhesus macaques against ZIKV challenge at 5 weeks after immunization. Six unvaccinated control macaques and five vaccinated macaques that received 50 μg ($n = 3$), 200 μg ($n = 1$) or 600 μg ($n = 1$) of ZIKV mRNA–LNP at week 0 were challenged by subcutaneous injection of 10^4 $TCID_{50}$ of ZIKV PRVABC59 at week 5. Viral loads were measured in plasma by qRT–PCR for ZIKV capsid RNA. Dotted lines indicate the threshold beneath which values are below the limit of detection (50 copies per ml), and undetectable values were staggered to show individual animals. Day 3 and 5 viraemia in vaccine and control groups was compared by Mann–Whitney test, $P < 0.001$.

that ZIKV-related mortality in immune-competent mice decreases between 1 and 4 weeks of age[24], but ZIKV replication in adult mice has not yet been well described.

In rhesus macaques, a single immunization with 50 μg ZIKV prM–E mRNA–LNP induced RVP nAb titres that were 50 times higher than those induced by one immunization with 1 mg DNA vaccine and over two times higher than those induced by two immunizations of DNA[12], as measured by the same assay in the same laboratory. ZIKV mRNA–LNP nAb titres may overlap with those elicited by one injection of PIV or RhAd52 ZIKV vaccines in macaques, although differences in assay formats prevent a precise comparison. The FRNT nAb titres elicited by ZIKV mRNA–LNP in macaques were maintained at a stable level until 12 weeks after immunization, suggesting that protection may be durable.

Future studies on the nucleoside-modified ZIKV mRNA–LNP vaccine will allow us to explore the effect of a boost, study the effect of this vaccine on other flavivirus infections and determine the efficacy in preventing fetal ZIKV infection and disease.

Online Content Methods, along with any additional Extended Data display items and Source Data, are available in the online version of the paper; references unique to these sections appear only in the online paper.

Received 14 October 2016; accepted 27 January 2017.
Published online 2 February 2017.

1. Pierson, T. C. & Graham, B. S. Zika virus: immunity and vaccine development. *Cell* **167,** 625–631 (2016).
2. Weissman, D. mRNA transcript therapy. *Expert Rev. Vaccines* **14,** 265–281 (2015).
3. Sahin, U., Karikó, K. & Türeci, Ö. mRNA-based therapeutics—developing a new class of drugs. *Nat. Rev. Drug Discov.* **13,** 759–780 (2014).
4. Dick, G. W., Kitchen, S. F. & Haddow, A. J. Zika virus. I. Isolations and serological specificity. *Trans. R. Soc. Trop. Med. Hyg.* **46,** 509–520 (1952).
5. Beck, A. S. & Barrett, A. D. Current status and future prospects of yellow fever vaccines. *Expert Rev. Vaccines* **14,** 1479–1492 (2015).
6. Jarmer, J. *et al.* Variation of the specificity of the human antibody responses after tick-borne encephalitis virus infection and vaccination. *J. Virol.* **88,** 13845–13857 (2014).
7. Guy, B. & Jackson, N. Dengue vaccine: hypotheses to understand CYD-TDV-induced protection. *Nat. Rev. Microbiol.* **14,** 45–54 (2016).
8. Kim, E. *et al.* Preventative vaccines for Zika virus outbreak: preliminary evaluation. *EBioMedicine* **13,** 315–320 (2016).
9. Muthumani, K. *et al. In vivo* protection against ZIKV infection and pathogenesis through passive antibody transfer and active immunisation with a prMEnv DNA vaccine. *npj Vaccines* **1,** 16021 (2016).
10. Abbink, P. *et al.* Protective efficacy of multiple vaccine platforms against Zika virus challenge in rhesus monkeys. *Science* **353,** 1129–1132 (2016).
11. Larocca, R. A. *et al.* Vaccine protection against Zika virus from Brazil. *Nature* **536,** 474–478 (2016).
12. Dowd, K. A. *et al.* Rapid development of a DNA vaccine for Zika virus. *Science* **354,** 237–240 (2016).
13. Ledgerwood, J. E. *et al.* A replication defective recombinant Ad5 vaccine expressing Ebola virus GP is safe and immunogenic in healthy adults. *Vaccine* **29,** 304–313 (2010).
14. Sumida, S. M. *et al.* Neutralizing antibodies and $CD8^+$ T lymphocytes both contribute to immunity to adenovirus serotype 5 vaccine vectors. *J. Virol.* **78,** 2666–2673 (2004).
15. Abbink, P. *et al.* Construction and evaluation of novel rhesus monkey adenovirus vaccine vectors. *J. Virol.* **89,** 1512–1522 (2015).
16. Minor, P. D. Live attenuated vaccines: historical successes and current challenges. *Virology* **479–480,** 379–392 (2015).
17. Baronti, C. *et al.* Complete coding sequence of zika virus from a French Polynesia outbreak in 2013. *Genome Announc.* **2,** e00500–14 (2014).
18. Andries, O. *et al.* N^1-methylpseudouridine-incorporated mRNA outperforms pseudouridine-incorporated mRNA by providing enhanced protein expression and reduced immunogenicity in mammalian cell lines and mice. *J. Control. Release* **217,** 337–344 (2015).
19. Pardi, N. *et al.* Expression kinetics of nucleoside-modified mRNA delivered in lipid nanoparticles to mice by various routes. *J. Control. Release* **217,** 345–351 (2015).
20. Wang, P. G. *et al.* Efficient assembly and secretion of recombinant subviral particles of the four dengue serotypes using native prM and E proteins. *PLoS One* **4,** e8325 (2009).
21. Weissman, D. *et al.* HIV gag mRNA transfection of dendritic cells (DC) delivers encoded antigen to MHC class I and II molecules, causes DC maturation, and induces a potent human *in vitro* primary immune response. *J. Immunol.* **165,** 4710–4717 (2000).
22. Dudley, D. M. *et al.* A rhesus macaque model of Asian-lineage Zika virus infection. *Nat. Commun.* **7,** 12204 (2016).
23. Dowd, K. A. *et al.* Broadly neutralizing activity of Zika virus-immune sera identifies a single viral serotype. *Cell Reports* **16,** 1485–1491 (2016).
24. Lazear, H. M. *et al.* A mouse model of Zika virus pathogenesis. *Cell Host Microbe* **19,** 720–730 (2016).

Supplementary Information is available in the online version of the paper.

Acknowledgements We thank R. Tesh at the UTMB World Reference Center for Emerging Viruses and Arboviruses for providing ZIKV stocks. We gratefully acknowledge the technical or administrative support of M. Bertrand, L. Arwood, C. Sample, M. J. Barr, C. Vivian, T. Gurley and M. A. Moody, E. E. Ooi, S. Lok, H.-X. Liao, S. Awasthi, L. Hook, F. Shaheen, and the UPenn CFAR. The Virology Unit of the Duke Regional Biocontainment Laboratory (Duke Human Vaccine Institute) received support from the NIH, UC6-AI058607. The Duke Center for HIV/AIDS Vaccine Immunology received support from NIH AI100645. D.V. received funding from the Department of Diagnostic Medicine and Pathobiology, College of Veterinary Medicine, Kansas State University. R.S.P., C.R.D., K.A.D., T.C.P. and B.S.G. were funded by the NIAID Division of Intramural Research and the Vaccine Research Center. S.E.H. received funding through NIH U19-AI057229. M.J.Hog. received funding from NIH T32 AI007632-14. D.W. received funding from NIH R01-AI050484, R01-AI124429 and R01-AI084860, and Takeda Pharmaceuticals, New Frontier Science.

Author Contributions N.P., M.J.Hog., B.F.H., T.C.P., B.S.G., M.G.L. and D.W. designed the studies and evaluated data. N.P. and H.M. conducted mouse studies. M.J.Hog. performed virologic and immunologic assays for mouse and non-human primate studies. D.W., M.J.Hog., N.P. and K.K. developed the mRNA construct and platform. E.W. and S.E.H. provided virologic technical assistance and reagents. V.M.H. provided molecular assay assistance. C.E.M., R.P., G.D.S., R.S.P., C.R.D., K.A.D. and T.C.P. conducted nAb and IgG assays. B.L.M., Y.K.T., T.D.M. and M.J.Hop. developed and provided LNPs. Y.-J.H., D.V. and S.H. provided non-human primate challenge stock. H.A., J.G. and M.W. conducted viral load analysis. M.G.L., L.L.S., R.M.S., W.W. and A.G. carried out the non-human primate immunization and challenge trial. J.-S.Y., S.San., H.B., S.Sah. and M.L. processed non-human primate samples and conducted assays for non-human primate studies. N.P., M.J.Hog. and D.W. wrote the paper with all co-authors.

Author Information Reprints and permissions information is available at www.nature.com/reprints. The authors declare competing financial interests: details are available in the online version of the paper. Readers are welcome to comment on the online version of the paper. Correspondence and requests for materials should be addressed to D.W. (dreww@upenn.edu).

Reviewer Information *Nature* thanks A. Barrett, G. Screaton and the other anonymous reviewer(s) for their contribution to the peer review of this work.

METHODS

Ethics statement. *Animals.* The investigators adhered to the Guide for the Care and Use of Laboratory Animals by the Committee on Care of Laboratory Animal Resources Commission on Life Sciences, National Research Council. Mouse studies were conducted under protocols approved by the University of Pennsylvania (UPenn) IACUCs. Rhesus macaques (*Macaca mulatta*) were housed at Bioqual, Inc. (Rockville, MD). Macaque experiments were reviewed and approved by Bioqual and UPenn Animal Care and Use Committees. All animals were housed and cared for according to local, state and federal policies in an Association for Assessment and Accreditation of Laboratory Animal Care International (AAALAC)-accredited facility.

Human cells. Research involving human cells complied with the Declaration of Helsinki. De-identified leukapheresis cells were obtained from the UPenn Immunology Core under their Institutional Review Board (IRB)-approved protocol, and were deemed exempt by the UPenn IRB.

Antibody reagents. The pan-flavivirus mouse monoclonal antibody 4G2, clone D1-4G2-4-15 (EMD Millipore MAB10216) was used to detect ZIKV E protein by western blot. The following antibodies were used for flow cytometry: anti-CD4 PerCP/Cy5.5 (clone GK1.5, Biolegend), anti-CD3 APC-Cy7 (clone 145-2C11, BD Biosciences), anti-CD27 PE (clone LG.3A10, BD Biosciences), anti-TNF PE-Cy7 (clone MP6-XT22, BD Biosciences), anti-IFNγ AF700 (clone XMG1.2, BD Biosciences), anti-IL-2 APC (clone JES6-5H4, BD Biosciences). The live/dead fixable aqua dead cell stain kit (Life Technologies) was used to discriminate dead cells and debris. The following antibodies were used for ELISA assays: goat anti-mouse IgG HRP (Sigma 4416), goat anti-monkey IgG HRP (Sigma 2054) and ZIKV E-protein-specific monoclonal antibody NR-4747 clone E19 (BEI Resources). ZIKV-neutralizing human monoclonal antibody Ab3594 was provided by the Duke University, Duke-NUS Graduate Medical School, National University of Singapore team of C.E.M, G.D.S., R.P., E. E. Ooi, B.F.H., M. A. Moody, S. Lok, and H.-X. Liao.

Protein reagents. Purified recombinant ZIKV E protein (Aalto Bioreagents AZ 6312) was used in ELISAs to detect E-protein-specific IgG, in western blots as a positive control and in mouse splenocyte stimulation.

mRNA production. mRNA was produced as previously described[25] using T7 RNA polymerase on linearized plasmid (pTEV-ZIKVprM-E-A101) encoding codon-optimized[26] ZIKV strain H/PF/2013 (Asian lineage, French Polynesia, 2013, GenBank: KJ776791) prM–E glycoproteins. mRNA was transcribed to contain a 101 nucleotide-long poly(A) tail. 1-methylpseudouridine-5′-triphosphate (TriLink) was used instead of UTP to generate modified nucleoside-containing mRNA. mRNA was capped using a m7G capping kit with 2′-*O*-methyltransferase to obtain cap1 and was purified by a fast protein liquid chromatography (FPLC) method, as described[27]. mRNA was analysed by agarose gel electrophoresis and stored frozen at −20 °C.

Cell culture. Human embryonic kidney (HEK)293T cells (ATCC) were cultured in Dulbecco's modified Eagle's medium (DMEM) supplemented with 2 mM L-glutamine (Life Technologies) and 10% fetal calf serum (FCS) (HyClone) (complete medium). The HEK293T cell line was tested for mycoplasma contamination after receipt from ATCC and before expansion and cryopreservation. Human dendritic cells were generated from monocytes, as described[28], and grown in RPMI1640 medium containing 2 mM L-glutamine (Life Technologies) and 10% FCS (HyClone) (complete medium) supplemented with 50 μg ml^{-1} recombinant human GM-CSF and 100 μg ml^{-1} recombinant human IL-4 (R&D systems). Cells were maintained by adding fresh medium containing IL-4 and GM-CSF every 3 days and were used on day 7. Mouse dendritic cells were generated from bone marrow cells obtained from the femurs of animals and grown in complete medium supplemented with 50 μg ml^{-1} mouse GM-CSF (R&D systems). Cells were maintained by adding fresh medium containing mouse GM-CSF every 3 days and were used on day 7.

mRNA transfection. Transfection of human and mouse dendritic cells and HEK293T cells was performed with TransIT-mRNA (Mirus Bio) according to the manufacturer's instructions: mRNA (0.3 μg) was combined with TransIT-mRNA reagent (0.34 μl) and boost reagent (0.22 μl) in 17 μl of serum-free medium, and the complex was added to 2×10^5 cells in 183 μl complete medium. Supernatant was collected and cells were lysed for 1 h on ice in RIPA buffer (Sigma) at 18 h after transfection.

Western blot analysis of envelope protein expression. Whole-cell lysates and supernatants from cells transfected with ZIKV prM–E were assayed for ZIKV E protein by non-denaturing SDS–PAGE western blot. Samples were combined with 4 × Laemmli buffer (Bio-Rad) and separated on a 4–15% precast polyacrylamide Criterion TGX gel (Bio-Rad) for 45 min at 200 V. Transfer to PVDF membrane was performed using a semi-dry apparatus (Ellard Instrumentation, Ltd) at 10 V for 1 h. The membrane was blocked with 5% non-fat dry milk in TBS buffer containing 0.5% Tween-20. E protein was detected using 1:10,000 4G2 ascites for 1 h, followed by secondary goat anti-mouse IgG HRP 1:10,000 for 1 h. Antibody incubations were performed at room temperature in blocking buffer. Blots were developed using Luminata Forte substrate (Millipore) and a Kodak X-OMAT 1000A processor. At least 2 independent experiments were performed.

Characterization of E protein in supernatant. Supernatant from HEK293T cells transfected with ZIKV prM–E mRNA was tested for whether E protein could be pelleted and disrupted with detergent, consistent with subviral particles. Supernatant was incubated in PBS alone or PBS with 0.5% Triton X-100 for 1 h on ice. Samples were then spun at 42,000 r.p.m. for 2.5 h in a Beckman TLA-55 rotor. The supernatant was then removed from the pellet, which was resuspended in 50 μl of PBS. Equal volumes of the input, pellet and post-centrifugation supernatant fractions were then analysed by western blot, as described above.

Lipid-nanoparticle encapsulation of the mRNA. FPLC-purified mRNA and polycytidylic acid (poly(C) RNA) (Sigma) were encapsulated in LNPs using a self-assembly process in which an aqueous solution of mRNA at pH 4.0 is rapidly mixed with a solution of lipids dissolved in ethanol[29]. LNPs used in this study were similar in composition to those described previously[29,30], which contain an ionizable cationic lipid (proprietary to Acuitas), phosphatidylcholine, cholesterol and PEG-lipid (with a ratio of 50:10:38.5:1.5 mol/mol) and were encapsulated at an RNA to total lipid ratio of around 0.05 (wt/wt). The LNPs had a diameter of around 80 nm as measured by dynamic light scattering using a Zetasizer Nano ZS instrument (Malvern Instruments Ltd). RNA–LNP formulations were stored at −80 °C at a concentration of RNA of about 1 μg μl^{-1}.

Administration of LNPs to mice and rhesus monkeys. *Mice.* Female BALB/c and C57BL/6 mice aged 8 weeks were purchased from Charles River Laboratories, and cages of mice were randomly allocated to groups. Power analysis was used to calculate the size of all animal groups to ensure statistically significant results. RNA–LNP was diluted in PBS and injected into animals intradermally with a 3/10cc 29½G insulin syringe (BD Biosciences). Four sites of injection (30 μl each) over the lower back were used.

Monkeys. Ketamine-anaesthetized animals were shaved on their back and injected with mRNA–LNP diluted in PBS. Ten sites of injection (60 μl each) were used. Animals of similar age and weight were allocated to each group.

Blood collection from mice and rhesus macaques. *Mice.* Blood was collected from the orbital sinus under isoflurane anaesthesia. Blood was centrifuged for 10 min at 13,000 r.p.m. and the serum was stored at −20 °C and used for ELISA and virus neutralization assays. EDTA-plasma was collected to isolate RNA for quantitative PCR with reverse transcription (qRT–PCR) analysis.

Monkeys. Blood was collected by femoral venipuncture under ketamine anaesthesia, and serum and EDTA–plasma were collected and stored at −80 °C for ELISA, neutralization analysis and to isolate RNA for qRT–PCR.

Stimulation and staining of splenocytes. Single-cell suspensions from spleens were made in complete medium. Splenocytes were washed once in PBS and resuspended in complete medium at 2×10^7 cells per ml. Subsequently, 2×10^6 cells (100 μl) per sample were stimulated for 6 h at 37 °C using 2 μg ml^{-1} purified, recombinant ZIKV E protein. GolgiPlug (brefeldin A, BD Biosciences) and GolgiStop (monensin, BD Biosciences) were diluted 1:100 and 1:143 in complete medium, respectively, and 20 μl from both diluted reagents was added to each sample to inhibit the secretion of intracellular cytokines after 1 h. An unstimulated sample for each animal was included. Samples stimulated with PMA (10 ng ml^{-1})–ionomycin (250 ng ml^{-1}) (Sigma) were used as positive controls.

After stimulation, cells were washed in PBS and stained using the live/dead fixable aqua dead cell stain kit (Life Technologies) and then surface stained for CD4 and CD27. Antibodies were incubated with cells for 30 min at room temperature. Following surface staining, cells were washed in FACS buffer and fixed using the Cytofix/Cytoperm kit (BD Biosciences) according to the manufacturer's instructions. Following fixation, the cells were washed in the appropriate perm buffer and incubated with antibodies against CD3, TNF, IFNγ and IL-2 for 1 h at room temperature. Following staining, the cells were washed with the appropriate perm buffer, fixed (PBS containing 1% paraformaldehyde) and stored at 4 °C until analysis. Results are obtained from one technical replicate.

Flow cytometry. Splenocytes were analysed on a modified LSR II flow cytometer (BD Biosciences). One hundred thousand events were collected per sample. After the gates for each function were created, the Boolean gate platform was used to create the full array of possible combination of cytokines, equating to seven response patterns when testing three cytokines. Data were expressed by subtracting the per cent positive unstimulated cells from the per cent positive cells stimulated with E protein.

Enzyme-linked immunosorbent assays (ELISA) for ZIKV E-specific IgG. Immulon 4HXB ELISA plates were coated with 6 μg ml^{-1} purified, recombinant ZIKV E protein in 0.1 M sodium bicarbonate buffer overnight at 4 °C. The plate was blocked with 2% BSA in PBS for 1 h, and washed three times with wash buffer (PBS

with 0.05% Tween-20). Mouse or rhesus macaque serum was diluted in blocking buffer and incubated on the plate for 1 h at room temperature, followed by four washes. Secondary HRP-conjugated antibody was diluted 1:10,000 in blocking buffer and incubated on the plate for 1 h, followed by four washes. TMB substrate (KPL) was applied to the plate and the reaction was stopped with 2 Normal sulfuric acid. The absorbance was measured at 450 nm using an MRX Revelation microplate reader. ZIKV E-protein-specific IgG was analysed in two ways: as an endpoint dilution titre, defined as the highest reciprocal dilution of serum to give an OD greater than the sum of the background plus 0.01 OD units; and as an estimate of the absolute IgG concentration, which was based on the mouse monoclonal antibody NR-4747 as a standard (applicable only to mouse samples). All samples were run in at least technical duplicates.

ZIKV MR-766 plaque reduction neutralization tests (PRNT). ZIKV strain MR-766 (African lineage, Uganda, 1947, GenBank: AY632535) (UTMB Arbovirus Reference Collection) was produced in Vero cells (ATCC CCL-81) and 50 PFU were incubated with increasing dilutions of heat-inactivated serum in serum-free DMEM (Corning) medium for 1 h at 37 °C. The virus–serum mixture (200 μl) was added to a confluent monolayer of Vero cells in 6-well format and incubated for 1.5 h at 37 °C with intermittent rocking. Then, 3 ml of overlay, containing a final concentration of 0.5% methylcellulose (4,000 centipoise) (Sigma), 1 × DMEM (Gibco), 16 mM HEPES, 0.56% sodium bicarbonate, 1.6× GlutaMAX (Gibco), 1 × penicillin/streptomycin (Corning), and 4 μg ml^{-1} amphotericin B (Gibco), was added to each well, and plates were incubated for 5 days at 37 °C in 5% CO_2. The overlay was aspirated and cells were fixed and stained with 0.5% crystal violet (Sigma) in 25% methanol, 75% deionized water. Wells were rinsed with deionized water to visualize plaques. Neutralization titres (EC_{50}) were determined by plotting a line through the linear portion of the curve that crossed 50% inhibition and calculating the reciprocal dilution of serum required for 50% neutralization of infection. EC_{50} titres are reported as the mean of one or two technical replicates and values below the limit of detection are reported as half of the limit of detection.

ZIKV MEX I-44 focus reduction neutralization tests (FRNT). ZIKV MEX I-44 (Asian lineage, Mexico, 2016, GenBank: KX856011) stocks were generated in Vero 76 cells (ATCC CRL-1587) and collected as clarified cell-culture lysate/supernatant. FRNT was performed by combining a standard dose of ZIKV with twofold serial dilutions of heat-inactivated serum for 1 h at 37 °C. Virus–serum mixtures (100 μl) were then inoculated onto Vero 76 monolayers, incubated at 37 °C for 1 h and overlayed with an Avicel (FMC Biopolymer)-containing growth medium. After 3 days of incubation, plates were formalin-fixed, permeabilized, blocked and stained by sequential incubation with a biotin-conjugated 4G2 monoclonal antibody (ATCC HB-112), streptavidin-HRP (BD Biosciences) and TrueBlue peroxidase substrate (KPL). Virus input was verified in parallel (acceptable range: 20–60 foci). $FRNT_{50}$ (EC_{50} titres) are reported as the highest reciprocal dilution giving a focus count ≤ the 50% neutralization cutoff, and the geometric mean was computed for technical duplicates.

Reporter virus particle (RVP) production. Pseudo-infectious RVPs were produced by complementation of a GFP-expressing WNV sub-genomic replicon[23,31] with a plasmid encoding the viral structural proteins (capsid-prM–E). Briefly, ZIKV MR-766 and ZIKV H/PF/2013 RVPs were produced via co-transfection of HEK293T cells with the structural gene and replicon plasmids (3:1 ratio by mass) using Lipofectamine 3000 per the manufacturer's protocol (Invitrogen). Transfected cells were incubated at 30 °C and RVP-containing supernatants were collected on days 3–6. Stocks were passed through a 0.2-μm filter and aliquots were stored at −80 °C until use. Stock titres were determined by infecting Raji-DCSIGNR cells with serial dilutions of filtered RVP supernatants. GFP-positive cells were assessed by flow cytometry at 48 h after infection and RVP titres were calculated.

RVP neutralization assay. Previously titred RVPs were diluted to ensure antibody excess at informative points on the dose–response curves and were incubated with serial dilutions of mouse or macaque serum for 1 h at 37 °C to allow for steady-state binding. Raji-DCSIGNR cells were then infected with antibody–RVP complexes in two technical replicates. Infections were carried out at 37 °C and GFP-positive infected cells were detected by flow cytometry 24–48 h later. Neutralization results were analysed by nonlinear regression to estimate the reciprocal dilution of serum required for half-maximal neutralization of infection (EC_{50} titre) (Prism 6, GraphPad). The initial dilution of serum (on the basis of the final volume of RVPs, cells, and serum) was set as the limit of confidence of the assay. Titres for which nonlinear regression was predicted to be below this threshold were reported as a titre half the limit of confidence. Individual EC_{50} titres are reported as the geometric mean of at least 2 technical replicates.

Preparation of challenge ZIKV virus. *Mice.* Challenge ZIKV strain PRVABC59 (Asian lineage, Puerto Rico, 2015, GenBank: KU501215) (BEI Resources NR-50240) was grown in Vero CCL81 cells. A T175 flask of cells at 75–90% confluency was inoculated with an MOI of 0.01 ZIKV in 10 ml of serum-free DMEM medium. The flask was incubated at 37 °C, 5% CO_2 for 1.5 h with intermittent rocking, then warmed medium was added to a final concentration of 1.5% FCS, 1 × GlutaMAX (Gibco) and 1 × penicillin/streptomycin (Corning) in a final volume of 25 ml. The flask was incubated for 4 days or until cytopathic effects were visible. Then, the supernatant was collected, clarified by low-speed centrifugation and ultra-centrifuged at 20,000 r.p.m. for 1 h at 4 °C in a Sorvall SureSpin 630 rotor. The supernatant was removed and the pellet was resuspended in 1 ml of serum-free DMEM, aliquoted and stored at −80 °C. Before challenge, virus was thawed and diluted in PBS to 2,000 PFU per ml.

Monkeys. Challenge ZIKV strain PRVABC59 was grown in Vero 76 CRL-1587 cells. T150 flasks of cells at 80–85% confluency were used for propagation. Infection was performed with 100 μl stock virus diluted in 4 ml of fresh L-15 medium (Gibco) supplemented with 10% FCS (Gibco), 10% tryptose phosphate broth (Sigma Aldrich), 1 × penicillin/streptomycin (Gibco) and L-glutamine (Gibco) and adsorbed for 1 h at room temperature with gentle agitation every 15 min. Each flask received 7 ml of fresh L-15 medium after adsorption and was incubated for 4 days at 37 °C. Cellular debris was removed by centrifugation at 1,200 r.p.m. for 5 min at 4 °C in an Eppendorf A-4-62 rotor. Virus stocks were aliquoted and stored at −80 °C.

Zika virus challenge in mice and rhesus macaques. *Mice.* At 2 or 20 weeks after vaccination, mice were bled and then challenged intravenously with 200 PFU of ZIKV PRVABC59 in 100 μl of PBS. Blood was collected 3 and 7 days after the challenge to determine viral loads (ZIKV RNA copies per ml) in plasma.

Monkeys. Macaques were anaesthetized with ketamine and injected subcutaneously in the hind thigh with 10^4 $TCID_{50}$ of ZIKV PRVABC59 in a volume of 1 ml in PBS. Blood was collected 1, 3, 5, and 7 days after the challenge to determine viral loads (ZIKV RNA copies per ml) in plasma.

Viral load quantification (qRT–PCR). Using blinded samples, RNA was isolated from 200 μl (macaque) or 50 μl (mouse) plasma using the QIAamp MinElute Virus spin kit (Qiagen). Extracted RNA was used for amplification using the SensiFAST Probe Lo-ROX One-Step Kit (Bioline BIO-78005) on a 7500 Real-Time PCR system (Applied Biosystems). Primers and probe were designed to amplify a conserved region of the capsid gene from ZIKV BeH815744, as follows: fwd 5′-GGAAAAAAGAGGCTATGGAAATAATAAAG-3′; rev 5′-CTCCTTCCTAGCATTGATTATTCTCA-3′; probe 5′-AGTTCAAGAA AGATCTGGCTG-3′.

Primers and probe were used at a final concentration of 2 μM, and the following program was run: 48 °C for 30 min, 95 °C for 10 min, followed by 40 cycles of 95 °C for 15 s and 1 min at 60 °C. Assay sensitivity was 50 copies per ml for macaque and 200 copies per ml for mouse samples. Results are calculated from at least two technical replicates.

Statistical analysis. No statistical methods were used to predetermine sample size, unless indicated. The investigators were not blinded to allocation during experiments and outcome assessment unless indicated (qRT–PCR). GraphPad Prism 5.0f was used to perform Mann–Whitney and Kruskal–Wallis (with Dunn's correction) tests to compare immune responses in vaccinated and control mice and in different dose groups of macaques, respectively. SPICE 5.35 and Microsoft Excel software was used to perform Student's *t*-tests to compare T cell responses in vaccinated and control mice.

Data availability. All data and full plasmid sequences are available upon request from the corresponding author.

25. Pardi, N., Muramatsu, H., Weissman, D. & Karikó, K. *In vitro* transcription of long RNA containing modified nucleosides. *Methods Mol. Biol.* **969,** 29–42 (2013).
26. Thess, A. *et al.* Sequence-engineered mRNA without chemical nucleoside modifications enables an effective protein therapy in large animals. *Mol. Ther.* **23,** 1456–1464 (2015).
27. Weissman, D., Pardi, N., Muramatsu, H. & Karikó, K. HPLC purification of *in vitro* transcribed long RNA. *Methods Mol. Biol.* **969,** 43–54 (2013).
28. Karikó, K. *et al.* Incorporation of pseudouridine into mRNA yields superior nonimmunogenic vector with increased translational capacity and biological stability. *Mol. Ther.* **16,** 1833–1840 (2008).
29. Maier, M. A. *et al.* Biodegradable lipids enabling rapidly eliminated lipid nanoparticles for systemic delivery of RNAi therapeutics. *Mol. Ther.* **21,** 1570–1578 (2013).
30. Jayaraman, M. *et al.* Maximizing the potency of siRNA lipid nanoparticles for hepatic gene silencing *in vivo*. *Angew. Chem. Int. Edn Engl.* **51,** 8529–8533 (2012).
31. Pierson, T. C. *et al.* A rapid and quantitative assay for measuring antibody-mediated neutralization of West Nile virus infection. *Virology* **346,** 53–65 (2006).

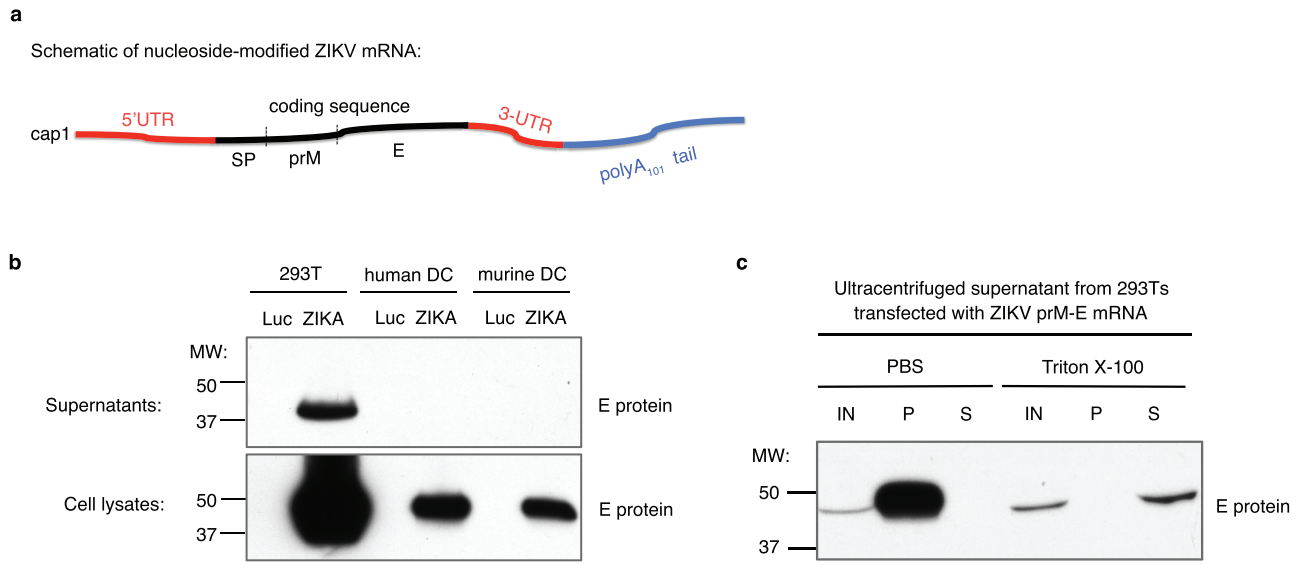

Extended Data Figure 1 | Design and characterization of ZIKV prM–E mRNA. a, The ZIKV mRNA encodes the signal peptide (SP) from MHC class II and pre-membrane (prM) and envelope (E) glycoproteins from ZIKV H/PF/2013. **b**, mRNA was transfected into HEK293T cells ($n = 3$), human ($n = 3$) or mouse dendritic cells ($n = 2$). E protein expression in cell lysate and supernatant was analysed by western blot, using firefly luciferase-encoding mRNA-transfected cells as a negative control. **c**, ZIKV mRNA supernatant from transfected HEK293T cells was characterized by ultracentrifugation in the presence and absence of 0.5% Triton X-100, followed by western blot of input (IN), pellet (P) and final supernatant (S) fractions ($n = 3$).

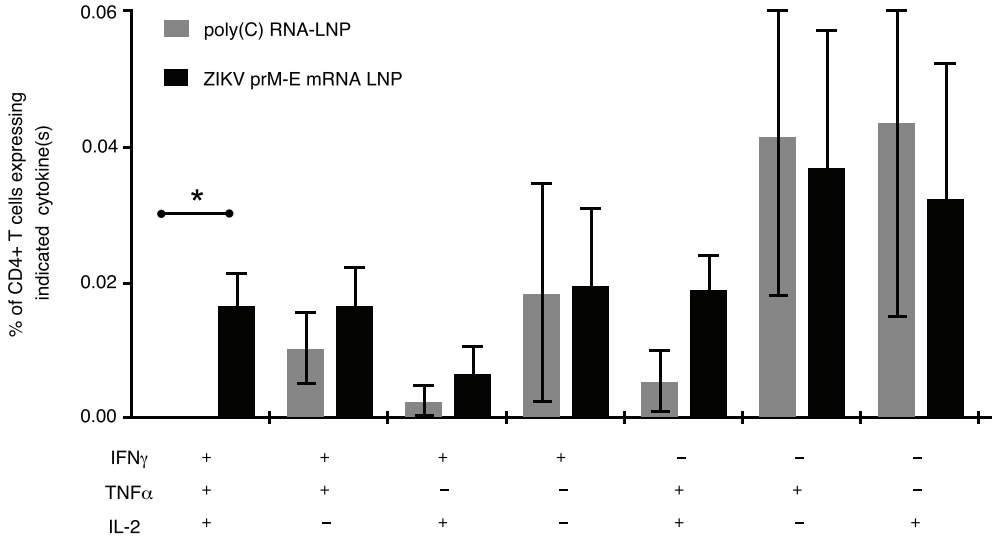

Extended Data Figure 2 | Nucleoside-modified ZIKV mRNA–LNP immunization elicits polyfunctional ZIKV E-protein-specific CD4$^+$ T cell responses. C57BL/6 mice were immunized with 30 μg of nucleoside-modified ZIKV prM–E mRNA–LNP ($n = 8$) or control poly(C) RNA–LNP ($n = 4$). At week 2, antigen-specific CD4$^+$ T cells were detected by intracellular cytokine staining. Graph shows mean ± s.e.m. of the frequencies of combinations of cytokines produced by CD4$^+$ T cells. *$P < 0.05$ (Student's t-test).

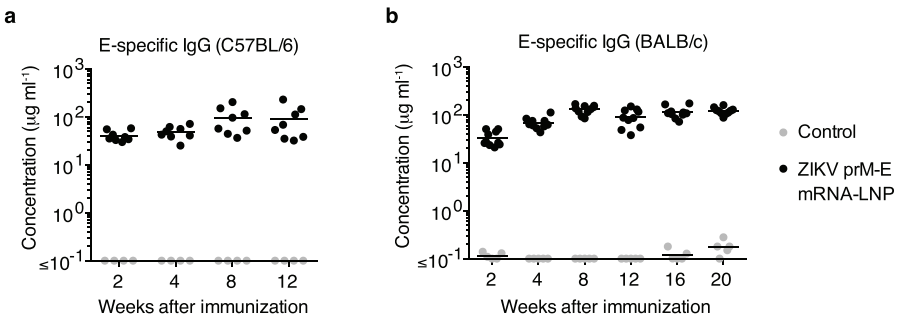

Extended Data Figure 3 | Concentration of ZIKV E-protein-specific IgG in mice. a, **b**, Serum from C57BL/6 mice (**a**; $n = 4$ control; $n = 8$ ZIKV mRNA–LNP) or BALB/c mice (**b**; $n = 5$ control; $n = 10$ ZIKV mRNA–LNP) was analysed by ELISA, and estimates of the concentration of ZIKV E-protein-specific IgG were calculated using the mouse monoclonal antibody NR-4747 as a standard. Points represent individual mice; horizontal lines indicate the mean. Responses in vaccine and control groups were compared at each time point by Mann–Whitney test, $P < 0.01$ for all comparisons.

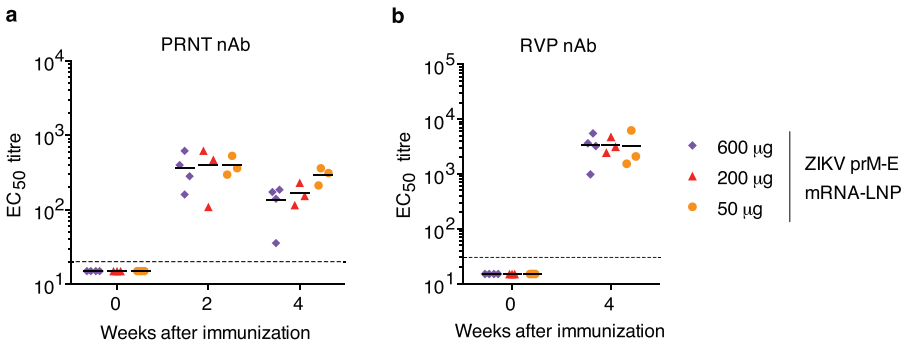

Extended Data Figure 4 | Neutralizing antibody responses against ZIKV MR-766 in macaques immunized with ZIKV prM–E mRNA–LNP. Serum from immunized macaques was analysed for neutralization of ZIKV MR-766 using the PRNT assay (**a**) or the RVP assay (**b**) at the indicated time points. Shaded area indicates values below the limit of detection; horizontal bars indicate mean; symbols indicate individual animals. Immune responses in dose groups were compared by Kruskal–Wallis test, $P > 0.05$ for all comparisons.

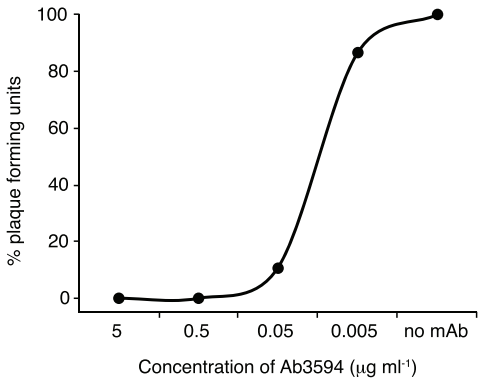

Extended Data Figure 5 | Neutralization curve for a human anti-ZIKV neutralizing monoclonal antibody. ZIKV MR-766 was neutralized by Ab3594, a human ZIKV-neutralizing monoclonal antibody, as a positive control in the PRNT assay. Shown is a representative curve ($n = 4$). $EC_{50} = 0.026 \pm 5.4\,\mu g\ ml^{-1}$ (mean ± s.d.).

Extended Data Table 1 | Characteristics of rhesus macaques in vaccination and challenge experiments

Immunization	Group	ID	Weight (kg)	Sex	DOB
ZIKV prM-E mRNA-LNP, 600 μg	1	6858	3.3	M	5/19/14
		150250	3.05	F	3/22/15
		150793	2.55	M	4/1/15
		150796 *	2.75	F	4/13/15
ZIKV prM-E mRNA-LNP, 200 μg	2	150251	2.95	M	3/22/15
		150795	2.55	M	4/12/15
		150798 *	2.35	F	4/26/15
ZIKV prM-E mRNA-LNP, 50 μg	3	6857 *	3.15	F	6/6/14
		150252 *	2.15	F	3/25/15
		150794 *	2.75	M	4/5/15
Challenge control group (unimmunized)	4	6143 *	7.85	F	7/3/09
		6154 *	8.95	F	4/6/10
		6076 *	7.6	M	10/20/11
		6150 *	11.55	M	1/26/10
		6211 *	8.65	M	5/2/10
		6157 *	10.15	F	4/3/10

*Animals that were challenged with ZIKV.

nature COMMUNICATIONS

ARTICLE

DOI: 10.1038/s41467-018-05482-0 OPEN

Nucleoside-modified mRNA immunization elicits influenza virus hemagglutinin stalk-specific antibodies

Norbert Pardi[1], Kaela Parkhouse[2], Ericka Kirkpatrick[3,4], Meagan McMahon[3], Seth J. Zost[2], Barbara L. Mui[5], Ying K. Tam[5], Katalin Karikó[6], Christopher J. Barbosa[5], Thomas D. Madden[5], Michael J. Hope[5], Florian Krammer[3], Scott E. Hensley[2] & Drew Weissman[1]

Currently available influenza virus vaccines have inadequate effectiveness and are reformulated annually due to viral antigenic drift. Thus, development of a vaccine that confers long-term protective immunity against antigenically distant influenza virus strains is urgently needed. The highly conserved influenza virus hemagglutinin (HA) stalk represents one of the potential targets of broadly protective/universal influenza virus vaccines. Here, we evaluate a potent broadly protective influenza virus vaccine candidate that uses nucleoside-modified and purified mRNA encoding full-length influenza virus HA formulated in lipid nanoparticles (LNPs). We demonstrate that immunization with HA mRNA-LNPs induces antibody responses against the HA stalk domain of influenza virus in mice, rabbits, and ferrets. The HA stalk-specific antibody response is associated with protection from homologous, heterologous, and heterosubtypic influenza virus infection in mice.

[1] Department of Medicine, University of Pennsylvania, Philadelphia, PA 19104, USA. [2] Department of Microbiology, Perelman School of Medicine, University of Pennsylvania, Philadelphia, PA 19104, USA. [3] Department of Microbiology, Icahn School of Medicine at Mount Sinai, New York, NY 10029, USA. [4] Graduate School of Biomedical Sciences, Icahn School of Medicine at Mount Sinai, New York, NY 10029, USA. [5] Acuitas Therapeutics, Vancouver, BC V6T 1Z3, Canada. [6] BioNTech RNA Pharmaceuticals, An der Goldgrube 12, 55131 Mainz, Germany. These authors contributed equally: Norbert Pardi, Kaela Parkhouse. These authors jointly supervised this work: Scott E. Hensley, Drew Weissman. Correspondence and requests for materials should be addressed to S.E.H. (email: hensley@pennmedicine.upenn.edu) or to D.W. (email: dreww@pennmedicine.upenn.edu)

Seasonal influenza virus epidemics pose a significant global health threat. Inactivated and live attenuated vaccines have limited effectiveness and need to be reformulated every year. These vaccines induce antibody responses primarily against the immunodominant globular head domain of influenza virus hemagglutinin (HA), but the virus can easily escape from protective immune responses due to the plasticity of the HA head (reviewed in ref. [1]). It may be possible to induce broader protection with vaccines that target more conserved viral regions, such as the stalk domain of HA that is less tolerant of escape mutations (reviewed in ref. [2]). In recent years, several HA immunogens have been developed that elicit HA stalk-specific immune responses. For example, headless HAs and chimeric HAs (cHAs) induce potent stalk-reactive antibodies[3–7]. Heterologous prime-boost immunizations were also shown to elicit HA stalk-specific antibodies in preclinical studies[6–11]. Notably, most HA stalk-based vaccines require multiple immunizations.

In vitro-transcribed messenger RNA (mRNA)-based vaccines have shown promise against cancer and infectious diseases (reviewed in ref. [12]). For example, a lipid nanoparticle (LNP) encapsulated[13] 1-methylpseudouridine-modified mRNA vaccine protected mice and non-human primates against Zika virus infection after a single low dose immunization[14]. Although, several recent studies indicate that mRNA-based vaccines can provide protection against influenza virus infection, none of these reports determined if mRNA-based influenza virus vaccines elicited broadly reactive antibodies capable of neutralizing antigenically distinct influenza virus strains after a single immunization[15–19].

Here, we demonstrate that vaccination with influenza virus HA-encoding, nucleoside-modified[20], and fast protein liquid chromatography (FPLC)-purified[21] mRNA-LNPs induces potent antibody responses that target the conserved HA stalk domain in mice, rabbits, and ferrets. These broadly reactive antibody responses were associated with protection from homologous, heterologous, and heterosubtypic influenza viruses in mice. We propose that nucleoside-modified, FPLC-purified mRNA-LNP vaccines represent a promising broadly protective influenza virus vaccine candidate.

Results

HA head and stalk-specific antibody responses in mice. To evaluate the immunogenicity of the nucleoside-modified HA mRNA-LNP vaccine, mice were immunized twice with 3, 10, or 30 µg of A/California/07/2009 (H1N1) (A/Cal09) HA-encoding mRNA-LNPs intradermally (i.d.) or 10, 30, or 90 µg of A/California/07/2009 HA mRNA-LNPs intramuscularly (i.m.) and antibody responses were assessed. The two immunizations were delivered 4 weeks apart. Control animals were vaccinated with 30 µg (i.d.) or 90 µg (i.m.) of poly(C) RNA-LNPs. A single immunization induced potent antibody responses targeting the HA globular head domain as determined by hemagglutination inhibition (HAI) assays using the homologous A/California/07/2009 virus (Fig. 1a, b). Higher vaccine doses elicited higher HAI titers with subtle differences between the i.d. and i.m.-immunized animals. A second immunization substantially increased HAI titers that reached 1:1280–1:20,480 at week 8 (Fig. 1a, b). As expected, antibodies elicited by the A/California/07/2009 HA mRNA-LNPs had no HAI activity against the A/Puerto Rico/8/1934 H1N1 virus (Fig. 1c, d), which possesses a genetically divergent HA globular head domain (Supplementary Fig. 1).

We next performed enzyme-linked immunosorbent assays (ELISAs) using cHA antigens to quantify HA stalk-reactive

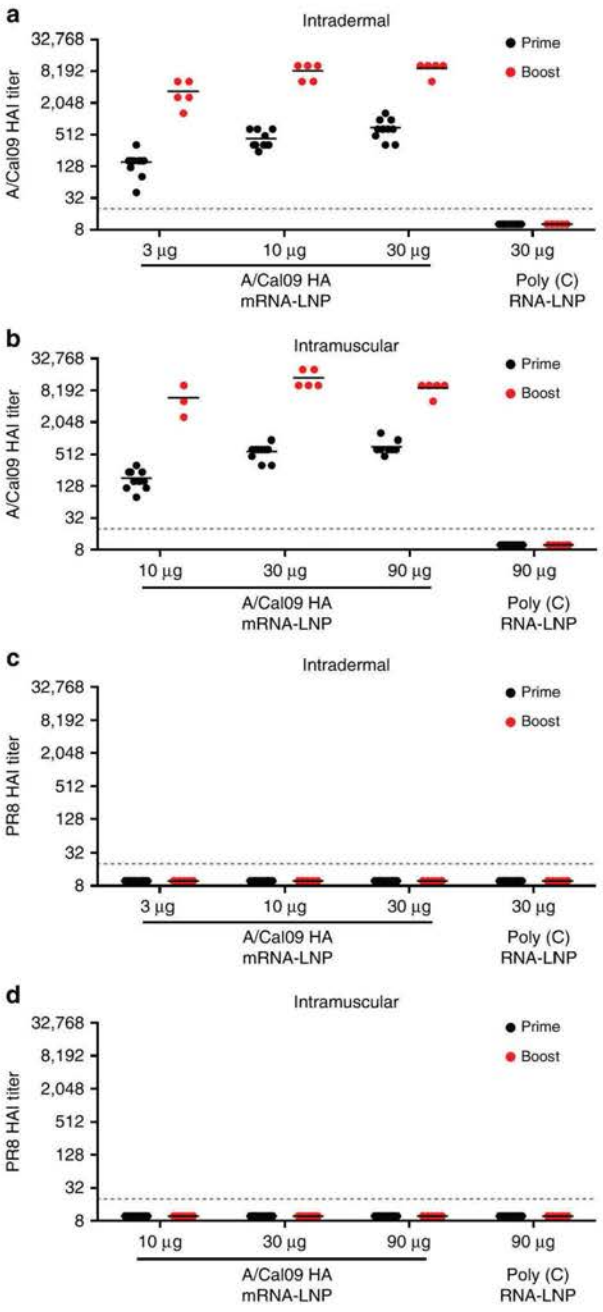

Fig. 1 Nucleoside-modified HA mRNA-LNP immunization elicits potent neutralizing antibody responses in mice. Mice received two i.d. (3, 10, or 30 µg) or i.m. (10, 30, or 90 µg) immunizations of A/California/07/2009 HA mRNA-LNPs or 30 (i.d.) or 90 (i.m.) µg of poly(C) RNA-LNPs at week 0 (prime) and 4 (boost). HA inhibition (HAI) titers against A/California/07/2009 (**a**, **b**) and A/Puerto Rico/8/1934 (**c**, **d**) viruses were determined at week 4 and 8. $n = 3$–10 mice and each symbol represents one animal. Two independent experiments were performed. Horizontal lines show the mean; dotted line indicates the limit of detection. Statistical analysis: **a**, **b** two-way ANOVA with Bonferroni correction on log-transformed data, $p < 0.05$; all comparisons across doses and time points were statistically significant except for (**a**) 10 µg HA prime vs. 30 µg HA prime and 10 µg HA boost vs. 30 µg HA boost and for (**b**) 10 µg HA boost vs. 90 µg HA boost, 30 µg HA prime vs. 90 µg HA prime and 30 µg HA boost vs. 90 µg HA boost

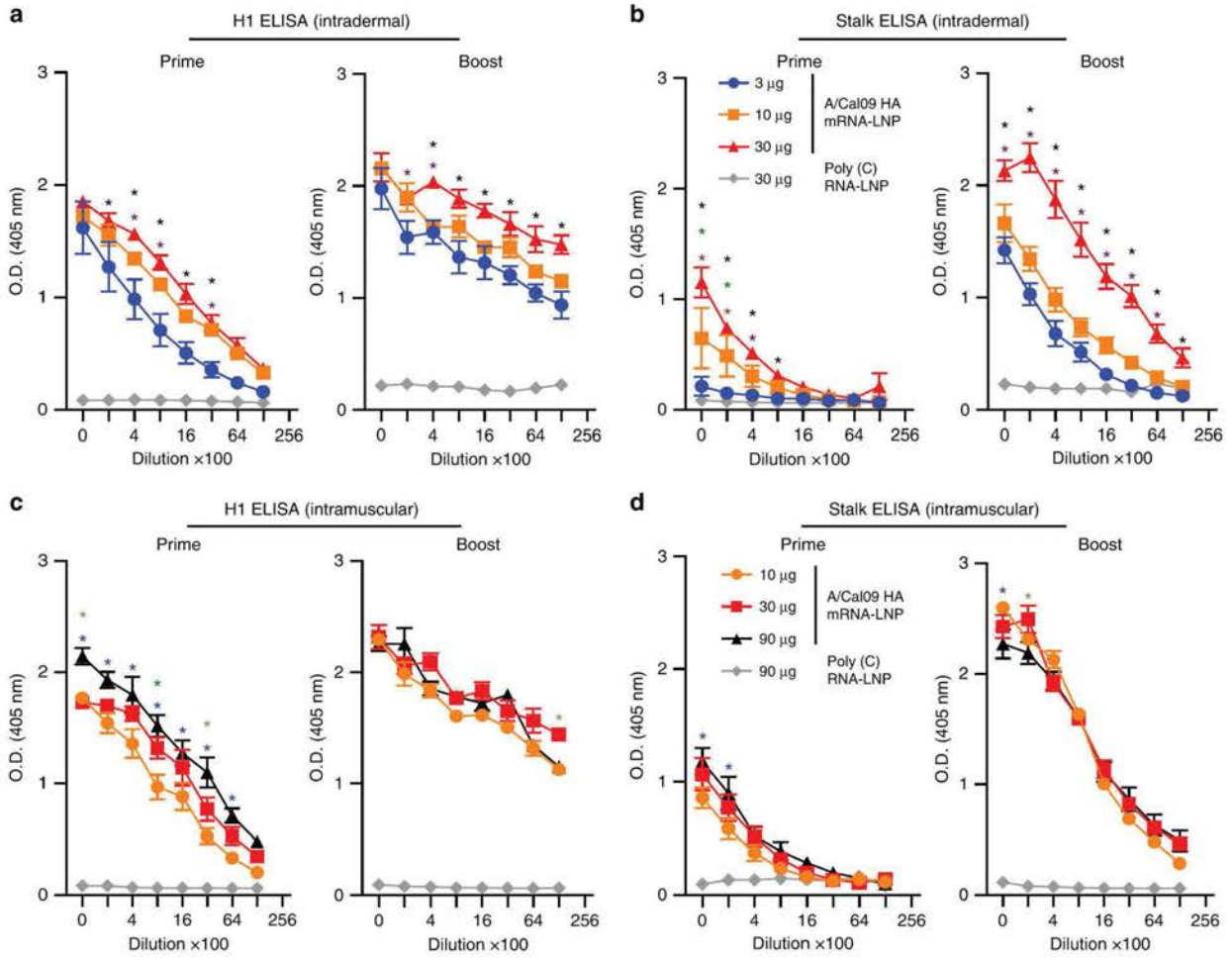

Fig. 2 Nucleoside-modified HA mRNA-LNP immunization elicits HA stalk-specific antibody responses in mice. Mice received two i.d. (3, 10, or 30 µg) (**a**, **b**) or i.m. (10, 30, or 90 µg) (**c**, **d**) immunizations of A/California/07/2009 HA mRNA-LNPs or 30 (i.d.) or 90 (i.m.) µg of poly(C) RNA-LNPs at weeks 0 and 4. IgG binding to full-length H1 HA (**a**, **c**) and cH6/1 HA (**b**, **d**) proteins was determined at week 4 and week 8. $n = 3$–10 mice. Two independent experiments were performed. Error bars are SEM. Statistical analysis: **a**, **b** two-way ANOVA with Bonferroni correction, $^*p < 0.05$ comparing A/California/07/2009 HA mRNA-LNP dose groups at each serum dilution, black star: significant difference in titers between the 3 and 30 µg groups, purple star: significant difference in titers between the 3 and 10 µg groups, green star: significant difference in titers between the 10 and 30 µg groups; **c**, **d** two-way ANOVA with Bonferroni correction, $^*p < 0.05$ comparing A/California/07/2009 HA mRNA-LNP dose groups at each serum dilution, blue star: significant difference in titers between the 10 and 90 µg groups, green star: significant difference in titers between the 10 and 30 µg groups, gray star: significant difference in titers between the 30 and 90 µg groups

antibodies elicited by nucleoside-modified HA mRNA-LNP vaccination. For these experiments, we measured antibody binding to full-length A/California/07/2009 HA and an H6/1 cHA (cH6/1 HA) that possesses an H1 stalk domain and an H6 "exotic" globular head domain. Previous studies have shown that H1 stalk-reactive antibodies bind to both the full-length H1 construct and the cH6/1 construct, whereas H1 globular head-reactive antibodies bind only to the full-length H1 construct and not the cH6/1 construct[22]. Antibodies from all A/California/07/2009 HA-vaccinated mice showed very strong binding to full-length A/California/07/2009 HA after a single immunization (Fig. 2a, c). Importantly, HA stalk-reactive antibodies capable of binding to cH6/1 HA were also elicited by a single immunization. A booster immunization significantly increased HA stalk-reactive antibodies capable of binding to cH6/1 HA (Fig. 2b, d).

To determine if HA stalk-specific antibodies could be elicited with a different influenza HA immunogen, mice were i.d. immunized with a single dose of 30 µg of A/Puerto Rico/8/1934 (PR8) influenza HA mRNA-LNPs or poly(C) RNA-LNPs and HAI activity and HA stalk-specific antibody responses were followed over time. A single immunization elicited high HAI titers against the homologous A/Puerto Rico/8/1934 virus (Fig. 3a). Consistent with our results using mRNA-LNPs expressing A/California/07/2009 HA, A/Puerto Rico/8/1934 HA mRNA-LNPs elicited high levels of antibodies to full-length A/Puerto Rico/8/1934 HA and a significant portion of these antibodies recognized the HA stalk domain of a cH5/1 HA construct (Fig. 3b, c). We also tested the durability of antibody responses in this experiment, and found that anti-HA antibody levels remained unchanged over 30 weeks post-vaccination, and, in fact, the stalk responses were stronger compared to 4 weeks post-immunization (Fig. 3).

Durable, protective responses toward the HA require $CD4^+$ T cell functions[23], thus we examined $CD4^+$ T cell responses after

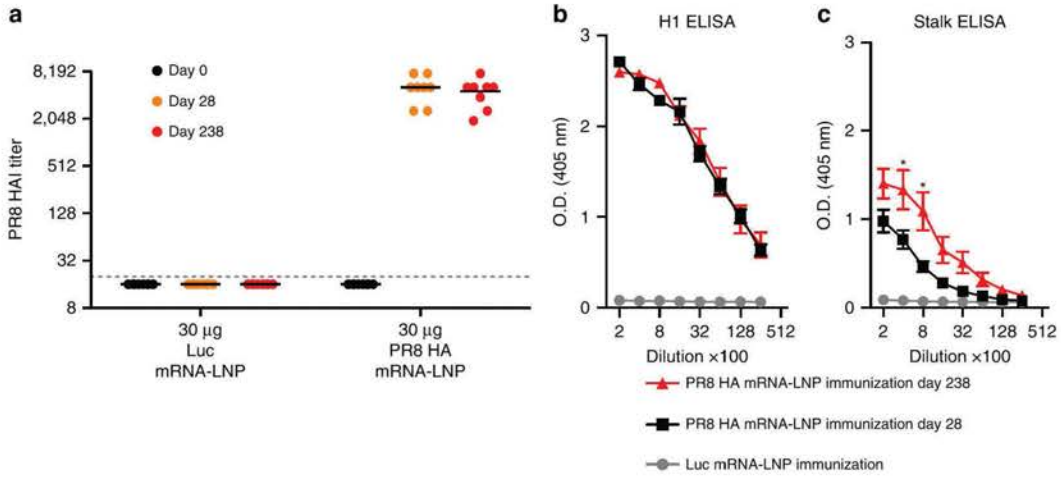

Fig. 3 Nucleoside-modified HA mRNA-LNP immunization elicits durable HA stalk-specific antibody responses in mice. Mice received a single i.d. dose of 30 µg of A/Puerto Rico/8/1934 HA mRNA-LNP vaccine and **a** HAI titers against A/Puerto Rico/8/1934 and IgG binding to full-length H1 HA (**b**) and cH5/1 HA (**c**) proteins in mouse serum obtained 28 and 238 days post single immunization were determined. $n = 8$ mice. **a** Each symbol represents one animal, horizontal lines show the mean, dotted line indicates the limit of detection. **b**, **c** Error bars are SEM. Statistical analysis: **a** two-way ANOVA with Bonferroni correction on log-transformed data, $p < 0.05$; all comparisons between the Luc and the day 28 and day 238 Puerto Rico/8/1934 HA groups were statistically significant. **b**, **c** Two-way ANOVA with Bonferroni correction comparing Puerto Rico/8/1934 HA day 28 and day 238 time points for different dilutions. $^*p < 0.05$

nucleoside-modified mRNA-LNP vaccination. Mice were immunized with a single 30 µg dose of A/California/07/2009 HA-encoding mRNA-LNPs i.d. and $CD4^+$ T cell responses were determined 12 days later. As a comparator, a group of mice were immunized with 3 µg of monovalent A/California/07/2009 virus vaccine. Unlike inactivated virus immunization, HA mRNA-LNP vaccination induced HA-specific $CD4^+$ T cell responses as measured by intracellular cytokine production (Supplementary Fig. 2).

HA stalk-reactive antibody responses in rabbits and ferrets. To further evaluate the potency of the nucleoside-modified mRNA-LNP influenza virus vaccine, immunogenicity was also evaluated in rabbits and ferrets. Rabbits were i.d. immunized twice with 50 µg of A/California/07/2009 HA mRNA-LNPs and antibody responses were evaluated. A single immunization elicited HAI titers ranging from 1:120 to 1:320, as well as, HA stalk-specific antibody responses (Supplementary Fig. 3). A second immunization significantly boosted antibody responses and resulted in increased HAI titers and stalk-specific antibodies (Supplementary Fig. 3).

Next, we evaluated the nucleoside-modified mRNA-LNP influenza virus vaccine in a ferret model. Animals were immunized i.m. twice with 60 µg of A/California/07/2009 HA mRNA-LNPs. Antibodies against the HA globular head domain were elicited in 8 out of 12 ferrets (≥1:40 HAI in all responders) 4 weeks after the first immunization as measured by HAI assays (Fig. 4a). Substantially increased HAI titers (≥1:160 in 10 out of 12 animals) were obtained after the boost. No HAI activity against the heterologous asH1N1 (A/swine/Jiangsu/40/2011, Supplementary Fig. 4) virus was detected (Fig. 4b). Importantly, animals generated HA stalk-reactive antibodies that bound to the cH6/1 HA protein (Fig. 4c). Moreover, as measured by in vitro microneutralization (MN) experiments, sera obtained from ferrets 4 weeks after the first and 9 weeks after the second immunization neutralized the closely related pH1N1 (A/Netherlands/602/2009) and the more antigenically distant asH1N1 virus (Supplementary Fig. 5).

Collectively, these studies indicate that nucleoside-modified HA mRNA-LNP vaccines elicit high levels of antibodies against both the HA head and stalk domains of influenza virus in mice, rabbits, and ferrets.

Protection from homologous and heterologous viruses in mice. To investigate the protective efficacy of mRNA immunization, mice that were immunized with two i.d. or i.m. doses of A/California/07/2009 HA mRNA-LNPs were challenged with the homologous A/California/07/2009 H1N1 virus or the heterologous A/Puerto Rico/8/1934 H1N1 virus 5 weeks after the last immunization. Both challenge viruses possessed A/Puerto Rico/8/1934 internal genes and the A/California/7/2009 HA possessed a D225G mutation to facilitate viral replication in mice. All HA mRNA-LNP-vaccinated animals were protected from both the homologous (Fig. 5a, b) and heterologous H1N1 virus infection (Fig. 5c, d), although some initial weight loss in the low dose groups was observed after challenge with the A/Puerto Rico/8/1934 virus (Fig. 5c). Mice injected with control poly(C) RNA-LNP lost weight and died or needed to be euthanized after viral challenge (Fig. 5).

Based on the high HAI titers and measurable HA stalk-reactive antibody responses elicited by the mRNA-LNP constructs, we hypothesized that a single HA mRNA-LNP immunization could elicit protective immunity. Mice were i.m. immunized with a single dose of 30 µg of A/California/07/2009 HA mRNA-LNPs or 30 µg of poly(C) RNA-LNPs. As a comparator, a group of mice were immunized with 3 µg of monovalent A/California/07/2009 virus vaccine. Four weeks after vaccination, mRNA-LNP vaccines induced HAI titers ranging between 320–960 against the autologous strain, whereas the monovalent virus vaccine elicited very low HAI titers of ~1:15 (Fig. 6a). No HAI activity against the PR8 virus was detected (Fig. 6a). High antibody titers elicited by the mRNA-LNP vaccine were associated with protection following challenge with the homologous A/California/07/2009 viral strain and the heterologous A/Puerto Rico/8/1934 viral strain (Fig. 6b, c). All mRNA-LNP-immunized and monovalent virus vaccine-injected animals survived A/

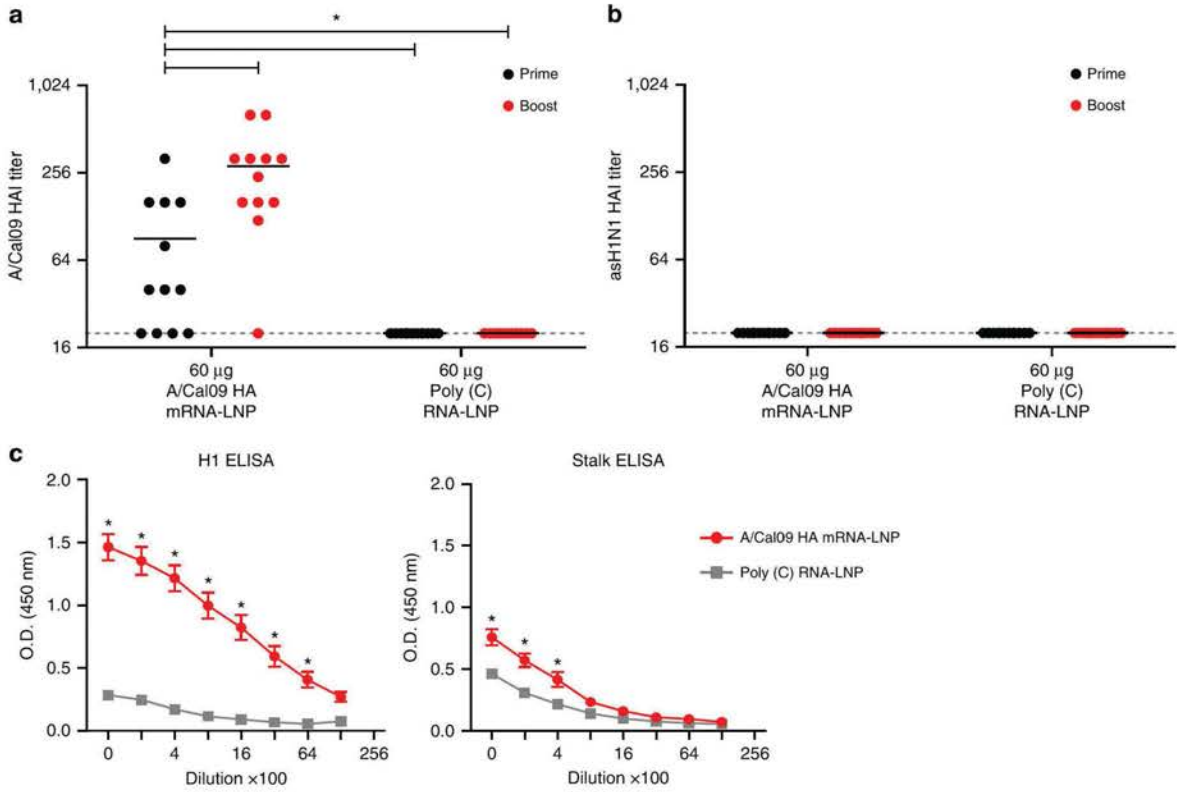

Fig. 4 Nucleoside-modified HA mRNA-LNP immunization induces HA stalk-reactive antibodies in ferrets. Ferrets were immunized two times i.m. with 60 µg of A/California/07/2009 HA mRNA-LNPs or 60 µg of poly(C) RNA-LNPs at week 0 (prime) and 4 (boost). HAI titers against the A/California/07/2009 (**a**) and A/swine/Jiangsu/40/2011 (**b**) viruses were determined at week 4 (prime) and week 13 (boost). **c** IgG binding to full-length H1 HA (total) and cH6/1 HA (stalk) proteins from serum samples obtained 9 weeks after the second immunization was determined. $n = 12$ ferrets. **a**, **b** Each symbol represents one animal, horizontal lines show the mean, dotted line indicates the limit of detection. **c** error bars are SEM. Statistical analysis: **a**, **b** one-way ANOVA with Bonferroni correction on log-transformed data, $^*p < 0.05$. **c** Two-way ANOVA with Bonferroni correction comparing A/California/07/2009 HA and poly(C) immunizations for different dilutions. $^*p < 0.05$

California/07/2009 virus infection; however, animals in both groups lost a substantial amount of weight following infection (Fig. 6b). mRNA-LNP-immunized animals displayed weight loss following A/Puerto Rico/8/1934 virus challenge, but they rapidly recovered and survived virus infection (Fig. 6c). In contrast, mice that were immunized with the monovalent A/California/07/2009 virus vaccine or the poly(C) RNA-LNP vaccine rapidly developed symptoms and 100% of the animals died following A/Puerto Rico/8/1934 virus challenge (Fig. 6c). These data demonstrate that a single mRNA-LNP immunization induced protection from an antigenically distant H1 virus (Supplementary Fig. 1) in the absence of HAI activity to this viral HA.

Protection from a heterosubtypic virus in mice. We next performed a series of studies with an H5N1 influenza virus to determine whether nucleoside-modified HA mRNA-LNP immunization elicits protective immune responses against more antigenically distant influenza virus subtypes. Mice were immunized twice with 30 µg of A/California/07/2009 HA mRNA-LNPs i.d. or 1 µg (total protein) of inactivated H5N1 influenza virus i.m.[24]. Mice were then challenged with a lethal dose of H5N1 virus (6:2 reassortant between A/Puerto Rico/8/1934 and A/Vietnam/1203/04, which donated HA and neuraminidase) 4 weeks after the second immunization and weight and morbidity were monitored for 14 days. Strikingly, all HA mRNA-LNP-immunized animals survived viral challenge, while those injected with poly (C) RNA-LNP needed to be euthanized (Fig. 7a). As expected, no measurable HAI activity against the H5N1 virus was observed in mice immunized with the A/California/07/2009 HA mRNA-LNP vaccine (Fig. 7b). Interestingly, sera from these animals also did not display neutralization activity against the H5N1 virus in in vitro MN experiments (Fig. 7c).

Discussion

Currently approved influenza virus vaccines offer protection against well-matched circulating strains. These regimens mostly elicit antibody responses against the continuously changing immunodominant globular HA head domain. There is a need to develop "universal" influenza virus vaccines that induce potent immune responses against conserved viral epitopes and offer protection from heterologous and heterosubtypic strains. There are several viral protein regions that are conserved among different influenza virus strains, including epitopes in the HA stalk domain, neuraminidase, the ectodomain of the ion channel M2, matrix protein, and nucleoprotein (reviewed in refs. [25,26]). Vaccines against these targets might be able to elicit broad and protective influenza virus-specific immune responses (reviewed in ref. [1]). One of the most extensively studied targets is the immunosubdominant HA stalk (reviewed in ref. [27]). Seasonal influenza vaccines elicit poor antibody responses against HA stalk[28,29] in most individuals; thus, the development of new vaccine platforms

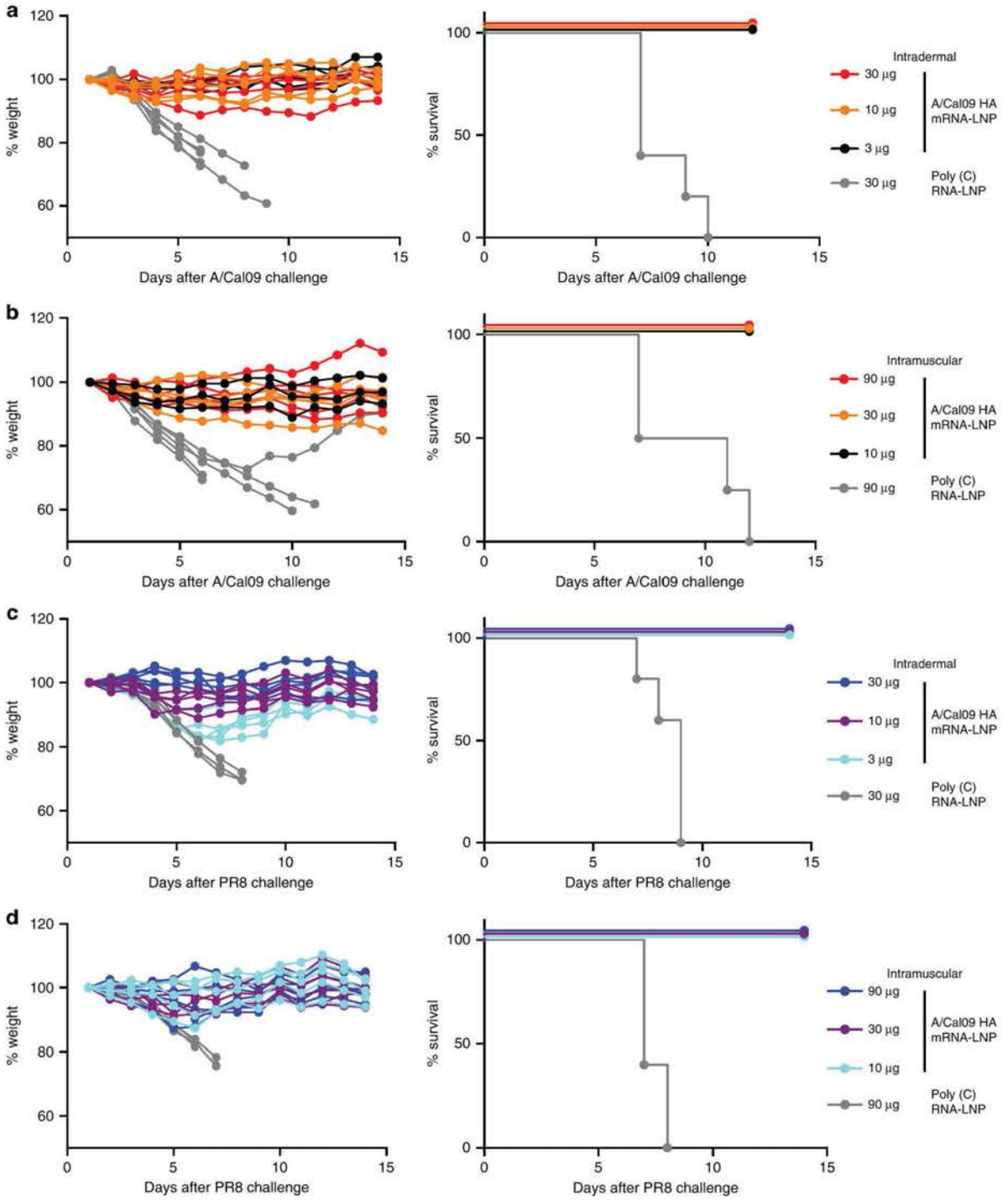

Fig. 5 Two immunizations with nucleoside-modified A/California/07/2009 HA mRNA-LNP vaccine elicits protection from A/California/07/2009 and Puerto Rico/8/1934 viruses. Mice received two i.d. (3, 10, or 30 µg) or i.m. (10, 30, or 90 µg) immunizations of A/California/07/2009 HA mRNA-LNPs or 30 (i.d.) or 90 (i.m.) µg of poly(C) RNA-LNPs at week 0 (prime) and 4 (boost). Animals were challenged with lethal doses of homologous A/California/07/2009 (**a**, **b**) or heterologous A/Puerto Rico/8/1934 viruses (**c**, **d**) 5 weeks after the second immunization and weight loss and survival were followed. Two independent experiments were performed. $n = 5$ mice and each weight loss line represents one animal

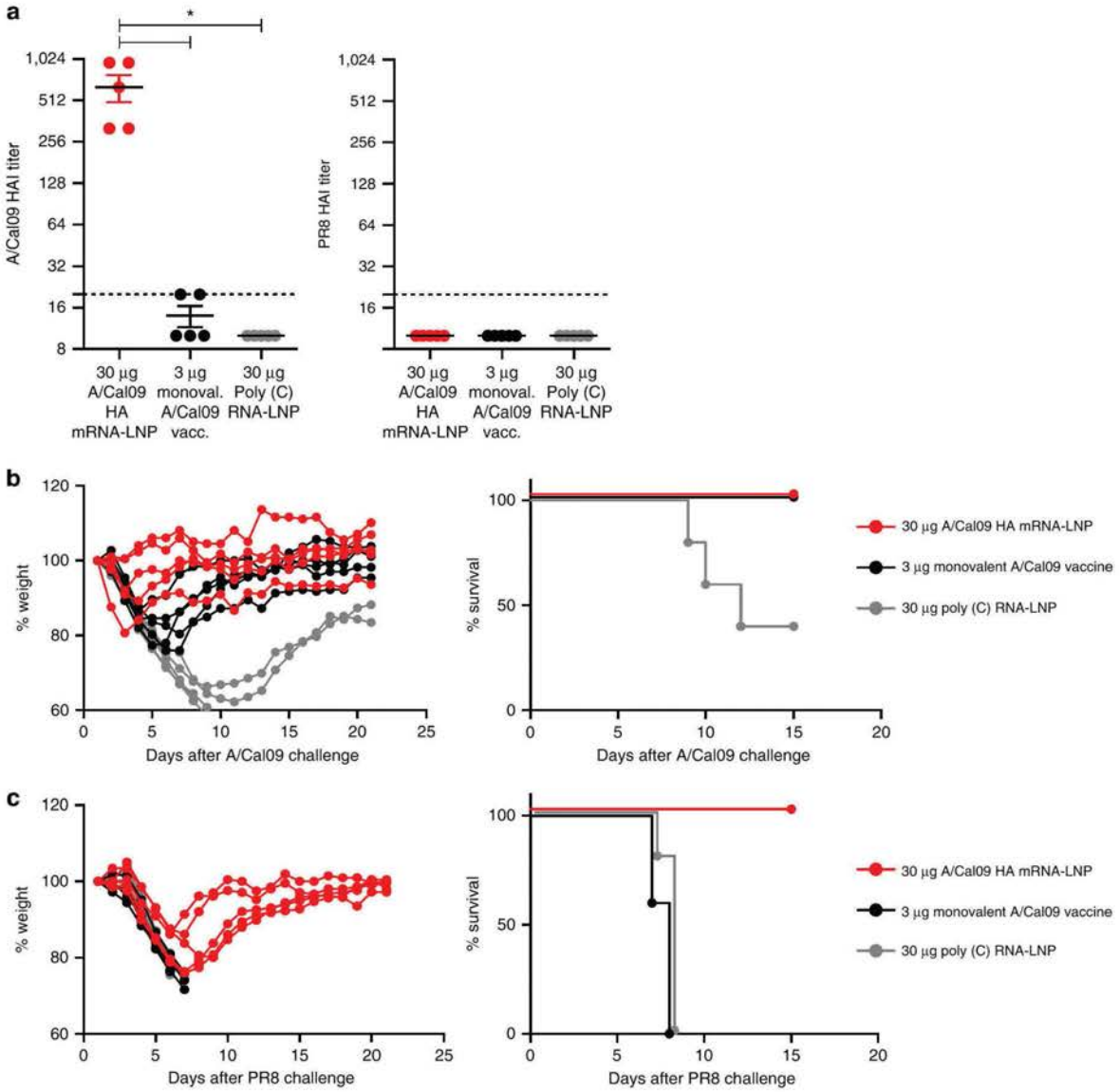

Fig. 6 Nucleoside-modified A/California/07/2009 HA mRNA-LNP vaccine elicits protection from A/California/07/2009 and A/Puerto Rico/8/1934 viruses after a single immunization. Mice received a single i.m. dose of 30 µg A/California/07/2009 HA mRNA-LNPs. Control animals were vaccinated i.m. with a single dose of 3 µg of monovalent A/California/07/2009 virus vaccine or 30 µg of poly(C) RNA-LNPs. HAI titers against the A/California/07/2009 and A/Puerto Rico/8/1934 virus (**a**) were determined 28 days post single immunization. Animals were challenged with lethal doses of homologous A/California/07/2009 (**b**) or heterologous A/Puerto Rico/8/1934 (**c**) viruses 28 days after immunization and weight loss and survival was followed. $n = 5$ mice. **a** Horizontal lines show the mean; dotted line indicates the limit of detection. **b**, **c** Each weight loss line represents one animal. Statistical analysis: **a** one-way ANOVA with Bonferroni correction on log-transformed data, $^*p < 0.05$; **b** two-way ANOVA with Bonferroni correction on weight loss graphs comparing A/California/07/2009 mRNA-immunized animals to inactivated virus-immunized animals. $p < 0.05$ on days 4–6

and optimized immunogens that specifically elicit antibodies against this region is critically important.

Previous studies, using stable, headless HA proteins[3,4] or cHA-encoding DNA and proteins (prime-boost)[6] demonstrated that HA stalk-specific antibodies can be elicited in mice and ferrets. Yassine and colleagues developed headless H1 HA immunogens and demonstrated that three immunizations elicited protective antibodies against H5N1 influenza virus in mice and ferrets[3]. Impagliazzo and coworkers generated various monomeric, dimeric, and trimeric headless H1 mini HAs and showed that three immunizations with the best working trimeric construct resulted in protection against an H5N1 virus in mice[4], and potent antibody responses in cynomolgus monkeys. Ermler and colleagues designed cHAs with HA heads from various influenza A viruses and HA stalks from influenza B viruses[6]. Sequential vaccination (one DNA prime and two protein boosts) with these constructs resulted in protection from influenza B viruses in mice. A recent study from the same laboratory used sequential immunization in ferrets and demonstrated protection from pandemic H1N1 virus challenge[7].

Here, we evaluated the efficacy of a newly developed influenza virus vaccine using nucleoside-modified, FPLC-purified full-length HA-encoding mRNA encapsulated in LNPs[30]. A single immunization with 3 µg of A/California/07/2009 HA mRNA-

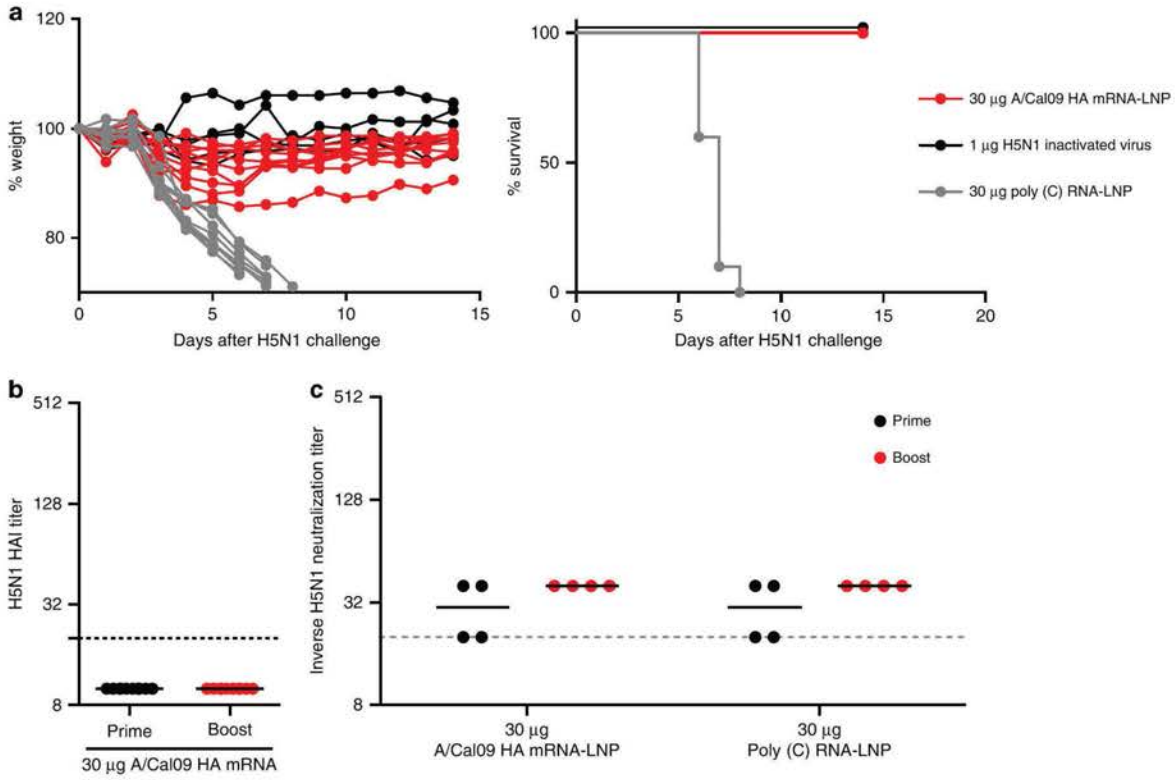

Fig. 7 Nucleoside-modified A/California/07/2009 HA mRNA-LNP vaccine elicits protection from the A/Vietnam/1203/04 (H5N1) virus after two immunizations. Mice received two i.d. doses of 30 µg of A/California/07/2009 HA mRNA-LNPs at weeks 0 and 4. Control animals were vaccinated with two i.d. doses of 30 µg of poly(C) RNA-LNPs or two i.m. doses of 1 µg of inactivated H5N1 virus. (**a**) Animals were challenged with a lethal dose of A/Vietnam/1203/04 virus 28 days after the second immunization and weight loss and survival were followed. $n = 10$ mice. HAI titers (**b**) and in vitro microneutralization activity (**c**) against the A/Vietnam/1203/04 virus were determined 28 days after the first and 28 days after the second immunization. Pooled serum samples were used for MN assays. **a** Each weight loss line represents one animal. **b**, **c** Horizontal lines show the mean; dotted line indicates the limit of detection. Statistical analysis: **a** two-way ANOVA with Bonferroni correction on weight loss graphs comparing A/California/07/2009 mRNA-immunized animals to inactivated virus-immunized animals, $p < 0.05$ on days 5–7. **b** Unpaired *t*-test comparing post prime and post boost samples, $^*p < 0.05$. **c** Two-way ANOVA with Bonferroni correction, $^*p < 0.05$

LNPs resulted in ≥1:120 A/California/07/2009 HAI titers at 4 weeks post-immunization in mice. A second dose induced HAI values ranging between 1280–20,480 depending on the dose and the route of delivery (Fig. 1a, b). Of note, vaccination with A/California/07/2009 mRNA-LNPs did not generate HAI activity against the A/Puerto Rico/8/1934 H1N1 influenza virus (Fig. 1c, d); however, the vaccine protected animals from A/Puerto Rico/8/1934 influenza virus challenge (Fig. 5c, d). This protection was likely mediated by HA stalk-reactive antibody responses that were measurable after a single immunization, and which were boosted by a subsequent immunization (Fig. 2).

A critical finding of this report is that a single immunization with A/California/07/2009 HA mRNA-LNPs resulted in protection against the homologous A/California/07/2009 and the heterologous A/Puerto Rico/8/1934 virus challenge in mice (Fig. 6b, c). Furthermore, we found that two immunizations with the A/California/07/2009 HA mRNA-LNP vaccine induced protection against H5N1 influenza virus infection (Fig. 7a). Of note, sera from these animals did not neutralize the challenge virus in in vitro MN experiments (Fig. 7c), which suggests a contribution of other effector immune mechanisms to heterosubtypic vaccine protection. These findings are in accordance with the literature as several recent studies demonstrated that the potency of HA stalk-specific antibodies were often enhanced by Fc receptor-mediated mechanisms such as antibody-dependent cell-mediated cytotoxicity or complement-dependent cytotoxicity[31–34]. Future studies will determine the correlates of protection after mRNA-LNP influenza vaccine administration. Several mRNA-based influenza vaccines have been described in recent years (reviewed in ref. [35]). For example, Bahl and colleagues demonstrated that a similar mRNA-LNP vaccine platform (using nucleoside-modified but not FPLC-purified H7 and H10 HA mRNAs) induced protection against the homologous influenza virus after a single dose immunization in mice and ferrets; however, no heterologous challenge data or evidence for the presence of stalk-specific antibodies was evaluated in these studies[18]. Another recent report using unmodified HA mRNA-LNPs demonstrated durable induction of HA-specific antibodies in non-human primates, but again, the generation of cross-protective HA stalk antibodies was not reported[36].

Ferrets are one of the best animal models for influenza virus research; however, a potential limitation of the use of ferrets for antiserum generation is that they usually generate more focused antibody responses to the variable head regions of HA than humans after natural infection[37,38]. We demonstrated that a single i.m. immunization with the A/California/07/2009 mRNA-LNP vaccine elicited ≥1:40 HAI activity against the A/California/07/2009 virus in 8 out of 12 animals 4 weeks after vaccination (Fig. 4a). A subsequent immunization resulted in ≥1:160 HAI titers in 10 out of 12 A/California/07/2009 HA mRNA-LNP-

immunized ferrets. The high variability in HAI activity may be due to the genetic heterogeneity of the out-bred animals, and thus it is possible that in some ferrets mRNA-LNP immunization skewed immune responses toward epitopes that neutralize viruses but do not induce HAI titers (Fig. 4a). The presence of stalk-reactive antibodies (Fig. 4c) and MN titers against the homologous and heterologous H1N1 strains in A/California/07/2009 HA mRNA-LNP-immunized animals (Supplementary Fig. 5) support this hypothesis. Additionally, rabbits were immunized with the A/California/07/2009 HA mRNA-LNP vaccine and found that a single immunization elicited HA stalk-reactive antibodies (Supplementary Fig. 3), demonstrating that our findings in mice were translated to two species of large animals.

Here, we demonstrate that the nucleoside-modified, FPLC-purified influenza virus HA-encoding mRNA-LNP vaccine elicited HA stalk-specific antibody responses in mice, rabbits, and ferrets with durable HA stalk titers in mice. Future studies will address if mRNA-LNP immunization preferentially induce HA stalk-specific responses or they are elicited as a consequence of the very potent immune response without refocusing the immunodominance. Additional studies using adoptive serum transfer and T cell depletions will further evaluate the contribution of stalk-specific antibodies to vaccine protection in the heterosubtypic influenza virus infection model. The mRNA-LNP vaccine platform has additional beneficial features over other vaccines, including a favorable safety profile and highly scalable and potentially inexpensive manufacture. In addition to potency, from an influenza virus vaccine perspective, the most critical advantages of the present platform are the rapid development and the ease of production. It is notable that these vaccines are not subject to cell culture and egg-adaptive mutations that commonly arise as conventional influenza virus vaccines are manufactured[39,40]. The use of the nucleoside-modified mRNA-LNP platform with optimized HA stalk-inducing immunogens[3,4,7] may offer a superior platform with easy clinical use. Currently available seasonal influenza virus vaccines do not protect well against antigenically drifted viral strains and they likely provide very little protection against emerging pandemic strains. Production of conventional, FDA-approved vaccines against new pandemic viruses could take at least 6 months, leaving the population unprotected during this period[1]. On the contrary, once the genetic sequence of the target HA antigen is known, mRNA-LNP vaccines can potentially be produced within weeks (reviewed in ref. [12]). mRNA-LNP vaccine production is sequence-independent and can be applied to virtually any pathogen. We believe that the data presented in this report combined with the additional beneficial features of nucleoside-modified and purified mRNA-LNPs makes the present platform a viable broadly protective influenza virus vaccine candidate.

Methods

Ethics statement. The investigators faithfully adhered to the "Guide for the Care and Use of Laboratory Animals" by the Committee on Care of Laboratory Animal Resources Commission on Life Sciences, National Research Council. The animal facilities at the University of Pennsylvania, The Wistar Institute, the Icahn School of Medicine at Mount Sinai and Noble Life Sciences vivarium are fully accredited by the American Association for Accreditation of Laboratory Animal Care. All studies were conducted under protocols approved by the University of Pennsylvania, Noble Life Sciences, the Icahn School of Medicine at Mount Sinai, and The Wistar Institute IACUCs. The Wistar IACUC does not use weight loss as a criteria for euthanasia in murine influenza virus experiments.

mRNA production. mRNAs were produced as previously described[41] using T7 RNA polymerase (Megascript, Ambion) on linearized plasmids (synthesized by GenScript) encoding codon-optimized[42] Puerto Rico/8/1934 influenza virus HA (pTEV-PR8 HA-A101), A/California/7/2009 influenza virus hemmaglutinin (pTEV-A/Cal09 HA-A101), and firefly luciferase (pTEV-Luc-A101). mRNAs were transcribed to contain 101 nucleotide-long poly(A) tails. One-methylpseudouridine (m1Ψ)-5′-triphosphate (TriLink) instead of UTP was used to generate modified nucleoside-containing mRNA. RNAs were capped using the m7G capping kit with 2′-*O*-methyltransferase (ScriptCap, CellScript) to obtain cap1. mRNA was purified by FPLC (Akta Purifier, GE Healthcare), as described[43]. All mRNAs were analyzed by denaturing or native agarose gel electrophoresis and were stored frozen at −20 °C.

LNP formulation of the mRNA. FPLC-purified m1Ψ-containing firefly luciferase and influenza virus HA-encoding mRNAs and poly(C) RNA (Sigma) were encapsulated in LNPs using a self-assembly process in which an aqueous solution of mRNA at pH = 4.0 is rapidly mixed with a solution of lipids dissolved in ethanol[44]. LNPs used in this study were similar in composition to those described previously[44,45], which contain an ionizable cationic lipid (proprietary to Acuitas)/phosphatidylcholine/cholesterol/PEG-lipid (50:10:38.5:1.5 mol/mol) and were encapsulated at an RNA to total lipid ratio of ~0.05 (wt/wt). They had a diameter of ~80 nm as measured by dynamic light scattering using a Zetasizer Nano ZS (Malvern Instruments Ltd., Malvern, UK) instrument. mRNA-LNP formulations were stored at −80 °C at a concentration of mRNA of ~1 μg/μl.

Immunization of mice, rabbits, and ferrets. Mice: Female BALB/c mice aged 8 weeks were purchased from Charles River Laboratories. mRNA-LNPs were diluted in phosphate-buffered saline (PBS) and injected into animals intradermally with a 3/10cc 29½G insulin syringe (BD Biosciences). Four sites of injection (30 μl each) over the lower back were used. For intramuscular injections, mRNA-LNPs were diluted in PBS and injected into animals using a 3/10cc 29½G insulin syringe. Monovalent A/California/7/2009 virus vaccine (3 μg in 50 μl) (BEI Resources, NR-20347) and inactivated A/Vietnam/1203/04 virus vaccine (1 μg in 50 μl) (the virus was grown in eggs and inactivated with 0.3% formalin) were intramuscularly injected into the quadriceps muscle of animals using a 3/10cc 29½G insulin syringe. Inactivated H5N1 whole-virus vaccine preparation was generated by concentration of A/Vietnam/1203/04 virus (vaccine strain, 6:2 re-assortant with PR8, polybasic cleavage site of HA was removed) via ultracentrifugation followed by inactivation with 0.03% formalin. Protein content was measured using the Bradford method and reflects total protein rather than HA concentration.

Rabbits: Female New Zealand White rabbits aged 6 weeks were purchased from Charles River Laboratories. mRNA-LNPs were diluted in PBS and injected into animals intradermally with a 3/10cc 29G syringe (BD Biosciences). Six sites of injection (45 μl each) over the lower back were used.

Ferrets: 7–10-week-old male and female ferrets were purchased from Triple F Farms Inc. mRNA-LNPs were diluted in PBS and injected intramuscularly into the upper thigh (100 μl).

Blood collection. Mice: Blood was collected prior to each immunization by submandibular bleeding. Blood was centrifuged for 10 min at 2000 × *g* in an Eppendorf microcentrifuge and the serum was stored at −80 °C and used for ELISA, MN, and HAI assays.

Rabbits: Blood was obtained from the lateral saphenous vein under anesthesia. Blood was centrifuged for 10 min at 3000 × *g* and the serum was stored at −80 °C and used for ELISA and HAI assays.

Ferrets: Blood was obtained from the vena cava under anesthesia. Blood was centrifuged for 10 min at 3000 × *g* and the serum was stored at −80 °C and used for ELISA, MN, and HAI assays.

Antibody reagents for flow cytometry. The following antibodies were used for flow cytometry: anti-CD4 PerCP/Cy5.5 (Clone GK1.5, BioLegend), anti-CD3 APC-Cy7 (Clone 145-2C11, BD Biosciences), anti-TNF-α PE-Cy7 (Clone MP6-XT22, BD Biosciences), anti-IFN-γ AF700 (Clone XMG1.2, BD Biosciences), anti-IL-2 APC (Clone JES6-5H4, BD Biosciences).

Mouse splenocyte stimulation/staining and flow cytometry. Single cell suspensions from mouse spleens were made in complete medium. Splenocytes were washed once in PBS and resuspended in complete medium at 2×10^7 cells/ml. 2×10^6 cells (100 μl) per sample were stimulated for 6 h at 37 °C using two overlapping influenza virus HA (A/California/07/2009) peptide pools (peptides are 14-mers or 15-mers, with 11 amino acid overlaps, provided by BEI resources, NR-19244) at 2 μg/ml per peptide. Golgi Plug (brefeldin A, BD Biosciences) and Golgi Stop (monensin, BD Biosciences) were diluted 1:100 and 1:143 in complete medium, respectively, and 20 μl from both were added to each sample to inhibit the secretion of intracellular cytokines after 1 h of stimulation. A PMA (10 ng/ml)-ionomycin (250 ng/ml) (Sigma) stimulated sample and unstimulated samples for each animal were included.

After stimulation, cells were washed in PBS and stained using the LIVE/DEAD Fixable Aqua Dead Cell Stain Kit and then surface stained for CD4 (2 μg/ml). Antibodies were incubated with cells for 30 min at RT. Following surface staining, cells were washed in FACS buffer and fixed using the Cytofix/Cytoperm kit (BD Biosciences), according to the manufacturer's instructions. Following fixation, the cells were washed in the permeabilization buffer and incubated with antibodies against CD3 (1.6 μg/ml), TNF-α (1.6 μg/ml), IFN-γ (4 μg/ml), and IL-2 (4 μg/ml) for 1 h at RT. Following staining, the cells were washed with the permeabilization

buffer, fixed (PBS containing 1% paraformaldehyde) and stored at 4 °C until analysis. Splenocytes were analyzed on a modified LSR II flow cytometer (BD Biosciences).

Recombinant influenza virus cHAs. Recombinant HAs including H1 HAs of A/California/04/09 and A/Puerto Rico/8/34 and chimeric cH6/1_{Calss} (an H6 head domain from A/mallard/Sweden/81/02 on top of an H1 stalk domain from A/California/04/09 with a stabilizing mutation in the stalk domain) and cH5/1_{PR8} (an H5 head domain from A/Vietnam/1203/04 on top of an H1 stalk domain from A/Puerto Rico/8/34) constructs were expressed in the baculovirus expression system, as previously described[46–48]. They were then purified via a hexahistidine tag and Ni-nitrilotriacetic acid (NTA) resin.

Influenza virus challenge studies. Mice were anesthetized with isoflurane and intranasally challenged with 200,000 $TCID_{50}$ of A/California/07/2009 influenza virus (6:2 virus with 6 A/Puerto Rico/8/1934 internal genes and A/California/07/2009 HA and NA) or 5000 $TCID_{50}$ of A/Puerto Rico/8/1934 influenza virus in 50 µl PBS. The A/California/7/2009 HA possessed a D225G mutation to facilitate viral replication in mice.

H5N1 challenges were performed with a 6:2 A/Vietnam/1203/04 reassortant virus (6 A/Puerto Rico/8/1934 internal genes and A/Vietnam/1203/04 HA and NA with the polybasic cleavage site removed from the HA). Animals were anesthetized using ketamine/xylazine (0.15 mg ketamine and 0.03 mg xylazine) delivered intraperitoneally in a volume of 100 µl. The mice were then inoculated with 50 µl of a virus dilution (in PBS) containing 5 murine 50% lethal doses (mLD_{50}) of virus.

Enzyme-linked immunosorbent assays. ELISA plates were coated overnight at 4 °C with 3 µg/ml of recombinant protein. ELISA plates were blocked with a 3% (w/vol) bovine serum albumin (BSA) solution in PBS for 2 h. Plates were then washed three times with PBS-Tween20 (0.1%) and serial dilutions of sera (diluted in 1% BSA in PBS) were added to the plates. After 2 h of incubation, plates were washed and alkaline phosphatase-conjugated or horseradish peroxidase (HRP)-conjugated secondary antibodies were added. After a 1 h incubation, plates were washed and a p-nitrophenyl phosphate or a 3,3′,5,5′-tetramethylbenzidine (TMB) substrate (Seracare, product number 50-00-03) was added. For HRP-based ELISAs, HCl was then added to stop the TMB reaction, and absorbance at 405 nm was measured using a plate reader. Results were obtained from technical duplicates.

HAI assays. A/Puerto Rico/8/1934 and A/California/07/2009 HAI assays: Mouse sera were heat-treated for 30 min at 55 °C. Ferret sera were treated with receptor destroying enzyme (RDE) from *Vibrio cholerae* (Denka Seiken, Chuo-ku, Tokyo, Japan) for 2 h at 37 °C and then heat-treated for 30 min at 55 °C. Rabbit sera were RDE-treated for 2 h at 37 °C, heat-treated for 30 min at 55 °C, and then absorbed with turkey erythrocytes. Titrations were performed in 96-well round bottom plates (BD Biosciences). First, 5 µl of sera were added to 95 µl of PBS (1:20 dilution), then two-fold serial dilutions were performed up to 1:2560 in a volume of 50 µl. Next, four agglutinating doses of virus were added to a total volume of 100 µl. Finally, 12.5 µl of turkey erythrocytes (Lampire) (2% (vol/vol) solution) was added to each well, and mixed thoroughly. Agglutination was read after incubating for 1 h at RT. HAI titers were expressed as the inverse of the highest dilution that inhibited four agglutinating doses of influenza virus.

A/swine/Jiangsu/40/2011 and A/Vietnam/1203/04 HAI assays: Mouse and ferret sera were treated with three volumes (based on original sera volume) of RDE for 18 h at 37 °C. Three volumes (based on original serum volume) of 2.5% sodium citrate solution was then added to the RDE-treated serum samples and were then incubated at 56 °C for 1 h. Three volumes of PBS (based on original serum volume) were added to each sample for a final dilution of 1:10. Titrations were performed in 96-well round bottom plates (BD Biosciences). First, 50 µl of RDE-treated serum was added to the first well, then two-fold serial dilutions were performed up to 1:2048. Next, eight agglutinating doses of virus were added to a total volume of 50 µl. Virus and sera were then incubated at RT for 30 min with shaking. Following this incubation, 50 µl of chicken erythrocytes (Charles River Laboratories) (0.5% (vol/vol) solution) was added to each well, and mixed thoroughly. Agglutination was read after incubating for 1 h at 4 °C. HAI titers were expressed as the inverse of the highest dilution that inhibited four agglutinating doses of influenza virus.

All samples were run in at least technical duplicates. The challenge virus strains (detailed in "Influenza virus challenge studies") were used for HAI assays.

MN assays. Mouse and ferret sera were treated with three volumes (based on original sera volume) of RDE for 18 h at 37 °C. Three volumes (based on original serum volume) of 2.5% sodium citrate solution was then added to the RDE-treated serum samples and were then incubated at 56 °C for 1 h. Three volumes of PBS (based on original serum volume) were added to each sample for a final dilution of 1:10.

Madin–Darby Canine Kidney (MDCK) cells (ATCC number PTA-6500) maintained in complete Dulbecco's Modified Eagle Medium with the addition of 10% fetal bovine serum, 1% Pen/Strep, 1% of a 1 M HEPES stock solution were plated at a concentration of 1.5×10^4 cells per well in a 96-well plate and left to grow overnight at 37 °C, 5% CO_2 until they reached 80–90% confluency.

RDE-treated sera was serially diluted two-fold in 1× minimal essential medium (MEM; 10% 10× MEM, 1% 200 mM L-glutamine, 1.6% of a 7.5% sodium bicarbonate stock solution (pH 7.5), 1% of a 1 M 4-(2-hydroxyethyl)-1-piperazineethanesulfonic acid (HEPES) stock solution, 1% of penicillin/streptomycin antibiotic cocktail (Pen/Strep, Gibco), 0.6% of a 35% BSA stock solution) containing 1 µg/ml L-1-tosylamide-2-phenylethyl chloromethyl ketone (TPCK)-treated trypsin. For ferret sera, half of the volume of the serial dilutions was incubated with 100×$TCID_{50}$ of each virus (at a 1:1 volume ratio) for 1 h at RT with shaking. The virus-sera mixture was then applied to 80–90% confluent MDCK cells after they had been washed one time with sterile, 1×PBS. The cells were then incubated with the virus-sera mixture for 1 h at 33 °C. After the incubation, the virus-ferret sera mixture was removed, cells were washed with 1×PBS, and then covered with the remaining half of the serial sera dilutions (supplemented with a 1:1 addition of 1×MEM with 1 µg/ml TPCK-treated trypsin).

For mouse sera, the entire amount of sera was incubated with 50×$TCID_{50}$ of H5N1 (at a 1:1 ratio) for 1 h at RT with shaking. The virus-sera mixture was then applied to 80–90% confluent MDCK cells after they had been washed one time with sterile 1×PBS. The cells were then incubated with the virus-sera mixture for 3 days at 33 °C. The difference in incubation time for the ferret sera vs. mouse sera on MDCK cells in these assays was due to the limited volumes of sera from mouse studies.

All samples were run in at least technical duplicates.

Multiple sequence alignment and phylogenetic tree. Sequences of the full-length HA protein of A/California/04/2009 (pH1N1), A/Michigan/45/2015, A/New Caledonia/20/1999, A/South Carolina/1/1918, A/swine/Jiangsu/40/2011 (asH1N1), A/Brisbane/59/2007, A/swine/4/Mexico/2009, A/swine/Aichi/10/2015, A/swine/Guangxi/QZ5/2014, and A/swine/Ohio/A02216472/2017 were downloaded from the Global Initiative for Sharing of all Influenza Data (GISAID) and aligned using the online server, Clustal Omega (https://www.ebi.ac.uk/Tools/msa/clustalo/). The phylogenetic tree produced from this alignment was downloaded, rooted to A/South Carolina/1/1918, and visualized using FigTree.

Mapping conservation of pH1N1 and asH1N1. The structure used for visualizing the conserved residues between pH1N1 and asH1N1 is PDB ID 3LZG[49]. A n alignment of pH1N1 and asH1N1 whole-HA protein sequences (downloaded from GISAID) was used to determine 100% conserved residues in Chimeria v1.12. These residues were then mapped onto a monomer of 3LZG in red. The alignment of pH1N1 and asH1N1 was also uploaded to the LALIGN server (https://embnet.vital-it.ch/software/LALIGN_form.html) to determine percent identity and similarity between the two HA proteins.

Statistical analyses. Statistical analyses were performed with Excel and Prism 5.0f software. Data were compared using one-way and two-way ANOVA corrected for multiple comparisons (Bonferroni method) and unpaired *t*-test. Survival analyses were perfomed using the log-rank (Mantel–Cox) test. The A/California/07/2009 crystal structure (PDB ID 3UBN) was visualized using PyMOL software.

Data availability. All data are available within the article and its Supplementary Information file or from the authors upon request.

Received: 21 December 2017 Accepted: 13 June 2018
Published online: 22 August 2018

References

1. Krammer, F. & Palese, P. Advances in the development of influenza virus vaccines. *Nat. Rev. Drug Discov.* **14**, 167–182 (2015).
2. Krammer, F. & Palese, P. Influenza virus hemagglutinin stalk-based antibodies and vaccines. *Curr. Opin. Virol.* **3**, 521–530 (2013).
3. Yassine, H. M. et al. Hemagglutinin-stem nanoparticles generate heterosubtypic influenza protection. *Nat. Med.* **21**, 1065–1070 (2015).
4. Impagliazzo, A. et al. A stable trimeric influenza hemagglutinin stem as a broadly protective immunogen. *Science* **349**, 1301–1306 (2015).
5. Valkenburg, S. A. et al. Stalking influenza by vaccination with pre-fusion headless HA mini-stem. *Sci. Rep.* **6**, 22666 (2016).
6. Ermler, M. E. et al. Chimeric hemagglutinin constructs induce broad protection against influenza B virus challenge in the mouse model. *J. Virol.* **91**, e00286-17 (2017).
7. Nachbagauer, R. et al. A universal influenza virus vaccine candidate confers protection against pandemic H1N1 infection in preclinical ferret studies. *NPJ Vaccines* **2**, 1–13 (2017).
8. Wei, C. J. et al. Induction of broadly neutralizing H1N1 influenza antibodies by vaccination. *Science* **329**, 1060–1064 (2010).

9. Babu, T. M. et al. Live attenuated H7N7 influenza vaccine primes for a vigorous antibody response to inactivated H7N7 influenza vaccine. *Vaccine* **32**, 6798–6804 (2014).
10. Talaat, K. R. et al. A live attenuated influenza A(H5N1) vaccine induces long-term immunity in the absence of a primary antibody response. *J. Infect. Dis.* **209**, 1860–1869 (2014).
11. Halliley, J. L. et al. High-affinity H7 head and stalk domain-specific antibody responses to an inactivated influenza H7N7 vaccine after priming with live attenuated influenza vaccine. *J. Infect. Dis.* **212**, 1270–1278 (2015).
12. Pardi, N., Hogan, M. J., Porter, F. W. & Weissman, D. mRNA vaccines—a new era in vaccinology. *Nat. Rev. Drug Discov.* **17**, 261–279 (2018).
13. Pardi, N. et al. Expression kinetics of nucleoside-modified mRNA delivered in lipid nanoparticles to mice by various routes. *J. Control Release* **217**, 345–351 (2015).
14. Pardi, N. et al. Zika virus protection by a single low-dose nucleoside-modified mRNA vaccination. *Nature* **543**, 248–251 (2017).
15. Brazzoli, M. et al. Induction of broad-based immunity and protective efficacy by self-amplifying mRNA vaccines encoding influenza virus hemagglutinin. *J. Virol.* **90**, 332–344 (2015).
16. Magini, D. et al. Self-amplifying mRNA vaccines expressing multiple conserved influenza antigens confer protection against homologous and heterosubtypic viral challenge. *PLoS ONE* **11**, e0161193 (2016).
17. Chahal, J. S. et al. Dendrimer-RNA nanoparticles generate protective immunity against lethal Ebola, H1N1 influenza, and Toxoplasma gondii challenges with a single dose. *Proc. Natl Acad. Sci. USA* **113**, E4133–E4142 (2016).
18. Bahl, K. et al. Preclinical and clinical demonstration of immunogenicity by mRNA vaccines against H10N8 and H7N9 influenza viruses. *Mol. Ther.* **25**, 1316–1327 (2017).
19. Petsch, B. et al. Protective efficacy of in vitro synthesized, specific mRNA vaccines against influenza A virus infection. *Nat. Biotechnol.* **30**, 1210–1216 (2012).
20. Kariko, K. et al. Incorporation of pseudouridine into mRNA yields superior nonimmunogenic vector with increased translational capacity and biological stability. *Mol. Ther.* **16**, 1833–1840 (2008).
21. Kariko, K., Muramatsu, H., Ludwig, J. & Weissman, D. Generating the optimal mRNA for therapy: HPLC purification eliminates immune activation and improves translation of nucleoside-modified, protein-encoding mRNA. *Nucleic Acids Res.* **39**, e142 (2011).
22. Pica, N. et al. Hemagglutinin stalk antibodies elicited by the 2009 pandemic influenza virus as a mechanism for the extinction of seasonal H1N1 viruses. *Proc. Natl Acad. Sci. USA* **109**, 2573–2578 (2012).
23. Swain, S. L. et al. CD4+ T-cell memory: generation and multi-faceted roles for CD4 +T cells in protective immunity to influenza. *Immunol. Rev.* **211**, 8–22 (2006).
24. Krammer, F., Pica, N., Hai, R., Margine, I. & Palese, P. Chimeric hemagglutinin influenza virus vaccine constructs elicit broadly protective stalk-specific antibodies. *J. Virol.* **87**, 6542–6550 (2013).
25. Krammer, F., Garcia-Sastre, A. & Palese, P. Is it possible to develop a "universal" influenza virus vaccine? Toward a universal influenza virus vaccine: potential target antigens and critical aspects for vaccine development. *Cold Spring Harb. Perspect. Biol.* **10**, a028845 (2017).
26. Andrews, S. F., Graham, B. S., Mascola, J. R. & McDermott, A. B. Is it possible to develop a "universal" influenza virus vaccine? Immunogenetic considerations underlying B-cell biology in the development of a pan-subtype influenza A vaccine targeting the hemagglutinin stem. *Cold Spring Harb. Perspect. Biol.* **10**, a029413 (2017).
27. Krammer, F. Novel universal influenza virus vaccine approaches. *Curr. Opin. Virol.* **17**, 95–103 (2016).
28. Corti, D. et al. Heterosubtypic neutralizing antibodies are produced by individuals immunized with a seasonal influenza vaccine. *J. Clin. Invest.* **120**, 1663–1673 (2010).
29. Sui, J. et al. Wide prevalence of heterosubtypic broadly neutralizing human anti-influenza A antibodies. *Clin. Infect. Dis.* **52**, 1003–1009 (2011).
30. Pardi, N. & Weissman, D. Nucleoside modified mRNA vaccines for infectious diseases. *Methods Mol. Biol.* **1499**, 109–121 (2017).
31. DiLillo, D. J., Tan, G. S., Palese, P. & Ravetch, J. V. Broadly neutralizing hemagglutinin stalk-specific antibodies require FcgammaR interactions for protection against influenza virus in vivo. *Nat. Med.* **20**, 143–151 (2014).
32. Henry Dunand, C. J. et al. Both neutralizing and non-neutralizing human H7N9 influenza vaccine-induced monoclonal antibodies confer protection. *Cell Host Microbe* **19**, 800–813 (2016).
33. Leon, P. E. et al. Optimal activation of Fc-mediated effector functions by influenza virus hemagglutinin antibodies requires two points of contact. *Proc. Natl Acad. Sci. USA* **113**, E5944–E5951 (2016).
34. Terajima, M. et al. Complement-dependent lysis of influenza a virus-infected cells by broadly cross-reactive human monoclonal antibodies. *J. Virol.* **85**, 13463–13467 (2011).
35. Scorza, F. B. & Pardi, N. New kids on the block: RNA-based influenza virus vaccines. *Vaccines* **6**, E20 (2018).
36. Lutz, J. et al. Unmodified mRNA in LNPs constitutes a competitive technology for prophylactic vaccines. *NPJ Vaccines* **2**, 1–9 (2017).
37. Li, Y. et al. Immune history shapes specificity of pandemic H1N1 influenza antibody responses. *J. Exp. Med.* **210**, 1493–1500 (2013).
38. Nachbagauer, R. et al. Defining the antibody cross-reactome directed against the influenza virus surface glycoproteins. *Nat. Immunol.* **18**, 464–473 (2017).
39. Zost, S. J. et al. Contemporary H3N2 influenza viruses have a glycosylation site that alters binding of antibodies elicited by egg-adapted vaccine strains. *Proc. Natl Acad. Sci. USA* **114**, 12578–12583 (2017).
40. Wu, N. C. et al. A structural explanation for the low effectiveness of the seasonal influenza H3N2 vaccine. *PLoS Pathog.* **13**, e1006682 (2017).
41. Pardi, N., Muramatsu, H., Weissman, D. & Kariko, K. In vitro transcription of long RNA containing modified nucleosides. *Methods Mol. Biol.* **969**, 29–42 (2013).
42. Thess, A. et al. Sequence-engineered mRNA without chemical nucleoside modifications enables an effective protein therapy in large animals. *Mol. Ther.* **23**, 1456–1464 (2015).
43. Weissman, D., Pardi, N., Muramatsu, H. & Kariko, K. HPLC purification of in vitro transcribed long RNA. *Methods Mol. Biol.* **969**, 43–54 (2013).
44. Maier, M. A. et al. Biodegradable lipids enabling rapidly eliminated lipid nanoparticles for systemic delivery of RNAi therapeutics. *Mol. Ther.* **21**, 1570–1578 (2013).
45. Jayaraman, M. et al. Maximizing the potency of siRNA lipid nanoparticles for hepatic gene silencing in vivo. *Angew. Chem. Int. Ed. Engl.* **51**, 8529–8533 (2012).
46. Krammer, F. et al. A carboxy-terminal trimerization domain stabilizes conformational epitopes on the stalk domain of soluble recombinant hemagglutinin substrates. *PLoS ONE* **7**, e43603 (2012).
47. Hai, R. et al. Influenza viruses expressing chimeric hemagglutinins: globular head and stalk domains derived from different subtypes. *J. Virol.* **86**, 5774–5781 (2012).
48. Margine, I., Palese, P. & Krammer, F. Expression of functional recombinant hemagglutinin and neuraminidase proteins from the novel H7N9 influenza virus using the baculovirus expression system. *J. Vis. Exp.* **81**, e51112 (2013).
49. Xu, R. et al. Structural basis of preexisting immunity to the 2009 H1N1 pandemic influenza virus. *Science* **328**, 357–360 (2010).

Acknowledgements

We thank Michael J. Hogan, Ph.D., and Istvan Tombacz, Ph.D., for assistance with statistical analysis and critical review of the manuscript. S.E.H. was supported by the National Institute of Allergy and Infectious Diseases (1R01AI113047, 1R01AI108686, and Centers of Influenza Virus Research and Surveillance (CEIRS) contract HHSN272201400005C). S.E.H. holds an Investigators in the Pathogenesis of Infectious Disease Award from the Burroughs Wellcome Fund. D.W. was supported by the NIAID of the NIH under award numbers R01-AI050484, R01-AI124429, and R01-AI084860, and the New Frontier Sciences division of Takeda Pharmaceuticals. Work in the Krammer Laboratory was supported by by NIAID U19 AI109946 and the Centers of Influenza Virus Research and Surveillance (CEIRS) contract HHSN272201400008C.

Author contributions

N.P., D.W., K.P., S.E.H., and F.K. designed vaccine studies. N.P., K.P., M.M., and E.L.K. performed the studies. S.J.Z. generated Fig. S1. B.L.M., Y.K.T., T.D.M., F.K., C.J.B., and M.J.H. supplied reagents. N.P., D.W., S.E.H., F.K., and K.K. wrote the manuscript with help from the co-authors.

Additional information

Supplementary Information accompanies this paper at https://doi.org/10.1038/s41467-018-05482-0.

Competing interests: In accordance with the University of Pennsylvania policies and procedures and our ethical obligations as researchers, we report that K.K. and D.W. are named on patents that describe the use of nucleoside-modified mRNA as a platform to deliver therapeutic proteins. D.W. and N.P. are also named on a patent describing the use of modified mRNA in lipid nanoparticles as a vaccine platform. We have disclosed those interests fully to the University of Pennsylvania, and we have in place an approved plan for managing any potential conflicts arising from licensing of our patents. S.E.H. has received consultancy fee from Lumen, Novavax, and Merck for work unrelated to this report. The remaining authors declare no competing interests.

Reprints and permission information is available online at http://npg.nature.com/reprintsandpermissions/

Publisher's note: Springer Nature remains neutral with regard to jurisdictional claims in published maps and institutional affiliations.

mRNA-based therapeutics — developing a new class of drugs

Ugur Sahin[1,2], Katalin Karikó[2,3] and Özlem Türeci[1]

Abstract | *In vitro* transcribed (IVT) mRNA has recently come into focus as a potential new drug class to deliver genetic information. Such synthetic mRNA can be engineered to transiently express proteins by structurally resembling natural mRNA. Advances in addressing the inherent challenges of this drug class, particularly related to controlling the translational efficacy and immunogenicity of the IVTmRNA, provide the basis for a broad range of potential applications. mRNA-based cancer immunotherapies and infectious disease vaccines have entered clinical development. Meanwhile, emerging novel approaches include *in vivo* delivery of IVT mRNA to replace or supplement proteins, IVT mRNA-based generation of pluripotent stem cells and genome engineering using IVT mRNA-encoded designer nucleases. This Review provides a comprehensive overview of the current state of mRNA-based drug technologies and their applications, and discusses the key challenges and opportunities in developing these into a new class of drugs.

The concept of nucleic acid-encoded drugs was conceived over two decades ago when Wolff *et al.*[1] demonstrated that direct injection of *in vitro* transcribed (IVT) mRNA or plasmid DNA (pDNA) into the skeletal muscle of mice led to the expression of the encoded protein in the injected muscle. At the time, mRNA was not pursued further as it is less stable than DNA, and the field focused on technologies based on pDNA and viral DNA. Nevertheless, since its discovery in 1961, mRNA has been the subject of consistent basic and applied research for various diseases (FIG. 1 (TIMELINE)). In the first decades after its discovery, the focus was on understanding the structural and functional aspects of mRNA and its metabolism in the eukaryotic cell. This is in addition to making tools for mRNA recombinant engineering more accessible to a broader research community. In the 1990s, preclinical exploration of IVT mRNA was initiated for diverse applications, including protein substitution and vaccination approaches for cancer and infectious diseases[2–11]. Consequently, accumulated knowledge enabled recent scientific and technological advances to overcome some of the obstacles associated with mRNA, such as its short half-life and unfavourable immunogenicity.

Conceptually, there are several important differences between IVT mRNA-based therapeutic approaches and other nucleic acid-based therapies. IVT mRNA does not need to enter into the nucleus to be functional; once it has reached the cytoplasm the mRNA is translated instantly. By contrast, DNA therapeutics need to access the nucleus to be transcribed into RNA, and their functionality depends on nuclear envelope breakdown during cell division. In addition, IVT mRNA-based therapeutics, unlike plasmid DNA and viral vectors, do not integrate into the genome and therefore do not pose the risk of insertional mutagenesis. For most pharmaceutical applications it is also advantageous that IVT mRNA is only transiently active and is completely degraded via physiological metabolic pathways. Moreover, the production of IVT mRNA is relatively simple and inexpensive, and so the development of IVT mRNA-based therapeutics has garnered broad interest (BOX 1).

In the field of therapeutic cancer vaccination, IVT mRNA has undergone extensive preclinical investigation and has reached Phase III clinical testing[12–18]. In other areas such as protein-replacement therapies in oncology[11,19–21], cardiology[22,23], endocrinology[24], haematology[25,26], pulmonary medicine[25,27] or the treatment of other diseases[6,28], the development of IVT mRNA-based therapeutics is at the preclinical stage. To advance protein replacement therapies, unresolved issues such as the targeted delivery of mRNA and its complex pharmacology need to be addressed.

Here, we provide a comprehensive overview of the current state of mRNA-based drug technologies and their various applications. We discuss the peculiarities of the biopharmaceutical development of mRNA-based therapeutics, as well as the strengths and the key challenges that might affect the progress of this drug class.

[1]*TRON Translational Oncology at the University Medical Center of the Johannes Gutenberg University, Langenbeckstrasse 1, 55131 Mainz, Germany.*
[2]*BioNTech Corporation, An der Goldgrube 12, 55131 Mainz, Germany.*
[3]*Department of Neurosurgery, University of Pennsylvania School of Medicine, Philadelphia, Pennsylvania 19104, USA.*
e-mails: ugur.sahin@tron-mainz.de; katalin.kariko@biontech.de; tureci@mail.uni-mainz.de
doi:10.1038/nrd4278
Published online
19 September 2014

Timeline | **Key discoveries and advances in the development of mRNA as a drug technology**

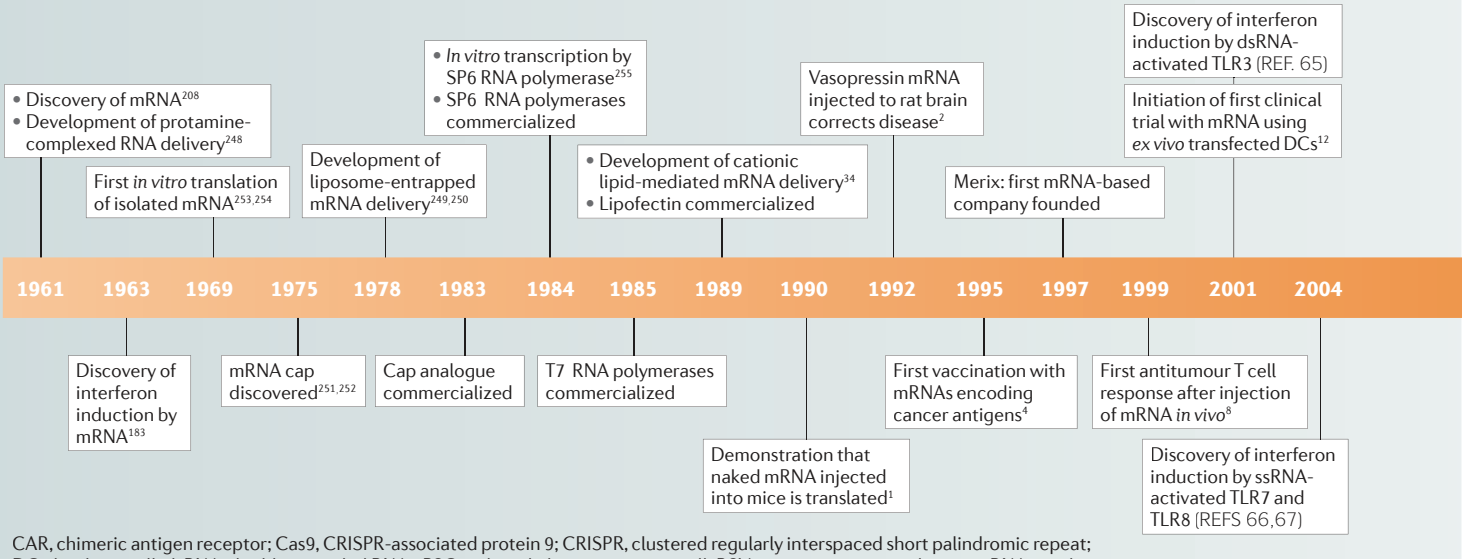

CAR, chimeric antigen receptor; Cas9, CRISPR-associated protein 9; CRISPR, clustered regularly interspaced short palindromic repeat; DC, dendritic cell; dsRNA, double-stranded RNA; iPSC, induced pluripotent stem cell; RSV, respiratory syncytial virus; ssRNA, single-stranded RNA; TALEN, transcription activator-like effector nuclease; TLR, Toll-like receptor.

Principal concept of mRNA pharmacology

The concept behind using IVT mRNA as a drug is the transfer of a defined genetic message into the cells of a patient for the ultimate purpose of preventing or altering a particular disease state.

In principle, two approaches of using IVT mRNA are being pursued. One is to transfer it into the patient's cells *ex vivo*; these transfected cells are then adoptively administered back to the patient. This method is being investigated for genome engineering, genetic reprogramming, T cell- and dendritic cell (DC)-based immunotherapies to treat cancer and infectious diseases, and some protein-replacement approaches. The second approach is direct delivery of the IVT mRNA using various routes. This is being developed for applications in oncology and infectious diseases, tolerization regimens to treat allergies and for other protein-replacement therapies. For both *ex vivo* transfection and direct vaccination, the following general principles of mRNA pharmacology apply.

The machinery of the transfected cell is utilized for *in vivo* translation of the message to the corresponding protein, which is the pharmacologically active product. Thus, therapeutic protein-coding mRNA works in an opposite manner to small interfering RNA (siRNA), which inhibits the expression of proteins. IVT mRNA is engineered to structurally resemble naturally occurring mature and processed mRNA in the cytoplasm of eukaryotic cells. Hence, the IVT mRNA is single-stranded, has a 5′ cap and a 3′ poly(A) tail. The open reading frame (ORF) encoding the protein of interest is marked by start and stop codons and is flanked by untranslated regions (UTRs) (FIG. 2).

The mRNA is synthesized in a cell-free system by *in vitro* transcription from a DNA template, such as a linearized plasmid or a PCR product. With the exception of the 5′ cap, this DNA template encodes all the structural elements of a functional mRNA. *In vitro* transcription is performed with T7 or SP6 RNA polymerase in the presence of nucleotides and thereafter the mRNA is capped enzymatically. The template DNA is then digested by DNases and the mRNA is purified by conventionally used methods for isolating nucleic acids.

The primary compartment of the pharmacodynamic activity of IVT mRNA is the cytoplasm. In contrast to natural mRNA that is produced in the nucleus and enters the cytoplasm through nuclear export, IVT mRNA has to enter the cytoplasm from the extracellular space.

Irrespective of whether the IVT mRNA is delivered to the cells *in vitro* or *in vivo*, two key factors determine its cytoplasmic bioavailability. One is rapid degradation by the highly active ubiquitous RNases, which are abundant in the extracellular space. The other is the cell membrane, which hampers the passive diffusion of the negatively charged large mRNA molecule into the cytoplasm. In principle, eukaryotic cells are capable of actively engulfing naked mRNA. However, in most cell types the uptake rate and cytoplasmic transfer is minimal (less than 1 in 10,000 molecules of the initial mRNA input). The transfection of cells can be improved by formulating the IVT mRNA with complexing agents, which protect the mRNA from degradation by RNases and also act as facilitators for its cellular uptake. Alternatively, techniques such as electroporation in RNase-free buffer can be used for efficient *ex vivo* mRNA transfer into cells.

Once IVT mRNA has entered the cytoplasm, its pharmacology is governed by the same complex cellular mechanisms that regulate the stability and translation of native mRNA.

The protein product translated from the IVT mRNA undergoes post-translational modification, and this protein is the bioactive compound. The half-lives of both the

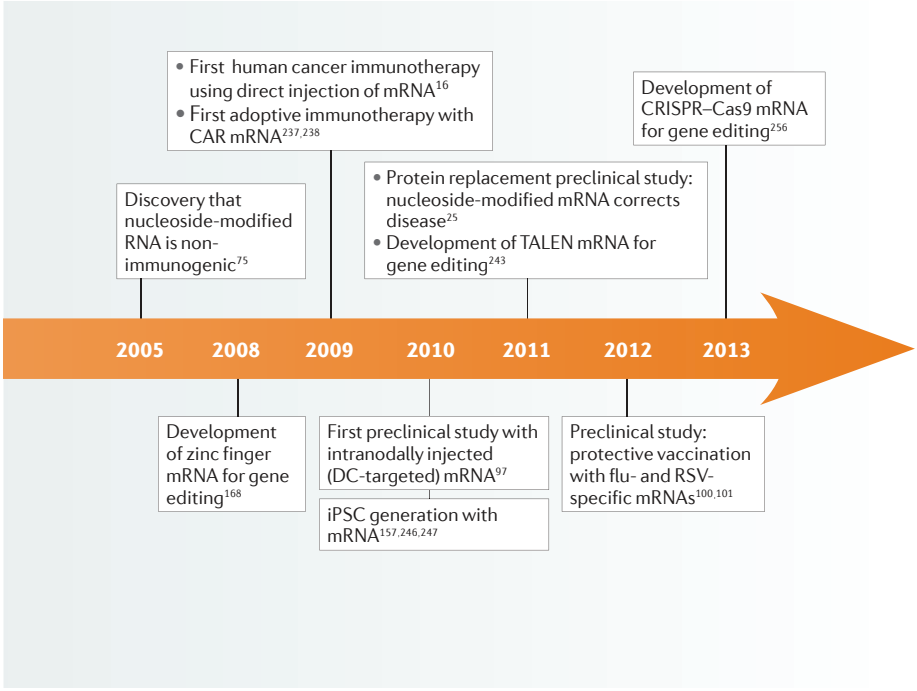

IVT mRNA template and the protein product are critical determinants of the pharmacokinetics of mRNA-based therapeutics.

Once the encoded protein has been generated, its destination is determined by signal peptides. These may be either intrinsic to the natural protein sequence or recombinantly engineered to direct the protein to the desired cell compartment within the host cell. Alternatively, the protein may be secreted to act on neighbouring cells or, if released into the bloodstream, to act on distant organs.

For immunotherapeutic approaches, the processing pathways of the encoded protein are crucial for determining its pharmacodynamics. Similar to the fate of endogenously generated protein, mRNA-encoded products are degraded by proteasomes and presented on major histocompatibility complex (MHC) class I molecules to $CD8^+$ T cells. In general, intracellular proteins do not reach the MHC class II processing pathway to induce T helper cell responses. However, by introducing a secretion signal into the antigen-encoding sequence, T helper cell responses can be achieved as the secretion signal redirects the protein antigen to the extracellular space.

Improving the translation and stability of mRNA

The amount of IVT mRNA required for a therapeutic effect and the treatment duration depends on many factors. These include the intended biological function of the encoded protein and its mode of action, as well as the potency and the circulation half-life of the protein, which will vary by several orders of magnitude for different applications. Nanogram to microgram amounts of highly antigenic proteins may be sufficient for the efficient induction of immune responses in humans. By contrast, milligram or even gram amounts of proteins may be required for the delivery of systemically active growth factors, hormones or monoclonal antibodies. Through iterative optimization of the translational potency and intracellular stability of IVT mRNA, the protein amounts that can be generated per unit of mRNA have considerably increased.

Substantial efforts have been invested in modifying structural elements of the IVT mRNA — notably the 5′ cap, 5′- and 3′-UTRs, the coding region, and the poly(A) tail — to systematically improve its intracellular stability and translational efficiency (FIG. 3). These improvements ultimately lead to the production of significant levels of the encoded protein over a longer timeframe; from a range of a few minutes to longer than 1 week[29–31]. The range of opportunities available for the modulation of mRNA pharmacology is still not fully explored, and a deeper understanding of mRNA-binding factors and their binding sites is likely to open up further opportunities for engineering mRNA vectors with diverse pharmacokinetic properties.

The 5′ cap. Robust translation of mRNA requires a functional 5′cap structure. Natural eukaryotic mRNA has a 7-methylguanosine (m^7G) cap linked to the mRNA during the transcription process by a 5′-5′-triphosphate bridge (ppp) (m^7GpppN structure). Binding of the 5′ cap to eukaryotic translation initiation factor 4E (EIF4E) is crucial for efficient translation, whereas its binding to the mRNA decapping enzymes DCP1, DCP2 or DCPS regulates mRNA decay[32]. One approach to cap IVT mRNA after its initial synthesis is to perform a second step with recombinant vaccinia virus-derived capping enzymes[33]. The resulting cap structure is identical to the most frequent naturally occurring eukaryotic cap structure. The other more commonly used approach is to add a synthetic cap analogue into the *in vitro* transcription reaction and perform capping and *in vitro* transcription in a single step. However, the main limitation of this approach is that the cap analogue and the GTP nucleotide required for *in vitro* transcription compete, resulting in some of the mRNA remaining uncapped and translationally inactive.

Early mRNA research was performed with IVT mRNAs generated with a m^7GpppG cap analogue[1,34], and most of the ongoing clinical trials still use this type of mRNA. However, a substantial proportion of the m^7GpppG analogue is incorporated in reverse orientation into the mRNA and therefore not recognized by the translational machinery, resulting in lower translational activity. Hence, so-called anti-reverse cap analogues (ARCAs; $m_2^{7,3'-O}GpppG$) were introduced[35,36]. ARCA-capped mRNAs exhibited superior translational efficiency in various cell types[37,38]. Recently, a phosphorothioate-containing ARCA cap analogue was developed[39]. This cap analogue confers resistance to decapping by DCP2, thus further extending the half-life of the mRNA[40]. Experiments in mice showed that IVT mRNA containing a phosphorothioate-modified cap induced potent immune responses against the encoded protein, and the responses were stronger than those induced by mRNAs with a control cap[41]. The impact of the cap analogues on the translation and stability of IVT mRNA appears to depend on the cell type and cell differentiation state[39].

Box 1 | **Academic and industrial interest in mRNA**

Recently, several universities have opened RNA centres to advance therapeutic applications of RNA, including *in vitro* transcribed (IVT) mRNA. These centres include the RNA Therapeutic Institute at the University of Massachusetts, USA, the Yale Center for RNA Science and Medicine, USA, and the RNA Institute at the University at Albany, State University of New York, USA. The preclinical and clinical development of mRNA-based therapeutics has also been accelerated at university spin-off companies (for example, Argos Therapeutics, BioNTech, CureVac, eTheRNA, Ethris, Factor Bioscience, Moderna and Onkaido), which are supported by considerable venture capital inflows.

Major pharmaceutical companies such as Novartis, Sanofi Pasteur, AstraZeneca, Alexion and Shire have entered into the development of mRNA-based products. IVT mRNA technologies are being in-licensed (for example, the US$240 million deal between AstraZeneca and Moderna in 2013, the Sanofi Pasteur deal with Curevac in 2014, the Shire collaboration with Ethris in 2013, and the $100 million upfront deal between Moderna and Alexion in 2014; see the FierceBiotech website for further information). In October 2013, the 1st International mRNA Health Conference was held in the historic town of Tübingen, Germany, where nucleic acid was discovered 140 years ago[207].

The poly(A) tail. The poly(A) tail regulates the stability and translational efficiency of mRNA in synergy with the 5′ cap, the internal ribosomal entry site and various other determinants[42]. IVT mRNA is tailed either by encoding the poly(A) stretch in the template vector from which it is transcribed or by a two-step reaction that extends the IVT mRNA enzymatically using recombinant poly(A)polymerase. Recombinant poly(A) polymerase enables the incorporation of modified nucleotides into the poly(A) tail to inhibit deadenylation by poly(A)-specific nucleases[43]. This approach has been explored for various nucleoside analogues, including cordycepin (3′-deoxyadenosine)[44]; however, cordycepin failed to increase the half-life of the mRNA[38]. This failure is most probably because cordycepin is a chain terminator and thus incorporates only at the ultimate 3′ position.

A limitation of enzymatic polyadenylation is that each RNA preparation consists of a mixture of RNA species differing in the length of the poly(A) tail. *In vitro* transcription of RNA from a DNA template, by contrast, yields RNA with a defined poly(A) tail length, and is therefore preferred, particularly if the mRNA is intended for clinical applications. Analyses in DCs demonstrated that the 3′ end of the poly(A) tail should not be masked by additional bases and that the optimal length of the poly(A) tail is between 120 and 150 nucleotides[29,37].

5′- and 3′-UTRs. Another strategy to optimize the translation and stability of IVT mRNA in cells is to incorporate 5′- and 3′-UTRs containing regulatory sequence elements that have been identified to modulate the translation and stability of endogenous mRNA.

For example, many IVT mRNAs contain the 3′-UTRs of α- and β-globin mRNAs that harbour several sequence elements that increase the stability and translation of mRNA[30,45]. The stabilizing effect of human β-globin 3′-UTR sequences is further augmented by using two human β-globin 3′-UTRs arranged in a head-to-tail orientation[29]. In addition, various regions of cellular and viral 5′- and 3′-UTRs enhance the stability and translational efficiency of mRNA. The 3′-UTR of the eukaryotic elongation factor 1α (*EEF1A1*) mRNA[46] and a 5′-UTR element present in many orthopoxvirus mRNAs, for example, inhibited both decapping and 3′–5′ exonucleolytic degradation[47] (reviewed in REF. 48). For some applications, destabilizing the mRNA might be desirable to limit the duration of protein production. This effect can be achieved by incorporating AU-rich elements into 3′-UTRs, thus ensuring rapid mRNA degradation and a short duration of protein expression[49].

The coding region. Codon composition is known to affect translation efficiency. Replacing rare codons with synonymous frequent codons improves translational yield[50] because reuse of the same tRNA accelerates translation owing to amino-acylation of tRNAs in the vicinity of the ribosomes[51]. Codon context (that is, neighbouring nucleotides and codons) also affects the translational elongation rate and translational efficiency[52]. Similar to recombinant DNA-based approaches (reviewed in REF. 53), codon-optimized IVT mRNAs have been successfully used in vaccine studies against viral infections[54] and for the expression of non-viral proteins[26].

However, there may be valid reasons to refrain from using optimized codons. Some proteins require slow translation, which is ensured by rare codons, for their proper folding[55]. It may also be beneficial for some IVT mRNA-encoded vaccines to maintain the original ORF. Potent cryptic T cell epitopes may be generated when the IVT mRNA is translated in different frames owing to ribosomal frame-shifting or when translation is initiated either internally or from a CUG start codon[56–58]. Codon optimization should eliminate these important sources of antigenic peptides.

Immune-stimulatory activity of IVT mRNA

For vaccination, the strong immune-stimulatory effect and intrinsic adjuvant activity of IVT mRNA are added benefits[59,60] and lead to potent antigen-specific cellular and humoral immune responses[9,61]. The type of immune response appears to depend on a range of factors, including the characteristics of the type and size of particles in which the IVT mRNA is incorporated[62–64]. In applications such as protein-replacement therapies, however, activation of the innate immune system by IVT mRNA is a major disadvantage. The recent progress in identifying RNA sensors in cells and the structural elements within mRNA that are involved in immune recognition provides opportunities to augment immune activation by IVT mRNA, or alternatively, to create 'de-immunized' mRNA as needed.

IVT mRNA induces immune stimulation by activating pattern recognition receptors, the natural role of which is to identify and respond to viral RNAs by inducing various downstream effects (FIG. 4).

In immune cells, the Toll-like receptors TLR3, TLR7 and TLR8, which reside in the endosomal compartment, are activated by endocytosed IVT mRNA and induce secretion of interferon. TLR3 recognizes double-stranded RNA (dsRNA)[65], whereas TLR7 and TLR8 sense single-stranded RNA (ssRNA)[66,67]. Poly(U) is the most potent interferon inducer, and acts through TLR7 (REFS 67,68).

By contrast, in non-immune cells, most of the interferon production is induced through the activation of the cytosolic receptors cytoplasmic retinoic acid-inducible gene I protein (RIG-I; also known as DDX58) and melanoma differentiation-associated protein 5 (MDA5; also known as IFIH1)[69,70]. RIG-1 is activated by short, double-stranded, 5′-triphosphate RNA[71], whereas MDA5 responds to long dsRNA and viral mRNAs lacking 2′-*O*-methylation[72,73].

Cytoplasmic RNA sensors mediate immune stimulation and affect the efficiency of mRNA translation, which eventually leads to stalled translation, RNA degradation and direct antiviral activity (FIG. 4). These effects are partly mediated by protein kinase RNA-activated (PKR; also known as EIF2AK2), which phosphorylates the eukaryotic translation initiation factor 2α (eIF2α) and ultimately inhibits mRNA translation[74]. De-immunized

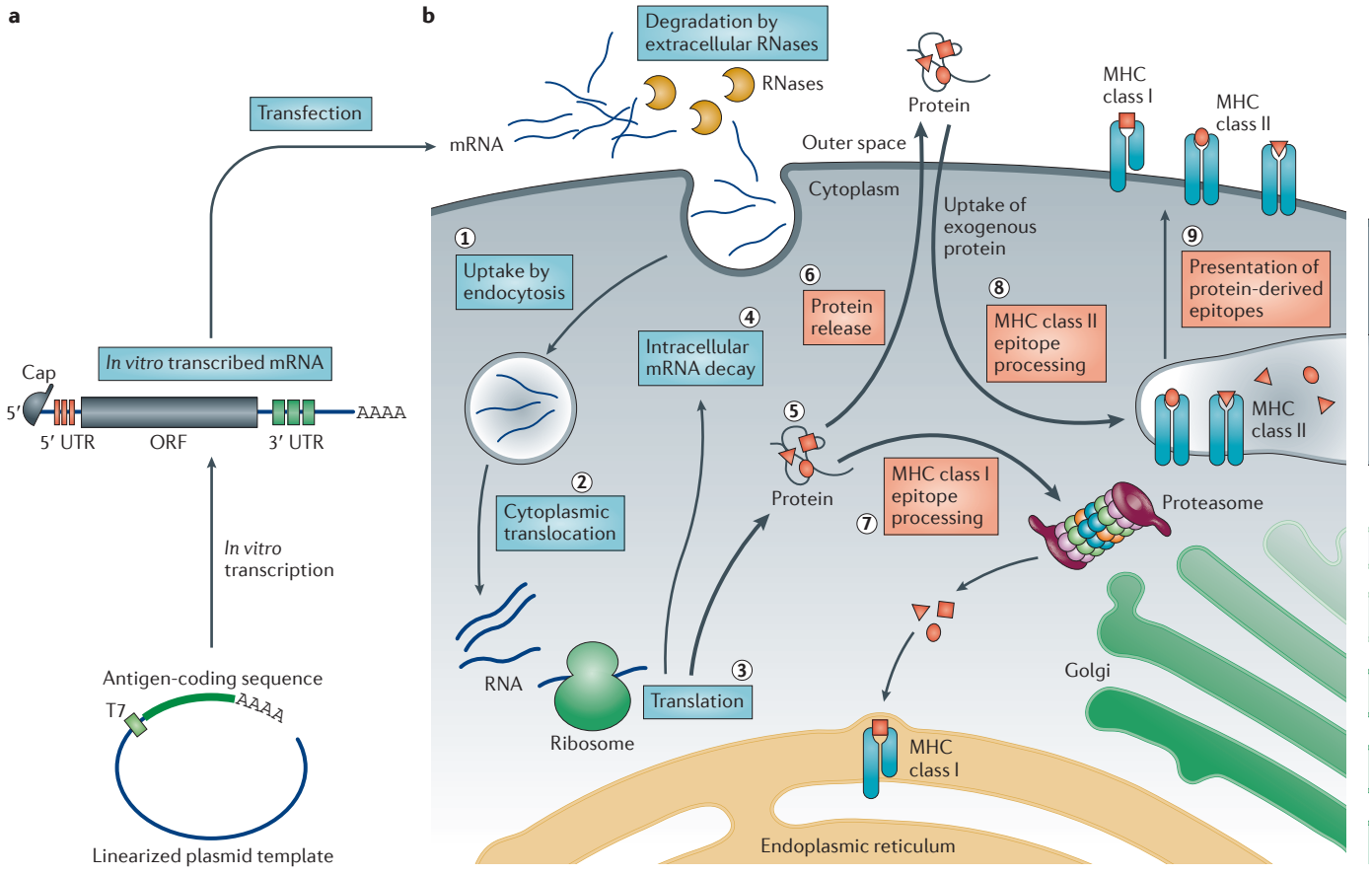

Figure 2 | **Principles of antigen-encoding mRNA pharmacology.** **a** | A linearized DNA plasmid template with the antigen-coding sequence is used for *in vitro* transcription. The *in vitro* transcribed mRNA contains the cap, 5′and 3′ untranslated regions (UTRs), the open reading frame (ORF) and the poly(A) tail, which determine the translational activity and stability of the mRNA molecule after its transfer into cells. **b** | Step 1: a fraction of exogenous mRNA escapes degradation by ubiquitous RNases and is spontaneously endocytosed by cell-specific mechanisms (for example, macropinocytosis in immature dendritic cells) and enters endosomal pathways. Step 2: release mechanisms of mRNA into the cytoplasm are not fully understood. Step 3: translation of mRNA uses the protein synthesis machinery of host cells. The rate-limiting step of mRNA translation is the binding of the eukaryotic translation initiation factor 4E (eIF4E) to the cap structure[222,223]. Binding of the mRNA to ribosomes, the eukaryotic initiation factors eIF4E and eIF4G, and poly(A)-binding protein, results in the formation of circular structures and active translation[224]. Step 4: termination of translation by degradation of mRNAs is catalysed by exonucleases[225,226]. The cap is hydrolysed by the scavenger decapping enzymes DCP1, DCP2 and DCPS[32], followed by digestion of the residual mRNA by 5′–3′ exoribonuclease 1 (XRN1). Degradation may be delayed if the mRNA is silenced and resides in cytoplasmic processing bodies[227]. Alternatively, endonucleolytic cleavage of mRNA in the exosome may occur[228–230]. The catabolism of aberrant mRNA (for example, mRNA with a premature stop codon) is controlled by various other mechanisms[231]. Step 5: the translated protein product undergoes post-translational modification, the nature of which depends on the properties of the host cell. The translated protein can then act in the cell in which it has been generated. Step 6: alternatively, the protein product is secreted and may act via autocrine, paracrine or endocrine mechanisms. Step 7: for immunotherapeutic use of mRNA, the protein product needs to be degraded into antigenic peptide epitopes. These peptide epitopes are loaded onto major histocompatibility complex (MHC) molecules, which ensure surface presentation of these antigens to immune effector cells. Cytoplasmic proteins are proteasomally degraded and routed to the endoplasmic reticulum where they are loaded on MHC class I molecules to be presented to $CD8^+$ cytotoxic T lymphocytes. MHC class I molecules are expressed by almost all cells. Step 8: in antigen-presenting cells, to obtain cognate T cell help for a more potent and sustainable immune response, the protein product needs to be routed to MHC class II loading compartments. This can be accomplished by incorporating routing signal-encoding sequences into the mRNA. Moreover, exogenous antigens that are taken up by dendritic cells can also be processed and loaded onto MHC class I molecules by a mechanism that is known as cross-priming[232]. Step 9: protein-derived epitopes can then be presented on the cell surface by both MHC class I and MHC class II molecules.

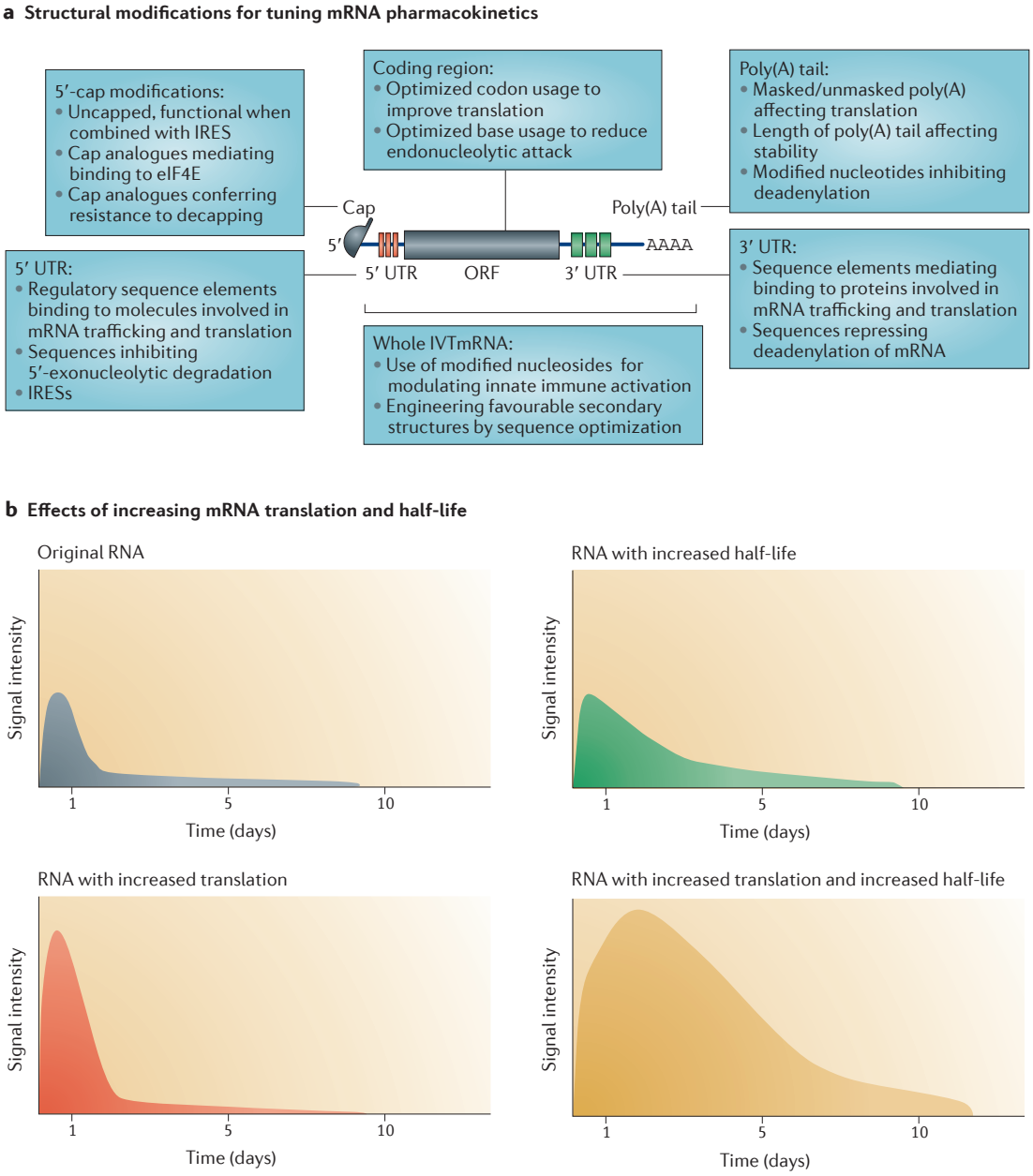

Figure 3 | **Tuning mRNA drug dose pharmacokinetics. a** | Key structural elements of *in vitro* transcribed (IVT) mRNA and strategies for their modifications. **b** | Depending on which elements (for example, modification of caps, untranslated regions (UTRs) or poly(A) tails) are used alone or in combination, the duration and kinetic profile of expression of the protein product can be modulated and fine-tuned. eIF4E, eukaryotic translation initiation factor 4E; IRES, internal ribosome entry site; ORF, open reading frame.

IVT mRNA can be created by incorporating naturally occurring modified nucleosides such as pseudouridine, 2-thiouridine, 5-methyluridine, 5-methylcytidine or N6-methyladenosine into the IVT mRNA; this has been shown to suppress both the intrinsic adjuvant activity of IVT mRNA as well as its inhibitory effects on translation[75,245]. Such modified IVT mRNAs appear to avoid the activation of TLR7 and TLR8 (REF. 75), and some of them, including pseudouridine and 2-thiouridine, were shown to make IVT mRNA undetectable by RIG-I and PKR[76–78]. When dsRNA contaminants (and thus any remaining TLR3 activation) were eliminated through high-performance liquid chromatography purification, the modified mRNA no longer induced any immune-stimulatory effect[63]. Superior translation of pseudouridine-modified mRNA has been attributed to its increased stability and reduced binding to PKR[78,185].

Progress in improving mRNA delivery

Many cell types can spontaneously take up naked mRNA. Naked mRNA internalized by scavenger-receptor-mediated endocytosis accumulates in the lysosome,

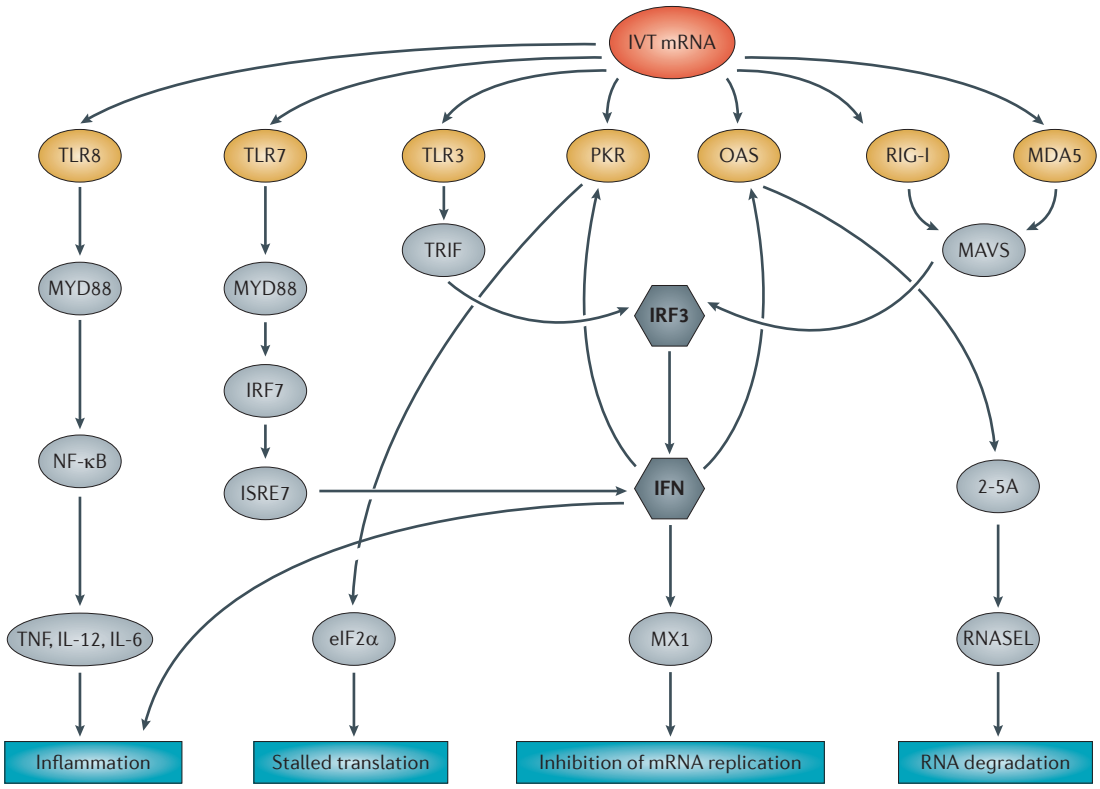

Figure 4 | **Inflammatory responses to synthetic mRNA.** *In vitro* transcribed (IVT) mRNA is recognized by various endosomal innate immune receptors (Toll-like receptor 3 (TLR3), TLR7 and TLR8) and cytoplasmic innate immune receptors (protein kinase RNA-activated (PKR), retinoic acid-inducible gene I protein (RIG-I), melanoma differentiation-associated protein 5 (MDA5) and 2′–5′-oligoadenylate synthase (OAS)). Signalling through these different pathways results in inflammation associated with type 1 interferon (IFN), tumour necrosis factor (TNF), interleukin-6 (IL-6), IL-12 and the activation of cascades of transcriptional programmes. Overall, these create a pro-inflammatory microenvironment poised for inducing specific immune responses. Moreover, downstream effects such as slow-down of translation by eukaryotic translation initiation factor 2α (eIF2α) phosphorylation, enhanced RNA degradation by ribonuclease L (RNASEL) overexpression and inhibition of replication of self-amplifying mRNA are of relevance for the pharmacokinetics and pharmacodynamics of the IVT mRNA. IRF, interferon regulatory factor; ISRE7, interferon-stimulated response element; MAVS, mitochondrial antiviral signalling protein; MDA5, melanoma differentiation-associated protein 5; MYD88, myeloid differentiation primary response protein 88; MX1, myxovirus (influenza) resistance 1; NF-κB, nuclear factor-κB; TRIF, Toll-IL-1 receptor domain-containing adapter protein inducing IFNβ.

from which only small amounts of mRNA leak into the cytoplasm[79]. The mechanisms of mRNA release into the cytoplasm are not well characterized and may differ between cell types. Moreover, mRNA is exchanged via exosomes between cells[80]. In most cells, active uptake of mRNA is inefficient and saturated at low mRNA doses. Immature DCs, which are specialized to constantly engulf extracellular fluid while sampling their environment, are an exception because they take up mRNA by macropinocytosis and thereby accumulate it with high efficiency in a linear non-saturable manner in concentration ranges over several orders of magnitudes[81]. As a consequence, for delivery into most cell types, suitable formulations are required to protect IVT mRNA against extracellular RNase-mediated degradation and facilitate its entry into cells.

There are two challenges associated with the delivery of IVT mRNA: one is to achieve a sufficiently high net level of the encoded protein and the other is to reach a high number of cells.

Most physiological and pathological processes, such as cell migration, cell growth, wound healing, inflammation and angiogenesis, are controlled by paracrine signalling. Accordingly, many intended clinical applications involve signalling molecules such as chemokines, cytokines and growth factors, which are secreted and exert their biological function in a paracrine manner. In these cases, the amount of total protein is crucial for their biological effect. IVT mRNA may be delivered to any cell type that is accessible via the bloodstream or other routes, as long as sufficient doses of the encoded protein are released and reach their target cells. For such applications, transfection with the synthetic mRNA is a suitable approach. For potent protein hormones such as erythropoietin, systemic delivery of mRNA appears to result in adequate plasma levels, as shown by preclinical studies in mice and primates[26]. Liver cells are accessible to many types of polymer and liposomal delivery platforms, so targeting the liver may be one approach to produce high amounts of recombinant protein.

The challenge is different if deficient or defective intracellular proteins are to be substituted through IVT mRNA. Here, the proportion of cells that are restored by IVT mRNA transfer has to be significant enough to have a biological impact. For such applications, the proportion of transfected target cells rather than the absolute protein dose is crucial. If cells are transfected *ex vivo*, transfection efficiencies of up to 80% of cells are achievable for most cell types. *In vivo* delivery of mRNA, by contrast, into a high fraction of defined target cell populations is challenging and depends on the accessibility of target cells.

In vitro *transfection strategies.* *In vitro* transfection strategies to obtain cells transfected with IVT mRNA for adoptive transfer have benefited from the development of formulations to protect mRNA against RNase-mediated degradation and to facilitate its entry into cells. In addition to various positively charged lipids, other transfection agents containing polymers, such as polyethylenimine, cationic polypeptides and dendrimers (reviewed in REF. 82), are commercially available. The number of mRNA transfection kits for *in vitro* and *in vivo* mRNA delivery is rapidly growing. Clinical applications using *ex vivo* IVT mRNA-transfected cells have benefited from these advances.

Electroporation, which was first applied to gene transfer in 1982 (REF. 83), is now established as a favoured method for *in vitro* mRNA transfection of haematopoietic cell types[84]. Immunotherapy with DCs electroporated with IVT or autologous tumour-derived mRNA was shown to be safe in patients with cancer[15,18,85–90]. In Phase IB trials, patients with advanced stage III and IV melanoma generated strong $CD4^+$ and $CD8^+$ immune responses against the antigens encoded by the IVT mRNAs[18,117]. In a Phase I trial, 19 of 20 patients with metastatic prostate cancer also responded to the treatment by developing antigen-specific $CD8^+$ T cells[15]. The development of novel devices for gentle electroporation of large numbers of cells under sterile conditions has enabled the development of a rapid clinical-grade protocol for a broad range of IVT mRNA-based cell therapy applications[91].

In vivo *transfection strategies.* Clinical trials in which naked or protamine-complexed mRNA vaccines are delivered either intradermally[16,17,92] (ClinicalTrials.gov identifiers: NCT01915524 and NCT01817738) or injected directly into lymph nodes (ClinicalTrials.gov identifier: NCT01684241) are ongoing. However, although the delivery of naked IVT mRNA appears to be sufficient to induce potent immune responses, it may not be sufficient for other clinical applications in which a substantially higher amount of protein is required and cell types other than DCs are targeted.

For systemic delivery, nucleic acid-based drugs are administered as nanosized drug formulations and reach organs via either fenestrated or non-fenestrated capillaries. Cells in the bloodstream, cells of the liver and reticuloendothelial cells in the spleen and bone marrow are accessible for intravenously delivered nanosized carriers. Systemic delivery of IVT mRNA to other tissues, however, is hindered by non-fenestrated, non-permeable vascular endothelia, intercellular junctions and dense extracellular fibril networks that limit the accessibility of target cells[93] (FIG. 5). The extensive but moderately successful efforts and difficulties experienced with siRNA and pDNA deliveries are predictive of what to expect for similar efforts in the mRNA field. However, it is important to consider the conceptual differences among these three platforms. In particular, the lessons learnt and improvements made in the delivery of siRNA (for example, clinically validated lipid nanoparticle formulations with excellent safety and efficacy profiles)[94,95] and pDNA need to be considered when deciding whether these improvements can be similarly adopted to advance mRNA delivery or whether novel mRNA-tailored approaches have to be explored.

It is particularly challenging to target cells such as neurons and myocardial or skeletal muscle cells, as they are not directly accessible to nanosized carriers delivered by systemic routes. Therefore, different routes of delivery are being tested for therapeutic applications of IVT mRNA *in vivo*, such as intramuscular, intradermal, intranodal, subcutaneous, intravenous, intratracheal and intrathecal delivery[4,7,9,25,26,96–102]. For drug delivery to the lung, IVT mRNA is either administered as aerosol or by intravenous targeting of the lung vasculature[27,103]. Cells in the central nervous system may be reached via intrathecal injection. For effective cancer targeting, the enhanced permeability and retention effect may be exploited, which is a unique phenomenon of solid tumours related to their anatomical and pathophysiological differences from normal tissues[21,104].

Preclinical and clinical applications

The progress in mRNA technology motivated the exploration of IVT mRNA for a broad range of therapeutic applications in numerous preclinical studies and a smaller number of clinical trials (FIG. 6; TABLE 1). The three major therapeutic areas for which mRNA drugs are currently being explored are immunotherapeutics, protein-replacement therapies and regenerative medicine applications.

Cancer immunotherapy. Cancer immunotherapy is the field in which mRNA-based technologies have the longest history of systematic exploration in integrated preclinical and clinical programmes.

In 1995, it was demonstrated that intramuscular injection of naked RNA encoding carcinoembryonic antigen elicited antigen-specific antibody responses[4]. A year later, it was demonstrated that DCs exposed to mRNA coding for specific antigens or to total mRNA extracted from tumour cells and subcutaneously administered into tumour-bearing mice induced T cell immune responses and inhibited the growth of established tumours[5]. These findings, together with the increasing availability of vaccine targets owing to cloning of novel tumour antigens[105,106], accelerated the development and clinical translation of the mRNA-transfected DC approach[12,107–109]. Since then, numerous clinical trials

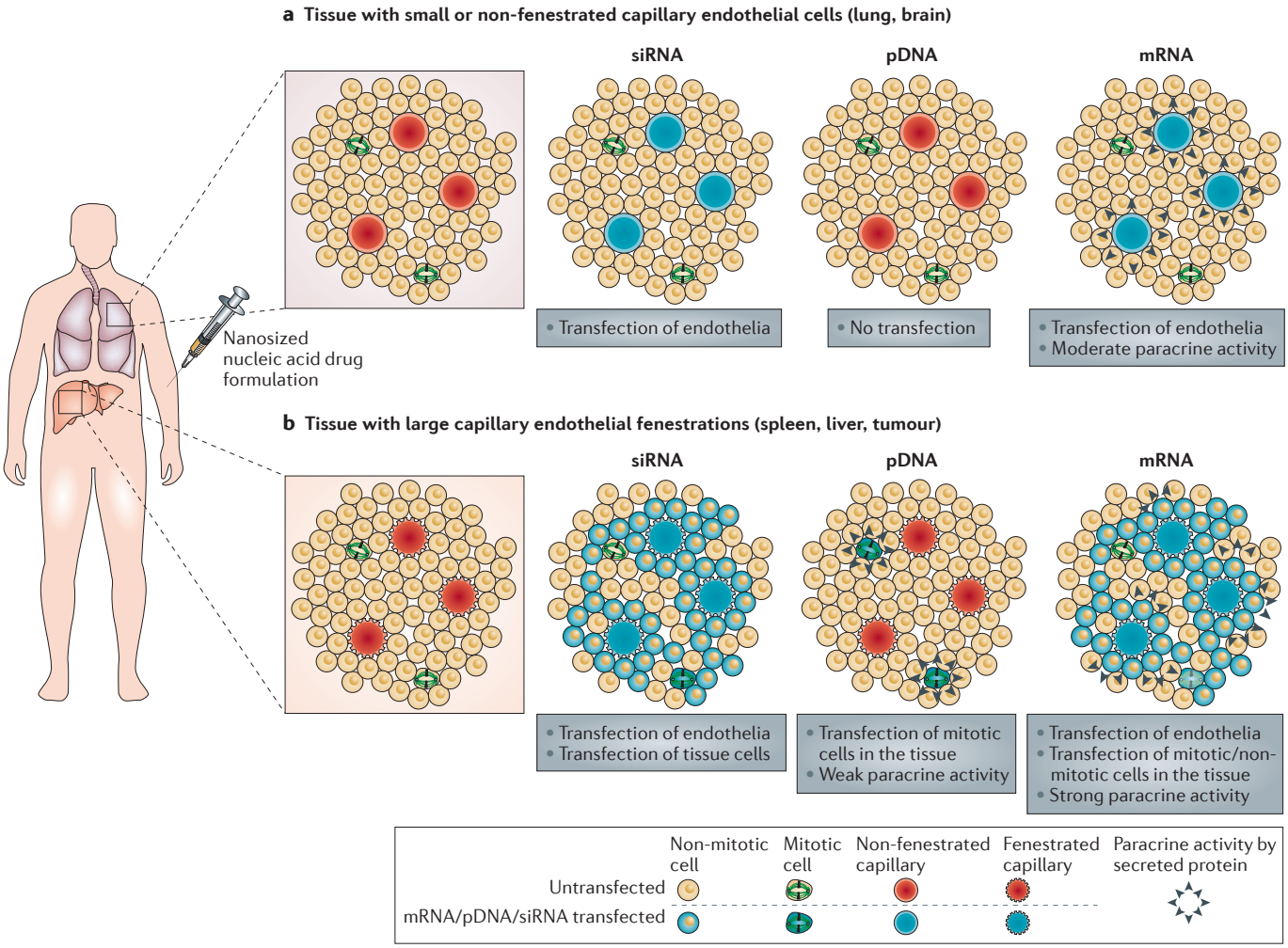

Figure 5 | **Differences in siRNA, pDNA and mRNA technologies in tissues with non-fenestrated or fenestrated capillaries.** All three nucleic acid-based drug modalities are applied as nanosized drug formulations for systemic delivery and reach organs via capillary systems with either non-fenestrated (**a**) or fenestrated (**b**) capillaries. The primary pharmacological effect of small interfering RNA (siRNA), namely the deletion of a defined protein function *in situ*, is restricted to those very cells it has entered. siRNA cannot act in cells that are not directly accessed owing to biological barriers such as non-fenestrated capillaries. In tissues with endothelial fenestration, siRNA may reach a few tissue layers adjacent to capillaries. Plasmid DNA (pDNA) is only incorporated and active in those cells undergoing mitosis at the time of exposure. This impairs its use for tissues with non-fenestrated capillaries and restricts the number of transfectable cells in tissues with endothelial fenestration to those undergoing mitosis at the time of exposure. In contrast to pDNA, mRNA enters and acts in endothelial cells of non-fenestrated tissues, and in fenestrated tissues it reaches both mitotic and non-mitotic cells in cell layers adjacent to the capillaries[233]. Non-target cells, such as vascular endothelial cells transfected with mRNA or pDNA, can express pharmacologically active proteins and, via paracrine secretion, can reach target cells that are located behind the mRNA delivery barriers[234] (obviously siRNA cannot rely on such a function). Proteins produced in transfected cells are able to diffuse after secretion into the target tissue and mediate the intended biological effects via paracrine activity on adjacent cell populations. Such paracrine activity may be of particular value in tissues that have non-fenestrated capillaries.

using vaccines based on *ex vivo* IVT mRNA-transfected DCs were performed in patients with cancer and thus established the feasibility and safety of this approach (reviewed in REFS 110,111).

Treatment protocols with IVT mRNA-transfected DCs were further refined, for example, by optimizing *ex vivo* maturation of DCs or by co-delivering IVT mRNA that encoded immune response modulators such as cytokines and co-stimulators[18,112–116], thus enhancing antitumoural activity in patients[87,117]. Meanwhile, Argos Therapeutics has initiated a Phase III clinical trial using DCs loaded with autologous tumour-derived amplified mRNA in patients with advanced renal cell cancer; data from this study are anticipated in 2015 (ClinicalTrials.gov identifier: NCT01582672).

Cell therapies are costly and complex. Therefore, direct *in vivo* administration of IVT mRNA that encodes the tumour antigen has been revisited by various groups. Different delivery strategies, such as cationic liposomes and bombardment using gene guns, were tested with varying success (reviewed in REF. 118).

For example, clinical trials of intradermal delivery of naked or protamine-complexed, sequence-optimized IVT mRNA demonstrated that expression of the encoded

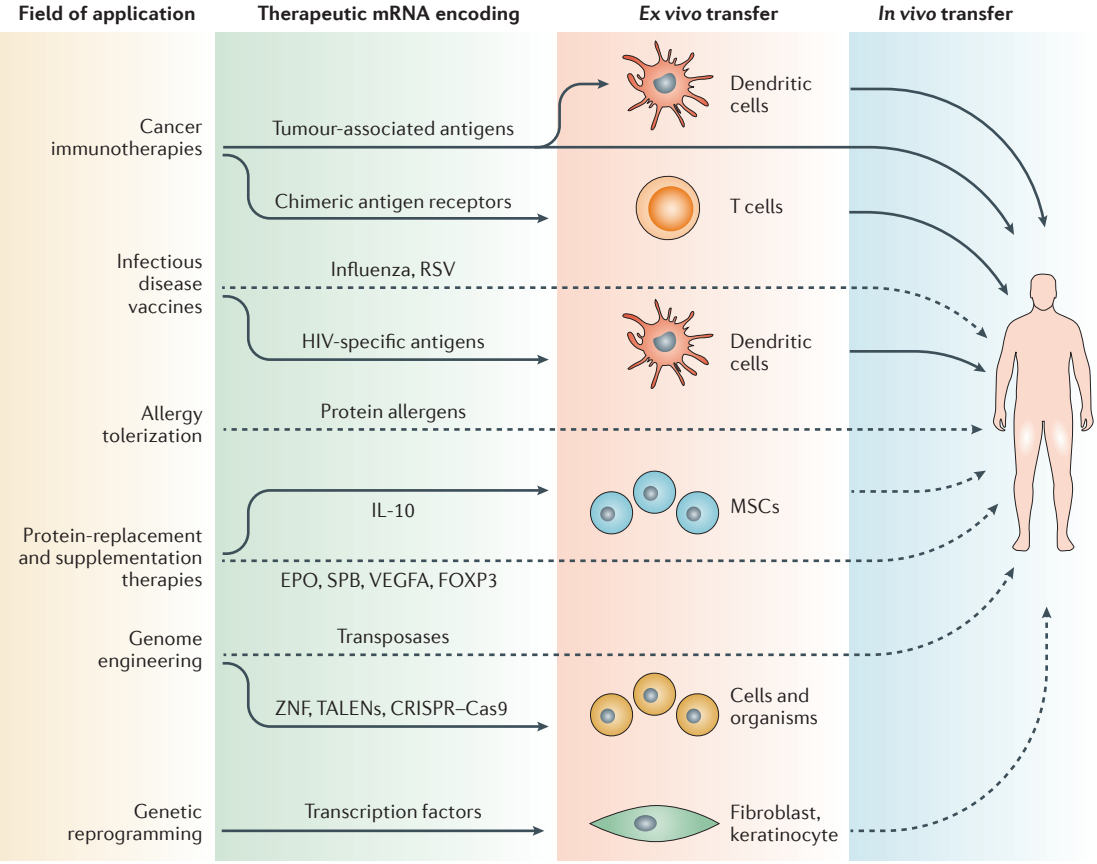

Figure 6 | **Potential therapeutic applications of IVT mRNA.** The therapeutic applications of *in vitro* transcribed (IVT) mRNA are summarized in detail in TABLE 1. The solid arrows pointing in the right hand column denote applications that are in the clinic, whereas stippled arrows refer to preclinical applications. Cas9, CRISPR-associated protein 9; CRISPR, clustered regularly interspaced short palindromic repeat; EPO, erythropoietin; FOXP3, forkhead box P3; IL-10, interleukin-10; MSC, mesenchymal stem cell; RSV, respiratory syncytial virus; SPB, surfactant protein B; TALEN, transcription activator-like effector nuclease; VEGFA, vascular endothelial growth factor A; ZNF, zinc finger nuclease.

antigen by skin cells occurred, and that this led to the induction of T cell and antibody responses[9]. In addition, intradermal application of naked mRNA alone led to the induction of a T helper 2 (T_H2)-type antigen-specific immune response. By contrast, a strong shift towards a T_H1-type response was accomplished by co-delivering adjuvants such as granulocyte–macrophage colony-stimulating factor (GM-CSF)[119] or complexing the IVT mRNA with protamine[120]. Early clinical trials with protamine-complexed IVT mRNA as well as mRNA combined with GM-CSF revealed that intradermal vaccination with these compounds is feasible, safe and can lead to the induction of antigen-specific antibody and T cell immune responses[17,92]. This approach was further optimized, resulting in a pharmaceutical-grade two-component vaccine combining a naked antigen-encoding mRNA plus a protamine-complexed mRNA adjuvant (developed by CureVac). This vaccine showed potent activity in preclinical studies[62] and is currently being tested in ongoing clinical trials in patients with prostate cancer (ClinicalTrials.gov identifiers: NCT00831467 and NCT01817738) and non-small-cell lung cancer (ClinicalTrials.gov identifiers: NCT00923312 and NCT01915524)[121].

In another strategy, the IVT mRNA was optimized for *in situ* transfection of DCs *in vivo*. The objectives of this approach were to improve the translation and stability of the IVT mRNA and to enhance the presentation of the mRNA-encoded antigen on MHC class I and II molecules of murine and human DCs[29,41,122–124]. Direct injection of naked IVT mRNA into lymph nodes was identified as the most effective route to induce potent T cell responses. The IVT mRNA was selectively and effectively taken up by lymph node-resident DCs through macropinocytosis and mediated their maturation via TLR7 signalling. Presentation of the IVT mRNA-encoded antigen and the immunostimulatory intralymphatic milieu induced strong antigen-specific T cell responses of the T_H1 pro-inflammatory type and profound antitumour immunity in animal models[81,97,98,125]. Immune responses of DCs following delivery of IVT mRNA can be further potentiated by either co-administering the DC-activating ligand FMS-related tyrosine kinase 3 (FLT3) as a recombinant protein[98] or co-transfecting DCs with the so-called TriMix, consisting of IVT mRNAs encoding the immunomodulators CD40L, CD70 and truncated, constitutively active TLR4 (REF. 99). First-in-human testing of the

Table 1 | **Therapeutic mRNA applications**

Phase	Method	mRNA encoding	Application
Cancer immunotherapy			
Preclinical	Direct injection of mRNA	CEA[4], NY-ESO[98], gp100 (REF. 8), TRP2, tyrosinase[99], PSA and STEAP[62]	Melanoma[8], prostate cancer[62]
	Injection of DCs transfected *ex vivo*	MUC1 (REF. 10), survivin[235], iLRP[236]	Haematological malignancies[235,236]
	Injection of T cells transfected *ex vivo*	CAR-HER2/neo[237], CAR-CD19 (REFS 131,132,238), CAR-mesothelin[129,132]	Ovarian cancer[237], lymphoma[131], leukaemia[131,132,238], mesothelioma[129]
Clinical	Direct injection of mRNA	Melan-A, tyrosinase, gp100, MAGEA1, MAGEA3 and survivin[16] MUC1, CEA, HER2, telomerase, MAGEA1 and survivin[17]	Melanoma[16], renal cell carcinoma[17]
	Injection of DCs transfected *ex vivo*	PSA[12]; telomerase[15]; CEA[13,14]; TriMix, MAGEA3, MAGEC2, gp100 and tyrosinase[18,89,90,239,241]; gp100 and tyrosinase[117]; WT1 (REF. 87)	Prostate cancer[12,15], pancreatic cancer[13], metastatic malignancies[14], colon cancer[14], melanoma[18,89,90,117,239,241], leukaemia[87]
	Injection of T cells transfected *ex vivo*	CAR containing mesothelin-targeted antibody[240]	Mesothelioma
Infectious disease vaccines			
Preclinical	Direct injection of mRNA	Influenza-associated Ag[3,100,133,140], TB-associated Hsp65 (REF. 242), RSV-Ag[101,140]	Influenza[3,100,133,140], tuberculosis[242], respiratory tract infection[101,140], tick-borne encephalitis[7,140]
Clinical	Injection of DCs transfected *ex vivo*	TriMix, HIV-specific Gag, Vpr, Rev, Tat and Nef mRNA[115,134,135]	HIV
Allergy tolerization			
Preclinical	Direct injection of mRNA	Allergens causing type I allergy e.g. peanut Ara h 2.02, ovalbumin, grass pollen Phl p 5, dust mite Der p 2 (REFS 147,148)	Allergies for peanut, egg white, grass pollen and dust mite[147,148]
Protein replacement			
Preclinical	Direct injection of mRNA	Vasopressin[2], AAT[6], EPO[25,26], SPB[25], FOXP3 (REF. 27), HSV1-TK[21], VEGFA[23], BAX[19]	Diabetes insipidus[2], anaemia[25,26], congenital lung disease[25], asthma[27], myocardial infarction[23], melanoma[19]
	Injection of DCs transfected *ex vivo*	IL-4 (REF. 24)	Autoimmune diabetes[24]
	Injection of monocytes, macrophages and MSCs transfected *ex vivo*	IL-10 (REF. 22), P-selectin glycoprotein ligand 1, SLeX[22,28]	Autoimmune myocarditis[22], inflammation[28]
Genome engineering, gene editing			
Preclinical	Transfection *ex vivo*	Sleeping beauty[177,178,181], piggyBac[181,182] and Tol2 (REFS 179,180) transposases	Genome engineering
		Zinc-finger nucleases[172]	Gene editing, engineered animal models
		TALE nucleases[171,244]	Gene editing, engineered animal models
		RNA-guided Cas9 nuclease[170,173–176]	Gene editing, engineered mice[170,173], rats[175], rabbits[174] and macaques[176]
Genetic reprogramming of cells, tissue engineering			
Preclinical	Transfection *ex vivo*	Transcription factors[157–159,161,246,247], progerin[161]	Generating iPSCs[157–159,161,246,247], model diseases[161]

AAT, α1 antitrypsin; Ag, antigen; Cas9, CRISPR-associated protein 9; CEA, carcinoembryonic antigen; CRISPR, clustered regularly interspaced short palindromic repeat; DC, dendritic cell; EPO, erythropoietin; FOXP3, forkhead box P3; HER2, human epidermal growth factor receptor 2; Hsp65, heat shock protein 65 kDa; HSV1-TK, herpes simplex virus type 1 thymidine kinase; iLRP, immature laminin receptor protein; iPSC, induced pluripotent stem cell; MAGE, melanoma antigen; MSC, mesenchymal stem cell; MUC1, mucin 1; PSA, prostate-specific antigen; RSV, respiratory syncytial virus; SPB, surfactant protein B; STEAP, six-transmembrane epithelial antigen of prostate 1; TALEN, transcription activator-like effector nuclease; TB, tuberculosis; TriMix, mRNAs encoding CD40L, CD70 and constitutively active TLR4; TRP2, tyrosinase-related protein 2; VEGFA, vascular endothelial growth factor A; WT1, Wilms tumour 1.

intranodal injection of naked IVT mRNA encoding cancer antigens (developed by BioNTech) has recently begun in patients with melanoma (ClinicalTrials.gov identifier: NCT01684241).

Personalization of cancer immunotherapy may be facilitated by *in vivo* administered mRNA technology owing to its versatility, robustness and relatively low cost[126–128]. The clinical testing of the first individualized vaccine for treating patients with cancer has just been initiated (ClinicalTrials.gov identifier: NCT02035956). Tumour specimens from each enrolled patient are subjected to next-generation sequencing and individual immunogenic mutations are selected to construct a personalized IVT mRNA vaccine encoding a polypeptide that consists of aligned epitopes with individual mutations. Thus, IVT mRNA may become the first drug that is engineered according to personal genome information.

In addition to active immunization and immunomodulation, IVT mRNA is being investigated as a multipurpose tool for the transient modulation of immune cells. For example, IVT mRNA encoding tumour antigen-specific T cell receptor (TCR) or chimeric antigen receptor (CAR) has been transfected into T cells or natural killer cells *ex vivo* by electroporation. Transfected cells carrying such mRNA-encoded receptors are able to recognize and kill tumour cells that express the target antigen. The transient nature of mRNA reduces the risk of unwanted side effects by the uncontrolled expansion of adoptively transferred immune cells. IVT mRNAs encoding various antigen-specific receptors have been evaluated and their antitumour activity was demonstrated in animal models[129–132]. Recently, cell therapy using T cells electroporated with IVT mRNA encoding CARs entered clinical testing (ClinicalTrials.gov identifier: NCT01897415).

Vaccines against infectious diseases. In 1993, it was demonstrated that liposome-entrapped IVT mRNA encoding an influenza nucleoprotein induced a virus-specific T cell response in mice[3]. Recently, intramuscularly delivered, self-amplifying IVT RNA formulated with synthetic lipid nanoparticles was shown to induce protective antibody responses against respiratory syncytial virus (RSV) and influenza virus in mice[101,133].

Currently, three types of IVT mRNA-based vaccine approaches for infectious diseases have entered pharmaceutical development.

For the treatment of HIV infections, patients under highly active antiretroviral therapy were immunized with DCs transfected with IVT mRNA encoding HIV proteins. Three Phase I/II clinical trials using IVT mRNA encoding combinations of different viral proteins showed that the vaccines are safe and that antigen-specific $CD8^+$ and $CD4^+$ T cell responses can be induced[115,134,135]. In one of these studies, increased HIV inhibition by antigen-specific $CD8^+$ T cells was documented *ex vivo*; however, no antiviral effects were observed in the clinical trial[135].

Two different strategies using IVT mRNA as prophylactic influenza vaccines are currently undergoing preclinical investigation. The first is based on an intradermally injected two-component vaccine containing an mRNA adjuvant and naked IVT mRNA encoding influenza haemagglutinin antigen alone or in combination with neuraminidase-encoding IVT mRNA. Both regimens induced protective immune responses against the corresponding influenza strains in aged and newborn mice, as well as long-lasting protective immunity in ferrets and pigs[100].

The second strategy uses self-amplifying IVT mRNA containing sequences of positive-stranded RNA viruses (BOX 2). Initially, this strategy was developed for a flavivirus model and protective immunity against flavivirus infection was achievable with intradermal delivery of less than 1 ng of IVT genomic mRNA, which corresponded to the attenuated virus[7]. Subsequent studies of RNA-based vaccines for infectious diseases focused on recombinant RNA replicon systems derived from the alphavirus family[136,137] (reviewed in REFS 138,139). RNA replicon vectors in which genes encoding structural proteins were replaced by genes encoding viral antigens have been used to elicit protective antibody responses in animal models of flavivirus, RSV, influenza and parainfluenza virus infection[140–142].

Vaccines to alleviate allergy. Antigen-specific immunotherapy is the only treatment modality for immunoglobulin E (IgE)-mediated type I allergic diseases. Modulating the type of T cell response and inducing IgG antibodies that compete with IgE antibodies for their binding sites on allergens are the primary modes of action of an effective immunotherapy[143].

The molecular identification of the most common hypersensitivity target antigens set the stage for recombinant vaccine approaches. In preclinical models, DNA-based genetic vaccines were shown to antagonize allergy mechanisms by inducing T_H1-type T cell immune responses that suppressed allergen-specific IgE production[144,145]. However, the clinical translation of DNA-based allergy vaccines is hampered by safety considerations. It was shown that the injected DNA persisted for 2 weeks and could spread from the injection site to immune and non-immune tissues throughout the body, thus posing the potential risk of inducing severe anaphylactic side effects[146]. In this respect, IVT mRNA-based approaches may be advantageous because IVT mRNA undergoes rapid degradation in the extracellular space and can be engineered to have a short intracellular half-life. Combined with the strong T_H1 immunostimulatory capacity of mRNA, it may be better suited than DNA for the development as an allergy vaccine. In a murine model of allergic rhinitis, intradermal injection of IVT mRNA before antigen sensitization induced long-lasting allergen-specific T_H1-type immune responses[147,148]. These responses protected the mice against the induction of allergen-specific IgE and inhibited lung inflammation mediated by allergen exposure[147,148].

Protein-replacement therapies. The supplementation of proteins that are not expressed or are not functional, as well as the substitution of foreign proteins that activate or inhibit cellular pathways (for example, therapeutic

Box 2 | **Self-amplifying mRNA**

The RNA genomes of positive-strand RNA viruses, such as picornaviruses, alphaviruses and flaviviruses, have a dual function[245]. They act as an mRNA template for the instant translation of RNA-dependent RNA polymerase (RDRP) and as a genomic template for replication by the respective RDRP. The negative-strand RNA resulting from the initial replication serves as a template for the continued synthesis of the positive-strand viral genome. In the later phase of infection, RNA polymerase switches to a downstream promoter on the same RNA molecule and starts to transcribe capped mRNA encoding structural viral proteins. The first cloning of an infective full-length genome of an animal RNA virus was accomplished in 1981 (REF. 209) and laid the foundation for genetic engineering of self-amplifying viral mRNA replicons. Such vectors harbour the RDRP genes and mimic the characteristic replicative features of positive-strand RNA viruses[136,210–216]. The replicon RNA can be produced easily by *in vitro* transcription from cDNA templates. The structural genes of the RNA virus are replaced by heterologous genes of interest, which are controlled by a subgenomic promoter[137,217–220]. This enables high levels of protein production from minute amounts of transfected recombinant replicon RNA by amplification of the transgene but avoids infective virus production. The intracellular replication is transient and the double-stranded RNA (dsRNA) induces interferon-mediated host-defence mechanisms by triggering pattern recognition receptors. This results in strong antigen-specific immune responses against the inserted target molecules. Thus, self-amplifying mRNA vector systems are ideally suited for vaccine development because they provide high transient transgene expression and inherent adjuvant effects.

antibodies), are the most obvious applications for IVT mRNA-based drugs. Several diseases are being studied in which the malfunctioning proteins are being replaced by the *in vivo* production of the therapeutic intracellular and secreted proteins from transfected IVT mRNA. All such endeavours are at the preclinical stages of development.

The first preclinical application of an IVT mRNA for replacing a deficient, physiologically relevant protein was reported in 1992 and it remained the only such work for almost two decades[2]. The discovery that modified nucleosides can reduce the immune-stimulatory activity of RNA was pivotal in advancing this field of application[75]. Preclinical experiments showed that the use of nucleoside-modified IVT mRNA together with improved mRNA purification protocols eliminates immune activation by mRNA and increases its translation[63], thereby opening the therapeutic application of IVT mRNA for the field of protein replacement.

IVT mRNA containing modified nucleosides (2-thiouridine and 5-methylcytidine) and encoding surfactant protein B (SPB) was tested in a mouse model of congenital lethal lung disease caused by the lack of the SPB protein. Aerosol delivery of *SPB* mRNA into the lung twice a week protected mice from respiratory failure and prolonged their average lifespan[25]. In experiments with mice and macaques, pseudouridine-modified IVT mRNA purified by high-performance liquid chromatography and encoding erythropoietin was administered, and therapeutically relevant levels of erythropoietin were detected[26]. In an asthma disease model, intratracheal delivery of a nucleoside-modified mRNA encoding the regulatory T cell transcription factor forkhead box protein P3 (FOXP3) rebalanced pulmonary T_H cell responses and protected the mice from allergen-induced tissue inflammation and airway hyperresponsiveness[27]. It was also demonstrated that direct intramyocardial injection of IVT mRNA containing pseudouridine and 5-methylcytidine, and encoding vascular endothelial growth factor A (VEGFA), improved heart function and enhanced long-term survival in a mouse model of myocardial infarction[23]. In another study, mouse mesenchymal stem cells were transfected *ex vivo* with pseudouridine-containing IVT mRNA encoding the immunosuppressive cytokine interleukin-10 (IL-10) and the tissue homing factors P-selectin glycoprotein ligand 1 (PSGL1) and Sialyl-Lewis(x) (SLeX). Upon re-injection, these cells homed to inflamed tissues and promoted rapid healing[28].

Despite these achievements, the development of IVT mRNA drugs for the purpose of protein replacement is still associated with technical challenges. For IVT mRNA-based protein delivery, cell type-specific differences in post-translational modification have to be considered. For example, for glycoproteins, the composition of the glycoconjugate is not encoded in the mRNA and depends on the tissue type in which the protein is generated. Not every cell has the capability to glycosylate each protein properly, particularly if highly complex glycosylation is required[149]. Another type of post-translational modification is proteolytic processing. Processing by endoproteases is an integral part of the maturation of various functional polypeptides, including growth factors, cytokines, receptors, neuropeptides, enzymes, hormones and plasma proteins[150]. Other proteins require well-defined cleavage by protein convertases to their biologically active form, which occurs intracellularly in the Golgi apparatus and the secretory granules[151]. Several convertase subtypes have been identified with different specificities and tissue distribution[152]. Cells that are transfected with IVT mRNA need to have the required convertase or endoprotease to process the encoded precursors to functional products.

When secreted proteins are expressed in heterologous tissues, their secretory signal peptides may be poorly recognized and most of the protein may remain within the cells. The relative secretory signal strengths differ[153]; thus, exchanging the natural signal peptides could lead to increased protein secretion. For example, in an animal model of plasmid-mediated expression of erythropoietin in muscles, significantly more erythropoietin was secreted when the natural signal peptide of erythropoietin was replaced with that of tissue plasminogen activator[154]. To achieve maximal effect, IVT mRNA should ideally be transfected into cells that naturally secrete the encoded protein, otherwise signal peptide optimization might be required[155].

It is of considerable interest to utilize IVT mRNA for a broad range of protein-replacement applications, including those that are currently being addressed with recombinant proteins as well as those for which recombinant protein technology cannot be used. Given the diversity of proteins that may be potential candidates for the IVT mRNA approach and are currently being explored as such, it is difficult to predict which of these will be the first to be advanced into clinical development. The developmental hurdles may be lower for proteins with a broad therapeutic window, activity at low doses and for which there is already an established pharmacokinetic and pharmacodynamic understanding in

humans. It may also be easier to develop IVT mRNA-based protein replacement approaches for proteins that are expressed in easily accessible organs such as the liver, as well as for proteins that are fully inactive in the respective patient population and therefore the substituted counterpart can be instantaneously and easily quantified for better control of its bioavailability.

Reprogramming of cell fates. Cell phenotype and function can be modulated *in vitro* using nucleoside-modified IVT mRNA. In 2010, it was demonstrated that IVT mRNA containing pseudouridine and 5-methylcytydine and encoding the Yamanaka stem cell factors[156] could be used as a safe strategy for efficiently reprogramming cells to pluripotency without leaving residual traces of transgenes[157]. The IVT mRNA was not only used to induce pluripotency but also to differentiate induced pluripotent stem cells (iPSCs). The introduction of nucleoside-modified IVT mRNA encoding myoblast determination protein into iPSCs resulted in their direct differentiation into myocyte-like cells.

Since then, several variants of the original approach have been described, which claim more effective induction of either pluripotent stem cells or cell fate conversion[158,159,204] (reviewed in REF. 160). The reprogramming and direct differentiation of cells with IVT mRNA profits from its high *in vitro* transfection efficiency, transient expression with no genomic integration and the ability to transfer complex mixtures. The lack of residual expression of transgenes in IVT mRNA-induced iPSCs not only facilitates their utilization for disease modelling[161] and toxicology testing[162] but also forms the basis for their application in regenerative medicine[163]. Similarly, IVT mRNA transfer may be utilized to generate differentiated cells of clinical value.

Genome editing with IVT mRNA-encoded engineered nucleases. In the past decade, genome editing has emerged as a potential alternative to gene therapy. Custom-designed zinc finger nucleases (ZFNs), transcription activator-like effector nucleases (TALENs) and CRISPR–Cas9 (clustered regularly spaced short palindromic repeat–CRISPR-associated protein 9) provide powerful tools for site-specific modification of genomes[164–166]. These approaches, however, have the risk of nonspecific editing. A prolonged presence of editing enzymes translated from DNA-based vectors resulted in off-target effects[167]. As the nucleases are only required for a short duration, their transient expression from IVT mRNA would minimize this nonspecific effect. IVT mRNAs encoding ZFNs, TALENs and Cas9 have been applied successfully to edit genomes by disrupting or integrating sequences *ex vivo* in embryonic cells from different species (for example, mice, rats and rabbits) and *in vivo* in rodents[168–175]. Most recently, cynomolgus monkeys with site-specific gene modifications were generated by injecting IVT mRNA encoding Cas9 at the one-cell embryonic stage, thus opening the opportunity to create primate models of human diseases[176].

Transposase-encoding IVT mRNA has also been utilized for transposon-mediated stable gene transfer both *in vitro* and *in vivo*. For example, the expression of transposases of the Sleeping Beauty, piggyBac or Tol2 transposon systems by injection of their mRNAs resulted in stable genomic transposition in mammalian cells[177] and *in vivo* in rodents[178–181].

The use of IVT mRNA rather than plasmids for the expression of the transposases increased the survival rate of the injected cells because injection in the cytoplasm is more gentle than pronuclear injection[179]. By narrowing the duration of peak translation, the biosafety of the approach is increased because the probability of remobilization of the transgenes is reduced[182].

Clinical translation of IVT mRNA

By relying on the patient's body to make the desired protein, IVT mRNA drugs provide an approach in which the robust and tunable production of a therapeutic protein is possible, bypassing the need for costly manufacturing of proteins in fermentation tanks. Associated with these unique features is the vision that utilizing IVT mRNA will help address challenges in newly emerging technologies such as targeted genome engineering, generation and reprograming of stem cells as well as production of on-demand personalized vaccines.

To enable the full potential of mRNA as a therapeutic modality to be realized, regulatory (BOX 3) and scientific issues concerning clinical and product development require diligent consideration.

So far, clinical experience of IVT mRNA drugs is limited to immunotherapeutic applications. Of the clinical programmes in the field of vaccine development with IVT mRNA alone or IVT mRNA-transfected DCs, few are advanced enough to provide a sufficiently broad knowledge base for other applications. For each application, the well-established systematic exploration of the variables of treatment protocols, such as dosing, treatment schedule and route of administration, have to be delineated to identify the appropriate regimen.

Common objectives of early clinical trials are to explore pharmacokinetic characteristics of the drug and to conduct dose finding. However, the pharmacology of mRNA drugs is complex because the IVT mRNA is not the final pharmacologically active agent. So far, it has not been fully investigated whether the bioavailability of the protein it encodes can be robustly and precisely controlled under clinical conditions, which are particularly challenging because of high inter- and intra-individual variability. Accompanying medication also requires consideration, particularly when IVT mRNA therapies are combined with other drugs that affect mRNA metabolism and translation, such as certain antibiotics and anticancer drugs.

Other key challenges related to the complex pharmacology of mRNA, and to its delivery in particular, concern applications in which precise targeting of a particular cell type and organ is required.

Safety considerations

Clinical experience with IVT mRNA for immunotherapy has demonstrated an excellent tolerability and safety profile and showed that mRNA drugs have no platform-inherent major risks.

Box 3 | **Regulatory framework for mRNA-based therapeutics**

Existing standard guidance for new molecular entities needs to be adapted to mRNA-based drugs. So far, no competent authority has officially stated its general position on how mRNA drugs will be classified, nor have any directions and guidelines been published. As the number of precedents is limited and the diversity of mRNA-based applications is broad, one cannot predict for each individual investigational mRNA drug how the United States, the European Union and European national competent authorities may view *in vitro* transcribed (IVT) mRNA from a regulatory perspective.

One would expect the classification of an mRNA drug to be a biologic, a gene therapy or a somatic cell therapy.

Most of the clinical trials using IVT mRNA have been initiated by European teams and have been performed in Europe. Thus, there are not many real-life examples of how mRNA-based therapeutics would be classified by the US Food and Drug Administration (FDA).

The FDA definition of gene therapy is as follows: "… modification of the genetic material of living cells. Cells may be modified *ex vivo* for subsequent administration to humans, or may be altered *in vivo* by gene therapy given directly to the subject. When the genetic manipulation is performed *ex vivo* on cells which are then administered to the patient, this is also a form of somatic cell therapy … Recombinant DNA materials used to transfer genetic material for such therapy are considered components of gene therapy." As RNA does not result in "modification of the genetic material of living cells", one would anticipate that its administration will not be classified as a gene therapy in the United States.

In the European Union, mRNA-based therapies are most likely to fall under the European Medicines Agency (EMA)'s regulation for advanced therapy medicinal products (Directive 2009/120/EC), which covers gene therapies, engineered somatic cells and tissue engineered products.

This regulation defines a gene therapy medicinal product as follows: "Gene therapy medicinal product means a biological medicinal product which has the following characteristics: "(a) it contains an active substance which contains or consists of a recombinant nucleic acid used in or administered to human beings with a view to regulating, repairing, replacing, adding or deleting a genetic sequence; (b) its therapeutic, prophylactic or diagnostic effect relates directly to the recombinant nucleic acid sequence it contains, or to the product of genetic expression of this sequence. Gene therapy medicinal products shall not include vaccines against infectious diseases."

In vivo administered mRNA drug products are presumably viewed as an added recombinant nucleic acid complying with the EU definition of a gene therapy product. An interesting exception is dendritic cells transfected *ex vivo* with IVT mRNA before administration to patients. The EMA's Committee for Advanced Therapies (CAT) did not classify such a product as gene therapy because mRNA was considered to be degraded within the cells at the time of their adoptive transfer to the patient. The CAT classified this cell product as a somatic cell therapy product. Furthermore, mRNA drugs, which are used to vaccinate against infectious disease, are unlikely to be classified as gene therapy. According to Part IV of Annex I to Directive 2001/83/EC, gene therapy medicinal products do not include vaccines against infectious diseases. Moreover, the legal definition of gene therapy only relates to biological medicinal products. Consequently, products that have been manufactured by chemical means do not fulfil this definition.

The guidelines established for gene therapies may provide a valuable roadmap for setting up the regulatory framework for RNA vaccines. However, in contrast to DNA and viral vectors, mRNA does not contain promoter elements and does not integrate into the genome, and disruption of genes does not occur unless mRNAs encoding DNA-modifying enzymes are delivered. mRNA expression is dose-dependent and transient. Thus, there is no scientifically sound rationale to test for genome integration, germline transmission, genotoxicity or carcinogenicity of IMPs (investigational medicinal products), or carry out long-term observation of patients in clinical studies. Future guidance should take these features into consideration, as they clearly distinguish mRNA products from (other) gene therapies with respect to the anticipated risks.

However, for most of the other applications of mRNA-based therapeutics, including mRNA-based protein-replacement therapies, there is no clinical experience yet, leaving developers and regulators uncertain about the nature and frequency of safety problems that might occur.

Various safety risks associated with other drug classes do not apply to mRNA-based therapeutics (BOX 3). IVT mRNA manufacturing is relatively simple and the manufacturing process as well as product quality is uniform and easy to control (BOX 4). With no cellular and animal components involved, process-related risks are considerably lower for IVT mRNA as compared to recombinant proteins.

Nevertheless, various risk factors have to be considered.

IVT mRNA-mediated activation of immune mechanisms. The immune-activating property of IVT mRNA is an important feature to be considered from a safety perspective, particularly for systemically administered IVT mRNA. The underlying mechanisms are being extensively investigated. As discussed above, several signalling receptors of the innate immune system, including TLR3, TLR7 and TLR8, have been shown to mediate mRNA-induced immune activation and cytokine secretion[65–67,183,184]. In preclinical studies, interferon-α, IL-6, tumour necrosis factor-α and interferon-γ-induced protein 10 (IP-10; also known as CXCL10) were determined as key cytokines that are upregulated by systemic IVT mRNA delivery. The immune activation and profiles of secreted cytokines depend on the formulation of the IVT mRNA, including the particle size[64].

Safety studies in animals are desirable but may not be fully conclusive owing to species-specific differences. To complement animal studies, IVT mRNA formulations should be tested *in vitro* for their pharmacodynamic effects on human leukocytes. As immune activation is

Box 4 | **GMP of mRNA-based therapeutics**

The production of mRNA by *in vitro* transcription is a well-defined procedure. The starting material is usually a plasmid DNA vector comprising a promoter for bacteriophage RNA polymerase, the open reading frame encoding the protein of interest, sequences corresponding to the untranslated regions (UTRs) and a poly(A) tail. The plasmid is linearized with a restriction enzyme that cleaves the DNA downstream from sequences encoding the poly(A) tail. Following purification of the linearized plasmid, an RNA polymerase *in vitro* transcribes the message in the presence of the four ribonucleoside triphosphates and a chemically synthesized cap analogue. All components can be obtained from commercial vendors as certified, quality-controlled, animal-component-free material. Residual plasmid DNA is removed by DNase digestion and the *in vitro* transcribed (IVT) RNA is purified using bead-based methods, precipitation or chromatography. After formulation, sterile filtration and vial filling, the IVT mRNA drug is ready for use.

The manufacturing process has to be conducted with strictly RNase-free materials requiring extensive testing of RNase contamination of all components and equipment used in the process.

As IVT mRNA is produced in cell-free systems, process development and manufacturing of clinical-grade material can be easily standardized. Once established, the same technology can be used with relatively minor adaptations for the production of almost any individual IVT mRNA sequence of similar size. Transfer of the process in a good manufacturing practice (GMP)-qualified environment and up-scaling are associated with extensive process optimization and protocol validation. Once a high degree of standardization is accomplished, batch-to-batch reproducibility is easily maintained.

On top of various in-process analytics, GMP release of the IVT mRNA drug substance and of the formulated drug products requires extensive testing and characterization. Typical analyses address identity, appearance, content, integrity, residual DNA, endotoxin contamination and sterility. Moreover, the ability of the IVT mRNA to be translated into a protein product has to be verified by a potency test. Typically, a subset of these assays is used for stability testing. Characterization of a product with respect to its quality attributes early in product development will assist in future comparability studies necessitated by process and manufacturing changes, thereby enabling faster product development. Evaluation of these attributes depends on a thorough understanding of the biology of the investigational product.

Stability is not an issue, as RNA is stable in RNase-free environments and can be kept at room temperature for at least 2 years without significant degradation.

Once IVT mRNA GMP production is established, the availability of highly pure, synthetic mRNAs to supply a standard Phase I/II clinical trial including manufacturing and release-relevant analytics within a few months can be accomplished cost-effectively. Depending on the dose and the number of patients, relatively small manufacturing plants may provide the drug material needed for early clinical testing. In recent clinical trials, an initial dose of 600 μg mRNA[16] or a total dose of 800 μg mRNA per patient[17] was administered to achieve efficient antigen-specific immune responses. However, it has to be considered that precise amounts depend on the mRNA backbone used, on the specific type of application and whether the IVT mRNA is administered *ex vivo* or *in vivo*. It has to be expected that in protein-replacement settings that require long-term or chronic treatment, total dosing per patient may be in the milligram scale. The capacity of GMP mRNA manufacturing is currently several grams per batch.

A further impact on ease and costs of manufacturing might result from progress in the field of chemical synthesis of functional mRNAs. So far, however, chemical synthesis of RNAs is limited to very short reading frames (less than 150 nucleotides corresponding to a maximum of 50 amino acids).

dose-dependent, conservative dose-escalation protocols with low starting doses and close monitoring of patients are advised. Future studies will show whether nucleoside-modified IVT mRNA will avoid the activation of human TLRs in the clinical setting.

For applications of IVT mRNA as vaccines, transient immune activation is desirable. However, it is important to dissect the exact nature of the immune-modifying effect of each individual mRNA drug as part of the clinical research programme and to assess whether it is indeed desired. For example, induction of interferon-α, which slows down the translation machinery, should be avoided[186].

The current data do not indicate that there is any induction of immunogenicity against IVT mRNA itself. However, mounting evidence suggests that patients with systemic lupus erythematosus and other autoimmune diseases can develop anti-self RNA autoantibodies that have a role in the induction and progression of autoimmunity[187]. Thus, under certain circumstances, such as long-term repetitive systemic application of mRNAs, anti-RNA antibodies may potentially form and mediate immune pathology. One might consider screening mRNA sequences to avoid conformations that are prone to inducing mRNA-specific antibodies[188]. Clinical monitoring of autoimmune phenomena and laboratory tests for antinuclear antibodies are therefore advised.

Immunogenicity of the IVT mRNA-encoded proteins. For recombinant proteins it is well established that unintended immunogenicity may result in adverse events such as anaphylaxis, cytokine release syndrome and infusion reactions. Moreover, immune responses may neutralize the biological activity of the protein drug as well as the endogenous protein counterpart[189–191]. A prominent example is the induction of neutralizing antibodies to therapeutic erythropoietin that caused red cell aplasia in monkeys and humans by crossreacting with endogenous erythropoietin[192–194].

In principle, antiprotein antibodies can develop against proteins expressed from any IVT mRNA, in particular if repeat administration regimens are pursued.

However, in contrast to recombinant protein drugs, *in vivo*-generated protein therapeutics are autologous, produced in human cells and are likely to undergo the correct post-translational modifications and folding. Moreover, risk factors for immunogenicity related to the protein manufacturing process, such as protein aggregation or impurities derived from cells or medium in which the protein was produced, do not occur with IVT mRNA.

Since most of the immune-mediated adverse effects against a therapeutic protein product are mediated by humoral mechanisms, circulating antibodies to the therapeutic protein product have been the main criterion for defining an immune response. These should be screened for in clinical studies of IVT mRNA-mediated protein-replacement approaches.

It is also conceivable that the expression of a foreign protein together with the pro-inflammatory effects mediated by the mRNA backbone may result in immunopathology on the tissue level. For immunotherapeutic approaches, this may be of minor relevance as antigen-presenting cells are the target cells of mRNA delivery and these are short-lived once they have transitioned into the mature state. If, however, other organs such as the liver, kidney, lungs or myocardium are targeted, this risk needs to be addressed. Various applications that are being pursued use the liver as the target organ, as it has been shown (at least for various siRNA delivery platforms)

that nucleic-acid-based drugs are routed to the liver by default, and therefore liver targeting can be accomplished without further optimizing delivery[195]. As hepatic toxicity may be life threatening, particular caution is warranted and liver enzymes such as transaminases need to be measured. However, given the unique immunological properties of this organ, it may even be de-risking to use the liver as a depot organ for protein expression of the first-generation of mRNA-based therapeutics for protein replacement, as its capacity to induce antigen-specific tolerance may counteract immunogenecity[196].

Risks associated with non-natural nucleotides. The highly abundant extracellular RNases have evolved as a powerful control mechanism of RNA levels in the extracellular space[197]. No significant risks are anticipated to be associated with the absorption, distribution, metabolism and excretion profile of IVT mRNA drugs that are composed of natural nucleotides because the human body breaks down much higher amounts of natural mRNA every day. However, this may not apply to investigational mRNA drugs containing unnatural modified nucleotides. Mechanisms of catabolism and excretion and potential unwanted cross-effects on other toxicity-relevant pathways of unnatural nucleotides in a polynucleotide structure or their metabolites and potential risks associated with these are still unknown.

This caveat is supported by observations from unnatural nucleoside analogues used as antiviral and anticancer drugs that interfere with viral and tumour cell replication. Many of these nucleoside analogues demonstrated unexpected mitochondrial toxicities[198,199] that are associated with functions of nucleoside transporters[200]. Nucleoside reverse transcriptase inhibitors used for treating HIV-infected patients caused severe clinical toxicities (for example, myopathy, polyneuropathy, lactic acidosis, liver steatosis, pancreatitis and lipodystrophy) "including fatal complications due to mitochondrial dysfunction[199]. These adverse effects of unnatural modified nucleosides were caused by the inhibition of DNA polymerase γ, an enzyme solely responsible for mitochondrial DNA replication, blocking *de novo* mitochondrial DNA synthesis[201]. These risks were not identified in preclinical studies performed in mice and rats owing to interspecies differences in the subcellular localization of nucleoside transporter 1 (REFS 202,203).

In clinical trial design, the potential toxicity of nucleoside analogues should be addressed diligently by conservative dose-escalation regimens and close assessment of risk organs. Safety monitoring has to consider that adverse effects may only occur after prolonged treatment with nucleoside analogues.

Safety considerations regarding the encoded protein. In addition to the risks described above, 'content'-specific risks determined by the nature of the encoded protein and by the type of application have to be considered. The number of genes and modes of action executed by these genes is highly diverse. Therefore, no general exhaustive risk assessment can be provided; instead, risks have to be evaluated with due diligence on a case-by-case basis.

Depending on the specific application, it may be an important safety measure to ensure that *in vivo* transferred RNA only enters the cell type it is intended for.

Another caveat concerns proteins that are challenging with regard to dosing, such as proteins with a narrow therapeutic window or with a steep dose–response relationship. The key challenge for such protein targets is to control the robustness and fidelity of their bioavailability and address potential inter-individual variations by closely monitored, individually adjusted dosing schedules.

Conclusions and perspectives

As outlined in this Review, cancer immunotherapy is the only field in which clinical testing and industrialization of the manufacturing of mRNA drugs is at an advanced stage. For vaccination against infectious diseases, IVT mRNA is in early clinical testing, whereas in all other medical applications, such as protein replacement, it is at the preclinical stage.

The instability of mRNA (originally perceived as the primary hurdle in RNA drug development) has been efficiently addressed. Intracellular stability can be achieved and the half-life of mRNA translational activity tuned from minutes to days by structural elements that modulate mRNA translation and mRNA metabolism, and that are now used in the design of IVT mRNAs. Extracellular stability is being addressed through the development of formulations — for example, protamine and nanoparticle carriers. Progress in de-immunization techniques of IVT mRNA has facilitated the control of the inflammatory activity of mRNA in animal models. Moreover, for the biopharmaceutical development of mRNA drugs, the initial foundations regarding patent and intellectual property issues have been laid (BOX 5). IVT mRNA can be manufactured at relatively low costs and within a few hours, and the production and purification processes are robust, enabling the generation of mRNA ranging from a few hundred to more than 10,000 nucleotides in length. The robustness and ease of the production process facilitates the implementation of high-throughput approaches for drug discovery and

Box 5 | **Patents and the intellectual property landscape**

The number of patent applications in the core field of mRNA-based therapeutics technology has been growing considerably in the past 10 years. The main mRNA-relevant intellectual property categories are "composition of matter" patents and applications related to the mRNA itself, applications covering formulations for mRNA delivery and patents claiming mRNA for certain applications. In contrast to the small interfering RNA (siRNA) field in which therapeutic use of the drug format itself is covered by fundamental patents[221], there are no basic patents limiting the broad industrial application of *in vitro* transcribed (IVT) mRNA for therapy. The current patent landscape is characterized by low fragmentation. The highest currently visible patenting activity stems from the small group of biotechnology companies specialized in mRNA-based therapeutics. These patent portfolios document the anticipated systematic and strategic approach to develop each of these company's own intellectual property estate as a basis for each company's business model. An increasing number of patent applications are from academic groups featuring findings in preclinical studies and from industry for the use of IVT mRNA to replace defined disease targets.

As the field is young, many patent applications have not yet been granted.

iterative drug optimization. Once the clinical mRNA drug candidate is identified, process optimization and clinical-grade good manufacturing practice (GMP) production can be carried out within several months. In our experience, production costs for GMP batches for clinical studies are on average five- to tenfold lower for IVT mRNA than for recombinant protein therapeutics produced in eukaryotic cells.

The major challenges for which satisfactory solutions are still pending, in particular for non-immunotherapy-related *in vivo* applications, are targeting to the desired organ or cell type *in vivo* and the complex pharmacology of IVT mRNA. This means that the question of consistent dosing across tissues and patients can become a significant roadblock for the clinical development of *in vivo* administered IVT mRNA. As discussed above, it is still unclear how to accurately deliver the IVT mRNA to the target cell type and how to achieve the right therapeutic dose level. Moreover, it has not been thoroughly investigated whether mRNA dose–protein-effect relationships vary inter-individually or even intra-individually when comparing independent routes of administration.

In this respect, the use of cells that are transfected *ex vivo* with IVT mRNA, particularly for immunotherapeutic approaches, can be viewed as the 'low-hanging fruit'. For immunotherapy, relatively small amounts of IVT mRNA encoding the corresponding antigen are sufficient to obtain robust efficacy signals, which is further supported by the intrinsic adjuvant activity of mRNA. Moreover, professional antigen-presenting cells, which are the targets for mRNA-based vaccine delivery, are constitutively equipped with a specialized mechanism for mRNA uptake. Beyond applications for cancer immunotherapy, mRNA-based vaccine development may also create opportunities to manage newly emerging pandemics. Recent progress in synthetic DNA technology has enabled the rapid and accurate synthesis of genes encoding any potential target antigen[205]. The large-scale manufacturing of rapidly assembled synthetic genes that are suitable DNA templates for *in vitro* transcription could accelerate the overall process of mRNA-based vaccine production.

When extending IVT mRNA therapeutics into applications such as protein-replacement therapies, delivery, dosability and robustness of dosing, as well as the tissue selectivity of the *in vivo* administered mRNA drug need to be carefully addressed. Moreover, immune stimulation is unwanted. As a consequence, the hurdle for advancing non-immunotherapy applications is higher and its acceleration through spill-over effects from the immunotherapy field is limited. For many protein-replacement therapy applications, IVT mRNA delivery may be successfully realized by optimizing existing delivery tools. The most reasonable approach would be to select diseases in which the target tissues are easily accessible and the encoded proteins are active even at low doses and have broad therapeutic windows.

For the development of mRNA as a biopharmaceutical, the mRNA technology platform has to become an industry-compatible process. For IVT mRNA that is used *ex vivo* in cell therapeutic applications, this will be limited by the challenging industrialization hurdles faced by cell therapy[206]. IVT mRNA for *in vivo* use, by contrast, follows 'platform'-specific patterns in terms of general pharmaceutical properties, and its manufacturing is straightforward, cost-effective and does not carry specific challenges. Progress will also depend on how process automation will evolve and whether specialized companies can deliver standard or customized equipment for that purpose. For product-based companies seeking to outsource manufacturing, the low number of service providers can impede project planning and timelines. The development of a diversified landscape of a service and supply industry around the core mRNA drug product has begun and will facilitate industrialization.

Under the shadow of disappointments and failures in the neighbouring fields of gene therapy and siRNA, the mRNA field has been advanced with due caution. Cardinal faults such as premature adoption of new technology, clinical trials with unnecessary safety risks, as well as unrealistic expectations of industry leaders and investors, have been avoided. Ongoing clinical testing programmes have been initiated based on thorough preclinical exploration and understanding of underlying mechanisms. It is advisable that this prudence is further maintained.

1. Wolff, J. A. *et al.* Direct gene transfer into mouse muscle *in vivo*. *Science* **247**, 1465–1468 (1990).
2. Jirikowski, G. F. *et al.* Reversal of diabetes insipidus in Brattleboro rats: intrahypothalamic injection of vasopressin mRNA. *Science* **255**, 996–998 (1992).
3. Martinon, F. *et al.* Induction of virus-specific cytotoxic T lymphocytes *in vivo* by liposome-entrapped mRNA. *Eur. J. Immunol.* **23**, 1719–1722 (1993).
4. Conry, R. M. *et al.* Characterization of a messenger RNA polynucleotide vaccine vector. *Cancer Res.* **55**, 1397–1400 (1995).
5. Boczkowski, D. *et al.* Dendritic cells pulsed with RNA are potent antigen-presenting cells *in vitro* and *in vivo*. *J. Exp. Med.* **184**, 465–472 (1996).
6. Qiu, P. *et al.* Gene gun delivery of mRNA *in situ* results in efficient transgene expression and genetic immunization. *Gene Ther.* **3**, 262–268 (1996).
7. Mandl, C. W. *et al. In vitro*-synthesized infectious RNA as an attenuated live vaccine in a flavivirus model. *Nature Med.* **4**, 1438–1440 (1998).
8. Zhou, W. Z. *et al.* RNA melanoma vaccine: induction of antitumor immunity by human glycoprotein 100 mRNA immunization. *Hum. Gene Ther.* **10**, 2719–2724 (1999).
9. Hoerr, I. *et al. In vivo* application of RNA leads to induction of specific cytotoxic T lymphocytes and antibodies. *Eur. J. Immunol.* **30**, 1–7 (2000).
10. Koido, S. *et al.* Induction of antitumor immunity by vaccination of dendritic cells transfected with *MUC1* RNA. *J. Immunol.* **165**, 5713–5719 (2000).
11. Schirmacher, V. *et al.* Intra-pinna anti-tumor vaccination with self-replicating infectious RNA or with DNA encoding a model tumor antigen and a cytokine. *Gene Ther.* **7**, 1137–1147 (2000).
12. Heiser, A. *et al.* Autologous dendritic cells transfected with prostate-specific antigen RNA stimulate CTL responses against metastatic prostate tumors. *J. Clin. Invest.* **109**, 409–417 (2002).
13. Morse, M. A. *et al.* The feasibility and safety of immunotherapy with dendritic cells loaded with CEA mRNA following neoadjuvant chemoradiotherapy and resection of pancreatic cancer. *Int. J. Gastrointest Cancer* **32**, 1–6 (2002).
14. Morse, M. A. *et al.* Immunotherapy with autologous, human dendritic cells transfected with carcinoembryonic antigen mRNA. *Cancer Invest.* **21**, 341–349 (2003).
15. Su, Z. *et al.* Telomerase mRNA-transfected dendritic cells stimulate antigen-specific $CD8^+$ and $CD4^+$ T cell responses in patients with metastatic prostate cancer. *J. Immunol.* **174**, 3798–3807 (2005).
16. Weide, B. *et al.* Direct injection of protamine-protected mRNA: results of a phase 1/2 vaccination trial in metastatic melanoma patients. *J. Immunother.* **32**, 498–507 (2009).
17. Rittig, S. M. *et al.* Intradermal vaccinations with RNA coding for TAA generate $CD8^+$ and $CD4^+$ immune responses and induce clinical benefit in vaccinated patients. *Mol. Ther.* **19**, 990–999 (2011).
18. Wilgenhof, S. *et al.* A phase IB study on intravenous synthetic mRNA electroporated dendritic cell immunotherapy in pretreated advanced melanoma patients. *Ann. Oncol.* **24**, 2686–2693 (2013).
19. Okumura, K. *et al. Bax* mRNA therapy using cationic liposomes for human malignant melanoma. *J. Gene Med.* **10**, 910–917 (2008).

20. Mitchell, D. A. *et al.* Selective modification of antigen-specific T cells by RNA electroporation. *Hum. Gene Ther.* **19**, 511–521 (2008).
21. Wang, Y. *et al.* Systemic delivery of modified mRNA encoding herpes simplex virus 1 thymidine kinase for targeted cancer gene therapy. *Mol. Ther.* **21**, 358–367 (2013).
22. Zimmermann, O. *et al.* Successful use of mRNA-nucleofection for overexpression of interleukin-10 in murine monocytes/macrophages for anti-inflammatory therapy in a murine model of autoimmune myocarditis. *J. Am. Heart Assoc.* **1**, e003293 (2012).
23. Zangi, L. *et al.* Modified mRNA directs the fate of heart progenitor cells and induces vascular regeneration after myocardial infarction. *Nature Biotech.* **31**, 898–907 (2013).
24. Creusot, R. J. *et al.* A short pulse of IL-4 delivered by DCs electroporated with modified mRNA can both prevent and treat autoimmune diabetes in NOD mice. *Mol. Ther.* **18**, 2112–2120 (2010).
25. Kormann, M. S. *et al.* Expression of therapeutic proteins after delivery of chemically modified mRNA in mice. *Nature Biotech.* **29**, 154–157 (2011).
26. Kariko, K. *et al.* Increased erythropoiesis in mice injected with submicrogram quantities of pseudouridine-containing mRNA encoding erythropoietin. *Mol. Ther.* **20**, 948–953 (2012).
27. Mays, L. E. *et al.* Modified *Foxp3* mRNA protects against asthma through an IL-10-dependent mechanism. *J. Clin. Invest.* **123**, 1216–1228 (2013).
28. Levy, O. *et al.* mRNA-engineered mesenchymal stem cells for targeted delivery of interleukin-10 to sites of inflammation. *Blood* **122**, e23–e32 (2013).
29. Holtkamp, S. *et al.* Modification of antigen-encoding RNA increases stability, translational efficacy, and T-cell stimulatory capacity of dendritic cells. *Blood* **108**, 4009–4017 (2006).
30. Karikó, K., Kuo, A. & Barnathan, E. Overexpression of urokinase receptor in mammalian cells following administration of the in vitro transcribed encoding mRNA. *Gene Ther.* **6**, 1092–1100 (1999).
31. Kallen, K.-J. & Theβ, A. A development that may evolve into a revolution in medicine: mRNA as the basis for novel, nucleotide-based vaccines and drugs. *Ther. Adv. Vaccines* **2**, 10–31 (2014).
32. Li, Y. & Kiledjian, M. Regulation of mRNA decapping. *Wiley Interdiscip. Rev. RNA* **1**, 253–265 (2010).
33. Martin, S. A., Paoletti, E. & Moss, B. Purification of mRNA guanylyltransferase and mRNA (guanine-7-) methyltransferase from vaccinia virions. *J. Biol. Chem.* **250**, 9322–9329 (1975).
34. Malone, R. W., Felgner, P. L. & Verma, I. M. Cationic liposome-mediated RNA transfection. *Proc. Natl Acad. Sci. USA* **86**, 6077–6081 (1989).
35. Stepinski, J. *et al.* Synthesis and properties of mRNAs containing the novel "anti-reverse" cap analogs 7-methyl(3′-O-methyl)GpppG and 7-methyl (3′-deoxy) GpppG. *RNA* **7**, 1486–1495 (2001).
36. Jemielity, J. *et al.* Novel "anti-reverse" cap analogs with superior translational properties. *RNA* **9**, 1108–1122 (2003).
37. Mockey, M. *et al.* mRNA transfection of dendritic cells: synergistic effect of ARCA mRNA capping with poly(A) chains in *cis* and in *trans* for a high protein expression level. *Biochem. Biophys. Res. Commun.* **340**, 1062–1068 (2006).
38. Rabinovich, P. M. *et al.* Synthetic messenger RNA as a tool for gene therapy. *Hum. Gene Ther.* **17**, 1027–1035 (2006).
39. Grudzien-Nogalska, E. *et al.* Phosphorothioate cap analogs stabilize mRNA and increase translational efficiency in mammalian cells. *RNA* **13**, 1745–1755 (2007).
40. Kowalska, J. *et al.* Synthesis and characterization of mRNA cap analogs containing phosphorothioate substitutions that bind tightly to eIF4E and are resistant to the decapping pyrophosphatase DcpS. *RNA* **14**, 1119–1131 (2008).
41. Kuhn, A. N. *et al.* Phosphorothioate cap analogs increase stability and translational efficiency of RNA vaccines in immature dendritic cells and induce superior immune responses *in vivo*. *Gene Ther.* **17**, 961–971 (2010).
42. Gallie, D. R. The cap and poly(A) tail function synergistically to regulate mRNA translational efficiency. *Genes Dev.* **5**, 2108–2116 (1991).
43. Korner, C. G. & Wahle, E. Poly(A) tail shortening by a mammalian poly(A)-specific 3′-exoribonuclease. *J. Biol. Chem.* **272**, 10448–10456 (1997).
44. Martin, G. & Keller, W. Tailing and 3′-end labeling of RNA with yeast poly(A) polymerase and various nucleotides. *RNA* **4**, 226–230 (1998).
45. Ross, J. & Sullivan, T. Half-lives of β and γ globin messenger RNAs and of protein synthetic capacity in cultured human reticulocytes. *Blood* **66**, 1149–1154 (1985).
46. Zinckgraf, J. W. & Silbart, L. K. Modulating gene expression using DNA vaccines with different 3′-UTRs influences antibody titer, seroconversion and cytokine profiles. *Vaccine* **21**, 1640–1649 (2003).
47. Bergman, N. *et al.* Lsm proteins bind and stabilize RNAs containing 5′ poly(A) tracts. *Nature Struct. Mol. Biol.* **14**, 824–831 (2007).
48. Kuhn, A. N. *et al.* mRNA as a versatile tool for exogenous protein expression. *Curr. Gene Ther.* **12**, 347–361 (2012).
49. Chen, C. Y. & Shyu, A. B. AU-rich elements: characterization and importance in mRNA degradation. *Trends Biochem. Sci.* **20**, 465–470 (1995).
50. Gustafsson, C., Govindarajan, S. & Minshull, J. Codon bias and heterologous protein expression. *Trends Biotechnol.* **22**, 346–353 (2004).
51. Cannarozzi, G. *et al.* A role for codon order in translation dynamics. *Cell* **141**, 355–367 (2010).
52. Bossi, L. & Ruth, J. R. The influence of codon context on genetic code translation. *Nature* **286**, 123–127 (1980).
53. Gustafsson, C. *et al.* Engineering genes for predictable protein expression. *Protein Expr. Purif.* **83**, 37–46 (2012).
54. Van Gulck, E. R. A. *et al.* Efficient stimulation of HIV-1-specific T cells using dendritic cells electroporated with mRNA encoding autologous HIV-1 Gag and Env proteins. *Blood* **107**, 1818–1827 (2006).
55. Kimchi-Sarfaty, C. *et al.* A "silent" polymorphism in the *MDR1* gene changes substrate specificity. *Science* **315**, 525–528 (2007).
56. Malarkannan, S. *et al.* Presentation of out-of-frame peptide/MHC class I complexes by a novel translation initiation mechanism. *Immunity* **10**, 681–690 (1999).
57. Saulquin, X. *et al.* +1 frameshifting as a novel mechanism to generate a cryptic cytotoxic T lymphocyte epitope derived from human interleukin 10. *J. Exp. Med.* **195**, 353–358 (2002).
58. Schwab, S. R. *et al.* Constitutive display of cryptic translation products by MHC class I molecules. *Science* **301**, 1367–1371 (2003).
59. Bourquin, C. *et al.* Immunostimulatory RNA oligonucleotides trigger an antigen-specific cytotoxic T-cell and IgG2a response. *Blood* **109**, 2953–2960 (2007).
60. Sander, L. E. *et al.* Detection of prokaryotic mRNA signifies microbial viability and promotes immunity. *Nature* **474**, 385–389 (2011).
61. Weissman, D. *et al.* HIV gag mRNA transfection of dendritic cells (DC) delivers encoded antigen to MHC class I and II molecules, causes DC maturation, and induces a potent human *in vitro* primary immune response. *J. Immunol.* **165**, 4710–4717 (2000).
62. Fotin-Mleczek, M. *et al.* Messenger RNA-based vaccines with dual activity induce balanced TLR-7 dependent adaptive immune responses and provide antitumor activity. *J. Immunother.* **34**, 1–15 (2011).
63. Karikó, K. *et al.* Generating the optimal mRNA for therapy: HPLC purification eliminates immune activation and improves translation of nucleoside-modified, protein-encoding mRNA. *Nucleic Acids Res.* **39**, e142 (2011).
64. Rettig, L. *et al.* Particle size and activation threshold: a new dimension of danger signaling. *Blood* **115**, 4533–4541 (2010).
65. Alexopoulou, L. *et al.* Recognition of double-stranded RNA and activation of NF-κB by Toll-like receptor 3. *Nature* **413**, 732–738 (2001).
66. Diebold, S. S. *et al.* Innate antiviral responses by means of TLR7-mediated recognition of single-stranded RNA. *Science* **303**, 1529–1531 (2004).
67. Heil, F. *et al.* Species-specific recognition of single-stranded RNA via Toll-like receptor 7 and 8. *Science* **303**, 1526–1529 (2004).
68. Diebold, S. S. *et al.* Nucleic acid agonists for Toll-like receptor 7 are defined by the presence of uridine ribonucleotides. *Eur. J. Immunol.* **36**, 3256–3267 (2006).
69. Yoneyama, M. *et al.* The RNA helicase RIG-I has an essential function in double-stranded RNA-induced innate antiviral responses. *Nature Immunol.* **5**, 730–737 (2004).
70. Yoneyama, M. *et al.* Shared and unique functions of the DExD/H-Box helicases RIG-I, MDA5, and LGP2 in antiviral innate immunity. *J. Immunol.* **175**, 2851–2858 (2005).
71. Schlee, M. *et al.* Recognition of 5′ triphosphate by RIG-I helicase requires short blunt double-stranded RNA as contained in panhandle of negative-strand virus. *Immunity* **31**, 25–34 (2009).
72. Pichlmair, A. *et al.* Activation of MDA5 requires higher-order RNA structures generated during virus infection. *J. Virol.* **83**, 10761–10769 (2009).
73. Zust, R. *et al.* Ribose 2′-*O*-methylation provides a molecular signature for the distinction of self and non-self mRNA dependent on the RNA sensor Mda5. *Nature Immunol.* **12**, 137–143 (2011).
74. Balachandran, S. *et al.* Essential role for the dsRNA-dependent protein kinase PKR in innate immunity to viral infection. *Immunity* **13**, 129–141 (2000).
75. Karikó, K. *et al.* Suppression of RNA recognition by Toll-like receptors: the impact of nucleoside modification and the evolutionary origin of RNA. *Immunity* **23**, 165–175 (2005).
76. Hornung, V. *et al.* 5′-triphosphate RNA is the ligand for RIG-I. *Science* **314**, 994–997 (2006).
77. Nallagatla, S. R. & Bevilacqua, P. C. Nucleoside modifications modulate activation of the protein kinase PKR in an RNA structure-specific manner. *RNA* **14**, 1201–1213 (2008).
78. Anderson, B. R. *et al.* Incorporation of pseudouridine into mRNA enhances translation by diminishing PKR activation. *Nucleic Acids Res.* **38**, 5884–5892 (2010).
79. Lorenz, C. *et al.* Protein expression from exogenous mRNA: uptake by receptor-mediated endocytosis and trafficking via the lysosomal pathway. *RNA Biol.* **8**, 627–636 (2011).
80. Valadi, H. *et al.* Exosome-mediated transfer of mRNAs and microRNAs is a novel mechanism of genetic exchange between cells. *Nature Cell Biol.* **9**, 654–659 (2007).
81. Diken, M. *et al.* Selective uptake of naked vaccine RNA by dendritic cells is driven by macropinocytosis and abrogated upon DC maturation. *Gene Ther.* **18**, 702–708 (2011).
82. Wang, W. *et al.* Non-viral gene delivery methods. *Curr. Pharm. Biotechnol.* **14**, 46–60 (2013).
83. Neumann, E. *et al.* Gene transfer into mouse lyoma cells by electroporation in high electric fields. *EMBO J.* **1**, 841–845 (1982).
84. Van Tendeloo, V. F. *et al.* Nonviral transfection of distinct types of human dendritic cells: high-efficiency gene transfer by electroporation into hematopoietic progenitor- but not monocyte-derived dendritic cells. *Gene Ther.* **5**, 700–707 (1998).
85. Kyte, J. A. *et al.* Phase I/II trial of melanoma therapy with dendritic cells transfected with autologous tumor-mRNA. *Cancer Gene Ther.* **13**, 905–918 (2006).
86. Van Driessche, A. *et al.* Clinical-grade manufacturing of autologous mature mRNA-electroporated dendritic cells and safety testing in acute myeloid leukemia patients in a phase I dose-escalation clinical trial. *Cytotherapy* **11**, 653–668 (2009).
87. Van Tendeloo, V. F. *et al.* Induction of complete and molecular remissions in acute myeloid leukemia by Wilms' tumor 1 antigen-targeted dendritic cell vaccination. *Proc. Natl Acad. Sci. USA* **107**, 13824–13829 (2010).
88. Wilgenhof, S. *et al.* Therapeutic vaccination with an autologous mRNA electroporated dendritic cell vaccine in patients with advanced melanoma. *J. Immunother.* **34**, 448–456 (2011).
89. Van Nuffel, A. M. *et al.* Intravenous and intradermal TriMix-dendritic cell therapy results in a broad T-cell response and durable tumor response in a chemorefractory stage IV-M1c melanoma patient. *Cancer Immunol. Immunother.* **61**, 1033–1043 (2012).
90. Van Nuffel, A. M. *et al.* Dendritic cells loaded with mRNA encoding full-length tumor antigens prime $CD4^+$ and $CD8^+$ T cells in melanoma patients. *Mol. Ther.* **20**, 1063–1074 (2012).
91. Geng, T. *et al.* Transfection of cells using flow-through electroporation based on constant voltage. *Nature Protoc.* **6**, 1192–1208 (2011).

92. Weide, B. *et al.* Results of the first phase I/II clinical vaccination trial with direct injection of mRNA. *J. Immunother.* **31**, 180–188 (2008).
93. Wang, T., Upponi, J. R. & Torchilin, V. P. Design of multifunctional non-viral gene vectors to overcome physiological barriers: dilemmas and strategies. *Int. J. Pharm.* **427**, 3–20 (2012).
94. Semple, S. C. *et al.* Rational design of cationic lipids for siRNA delivery. *Nature Biotech.* **28**, 172–176 (2010).
95. Coelho, T. *et al.* Safety and efficacy of RNAi therapy for transthyretin amyloidosis. *N. Engl. J. Med.* **369**, 819–829 (2013).
96. Granstein, R. D., Ding, W. & Ozawa, H. Induction of anti-tumor immunity with epidermal cells pulsed with tumor-derived RNA or intradermal administration of RNA. *J. Invest. Dermatol.* **114**, 632–636 (2000).
97. Kreiter, S. *et al.* Intranodal vaccination with naked antigen-encoding RNA elicits potent prophylactic and therapeutic antitumoral immunity. *Cancer Res.* **70**, 9031–9040 (2010).
98. Kreiter, S. *et al.* FLT3 ligand enhances the cancer therapeutic potency of naked RNA vaccines. *Cancer Res.* **71**, 6132–6142 (2011).
99. Van Lint, S. *et al.* Preclinical evaluation of TriMix and antigen mRNA-based antitumor therapy. *Cancer Res.* **72**, 1661–1671 (2012).
100. Petsch, B. *et al.* Protective efficacy of *in vitro* synthesized, specific mRNA vaccines against influenza A virus infection. *Nature Biotech.* **30**, 1210–1216 (2012).
101. Geall, A. J. *et al.* Nonviral delivery of self-amplifying RNA vaccines. *Proc. Natl Acad. Sci. USA* **109**, 14604–14609 (2012).
102. Uchida, S. *et al. In vivo* messenger RNA introduction into the central nervous system using polyplex nanomicelle. *PLoS ONE* **8**, e56220 (2013).
103. Azarmi, S., Roa, W. H. & Lobenberg, R. Targeted delivery of nanoparticles for the treatment of lung diseases. *Adv. Drug Deliv. Rev.* **60**, 863–875 (2008).
104. Torchilin, V. Tumor delivery of macromolecular drugs based on the EPR effect. *Adv. Drug Deliv. Rev.* **63**, 131–135 (2011).
105. van der Bruggen, P. *et al.* A gene encoding an antigen recognized by cytolytic T lymphocytes on a human melanoma. *Science* **254**, 1643–1647 (1991).
106. Sahin, U. *et al.* Human neoplasms elicit multiple specific immune responses in the autologous host. *Proc. Natl Acad. Sci. USA* **92**, 11810–11813 (1995).
107. Nair, S. K. *et al.* Induction of cytotoxic T cell responses and tumor immunity against unrelated tumors using telomerase reverse transcriptase RNA transfected dendritic cells. *Nature Med.* **6**, 1011–1017 (2000).
108. Nair, S. K. *et al.* Induction of primary carcinoembryonic antigen (CEA)-specific cytotoxic T lymphocytes *in vitro* using human dendritic cells transfected with RNA. *Nature Biotech.* **16**, 364–369 (1998).
109. Morse, M. A. *et al.* Optimization of the sequence of antigen loading and CD40-ligand-induced maturation of dendritic cells. *Cancer Res.* **58**, 2965–2968 (1998).
110. Van Lint, S. *et al.* mRNA: From a chemical blueprint for protein production to an off-the-shelf therapeutic. *Hum. Vaccin. Immunother.* **9**, 265–274 (2013).
111. Kreiter, S. *et al.* Tumor vaccination using messenger RNA: prospects of a future therapy. *Curr. Opin. Immunol.* **23**, 399–406 (2011).
112. Cisco, R. M. *et al.* Induction of human dendritic cell maturation using transfection with RNA encoding a dominant positive Toll-like receptor 4. *J. Immunol.* **172**, 7162–7168 (2004).
113. Bonehill, A. *et al.* Enhancing the T-cell stimulatory capacity of human dendritic cells by co-electroporation with CD40L, CD70 and constitutively active TLR4 encoding mRNA. *Mol. Ther.* **16**, 1170–1180 (2008).
114. Calderhead, D. M. *et al.* Cytokine maturation followed by CD40L mRNA electroporation results in a clinically relevant dendritic cell product capable of inducing a potent proinflammatory CTL response. *J. Immunother.* **31**, 731–741 (2008).
115. Routy, J.-P. *et al.* Immunologic activity and safety of autologous HIV RNA-electroporated dendritic cells in HIV-1 infected patients receiving antiretroviral therapy. *Clin. Immunol.* **134**, 140–147 (2010).
116. Bontkes, H. J. *et al.* Dendritic cells transfected with interleukin-12 and tumor-associated antigen messenger RNA induce high avidity cytotoxic T cells. *Gene Ther.* **14**, 366–375 (2007).
117. Aarntzen, E. H. J. G. *et al.* Vaccination with mRNA-electroporated dendritic cells induces robust tumor antigen-specific $CD4^+$ and $CD8^+$ T cells responses in stage III and IV melanoma patients. *Clin. Cancer Res.* **18**, 5460–5470 (2012).
118. Pascolo, S. Vaccination with messenger RNA (mRNA). *Handb Exp. Pharmacol.* **183**, 221–235 (2008).
119. Carralot, J. P. *et al.* Polarization of immunity induced by direct injection of naked sequence-stabilized mRNA vaccines. *Cell. Mol. Life Sci.* **61**, 2418–2424 (2004).
120. Scheel, B. *et al.* Toll-like receptor-dependent activation of several human blood cell types by protamine-condensed mRNA. *Eur. J. Immunol.* **35**, 1557–1566 (2005).
121. Fotin-Mleczek, M. *et al.* Highly potent mRNA based cancer vaccines represent an attractive platform for combination therapies supporting an improved therapeutic effect. *J. Gene Med.* **14**, 428–439 (2012).
122. Kreiter, S. *et al.* Simultaneous *ex vivo* quantification of antigen-specific $CD4^+$ and $CD8^+$ T cell responses using *in vitro* transcribed RNA. *Cancer Immunol. Immunother.* **56**, 1577–1587 (2007).
123. Kreiter, S. *et al.* Increased antigen presentation efficiency by coupling antigens to MHC class I trafficking signals. *J. Immunol.* **180**, 309–318 (2008).
124. Diken, M. *et al.* Antitumor vaccination with synthetic mRNA: strategies for *in vitro* and *in vivo* preclinical studies. *Methods Mol. Biol.* **969**, 235–246 (2013).
125. Diken, M. *et al.* mTOR inhibition improves antitumor effects of vaccination with antigen-encoding RNA. *Cancer Immunol. Res.* **1**, 386–392 (2013).
126. Castle, J. C. *et al.* Exploiting the mutanome for tumor vaccination. *Cancer Res.* **72**, 1081–1091 (2012).
127. Kreiter, S. *et al.* Targeting the tumor mutanome for personalized vaccination therapy. *Oncoimmunology* **1**, 768–769 (2012).
128. Britten, C. M. *et al.* The regulatory landscape for actively personalized cancer immunotherapies. *Nature Biotech.* **31**, 880–882 (2013).
129. Zhao, Y. *et al.* Multiple injections of electroporated autologous T cells expressing a chimeric antigen receptor mediate regression of human disseminated tumor. *Cancer Res.* **70**, 9053–9061 (2010).
130. Almasbak, H. *et al.* Transiently redirected T cells for adoptive transfer. *Cytotherapy* **13**, 629–640 (2011).
131. Barrett, D. M. *et al.* Treatment of advanced leukemia in mice with mRNA engineered T cells. *Hum. Gene Ther.* **22**, 1575–1586 (2011).
132. Barrett, D. M. *et al.* Regimen specific effects of RNA-modified chimeric antigen receptor T cells in mice with advanced leukemia. *Hum. Gene Ther.* **24**, 717–727 (2013).
133. Hekele, A. *et al.* Rapidly produced SAM® vaccine against H7N9 influenza is immunogenic in mice. *Emerg. Microbes Infect.* **2**, e52 (2013).
134. Allard, S. D. *et al.* A phase I/IIa immunotherapy trial of HIV-1-infected patients with Tat, Rev and Nef expressing dendritic cells followed by treatment interruption. *Clin. Immunol.* **142**, 252–268 (2012).
135. Van Gulck, E. *et al.* mRNA-based dendritic cell vaccination induces potent antiviral T-cell responses in HIV-1-infected patients. *AIDS* **26**, F1–F12 (2012).
136. Liljestrom, P. & Garoff, H. A new generation of animal cell expression vectors based on the Semliki Forest virus replicon. *Biotechnology* **9**, 1356–1361 (1991).
137. Zhou, X. *et al.* Self-replicating Semliki Forest virus RNA as recombinant vaccine. *Vaccine* **12**, 1510–1514 (1994).
138. Ulmer, J. B. *et al.* RNA-based vaccines. *Vaccine* **30**, 4414–4418 (2012).
139. Geall, A. J., Mandl, C. W. & Ulmer, J. B. RNA: the new revolution in nucleic acid vaccines. *Semin. Immunol.* **25**, 152–159 (2013).
140. Fleeton, M. N. *et al.* Self-replicative RNA vaccines elicit protection against influenza A virus, respiratory syncytial virus, and a tickborne encephalitis virus. *J. Infect. Dis.* **183**, 1395–1398 (2001).
141. Anraku, I. *et al.* Kunjin virus replicon vaccine vectors induce protective $CD8^+$ T-cell immunity. *J. Virol.* **76**, 3791–3799 (2002).
142. Greer, C. E. *et al.* A chimeric alphavirus RNA replicon gene-based vaccine for human parainfluenza virus type 3 induces protective immunity against intranasal virus challenge. *Vaccine* **25**, 481–489 (2007).
143. Valenta, R. *et al.* From allergen genes to allergy vaccines. *Annu. Rev. Immunol.* **28**, 211–241 (2010).
144. Raz, E. *et al.* Preferential induction of a Th1 immune response and inhibition of specific IgE antibody formation by plasmid DNA immunization. *Proc. Natl Acad. Sci. USA* **93**, 5141–5145 (1996).
145. Chua, K. Y., Kuo, I. C. & Huang, C. H. DNA vaccines for the prevention and treatment of allergy. *Curr. Opin. Allergy Clin. Immunol.* **9**, 50–54 (2009).
146. Slater, J. E. *et al.* The latex allergen Hev b 5 transcript is widely distributed after subcutaneous injection in BALB/c mice of its DNA vaccine. *J. Allergy Clin. Immunol.* **102**, 469–475 (1998).
147. Roesler, E. *et al.* Immunize and disappear-safety-optimized mRNA vaccination with a panel of 29 allergens. *J. Allergy Clin. Immunol,* **124**, 1070–1077.e11 (2009).
148. Weiss, R. *et al.* Prophylactic mRNA vaccination against allergy. *Curr. Opin. Allergy Clin. Immunol.* **10**, 567–574 (2010).
149. Kolarich, D. *et al.* Comprehensive glyco-proteomic analysis of human α1-antitrypsin and its charge isoforms. *Proteomics* **6**, 3369–3380 (2006).
150. Seidah, N. G. & Chrétien, M. Proprotein and prohormone convertases: a family of subtilases generating diverse bioactive polypeptides. *Brain Res.* **848**, 45–62 (1999).
151. Nakayama, K. Furin: a mammalian subtilisin/Kex2p-like endoprotease involved in processing of a wide variety of precursor proteins. *Biochem. J.* **327**, 625–635 (1997).
152. Seidah, N. G. *et al.* Precursor convertases: an evolutionary ancient, cell-specific, combinatorial mechanism yielding diverse bioactive peptides and proteins. *Ann. NY Acad. Sci.* **839**, 9–24 (1998).
153. Barash, S., Wang, W. & Shi, Y. Human secretory signal peptide description by hidden Markov model and generation of a strong artificial signal peptide for secreted protein expression. *Biochem. Biophys. Res. Commun.* **294**, 835–842 (2002).
154. Fattori, E. *et al.* Gene electro-transfer of an improved erythropoietin plasmid in mice and non-human primates. *J. Gene Med.* **7**, 228–236 (2005).
155. Roberts, A. A. *et al.* Engineering factor Viii for hemophilia gene therapy. *J. Genet. Syndr. Gene Ther.* **1**, S1–006 (2011).
156. Takahashi, K. & Yamanaka, S. Induction of pluripotent stem cells from mouse embryonic and adult fibroblast cultures by defined factors. *Cell* **126**, 663–676 (2006).
157. Warren, L. *et al.* Highly efficient reprogramming to pluripotency and directed differentiation of human cells with synthetic modified mRNA. *Cell Stem Cell* **7**, 618–630 (2010).
158. Warren, L. *et al.* Feeder-free derivation of human induced pluripotent stem cells with messenger RNA. *Sci. Rep.* **2**, 657 (2012).
159. Mandal, P. K. & Rossi, D. J. Reprogramming human fibroblasts to pluripotency using modified mRNA. *Nature Protoc.* **8**, 568–582 (2013).
160. Bernal, J. A. RNA-based tools for nuclear reprogramming and lineage-conversion: towards clinical applications. *J. Cardiovasc. Transl. Res.* **6**, 956–968 (2013).
161. Miller, J. D. *et al.* Human iPSC-based modeling of late-onset disease via progerin-induced aging. *Cell Stem Cell* **13**, 691–705 (2013).
162. Scott, C. W., Peters, M. F. & Dragan, Y. P. Human induced pluripotent stem cells and their use in drug discovery for toxicity testing. *Toxicol. Lett.* **219**, 49–58 (2013).
163. Okano, H. *et al.* Steps toward safe cell therapy using induced pluripotent stem cells. *Circ. Res.* **112**, 523–533 (2013).
164. Miller, J. C. *et al.* An improved zinc-finger nuclease architecture for highly specific genome editing. *Nature Biotech.* **25**, 778–785 (2007).
165. Hockemeyer, D. *et al.* Genetic engineering of human pluripotent cells using TALE nucleases. *Nature Biotech.* **29**, 731–734 (2011).
166. Mali, P. *et al.* RNA-guided human genome engineering via Cas9. *Science* **339**, 823–826 (2013).
167. Fu, Y. *et al.* High-frequency off-target mutagenesis induced by CRISPR-Cas nucleases in human cells. *Nature Biotech.* **31**, 822–826 (2013).

168. Doyon, Y. *et al.* Heritable targeted gene disruption in zebrafish using designed zinc-finger nucleases. *Nature Biotech.* **26**, 702–708 (2008).
169. Tesson, L. *et al.* Knockout rats generated by embryo microinjection of TALENs. *Nature Biotech.* **29**, 695–696 (2011).
170. Wang, H. *et al.* One-step generation of mice carrying mutations in multiple genes by CRISPR/Cas-mediated genome engineering. *Cell* **153**, 910–918 (2013).
171. Wefers, B. *et al.* Generation of targeted mouse mutants by embryo microinjection of TALEN mRNA. *Nature Protocols* **8**, 2355–2379 (2013).
172. Geurts, A. M. *et al.* Knockout rats via embryo microinjection of zinc-finger nucleases. *Science* **325**, 433 (2009).
173. Shen, B. *et al.* Generation of gene-modified mice via Cas9/RNA-mediated gene targeting. *Cell Res.* **23**, 720–723 (2013).
174. Yang, D. *et al.* Effective gene targeting in rabbits using RNA-guided Cas9 nucleases. *J. Mol. Cell Biol.* **6**, 97–99 (2014).
175. Ma, Y. *et al.* Generating rats with conditional alleles using CRISPR/Cas9. *Cell Res.* **24**, 122–125 (2014).
176. Niu, Y. *et al.* Generation of gene-modified cynomolgus monkey via Cas9/RNA-mediated gene targeting in one-cell embryos. *Cell* **156**, 836–843 (2014).
177. Dupuy, A. J. *et al.* Mammalian germ-line transgenesis by transposition. *Proc. Natl Acad. Sci. USA* **99**, 4495–4499 (2002).
178. Wilber, A. *et al.* RNA as a source of transposase for sleeping beauty-mediated gene insertion and expression in somatic cells and tissues. *Mol. Ther.* **13**, 625–630 (2006).
179. Sumiyama, K., Kawakami, K. & Yagita, K. A simple and highly efficient transgenesis method in mice with the Tol2 transposon system and cytoplasmic microinjection. *Genomics* **95**, 306–311 (2010).
180. Suster, M. L., Sumiyama, K. & Kawakami, K. Transposon-mediated BAC transgenesis in zebrafish and mice. *BMC Genomics* **10**, 477 (2009).
181. Furushima, K. *et al.* Insertional mutagenesis by a hybrid piggyBac and sleeping beauty transposon in the rat. *Genetics* **192**, 1235–1248 (2012).
182. Bire, S. *et al.* Exogenous mRNA delivery and bioavailability in gene transfer mediated by piggyBac transposition. *BMC Biotechnol.* **13**, 75 (2013).
183. Isaacs, A., Cox, R. A. & Rotem, Z. Foreign nucleic acids as the stimulus to make interferon. *Lancet* **282**, 113–116 (1963).
184. Tytell, A. A. *et al.* Inducers of interferon and host resistance. 3. Double-stranded RNA from reovirus type 3 virions (reo 3-RNA). *Proc. Natl Acad. Sci. USA* **58**, 1719–1722 (1967).
185. Anderson, B. R. *et al.* Nucleoside modifications in RNA limit activation of 2′-5′-oligoadenylate synthetase and increase resistance to cleavage by RNase L. *Nuc. Acids Res.* **39**, 9329–9338 (2011).
186. Pollard, C. *et al.* Type I IFN counteracts the induction of antigen-specific immune responses by lipid-based delivery of mRNA vaccines. *Mol. Ther.* **21**, 251–259 (2013).
187. Hwang, S. H. *et al.* B cell TLR7 expression drives anti-RNA autoantibody production and exacerbates disease in systemic lupus erythematosus-prone mice. *J. Immunol.* **189**, 5786–5796 (2012).
188. Lipes, B. D. & Keene, J. D. Autoimmune epitopes in messenger RNA. *RNA* **8**, 762–771 (2002).
189. Murphy, K. (ed) in *Janeway's Immunobiology* 367–408 (Garland Science Publishing, 2011).
190. Worobec, A. & Rosenberg, A. S. A risk-based approach to immunogenicity concerns of therapeutic protein products, part 1: considering consequences of the immune response to a protein. *BioPharm International* 22–26 (2004).
191. Koren, E. *et al.* Recommendations on risk-based strategies for detection and characterization of antibodies against biotechnology products. *J. Immunol. Methods* **333**, 1–9 (2008).
192. Casadevall, N. *et al.* Pure red-cell aplasia and antierythropoietin antibodies in patients treated with recombinant erythropoietin. *N. Engl. J. Med.* **346**, 469–475 (2002).
193. Gao, G. *et al.* Erythropoietin gene therapy leads to autoimmune anemia in macaques. *Blood* **103**, 3300–3302 (2004).
194. Kromminga, A. & Schellekens, H. Antibodies against erythropoietin and other protein-based therapeutics: an overview. *Ann, NY Acad. Sci.* **1050**, 257–265 (2005).
195. Czech, M. P., Aouadi, M. & Tesz, G. J. RNAi-based therapeutic strategies for metabolic disease. *Nature Rev. Endocrinol.* **7**, 473–484 (2011).
196. Racanelli, V. & Rehermann, B. The liver as an immunological organ. *Hepatology* **43** (Suppl. 1), S54–S62 (2006).
197. Dyer, K. D. & Rosenberg, H. F. The RNase a superfamily: generation of diversity and innate host defense. *Mol. Divers.* **13**, 13 (2006).
198. McKenzie, R. *et al.* Hepatic failure and lactic acidosis due to fialuridine (FIAU), an investigational nucleoside analogue for chronic hepatitis B. *N. Engl. J. Med.* **333**, 1099–1105 (1995).
199. Lewis, W. Defective mitochondrial DNA replication and NRTIs: pathophysiological implications in AIDS cardiomyopathy. *Am. J. Physiol. Heart Circ. Physiol.* **284**, H1–H9 (2003).
200. Griffiths, M. *et al.* Cloning of a human nucleoside transporter implicated in the cellular uptake of adenosine and chemotherapeutic drugs. *Nature Med.* **3**, 89–93 (1997).
201. Lewis, W. *et al.* Fialuridine and its metabolites inhibit DNA polymerase γ at sites of multiple adjacent analog incorporation, decrease mtDNA abundance, and cause mitochondrial structural defects in cultured hepatoblasts. *Proc. Natl Acad. Sci. USA* **93**, 3592–3597 (1996).
202. Lai, Y., Tse, C.-M. & Unadkat, J. D. Mitochondrial expression of the human equilibrative nucleoside transporter 1 (hENT1) results in enhanced mitochondrial toxicity of antiviral drugs. *J. Biol. Chem.* **279**, 4490–4497 (2004).
203. Lee, E.-W. *et al.* Identification of the mitochondrial targeting signal of the human equilibrative nucleoside transporter 1 (hENT1): implications for interspecies differences in mitochondrial toxicity of fialuridine. *J. Biol. Chem.* **281**, 16700–16706 (2006).
204. Yoshioka, N. *et al.* Efficient generation of human iPSCs by a synthetic self-replicative RNA. *Cell Stem Cell* **13**, 246–254 (2013).
205. Dormitzer, P. R. *et al.* Synthetic generation of influenza vaccine viruses for rapid response to pandemics. *Sci. Transl. Med.* **5**, 185ra68 (2013).
206. Prieels, J.-P. *et al.* Mastering industrialization of cell therapy products. *BioProcess Int.* **10**, S12–S15 (2012).
207. Dahm, R. Friedrich Miescher and the discovery of DNA. *Dev. Biol.* **278**, 274–288 (2005).
208. Brenner, S., Jacob, F. & Meselson, M. An unstable intermediate carrying information from genes to ribosomes for protein synthesis. *Nature* **190**, 576–581 (1961).
209. Racaniello, V. R. & Baltimore, D. Cloned poliovirus complementary DNA is infectious in mammalian cells. *Science* **214**, 916–919 (1981).
210. Rice, C. M. *et al.* Production of infectious RNA transcripts from Sindbis virus cDNA clones: mapping of lethal mutations, rescue of a temperature-sensitive marker, and *in vitro* mutagenesis to generate defined mutants. *J. Virol.* **61**, 3809–3819 (1987).
211. Etchison, D. & Ehrenfeld, E. Comparison of replication complexes synthesizing poliovirus RNA. *Virology* **111**, 33–46 (1981).
212. Mizutani, S. & Colonno, R. J. *In vitro* synthesis of an infectious RNA from cDNA clones of human rhinovirus type 14. *J. Virol.* **56**, 628–632 (1985).
213. van der Werf, S. *et al.* Synthesis of infectious poliovirus RNA by purified T7 RNA polymerase. *Proc. Natl Acad. Sci. USA* **83**, 2330–2334 (1986).
214. Khromykh, A. A. & Westaway, E. G. Subgenomic replicons of the flavivirus Kunjin: construction and applications. *J. Virol.* **71**, 1497–1505 (1997).
215. Perri, S. *et al.* An alphavirus replicon particle chimera derived from venezuelan equine encephalitis and sindbis viruses is a potent gene-based vaccine delivery vector. *J. Virol.* **77**, 10394–10403 (2003).
216. Rolls, M. M. *et al.* Novel infectious particles generated by expression of the vesicular stomatitis virus glycoprotein from a self-replicating RNA. *Cell* **79**, 497–506 (1994).
217. Xiong, C. *et al.* Sindbis virus: an efficient, broad host range vector for gene expression in animal cells. *Science* **243**, 1188–1191 (1989).
218. Ying, H. *et al.* Cancer therapy using a self-replicating RNA vaccine. *Nature Med.* **5**, 823–827 (1999).
219. Lundstrom, K. Alphaviruses in gene therapy. *Viruses* **1**, 13–25 (2009).
220. Hewson, R. RNA viruses: emerging vectors for vaccination and gene therapy. *Mol. Med. Today* **6**, 28–35 (2000).
221. Lundin, P. Is silence still golden? Mapping the RNAi patent landscape. *Nature Biotech.* **29**, 493–497 (2011).
222. Modrak-Wojcik, A. *et al.* Eukaryotic translation initiation is controlled by cooperativity effects within ternary complexes of 4E-BP1, eIF4E, and the mRNA 5′ cap. *FEBS Lett.* **587**, 3928–3934 (2013).
223. Rau, M. *et al.* A reevaluation of the cap-binding protein, eIF4E, as a rate-limiting factor for initiation of translation in reticulocyte lysate. *J. Biol. Chem.* **271**, 8983–8990 (1996).
224. Wells, S. E. *et al.* Circularization of mRNA by eukaryotic translation initiation factors. *Mol. Cell* **2**, 135–140 (1998).
225. Houseley, J. & Tollervey, D. The many pathways of RNA degradation. *Cell* **136**, 763–776 (2009).
226. Balagopal, V., Fluch, L. & Nissan, T. Ways and means of eukaryotic mRNA decay. *Biochim. Biophys. Acta* **1819**, 593–603 (2012).
227. Shyu, A. B., Wilkinson, M. F. & van Hoof, A. Messenger RNA regulation: to translate or to degrade. *EMBO J.* **27**, 471–481 (2008).
228. Tomecki, R. & Dziembowski, A. Novel endoribonucleases as central players in various pathways of eukaryotic RNA metabolism. *RNA* **16**, 1692–1724 (2010).
229. Li, W. M., Barnes, T. & Lee, C. H. Endoribonucleases — enzymes gaining spotlight in mRNA metabolism. *FEBS J.* **277**, 627–641 (2010).
230. Wilusz, J. RNA stability: is it the endo' the world as we know it? *Nature Struct. Mol. Biol.* **16**, 9–10 (2009).
231. Garneau, N. L., Wilusz, J. & Wilusz, C. J. The highways and byways of mRNA decay. *Nature Rev. Mol. Cell Biol.* **8**, 113–126 (2007).
232. Bevan, M. J. Cross-priming. *Nature Immunol.* **7**, 363–365 (2006).
233. Thomsen, L. B. *et al.* Nanoparticle-derived non-viral genetic transfection at the blood–brain barrier to enable neuronal growth factor delivery by secretion from brain endothelium. *Curr. Med. Chem.* **18**, 3330–3334 (2011).
234. Hayashi, S. *et al.* Autocrine-paracrine effects of overexpression of hepatocyte growth factor gene on growth of endothelial cells. *Biochem. Biophys. Res. Commun.* **220**, 539–545 (1996).
235. Zeis, M. *et al.* Generation of cytotoxic responses in mice and human individuals against hematological malignancies using survivin-RNA-transfected dendritic cells. *J. Immunol.* **170**, 5391–5397 (2003).
236. Siegel, S. *et al.* Induction of cytotoxic T-cell responses against the oncofetal antigen-immature laminin receptor for the treatment of hematologic malignancies. *Blood* **102**, 4416–4423 (2003).
237. Yoon, S. H. *et al.* Adoptive immunotherapy using human peripheral blood lymphocytes transferred with RNA encoding Her-2/neu-specific chimeric immune receptor in ovarian cancer xenograft model. *Cancer Gene Ther.* **16**, 489–497 (2009).
238. Rabinovich, P. M. *et al.* Chimeric receptor mRNA transfection as a tool to generate antineoplastic lymphocytes. *Hum. Gene Ther.* **20**, 51–61 (2009).
239. Bonehill, A. *et al.* Single-step antigen loading and activation of dendritic cells by mRNA electroporation for the purpose of therapeutic vaccination in melanoma patients. *Clin. Cancer Res.* **15**, 3366–3375 (2009).
240. Maus, M. V. *et al.* T cells expressing chimeric antigen receptors can cause anaphylaxis in humans. *Cancer Immunol. Res.* **1**, 26–31 (2013).
241. Benteyn, D. *et al.* Characterization of $CD8^+$ T-cell responses in the peripheral blood and skin injection sites of melanoma patients treated with mRNA electroporated autologous dendritic cells (TriMixDC-MEL). *Biomed Res Int* http://dx.doi.org/10.1155/2013/976383 (2013).
242. Lorenzi, J. C. *et al.* Intranasal vaccination with messenger RNA as a new approach in gene therapy: use against tuberculosis. *BMC Biotechnol.* **10**, 77 (2010).
243. Wood, A. J. *et al.* Targeted genome editing across species using ZFNs and TALENs. *Science* **333**, 307 (2011).
244. Davies, B. *et al.* Site specific mutation of the *Zic2* locus by microinjection of TALEN mRNA in mouse CD1, C3H and C57BL/6J oocytes. *PLoS ONE* **8**, e60216 (2013).

245. Karikó, K. *et al*. Incorporation of pseudouridine into mRNA yields superior nonimmunogenic vector with increased translational capacity and biological stability. *Mol Ther.* **16**, 1833–1840 (2008).
246. Angel, M. & Yanik, M. F. Innate immune suppression enables frequent transfection with RNA encoding reprogramming proteins. *PLoS ONE* **5**, e11756 (2010).
247. Yakubov, E. *et al.* Reprogramming of human fibroblasts to pluripotent stem cells using mRNA of four transcription factors. *Biochem. Biophys. Res. Commun.* **394**, 189–193 (2010).
248. Smull, C. E., Mallette, M. F. & Ludwig, E. H. The use of basic proteins to increase the infectivity of enterovirus ribonucleic acid. *Biochem. Biophys. Res. Commun.* **5**, 247–249 (1961).
249. Papahadjopoulos, D. *et al.* Cochleate lipid cylinders: formation by fusion of unilamellar lipid vesicles. *Biochim. Biophys. Acta* **394**, 483–491 (1975).
250. Dimitriadis, G. J. Translation of rabbit globin mRNA introduced by liposomes into mouse lymphocytes. *Nature* **274**, 923–924 (1978).
251. Muthukrishnan, S., Both, G. W., Furuichi, Y. & Shatkin, A. J. 5'-Terminal 7-methylguanosine in eukaryotic mRNA is required for translation. *Nature* **255**, 33–37 (1975).
252. Furuichi, Y. & Miura, K. A blocked structure at the 5' terminus of mRNA from cytoplasmic polyhedrosis virus. *Nature* **253**, 374–375 (1975).
253. Lockard, R. E. & Lingrel, J. B. The synthesis of mouse hemoglobin β-chains in a rabbit reticulocyte cell-free system programmed with mouse reticulocyte 9S RNA. *Biochem. Biophys. Res. Commun.* **37**, 204–212 (1969).
254. Gurdon, J. B. *et al.* Use of frog eggs and oocytes for the study of messenger RNA and its translation in living cells. *Nature.* **233**, 177–182 (1971).
255. Krieg, P. A. & Melton, D. A. Functional messenger RNAs are produced by SP6 *in vitro* transcription of cloned cDNAs. *Nucl. Acids Res.* **12**, 7057–7070 (1984).
256. Hwang, W. Y. *et al.* Efficient genome editing in zebrafish using a CRISPR-Cas system. *Nature Biotech.* **31**, 227–229 (2013).

Competing interests statement
The authors declare competing interests: see Web version for details.

FURTHER INFORMATION

2nd International mRNA Health Conference; Boston, November 11-12, 2014: http://www.mrna-conference.com
ClinicalTrials.gov database: https://clinicaltrials.gov
FierceBiotech (Industry Voices: mRNA-Based Therapies — Blueprints for Therapeutics; 25 Jul 2013): http://www.fiercebiotech.com/story/industry-voices-mrna-based-therapies-blueprints-therapeutics/2013-07-25
How Messenger mRNA therapeutics work: https://www.youtube.com/watch?v=lvp9ZdwX-PA
RNA vaccines: https://www.youtube.com/watch?v=EthhhCmn5gw
Zone in with Zon (What's trending in nucleic acid research): Modified mRNA Mania; 2 Dec 2013: http://zon.trilinkbiotech.com/2013/12/02/modified-mrna/

ALL LINKS ARE ACTIVE IN THE ONLINE PDF

Veterinary Pathology
2018, Vol. 55(2) 341-354

DOI: 10.1177/0300985817738095
journals.sagepub.com/home/vet

Safety Evaluation of Lipid Nanoparticle–Formulated Modified mRNA in the Sprague-Dawley Rat and Cynomolgus Monkey

Maja Sedic[1], Joseph J. Senn[1], Andy Lynn[1], Michael Laska[1], Mike Smith[1], Stefan J. Platz[2], Joseph Bolen[3], Stephen Hoge[1], Alex Bulychev[1], Eric Jacquinet[1], Victoria Bartlett[4], and Peter F. Smith[5]

Abstract

The pharmacology, pharmacokinetics, and safety of modified mRNA formulated in lipid nanoparticles (LNPs) were evaluated after repeat intravenous infusion to rats and monkeys. In both species, modified mRNA encoding the protein for human erythropoietin (hEPO) had predictable and consistent pharmacologic and toxicologic effects. Pharmacokinetic analysis conducted following the first dose showed that measured hEPO levels were maximal at 6 hours after the end of intravenous infusion and in excess of 100-fold the anticipated efficacious exposure (17.6 ng/ml) at the highest dose tested.[24] hEPO was pharmacologically active in both the rat and the monkey, as indicated by a significant increase in red blood cell mass parameters. The primary safety-related findings were caused by the exaggerated pharmacology of hEPO and included increased hematopoiesis in the liver, spleen, and bone marrow (rats) and minimal hemorrhage in the heart (monkeys). Additional primary safety-related findings in the rat included mildly increased white blood cell counts, changes in the coagulation parameters at all doses, as well as liver injury and release of interferon γ–inducible protein 10 in high-dose groups only. In the monkey, as seen with the parenteral administration of cationic LNPs, splenic necrosis and lymphocyte depletion were observed, accompanied with mild and reversible complement activation. These findings defined a well-tolerated dose level above the anticipated efficacious dose. Overall, these combined studies indicate that LNP-formulated modified mRNA can be administered by intravenous infusion in 2 toxicologically relevant test species and generate supratherapeutic levels of protein (hEPO) in vivo.

Keywords

modified mRNA, lipid nanoparticle, toxicology, pharmacokinetics, drug discovery

The promise of mRNA as a novel modality to deliver therapeutic proteins in humans is vast, as evidenced by the growth and success of recombinant human therapeutic proteins over the last 3 decades, such as recombinant human insulin for the treatment of diabetes mellitus.[17] Protein expression directed by exogenous mRNA offers many advantages over other nucleic acid–based concepts, as well as recombinant proteins. Potential advantages of mRNA over DNA-based technology include (1) no integration into the host genome thereby circumventing the risk of deleterious chromosomal changes, and (2) faster and more efficient expression with proper modifications, since mRNA therapeutics only require access to the cytoplasm. In comparison with recombinant proteins, mRNA would have lower manufacturing costs and could enable access to intracellular as well as cell membrane–bound therapeutic targets. The biggest challenges of mRNA technology are its potential for immunogenicity and its relatively poor in vivo stability. These challenges have been addressed through progress in chemistry and sequence engineering (eg, optimization of the 5′ cap, 5′-, and 3′-untranslated regions and coding sequences) and through the use of specific nucleotide modifications.[16,21,29]

Nucleotide-modified mRNA is nearly identical to naturally occurring mammalian mRNA, with the exception that certain nucleotides, normally present in mammalian mRNA, are partially or fully replaced with nucleosides, such as pyrimidine nucleosides—specifically, pseudouridine, 2-thiouridine,

[1]Moderna Therapeutics, Cambridge, MA
[2]AstraZeneca, Melbourn, Royston, UK
[3]PureTech Health, Boston, MA
[4]Akcea Therapeutics, Cambridge, MA
[5]Alnylam Pharmaceuticals Inc, Cambridge, MA

Supplementary material for this article is available online.

Corresponding Author:
Joseph J. Senn, Moderna Therapeutics, 200 Technology Square, Cambridge, MA 02139, USA.
Email: Joe.Senn@modernatx.com

5-methyl cytosine, or N1-methyl-pseudouridine.[2,14,16,21,29] These naturally occurring pyrimidine nucleotides are present in mammalian tRNA, rRNA, and small nuclear RNAs.[20] Incorporation of these nucleotides in place of the normal pyrimidine base has been shown to minimize the indiscriminate recognition of exogenous mRNA by pathogen-associated molecular pattern receptors, such as toll-like receptors, retinoic acid–inducible gene 1, melanoma differentiation-associated protein 5, nucleotide-binding oligomerization domain-containing protein 2, and protein kinase R.[7]

Given the lability of a naked mRNA molecule, the development of mRNA therapeutics has been further hampered by the lack of appropriate formulations for delivery and potentially as a targeting mechanism to a diseased organ or tissue.[12] However, the application of lipid-based nanoparticle delivery systems, initially developed for the in vivo delivery of siRNA, has enabled systemic administration of modified mRNA.[22] Adequate delivery of mRNA with lipid nanoparticles (LNPs) has been demonstrated for mRNA-based vaccines, where intramuscular injection of low doses of mRNA formulated in either LNPs or nanoemulsion induced immune protection from influenza and respiratory syncytial virus in mice, as well as cytomegalovirus and respiratory syncytial virus in monkeys.[9] Furthermore, a single administration of modified mRNA-LNP complexes in mice by various routes resulted in high, sustained protein production.[19] Finally, Thess et al[25] reported that repeated administration of unmodified mRNA in combination with the nonliposomal polymeric delivery system (*Trans*IT) induced high systemic protein levels and strong physiologic responses in mice. These authors also noted similar observations following single-dose administration of erythropoietin (EPO)–mRNA in LNPs to pigs and monkeys.

LNPs have been reported to be clinically effective for the delivery of siRNA.[6] The LNP vehicle is currently in late-phase clinical trials of a synthetic siRNA in patients suffering from transthyretin amyloidosis and has been well tolerated in this population.[6] Therefore, considerable work has been done to understand the safety profile of systemic administration of siRNA-LNPs.[3] Here, we set out to describe, for the first time, the pharmacology and toxicologic effects of repeated administration of hEPO-mRNA in LNPs in male Sprague-Dawley rats and female cynomolgus monkeys.

Materials and Methods

Animals and Husbandry

The study plan and any amendments or procedures involving the care and use of animals in these studies were reviewed and approved by the Institutional Animal Care and Use Committee of Charles River Laboratories Preclinical Services (Montreal and Sherbrooke, Canada). During the study, the care and use of animals were conducted according to the guidelines of the US National Research Council and the Canadian Council on Animal Care.

Male Sprague-Dawley rats (Charles River Laboratories) were 11 to 12 weeks old and weighed between 390 and 497 g at dose initiation. Animals were group housed in polycarbonate bins and separated during designated procedures. The temperature of the animal room was kept between 19°C and 25°C, with humidity between 30% and 70%. The light cycle was 12 hours light and 12 hours dark, except during designated procedures. Animals were fed PMI Nutrition International Certified Rodent Chow No. 5CR4 (14% protein) ad libitum throughout the in-life studies, except during designated procedures. Municipal tap water treated by reverse osmosis and ultraviolet irradiation was freely available to each animal via an automatic watering system. Environmental enrichment was provided to animals per standard operating procedures of Charles River Laboratories (Montreal, Canada), except during study procedures and activities.

Female cynomolgus monkeys (Charles River Laboratories) were 1.5 to 6 years old and weighed 2.5 to 5.1 kg at the initiation of dosing. Animals were housed in stainless-steel cages and separated during designated procedures. The temperature of the animal room was kept between 20°C and 26°C, with humidity between 30% and 70%. The light cycle was 12 hours light and 12 hours dark except during designated procedures. Animals were fed PMI Nutrition International Certified Primate Chow No. 5048 (25% protein). Municipal tap water treated by reverse osmosis and ultraviolet irradiation was freely available to each animal via an automatic watering system. Psychological and environmental enrichment was provided to animals per standard operating procedures of Charles River Laboratories (Montreal, Canada) except during study procedures and activities.

Control, Test, and Reference Items

An 850-nucleotide messenger RNA was prepared by in vitro transcription from a linearized DNA template with T7 RNA Polymerase. The DNA template encoded the T7 promoter, a 5′ untranslated region, the 579-nucleotide open reading frame encoding human EPO (hEPO) mature protein with signal sequence, a 3′untranslated region, and a polyadenylated tail. The in vitro transcription was performed with the canonical nucleotides adenosine triphosphate and guanosine triphosphate and the modified nucleotides 1-methylpseudouridine triphosphate and 5-methylcytidine triphosphate. The mRNA contains a 5′ Cap 1 structure, which consisted of 7-methylguanosine linked to the 5′ nucleoside of the mRNA chain through a 5′–5′ triphosphate bridge and 2′-O-methyl group present on the first nucleotide of the mRNA.[23] The messenger RNA was purified and buffer exchanged into low ionic strength buffer for formulation.[18] The final mRNA had a calculated molecular weight of 277 786 Da.

The mRNA-loaded LNPs were generated via stepwise ethanol dilution, with an approach adapted from previously demonstrated methods.[13,30] The LNP formulation was prepared by dissolving the lipids (6Z,9Z,28Z,31Z)-heptatriaconta-6,9,28,31-tetraen-19-yl 4-(dimethylamino)butanoate (MC3),

Table 1. Experimental Design for Safety Study: Rat.[a]

Group No.	Test Material	Dose Level, mg/kg[b]	Intravenous Administration	Dose Concentration mg/ml
1	PBS	0	10-min infusion, 2×/wk	0
2	mRNA EPO	0.03	10-min infusion, 2×/wk	0.006
3	mRNA EPO	0.1	10-min infusion, 2×/wk	0.02
4	mRNA EPO	0.3	10-min infusion, 2×/wk	0.06
5	mRNA EPO	0.3	10-min infusion, 1×/wk	0.06
6	Empty LNP	0.3	10-min infusion, 2×/wk	0.06

Abbreviations: EPO, erythropoietin; LNP, lipid nanoparticle; PBS, phosphate-buffered saline.
[a]No. of males per group, $n = 24$. Dose volume per group, 5 ml/kg. Dose rate per group, 30 ml/kg/h.
[b]Dose levels in terms of mRNA content. For group No. 6, the dose level is listed in terms of the same amount of lipid:mRNA ratio (by weight).

Table 2. Experimental Design for Safety Study: Monkey.[a]

Group No.	Test Material	Dose Level (mg/kg)[b]	Intravenous Administration	Dose Concentration (mg/mL)
1	PBS	0	60-min infusion (2×/wk)	0
2	mRNA EPO	0.03	60-min infusion (2×/wk)	0.006
3	mRNA EPO	0.1	60-min infusion (2×/wk)	0.02
4	mRNA EPO	0.3	60-min infusion (2×/wk)	0.06
5	mRNA EPO	0.3	60-min infusion (1×/wk)	0.06
6	Empty LNP	0.3	60-min infusion (2×/wk)	0.06

Abbreviations: EPO, erythropoietin; LNP, lipid nanoparticle; PBS, phosphate-buffered saline.
[a]No. of females per group, $n = 3$. Dose volume per group, 5 ml/kg. Dose rate per group, 5 ml/kg/h.
[b]Dose levels in terms of mRNA content. For group No. 6, the dose level is listed in terms of the same amount of lipid to mRNA ratio (by weight).

1,2-distearoyl-sn-glycero-3-phosphocholine (DSPC), cholesterol, and 1,2-dimyristoyl-rac-glycerol, methoxypolyethylene glycol (PEG2000-DMG) in ethanol. The 4 lipids were prepared as a combined stock, with a total concentration of 12.5 mM (molar ratio of 50:10:38.5:1.5, MC3:DSPC:cholesterol: PEG2000-DMG). In brief, the solution containing lipids was mixed with an acidic aqueous buffer containing mRNA (0.18 mg/ml, pH 4.0) in a T-mixer device. The resulting LNP dispersion was diluted and subsequently purified and concentrated by tangential flow filtration. The formulation was filtered through a clarification filter (0.8/0.2 μm nominal). Prior to storage, the formulation was additionally filtered through 2 in-line sterile filters (0.2 μm) and aseptically filled into sterilized vials, stoppered, and capped. Empty LNPs were generated with a similar approach, whereby mRNA was excluded from the process.

The final LNP lipid concentration was determined with an ultraperformance liquid chromatography system with online charged aerosol detection. The total concentrations of lipids in the final mRNA-LNPs and empty LNPs were 22.0 and 13.1 mg/ml, respectively. The final mRNA content in hEPO LNPs was quantified by ultraviolet analysis, resulting in an mRNA concentration of 1.2 mg/ml. Measured lipid and mRNA concentration values enabled dilution with phosphate-buffered saline (PBS) to target levels for dosing (Tables 1, 2). Particle hydrodynamic diameters were determined by dynamic light scattering. Resulting diameters for mRNA and empty LNPs were 81 nm (0.08 polydispersity index) and 61 nm (0.10 polydispersity index), respectively. Total mRNA encapsulation was quantified with the Ribogreen assay (ThermoFisher Scientific). The final value for hEPO-mRNA in LNP encapsulation was 97%. Additional information for the control, test, and reference items is provided in Supplemental Table 1.

Male Rat Study Design

Only male rats were used for this study, as there was no expected sex-specific differences in metabolism, distribution, or toxicity. The negative control, test, or reference items were administered over the course of 2 weeks in a 10-minute intravenous (IV) infusion via a caudal vein at a dose level, dose volume, and frequency listed in Table 1. Dose levels for each study were based on previous pharmacology data demonstrating production of efficacious levels of hEPO in the rat and cynomolgus monkey at doses $\leq$0.03 mg/kg of mRNA. Based on pharmacokinetic (PK) data indicating predictable increases in protein expression with dose, the mid- and high doses for these studies were selected to achieve significant multiples of the efficacious dose level. Since PK behavior and physiologic consequences are well defined for EPO therapy, we employed a similar approach in our study of hEPO-mRNA in LNPs.[15,16,25] Each infused dose was administered with a temporary indwelling catheter inserted in a caudal vein connected to an injection set and infusion pump. The animals were temporarily restrained for the dose administration and not sedated. The dose volume for each animal was based on the most recent body weight measurement. The first day of dosing was designated as day 1. Six males per group were used for toxicity assessment, 12 males per group for immunology assessment, and 6 males per group for PK / pharmacodynamic (PD) assessment. The following end points were evaluated: clinical signs (including observations of the infusion sites), body weights, food consumption, PK/PD, clinical pathology (hematology, coagulation, and clinical chemistry), macro- and microscopic examination of tissues, and immunotoxicology markers: histamine, interleukin 6 (IL-6), interferon γ–induced protein 10 (IP-10), tumor necrosis factor α (TNF-α), interferon α (IFN-α), and complement (C3).

Blood samples were collected from nonfasted animals and analyzed for hematology on day 9 and from fasted animals for hematology, coagulation, and clinical chemistry on day 16 (at necropsy). For PD (hEPO) or PK (hEPO-mRNA), blood samples were collected and processed to plasma prestudy and at 2, 6, 24, and 48 hours after the end of injection/infusion on days 1 and 15. After processing, the plasma samples were stored in a freezer set to maintain −80°C until analyzed. For cytokines (ie, IL-6, IP-10, TNF-α), histamine, and complement (C3) analysis, blood samples were collected prestudy and at 5 minutes and 2,

6, and 24 hours after the end of injection/infusion on days 1 and 15 in K_3EDTA tubes and processed to plasma or serum (no anticoagulant) for IFN-α analysis.

Female Monkey Study Design

Female monkeys were used for this study, as there was no expected sex-specific differences in metabolism, distribution, or toxicity. The negative control, test, and reference items were administered over the course of 2 weeks in a 60-minute IV infusion via an appropriate peripheral vein (eg, saphenous or brachial) at the dose level, dose volume, and frequency listed in Table 2. The dose volume for each animal was based on the most recent body weight measurement. The animals were temporarily restrained (on a sling or a chair) for the dose administration and not sedated. Each infused dose was administered with a temporary indwelling catheter inserted in a peripheral vein connected to an injection set and infusion pump. The first day of dosing was designated as day 1. The end points in this study included clinical signs (including observation of the infusion sites), body weights, food consumption, PK/PD, clinical pathology (hematology, coagulation, and serum chemistry), macro- and microscopic examination of tissues, and selected cytokines (interleukin 1 β [IL-1β], IL-6, TNF-α, and IP-10) and complement (C3a and C5b-9).

Blood samples were collected from overnight-fasted animals for hematology, coagulation, and clinical chemistry parameters at predose (baseline) and on day 16. Additionally, blood was analyzed on day 8 for hematology parameters only. For PK/PD assessments, blood samples were collected and processed to plasma at the following time points: predose; 2, 6, 24, and 48 hours after the first dose; and 6 hours after subsequent dosing occasions. After processing, the plasma samples were stored in a freezer set to −80°C until analyzed. Blood samples were collected in K_3EDTA tubes and processed to plasma for analysis of cytokines (ie, IL-1β, IL-6, TNF-α) and complement (ie, C3a and C5b-9) or to serum for analysis of IFN-α and IP-10 at the following time points for all groups: predose; at 2, 6, and 24 hours after the end of infusion on day 1; and at 2, 6, and 24 hours after the end of infusion on day 15. Additionally, for complement analysis only, blood samples were collected 2, 6, and 24 hours after the end of infusion on day 4 (groups 1–4 and 6).

Clinical Pathology

Hematology parameters were measured with Bayer Advia 120 Automated Hematology Analyzer (Siemens Healthcare). Standard coagulation parameters were measured on a START 4 Compact Stago Analyzer (Diagnostica Stago). Standard clinical chemistry parameters were measured with Modular Analytics (Roche/Hitachi).

Histamine, Cytokine and Complement Levels

Histamine levels in the rat plasma were determined with the Histamine EIA Kit (IM-2015; Immunotech). Serum levels of IFNα were determined with the Rat IFNα ELISA Kit (KT-60242; Kamiya Biomedical Company) and the Human IFNα Multi-subtype ELISA Kit (41105-1 or 41105-2; PBL Biomedical Laboratories). IL-6, IP-10, and TNFα in rat plasma were determined with the Rat Cytokine/Chemokine Magnetic Panel Kit (RECYMAG-65K; Millipore). IL1β, IL-6, and TNFα in monkey plasma were determined with the Non-Human Primate Cytokine/Chemokine Magnetic Panel Kit (PRCYTOMAG-40K; Millipore). IP-10 in the monkey serum was determined with the Monkey IP-10 Singleplex Magnetic Kit (LHB0001; Invitrogen). C3 levels in the rat plasma were determined with the Rat C3 ELISA Kit (GWB-A8B8AF; Genway). C3a levels in the monkey plasma were determined with the Human C3a EIA Kit (A031; Quidel). C5b-9 levels in the monkey plasma were determined with the Human C5b-9 ELISA Kit (558315; BD Bioscience).

Histopathology

Representative samples of the following tissues from all animals were preserved in 10% neutral buffered formalin: bone marrow (sternum), heart, infusion site (last dose), kidney, liver, lung, spleen, and thymus. Tissues were embedded in paraffin, sectioned, mounted on glass slides, and stained with hematoxylin and eosin. The histopathologic evaluation was internally peer reviewed.

hEPO bDNA

The bioanalysis of plasma samples for quantification of hEPO-mRNA levels was conducted at AxoLabs according to the bDNA method for mRNA detection developed by QuantiGene (Affymetrix).[26] Briefly, plasma samples were directly diluted in lysis buffer. On each bDNA plate, including a customized assay-specific set of probes, a dilution curve was pipetted with spiked standards into untreated plasma. Signal amplification was carried out with oligonucleotides bound to the enzyme alkaline phosphatase. The calculated amount in picograms was normalized to the amount of plasma in the lysate and to the amount of lysate applied to the plate. Since measurements in the PBS-treated control group were within the background level range, cross-reactivity of hEPO-mRNA to rat or monkey EPO mRNA was considered negligible.

hEPO ELISA

hEPO levels were measured with a human EPO Sandwich ELISA Kit (01630; Stemcell Technologies). For this assay, the lower and upper limits of quantitation were 12 and 800 pg/ml, respectively. Since predose measurements were within the background level range, cross-reactivity of hEPO to rat or monkey EPO was considered negligible.

Data Analysis and Reporting

The toxicokinetic parameters of human modified hEPO-mRNA and its expressed protein in plasma were calculated with a noncompartmental approach in WinNonlin Phoenix 64, version 6.3 (Pharsight). Dose-normalized maximum serum concentration (C_{max}/dose) and area under the curve (AUC/dose) were determined by dividing the respective parameters by dose and calculated by either WinNonlin or Excel. The mean, standard deviation, and percentage coefficient of variation of the toxicokinetic parameters were calculated in WinNonlin. All reported values were rounded to either 3 significant figures or 1 decimal place (time to reach maximum serum concentration [T_{max}], half-life [$t_{1/2}$]).

Results

Administration of hEPO-mRNA in LNP Results in Detection of Significant Serum hEPO Levels and Corresponding PD Effects in the Rat and Monkey

Toxicokinetic analysis in the rat revealed that hEPO-mRNA had a moderate half-life (2.9–5.7 hours) and low clearance (49.0–97.2 ml/h/kg; Fig. 1, Table 3). The C_{max}/dose values were consistent among the 4 dose groups, ranging from 2270 to 3320 ng/ml/mg/kg (Table 3). Measured hEPO levels were maximal approximately 6 hours after the 10-minute infusion (Fig. 2, Table 4). The AUC values (for hEPO-mRNA and hEPO) increased in more than a dose-proportional manner, between 0.03 and 0.3 mg/kg (Table 4). Plasma samples collected at 6 hours after each dose indicated that hEPO levels were constant at C_{max} at all dose levels until day 15, when measured hEPO levels were significantly decreased in the mid- and high-dosed groups (Fig. 3). Consistent with literature data,[1] peak reticulocytosis (PD marker described later) was observed by day 9, and levels remained elevated during the 15-day period. Overall, these results indicate that plasma concentrations of hEPO were mostly consistent throughout the study and exhibited greater-than-dose-proportional increases in AUC after IV administration.

Significant increases were noted in red blood cell and associated parameters (hemoglobin, hematocrit) in all male rat groups dosed with hEPO-mRNA in LNPs as compared with the PBS group and the group dosed with empty LNPs. Interestingly, the changes in red blood cell parameters (except mean corpuscular volume) were similar across all hEPO-mRNA-dosed groups and did not seem to be dose related (Fig. 4, Suppl. Fig. 1). In addition, dose-dependent increases in platelet counts and reticulocytes were noted, particularly at the highest doses administered twice weekly (Suppl. Fig. 1). Overall, these results indicate that repeated administration of hEPO-mRNA in LNPs achieves physiologically relevant and persistent hEPO levels that result in significant changes in precursor cells and mature red blood cell count at doses as low as 0.03 mg/kg.

Like in male rats, toxicokinetic findings in female monkeys indicated that the total exposure (AUC) to hEPO-mRNA and

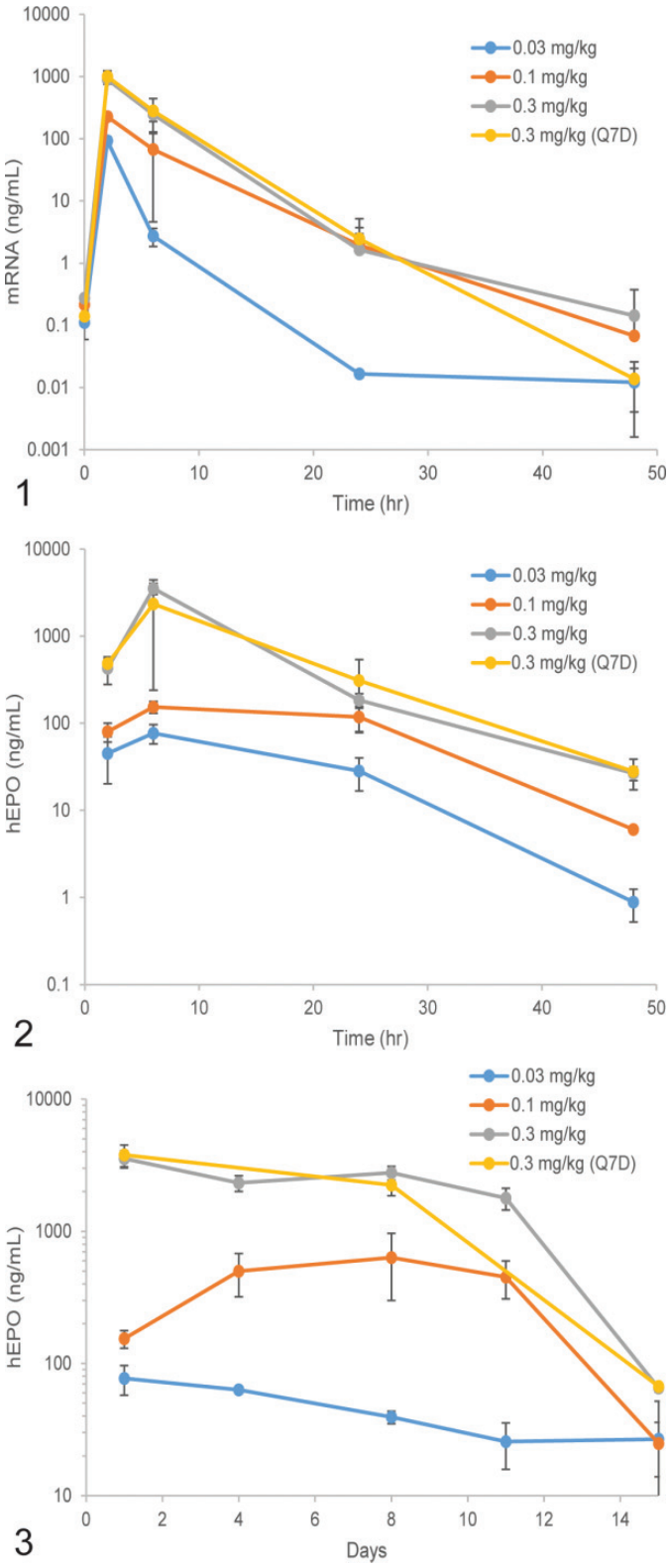

Figures 1–3. Plasma concentration of hEPO-mRNA (ng/ml; Fig. 1) and hEPO (ng/ml; Figs. 2, 3) in rats. Graphs represent mean values ($n = 6$); error bars indicate SD. Following a 10-minute infusion, peak plasma concentrations of hEPO-mRNA appear to occur at approximately 2 hours, while peak plasma concentrations of hEPO are approximately at 6 hours. Note that hEPO levels appear constant at all dose levels until day 15. hEPO, human erythropoietin; Q7D, 1 dose per week.

Table 3. Toxicokinetic Values for hEPO-mRNA in the Rat.[a]

Dose, mg/kg	$t_{1/2}$, h	Cmax, ng/ml	Cmax/Dose, ng/ml	AUC, h × ng/ml	AUC/Dose, h × ng/ml	Cl, ml/h/kg
0.03	5.7	92.6	3090	309	10,300	97.2
0.1	4.3	227	2270	1460	14,600	68.5
0.3	4	902	3010	5450	18,200	55.1
0.3[b]	2.9	995	3320	6120	20,400	49

Abbreviations: AUC, area under the curve; Cl, clearance; Cmax, maximum serum concentration; hEPO, human erythropoietin; $t_{1/2}$, half-life; Tmax, time to reach maximum serum concentration.
[a]Tmax per dose, 2 hours.
[b]One dose per week.

Table 4. Toxicokinetic Values for hEPO in the Rat.[a]

Dose, mg/kg	Cmax, ng/ml	AUC, h × ng/ml	$t_{1/2}$, h
0.03	77.1	1590	6.4
0.1	154	4480	8.7
0.3	3540	44 400	6.1
0.3[b]	2340	34 100	6.6

Abbreviations: AUC, area under the curve; Cmax, maximum serum concentration; hEPO, human erythropoietin; $t_{1/2}$, half-life; Tmax, time to reach maximum serum concentration.
[a]Tmax per dose, 6 hours.
[b]One dose per week.

hEPO increased in a dose-related manner after IV administration of 0.1 to 0.3 mg/kg/d of hEPO-mRNA in LNPs (Figs. 5, 6; Tables 5, 6). There was a notable difference in hEPO-mRNA exposure after the first dose between the groups administered 0.3 mg/kg twice and once per week, which could be due to the small sample size and large intragroup variability (Table 5). In addition, the results showed that hEPO-mRNA had a relatively long half-life (5.9–9.3 hours) and low clearance (9.03–27.0 ml/h/kg; Table 5). After a 60-minute infusion of hEPO-mRNA in LNPs, maximum plasma concentration of hEPO was estimated to occur between 6 and 24 hours (Table 6). The delay in estimated T_{max} observed in group 5 could be a consequence of

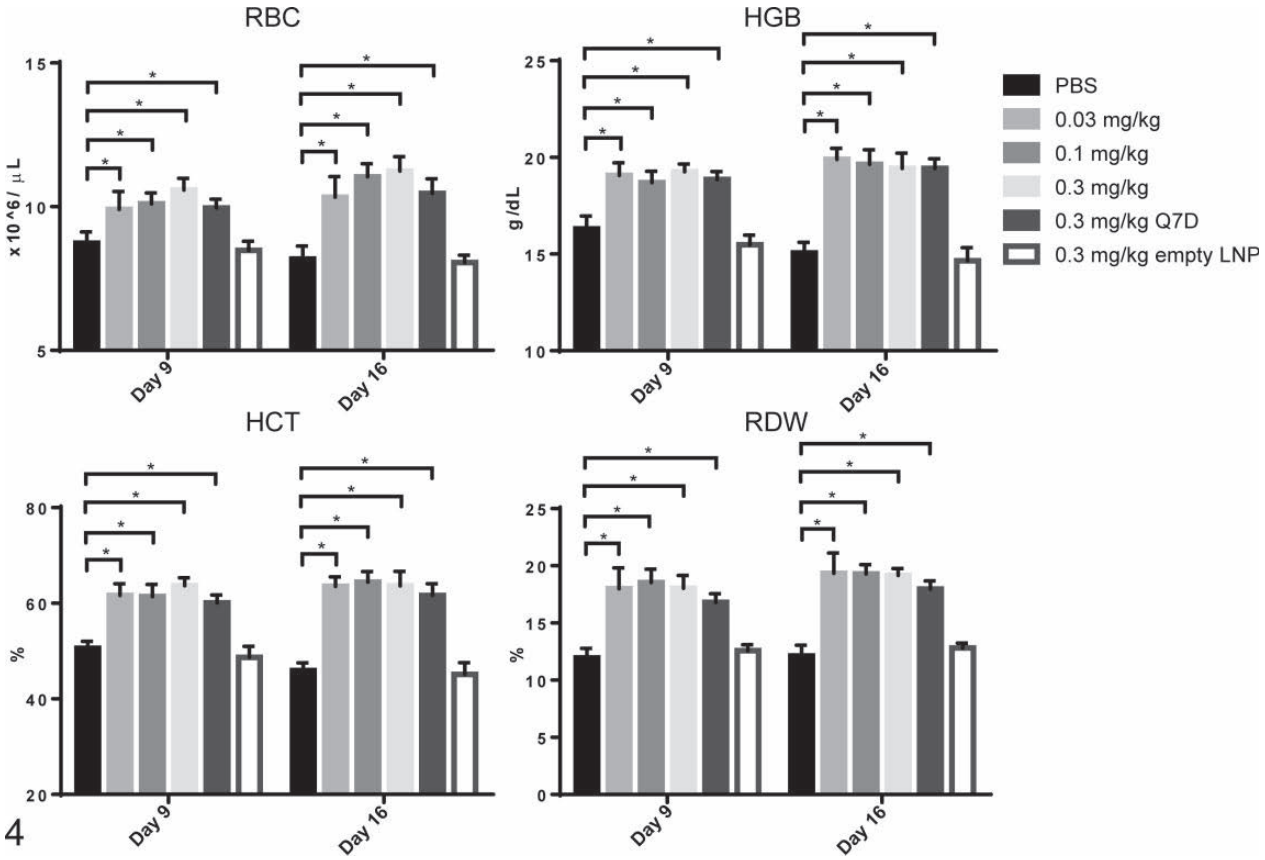

Figure 4. Red blood cell (RBC) mass parameters in rats: RBCs ($\times 10^6$ cells/µl), hemoglobin (HGB; g/dl), hematocrit (HCT; %), and erythrocyte distribution width (RDW; %). Graphs represent mean values ($n = 6$); error bars indicate SD. Ordinary one-way analysis of variance (multiple comparisons) was used to calculate the *P* values. *$P < .05$. LNP, lipid nanoparticle; PBS, phosphate-buffered saline; Q7D, 1 dose per week.

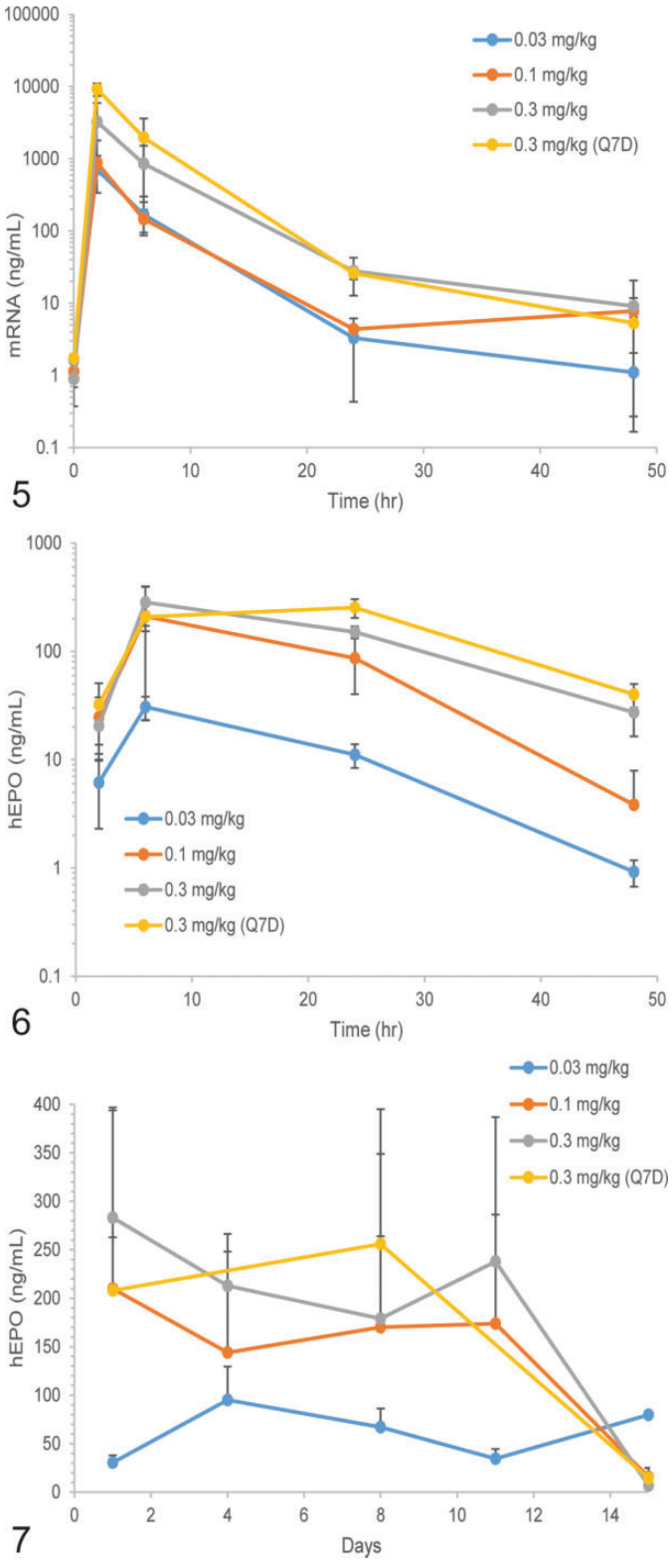

Figures 5–7. Plasma concentrations of hEPO-mRNA (ng/ml; Fig. 5) and hEPO (ng/ml; Figs. 6, 7) in monkeys. Graphs represent mean values ($n = 3$); error bars indicate SD. Following a 60-minute infusion, peak plasma concentrations of hEPO-mRNA appear to be at 2 hours, while peak plasma concentrations of hEPO are approximately at 6 hours. Note that hEPO levels appear relatively constant at all dose levels until day 15. hEPO, human erythropoietin; Q7D, 1 dose per week.

increased hEPO-mRNA exposure in this particular group or, as mentioned before, could be an artifact of high variability within that group. Also, as in male rats, serum hEPO concentrations at C_{max} were well maintained at all dose levels throughout the study until day 15, when measured hEPO levels significantly decreased in the mid- and high-dose groups (Fig. 7).

As expected, hEPO expression in monkeys led to significant changes in red blood cell mass. By day 8 of the study, absolute reticulocyte counts increased in all dose groups (Fig. 8). By the end of the study, a significant spike was noted in all other red blood cell parameters, such as absolute red blood cells, hematocrit, hemoglobin, and erythrocyte distribution width, whereas reticulocytes returned to baseline levels. Like in rats, the increases in red blood cell parameters were similar across all groups and did not seem to be dose related. These changes were not observed in the group dosed with empty LNPs.

Tolerability of hEPO-mRNA in LNPs in Male Rats

There were no notable clinical observations or body weights/food consumption changes in any group (data not shown). Slight changes were observed in coagulation parameters. Specifically, activated partial thromboplastin time was prolonged in all animals dosed with hEPO-mRNA in LNPs, and prothrombin time was prolonged in all animals dosed with hEPO-mRNA twice per week. In addition, fibrinogen levels were elevated for animals receiving 0.3 mg/kg of hEPO-mRNA once and twice per week (Suppl. Fig. 2).

Assessment of hematologic parameters on days 9 and 16 of the study indicated that white blood cells increased at doses $\geq$0.1 mg/kg of hEPO-mRNA in LNPs given twice weekly. Consistent with this, neutrophil, monocyte, and atypical lymphocyte counts were elevated across all groups dosed with hEPO-mRNA in LNPs. Interestingly, administration of hEPO-mRNA in LNPs once weekly or empty LNPs did not elicit the same increase in white blood cells (Fig. 9).

In addition, histamine release and serum levels of cytokines were evaluated. IP-10 was elevated 6 to 24 hours postdose on days 1 and 15 only in the groups dosed with 0.3 mg/kg of hEPO-mRNA in LNPs once and twice weekly (Fig. 10). No changes in IP-10 or histamine were seen in the group given empty LNPs (Fig. 10 and data not shown). No changes in other cytokines (IL-6, TNF-α, IFN-α) or complement (C3) were observed in any study group (data not shown).

Administration of hEPO-mRNA in LNPs at doses $\geq$0.03 mg/kg resulted in several macro- and microscopic findings in the spleen, bone marrow, liver, lungs, and stomach. Primary findings were considered to be related to increased hEPO expression and included an increase in extramedullary hematopoiesis in the spleen, liver, and bone marrow (Figs. 11–16).[1] In addition, macroscopic enlargement of the spleen was noted. These findings correspond to the hematologic changes (reticulocyte counts, red blood cells, and red cell mass parameters). Minimal hemorrhage in the lung and glandular stomach was noted at all doses of hEPO-mRNA in LNPs, which corresponds to macroscopic observations of dark foci in these tissues.

Table 5. Toxicokinetic Values for hEPO-mRNA in the Monkey.[a]

	Cmax, ng/mL			AUC, h × ng/ml			$t_{1/2}$, h		Cl, mL/h/kg	
Dose, mg/kg	Mean	SD	Mean Cmax/Dose, ng/mL	Mean	SD	Mean AUC/Dose, h × ng/ml	Mean	SD	Mean	SD
0.03	715	379	23 800	4090	1870	136 000	5.89	0.554	9.03	5.57
0.1	882	904	8820	4440	3140	44 400	9.31	8.12	27	13
0.3	3270	2620	10 900	19 900	15 400	66 300	6.99	1.22	21.3	12.8
0.3[b]	9240	1860	30 800	49 900	13 600	166 000	7.36	6.51	6.33	1.87

Abbreviations: AUC, area under the curve; Cl, clearance; Cmax, maximum serum concentration; hEPO, human erythropoietin; $t_{1/2}$, half-life; Tmax, time to reach maximum serum concentration.
[a]Mean Tmax per dose, 2 hours.
[b]One dose per week.

Table 6. Toxicokinetic Values for hEPO in the Monkey.

		Cmax, ng/ml		AUC, h × ng/ml	
Dose, mg/kg	Mean Tmax, h	Mean	SD	Mean	SD
0.03	6	30.6	7.42	600	39.8
0.1	6	210	187	4240	2530
0.3	6	283	111	6660	915
0.3[a]	24	253	49.4	8170	1550

Abbreviations: AUC, area under the curve; Cmax, maximum serum concentration; hEPO, human erythropoietin; Tmax, time to reach maximum serum concentration.
[a]One dose per week.

Additional findings observed in groups dosed with hEPO-mRNA in LNPs or empty LNPs included increased mononuclear cell infiltration and a minimal to moderate extent of single-cell necrosis in the liver at doses ≥0.1 mg/kg (Figs. 17, 18). At 0.3 mg/kg per dose of hEPO-mRNA, minimal to mild hypertrophy/hyperplasia of the sinusoidal endothelial cells was observed in the liver. These liver findings were accompanied with mild elevations in alanine aminotransferase (ALT) and aspartate aminotransferase (AST; Fig. 19). Overall, these data suggest that doses ≥0.1 mg/kg result in minor liver injury that seems to be primarily driven by the vehicle (LNPs).

Tolerability of hEPO-mRNA in LNPs in Female Monkey

There were no clinical signs or effects on body weights and food consumption related to hEPO-mRNA in LNPs (data not shown). Mild decreases in phosphorus and albumin levels were noted only in animals given 0.3 mg/kg of hEPO-mRNA in LNPs once or twice weekly (Suppl. Fig. 3) and were likely related to the mild proinflammatory changes observed.

There were no changes in leukocytes when compared with PBS in all groups throughout the duration of the study (data not shown). No significant changes in cytokine release (IL-1β, IL-6, TNF-α, IP-10) were observed (data not shown). However, complement activation (C3a, C5b-9) was detected in the mid- and high-dose groups given hEPO-mRNA in LNPs once and twice a week. The magnitude of complement change appears to increase with repeat dosing; significant changes were observed at 2 to 6 hours postdosing on day 1, 6 hours postdosing on day 4, and at 2 to 6 hours postdosing on day 15. By day 15 (2–6 hour postdosing), a mild but not statistically significant trend in complement activation was observed in all groups dosed with hEPO-mRNA in LNPs as well as empty LNPs (Fig. 20).

Macro- and microscopic pathology findings were minimal and mainly present in the heart and spleen. Minimal hemorrhage was noted in the heart at doses ≥0.1 mg/kg and was consistent with suprapharmacologic effects of hEPO.[1] Findings in the spleen were primarily related to administration of the drug product (hEPO-mRNA in LNPs) once weekly at 0.3 mg/kg and included minimal lymphoid depletion in the periarteriolar lymphoid sheaths in the white pulp of the spleen in 3 animals, as well as mild multifocal white pulp necrosis and decreased cellularity of the red pulp in only 1 animal (data not shown).

Discussion

The ability to deliver therapeutic levels of proteins with modified mRNA opens the door to potential life-saving therapies in various indications. The modified mRNA platform has the potential to enable the development of single as well as combination therapeutic agents. However, like siRNA, mRNA is a labile biological molecule and therefore requires the use of protective delivery systems to effectively harness its potential. Indeed, systemic administration of unformulated and unmodified RNA molecules leads to degradation by RNAses, rapid renal clearance, and potential stimulation of an immune response, resulting in very short half-lives (<5 minutes postdosing).[5,11,16,27] Therefore, LNPs were utilized in our studies to improve the PK profile and cellular uptake of mRNA.[10]

In our studies, plasma AUC of hEPO-mRNA increased in a dose-proportional manner in monkeys and in a greater-than-dose-proportional manner in rats. In addition, hEPO-mRNA had moderate to long half-life and relatively low clearance in both species. Finally, hEPO expression resulted in supratherapeutic levels (~100-fold the projected clinically efficacious dose) in rats and monkeys.[24] The protein produced had expected PK and PD properties ($t_{1/2}$) as evidenced by exaggerated pharmacologic effects associated with supratherapeutic

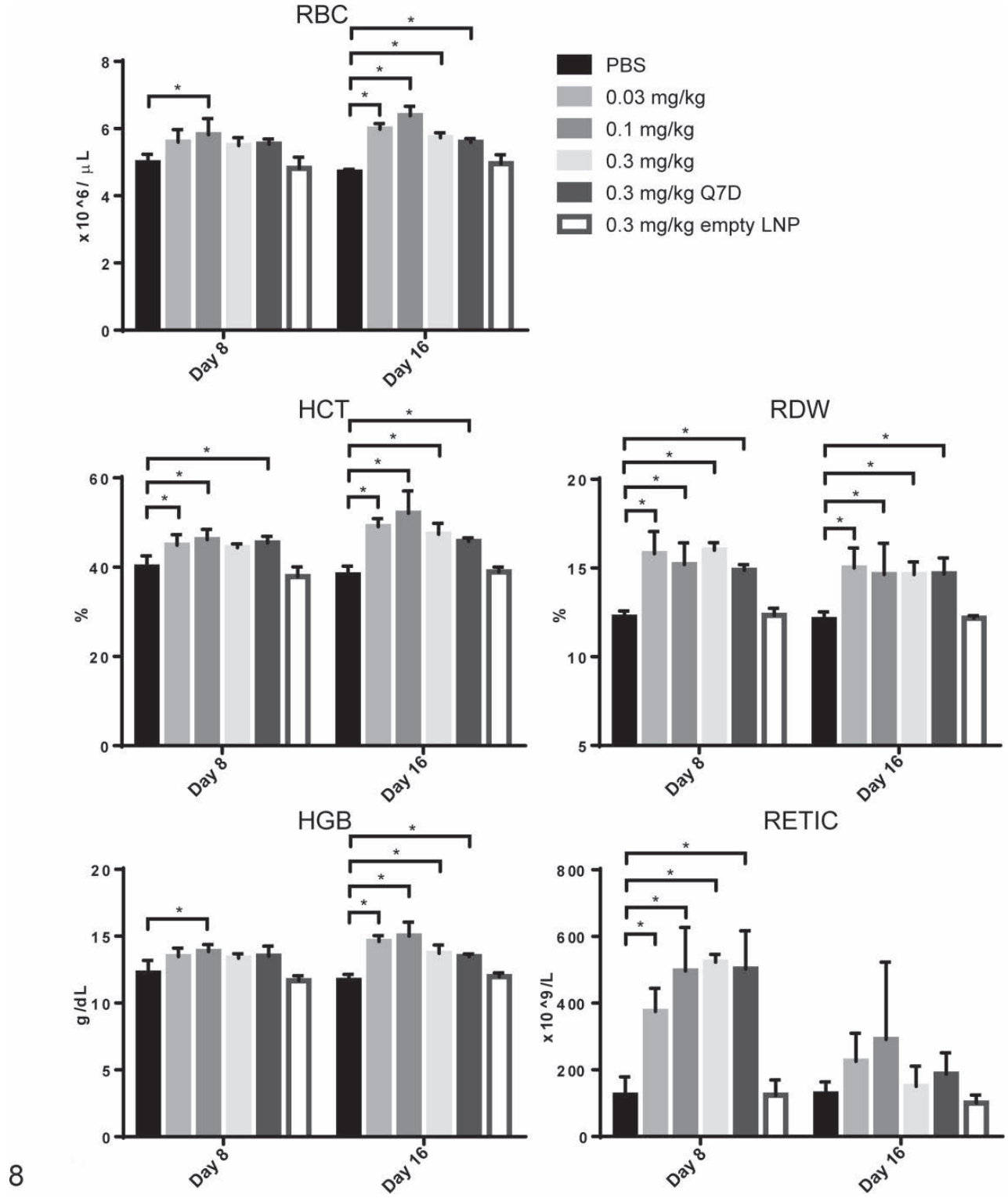

Figure 8. Red blood cell (RBC) mass parameters in monkeys: RBCs ($\times 10^6$ cells/µl), hemoglobin (HGB; g/dl), hematocrit (HCT; %), erythrocyte distribution width (RDW; %), and reticulocytes (RETIC; $\times 10^9$ cells/µl). Graphs represent mean values ($n = 3$); error bars indicate SD. Ordinary one-way analysis of variance (multiple comparisons) was used to calculate the *P* values. **P* < .05. LNP, lipid nanoparticle; PBS, phosphate-buffered saline; Q7D, 1 dose per week.

doses of hEPO observed in both species (increased red blood cell mass parameters; mild hemorrhages in the heart, stomach, and lungs; extramedullary hematopoiesis in the liver and spleen; and increased hematopoiesis in bone marrow). These data suggest that hEPO-mRNA (and putatively modified mRNA in general) administered in LNPs has acceptable

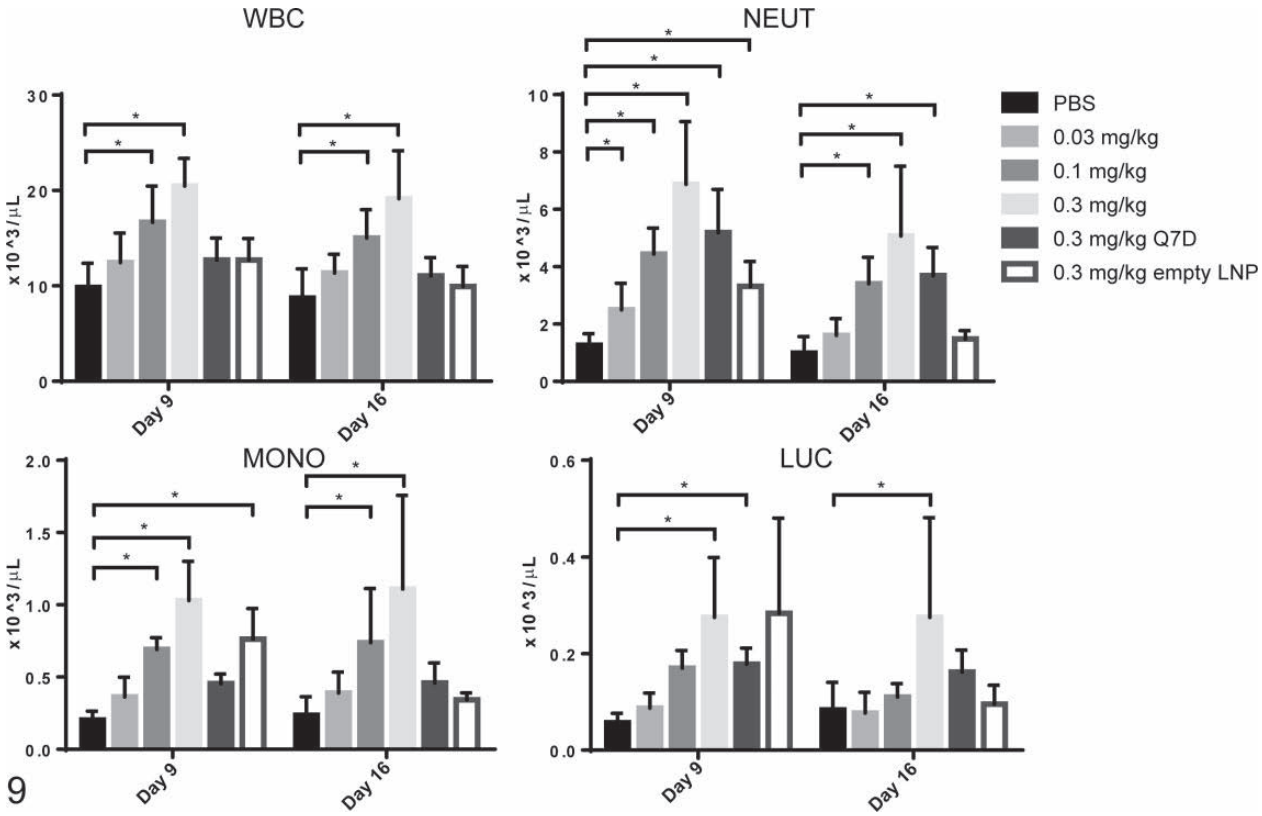

Figure 9. Leukocyte parameters in rats: white blood cells (WBC; $\times 10^3$ cells/µL), neutrophils (NEUT; $\times 10^3$ cells/µL), monocytes (MONO; $\times 10^3$/µL), and large unstained cells (LUC; $\times 10^3$/µL). Graphs represent mean values ($n = 6$); error bars indicate SD. Ordinary one-way analysis of variance (multiple comparisons) was used to calculate the *P* values. **P* < .05. LNP, lipid nanoparticle; PBS, phosphate-buffered saline; Q7D, 1 dose per week.

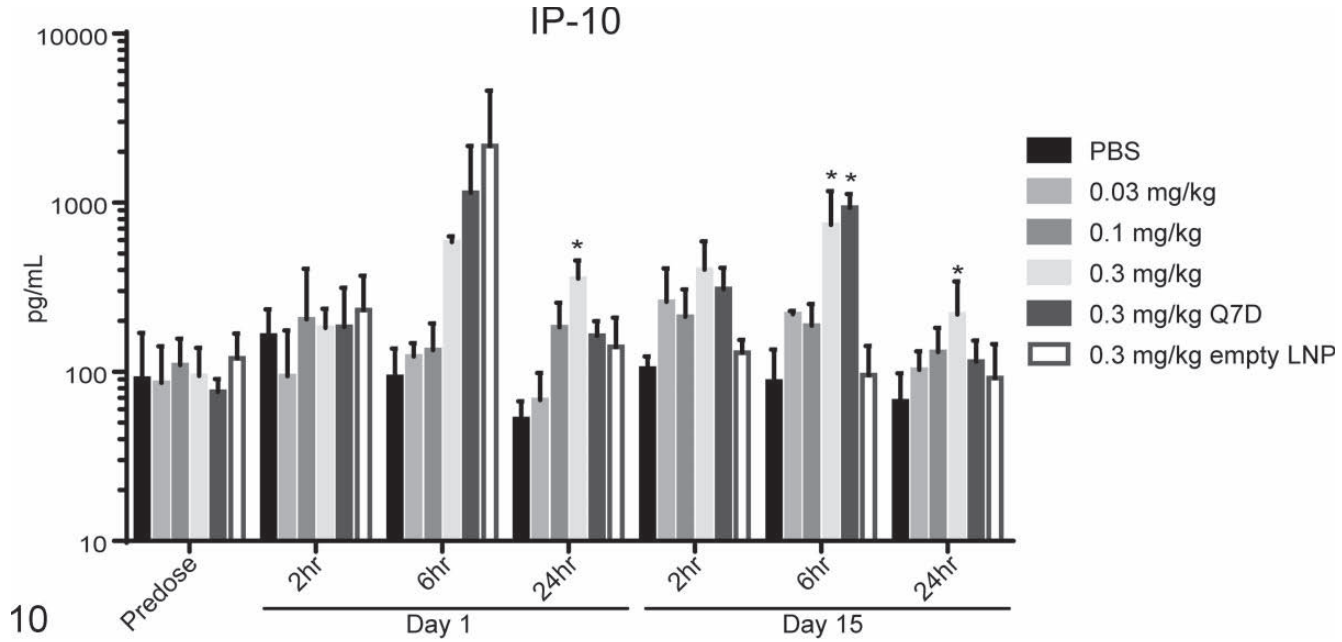

Figure 10. Plasma interferon γ–inducible protein 10 (IP-10) levels in rats. Graph represents mean values ($n = 6$); error bars indicate SD. Ordinary one-way analysis of variance (multiple comparisons) was used to calculate the *P* values. **P* < .05. LNP, lipid nanoparticle; PBS, phosphate-buffered saline; Q7D, 1 dose per week.

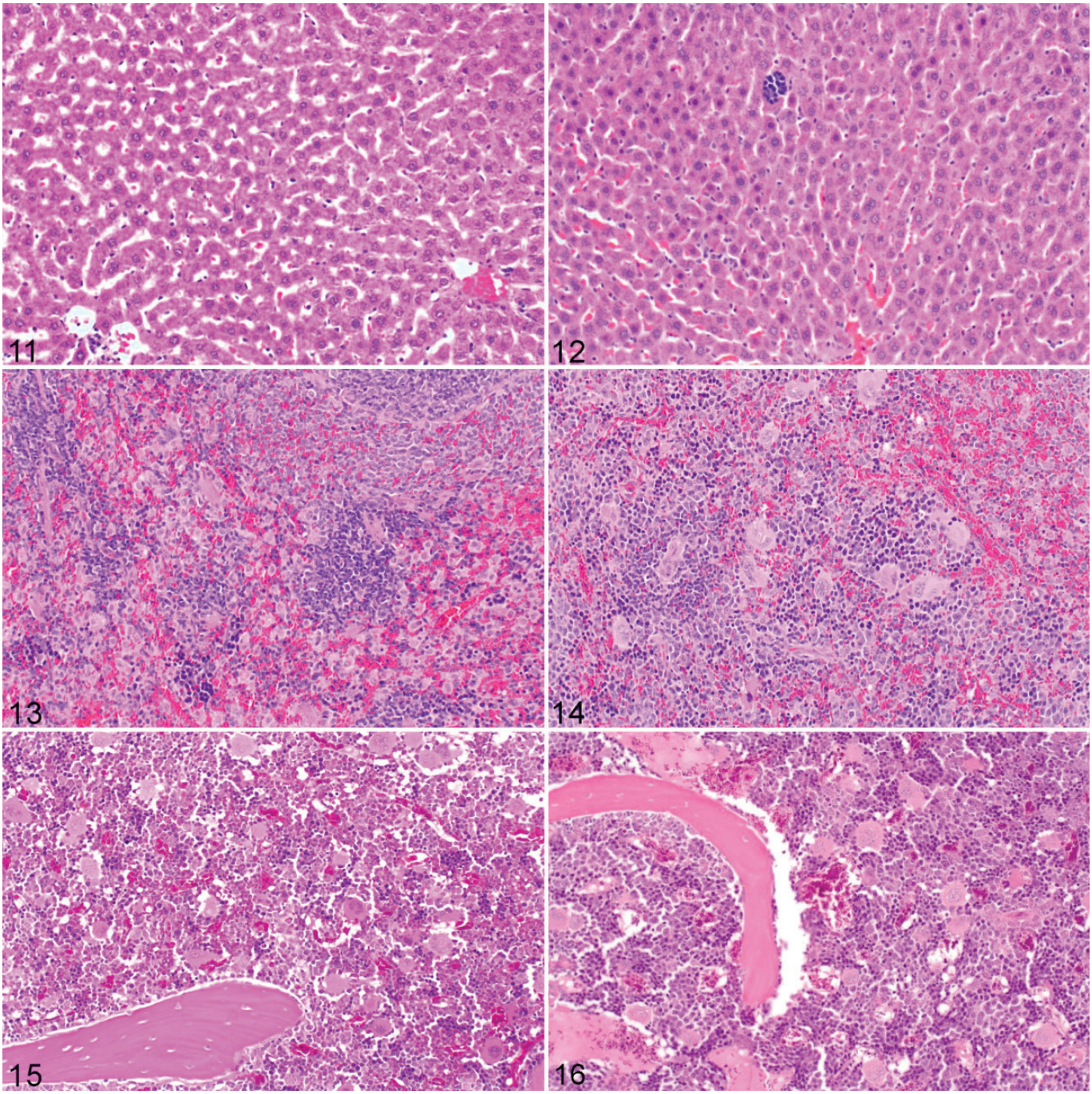

Figures 11–16. Histologic findings in control rats and in rats dosed with 0.3 mg/kg of hEPO-mRNA twice a week. Hematoxylin and eosin. **Figure 11.** Liver, control rat. **Figure 12.** Liver, rat dosed with hEPO-mRNA. There is extramedullary hematopoiesis. **Figure 13.** Spleen, control rat. **Figure 14.** Spleen, rat dosed with hEPO-mRNA. There is increased extramedullary hematopoiesis. **Figure 15.** Bone marrow (sternal), control rat. **Figure 16.** Bone marrow (sternal), rat dosed with hEPO-mRNA. There is increased hematopoiesis. hEPO, human erythropoietin.

properties for a drug product at least when administered over a 2-week period.

A marked decrease of the plasma concentration of hEPO was observed by day 15 in the mid- and high-dose groups in both species. This reduction in hEPO levels may have been mediated by antibodies against the expressed protein since animals were exposed to a nonhomologous protein.[4,8] To further investigate for the presence of antiprotein antibodies, we have subsequently developed appropriate bioanalytical methods, and the data collected from subsequent in vivo studies exploring the levels of species-specific anti-hEPO antibodies support this hypothesis (data not shown).

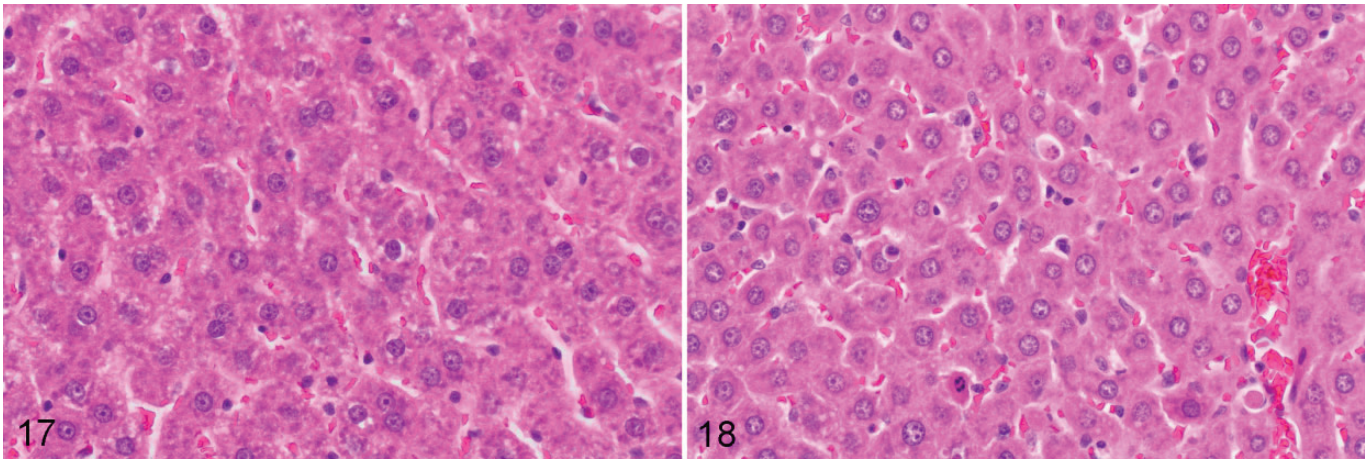

Figures 17 and 18. Histologic findings in control rat and in rat dosed with 0.3 mg/kg of empty lipid nanoparticles twice a week. **Figure 17.** Liver, control rat. **Figure 18.** Liver, rat dosed with empty empty lipid nanoparticles. There is single-cell necrosis of hepatocytes.

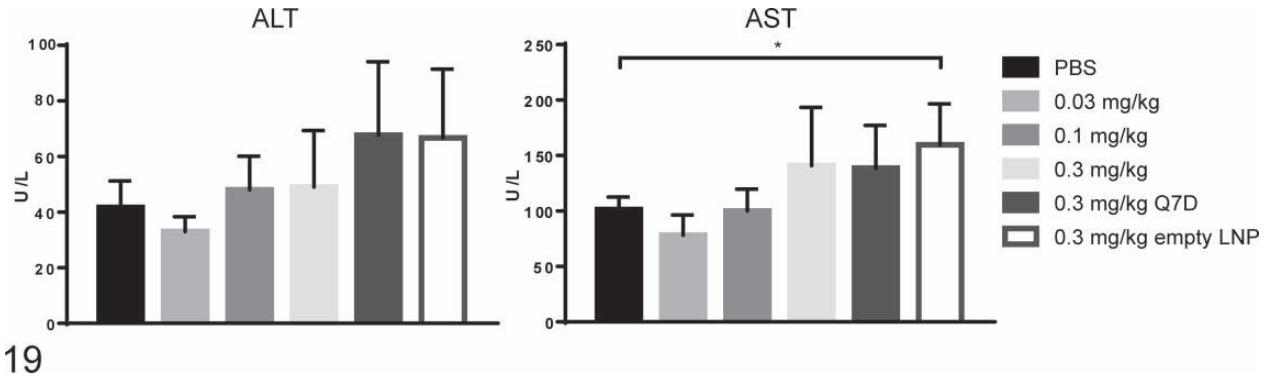

Figure 19. Serum levels of liver enzymes in rats. Graphs represent mean values ($n = 6$); error bars indicate SD. Ordinary one-way analysis of variance (multiple comparisons) was used to calculate the *P* values. *$P < .05$. ALT, alanine aminotransferase; AST, aspartate aminotransferase; LNP, lipid nanoparticle; PBS, phosphate-buffered saline; Q7D, 1 dose per week.

From a safety perspective, modified mRNA delivered in LNPs is a complex molecule that requires the assessment of safety of the delivery system (LNPs), mRNA, and the translated protein product. Overall, administration of 0.3 mg/kg of LNPs alone via IV infusion was well tolerated. In male rats, increases in neutrophils and monocytes were observed, and microscopic changes in liver were noted that correlated with mild and monitorable increases in liver enzymes (ALT and AST). In female monkeys, only minimal and transient complement activation was induced by LNPs alone. Similar changes have been reported for LNP vehicle.[3]

IV infusion of hEPO-mRNA in LNPs was well tolerated in both species. A mild and reversible proinflammatory profile was noted that consisted of elevations in IP-10 (rat) and detection of complement cleavage products (monkey). These findings correlated with slight changes in both species in terms of hematology parameters (white blood cell counts, lymphocytes, neutrophils, and monocytes) and coagulation parameters (activated partial thromboplastin time, prothrombin time, and fibrinogen), although more consistently observed in the rat. In the rat, liver microscopic changes with elevations of serum ALT and/or AST were similar to those observed in the group dosed with empty LNPs. In addition, changes in the spleen (depletion in the periarteriolar lymphoid sheaths and splenic necrosis) were observed in monkeys. These findings suggest that the administration of mRNA in LNPs at doses as high as 0.3 mg/kg per dose induces a mild to moderate and reversible proinflammatory response. Furthermore, it is evident that this immune activation can be mitigated by either lowering the dose or decreasing the frequency of dosing.

These findings (serum complement activation, cytokine elevation, and potential liver and spleen effects) are in agreement with those previously reported for LNPs loaded with siRNA in nonclinical and clinical studies.[3,6] Comparable toxicologic profiles of modified siRNA and mRNA in LNPs suggest that the toxicologic effects and possibly the distribution properties (primarily liver and monocyte phagocytic system) of the drug product are predominantly vehicle driven. Note that an empty LNP may have slightly different surface properties than the one loaded with mRNA; thus, small differences in magnitude or

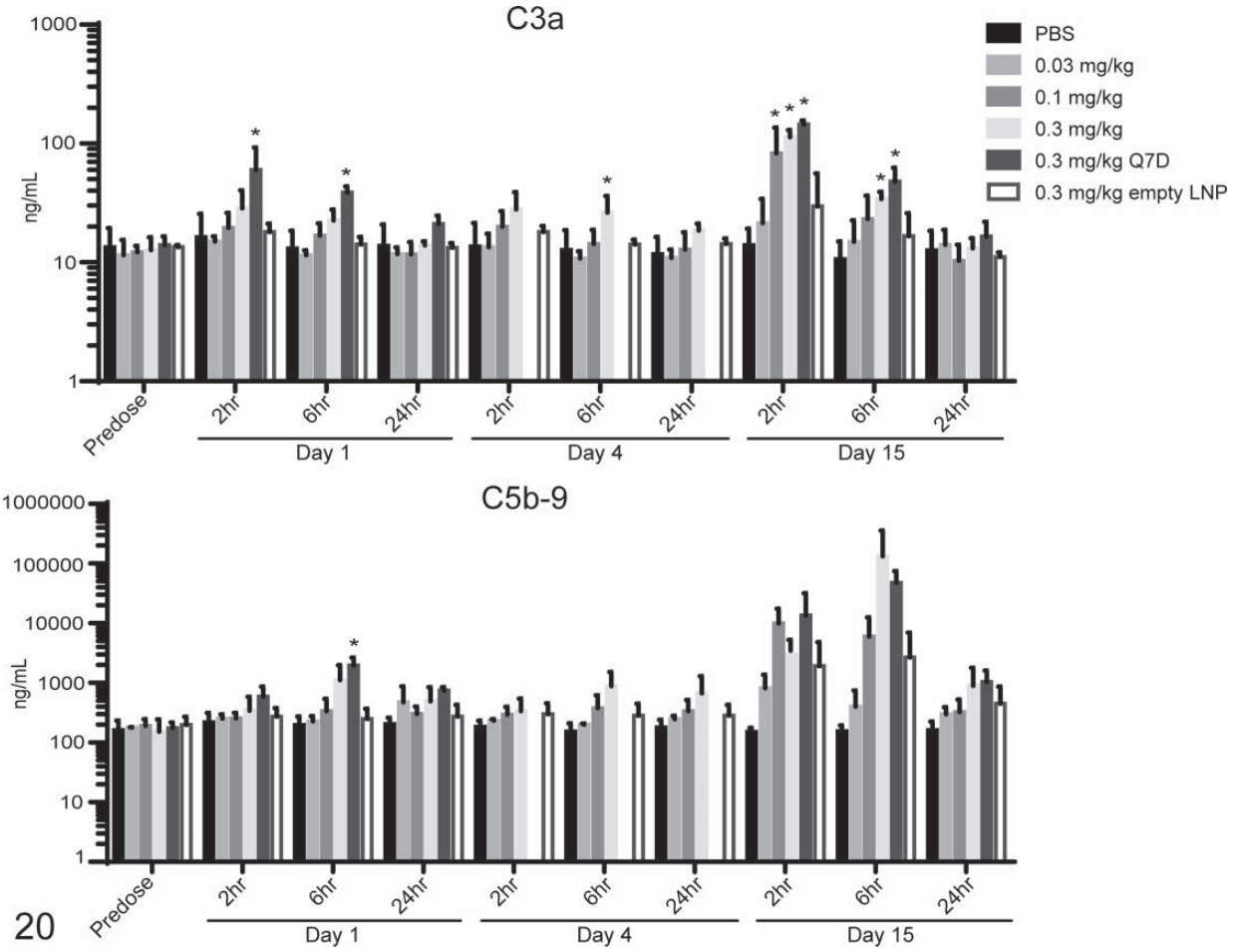

Figure 20. Plasma levels of complement components (C3a and C5b-9) in monkeys. Graphs represent mean values ($n = 3$); error bars indicate SD. Ordinary one-way analysis of variance (multiple comparisons) was used to calculate the *P* values. *$P < .05$. LNP, lipid nanoparticle; PBS, phosphate-buffered saline; Q7D, 1 dose per week.

effects may occur.[28] Therefore, a preferred control instead of the empty LNPs would be LNPs loaded with nonsense mRNA with equivalent base modifications.

In conclusion, the PK, PD, and toxicologic properties of modified mRNA loaded in LNPs are generally consistent between species. The primary toxicologic findings of hEPO-mRNA in LNPs are related to the supratherapeutic exposure to hEPO and inflammatory findings that are mainly LNP driven. Given the similarities in LNP-related toxicities between the rat and the monkey, it is likely that similar effects will translate to the clinic and be monitorable with the parameters identified in nonclinical species. Although the studies were not conducted to support advancement of a clinical candidate, they suggest that the mRNA-in-LNP approach might be feasible to safely deliver therapeutic levels of an exogenous protein. This would enable novel therapies for a variety of indications. Future work will be geared toward evaluating different routes of administration, the effects of chronic dosing, and the risk to juvenile animals, as juveniles may be particularly important in the setting of rare disease.

Acknowledgements

We thank everyone involved in execution, analysis, and discussion of these studies at Charles River Laboratories, Moderna, AxoLabs, and AstraZeneca.

Declaration of Conflicting Interests

The author(s) declared the following potential conflicts of interest with respect to the research, authorship, and/or publication of this article: All authors except Stefan J. Platz are employed by Moderna or were employed by Moderna at the time when these studies were conducted. Stefan J. Platz is employed by AstraZeneca, Moderna's collaborator on the project.

Funding

The author(s) received the following financial support for the research, authorship, and/or publication of this article: Moderna and AstraZeneca provided financing for this project.

References

1. Andrews DA, Boren BM, Turk JR, et al. Dose-related differences in the pharmacodynamic and toxicologic response to a novel hyperglycosylated analog of recombinant human erythropoietin in Sprague-Dawely rats with similarly high hematocrit. *Toxicol Pathol*. 2013;**42**(3):524–539.

2. Andries O, McCafferty S, DeSmedt SC, et al. N(1)-methylpseudouridine-incorporated mRNA outperforms pseudouridine-incorporated mRNA by providing enhanced protein expression and reduced immunogenicity in mammalian cell lines and mice. *J Control Release*. 2015;**217**:337–344.
3. Barros SA, Gollob JA. Safety profile of RNAi nanomedicines. *Adv Drug Deliv Rev*. 2012;**64**(15):1730–1737.
4. Casadevall N. Pure red cell aplasia and anti-erythropoietin antibodies in patient treated with epoetin. *Nephrol Dial Transplant*. 2003;**18**(8):viii37–viii41.
5. Christensen J, Litherland K, Faller T, et al. Biodistribution and metabolism studies of lipid nanoparticle-formulated internally [^{3} H]-labeled siRNA in mice. *Drug Metab Dispos*. 2014;**42**(3):431–440.
6. Coelho T, Adams D, Silva A, et al. Safety and efficacy of RNAi therapy for transthyretin amyloidosis. *N Engl J Med*. 2013;**369**(9):819–829.
7. Desmet CJ, Ishii KJ. Nucleic acid sensing at the interface between innate and adapted immunity in vaccination. *Nat Rev Immunol*. 2012;**12**(7): 479–491.
8. Frost H. Antibody-mediated side effects of recombinant proteins. *Toxicology*. 2005;**209**(2):155–160.
9. Geall AJ, Verma A, Otten GR, et al. Nonviral delivery of self-amplifying RNA vaccines. *Proc Natl Acad Sci U S A*. 2012;**109**(36):14604–14609.
10. Gilleron J, Querbes W, Zeigerer A, et al. Image-based analysis of lipid nanoparticle-mediated siRNA delivery, intracellular trafficking and endosomal escape. *Nat Biotechnol*. 2013;**31**(7):638–646.
11. Gilmore IR, Fox SP, Hollins AJ, et al. Delivery strategies for siRNA-mediated gene silencing. *Curr Drug Deliv*. 2006;**3**(2):147–155.
12. Islam MA, Reesor EK, Xu Y, et al. Biomaterials for mRNA delivery. *Biomater Sci*. 2015;**3**(12):1519–1533.
13. Jeffs LB, Palmer LR, Ambegia EG, et al. A scalable, extrusion-free method for efficient liposomal encapsulation of plasmid DNA. *Pharm Res*. 2005;**22**(3): 362–372.
14. Kariko K, Buckstein M, Ni H, et al. Suppression of RNA recognition by Toll-like receptors: the impact of nucleoside modification and the evolutionary origin of RNA. *Immunity*. 2005;**23**(2):165–175.
15. Kariko K, Muramatsu H, Keller JM, et al. Increased erythropoiesis in mice injected with submicrogram quantities of pseudouridine-containing mRNA encoding erythropoietin. *Mol Ther*. 2012;**20**(5):948–953.
16. Kormann MS, Hasenpusch G, Aneja MK, et al. Expression of therapeutic proteins after delivery of chemically modified mRNA in mice. *Nat Biothechnol*. 2011;**29**(2):154–157.
17. Leader B, Baca QJ, Golan DE. Protein therapeutics: a summary and pharmacological classification. *Nat Rev Drug Discov*. 2008;**7**(1):21–39.
18. Martins R, Queiroz JA, Sousa F. Ribonucleic acid purification. *J Chromatogr A*. 2014;**1355**:1–14.
19. Pardi N, Tuyishime S, Muramatsu H, et al. Expression kinetics of nucleoside-modified mRNA delivered in lipid nanoparticles to mice by various routes. *J Control Release*. 2015;**217**:345–351.
20. Rozenski J, Crain PF, McCloskey JA. The RNA modifications database: 1999 update. *Nucleic Acids Res*. 1999;**27**(1):196–197.
21. Sahin U, Kariko K, Tureci O. mRNA-based therapeutics—developing a new class of drugs. *Nat Rev Drug Discov*. 2014;**13**(10):759–780.
22. Semple SC, Akinc A, Chen J, et al. Rational design of cationic lipids for siRNA delivery. *Nat Biotechnol*. 2010;**28**(2):172–176.
23. Shatkin AJ. Capping of eukaryotic mRNAs. *Cell*. 1976;**9**(4, pt 2):645–653.
24. Sörgel F, Thyroff-Friesinger U, Vetter A, et al. Bioequivalence of HX575 (recombinant human epoetin alfa) and a comparator epoetin alfa after multiple intravenous administrations: an open-label randomized controlled trial. *BMC Clin Pharmacol*. 2009;**9**:10.
25. Thess A, Grund S, Mui BL, et al. Sequence-engineered mRNA without chemical nucleoside modifications enables an effective protein therapy in large animals. *Mol Ther*. 2015;**23**(9):1456–1464.
26. Tsongalis GJ. Branched DNA technology in molecular diagnostics. *Am J Clin Pathol*. 2006;**126**(3):448–453.
27. Wang Y, Su H, Yang Y, et al. Systemic delivery of modified mRNA encoding herpes simplex virus 1 thymidine kinase for targeted cancer gene therapy. *Mol Ther*. 2013;**21**(2):358–367.
28. Xue HY, Guo P, Wen WC, et al. Lipid-based nanocarriers for RNA delivery. *Curr Pharm Des*. 2015;**21**(22):3140–3147.
29. Zangi L, Lui KO, von Gise A, et al. Modified mRNA directs the fate of heart progenitor cells and induces vascular regeneration after myocardial infarction. *Nat Biotechnol*. 2013;**31**(10):898–907.
30. Zimmermann TS, Lee AC, Akinc A, et al. RNAi-mediated gene silencing in non-human primates. *Nature*. 2006;**441**(7089):111–114.

Toxicologic Pathology
2020, Vol. 48(2) 257-276

DOI: 10.1177/0192623319875085
journals.sagepub.com/home/tpx
SAGE

*This Points to Consider article is a product of a Society of Toxicologic Pathology (STP) Working Group commissioned by the Scientific and Regulatory Policy Committee (SRPC) of the STP. It has been reviewed and approved by the SRPC and Executive Committee of the STP but does not represent a formal best practice recommendation. The views expressed in this article are those of the authors and do not necessarily represent the policies, positions, or opinions of their respective agencies and organizations. Readers of Toxicologic Pathology are encouraged to send their thoughts on these articles or ideas for new topics to the editor.

Scientific and Regulatory Policy Committee Points to Consider*: Approaches to the Conduct and Interpretation of Vaccine Safety Studies for Clinical and Anatomic Pathologists

Rani S. Sellers[1], Keith Nelson[2], Bindu Bennet[3], Jayanthi Wolf[4], Niraj Tripathi[5], Ronnie Chamanza[6], Marie-France Perron Lepage[7], Karissa Adkins[8], Sebastien Laurent[9], and Sean P. Troth[4]

Abstract

The design and execution of toxicology studies supporting vaccine development have some unique considerations relative to those supporting traditional small molecules and biologics. A working group of the Society of Toxicologic Pathology Scientific and Regulatory Policy Committee conducted a review of the scientific, technical, and regulatory considerations for veterinary pathologists and toxicologists related to the design and evaluation of regulatory toxicology studies supporting vaccine clinical trials. Much of the information in this document focuses on the development of prophylactic vaccines for infectious agents. Many of these considerations also apply to therapeutic vaccine development (such as vaccines directed against cancer epitopes); important differences will be identified in various sections as appropriate. The topics addressed in this *Points to Consider* article include regulatory guidelines for nonclinical vaccine studies, study design (including species selection), technical considerations in dosing and injection site collection, study end point evaluation, and data interpretation. The intent of this publication is to share learnings related to nonclinical studies to support vaccine development to help others as they move into this therapeutic area.

Keywords

vaccine, regulatory toxicology, species selection, injection site, adjuvant, vaccine study design

Introduction

The development and use of vaccines have evolved substantially since Edward Jenner first used exudate from cowpox lesions to inoculate people against smallpox. The underlying concept for vaccine development, however, is essentially the same today as it was then: expose people to an antigen to prime development of protective immunity against disease. Vaccines may be prophylactic or therapeutic. Prophylactic vaccine development is different from traditional drug development, as the target is a foreign protein that should have no or very little homology to human- or animal-expressed proteins. Therapeutic vaccines, in contrast, typically target endogenous proteins or neoantigens to cure existing disease, and as such have

[1] Pfizer Inc, Pearl River, New York, NY, USA
[2] Charles River Laboratories, Mattawan, MI, USA
[3] Janssen Research & Development LLC, Spring House, PA, USA
[4] Merck & Co, Inc, West Point, PA, USA
[5] Covance, Madison, WI, USA
[6] Janssen Pharmaceutical Companies of Johnson & Johnson, Beerse, Belgium
[7] Charles River Laboratories, St-Germain-Nuelles, France
[8] Sanofi US, Framingham, MA, USA
[9] Sanofi R&D, Preclinical Safety Department, Montpellier, France

Corresponding Author:
Rani S. Sellers, Drug Safety Research & Development, Pfizer Inc, 401 North Middletown Road, Pearl River, New York, NY 10965, USA.
Email: rani.sellers@pfizer.com

some different nonclinical considerations. Several therapeutic vaccines are currently being or have been investigated for potential treatment of a diverse number of diseases such as Alzheimer disease, Parkinson disease, and multiple types of cancer.[1–3] Vaccines are being developed using a wide variety of modalities, and formulations/therapies may include adjuvants or other immunological modulators to promote the desired immune response.

Regulatory toxicology studies in support of vaccine clinical trials incorporate similar design elements to standard small molecule and biotherapeutic toxicity studies, with inclusion of additional points intended to evaluate acute phase and immunogenic responses to the vaccine antigens. With respect to pathology, regulatory toxicology studies for vaccines share many of the same fundamental points as routine toxicology studies, such as macroscopic and microscopic observations, organ weights, and clinical pathology parameters. However, there are considerations that the pathologist involved in vaccine development programs should be aware of to help guide protocol development, tissue collection, and study interpretation. Specifically, these include species selection, route of administration, nonantigen vaccine components, coadministered compounds such as adjuvants, the use of devices or techniques for accurate dose administration and draining lymph node and injection site tissue collection. In addition to the standard toxicology studies conducted for vaccines, other studies such as neurovirulence, biodistribution, or environmental risk (eg, livestock transmission) studies may be required depending on the vaccine modality and indication, and veterinary pathologists may be involved in study design and interpretation of study data as well. A host of other studies may be conducted for vaccines, and pathologists may be enlisted to provide support.

The purpose of this article is to serve as a "Points to Consider" document for toxicologic pathologists in vaccine development and includes practical information to help guide pathologists in the conduct of these studies. The focus of the discussions here is related to the development of vaccines for human use. Although regulatory aspects differ slightly, the same principles and practices described here could be applied to vaccines being developed for veterinary use.

Regulatory Guidelines for the Nonclinical Safety Assessment of Vaccines and Adjuvants

Until the 1990s, there was little regulatory guidance on vaccine development. The first comprehensive nonclinical pharmacology and toxicology prophylactic vaccine regulatory guideline was issued in 1997 by the European Medicines Agency (EMA),[4] which has subsequently been replaced by World Health Organization (WHO) guidance documents on assessment of vaccine safety.[5] Guidelines specifically addressing the use of adjuvants in vaccines include a WHO guidance[6] (2014) and an EMA guidance (2005).[7] The Food and Drug Administration (FDA) defers to the WHO guidelines for the development of prophylactic vaccines intended to protect against microbial disease. The WHO guidance documents guide the nonclinical development of vaccines for many countries, although additional studies on vaccine safety may be expected in some countries. There are several disease-specific vaccine guidances that should be referred to for certain indications (eg, dengue, Ebola, HIV).[8–10] There are no International Council for Harmonisation of Technical Requirements for Pharmaceuticals for Human Use guidances specifically for vaccine development and nonclinical safety assessment. It is important to note that regulatory expectations for vaccine development are evolving, and for these reasons, vaccine developers and producers need to keep apprised of current global regulatory requirements to meet regulatory expectations for marketing approval worldwide. Regulatory guidance in the development of therapeutic vaccines is currently limited and includes US FDA's "Clinical Considerations for Therapeutic Cancer Vaccines"[11] and EMA's "Guideline on the evaluation of anticancer medicinal products in man."[12] Although these guidelines focus primarily on clinical development, they briefly include considerations for nonclinical studies.

Regulatory requirements may vary depending on the nature of the vaccine (eg, peptide, conjugate, nucleic acid, viral vector, live virus); its components including the presence of adjuvants, adsorbants, or other; and the intended target population. Specific guidelines (general list can be found in Table 1) should be referred to when designing nonclinical studies for new vaccine candidates. Most prophylactic vaccines require only 1 repeat-dose toxicology study in a single species, which is generally expected to include a recovery arm to assess the reversibility and to detect any delayed toxicity, such as a delayed immune response. Regulatory requirements to support administration in humans are similar to those for other biopharmaceuticals, with some exceptions (Table 2). Generally, standalone single-dose toxicity and safety pharmacology studies prior to clinical studies are not required for vaccines (with the exception Japanese regulatory authorities, which presently do ask for safety pharmacology assessments for vaccines). If it is determined that such studies are necessary, it is generally sufficient to assess these effects within the repeat-dose toxicology study supporting the first-in-human clinical trial. Additionally, nucleic acid–based vaccines using DNA or RNA vectors will likely require biodistribution and possibly persistence studies and may require other safety studies, for example, neurovirulence in the case of potentially neurotropic live virus constructs. For additional information, the reader is referred to the many excellent reviews published on vaccine study design and regulatory considerations.[13–17]

Therapeutic vaccines are a heterogeneous class of vaccines that contain immunogenic substances capable of inducing antigen-specific, active (humoral or cell-mediated) immunity for use in treating a number of diverse diseases (eg, Alzheimer disease, Parkinson disease, multiple types of cancer).[1] Therapeutic vaccine regimens may include administration of active components that modulate the immune system, such as programmed cell death protein-1 and programmed death ligand-1 (PD-1/PDL-1) inhibitors, cytotoxic T-lymphocyte associated

Table 1. Selected Regulatory Guidelines for Vaccines.

Vaccine Type[a]	Guideline
All vaccines	World Health Organization (WHO): Guidelines on nonclinical evaluation of vaccines (WHO, 2005)
All adjuvanted vaccines	WHO: Guidelines on the nonclinical evaluation of vaccine adjuvants and adjuvanted vaccines (WHO, 2013) European Medicines Agency (EMA): Guideline on adjuvants in vaccines for human use (EMA, 2005)
Prophylactic vaccines (country-specific examples)	Ministry of Health, Labour and Welfare (MHLW), Japan: Guideline for nonclinical studies of vaccines for preventing infectious diseases (MHLW, 2010) State Food and Drug Administration (SFDA), China: Technical guidelines for preclinical research on preventive vaccines (SFDA, 2010)
Vaccines for women of childbearing potential and pregnant women	US Food and Drug Administration (US FDA): Guidance for industry: considerations for developmental toxicology studies for preventative and therapeutic vaccines for infectious disease indications (FDA, 2006) International Council for Harmonisation (ICH) S5: Detection of toxicity to reproduction for human pharmaceuticals is currently being revised (R3, Step 2, 2017)
DNA vaccines	US FDA: Guidance for industry: considerations for plasmid DNA vaccines for infectious disease indications (FDA, 2007) WHO: Guidelines for assuring the quality and nonclinical safety evaluation of DNA vaccines (WHO, 2005)
Viral-vectored vaccines	EMA: Guideline on quality, nonclinical, and clinical aspects of live recombinant viral vectored vaccines (EMA, 2010) FDA: Characterization and qualification of cell substrates and other biological materials used in the production of viral vaccines for infectious disease indications (FDA, 2010)
Recombinant protein/peptide vaccines	US FDA: Points to consider in the production and testing of new drugs and biologicals produced by recombinant DNA technology (FDA, 1985) ICH S6 and ICH S6 (R1): Preclinical safety evaluation of biotechnology-derived pharmaceuticals (ICH, 1997; ICH, 2011)
Combination vaccines	EMA: Note for guidance on pharmaceutical and biological aspects of combined vaccines (EMA, 1998) US FDA: Guidance for industry for the evaluation of combination vaccines for preventable diseases production, testing, and clinical studies (FDA, 1997)
Therapeutic cancer vaccines	US FDA: Clinical considerations for therapeutic cancer vaccines (FDA, 2011) EMA: Guideline on the evaluation of anticancer medicinal products in man (EMA, 2013)

Abbreviations: EMA, European Medicines Agency; FDA, Food and Drug Administration; ICH, International Council for Harmonisation; WHO, World Health Organization.
[a]Disease-specific and oncolytic vaccine guidelines are not included in this table, but should be consulted.

protein 4 (CTLA-4) inhibitors, and tyrosine kinase inhibitors. Inclusion of these components is essential for overcoming tolerance to self-antigens, which would prevent elicitation of the immune response needed for a therapeutic effect. Any active components should have a complete safety package to support the route of administration, dose, and so on. Additionally, devices intended for clinical administration of vaccines must have an adequate safety package for submission to the FDA (and subject to device-specific guidelines), and the pathologist may or may not be involved in the evaluation of these devices.

Adjuvants

Many vaccine formulations contain adjuvants. Adjuvants used in conjunction with a vaccine antigen may increase or prolong an immune response, retain an antigen at the site of injection, and/or modulate the type of immune response to the antigen (Th1 vs Th2) to enhance the success of the vaccine.[6,18–20] Although adjuvants have an immune-stimulatory effect, regulatory authorities in the United States and European Union do not consider them to be active components of the formulation. Instead, they are considered vaccine constituents as described

Table 2. Types of Studies Performed for Different Modalities.

Study Type	Vaccine	Small Molecule	Biologic	Biosimilar
In vivo safety pharmacology	Not required. Safety pharmacology end points within repeat-dose toxicology study in large animal species may be included	Stand-alone studies in 2 species	CV telemetry in single relevant species	Generally not performed
In vitro (*hERG*) electrophysiology	Not performed	Performed	Generally not performed (depends on target)	Generally not performed
Genotoxicology studies	Generally not performed (exception may be novel adjuvants)	Performed (unless no cause for concern based on structure)	Generally not performed	Generally not performed
Carcinogenicity studies	Not performed (tumorigenicity for novel production cell lines)	Performed	Generally not performed	Generally not performed
Repeat-dose toxicity	Single species; immunogenicity assessed	Two species	Single species; immunogenicity assessed	Either not needed or limited evaluation
DART	Single species	Two species	Single species	Generally not performed
Juvenile toxicology studies	Generally not performed	Performed only if relevant for the proposed indication	Performed only if relevant for the proposed indication	Generally not performed
Other	Biodistribution and persistence for nucleic acid and viral-vector–based vaccines as needed; neurovirulence studies (for neurotropic viruses on a case-by-case basis)	NA	Tissue cross-reactivity for monoclonal antibodies	NA

Abbreviations: CV, cardiovascular; DART, developmental and reproductive toxicity; hERG, human Ether-à-go-go-Related Gene; NA, not applicable.

in the Code of Federal Regulations (US 21CFR 610.15 (USCFR [2015]). Established adjuvants include those that are used in marketed vaccines, of which the most common are the aluminum salts (eg, aluminum hydroxide, aluminum phosphate, potassium aluminum sulfate) that have been in many products and have decades of safety information. In contrast, novel adjuvants are those that have a limited safety database and/or are not yet used in marketed products. It should be noted that there is not complete uniformity in the regulatory expectations for novel adjuvants between the EMA and WHO guidelines. The EMA Guideline on Adjuvants in Vaccines for Human Use recommends that adjuvants be tested alone in 2 species (rodent and nonrodent) unless otherwise justified, whereas the WHO guidelines indicate that including an adjuvant alone arm in the repeat-dose toxicology study in single species is generally acceptable. Therefore, decisions around species selection for adjuvanted vaccines may require scientific discussion with regulatory authorities. There are several adjuvants that were initially developed as novel adjuvants (eg, MF59 [Fluad], AS01B [Shingrix], CpG [22-mer ODN 1018 ISS] [Heplisav-B]), but which are now in approved products and have postapproval safety data.

Vaccine Study Design

Considerations for the design of nonclinical studies for vaccines include species selection, dose selection, and dosing regimen and may be different between therapeutic and prophylactic vaccines. In addition, the components of the vaccine should reflect the anticipated clinical doses and administration routes. Any specialized equipment for vaccine delivery (eg, electroporation units, microneedles) in nonclinical studies should, as closely as possible, match the device intended for clinical use. However, there may be equipment limitations due to the small body size of some nonclinical species.

Species Selection

The key criterion for species selection in vaccine toxicity testing is a demonstrable immune response to the administered antigen(s). The WHO guidelines[5] specify that the animal species should develop "an immune response similar to the expected human response after vaccination." However, this may not be feasible as even in nonhuman primates (NHP) the immune response does not necessarily translate to that of humans[21] and the immune response need not necessarily reflect the type of immune response anticipated in humans (eg, a humoral response may be assessed even if the vaccine elicits a cellular response). The WHO guidelines[5] also suggest that the chosen animal species ideally "be sensitive to the pathogenic organism or toxin under consideration." Presumably, this is a consideration for modified live viruses, which may revert to a more virulent form or inactivated viruses that may be incompletely inactivated. Selecting a species that is susceptible to the pathogen or reflects the course of infection in humans may be difficult. Therefore, in practical terms, demonstrable

immunogenicity to the vaccine (antigen) is accepted for most vaccine toxicology studies.

The rat and rabbit are the most commonly used species for vaccine studies, as their small size is cost-effective and they both tend to generate immune responses to administered vaccine antigens. Other laboratory animal species such as mice, guinea pigs, ferrets,[22] NHP, dogs, and minipigs[23] are also used both in vaccine toxicology studies and as nonclinical models for vaccine development. For therapeutic cancer vaccines, the choice of the appropriate species for evaluation is often on a case-by-case basis with consideration of antigen sequence homology versus endogenous human proteins and pharmacologic activity of coadministered materials (eg, CTLA-4 and/or PD-1/PDL1 antagonists).[24] Specific considerations for the various test species for vaccine toxicology studies are included below.

Rabbits

The rabbit has been the traditional species for vaccine toxicology studies, as they tend to generate a robust immune response to administered antigens. Their larger size also allows for administration of the full human dose/dose volume (typically 0.5 mL) into a single intramuscular (IM) site, and their blood volume permits a greater number of repeated blood samplings than from rodents.[25] The disadvantages of using the rabbit can include less familiarity of necropsy staff and pathologists with rabbit anatomy, a paucity of publications on background pathology findings in rabbits, a limited historical control database (HCD), housing costs, and the current lack of a standardized system of nomenclature, tissue sampling, and trimming guidelines for rabbit. The forthcoming International Harmonization of Nomenclature and Diagnostic Criteria publication on neoplastic and non-neoplastic findings in rabbits will substantially improve consistency in nomenclature and pathology findings in this species. Rabbits have also been reported to have a limited immune response to adjuvants that trigger a toll-like receptor-9 (TLR9) response in mice and humans, such as CpG oligodinucleotides (ODN).[26] Therefore, the rabbit may not be an ideal toxicology species for vaccine formulations that contain CpG ODN. A recent publication also suggested that stress in rabbits may lead to inflammation in the heart, which may confound study interpretations.[27] For these reasons, some companies have transitioned to using the rat as their primary toxicology species for vaccine studies.

Rats

Rats are small and easy to handle, have relatively low housing costs, and do not require specialized training for necropsy. In addition, the rat anatomy is well understood by most technicians, and tissue trimming guides are readily available. For the pathologist, the advantages of the rat include a well-harmonized and standardized nomenclature[28] and a more ubiquitous understanding of background or spontaneous histopathology and variability of clinical pathology parameters. The primary disadvantages of using the rat are limited blood volume and small muscle mass for vaccines administered by IM injection. The small muscle mass constraints may be overcome by administering in multiple sites or using a lower dose volume that is allowed per the WHO guideline (dosing on a milligram per kilogram [mg/kg] basis) IM.[25] The small muscle mass makes IM administration challenging, and errors in precision of the injection are common with individuals inexperienced in this technique. Brief anesthesia with isoflurane may be used to improve the placement accuracy of IM injection without apparent impact in other study parameters. Many companies have transitioned from using the Sprague-Dawley (SD) rat to using the Wistar Han (WH) rat as they generally have fewer age-related background findings.[29] Because the WH rat strain is smaller than other rat strains commonly used for toxicology (eg, SD), it may be advisable to initiate vaccine studies in 10- to 12-week-old WH rats rather than the more typical age of 8 to 10 weeks so that they are slightly larger in size at study start.

Mice

Mice have been less commonly used than rabbits or rats as the toxicology species for vaccine development, primarily because of their small size. However, if the mouse has been used as the model in nonclinical pharmacology or efficacy studies, there is no reason they cannot be used as the toxicology species as long as a reliable and consistent immune response is generated to the vaccine antigens. Since administration of a full human dose is not generally possible, vaccine studies in mice are conducted using a dose that achieves some multiple(s) of the anticipated human clinical dose on a mg/kg basis. Historical control database may be limited within an institution on the specific strain utilized; however, for the standard mouse strains, there is published literature and databases (eg, Registry of Industrial Toxicology-Animal Data; https://reni.item.fraunhofer.de/reni/public/rita/) on background findings to serve as a good resource to the pathologist.[30] In addition, as in the rat, the mouse anatomy is well understood by most technicians and tissue trimming guides,[31–33] and a harmonized and standardized system of nomenclature is readily available.[34]

Other Small Nonclinical Species

Other small animals, such as the ferret, guinea pig, cotton rat, and hamster, have also been used for vaccine safety studies.[25,35] The guinea pig is occasionally used for local tolerance studies and routinely for the abnormal toxicity/general safety test[36] (a quality control test conducted to ensure no contaminants have been introduced during product manufacturing), which is required by some countries (eg, Russia, China). Guinea pigs are relatively unique in that mast cell degranulation may be initiated with immunoglobulin G (IgG) as well as IgE, so high IgG titers may result in a species-specific anaphylactic-like response.[37] Ferrets have been used primarily for vaccine safety studies for influenza vaccines, as they are susceptible to

the disease and often serve as both the nonclinical efficacy and toxicology species.[38,39] These species have the disadvantages of small size, generally limited HCD, and limited published strain-specific background findings with incidences.[25] There may also be limitations on the availability of assays and reagents (eg, for measuring immune responses, acute-phase reactants) for some of these species.

Nonhuman Primates

Nonhuman primates have a number of advantages for vaccine studies, such as having relatively large muscles to enable IM administration of a full human dose and a high blood volume for sampling. The muscle size also enables use of special delivery techniques, such as electroporation devices. Nonhuman primates are not commonly used for toxicology studies of vaccines against infectious disease, although they are used often as nonclinical models to evaluate immune induction to vaccine candidates and sometimes to support juvenile studies. Nonhuman primates should be used for toxicology studies only if there are no other relevant animal species, which is may be the case with therapeutic vaccines, with or without coadministeration with biotherapeutic molecules. When using NHP, the source of the animals should be considered. For example, cynomolgus monkeys (*Macaca fascicularis*) of Mauritian, Indian, or Chinese origin have differences in immune responses and background incidence of tissue inflammatory cell infiltrates that have been attributed to differences in their genetics.[40–42]

Minipigs

As with NHP, minipigs have the advantage of a large muscle mass to facilitate IM administration of a full human dose and have ample blood volume for repeated blood collections. They are not commonly used as a toxicology species for vaccines, but have been developed as a model for studying intradermal or topical vaccines.[43] Minipigs have the advantage of having similar physiological, skin microanatomical, and immunological characteristics as humans.[44,45] A recent increase in minipig publications[46] may make this a more commonly used species going forward. There may be limitations on anatomic knowledge for technical staff, tissue trimming guidelines, availability of assays and reagents (eg, for measuring immune responses, acute-phase reactants), varying degrees of pathologist familiarity with evaluating the species, and HCD.

Dogs

From a practical perspective, the dog could be viewed as a good candidate species for vaccine toxicology studies due to their large size (amenable to full human dose), substantial blood volume enabling serial sampling, and an abundance of publicly available and/or proprietary HCD. However, dogs have seldom been used as models for studying vaccine pharmacology, efficacy, or safety. An important consideration in the use of dogs is their high sensitivity to polysorbate 80 (Tween80), a common component of vaccines, which causes an anaphylactic-like reaction.[47,48] There is also little historical immunology-specific data, limited availability of assays and reagents for Beagle dogs as compared to rodents,[49] and studies of comparative immunology between humans and dogs are limited.

Study Groups

Study groups should include, at a minimum, a saline control group (formulation buffer may also be used but is less common) and vaccine group(s). If an adjuvant is a component of the vaccine formulation, inclusion of an adjuvant control group should be considered to comfortably interpret the clinical pathology and histological findings in those vaccine groups. If the adjuvant has an extensive safety database and is in numerous marketed products, an adjuvant control group may not be necessary (eg, aluminum salt adjuvants such as $AlPO_4$, $Al[OH]_3$). Dose groups for therapeutic vaccines may vary depending on the components of the vaccine. Animal numbers for vaccine studies are determined similarly as in other routine toxicology studies and specific recommendations are included in the WHO guidance documents.[5,6]

Dose Volume and Administration Location

Most vaccines are administered IM, although intradermal, subcutaneous, oral, and intranasal (IN) administrations are also sometimes used. Although uncommon, intravenous administration of vaccines may be effective.[50] Because the WHO guidance documents indicate that the full human dose should be administered whenever feasible, IM administration of the full human dose (typically 0.5 mL) to the rabbit or other large animals is straightforward, and the hindlimb or the dorsolumbar musculature is most commonly used. When the dosing regimen requires multiple administrations, IM dosing may alternate between the left and right sides. Administration of the full human dose volume into a single muscle of rodents or other small animals, however, is generally not feasible. A maximum IM dose volume in the rat at one site is recommended to be $\leq$250 µL and must be in a muscle large enough to support the dose volume.[25,51] In general, this limits the injection sites to the hindlimb and the volume is typically split between both hindlimbs, although lower dose volumes may be administered in the lumbar muscles. In the rat, the quadriceps muscles are most commonly used; however, other muscles of the hindlimb, including the biceps femoris or gastrocnemius muscles, may be utilized.

Mice or other small species will require much lower dose volumes ($\leq$100 µL) per IM site. When administering lower doses than those anticipated for use in humans, there should be immunological data to support an immune response to the dose administered. A mg/kg exposure multiple for the formulation components may be a scientifically valid alternative for discussion with regulatory agencies.[5,6] Alternatively, it may be possible in some cases to increase the concentration of the vaccine antigens and adjuvants such that the full human dose

of these components may be administered. However, this is not a commonly used approach and there are possible concentration-based immunological or physical confounding effects that could be introduced. If such an approach is taken, however, risk may be mitigated through evaluation in non-Good Laboratory Practices studies prior to initiating the pivotal toxicology studies.

Subcutaneous vaccine administration sites may differ by species, although most species may be readily injected in the interscapular region, dorsal neck, shoulder, or flank. Subcutaneous locations in most species except for mouse may accommodate up to 5 mL/kg/site or the full human dose.[52]

Intranasal administration delivers the vaccine to the nasal mucosa and IN vaccines have been developed mainly for influenza but have been tested for a number of respiratory viruses.[39,53] The IN route offers the induction of both a systemic and local/mucosal immunity and the production of higher local IgA antibody and cell-mediated immunity compared to parental routes, as its main advantages.[54] It also provides a noninvasive or needle-free delivery system, which contributes to patient comfort/compliance, and requires a relatively smaller antigenic dose.[55] Clinically, the main challenges for IN delivery of vaccines include the potential passage of the vaccine to the olfactory bulb of the brain and other potentially adverse effects in patients with allergies or asthma.[55] To adequately assess the potential effects of vaccine delivery to the brain, species with nasal anatomy closer to that of humans, such as the cynomolgus monkey, should be considered.[55,56] Species such as the rat and dog, in which the olfactory bulb is protected by the presence of a transverse lamina, are generally not considered suitable, as the vaccine may not reach the olfactory bulb, limiting reliable prediction of brain delivery-associated effects.[56] A further disadvantage of using rodents and other smaller animals for safety testing of IN vaccines includes the potential for the vaccine to reach the lungs. Evaluation of the administration site in IN vaccines may be challenging, particularly in species with a large nasal mucosal surface area. Mucosal delivery of vaccines also includes oral vaccines as have been developed for *Vibrio cholerae*, *Salmonella typhi*, poliovirus, and rotavirus.[57]

Intradermal or transcutaneous vaccine administration has appeal, as this method of delivery tends to use less material (dose-sparing), generally does not require adjuvant, and serves as a "needle-free" alternative to vaccination.[58] Microneedle techniques are also utilized for intradermal vaccine administration.[59] To date, there has been mixed success with intradermal delivery of live-attenuated vaccines.[58,60–63] These methods of delivery require use of adequate delivery devices, of which there are several in development.[64–66] Because of the similarity with human skin, the pig is often used as a nonclinical model for safety testing.[67] The pathologist should be aware of "dippity pig syndrome" that is characterized by reddened skin and open sores along the dorsum in healthy young pigs, which may overlap the region of dose administration and confound the toxicology interpretation (Figure 1). The lesion usually begins resolving within a few days of onset. A cause for this syndrome is uncertain.[68]

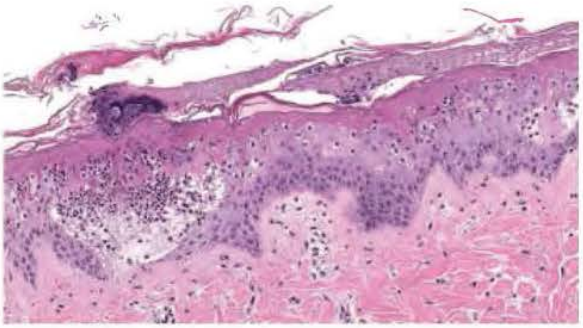

Figure 1. Photomicrograph of dorsal skin from a minipig with "dippity pig" syndrome stained with hematoxylin and eosin. Note the presence of epithelial edema, infiltrates of neutrophils, and superficial crust.

Dose Number and Dosing Interval

The dose number and dosing interval should reflect the strategy planned for clinical use. The number of doses should, at a minimum, represent the anticipated number of clinical doses given in a regimen over a year; however, it is suggested in repeat-dose toxicology studies to add an additional dose (N + 1, where N = the number of doses to be administered clinically). Prophylactic vaccines against infectious agents are often clinically administered periodically, with months or even years between administrations. In toxicology studies, the time between dose administrations may be shortened. Doses are usually administered 2 to 3 weeks apart, based on the kinetics of the primary and secondary antibody response in the animal species. Time points separated by less than 2 weeks are generally not used. For therapeutic vaccines, the timing of dose administration and number of doses generally reflect the clinical dosing regimen for at least 1 cycle (for cancer treatment expectations, refer to ICHS9; Non-Clinical Evaluation of Anticancer Pharmaceuticals), and dose administration methods should be as close to that used in the clinic as possible (eg, electroporation devices).

Technical Considerations of Dose Administration

Since the primary target tissue in most vaccine studies is the injection site, accurate administration of the test material is essential to facilitate identification and precise collection of the injection site(s) at necropsy. Some test facilities have found it advantageous to briefly anesthetize small species with isoflurane for the IM injections to ensure accuracy of administration and reduce local trauma due to animal movement during the injection. In the authors' experience, use of anesthesia has not been associated with any confounding effects in study parameters. In-life techniques for facilitating the accurate administration of the test material include (1) anatomic localization of

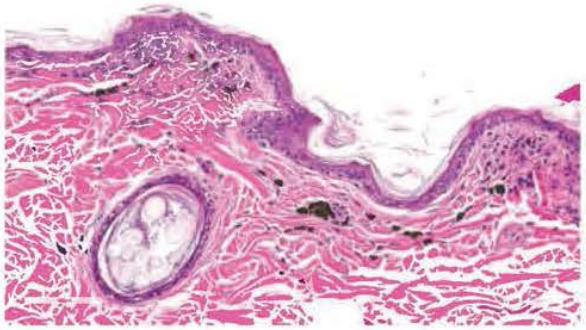

Figure 2. Photomicrograph of skin from tattoo site near intramuscular injection site in a ferret stained with hematoxylin and eosin. Pigment-laden macrophages and small numbers of mixed lymphocytes and plasma cells infiltrate the superficial dermis in a focal area.

the injection site; (2) application of specific dosing parameters, including needle length/gauge, injection approach, and directionality; (3) consideration of species variation in anatomy; (4) manual or chemical restraint as necessary; and (5) utilization of appropriate marking of the area of the injection. At necropsy, these techniques may be coupled with collection of wide margins to ensure the accurate collection of the injection site(s).

Injection Sites

Injection site delineation is important to ensure accurate collection at necropsy. Injection site collection from animals with larger muscle area, such as the rabbit and NHP, may be more challenging to sample as compared to those with much smaller muscles. The injection site may be shaved and marked to delineate the location of needle entry and vaccine deposition. This is often done with a superficial pen or ink marking at the time of injection, which sometimes requires repeated application at regular intervals due to fading. An alternative method of marking has been to delineate an injection area by permanent tattoos to surround or otherwise highlight a central area for injection. This requires tattoo administration at least a week prior to dosing but can reduce staff effort and time in remarking the skin over the course of the study. Histologically, tattoo ink pigment may be associated with minimal lymphohistiocytic infiltrates within the dermis (Figure 2).

Exterior marking has the benefit of easy identification of the injection site for the technical staff and may have benefit for the necropsy staff. However, the highly pliant nature of rabbit skin may make skin marking an inconsistent way to delineate the desired IM target. Alternative methods of identifying the injection site other than by marking may allow for more consistent and better dosing and collection. The use of anatomic landmarks may provide consistent localization of the site of administration, assisting staff during in-life and postmortem procedures (Figure 3A-C). The most reliable anatomic landmarks tend to be bones in the region of the injection site(s). For

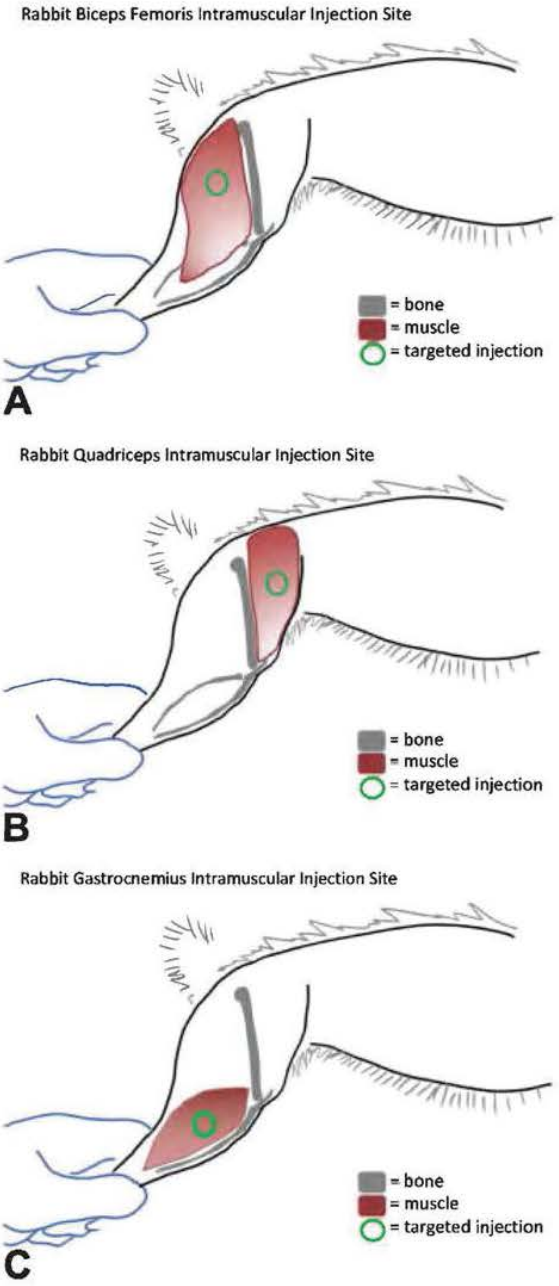

Figure 3. Diagram of injection site localization in rabbits. A, Diagram of injection site location in biceps femoris. Injection should be perpendicular to skin/muscle belly, at approximate midpoint of femur and 1 to 2 cm caudal to femur. B, Diagram of injection site location in quadriceps. Injection should be perpendicular to skin/muscle belly, at approximate midpoint of femur and 1 to 2 cm cranial to femur. C, Diagram of injection site location in gastrocnemius. Injection should be perpendicular to skin/muscle belly, just proximal to the midpoint of tibia/fibula and ~1 cm caudal to tibia.

Figure 4. Macroscopic photo after intramuscular injection of green marking dye in a rabbit. Note that the injected material is in line with or external to the circle inked on the skin to mark the outer rim of the injection site. Careful attention to needle direction during dose administration is essential for accurate injection site collection at necropsy.

example, the femur is a commonly used landmark for injections into the quadriceps or biceps femoris muscles, with the articulation of the hip and the knee forming 2 points of reference and the length of the femur forming another. By palpating hip and knee joints, the midfemur may be located, and the vaccine consistently administered into the adjacent defined muscle belly such as quadriceps or biceps femoris muscles. This method also improves collection of sites, as necropsy and tissue trimming staff can use the same landmarks to locate the injection site region.

Directionality and Depth of Injections

The direction and depth of injection should be considered. The technical staff should be trained to have consistent orientation, injection site direction, and injection depth. For example, if the area of injection is marked on the skin, the technical staff should pay attention to where the material is ultimately injected—the needle might enter the skin in the delineated region, but be injected outside the demarcated area (Figure 4). This is particularly a concern for subcutaneous injections, but is also important for IM injections. Additionally, needles for IM injections should be oriented consistently (preferably perpendicular to the muscle) to provide greater accuracy and consistency, and reduced effects on regional structures such as the sciatic nerve and knee joint.

Needle Length

Needle length is important to consider both within a study and between studies to reduce nonspecific variation in the injection site histology. For IM injections, longer needles in rodents may run the risk of causing deeper than desired injection of material, such as into the stifle joint region, muscle bundles deep to the targeted muscle, and in or around the sciatic nerve. A needle length of 3/8″ is appropriate for IM delivery in many animals, including rabbits, monkeys, dogs, and ferrets. Longer needles such as 5/8″ may be associated with administration of material into underlying muscle beds, even in NHP. Shorter needles may be appropriate in smaller species, such as mice, rats, and hamsters (eg, 3/16″) and should be considered on a case-by-case basis. In general, the proximal portion of the muscle is thicker than the distal portions; thus, there is a lower risk of passing through the intended muscle. Variations in needle length may impact the consistency of the location of where material is injected, even if directionality is consistent.

In-Life Assessments

The in-life assessments in vaccine studies are the same as for other repeat-dose toxicology studies with inclusion of postvaccine administration-specific end points, such as body temperature and injection site evaluations. Specific recommendations are detailed in the WHO[5,6] and other regulatory guidance documents.

Local Toxicity/Reactogenicity

Evaluation of the vaccine administration site is an important component of the in-life assessment in vaccine studies. Assessment of the injection site often utilizes a prospectively defined scoring system for erythema (redness) and edema (swelling) for which many use a modification of scoring of skin irritation described by Draize et al,[69] as well as characterization of other injection site changes such as vesiculation, ulceration, eschar formation, and any potential evidence of significant toxicity, including limb impairment. However, use of a specific scoring system is not a requirement if injection site observations over the course of the study are accurately captured and described. Additionally, body temperature before and after vaccine administration is evaluated and may be measured at the same time as the injection site observations.[6]

Clinical Pathology

The clinical pathology panels in vaccine studies are similar to those for small molecules and include blood (hematology, clinical chemistry, and coagulation) and urine (urinalysis).[70,71] Additionally, 1 or more serum acute-phase proteins (APPs) are typically measured as indicators of an immune response.[72,73] Cytokines may also be used as a measure of the immune response, but are less common because of their short half-life, wide physiological range, and high inter and intra-animal variation.

Timing of blood collection for clinical pathology is usually 1 to 3 days after the first and last dose administrations and at the recovery-phase necropsy, although other time points may be included. Blood collection 1 to 3 days after dosing is timed to capture any acute-phase response, which is usually short-lived, depending on the parameter being evaluated. For rodent

studies, blood volume and collection limitations are often an issue. For studies in which multiple blood collections for clinical pathology and serology are required, rats may be divided into subgroups to allow collection for various assays (such as half for hematology and other half for chemistry; other biomarkers or serology may be accommodated with either subset of animals depending on the volume requirements or, if needed, an additional cohort of animals). Serum collection for assessing the antigen-induced immune response usually occurs prior to dose initiation and at the end of the dosing and recovery phases; however, time points could vary depending on study needs (eg, when comparing different prime-boost regimens).

Clinical Chemistry and APPs

The clinical chemistry panel includes various end points for assessment of general health as well as markers for inflammation and APP. Creatine kinase (CK) is occasionally included as a marker of muscle damage at the injection site and may help differentiate acute-phase responses associated with the vaccine components from those occurring secondary to physical trauma. However, often there is poor concordance between local tissue injury (measured by CK) and the systemic inflammatory response (measured by APPs).[72]

Due to the lack of sensitivity in the routine clinical chemistry parameters to monitor an acute-phase response, fibrinogen and species-specific APPs are routinely measured to assess potential vaccine reactogenicity. Hepatic synthesis of APPs (positive APPs) may downregulate the synthesis of other proteins, including albumin, which are identified as negative APPs. However, there are no defined cutoffs for changes in these APPs to help with decision-making. The presence of an acute-phase response in vaccine studies is of little significance to the overall study conclusions if the immune response to the antigen is as expected and no unexpected or adverse systemic findings are observed.

Species differences in APPs must be considered when designing a vaccine toxicology study. For example, C-reactive protein (CRP) is a sensitive indicator of the acute-phase response and the most commonly utilized major APP for humans, rabbits, dogs, and NHP.[72] However, CRP is a poor marker of an acute-phase response in rodents. Instead, the major APPs for rodents are α1-acid glycoprotein and α2-macroglobulin.[73] When measuring APPs, it is very important to understand how an assay is being performed; there may be notable differences in results due to differences in assay sensitivity between different instruments and reagent systems, and thus data should not be compared between different methods and laboratories. Some of these APPs (such as CRP, haptoglobin, and serum amyloid A) may utilize human assays or species-specific assays, so species cross-reactivity should be critically evaluated and assay validation should be performed in relevant species to assure satisfactory performance.

Evidence of an acute-phase response indicative of reactogenicity to the vaccine formulation may be evident in the routine chemistry panel as increases in globulins and decreases in albumin. Globulins increase slowly after vaccine administration and are long-lived, sometimes remaining elevated until the end of the recovery period. These elevations are often very slight (<1.2× relevant control) and not always statistically significant. Decreases in albumin are often evident within days of vaccine administration and as with globulins; the change may be slight and variably statistically significant. Therefore, reductions in the albumin:globulin (A:G) ratio after the first vaccine administration may reflect reduced albumin, whereas later in the study, the decreased A:G ratio may reflect increased globulins.

Hematology

Changes in hematology (complete blood count) parameters are useful in assessing the inflammatory response caused by the administration of vaccines and their components. Findings should be compared to concurrent controls, even when baseline data (prior to dose administration) are available, as hematology data can be influenced by study procedures. Most commonly observed changes in hematology parameters include increased white blood cells with increased neutrophils, monocytes, and/or lymphocytes. Eosinophils and basophils are not reliable as indicators for inflammation, as they are generally present in very small numbers. The inflammatory response is often more prominent with vaccines formulated with adjuvants. The inflammatory leukogram tends to be variable depending on the antigen and adjuvant and may range from negligible to remarkable. Different adjuvants can impact the severity and character of hematology changes. Stress/excitement may also result in increased neutrophils, monocytes, and/or lymphocyte counts, and study procedures should be taken into consideration for identifying vaccine/adjuvant-related hematology changes.

Coagulation

The coagulation panel typically includes coagulation times (prothrombin time and activated partial thromboplastin time [aPTT]) and fibrinogen. Fibrinogen is a clotting factor and an APP that is present at a higher basal concentration (generally 200-300 mg/dL range) in the blood to maintain normal clotting. Due to its high basal concentration and the upper limit of the assay, the maximal increase in fibrinogen is typically not more than 4- to 5-fold, making it a minor to moderate reactant for most species. However, fibrinogen is still an effective marker for inflammation/acute-phase reaction in most species, and small increases are usually meaningful. Clinically increased CRP levels are known to cause false increases in aPTT, as CRP has binding affinity for phospholipids, interfering with the aPTT assay.[74]

Other Considerations in Clinical Pathology Findings

Intramuscular injection, a common route of administration for vaccines, causes local tissue injury and incites an inflammatory response, creating more variability in data. Sometimes, it can

be difficult to parse out changes attributed to the injection procedure from those caused by the immune response to vaccine/adjuvants. In such cases, the saline control group is often helpful in identifying changes attributed to the injection procedure, as well as the evaluation of CK, a marker of muscle damage that could indicate injection site muscle trauma.

Therapeutic vaccines, which contain other active components, may have changes related to those components or to the vaccine target. Immune oncology checkpoint inhibitors, for example, can elevate the white blood cell count, particularly lymphocytes.[75] Therapeutic vaccines may also have intended alterations in clinical pathology parameters. For instance, vaccines targeting cholesterol biogenesis would be anticipated to have reductions in serum cholesterol concentrations as a therapeutic end point.

Anatomic Pathology

In toxicology studies for prophylactic vaccines, the pathology evaluation focuses primarily on the local response to the vaccine at the injection site and draining lymph node. Different concentrations of antigen infrequently alter the findings at the injection site and draining lymph node, so in this way, antigen dose often has little impact on the pathology findings. The dose and type of adjuvant in the vaccine formulation may have a greater impact on the pathology data than the antigens, and thus different formulations under consideration for human testing should be evaluated in the toxicology study. Because the antigen is a foreign protein, there is rarely a concern for immune cross-reactivity with an endogenous protein. This is in contrast to therapeutic vaccines, for which an endogenous antigen is used, and therefore tissues in which cross-reactivity may be of concern should be evaluated histologically.

Necropsy

Macroscopic Findings

Vaccines formulated with an adjuvant often have gross enlargement of the draining lymph nodes, in contrast to vaccines formulated without adjuvant in which lymph node enlargement is less frequent. The spleen may also be enlarged. Macroscopic injection site findings may range from unremarkable to ulceration or scabbing. Changes at the injection site should be differentiated from damage associated with injection site preparation (shaving and disinfection). However, most often, there are either no findings or slight discoloration of the skin or underlying muscle in the injection site region. Therapeutic vaccines may contain other active components, which may be associated with gross treatment-related findings (although in the experience of the working group, this is uncommon).

Tissue Lists and Organ Weights

Organ weights are routinely collected in vaccine toxicology studies consistent with the Society of Toxicologic Pathology (STP) best-practice guidance on organ weight collection.[76,77] In vaccines against infectious diseases, there is often no change in organ weights, although the spleen may on occasion have slight increases in absolute and/or relative weight. Although not recommended in the STP best-practice guideline, draining lymph nodes may be weighed to help in the assessment of immunogenicity and lymphoid reactivity. However, the value should be considered on a study- and species-specific basis.[78] The value of weighing draining lymph nodes in rodents and other small laboratory animals may be limited by interanimal variation in immune reactivity, sampling error, and small size, all of which may contribute to wide variation in lymph node weight.

The WHO guidelines include an extensive tissue list.[5] The majority of tissues suggested for collection are consistent with those collected for routine toxicology studies (including the injection site[s] and draining lymph nodes), but with the addition of larynx and lacrimal gland. Presumably, microscopic evaluation of the larynx is intended for inhaled or ingested vaccines. The inclusion of lacrimal gland was a result of a squalene-based adjuvant-related finding in rabbit lacrimal glands.[79] Because of the nature of vaccine study design (ie, generally no dose ranges), all tissues from all dose groups are processed to slide and evaluated at the end of the dosing period. In the case that multiple dose levels of the same formulation are evaluated, limiting evaluation to targets only at lower dose groups may be acceptable. Adequate collection of the injection site(s) and their corresponding draining lymph node(s) (Table 3) is essential, so care must be taken in ensuring that these are properly and consistently collected. Reliable collection of the injection site depends on consistency in the location of dose administration (see section "Dose Administration"). The draining lymph nodes can easily be identified or verified prestudy by methylene blue injection at the site of intended administration in the toxicology species of choice. Tissue collection at the recovery phase is intended to evaluate resolution of findings observed at the end of the dosing phase and potential delayed toxicities. The same tissues should be collected at the recovery-phase necropsy as at the dosing-phase necropsy. Microscopic evaluation of tissues from recovery phase animals may include all tissues collected or could be limited to the injection site, draining lymph nodes, spleen, and any organs with changes at the end of the dosing phase, with or without a subset of additional tissues as deemed appropriate.

Collection and Trimming of the Injection Site

For IM injections, the injection site muscle and overlying skin should be collected and evaluated. These do not need to be kept together and may be evaluated separately, although retaining the overlying skin with the muscle may reveal the needle tract. In rabbits, where the skin is only loosely connected to the underlying muscle, maintenance of the muscle with overlying skin may not add value for identifying injection tracts. At the time of collection, staples may be used at the edge of the excision site in rabbits to securely attach the skin to the underlying musculature and avoid the slipping of the skin over the muscle

Table 3. Draining Lymph Nodes.

	Subcutaneous	Intramuscular	Intravenous
Rat[80]	Interscapular: Brachial LN Interscapular: Axillary Dorsal thoracic: Axillary Dorsal Lumbar: Axillary Dorsal sacrum: Inguinal	Dorsolumbar or gluteal: Inguinal Hindleg (cranial): Inguinal, iliac Hindleg (caudal): Inguinal, iliac	Tail vein: Inguinal
NHP[81]	Interscapular: Axillary Dorsal thoracic: Axillary Dorsal lumbar: Iliac Dorsal sacral: Iliac Midline dorsal lumbar: Superficial inguinal Midline dorsal sacral: Superficial inguinal	Dorsolumbar or gluteal: Iliac Hindleg (cranial): inguinal, iliac Hindleg (caudal): Inguinal (popliteal for distal part of limb)	Saphenous: Inguinal, popliteal, iliac Cephalic: Axillary
Rabbit[82]	Interscapular: Axillary Dorsal thoracic: Axillary Dorsal lumbar: Subiliac Dorsal sacral: Subiliac Midline dorsal lumbar: Axillary Midline dorsal sacral: Iliac	Dorsolumbar or gluteal: Iliac Hindleg (cranial): Inguinal, iliac Hindleg, caudal: Inguinal, iliac, popliteal	Ear vein: Parotid, mandibular
Dog[83]	Interscapular: Superficial cervical Dorsal thoracic: Axillary Dorsal lumbar: Iliac Dorsal sacral: Iliac Midline dorsal lumbar: Axillary	Dorsolumbar or gluteal: Iliac Hindleg (cranial): Inguinal Hindleg, caudal: Iliac	Cephalic: Superficial cervical, axillary Saphenous: Inguinal, popliteal Jugular: Superficial cervical Femoral: Inguinal
Minipig[84]	Interscapular: Dorsal superficial cervical Dorsal thoracic: Dorsal superficial cervical Dorsal lumbar: Iliac Dorsal sacral: Iliac	Dorsolumbar or gluteal: Iliac Hindleg (cranial): Subiliac Hindleg (caudal): Inguinal	

Abbreviations: LN, lymph node; NHP, nonhuman primates.

Figure 5. Macroscopic photo of an excised intramuscular injection site in the rabbit epaxial musculature and skin (circles indicate injection sites 1 and 2). The use of surgical staples along the cut edge of skin and muscle helps to maintain in vivo orientation. Every cut edge of skin *must* be anchored to the muscle to avoid severe shrinkage and distortion during the fixation process. Injection sites successfully fixed with minimal skin movement results in correct sectioning of injected muscle, subcutaneous tissues, and skin. Note: proper fixation is not a problem with these sites.

and the eventual differential shrinkage of the skin compared to the muscle upon fixation (Figure 5). After fixation, the staples may be removed, and the tissues will remain opposed for trimming. To preserve anatomical correlation after necropsy, the hindlimb of animals up to rabbit size may be successfully removed and fixed in totality prior to trimming and embedding. For evaluation of the muscle of the injection site, it is helpful to have 3 to 5 cross sections of the region for histological evaluation (depending on the animal size), as there will be variation in the extent of the change depending on whether the evaluation is at the center of the injection site or along the margins (Figure 6). However, other strategies may also be successful. Inclusion of the deep margins of the muscle at the injection site is often helpful in evaluating the full extent of the changes.

For subcutaneous injections, the underlying muscle, overlying skin, and the subcutaneous compartment are typically collected and evaluated. These are often kept together and evaluated as a whole. Similar to IM injection sites, evaluation of multiple spaced cross sections provides a method of ensuring accurate assessment of the injection site despite possible dosing variability.

For IN vaccines, multiple levels of the nasal cavity should be collected for histopathology[85–87] along with the nasal-associated lymphoid tissue (NALT), tonsillar tissue (if applicable), the nasopharynx/pharynx, larynx, trachea, draining lymph node for the respiratory tract such as (tracheo)bronchial lymph nodes, lungs, and the brain. In rodents (which lack tonsils), NALT located in the ventral aspects of the caudal nasal cavity at the entrance of the nasopharynx is considered to be the equivalent of the Waldeyer ring in humans and can be assessed on nasal cavity sections; in monkeys, NALT is present

Figure 6. Macroscopic photo of 5 cross sections through an intramuscular (IM) injection site in rabbit after IM injection of green marking dye. Note that the injection site is seen only in the middle 3 sections. Injected dye is seen at varying depths in the muscle as well.

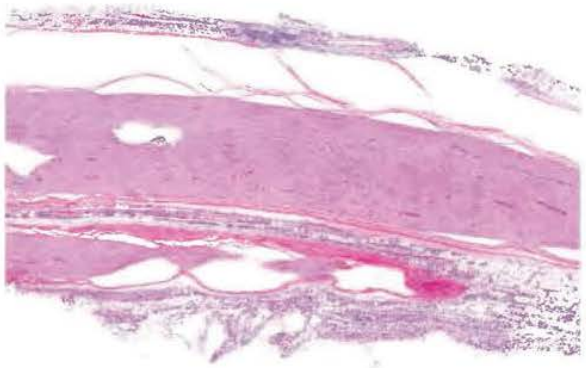

Figure 7. Photomicrograph of sciatic nerve stained by hematoxylin and eosin from a Wistar (Han) rat administered ISCOMATRIX. Perineural inflammatory cell infiltrates are present around the nerve due to vaccine administration at or near the sciatic nerve.

throughout the nasal cavity and tonsillar tissue is present within the nasopharyngeal septum.[56] Dogs have abundant tonsillar tissue that can be sampled separately, but as discussed before, dogs are rarely used in IN vaccine studies since the presence of a transverse lamina and olfactory recess in the nasal cavity in this species limits their use to predict brain delivery-associated effects.

Other Considerations for Tissue Collection

Although damage to the skeletal muscle and trauma or vaccine-induced inflammation in the region around the sciatic nerve or joint may be common issues in IM vaccine studies, they may become particularly problematic if they are more frequently identified in the vaccine groups (Figure 7). To rule out any potential questions regarding systemic effects on the skeletal muscle, nerves, or joints, it may be of value to collect these tissues from sites distant to the site of vaccine administration. For example, if both the hindlimbs were used for injection, collection of a skeletal muscle, joint, and nerve from the forelimb or, for rodents, the entire forelimb, may be beneficial. These additional tissues may be held in reserve for evaluation if needed or may be processed to slide and evaluated as part of the study.

Microscopic Findings

Microscopic findings in vaccine studies are usually at the injection site and surrounding tissues and in the draining lymph nodes. There may also be findings in other lymphoid organs, such as the spleen. Comparing the microscopic findings of the vaccine to those of the saline controls is important to understand the effect of the vaccine formulation in its entirety. However, within the microscopic component of the pathology report, it is important to differentiate, where possible, the effects of adjuvant from the effects of antigen. For studies that lack an adjuvant control, this may require reference to historical data. Differences between microscopic findings with the adjuvant alone and the vaccine formulated with the adjuvant are relatively infrequent. Since other components such as immune checkpoint inhibitors are included in therapeutic vaccines, changes specific to those components may be evident histologically (such as increased immune cell infiltrates into tissues).[75,88] However, details on the microscopic findings outside the injection site(s) and draining lymph nodes with various therapeutic vaccine regimens are beyond the scope of this article.

Injection Sites

Most vaccine studies have multiple doses administered over the period of 2 weeks or more. Therefore, microscopic findings may be complex, as they range from acute to chronic with responses not only to the injected material but also to physical trauma from the needle or injected material (eg, tissue compression). Determining how many injection sites should be evaluated microscopically should be based on the study design. If a full dose was administered in alternating sites, then evaluation of all sites can give a more temporal understanding of the

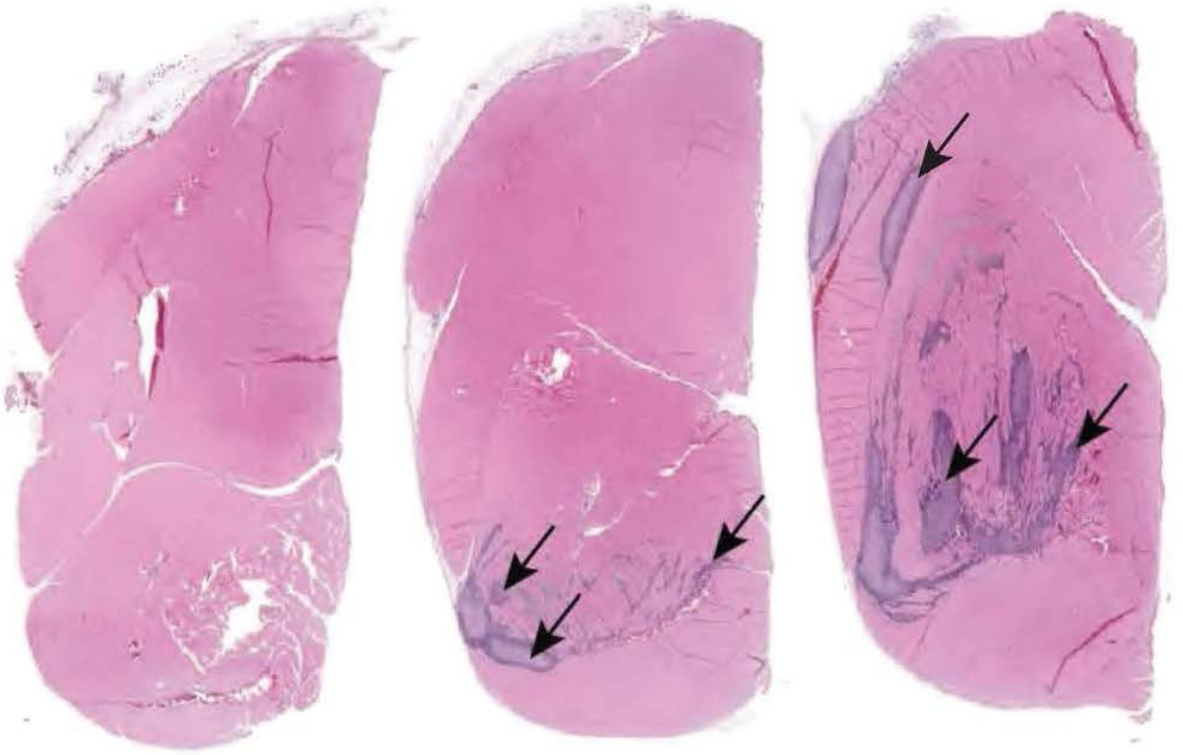

Figure 8. Photomicrograph of the quadriceps muscle injection site stained with hematoxylin and eosin from a Wistar Han rat administered aluminum phosphate adjuvant. Note that inflammatory cell infiltrates are negligible in the section to the left, slight in the middle section, and prominent in the section to the right (arrows). It is important that more than 1 section be evaluated to accurately identify and diagnose injection site findings.

injection site findings. In this case, the injection sites should be independently identified and evaluated. If the dose was administered at multiple sites at each dosing day, then it would be adequate to evaluate a single site (with collection of all sites). In this case, if multiple sites are evaluated, findings may be recorded individually or as a composite diagnosis(es). For therapeutic vaccines, different components of the regimen may be administered at different sites; injection sites for each unique component are usually evaluated independently. Regardless of how many injection sites are evaluated, it is helpful to include multiple levels of each injection site, if possible, to accurately capture the microscopic characteristics and severity (Figures 6 and 8). If microscopic findings are not identified, particularly with formulations containing adjuvants, it may be of value to either section deeper into the block (rats and mice) or retrim wet tissue to ensure accurate evaluation of injection site findings.

The severity of lesions and type of inflammatory cell infiltrates at the injection site will vary depending on the vaccine components. Most injection sites include some degree of inflammation or inflammatory cell infiltrate, muscle degeneration or necrosis, edema, hemorrhage, and/or fibrosis,

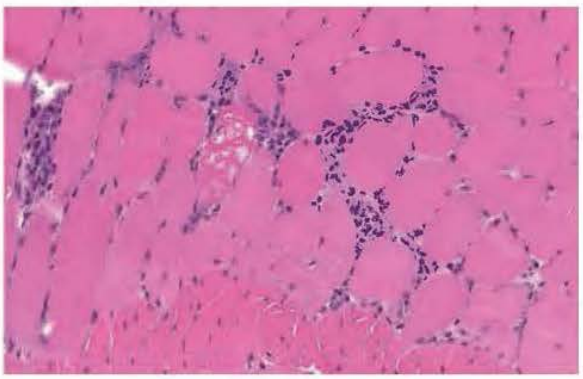

Figure 9. Photomicrograph of an intramuscular injection site stained with hematoxylin and eosin from a rat after administration of saline. Note the myofiber degeneration/necrosis and minimal inflammatory cell infiltrate.

depending on the timing of necropsy after administration. Intramuscular administration of saline causes scant inflammation, often comprised of scattered small aggregates of macrophages

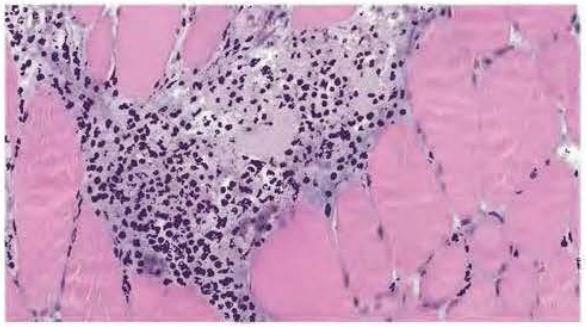

Figure 10. Photomicrograph of the quadriceps muscle injection site stained with hematoxylin and eosin from a Wistar Han rat administered aluminum phosphate adjuvant intramuscular. Note the presence of macrophages and granulocytes (including eosinophils) admixed with granular material and necrotic skeletal myofibers. Original objective 20×.

or other mononuclear inflammatory cells with or without individual myocyte degeneration or necrosis, edema, hemorrhage, and/or fibrosis (Figure 9).[2] Some antigens alone are highly immunogenic and may cause notable inflammation at the injection site, even when formulated without an adjuvant, although many have changes similar to those identified with saline administration.

Aluminum-containing formulations consistently result in inflammation at the injection site. Acute changes are characterized by infiltrates of macrophages (multinucleated cells are uncommon), neutrophils (heterophils in rabbits), and eosinophils, with variable degrees of hemorrhage, inflammation, and individual muscle cell degeneration/necrosis (Figure 10). Aggregates of neutrophils may be present within the lesion and generally resolve; these should not be confused with bacterial contamination of the injection site. Basophilic to gray granular material (interpreted to be aluminum) is typically present both within macrophages and extracellularly at the injection site. Adjuvant material may collect along and distend fascial planes at the injection site. Macrophages may surround moderate amounts of extracellular adjuvant material displacing tissue. In the chronic stage, the injection site will have fewer granulocytic cells and the adjuvant-containing macrophages will often be surrounded by lymphocytes and fewer plasma cells (Figure 11A–B). This change is considered an indicator of the recovery process. Adjuvant material and the associated macrophages are usually present at recovery, although often slightly less prominent.

Non aluminum–containing adjuvants variably incite inflammation and/or necrosis at the injection site. Inflammation, hemorrhage, and edema tracking along the muscle fascial planes may also be evident with these adjuvants (Figure 12A–B). Administration of ODN adjuvants (eg, CpG-ODN), which drive TLR-9 activation, has histological changes similar to saline. However, when they are coadministered with aluminum, changes are generally more severe than aluminum

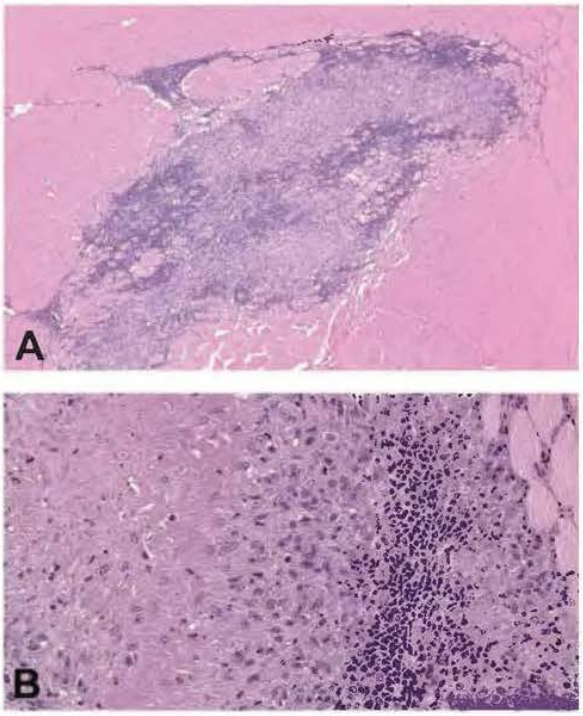

Figure 11. Photomicrographs of the quadriceps muscle injection site stained with hematoxylin and eosin from a Sprague-Dawley rat administered aluminum-containing adjuvant. Chronic inflammation characterized by central adjuvant, cellular debris, and accumulations of macrophages surrounded by lymphocytic infiltrates. (A) Original objective 20× and (B) Original objective 20×.

alone. Squalene-based oil emulsion adjuvants may elicit inflammation with vacuolated macrophages.

Consistent diagnostic terminology is important for comparisons of findings between studies, programs, and organizations. For injection sites that have both the muscle and the skin, it may be helpful to subcategorize the injection site into injection site: muscle and injection site: skin. Because injection sites may be quite complex, splitting diagnoses in the data capture system may reduce, rather than improve, clarity of the injection site findings. Instead, the use of simple diagnostic terms with microscopic details (eg, specific inflammatory cell types, muscle degeneration/necrosis, edema, hemorrhage) specified and/or elaborated upon in the study report narrative may be beneficial. The use of other diagnoses should be included as needed to differentiate test groups (eg, fibrosis). Most injection site inflammatory findings can be diagnosed as infiltrate, cell type or as inflammation, cell type (eg, neutrophilic, mixed, lymphocytic, plasmacytic, mononuclear). The addition of chronicity modifiers may be included (acute, subacute, chronic, or chronic-active).[89] When inflammation includes many macrophages, the authors prefer the use of macrophage or histiocyte as a modifier rather than granulomatous. The use of the term

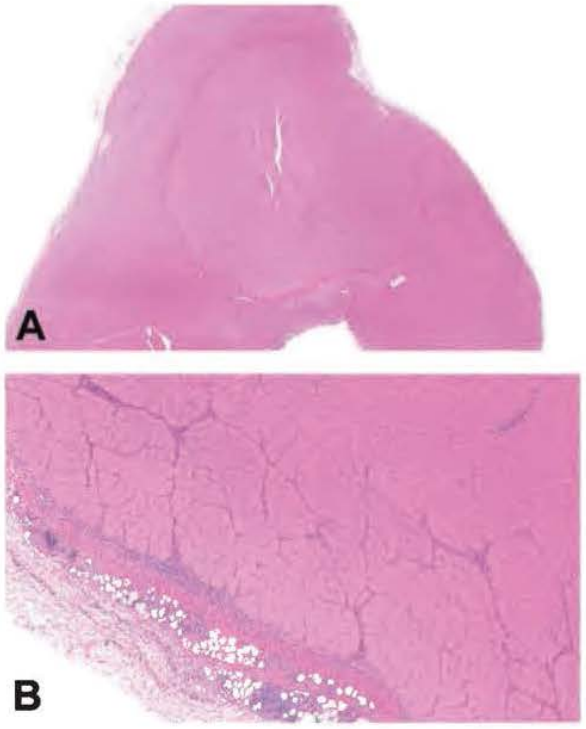

Figure 12. Photomicrograph of the quadriceps muscle injection site stained with hematoxylin and eosin from a Wistar Han rat administered ISCOMATRIX adjuvant intramuscular. Inflammatory cell infiltrates dissect between muscles and muscle fascicles, rather than displacing tissue. (A) Original objective 2× and (B) Original objective 10×.

"granulomatous inflammation" may be misleading, as it is evocative of etiologies such as fungal or mycobacterial infection. However, some formulations that contain oil or crystalline material may induce a foreign-body response, and in such cases, the pathologist may opt to use the modifier "granulomatous." Severity grading should take into consideration the amount of tissue affected, the intensity of the inflammatory infiltrate, and the degree of associated tissue damage. Thus, if multiple sections of the injection site were evaluated microscopically, the severity modifier would be based on the average severity across all 3 sections. In rats, the severity of findings can be greater at the injection site in females than in males, attributable to their smaller muscle size. The criteria for the severity modifiers are typically described within the pathology text.

With IM administration, it is common to see injection material outside the region of administration, whether by extension along fascial planes, movement out through the injection tract, or from inaccurate administration (Figures 7, 12, and 13). Particularly with rats and mice, inadvertent administration of material into an incorrect location is occasionally encountered, including unintentional administration of the vaccine into the

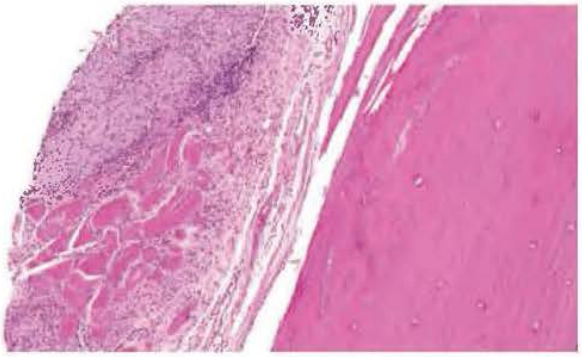

Figure 13. Photomicrograph of connective tissue adjacent to the femur stained with hematoxylin and eosin from a Wistar Han rat administered an aluminum-containing adjuvant intramuscular. Note the accumulation of macrophages containing lightly basophilic granular material (adjuvant).

wrong muscle bed (eg, administration into the gastrocnemius rather than the caudal thigh muscles such as the biceps femoris muscle). Because of this, regional structures may be at risk for needle-related damage or vaccine-associated inflammation. The extent of this effect will vary depending on the site of administration, the size of the test species, and the experience of the technicians administering the material. In the hindlimb, inflammation around the sciatic nerve due to local extension of the vaccine is sometimes observed (regardless of the species; Figure 7). In smaller species, such as the rat and mouse, periosteal or periarticular extracapsular inflammatory infiltrates may occasionally be observed around the knee joint in the hindlimb (Figure 13), and rarely, inflammatory infiltrates, with or without injection material, may be seen within the joint capsule. In the pathology report, these findings may be described as an extension of the injection site, to differentiate it from a systemic (immune-mediated) effect. When designing a vaccine study in rodents, consider collection of joint(s) distant from the injection site for potential microscopic evaluation in case there is any ambiguity as to the cause of any joint findings encountered near the local injection site.

Draining Lymph Nodes and Spleen

Microscopic evaluation of the draining lymph nodes may be challenging simply because of inconsistencies in orientation at tissue embedding and sectioning, particularly for rodents. This variation should be taken into consideration when interpreting the findings. The most common finding is increased cellularity and/or number of the germinal centers in association with antigens with or without adjuvants, although adjuvants may increase the incidence/severity of this finding. This finding may also be present in the spleen, although this is not as common as in the draining lymph nodes and may vary with the formulation. In animals administered aluminum-containing formulations, the draining lymph nodes will have aggregates

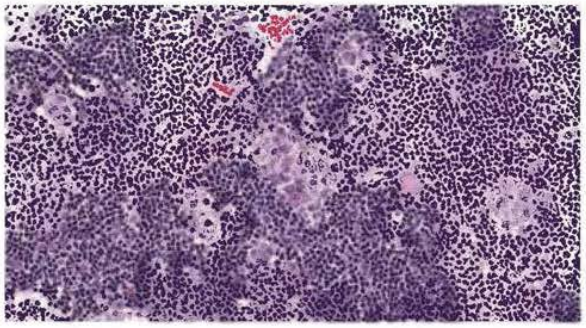

Figure 14. Photomicrograph of the draining lymph node stained with hematoxylin and eosin from a Wistar Han rat administered an aluminum-containing adjuvant formulation. Note the aggregates of macrophages containing granular material (adjuvant).

of macrophages containing basophilic to gray granular material, reflecting accumulation of aluminum draining from the injection site (Figure 14). The region of the lymph node within the histological section can dramatically impact the severity of macrophage aggregates. Aggregates may be evident both within the cotex and sinusoids of the lymph nodes. Additionally, there may be significant plasmacytosis within the draining lymph node(s). While germinal center changes may be recovered 4 weeks from the last dose, the accumulation of aluminum-containing macrophages is often unchanged 4 weeks from the end of the dosing phase.

Other Tissues

Treatment-related microscopic findings in other tissues beyond injection site, draining lymph node, and the spleen are uncommon in prophylactic vaccines, although there may be exacerbations of species-specific background findings (eg, cardiac changes in rabbits) as a result of study activity-related stress.[27] Therapeutic vaccines may have histological findings related to coadministration of other components.[88,90,91] Many therapeutic vaccines are evaluated in NHP. Studies using NHP have fewer animals per group and NHP have notable interanimal variation in background inflammatory infiltrates (particularly in Macaques of Chinese origin),[40] which may make interpretation of treatment-related immune cell infiltrates into tissues challenging. In these cases, the HCD may be of notable value in interpreting the study findings.

Data Integration

Vaccine-associated inflammatory reactions at the injection sites or systemically may be correlated with elevations in body temperature, elevations in white blood cells, and alterations in clinical chemistry and coagulation (ie, fibrinogen) findings. Animals administered saline often have no or only limited clinical signs, clinical pathology findings, or microscopic observations, and depending on the immunogenicity of the antigen, there may also be limited findings in vaccines administered without adjuvants. When adjuvants are included in the formulation, most anatomic and clinical pathology findings will be related to the adjuvant with some contribution from the antigens. It may be of value to parse out the impact of the adjuvant component of the formulation, when possible, as this may help identify antigen-specific effects of the vaccine. Elevations in sensitive biomarkers (eg, CRP, α2-macroglobulin, α1-acid glycoprotein, fibrinogen) may correlate with findings at the injection site (including inflammation, tissue trauma, myofiber degeneration/necrosis, and/or hemorrhage). However, good concordance between clinical pathology findings and microscopic findings at the injection site and draining lymph nodes may not be observed. In these cases, the clinical pathology findings may be more sensitive than the injection site and lymphoid organs in reflecting acute-phase response or immune stimulation by the antigen(s).

The injection site inflammation may be robust, particularly when formulated with an immune activator (ie, adjuvant). When unaccompanied by clinical signs (other than transient elevations in body temperature and redness/swelling at the injection site) and with evidence of reversibility (ie, no evidence of long-term impairment, excessive scarring/fibrosis, progression, etc), injection site findings, even marked to severe, are generally considered nonadverse. Microscopic inflammatory changes at the injection site and draining lymph nodes/spleen are typically ascribed as consistent with those observed with administration of other vaccines or aluminum-containing formulations. Occasionally, however, a vaccine or an adjuvant development candidate can be associated with atypical findings, which may be considered adverse (ie, any effect that impairs the animals' physical or physiological functions[92]). Ulceration of the skin overlying the IM injection site, severe edema or abscessation, extensive necrosis, progression rather than reversibility, and so on may require additional efforts and discussions to determine adversity. Therapeutic vaccines may have similar findings at the injection sites and in lymphoid tissues, although target- or modality-related findings may also be present in other tissues. Ultimately, the decision to proceed into the clinic with any vaccine, prophylactic, or therapeutic demonstrating more severe or unusual local inflammatory changes will have to include a risk–benefit analysis. Since a precise threshold for local tolerability may be difficult to define, it is often helpful to place nonclinical study findings in context by comparison to other marketed compounds.

Conclusions

Regulatory toxicology studies supporting human vaccine clinical trials have many similarities to studies supporting other biopharmaceutical products. With respect to pathology, toxicology studies for vaccines share the same fundamental end points as routine toxicology studies (ie, macroscopic and microscopic evaluation, organ weights, and clinical pathology parameters). Clinical pathology typically includes additional

biomarkers to measure the acute-phase response and the selection of the APP(s) must be appropriate to the species being evaluated. Key histological end points in vaccine studies are the findings in the injection sites and draining lymph nodes. Therefore, accurate and consistent vaccine administration is essential for optimized injection site collection at necropsy and trimming postnecropsy. The information presented here is intended to help pathologists and other team members involved in vaccine development programs. This "Points to Consider" paper reviewed some basic vaccine regulatory and study design considerations, addressed important technical concerns for vaccine studies, and discussed the microscopic and clinical pathology findings that are commonly identified in vaccine studies.

Acknowledgments

The authors thank Amber Doan and Beth Mahler for their artistic contributions to this article (Figure 3), and Xavier Palazzi for contributing figure 1.

Declaration of Conflicting Interests

The author(s) declared no potential, real, or perceived conflicts of interest with respect to the research, authorship, and/or publication of this article.

Funding

The author(s) received no financial support for the research, authorship, and/or publication of this article.

ORCID iD

Rani S. Sellers https://orcid.org/0000-0001-8870-4675
R. Chamanza https://orcid.org/0000-0002-8803-1412
S. Troth https://orcid.org/0000-0002-4696-5129

References

1. Guo C, Manjili MH, Subjeck JR, Sarkar D, Fisher PB, Wang XY. Therapeutic cancer vaccines: past, present, and future. *Adv Cancer Res*. 2013; 119:421-475.
2. Martins YA, Tsuchida CJ, Antoniassi P, Demarchi IG. Efficacy and safety of the immunization with DNA for Alzheimer's disease in animal models: a systematic review from literature. *J Alzheimer's Dis Rep*. 2017;1(1): 195-217.
3. Doucet M, El-Turabi A, Zabel F, et al. Preclinical development of a vaccine against oligomeric alpha-synuclein based on virus-like particles. *PLoS One*. 2017;12(8):e0181844-e0181844.
4. European Medicines Agency. Note for guidance on preclinical pharmacological and toxicological testing of vaccines. 1997. https://www.ema.europa.eu/en/documents/scientific-guideline/note-guidance-preclinical-pharmacological-toxicological-testing-vaccines_en.pdf. Accessed March 15, 2019.
5. World Health Organization. *Annex 1. Guidelines on the Nonclinical Evaluation of Vaccines*. Geneva, Switzerland: World Health Organization; 2005:31-63.
6. World Health Organization. *Annex 2. Guidelines on the Nonclinical Evaluation of Vaccine Adjuvants and Adjuvanted Vaccines*. Geneva, Switzerland: World Health Organization; 2014.
7. European Medicines Agency. Guideline on adjuvants in vaccines for human use. 2005. https://www.ema.europa.eu/en/documents/scientific-guideline/guideline-adjuvants-vaccines-human-use-see-also-explanatory-note_en.pdf. Accessed March 15, 2019.
8. World Health Organization. *Guidelines for the Clinical Evaluation of Dengue Vaccines in Endemic Areas*. In: Immunization, Vaccines and Biologicals. Geneva, Switzerland: World Health Organization; 2008.
9. Food and Drug Administration. Guidance for Industry: *Development of Preventive HIV Vaccines for Use in Pediatric Populations*. Washington, DC: U.S. Department of Health and Human Services, Food and Drug Administration, Center for Biologics Evaluation and Research; 2006.
10. World Health Organization. *Guidelines on the Quality, Safety and Efficacy of Ebola Vaccines (Proposed New Guidelines)*. Geneva, Switzerland: World Health Organization; 2016.
11. Food and Drug Administration, Center for Biologics Evaluation and Research. Guidance for industry: clinical considerations for therapeutic cancer vaccines. 2011. https://www.fda.gov/downloads/biologicsbloodvaccines/guidancecomplianceregulatoryinformation/guidances/vaccines/ucm278673.pdf. Accessed March 15, 2019.
12. European Medicines Agency. Guideline on the evaluation of anticancer medicinal products in man. 2017. https://www.ema.europa.eu/en/documents/scientific-guideline/guideline-evaluation-anticancer-medicinal-products-man-revision-5_en.pdf. Accessed March 15, 2019.
13. Ferraro B, Morrow MP, Hutnick NA, Shin TH, Lucke CE, Weiner DB. Clinical applications of DNA vaccines: current progress. *Clin Infect Dis*. 2011;53(3):296-302.
14. Wolf JJ, Kaplanski CV, Lebron JA. Nonclinical safety assessment of vaccines and adjuvants. In: Davies G, ed. *Vaccine Adjuvants: Methods and Protocols*. Totowa, NJ: Humana Press; 2010:29-40.
15. Al-Humadi N. Pre-clinical toxicology considerations for vaccine development. *Vaccine*. 2017;35(43):5762-5767.
16. Green MD, Al-Humadi NH. Preclinical toxicology of vaccines disclaimer: the findings and conclusions in this chapter have not been formally disseminated by the food and drug administration and should not be construed to represent any agency determination or policy. In: Faqi AS, ed. *A Comprehensive Guide to Toxicology in Nonclinical Drug Development*. 2nd ed. Boston, MA: Academic Press; 2017:709-735. Chapter 27.
17. Plitnick LM. Global regulatory guidelines for vaccines. In: Plitnick L, Herzyk D, ed. *Nonclinical Development of Novel Biologics, Biosimilars, Vaccines and Specialty Biologics*. Amsterdam, the Netherlands: Elsevier; 2013.
18. Batista-Duharte A, Portuondo D, Perez O, Carlos IZ. Systemic immunotoxicity reactions induced by adjuvanted vaccines. *Int Immunopharmacol*. 2014;20(1):170-180.
19. Garçon N, Segal L, Tavares F, Van Mechelen M. The safety evaluation of adjuvants during vaccine development: the AS04 experience. *Vaccine*. 2011;29(27):4453-4459.
20. Mastelic B, Garcon N, Del Giudice G, et al. Predictive markers of safety and immunogenicity of adjuvanted vaccines. *Biologicals*. 2013;41(6): 458-468.
21. Herati RS, Wherry EJ. What is the predictive value of animal models for vaccine efficacy in humans? Consideration of strategies to improve the value of animal models. *Cold Spring Harb Perspect Biol*. 2018;10(4):pii: a031583.
22. Jin H, Manetz S, Leininger J, et al. Toxicological evaluation of live attenuated, cold-adapted H5N1 vaccines in ferrets. *Vaccine*. 2007;25(52): 8664-8672.
23. Gerdts V, Wilson HL, Meurens F, et al. Large animal models for vaccine development and testing. *ILAR J*. 2015;56(1):53-62.
24. Collins JM, Redman JM, Gulley JL. Combining vaccines and immune checkpoint inhibitors to prime, expand, and facilitate effective tumor immunotherapy. *Exp Rev Vaccines*. 2018;17(8):697-705.
25. Forster R. Study designs for the nonclinical safety testing of new vaccine products. *J Pharmacol Toxicol Meth*. 2012;66(1):1-7.
26. Liu J, Xu C, Liu Y-L, et al. Activation of rabbit TLR9 by different CpG-ODN optimized for mouse and human TLR9. *Comp Immunol Microbiol Infect Dis*. 2012;35(5):443-451.
27. Sellers RS, Pardo I, Hu G, et al. Inflammatory cell findings in the female rabbit heart and stress-associated exacerbation with handling and procedures used in nonclinical studies. *Toxicol Pathol*. 2017;45(3):416-426.

28. Keenan CM, Baker JF, Bradley AE, et al. International Harmonization of Nomenclature and Diagnostic Criteria (INHAND) progress to date and future plans. *J Toxicol Pathol*. 2015;28(1):51-53.
29. Weber K, Razinger T, Hardisty JF, et al. Differences in rat models used in routine toxicity studies. *Int J Toxicol*. 2011;30(2):162-173.
30. Brayton CF, Treuting PM, Ward JM. Pathobiology of aging mice and GEM: background strains and experimental design. *Vet Pathol*. 2012; 49(1):85-105.
31. Ruehl-Fehlert C, Kittel B, Morawietz G, et al. Revised guides for organ sampling and trimming in rats and mice-part 1. *Exp Toxicol Pathol*. 2003; 55(2-3):91-106.
32. Morawietz G, Ruehl-Fehlert C, Kittel B, et al. Revised guides for organ sampling and trimming in rats and mice—part 3. A joint publication of the RITA and NACAD groups. *Exp Toxicol Pathol*. 2004;55(6):433-449.
33. Kittel B, Ruehl-Fehlert C, Morawietz G, et al. Revised guides for organ sampling and trimming in rats and mice—part 2. A joint publication of the RITA and NACAD groups. *Exp Toxicol Pathol*. 2004;55(6):413-431.
34. Keenan CM, Baker J, Bradley A, et al. International Harmonization of Nomenclature and Diagnostic Criteria (INHAND): progress to date and future plans. *Toxicol Pathol*. 2015;43(5):730-732.
35. Potter CW, Jennings R. The hamster as a model system for the study of influenza vaccines. *Postgrad Med J*. 1976;52(608):345-351.
36. Garbe JHO, Ausborn S, Beggs C, et al. Historical data analyses and scientific knowledge suggest complete removal of the abnormal toxicity test as a quality control test. *J Pharm Sci*. 2014;103(11):3349-3355.
37. Al-Laith M, Weyer A, Havet N, Dumarey C, Vargaftig BB, Bachelet M. Immunoglobulin-G-dependent stimulation of guinea pig lung mast cells and macrophages. *Allergy*. 1993;48(8):608-614.
38. Belser JA, Katz JM, Tumpey TM. The ferret as a model organism to study influenza A virus infection. *Dis Model Mech*. 2011;4(5):575-579.
39. Albrecht RA, Liu W-C, Sant AJ, et al. Moving forward: recent developments for the ferret biomedical research model. *mBio*. 2018;9(4): e01113-e01118.
40. Kozlosky JC, Mysore J, Clark SP, et al. Comparison of physiologic and pharmacologic parameters in Asian and Mauritius cynomolgus macaques. *Regul Toxicol Pharmacol*. 2015;73(1):27-42.
41. Ogawa LM, Vallender EJ. Genetic substructure in cynomolgus macaques (*Macaca fascicularis*) on the island of Mauritius. *BMC Genomics*. 2014; 15(1):748.
42. Colman K. Impact of the genetics and source of preclinical safety animal models on study design, results, and interpretation. *Toxicol Pathol*. 2016; 45(1):94-106.
43. Gerdts V, Little-van den Hurk S, Griebel PJ, Babiuk LA. Use of animal models in the development of human vaccines. *Future Microbiol*. 2007; 2(6):667-675.
44. Rubic-Schneider T, Christen B, Brees D, Kammüller M. Minipigs in translational immunosafety sciences: a perspective. *Toxicol Pathol*. 2016;44(3): 315-324.
45. Mair KH, Sedlak C, Kaser T, et al. The porcine innate immune system: an update. *Dev Comp Immunol*. 2014;45(2):321-343.
46. Helke KL, Nelson KN, Sargeant AM, et al. Background pathological changes in minipigs: a comparison of the incidence and nature among different breeds and populations of minipigs. *Toxicol Pathol*. 2016; 44(3):325-337.
47. Moghimi SM, Wibroe PP, Szebeni J, Hunter AC. Surfactant-mediated complement activation in beagle dogs. *Int Immunopharmacol*. 2013; 17(1):33-34.
48. Qiu S, Liu Z, Hou L, et al. Complement activation associated with polysorbate 80 in beagle dogs. *Int Immunopharmacol*. 2013;15(1):144-149.
49. Klotz D, Baumgärtner W, Gerhauser I. Type I interferons in the pathogenesis and treatment of canine diseases. *Vet Immunol Immunopathol*. 2017; 191:80-93.
50. Mordmüller B, Surat G, Lagler H, et al. Sterile protection against human malaria by chemoattenuated PfSPZ vaccine. *Nature*. 2017;542:445.
51. Diehl KH, Hull R, Morton D, et al. A good practice guide to the administration of substances and removal of blood, including routes and volumes. *J Appl Toxicol*. 2001;21(1):15-23.
52. Turner PV, Brabb T, Pekow C, Vasbinder MA. Administration of substances to laboratory animals: routes of administration and factors to consider. *J Am Assoc Lab Anim Sci*. 2011;50(5):600-613.
53. Hatta Y, Boltz D, Sarawar S, Kawaoka Y, Neumann G, Bilsel P. Novel influenza vaccine M2SR protects against drifted H1N1 and H3N2 influenza virus challenge in ferrets with pre-existing immunity. *Vaccine*. 2018; 36(33):5097-5103.
54. Lycke N. Recent progress in mucosal vaccine development: potential and limitations. *Nat Rev Immunol*. 2012;12:592.
55. Emami A, Tepper J, Short B, et al. Toxicology evaluation of drugs administered via uncommon routes: intranasal, intraocular, intrathecal/intraspinal, and intra-articular. *Int J Toxicol*. 2017;37(1):4-27.
56. Chamanza R, Wright JA. A review of the comparative anatomy, histology, physiology and pathology of the nasal cavity of rats, mice, dogs and non-human primates. Relevance to inhalation toxicology and human health risk assessment. *J Comp Pathol*. 2015;153(4):287-314.
57. Azegami T, Yuki Y, Kiyono H. Challenges in mucosal vaccines for the control of infectious diseases. *Int Immunol*. 2014;26(9):517-528.
58. Hickling JK, Jones KR, Friede M, Zehrung D, Chen D, Kristensen D. Intradermal delivery of vaccines: potential benefits and current challenges. *Bull World Health Organ*. 2011;89(3):221-226.
59. Prausnitz MR, Mikszta JA, Cormier M, Andrianov AK. Microneedle-based vaccines. In: Compans RW, Orenstein WA, eds. *Vaccines Pandemic Influenza*. Berlin, Heidelberg: Springer; 2009:369-393.
60. Sangaré L, Manhart L, Zehrung D, Wang CC. Intradermal hepatitis B vaccination: a systematic review and meta-analysis. *Vaccine*. 2009; 27(12):1777-1786.
61. Seaman MS, Wilck MB, Baden LR, et al. Effect of vaccination with modified vaccinia ankara (ACAM3000) on subsequent challenge with Dryvax. *J Infect Dis*. 2010;201(9):1353-1360.
62. Mohammed AJ, AlAwaidy S, Bawikar S, et al. Fractional doses of inactivated poliovirus vaccine in Oman. *N Engl J Med*. 2010;362(25): 2351-2359.
63. Resik S, Tejeda A, Mas Lago P, et al. Randomized controlled clinical trial of fractional doses of inactivated poliovirus vaccine administered intradermally by needle-free device in Cuba. *J Infect Dis*. 2010;201(9):1344-1352.
64. Waghule T, Singhvi G, Dubey SK, et al. Microneedles: a smart approach and increasing potential for transdermal drug delivery system. *Biomed Pharmacother*. 2019;109:1249-1258.
65. Bussio JI, Molina-Perea C, González-Aramundiz JV. Lower-sized chitosan nanocapsules for transcutaneous antigen delivery. *Nanomaterials (Basel)*. 2018;8(9):659.
66. Alkilani AZ, McCrudden MTC, Donnelly RF. Transdermal drug delivery: innovative pharmaceutical developments based on disruption of the barrier properties of the stratum corneum. *Pharmaceutics*. 2015;7(4):438.
67. Todo H. Transdermal permeation of drugs in various animal species. *Pharmaceutics*. 2017;9(3):pii:E33.
68. Lawhorn DB. Diseases of potbellied pigs. *Merck Vet Manual*. Merck Sharp & Dohme Corp; 2019. https://www.merckvetmanual.com/exotic-and-laboratory-animals/potbellied-pigs/diseases-of-potbellied-pigs.
69. Draize JH, Woodard G, Calvery HO. Methods for the study of irritation and toxicity of substances applied topically to the skin and mucous membranes. *J Pharmacol Exper Therap*. 1944;82(3):377-390.
70. Tomlinson L, Boone LI, Ramaiah L, et al. Best practices for veterinary toxicologic clinical pathology, with emphasis on the pharmaceutical and biotechnology industries. *Vet Clin Pathol*. 2013;42(3):252-269.
71. Weingand K, Brown G, Hall R, et al. Harmonization of animal clinical pathology testing in toxicity and safety studies. The Joint Scientific Committee for International Harmonization of Clinical Pathology Testing. *Fundam Appl Toxicol*. 1996;29(2):198-201.
72. Green MD. Acute phase responses to novel, investigational vaccines in toxicology studies: the relationship between C-reactive protein and other acute phase proteins. *Int J Toxicol*. 2015;34(5):379-383.
73. Cray C, Zaias J, Altman NH. Acute phase response in animals: a review. *Comp Med*. 2009;59(6):517-526.
74. van Rossum AP, Vlasveld LT, van den Hoven LJ, de Wit CW, Castel A. False prolongation of the activated partial thromboplastin time (aPTT) in

inflammatory patients: interference of C-reactive protein. *Br J Haematol*. 2012;157(3):394-395.
75. Du X, Liu M, Su J, et al. Uncoupling therapeutic from immunotherapy-related adverse effects for safer and effective anti-CTLA-4 antibodies in CTLA4 humanized mice. *Cell Res*. 2018;28(4):433-447.
76. Sellers RS, Morton D, Michael B, et al. Society of Toxicologic Pathology position paper: organ weight recommendations for toxicology studies. *Toxicol Pathol*. 2007;35(5):751-755.
77. Michael B, Yano B, Sellers RS, et al. Evaluation of organ weights for rodent and non-rodent toxicity studies: a review of regulatory guidelines and a survey of current practices. *Toxicol Pathol*. 2007;35(5):742-750.
78. Haley P, Perry R, Ennulat D, et al. STP position paper: best practice guideline for the routine pathology evaluation of the immune system. *Toxicol Pathol*. 2005;33(3):404-407.
79. European Medicines Agency. Humanza EPAR public assessment report. 2010. https://www.ema.europa.eu/en/documents/assessment-report/humenza-epar-public-assessment-report_en.pdf. Accessed March 15, 2019.
80. Tilney NL. Patterns of lymphatic drainage in the adult laboratory rat. *J Anat*. 1971;109(pt 3):369-383.
81. Gooneratne BW. The lymphatic system in rhesus monkeys (*Macaca mulatta*) outlined by lower limb lymphography. *Acta Anat (Basel)*. 1972;81(4):602-608.
82. Soto-Miranda MA, Suami H, Chang DW. Mapping superficial lymphatic territories in the rabbit. *Anat Rec (Hoboken)*. 2013;296(6):965-970.
83. Suami H, Yamashita S, Soto-Miranda MA, Chang DW. Lymphatic territories (lymphosomes) in a canine: an animal model for investigation of postoperative lymphatic alterations. *PLoS One*. 2013;8(7):e69222-e69222.
84. Ito R, Suami H. Lymphatic territories (lymphosomes) in swine: an animal model for future lymphatic research. *Plast Reconstr Surg*. 2015;136(2):297-304.
85. Randall HW, Monticello TM, Morgan KT. Large area sectioning for morphologic studies of nonhuman primate nasal cavities. *Stain Technol*. 1988;63(6):355-362.
86. Pereira ME, Macri NP, Creasy DM. Evaluation of the rabbit nasal cavity in inhalation studies and a comparison with other common laboratory species and man. *Toxicol Pathol*. 2011;39(5):893-900.
87. Young JT. Histopathologic examination of the rat nasal cavity. *Fundam Appl Toxicol*. 1981;1(4):309-312.
88. Iwama S, De Remigis A, Callahan MK, Slovin SF, Wolchok JD, Caturegli P. Pituitary expression of CTLA-4 mediates hypophysitis secondary to administration of CTLA-4 blocking antibody. *Sci Transl Med*. 2014;6(230):230ra245.
89. Greaves P, Chouinard L, Ernst H, et al. Proliferative and non-proliferative lesions of the rat and mouse soft tissue, skeletal muscle and mesothelium. *J Toxicol Pathol*. 2013;26(3 suppl):1S-26S.
90. Selby MJ, Engelhardt JJ, Johnston RJ, et al. Preclinical development of ipilimumab and nivolumab combination immunotherapy: mouse tumor models, in vitro functional studies, and cynomolgus macaque toxicology. *PLoS One*. 2016;11(9):e0161779.
91. Hughes J, Vudattu N, Sznol M, et al. Precipitation of autoimmune diabetes with anti-PD-1 immunotherapy. *Diabetes Care*. 2015;38(4):e55-e57.
92. Kerlin R, Bolon B, Burkhardt J, et al. Scientific and Regulatory Policy Committee: recommended ("best") practices for determining, communicating, and using adverse effect data from nonclinical studies. *Toxicol Pathol*. 2015;44(2):147-162.

Title: SARS-CoV-2 infection leads to acute infection with dynamic cellular and inflammatory flux in the lung that varies across nonhuman primate species

Authors: Dhiraj Kumar Singh[1,2], Shashank R. Ganatra[1,2], Bindu Singh[1,2], Journey Cole[1,2], Kendra J. Alfson[2], Elizabeth Clemmons[1,2], Michal Gazi[2], Olga Gonzalez[1,2], Ruby Escobedo[1,2], Tae-Hyung Lee[1,2], Ayan Chatterjee[1,2], Yenny Goez-Gazi[2], Riti Sharan[1,2], Rajesh Thippeshappa[1,2], Maya Gough[1,2], Cynthia Alvarez[1,2], Alyssa Blakley[1,2], Justin Ferdin[1,2], Carmen Bartley[1,2], Hilary Staples[1,2], Laura Parodi[1,2], Jessica Callery[1,2], Amanda Mannino[1,2], Benjamin Klaffke[2], Priscilla Escareno[2] , Roy N. Platt II[2], Vida Hodara[1,2], Julia Scordo[2], Adelekan Oyejide[3], Dharani K. Ajithdoss[3], Richard Copin[3], Alina Baum[3], Christos Kyratsous[3], Xavier Alvarez[1,2], Bruce Rosas[4], Mushtaq Ahmed[4], Anna Goodroe[1,2], John Dutton[1,2], Shannan Hall-Ursone[1,2], Patrice A. Frost[1,2], Andra K. Voges[5], Corinna N. Ross[1,2], Ken Sayers[1,2], Christopher Chen[1,2], Cory Hallam[2], Shabaana A. Khader[4] , Makedonka Mitreva[4], Timothy J. C. Anderson[2], Luis Martinez-Sobrido[2], Jean L. Patterson[2], Joanne Turner[2], Jordi B.Torrelles[2], Edward J. Dick, Jr.[1,2], Kathleen Brasky[1,2], Larry S. Schlesinger[1,2], Luis D. Giavedoni[1,2#], Ricardo Carrion, Jr.[1,2#], Deepak Kaushal[1,2#]

Affiliations: [1]Southwest National Primate Research Center, [2]Texas Biomedical Research Institute, San Antonio, TX, 78227, [3]Regeneron Pharmaceuticals, Inc., Tarrytown, NY 10591; [4]Washington University in St Louis School of Medicine, St Louis, MO; [5]Veterinary Imaging Consulting of South Texas, San Antonio, TX, 78258.

[#]To whom correspondence may be addressed: Deepak Kaushal, PhD, Director, Southwest National Primate Research Center, Professor, Texas Biomedical Research Institute, 8715 W. Military Drive, San Antonio, TX, 78227, Email: dkaushal@txbiomed.org, Tel. (210)258-9209; OR Ricardo Carrion, Jr., PhD, Professor, Texas Biomedical Research Institute, 8715 W. Military Drive,

San Antonio, TX, 78227; Email: rcarrion@txbiomed.org, Tel. (210)258-9479 OR Luis D. Giavedoni, PhD, Professor, Texas Biomedical Research Institute, 8715 W. Military Drive, San Antonio, TX, 78227, Email: lgiavedoni@txbiomed.org, Tel. (210)258-9603.

Abbreviations: COVID-19, Coronavirus disease 2019; SARS-CoV-2, Severe Acute Respiratory Syndrome Coronavirus-2; BAL, bronchoalveolar lavage; PFU, Plaque Forming Unit; CRP, C-reactive protein; CXR, thoracic radiograph; NHP, nonhuman primate; PBMC, peripheral blood mononuclear cell; dpi, days post-infection.

Key words: COVID-19, SARS-CoV-2, nonhuman primates, rhesus macaques, baboons, marmosets, animal models, BAL, CT

Summary

There are no known cures or vaccines for COVID-19, the defining pandemic of this era. Animal models are essential to fast track new interventions and nonhuman primate (NHP) models of other infectious diseases have proven extremely valuable. Here we compare SARS-CoV-2 infection in three species of experimentally infected NHPs (rhesus macaques, baboons, and marmosets). During the first 3 days, macaques developed clinical signatures of viral infection and systemic inflammation, coupled with early evidence of viral replication and mild-to-moderate interstitial and alveolar pneumonitis, as well as extra-pulmonary pathologies. Cone-beam CT scans showed evidence of moderate pneumonia, which progressed over 3 days. Longitudinal studies showed that while both young and old macaques developed early signs of COVID-19, both groups recovered within a two-week period. Recovery was characterized by low-levels of viral persistence in the lung, suggesting mechanisms by which individuals with compromised immune

systems may be susceptible to prolonged and progressive COVID-19. The lung compartment contained a complex early inflammatory milieu with an influx of innate and adaptive immune cells, particularly interstitial macrophages, neutrophils and plasmacytoid dendritic cells, and a prominent Type I-interferon response. While macaques developed moderate disease, baboons exhibited prolonged shedding of virus and extensive pathology following infection; and marmosets demonstrated a milder form of infection. These results showcase in critical detail, the robust early cellular immune responses to SARS-CoV-2 infection, which are not sterilizing and likely impact development of antibody responses. Thus, various NHP genera recapitulate heterogeneous progression of COVID-19. Rhesus macaques and baboons develop different, quantifiable disease attributes making them immediately available essential models to test new vaccines and therapies.

Main

A novel coronavirus, designated severe acute respiratory syndrome coronavirus 2 (SARS-CoV-2), emerged in Wuhan, China in 2019, and was proven to be the cause of an unspecified pneumonia. It has since spread globally, causing Coronavirus Disease 2019 (COVID-19) [1]. The World Health Organization (WHO) declared COVID-19 a pandemic. It is clear that community spread of SARS-CoV-2 is occurring rapidly and the virus has very high infectivity and transmission rates, even compared to SARS-CoV-1, the causative agent of an outbreak 15 years earlier. It has been estimated that between up to 250,000 American lives may be lost due to COVID-19. The world over, these numbers could be 10-50 times worse. Clearly, COVID-19 is the most defining

pandemic of this era, requiring significant biomedical research input, in order to most effectively fast track the development of new therapies and vaccines.

Human COVID-19 disease presents with a broad clinical spectrum ranging from asymptomatic to mild and severe cases. Patients with COVID pneumonia exhibit high-grade pyrexia, fatigue, dyspnea and dry cough accompanied by a rapidly progressing pneumonia, with bilateral opacities on x-ray and patchy, ground glass opacities on lung Computed Tomography (CT) scans. Individuals with immunocompromised conditions and comorbidities are at highest risk for worse outcomes of COVID-19.

Nonhuman primate (NHP) models of infectious diseases have proven useful for both investigating the pathogenesis of infection and testing therapeutic and vaccine candidates [2]. During the SARS and MERS outbreaks, NHP models were developed with a moderate degree of success[3]. Early reports also indicate the utility of NHPs for SARS-CoV-2 infection, and for evaluating vaccine candidates[4,5,6,7]. We hypothesized that the heterogeneity of human responses to SARS-CoV-2 infection can be recapitulated using multiple NHP species. Furthermore, we sought to gain a detailed characterization of the early cellular immune events following SARS-CoV-2 infection in the lung compartment, which has not yet been reported. Here, we compare SARS-CoV-2 infection in three species of NHPs (Specific Pathogen-free [SPF] Indian rhesus macaques, African-origin baboons, and New-World origin common marmosets). We assess age as a variable and focus our studies on high resolution imaging and the critical nature of the early cellular immune response in the lung which likely impacts disease outcome.

Early events in SARS-CoV-2 infection in rhesus macaques

We first assessed the ability of SARS-CoV-2 to infect rhesus macaques during an acute 3-day infection study. Four Indian-origin mycobacteria- and SPF-naïve rhesus macaques (*Macaca mulatta*) (Table S1) were infected by multiple routes (ocular, intratracheal and intranasal) with sixth-passage virus at a target dose of $1.05x10^6$ PFU/per animal. All animals developed clinical signs of viral infection as evidenced by a doubling of serum C-Reactive Protein (CRP) levels relative to baseline, indicating systemic inflammation (Fig 1a); significantly decreased serum albumin (Fig 1b) and hemoglobin (Fig 1c) levels, indicating viral-induced anemia; and progressively increasing total serum CO_2 levels (Fig S1a) indicative of pulmonary dysfunction. These observations were accompanied by a decrease in red blood cells (RBCs) (Fig S1b), reticulocytes (Fig S1c), white blood cells (WBCs) (Fig S1d), and platelet counts (Fig S1e); and a decrease in both the total number and percentage of neutrophils (Fig S1f, g), the latter suggesting that neutrophils are recruited to the lung compartment in response to SARS-CoV-2 infection as first responders. In contrast, systemic influx of monocytes was observed, indicating viral infection-induced myelopoiesis (Fig S1h). Monocytes are crucial for successful antiviral responses via recognition of pathogen-associated molecular patterns, thereby initiating a signaling cascade that invokes an interferon response to control infections. No significant pyrexia or weight loss was observed in this acute study. Overall, our results suggest that rhesus macaques develop several clinical signs of viral infection following experimental exposure to SARS-CoV-2.

Viral RNA was detected in BAL, and from nasal or nasopharyngeal (NS) and buccopharyngeal (BS) swabs at 1-3 days post-infection (dpi), but not at pre-infection time points (Fig 1d-f). Viral RNA was also detected in saliva and from rectal swabs (RS) in a small subset of animals (Fig S1i-j). Unlike other samples, viral RNA was only detected in RS at later time points (i.e., after 1 dpi). At necropsy (3 dpi), we performed random sampling from every lung lobe and SARS-CoV-2 RNA could be detected in 23/24 total lung sections analyzed. An average of 4-6 log copies/100 mg of lung tissue could be detected from every lobe (Fig 1g). The ~4-log increase in viral RNA from 1 to 2 dpi in the BAL (Fig 1d) provided clear evidence of early active replication of SARS-CoV-2 in rhesus macaques.

Examination at necropsy (3 dpi) revealed findings of interstitial and alveolar pneumonia (Fig 1h, i). While gross appearance of the lungs of most infected animals was unremarkable (Fig S2a), multifocal to coalescing red discoloration of the left lung lobes in one macaque was observed (Fig S2b). Table S2 summarizes the histopathologic findings in descending order of occurrence by anatomic location. The lung was the most affected organ ((Fig 1h, i, Table S2, Fig S2). Multifocal, mild to moderate interstitial pneumonia characterized by infiltrates of neutrophils, macrophages, lymphocytes, and eosinophils was present in all four animals (Fig 1 i, Fig S2d, e, g, h), and was accompanied by variable fibrosis (4/4, Fig S2e), fibrin deposition (3/4, Fig S2c), vasculitis (3/4, Fig S2f), edema (2/4, Fig S2h), necrosis (Fig S2g), and areas of consolidation (2/4, Fig S2c). All four macaques exhibited the following: 1) Syncytial cells in the epithelial lining and/or alveolar lumen (Fig S2e, g, k); 2) Bronchitis characterized by infiltrates of eosinophils within the bronchial wall

and epithelium (Fig 1h, Fig S2i, j, k); Bronchus-associated lymphoid tissue (BALT) hyperplasia (Fig S2i); and 4) Minimal to moderate lymphoplasmacytic and eosinophilic tracheitis and rhinitis.

The presence of SARS-CoV-2 in tissue sections collected at necropsy (3 dpi) was determined by multi-label confocal immunofluorescence using antibodies specific for Nucleocapsid (N) (Fig 1j, k, Fig S3) and Spike(S) proteins (Fig S4) and their respective isotype controls (Fig S3, S4). Fluorescence immuno-histochemical analysis revealed the presence of SARS CoV-2 proteins in lungs (Fig 1j, Fig S3a, g, Fig S4a, d, g, j), nasal epithelium (Fig 1k, Fig S3b, h, Fig S4b, e, h, k) and tonsils (Fig S3c, i, Fig S4c, f, I, l). In all tissues, including lungs (Fig 1j, Fig S3 a, g), nasal epithelium (Fig 1k, Fig S3 b, h) and tonsils (Fig S3 c, i), N antigen signal was present in cells expressing ACE2, which has been shown to be a receptor for SARS-CoV-2, or in cells adjoining those expressing ACE2. No signal was detected in N isotype control staining in lungs, nasal epithelium or tonsils (Fig S3d-f), and no signal for viral antigen was detected in naïve tissues (Fig S3 m, n). It appeared that the expression levels of ACE2 protein were much lower in lung tissues derived from naïve animals compared to those from macaques exposed to SARS-CoV-2 (Fig S3 m, n). The majority of the S signal was detected in the epithelial layer with discrete distribution throughout the lung tissue (Fig S4a, d). In the nasal cavity, the virus was observed in cells of the epithelial linings (Fig S4b, h) but in tonsils, the virus appeared distributed throughout the tissue (Fig 3c, i). Together, these results show that SARS-CoV-2 exposure induces a respiratory tract infection in rhesus macaques. Viral replication is supported in the upper and lower lung compartments during the first three days of infection and viral antigens are detected at high levels in the lungs.

To complement the lung histopathology in rhesus macaques, radiographs were performed at baseline and each day post-infection. All four infected macaques showed progressive increase in CXR abnormality scores, consistent with an infectious disease (Fig 2a, Fig S5a). The 2 and 3 dpi CXR scores were significantly elevated relative to baseline (Fig 2a), despite evidence of partial resolution of specific lesions at 2 or 3 dpi versus 1 dpi (Fig S5a). There were mild-to-severe multifocal interstitial-to-alveolar patterns with soft tissue opacities (seen as ground glass opacities described in the CT scans below) in various lobes or diffusely in some animals, with more severe abnormalities in the lower lung lobes, and with the most severe findings at 3 dpi (Fig S5a). Pleural effusions were also observed.

Lung CT scans prior to infection showed a normal thorax cavity with the exception of atelectasis (Fig 2b-d, top panel). Within 1 dpi, CT scans showed increased multifocal pulmonary infiltrates with ground glass opacities in various lung lobes, linear opacities in the lung parenchyma, nodular opacities in some lung lobes, and increased soft tissue attenuation extending primarily adjacent to the vasculature (Fig 2c, Fig S5b-e). In some animals, multifocal alveolar pulmonary patterns and interstitial opacities were observed in lobe subsections, with soft tissue attenuation and focal border effacement with the pulmonary vasculature. Features intensified at 2-3 dpi, primarily in the lung periphery, but also adjacent to the primary bronchus and the vasculature (Fig 2d, Fig S5b). In other animals, progressive alveolar or interstitial pulmonary patterns were observed at 2 dpi (Fig 2c). While ground glass opacities in some lobes intensified at 2 dpi relative to 1 dpi, others resolved (Fig S5c, d). In one animal, the individual nodular pattern at 1 dpi evolved to a multifocal soft tissue nodular pattern in multiple lobes with associated diffuse ground glass

opacities (Fig S5d). At 3 dpi, persistent, patchy, fairly diffuse ground glass pulmonary opacities existed in many lung lobes with multifocal nodular tendency (Fig S5e). Overall, CT abnormality scores continuously increased at over the 3 days relative to baseline (Fig 2e). Percent change in the hyperdensity volume was calculated using CT scans to quantify pathological changes over the course of disease [8]. We observed a significant increase in lung hyperdense areas between 1-3 dpi compared to the baseline scans (Fig 2f-i). Measurement of volume involved in hyperdensity showed a significant, progressive increase over time (Fig 2j). Pneumonia was evident in all infected animals relative to their baseline (Fig 2j), suggesting that while some lesions formed and resolved within the three-day infection protocol, others persisted or progressed. Together, CXR and CT scans revealed moderate multi-lobe pneumonia in infected animals, confirming the histopathology results (Fig 1h, i, Fig S2) in the very early phase of SARS-CoV-2 infection in rhesus macaques.

We measured the levels of pro-inflammatory, Type I cytokines in the BAL fluid (Fig 3) and plasma (Fig S6a-l) of acutely infected rhesus macaques. Levels of IL-6 (Fig 3a), IFN-α (Fig 3b), IFN-γ (Fig 3c), IL-8 (Fig 3d), perforin (Fig 3e), IP-10 (Fig 3f), MIP1-α (Fig 3g) and MIP1-β (Fig 3h) were all significantly elevated in the BAL fluid. The levels of IL-12p40 (Fig 3i), IL-18 (Fig 3j), TNF (Fig 3k) and IL-1Ra (Fig 3l) increased over time. Of particular interest was the elevation of Type I IFN-α (Fig 3b), which has critical anti-viral activity including against SARS-CoV-2 [9]. Expression of a downstream Type-I interferon-regulated gene IP-10 (CXCL-10), which promotes the recruitment of CXCR3^{+} Th1 thymocytes, was also induced (Fig 3f). Therefore, we observed that rhesus macaques mount an early anti-viral response to SARS-CoV-2 infection. Type I IFNs and IL-6 (both

significantly expressed) are key components of a "cytokine-storm" which promote acute respiratory distress syndrome (ARDS) associated with both SARS-CoV-1 and -2, when induced uncontrollably[10]. IFN-α and IP-10 were also significantly elevated in plasma samples at 2 and 3 dpi (Fig S6).

Thus, clinical, imaging, pathology and cytokine analyses provide evidence for an acute infection in macaques following exposure to SARS-CoV-2, which leads to a moderate pneumonia and pathology, with early activation of anti-viral responses. To study progression of infection, and assess the effect of age on SARS-CoV-2 infection, we infected six young and six old Indian-origin rhesus macaques as described above and longitudinally followed the outcome over 14-17 days (Table S1). We included four macaques as procedural controls, which were sham-infected and underwent all procedures (with the exception of necropsy) to control for the impact of multiple procedures over the course of the study (Table S1). We also infected six baboons and an equal number of marmosets with SARS-CoV-2 in order to compare the progression of COVID-19 in different NHP models.

Long-term study of SARS-CoV-2 infection in rhesus macaques, baboons and marmosets demonstrates heterogeneity in progression to COVID-19

Results of the longitudinal study showed that the acute signs of SARS-CoV-2 infection and mild-to-moderate COVID-19 disease in rhesus macaques markedly improved over time (Fig S7). In general, no major differences were observed as a consequence of age, and subsequent data from young and old animals are combined (N=12), unless specified. A small subset (3/12) of animals

exhibited elevated serum CRP past 3 dpi (Fig S7a), although metabolic signs of dysfunction likely induced by infection (e.g. tCO2 elevation) continued for the duration of the study (Fig S7b). No alterations were observed in the levels of serum albumin or hemoglobin during this timeframe (not shown). There was a significant decline in RBCs (Fig S7c) at 3 and 6 dpi which normalized or reverted by 9 dpi. The percentage of neutrophils in the peripheral blood remained unchanged between 3-14 dpi (not shown). The significant decline in blood platelets and increase in the percentage of monocytes observed at 3 dpi, were short-lived (Fig S7d, e). Despite these modest changes, the majority of animals in both age groups exhibited weight loss throughout the study duration (Fig S7f), although pyrexia was not observed (not shown).

Viral RNA was detected in BAL of 10/12 macaques at 3 dpi, but declined thereafter (Fig 4a). Detection of viral RNA was equivalent between young (5/6) and old (5/6) macaques (Fig S8a). Very low viral RNA copy numbers were detected in BAL at 9 dpi with only one young macaque testing positive, and none by 12 dpi (Fig 4a). Viral RNA appeared to persist for much longer in NS than BAL, including at study endpoint (Fig 4b). Viral RNA was detected from NS in 6/12 macaques at 3 dpi and on average young macaques harbored more virus in their nasal cavity at 3 dpi relative to old animals but the differences were not significant (Fig S8b). SARS-CoV-2 RNA was detected in 10/12 macaques (6 young, 4 old, respectively) at 9 dpi and 6/12 macaques at the end of the study period (Fig S8b). These results suggest that the virus persists for at least two weeks in the respiratory compartment of immunocompetent macaques that clinically recovered from COVID-19. Viral RNA was detected from BS in 4/12 animals at 3 and 6 dpi, but not at later time points (Fig S8c, d). No significant difference was detected between age groups. Viral RNA was also

detected from RS in 2/12 animals at 3, 6 and 9 dpi (Fig S8e, f). Significantly lower levels of viral RNA (2.5 logs) were detectable at the end of the study (14-17 days) when compared to viral RNA detected at the end of the 3-day protocol (Fig 4c, Fig S9a). Viral RNA was detected in the lungs of two-thirds (8/12) of all macaques and no effect of age was apparent. No viral RNA was detected in any serum samples (Fig S9b) or in randomly selected urine samples (Fig S9c). The presence of viral RNA in the lungs of macaques after two weeks following recovery from acute COVID-19 indicates that while macaques control SARS-CoV-2 infection, immune responses are not sterilizing.

Gross examination of the lungs of most infected animals at necropsy (14 to 17 dpi) was unremarkable (Fig S10a); however, red discoloration of the dorsal aspect of the lung lobes was seen in four young and two aged animals (Fig S10b). Table S3 summarizes the histopathologic findings in descending order of occurrence by anatomic location. The lungs were the most affected organ (Fig 4d, e, Table S3). Multifocal minimal to mild interstitial mononuclear inflammation was seen in 11/12 animals (Fig 4n, 0, Fig S10c), generally composed of macrophages and lymphocytes that expanded the alveolar septa (Fig 4n, Fig S10d, e, f, g), with variable neutrophil infiltrates (5/12, Fig S10e), fibrosis (5/12, Fig 4o, Fig S10f, g) or vasculitis (3/12, Fig S10i). Alveolar epithelium often contained areas of type II pneumocyte hyperplasia (4/12, Fig S10e) and bronchiolization (2/12, Fig S10h). Alveolar lumina contained increased alveolar histiocytosis (9/12, Fig 4o, Fig S10d, e) occasionally admixed with neutrophils (5/12, Fig S10e). Syncytial cells (Fig S10e, f) were observed most frequently in the alveolar lumen in all 12 animals. Bronchitis was observed in 4/12, characterized by infiltrates of eosinophils within the bronchial

wall and epithelium (Fig S10j). Prominent perivascular lymphocytes (7/12, Fig S10k) and BALT hyperplasia (5/12, Fig S10i) were frequently observed. The majority of the animals (11/12) exhibited minimal to moderate lymphoplasmacytic and eosinophilic tracheitis.

Early detection of viral RNA in BAL was comparable between macaques and baboons (Fig 4a, f) and NS (Fig 4b, g). A third of the baboons had detectable viral RNA in NS at 12 dpi (Fig 4g), and a similar number of animals remained positive at 9 dpi in the BS (Fig S11a). The number of baboons from which viral RNA could be detected in RS increased over time from 1/6 at 3 dpi to 3/6 at 6 dpi, 4/6 at 9 dpi and 3/6 at 12 dpi, underscoring long-term viral persistence of SARS-CoV-2 in baboons relative to rhesus macaques (Fig S11b). Postmortem gross examination at 14 to 17 dpi identified red discoloration of the lung lobes in all six baboons (Fig S11c, d). Table S4 summarizes the histopathologic findings in descending order of occurrence by anatomic location. Like macaques, the lungs were the most affected organ in the baboons (Fig 4h, i, Table S6, Fig S11). Multifocal minimal to moderate interstitial mononuclear inflammation was seen in 6/6 animals (Fig 4h, Fig S11f, g, h, i), generally composed of macrophages and lymphocytes that expanded the alveolar septa, with variable neutrophil infiltrates (3/6, Fig S11f, g, j, k) or fibrosis (2/6, Fig S11j, k). Alveolar epithelium often contained areas of type II pneumocyte hyperplasia (4/6, Fig 4i, Fig S11i) and bronchiolization (1/6, Fig S11l). Alveolar lumina contained increased alveolar histiocytosis (6/6, Fig 4h) occasionally admixed with neutrophils (3/6) (Fig S11f, g, h, i). Syncytial cells were observed most frequently in the alveolar lumen in all 6 animals (Fig 4h, Fig S11m). Bronchitis was observed in 6/6, characterized by infiltrates of eosinophils within the bronchial wall and epithelium (Fig S11n). BALT hyperplasia (5/6, Fig S11k) was frequently observed. The

majority of the animals exhibited minimal to moderate lymphoplasmacytic and eosinophilic tracheitis (5/6) and rhinitis (4/6).

SARS-CoV-2 infection was milder in marmosets. Less than 4 logs of viral RNA could be detected in NS from infected marmosets, peaking at 3 dpi, and 1/6 animals was also positive at 6 dpi. No viral RNA was detected at later time points (Fig 4j). No viral RNA was detected in BS (Fig 4k). A subset of six marmosets was euthanized at 3 dpi (n=2), while others were necropsied at 14 dpi. Approximately 2 logs of viral RNA could be detected in the lungs of marmosets at both time points. Evidence of SARS-CoV-2 infection-induced pathology, including interstitial and alveolar pneumonitis was observed in marmoset lungs as well (Fig 4m, n), although not as prevalent as in macaques or baboons. Thus, our results show that three genera of NHPs develop different degrees of COVID-19 following SARS-CoV-2 infection when evaluated side by side, with baboons exhibiting moderate to severe pathology, macaques exhibiting moderate pathology and marmosets exhibiting mild pathology. Viral RNA levels in BAL, NS and lungs are consistent with the levels of pathology. While other results also suggest that marmosets are unaffected by SARS-CoV-2 infection [4] (https://www.biorxiv.org/content/10.1101/2020.03.21.001628v1), we show that these NHPs do develop non-negligible, mild COVID-19-related pathology and some degree of viral persistence.

We performed detailed imaging of macaques in the longitudinal study. Similar to the acute study, imaging revealed the development of viral pneumonia. All macaques infected with SARS-CoV-2 exhibited low baseline CXR scores (Fig 5a, Table S5) with no difference due to age (Fig 5b). Several

infected macaques showed changes consistent with pneumonia (Table S5) with peak severity seen between 3-6 dpi, followed by a decline by study end (Fig 5a, b, Table S5). Examples of the development of extensive pneumonia by CXR can be seen in macaques at 6 dpi, relative to baseline with subsequent resolution (Fig 5 c-e). Several animals exhibited multi-lobe alveolar infiltrates and/or interstitial opacities at 6 dpi. In other animals, there were progressive, moderate to severe interstitial and alveolar infiltrates at 6 dpi, which resolved by day 14. Conversely, the radiographs of all procedure control animals (which underwent repeated BAL procedures) exhibited normal a thorax cavity with minimal to no findings.

High resolution CT imaging of the lungs was performed prior to and following SARS-CoV-2 infection on six young and six old macaques. Pneumonia was present in all animals, post-infection, but to a significantly higher degree in old macaques relative to young (Fig 5f, Fig S12a-f, Table S6). At 6 dpi, severe patchy alveolar patterns were observed in some lobes, while other lobes had milder, interstitial patterns, with moderate to severe ground glass opacities primarily in the lungs of old macaques (Fig S12a-f). In all animals, resolution of many ground glass opacities and nodular as well as multifocal lesions was observed at 12 dpi (Fig 5f, Fig S12a, b, d-f). At 12 dpi, all but one of the older macaques exhibited a normal or nearly normal thorax cavity, the latter with minimal ground glass opacities in all lung lobes studied at this time. Findings in one older macaque was considerably improved but retained patchy round glass opacities in all lobes and alveolar patterns in some lobes at 12 dpi (Fig S12c). This animal had the highest overall score by CT (Fig 5f) and CXRs (Fig 5 a-b). These results suggest that pneumonia in some older macaques may persist longer than in younger animals. Similar to the acute study, hyperdensity analysis

328 revealed a significant, progressive increase in the volume of lung involved in pneumonia at 6 dpi,
329 which normalized by 12 dpi (Fig 5g-o).
330
331 **SARS-CoV-2 infection in macaques results in a dynamic myeloid cell response in the lungs of**
332 **rhesus macaques**
333 Cellular composition in BAL samples and peripheral blood[11,12] at necropsy showed markedly
334 altered immune cell responses in the lung compartment following infection of macaques. In
335 healthy lungs, BAL is predominantly comprised of alveolar macrophages (AMs)[13] but respiratory
336 tract infections result in the influx of other immune cells. SARS-CoV-2 infection moderately
337 increased the proportions of myeloid cells in the BAL 3 dpi, with most returning to normal by 9
338 dpi (Fig S13a). There was no effect of age (Fig S13b). The myeloid influx included cells phenotyped
339 as interstitial macrophages (IMs, Fig 6a, e), neutrophils (Fig 6c, g) and plasmacytoid dendritic cells
340 (pDCs, Fig 6d, h). In contrast, the levels of resident AMs in BAL declined significantly at 3 dpi (Fig
341 6b, f). The increase in IMs, neutrophils and pDCs at 3 dpi was highly correlated with the levels of
342 viral RNA (Fig 6i-j, Fig S13i), while AMs exhibited an opposite trend. The frequency of
343 conventional dendritic cells (cDCs) declined as pDCs increased in BAL (Fig S13c). An increase in
344 the levels of both classical ($CD14^+CD16^-$) (not shown) and intermediate/inflammatory
345 ($CD14^+CD16^+$) monocytes in BAL was also observed at 3 dpi (Fig S13d). The frequency of myeloid
346 subpopulations increased in BAL was generally reduced in blood (Fig S13e-h), with two
347 exceptions - pDCs and $CD14^+CD16^+$ monocytes, which were increased in the blood as well as BAL
348 (Fig S13g-h). Relative to AMs, IMs have a shorter half-life, exhibit continuous turnover, and may
349 help to maintain homeostasis and protect against continuous pathogen exposure from the

environment[14]. Increased recruitment of pDCs to the lungs suggests a potentially important feature of protection from advanced COVID-19 disease in the rhesus macaque model since they are a major source of anti-viral Type I interferons such as IFN-α, the levels of which were elevated in the BAL within 1-3 dpi (Fig 3b).

Multi-label confocal imaging of lung tissues following Ki67 staining depicted that only few of the virally-infected cells in the lung tissue actively proliferated (Fig 5k-p). Detailed analysis of the lung tissue revealed that neutrophils (Fig 6k, l, Fig S14a, d), macrophages (Fig 6m, n, Fig S14b, h) and pDCs (Fig 6o, p, Fig S14c, i) recruited to the lung compartment (Fig 6a-h) harbored high levels of viral proteins (Fig 6k-p, Fig S14). Apart from these, many of the other cell-types contained viral proteins, suggesting a capacity of the virus to infect many cell types and that intact virus may also persist in the lungs. These novel data suggest that rapid influx of specialized subsets of myeloid cells to the lung that are known to express Type I IFNs and other pro-inflammatory cytokines is a key event in the control of SARS-CoV-2 infection.

Infection of macaques also resulted in a significant influx of T cells to the alveolar space by 3 dpi, which normalized by 9 dpi (Fig 7a, b, g). After infection, $CD4^+$ T cells expressed significantly lower levels of antigen-experience/tissue residence (CD69; Fig 6c), Th1 (CXCR3; Fig 6d), memory (CCR7; Fig 6f), and activation (HLA-DR) (Fig 6m) markers in BAL. In contrast, the levels of $CD4^+$ T cells expressing PD-1 (Fig 6e) and LAG-3 (Fig 6n) were significantly elevated, while those of $CD4^+$ T cells expressing CCR5 (Fig 6l) were unchanged. A similar effect was observed in $CD8^+$ T cell subsets, where the expression of CD69 (Fig 6h), CXCR3 (Fig 6i), and CCR7 (Fig 6k) was significantly reduced

in BAL following infection whereas expression of PD-1 (Fig 6j) and LAG-3 (Fig 6q) in the $CD8^+$ T cells was significantly increased. CCR5 (Fig 6o) and HLA-DR (Fig 6p) were unchanged. No differences were observed in T cell responses in young relative to old animals. Taking data from myeloid cells and lymphocytes together, we postulate that the rapid influx of myeloid cells capable of producing high levels of Type I IFNs result in immune control of SARS-CoV-2 infection in macaques, but that this control is not sterilizing. This allows for viral antigens to persist leading T cell recruitment, but with a T cell profile associated with immune modulation and promotion of antigen-mediated T cell anergy/exhaustion (PD-1, LAG3 expression)[15].

To extrapolate from phenotype to function, we explored proliferation, immune mediator production, and memory phenotypes. $CD4^+$ and $CD8^+$ T cells exhibiting proliferative (Fig 8a, g) and memory markers (Fig 8b, h) were significantly increased in BAL after infection whereas $CD4^+$ and $CD8^+$ T cells expressing naïve (Fig 8c, i) and effector (Fig 8d, j) phenotypes were significantly reduced. The percentage of $CD4^+$ (Fig 8e) and $CD8^+$ (Fig 8k) T cells expressing IL-2 was significantly elevated in the BAL at 9 dpi. A similar effect was observed for Granzyme-B (GZMB) (Fig 8f, l) which was sustained through 9 dpi. No significant effect of age was observed, although the expression of IL-2 on T cells was higher for young compared old rhesus macaques. Frequencies of $CD4^+$ and $CD8^+$ expressing interferon-γ (IFNG) (Fig S15a, d) and IL-17 (Fig S15b, e) were elevated, but unchanged for TNF-α (Fig S15c, f). Greater expression of IFNγ was measured on $CD4^+$ T cells recruited to the BAL in younger animals, but the differences were not statistically significant. These results suggest that robust cellular immune responses (both $CD4^+$ and $CD8^+$ T cells) are generated in the lung compartment (BAL) as early as day 3 and maintained at 9 dpi in many

394 instances. Following ex vivo re-stimulation of T cells from BAL at 9 dpi with CoV-specific peptide
395 pools, $CD4^+$ T cells expressing IL-2 (Fig 8m), GZMB (Fig 8n), IFN-γ (Fig S15g), IL-17 (Fig S15h) and
396 TNF-α (Fig S15i) were not statistically elevated beyond baseline values. This was similar for $CD8^+$
397 T cells expressing IL-2 (Fig 8o), GZMB (Fig 8p), IFN-γ (Fig S15j), IL-17 (Fig S15k) and TNF-α (Fig
398 S15l). In combination with increased expression of the immune-regulatory markers PD-1 and
399 LAG-3, our results suggest that T cells recruited to the lung compartment following SARS-CoV-2
400 infection are capable of secreting cytokine but fail to generate robust antigen specific responses
401 highlighting the fact that persistent T cell stimulation by viral antigens may generate T cell anergy
402 relatively early in infection and this is promoted by our findings of viral persistence in the
403 respiratory tract.
404
405 Immunophenotyping results were confirmed by studying cytokine production in BAL and plasma
406 (Fig S16)[16]. Our results show that the levels of IFN-α (Fig S16a), IL-1Ra (Fig S16b), and IL-6 (Fig
407 S16d) were elevated in BAL following infection, but levels rapidly normalized after the 3 dpi peak.
408 Levels of IFN-α were also induced in plasma (Fig S16g), but not those of IL-1Ra (Fig S16h), and IL-
409 6 (Fig S16j) or other cytokines studied. Cytokines were not induced at baseline or in procedure
410 control animals. Overall, the longitudinal study results were consistent with the acute infection
411 study in the expression of Type I pro-inflammatory cytokines responsible for viral control (IFN-α)
412 and expression of IL-6, which may contribute to a cytokine storm and development of ARDS in a
413 subset of hosts during COVID-19.
414

Protein levels of ACE-2, one presumed receptor for SARS-CoV-2 in humans, were detected at higher levels in the lungs and nasal epithelia of infected macaques than those in the lungs of naive rhesus macaques (Fig 1j, k). Using RNAseq we also studied if expression of ACE-2 could be detected in macaque lung tissues and elevated in in SARS-CoV-2 infected animals. This was indeed the case (Fig S17a-d) in a statistically significant manner two weeks after infection despite multiple hypothesis correction (Fig S17a, b). Interestingly, ACE-2 expression was significantly higher in young compared to old macaques (Fig S17c, d). These results potentially explain the higher levels of virus that we observed in several samples derived from young macaques in these two cohorts (Fig S8). Expression of transcripts specific for other viral receptors/co-receptors e.g., Cathepsin-L, CD147 or TMPRSS2 was not significantly altered in the lung two weeks after infection (Fig S17a).

Altogether, our results show that rhesus macaques, baboons and marmosets can all be infected with SARS-CoV-2 but exhibit differential progression to COVID-19. While marmosets exhibit mild infection, macaques are characterized by the presence of moderate progressive pneumonia that is rapidly resolved. This is accompanied by a marked reduction in lung and nasal viral loads. Baboons appear to have the most lung pathology, and the level of viral shedding and persistence in extra-respiratory compartment is also greater in this model. Furthermore, we show the importance of state-of-the-art, non-invasive imaging – cone beam CT scanning, and the application of innovative algorithms to identify the extent of lung involved in pneumonia, in developing models of COVID-19. This provided us with a quantifiable metric that lent itself to accurately assessing the efficacy of vaccines or the impact of therapeutic interventions.

Our results also point out, for the first time, that SARS-CoV-2 infection is associated with dynamic influxes of specific subsets of myeloid cells to the lung, particularly IMs, neutrophils and pDCs, and that viral proteins can be detected in these cells. These cellular influxes are likely due to a strong viral-induced myelopoeisis. This may help explain both development of COVID-19 pneumonia and subsequent control via expression of a strong Type I IFN response and expression of other pro-inflammatory cytokines. We speculate that these responses clear the majority of virus, and, in doing so, lead to eventual resolution of pneumonia, while limiting a progressive cytokine storm and ARDS in the majority of hosts. Macaques have served as excellent models of infectious diseases and vaccine development efforts[17-19], and this model permits lung imaging and detailed immune evaluations. Given the ability to reproducibly measure viral loads in NS and BAL, and quantify lung involvement by CT scans and hyperdensity analyses, we expect this model to play a critical role in the preclinical testing of novel candidate vaccines against SARS-CoV-2 infection and/or COVID-19 disease in development. Experiments in rhesus macaques can also evaluate safety and immunogenicity, including the important issue of antibody-mediated immune enhancement. Since mild-to-moderate COVID-19 disease that follows SARS-CoV-2 infection in rhesus macaques is short-lived, it follows that vaccine safety and efficacy studies can be evaluated in short term studies.

However, detection of both virus and its protein antigens over two weeks in macaques, baboons and even marmosets, indicates viral persistence rather than sterilizing immunity. Support for this comes from the finding of PD-1 and LAG-3 expression by $CD4^+$ and $CD8^+$ T cells in the lung and

lack of induction of antigen-specific immune effector cytokine production by these cells. Characterization of these responses is particularly important considering that T cell responses, particularly T helper responses, play key roles in shaping the nature of downstream B cell responses and production of antibodies. It is likely that in immunocompromised patients, persistent presence of SARS-CoV-2 could lead to exacerbated disease. Since COVID-19 has disproportionately affected the aging human population, we included age as an independent variable in our studies. Although there were several smaller changes observed in older animals, old and young animals both resolved infection. While it is possible that NHPs do not completely model all aspects of COVID-19 in humans, these findings suggest that underlying conditions which impact immunity such as defined and undefined co-morbidities, rather than aging per se, may be responsible for the greater morbidity and mortality observed due to COVID-19 in the aged human population (and a subset of younger individuals). Baboons developed more extensive disease and pathology with more widespread and severe inflammatory lesions compared to rhesus macaques. Baboons are also a preferred model of cardiovascular and metabolic diseases including diabetes [20-22], and therefore further development of the baboon model may prove especially useful for the study of co-morbidities with COVID-19 such as diabetes, cardiovascular disease, and aging.

Methods

Study approval. All of the infected animals were housed in Animal Biosafety Level 3 or 4 (ABSL3, ABSL4) at the Southwest National Primate Research Center where they were treated per the

481 standards recommended by AAALAC International and the NIH Guide for the Care and Use of
482 Laboratory Animals. Sham controls were housed in ABSL2. The animal studies in each of the
483 species were approved by the Animal Care and Use Committee of the Texas Biomedical Research
484 Institute and as an omnibus Biosafety Committee protocol.
485
486 **Animal studies and clinical evaluations**. 16 (eight young and eight young, see Table S1 for details)
487 Indian-origin rhesus macaques *(Macaca mulatta)*, and six African-origin baboons (*Papio*
488 *hamadryas*) all from SNPRC breeding colonies, were exposed via multiple routes (ocular, 100 μL;
489 intranasal, 200 μL - using a Teleflex Intranasal Mucosal Atomization Device; intratracheal, 200 μL
490 - using a Teleflex Laryngo-Tracheal Mucosal Atomization Device) of inoculation to 500 μL of an
491 undiluted stock of SARS-CoV-2, which had a titer of 2.1E+06 pfu/mL, resulting in the
492 administration of 1.05x106 pfu SARS-CoV-2. SARS-CoV-2 generated from isolate USA-WA1/2020
493 was used for animal exposures. A fourth cell-culture passage (P4) of SARS-CoV-2 was obtained
494 from Biodefense and Emerging Infections Research Resources Repository (BEI Resources, catalog
495 number NR-52281, GenBank accession number MN985325.1) and propagated at Texas Biomed.
496 The stock virus was passaged for a fifth time in Vero E6 cells at a multiplicity of infection (MOI)
497 of approximately 0.001. This master stock was used to generate a sixth cell culture passage
498 exposure stock by infecting VeroE6 cells at a MOI of 0.02. The resulting stock had a titer of 2.10
499 x 106 PFU/mL and was attributed the Lot No. 20200320. The exposure stock has been confirmed
500 to be SARS-CoV-2 by deep sequencing and was identical to published sequence (MN985325).
501 strain USA-WA1/2020 (BEI Resources, NR-52281, Manassas, VA). Six Brazilian-origin common
502 marmosets (*Callithrix jacchus*) were also infected via the combined routes (80μL intranasal; 40μL

ocular [20µL/eye]; 40µL oral performed twice for a total of 160µL intranasal, 80µL ocular; 80µL oral and 100µL IT) of the same stock. The total target dose presented to marmosets was 8.82E+05 pfu/mL. Four macaques, baboons and marmosets each were sham-infected with DMEM-10 media (the storage vehicle of the virus), to be used as procedural controls. Infected animals were euthanized for tissue collection at necropsy, and control animals were returned to the colony. Macaques were enrolled from a specific pathogen-free colony maintained at the SNPRC and were tested free from SPF-4 (simian retrovirus D, SIV, STLV-1 and herpes B virus). All animals including the baboons and the marmosets were also free of *Mycobacterium tuberculosis*. Animals were monitored regularly by a board-certified veterinary clinician for rectal body temperature, weight and physical examination. Collection of blood, BAL, nasal swab, and urine, under tiletamine-zolazepam (Telazol) anesthesia was performed as described (Table S1), except that BAL was not performed in marmosets. Four macaques were sampled daily until euthanized at 3dpi. All other macaques and all the baboons were sampled at 0, 3, 6, 9, 12 dpi and at euthanasia (BAL performed weekly). Blood was collected for complete blood cell analysis and specialized serum chemistries. Animals were observed daily to record alert clinical measurements. Nasal (longitudinal) or nasopharyngeal (acute) swabs and BALs were obtained to measure viral loads in a longitudinal manner, as described earlier [11]. Briefly, in a sitting position, the larynx was visualized and a sterile feeding tube inserted into the trachea and advanced until met with resistance. Up to 80ml of warm sterile saline was instilled, divided into multiple aliquots. Fluid was aspirated and collected for analysis.

Chest X-Rays. Clinical radiographic evaluation was performed as following: The lungs of all animals were imaged by conventional (chest radiography, CXR), as previously described [23]. Three

view thoracic radiographs (ventrodorsal, right and left lateral) were performed at all sampling time points. High-resolution computed tomography (CT) was performed daily through 3 dpi in 4 infected macaques and on 6 and 12 dpi in 3 young and 3 old macaques as described in the next section. Images were evaluated by a board-certified veterinary radiologist and scored as normal, mild moderate or severe disease. The changes were characterized as to location (lung lobe) and distribution (perivascular/peribronchial, hilar, peripheral, diffuse, multifocal/patchy).

CT Imaging and quantitative analysis of lung pathology. The animals were anesthetized using Telazol (2-6mg/kg) and maintained by inhaled isoflurane delivered through Hallowell 2002 ventilator anesthesia system (Hallowell, Pittsfield, MA). Animals were intubated to perform end-inspiratory breath-hold using a remote breath-hold switch. Lung field CT images were acquired using Multiscan LFER150 PET/CT (MEDISO Inc., Budapest, Hungary) scanner. Image analysis was performed using 3D ROI tools available in Vivoquant (Invicro, Boston, MA). Percent change in lung hyperdensity was calculated to quantify lung pathology (1, 2). The lung volume involved in pneumonia, was quantified as follows: briefly, lung segmentation was performed using a connected thresholding feature, to identify lung ROI by classifying all the input voxels of scan in the range of -850 HU to -500 HU. Smoothing filters were used to reassign every ROI voxel value to the mode of the surrounding region with defined voxel radius and iterations to reconstruct the Lung ROI. Thereafter, global thresholding was applied to classify the voxels within Lung ROI in the range of -490 HU to +500 HU to obtain Lung hyperdensity ROI. The resultant ROIs were then rendered in the maximum intensity projection view using the VTK feature.

Viral RNA determination. Viral RNA from plasma/sera, BAL, urine, saliva, and swabs (nasal/nasopharyngeal, oropharyngeal, rectal) and lung homogenates was determined by RT-qPCR and viral RNA isolation as previously described for MERS-CoV and SARS-CoV (12, 27, 28). RNA extraction from fluids was performed using the EpMotion M5073c Liquid Handler (Eppendorf) and the NucleoMag Pathogen kit (Macherey-Nagel). 100 µL of test sample were mixed with 150 µL of 1X DPBS (Gibco) and 750 µL TRIzol LS. Inactivation controls were prepared with each batch of samples to ensure no cross contamination occurred during inactivation. Samples were thawed at room temperature and then, for serum, swabs and urine samples 10µg yeast tRNA was added, along with 1 x 103 pfu of MS2 phage (*Escherichia coli* bacteriophage MS2, ATCC). DNA LoBind Tubes (Eppendorf) were prepared with 20 µL of NucleoMag B-Beads (NucleoMag Pathogen kit, Macherey-Nagel) and 975 µL of Buffer NPB2 (NucleoMag Pathogen kit, Macherey-Nagel). After centrifugation, the upper aqueous phase of each sample was transferred to the corresponding new tube containing NucleoMag B-Beads and Buffer NPB2. The samples were mixed using HulaMixer (Thermo Fisher Scientific Inc.) rotating for 10 min at room temperature. Samples were then transferred to the sample rack on EpMotion M5073c Liquid Handler (Eppendorf) for further processing according to NucleoMag Pathogen kit instructions. For viral RNA determination from tissues, 100mg of tissue was homogenized in 1mL Trizol Reagent (Invitrogen, Grand Island, NY, USA) with a Qiagen (Germantown, MD, USA) steel bead and Qiagen Stratagene TissueLyser. For detection of infectious virus, briefly, tissues were homogenized 10% w/v in viral transport medium using Polytron PT2100 tissue grinders (Kinematica). After low-speed centrifugation, the homogenates were frozen at −70°C until they were inoculated on Vero E6 cell cultures in 10-fold serial dilutions. The SARS-CoV-2 RT-qPCR was

performed using a CDC-developed 2019-nCoV_N1 assay with the TaqPath™ 1-Step RT-qPCR Master Mix, CG (ThermoFisher). The assays were performed on a QuantStudio 3 instrument (Applied Biosystems) with the following cycling parameters: Hold stage 2 min at 25°C, 15 min at 50°C, 2 min at 95°C. PCR stage 45 cycles of 3 s at 95°C, 30 s at 60°C. Primer and probe info: 2019-nCoV_N1-F: GACCCCAAAATCAGCGAAAT (500nM); 2019-nCoV_N1-R: TCTGGTTACTGCCAGTTGAATCTG (500 nM); 2019-nCoV_N1-P FAM/MGB probe: ACCCCGCATTACGTTTGGTGGACC (125nM).

Pathology. Animals were euthanized and complete necropsy was performed. Gross images (lung, spleen, liver) and organ weights (lymph nodes, tonsil, spleen, lung, liver, adrenal glands) were obtained at necropsy. Representative samples of lung lymph nodes (inguinal, axillary, mandibular and mediastinal), tonsil, thyroid gland, trachea, heart, spleen, liver, kidney, adrenal gland, digestive system (stomach, duodenum, jejunum, ileum, colon, and rectum), testes or ovary, brain, eye, nasal tissue, and skin were collected for all animals. Tissues were fixed in 10% neutral buffered formalin, processed to paraffin, sectioned at 5 um thickness, stained with hematoxylin and eosin utilizing standard methods, and evaluated by a board-certified veterinary pathologist.

Tissue processing, flow cytometry, multiplex cytokine analyses, immunohistochemistry, multicolor confocal microscopy and RNAseq for immune evaluations.

Flow cytometry was performed as previously described [24-26] on blood and BAL samples collected on time points days 3, 6, 9, 12, and at endpoint, which occurred at 14-17 dpi for various animals. A comprehensive list of antibodies used in these experiments is provided in Table S7. For

evaluations on peripheral blood, PBMC were prepared as previously described. Briefly, Cellular phenotypes were studied using antibodies: CD3 (clone SP34-2), CD4 (clone L200), CD69 (clone FN50), CD20 (2H7), CD95 (clone DX2), KI67 (B56), CCR5 (3A9), CCR7(clone 3D12), CD28 (clone CD28.2), CD45 (clone D058-1283), CXCR3 (clone 1C6/CXCR3), HLA-DR (clone L243), CCR6 (clone 11A9), LAG-3 (Polyclonal, R&D Systems, Minneapolis, MN, USA), CD123 (clone 7G3), CD14 (clone M5E2), CD206 (clone 206), CD16 (clone 3G8), CD163 (GHI/61), CD66abce (Clone TET2, Miltenyi Biotech, USA), CD40 (clone 5C3), IL-2(clone MQ1-17H12) , Granzyme-B (clone GB11) all purchased from BD Biosciences (San Jose, CA, USA) unless specified. CD8 (clone RPA-T8), CD11c (clone 3.9), TNF-alpha (clone MAb11), IFN-gamma (clone B27), IL-17 (clone BL168) and PD-1 (clone EH12.2H7) were purchased from BioLegend, San Diego, CA, US. For antigenic stimulation cells were cultured overnight with SARS-CoV-2 specific peptide pools of the nucleocapsid (N), membrane (M) and spike (S) proteins (PepTivator SARS-CoV-2 peptide pool, Miltenyi Biotech, USA). A detailed gating strategy for detection and enumeration of various cellular phenotypes is described (Fig S18).

Immuno-histochemistry was performed on 4 μm thick sections of lung, nasal cavity and tonsils. The sections were baked at 65^0C for 30 min followed by de-paraffinization using Xylene and subsequent hydration with decreasing gradations of ethanol as described [11,27]. Heat induced antigen retrieval was performed using Sodium citrate buffer (10mM, pH 6.0) followed by blocking (3 % BSA in TBST for 1 h at 37^0C). For SARS CoV-2 detection, specimens were incubated with rabbit SARS CoV-2 spike (S) antibody (ProSci, USA, 1:200, 37^0C for 2 h) or anti-SARS CoV-2 nucleocapsid (N) antibody (Sino Biologicals, USA, 1:100, 2h at 37^0C). Antihuman ACE-2 (R&D Systems, USA, 1:50, 2h at 37^0C) was used for identification of ACE-2. Mouse anti-human

CD66abce-PE conjugated (Miltenyi Biotech, USA, 1:20, 2 h at 37^0C) was used for identification of neutrophils; mouse CD68 (Thermo Fisher Scientific, USA, 1:100, 2 h at 37^0C) for macrophages and pDC's were identified by co-staining of PE conjugated mouse anti-human CD123 (BD Biosciences, USA, 1:20, 37^0C for 2h) and mouse anti-human HLA-DR antibody (Thermo Fisher Scientific, USA, 1:100, 2 h at 37^0C). Also, mouse anti-Ki67 (BD Biosciences, USA, 1:50, 2 h at 37^0C) was used for detection of actively proliferating cells. Chicken anti-rabbit IgG (H+L), Alexa Fluor 488 conjugate; goat anti-mouse IgG (H+L), Alexa Fluor 647 conjugate; donkey anti-mouse IgG (H+L), Alexa-Fluor 555 conjugate secondary antibodies (Thermo Fisher Scientific, USA, 1:400, 1 h at 37^0C) were used for labelling Spike, Ki67 and HLA-DR, CD68 primary antibodies respectively. Tissue sections were then stained with DAPI (Thermo Fisher Scientific, USA, 1:5000, 5 min at 37^0C) with subsequent mounting with Prolong Diamond Antifade mountant (Thermo Fisher Scientific, USA). Ziess LSM 800 confocal microscope was used to visualize the stained sections (10X, 20X and 63X magnification).

RNA was isolated, RNAseq performed and data analyzed as described [16].

Statistical analyses. **Statistical analyses**. Graphs were prepared and statistical comparisons applied using GraphPad Prism version 8 (La Jolla, CA). Various statistical comparisons were performed viz. 2-tailed Student's t-test, ordinary analysis of variance (ANOVA) or one-way or two-way repeated measure analysis of variance (rmANOVA) with Geisser-Greenhouse correction for sphericity and Tukey's post hoc correction for multiple-testing (GraphPad Prism 8) was applied wherever applicable and as described in the figure legends. For Correlation analysis, Spearman's

636 rank test was applied. Statistical differences between groups were reported significant when the
637 p-value is less than or equal to 0.05. The data are presented in mean ± SEM.
638
639 **Author Contributions.** DK, LSS, RC, LDG designed these studies. DKS, SRG, BS, JC, KJA, RE, T-HL,
640 MG, YG-G, RS, AC, RT, MG, CA, AB, JF, CB, HS, LP, JC, AM, BK, RNP, PE, VH, XA, AB, CK, MA, BR
641 conducted the experiments and acquired the data. EC, AG, JD, SH-U, PAF, CNR, KS, CC, CH, OG,
642 JD, AKV, CH, EJD and KB provided veterinary, veterinary pathology, imaging, colony management
643 or management expertise; DKS, SRG, BS, KJA, AC, MG, EC, RNP, JS, AO, DKA, RC, BR, TJCA, SAK,
644 MM, LDG, RC and DK analyzed the data; DK wrote the paper; LSS, JT, LDG, RC, JBT, KB, EC, LMS,
645 JLP, SG and DKS provided assistance with writing the paper.
646
647 **Acknowledgments**. We acknowledge exceptional work by our SNPRC veterinary technical and
648 care staff (especially the veterinary technical/animal care groups headed by Tyneshia Camp,
649 Wade Hodgkins, Manuel Aguilar, David Vandenberg and Laura Rumpf) as well as the entire SNPRC
650 and Texas Biomed administrative staff, especially Helen Hawn, for assistance with this study,
651 especially during trying times.
652
653 **Statement on conflict of interests:** "RC, Jr is funded by Regeneron, Inc. This funder had no role,
654 however, in the design and execution of the experiments and the interpretation of data. The
655 authors declare that no other financial conflict of interest exists."
656

Financial support. This work was primarily supported by a philanthropic award to Texas Biomed Coronavirus Working Group; a SNPRC Pilot study award to LDG, RC, JP, LM and JBT; an award to RC, Jr from Regeneron Pharmaceuticals, (contract # 2020_004110) in part with federal funds from the Department of Health and Human Services; Office of the Assistant Secretary for Preparedness and Response; Biomedical Advanced Research and Development Authority, under Contract No. HHSO100201700020C; and institutional NIH awards P51OD111033 and U42OD010442. The views expressed here are those of the authors and do not necessarily represent the views or official position of the funding agencies.

References

1 Callaway, E., Cyranoski, D., Mallapaty, S., Stoye, E. & Tollefson, J. The coronavirus pandemic in five powerful charts. *Nature* **579**, 482-483, doi:10.1038/d41586-020-00758-2 (2020).

2 Bucsan, A. N., Mehra, S., Khader, S. A. & Kaushal, D. The current state of animal models and genomic approaches towards identifying and validating molecular determinants of Mycobacterium tuberculosis infection and tuberculosis disease. *Pathog Dis* **77**, doi:10.1093/femspd/ftz037 (2019).

3 Gretebeck, L. M. & Subbarao, K. Animal models for SARS and MERS coronaviruses. *Curr Opin Virol* **13**, 123-129, doi:10.1016/j.coviro.2015.06.009 (2015).

4 Rockx, B. *et al.* Comparative pathogenesis of COVID-19, MERS, and SARS in a nonhuman primate model. *Science*, doi:10.1126/science.abb7314 (2020).

5 Munster, V. J. *et al.* Respiratory disease in rhesus macaques inoculated with SARS-CoV-2. *Nature*, doi:10.1038/s41586-020-2324-7 (2020).

6 Yu, J. *et al.* DNA vaccine protection against SARS-CoV-2 in rhesus macaques. *Science*, doi:10.1126/science.abc6284 (2020).

7 Chandrashekar, A. *et al.* SARS-CoV-2 infection protects against rechallenge in rhesus macaques. *Science*, doi:10.1126/science.abc4776 (2020).

8 Cockrell, A. S. *et al.* A spike-modified Middle East respiratory syndrome coronavirus (MERS-CoV) infectious clone elicits mild respiratory disease in infected rhesus macaques. *Sci Rep* **8**, 10727, doi:10.1038/s41598-018-28900-1 (2018).

9 Mantlo, E., Bukreyeva, N., Maruyama, J., Paessler, S. & Huang, C. Antiviral activities of type I interferons to SARS-CoV-2 infection. *Antiviral Res* **179**, 104811, doi:10.1016/j.antiviral.2020.104811 (2020).

10 Nile, S. H. *et al.* COVID-19: Pathogenesis, cytokine storm and therapeutic potential of interferons. *Cytokine Growth Factor Rev*, doi:10.1016/j.cytogfr.2020.05.002 (2020).

11 Bucsan, A. N. *et al.* Mechanisms of reactivation of latent tuberculosis infection due to SIV co-infection. *J Clin Invest*, doi:10.1172/JCI125810 (2019).

12 Gautam, U. S. *et al.* In vivo inhibition of tryptophan catabolism reorganizes the tuberculoma and augments immune-mediated control of Mycobacterium tuberculosis. *Proc Natl Acad Sci U S A* **115**, E62-E71, doi:10.1073/pnas.1711373114 (2018).

13 Cai, Y. *et al.* In vivo characterization of alveolar and interstitial lung macrophages in rhesus macaques: implications for understanding lung disease in humans. *J Immunol* **192**, 2821-2829, doi:10.4049/jimmunol.1302269 (2014).

14 Kuroda, M. J. *et al.* High Turnover of Tissue Macrophages Contributes to Tuberculosis Reactivation in Simian Immunodeficiency Virus-Infected Rhesus Macaques. *J Infect Dis*, doi:10.1093/infdis/jix625 (2018).

15 Barber, D. L. *et al.* Restoring function in exhausted CD8 T cells during chronic viral infection. *Nature* **439**, 682-687, doi:10.1038/nature04444 (2006).

16 Ahmed, M. *et al.* Immune correlates of tuberculosis disease and risk translate across species. *Sci Transl Med* **12**, doi:10.1126/scitranslmed.aay0233 (2020).

17 Darrah, P. A. *et al.* Prevention of tuberculosis in macaques after intravenous BCG immunization. *Nature* **577**, 95-102, doi:10.1038/s41586-019-1817-8 (2020).

18 Veazey, R. S. *et al.* Gastrointestinal tract as a major site of CD4+ T cell depletion and viral replication in SIV infection. *Science* **280**, 427-431 (1998).

19 Barouch, D. H., Klasse, P. J., Dufour, J., Veazey, R. S. & Moore, J. P. Macaque studies of vaccine and microbicide combinations for preventing HIV-1 sexual transmission. *Proc Natl Acad Sci U S A* **109**, 8694-8698, doi:10.1073/pnas.1203183109 (2012).

20 Cox, L. A. *et al.* Nonhuman Primates and Translational Research-Cardiovascular Disease. *ILAR J* **58**, 235-250, doi:10.1093/ilar/ilx025 (2017).

21 Rincon-Choles, H. *et al.* Renal histopathology of a baboon model with type 2 diabetes. *Toxicol Pathol* **40**, 1020-1030, doi:10.1177/0192623312444025 (2012).

22 Cole, S. A., Laviada-Molina, H. A., Serres-Perales, J. M., Rodriguez-Ayala, E. & Bastarrachea, R. A. The COVID-19 Pandemic during the Time of the Diabetes Pandemic: Likely Fraternal Twins? *Pathogens* **9**, doi:10.3390/pathogens9050389 (2020).

23 Kaushal, D. *et al.* Mucosal vaccination with attenuated Mycobacterium tuberculosis induces strong central memory responses and protects against tuberculosis. *Nat Commun* **6**, 8533, doi:10.1038/ncomms9533 (2015).

24 Bucsan, A. N. *et al.* Mechanisms of reactivation of latent tuberculosis infection due to SIV coinfection. *J Clin Invest* **129**, 5254-5260, doi:10.1172/JCI125810 (2019).

25 Foreman, T. W. *et al.* Isoniazid and Rifapentine Treatment Eradicates Persistent Mycobacterium tuberculosis in Macaques. *Am J Respir Crit Care Med*, doi:10.1164/rccm.201903-0646OC (2019).

26 Foreman, T. W. *et al.* CD4+ T-cell-independent mechanisms suppress reactivation of latent tuberculosis in a macaque model of HIV coinfection. *Proc Natl Acad Sci U S A* **113**, E5636-5644, doi:10.1073/pnas.1611987113 (2016).

27 Mehra, S. *et al.* Granuloma correlates of protection against tuberculosis and mechanisms of immune modulation by Mycobacterium tuberculosis. *J Infect Dis* **207**, 1115-1127, doi:10.1093/infdis/jis778 (2013).

28 Joosten, S. A. *et al.* Mycobacterium tuberculosis peptides presented by HLA-E molecules are targets for human CD8 T-cells with cytotoxic as well as regulatory activity. *PLoS Pathog* **6**, e1000782, doi:10.1371/journal.ppat.1000782 (2010).

29 Raju, R. M. *et al.* Post-translational regulation via Clp protease is critical for survival of Mycobacterium tuberculosis. *PLoS Pathog* **10**, e1003994, doi:10.1371/journal.ppat.1003994 (2014).

30 Winglee, K. *et al.* Aerosol Mycobacterium tuberculosis infection causes rapid loss of diversity in gut microbiota. *PLoS One* **9**, e97048, doi:10.1371/journal.pone.0097048 (2014).

760 **Figure legends**

761

762 **Figure 1. Clinical correlates of SARS-CoV-2 infection in rhesus macaques over 0-3 dpi**. Changes
763 in serum CRP (mg/L) (a), albumin (ALB) (g/dL) (b), hemoglobin (HGB) content (g/dL) (c),
764 longitudinally in peripheral blood. Viral RNA (log_{10} copies/mL were measured by RT-PCR in BAL
765 fluid (d), nasopharyngeal (e), and buccopharyngeal (f) swabs longitudinally (red – 0 dpi; purple –
766 1 dpi; blue – 2 dpi; green – 3 dpi). Viral RNA was also measured in lung tissue homogenates at
767 endpoint (3 dpi) and data is expressed as log_{10} copies/gram of the lung tissue for random samples
768 from three lobes in left (orange) and right (teal) lungs (g Hematoxylin and eosin (H&E) staining
769 was performed on formalin-fixed paraffin-embedded (FFPE) lung sections from infected animals
770 for pathological analysis Histopathologic analysis revealed bronchitis characterized by infiltrates
771 of macrophages, lymphocytes, neutrophils, and eosinophils that expanded the wall (bracket),
772 and along with syncytial cells (arrows) filled the bronchiole lumen and adjacent alveolar spaces.
773 (h); Suppurative interstitial pneumonia with Type II pneumocyte hyperplasia (arrowheads) and
774 alveolar space filled with neutrophils, macrophages and fibrin (*). Bracket denotes alveolar
775 space. (i). Multilabel confocal immunofluorescence microscopy of lungs (j) and nasal epithelium
776 (k) at 63x with Nucleocapsid (N) specific antibody (green) DAPI (blue), and ACE2 (red). (a-f) Data
777 is represented as mean$\pm$ SEM (n=4).). (c-g) Undetectable results are represented as 1 copy. One
778 way Repeated-measures ANOVA with Geisser-Greenhouse correction for sphericity and Tukey's
779 post hoc correction for multiple-testing (GraphPad Prism 8) was applied. * P<0.005, ** P<0.005,
780 *** P<0.0005.

781

Fig 1

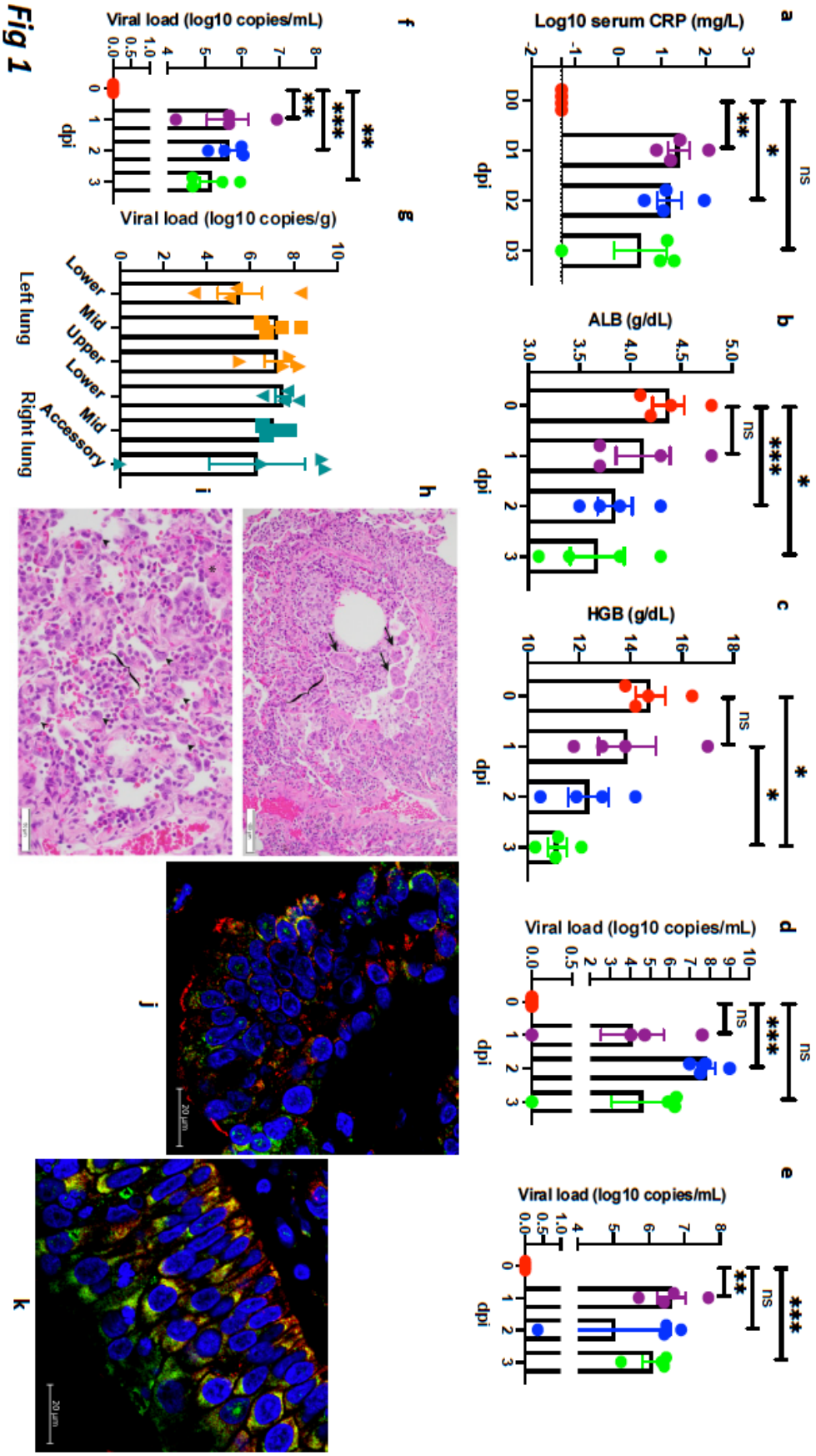

Figure 2. Radiologic evaluation of the lung compartment following SARS-CoV-2 infection in rhesus macaques over 0-3 dpi including by hyperdensity analyses. CXR (a) and CT (e) scores generated by a veterinary radiologist blinded to the experimental group (red – 0 dpi; purple – 1 dpi; blue – 2 dpi; green – 3 dpi). (a) Data is represented as mean± SEM (n=4). One way Repeated-measures ANOVA with Geisser-Greenhouse correction for sphericity and Tukey's post hoc correction for multiple-testing (GraphPad Prism 8) was applied. * $P<0.05$. Representative CT scan images performed on Day 0-2 dpi show (b) transverse, (c) vertical, (d) longitudinal view of left caudal lobe ground glass opacity on 1 dpi (middle), 2 dpi [28] and baseline at 0 dpi (upper inset). CT scans (b-d) revealed evidence of pneumonia and lung abnormalities in the infected animals relative to controls which resolved between 1 to 2 dpi (red arrow). 3D reconstruction (f) of ROI volume representing the location of lesion. (Fig 2g-i) represent image for quantification of lung lesion with green area representing normal intensity lung voxels (-850 HU to -500 HU), while red areas represent hyperdense voxels (-490 HU to 500 HU). Percent change in lung hyperdensity in SARS-CoV2 infected animals over Day 1-3 dpi compared to the baseline(j). (red – 0 dpi; purple – 1 dpi; blue – 2 dpi; green – 3 dpi). (e, j) Data represented as (mean ± SEM) (n=4 for 0-2 dpi, n=2 for 3dpi). Ordinary one-way ANOVA with Dunnett's post hoc test was applied.

Fig 2

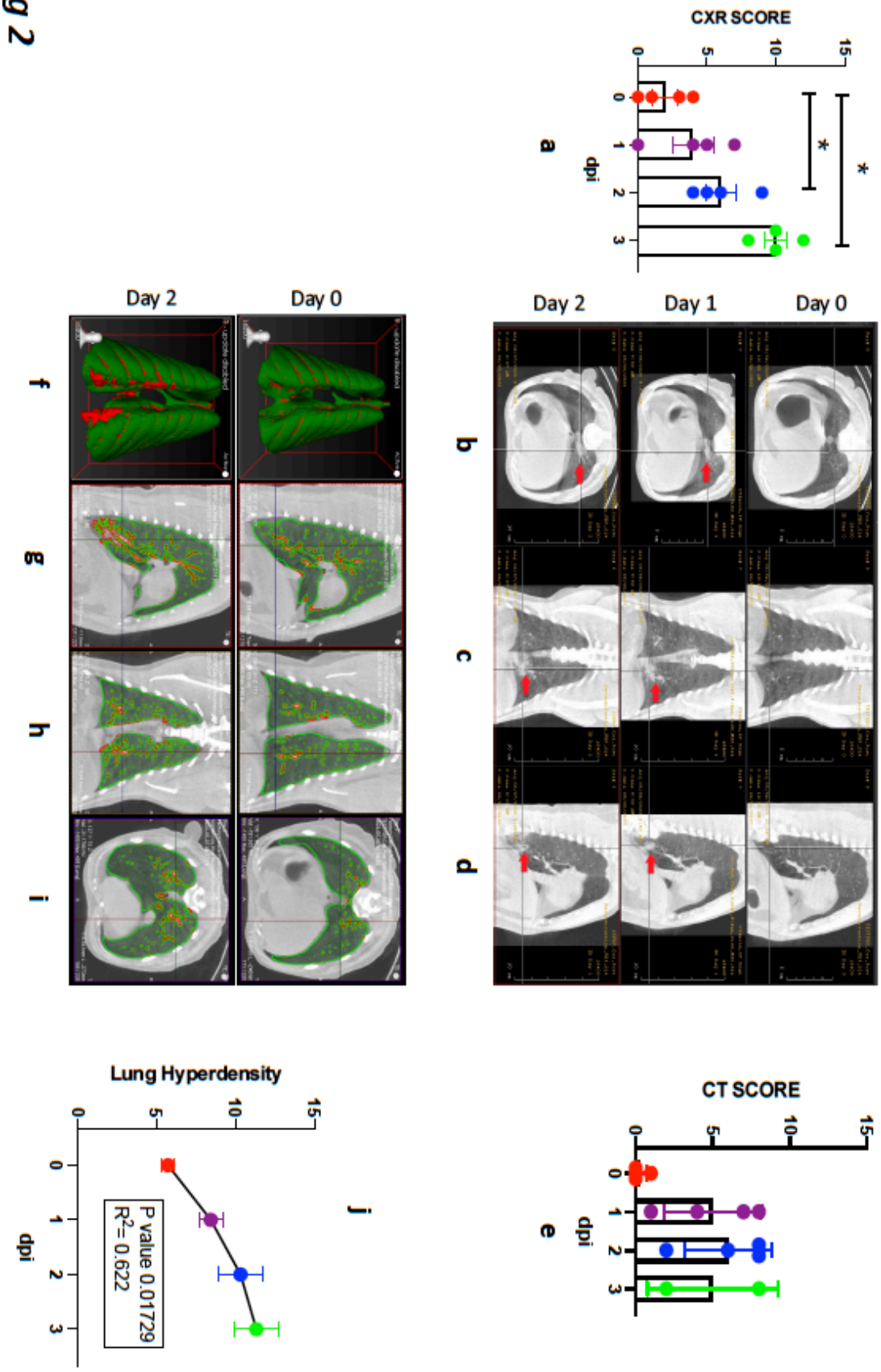

Figure 3. SARS-CoV-2 induced alveolar inflammation. Simultaneous analysis of multiple cytokines by Luminex technology in the BAL fluid of rhesus macaques over 0-3 dpi. Levels of IL-6 (a), IFN-a (b), IFN-g (c), IL-8 (d), perforin (e), IP-10 (f), MIP1a (g), MIP1b (h), IL-12p40 (i), IL-18 (j), TNF (k) and IL-1Ra (l) are expressed in Log10 concentration in picogram per mL of BAL fluid. (red – 0 dpi; purple – 1 dpi; blue – 2 dpi; green – 3 dpi). Data is represented as mean± SEM (n=4). One way Repeated-measures ANOVA with Geisser-Greenhouse correction for sphericity and Tukey's post hoc correction for multiple-testing (GraphPad Prism 8) was applied. * P<0.005, ** P<0.005, *** P<0.0005.

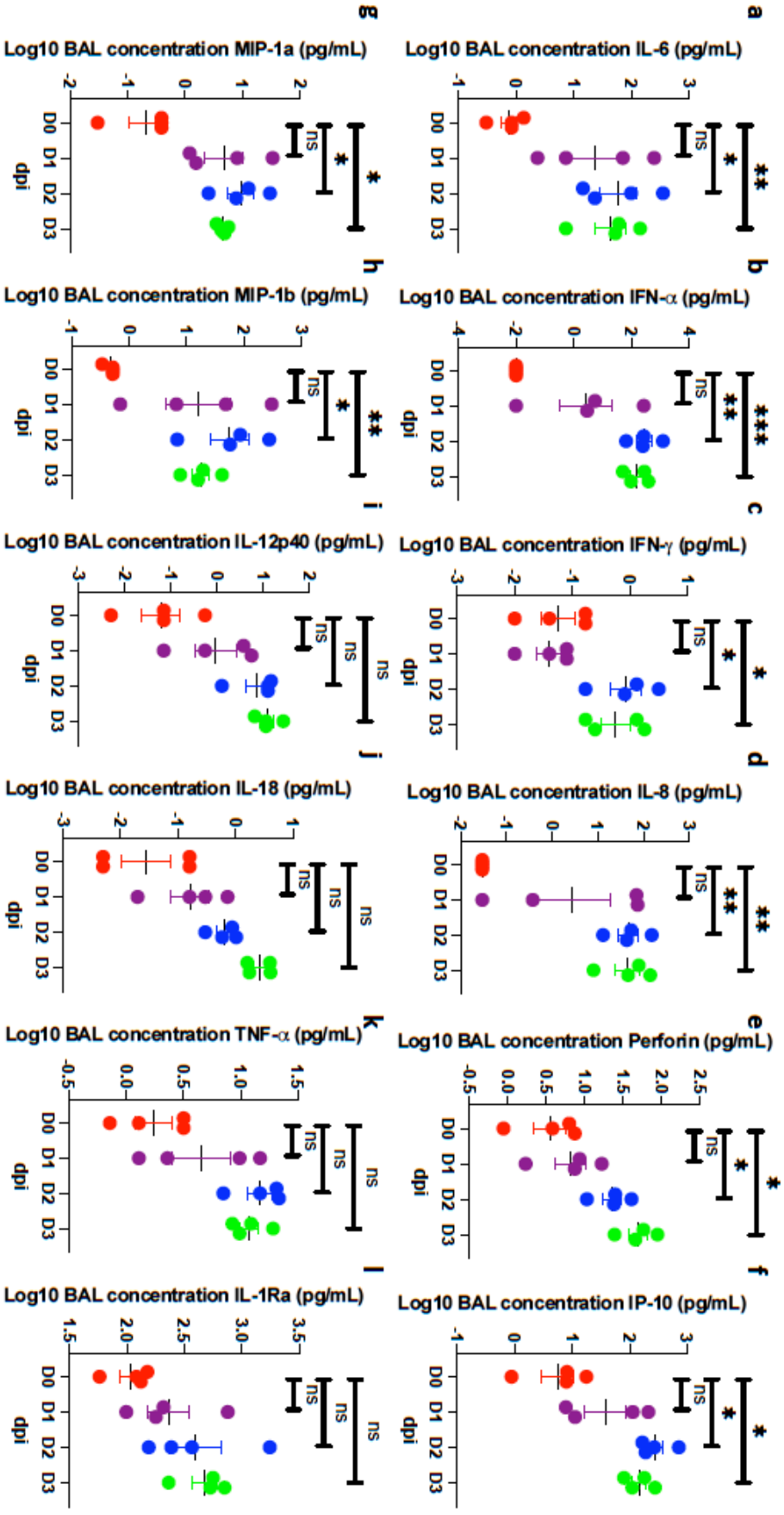

Fig 3

Figure 4. Longitudinal clinical and histopathological correlates of SARS-CoV-2 infection in rhesus macaques, baboons and marmosets over two weeks. Viral RNA (log_{10} copies/mL were measured by RT-PCR in BAL fluid (a) and nasopharyngeal (b) swabs of SARS-CoV-2 infected rhesus macaques longitudinally (red – 0 dpi; purple – 3 dpi; black – 6 dpi: blue – 9 dpi; orange – 12 dpi: green – 14-17 dpi). (n=12) One way Repeated-measures ANOVA with Geisser-Greenhouse correction for sphericity and Tukey's post hoc correction for multiple-testing (GraphPad Prism 8) was applied. * P<0.005, *** P<0.0005. Viral RNA was also measured in lung tissue homogenates of infected rhesus macaques at endpoint (14-17 dpi) and data is expressed as log_{10} copies/gram of the lung tissue for random samples from three lobes in left (orange) and right (teal) lungs (c). Histopathologic analysis revealed regionally extensive interstitial lymphocytes, plasma cells, lesser macrophages and eosinophils expanding the alveolar septa (bracket) and alveolar spaces filled with macrophages (*). Normal alveolar wall is highlighted (arrow) for comparison (d). Alveolar spaces with extensive interstitial alveolar wall thickening by deposits of collagen (*) and scattered alveolar macrophages (arrow) (e). Viral RNA (log_{10} copies/mL were measured by RT-PCR in BAL fluid (f) and Nasopharyngeal (g) swab from SARS-CoV-2 infected baboons. (n=6) One way Repeated-measures ANOVA with Geisser-Greenhouse correction for sphericity and Tukey's post hoc correction for multiple-testing (GraphPad Prism 8) was applied. Histopathologic analysis revealed regionally extensive interstitial lymphocytes, plasma cells, lesser macrophages and eosinophils expanding the alveolar septa (bracket) and alveolar spaces filled with macrophages (*), (h). Alveolar wall thickening by interstitial deposits of collagen (*), alveoli lined by occasional type II pneumocytes (arrowhead) and alveolar spaces containing syncytial cells (arrow) and alveolar macrophages (i). Viral RNA (log_{10} copies/mL were measured by RT-PCR in marmoset

nasal wash (j) and oral (k) swabs longitudinally (red – 0 dpi; purple – 3 dpi; blue – 6 dpi; green – 9 dpi; black – 14-17 dpi). n=6 for 0-3 dpi and n=4 for 6-14 dpi). .Histopathologic analysis revealed milder form of interstitial lymphocytes, and macrophages recruited to the alveolar space (m, n). Ordinary one-way ANOVA with Dunnett's post hoc test was applied. Viral RNA was also measured in lung homogenates at endpoint (3 dpi & 14 dpi) and data is expressed as $\log_{10}$ copies/gram of the lung for random samples from left and right lobes at 3 dpi (orange) and 14 dpi (teal) (g). Data is represented as mean± SEM. ** P<0.005, **** P<0.00005.

873

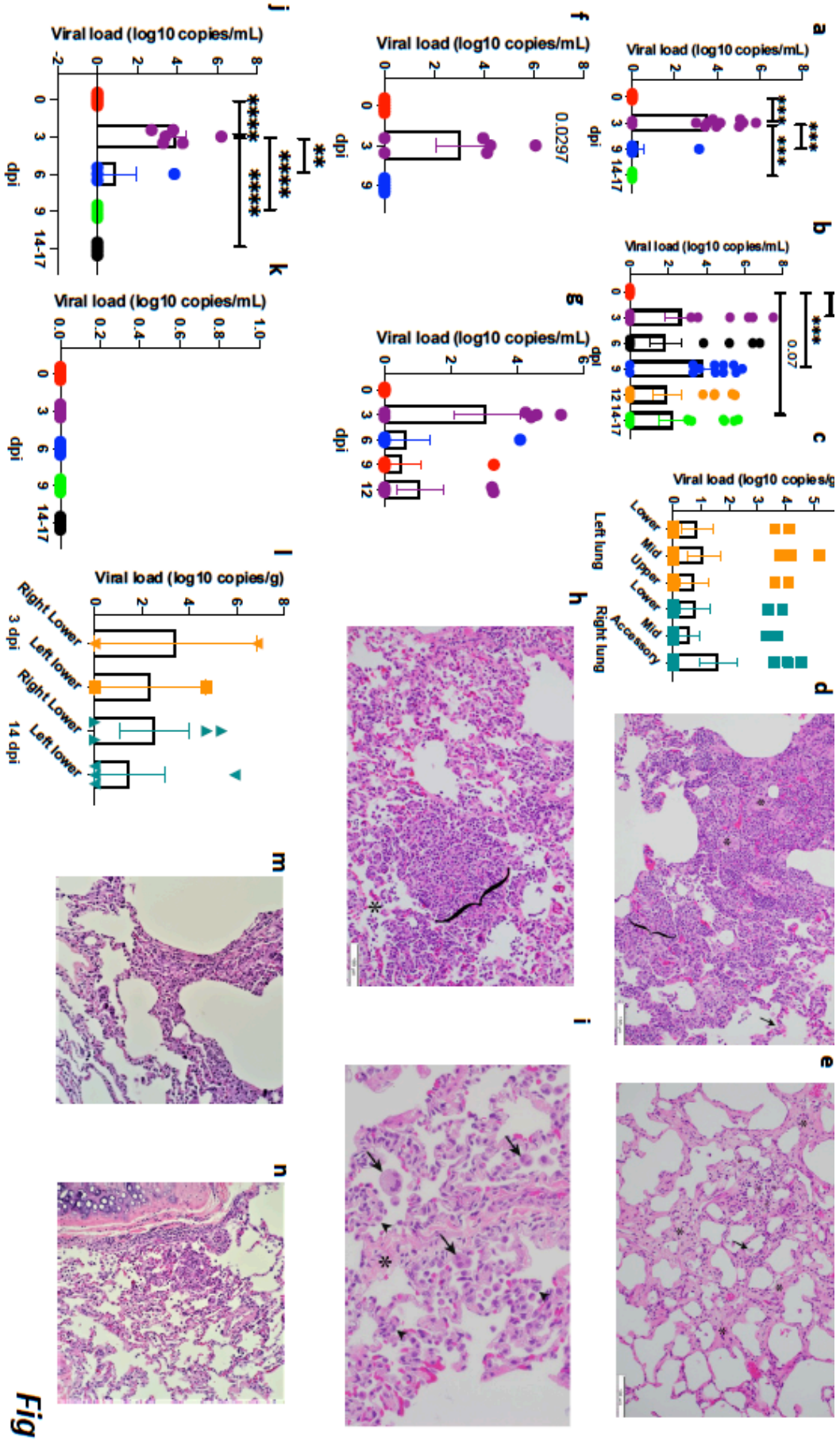

Fig 4

Figure 5. CXR (a) scores generated by a veterinary radiologist blinded to the experimental group (n=12) and (b) CXR scores split in old and young macaques (n=6). CXR radiographs showing minimal right caudal interstitial pattern at 0 dpi (c), Alveolar pattern associated with the caudal sub segment of the left cranial lung lobe and left caudal lung lobe with patchy right caudal interstitial opacity at 6 dpi (d) and Minimal left caudal interstitial pattern at 14dpi (e). CT (f) scores generated by a blinded veterinary radiologist (n=6). 3D reconstruction (g,k) of ROI volume representing the location of lesion. (h-j, l-n) represent image for quantification of lung lesion with green area representing normal intensity lung voxels (-850 HU to -500 HU), while red areas represent hyperdense voxels (-490 HU to 500 HU). Percent change in lung hyperdensity in SARS-CoV2 infected animals over 6 dpi compared to 12 dpi (o) (n=6). Data is represented as mean± SEM. (a) One way & (b) two way Repeated-measures ANOVA with Geisser-Greenhouse correction for sphericity and Tukey's post hoc correction for multiple-testing and (f,o) Paired T test (GraphPad Prism 8) was applied. * P<0.005, ** P<0.005, *** P<0.0005.

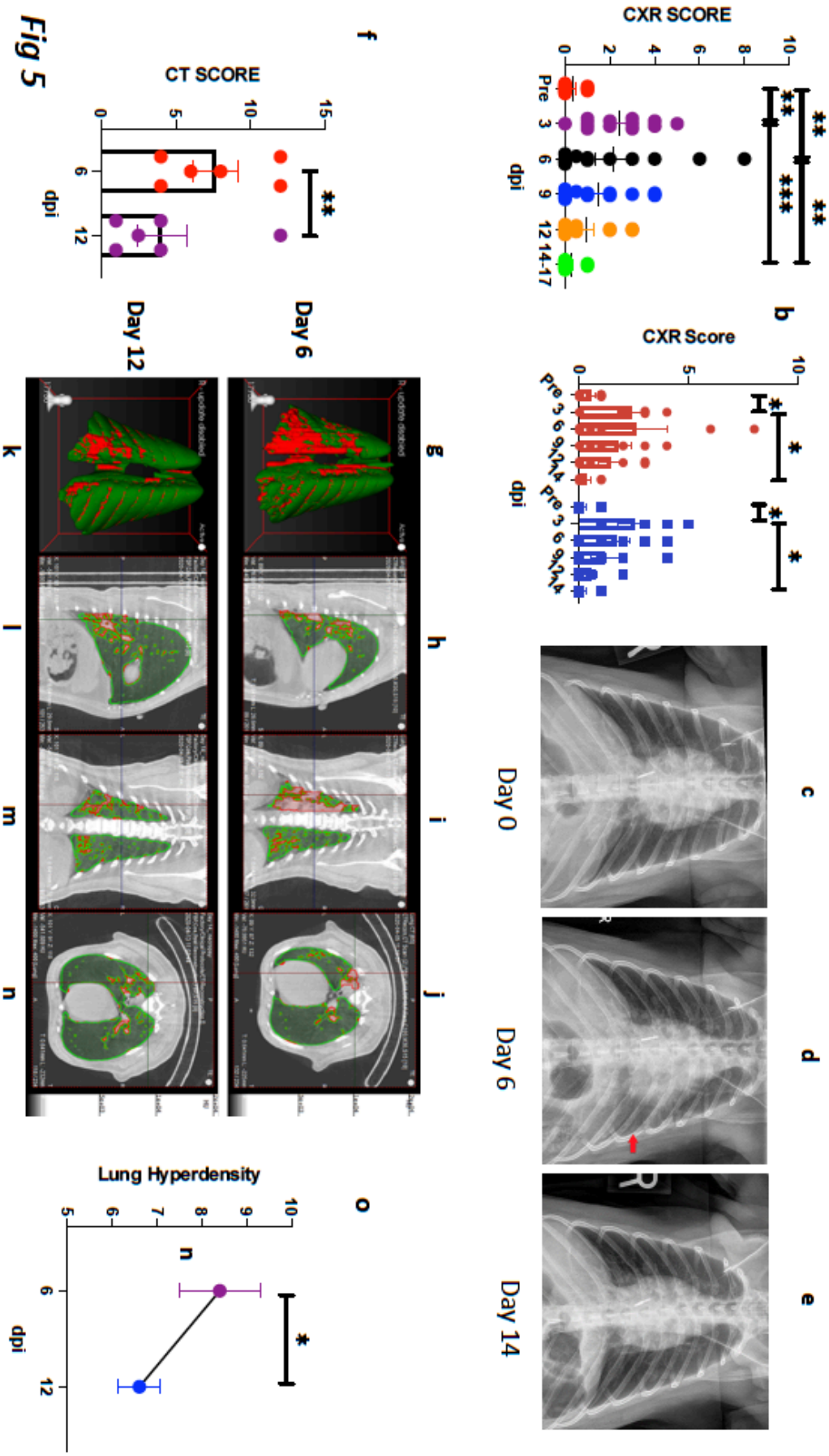

Figure 6. Longitudinal accumulation of myeloid cells in BAL following SARS-CoV-2 infection in rhesus macaques. Flow cytometric analysis of BAL IMs (a, e), AMs (b, f), neutrophils (c,g), and pDCs (d, h). Data shown combined for age (a-d) (n=12); data split by age (g-h) (n=6). Data is represented as mean± SEM. (a-d) One way and (e-h) two way Repeated-measures ANOVA with Geisser-Greenhouse correction for sphericity and Tukey's post hoc correction for multiple-testing (GraphPad Prism 8) was applied. * P<0.005, ** P<0.005, *** P<0.0005. Coloring scheme for e-h – young (blue), old (red). Correlations with Spearman's rank test between cellular fraction and Log10 viral RNA copy number in BAL (i) and corresponding values for Spearman's rank correlation coefficient (j) and P value (Suppl. Fig13i). Coloring scheme for i – Neutrophil (blue), IM (red), AM (orange, pDC (green). Multilabel confocal immunofluorescence microscopy of FFPE lung sections from SARS CoV-2 infected Rhesus macaques having a high viral titer at 3 dpi (k-p) with SARS CoV-2 Spike specific antibody (green), KI-67 [29], neutrophil marker CD66abce (red) and DAPI (blue) at 10X (k) and 63X (l); SARS CoV-2 Spike (green), pan-macrophage marker CD68 (red) and DAPI (blue) at 10X (m) and 63X (n); SARS CoV-2 Spike (green), HLA-DR [29], pDC marker CD123 (red) and DAPI (blue) at 10X (o) and 63X (p).

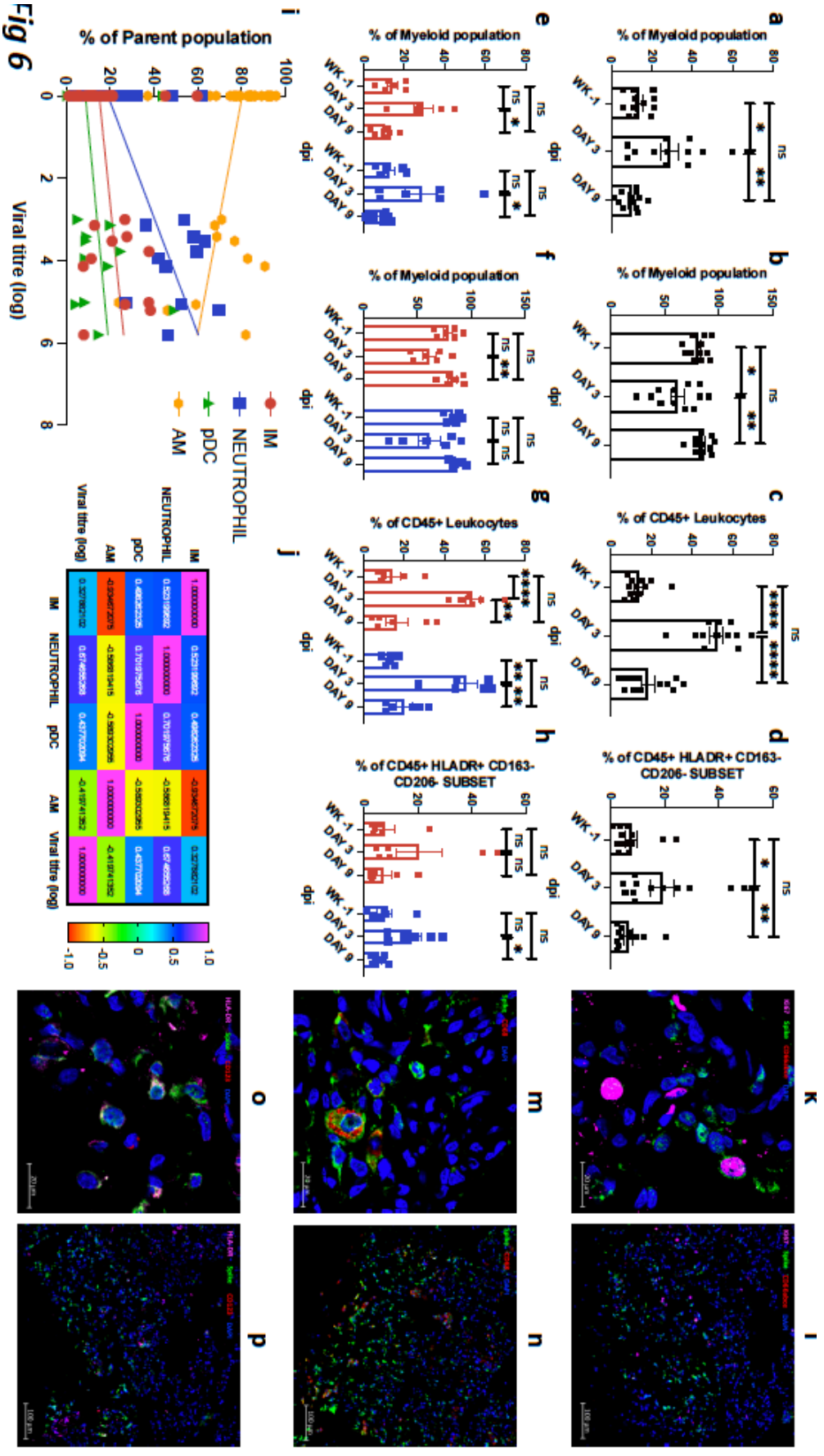

Figure 7. Longitudinal changes in T cells in BAL following SARS-CoV-2 infection in rhesus macaques. BAL Frequencies of $CD3^+$ T cells (a), $CD4^+$ T cells (b), $CD8^+$ T cells (g), $CD4^+$ T cell subsets expressing early activation marker CD69 (c), CXCR3 (d), PD-1 (e) and memory marker CCR7 (f), CCR5 (l), HLA-DR (m) and LAG-3 (n); $CD8^+$ T cell subsets expressing early activation marker CD69 (h), CXCR3 (i), PD-1 (j) and memory marker CCR7 (k), CCR5 (o), HLA-DR (p) and LAG-3 (q). Coloring scheme – young (blue), old (red). Data is represented as mean± SEM. (n=6) Two way Repeated-measures ANOVA with Geisser-Greenhouse correction for sphericity and Tukey's post hoc correction for multiple-testing (GraphPad Prism 8) was applied. * P<0.005, ** P<0.005, *** P<0.0005.

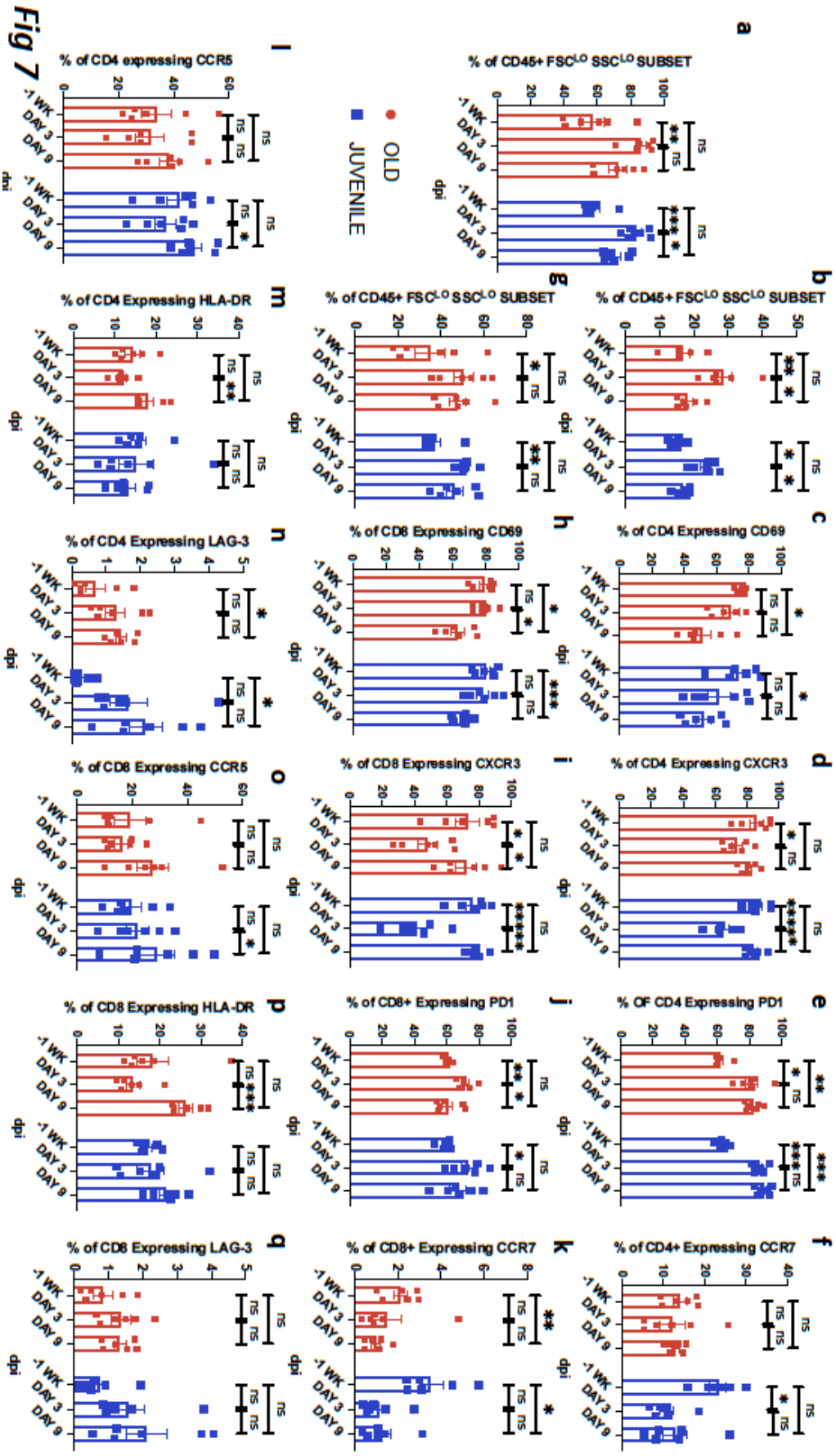

Figure 8. Longitudinal changes in memory T cells in BAL following SARS-CoV-2 infection in rhesus macaques. BAL Frequencies of CD4+ T cell subsets expressing KI67 (a), Memory (b), Naïve (c), Effector (d), IL-2 (e) and Granzyme B (f). Frequencies of CD8+ T cell subsets expressing KI67 (g), Memory (h), Naïve (i), Effector (j), IL-2 (k) and Granzyme B (l). BAL cells were stimulated overnight (12-14 hours) with either Mock control (U); PMA-Ionomycin (P/I) or SARS-CoV-2 - specific peptide pools of the nucleocapsid (N), membrane (M) and spike (S) proteins. Antigen specific cytokine secretion in T cells was estimated by flow cytometry. Fraction of $CD4^+$ T cells secreting IL-2 (m), Granzyme B (n); CD8+ T cells secreting IL-2 (o) and Granzyme B (p). Coloring scheme – young (blue), old (red). Data is represented as mean± SEM. (n=6) two way Repeated-measures ANOVA with Geisser-Greenhouse correction for sphericity and Tukey's post hoc correction for multiple-testing (GraphPad Prism 8) was applied. * P<0.005, ** P<0.005, *** P<0.0005.

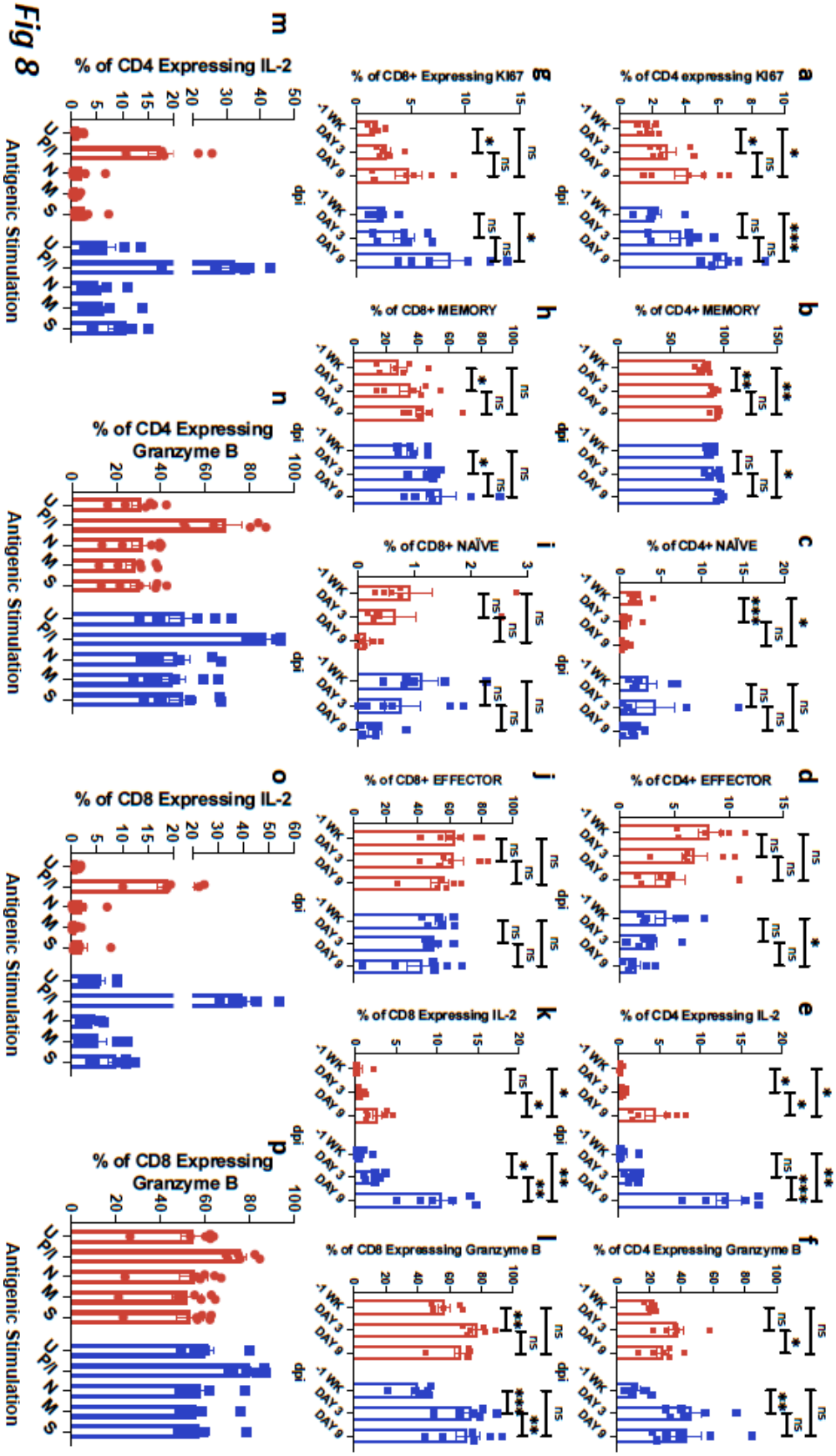

Figure S1. Clinical correlates in short-term (0-3 dpi) rhesus macaques. Serum levels of tCO2 (D-mmol/L) (a), and whole blood levels of Red Blood Cells (RBCs) (million/mL) (b), reticulocytes (K/mL) (c), White Blood Cells (WBCs) (K/mL) (d), platelets (K/uL) (e), Neutrophils (K/mL) (f), percentage of Neutrophils (g), percentage of monocytes (h). Viral RNA (log_{10} copies/mL were measured by RT-PCR in saliva (i), and rectal swab (j).) Data is represented as mean± SEM (n=4). One way Repeated-measures ANOVA with Geisser-Greenhouse correction for sphericity and Tukey's post hoc correction for multiple-testing (GraphPad Prism 8) was applied. * P<0.005, ** P<0.005, *** P<0.0005.

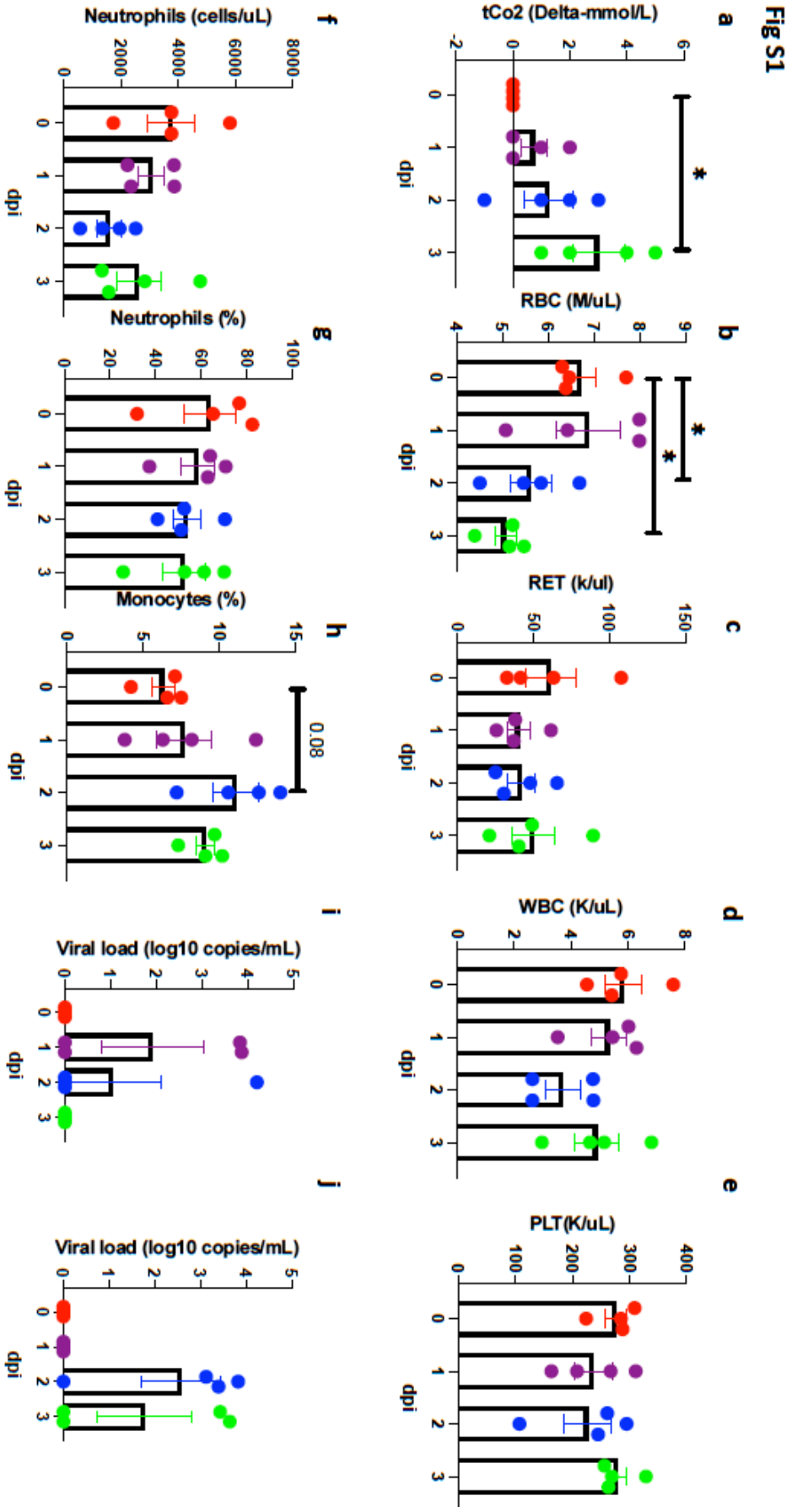

Figure S2. **Gross and histopathologic findings of young and aged male and female Rhesus macaques experimentally exposed to COVID19 - 3 dpi.** Young male Rhesus macaque. Lung was grossly unremarkable (a). Aged male Rhesus macaque. Lung. The dorsal aspect of the lungs was mottled red (*) (b). Aged male Rhesus macaque. Lung. Sub gross image showing extensive areas of consolidation (*) (c). Aged male Rhesus macaque. Lung. Moderate interstitial pneumonia with scattered type II pneumocytes (arrow), neutrophils (arrowhead), and intra-alveolar fibrin deposition (*) (d). Aged female Rhesus macaque. Lung. Mild interstitial pneumonia with scattered syncytial cells (arrow), neutrophils (arrowhead), and expansion of alveolar walls by fibrosis (bracket) (e). Young female Rhesus macaque. Lung. Vasculitis. Vascular wall disrupted by infiltrates of mononuclear cells and lesser neutrophils. Vessel lumen marked by (*) (f). Young female Rhesus macaque. Lung. Mild interstitial pneumonia. Alveolar spaces contain neutrophils and cellular debris (necrosis, arrow) (g). Young female Rhesus macaque. Lung. Mild interstitial pneumonia. Alveolar spaces (*) contain neutrophils and eosinophilic fluid (edema) (h). Young female Rhesus macaque. Lung. Bronchiolitis. Bronchiolar wall expanded by infiltrates of lymphocytes and macrophages (bracket) (i). Young male Rhesus macaque. Lung. Bronchitis. Bronchial wall expanded by infiltrates of eosinophils that expand and disrupt the epithelium and smooth muscle (bracket) (j). Young female Rhesus macaque. Lung. Bronchitis. Bronchial lumen contains macrophages (arrowhead), cellular debris, and syncytial cells (arrow) (k). Aged female Rhesus macaque. Lung. Area of bronchiolar associated lymphoid tissue (BALT) (*) (l). All slides were stained with H&E.

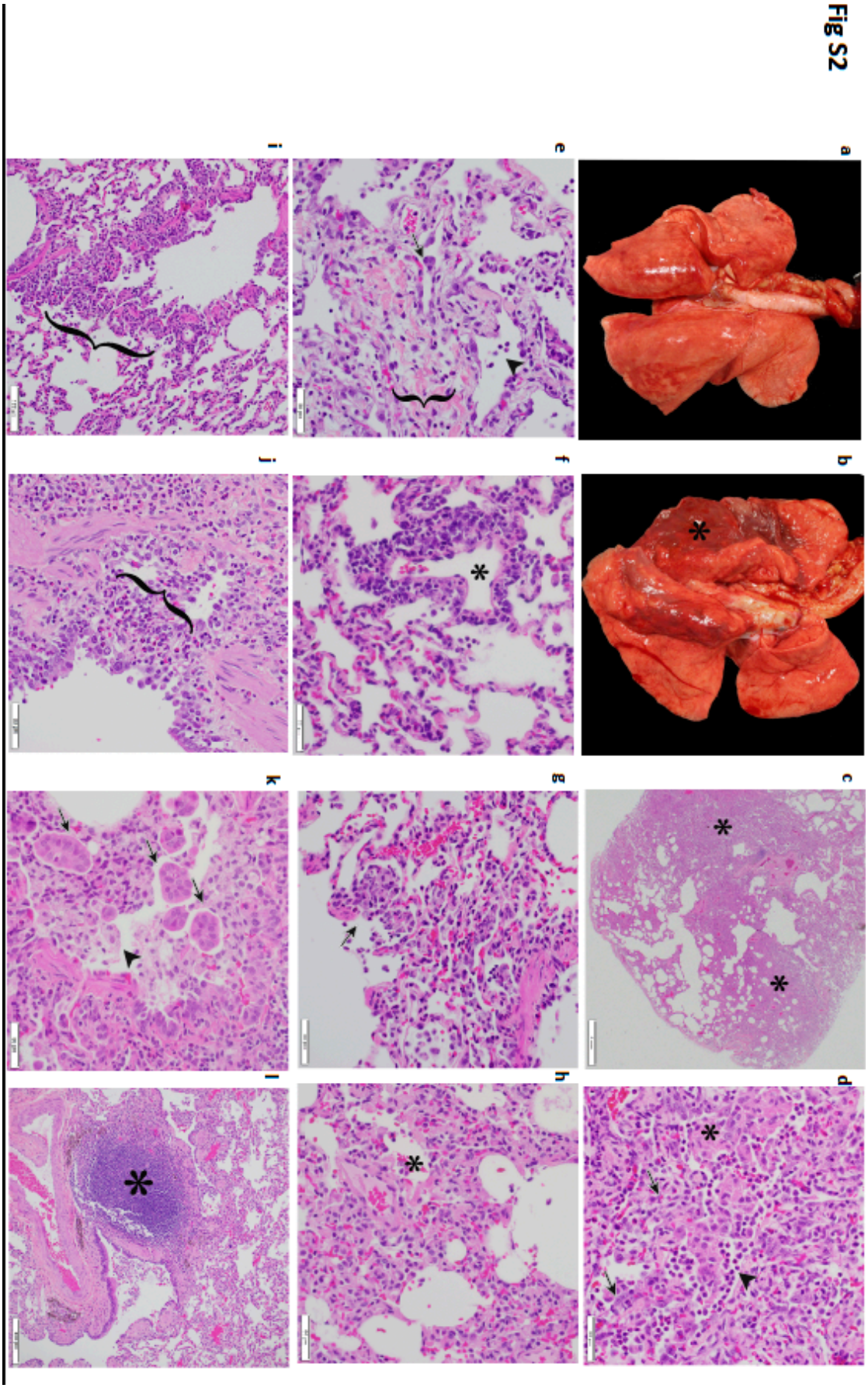

Fig S2

Fig S3. Multi-label confocal immunofluorescence microscopy of lungs (20X-a, 63X-g), nasal epithelium (20X-b, 63x-h) and tonsil (20X-c,63X-i) with SARS CoV-2 N specific antibody (green), DAPI (blue) and ACE-2 (red). Rabbit IgG isotype control antibody was used to rule out non-specific staining in lungs (20X-d, 63X-j), nasal epithelium (20X-e, 63x-k) and tonsil (20X-f, 63X-l). Staining in naïve rhesus macaque lung tissues did not show N signal in lungs (m) or nasal epithelium (n).

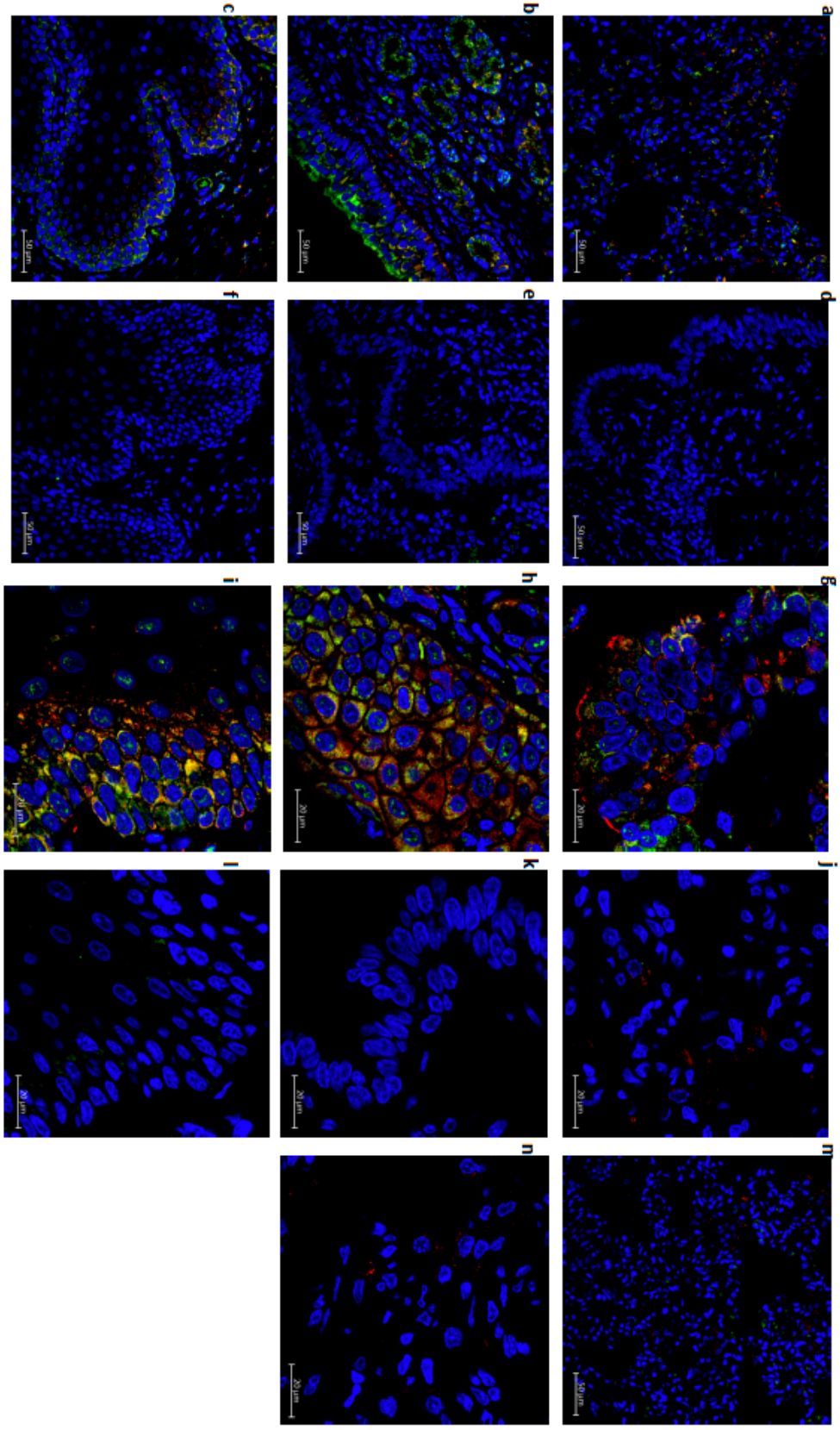

Fig S3

Figure S4. Multi-label confocal immunofluorescence microscopy of lungs (10X-a, 63X-g), nasal epithelium (10X-b, 63x-h) and tonsil (10X-c,63X-i) with SARS CoV-2 S specific antibody (green) and DAPI (blue). Rabbit IgG isotype control antibody was used to stain the tissues to rule out any non-specific staining. The panels showing isotype control staining include: lungs (10X-d, 63X-j), nasal epithelium (10X-e, 63X-k) and tonsil (10X-f, 63X-l).

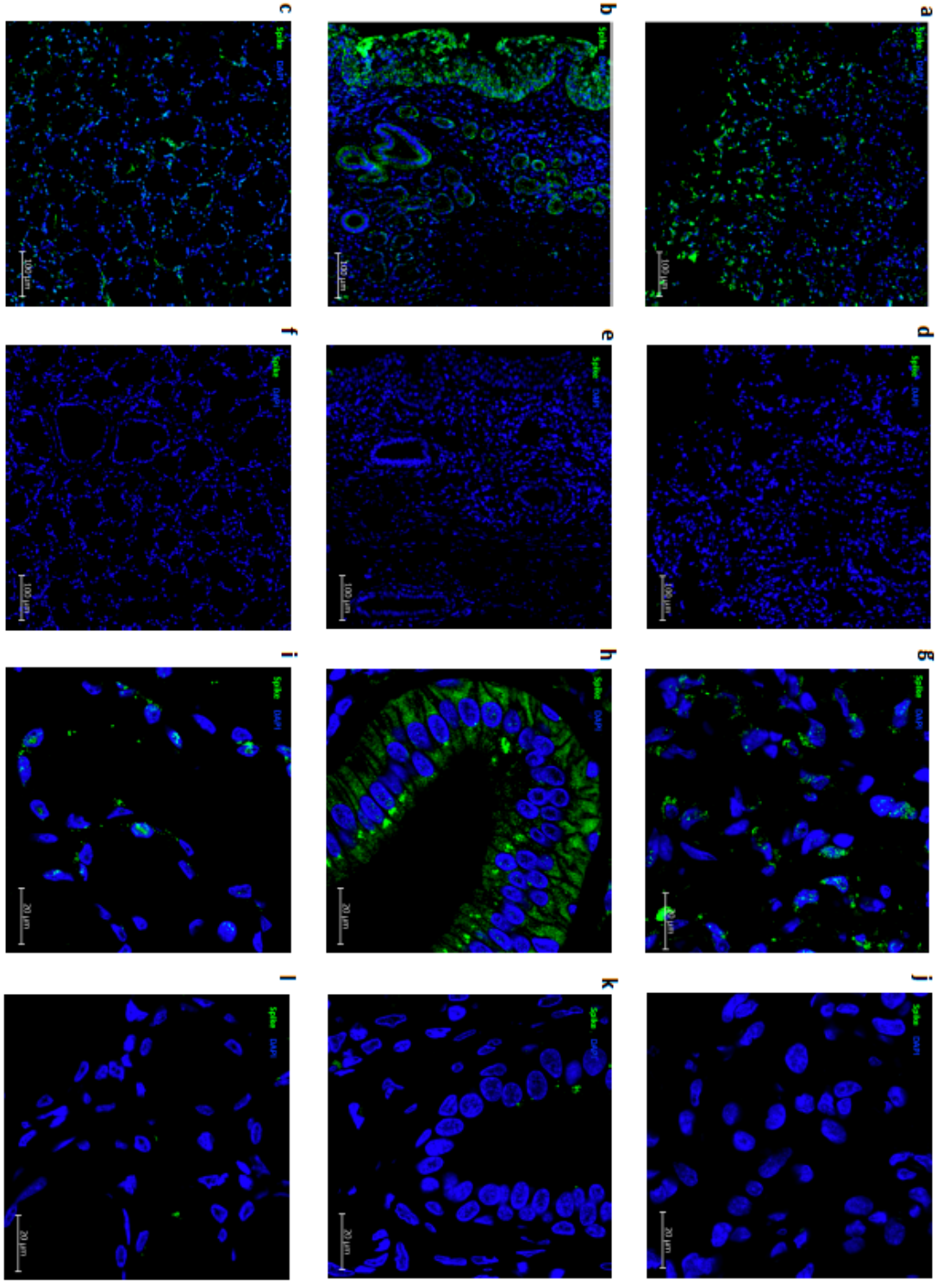

Figure S5. **Radiology of Rhesus macaques experimentally exposed to COVID19 - 3 dpi.** CXR Radiographs showing ventrodorsal and right lateral views(a). Day 0: Normal, Day 1: Mild left caudal interstitial opacity with minimal diffuse right interstitial opacity, Day 2: Mild multifocal interstitial pattern (red arrow), Day 3: Mild multifocal interstitial pattern with patchy region in left caudal lobe (red arrow). CT scan axial view showing lesion characteristics in rhesus macaques infected with SARS-CoV-2 (b) at baseline and Day 1-3 dpi. As seen in (b) ground glass opacity seen on Day 2 dpi intensified on Day 3 dpi. (c) and (d) show lesions that appear on Day 1 show gradual resolution on Day 2-3 dpi whereas lesion in panel (e) observed on Day 1 dpi showed only minimal changes on Day 2. Red arrow point towards lung lesions with high attenuation.

Figure S6. SARS-CoV-2 induced cytokines in plasma. Simultaneous analysis of multiple cytokines by Luminex technology in the plasma of rhesus macaques over 0-3 dpi. Levels of IL-6 (a), IFN-a (b), IFN-g (c), IL-8 (d), perforin (e), IP-10 (f), MIP1a (g), MIP1b (h), IL-12p40 (i), IL-18 (j), TNF-a (k) and IL-1Ra (l)are expressed in Log10 concentration in picogram per mL of plasma. (red – 0 dpi; purple – 1 dpi; blue – 2 dpi; green – 3 dpi). (n=4) Data is represented as mean± SEM. One way repeated-measures ANOVA with Geisser-Greenhouse correction for sphericity and Tukey's post hoc correction for multiple-testing (GraphPad Prism 8) was applied. * P<0.005, ** P<0.005, *** P<0.0005.

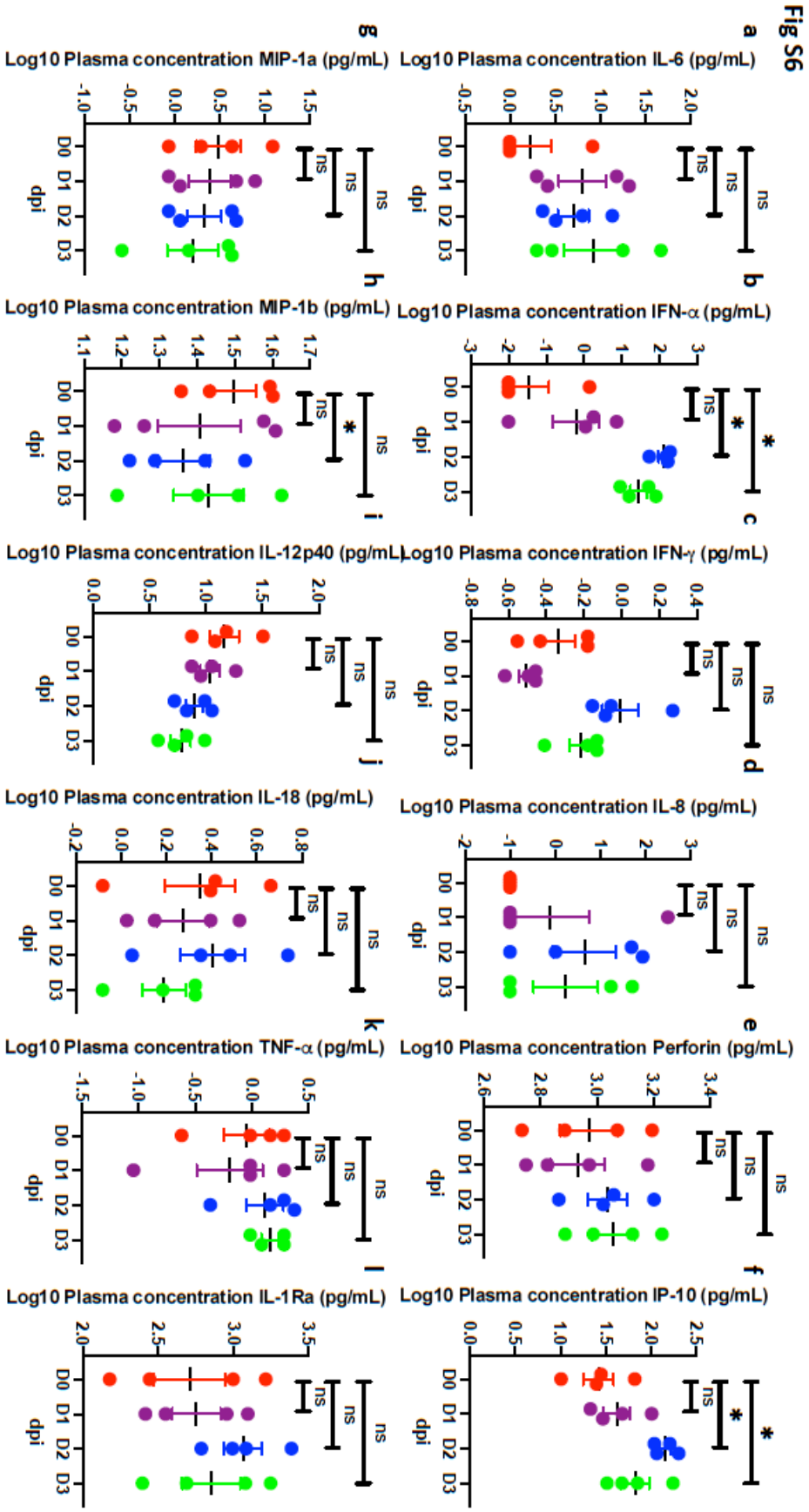

Figure S7. Clinical correlates in long-term (14-17 dpi) rhesus macaques. Serum levels of CRP (mg/L) (a), tCO2 (D-mmol/L) (b), and whole blood levels of Red Blood Cells (RBCs) (million/mL) (c), reticulocytes (K/mL) (d), percentage of Neutrophils (g), Neutrophils (K/mL) (f), platelets (K/uL) (e), percentage of monocytes (h) and percent change in weight (i) (Coloring scheme for I – young (blue), old (red).). (a-e) (n=12) Data is represented as mean± SEM. One way repeated-measures ANOVA with Geisser-Greenhouse correction for sphericity and Tukey's post hoc correction for multiple-testing (GraphPad Prism 8) was applied. * P<0.005, ** P<0.005, *** P<0.0005.

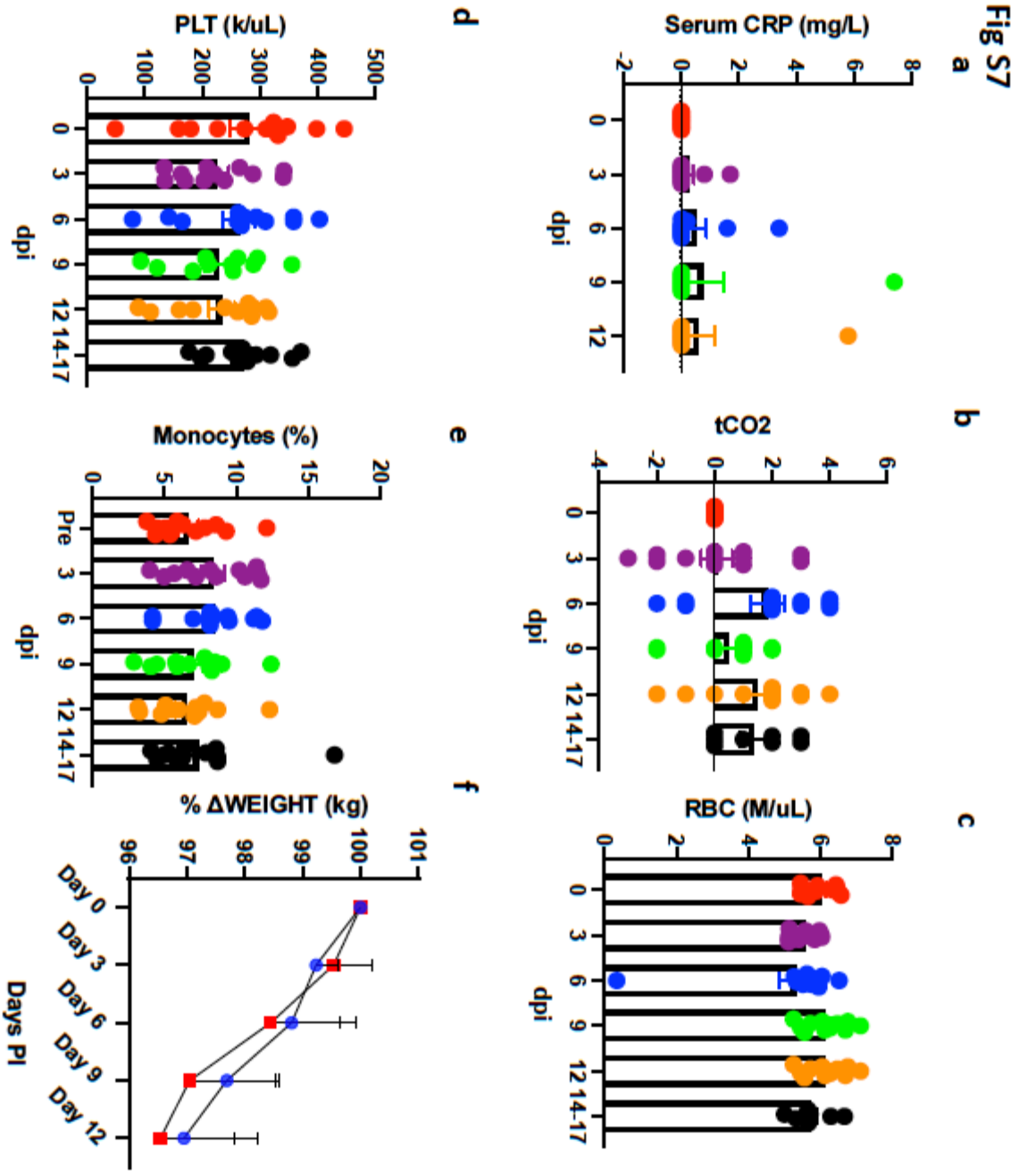

Figure S8. Longitudinal viral RNA determination following SARS-CoV-2 infection in rhesus macaques. Viral RNA (log_{10} copies/mL measured by RT-PCR in BAL fluid (a) and nasopharyngeal (b), buccopharyngeal (c-d) and rectal [30] swabs longitudinally. Data is depicted as combined for age (c,e) and data split by age a; b; d; f). Coloring scheme for c; e – (red – 0 dpi; purple – 3 dpi; blue – 6 dpi: green – 9 dpi; orange – 12 dpi: black – 14-17 dpi). (n=12) One way Repeated-measures ANOVA with Geisser-Greenhouse correction for sphericity and Tukey's post hoc correction for multiple-testing (GraphPad Prism 8) was applied. * P<0.005, ** P<0.005, *** P<0.0005. Coloring scheme for a; b; d; f – young (blue), old (red). (n=6) Data is represented as mean± SEM. Two way Repeated-measures ANOVA with Geisser-Greenhouse correction for sphericity and Tukey's post hoc correction for multiple-testing (GraphPad Prism 8) was applied. ** P<0.005.

Fig S8

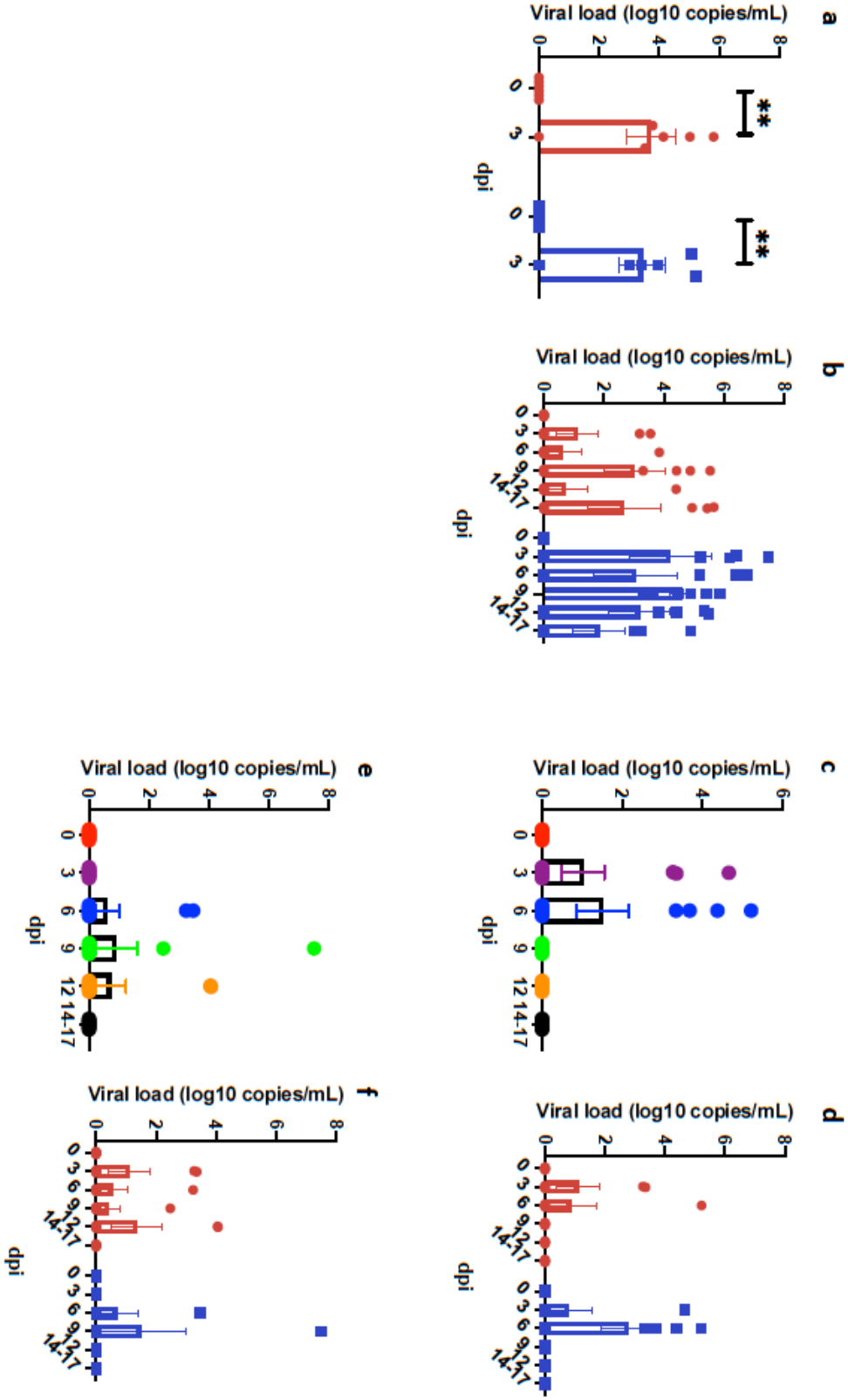

Figure S9. Longitudinal viral RNA determination following SARS-CoV-2 infection in rhesus macaques. Viral RNA was determined at endpoint in Lungs (a) and longitudinally in plasma (b) and urine (c).

Fig S9

a

b

Viral RNA (copies/mL) titre in plasma of Rhesus macaques

ID	Sex	Cohort	Day 0	Day 3	Day 6	Day 9	Day 12
16653	M	old	*UD	*UD	*UD	*UD	*UD
17736	F	old	*UD	*UD	*UD	*UD	*UD
19314	F	old	*UD	*UD	*UD	*UD	*UD
19853	F	old	*UD	*UD	*UD	*UD	*UD
20083	F	old	*UD	*UD	*UD	*UD	*UD
33926	M	old	*UD	*UD	*UD	*UD	*UD
35951	M	juvenile	TBD	*UD	*UD	*UD	*UD
35969	M	juvenile	*UD	*UD	*UD	*UD	*UD
36052	F	juvenile	TBD	*UD	*UD	*UD	*UD
36056	F	juvenile	*UD	*UD	*UD	*UD	*UD
36189	F	juvenile	*UD	*UD	*UD	*UD	*UD
36207	M	juvenile	TBD	*UD	*UD	*UD	*UD

c

Viral RNA (copies/mL) titre in urine of Rhesus macaques

SNPRC ID	Sex	Cohort	Day 0	Day 3	Day 6	Day 9	Day 12
16653	M	old		*UD	*UD		
17736	F	old			*UD		
19314	F	old		*UD			
19853	F	old					
20083	F	old					
33926	M	old		*UD	*UD		
35951	M	juvenile			*UD		
35969	M	juvenile		*UD	*UD		
36052	F	juvenile		*UD	*UD		
36056	F	juvenile		*UD	*UD		
36189	F	juvenile					

Figure S10. **Gross and histopathologic findings of young and aged male and female Rhesus macaques experimentally exposed to SARS-CoV-2 - 14-17 dpi.** Young male Rhesus macaque. Lung was grossly unremarkable (a). Aged male Rhesus macaque. The dorsal aspect of the lungs was mottled red (b). Young male Rhesus macaque. Lung. Subgross image showing multifocal areas of minimal interstitial pneumonia (*) (c). Young female Rhesus macaque. Lung. Mild lymphocytic interstitial pneumonia with alveolar septa (bracket) expanded by mononuclear cells (lymphocytes and macrophages) (d). Aged female Rhesus macaque. Lung. Mild lymphocytic interstitial pneumonia with increased alveolar macrophages and few syncytial cells (arrow) within the alveolar lumen (*; a neutrophil is just to the left of the *) and type II pneumocytes lining alveoli (arrowhead) (e). Aged female Rhesus macaque. Lung. Minimal interstitial pneumonia with alveolar septa expanded by fibrosis (*) and few syncytial cells (arrow) within alveoli (f). Young male Rhesus macaque. Lung. Alveolar septa expanded by fibrosis (*) and lymphocyte infiltrates (g). Aged male Rhesus macaque. Lung. Areas of bronchiolization (arrows) (h). Young female Rhesus macaque. Lung. Vasculitis. Vascular wall disrupted by infiltrates of mononuclear cells and lesser neutrophils (arrow) (i). Young female Rhesus macaque. Lung. Bronchitis. Bronchial epithelium infiltrated by eosinophils (arrow). Fibrosis adjacent to bronchus (*) (j). Young female Rhesus macaque. Lung. Area of perivascular lymphocyte infiltrates (*) (k). Young female Rhesus macaque. Lung. Area of bronchiolar associated lymphoid tissue (BALT) (*) (l). All slides were stained with H&E.

Fig S10

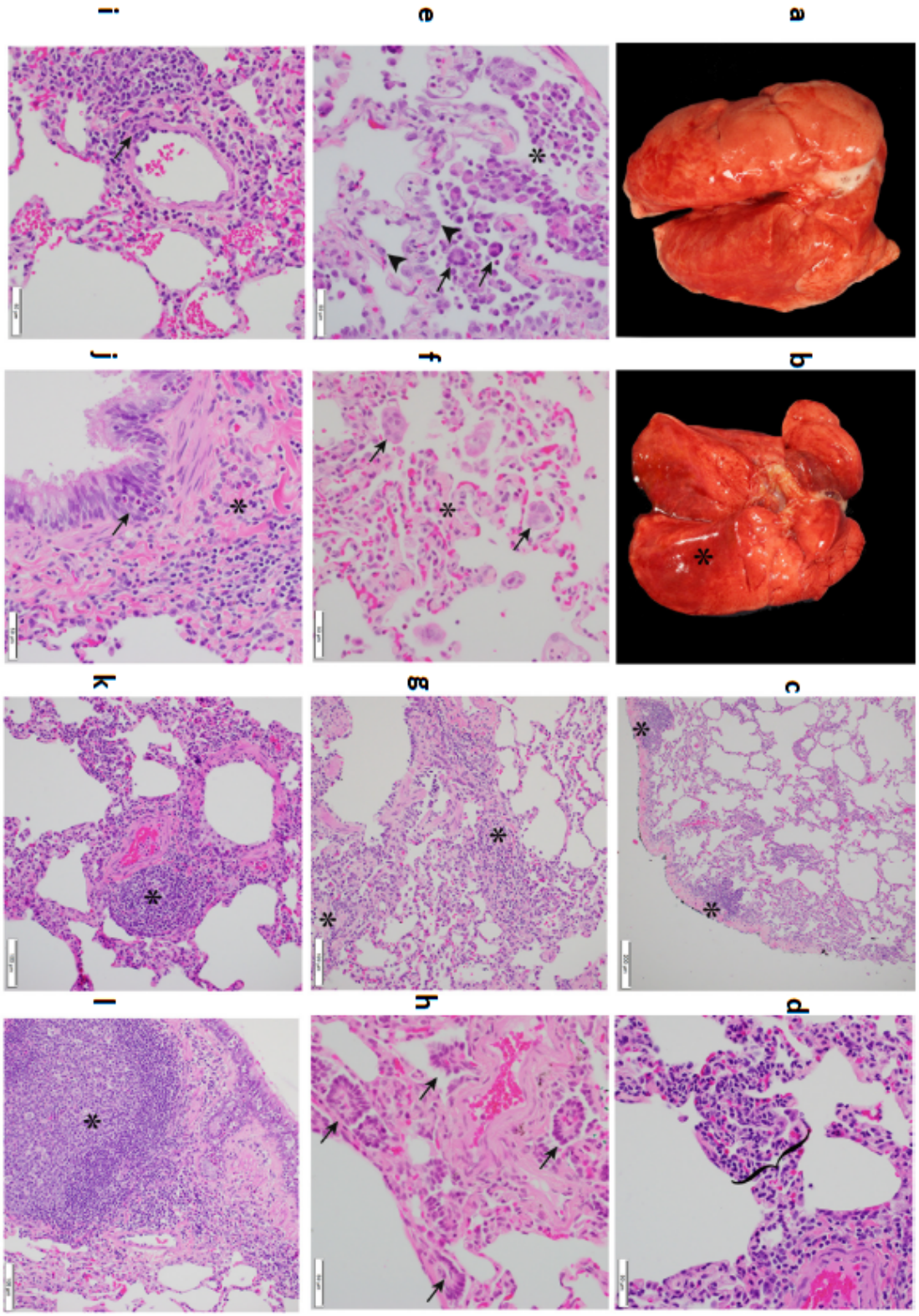

Figure S11. Viral, Gross and histopathologic findings of young male and female baboons experimentally exposed to COVID19 - 14-17 dpi. Viral RNA (log_{10} copies/mL were measured by RT-PCR in buccopharyngeal (a) and rectal (b) swabs longitudinally. Young male baboon. The dorsal aspect of the lungs was mottled red (*) (c). Young female baboon. The dorsal aspect of the lungs was mottled red (*) (d). Young male baboon. Lung. Subgross image showing areas of consolidation (*) (e). Young female baboon. Moderate lymphocytic interstitial pneumonia with scattered neutrophils (arrowhead) (f). Young female baboon. Moderate lymphocytic interstitial pneumonia with alveolar septa (bracket) markedly expanded by mononuclear cells (lymphocytes and macrophages) and increased alveolar macrophages within the alveolar lumen (*) (g). Young male baboon. Lung. Mild lymphocytic interstitial pneumonia with increased alveolar macrophages and few syncytial cells (arrow) within the alveolar lumen (*) (h). Young female baboon. Mild lymphocytic interstitial pneumonia with scattered type II pneumocytes (arrows) and increased alveolar macrophages and neutrophils within the alveolar lumen (*) (i). Young male baboon. Lung. Alveolar septa expanded by fibrosis (*) (j). Young male baboon. Lung. Alveolar septa expanded by fibrosis (*) (k). Young female baboon. Area of bronchiolization (bracket) (l). Young male baboon. Lung. Syncytial cells within airways (arrows) (m). Young male baboon. Lung. Bronchitis. Bronchial wall expanded by infiltrates of eosinophils that expand and disrupt the epithelium (arrow). Area of bronchiolar associated lymphoid tissue (BALT) (*) (n). All slides were stained with H&E.

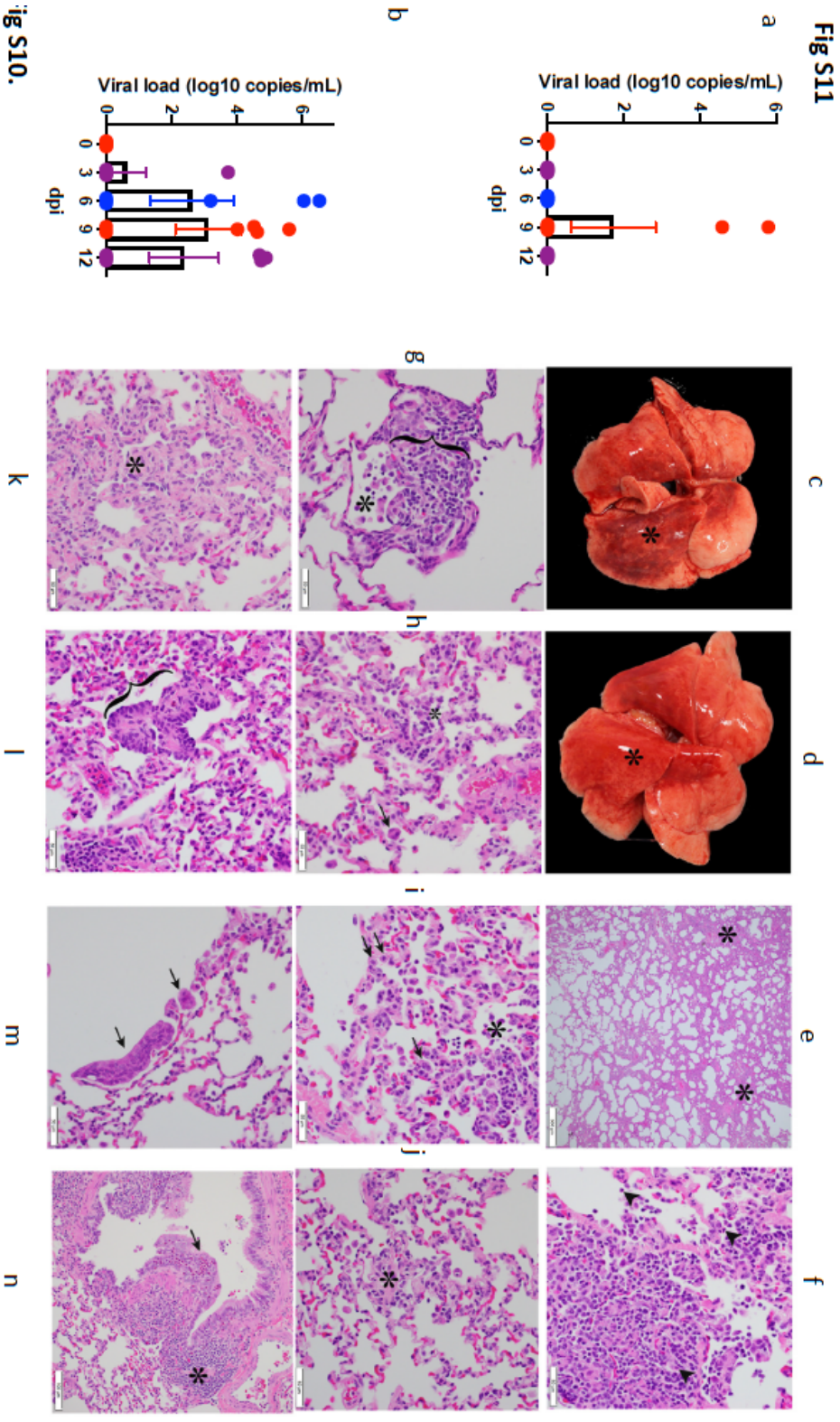

ig S10.

Figure S12. CT scan in axial view showing lesion characteristics in rhesus macaques infected with SARS-CoV-2 from Day 6-12 dpi. As seen in panel A, B, D, E and F patchy alveolar patterns, nodular and/or multifocal ground glass opacities (red arrow) seen on Day 6 dpi show dramatic resolution by Day 12 dpi, whereas panel C shows persistent patchy ground glass opacity on Day 6 dpi and Day 12 dpi.

Fig S12

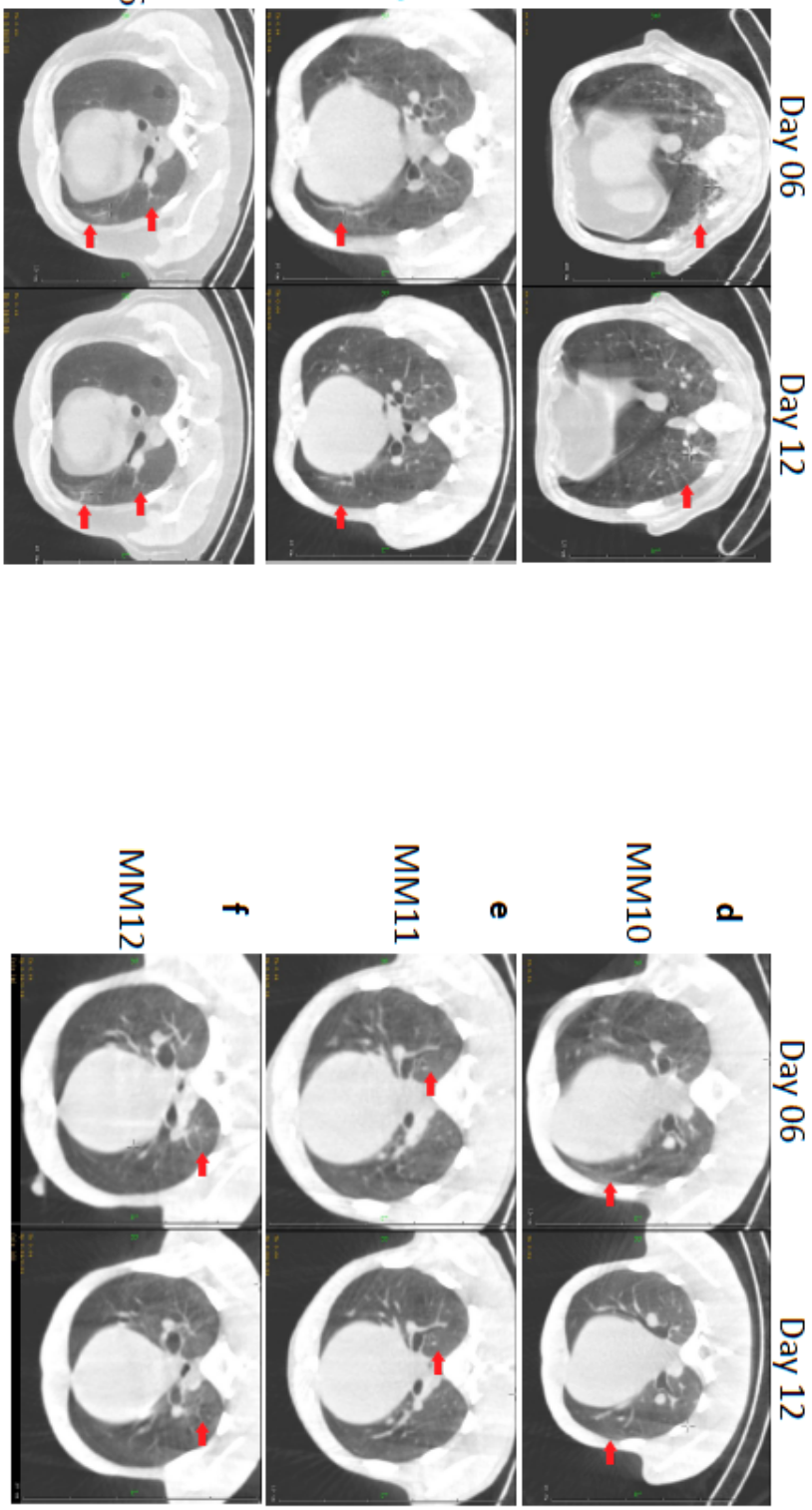

Figure S13. Accumulation of various types of myeloid cells in BAL (a-d) and PBMCs (c-h). Total myeloid cell compartment in the BAL in all animals (a) (n=12), and in two groups of macaques split by age (b). percentage of cDCs (c) and intermediate monocytes (d) in BAL. Percentage of interstitial (e) and alveolar (f) macrophages, pDCs (g) and intermediate macrophages (h) in the peripheral blood. Coloring scheme for b-h – young (blue), old (red) (n=6). (i) P value table for Spearman's correlation curve in Fig 5i.

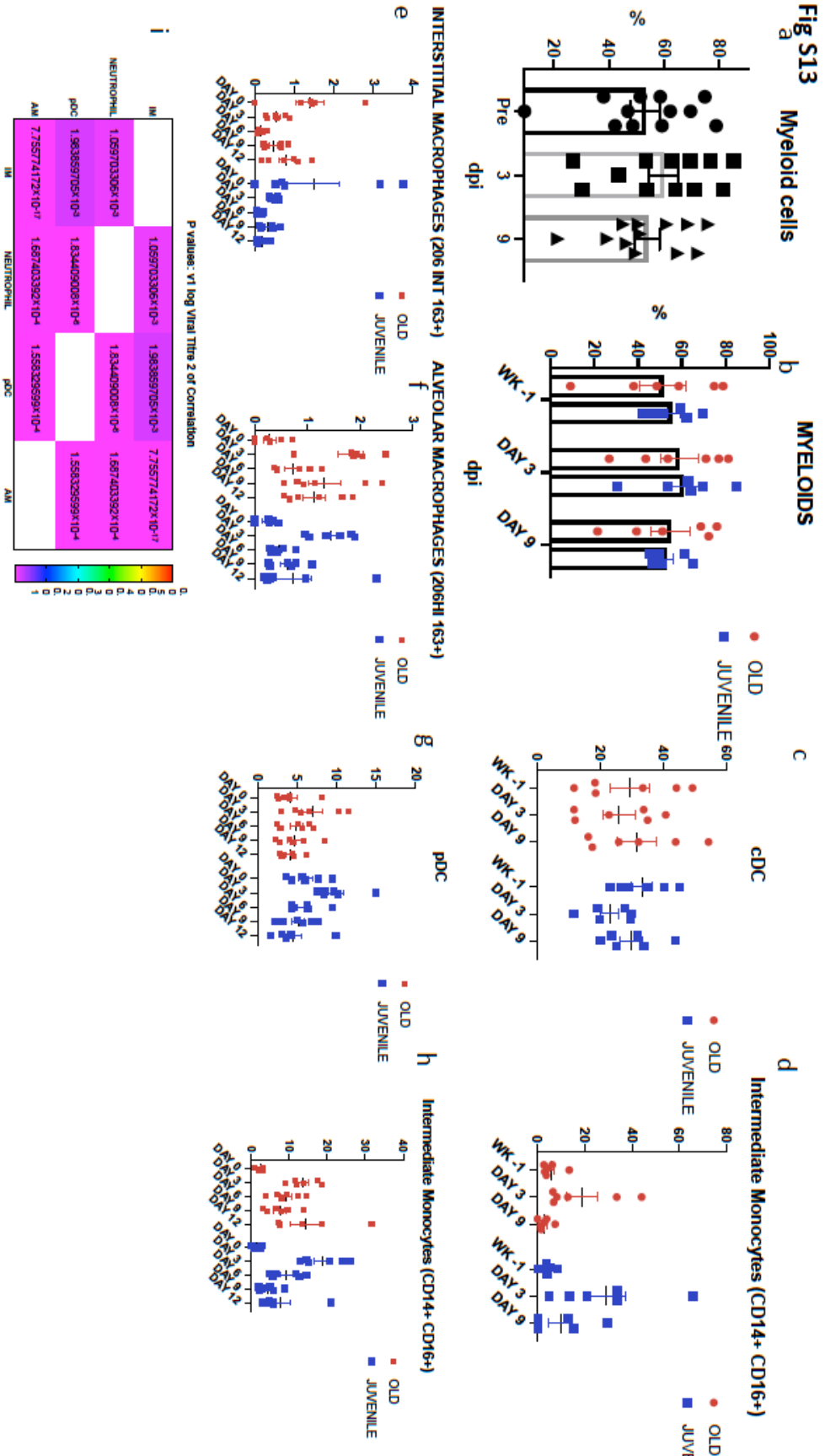

Figure S14. Detection of SARS-CoV-2 signal in host lung cells by confocal microscopy. Multi-label confocal immunofluorescence microscopy of a high viral titer lung lobe from SARS CoV-2 infected Rhesus macaque at 3 dpi with SARS CoV-2 Spike specific antibody (green), neutrophil marker CD66abce (red) and DAPI (blue)- (10X-a, 63X-g) vs the naïve control lungs (10X-d, 63X-j). SARS CoV-2 Spike (green), pan-macrophage marker CD68 (red) and DAPI (blue) in infected lungs (10X-b and 63X-h) vs the naïve control lungs (10X-e, 63X-k). SARS CoV-2 Spike (green), HLA-DR [29], pDC marker CD123 (red) and DAPI (blue) specific staining in infected lungs (10X-c,63X-i) vs naïve control lungs(10X-f, 63X-l).

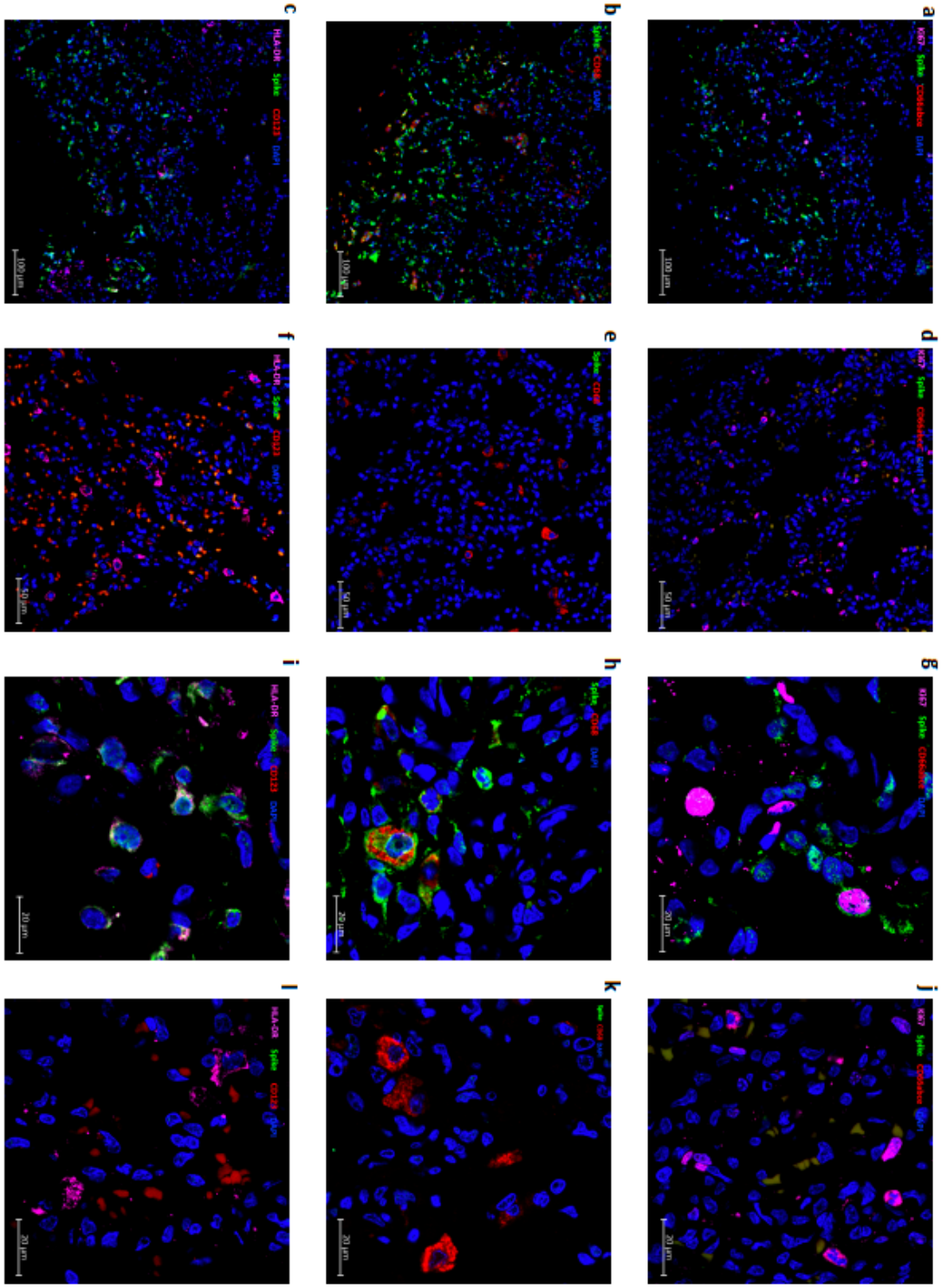

Fig S14

Figure S15. Longitudinal changes in cytokine secretion profile in BAL T cells following SARS-CoV-2 infection in rhesus macaques. BAL Frequencies of $CD4^+$ T cell subsets expressing Interferon-$\boldsymbol{\gamma}$ (a), IL-17 (b), TNF-$\boldsymbol{\alpha}$ (c), CD8+ T cells expressing Interferon-$\boldsymbol{\gamma}$ (d), IL-17 (e), TNF-$\boldsymbol{\alpha}$ (f) cultured overnight without any external antigenic stimulation. BAL cells were also stimulated overnight (12-14 hours) with either Mock control (U); PMA-Ionomycin (P/I) or SARS-CoV-2 -specific peptide pools of the nucleocapsid (N), membrane (M) and spike (S) proteins. Antigen specific cytokine secretion in T cells was estimated by flow cytometry. Fraction of CD4+ T cell subsets expressing Interferon-γ (g), IL-17 (h), TNF-α (i), CD8+ T cells expressing Interferon-γ (j), IL-17 (k), TNF-α (l). Coloring scheme– young (blue), old (red). Data is represented as mean$\pm$ SEM. (n=6) Two way Repeated-measures ANOVA with Geisser-Greenhouse correction for sphericity and Tukey's post hoc correction for multiple-testing (GraphPad Prism 8) was applied. * P<0.005, ** P<0.005, *** P<0.0005.

Fig S15

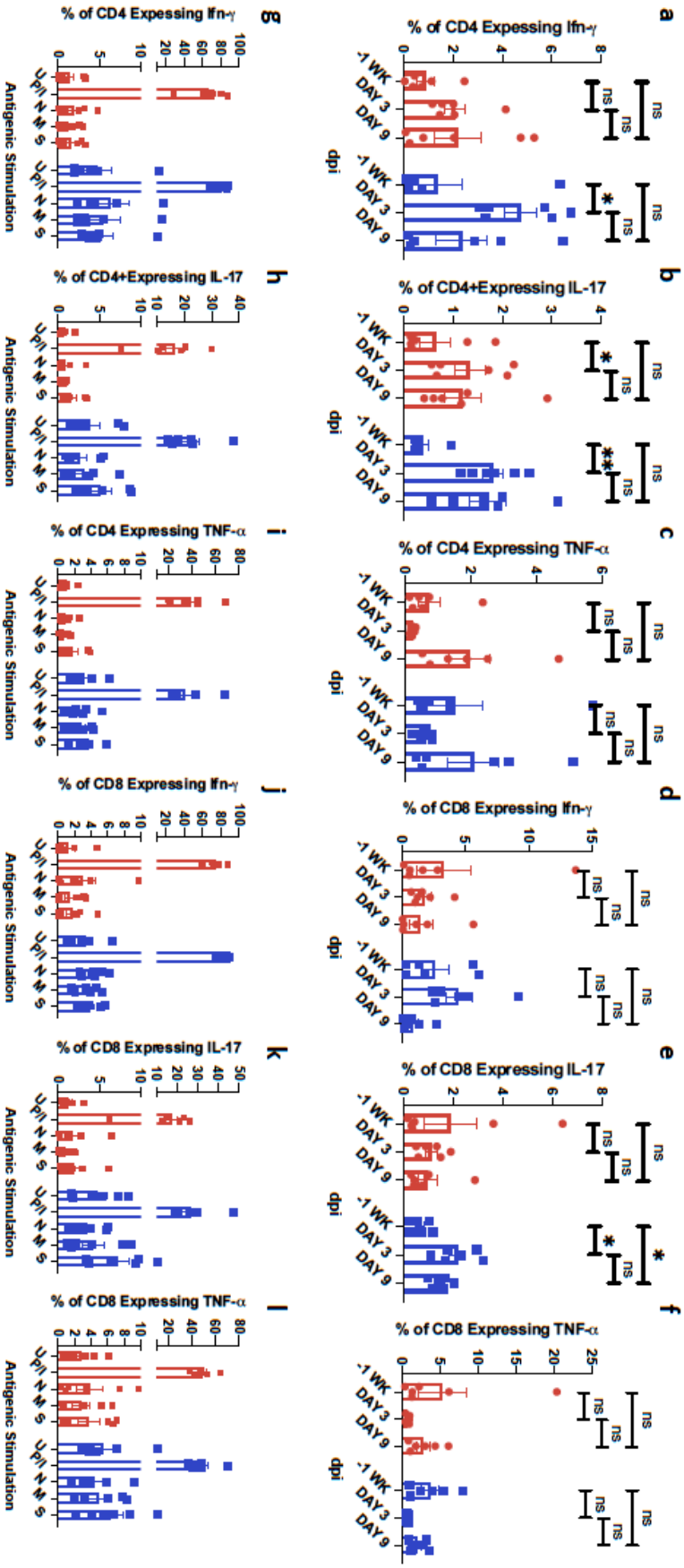

Figure S16. Longitudinal changes in SARS-CoV-2 induced cytokines in BAL fluid and plasma following SARS-CoV-2 infection in rhesus macaques over two weeks. Simultaneous analysis of multiple cytokines by Luminex technology in the BAL fluid and plasma of rhesus macaques over 0-15 dpi. Levels of IFN-α (a), IL-1Ra (b), IFN-γ (c), TNF-α (d), IL-6 (e), Perforin (f) are expressed in Log10 concentration in picogram per mL of BAL fluid. Levels of IFN-α (g), IL-1Ra (h), IFN-γ (i), TNF-a (j), IL-6 (k), Perforin (l) are expressed in Log10 concentration in picogram per mL of BAL fluid. Coloring scheme – young (blue), old (red). Data is represented as mean$\pm$ SEM. (n=12) Two way Repeated-measures ANOVA with Geisser-Greenhouse correction for sphericity and Tukey's post hoc correction for multiple-testing (GraphPad Prism 8) was applied. * P<0.005, ** P<0.005, *** P<0.0005.

Fig S16

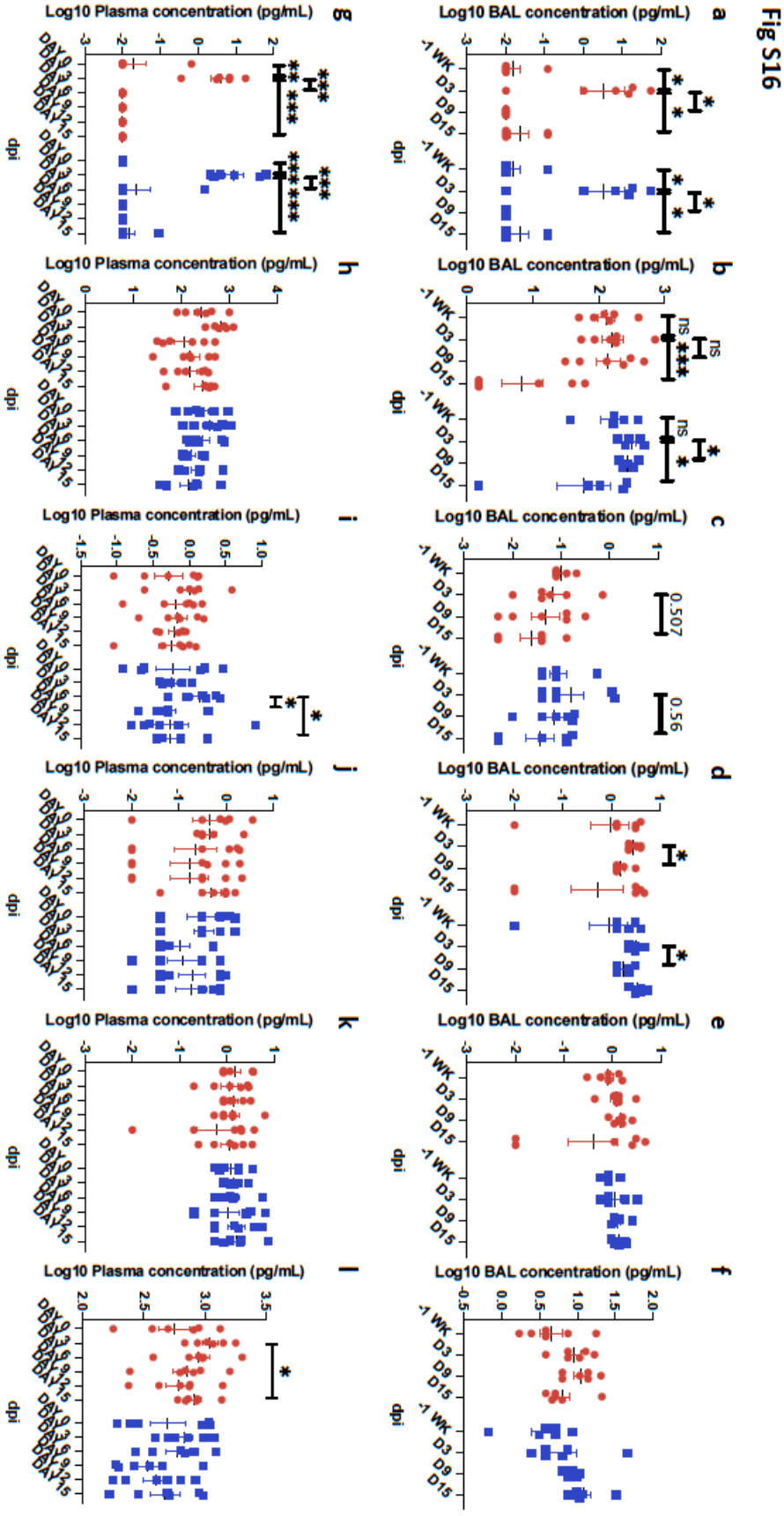

Figure S17. SARS-CoV-2 infection induces ACE-2 expression. RNAseq was performed on total RNA isolated from the lungs of naïve (n=3) and SARS-CoV-2 infected (14-17dpi) rhesus macaques (n=8, 3 young and 5 old macaques) as described earlier [16]. Results indicate that the expression of ACE2, which is lower in naïve animals (denoted by red color in the heat map) (a), was induced following SARS-CoV-2 infection (denoted by blue color in the heat map) (a). Relative expression level of ACE-2 was significantly higher than in naïve tissues (b). Higher expression of ACE-2 was observed in lung tissues obtained at necropsy from young relative to old macaques (c, d), such that the difference between naïve animals and young SARS-CoV-2 infected animals in ACE-2 expression levels was statistically significant by itself. All p-values shown on expression swarm plots (b-d) are FDR-corrected significance values for differential expression calculated by DESEQ2 [16].

Fig S17

Figure S18. Flow cytometry Gating Strategy. Gating strategy for T cell phenotyping is described.

Fig S18

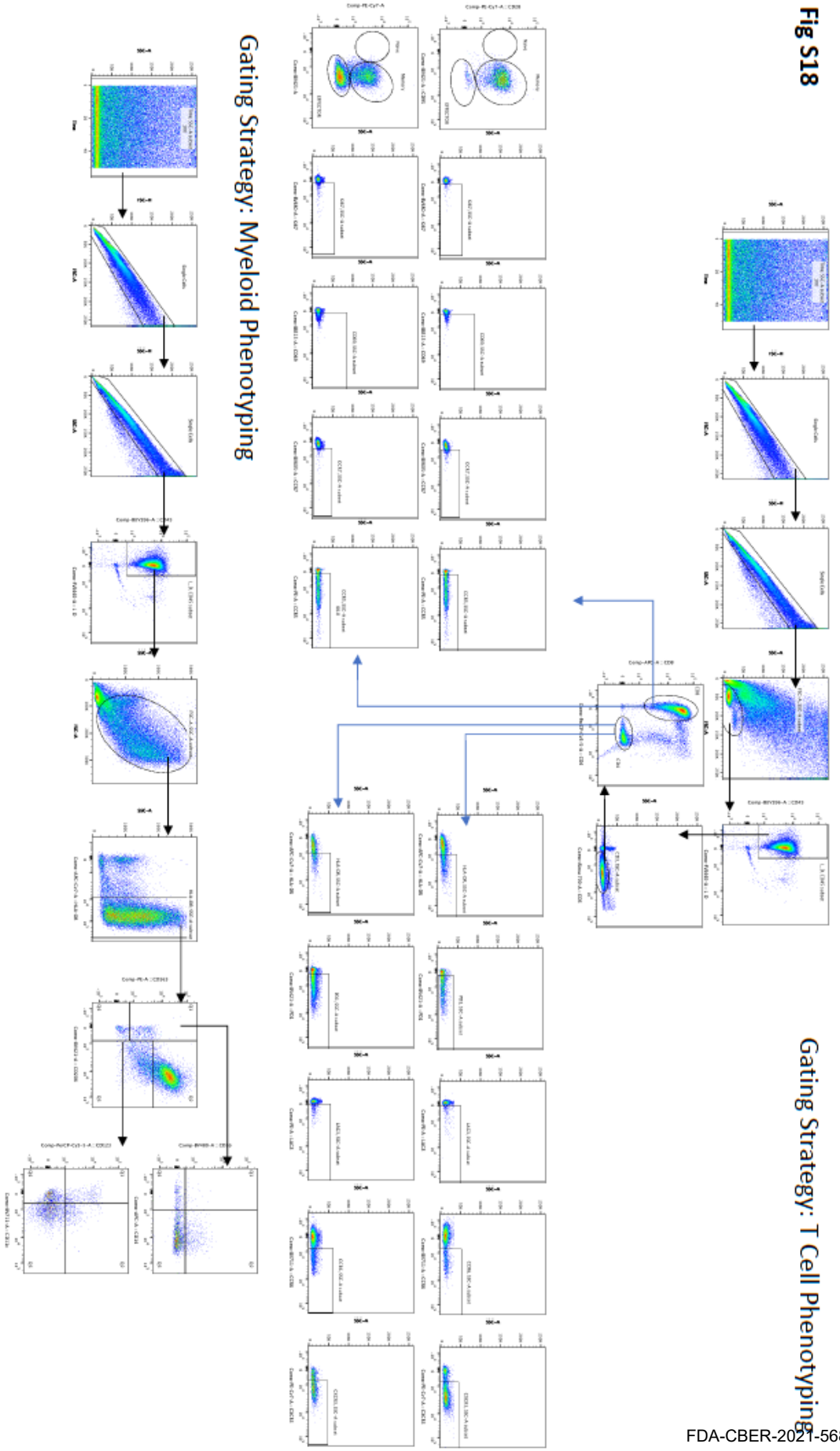

Supplemental tables

Table S1. In vivo experimental design. A. short-term rhesus macaque pilot. B-D. 14-day multispecies comparison in rhesus macaques, baboons, marmosets.

Table S2. Distribution of lesions by anatomic location and morphologic diagnosis of young and aged rhesus macaques experimentally exposed to SARS-CoV-2 - 3 dpi.

Table S3. Distribution of lesions by anatomic location and morphologic diagnosis of young and aged rhesus macaques experimentally exposed to SARS-CoV-2 – 14-17 dpi.

Table S4. Distribution of lesions in baboons experimentally exposed to SARS-CoV-2 – 14-17 dpi.

Table S5. CXR scores in rhesus macaques experimentally exposed to SARS-CoV-2 – 14-17 dpi.

Table S6. CT scores in rhesus macaques experimentally exposed to SARS-CoV-2 – 14-17 dpi.

Table S7. List of antibodies used for immunophenotyping studies.

Immunity, Vol. 13, 529–538, October, 2000, Copyright ©2000 by Cell Press

Enhanced Antigen-Specific Antitumor Immunity with Altered Peptide Ligands that Stabilize the MHC-Peptide-TCR Complex

Jill E. Slansky,* Frédérique M. Rattis,*‖ Lisa F. Boyd,† Tarek Fahmy,‡ Elizabeth M. Jaffee,* Jonathan P. Schneck,‡ David H. Margulies,† and Drew M. Pardoll*§

*Department of Oncology
Johns Hopkins University School of Medicine
Baltimore, Maryland 21231
†Molecular Biology Section
Laboratory of Immunology
Building 10, Room 11N311
National Institutes of Allergy and Infectious Diseases
National Institutes of Health
Bethesda, Maryland 20892
‡Department of Pathology and Medicine
Division of Immunopathology
Johns Hopkins University
Baltimore, Maryland 21205

Summary

T cell responsiveness to an epitope is affected both by its affinity for the presenting MHC molecule and the affinity of the MHC-peptide complex for TCR. One limitation of cancer immunotherapy is that natural tumor antigens elicit relatively weak T cell responses, in part because high-affinity T cells are rendered tolerant to these antigens. We report here that amino acid substitutions in a natural MHC class I–restricted tumor antigen that increase the stability of the MHC-peptide-TCR complex are significantly more potent as tumor vaccines. The improved immunity results from enhanced in vivo expansion of T cells specific for the natural tumor epitope. These results indicate peptides that stabilize the MHC-peptide-TCR complex may provide superior antitumor immunity through enhanced stimulation of specific T cells.

Introduction

A major endeavor in modern medicine is the enhancement of vaccine potency via manipulation of both the antigen and the delivery system. Success in this effort is critical in the development of effective cancer immunotherapy. In particular, enhancement of T cell responses to tumor antigens would lead to more potent treatments (Pardoll, 2000). Endogenous T cell responses to both murine and human cancers can be readily identified (reviewed in De Plaen et al., 1997; Robbins and Kawakami, 1996). Tumor antigens recognized by T cells typically fall into one of three categories (reviewed in Boon et al., 1997; Gilboa, 1999): (1) antigens whose peptide epitopes incorporate the product of a mutation specific to the individual tumor (e.g., mutated oncogenes); (2) nonmutated antigens expressed by a significant proportion of tumors of certain histologic types but silent in most normal tissues in the adult (e.g., MAGE1-3); (3) tissue-specific differentiation antigens specific to the tissue type from which the tumor arose (e.g., gp100 and tyrosinase). The latter two categories of tumor antigen represent attractive candidates for incorporation into antigen-specific cancer vaccines with broad applicability in treatment of many tumors. Despite the growing list of candidate tumor antigens recognized by T cells, antigen-specific vaccination for established cancer has thus far seen relatively limited success. A major limitation to the efficacy of cancer vaccines is that endogenous T cell responses against tumor antigens tend to be relatively weak. In some cases, the weak T cell responses to tumor antigens appear to be related to the low affinity of the peptide antigen for its presenting MHC molecule (Cox et al., 1994). This low affinity results in weak association of peptide with MHC molecules at the surface of antigen-presenting cells resulting in poor presentation of MHC-peptide ligand to T cells. Such antigens are often characterized by an absence of favored residues at critical anchor positions involved in MHC binding. For weak tumor antigens that fall into the low-affinity MHC binding category, replacement or mutation of unfavorable anchor residues with more effective ones may greatly enhance MHC binding properties (Lurquin et al., 1989; Gervois et al., 1996; Parkhurst et al., 1996; Bakker et al., 1997; Dyall et al., 1998; Overwijk et al., 1998; Valmori et al., 1999). These altered peptides may more effectively activate T cell responses against the wild-type peptide antigen by virtue of the increased efficiency of presentation of the MHC-peptide complex to specific T cells. In both mouse and human studies, these anchor-modified peptides can elicit superior T cell responses against the original antigen in vivo (Dyall et al., 1998; Rosenberg et al., 1998). Thus, enhanced stability of the MHC-peptide complex afforded by the favorable anchor residue may result in a more efficacious T cell response due to the presentation of increased numbers of MHC-peptide ligands.

Some tumor antigens bind to their presenting MHC with affinities in a similar range to strong viral antigens yet elicit weak endogenous immune responses (Lee et al., 1999). For tumor antigens with high MHC affinities, the proposed mechanism for weak endogenous immune responses is that high-affinity T cells are actively tolerized via anergy or deletion, thereby leaving a functional repertoire consisting of T cells bearing T cell receptors (TCR) with low affinity for MHC-peptide complexes. This residual T cell repertoire is postulated to have escaped active tolerance induction by virtue of its low affinity for MHC-peptide ligand. This mechanism is particularly relevant for shared tumor antigens, which, because they are self-antigens, have had a long time period to induce tolerance (Morgan et al., 1998).

The current study was designed to investigate the effect of immunization with altered peptides in which amino acids were substituted that affect the affinity of the MHC-peptide complex for TCR rather than the affinity of peptide for MHC. We focused on a nonmutated H-2L^d-

§To whom correspondence should be addressed (e-mail: dmpardol@jhmi.edu).
‖Present address: Genoway, 46 Allée d'Italie, 69007 Lyon, France.

restricted peptide antigen derived from gp70 amino acids 423–431, referred to as AH1 (SPSYVYHQF), which is the dominant target for the CD8 T cell responses against the CT26 colorectal tumor (Huang et al., 1996). gp70 expression is silent in most normal tissues but is active in many mouse tumors (Huang et al., 1996). According to a computer algorithm developed to rank order the half-time of disassociation of peptide to MHC, AH1 is predicted to bind H-2L^d with higher affinity than other peptides derived from gp70 (Parker et al., 1994). AH1 features a proline in position two and an aliphatic residue in position nine, consistent with the consensus residues for H-2L^d binding peptides (Corr et al., 1992).

Here, we show that AH1 has relatively high affinity for H-2L^d but provides relatively weak immunization against CT26 challenge. An amino acid substitution in AH1 that does not alter MHC binding but rather increases the stability of the MHC-peptide-TCR complex by decreasing the off rate of TCR from MHC-peptide is significantly more potent in activating T cells in vivo specific for the natural tumor epitope, resulting in enhanced systemic antitumor immunity.

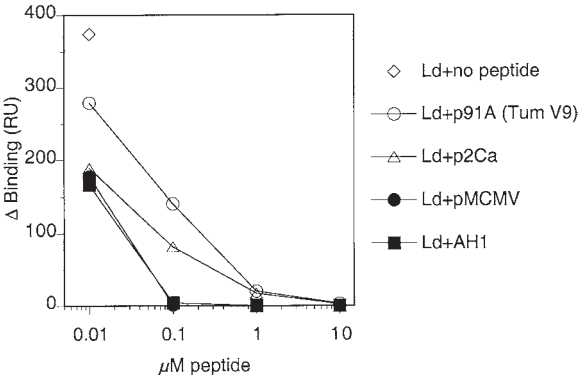

Figure 1. AH1 and pMCMV Peptides Bind H-2L^d with Similar Affinity

Either buffer alone or graded concentrations of the indicated peptide (pMCMV [YPHFMPTNL], p2Ca [LSPFSFDL], p91A-Tum V9 [QNHRALDLV]) were combined with 40 μM H-2L^d produced in mammalian cells and exposed to immobilized pMCMV-C4 peptide on the biosensor surface. The cysteine substitution at position 4 of pMCMV facilitated immobilization of the peptide to the biosensor surface and exhibits similar binding to H-2L^d as the native peptide. The amount of H-2L^d bound to pMCMV-C4 is reflected by the change in resonance units after 4 min.

Results

Tumor Antigen AH1 Binds MHC with High Affinity

To analyze the role of MHC and TCR binding properties on the immunogenicity of a tumor antigen, we chose the well-characterized mouse colorectal cancer, CT26. AH1, an H-2L^d-restricted peptide, was identified as the immunodominant antigen from CT26 recognized by CD8$^+$ T cells in animals immunized with autologous whole cell tumor vaccines (Huang et al., 1996). As with most natural tumor antigens derived from self-proteins, AH1 peptide is a relatively weak immunogen when used independently from the tumor as a vaccine against CT26 even though it is a good target for activated antigen-specific CTL (Huang et al., 1996). To understand why the peptide antigen does not immunize efficiently against tumor formation and to determine if substitutions that alter the stability of the trimeric complex might result in stronger antitumor immunity, we first studied the physical parameters of the interaction between H-2L^d and AH1 as well as the H-2L^d-AH1 complex and a cognate TCR.

To compare binding of the AH1 peptide to the MHC class I molecule H-2L^d relative to other tumor antigens and known H-2L^d binding peptides, we employed a previously described assay using immobilized peptides and surface plasmon resonance (Khilko et al., 1993; reviewed in Khilko et al., 1995). In this assay, the binding of an "empty" soluble H-2L^d to an immobilized peptide is competed for by graded concentrations of a test peptide. The peptide pMCMV-C4 was immobilized, and the indicated competing peptides and H-2L^d were offered in solution phase. AH1 bound H-2L^d as well as pMCMV and better than the other peptides tested as indicated by the decreased change in resonance units, especially at the lower peptide concentrations (Figure 1). pMCMV has previously been shown to be a high-affinity H-2L^d binding peptide (Margulies et al., 1993). p2Ca and p91A-Tum V9, another H-2L^d-restricted tumor antigen, are intermediate affinity MHC binding peptides (Alexander-Miller et al., 1994; Corr et al., 1994). These results indicate that AH1 is a high-affinity binding peptide of H-2L^d. Thus, weak MHC binding does not account for the failure of the AH1 peptide to serve as an effective immunogen.

Alanine Substitution of Residue Five in the AH1 Peptide Enhances Stability of the MHC-Peptide-TCR Complex

To determine the influence of TCR affinity for MHC-peptide complex on immunogenicity, we studied TCR binding to the natural H-2L^d-AH1 complex as well as to a panel of alanine-substituted variant peptides. To overcome the intrinsically low affinity of MHC-peptide for TCR, we used the general approach of making multivalent MHC and TCR complexes (Altman et al., 1996; O'Herrin et al., 1997; Murali-Krishna et al., 1998). We generated dimeric forms of TCR and MHC-peptide using an Ig scaffold to produce fusion proteins (Dal Porto et al., 1993; O'Herrin et al., 1997; Greten et al., 1998). Binding was measured in both directions by flow cytometry by adding peptide-loaded dimeric H-2L^d, Ld-Ig, to AH1-specific T cells and dimeric TCR, CT-Ig, to peptide-loaded antigen-presenting cells. The rank order of binding of either TCR to MHC-peptide on cells or MHC-peptide to TCR expressing cells was essentially the same (Figure 2). Substitution of the consensus MHC anchor residue 2 (proline) resulted in reduced binding, although the interaction was not totally abolished in either the TCR or MHC binding assay. Other amino acids can be tolerated in position 2 in the presence of strong C′ terminal anchor residues as in p2Ca (LSPFSFDL) and Tum (QNHRALDL) (Robinson and Lee, 1996). Peptides with substituted residues 4, 6, 7, 8, and 9 resulted in background-level binding similar to the negative control pMCMV. In contrast, peptides with substituted residues 1, 3, and 5 each mediated more binding than wild-type AH1. Since AH1-A5 mediated the greatest binding of all the peptides tested, we chose to fully characterize the binding of AH1-A5

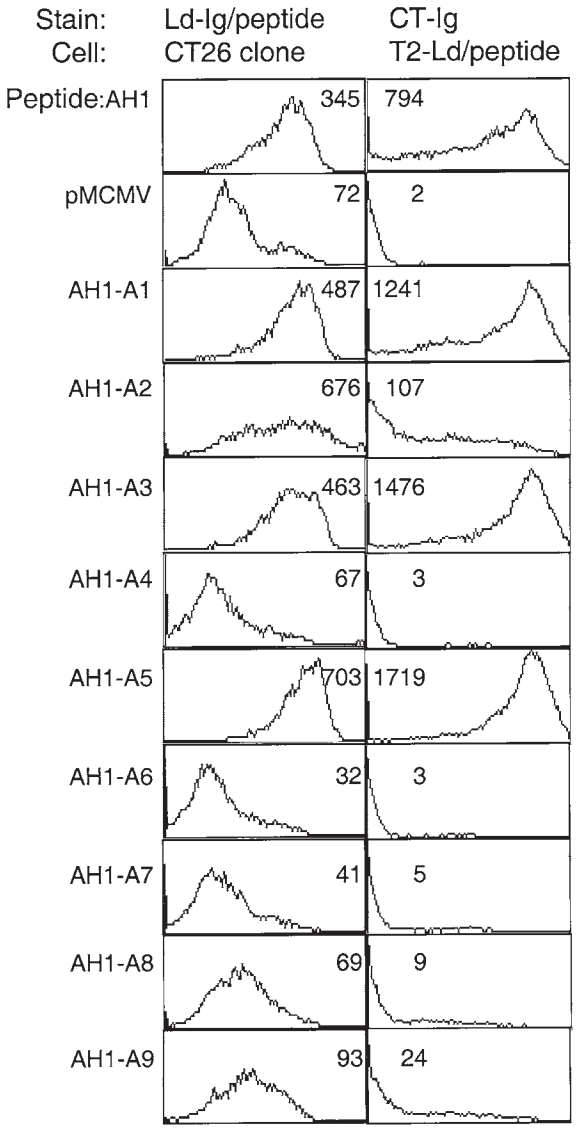

Figure 2. Binding of TCR to Ligand as Mediated by AH1 and AH1 with Alanine Substitutions

In the left panel, the AH1-specific T cell clone was stained with divalent H-2L^d, Ld-Ig, which had been loaded with the indicated peptides, and analyzed by flow cytometry. In the right panel, T2-Ld cells were incubated in 10 μM of the indicated peptide, stained with a divalent single chain form of the TCR from the AH1-specific clone, CT-Ig, and analyzed by flow cytometry. Both Ld-Ig and CT-Ig proteins were added in excess and visualized with IgG1-biotin and Avidin-PE. Histograms of the relative cell number versus fluorescence are shown. The mean channel fluorescence is indicated in each histogram.

for H-2L^d and H-2L^d-AH1-A5 for TCR compared with the wild-type AH1 peptide.

AH1 and AH1-A5 Peptides Bind MHC with Similar Affinities

One possible mechanism to explain the increased binding of TCR to MHC-peptide complexes containing AH1-A5 relative to the wild-type AH1 peptide is enhanced MHC binding. We therefore compared the ability of the peptides to bind H-2L^d as described in Figure 1. Again, the AH1 peptide competed for soluble H-2L^d as well as pMCMV and nominally better than the other peptides tested including AH1-A5 (Figure 3). Thus, the enhanced binding mediated by the AH1-A5 peptide relative to the AH1 peptide shown in Figure 2 is not a result of an increased affinity for MHC.

H-2L^d-AH1-A5 Binds TCR with Higher Affinity than H-2L^d-AH1

Surface plasmon resonance was used to directly measure the binding properties between TCR and the different peptides complexed with H-2L^d. The CT26 TCR-Ig was immobilized to the biosensor surface to measure the binding characteristics of graded concentrations H-2L^d complexed with AH1, AH1-A5, AH1-A7, and pMCMV. Binding of MHC-peptide complexes to the immobilized TCR was visualized as the time-dependent increase in resonance units (Figure 4A). Based on steady-state binding levels, the equilibrium constants for dissociation, K_D for the interaction of the TCR-Ig protein to the soluble H-2L^d complexes were determined (Figure 4B; Table 1). H-2L^d-AH1-A5 resulted in more binding than H-2L^d-AH1 reflecting the stronger affinity (K_D). Significant binding of pMCMV-H-2L^d to the TCR was not detected as expected demonstrating specificity. Independently, the kinetic dissociation rate constants (k_{off}) for each interaction were determined using a direct fit algorithm (Table 1) with the assumption of 1:1 Langmuir binding. Based on the measured K_D and k_{off}, the kinetic association rate constants, k_{on}, were calculated. As shown in Table 1, the on rates of the AH1 and AH1-A5 peptide complexes were similar. However, the off rate of the AH1-A5 complex was about 3-fold slower than the AH1 complex accounting for the difference in affinity. The on rate of the H-2L^d-AH1-A7 complex was about 4-fold slower than the H-2L^d-AH1 complex, although the off rates were similar. Table 1 also summarizes the half-time of binding of the MHC-peptide binding to the TCR based on the k_{off}.

AH1-A5 Peptide Improved Cytolytic Activity Mediated by an AH1-Specific T Cell Clone

As an initial step toward correlating TCR binding properties with immunogenicity, we analyzed the reactivity of the AH1-specific T cell clone to the AH1 peptide as well as the panel of alanine-substituted variant peptides in chromium release assays (Figure 5). 10 ng/ml (8.3 nM) AH1 peptide resulted in maximal specific lysis by the AH1-specific clone. When the anchor residues were changed to an alanine (AH1-A2 and AH1-A9), peptide-dependent sensitization for lysis was abolished. Substitution at positions 4, 6, and 7 also resulted in background-level lysis similar to the negative control pMCMV. Substitution in positions 1, 3, and 8 mediated approximately the same level of lysis at AH1. However, the alanine substitution at position 5 sensitized target cells for maximal lysis at ~10-fold lower concentration of peptide (1 ng/ml) and shifted the entire dose response curve. With the exceptions of AH1-A2 and AH1-A8, the cytolysis results correlated with those obtained in the binding experiments (Figure 2). Thus, the increased affinity of the AH1-A5-mediated MHC-TCR complex correlated with increased sensitization of targets for cytolysis by the AH1-specific T cell clone.

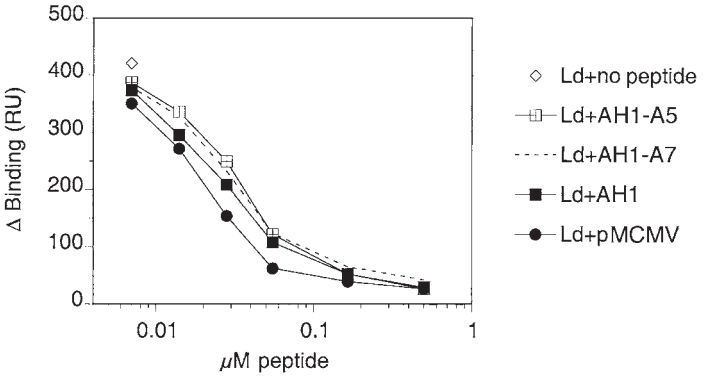

Figure 3. AH1 and AH1-A5 Bind H-2L^d with Similar Affinity

Either buffer alone or graded concentrations of indicated peptide were combined with 40 μM H-2L^d and exposed to immobilized pMCMV-C4 peptide on the biosensor surface, as in Figure 1. The amount of H-2L^d bound to pMCMV-C4 is reflected by the change in resonance units on the Y axis after 1 min.

Vaccination Using AH1-A5 Peptide Improved In Vivo T Cell Immunity to AH1 Peptide and CT26 Tumor

The enhanced apparent TCR affinity and stimulatory capacity of AH1-A5 for an individual T cell clone prompted us to evaluate in vivo immunogenicity of AH1-A5 relative to the wild-type AH1 peptide. At issue is whether a significant proportion of the AH1-specific T cell repertoire in vivo mimics that of the isolated CD8$^+$ T cell clone. Of relevance to cancer immunotherapy is whether the increased binding between the cloned T cell receptor and the H-2L^d-AH1-A5 complex as compared to the H-2L^d-AH1 complex can result in a more robust immune response in vivo against the AH1 epitope and ultimately the tumor, CT26. To determine if AH1-A5

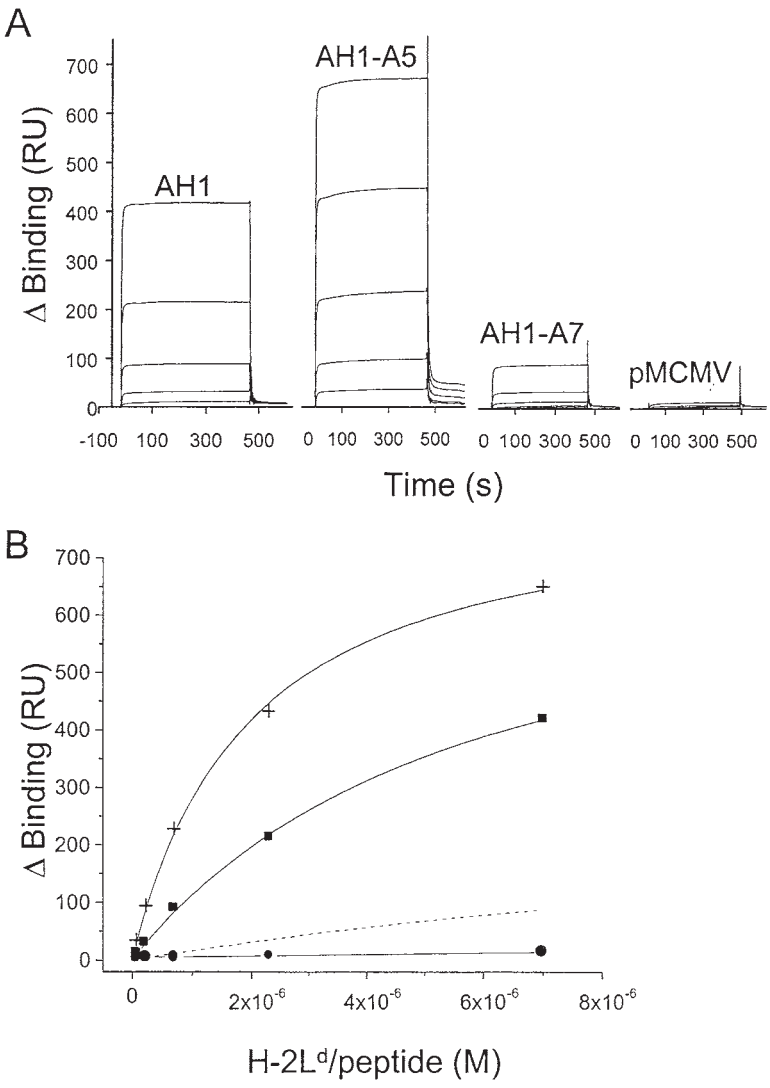

Figure 4. AH1-A5 Has a Stronger Affinity and a Longer Dissociation Time Than AH1

(A) Profiles from the biosensor of H-2L^d-peptide binding to the TCR derived from the AH1-specific clone are shown. Graded concentrations (7.00, 2.33, 0.70, 0.233, and 0.07 mM) of H-2L^d produced in bacteria complexed with the indicated peptide were injected over 5300 resonance units of immobilized CT-Ig at a flow rate of 5 μl/min. The change in resonance units (RU) reflects binding of H-2L^d-peptide to the surface over time. Data extrapolated from these curves were used to determine the dissociation rates (k_{off}) using Biaevaluation 3.0 software and to the graph in Figure 4B. Results of these analyses are shown in Table 1.

(B) Equilibrium binding constants (K_D) were derived from these curves using a nonlinear 1:1 Langmuir binding curve-fit on the Origin program from Microcal 1.4 software (+, AH1-A5; square, AH1; dotted line, AH1-A7; and circle, pMCMV).

Table 1. Affinity and Kinetic Constants for Binding of H-2L^d/Peptide[a] to T Cell Receptor[b]

Ld/Peptide	k_{off} (s^{-1})[c]	k_{on} ($s^{-1}M^{-1}$)[d]	K_D (μM)[e]	$t_{1/2}$ (s)[f]
AH1	0.35 ± 0.025	$6.1 \times 10^4 \pm 6.5 \times 10^3$	5.7 ± 0.45	2.0 ± 0.14
AH1-A5	0.11 ± 0.017	$5.8 \times 10^4 \pm 1.0 \times 10^4$	1.9 ± 0.18	6.3 ± 0.97
AH1-A7	0.28 ± 0.023	$1.6 \times 10^4 \pm 6.4 \times 10^3$	18 ± 7.3	2.4 ± 0.20
pMCMV[g]			<<60 ± 50	

[a] H-2L^d protein was produced in *E. coli* and folded separately around each peptide.
[b] The single-chain CT26 T cell receptor was produced in plasmacytoma cells and immobilized to a CM5 chip with amine coupling.
[c] The k_{off} values were determined using the BIAevaluation 3.0 program for 1:1 Langmuir dissociation kinetics.
[d] The k_{on} values were calculated from k_{off} and K_D.
[e] The K_D values were obtained from equilibrium binding data.
[f] $T_{1/2}$ equals ln 2 divided by k_{off}.
[g] H-2L^d/pMCMV interaction with CT26 T cell receptor was too weak to permit accurate assessment of binding parameters.

is a stronger tumor antigen than endogenous AH1, we compared these two peptides in a vaccination study.

For this study, we used dendritic cells as antigen-presenting cells (Mayordomo et al., 1995) derived from the spleen and loaded overnight with peptide in serum-free medium. The phenotype of these cells is similar to that of dendritic cells described by others (reviewed in Banchereau and Steinman, 1998); they express high levels of MHC class II, costimulatory molecules (B7.1 and B7.2), and CD11c (Figure 6A). By staining the cells with the dimeric TCR, CT-Ig, as described in Figure 2, we determined the most efficient conditions for peptide loading. Then, using the same method, we determined that the dendritic cells were loaded with similar amounts of AH1 and AH1-A5 peptides.

To determine the relative effect of these peptide-loaded dendritic cells on the tumor-specific T cell response, we primed and boosted mice with dendritic cells before removing the spleen. After a single in vitro stimulation, we analyzed the cells for both CT26-specific lysis and binding to the Ld-Ig loaded with AH1. Vaccination with AH1-A5 peptide resulted in significantly greater lysis of CT26 targets (Figure 6B). This increased activity was associated with an increase in the percentage of CD8$^+$ H-2L^d-AH1-specific T cells as assessed by staining with Ld-Ig loaded with AH1 (Figure 6C). Vaccination with AH1-A5 loaded dendritic cells resulted in a 5- to 10-fold greater expansion of AH1-specific T cells relative to the AH1-loaded dendritic cell vaccine. Although qualitative differences of the T cell populations after vaccination with different dendritic cells are not measured here, these results show a significant quantitative difference in the T cell populations.

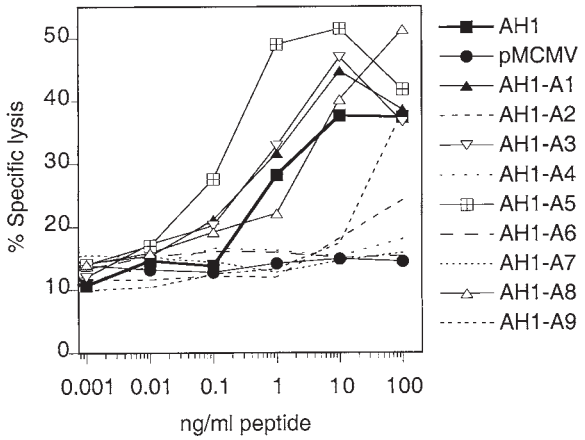

Figure 5. AH1-A5 Mediates More Cytolytic Activity Than the Wild-Type Tumor Antigen, AH1

^{51}Cr-labeled MC57G-Ld cells (3×10^3) were combined with the AH1-specific T cell clone (1.5×10^4) and graded concentrations of peptide as indicated on the X axis. Percent lysis was calculated after 4 hr at 37°.

Using the same vaccination protocol, we evaluated whether the increased in vivo stimulation of AH1-specific T cells by the AH1-A5 peptide resulted in enhanced antitumor immunity (Figure 6D). Development of tumors in mice treated with unpulsed dendritic cells, dendritic cells pulsed with pMCMV, or AH1-A7 occurred at the same rate as in untreated mice. Vaccination with AH1-loaded dendritic cells induced a significant delay in tumor growth relative to untreated mice ($p = 0.001$). Tumor-free survival was also significantly increased with the treatment of AH1-A5-pulsed dendritic cells relative to AH1-pulsed dendritic cells ($p = 0.025$). Thus, selection of a peptide variant that stabilized the trimolecular complex by decreasing TCR off rate resulted in enhanced in vivo activation and expansion of antigen-specific T cells and superior antitumor immunity.

Discussion

A structural understanding of the formation of a ternary MHC-peptide-TCR complex suggests that particular amino acid residues of the bound peptide contribute predominantly either to MHC interactions (anchor or agretopic residues) or to TCR interactions (epitopic or antigenic residues). This compartmentalized view of peptide interactions with MHC and TCR is most likely incorrect in detail but nevertheless offers a simplified framework of conceptualizing the effects of single residue amino acid substitutions of antigenic peptides. With the initial demonstrations that amino acid alterations in T cell epitopes could enhance stimulation of T cell populations specific for the original epitope, epitope modification has become an attractive approach to augment antigen-specific immunotherapies (Solinger et al., 1979; Boehncke et al., 1993; Chen, 1999). Indeed, amino acid substitutions that enhance binding affinity of peptide for the presenting MHC molecule have been demonstrated to improve the immunogenicity of a number of MHC class I–restricted

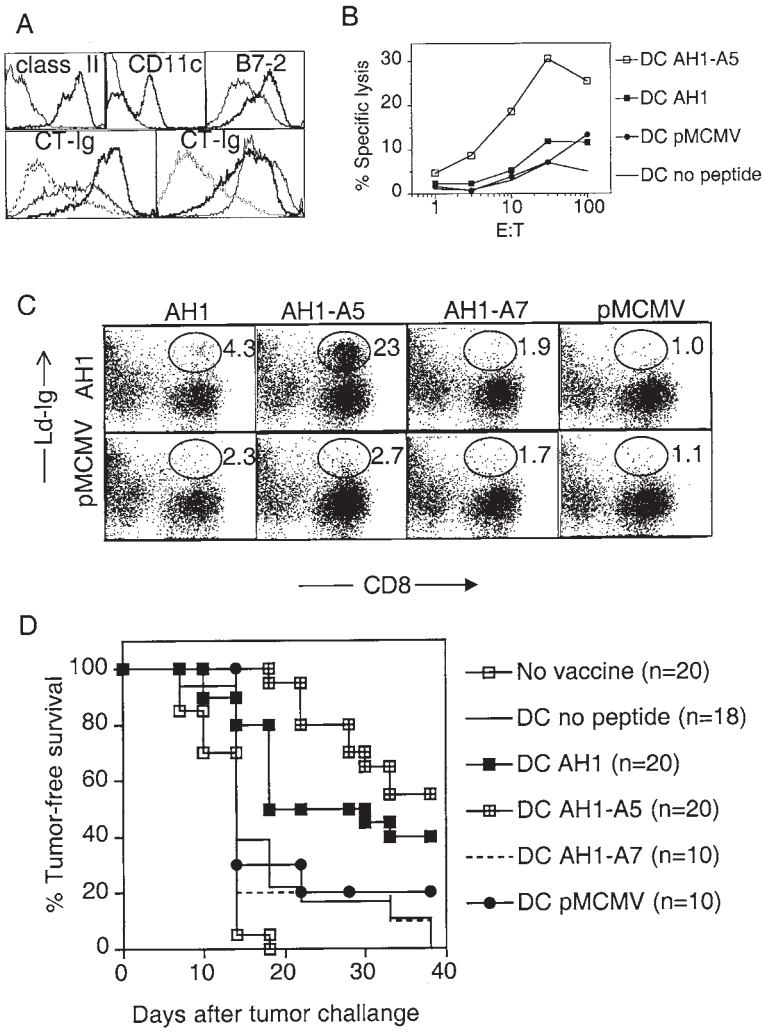

Figure 6. Immunization with AH1-A5-Loaded Dendritic Cells Results in Enhanced Lytic Activity, Frequency of $CD8^+$ CT26-Specific T Cells, and Tumor-Free Survival Relative to Immunization with AH1-Loaded Dendritic Cells

(A) Characteristics of cell surface markers and peptide loading of dendritic cells derived from the spleen are shown. Dendritic cell populations from the spleen were enriched to 60%–80% with a BSA gradient and adherence to plastic. After a 12 hr incubation with 100 or 300 μg/ml peptide, the cells were analyzed for cell surface markers. Expression of MHC class II, CD11c, and B7-2 were examined. In the first row, the thick line represents staining with the indicated antibody, and the thin line represents background fluorescence from an isotype-matched control antibody. In the second row, dendritic cells are stained with CT-Ig. In the left panel, the thick line represents cells incubated with 300 μg/ml AH1 peptide, the thin line represents cells incubated with 100 μg/ml AH1 peptide, and the dotted line represents cells incubated without peptide. In the right panel, the thick line represents cells incubated with 300 μg/ml AH1 peptide, the thin line represents cells incubated with 300 μg/ml AH1-A5 peptide, and the dotted line represents cells incubated without peptide.

(B–D) BALB/c mice were injected on day –14 and day –7 subcutaneously in both hind flanks with 1×10^5 dendritic cells pulsed with 300 μg/ml of the indicated peptides. (B) Lytic activity specific for CT26 targets from mice immunized with peptide-pulsed dendritic cells. CTL derived from mice were examined 5 days after in vitro stimulation with CT26 expressing B7. Background lytic activity from spleen cells of a naive mouse treated in parallel was subtracted. A representative experiment of two mice per group is shown. (C) Frequency of AH1-specific T cells was measured 7 days after in vitro stimulation. The peptide used to pulse the dendritic cells is indicated on top. The numbers in the right-hand corner indicate the percent antigen-specific $CD8^+$ cells measured. (D) On day 0, 5×10^4 CT26 tumor cells were injected subcutaneously in the left hind flank and tumor-free survival was monitored for 38 days. N represents the number of mice in each group pooled from two independent experiments performed under identical conditions. The survival differences analyzed on a Kaplan-Meier curve with Mantel-Cox statistics indicates that the difference between treatment with DC pulsed with no peptide verses DC pulsed with AH1 ($p = 0.001$) and DC pulsed with AH1 verses DC pulsed with A5 ($p = 0.025$) are significant.

tumor antigens (Gervois et al., 1996; Parkhurst et al., 1996; Bakker et al., 1997; Dyall et al., 1998; Overwijk et al., 1998; Valmori et al., 1999). Here, we have demonstrated that an amino acid substitution that enhances the affinity of the MHC-peptide complex for the TCR also enhances expansion and activation of polyclonal T cell responses specific for the wild-type antigen. In the case of the immunodominant AH1 tumor antigen studied here, this enhanced in vivo immunization results in superior immunity against challenge with the CT26 tumor.

Substitution of alanine for valine at position five (P5) of the AH1 peptide does not significantly change peptide binding to MHC but increases the affinity of MHC-peptide for TCR, suggesting that it is epitopic. Consistent with our interpretations, analysis of H-$2L^d$ binding to the tum peptide suggests that arginine at P5 also binds the TCR (Robinson and Lee, 1996). Amino acids at this position are predicted to have high solvent accessibility that correlates with increased TCR interactions (Zhang et al., 1992; Balendiran et al., 1997). However, using an H-$2L^d$ crystal structure to predict the orientation of the fifth residue of the QL9 peptide (phenylalanine) suggests that it is buried in pocket C of H-$2L^d$ (Speir et al., 1998). The crystal structure of p29 peptide complexed with H-$2L^d$ shows the asparagine at P5 is pointing toward the α1 helix of the MHC (Balendiran et al., 1997). Pocket C of the mid-cleft region of H-$2L^d$ is shallow, hydrophobic, and does not require binding of a consensus residue (Balendiran et al., 1997). Given these disparities in orientation of P5 for different H-$2L^d$ binding peptides, one cannot accurately predict the orientation of P5 in the AH1 peptide. It is thus unclear whether the altered TCR affinity afforded by the valine to alanine substitution of AH1 is due to direct contact of P5 with the TCR or rather through affects on the relative orientation of the adjacent tyrosines.

Since the AH1-A5 peptide was originally identified

using only a single AH1-specific T cell clone in vitro, the heteroclitic properties were somewhat unexpected. Differences in in vitro reactivity using a single T cell clone might not necessarily predict the relative reactivities between wild-type AH1 and AH1-A5 among the diverse in vivo polyclonal T cell response. The finding that AH1-A5 was so much more efficient at expanding and activating T cells specific for wild-type AH1 suggests that a large T cell repertoire exists in vivo whose TCR displays common structural features and reactivity patterns to the original T cell clone.

As with many other antigens, certain Vβ segments dominate the AH1-specific T cell response. We found a predominance of Vβ8.3, the Vβ segment expressed by the T cell clone, within polyclonal AH1-specific T cell lines. Colombo and colleagues have identified T cell populations specific to AH1 expressing other Vβ regions (personal communication). We are currently determining if there are qualitative differences in the repertoire of AH1-specific T cells activated by in vivo immunization with AH1-A5 versus wild-type AH1. It is possible that the AH1-reactive T cell repertoire specifically expanded by AH1-A5 represents a subset of the total AH1-reactive repertoire. Whether or not this is the case, the enhanced TCR binding properties of AH1-A5 relative to wild-type AH1 clearly provides enough of an advantage at the population level in vivo to result in a net enhancement in activation and expansion of AH1-specific T cells.

The overall antitumor immune response afforded by various immunotherapies is a combination of multiple types of responses to multiple tumor antigens not limited to, for example, a single antigen. The finding that modification of a single epitope can significantly affect antitumor immunity raises the possibility that additive effects of multiple antigenic modifications in a polyvalent vaccine may provide more potent protection. While substitution of MHC binding anchor residues is a reasonable approach to modify epitopes displaying low MHC affinities, it is likely that the poor immunogenicity of most tumor antigens is due instead to tolerization of high-affinity T cells, thereby leaving an available repertoire of low-affinity T cells. The feasibility of activating these remaining low-affinity populations of T cells was demonstrated in studies using HA as a model self- and tumor antigen (Morgan et al., 1998).

The gp70 antigen from which the AH1 epitope is derived represents a prototype example of a shared tumor antigen whose expression has been selectively upregulated in CT26 and in many other mouse tumors (Jaffee and Pardoll, 1996). Although gp70 expression was not detected in the thymus in our previous study (Huang et al., 1996), it is quite possible that natural expression of gp70 tolerizes high-affinity T cells. Evidence for such a mechanism has indeed been observed with other endogenous retroviral gene products such as the MMTV-derived superantigens (Marrack et al., 1993). Consistent with this idea, AH1 peptide is a weak immunogen despite the fact that it is the dominant target for CT26-specific CTL responses. For example, immunization with recombinant vaccinia expressing either full-length gp70 or an AH1 minigene downstream of an endoplasmic reticulum signal sequence fails to protect animals against CT26 challenge (K. Gorski, E. M. J., and D. M. P., unpublished data). In contrast, immunization with vaccinia virus expressing β-galactosidase efficiently protects animals against challenge with CT26-expressing β-galactosidase (Bronte et al., 1995).

The measured affinity of the H-2L^d-AH1 complex for the cognate TCR was at the low end of the range of reported affinities for other agonist MHC class I–restricted antigen TCR pairs (reviewed in Davis et al., 1998). However, given the variabilities in construction of soluble TCRs and MHCs used in the different studies as well as variations affecting surface plasmon resonance measurements, it is difficult to make reliable comparisons among different studies. The roughly 3-fold enhanced TCR affinity of H-2L^d-AH1-A5 relative to H-2L^d-AH1 is reflected in a 3-fold decreased k_d; the k_a for H-2L^d-AH1 and H-2L^d-AH1-A5 is essentially identical. This 3-fold difference in affinity and off rate results in a roughly 10-fold enhancement in activation of the AH1 T cell clone. The elements of MHC-peptide binding to TCR that are most relevant to T cell stimulation are still not yet completely resolved. While some groups have presented data favoring a strong correlation between off rate and stimulatory capacity (Chen et al., 1994; Savage et al., 1999), others have argued for an important contribution of on rate and/or overall affinity in determining functional T cell reactivity (Alam et al., 1996). For other cases, a clear cut correlation is lacking and other characteristics may be involved (Al-Ramadi et al., 1995; reviewed in Manning and Kranz, 1999). Of note, the measured off rates of H-2L^d-AH1-A7 and H-2L^d-AH1 for TCR are similar though AH1-A7 fails to stimulate the AH1-specific T cell clone. This result further suggests that off rate of MHC-peptide from TCR is not the sole determinant of biological activity.

While the TCR affinity of H-2L^d-AH1 and its biological activity in stimulating the AH1 clone are consistent with AH1 being a weak agonist, it is possible that AH1 has partial antagonist properties as well. Indeed, it has been suggested that low TCR affinities for tumor antigens could lead to tolerance in tumor-specific T cells. A recent study in melanoma patients identified an unresponsive or "anergic" phenotype among populations of tyrosinase-specific T cells from draining lymph nodes containing melanoma metastases (Lee et al., 1999). If tolerance is being induced, amino acid substitutions in tumor antigens that result in increased TCR affinity may enhance immunogenicity by converting peptides from partial antagonists to full agonists for populations of specific T cells in vivo. Further functional analysis of the populations of AH1-specific T cells activated in vivo by wild-type AH1 versus AH1-A5 may shed light on how peptide substitutions effecting the stability of the MHC-peptide-TCR complex affect the balance between activation and tolerance of tumor-specific T cells.

Experimental Procedures

Peptides

All peptides were purified to greater than 95% purity and purchased from Macromolecular Resources (CO), Chiron (CA), or Princeton BioMolecules (OH). The sequences of the peptides are SPSYVYHQF (AH1), A**P**SYVYHQF (AH1-A1), S**A**SYVYHQF (AH1-A2), SP**A**YVYHQF (AH1-A3), SPS**A**VYHQF (AH1-A4), SPSY**A**YHQF (AH1-A5), SPSY**V**AHQF (AH1-A6), SPSYVY**A**QF (AH1-A7), SPSYVYH**A**F (AH1-A8), SPSYVYHQ**A** (AH1-A9), YPHFMPTNL (pMCMV), and YPH**C**MPTNL (pMCMV-C4), LSPFSFDL (p2Ca), and QNHRALDLV (p91A-Tum V9).

Biosensor Analysis

The real-time surface plasmon resonance experiments utilized the Biacore 2000. All immobilization and binding experiments were performed at 25°C at a flow rate of 5 μl/minute. The binding buffer, HBST (10 mM Hepes [pH 7.5], 3.4 mM EDTA, 15 mM sodium chloride, and 0.005% Tween 20), was used to dilute the solution phase ligand. The cell culture–produced H-2L^d used in the peptide binding experiments have been described (Boyd et al., 1992; Goldstein et al., 1997). 40 mM H-2L^d was used in each reaction. The change in binding (resonance units) was determined 1 min after addition to the peptide surface. Sulfo-SMCC (sulfosuccinimidyl 4-(N-maleimidomethyl)cyclohexane-1-carboxylate) (Pierce) was used to couple between 100 and 200 resonance units of peptides through a cysteine to the dextran-coated CM5 sensor chip as previously reviewed and described (Margulies et al., 1996). After binding the MHC to the peptide surface, the surface was regenerated with 50 mM phosphoric acid. Approximately 5000 resonance units of the single chain TCR in 25 mM sodium acetate (pH 5.1) was coupled to the CM5 chip with amine chemistry (NHS/EDC) as determined by the BIAevaluation 3.0 Application Wizard. A blank surface was prepared using the same method without protein. The TCR surface was cleared of MHC-peptide binding with a 5 min wash with HBST. The fit of curves with a standard error of less than 5% of the calculated k_{off} and residuals less than 2 were considered.

To obtain equilibrium constants, the data were nonlinearly fit to the following equation using the Origin program from Microcal software: $R = (R_{max}c)-(K_D+c)$ where R = resonance units, R_{max} = maximum resonance units as determined by the nonlinear fit, c = concentration of analyte, and K_D = the affinity constant.

Cells

CT26, CT26-B7 that express human B7.1, and MC57G-Ld were cultured in complete medium (RPMI-1640 supplemented with 10% fetal calf serum, 100 units/ml penicillin, 100 units/ml streptomycin, 1× MEM nonessential amino acids [Sigma], 1 mM sodium pyruvate, 10 mM Hepes [pH 7.5], 2 mM L-glutamine, and 0.1 mM β-mercaptoethanol) as described (Griswold and Corbett, 1975; Huang et al., 1996). T2-Ld cells were cultured in the same medium (O'Herrin et al., 1997).

The AH1-specific T cell clone was generated from limiting dilution of a CT26 CTL line that was isolated from a spleen of a BALB/c mouse vaccinated with CT26 transduced with GM-CSF (Huang et al., 1996). The T cell clones were stimulated in vitro every 7 days as described (Huang et al., 1996). Splenocytes were stimulated in vitro by the same method. In brief, the spleens were crushed and red blood cells were lysed (Kruisbeek, 1993). After two washes in complete medium, the 4×10^6 cells were combined with 1×10^5 mitomycin C-treated CT26-B7 and 10 units/ml IL-2 in 2 ml complete medium in 24-well plates.

Dendritic cells were generated from the spleen as described (Inaba et al., 1998). The dendritic cells were loaded overnight in 100 or 300 μg/ml peptide in serum-free AIMV medium supplemented with 0.1 mM β-mercaptoethanol, 100 units/ml penicillin, and 100 units/ml streptomycin. Excess peptide was removed in three washes of Hanks buffer (Gibco).

Construction, Expression, and Purification of Ld-Ig and CT-Ig

Ld-Ig, the divalent H-2L^d protein was constructed, expressed, and purified using described methods (Schneck et al., 1999). In brief, the BALB/c H-2L^d cDNA from pLd.444 (Huang et al., 1996) was amplified using primers 5′LdMluI ATACGCGTCGCAGATGGGGGC GATGGCTCC and 3′LdXhoI ACCTCGAGTGCGGCCGCCCATCTC AGGGTGAGGGG. The fragment was digested with MluI and XhoI and inserted into the same sites of pX-Ig (Dal Porto et al., 1993). The sequence was verified. The resulting plasmid was cotransfected by electroporation with a human β2-microglobulin expression plasmid into J558L plasmacytoma cells. A clone that secreted relatively high levels of protein, as determined by ELISAs specific for H-2L^d or the IgG1 portion of the molecule, was grown in Hybridoma-SFM (Gibco), and protein was purified from supernatants by affinity chromatography to the variable region of the Ig portion. Purified Ld-Ig was loaded with peptide by incubating it with ~200-fold excess peptide for 1–5 days. The resulting protein was used to stain antigen-specific T cells.

CT-Ig was generated similarly to Ld-Ig and to other divalent TCRs constructed (Plaksin et al., 1997; Lebowitz et al., 1998). In place of the MHC fragment in Ld-Ig, a fragment encoding a single chain TCR from the AH1-specific T cell clone was inserted. The variable domain of the β chain of the T cell clone was identified by recognition of the vβ8.3 antibody (1B3.3). The variable region family of the α chain of the T cell clone was identified by PCR (as determined by David Woodland). The family member was identified as vα4.11 by sequencing. The α and β chains were amplified from cDNA from the AH1-specific clone using these primers: 5′vα4.11.AseI GGAATTCATT AATGACTCAGTAACCCAGATGCAA, 3′vαHindIII ATAAGAAAGCTT TCCTGGTTTTACTGATAATTT, 5′β8.3NdeI ATAAGAATGCGGCCG CCGAGGTCGCAGTCACCCAAAGCCCTA, and 3′cβXhoI CCGCCTC GAGTCAGTCTGCTCGGCCCCAGGCCTCTGC. The fragments were inserted into pCR2.1 (Invitrogen) to verify the sequence. The NotI-XhoI fragment harboring the coding region of v-d-j-c of the β chain was inserted into the same sites of pET-scTCR to replace the existing β chain (Plaksin et al., 1997). The AseI-HindIII fragment encoding the v-j region of the α chain was then inserted NdeI-HindIII of pET-scTCR leaving the linker between the α and the β chain (Chung et al., 1994) and the rest of the vector, pET21+ (Novagen) intact. The single chain TCR was amplified with primers 5′MluITCR GATCACG CGTCGATGGACTCAGTAACCCAGA and 3′SalITCR GATCGTCGA CGTCTGCTCGGCCCCAGGCCTC. The resulting fragment was inserted into pCR2.1 for sequencing and then the MluI-SalI fragment was inserted into the MluI and XhoI sites of pX-Ig. As with Ld-Ig, this plasmid was electroporated into J558L cells, and a clone that reacted with antibodies to the cβ region (H57-597, PharMingen), vβ8 (F23.1, PharMingen), and IgG1 (Caltag) (data not shown), was expanded to produce protein for staining antigen presenting cells and binding experiments.

Antibodies, Cell Staining, and Flow Cytometric Analysis

To examine peptide-mediated binding, 2×10^5 CT26 T cell clone was incubated on ice with ~1 μg Ld-Ig loaded with different peptides for 1–2 hr in flow cytometry wash buffer (1×HBSS (Gibco), 2% fetal calf serum, 10 mM Hepes [pH 7.5], and 0.1% sodium azide). The Ld-Ig-peptide was visualized with IgG1-biotin (PharMingen) and avidin-PE (Caltag) on a Becton-Dickinson FACScan flow cytometer. When visualizing antigen-specific T cells after an in vitro stimulation, CD4-FITC (RM2501-3, Caltag), B220-FITC (PharMingen), and CD8-cychrome (PharMingen) were also included with the avidin-PE to facilitate detection of the $CD8^+$ cells.

For visualization of peptide-loaded H-2L^d complexes, T2-Ld cells were incubated overnight at 25°C. T2-Ld cells were then incubated with 10 μM peptide for 2 hr at 37°C. Approximately 1 μg CT-Ig was added to either 3×10^5 T2-Ld cells or peptide-pulsed dendritic cells, the cells were incubated on ice for 1–2 hr, and, then visualized by flow cytometry as described with Ld-Ig. The antibody 14-4-4, which recognizes MHC class II (American Type Cell Collection), anti-CD80, which recognizes B7.1 (PharMingen), and CD11c (PharMingen) were used in analyzing the cell surface marker of the dendritic cells.

Chromium Release Assays

One million target cells were labeled in 100 μl complete medium and 200 μCi ^{51}Cr at 37°C for 1–1.5 hr. Target cells were washed three times to remove excess chromium. To determine which peptides mediate lysis of the AH1-specific clone, ^{51}Cr-labeled MC57G-Ld cells (3×10^3) and AH1-specific T cell clone (1.5×10^4) were added to 10-fold serial dilutions of the indicated peptides in a total of 200 μl in a round-bottom 96-well plate for 4 hr at 37°C. Half of the supernatant was removed and the gamma irradiation was counted. To determine the tumor specific lysis from splenocytes after vaccination, 3×10^3 ^{51}Cr-labeled CT26 cells were added to varying concentrations of splenocytes that had been stimulated in vitro for 5 days at a 40:1 ratio with mitomycin C-treated CT26-B7. Each data point was performed in triplicate and then averaged. The shown experiments are a representative of an example of at least two experiments performed with each peptide. Data are expressed as % specific lysis = (measured release − spontaneous release) − (maximum release − spontaneous release) × 100. Activity of splenocytes from naive mice was subtracted from activity of splenocytes from vaccinated mice.

Protein Expression and Purification

H-2L^d (Balendiran et al., 1997) and β2-microglobulin (Shields et al., 1998) were produced in bacteria similarly to a described procedure (Kurucz et al., 1993; Li et al., 1998). The H-2L^d preparations were made in parallel; each of the indicated peptides were folded with H-2L^d and β2-microglobulin separately. The H-2L^d-β2-microglobulin-peptide complexes were purified from aggregates on a Sephadex 75 gel filtration column, dialyzed against HBST, and quantitated using the UV-1601 Shimadzu spectrophotometer before using in binding experiments.

Mice and Immunizations

Six- to eight-week-old female BALB-CanNCr mice were purchased from the National Cancer Institute. Mice were injected with 1×10^5 dendritic cells in the left- and right-hind flank subcutanously on days –14 and –7. On day 0, mice were injected subcutanously in the left flank with 5×10^4 CT26 cells. Tumor-free survival was assessed by detection of a palpable solid tumor at the site of injection. At 6 days, we began to monitor for palpable tumors. Tumors developed in most of the untreated mice within 2 weeks. The statistics were analyzed using the software StatView 5.0.1 (SAS Institute).

Acknowledgments

J. E. S. dedicates this paper to the memory of Dick Slansky. We appreciate the help in identification of the Vα family from David Woodland, protein production from Kannan Natarajan, and cell culture from Amy Morck. This work was supported in part by National Institutes of Health Grant CA57842 (D. M. P.) and CA76669 (J. E. S.), Dorothy H. Needle Charitable Trust, Mr. and Mrs. William Topercer Endowment, and the Janny Foundation.

Received June 15, 2000; revised September 18, 2000.

References

Alam, S.M., Travers, P.J., Wung, J.L., Nasholds, W., Redpath, S., Jameson, S.C., and Gascoigne, N.R.J. (1996). T-cell-receptor affinity and thymocyte positive selection. Nature *381*, 616–620.

Alexander-Miller, M., Robinson, R.A., Smith, J.D., Gillanders, W.E., Harrison, L.G., Hansen, T.H., Connolly, J.M., and Lee, D.R. (1994). Definition of TCR recognition sites on L^d-tum$^-$ complexes. Int. Immunol. *6*, 1699–1707.

Al-Ramadi, B.K., Jelonek, M.T., Boyd, L.F., Margulies, D.H., and Bothwell, A.L.M. (1995). Lack of strict correlation of functional sensitization with the apparent affinity of MHC/peptide complexes for the TCR. J. Immunol. *155*, 662–673.

Altman, J.D., Moss, P.A.H., Goulder, P.J.R., Barouch, D.H., McHeyzer-Williams, M.G., Bell, J.I., McMichael, A.J., and Davis, M.M. (1996). Phenotypic analysis of antigen-specific T lymphocytes. Science *274*, 94–96.

Bakker, A.B.H., van der Burg, S.H., Huijbens, R.J.F., Drijfhout, J., Melief, C.J.M., Adema, G.J., and Figdor, C.G. (1997). Analogues of CTL epitopes with improved MHC class-I binding elicit anti-melanoma CTL recognizing the wild-type epitope. Int. J. Cancer *70*, 302–309.

Balendiran, G.K., Solheim, J.C., Young, A.C.M., Hansen, T.H., Nathenson, S.G., and Sacchettini, J.C. (1997). The three-dimensional structure of an H-2L^d-peptide complex explains the unique interaction of L^d with beta-2 microglobulin and peptide. Proc. Natl. Acad. Sci. USA *94*, 6880–6885.

Banchereau, J., and Steinman, R.M. (1998). Dendritic cells and the control of immunity. Nature *392*, 245–252.

Boehncke, W.-H., Takeshita, T., Pendleton, C.D., Houghten, R.A., Sadegh-Nasseri, S., Racioppi, L., Berzofsky, J.A., and Germain, R.N. (1993). The importance of dominant negative effects of amino acid side chain substitution in peptide-MHC molecule interactions and T cell recognition. J. Immunol. *150*, 331–341.

Boon, T., Coulie, P.G., and Van den Eynde, B. (1997). Tumor antigens recognized by T cells. Immunol. Today *18*, 267–268.

Boyd, L.F., Kozlowski, S., and Margulies, D.H. (1992). Solution binding of an antigenic peptide to a major histocompatibility complex class I molecule and the role of β_2-microglobulin. Proc. Natl. Acad. Sci. USA *89*, 2242–2246.

Bronte, V., Tsung, K., Rao, J.B., Chen, P.W., Wang, M., Rosenberg, S.A., and Restifo, N.P. (1995). IL-2 enhances the function of recombinant poxvirus-based vaccines in the treatment of established pulmonary metastases. J. Immunol. *154*, 5282–5292.

Chen, L. (1999). Mimotopes of cytolytic T lymphocytes in cancer immunotherapy. Curr. Opin. Immunol. *11*, 219–222.

Chen, W., Khilko, S., Fecondo, J., Margulies, D.H., and McCluskey, J. (1994). Determinant selection of major histocompatibility complex class I-peptide affinity and is strongly influenced by nondominant anchor residues. J. Exp. Med. *180*, 1471–1483.

Chung, S., Wucherpfennig, K.W., Friedman, S.M., Hafler, D.A., and Strominger, J.L. (1994). Functional three-domain single-chain T-cell receptor. Proc. Natl. Acad. Sci. USA *91*, 12654–12658.

Corr, M., Boyd, L.F., Frankel, S.R., Kozlowski, S., Padlan, E.A., and Margulies, D.H. (1992). Endogenous peptides of a soluble major histocompatibility complex class I molecule, H-2L^d_s: sequence motif, quantitative binding, and molecular modeling of the complex. J. Exp. Med. *176*, 1681–1692.

Corr, M., Slanetz, A.E., Boyd, L.F., Jelonek, M.T., Khilko, S., Al-Ramadi, B.K., Kim, Y.S., Maher, S.E., Bothwell, A.L.M., and Margulies, D.H. (1994). T cell receptor-MHC class I peptide interactions: affinity, kinetics, and specificity. Science *265*, 946–949.

Cox, A.L., Skipper, J., Chen, Y., Henderson, R.A., Darrow, T.L., Shabanowitz, J., Engelhard, V.H., Hunt, D.F., and Slingluff, C.L. (1994). Identification of a peptide recognized by five melanoma-specific human cytotoxic T cell lines. Science *264*, 716–719.

Dal Porto, J., Johansen, T.E., Catipovic, B., Parfiit, D.J., Tuveson, D., Gether, U., Kozlowski, S., Fearon, D.T., and Schneck, J.P. (1993). A soluble divalent class I major histocompatibility complex molecule inhibits alloreactive T cells at nanomolar concentrations. Proc. Natl. Acad. Sci. USA *90*, 6671–6675.

Davis, M.M., Boniface, J.J., Reich, Z., Lyons, D., Hampl, J., Arden, B., and Chien, Y. (1998). Ligand recognition by aβ T cell receptors. Annu. Rev. Immunol. *16*, 523–544.

De Plaen, E., Lurquin, C., Lethé, B., van der Bruggen, P., Brichard, V., Renauld, J.-P., Coulie, P., Van Pel, A., and Boon, T. (1997). Identification of genes coding for tumor antigens recognized by cytolytic T lymphocytes. Methods: a companion to Methods Enzymol. *12*, 125–142.

Dyall, R., Bowne, W.B., Weber, L.W., LeMaoult, J., Szabo, P., Moroi, Y., Piskun, G., Lewis, J.J., Houghton, A.N., and Nikolic-Zugic, J. (1998). Heteroclitic immunization induces tumor immunity. J. Exp. Med. *188*, 1553–1561.

Gervois, N., Guilloux, Y., Diez, E., and Jotereau, F. (1996). Suboptimal activation of melanoma infiltrating lymphocytes (TIL) due to low avidity of TCR/MHC-tumor peptide interactions. J. Exp. Med. *183*, 2403–2407.

Gilboa, E. (1999). The makings of a tumor rejection antigen. Immunity *11*, 263–270.

Goldstein, J., Mostkowsky, H., Tung, J., Hon, H., Brunswick, M., and Kozlowski, S. (1997). Naive alloreactive CD8 T cells are activated by purified major histocompatibility complex class I and antigenic peptide. Eur. J. Immunol. *27*, 871–878.

Greten, T.F., Slansky, J.E., Kubota, R., Soldan, S.S., Jaffee, E.M., Leist, T.P., Pardoll, D.M., Jacobson, S., and Schneck, J.P. (1998). Direct visualization of antigen-specific T cells: HTLV-1 Tax11-19 specific CD8+ T cells are activated in peripheral blood and accumulate in cerebrospinal fluid from HAM/TSP patients. Proc. Natl. Acad. Sci. USA *95*, 7568–7573.

Griswold, D.P., and Corbett, T.H. (1975). A colon tumor model for anticancer agent evaluation. Cancer *36*, 2441–2444.

Huang, A.Y.C., Gulden, P.H., Woods, A.S., Thomas, M.C., Tong, C.D., Wang, W., Engelhard, V.H., Pasternack, G., Cotter, R., Hunt, D., et al. (1996). The immunodominant major histocompatibility class I-restricted antigen of a murine colon tumor derives from an endoge-

nous retroviral gene product. Proc. Natl. Acad. Sci. USA *93*, 9730–9735.

Inaba, K., Swiggard, W.J., Steinman, R.M., Romani, N., and Schuler, G. (1998). Isolation of dendritic cells. In Current Protocols in Immunology, J.E. Coligan, A.M. Kruisbeek, D.H. Margulies, E.M. Shevach, and W. Strober, eds. (United States: John Wiley & Sons), pp. 3.7.1–3.7.15.

Jaffee, E.M., and Pardoll, D.M. (1996). Murine tumor antigens: is it worth the search? Curr. Opin. Immunol. *8*, 622–627.

Khilko, S.N., Corr, M., Boyd, L.F., Lees, A., Inman, J.K., and Margulies, D.H. (1993). Direct detection of major histocompatibility complex class I binding to antigenic peptides using surface plasmon resonance. Peptide immobilization and characterization of binding specificity. J. Biol. Chem. *268*, 15425–15434.

Khilko, S.N., Jelonek, M.T., Corr, M., Boyd, L.F., Bothwell, A.L., and Margulies, D.H. (1995). Measuring interactions of MHC class I molecules using surface plasmon resonance. J. Immunol. Methods *183*, 77–94.

Kruisbeek, A.M. (1993). Isolation and fractionation of mononuclear cell populations. In Current Protocols in Immunology, J.E. Coligan, A.M. Kruisbeek, D.H. Margulies, E.M. Shevach, and W. Strober, eds. (United States: John Wiley & Sons, Inc.), pp. 3.1.1–3.1.5.

Kurucz, I., Jost, C.R., George, A.J., Andrew, S.M., and Segal, D.M. (1993). A bacterially expressed single-chain Fv construct from the 2B4 T-cell receptor. Proc. Natl. Acad. Sci. USA *90*, 3830–3834.

Lebowitz, M.S., O'Herrin, S.M., Hamad, A.-R.A., Fahmy, T., Marguet, D., Barnes, N.C., Pardoll, D., Bieler, J.G., and Schneck, J.P. (1998). Soluble, high-affinity dimers of the T-cell receptors and class II major histocompatibility complexes: biochemical probes for analysis and modulation of immune responses. Cell. Immunol. *192*, 175–184.

Lee, P.P., Yee, C., Savage, P.A., Fong, L., Brockstedt, D., Weber, J.S., Johnson, D., Swetter, S., Thompson, J., Greenberg, P.D., et al. (1999). Characterization of circulating T cells specific for tumor-associated antigens in melanoma patients. Nat. Med. *5*, 677–685.

Li, H., Natarajan, K., Malchiodi, E.L., Margulies, D.H., and Mariuzza, R.A. (1998). Three-dimentional strcture of H-2D^d complexed with an immunodominant peptide from human immunodeficiency virus envelope glycoprotein 120. J. Mol. Biol. *283*, 179–191.

Lurquin, C., Van Pel, A., Marime, B., De Plaen, E., Szikora, J.-P., Janssens, C., Reddehase, M.J., Lejeune, J., and Boon, T. (1989). Structure of the gene of tum$^-$ transplantation antigen P91A: the mutated exon encodes a peptide recognized with L^d by cytolytic T cells. Cell *58*, 293–303.

Manning, T.C., and Kranz, D.M. (1999). Binding energetics of T-cell receptors: correlation with immunological consequences. Immunol. Today *20*, 417–422.

Margulies, D.H., Corr, M., Boyd, L.F., and Khilko, S.N. (1993). MHC class I/peptide interactions: binding specificity and kinetics. J. Mol. Recog. *6*, 59–69.

Margulies, D.H., Plaksin, D., Khilko, S.N., and Jelonek, M.T. (1996). Studying interactions involving the T-cell antigen receptor by surface plasmon resonance. Curr. Opin. Immunol. *8*, 262–270.

Marrack, P., Winslow, G.M., Choi, Y., Scherer, M., Pullen, A., White, J., and Kappler, J.W. (1993). The bacterial and mouse mammary tumor virus superantigens; two different families of proteins with the same functions. Immunol. Rev. *131*, 79–92.

Mayordomo, J.I., Zorina, T., Storkus, W.J., Zitvogel, L., Celluzzi, C., Falo, L.D., Melief, C.J., Ildstad, S.T., Kast, M.W., Deleo, A.B., and Lotze, M.T. (1995). Bone marrow-derived dendritic cells pulsed with synthetic tumor peptides elicit protective and therapeutic antitumor immunity. Nat. Med. *1*, 1297–1302.

Morgan, D.J., Kreuwel, H.T.C., Fleck, S., Levitsky, H.I., Pardoll, D.M., and Sherman, L.A. (1998). Activation of low avidity CTL specific for a self epitope results in tumor rejection but not autoimmunity. J. Immunol. *160*, 643–651.

Murali-Krishna, K., Altman, J.D., Suresh, M., Sourdive, D.J.D., Zajac, A.J., Miller, J.D., Slansky, J.E., and Ahmed, R. (1998). Counting antigen-specific CD8 T cells: a re-evaluation of bystander activation during viral infection. Immunity *8*, 177–187.

O'Herrin, S.M., Lebowitz, M.S., Bieler, J.G., al-Ramadi, B.K., Utz, U., Bothwell, A.L.M., and Schneck, J.P. (1997). Anaylsis of the expression of peptide-major histocompatibility complexes using high affinity soluble divalent T cell receptors. J. Exp. Med. *186*, 1333–1345.

Overwijk, W.W., Tsung, A., Irvine, K.R., Parkhurst, M.R., Goletz, T.J., Tsung, K., Carroll, M.W., Liu, C., Moss, B., Rosenberg, S.A., and Restifo, N.P. (1998). gp100/pmel 17 is a murine tumor rejection antigen: induction of "self"-reactive, tumoricidal T cells using high-affinity, altered peptide ligand. J. Exp. Med. *188*, 277–286.

Pardoll, D.M. (2000). Therapeutic vaccination of cancer. Clin. Immunol. *95*, S44–S62.

Parker, K.C., Bednarek, A.M., and Coligan, J.E. (1994). Scheme for ranking potential HLA-A2 binding peptides based on independent binding of individual peptide side-chains. J. Immunol. *152*, 163–175.

Parkhurst, M.R., Salgaller, M.L., Southwood, S., Robbins, P.F., Sette, A., Rosenberg, S.A., and Kawakami, Y. (1996). Improved induction of melanoma-reactive CTL with peptide from the melanoma antigen gp100 modified at HLA-A*0201-binding residues. J. Immunol. *157*, 2539–2548.

Plaksin, D., Polakova, K., McPhie, P., and Margulies, D.H. (1997). A three-domain T cell receptor is biologically active and specifically stains cell surface MHC/peptide complexes. J. Immunol. *158*, 2218–2227.

Robbins, P.F., and Kawakami, Y. (1996). Human tumor antigens recognized by T cells. Curr. Opin. Immunol. *8*, 628–636.

Robinson, R.A., and Lee, D.R. (1996). Studies of tum$^-$ peptide analogs define an alternative anchor that can be utilized by L^d ligands lacking the consensus P2 anchor. J. Immunol. *156*, 4266–4273.

Rosenberg, S.A., Yang, J.C., Schwartzentruber, D.J., Hwu, P., Marincola, F.M., Topalian, S.L., Restifo, N.P., Dudley, M.E., Schwarz, S.L., Spiess, P.J., et al. (1998). Immunologic and therapeutic evaluation of a synthetic peptide vaccine for the treatment of patients with metastatic melanoma. Nat. Med. *4*, 321–327.

Savage, P.A., Boniface, J.J., and Davis, M.M. (1999). A kinetic basis for T cell receptor repertoire selection during an immune response. Immunity *10*, 485–492.

Schneck, J.P., Slansky, J.E., O'Herrin, S.M., and Greten, T.F. (1999). Monitoring antigen-specific T cells using MHC-Ig dimers. In Current Protocols in Immunology, J.E. Coligan, A.M. Kruisbeek, D.H. Margulies, E.M. Shevach, and W. Strober, eds. (United States: John Wiley & Sons), pp. 17.2.1–17.2.17.

Shields, M.J., Assefi, N., Hodgson, W., Kim, E.J., and Ribaudo, R.K. (1998). Characterization of the interactions between MHC class I subunits: a systematic approach for the engineering of higher affinity variants of β_2-microglobulin. J. Immunol. *160*, 2297–2307.

Solinger, A.M., Ultee, M.E., Margoliash, E., and Schwartz, R. (1979). T-lymphocyte response to cytochrome c. J. Exp. Med. *150*, 830–848.

Speir, J.A., Garcia, K.C., Brunmark, A., Degano, M., Peterson, P.A., Teyton, L., and Wilson, I.A. (1998). Stuctural basis of 2C TCR allorecognition of H-2Ld peptide complexes. Immunity *8*, 553–562.

Valmori, D., Fonteneau, J., Valitutti, S., Gervois, N., Dunbar, R., Liénard, D., Rimoldi, D., Cerundolo, V., Jotereau, F., Cerottini, J., et al. (1999). Optimal activation of tumor-reactive T cells by selected antigenic peptide analogues. Int. Immunol. *11*, 1971–1979.

Zhang, W., Young, A.C., Imarai, M., Nathenson, S.G., and Sacchettini, J.C. (1992). Crystal structure of the major histocompatibility complex class I H-2K^b molecule containing a signal viral peptide: implications for peptide and T-cell receptor recognition. Proc. Natl. Acad. Sci. USA *89*, 8403–8407.

Lipid nanoparticle-targeted mRNA therapy as a treatment for the inherited metabolic liver disorder arginase deficiency

Brian Truong[a,b], Gabriella Allegri[c], Xiao-Bo Liu[b], Kristine E. Burke[d], Xuling Zhu[d], Stephen D. Cederbaum[e,f,g], Johannes Häberle[c], Paolo G. V. Martini[d], and Gerald S. Lipshutz[a,b,e,f,g,1]

[a]Department of Molecular and Medical Pharmacology, David Geffen School of Medicine at UCLA, Los Angeles, CA 90095; [b]Department of Surgery, David Geffen School of Medicine at UCLA, Los Angeles, CA 90095; [c]Division of Metabolism and Children's Research Center, University Children's Hospital, 8032 Zurich, Switzerland; [d]Moderna, Inc., Cambridge, MA 02139; [e]Department of Psychiatry, David Geffen School of Medicine at UCLA, Los Angeles, CA 90095; [f]Intellectual and Developmental Disabilities Research Center at UCLA, David Geffen School of Medicine at UCLA, Los Angeles, CA 90095; and [g]Semel Institute for Neuroscience, David Geffen School of Medicine at UCLA, Los Angeles, CA 90095

Edited by Dwight Koeberl, Duke University, Durham, NC, and accepted by Editorial Board Member David J. Mangelsdorf August 9, 2019 (received for review April 10, 2019)

Arginase deficiency is caused by biallelic mutations in arginase 1 (ARG1), the final step of the urea cycle, and results biochemically in hyperargininemia and the presence of guanidino compounds, while it is clinically notable for developmental delays, spastic diplegia, psychomotor function loss, and (uncommonly) death. There is currently no completely effective medical treatment available. While preclinical strategies have been demonstrated, disadvantages with viral-based episomal-expressing gene therapy vectors include the risk of insertional mutagenesis and limited efficacy due to hepatocellular division. Recent advances in messenger RNA (mRNA) codon optimization, synthesis, and encapsulation within biodegradable liver-targeted lipid nanoparticles (LNPs) have potentially enabled a new generation of safer, albeit temporary, treatments to restore liver metabolic function in patients with urea cycle disorders, including ARG1 deficiency. In this study, we applied such technologies to successfully treat an ARG1-deficient murine model. Mice were administered LNPs encapsulating human codon-optimized *ARG1* mRNA every 3 d. Mice demonstrated 100% survival with no signs of hyperammonemia or weight loss to beyond 11 wk, compared with controls that perished by day 22. Plasma ammonia, arginine, and glutamine demonstrated good control without elevation of guanidinoacetic acid, a guanidino compound. Evidence of urea cycle activity restoration was demonstrated by the ability to fully metabolize an ammonium challenge and by achieving near-normal ureagenesis; liver arginase activity achieved 54% of wild type. Biochemical and microscopic data showed no evidence of hepatotoxicity. These results suggest that delivery of *ARG1* mRNA by liver-targeted nanoparticles may be a viable gene-based therapeutic for the treatment of arginase deficiency.

arginase deficiency | hyperargininemia | lipid nanoparticle | mRNA | ureagenesis

Arginase deficiency (Online Mendelian Inheritance in Man phenotype [OMIM]:207800) is an uncommon autosomal recessive disorder [estimated incidence of 1:950,000 in the United States (1)] that results from loss of arginase 1 (ARG1) (Enzyme Commission 3.5.3.1). ARG1 is the final enzyme of the urea cycle completing the major metabolic pathway for the disposal of excess nitrogen in terrestrial mammals. Along with red blood cells, the cytosolic enzyme is most prevalent in hepatocytes hydrolyzing arginine into ornithine, which then reenters the cycle, while nitrogen, in the form of urea, is excreted as waste in the urine (2).

The typical presentation of arginase deficiency is different from that of the other urea cycle disorders (UCDs), with the onset of symptoms typically in late infancy. Outcomes include microcephaly, seizures, loss of ambulation, clonus, spastic diplegia, intellectual disability (from mild to severe), growth deficiency, and failure to thrive (3, 4); the exact cause of these neurological manifestations and the progressive intellectual decline are not known but are hypothesized to be related to hyperargininemia and the accumulation of guanidino compounds (as putative neurotoxins) found in the plasma, urine, and cerebrospinal fluid of these patients (5–10). Unlike the other enzyme deficiencies of the urea cycle, hyperammonemia is uncommon (11), and thus patients typically avoid the severe nitrogen vulnerability and catastrophic crises that occur in the other UCDs. However, the neurological decline is progressive and unrelenting, and the mainstay of current-day therapy, which includes provision of a very strict protein-restricted diet, amino acid supplementation, and administration of the nitrogen scavengers sodium benzoate and sodium phenylbutyrate (3, 4), only partially alleviates the disorder, as there exists no medical therapy that is completely efficacious. While liver transplantation has not been commonly employed for patients with this disorder, long-term follow-up of 2 patients who underwent liver transplantation showed normalization of plasma arginine and guanidino compounds with lack of progressive neurological decline (12, 13), further supporting

Significance

Systemically administered lipid nanoparticles (LNPs) targeting the liver were able to express the cytoplasmic enzyme arginase 1 (ARG1) in a conditional knockout model of ARG1 deficiency. Metabolically, this resulted in maintaining normal plasma ammonia and arginine, preventing the build-up of excessive hepatic arginine, and obviated the development of guanidino compounds, a hallmark of this enzyme deficiency. Unlike controls, repeat dosing of LNPs encapsulating human codon-optimized *ARG1* messenger RNA led to long-term survival without evidence of toxicity, restoration of ureagenesis, and the ability to handle toxic ammonia loading. These findings have implications for therapy of ARG1 deficiency, which is presently inadequately treated and leads to progressive neurological decline.

Author contributions: B.T. and G.S.L. designed research; B.T., G.A., X.-B.L., K.E.B., X.Z., and G.S.L. performed research; J.H. and P.G.V.M. contributed new reagents/analytic tools; B.T., X.-B.L., S.D.C., J.H., P.G.V.M., and G.S.L. analyzed data; and B.T. and G.S.L. wrote the paper.

Conflict of interest statement: G.S.L. has served as a consultant to Audentes Therapeutics in an area unrelated to this work. S.D.C. is a consultant for Synlogic and Cobalt Biomedicine in areas unrelated to this work. K.E.B., X.Z., and P.G.V.M. are current or previous employees of Moderna, Inc. and receive salary and stock options as compensation for their employment.

This article is a PNAS Direct Submission. D.K. is a guest editor invited by the Editorial Board.

See Commentary on page 20804.

[1]To whom correspondence may be addressed. Email: glipshutz@mednet.ucla.edu.

This article contains supporting information online at www.pnas.org/lookup/suppl/doi:10.1073/pnas.1906182116/-/DCSupplemental.

First published September 9, 2019.

methods of normalization of plasma arginine levels as tenets of therapy.

With the development of transgenic technology and the advances of the last 2.5 decades in the progress and application of gene therapy to monogenic disorders of the liver, our group has been successful in the development of a mouse model of hyperargininemia (14), along with the preclinical application of viral-based gene therapy approaches in treating this enzyme deficiency (15–17). The beginning of therapy before (18, 19) or shortly after (20, 21) birth, before the onset of phenotypic disease, has advantages, as early gene therapy has the potential to ameliorate genetic abnormalities before the development of phenotypic disease. For example, initiating therapy shortly after birth has demonstrated that both restoring hepatic arginase activity and controlling hyperargininemia and guanidino compounds lead to normal neurological development, cognitive activity, and behavior in Arg1-deficient mice (22, 23).

However, such therapy with episomal viral vectors [as adeno-associated virus (AAV) typically only integrates at a low frequency (24)] is faced with greater challenges in rapidly dividing tissues and organs than therapy of postmitotic tissues (25). In neonates, the rate of hepatocellular proliferation is much higher and affects the maintenance of episomal vector genomes (26, 27), while rapid cellular proliferation in adults is uncommon. For example, individual hepatocytes in the adult mouse liver are replaced once every 180 to 400 d (28, 29), while the neonatal murine liver increases from 50 mg to over 1 gram in the first 5 postnatal weeks (25). When administered to neonatal mice, this results in a decline in AAV copy number of over 3 logs (25) leaving relatively few arginase-expressing hepatocytes over the long term in adult animals and the potential for nitrogen vulnerability (16, 17). While enzyme replacement has led to successful therapies for a number of other genetic disorders, when tested in arginase-deficient mice, plasma arginine was reduced (11); however, repeat dosing did not result in improved survival or prevention of weight loss, likely due to the inability of the PEGylated enzyme to enter hepatocytes. Thus, today, there remains an unmet need for these patients.

Messenger RNA (mRNA) therapy with nanoparticle encapsulation for systemic delivery to hepatocytes has the potential to restore metabolic enzymatic activity for a number of hepatic metabolic disorders (30, 31), including arginase deficiency. Until recently, RNA-based therapeutics have suffered from problems of poor translatability, lack of stability, immune responses, hepatotoxicity (32), and inefficient delivery (30, 33). Recent advances have improved the stability and translatability of RNAs and have made them immunologically inactive (30). While the advantages include avoidance of insertional mutagenesis and lack of constitutive gene activation, the use of mRNA technology may also allow for restoration of inaccessible targets (31), such as cytoplasmic arginase activity, which was unachievable with PEGylated enzymatic therapy (11).

In this study, we encapsulated and systemically administered human codon-optimized *ARG1* (h*ARG1*) mRNA to a conditional knockout murine model of ARG1 deficiency. We achieved delivery of mRNA to the liver by lipid nanoparticles (LNPs) at therapeutic levels in this preclinical model. We successfully demonstrated high-level hepatic arginase expression and function with restoration of ureagenesis, while achieving long-term survival, maintenance of weight, normalization of plasma ammonia and arginine, lack of hepatic guanidinoacetic acid (GAA; a guanidino compound), and normalization of hepatic arginine without evidence of hepatotoxicity. These findings demonstrate the efficacy of this approach in arginase deficiency.

Results

LNPs Successfully Deliver mRNA to Murine Livers. The liver is the primary location of nitrogen detoxification and urea cycle function. Therefore, targeted delivery of the LNPs and proper release of the encapsulated mRNA for therapeutic protein translation in the liver are crucial to the potential success of this treatment modality for arginase deficiency. To examine the ability of our engineered LNPs to traffic to the liver, we administered a single intravenous (IV) bolus of 2 mg/kg of LNP-encapsulated firefly (*Photinus pyralis*) luciferase mRNA (LNP-*luc*) to wild-type (WT) conditional arginase-deficient ($Arg1^{flox/flox}$) mice ($n = 5$ males). Beginning 2 h after LNP-*luc* injection, mice were administered the luciferase substrate D-Luciferin and underwent serial bioluminescent imaging (BLI). Imaging revealed proper localization of functional luciferase protein to the liver as early as 2 h after LNP-*luc* injection that remained detectable by BLI in some animals up to 36 h postinjection (Fig. 1*A*). At 72 h after the initial LNP-*luc* injection, luciferase protein was undetectable by BLI, and an additional IV bolus of 2 mg/kg of LNP-*luc* was administered at 73 h after the first injection. Repeat serial BLI revealed liver trafficking and luciferase protein translation and stability kinetics comparable to the initial LNP-*luc* injection (Fig. 1 *A* and *B*). Although the protein translation kinetics and half-life will be variable and determined by the specific mRNA encapsulated within the LNPs, BLI demonstrated the ability of LNPs to reliably and repeatedly deliver mRNA to the liver without overt evidence of short-term abnormalities.

Pharmacokinetic Characterization of LNP-Encapsulated Arginase mRNA in Murine Livers. The h*ARG1* mRNA was designed, synthesized, and encapsulated within our biodegradable liver-targeting LNPs (LNP-h*ARG1*). To characterize the kinetics of the h*ARG1* mRNA release from the LNPs and stability within the liver, we performed a pharmacokinetic (PK) study in WT $Arg1^{flox/flox}$ mice ($n = 3$ mice per time point). We administered a single IV bolus of 2 mg/kg of LNP-h*ARG1* and collected livers at the time points of 0, 2, 6, 12, and 24 h and then daily from days 2 to 7 postinjection. Using quantitative real-time-PCR (qRT-PCR) primers specific for the h*ARG1* mRNA encapsulated within the LNPs, h*ARG1* mRNA levels in treated livers were determined relative to murine *Gapdh* housekeeping transcript levels. We observed peak and substantial h*ARG1* mRNA levels in the liver at the earliest time point 2 h postinjection compared with 0-h mice that did not receive LNP-h*ARG1* (0 h: 0.934 ± 9.934 vs. 2 h: $1.49 \times 10^5 \pm 2.06 \times 10^4$ relative transcript levels; $P < 0.001$) (Fig. 1*C*). After the observed peak at 2 h, h*ARG1* mRNA levels significantly decreased by 33.1% by 6 h ($P = 0.005$) and 84.2% by 12 h ($P < 0.001$) relative to 2-h postinjection mRNA levels. By 24 h, only 4.4% of the 2-h postinjection mRNA levels remained ($P < 0.001$), and levels were maintained below 0.25% from days 2 to 7 ($P < 0.001$ each day).

Long-Term Animal Survival after Systemic Delivery of LNP-h*ARG1*. Hepatic loss of murine Arg1 expression leads to hyperargininemia, hyperammonemia, and death in $Arg1^{-/-}$ mice (34). Previous studies have demonstrated that delivery of the murine Arg1 complementary DNA (cDNA) by AAVrh10 can rescue a juvenile-lethal arginase-deficient murine model, whose therapeutic efficacy may be limited due to hepatocellular division, leading to eventual dilution and a substantial reduction of the transgene expression (16). To demonstrate the long-term efficacy of LNP-mediated delivery of codon-optimized h*ARG1* mRNA to successfully treat arginase deficiency, adult $Arg1^{flox/flox}$ mice were administered 2.0×10^{11} genome copies of AAV8-thyroxine binding globulin promoter (TBG)-Cre recombinase (Cre) on day 0 to disrupt hepatic expression of the endogenous functional murine Arg1 by excision of exons 7 and 8. Beginning on day 14 after AAV8-TBG-Cre administration, mice were administered IV either 2 mg/kg of LNP-*luc* or LNP-h*ARG1* ($n = 10$, 5 males and 5 females per group). One group was administered LNP-mRNA weekly, and another group was administered LNP-mRNA every 3 d (q3D). Weight was recorded daily, blood was collected weekly, and livers were collected at the end of the study or at the time of euthanasia

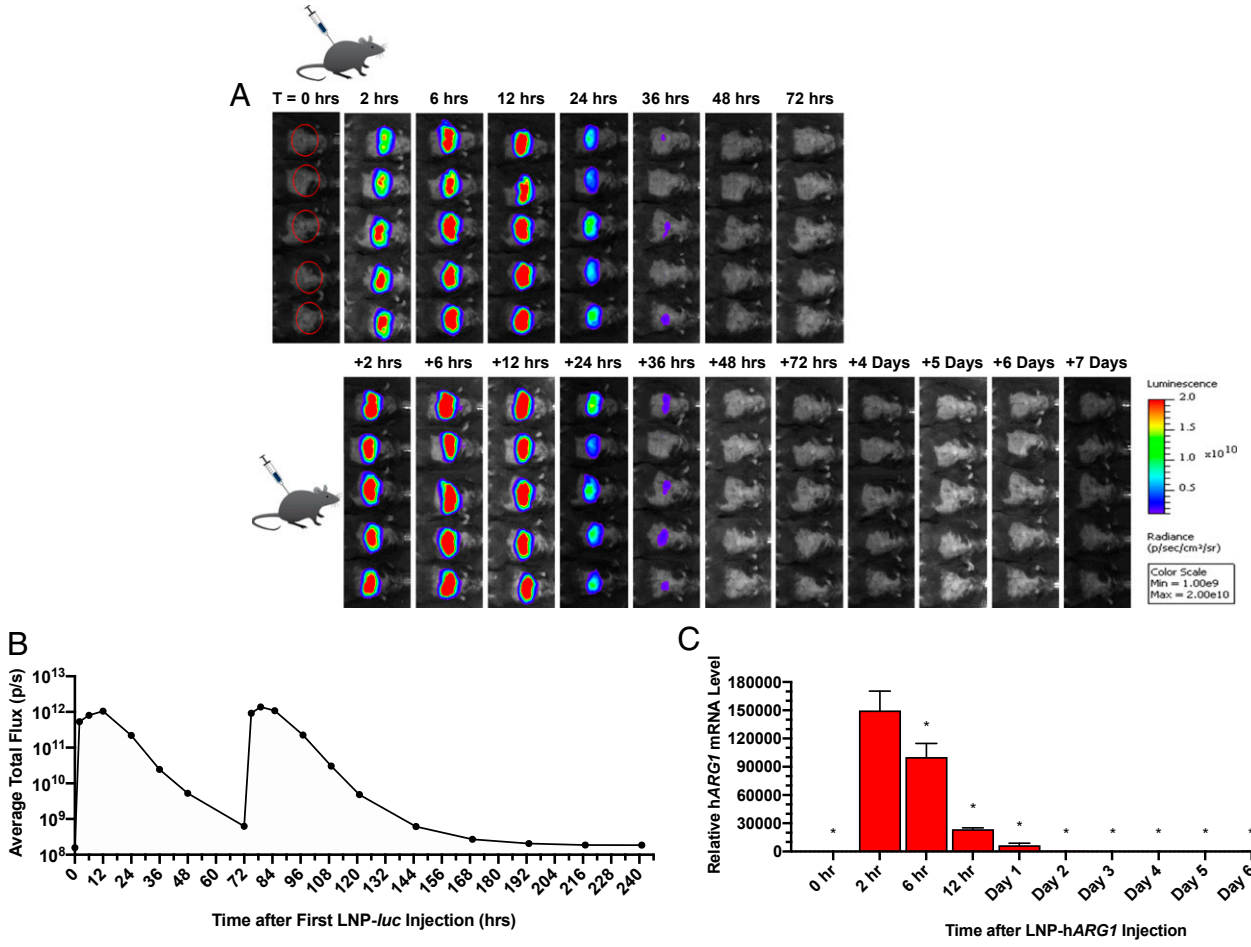

Fig. 1. LNP-mediated mRNA delivery to the liver results in repeatable hepatic expression. WT conditional Arg1 knockout mice were administered an IV bolus dose of 2 mg/kg of LNP-*luc* or LNP-h*ARG1*. (*A*) BLI of hepatic luciferase expression represented by a pseudocolor scale was performed at various time (T) points (0, 2, 6, 12, 24, 36, 48, and 72 h) after the first LNP-*luc* dose, with repeat imaging after the second bolus administration (2, 6, 12, 24, 36, 48, and 72 h; 4, 5, 6, and 7 d; $n = 5$ mice per time point). All images were acquired and processed with the same settings. Max, maximum; Min, minimum; p, photons; sr, steradian. (*B*) Quantitation of hepatic expression of firefly luciferase was performed after the initial LNP-*luc* bolus injection and after repeat administration. (*C*) PK characterization of h*ARG1* mRNA in the liver was determined by qRT-PCR after liver collection at various time points (0, 2, 6, 12, 24 h; 2, 3, 4, 5, 6, and 7 d; $n = 3$ per time point). *P* values were obtained from 1-way ANOVA with Tukey's multiple comparison test. *$P < 0.001$ compared with 2-h postinjection h*ARG1* mRNA levels. Data are presented as mean ± SEM.

for humane end points or death. Weekly LNP-h*ARG1* mice demonstrated significant life extension compared with weekly LNP-*luc* control mice ($P < 0.001$), but none exhibited long-term survival and stable weights; all weekly LNP-h*ARG1* mice died or were euthanized for humane end points by day 62, while all weekly LNP-*luc* mice perished by day 27 (Fig. 2 *A* and *B*). In contrast, q3D LNP-h*ARG1* mice exhibited significant life extension ($P < 0.001$) with 100% survival and without physiological signs of hyperammonemia or weight loss to beyond day 77 compared with q3D LNP-*luc* mice, which all perished by day 22 (Fig. 2 *C* and *D*). These data demonstrate that delivery of 2 mg/kg of LNP-h*ARG1* q3D is a therapeutic dose and frequency of administration that can successfully extend and maintain long-term survival and health of arginase-deficient mice. No period of multiday loading of LNP-h*ARG1* by daily injections is necessary (*SI Appendix*, Fig. S1).

Functional Metabolic Recovery of Arg1$^{-/-}$ Mice after Systemic Delivery of LNP-h*ARG1*. To evaluate the metabolic function of conditional Arg1$^{-/-}$ mice in response to LNP-mRNA treatment, plasma was collected over the course of the study and analyzed for various criteria. Due to the transient nature of LNP-mRNA treatment, plasma metabolite levels were expected to fluctuate depending on timing of plasma collection within the therapeutic q3D dosing interval. Therefore, mice ($n = 6$ per group) were bled every 7 d regardless of timing within the dosing interval to collect time points representing the full spectrum within the dosing interval. In weekly LNP-*luc* mice, plasma ammonia levels were measured on day 0 (183.7 ± 26.9 μM) and demonstrated significantly increased concentrations that peaked at death on day 21 (692.9 ± 23.5 μM; $P < 0.001$) (Fig. 3*A*). Similarly, significantly increased plasma ammonia concentrations at death compared with day 0 levels were also found in weekly LNP-h*ARG1* mice (day 0: 120.0 ± 17.8 vs. d 42: 1,409.6 ± 449.5 μM; $P = 0.002$) (Fig. 3*A*) and in q3D LNP-*luc* mice (day 0: 174.1 ± 32.6 vs. d 21: 1505.6 ± 414.5 μM; $P = 0.003$) (Fig. 3*B*). However, q3D LNP-h*ARG1* mice showed good control and no statistically significant increases in plasma ammonia throughout the study compared with day 0 levels, demonstrating amelioration of hyperammonemic episodes induced by hepatic Arg1 disruption (day 0: 112.8 ± 36.7 vs. d 14: 146.2 ± 42.2, day 21: 122.2 ± 35.2, day 28: 130.5 ± 33.4, day 42: 146.5 ± 22.7, day 56: 101.3 ± 31.9, day 70: 123.4 ± 24.5, and day 77: 163.1 ± 33.7 μM; $P > 0.05$) (Fig. 3*B*). Plasma ammonia in mice administered LNP-h*ARG1* q3D was measured at days 0, 14, 21, 28, 42, 56, 70, and 77, demonstrating levels corresponding to 0, 0, 1, 2, 1, 3, 2, and 1 d post-last dose (post-LD), respectively (Fig. 3*B*). Mice ($n = 5$ males per group) administered q3D LNP-h*ARG1* on day 72 (1 d post-LD) were also

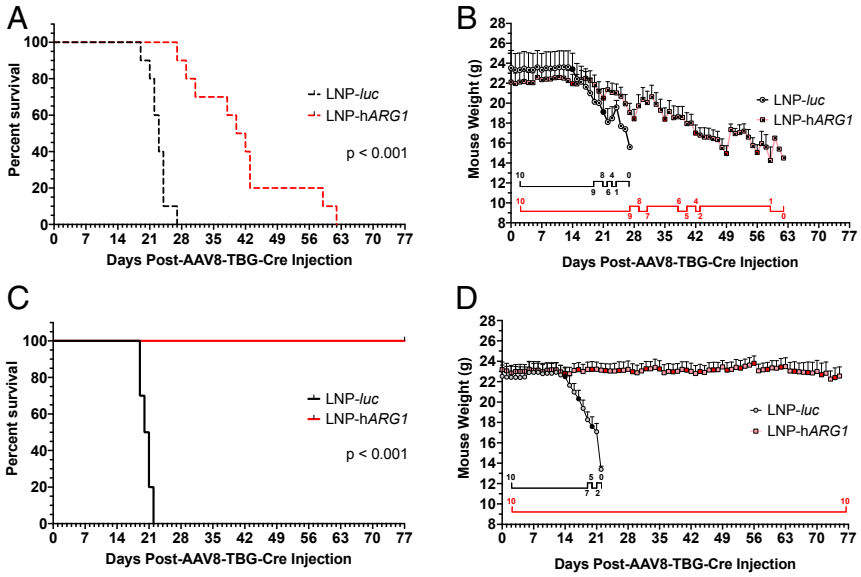

Fig. 2. Survival and weights of conditional ARG1 knockout mice were stable over the long term in mice administered LNP-formulated h*ARG1* mRNA every 3 d. Conditional arginase knockout mice were administered 2×10^{11} genome copies of AAV8-TBG-Cre (day 0) to induce Cre-Lox excision in the endogenous murine Arg1 gene, resulting in loss of function. Mice were administered an IV bolus of 2 mg/kg of LNP-*luc* (control, black line) or 2 mg/kg of LNP-h*ARG1* (experimental, red line) weekly (*A* and *B*) or q3D (*C* and *D*) beginning on day 14. Mice were monitored for survival and clinical evidence of deterioration in both the weekly dosed and q3D-dosed groups up to 11 wk after initiating Cre-Lox recombination ($n = 10$ per group, 5 males and 5 females). (*B* and *D*) Solid black line (LNP-*luc*) and red line (LNP-h*ARG1*) parallel to the *x* axis of weight logs represent surviving animals in each treatment study. (*A* and *C*) $P < 0.001$ obtained by log-rank. Data are presented as mean ± SEM. (*B* and *D*) Day of LNP injection is represented by a darkened red square for LNP-h*ARG1* and solid black circle for LNP-*luc*. g, gram.

able to similarly metabolize an ammonium challenge compared with WT control mice after 60 min, demonstrating an adequate ability to handle exogenous nitrogen loading (Fig. 3*C*).

To further confirm recovery of ureagenesis, q3D LNP-h*ARG1* mice on day 72 (1 d post-LD) and WT control mice ($n = 8$ per group, 4 male and 4 female) were administered intraperitoneal ^{15}N ammonium chloride, which was allowed to metabolize into ^{15}N urea for 60 min before collected blood was measured by gas chromatography-mass spectrometry for ^{15}N urea enrichment (Fig. 3 *D*, *Left*); q3D LNP-h*ARG1* mice metabolized 81.9 ± 11.3% of total WT control ^{15}N urea enrichment levels, demonstrating no statistically significant difference between the 2 groups ($P > 0.05$) (Fig. 3 *D*, *Right*).

Plasma and liver ($n = 6$ per group) were also analyzed for selected amino acids critical to the urea cycle and nitrogen metabolism pathways. Plasma amino acids were measured on days 0, 28, 56, and 77, demonstrating levels corresponding to 0, 2, 3, and 1 d post-LD, respectively. Plasma arginine and glutamine, both typically found elevated in mice with arginase deficiency, were significantly increased at the time of euthanasia in q3D LNP-*luc* mice compared with day 0 (ARG_{D0}: 114.6 ± 1.5 μM vs. ARG_{D21}: 832.5 ± 102.1 μM; $P < 0.001$) (GLN_{D0}: 731.8 ± 47.2 μM vs. GLN_{D21}: 1,277.0 ± 243.0 μM; $P = 0.020$) (Fig. 4 *A* and *B*). However, in q3D LNP-h*ARG1* mice, there was no statistically significant increase in plasma arginine or glutamine observed throughout the course of the study compared with day 0 (ARG_{D0}: 82.3 ± 8.3 μM vs. ARG_{D28}: 127.5 ± 12.09 μM, ARG_{D56}: 165.2 ± 36.47 μM, ARG_{D77}: 151.2 ± 34.4 μM; $P > 0.05$) (GLN_{D0}: 584.5 ± 19.1 μM vs. GLN_{D28}: 643.4 ± 32.5 μM, GLN_{D56}: 628.0 ± 90.86 μM, GLN_{D77}: 784.2 ± 66.7 μM; P = not significant) (Fig. 4 *A* and *B*). Plasma ornithine and lysine were also examined, and while neither the q3D LNP-*luc* group nor the q3D LNP-h*ARG1* group demonstrated statistically significant increases throughout the study, plasma lysine in q3D LNP-*luc* at the time of euthanasia was trending toward statistical significantly increased levels when compared with day 0 (LYS_{D0}: 182.5 ± 21.1 μM vs. LYS_{D21}: 356.9 ± 103.6 μM; $P = 0.096$) (Fig. 4 *C* and *D*).

Hepatic amino acids ($n = 6$ per group unless otherwise noted) were measured for q3D LNP-*luc* mice at the time of euthanasia and for q3D LNP-h*ARG1* mice on day 35 (3 d post-LD) and day 77 (1 d post-LD). Hepatic arginine concentrations in q3D LNP-*luc* mice (34.6 ± 5.7 nmol/mg of protein) were significantly higher compared with q3D LNP-h*ARG1* mice on both day 35 (2.6 ± 1.1 nmol/mg of protein; $P < 0.001$; $n = 4$) and day 77 (3.1 ± 0.2 nmol/mg of protein; $P < 0.001$) and WT control mice (2.5 ± 0.2 nmol/mg of protein; $P < 0.001$) (Fig. 4*E*). Liver glutamine concentrations in q3D LNP-*luc* mice (9.0 ± 1.2 nmol/mg of protein) were significantly lower compared with q3D LNP-h*ARG1* mice on day 77 (26.4 ± 1.8 nmol/mg of protein; $P < 0.001$), but not significantly different from q3D LNP-h*ARG1* mice on day 35 (19.92 ± 4.6 nmol/mg of protein; $P > 0.05$; $n = 4$) or WT control mice (18.0 ± 3.6 nmol/mg of protein; $P > 0.05$) (Fig. 4*F*); ammonia does result in the short-term activation of hepatic glutaminase (35) and may be the cause of this intracellular glutamine reduction in LNP-*luc* mice as plasma ammonia is markedly elevated in this group (Fig. 3*B*). Hepatic ornithine concentrations, when compared with WT controls (2.0 ± 0.2 nmol/mg of protein), were significantly elevated in q3D LNP-*luc* mice (12.1 ± 2.8 nmol/mg of protein; $P = 0.003$) and q3D LNP-h*ARG1* mice on day 35 (11.0 ± 2.3 nmol/mg of protein; $P = 0.017$; $n = 4$), but not significantly elevated in q3D LNP-h*ARG1* mice on day 77 (4.1 ± 0.7 nmol/mg of protein; $P > 0.05$) (Fig. 4*G*). Hepatic lysine concentrations in q3D LNP-*luc* mice (36.2 ± 7.6 nmol/mg of protein) were significantly higher compared with q3D LNP-h*ARG1* mice on both day 35 (7.7 ± 1.8 nmol/mg of protein; $P = 0.002$; $n = 4$) and day 77 (5.9 ± 0.6 nmol/mg of protein; $P < 0.001$) and WT control mice (5.1 ± 0.7 nmol/mg of protein; $P < 0.001$) (Fig. 4*H*).

Guanidino compounds have been found to accumulate in patients with arginase deficiency (6, 8, 36). Therefore, we quantified the accumulation of GAA ($n = 6$ per group unless otherwise stated) in plasma of q3D LNP-*luc* mice at the time of euthanasia and for q3D LNP-h*ARG1* mice on day 35 (3 d post-LD) and day 77 (1 d post-LD). There was no statistically significant increase between q3D LNP-h*ARG1* mice on day 35 (3.9 ± 0.6 nM; $n = 4$) and on day 77 (3.0 ± 0.4 nM) and WT controls (2.3 ± 0.2 nM);

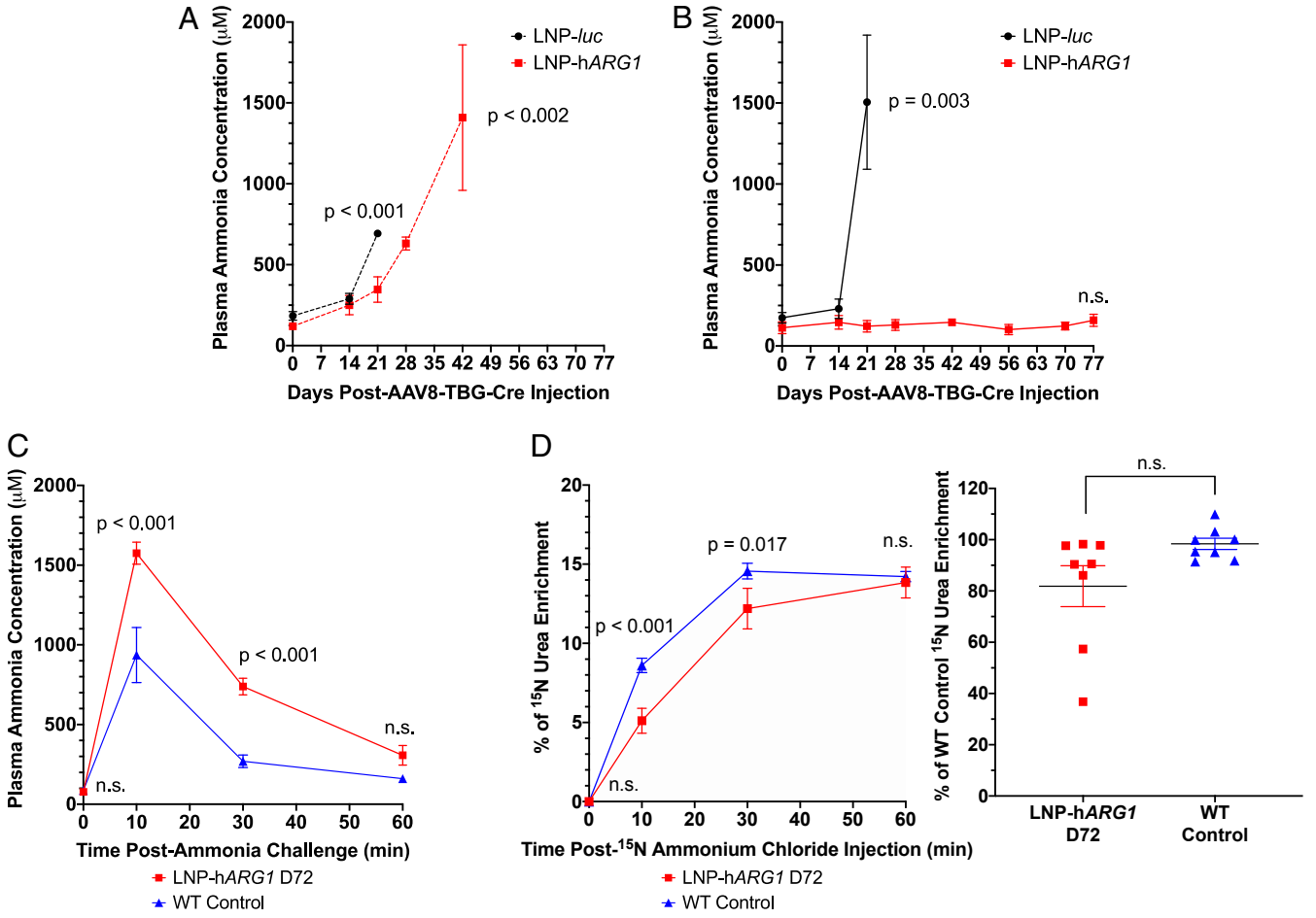

Fig. 3. Administration of LNP-h*ARG1* every 3 d results in controlled plasma ammonia and near-normal ureagenesis. Conditional arginase knockout mice were administered 2×10^{11} genome copies of AAV8-TBC-Cre (day 0) to induce Cre-Lox excision in the endogenous Arg1. Mice were administered an IV bolus of 2 mg/kg LNP-*luc* (control, black line) or 2 mg/kg LNP-h*ARG1* (experimental, red line) weekly (*A*) or q3D (*B*) ($n = 6$ per group) beginning on day 14. (*A*) Plasma ammonia was measured in weekly dosed mice on days 0, 14, 21, 28, and 42 in the morning before subsequent injection of LNP-mRNA in the afternoon ($n = 6$ per group). (*B*) Plasma ammonia was measured in q3D-dosed mice on days 0, 14, 21, 28, 42, 56, 70, and 77, demonstrating levels corresponding to 0, 0, 1, 2, 1, 3, 2, and 1 d post-LD, respectively ($n = 6$ per group). (*C*) q3D LNP-h*ARG1*–treated mice on day 72 (1 d post-LD) (red line; $n = 6$) and WT controls ($Arg1^{flox/flox}$; blue line; $n = 6$) were administered 0.4 M ammonium chloride intraperitoneally (IP), and plasma ammonia was measured 10, 30, and 60 min postchallenge. (*D*) Ureagenesis was assessed at 10, 30, and 60 min after IP administration of 0.4 M ^{15}N ammonium chloride on day 72 (1 d post-LD) in q3D LNP-h*ARG1* and WT control mice by ^{15}N urea enrichment quantitation using gas chromatography-mass spectrometry ($n = 8$ per group). (*Left*) Graph demonstrates the progression of ^{15}N urea enrichment at each time point. (*Right*) Graph demonstrates the total calculated area under the curve to depict the total accumulated quantity of ^{15}N urea enrichment of each group. In this graph, values are normalized to the average total area under the curve value of WT control mice. D, day. In all graphs, *P* values were obtained from 1-way ANOVA with Tukey's multiple comparison test (*A* and *B*), 2-way ANOVA with Sidak's multiple comparison test (*C* and *D*, *Left*), and an unpaired *t* test (*D*, *Right*). Data are presented as mean ± SEM. n.s., not significant.

however, GAA levels of q3D LNP-*luc* mice at the time of euthanasia were trending toward significantly increased levels (3.8 ± 0.6 nM; $P = 0.100$) compared with the WT controls (Fig. 4*I*).

To support the plasma GAA studies, hepatic levels were also quantified for q3D LNP-*luc* mice at the time of euthanasia and for q3D LNP-h*ARG1* mice on day 35 (3 d post-LD) and on day 77 (1 d post-LD) ($n = 4$ per group). Liver GAA levels in q3D LNP-*luc* mice (61.5 ± 12.7 pmol/mg of tissue) were significantly elevated compared with q3D LNP-h*ARG1* mice on day 77 (27.3 ± 6.9 pmol/mg of tissue; $P = 0.047$) and WT controls (18.8 ± 4.3 pmol/mg of tissue; $P = 0.013$); levels were trending toward significance compared with q3D LNP-h*ARG1* mice on day 35 (30.5 ± 5.6 pmol/mg of tissue; $P = 0.077$) (Fig. 4*J*).

To examine for potential liver toxicity induced by long-term administration of LNPs, plasma was examined for levels of alanine aminotransferase (ALT; $n = 6$ per group), a marker of liver injury, in q3D LNP-*luc* mice at the time of euthanasia (49.3 ± 17.5 units [U]/L) and q3D LNP-h*ARG1* mice on D77 (1 d post-LD) (33.6 ± 3.8 U/L); differences in levels in both groups were not statistically significant compared with WT control levels (27.3 ± 3.7 U/L) ($P > 0.05$ for both comparisons) (Fig. 4*K*). Altogether, these data demonstrate the ability for this treatment modality to completely and safely recover the metabolic profile of adult arginase-deficient mice.

LNP-h*ARG1* Levels and Localization Characteristics within $Arg1^{-/-}$ Livers. After the completion of our in vivo and plasma biochemical studies, LNP-mRNA–treated mice were euthanized and their livers were collected, sectioned, and analyzed to characterize LNP-h*ARG1* levels and distribution. The h*ARG1* mRNA in LNP-mRNA–treated livers was determined relative to the murine *Gapdh* housekeeping transcript levels ($n = 6$ per group). The q3D LNP-h*ARG1* mice were euthanized on day 77 (1 d post-LD). Mice were found to have a markedly and significantly increased level of h*ARG1* mRNA compared with LNP-*luc* and WT control mice ($P = 0.022$ for both) (Fig. 5*A*). In contrast, weekly LNP-h*ARG1*

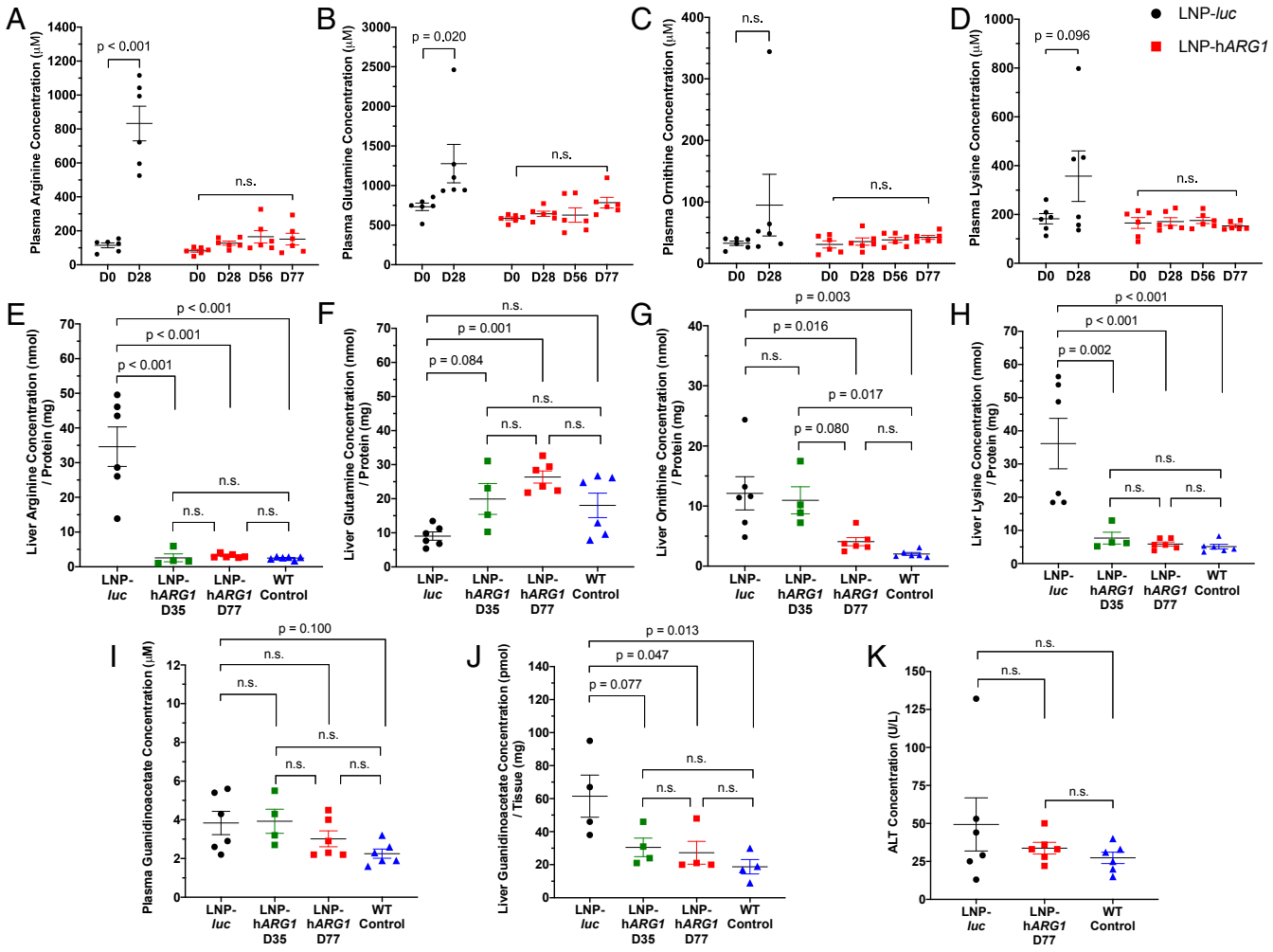

Fig. 4. LNP-h*ARG1* administration every 3 d prevents elevated plasma and hepatic arginine, controls plasma glutamine, and prevents GAA accumulation in the plasma. Plasma arginine (*A*), glutamine (*B*), ornithine (*C*), and lysine (*D*) were assessed in q3D control LNP-*luc* mice ($n = 6$; black) at days 0 and 28 and in q3D LNP-h*ARG1* mice ($n = 6$; red) at days 0, 28, 56, and 77, demonstrating levels corresponding to 0, 2, 3, and 1 d post-LD, respectively. Hepatic arginine (*E*), glutamine (*F*), ornithine (*G*), and lysine (*H*) were similarly assessed in control q3D LNP-*luc* mice at the time of euthanasia ($n = 6$; black) and in q3D LNP-h*ARG1* mice on day 35 (3 d post-LD; $n = 4$; green) and on day 77 (1 d post-LD; $n = 6$; red) and compared with WT control liver ($n = 6$; blue). (*I*) Plasma guanidino compounds, represented by GAA, were assessed in q3D LNP-h*ARG1* mice on day 35 (3 d post-LD; $n = 4$; green) and on day 77 (1 d post-LD; $n = 6$; red) and compared with q3D LNP-*luc* mice ($n = 6$; black) and WT controls ($n = 6$; blue). (*J*) Liver GAA was assessed using a method similar to that in *I* ($n = 4$ per group). (*K*) Plasma ALT was assessed in q3D LNP-h*ARG1* on day 77 (1 d post-LD; $n = 6$; red) and compared with q3D LNP-*luc* at the time of euthanasia ($n = 6$; black) and in WT controls ($n = 6$; blue). In all graphs, *P* values were obtained from 1-way ANOVA with Tukey's multiple comparison test. Data are presented as mean ± SEM. D, day; n.s., not significant.

mice showed levels of h*ARG1* mRNA in large variation and demonstrated no statistically significant differences compared with weekly LNP-*luc* and WT control mice (*SI Appendix*, Fig. S2*A*).

Liver lysates from LNP-mRNA–treated mice ($n = 6$ per group) were analyzed for functional ARG1 protein. The q3D LNP-h*ARG1* mice on day 77 (1 d post-LD) recovered 53.6 ± 6.3% of functional ARG1 activity relative to WT control mice ($P < 0.001$) (Fig. 5*B*). In contrast, while weekly LNP-h*ARG1* mice at time of euthanasia recovered 10.9 ± 1.5% of functional ARG1 activity relative to WT control mice ($P < 0.001$), these activity levels were found to be not significantly different from those of weekly LNP-*luc* mice at the time of euthanasia with 6.4 ± 0.6% of functional ARG1 activity ($P > 0.05$), whose expression was too low to maintain survival (*SI Appendix*, Fig. S2*B*). To further confirm these findings, Western blot analysis was performed with q3D LNP-h*ARG1* liver collected on day 77 (1 d post-LD), which revealed the strong presence of a single 35-kilodalton (kDa) isoform of ARG1 derived from LNP-h*ARG1* compared with WT mouse liver that demonstrates both 35- and 37-kDa endogenous Arg1 isoforms (Fig. 5*C*). Weekly LNP-h*ARG1* livers collected at the time of euthanasia demonstrated a minimal presence of ARG1 protein (*SI Appendix*, Fig. S2*C*).

To confirm that any survival extension was due to LNP-h*ARG1* treatment and not to maintenance of endogenous murine Arg1 expression, qRT-PCR primers were designed to span the endogenous murine *Arg1* exon 7 and 8 mRNA junction excised after AAV8-TBG-Cre activation. In weekly LNP-mRNA–treated and q3D LNP-*luc*–treated livers collected at the time of euthanasia and in q3D LNP-h*ARG1*–treated mice on day 77 (1 d post-LD), there was an absence of endogenous murine *Arg1* mRNA compared with WT control levels ($P > 0.05$ for both) (*SI Appendix*, Fig. S2 *D* and *E*).

Livers collected from weekly LNP-h*ARG1* and q3D LNP-*luc* mice collected at the time of euthanasia and from q3D LNP-h*ARG1* mice on day 77 (1 d post-LD) were sectioned and underwent various imaging analyses. The presence of h*ARG1* mRNA in LNP-mRNA–treated livers was visualized using in situ hybridization (ISH) probes designed specifically for h*ARG1* mRNA that

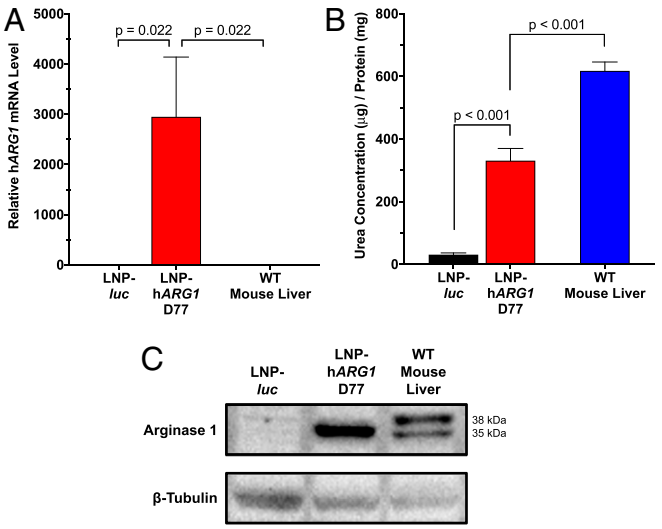

Fig. 5. LNP-h*ARG1* administration results in restoration of hepatic arginase mRNA and protein. The h*ARG1* mRNA hepatic levels relative to the murine *Gapdh* housekeeping gene were assessed by qRT-PCR (A), and functional hepatic ARG1 activity was assessed by a biochemical functional arginase assay (*B*) q3D in LNP-h*ARG1* mice on day 77 (1 d post-LD) and compared with q3D LNP-*luc* at the time of euthanasia and in WT controls ($n = 6$ per group). (*C*) Western blot analysis of hepatic ARG1 transgene expression in q3D LNP-h*ARG1* mice on day 77 (1 d post-LD) was compared with q3D LNP-*luc* at the time of euthanasia and in WT control liver. *P* values were obtained from 1-way ANOVA with Tukey's multiple comparison test. Data are presented as mean ± SEM. D, day.

was LNP-encapsulated. ISH of q3D LNP-h*ARG1* livers on day 77 collected 24 h after the final LNP-h*ARG1* dose revealed a positive but low presence of h*ARG1* mRNA in both hepatocytes and Kupffer cells (Fig. 6); h*ARG1* mRNA levels were in accordance with previous PK data that demonstrated a significant reduction in h*ARG1* mRNA after 24 h post–LNP-h*ARG1* injection (Fig. 1*C*). Weekly LNP-h*ARG1* mice similarly euthanized 24 h after the final LNP-h*ARG1* dose also demonstrated the positive, but lower, presence of h*ARG1* mRNA compared with q3D LNP-h*ARG1* livers by ISH (*SI Appendix*, Fig. S3). Immunofluorescent staining for ARG1 and glutamine synthetase (GS), to differentiate periportal ($GS^{Negative}$) and perivenous ($GS^{Positive}$) vasculature, was performed on weekly and q3D LNP-mRNA–treated liver sections to visualize localization of ARG1 expression. For weekly LNP-h*ARG1* livers collected at the time of euthanasia, no expression of ARG1 could be visualized, further confirming results from the molecular analysis (*SI Appendix*, Fig. S3). However, q3D LNP-h*ARG1* livers on day 77 (1 d post-LD) revealed strong ARG1 expression primarily localized in the periportal and interportal spaces consistent with LNP-h*ARG1* hepatic entrance via periportal vasculature and diffusion out to peripheral hepatocytes (Fig. 6). All liver sections were also stained with hematoxylin/eosin (H&E), revealing no overt pathological hepatic abnormalities or lymphocytic infiltrates, and with Masson's trichrome, where the absence of dark blue staining indicated lack of hepatic fibrosis or collagen deposition (Fig. 6). Furthermore, liver sections were imaged by electron microscopy to reveal intricate subcellular structures. All groups showed regular organization of the hepatic tissue without evidence of accumulation of electron-dense inclusions or bundles of collagen fibers. Hepatocytes demonstrated normal nuclear membranes, rough endoplasmic reticulum, and mitochondrial morphology. Compared with the WT and LNP-h*ARG1*–treated mice, LNP-*luc* hepatocytes did reveal mitochondria that were slightly enlarged (Fig. 6 and *SI Appendix*, Fig. S3) and the occasional presence of a lipid droplet (Fig. 6, arrows).

Discussion

UCDs are a family of inherited metabolic conditions of the liver in any of 6 enzymes or 2 transporters that impair ureagenesis and normal nitrogen detoxification produced as a consequence of protein metabolism (37). They are caused by monogenic loss of enzyme or transporter function, and are combined with straightforward medical treatments (i.e., protein-restricted diet, ammonia scavengers) that do not address the underlying cause. UCDs can result in the rapid development of hyperammonemia characterized by symptoms and signs, including headaches, hypo/hyperventilation, seizures, coma, and potentially death (38). Survivors typically have intellectual disabilities and remain vulnerable to repeat episodes of hyperammonemia with their cumulative and permanent neurological injury.

Arginase deficiency (OMIM:207800), caused by biallelic mutations in ARG1, tends to be recognized in late infancy to early childhood, unlike the other UCDs, where hyperammonemia and related signs often occur within a few days of birth (4, 38). Often identified by a presentation of spastic paraparesis or quadriparesis, the condition has progressive neurological decline, including developmental delays, psychomotor and growth retardation, and seizures as characteristic findings (4). While the potential for

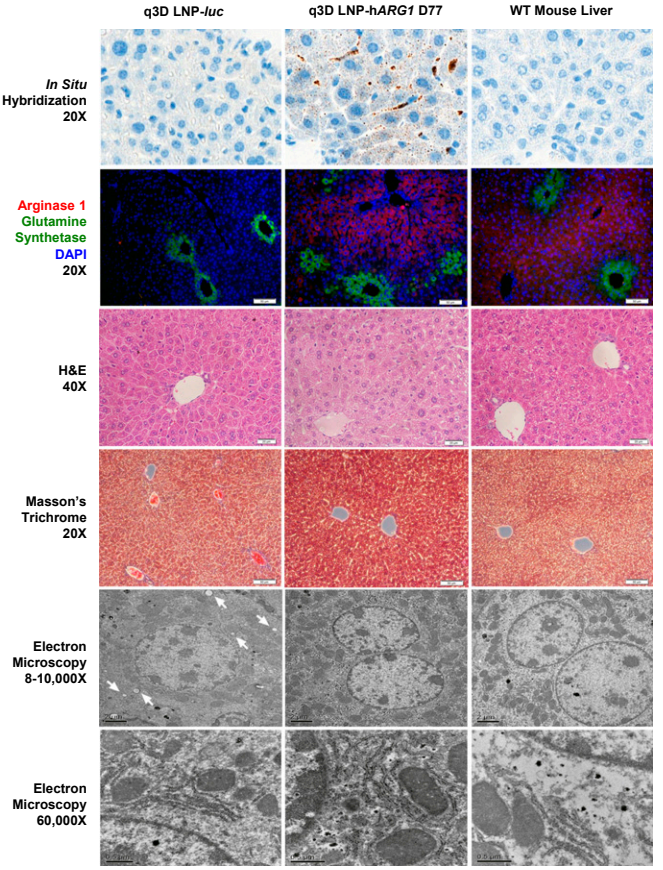

Fig. 6. LNP-h*ARG1*–mediated protein is detected in the liver when administered by LNP without evidence of inflammatory infiltrates, fibrosis, or subcellular injury. Liver sections of representative images of q3D LNP-*luc* mice at the time of euthanasia, q3D LNP-h*ARG1* mice on day 77 (1 d post LD), and WT control mice were examined for h*ARG1* mRNA presence by ISH (RNAScope) (first row, 20× magnification), for ARG1 transgene expression with greater perivenous vascular localization by immunostaining for ARG1 (red) and GS (green) (second row, 20× magnification), for hepatic histology by H&E staining (third row, 40× magnification); for collagen deposition/fibrosis by Masson's trichrome staining (fourth row, 20× magnification), and by electron microscopy (fifth row, 8,000× to 10,000× magnification; sixth row, 60,000× magnification). Arrows denote lipid droplets.

diagnosis by newborn screening would enable earlier therapeutic intervention (39), the current treatment is less than fully effective at best, resulting in progressive neurological injury. As such, arginase deficiency is another example of the growing number of metabolic diseases that can be detected by newborn screening but lack fully effective therapies.

In these present studies, we asked the question whether encapsulation of h*ARG1* mRNA within liver-targeting LNPs and their systemic delivery to arginase-deficient mice can achieve therapeutic recovery of urea cycle function at a reasonable concentration, dosage, and frequency and result in normal biochemical parameters. We demonstrate that administration of 2 mg/kg of LNP-h*ARG1* every 3 d results in both biochemical and functional efficacy of h*ARG1* mRNA. Unlike ARG1-deficient mice treated with a control mRNA (2 mg/kg of LNP-*luc* q3D), where all mice perished by day 22, we achieved 100% survival beyond 11 wk, stable weight, and recovery of urea cycle function with LNP-h*ARG1*, as demonstrated, in part, by maintenance of normal plasma ammonia and urea cycle-related amino acid levels, including glutamine. Notably, maintenance of normal plasma ammonia and amino acid levels was sustained throughout the q3D dosing interval with analysis occurring 1, 2, and 3 d post-LD. Importantly, unlike some other metabolic disorders where restored hepatic expression results in incomplete correction due to other metabolite-producing uncorrected tissues [e.g., methylmalonic acidemia (40)], plasma arginine was completely normalized as the urea cycle is exclusive to the liver. In addition, the generation of disease-related metabolites (i.e., GAA) is prevented, and repeat administration of h*ARG1* mRNA led to stable weights, an indication of the overall health of the mice. The distribution of the exogenous arginase protein was panhepatic, as occurs naturally, and is in contrast to the other urea cycle enzymes that concentrate in the periportal areas.

PK studies revealed the LNP as an effective delivery vehicle of h*ARG1* mRNA in vivo, leading to peak levels of h*ARG1* mRNA in the liver shortly after administration. Significant degradation of LNP-mRNA within 24 h is consistent with other studies (40). Functionally, whereas control mice demonstrated no hepatic arginase activity and perished, translated ARG1 protein from LNP-h*ARG1* persisted even after significant h*ARG1* mRNA degradation, leading to 54% of normal hepatic arginase activity 24 h after administration. This led to mice (1 d post-LD) being able to completely metabolize an exogenous challenge of ammonia into urea. In addition, ureagenesis was reestablished with similar ^{15}N incorporation in mice (1 d post-LD) compared with WT mice. While analyses aimed to quantify h*ARG1* mRNA and translated protein levels in the liver, as well as in vivo efficacy of LNP-h*ARG1* through exogenous ammonia challenges and recovery of ureagenesis, were performed on mice 1 d post-LD, a time point expected to have high ARG1 expression, we nonetheless have demonstrated the sustained efficacy of LNP-h*ARG1* throughout the q3D dosing interval, as evidenced by maintenance of normal weight, plasma amino acids, and prevention of GAA accumulation in mice 3 d post-LD.

LNP-h*ARG1* also led to normalization of intracellular arginine levels in hepatocytes; this is not achievable with enzyme replacement therapy (presently in clinical trial NCT03378531) due to the inability of the PEGylated enzyme to enter hepatocytes (11). Although further studies need to be performed, we hypothesize that normalization of intrahepatic arginine levels (not only plasma arginine levels) is needed to avoid the accumulation of disease-related metabolites such as GAA.

With concern for long-term toxicity issues related to repeat dosing of LNPs, we demonstrated that at the end of the 11-wk study, there was no histological or enzymatic evidence of liver injury. Further examination with electron microscopy demonstrated hepatocytes with normal nuclear membranes, rough endoplasmic reticulum, and mitochondrial morphology. Taken together, within the duration and scope of our study, repeat LNP-h*ARG1* dosing allowed for long-term survival and maintenance of normal plasma ammonia without evidence of hepatocellular injury.

We did find better survival and normalization of plasma ammonia during the q3D dosing period than with weekly administration. Whereas human arginase-deficient patients uncommonly have hyperammonemia, the murine model presents with both hyperammonemia and hyperargininemia, with the former leading to death. In this model, the q3D dosing is needed for extended therapeutic efficacy and survival. Along with q3D dosing, we examined 2 mg/kg of LNP-h*ARG1* administered weekly and demonstrated significant life extension; however, the weekly dosed mice exhibited unstable weights and significant increases of plasma ammonia by the end of each week, and they eventually succumbed to hyperammonemia. Notably, some weekly dosed mice had the positive presence of h*ARG1* mRNA by the time of death or euthanasia; however, Western blot and a functional assay demonstrated minimal hARG1 protein expression, potentially due to inadequate time for proper protein translation and the progression of disease in the mice. Thus, while further frequency optimization will be necessary for clinical application, human patients may not require the frequency of administration utilized in these murine studies.

Although progress has been made by way of advancements with both integrating and nonintegrating viral vector- and non–viral-based technologies to restore enzyme function, these gene therapy methods, for arginase deficiency, generally remain in the preclinical stage (16, 17, 41) and exhibit potential disadvantages. These include risk for insertional mutagenesis (24) and limited efficacy due to hepatocellular division (25) with viral-based strategies, lack of availability of cellular-based strategies (42) and organ-based strategies (43), and inability for hepatocyte penetrance with PEGylated enzyme replacement (11). Although highly promising and potentially curative, these strategies must be studied further to ensure effectiveness and safety before consideration of clinical applicability. Delivering mRNA to the liver is an alternative strategy to provide missing or defective enzyme function. The ability to repeatedly dose LNPs that carry h*ARG1* mRNA, supported by the PK studies that demonstrate rapid onset of expression and the tolerability of multiple dosing, suggests the value and preclinical proof-of-concept efficacy of LNP-based ARG1 mRNA therapy as an effective therapy for arginase deficiency.

Materials and Methods

Mouse Procedures. Conditional arginase-deficient mice on a C57BL/6 background (stock no. 008817; The Jackson Laboratory) were housed under specific pathogen-free conditions with food and water provided ad libitum. All mice were kept according to NIH guidelines, and all experimental procedures were conducted in accordance with guidelines for the care and use of research animals by the Chancellor's Animal Research Committee at the University of California, Los Angeles. At day 0, 8- to 12-wk-old animals were IV administered 2.0×10^{11} genome copies of AAV8-TBG-Cre (University of Pennsylvania Vector Core, Philadelphia, PA) prepared in sterile pharmaceutical grade saline. Male and female mice were distributed evenly throughout the study unless otherwise stated. Scheduled blood collections were taken from the retroorbital plexus under isoflurane anesthesia. Plasma was frozen immediately and stored at −80 °C. Mice were euthanized if they showed symptoms of lethargy, lying on their side, or inability to right themselves as signs of hyperammonemia. Beginning day 14 after AAV8-TBG-Cre injection, mice were administered IV LNP-encapsulated mRNA prepared at 2 mg/kg in sterile phosphate-buffered saline (PBS). One group of mice was injected with LNP-mRNA weekly, while 2 groups were injected every 3 d, one of which also received daily LNP-mRNA loading from days 14 to 21.

mRNA Synthesis and Formulation. The h*ARG1* mRNA codon optimization was performed using typical methods in the field (44). The mRNAs encoding luciferase and h*ARG1* were synthesized in vitro by T7 RNA polymerase-mediated transcription using a linearized DNA template that incorporated both the 5′ and 3′ untranslated regions with a poly-A tail and then purified and formulated for IV delivery as previously described (45) (the open reading frame for h*ARG1* is provided in *SI Appendix*).

BLI. Mice were shaved prior to imaging to minimize absorption of light by black fur and then imaged; total flux values in photons per second were calculated as previously described (25).

ALT Analysis. ALT level determination was performed from plasma samples using a Vet Excel Clinical Chemistry Analyzer (Alfa Wassermann Diagnostic Technologies) per the manufacturer's instructions.

Ammonia Analysis. Ammonia determination was performed in duplicate from plasma samples per the manufacturer's instructions (Abcam). Prolonged storage of plasma was avoided, and testing was generally performed with all samples simultaneously to avoid any batch effect.

Plasma and Liver Amino Acids. The concentration of amino acids in plasma and liver was determined by high performance liquid chromatography as previously described (46).

Guanidino Compounds. The concentration of GAA in the plasma and liver was determined by using a normal phase hydrophilic interaction column after analyte derivatization as previously described (47).

Ammonia Challenge and Ureagenesis. Mice were fasted for 3 to 4 h prior to the beginning of ammonia challenging, as previously described (23), using 4 mmol/kg of ^{15}N ammonium chloride ($^{15}NH_4Cl$; Cambridge Isotope Laboratories). Blood collections were performed immediately before and at 10, 30, and 60 min after injection, also allowing for ureagenesis determination as previously described (48).

Functional Arginase Analysis. Hepatic arginase activity was measured in duplicate from liver tissue lysates as previously described (16).

Histology and Immunohistochemistry. Liver tissues were fixed in 10% (vol/vol) buffered formalin for 48 h and then stored in 70% ethanol. Fixed tissue was embedded in paraffin blocks using standard procedures from which 4-μm-thick sections were collected on microscope slides. Section deparaffinization, rehydration, antigen retrieval, and permeabilization were performed as previously described (46). Sections were blocked with 10% (vol/vol) normal goat serum in PBS for 30 min. Sections were coincubated with primary antibodies for arginase (sc-20150; Santa Cruz Biotechnology) and GS (ab64613; Abcam) overnight at 4 °C. Sections were then coincubated with the fluorescent antibodies donkey anti-goat Alexa Fluor 594 (A11058; Invitrogen) and goat anti-mouse Alexa Fluor 488 (A11001; Invitrogen) for 1 h at room temperature. Section cell nuclei were counterstained with DAPI, mounted with VECTASHIELD Antifade Mounting Medium with DAPI (Vector Laboratories), and then visualized.

H&E and Masson's trichrome staining was performed by standard methods.

mRNA ISH. mRNA ISH was performed using RNAScope technology on an automated Leica BOND RX autostainer platform using the RNAScope 2.5 LS Reagent Kit-BROWN from Advanced Cell Diagnostics (ACD). An exclusive target probe with proprietary sequences was designed by ACD to target ARG1 mRNA. Control probes to the housekeeping gene *Mus musculus* peptidylprolyl isomerase B mRNA (catalog no. 313918; ACD), as a positive control, or the bacterial gene dihydrodipicolinate reductase (catalog no. 312038; ACD), as a negative control, was also used as a quality control check for tissues. Slides were processed using a Leica staining protocol per the user manual (document no. 322100-USM; ACD). All images were captured at 20× magnification with the Panoramic 250 Flash II (3DHISTECH) digital slide scanner.

Electron Microscopy. Four groups of liver tissues were collected and fixed in 4% (vol/vol) paraformaldehyde (Electron Microscopy Sciences) plus 2.5% (vol/vol) glutaraldehyde (Thermo Fisher Scientific) in PBS solution at 4 °C for several weeks. Each liver sample was prepared for imaging by standard methods (details of the methods used are provided in *SI Appendix*).

RNA Isolation. Total RNA was isolated from ∼20 mg of homogenized liver tissue with a Roche High Pure RNA Isolation Kit (Roche Applied Sciences) per the manufacturer's instructions.

Residual Endogenous Murine Arg1 mRNA qRT-PCR. One microgram of total RNA was reverse-transcribed to cDNA with a Transcriptor First Strand cDNA Synthesis Kit (Roche Applied Sciences) per the manufacturer's instructions. Primers for endogenous murine *Arg1* mRNA were designed to bind to the exon 7/8 junction: forward primer 5′-ACATCACAGAAGAAATTTACAAGACAG/reverse primer 5′-TGCCGTGTTCACAGTACTCTTC, with an amplicon length of 113 nucleotides. After cDNA synthesis, qRT-PCR was performed using SsoAdvanced Universal SYBR Green Supermix (Bio-Rad) on a MyiQ2 Two-Color Real-Time PCR Detection System (Bio-Rad). Transcript levels were analyzed in triplicate using the C_T (threshold cycle) values. Target transcript levels were normalized to endogenous murine *β-Actin* mRNA, and fold enrichment was measured using the $2^{-\Delta\Delta Ct}$ method.

h*ARG1* mRNA qRT-PCR. Total RNA was diluted to 10 ng/μL in water. LNP-encapsulated mRNA quantification was performed in triplicate with a Taqman RNA-to-CT 1 Step Kit (Thermo Fisher Scientific) per the manufacturer's instructions. For relative quantification of h*ARG1* mRNA, sample mRNA quantification was calculated relative to the Taqman-validated primer/probe pair for the murine *Gapdh* housekeeping gene (catalog no. 4331182, assay ID no. Hs02786624_g1; Thermo Fisher Scientific) using the $2^{-\Delta\Delta Ct}$ method, with ARG1 forward primer: CAAGGACATCGTCTACATCGG/reverse primer: ACCTCGGTCATGGAGAAGTA.

Western Blot. Liver tissue was homogenized, and 50 μg of protein was transferred and coincubated with the target primary arginase antibody (sc-20150; Santa Cruz Biotechnology) and the loading control primary antibody β-tubulin (sc-9104; Santa Cruz Biotechnology), followed by incubation with secondary horseradish peroxidase-conjugated goat anti-rabbit antibody (sc-2004; Santa Cruz Biotechnology). (details are provided in *SI Appendix*).

Statistical Analysis. All collected data were analyzed with the GraphPad Prism8 statistical package. Results were expressed as mean ± SEM, and *P* values were determined using 1-way ANOVA with Tukey's multiple comparison test, 2-way ANOVA with Sidak's multiple comparison test, or an unpaired *t* test when applicable. Error bars represent SEM. $P < 0.05$ was considered significant.

ACKNOWLEDGMENTS. We are grateful for the performance of the amino acid profiles by Drs. Itzhak and Ilana Nissim (Metabolomics Core facility, The Children's Hospital of Philadelphia; https://metabolomic.research.chop.edu/) and for the determination of plasma guanidino acetoacetate by Dr. Qin Sun (Baylor Genetics). We also thank Sarah Pyle for the illustrations included in Fig. 1. The studies were supported by NIH Grant 5 R01 NS100979-03 (to G.S.L.). We acknowledge the use of instruments at the Electron Imaging Center for NanoMachines supported by NIH Grant 1S10RR23057 (to Z. Hong Zhou) and the California NanoSystems Institute at UCLA.

1. M. L. Summar *et al.*; European Registry and Network for Intoxication Type Metabolic Diseases (E-IMD); Members of the Urea Cycle Disorders Consortium (UCDC), The incidence of urea cycle disorders. *Mol. Genet. Metab.* **110**, 179–180 (2013).
2. S. D. Cederbaum *et al.*, Arginases I and II: Do their functions overlap? *Mol. Genet. Metab.* **81** (suppl. 1), S38–S44 (2004).
3. T. Uchino *et al.*, Molecular basis of phenotypic variation in patients with argininemia. *Hum. Genet.* **96**, 255–260 (1995).
4. D. R. Carvalho *et al.*, Clinical features and neurologic progression of hyperargininemia. *Pediatr. Neurol.* **46**, 369–374 (2012).
5. J. L. Deignan *et al.*, Guanidino compound levels in blood, cerebrospinal fluid, and post-mortem brain material of patients with argininemia. *Mol. Genet. Metab.* **100** (suppl. 1), S31–S36 (2010).
6. B. Marescau *et al.*, Guanidino compounds in plasma, urine and cerebrospinal fluid of hyperargininemic patients during therapy. *Clin. Chim. Acta* **146**, 21–27 (1985).
7. N. Mizutani *et al.*, Guanidino compounds in hyperargininemia. *Tohoku J. Exp. Med.* **153**, 197–205 (1987).
8. P. Wiechert *et al.*, Excretion of guanidino-derivates in urine of hyperargininemic patients. *J. Genet. Hum.* **24**, 61–72 (1976).
9. P. Wiechert, B. Marescau, P. P. De Deyn, A. Lowenthal, Hyperargininemia, epilepsy and the metabolism of guanidino compounds. *Padiatr. Grenzgeb.* **28**, 101–106 (1989).
10. J. L. Deignan *et al.*, Increased plasma and tissue guanidino compounds in a mouse model of hyperargininemia. *Mol. Genet. Metab.* **93**, 172–178 (2008).
11. L. C. Burrage *et al.*; Members of Urea Cycle Disorders Consortium, Human recombinant arginase enzyme reduces plasma arginine in mouse models of arginase deficiency. *Hum. Mol. Genet.* **24**, 6417–6427 (2015).
12. E. Santos Silva *et al.*, Liver transplantation in a case of argininaemia. *J. Inherit. Metab. Dis.* **24**, 885–887 (2001).
13. E. S. Silva *et al.*, Liver transplantation prevents progressive neurological impairment in argininemia. *JIMD Rep.* **11**, 25–30 (2013).
14. R. K. Iyer *et al.*, Mouse model for human arginase deficiency. *Mol. Cell. Biol.* **22**, 4491–4498 (2002).
15. C. L. Gau *et al.*, Short-term correction of arginase deficiency in a neonatal murine model with a helper-dependent adenoviral vector. *Mol. Ther.* **17**, 1155–1163 (2009).
16. E. K. Lee *et al.*, Long-term survival of the juvenile lethal arginase-deficient mouse with AAV gene therapy. *Mol. Ther.* **20**, 1844–1851 (2012).
17. C. Hu *et al.*, Myocyte-mediated arginase expression controls hyperargininemia but not hyperammonemia in arginase-deficient mice. *Mol. Ther.* **22**, 1792–1802 (2014).

18. G. S. Lipshutz, R. Sarkar, L. Flebbe-Rehwaldt, H. Kazazian, K. M. Gaensler, Short-term correction of factor VIII deficiency in a murine model of hemophilia A after delivery of adenovirus murine factor VIII in utero. *Proc. Natl. Acad. Sci. U.S.A.* **96**, 13324–13329 (1999).
19. S. DeWeerdt, Prenatal gene therapy offers the earliest possible cure. *Nature* **564**, S6–S8 (2018).
20. C. Hu, G. S. Lipshutz, AAV-based neonatal gene therapy for hemophilia A: Long-term correction and avoidance of immune responses in mice. *Gene Ther.* **19**, 1166–1176 (2012).
21. S. N. Waddington *et al*., Fetal and neonatal gene therapy: Benefits and pitfalls. *Gene Ther.* **11** (suppl. 1), S92–S97 (2004).
22. G. Cantero *et al*., Rescue of the functional alterations of motor cortical circuits in arginase deficiency by neonatal gene therapy. *J. Neurosci.* **36**, 6680–6690 (2016).
23. E. K. Lee *et al*., AAV-based gene therapy prevents neuropathology and results in normal cognitive development in the hyperargininemic mouse. *Gene Ther.* **20**, 785–796 (2013).
24. R. J. Chandler *et al*., Vector design influences hepatic genotoxicity after adeno-associated virus gene therapy. *J. Clin. Invest.* **125**, 870–880 (2015).
25. C. Hu, R. W. Busuttil, G. S. Lipshutz, RH10 provides superior transgene expression in mice when compared with natural AAV serotypes for neonatal gene therapy. *J. Gene Med.* **12**, 766–778 (2010).
26. Z. Wang *et al*., Adeno-associated virus serotype 8 efficiently delivers genes to muscle and heart. *Nat. Biotechnol.* **23**, 321–328 (2005).
27. S. C. Cunningham, A. P. Dane, A. Spinoulas, G. J. Logan, I. E. Alexander, Gene delivery to the juvenile mouse liver using AAV2/8 vectors. *Mol. Ther.* **16**, 1081–1088 (2008).
28. N. Fausto, J. S. Campbell, The role of hepatocytes and oval cells in liver regeneration and repopulation. *Mech. Dev.* **120**, 117–130 (2003).
29. Y. Magami *et al*., Cell proliferation and renewal of normal hepatocytes and bile duct cells in adult mouse liver. *Liver* **22**, 419–425 (2002).
30. S. Ramaswamy *et al*., Systemic delivery of factor IX messenger RNA for protein replacement therapy. *Proc. Natl. Acad. Sci. U.S.A.* **114**, E1941–E1950 (2017).
31. D. An *et al*., Systemic messenger RNA therapy as a treatment for methylmalonic acidemia. *Cell Rep.* **24**, 2520 (2018).
32. M. S. Kormann *et al*., Expression of therapeutic proteins after delivery of chemically modified mRNA in mice. *Nat. Biotechnol.* **29**, 154–157 (2011).
33. T. S. Zatsepin, Y. V. Kotelevtsev, V. Koteliansky, Lipid nanoparticles for targeted siRNA delivery–Going from bench to bedside. *Int. J. Nanomedicine* **11**, 3077–3086 (2016).
34. J. Kasten *et al*., Lethal phenotype in conditional late-onset arginase 1 deficiency in the mouse. *Mol. Genet. Metab.* **110**, 222–230 (2013).
35. M. I. Chung-Bok, M. Watford, Characterization of the hepatic glutaminase promoter. *Contrib. Nephrol.* **121**, 43–47 (1997).
36. W. Amayreh, U. Meyer, A. M. Das, Treatment of arginase deficiency revisited: Guanidinoacetate as a therapeutic target and biomarker for therapeutic monitoring. *Dev. Med. Child Neurol.* **56**, 1021–1024 (2014).
37. A. Jichlinski, L. Clarke, M. T. Whitehead, A. Gropman, "Cerebral palsy" in a patient with arginase deficiency. *Semin. Pediatr. Neurol.* **26**, 110–114 (2018).
38. N. Ah Mew *et al*., "Urea cycle disorders overview" in *GeneReviews*, M. P. Adam *et al*., Eds. (University of Washington, Seattle, 2003).
39. B. L. Therrell, R. Currier, D. Lapidus, M. Grimm, S. D. Cederbaum, Newborn screening for hyperargininemia due to arginase 1 deficiency. *Mol. Genet. Metab.* **121**, 308–313 (2017).
40. R. J. Chandler *et al*., Metabolic phenotype of methylmalonic acidemia in mice and humans: The role of skeletal muscle. *BMC Med. Genet.* **8**, 64 (2007).
41. C. Hu *et al*., Minimal ureagenesis is necessary for survival in the murine model of hyperargininemia treated by AAV-based gene therapy. *Gene Ther.* **22**, 111–115 (2015). Correction in: *Gene Ther.* 22, 216 (2015).
42. S. A. K. Angarita *et al*., Human hepatocyte transplantation corrects the inherited metabolic liver disorder arginase deficiency in mice. *Mol. Genet. Metab.* **124**, 114–123 (2018).
43. E. K. Hsu *et al*., Analysis of liver offers to pediatric candidates on the transplant wait list. *Gastroenterology* **153**, 988–995 (2017).
44. C. Gustafsson, S. Govindarajan, J. Minshull, Codon bias and heterologous protein expression. *Trends Biotechnol.* **22**, 346–353 (2004).
45. D. An *et al*., Systemic messenger RNA therapy as a treatment for methylmalonic acidemia. *Cell Rep.* **21**, 3548–3558 (2017).
46. S. Khoja *et al*., Conditional disruption of hepatic carbamoyl phosphate synthetase 1 in mice results in hyperammonemia without orotic aciduria and can be corrected by liver-directed gene therapy. *Mol. Genet. Metab.* **124**, 243–253 (2018).
47. Q. Sun, W. E. O'Brien, Diagnosis of creatine metabolism disorders by determining creatine and guanidinoacetate in plasma and urine. *Methods Mol. Biol.* **603**, 175–185 (2010).
48. G. Allegri *et al*., A simple dried blood spot-method for in vivo measurement of ureagenesis by gas chromatography-mass spectrometry using stable isotopes. *Clin. Chim. Acta* **464**, 236–243 (2017).

Contains Nonbinding Recommendations

Development and Licensure of Vaccines to Prevent COVID-19

Guidance for Industry

U.S. Department of Health and Human Services
Food and Drug Administration
Center for Biologics Evaluation and Research
June 2020

Preface

Public Comment

This guidance is being issued to address the coronavirus disease 2019 (COVID-19) public health emergency. This guidance is being implemented without prior public comment because the Food and Drug Administration (FDA or Agency) has determined that prior public participation for this guidance is not feasible or appropriate (see section 701(h)(1)(C) of the Federal Food, Drug, and Cosmetic Act (FD&C Act) (21 U.S.C. 371(h)(1)(C)) and 21 CFR 10.115(g)(2)). This guidance document is being implemented immediately, but it remains subject to comment in accordance with the Agency's good guidance practices.

Comments may be submitted at any time for Agency consideration. Submit written comments to the Dockets Management Staff (HFA-305), Food and Drug Administration, 5630 Fishers Lane, Rm. 1061, Rockville, MD 20852. Submit electronic comments to https://www.regulations.gov. All comments should be identified with the docket FDA-2020-D-1137 and complete title of the guidance in the request.

Additional Copies

Additional copies are available from the FDA webpage titled "COVID-19-Related Guidance Documents for Industry, FDA Staff, and Other Stakeholders," *available at* https://www.fda.gov/emergency-preparedness-and-response/mcm-issues/covid-19-related-guidance-documents-industry-fda-staff-and-other-stakeholders, the FDA webpage titled "Search for FDA Guidance Documents," *available at* https://www.fda.gov/regulatory-information/search-fda-guidance-documents, and the FDA webpage titled "Biologics Guidances," *available at* https://www.fda.gov/vaccines-blood-biologics/guidance-compliance-regulatory-information-biologics/biologics-guidances. You may also send an email request to ocod@fda.hhs.gov to receive an additional copy of the guidance. Please include the docket number FDA-2020-D-1137 and complete title of the guidance in the request.

Questions

For questions about this document, contact the Office of Communication, Outreach, and Development (OCOD) by email at ocod@fda.hhs.gov or at 800-835-4709 or 240-402-8010.

Table of Contents

Contains Nonbinding Recommendations

Development and Licensure of Vaccines to Prevent COVID-19

Guidance for Industry

This guidance represents the current thinking of the Food and Drug Administration (FDA or Agency) on this topic. It does not establish any rights for any person and is not binding on FDA or the public. You can use an alternative approach if it satisfies the requirements of the applicable statutes and regulations. To discuss an alternative approach, contact the FDA staff responsible for this guidance as listed on the title page.

I. INTRODUCTION

FDA plays a critical role in protecting the United States from threats such as emerging infectious diseases, including the Coronavirus Disease 2019 (COVID-19) pandemic which has been caused by the severe acute respiratory syndrome coronavirus 2 (SARS-CoV-2). FDA is committed to providing timely guidance to support response efforts to this pandemic.

FDA is issuing this guidance to assist sponsors in the clinical development and licensure of vaccines for the prevention of COVID-19.

This guidance is intended to remain in effect for the duration of the public health emergency related to COVID-19 declared by the Secretary of Health and Human Services (HHS) on January 31, 2020, effective January 27, 2020, including any renewals made by the HHS Secretary in accordance with section 319(a)(2) of the Public Health Service Act (PHS Act) (42 U.S.C. 247d(a)(2)). The recommendations described in the guidance are expected to assist the Agency and sponsors in the clinical development and licensure of vaccines for the prevention of COVID-19 and reflect the Agency's current thinking on this issue.

Given this public health emergency, and as discussed in the Notice in the *Federal Register* of March 25, 2020, titled "Process for Making Available Guidance Documents Related to Coronavirus Disease 2019" (85 FR 16949), *available at* https://www.govinfo.gov/content/pkg/FR-2020-03-25/pdf/2020-06222.pdf, this guidance is being implemented without prior public comment because FDA has determined that prior public participation for this guidance is not feasible or appropriate (see section 701(h)(1)(C) of the Federal Food, Drug, and Cosmetic Act (FD&C Act), (21 U.S.C. 371(h)(1)(C)), and 21 CFR 10.115(g)(2)). This guidance document is being implemented immediately, but it remains subject to comment in accordance with the Agency's good guidance practices. However, FDA expects that the recommendations set forth in this revised guidance will continue to apply outside the context of the current public health emergency.

Therefore, within 60 days following the termination of the public health emergency, FDA intends to revise and replace this guidance with an updated guidance that incorporates any appropriate changes based on comments received on this guidance and the Agency's experience with implementation.

In general, FDA's guidance documents, including this guidance, do not establish legally enforceable responsibilities. Instead, guidances describe the Agency's current thinking on a topic and should be viewed only as recommendations, unless specific regulatory or statutory requirements are cited. The use of the word *should* in Agency guidance means that something is suggested or recommended, but not required.

II. BACKGROUND

There is currently an outbreak of respiratory disease caused by a novel coronavirus. The virus has been named "SARS-CoV-2" and the disease it causes has been named "COVID-19." On January 31, 2020, the Secretary of HHS issued a declaration of a public health emergency related to COVID-19 and mobilized the Operating Divisions of HHS.[1] In addition, on March 13, 2020, the President declared a national emergency in response to COVID-19.[2]

The SARS-CoV-2 pandemic presents an extraordinary challenge to global health. There are currently no FDA-licensed vaccines to prevent COVID-19. Commercial vaccine manufacturers and other entities are developing COVID-19 vaccine candidates using different technologies including RNA, DNA, protein, and viral vectored vaccines.

This guidance describes FDA's current recommendations regarding the data needed to facilitate clinical development and licensure of vaccines to prevent COVID-19. There are currently no accepted surrogate endpoints that are reasonably likely to predict clinical benefit of a COVID-19 vaccine. Thus, at this time, the goal of development programs should be to pursue traditional approval via direct evidence of vaccine safety and efficacy in protecting humans from SARS-CoV-2 infection and/or clinical disease.

This guidance provides an overview of key considerations to satisfy regulatory requirements set forth in the investigational new drug application (IND) regulations in 21 CFR Part 312 and licensing regulations in 21 CFR Part 601 for chemistry, manufacturing, and controls (CMC), and nonclinical and clinical data through development and licensure, and for post-licensure safety evaluation of COVID-19 preventive vaccines.[3] FDA is committed to supporting all scientifically sound approaches to attenuating the clinical impact of COVID-19. Sponsors engaged in the development of vaccines to prevent COVID-19 should also see the guidance for industry and investigators, *COVID-19 Public Health Emergency: General Considerations for Pre-IND Meeting Requests for COVID-19 Related Drugs and Biological Products* (Ref. 1).

---

[1] Secretary of Health and Human Services Alex M. Azar, Determination that a Public Health Emergency Exists. (Jan. 31, 2020, renewed April 21, 2020), *available at* https://www.phe.gov/emergency/news/healthactions/phe/Pages/default.aspx.

[2] Proclamation on Declaring a National Emergency Concerning the Novel Coronavirus Disease (COVID-19) Outbreak (Mar. 13, 2020), *available at* https://www.whitehouse.gov/presidential-actions/proclamation-declaring-national-emergency-concerning-novel-coronavirus-disease-covid-19-outbreak/.

[3] Novel devices used to administer COVID-19 vaccines raise additional issues which are not addressed in this guidance.

There are many COVID-19 vaccines currently in development and FDA recognizes that the considerations presented here do not represent all the considerations necessary to satisfy statutory and regulatory requirements applicable to the licensure of vaccines intended to prevent COVID-19. The nature of a particular vaccine and its intended use may impact specific data needs. We encourage sponsors to contact the Center for Biologics Evaluation and Research (CBER) Office of Vaccines Research and Review (OVRR) with specific questions.

III. CHEMISTRY, MANUFACTURING, AND CONTROLS – KEY CONSIDERATIONS

A. General Considerations

- COVID-19 vaccines licensed in the United States must meet the statutory and regulatory requirements for vaccine development and approval, including for quality, development, manufacture, and control (section 351(a) of the Public Health Service Act (PHS Act), (42 U.S.C. 262)). The vaccine product must be adequately characterized and its manufacture in compliance with applicable standards including current good manufacturing practice (cGMP) (section 501(a)(2)(B) of the FD&C Act (21 U.S.C. 351(a)(2)(B)) and 21 CFR Parts 210, 211, and 610). It is critical that vaccine production processes for each vaccine are well defined and appropriately controlled to ensure consistency in manufacturing.

- COVID-19 vaccine development may be accelerated based on knowledge gained from similar products manufactured with the same well-characterized platform technology, to the extent legally and scientifically permissible. Similarly, with appropriate justification, some aspects of manufacture and control may be based on the vaccine platform, and in some instances, reduce the need for product-specific data. FDA recommends that vaccine manufacturers engage in early communications with OVRR to discuss the type and extent of chemistry, manufacturing, and control information needed for development and licensure of their COVID-19 vaccine.

B. Manufacture of Drug Substance and Drug Product

- Data should be provided to show that all source material used in manufacturing is adequately controlled, including, for example, history and qualification of cell banks, history and qualification of virus banks, and identification of all animal derived materials used for cell culture and virus growth.

- Complete details of the manufacturing process must be provided in a Biologics License Application (BLA) to support licensure of a COVID-19 vaccine (21 CFR 601.2). Accordingly, sponsors should submit data and information identifying critical process parameters, critical quality attributes, batch records, defined hold times, and the in-process testing scheme. Specifications should be established for

each critical parameter. Validation data from the manufacture of platform-related products may provide useful supportive information, particularly in the identification of critical parameters.

- In-process control tests must be established that allow quality to be monitored for each lot for all stages of production (section 501(a)(2)(B) of the FD&C Act (21 U.S.C. 351(a)(2)(B)) and, as applicable, 21 CFR 211.110(a)).

- Data to support the consistency of the manufacturing process should be provided, including process validation protocols and study reports, data from engineering lots, and drug substance process performance qualification.

- The manufacturing process must be adequately validated (section 501(a)(2)(B) of the FD&C Act (21 U.S.C. 351(a)(2)(B)) and, as applicable, 21 CFR 211.100(a) and 211.110). Validation would typically include a sufficient number of commercial-scale batches that can be manufactured routinely, meeting predetermined in-process controls, critical process parameters, and lot release specifications. Typically, data on the manufacture of at least three commercial-scale batches are sufficient to support the validation of the manufacturing process (Ref. 2).

- A quality control system should be in place for all stages of manufacturing, including a well-defined testing program to ensure in process/intermediate product quality and product quality throughout the formulation and filling process. This system should also include a well-defined testing program to ensure drug substance quality profile and drug product quality for release. Data on the qualification/validation for all quality indicating assays should be submitted to the BLA to support licensure.

- All quality-control release tests, including key tests for vaccine purity, identity and potency, should be validated and shown to be suitable for the intended purpose. Release specifications are product specific and will be discussed with the sponsor as part of the review of a BLA.

- If adequately justified, final validation of formulation and filling operations may be completed after product approval if the impact on product quality is not compromised. It is important that any data that will be submitted after product approval be agreed upon prior to licensure and be submitted as a postmarketing commitment using the appropriate submission category.

- For vaccine licensure, the stability and expiry date of the vaccine in its final container, when maintained at the recommended storage temperature, should be demonstrated using final containers from at least three final lots made from different vaccine bulks.

- Storage conditions, including container closure integrity, must be fully validated (21 CFR 211.166).

- The vaccine must have been shown to maintain its potency for a period equal to that from the date of release to the expiry date (21 CFR 601.2 and 610.10). Post marketing commitments to provide full shelf life data may be acceptable with appropriate justification.

- A product specific stability program should be established to verify that licensed product maintains quality over the defined shelf life.

C. Facilities and Inspections

- Facilities must be of suitable size and construction to facilitate operations and should be adequately designed to prevent contamination, cross-contamination and mix-ups (section 501(a)(2)(B) of the FD&C Act (21 U.S.C. 351(a)(2)(B)) and, as applicable,21 CFR 211.42(a)). All utilities (including plumbing and sanitation) must be validated, and HVAC systems must provide adequate control over air pressure, micro-organisms, dust, humidity, and temperature, and sufficient protection or containment as needed (section 501(a)(2)(B) of the FD&C Act (21 U.S.C. 351(a)(2)(B)) and, as applicable, 21 CFR 211.46(c)) (Ref. 3). Facility and equipment cleaning and maintenance processes must be developed and validated (section 501(a)(2)(B) of the FD&C Act (21 U.S.C. 351(a)(2)(B)) and, as applicable, 21 CFR 211.56(c) and 211.67(b)).

- Manufacturing equipment should be qualified and sterile filtration and sterilization processes validated. Aseptic processes should be adequately validated using media simulations and personnel should be trained and qualified for their intended duties.

- A quality control unit must be established and must have the responsibility for oversight of manufacturing, and review and release of components, containers and closures, labeling, in-process material, and final products (section 501(a)(2)(B) of the FD&C Act (21 U.S.C. 351(a)(2)(B)) and, as applicable, 21 CFR 211.22). The quality control unit must have the responsibility for approving validation protocols, reports, investigate deviations, and institute corrective and preventive actions.

- FDA recommends that vaccine manufacturers engage in early communication with CBER's Office of Compliance and Biologics Quality, Division of Manufacturing and Product Quality to discuss facility preparation and inspection timing.

- Pre-license inspections of manufacturing sites are considered part of the review of a BLA and are generally conducted following the acceptance of a BLA filing (21 CFR 601.20). During the COVID-19 public health emergency, FDA is utilizing all available tools and sources of information to support regulatory decisions on applications that include sites impacted by FDA's ability to inspect due to COVID-19. During this interim period, we are using additional tools, where available, to determine the need for an on-site inspection and to support the

application assessment, such as reviewing a firm's previous compliance history, and requesting records in advance of or in lieu of on-site inspections or voluntarily from facilities and sites.

IV. NONCLINICAL DATA – KEY CONSIDERATIONS

A. General Considerations

- The purpose of nonclinical studies of a COVID-19 vaccine candidate is to define its immunogenicity and safety characteristics through *in vitro* and *in vivo* testing. Nonclinical studies in animal models[4] help identify potential vaccine related safety risks and guide the selection of dose, dosing regimen, and route of administration to be used in clinical studies. The extent of nonclinical data required to support proceeding to first in human (FIH) clinical trials depends on the vaccine construct, the supportive data available for the construct and data from closely related vaccines.

- Data from studies in animal models administered certain vaccine constructs against other coronaviruses (SARS-CoV and MERS-CoV) have raised concerns of a theoretical risk for COVID-19 vaccine-associated enhanced respiratory disease (ERD). In these studies, animal models were administered vaccine constructs against other coronaviruses and subsequently challenged with the respective wild-type virus. These studies have shown evidence of immunopathologic lung reactions characteristic of a Th-2 type hypersensitivity similar to ERD described in infants and animals that were administered formalin-inactivated respiratory syncytial virus (RSV) vaccine and that were subsequently challenged with RSV virus due to natural exposure or in the laboratory, respectively (Refs. 4-9). Vaccine candidates should be assessed in light of these studies as described in section D, below.

- FDA recommends that vaccine manufacturers engage in early communications with FDA to discuss the type and extent of nonclinical testing required for the particular COVID-19 vaccine candidate to support proceeding to FIH clinical trials and further clinical development.

B. Toxicity Studies (Refs. 10-14)

- For a COVID-19 vaccine candidate consisting of a novel product type and for which no prior nonclinical and clinical data are available, nonclinical safety studies will be required prior to proceeding to FIH clinical trials 21 CFR 312.23(a)(8).

[4] The preclinical program for any investigational product should be individualized with respect to scope, complexity, and overall design. We support the principles of the "3Rs," to reduce, refine, and replace animal use in testing when feasible. Proposals, with justification for any potential alternative approaches (e.g., in vitro or in silico testing), should be submitted during early communication meetings with FDA (see section VI of this document). We will consider if such an alternative method could be used in place of an animal test method.

- In some cases, it may not be necessary to perform nonclinical safety studies prior to FIH clinical trials because adequate information to characterize product safety may be available from other sources. For example, if the COVID-19 vaccine candidate is made using a platform technology utilized to manufacture a licensed vaccine or other previously studied investigational vaccines and is sufficiently characterized, it may be possible to use toxicology data (e.g., data from repeat dose toxicity studies, biodistribution studies) and clinical data accrued with other products using the same platform to support FIH clinical trials for that COVID-19 vaccine candidate. Vaccine manufacturers should summarize the findings and provide a rationale if considering using these data in lieu of performing nonclinical safety studies.

- When needed to support proceeding to FIH clinical trials, nonclinical safety assessments including toxicity and local tolerance studies must be conducted under conditions consistent with regulations prescribing good laboratory practices for conducting nonclincial laboratory studies (GLP) (21 CFR Part 58). Such studies should be completed and analysed prior to initiation of FIH clinical trials. When toxicology studies do not adequately characterize risk, additional safety testing should be conducted as appropriate.

- Data from toxicity studies may be submitted as unaudited final draft toxicicologic reports to accelerate proceeding to FIH clincial trials with COVID-19 vaccine candidates. The final, fully quality-assured reports should be available to FDA within 120 days of the start of the FIH clinical trial.

- Use of COVID-19 preventive vaccines in pregnancy and in women of childbearing potential will be an important consideration for vaccination programs. Therefore, FDA recommends that prior to enrolling pregnant women and women of childbearing potential who are not actively avoiding pregnancy in clinical trials, sponsors conduct developmental and reproductive toxicity (DART) studies with their respective COVID-19 vaccine candidate. Alternatively, sponsors may submit available data from DART studies with a similar product using comparable platform technology if, after consultation with the agency, the agency agrees those data are scientifically sufficient.

- Biodistribution studies in an animal species should be considered if the vaccine construct is novel in nature and there are no existing biodistribution data from the platform technology. These studies should be conducted if there is a likelihood of altered infectivity and tissue tropism or if a novel route of administration and formulation is to be used.

C. Characterization of the Immune Response in Animal Models

- Immunogenicity studies in animal models responsive to the selected COVID-19 vaccine antigen should be conducted to evaluate the immunologic properties of the COVID-19 vaccine candidate and to support FIH clinical trials. The aspects of

immunogenicity to be measured should be appropriate for the vaccine construct and its intended mechanism of action.

- Studies should include an evaluation of humoral, cellular, and functional immune responses, as appropriate to each of the included COVID-19 antigens. Use of antigen-specific enyzme linked immunosorbent assays (ELISA) should be considered to characterize the humoral response. Evaluation of cellular reponses should include the examination of CD8+ and CD4+ T cell responses using sensitive and specific assays. The functional activity of immune responses should be evaluated *in vitro* in neutralization assays using either wild-type virus or pseudovirion virus. The assays used for immunogencity evaluation should be demonstrated to be suitable for their intended purpose.

D. Studies to Address the Potential for Vaccine-associated Enhanced Respiratory Disease

- Current knowledge and understanding of the potential risk of COVID-19 vaccine associated ERD is limited, as is understanding of the value of available animal models in predicting the likelihood of such occurrence in humans. Nevertheless, studies in animal models (e.g., rodents and non-human primates) are considered important to address the potential for vaccine-associated ERD.

- Post-vaccination animal challenge studies and the characterization of the type of the nonclinical and clinical immune response induced by the particular COVID-19 vaccine candidate can be used to evaluate the likelihood of the vaccine to induce vaccine-associated ERD in humans.

- To support proceeding to FIH clinical trials, sponsors should conduct studies characterizing the vaccine-induced immune response in animal models evaluating immune markers of potential ERD outcomes. These should include assessments of functional immune responses (e.g., neutralizing antibody) versus total antibody responses and Th1/Th2 balance in animals vaccinated with clinically relevant doses of the COVID-19 vaccine candidate.

- COVID-19 vaccine candidates with immunogenicity data demonstrating high neutralizing antibody titers and Th1-type T cell polarization may be allowed to proceed to FIH trials without first completing postvaccination challenge studies in appropriate animal models, provided adequate risk mitigation strategies are put in place in the FIH trials. In these situations, postvaccination challenge studies are expected to be conducted in parallel with FIH trials to ensure the potential for vaccine-associated ERD is addressed prior to enrolling large numbers of human subjects into Phase 2 and 3 clinical trials. For COVID-19 vaccine candidates for which other data raise increased concerns about ERD, postvaccination animal challenge data and/or animal immunopathology studies are critical to assess protection and/or ERD *prior* to advancing to FIH clinical trials.

- The totality of data for a specific COVID-19 vaccine candidate, including data from postvaccination challenge studies in small animal models and from FIH clinical trials characterizing the type of immune responses induced by the vaccine will be considered in determining whether Phase 3 studies can proceed in the absence of postvaccination challenge data to address risk of ERD.

V. CLINICAL TRIALS – KEY CONSIDERATIONS

A. General Considerations

- Understanding of SARS-CoV-2 immunology, and specifically vaccine immune responses that might predict protection against COVID-19, is currently limited and evolving. Thus, while evaluation of immunogenicity is an important component of COVID-19 vaccine development, at this time, the goal of development programs should be to pursue traditional approval via direct evidence of vaccine efficacy in protecting humans from SARS-CoV-2 infection and/or disease.

- Clinical development programs for COVID-19 vaccines might be expedited by adaptive and/or seamless clinical trial designs (described below) that allow for selection between vaccine candidates and dosing regimens and for more rapid progression through the usual phases of clinical development.

- Regardless of whether clinical development programs proceed in discrete phases with separate studies or via a more seamless approach, an adequate body of data, including data to inform the risk of vaccine-associated ERD, will be needed as clinical development progresses to support the safety of vaccinating the proposed study populations and number of participants and, for later stage development, to ensure that the study design is adequate to meet its objectives.

- FDA can provide early advice, and potentially concurrence in principle, on plans for expedited/seamless clinical development. However, sponsors should plan to submit summaries of data available at each development milestone for FDA review and concurrence prior to advancing to the next phase of development.

- Conducting clinical trials in the setting of a public health emergency presents operational challenges. FDA has issued guidance to provide general considerations to assist sponsors in assuring the safety of trial participants, maintaining compliance with good clinical practice (GCP), and minimizing risks to trial integrity for the duration of the COVID-19 public health emergency. It should be noted that not all of the recommendations in that guidance may be applicable to vaccine development, given some of the different considerations for these products (Ref. 15).

B. Trial Populations

- Once acceptable pre-clinical data are available, FIH and other early phase studies (which typically expose 10–100 participants to each vaccine candidate being evaluated) should first enroll healthy adult participants who are at low risk of severe COVID-19. Exclusion of participants at higher risk of severe COVID-19 from early phase studies is necessary to mitigate potential risk of vaccine-associated ERD until additional data to inform that potential risk becomes available through ongoing product development.

    - As the understanding of COVID-19 pathogenesis continues to evolve, exclusion criteria should reflect the current understanding of risk factors for more severe COVID-19, such as those described by the Centers for Disease Control and Prevention (Ref. 16).

    - Older adult participants (e.g., over 55 years of age) may be enrolled in FIH and other early phase studies so long as they do not have medical comorbidities associated with an increased risk of severe COVID-19. Some preliminary safety data in younger adults (e.g., 7 days after a single vaccination) should be available prior to enrolling older adult participants, especially for vaccine platforms without prior clinical experience.

    - If possible, early clinical studies should also exclude participants at high risk of SARS-CoV-2 exposure (e.g., healthcare workers).

- Sponsors should collect and evaluate at least preliminary clinical safety and immunogenicity data for each dose level and age group (e.g., younger versus older adults) to support progression of clinical development to include larger numbers (e.g., hundreds) of participants and participants at higher risk of severe COVID-19.

    - Preliminary immunogenicity data from early phase development should include assessments of neutralizing vs. total antibody responses and Th1 vs. Th2 polarization.

    - Additional data to further inform potential risk of vaccine-associated ERD and to support progression of clinical development, if available, may include preliminary evaluation of COVID-19 disease outcomes from earlier clinical development and results of non-clinical studies evaluating protection and/or histopathological markers of vaccine-associated ERD following SARS-CoV-2 challenge.

- To generate sufficient data to meet the BLA approval standard, late phase clinical trials to demonstrate vaccine efficacy with formal hypothesis testing will likely need to enroll many thousands of participants, including many with medical comorbidities for trials seeking to assess protection against severe COVID-19.

    - Initiation of late phase trials should be preceded by adequate characterization of safety and immunogenicity (e.g., in a few hundred participants for each

vaccine candidate, dose level, and age group to be evaluated) to support general safety, potential for vaccine efficacy, and low risk of vaccine-associated ERD.

- Results of non-clinical studies evaluating protection and/or histopathological markers of vaccine-associated ERD following SARS-CoV-2 challenge and COVID-19 disease outcomes from earlier clinical development are other potentially important sources of information to support clinical trials with thousands of participants.

- Although establishing vaccine safety and efficacy in SARS-CoV-2 naïve individuals is critical, vaccine safety and COVID-19 outcomes in individuals with prior SARS-CoV-2 infection, which might have been asymptomatic, is also important to examine because pre-vaccination screening for prior infection is unlikely to occur in practice with the deployment of licensed COVID-19 vaccines. Therefore, COVID-19 vaccine trials need not screen for or exclude participants with history or laboratory evidence of prior SARS-CoV-2 infection. However, individuals with acute COVID-19 (or other acute infectious illness) should be excluded from COVID-19 vaccine trials.

- FDA encourages the inclusion of diverse populations in all phases of vaccine clinical development. This inclusion helps to ensure that vaccines are safe and effective for everyone in the indicated populations.

  - FDA strongly encourages the enrollment of populations most affected by COVID-19, specifically racial and ethnic minorities.

  - Evaluation of vaccine safety and efficacy in late phase clinical development in adults should include adequate representation of elderly individuals and individuals with medical comorbidities.

  - FDA encourages vaccine developers to consider early in their development programs data that might support inclusion of pregnant women and women of childbearing potential who are not actively avoiding pregnancy in pre-licensure clinical trials (Ref. 17).

  - It is important for developers of COVID-19 vaccines to plan for pediatric assessments of safety and effectiveness, given the nature of the COVID-19 public health emergency, and to help ensure compliance with the Pediatric Research Equity Act (PREA) (section 505B of the FD&C Act (21 U.S.C. 355c)) (Ref. 18). The epidemiology and pathogenesis of COVID-19, and the safety and effectiveness of COVID-19 vaccines, may be different in children compared with adults. In order to ensure compliance with 21 CFR Part 50 Subpart D (Additional safeguards for children in clinical investigations), considerations on the prospect of direct benefit and acceptable risk to support initiation of pediatric studies, and the appropriate design and endpoints for pediatric studies, should be discussed in the context of specific vaccine development programs.

C. Trial Design

- Early phase trials often aim to down-select among multiple vaccine candidates and/or dosing regimens via randomization of participants to different treatment groups. While including a placebo control and blinding are not required for early phase studies, doing so may assist in interpretation of preliminary safety data.

- Later phase trials, including efficacy trials, should be randomized, double-blinded, and placebo controlled.

    - An individually randomized controlled trial with 1:1 randomization between vaccine and placebo groups is usually the most efficient study design for demonstrating vaccine efficacy. Other types of randomization, such as cluster randomization, may be acceptable but require careful consideration of potential biases that are usually avoided with individual randomization.

    - An efficacy trial that evaluates multiple vaccine candidates against a single placebo group may be an acceptable approach to further increase efficiency, provided that the trial is adequately designed with appropriate statistical methods to evaluate efficacy.

    - If the availability of a COVID-19 vaccine proven to be safe and effective precludes ethical inclusion of a placebo control group, that vaccine could serve as the control treatment in a study designed to evaluate efficacy with non-inferiority hypothesis testing.

- Protocols for adaptive trials should include pre-specified criteria for adding or removing vaccine candidates or dosing regimens, and protocols for seamless trials should include pre-specified criteria (e.g., safety and immunogenicity data) for advancing from one phase of the study to the next.

- Follow-up of study participants for COVID-19 outcomes (in particular, for severe COVID-19 disease manifestations) should continue as long as feasible, ideally at least one to two years, to assess duration of protection and potential for vaccine-associated ERD as immune responses to the vaccine wane.

- Efficacy trials should include contingency plans for continued follow up and analysis of safety and effectiveness outcomes in the event that a safe and effective vaccine becomes available (e.g., as demonstrated in a planned interim analysis or as demonstrated in another clinical trial). In that case, discussion with the agency may be necessary to address ethical arguments to break the blind and offer vaccine to placebo recipients.

- In cases where statistical equivalency testing of vaccine immune responses in humans is required to support manufacturing consistency (clinical lot-to-lot consistency trial), this testing can be incorporated into the design of an efficacy trial and does not need to be conducted in a separate study.

D. Efficacy Considerations

- Either laboratory-confirmed COVID-19 or laboratory-confirmed SARS-CoV-2 infection is an acceptable primary endpoint for a COVID-19 vaccine efficacy trial.

  - Acute cases of COVID-19 should be virologically confirmed (e.g., by RT-PCR).

  - SARS-CoV-2 infection, including asymptomatic infection, can be monitored for and confirmed either by virologic methods or by serologic methods evaluating antibodies to SARS-CoV-2 antigens not included in the vaccine.

- Standardization of efficacy endpoints across clinical trials may facilitate comparative evaluation of vaccines for deployment programs, provided that such comparisons are not confounded by differences in trial design or study populations. To this end, FDA recommends that either the primary endpoint or a secondary endpoint (with or without formal hypothesis testing) be defined as virologically confirmed SARS-CoV-2 infection with one or more of the following symptoms:

  - Fever or chills
  - Cough
  - Shortness of breath or difficulty breathing
  - Fatigue
  - Muscle or body aches
  - Headache
  - New loss of taste or smell
  - Sore throat
  - Congestion or runny nose
  - Nausea or vomiting
  - Diarrhea

- As it is possible that a COVID-19 vaccine might be much more effective in preventing severe versus mild COVID-19, sponsors should consider powering efficacy trials for formal hypothesis testing on a severe COVID-19 endpoint. Regardless, severe COVID-19 should be evaluated as a secondary endpoint (with or without formal hypothesis testing) if not evaluated as a primary endpoint. FDA recommends that severe COVID-19 be defined as virologically confirmed SARS-CoV-2 infection with any of the following:

  - Clinical signs at rest indicative of severe systemic illness (respiratory rate $\geq$ 30 per minute, heart rate $\geq$ 125 per minute, SpO2 $\leq$ 93% on room air at sea level or PaO2/FiO2 < 300 mm Hg)
  - Respiratory failure (defined as needing high-flow oxygen, noninvasive ventilation, mechanical ventilation or ECMO)
  - Evidence of shock (SBP < 90 mm Hg, DBP < 60 mm Hg, or requiring vasopressors)
  - Significant acute renal, hepatic, or neurologic dysfunction

- Admission to an ICU
- Death

- SARS-CoV-2 infection (whether or not symptomatic) should be evaluated as a secondary or exploratory endpoint, if not evaluated as a primary endpoint.

- The above diagnostic criteria may need to be modified in certain populations; for example, in pediatric patients and those with respiratory comorbidities. Sponsors should discuss their proposed case definitions with the Agency prior to initiating enrollment.

E. Statistical Considerations

- To ensure that a widely deployed COVID-19 vaccine is effective, the primary efficacy endpoint point estimate for a placebo-controlled efficacy trial should be at least 50%, and the statistical success criterion should be that the lower bound of the appropriately alpha-adjusted confidence interval around the primary efficacy endpoint point estimate is >30%.

  - The same statistical success criterion should be used for any interim analysis designed for early detection of efficacy.

  - A lower bound ≤30% but >0% may be acceptable as a statistical success criterion for a secondary efficacy endpoint, provided that secondary endpoint hypothesis testing is dependent on success on the primary endpoint.

- For non-inferiority comparison to a COVID-19 vaccine already proven to be effective, the statistical success criterion should be that the lower bound of the appropriately alpha-adjusted confidence interval around the primary relative efficacy point estimate is >-10%.

- For each vaccine candidate, appropriate statistical methods should be used to control type 1 error for hypothesis testing on multiple endpoints and/or interim efficacy analyses.

- Late phase studies should include interim analyses to assess risk of vaccine-associated ERD (see section F) and futility.

- Study sample sizes and timing of interim analyses should be based on the statistical success criteria for primary and secondary (if applicable) efficacy analyses and realistic, data-driven estimates of vaccine efficacy and incidence of COVID-19 (or SARS-CoV-2 infection) for the populations and locales in which the trial will be conducted.

F. Safety Considerations

- The general safety evaluation of COVID-19 vaccines, including the size of the safety database to support vaccine licensure, should be no different than for other preventive vaccines for infectious diseases. Safety assessments throughout clinical development should include:

  - Solicited local and systemic adverse events for at least 7 days after each study vaccination in an adequate number of study participants to characterize reactogenicity (including at least a subset of participants in late phase efficacy trials).

  - Unsolicited adverse events in all study participants for at least 21–28 days after each study vaccination.

  - Serious and other medically attended adverse events in all study participants for at least 6 months after completion of all study vaccinations. Longer safety monitoring may be warranted for certain vaccine platforms (e.g., those that include novel adjuvants).

  - All pregnancies in study participants for which the date of conception is prior to vaccination or within 30 days after vaccination should be followed for pregnancy outcomes, including pregnancy loss, stillbirth, and congenital anomalies.

- The pre-licensure safety database for preventive vaccines for infectious diseases typically consists of at least 3,000 study participants vaccinated with the dosing regimen intended for licensure. FDA anticipates that adequately powered efficacy trials for COVID-19 vaccines will be of sufficient size to provide an acceptable safety database for each of younger adult and elderly populations, provided that no significant safety concerns arise during clinical development that would warrant further pre-licensure evaluation.

- COVID-19 vaccine trials should periodically monitor for unfavorable imbalances between vaccine and control groups in COVID-19 disease outcomes, in particular for cases of severe COVID-19 that may be a signal for vaccine-associated ERD.

  - Studies should include pre-specified criteria for halting based on signals of potential vaccine-associated ERD.

  - FDA recommends use of an independent data safety monitoring board (DSMB) (Ref. 18) for vaccine-associated ERD and other safety signal monitoring, especially during later stage development.

VI. POST-LICENSURE SAFETY EVALUATION – KEY CONSIDERATIONS

A. General Considerations

- As with all licensed vaccines, there can be limitations in the safety database accrued from the pre-licensure clinical studies of a COVID-19 vaccine. For example:
    - The number of subjects receiving a COVID-19 vaccine in pre-licensure clinical studies may not be adequate to detect some adverse reactions that may occur infrequently.
    - Pre-licensure safety data in some subpopulations likely to receive a COVID-19 vaccine (e.g., pregnant individuals, or individuals with medical comorbidities) may be limited at the time of licensure.
    - For some COVID-19 vaccines, the safety follow-up period to monitor for possible vaccine-associated ERD and other adverse reactions may not have been completed for all subjects enrolled in pre-licensure clinical studies before the vaccine is licensed.

- For COVID-19 vaccines, it is likely that during the early postmarketing period, a large population might be vaccinated in a relatively short timeframe. Thus, FDA recommends early planning of pharmacovigilance activities before licensure.

- To facilitate accurate recording and identification of vaccines in health records, manufacturers should consider establishment of individual Current Procedural Terminology (CPT) codes and the use of bar codes to label the immediate container.

B. Pharmacovigilance Activities for COVID-19 Vaccines

- Routine pharmacovigilance for licensed biological products includes expedited reporting of serious and unexpected adverse events as well as periodic safety reports in accordance with 21 CFR 600.80 (Postmarketing reporting of adverse experiences).

- FDA recommends that at the time of a BLA submission for a COVID-19 vaccine, applicants submit a Pharmacovigilance Plan (PVP) as described in the FDA Guidance for Industry; E2E Pharmacovigilance Planning (Ref. 20). The contents of a PVP for a COVID-19 vaccine will depend on its safety profile and will be based on data, which includes the pre-licensure clinical safety database, preclinical data, and available safety information for related vaccines, among other considerations.

- The PVP should include actions designed to address all important identified risks, important potential risks or important missing information. Pharmacoepidemiologic studies or other actions to evaluate notable potential risks, such as vaccine-associated ERD, should be considered. FDA may recommend one or more of the following as components of a PVP for a COVID-19 vaccine:

- Submission of reports of specific adverse events of interest in an expedited manner beyond routine required reporting;
- Submission of adverse event report summaries at more frequent intervals than specified for routine required reporting;
- Ongoing and/or extended safety follow-up (under an IND) for vaccine-associated ERD of subjects enrolled in pre-licensure clinical studies;
- A pharmacoepidemiologic study to further evaluate (an) important identified or potential risk(s) from the clinical development program, such as vaccine-associated ERD or other uncommon or delayed-onset adverse events of special interest;
- A pregnancy exposure registry that actively collects information on vaccination during pregnancy and associated pregnancy and infant outcomes (Ref. 21).

C. Required Postmarketing Safety Studies

- Section 505(o)(3) of the FD&C Act (21 U.S.C. 355(o)(3)) authorizes FDA to require certain postmarketing studies or clinical trials for prescription drugs approved under section 505(b) of the FD&C Act (21 U.S.C. 355(b)) and biological products approved under section 351 of the PHS Act (42 U.S.C. 262) (Ref. 22). Under section 505(o)(3), FDA can require such studies or trials at the time of approval to assess a known serious risk related to the use of the drug, to assess signals of serious risk related to the use of the drug, or to identify an unexpected serious risk when available data indicate the potential for a serious risk. Under section 505(o)(3), FDA can also require such studies or trials after approval if FDA becomes aware of new safety information, which is defined at section 505-1(b)(3) of the FD&C Act (21 U.S.C. 355-1(b)(3)).

- For COVID-19 vaccines, FDA may require postmarketing studies or trials to assess known or potential serious risks when such studies or trials are warranted.

VII. DIAGNOSTIC AND SEROLOGICAL ASSAYS – KEY CONSIDERATIONS

- Diagnostic assays used to support the pivotal efficacy analysis (e.g., RT-PCR) should be sensitive and accurate for the purpose of confirming infection and should be validated before use.

- Assays used for immunogenicity evaluation should be suitable for their intended purpose of assessing relevant immune responses to vaccination and be validated before use in pivotal clinical trials.

VIII. ADDITIONAL CONSIDERATIONS

A. Additional Considerations in Demonstrating Vaccine Effectiveness

- Given the current state of knowledge about COVID-19, the most direct approach to demonstrate effectiveness for a COVID-19 vaccine candidate is based on clinical endpoint efficacy trials showing protection against disease (see section V. D. above).

- Once additional understanding of SARS-CoV-2 immunology, and specifically vaccine immune responses that might be reasonably likely to predict protection against COVID-19, is acquired, accelerated approval of a COVID-19 vaccine pursuant to section 506 of the FD&C Act (21 U.S.C. 356) and 21 CFR 601.40 may be considered if an applicant provides sufficient data and information to meet the applicable legal requirements. For a COVID-19 vaccine, it may be possible to approve a product under these provisions based on adequate and well-controlled clinical trials establishing an effect of the product on a surrogate endpoint (e.g., immune response) that is reasonably likely to predict clinical benefit.

- A potential surrogate endpoint likely would depend on the characteristics of the vaccine, such as antigen structure, mode of delivery, and antigen processing and presentation in the individual vaccinated. For example, an immune marker established for an adenovirus-based vaccine cannot be presumed applicable to a VSV-based vaccine, given that the two vaccines present antigen in different ways and engender different types of protective immune responses.

- Since SARS-CoV-2 represents a novel pathogen, a surrogate endpoint reasonably likely to predict protection from COVID-19 should ideally be derived from human efficacy studies examining clinical disease endpoints. If the surrogate endpoint is derived from other data sources, sponsors should consult the FDA to reach agreement on the use of the surrogate endpoint.

- An adequate dataset evaluating the safety of the vaccine in humans would need to be provided for consideration of licensure.

- For drugs granted accelerated approval, postmarketing confirmatory trials have been required to verify and describe the predicted effect on clinical benefit. These studies should usually be underway at the time of the accelerated approval, 21 CFR Part 601, Subpart E, and must be completed with due diligence (section 506(c)(3)(A) of the FD&C Act (21 U.S.C. 356(c)(3)(A)) and 21 CFR 601.41).

- If it is no longer possible to demonstrate vaccine effectiveness by way of conducting clinical disease endpoint efficacy studies, the use of a controlled human infection model to obtain evidence to support vaccine efficacy may be considered. However, many issues, including logistical, human subject protection, ethical, and scientific issues, would need to be satisfactorily addressed. At this

time no controlled human infection models for SARS-CoV-2 have been established or characterized.

B. Emergency Use Authorization

- An Emergency Use Authorization (EUA) may be issued only after several statutory requirements are met (section 564 of the FD&C Act (21 U.S.C. 360bbb-2)) (Ref. 23). Among these requirements is a determination by FDA that the known and potential benefits of a product, when used to diagnose, prevent, or treat serious or life-threatening diseases, outweigh the known and potential risks of the product.

- Issuance of an EUA (Ref. 23) may be appropriate for a COVID-19 vaccine provided the standard for issuing an EUA is met. Issuance of an EUA for a COVID-19 vaccine prior to the completion of large randomized clinical efficacy trials could reduce the ability to demonstrate effectiveness of the investigational vaccine in a clinical disease endpoint efficacy trial to support licensure, and such clinical disease endpoint efficacy trials may be needed to investigate the potential for vaccine-associated ERD. Thus, for a vaccine for which there is adequate manufacturing information, issuance of an EUA may be appropriate once studies have demonstrated the safety and effectiveness of the vaccine but before the manufacturer has submitted and/or FDA has completed its formal review of the biologics license application.

- In the case of investigational vaccines being developed for the prevention of COVID-19, any assessment regarding an EUA would be made on a case by case basis considering the target population, the characteristics of the product, the preclinical and human clinical study data on the product, and the totality of the available scientific evidence relevant to the product.

IX. REFERENCES

1. COVID-19 Public Health Emergency: General Considerations for Pre-IND Meeting Requests for COVID-19 Related Drugs and Biological Products; Guidance for Industry, May 2020, https://www.fda.gov/media/137927/download.

2. Guidance for Industry: Process Validation: General Principles and Practices, January 2011, https://www.fda.gov/media/71021/download.

3. Guidance for Industry: Content and Format of Chemistry, Manufacturing and Controls Information and Establishment Description Information for a Vaccine or Related Product, January 1999, https://www.fda.gov/media/73614/download.

4. Perlman S and Dandekar AA, 2005, Immunopathogenesis of Coronavirus Infections: Implications for SARS, Nat Rev Immunol 5: 917-927, https://doi.org/10.1038/nri1732.

5. Haagmans BL, Boudet F, Kuiken T, deLang A, et al., 2005, Protective immunity induced by the inactivated SARS coronavirus vaccine, Abstract S 12-1 Presented at the X International Nidovirus Symposium, Colorado, Springs, CO.

6. Tseng C-T, Sbrana E, Iwata-Yoshikawa N, Newman P, et al., 2012, Immunization with SARS Coronavirus Vaccines Leads to Pulmonary Immunopathology on Challenge with the SARS Virus, PloS One, 7(4): e35421, https://journals.plos.org/plosone/article?id=10.1371/journal.pone.0035421.

7. Yasui F, Kai C, Kitabatake M, Inoue S, et al., 2008, Prior Immunization With Severe Acute Respiratory Syndrome (SARS) – associated Coronavirus (SARS-CoV) Nucleocapsid Protein Causes Severe Pneumonia in Mice Infected with SARS-CoV, J Immunol, 181(9): 6337-6348, https://www.jimmunol.org/content/181/9/6337.long.

8. Bolles M, Deming D, Long K, Agnihothram S, et al., 2011, A Double-Inactivated Severe Acute Respiratory Syndrome Coronavirus Vaccine Provides Incomplete Protection In Mice And Induces Increased Eosinophilic Proinflammatory Pulmonary Response Upon Challenge, J Virol 85(23) 12201-12215, https://www.ncbi.nlm.nih.gov/pmc/articles/PMC3209347/.

9. Agrawal AS, Tao X, Algaissi A, Garron T, et al., 2016, Immunization With Inactivated Middle East Respiratory Syndrome Coronavirus Vaccine Leads To Lung Immunopathology On Challenge With Live Virus, Hum Vaccin Immunother, 12(9): 2351-2356, https://www.ncbi.nlm.nih.gov/pmc/articles/PMC5027702/.

10. Guidance for Industry: Considerations For Plasmid DNA Vaccines For Infectious Disease Indications, November 2007, https://www.fda.gov/media/73667/download.

11. Guidance for Industry: Content And Format Of Chemistry, Manufacturing, And Controls Information And Establishment Description Information For A Vaccine Or Related Product, January 1999, https://www.fda.gov/media/73614/download.

12. Guidance for Industry: Considerations For Developmental Toxicity Studies For Preventive

And Therapeutic Vaccines For Infectious Disease Indications, February 2006, https://www.fda.gov/media/73986/download.

13. World Health Organization, WHO Guidelines On Nonclinical Evaluation Of Vaccines, Annex 1, WHO Technical Report Series, 2005; 927:31-63, https://www.who.int/biologicals/publications/trs/areas/vaccines/nonclinical_evaluation/ANNEX%201Nonclinical.P31-63.pdf?ua=1.

14. World Health Organization, Guidelines On The Nonclinical Evaluation Of Vaccine Adjuvants And Adjuvanted Vaccines, Annex 2, WHO Technical Report Series, TRS 987:59-100, https://www.who.int/biologicals/areas/vaccines/TRS_987_Annex2.pdf?ua=1.

15. FDA Guidance on Conduct of Clinical Trials of Medical Products during COVID-19 Public Health Emergency; Guidance for Industry, Investigators, and Institutional Review Boards, March 2020 and updated June 2020, https://www.fda.gov/media/136238/download.

16. Centers for Disease Control and Prevention, Coronavirus Disease 2019 (COVID-19) At Risk for Severe Illness, last reviewed May 14, 2020, https://www.cdc.gov/coronavirus/2019-ncov/need-extra-precautions/groups-at-higher-risk.html.

17. Pregnant Women: Scientific and Ethical Considerations for Inclusion in Clinical Trials; Draft Guidance for Industry, April 2018, https://www.fda.gov/media/112195/download.*

18. Draft Guidance for Industry: How to Comply with the Pediatric Research Equity Act, September 2005, https://www.fda.gov/media/72274/download.*

19. Guidance for Industry: Establishment and Operation of Clinical Trial Data Monitoring Committees, March 2006, https://www.fda.gov/media/75398/download.

20. Guidance for Industry: E2E Pharmacovigilance Planning, April 2005, https://www.fda.gov/media/71238/download.

21. Postapproval Pregnancy Safety Studies; Draft Guidance for Industry, May 2019, https://www.fda.gov/media/124746/download.*

22. Guidance for Industry: Postmarketing Studies and Clinical Trials — Implementation of Section 505(o)(3) of the Federal Food, Drug, and Cosmetic Act, April 2011, https://www.fda.gov/media/133746/download.

23. Emergency Use Authorization of Medical Products and Related Authorities; Guidance for Industry and Other Stakeholders, January 2017, https://www.fda.gov/media/97321/download.

* When finalized, this guidance will represent FDA's current thinking on this topic.

WHO Technical Report Series, No. 927, 2005

Annex 1
WHO guidelines on nonclinical evaluation of vaccines

This document provides guidance to national regulatory authorities (NRAs) and vaccine manufacturers on the nonclinical evaluation of vaccines by outlining the international regulatory expectations in this area. It should be read in conjunction with the Guidelines on clinical evaluation of vaccines: regulatory expectations (1), in order to complete the understanding of the whole process of vaccine evaluation. Vaccines are a diverse class of biological products and their nonclinical testing programmes will depend on product-specific features and clinical indications. The following text has therefore been written in the form of guidelines rather than recommendations. Guidelines allow greater flexibility than recommendatisons with respect to specific issues related to particular vaccines.

Introduction

Recent progress in biotechnology and basic immunology has led to the development of a broad range of novel vaccines raising exciting possibilities for the prevention of infectious diseases (*2*, *3*). Improvements to already licensed vaccines are also being considered; such improvements will lead to new products as well as to the introduction of new adjuvants. However, the complexity and novelty of these products presents scientific and regulatory challenges because criteria for their safety, potency and quality assessment may not exist. Product diversity and new approaches, technologies and methodologies develop over time; therefore, judgement based on the best science available should always form the basis for deciding on the type and extent of nonclinical evaluation for these products.

Although nonclinical evaluation plays an essential part in the overall development of vaccine candidates, there is at present limited guidance regarding nonclinical evaluation programmes for these products. In this guidance document, the general principles of nonclinical evaluation of vaccines are discussed, with particular attention being given to the regulatory expectations for new and novel vaccines.

Preclinical testing is a prerequisite to moving a candidate vaccine from the laboratory to the clinic and includes all aspects of testing, product characterization, proof of concept/immunogenicity studies and safety testing in animals conducted prior to clinical testing of the product in humans. Nonclinical evaluation, within the context of this document, refers to all in vivo and in vitro testing performed before and during the clinical development of vaccines. For example, nonclinical evaluation may be necessary when changes in the manufacturing process or product formulations are made or to further study potential safety concerns that may have arisen from phase I and II trials or that have been described in the literature for similar products.

1 General remarks

Nonclinical studies are aimed at defining the in vitro and in vivo characteristics of candidate vaccines including those relating to safety and immunogenicity. Nonclinical studies in animals are valuable tools for identifying possible risks to the vaccinees and helping to plan protocols for subsequent clinical studies in human subjects. However, in all cases, when safety testing in animals is performed, there should be a clear rationale for doing so and the study should be performed in

compliance with the national and international laws for the protection of laboratory animals (*4*), biosafety requirements (*5*) and with good laboratory practice (GLP) (*6*). However, there may be situations where full compliance with GLP is not possible. If the study, or part of the study, was not conducted in compliance with GLP, areas of noncompliance should be defined and a statement of the reason for noncompliance should be drawn up.

Potential safety concerns for a vaccine product include those due to inherent toxicities of the product, toxicities of impurities and contaminants, and toxicities that result from interactions between the vaccine components present in the vaccine formulation. In addition, the immune response induced by the vaccine may lead to toxic side-effects.

Despite efforts to maximize the predictive value of nonclinical toxicity studies there is always the possibility that not all risks are identified. The limitations of animal testing in reflecting clinical safety and efficacy in humans should be recognized as pathogenesis and immune responses are frequently species-specific. Moreover, potential safety concerns identified during animal testing may not necessarily indicate a problem in humans. However, any signal observed in nonclinical toxicity studies should be carefully addressed in human clinical trials and may require additional nonclinical testing. It should be noted that the absence of detectable toxicity in animal studies does not necessarily mean a vaccine will be safe in humans. Potential safety concerns related to specific types of vaccine candidate are considered in section 6.

The development and subsequent validation of in vitro tests for use as alternatives to nonclinical evaluation of vaccine candidates in animals is encouraged as it may lead to the improvement of nonclinical testing as well as to a reduction of animal usage.

The need for and extent of nonclinical testing will depend on the product under consideration. For example, for a product for which there is no prior nonclinical and clinical experience, nonclinical testing would be expected to be more extensive than for those vaccines previously licensed and used in humans. In some cases, it may not be necessary to perform preclinical safety studies prior to the initiation of phase 1 clinical trials. For example, in the case of transfer of technology, where access to the database of the originally developed vaccine is available, data from nonclinical bridging studies (e.g. physicochemical characterization and abbreviated in vivo studies) may be an acceptable basis for further development of the product.

Early communication between the vaccine manufacturer and the responsible national regulatory authority to agree on the requirements for and type of nonclinical testing is recommended.

1.1 *Scope*

For the purposes of this document, vaccines are considered to be a heterogeneous class of medicinal products containing immunogenic substances capable of inducing specific, active and protective host immunity against infectious disease.

Although most vaccines are being developed for pre- and post-exposure prophylaxis, in some cases, they may be indicated for therapeutic use against infectious diseases, e.g. human immunodeficiency virus (HIV), and human papillomavirus (HPV). Both prophylactic and therapeutic vaccines for infectious disease indications are considered in this document.

Vaccines for human use include one or more of the following: microorganisms inactivated by chemical and/or physical means that retain appropriate immunogenic properties; living microorganisms that have been selected for their attenuation whilst retaining immunogenic properties; antigens extracted from microorganisms, secreted by them or produced by recombinant DNA technology; chimeric microorganisms; antigens produced in vivo in the vaccinated host following administration of a live vector or nucleic acid or antigens produced by chemical synthesis in vitro. The antigens may be in their native state, truncated or modified following introduction of mutations, detoxified by chemical or physical means and/or aggregated, polymerized or conjugated to a carrier to increase immunogenicity. Antigens may be presented plain or in conjunction with an adjuvant, or in combination with other antigens, additives and other excipients.

Therapeutic vaccines for non-infectious diseases (e.g. certain cancer vaccines) and monoclonal antibodies used as immunogens (e.g. anti-idiotypic antibodies) are *not* considered here.

1.2 *Glossary*

The definitions given below apply to the terms used in these guidelines. They may have different meanings in other contexts.

Adjuvants
Substances that are intended to enhance relevant immune response and subsequent clinical efficacy of the vaccine.

Booster vaccination
Vaccination given at a certain time interval after primary vaccination to enhance immune responses and induce long-term protection.

Combination vaccine
A vaccine that consists of two or more antigens, either combined by the manufacturer or mixed immediately before administration and intended to protect against either more than one disease, or against one disease caused by different strains or serotypes of the same organism.

Genetically modified organism (GMO)
An organism or a microorganism in which the genetic material has been altered in a way that does not occur naturally by mating and/or natural recombination. This definition covers microorganisms including viruses, viroids and cell cultures including those from animals, but does not cover naked recombinant DNA or naked recombinant plasmids.

Good clinical practice (GCP)
A standard for clinical studies that encompasses their design, conduct, monitoring, termination, audit, analyses, reporting and documentation and which ensures that the studies are scientifically and ethically sound and that the clinical properties (diagnostic, therapeutic or prophylactic) of the pharmaceutical product under investigation are properly documented.

Good laboratory practice (GLP)
A quality system concerned with the organizational process and the conditions under which nonclinical health and environmental safety studies are planned, performed, monitored, recorded, archived and reported. GLP principles may be considered as a set of criteria to be satisfied as a basis for ensuring the quality, reliability and integrity of studies, the reporting of verifiable conclusions and the traceability of data.

Good manufacturing practice (GMP)
A part of the pharmaceutical quality assurance which ensures that products are consistently produced and controlled according to the quality standards appropriate to their intended use and as required by the marketing authorization. In these guidelines, GMP refers to the current GMP guidelines published by WHO.

Immunogenicity
Capacity of a vaccine to induce antibody-mediated and/or cell-mediated immunity and/or immunological memory.

Nonclinical evaluation of vaccines
All in vivo and in vitro testing performed before and during clinical development of vaccines. The potential toxicity of a vaccine should be assessed not only prior to initiation of human trials, but throughout clinical development.

Plasmid
Double-stranded circular DNA molecules capable of replicating in bacterial cells.

Potency
The measure of biological activity, using a suitable quantitative biological assay, based on the attribute of the product that is linked to the relevant biological properties.

Preclinical evaluation of vaccine
All in vivo and in vitro testing carried out prior to the first testing of vaccines in humans. This is a prerequisite to the initiation of clinical trials and includes product characterization, proof of concept/immunogenicity studies and animal safety testing.

Preclinical toxicity study
A study designed with the primary purpose of demonstrating the safety and tolerability of a candidate vaccine product. The design of the preclinical toxicity study should meet the criteria outlined in the section on study design to be considered supportive of the intended clinical trial.

Primary vaccination
First vaccination or series of vaccinations given within a predefined period, with an interval of less than 6 months between doses, to induce clinical protection.

Product characterization
A full battery of physical, chemical and biological tests conducted for a particular product. These tests include, but are not limited to, in-process control testing, testing for adventitious agents, testing process additives and process intermediates, and lot release.

Protocol or study plan
A document that states the background, rationale and objectives of the nonclinical studies and describes its design, methodology and organization, including statistical considerations, and the conditions under which it is to be performed and managed.

Relevant animal model
An animal that develops an immune response similar to the expected human response after vaccination. It is acknowledged that species-specific differences in immune responses are likely. Ideally, the animal species chosen should be sensitive to the pathogenic organism or toxin under consideration.

Route of administration
The means by which the candidate vaccine product is introduced to the host. Possible routes of administration include the intravenous, intramuscular, subcutaneous, transcutaneous, intradermal, transdermal, oral, intranasal, intranodal, intravaginal and intrarectal routes.

Seroconversion
Predefined increase in antibody concentration, considered to correlate with the transition from seronegative to seropositive, providing information on the immunogenicity of a vaccine. If there are pre-existing antibodies, seroconversion is defined as a transition from a predefined low level to a significantly higher defined level, such as a fourfold increase in geometric mean antibody concentration.

Validation
The action of proving, in accordance with the principles of good manufacturing practice, that any procedure, process, equipment (including the computer software or hardware used), material, activity or system actually leads to the expected results.

2 Characterization of candidate vaccines

2.1 *Vaccine production*

The biological nature of the starting materials, the manufacturing process and the test methods needed to characterize batches of the product are important elements to be considered in the design and the interpretation of nonclinical testing of vaccines. Many vaccines are produced using prokaryotic or eukaryotic microorganisms and subtle changes in these organisms may radically affect the vaccine product. Therefore, the establishment of a seed-lot system is essential for vaccine production. Moreover, the quality, safety and potency of

these products are usually sensitive to changes in manufacturing conditions. The quality and safety of vaccine preparations cannot be assured solely by testing of the end-product, but depends on the strict control of the manufacturing process following the principles of good manufacturing practice (GMP) (*7*). This includes demonstration of the purity and quality of the starting material (raw materials and seeds), in-process control testing, testing for process additives and process intermediates and the development and establishment of lot release tests. Moreover, as the relationship between physical and chemical characteristics, and the immunogenicity and efficacy of these products is frequently not completely understood, biological characterization through the use of biological assays should always complement the physical and chemical product characterization. The development of appropriate laboratory methods to characterize a vaccine formulation with respect to its components, as well as its safety and potency, is a prerequisite to the clinical use of any new or novel vaccines against bacteria, viruses or parasites.

Consistency of production is essential, and the demonstration that the product does not differ from vaccine lots that have been shown to be safe and adequately immunogenic and protective in clinical studies is a crucial component of vaccine evaluation, licensing and batch release. For this reason, manufacturers should make every effort to characterize these clinical lots and if possible to keep some of these lots for future reference.

Where no appropriate animal model exists for testing potency or where direct serological or immunological correlates of clinical protection are not available, the challenge is to ensure that each production batch has the same protective efficacy as those batches shown to be protective in clinical trials. In such cases, emphasis is increasingly being placed on assuring the consistency of production using modern physical, chemical and immunological methods that enable characterization of some products to a degree of precision not previously possible.

The vaccine lots used in preclinical studies should be adequately representative of the formulation intended for use in the clinical investigation and, ideally, preclinical testing should be done on the same lot as that proposed for the clinical trials. If this is not feasible, then the lots studied should be comparable with respect to physicochemical data, stability and formulation.

At a minimum, candidate vaccines for clinical trials should be prepared under conditions of good manufacturing practice (GMP) for

clinical trial material (*8*). However full GMP will be required at the later stages of clinical development (*7*, *9*).

Any change proposed to the manufacturing process during vaccine development should be considered carefully to evaluate its impact on the quality, safety and efficacy of the vaccine and the possible need for additional nonclinical and clinical investigations.

Subsequent changes in production methods or scale-up following product licensure will necessitate further product characterization to demonstrate comparability with the original lot(s) used to demonstrate safety and efficacy of the product. The extent of comparability testing needed depends on the nature of the changes implemented (*10*). These changes should be documented and the national regulatory authority consulted. Regulatory authorities should clearly define and implement in their regulations what changes require only a notification and which changes require formal approval before implementation (*11*).

The procedures used in the characterization and control of existing licensed traditional vaccines are not likely to be applicable to newer products developed using state-of-the-art technology to protect against the same infection. For example, specific guidelines have been developed for the production and control of acellular pertussis vaccines that differ from those applied to whole cell pertussis vaccine (*12*). Likewise, the tests applied to the characterization and control of traditional inactivated cholera vaccine for parenteral use are not necessarily applicable to the new inactivated whole-cell cholera vaccine intended for oral administration, and an appropriate potency test for the oral vaccine needs to be developed.

2.2 *Potency*

Potency tests measure the biological activity of a vaccine but do not necessarily reflect the mechanism of protection in humans. Potency measurement is often used to verify the consistency of the manufacturing process. The initial concept of potency testing for vaccines was to quantify the biological activity of the vaccine in comparison with a reference preparation of known bioactivity, where the antigenic component(s) were not well-defined.

Classical challenge studies in animals immunized with the vaccine under consideration have been developed into routine potency assays (e.g. for diphtheria and tetanus toxoids). In the case of the whole-cell pertussis potency assay, which consists of intracerebral challenge of immunized and nonimmunized animals, a correlation was established with clinical protection in humans (*11*). Where no suitable animal

challenge model exists, potency is often based on measurement of immune responses, usually serological (e.g. influenza and hepatitis B vaccines).

More recently, recombinant DNA methodology and modern physicochemical techniques have resulted in the manufacture of highly purified products that can be better characterized than the classic biologicals. However, the ability to measure the "relevant" biological activity for such products may still be lacking. For these products, characterization using physicochemical parameters, such as amount of antigen, size of the antigen, protein content and others can be used as a measure of consistency, but not necessarily of the potency of a vaccine.

For live attenuated vaccines, the approach to potency measurement is generally different. The potency of live viral vaccines is usually based on titration of the minimum infective dose in cell culture or chicken embryos, which may be considered as a surrogate marker of potency, but not as a measure of potency itself. A similar approach is taken to the potency measurement of live attenuated bacterial vaccines, bacille Calmette–Guérin (BCG), and typhoid vaccine (live Ty21A oral), where the number of live organisms present is the measure of potency.

For vaccines that express inserts encoding heterologous vaccine antigens (vaccines based on viral or bacterial vectors), it is not sufficient to determine the "biological activity" of the entire construct by measuring colony forming units (CFU) or infectious titre. For these vaccines, the use of other methods such as the quantitation of the expression of the insert, or the evaluation of the effective dose (ED_{50}) of the vectored vaccine should be considered.

2.3 *Stability*

The evaluation of vaccine stability is complex, as they are very susceptible to inactivation by environmental factors. Potency, as defined in the glossary, should be measured as a part of the stability testing, except in those cases where potency testing based on biological activity is not possible. Physical and chemical product characterization should be included in the stability evaluation. For a product entering human clinical trials, sufficient data should be collected to support the stability of the product for the duration of the preclinical and clinical trial. In certain cases, accelerated stability data may be used to support preliminary data obtained at the normal storage temperature. Stability data to support licensure should be obtained under the proposed storage conditions and should be based on long-term,

real-time stability studies. Finally, the stability of standards and reference materials also needs to be considered to ensure that the procedures used to measure relevant parameters are reliably standardized.

2.4 *International and national guidelines*

The World Health Organization (WHO), through considerable international consultation, develops Recommendations and Guidelines on the production and control of vaccines and other important biologicals (*13*), and these form the basis for assuring the acceptability of products globally. These documents specify the need for appropriate starting materials, including seed lot system and cell banks; strict adherence to established protocols; tests for purity, potency, and safety at specific steps during production; and the keeping of proper records. Guidelines allow greater flexibility than Recommendations with respect to specific issues related to particular vaccines.

WHO also provides Guidelines on manufacturing establishments involved in vaccine production. Recommendations can be found in the WHO document on good manufacturing practice for biologicals (*7*). Particular attention should be given to developing documented standard operating procedures for both production processes and testing procedures. These should be introduced as early as possible during the development of a vaccine and be well established by the time phase III clinical studies are undertaken and an application for marketing authorization is filed. The basic principles for the production and control of vaccines are published in the WHO Technical Report Series (*7*, *14–18*). Specific WHO guidelines and recommendations for particular vaccines are also available and should be consulted where appropriate.

WHO Recommendations and Guidelines are intended to be scientific and advisory in nature and to provide guidance for national regulatory authorities and for vaccine manufacturers. These documents may be adopted by national health authorities as definitive national regulations or used as the basis of such regulations. They are also used as the basis for deciding the acceptability of vaccines for purchase by United Nations agencies such as the United Nations Children's Fund (UNICEF) for use in global immunization programmes. Regulatory requirements for vaccines and other biologicals are also produced by other bodies, such as the European Agency for the Evaluation of Medicinal Products (EMEA) and the US Center for Biologics Evaluation and Research (CBER) (*19*); these documents can be found on the appropriate web sites (www.emea.eu.int and www.fda.gov/cber). In addition, pharmacopoeial requirements, such as those of the

European Pharmacopoeia, are also established for vaccines and are available at www.pheur.org.

For newly developed products, specific WHO, national or pharmacopoeial requirements may not be available and a national regulatory authority will need to agree on specifications with the manufacturer on a case-by-case basis during the evaluation of products for clinical trials and for licensing. For some of these novel products general guidance on production and control from WHO can be found in relevant documents, such as those describing DNA and peptide vaccines (*14*, *16*), as well as recommendations on animal cell substrates used for production of biologicals (*14*).

In addition, information on how to assure the quality of biologicals in general and on procedures for approving manufacture and for setting up a national control laboratory, can be found in the relevant WHO guidelines (*17*, *18*). For a vaccine intended to be marketed worldwide, the development of which also involves much international collaboration, it will be essential to ensure consistency of a regulatory approach for novel products such as vaccines for HIV prevention (*19*).

2.5 *Batch release and independent laboratory evaluation*

The potential variability of methods for the production of biologicals has led to the establishment of national and international requirements to define procedures for assuring the quality of vaccines and for assessing consistency both among manufacturers and over long periods of time. Licensed vaccines are subject to independent batch release (review, testing and authorizing release of a batch of vaccine independent of the manufacturer) by a national regulatory authority or national control laboratory, before release on to the market. Independent evaluation entails at least an evaluation of a manufacturer's batch release data (protocol review), but in many instances it also includes independent laboratory testing in addition to that carried out by the manufacturer.

Batch or lot release tests are those tests chosen during full product characterization to demonstrate the purity, safety and potency of the product. Lot release testing provides one measure of assurance that a lot can be manufactured consistently. Validation and establishment of lot release tests and specifications is a process that continues throughout product development and should be finalized prior to licensure.

In some countries, samples of vaccine for clinical trials are required by the national regulatory authority, as a part of the approval process for clinical trials. Vaccine developers are encouraged to consult the

appropriate regulatory agency early on during the development of a vaccine.

2.6 *Standards and reference materials*

Standards and reference materials play a vital part in the licensing and quality control process, their role ranging from use in specific antigen recognition tests to assays of vaccine toxicity, immunogenicity and potency. The standardization of the methods used to evaluate vaccines, as well as those used to evaluate immune responses to vaccine antigens, is also vital so that results may be compared directly between laboratories both within and between countries, and between clinical trials.

WHO International Biological Standards and Reference Reagents are the primary standards in use worldwide. In addition, national regulatory authorities and manufacturers may establish secondary (regional, national), working standards for the purpose of testing vaccine quality on a lot-to-lot basis. Such standards should be calibrated against International Standards, when they exist. There is concern that different secondary standards may result in "drifting" from the International Standard. Production of secondary standards on a large scale (e.g. on a regional basis) reduces the number of secondary standards in use, and should improve accuracy of testing vaccine quality. For example, the European Department for the Quality of Medicines of the Council of Europe, has been active in establishing working standards for vaccines that are calibrated against the WHO International Standards, where appropriate. The complete list of WHO International Standards and Reference Reagents can be found on the WHO web site at: www.who.int/ biologicals.

3 Immunogenicity and other pharmacodynamic studies

A pharmacodynamic study for a vaccine product is generally conducted to evaluate the immunogenicity. However, a pharmacodynamic study may also extend to include the pharmacology of an adjuvant.

Immunization studies in animal models should be conducted because they may provide valuable "proof of concept" information to support a clinical development plan. In addition, immunogenicity data derived from appropriate animal models are useful in establishing the immunological characteristics of the product and may guide selection of the doses, schedules and routes of administration to be evaluated in clinical trials. Nonclinical immunogenicity studies should assess the relevant immune response, e.g. humoral and/or cell-mediated

immune response, induced in the vaccinated animals. Depending on the immune response induced, such studies may include an evaluation of seroconversion rates, geometric mean antibody titres, or cell-mediated immunity in vaccinated animals. Nonclinical studies should, where possible, be designed to assess relevant immune responses, including functional immune response (e.g. neutralizing antibodies, opsonophagocytic activity, etc.) leading to protection. These studies may also be designed to address interference between antigens and/or live viruses. If a vaccine consists of more than one defined antigen (e.g. acellular pertussis vaccine consisting of 3–5 protein products) the response to each antigen should be evaluated. Where appropriate, challenge/protection studies with the corresponding infectious agent may be conducted to confirm the relevance of the animal models. A primary concern in interpreting the data obtained from such studies should be to determine how closely the animal model resembles the disease and immune response in humans. It should be recognized that animal models frequently fail to predict immunogenicity and efficacy in humans.

4 Toxicity assessment

The nonclinical safety assessment of vaccines needs to be viewed in the context of the evolving field of vaccine development. Thus, judgement based on the best science available should always form the basis for any decisions regarding the need for nonclinical safety studies, types of study and study designs. Similarly, scientific judgement should be applied to the interpretation of data from preclinical studies, regarding the risk–benefit ratio, animal model, dosing etc. For example, the observation of hypersensitivity reactions in an animal model may not necessarily preclude proceeding to clinical trials, but may indicate the necessity for careful monitoring of a particular clinical parameter.

Section 4.1 provides a general framework for designing a preclinical toxicity study for a vaccine. The parameters set out in this section are considered the minimum necessary for a safety assessment prior to the initiation of clinical trials in humans, in situations where preclinical safety studies are deemed necessary. As the design of any toxicity study is product-specific and based on indications, modifications to the framework outlined below may be necessary in response to particular product features, availability of animal models, methodologies, etc.

Section 4.2 provides additional considerations for performing special toxicity assessments that may be required on a case-by-case basis.

4.1 *Basic toxicity assessment*

4.1.1 *Study design*

The preclinical toxicity study should be adequate to identify and characterize potential toxic effects of a vaccine to allow investigators to conclude that it is reasonably safe to proceed to clinical investigation. The parameters to be considered in designing animal toxicology studies are the relevant animal species and strain, dosing schedule and method of vaccine administration, as well as timing of evaluation of end-points (e.g. sampling for clinical chemistry, antibody evaluation and necropsy). The route of administration should correspond to that intended for use in the clinical trials. When the vaccine is to be administered in human clinical trials using a particular device, the same device should be used in the animal study, where feasible (e.g. measles aerosol vaccine in the monkey model). Potential toxic effects of the product should be evaluated with regard to target organs, dose, route(s) of exposure, duration and frequency of exposure, and potential reversibility. The toxicity assessment of the vaccine formulation can be done either in dedicated-stand alone toxicity studies or in combination with studies of safety and activity that have toxicity end-points incorporated into the design. The study should also include an assessment of local tolerance.

4.1.2 *Animal species, sex, age and size of groups*

Data to be recorded on the animals used for toxicity testing should include information on the source, species and animal husbandry procedures (e.g. housing, feeding, handling and care of animals). In general, the use of outbred animals is recommended. The health of the animal will need to be evaluated in accordance with acceptable veterinary medical practice to ensure that animals are free of any condition that might interfere with the study. For instance, individual housing of laboratory animals may be required to minimize the risk of cross-infection.

Where possible, the safety profile of a product should be characterized in a species sensitive to the biological effects of the vaccine being studied. Ideally, the species chosen should be sensitive to the pathogenic organism or toxin. The animal species used should develop an immune response to the vaccine antigen. In general, one relevant animal species is sufficient for use in toxicity studies to support initiation of clinical trials. However, there may be situations in which two or more species may be necessary to characterize the product, for example where the mechanism of protection induced by the vaccine is not well understood (for example, intranasal influenza vaccine and intranasal measles vaccine).

In addition, when species-specific or strain-specific differences in the pharmacodynamics of the product are observed, it may be necessary to address the nonclinical safety of the product in more than one safety study and in more than one animal model.

The size of the treatment group depends on the animal model chosen. The number of animals used in studies using non-human primates would be expected to be less than that in studies that used rodents. For small animal models, e.g. rats and mice, it is recommended that approximately 10 males + 10 females per group be studied.

In general, the approximate age at the start of the study for rodents is 6–8 weeks, and for rabbits, 3–4 months.

4.1.3 *Dose, route of administration and control groups*

The toxicity study should be performed using a dose that maximizes exposure of the animal to the candidate vaccine and the immune response induced, for example, peak antibody response. In general, an evaluation of the dose–response is not required as part of the basic toxicity assessment and the lethal dose does not have to be determined. However, pilot dose–response studies may be conducted to determine which dose induces the highest antibody production in the animal model. If feasible, the highest dose (in absolute terms) to be used in the proposed clinical trial should be evaluated in the animal model. However, the dose is sometimes limited by the total volume that can be administered in a single injection, and guidelines on animal welfare should be followed. In such cases, the total volume may be administered at more than one site using the same route of administration. Alternatively, a dose that exceeds the human dose on a mg/kg basis and that induces an immune response in the animal model may be used. In such cases, the factor between human and animal dose should be justified.

The number of doses administered to the test animals should be equal to or more than the number of doses proposed in humans. To better simulate the proposed clinical usage, vaccine doses should be given at defined time intervals rather than as daily doses; the dosing interval used in the toxicity study may be shorter (e.g. an interval of 2–3 weeks) than the proposed interval in clinical trials in humans. The dosing interval in nonclinical trials may be based on the kinetics of the primary and secondary antibody responses observed in the animal model. A single-dose study may be performed in situations in which vaccine-induced antibodies are expected to neutralize a live viral vector, thus limiting the expression of the gene of interest (e.g. anti-adenovirus immune response), or when immune responses induced in

animals are expected to react with species-specific proteins present in the vaccine formulation (e.g. human recombinant cytokines used as adjuvants).

The route of administration should correspond to that intended for use in the human clinical trials. If toxic effects are observed in safety studies using a particular route of administration (e.g. intranasal), further toxicity studies using a different route of administration (e.g. intravenous) may be helpful in understanding the full spectrum of toxicity of the product.

The study design should include a negative control group(s) to evaluate a baseline level of treatment. If appropriate, active control groups (e.g. vaccine formulation without antigen) may also be included in the study. The study should include an additional treatment group of animals to be killed and evaluated as described below at later timepoints after treatment, to investigate the reversibility of any adverse effects observed during the treatment period and to screen for possible delayed adverse effects.

4.1.4 *Parameters monitored*

Toxicity studies should address the potential of the product for causing local inflammatory reactions, and possible effects on the draining lymph nodes, systemic toxicity and on the immune system. A broad spectrum of information should be obtained from the toxicity studies. Parameters to be monitored should include daily clinical observations, weekly body weights and weekly food consumption. During the first week of administration frequent measurements of body weight and food consumption are recommended, if feasible, as these are sensitive parameters indicating "illness". Interim analysis of haematology and serum chemistry should be considered approximately 1–3 days following the administration of the first and last dose and at the end of the recovery period. Haematology and serum chemistry analyses should include, at the minimum, an evaluation of relative and absolute differential white blood cell counts (lymphocytes, monocytes, granulocytes, abnormal cells) and albumin/globulin ratio, enzymes and electrolytes. In some cases, it may also be useful to evaluate coagulation parameters, urine samples and serum immunoglobulin classes. Data should be collected not only during treatment, but also following the recovery phase (e.g. 2 weeks or more following the last dose) to determine persistence, and look at exacerbation and/or reversibility of potential adverse effects.

At study termination, final body weights (after a period of fasting) should be measured. Terminal blood samples should be collected and

serum chemistry, haematology and immunological investigations should be done as described in the preceding paragraph. The immune response induced by the candidate vaccine should be assessed in order to confirm that the relevant animal model has been selected. A complete gross necropsy should be conducted and tissues collected and preserved, gross lesions should be examined and organ weights recorded (*23*). Histopathological examinations of tissues should be performed and special attention paid to the immune organs, i.e. lymph nodes (both local and distant from site of administration), thymus, spleen, bone marrow and Peyer's patches or bronchus-associated lymphoid tissue, as well as organs that may be expected to be affected as a result of the particular route of administration chosen. Histopathological examinations should always include pivotal organs (e.g. brain, kidneys, liver and reproductive organs) and the site of vaccine administration. The choice of tissues to be examined (ranging from a short list limited to immune and pivotal organs to a full list as provided in the Appendix) will depend on the vaccine in question, and the knowledge and experience obtained from previous nonclinical and clinical testing of the vaccine components. For example, full tissue examination will be required in the case of novel vaccines for which no prior nonclinical and clinical data are available. Therefore, the list of tissues to be tested should be defined on a case-by-case basis, following consultation with the relevant regulatory authority. Data should be reported in full listing the original collection of values, and summarized.

4.1.5 *Local tolerance*

The evaluation of local tolerance should be conducted either as a part of the repeated dose toxicity study or as a stand-alone study. Tolerance should be determined at those sites that come into contact with the vaccine antigen as a result of the method of administration, and also at those sites inadvertently exposed (e.g. eye exposure during administration by aerosol) to the vaccine. More details have been published elsewhere (*24*).

If abnormalities are observed in the basic toxicity study outlined in section 4.1., further studies may be necessary to evaluate the mechanism of the toxic effect.

4.2 ***Additional toxicity assessments***

4.2.1 *Special immunological investigations*

In certain cases, the results from evaluations of immune response from nonclinical and clinical studies, or from data on natural disease, may indicate immunological aspects of toxicity, e.g. precipitation of

immune complexes, humoral or cell-mediated immune response against antigenic determinants of the host itself as a consequence of molecular mimicry or exacerbation of the disease (e.g. inactivated measles vaccine). In such cases, additional studies to investigate the mechanism of the effect observed might be necessary.

Great similarity of vaccine determinants and host molecules could cause autoimmune reactions induced by molecular mimicry (*26*). Therefore, any vaccine antigen whose characteristics might mimic those of a host antigen should be treated with caution, even though it is recognized that molecular mimicry does not necessarily predispose to autoimmunity.

Because considerable efforts may be required in selecting and developing relevant animal models to address the above issues, caution should be exercised and a strong rationale provided when developing vaccines for diseases associated with autoimmune pathology.

If data suggest that the pathogen against which the vaccine is directed may cause autoimmune pathology, studies may be needed to address this concern on a case-by-case basis, if an appropriate animal model exists.

It should be noted that observations of biological markers for autoimmune reactions are not necessarily linked to pathogenic consequences. For instance, the presence of autoimmune antibodies does not necessarily indicate the induction of autoimmune disease (*25*).

When hypersensitivity reactions induced by the antigen(s), adjuvants, excipients or preservatives are of concern, additional investigations may be warranted.

4.2.2 *Developmental toxicity studies*

Developmental toxicity studies are usually not necessary for vaccines indicated for immunization during childhood. However, if the target population for the vaccine includes pregnant women and women of childbearing potential, developmental toxicity studies should be considered, unless a scientific and clinically sound argument is put forward by the manufacturer to show that conducting such studies is unnecessary. For a preventive vaccine, reproductive toxicity assessments are generally restricted to prenatal and postnatal developmental studies, because the primary concern is any potential untoward effect on the developing embryo, fetus or newborn. The need to conduct fertility and post-weaning assessments should be considered on a case-by-case basis. The animal model chosen should develop

an immune response to the vaccine, which is usually determined by serum antibody measurements. In addition, it is important to evaluate maternal antibody transfer by measuring vaccine-induced antibody in cord or fetal blood to verify exposure of the embryo or fetus to maternal antibody. The route of administration should mimic the clinical route of administration. Ideally, the maximal human dose should be administered to the test animal. If it is not possible to administer the full human dose, e.g. limitations on the total volume that can be administered, or if local toxicity is observed that may result in maternal stress, a dose that exceeds the human dose on a mg/kg basis and is able to induce an immune response in the animal should be used.

To assess any potential adverse effects of the vaccine during the period of organogenesis, the gestating animal is usually exposed to the vaccine during the period from implantation until closure of the hard palate and end of gestation defined as stages C, D and E in the ICH S5a document (*27*). Because of the relatively short gestation period of most animal models used, pre-mating treatment is frequently required to ensure maximal exposure of the embryo or fetus to the vaccine-induced immune response. For a preventive vaccine, the number of doses administered depends on the time of onset and duration of the response. Booster immunizations may be necessary at certain times during the period of gestation to maintain a high level of antibody throughout the gestation period and to expose the developing embryo to the components of the vaccine formulation. End-points include, but are not limited to, viability, resorptions, abortions, fetal body weight and morphology. The reader is referred to other publications for guidance on end-points used to evaluate potential toxic effects of the product on development of the embryo or fetus (*27*). It is also recommended that a period of postnatal follow-up of pups from birth to weaning be incorporated in the study design to assess normality of growth, body weight gain, suckling activity and viability. Studies should therefore be designed so that test groups are divided into subgroups. Half of the animals should be delivered by Caesarean section and the other half allowed to deliver their pups without surgical intervention.

4.2.3 *Genotoxicity and carcinogenicity studies*

Genotoxicity studies are normally not needed for the final vaccine formulation. However, they may be required for particular vaccine components such as novel adjuvants and additives. If needed, the in vitro tests for mutations and chromosomal damage should be done prior to first human exposure. The full battery of tests for genotoxicity may be performed in parallel with clinical trials (*28*).

Carcinogenicity studies are not required for vaccine antigens. However, they may be required for particular vaccine components such as novel adjuvants and additives.

4.2.4 *Safety pharmacology*

The purpose of safety pharmacology is to investigate the effects of the candidate vaccine on vital functions. If data from nonclinical and/or human clinical studies suggest that the vaccine (e.g. one based on specific toxoids) may affect physiological functions (e.g. central nervous system, respiratory, cardiovascular and renal functions) other than those of the immune system, safety pharmacology studies should be incorporated into the toxicity assessment. Useful information on this topic can be found in the *Note for Guidance on safety pharmacology studies for human pharmaceuticals* (*29*).

4.2.6 *Pharmacokinetic studies*

Pharmacokinetic studies (e.g. for determining serum or tissue concentrations of vaccine components) are normally not needed. The need for specific studies should be considered on a case-by-case basis (e.g. when using novel adjuvants or alternative routes of administration) and may include local deposition studies that would assess the retention of the vaccine component at the site of injection and its further distribution (e.g. to the draining lymph nodes). Distribution studies should be considered in the case of new formulations, novel adjuvants or when alternative routes of administration are intended to be used (e.g. oral or intranasal).

5 Special considerations

5.1 ***Adjuvants***

Adjuvants may be included in vaccine formulations or co-administered with vaccines to enhance the immune responses to particular antigen(s), or to target a particular immune response. It is important that the adjuvants used comply with pharmacopoeial requirements where they exist, and that they do not cause unacceptable toxicity.

Adjuvant activity is a result of many factors and the immune response obtained with one particular antigen/adjuvant formulation cannot, as a rule, be extrapolated to another antigen. Individual antigens vary in their physical and biological properties and antigens may interact differently with an adjuvant. Adjuvants must be chosen according to the type of immune response desired and they must be formulated with the antigen in such a way that distribution of both is optimized to ensure availability to the relevant lymphatic tissues. The route of

administration of the vaccine is also an important factor influencing the efficacy and safety of an adjuvant.

The effect of the adjuvant should be demonstrated in preclinical immunogenicity studies. If no toxicological data exist for a new adjuvant, toxicity studies of the adjuvant alone should first be performed. In general, assessment of new or novel adjuvants should be undertaken as required for new chemical entity (*30–32*). These data may be obtained by the vaccine manufacturer or by the producer of the adjuvant. In addition to assessing the safety of the adjuvant by itself it is also important to assess whether the combination of antigen and adjuvant exerts a synergistic adverse effect in the animal model (*33*, *34*). When species-specific proteins (e.g. cytokines) are used as novel adjuvants, the issue of species-specific response should be considered.

When evaluating the safety profile of the combination of adjuvant and vaccine, the formulation proposed for clinical use should be used.

Compatibility of the adjuvant(s) (e.g. lack of immune interference) with all antigenic components present in the vaccine should be evaluated.

If applicable, adsorption of all antigenic components present in the vaccine should be shown to be consistent on a lot-to-lot basis. Potential desorption of antigen during the shelf-life of the product should be performed as a part of stability studies, the results reported and specifications set, as this may affect not only immunogenicity, but also the toxicity profile of the product.

It should be noted that no adjuvant is licensed in its own right, but only as a component of a particular vaccine.

5.2 *Additives (excipients and preservatives)*

Where a new additive is to be used, for which no toxicological data exist, toxicity studies of the additive alone should first be performed and the results documented according to the guidelines for new chemical entities (*31*). The compatibility of a new additive with all vaccine antigens should be documented together with the toxicological profile of the final vaccine formulation under consideration in animal models as outlined in section 4.

5.3 *Vaccine formulation and delivery device*

The vaccine formulation (i.e. liquid form, capsules or powder), as well as the delivery device, may have an impact on the uptake of

the vaccine, its effectiveness and safety. Ideally, the delivery device and vaccine formulation tested in an animal safety study should be identical to those intended to be used clinically. However, animal models in which delivery devices intended for clinical use can be tested may not be available. In these instances, in order to develop an appropriate animal model, it may be necessary to conduct pilot studies to define and optimize the conditions for drug delivery in the animal model before it can be used to assess the preclinical safety of the product.

5.4 *Alternative routes of administration*

When using a vaccine formulation administered by alternative routes (e.g. intranasal, oral, intradermal, rectal and intravaginal routes), it can be assumed that their potency, relevant immunogenicity, tolerability, toxicity, and long-term safety may differ from that of products delivered by the parenteral route. Thus, when different routes of administration are proposed, nonclinical safety studies may have to be conducted using vaccine formulation and/or adjuvant alone in a suitable animal model to address the specific safety concerns associated with vaccine administration by these routes. Particular issues relevant to vaccines administered using alternative routes that may need to be considered are discussed below.

5.4.1 *Animal models*

A special consideration for vaccines administered by alternative routes should be the anatomy and physiology of the site of vaccine administration of the particular animal model chosen and its accessibility for the administration of the vaccine. For example, for intranasally administered products, the species chosen should ideally be receptive to spray administration of the product. In general, rabbits and dogs are useful test models for use of spray devices; however, their olfactory bulbs are highly protected and special techniques would be required to ensure that the test product reached this organ. Although mice and rats are useful models, intranasal administration to these species presents technical difficulties. Intranasal administration to non-human primates may be preferable, if they are susceptible to the infectious agent in question.

Depending on the level of concern regarding a particular route of administration or when there are species-specific differences between the animal models in their sensitivity to the candidate vaccine, it may be necessary to address the preclinical safety of the product in more than one safety study and in more than one animal model.

5.4.2 *Dose*

As the optimal dose derived from studies using the parenteral route of administration may differ from the dose used for alternative route(s) of administration, dose-finding studies may need to be conducted for a particular route of administration. Also, consideration should be given to the total volume of the vaccine administered as it may affect the outcome of the safety study. For example, intranasal administration of more than 5 µl of test preparation per nostril to a mouse would result in the test preparation being swallowed, rather than being adsorbed by the nasal mucosa.

5.4.3 *End-points*

The toxicity end-points would include those described in section 4 and may include additional outcome measures that would depend on the route of administration and specific concerns associated with the particular route and target organ. For example, if there is concern about the potential passage of vaccine components to the brain following intranasal administration, immunohistology and "in situ" methods and/or neurological assays and examinations may be necessary. For vaccines administered by inhalation, outcome measures may include pulmonary function tests and data on histopathology of the lungs. Considerable efforts may be required to develop appropriate methods to address potential safety concerns associated with the use of new routes of administration.

5.4.4 *Immunogenicity assessment*

The development of appropriate assays for measuring mucosal immune responses is critical for vaccines that are expected to function as mucosal immunogens because serological assays alone may not reflect the relevant immune response for a mucosal vaccine. Thus, in addition to measuring serological responses, it may be necessary to evaluate T cell responses, antibody-secreting cells and cytokine production. In addition, assays may need to be developed to assess the induction of local and systemic responses at sites distant from administration of the vaccine antigen.

6 Specific considerations for particular types of vaccines

In addition to the testing strategies outlined in sections 3, 4 and 5, studies may be necessary to address specific safety concerns associated with particular product types using suitable in vitro and in vivo test methods. The specific testing requirements for live attenuated and combination vaccines are discussed below. Detailed information regarding the production and control of other types of vaccine is available in the WHO guidance documents for production and con-

trol (13), and should be consulted. For example, in the recently developed guidelines for DNA (16) and synthetic peptide vaccines (18, 35), as well as for particular vaccines such as Hib conjugated vaccine (26), the issues relevant for nonclinical testing are discussed and should be considered in the development of an appropriate design for the nonclinical study of the vaccine in question.

6.1 *Live attenuated vaccines*

An assessment of the degree of attenuation, and the stability of the attenuated phenotype, are important considerations for the nonclinical testing programme of a live attenuated vaccine. Laboratory markers of attenuation are invaluable for this purpose. These markers should be capable of distinguishing the attenuated vaccine from fully virulent wild-type strains and, ideally, of detecting partial reversion to full virulence. To assess the stability of the attenuation phenotype, the vaccine may be passaged under production conditions beyond the maximum passage number to be used for production. Stability of attenuation may also be assessed by passage under conditions that are outside the conditions to be used for vaccine production. For example, higher or lower temperatures may exert selection pressure for reversion to virulence. The marker(s) of attenuation may subsequently be used to qualify new vaccine seed preparations and to monitor the effect of any significant changes in production conditions of the attenuated phenotype.

If the wild-type organism is neurotropic, or if passages through neural tissue have been used in the attenuation of a virus vaccine, then a test for neurovirulence should be performed at least at the level of the vaccine seed. A neurovirulence test is not necessarily required for all live attenuated vaccines. The specifications for an appropriate neurovirulence test depend on the organism under test and should be capable of distinguishing the attenuated vaccine from fully virulent wild-type strains and, ideally, of detecting partial reversion to full virulence. Specific reference preparations may be needed for this purpose. Neurovirulence tests in small animal models may be acceptable.

If the live attenuated vaccine is based on a genetically modified organism, then an environmental risk assessment may be required as part of the preclinical evaluation. An investigation into the possible shedding of vaccine organisms following administration contributes to the environmental risk assessment. For all live attenuated vaccines, information on the likelihood of exchange of genetic information with non-vaccine strains may be required and suitable nonclinical tests may be designed to provide data for this purpose.

6.2 *Combined vaccines*

New combinations produced either by formulation or at the time of reconstitution of antigens or serotypes should be studied for appropriate immunogenicity in an animal model, if available, before initiation of human clinical trials (*36*, *37*). Combined antigens should be examined by appropriate physicochemical means to evaluate possible changes to antigen properties on combination, such as degree of adsorption to aluminium adjuvants, as well as stability of the combination.

The immune response to each of the antigens in the vaccine should be assessed, including the quality of response and any potential interference and incompatibilities between combined antigens. It is preferable to study a new combination in comparison with the individual antigens in animals to determine whether augmentation or diminution of response occurs.

The need to evaluate the safety of the new combination in an animal model should be considered on a case-by-case basis. Such evaluation is likely to be necessary if there is concern that combining antigens and/or adjuvants may lead to problems of toxicity (e.g. novel adjuvant).

Similar consideration for nonclinical testing will also apply to cases where a new candidate single-component vaccine is developed from an already licensed combined vaccine (e.g. monovalent oral polio vaccine versus trivalent oral polio vaccine).

Authors

The first draft of these Guidelines on preclinical evaluation of vaccines was prepared by the members of the WHO drafting group following the meeting held at the National Institute of Public Health and the Environment (RIVM), the Netherlands 14–15 March 2002 attended by:

Dr M. Gruber, Scientific Reviewer, Division of Vaccines and Related Products Application, Center for Biologics Evaluation and Research, Food and Drug Administration, Rockville, MD, USA; Dr A. Homma, Bio-Manguinhos Oswaldo Cruz Foundation, Rio de Janeiro, Brazil; Dr J.G. Kreeftenberg, Bureau for International Cooperation, National Institute of Public Health and the Environment, Bilthoven, the Netherlands; Dr J.W. van der Laan, National Institute of Public Health and the Environment, Bilthoven, the Netherlands; Dr E. Griffiths, Coordinator, Quality Assurance and Safety of Biologicals, World Health Organization, Geneva, Switzerland; Dr I. Knezevic, Quality Assurance and Safety of Biologicals, World Health Organization, Geneva, Switzerland.

A second draft was prepared following a discussion on special immunological considerations held at Agence Française de Sécurité Sanitaire des Produits de

Santé, Lyon, France, 17 June 2002 attended by the following: Dr F. Fuchs, Agence Française de Sécurité Sanitaire des Produits de Santé, Lyon, France; Dr D. Masset, Agence Française de Sécurité Sanitaire des Produits de Santé (AFSSAPS), St Denis, France; Dr C. Ratignier Agence Française de Sécurité Sanitaire des Produits de Santé, St Denis, France; Dr Marc Pallardy, Agence Française de Sécurité Sanitaire des Produits de Santé (AFSSAPS), St Denis, France, and a further meeting of drafting group held in Geneva from 1–2 July 2002.

A third draft was prepared by the drafting group after an informal WHO Consultation on preclinical evaluation of vaccines: regulatory expectations, held in Geneva from 12–13 December 2002, attended by the following participants:

Dr T. Bektimirov, Deputy Director, Tarasevic State Research Institute for Standardization and Control of Medical Biological Preparations, Moscow, Russian Federation; Dr E. Chaves Leal, Vice Director, Instituto Nacional de Control de Qualidad Saude, Rio de Janeiro, Brazil; Dr W. Egan, Acting Director, Office of Vaccines Research and Review, Center for Biologics Evaluation and Research, Food and Drug Administration, Rockville, MD, USA; Dr E. Griffiths, Associate Director General, Biologics and Genetic Therapies, Health Canada, Ottawa, Canada; Dr M. Gruber, Scientific Reviewer, Division of Vaccines and Related Products Application, Center for Biologics Evaluation and Research, Food and Drug Administration, Rockville, MD, USA; Dr M. Haase, Paul Ehrlich Institute, Langen, Germany; Dr A. Homma, Developing Country Vaccine Manufacturer's Network, c/o Bio-Manguinhos Oswaldo Cruz Foundation, Rio de Janeiro, Brazil; Dr J.G. Kreeftenberg, Bureau for International Cooperation, National Institute of Public Health and the Environment, Bilthoven, the Netherlands; Dr J.W. van der Laan, National Institute of Public Health and the Environment, Bilthoven, the Netherlands; Dr R. Leke, Department of Immunology and Microbiology, Faculty of Medicine, University of Yaounde, Yaounde, Cameroon; Dr Lei Dianliang, Deputy Director, National Institute for the Control of Pharmaceutical and Biological Products, Beijing, People's Republic of China; Dr Lazara Martínez Muñoz, Centro para el Control Estatal de la Calidad de los Medicamentos, Havana, Cuba; Dr D. Masset, Agence française de Sécurité Sanitaire des Produits de Santé, Saint-Denis, France; Dr R. Mignolet, RLM Consulting, Wavre, Belgium; Dr P. Minor, Head, Division of Virology, National Institute for Biological Standards and Control, Potters Bar, Herts., England; Dr G. Orefici, Istituto Superiore di Sanità, Rome, Italy; Dr M. Pallardy, Agence Française de Sécurité Sanitaire des Produits de Santé, Veille Toxicologique/Vigilance, St Denis, France; Dr J. Petricciani, Carlsbad, USA; Dr P. Pitisuttithum, Vaccine Trial Centre, Faculty of Tropical Medicine, Mahidol University, Bangkok, Thailand; Dr F. Reigel, Vice Director, Swissmedic, Biological Medicines and Laboratories, Berne, Switzerland; Dr J. Robertson, National Institute for Biological Standards and Control, Potters Bar, Herts., England; Dr L. Slamet, Deputy for Therapeutic Products, Narcotic, Psychotropic and Addictive Substance Control, Directorate General of Food and Drug Control, Ministry of Health, Jakarta, Indonesia; Dr A.K. Tahlan, Central Drugs Laboratory, Central Research Institute, Kasauli, India; Ms C. Chamberlin, Scientific Secretary of European Pharmacopoeia Group of Experts on Vaccines, Strasbourg, France; Dr B. Meignier, IABS c/o Director, External R & D, Aventis Pasteur SA, Marcy l'Etoile, France; Dr B.J. Ledwith, Director, Biologics Safety Assessment, Merck Research Laboratories, West Point, PA, USA; Dr F. Verdier, Head, Product Safety Assessment, Aventis Pasteur, Marcy l'Etoile, France; Dr G. del Giudice, Head, Animal Models and Serology, Research Center, Chiron SpA, Siena, Italy.

WHO secretariat: Dr M.P. Kieny, Director, Initiative to Vaccine Research; Dr L. Rago, Coordinator, Quality Assurance and Safety of Medicines; Dr D. Wood, Acting Coordinator, Quality Assurance and Safety of Biologicals; Mr L. Belgharbi, Access to Technologies; Dr N. Dellepiane, Access to Technologies; Dr P. Duclos, Vaccine Assessment and Monitoring; Dr D. Kioy, Tropical Disease Research; Dr I. Knezevic, Quality Assurance and Safety of Biologicals; Dr E. Uramis Diaz, Access to Technologies; Dr S. Osmanov, Initiative to Vaccine Research/HVI.

The final draft (WHO/BS/03.1969) was prepared by Dr E. Griffiths, Dr M. Gruber, Dr D. Masset, Dr F. Verdier, Dr D. Wood and Dr I. Knezevic, following a meeting held in Geneva, 9–10 June 2003, and taking into account comments made by the Expert Committee on Biological Standardization at its meeting in February 2003 as well as comments made by the reviewers of the document.

References

1. WHO guidelines for clinical evaluation of vaccines: regulatory expectations. In: *WHO Expert Committee on Biological Standardization. Fifty-second Report.* Geneva, World Health Organization, 2004 (WHO Technical Report Series, No. 924 Annex 1).
2. *Biological standardization and control. A scientific review commissioned by the UK National Biological Standards Board*. Geneva, World Health Organization, 1997 (WHO/BLG/97.1).
3. *Biotechnology and world health. Risks and benefits of vaccines and other medical products produced by genetic engineering. Proceedings of a WHO meeting*. Geneva, World Health Organization, 1997 (WHO/VRD/BLG/97.01).
4. *WHO Manual of laboratory methods for testing vaccines used in the WHO Expanded Programme on Immunization*. Geneva, World Health Organization, 1997, Annex 1 (WHO/VSQ/97.04).
5. World Health Organization. *Laboratory biosafety manual*, 2nd ed. (revised) Geneva, World Health Organization, 2003.
6. *OECD principles on Good Laboratory Practice* (revised 1997). Paris, Organisation for Economic Co-operation and Development, 1997 (ENV/MC/CHEM (98) 17).
7. Good manufacturing practices for biological products. In: *WHO Expert Committee on Biological Standardization. Forty-second Report*. Geneva, World Health Organization, 1992 (WHO Technical Report Series, No. 822):20–30.
8. Good manufacturing practice: supplementary guidelines for the manufacture of the investigational pharmaceutical products for clinical trials in humans. In: *WHO Expert Committee on Specifications for Pharmaceutical Preparations: Thirty-Fourth Report.* Geneva, World Health Organization, 1996, Annex 7 (WHO Technical Report. Series, No. 863).
9. Good manufacturing practices for pharmaceutical products. In: *WHO Expert Committee on Specifications for Pharmaceutical Preparations. Thirty-second*

Report. Geneva, World Health Organization, 1992 Annex 1 (WHO Technical Report Series, No. 823).

10. *Note for guidance on comparability of medicinal products containing biotechnology-derived proteins as drug substance*. London, Committee for Proprietary Medicinal Products, 2000 (CPMP/BWP/3207/00).
11. European Commission Regulations No. 541/95, 542/95, 1146/98 and 1069/98.
12. Griffiths E. Efficacy of whole-cell pertussis vaccine. In: Wardlaw AC, Parton R, eds. *Pathogenesis and immunity in pertussis*. Chichester, Wiley, 1988: pp. 353–374.
13. Recommendations and guidelines for biological substances used in medicine and other documents. Geneva, World Health Organization, 2002 (WHO Technical Report Series, No. 910):99–102.
14. Requirements for the use of animal cells as *in vitro* substrates for the production of biologicals. In: *WHO Expert Committee on Biological Standardization. Forty-seventh Report.* Geneva, World Health Organization, 1998, Annex 1 (WHO Technical Report Series, No. 878).
15. *Guidelines on transmissible spongiform encephalopathies in relation to biological and pharmaceutical products*. Geneva, World Health Organization, 2003 (WHO/BCT/QSD/03.01).
16. Guidelines for assuring quality of DNA vaccines. In: *WHO Expert Committee on Biological Standardization. Forty-seventh Report.* Geneva, World Health Organization, 1998, Annex 3 (WHO Technical Report Series, No. 878).
17. Guidelines for assuring the quality of pharmaceutical and biological products prepared by recombinant DNA technology. In: *WHO Expert Committee on Biological Standardization. Forty-first Report.* Geneva, World Health Organization, 1991, Annex 3 (WHO Technical Report Series, No. 814).
18. Guidelines for the production and quality control of synthetic peptide vaccines. In: *WHO Expert Committee on Biological Standardization. Forty-eighth Report*. Geneva, World Health Organization, 1999, Annex 1 (WHO Technical Report Series, No. 889).
19. *Guidance for industry: content and format of chemistry, manufacturing and controls information and establishment description information for a vaccine or related product. Federal Register*, 1999, **2**:518–519 (Center for Biologics Evaluation and Research, US Food and Drug Administration).
20. Guidelines for national authorities on quality assurance for biological products. In: *WHO Expert Committee on Biological Standardization. Forty-second Report.* Geneva, World Health Organization, 1992 (WHO Technical Report Series, No. 822):31–46.
21. Regulation and licensing of biological products in countries with newly developing regulatory authorities. In: *WHO Expert Committee on Biological Standardization. Forty-fifth Report.* Geneva, World Health Organization, 1995 (WHO Technical Report Series No. 858):21–35.

22. Scientific considerations for the regulation and clinical evaluation of HIV/AIDS preventive vaccines: report from a WHO–UNAIDS Consultation 13–15 March 2001, Geneva Switzerland. *AIDS*, 2002, **16**:W15–W25.

23. *Note for guidance on repeated dose toxicity*. London, Committee for Proprietary Medicinal Products, 1999 (CPMP/SWP/1042/99).

24. *Note for guidance on non-clinical local tolerance testing of medicinal products.* London, Committee for Proprietary Medicinal Products, 2000 (CPMP/SWP/2145/00).

25. **Wraith DC, Goldman M, Lambert PH.** Vaccination and autoimmune disease: what is the evidence? *Lancet*, 2003, **362**:1659–1666.

26. Recommendations for *Haemophilus influenzae* type b conjugate vaccines. In: *WHO Expert Committee on Biological Standardization. Forty-ninth Report.* Geneva, World Health Organization, 2000 (WHO Technical Report Series, No. 897).

27. *Note for guidance for reproductive toxicology: detection of toxicity to reproduction for medicinal products*. London, Committee for Proprietary Medicinal Products (CPMP/ICH/386/95).

28. *Note for guidance on genotoxicity: a standard battery for genotoxicity testing of pharmaceuticals*. London, Committee for Proprietary Medicinal Products, 1995 (CPMP/ICH/174/95).

29. *Note for guidance on safety pharmacology studies for human pharmaceuticals*. London, Committee for Proprietary Medicinal Products (CPMP/ICH/539/00).

30. ICH M3(M) *Nonclinical safety studies for the conduct of human clinical trials for pharmaceuticals*. London, Committee for Proprietary Medicinal Products, 2000 (CPMP/ICH/286/95 modification).

31. *Guidance for industry: nonclinical studies for development of pharmaceutical excipients*. Draft. September 2002.

32. *Note for guidance on excipients, antioxidants and antimicrobial preservatives in the dossier for application for marketing authorisation of a medicinal product.* London, Committee for Proprietary Medicinal Products, 2003 (CPMP/QWP/419/03).

33. *Note for guidance on preclinical pharmacological and toxicological testing of vaccines*. London, Committee for Proprietary Medicinal Products, 1998 (CPMP/SWP/465/95).

34. **Goldenthal KL, Cavagnaro JA, Alving CR, Vogel FR.** Safety evaluation of vaccine adjuvants: National Cooperative Vaccine Development Meeting Working Group. *AIDS Research and Human Retroviruses*, 1993, **9**(suppl 1):S47–S51.

35. *Guidance for industry for the submission of chemistry, manufacturing, and controls information for synthetic peptide substances*. Center for Drug Evaluation and Research and Center for Biologics Evaluation and Research, 1994.

36. **Verdier F, Patriarca C, Descotes J.** Autoantibodies in conventional toxicity testing. *Toxicology*, 1997, **119**:51–58.

37. *Guidance for industry for the evaluation of combination vaccines for preventable diseases: production, testing and clinical studies*. US Food and Drug Administration, 1997.

38. *Note for guidance on pharmaceutical and biological aspects of combined vaccines*. London, Committee for Proprietary Medicinal Products, 1999 (CPMP/BWP/477/97). Geneva, World Health Organization, 2003.

Appendix

List of tissues to be collected in a repeated dose toxicity study

adrenal glands

aorta

bone (femur) and articulation

bone (sternum) with bone marrow

bone marrow smears[1]

brain

bronchi (main-stem)

caecum

colon

duodenum

epididymides

eyes

heart

ileum

injection site(s) (a sample should be taken from the area of injection)

jejunum

kidneys and ureters

larynx

liver

lungs

lymph node (mandibular)

lymph node (mesenteric)

mammary gland

oesophagus

optic nerves

[1] Bone marrow smears should be prepared at the scheduled necropsy for all animals including any moribund animals killed during the study. The smears should be fixed in methanol and then stained by the May-Grunwald-Giemsa method.

ovaries and oviducts
pancreas
parathyroid glands
Peyer's patches
pituitary gland
prostate
rectum
salivary glands (mandibular, parotid, sublingual)
sciatic nerves
seminal vesicles
skeletal muscle
skin
spinal cord (cervical, thoracic, lumbar)
spleen
stomach
testes
thymus
thyroid glands
tongue
trachea
ureters
urinary bladder
uterus (horns + cervix)
vagina
all gross lesions

WHO Technical Report Series
987

WHO Expert Committee on Biological Standardization

Sixty-fourth report

This report contains the collective views of an international group of experts and does not necessarily represent the decisions or the stated policy of the World Health Organization

WHO Library Cataloguing-in-Publication Data

WHO Expert Committee on Biological Standardization, sixty-fourth report.

(WHO technical report series ; no. 987)

1. Biological products - standards. 2. Vaccines - standards. 3. Reference standards.
4. Guideline. I. World Health Organization. II. WHO Expert Committee on Biological Standardization (2013: Geneva, Switzerland). III. Series.

ISBN 978 92 4 120987 8 (NLM classification: QW 800)
ISSN 0512-3054

Printed in Italy

Annex 2

Guidelines on the nonclinical evaluation of vaccine adjuvants and adjuvanted vaccines

Guidelines published by WHO are intended to be scientific and advisory in nature. Each of the following sections constitutes guidance for national regulatory authorities (NRAs) and for manufacturers of biological products. If an NRA so desires, these Guidelines may be adopted as definitive national requirements, or modifications may be justified and made by the NRA. It is recommended that modifications to these Guidelines are made only on condition that such modifications ensure that the product is at least as safe and efficacious as that prepared in accordance with the guidance set out below.

Introduction

These Guidelines are intended to provide guidance to NRAs and manufacturers on the nonclinical and initial clinical evaluation of vaccine adjuvants and adjuvanted vaccines by outlining international regulatory expectations in this area. The Guidelines should be read in conjunction with existing WHO guidelines on nonclinical (*1*) and clinical (*2*) evaluation of vaccines. There is substantial diversity among vaccine adjuvants and adjuvanted vaccines and their nonclinical and clinical testing programmes will depend upon product-specific features and their clinical indications. Therefore, the following text is written in the form of WHO Guidelines instead of Recommendations. Guidelines allow greater flexibility than Recommendations with respect to specific issues related to particular adjuvanted vaccines.

Over the past decades, strategies and approaches for the development and delivery of vaccine antigens have been expanded. Some of these antigens are weakly immunogenic and require the presence of adjuvants for the induction or enhancement of an adequate immune response. Vaccines with aluminium-based adjuvants have been used extensively in immunization programmes worldwide and a significant body of safety information has accumulated for them (*3*, *4*). As the knowledge of immunology and the mechanisms of vaccine adjuvant action have developed, the number of vaccines containing novel adjuvants being evaluated in clinical trials has increased. Vaccines containing adjuvants other than aluminium-containing compounds have been authorized for use in many countries (e.g. human papillomavirus and hepatitis B vaccines), and a number of vaccines with novel adjuvants are currently under development, including, but not limited to, vaccines against human immunodeficiency virus (HIV), malaria and tuberculosis, as well as new-generation vaccines against influenza and other diseases. However, the development and evaluation of adjuvanted vaccines present regulatory challenges. Vaccine manufacturers and regulators have questions about the type of information and extent of data that would be required to support proceeding to clinical trials with adjuvanted vaccines and to eventual authorization.

Existing WHO guidelines on nonclinical evaluation of vaccines (*1*) provide valuable general guidance; however, they provide limited information specifically related to new adjuvants and adjuvanted vaccines. Some of the issues addressed here are also discussed in national or regional guidance documents (*5*, *6*). Given the importance and the complexity of the issues, this updated and more extensive guidance on the nonclinical and preclinical testing of adjuvants and adjuvanted vaccines should allow manufacturers and regulators to proceed in an efficient manner on the critical path towards development and licensure of adjuvanted vaccines indicated for the control of diseases with an important global public health impact.

Background

Over the past decades, there have been a number of international workshops and meetings in which the issues covered by these WHO Guidelines have been discussed (*7–12*). To address the need for additional international guidance on nonclinical evaluation of adjuvanted vaccines, a consultation was organized by WHO on 7–8 September 2011 in Rockville, Maryland, United States, to initiate the process of developing new WHO guidance on the subject. The consultation was attended by experts from academia, NRAs, national control laboratories and industry involved in the research, manufacture and approval of adjuvanted vaccines from countries around the world. The purpose was to review the scientific information and available data and to discuss and identify the issues to be considered for the development of such international guidance. On 27–28 November 2012, WHO organized an informal consultation at its headquarters in Geneva, Switzerland attended by academics, researchers, vaccine manufacturers and regulators involved in the evaluation of adjuvanted vaccines, to review draft WHO Guidelines prepared by the drafting group and to seek consensus on key regulatory issues. The approaches to nonclinical and initial clinical evaluation of vaccine adjuvants and adjuvanted vaccines discussed in this document are a result of the efforts of this and other international working groups.

Scope

This document addresses regulatory considerations related to the nonclinical and initial clinical evaluation of adjuvanted vaccines. The goal of this document is to provide consistent and harmonized guidance on nonclinical testing approaches to support the use of candidate adjuvanted vaccines in all stages of clinical development and ultimately for marketing authorization of the product. However, each NRA may determine the regulatory requirements applicable for adjuvanted vaccines to be marketed and used in their country.

Vaccine adjuvants are substances or combinations of substances that are used in conjunction with a vaccine antigen to enhance (e.g. increase, accelerate, prolong and/or possibly target) or modulate to a different type (e.g. switch a Th1 immune response to a Th2 response, or a humoral response to a cytotoxic T-cell response) the specific immune response to the vaccine antigen in order to enhance the clinical effectiveness of the vaccine (see "Terminology" section below). For the purposes of this document, the term "adjuvant" includes formulations that contain one individual adjuvant as well as adjuvant combinations that contain multiple adjuvants. These WHO Guidelines specifically address vaccine adjuvants that are either separate substances that are mixed with vaccine antigens and administered at the same time and location as the vaccine antigen, or immunostimulatory

moieties that are engineered by recombinant DNA technology to be an inherent part of the antigen molecule (e.g. fusion proteins) or the immunogen (e.g. vectored vaccines). In this context, it should be noted that no vaccine adjuvant is authorized in its own right, but only as a component of a particular adjuvanted vaccine. This document does not deal with the carrier proteins that are covalently linked to polysaccharide antigens in conjugate vaccines. Also, the immune enhancing properties that are intrinsic to certain vaccine antigen preparations, such as the naturally occurring adjuvant activity of whole-cell pertussis vaccines, are not considered "adjuvants" within this document.

This document covers adjuvanted vaccines used in both prophylactic and therapeutic indications against infectious diseases. Nevertheless, some of the principles outlined below may be applicable to the nonclinical and initial clinical testing of adjuvanted therapeutic vaccines for other indications as well (e.g. cancer).

Nonclinical evaluation, within the context of this document, refers to all in vivo (in animal) and in vitro testing performed before and during the clinical development of adjuvanted vaccines and includes product characterization, proof-of-concept and immunogenicity studies, as well as safety testing in animals. Preclinical testing specifically refers to the nonclinical testing done prior to initiation of any human testing and is a prerequisite to movement of a candidate adjuvanted vaccine from the laboratory to the clinic. Thus, for the remainder of this document, the term "preclinical" will be used only when referring specifically to the nonclinical evaluation done prior to the first-in-human clinical trials.

Many regulatory agencies, in addition to defining an adjuvant based on its immune-enhancing biological activity, provide a regulatory and/or legal classification for the adjuvant component of a vaccine (e.g. excipient, active ingredient or constituent material). It is possible that depending on the particular definition used by the regulatory authority, additional testing may be required. These regulatory and legal issues are specific for each regulatory authority and are beyond the scope of this document.

General considerations

Adjuvants have been used for decades to enhance the immune response to vaccine antigens (*7*). Possible benefits of administering antigens in conjunction with adjuvants include the induction of long-term protection, better targeting of effector responses, induction of long-term memory, reduction of the antigen amount and/or the number of vaccine doses needed for a successful immunization and optimization of the immune response for populations with poor responsiveness. For certain complex diseases, stimulation of cell-mediated immune responses appears to be critical, and adjuvants can be employed to

optimize a desired immune response, such as the induction of cytotoxic or helper T lymphocyte responses. In addition, certain adjuvants can be used to promote antibody responses in a relevant immunoglobulin class or at mucosal surfaces.

Successful preclinical evaluation of adjuvanted vaccines, including physicochemical characterization, proof-of-concept testing in animals, and toxicity testing, is an important step towards their clinical development. In addition, studies in animals are valuable tools to help select a safe dose, schedule and route of administration, and to identify unexpected or potential adverse effects for specific monitoring in clinical trials. Safety concerns include potential inherent toxicities of the vaccine antigen and/or adjuvant, potential toxicities of any impurities and contaminants, and potential toxicities due to interactions of the components present in the final formulation. The regulatory considerations for adjuvanted vaccines are similar to those for vaccines in general, with additional issues being considered that are unique to novel adjuvants. For the purposes of these WHO Guidelines, a novel adjuvant is defined as an adjuvant that has not been included in a licensed vaccine.

Throughout this document, guidance is provided related to the evaluation of new adjuvants and adjuvanted vaccines, to include:

- unlicensed adjuvanted vaccines;
- antigens and adjuvants that have been included in licensed vaccines, but for which the production process has undergone significant changes;
- previously licensed products that have undergone major formulation changes (e.g. a change in adjuvant or addition or removal of one of the components);
- previously licensed products given by a new route of administration.

Where appropriate, considerations specific to the evaluation of novel adjuvants will be provided.

The established benefits and increased availability of adjuvants have stimulated an interest in transferring adjuvant production technology from one adjuvant or adjuvanted vaccine manufacturer to another. As stated above, adjuvants are not approved in their own right. In the context of vaccines against infectious diseases, adjuvants may only exist as components in licensed vaccines that consist of specific antigen/adjuvant combinations. Thus, each new adjuvanted vaccine is considered a new entity that will require appropriate physicochemical characterization and nonclinical and clinical evaluations. However, in cases of technology transfer, existing data from similar antigen and adjuvant components and/or adjuvanted vaccines held by the original manufacturer can provide important information to guide and potentially accelerate the nonclinical and clinical studies (e.g. data from adjuvant-alone study arms). The need for and

extent of nonclinical testing will depend on the adjuvanted vaccine under consideration; manufacturers are encouraged to consult with the NRA regarding the nonclinical testing needed.

Vaccine adjuvants have been divided broadly into two main types – those known as vaccine delivery systems, which enhance the delivery of the antigen to the local lymph node, and those known as immunostimulators, although this division has become less clear since some delivery systems are now known to have direct immune stimulatory effects in addition to their ability to enhance the delivery of the antigen to the local lymph node. Delivery systems include, but are not limited to, particles, carriers, emulsions and liposomes. Immunostimulators in general include substances that enhance the immune response to vaccine antigens by activating the innate immune system, which usually sets off a cascade of events including, but not limited to, increased antigen uptake into antigen-presenting cells, increased release of stimulatory molecules such as cytokines and increased localization of the antigen in the local lymph node. Immunostimulators may include cytokines or other substances that are generally described as "immune potentiators" because they exert direct effects on immune cells.

Adjuvants also can be classified according to their source (e.g. synthetic or microbial-derived), mechanism of action and physical or chemical properties. A list of the most commonly described adjuvant classes, with specific examples, is provided in Appendix 1. It should be noted that a given vaccine adjuvant may be a combination adjuvant (see "Terminology" section below) that consists of multiple types of adjuvants and thus can fall into more than one of the listed categories.

Terminology

The definitions given below apply to the terms used in these WHO Guidelines. They may have different meanings in other contexts.

Adjuvanted vaccine: the complete formulation that includes one or more antigens, an adjuvant(s), and any additives (which may include, for example, excipients or preservatives), the administration of which is intended to stimulate the immune system to result in an immune response that leads to the prevention or treatment of an infection or infectious disease.

First-in-human trial: for the purposes of this document, this refers to the first evaluation in human subjects. Most commonly, the first-in-human clinical trials are carried out in small numbers of healthy and immunocompetent adults to test the properties of a vaccine, its tolerability and, if appropriate, clinical laboratory and pharmacological parameters. These trials are considered phase I trials (*2*) and are primarily concerned with safety.

Good laboratory practice (GLP): a quality system concerned with the organizational process and the conditions under which nonclinical health and environmental safety studies are planned, performed, monitored, recorded,

archived and reported. GLP principles may be considered as a set of criteria to be satisfied as a basis for ensuring the quality, reliability and integrity of studies, the reporting of verifiable conclusions and the traceability of data (*1*, *13*).

Good manufacturing practice (GMP): a part of the pharmaceutical quality assurance which ensures that products are consistently produced and controlled according to the quality standards appropriate to their intended use and as required in the marketing authorization. In these Guidelines, GMP refers to the current GMP guidance published by WHO (*14*, *15*).

Immunogenicity: the capacity of a vaccine/adjuvanted vaccine to induce antibody-mediated immunity, cell-mediated immunity and/or immunological memory.

In vitro studies: refers to studies that are conducted in a laboratory environment using components (e.g. serum, cells or tissues) that were originally obtained from a living organism.

In vivo studies: refers to studies that are conducted with living organisms.

Nonclinical evaluation of vaccine adjuvants and adjuvanted vaccines: nonclinical testing includes all in vivo and in vitro testing performed before and in parallel with the clinical development of adjuvanted vaccines. Nonclinical testing includes product characterization, proof-of-concept studies and animal in vivo/in vitro toxicity testing. The potential toxicity of an adjuvanted vaccine should be defined not only prior to initiation of human trials, but throughout clinical development, if appropriate (see also the definition of preclinical evaluation of vaccine adjuvants and adjuvanted vaccines).

Novel adjuvant: a novel adjuvant is an adjuvant that has not been contained in a licensed vaccine.

Potency: a measure of biological activity, using a suitably quantitative biological assay, based on an attribute of the product (e.g. adjuvanted vaccine) that is believed to be linked to the relevant biological properties. Other measures of potency (e.g. physicochemical analyses) may be appropriate based on the nature of the products (e.g. polysaccharides).

Preclinical evaluation of vaccine adjuvants and adjuvanted vaccines: preclinical testing refers specifically to the nonclinical testing (see definition of nonclinical evaluation of vaccine adjuvants and adjuvanted vaccines) done prior to the first-in-human clinical trials. Preclinical evaluation is a prerequisite to the initiation of clinical trials.

Process intermediates: the antigen(s) and the adjuvant(s) used to produce the formulated adjuvanted vaccine.

Product characterization: a full battery of physical, chemical and biological tests conducted for a particular product (e.g. adjuvanted vaccine). These tests include, but are not limited to, in-process control testing, testing for adventitious agents, testing of process additives and process intermediates, and lot-release testing (*1*).

Proof-of-concept studies: proof-of-concept studies as discussed in this document include the in vivo and in vitro nonclinical testing conducted to evaluate the immune response to the adjuvanted vaccine, the enhancement of the immune response to the antigen by the adjuvant and/or the demonstration of the resulting protection against challenge with the infectious agent targeted by the adjuvanted vaccine. For therapeutic vaccines, proof-of-concept studies would include, when possible, studies to evaluate the capacity to control or ameliorate disease and/or clear infection.

Protocol or study/trial plan: a document that states the background, rationale and objectives of the nonclinical study or clinical trial, and describes its design, methodology and organization, including statistical considerations, and the conditions under which it is to be performed and managed (*1*).

Raw materials: ingredients used to produce process intermediates.

Route of administration: the means by which the candidate adjuvanted vaccine is introduced to the recipient. Routes of administration for adjuvanted vaccines may include, for example, the intramuscular, subcutaneous, transcutaneous (with or without scarification), intradermal, oral, intranasal, inhaled (aerosol), intravenous, intranodal, intravaginal or intrarectal routes.

Safety: the relative freedom from direct or indirect harmful effect to animals or persons by a product when appropriately administered, taking into consideration the character of the product in relation to the condition of the recipient at the time.

Vaccine adjuvants: substances or combinations of substances that are used in conjunction with a vaccine antigen to enhance (e.g. increase, accelerate, prolong and/or possibly target) or modulate to a different type (e.g. switch a Th1 immune response to a Th2 response or a humoral response to a cytotoxic T-cell response) the specific immune response to the vaccine antigen in order to enhance the clinical effectiveness of the vaccine. It may be any of the types of substances identified as examples of adjuvants in Appendix 1. The term "adjuvant" is used throughout the document to include adjuvants that exist as one individual substance as well as combination adjuvants that consist of multiple adjuvants and sometimes other additives.

Vaccine and adjuvanted vaccine: the complete formulation that includes an antigen (or an immunogen, e.g. a plasmid DNA vaccine) and any additives such as adjuvants, excipients or preservatives, the administration of which is intended to stimulate the immune system to result in an immune response to the vaccine antigen leading to the prevention or treatment of an infection or infectious disease. When the vaccine contains an adjuvant, it may be referred to as an adjuvanted vaccine.

Vaccine antigen: the active ingredient in a vaccine (or generated by a vaccine) against which a specific immune response is raised. The vaccine antigen may be a live, attenuated preparation of bacteria, viruses or parasites; inactivated

(killed) whole organisms; crude cellular fractions or purified antigens, including recombinant proteins (i.e. those derived from recombinant DNA expressed in a host cell); polysaccharides and conjugates formed by covalent linkage of polysaccharides to components such as mutated or inactivated proteins and/or toxoids, synthetic antigens, or heterologous proteins expressed by plasmid DNA or viral or bacterial vectors. It may also be a combination of the antigens or immunogens listed above.

Part A. Manufacturing and quality considerations for the nonclinical and clinical evaluation of vaccine adjuvants and adjuvanted vaccines

Adjuvanted vaccine manufacturers are encouraged to discuss with the NRA the extent of the manufacturing and quality-related information necessary to support the intended use of the antigen, the adjuvant and the adjuvanted vaccine. The extent of information necessary to evaluate and assure the consistent safety and effectiveness of adjuvanted vaccines will vary with the phase of nonclinical and clinical investigation. Similarly, the nature and extent of the manufacturing controls needed to achieve, and testing needed to demonstrate, appropriate adjuvanted vaccine quality differ not only among the various phases of product development (that is, research, pilot, investigational and commercial manufacture) but also among the various phases of clinical evaluation.

A.1 Production, characterization and quality assurance of lots to be used in nonclinical pharmacology studies

It is generally accepted that nonclinical pharmacology studies (e.g. the proof-of-concept and mechanism-of-action studies) may be done as non-GLP studies, and that they are often conducted with research or pilot-scale lots of antigen, adjuvant and/or adjuvanted vaccine formulations. Also, these studies are often dose-optimization studies in which the antigen and adjuvant components may be provided in two separate containers to allow for the mixing of different amounts of each component prior to administration, and the generation of data that support the proposed dose of antigen and adjuvant to be used in the investigational adjuvanted vaccine. While the level of characterization of the lots of antigen and adjuvant used in these exploratory studies may be less extensive than those to be used in the nonclinical toxicology and clinical studies, the same raw materials should be used, where possible, in their preparation, and the source and any testing of the raw materials – for example, purity and assessment of levels of metal ions (such as copper) in aluminium-containing compounds – should be documented. Ideally, the lots of antigen and adjuvant used to formulate the final

product should be manufactured by the same process as the lots to be tested in the nonclinical toxicology studies. The general quality of the adjuvanted vaccine components (that is, antigen and adjuvant intermediates) used in the nonclinical pharmacology studies should be adequately characterized preliminarily. As the relationship between physical and chemical characteristics of the adjuvanted vaccine and its components and the immunogenicity and efficacy of the adjuvanted vaccine is not completely understood in many cases, biological characterization (i.e. through the use of biological assays) should complement the physical and chemical characterization of the intermediates and the adjuvanted vaccine (see section A.2 and Table 2.1).

A.2 Production, characterization and quality assurance of lots to be used in nonclinical toxicology studies and first-in-human clinical trials

Ideally, the lots of the antigen, the adjuvant, and the adjuvanted vaccine used in the nonclinical toxicology studies should be the same lots as those proposed for use in the first-in-human trials; these lots should be manufactured in compliance with the GMPs that are appropriate for phase I clinical trial materials (*16*, *17*). Additionally, the quality and stability of the antigen, adjuvant and final adjuvanted vaccine formulation should be characterized adequately prior to, if not in parallel with, their use in a toxicology study (see section A.2.1 and Table 2.1).

If use of the same lots is not feasible, the lots used for the nonclinical toxicology studies should be comparable to those proposed for use in the first-in-human trials with respect to manufacturing process, physicochemical data, formulation and stability. Where there are significant differences in the manufacture of the antigen or the adjuvant (or in the formulation of the adjuvanted vaccine) to be used in the nonclinical toxicology studies and the first-in-human clinical trial, a detailed description of the differences should be provided. This information will allow the NRA to evaluate the potential impact of such changes on the safety of the adjuvanted vaccine and to determine whether or not the differences are sufficient to warrant the conduct of additional toxicology studies to support the safety of the proposed clinical use.

With respect to the control and testing of adjuvanted vaccine lots manufactured for use in first-in-human clinical trials, emphasis should generally be placed on elements that assure the safety of subjects. This usually includes identification and control of the raw materials used to manufacture the antigen and the adjuvant. For this reason, Certificates of Analysis, with test specifications and results indicated, should be provided for ingredients that are acquired from contract suppliers for use in manufacturing the adjuvanted vaccine. For some adjuvanted vaccines, additional considerations related to the manufacturing and testing of the vaccine adjuvant and its individual components may be needed

to provide assurance that the adjuvant is manufactured consistently and has a consistent composition. This may apply particularly when one or more of the components of the adjuvant is biological in nature, when the vaccine contains a complex adjuvant mixture, or when the antigens are adsorbed to mineral salts or gels. Therefore, it is important to use established quality control procedures that ensure the consistent manufacture of adjuvants and antigens to be used in the preparation of adjuvanted vaccines. The antigen and adjuvant, or formulated adjuvanted vaccine, used in the first-in-human trial should be manufactured under GMPs that are appropriate for phase I clinical trial materials (*16*, *17*). Compliance with GMPs will ensure that the lots of antigen, adjuvant and adjuvanted vaccine are consistently manufactured and controlled to the quality standards appropriate to their intended use. Compliance with all aspects of GMPs will be required at the later stages of clinical development (*14*, *15*) as discussed below (see section A.3 and Table 2.1).

The clinical lot(s) of adjuvanted vaccine, or separate lots of antigen and adjuvant if provided in separate final containers, should be demonstrated to be stable for the duration of the clinical trial. Additionally, if the adjuvant is provided in a separate container (e.g. vial or syringe) to be used to reconstitute or be added to the antigen prior to vaccine administration, a detailed description of the procedure for mixing the components should be provided. A clear statement of the appropriate time and conditions for storage of the individual components and the final adjuvanted vaccine should be provided. Also, the appearance of the adjuvanted vaccine after mixing should be described, and stability data to support the storage of the adjuvanted vaccine up to the time of administration should be provided.

A.2.1 Analytical testing of adjuvant, antigen and adjuvanted vaccine

A detailed description of the adjuvant, antigen and adjuvanted vaccine should be provided and include information regarding the characterization conducted to assure the quality (e.g. identity, purity, sterility) and quantity of the antigen and adjuvant as well as the potency of the adjuvanted vaccine. It should be demonstrated that the adjuvant does not adversely affect the potency of the antigen upon mixing. In addition, information on the methods of manufacture and testing for the intermediates and final product, together with their preliminary release specifications, should be provided. Although it is not necessary to have validated methods for testing the lots of antigen and adjuvant or adjuvanted vaccine to be used in nonclinical toxicology studies and first-in-human clinical trials, the scientific background should justify the choice of the testing methods and the selected preliminary specifications. It is recommended that the NRA be consulted when designing analytical protocols appropriate for establishing the identity and quantity of the antigen(s), adjuvant(s) and any additives. It is important to

assess attributes of each of the antigen and the adjuvant components that may be relevant for adjuvant activity and adjuvanted vaccine potency. Additionally, the properties of the antigen and the adjuvant that are most indicative of stability, both when stored individually and as a formulated final adjuvanted vaccine, should be identified.

Assays used for characterization of the adjuvant may or may not be related to its mode of action, but should be adequate to ensure consistency of adjuvant production and to evaluate adjuvant stability. These may include, for example, assays for appearance, particle size distribution, presence of aggregates and pH for the adjuvant, and the amount of aluminium and degree of antigen adsorption for a vaccine adsorbed to an aluminium-containing compound. Analytical methods to evaluate the antigen and the adjuvant in an adjuvanted vaccine should be developed and validated as adjuvanted vaccine product development and clinical evaluation proceed. If relevant, the methods to be developed for characterization purposes should include, where possible, methods to assess compatibility and/or physical interactions between the antigen and adjuvant (and between the components of the adjuvant, if a combination adjuvant is used). Validation of these methods should be completed if they are intended for quality control batch release during later-stage clinical development or commercial distribution.

A quality-control test evaluating the potency of the final adjuvanted vaccine should be developed as one of the assays to assess consistency of manufacture. Depending on the type of potency assessment conducted on the adjuvanted vaccine and the requirements of the NRA, the assessment may or may not reflect the contribution of the adjuvant to the potency of the adjuvanted vaccine. If it does not, it will be important to conduct assessments of the identity and content of the adjuvant in the final adjuvanted vaccine. Also, the purity and sterility of the final adjuvanted vaccine will need to be assessed to ensure its safety. If the adjuvant or adjuvanted vaccine is tested for endotoxin via the Limulus amoebocyte lysate (LAL) test method, evidence that the adjuvant or adjuvanted vaccine does not interfere with the LAL test (e.g. data from lipopolysaccharide spiking experiments with and without adjuvant) should be provided, as certain adjuvants, such as cationic liposomes, may interfere with the LAL test method. If interference is observed, alternative tests (e.g. pyrogen test or macrophage-activation test) should be investigated.

If the final adjuvanted vaccine consists of co-packaged antigen and adjuvant, where each is provided in a separate container to be mixed prior to administration, both the antigen and the adjuvant should be evaluated prior to mixing for relevant parameters, such as identification, purity and sterility. In addition, the potency of the antigen and the content of the adjuvant per dose should be assessed. Also, where feasible, evidence should be provided as mentioned previously to demonstrate that the adjuvant does not adversely affect the potency of the final adjuvanted vaccine. Thus, the potency of the extemporaneously mixed,

adjuvanted vaccine formulation should be demonstrated. For some adjuvanted vaccines (e.g. aluminium-adsorbed vaccines), it may not be possible, depending on the nature of the potency assay, to evaluate the potency of the final formulated vaccine by certain assays. In this case, the determination of the potency of the antigen alone prior to adsorption may be recommended as well as the development of an in vivo method for potency assessment of the final formulation.

Consultation with the NRA is recommended to discuss both the need for and design of the quality control test known as the innocuity, general safety, or abnormal toxicity test for the adjuvanted vaccine. Additionally, if a particular NRA requires such a test for a formulated adjuvanted vaccine, it should be clarified whether only the antigen or both the antigen and adjuvant are to be tested when provided in separate final containers. While some regulatory authorities and WHO no longer require this test to be performed on a routine basis once the consistency of production has been established, some have further questioned the relevance of this test (*18–20*). In some countries there is a legal requirement to conduct an innocuity test with the objective of assessing the potential introduction of extraneous impurities into the final adjuvanted vaccine; however, this is not considered a toxicity test. If the innocuity test is required, and the investigational adjuvant or adjuvanted vaccine does not pass the innocuity test when administered according to the prescribed protocol, which is typically volume based and administered by the intraperitoneal route, it will be necessary to define the appropriate dose and route of administration for the adjuvanted vaccine. The manufacturer of the vaccine will need to provide justification for a modification of the innocuity test in regulatory submissions. Such modifications should be discussed with the NRAs. In the countries where the innocuity test is still necessary, once test data from many lots have been accumulated, and consistency of production has been well established to the satisfaction of the NRA, it may be possible to request an exemption from conduct of the innocuity test as part of routine lot-release testing.

A.3 Information required for later-stage clinical trials

In general, in the course of adjuvanted vaccine product development, the analytical technology and methodology is developed in parallel with the clinical investigations. As the adjuvanted vaccine product development and clinical evaluation proceed, the quality control and quality assurance of the antigen and adjuvant should be refined. When clinical trials to collect safety and efficacy data to support licensure are initiated, the manufacturing processes should be demonstrated to be consistent and validated, and a detailed description with appropriate validation information should be provided for all analytical procedures (except for those that are from an official pharmacopeial compendium) (*14*, *15*). If a national or international standard is not yet available for a particular

antigen, adjuvant or adjuvanted vaccine, the manufacturer should establish its own primary reference material during later-stage clinical trials.

A minimum of three consecutive lots of each of the antigen and the adjuvant intermediates (or final containers if provided separately) and formulated adjuvanted vaccine should be manufactured and tested for purposes of demonstrating consistency of manufacture of the vaccine antigen, the adjuvant and the formulated adjuvanted vaccine. Any changes in the manufacture or formulation should be carefully assessed to determine if such changes directly or indirectly affect the quality or safety of the adjuvanted vaccine. When analytical data from tests conducted on the adjuvanted vaccine demonstrate that the antigen, adjuvant or adjuvanted vaccine manufactured before and after such changes is not comparable, additional qualification and/or bridging studies should be undertaken to support the safety of the materials proposed for continued clinical evaluation.

To ensure that appropriate stability data are collected during later stage clinical trials of the adjuvanted vaccine, a stability protocol to be used for the formal stability studies should be developed for the antigen, the adjuvant and the adjuvanted vaccine. Stability programmes should be designed to monitor the chemical, physical, biological and microbiological stability of the antigen, the adjuvant, and the adjuvanted vaccine throughout the clinical testing programme. The properties of each antigen and adjuvant that are most indicative of stability, both when stored individually and as a mixed final adjuvanted vaccine, should be identified as stability evaluations proceed (as mentioned in section A.2.1). If it is determined that degradation products accumulate from either the antigen or the adjuvant over the shelf-life of the adjuvanted vaccine, these should be evaluated during stability testing of the final product. It is recommended that the NRA be consulted to determine whether additional suitable nonclinical toxicological testing should be undertaken to confirm their safety. Additional guidance on stability testing of vaccines can be found in WHO Guidelines on stability evaluation of vaccines (*21*).

Part B. Rationale for the use of the adjuvant

Adjuvant activity is a result of multiple factors and an adjuvant-mediated enhancement of the immune response to one vaccine antigen, as a rule, cannot be extrapolated to the enhancement of the immune response to another antigen. Individual antigens vary in their physical, biological and immunogenic properties and antigens may have different needs for immunological help from an adjuvant (*5*). Manufacturers should justify the choice of the adjuvant based on the immune response desired, which may include effects on the magnitude, the breadth and/or the type of immune response to specific antigens and on the safety profile. In addition, adjuvants are also used in antigen dose-sparing strategies with the aim of

increasing the availability and supply of vaccines – for example, under emergency situations of an influenza pandemic (*22*) or as a strategy to decrease the cost of the vaccine (e.g. use of inactivated poliovirus vaccine for polio eradication) (*23*).

Many advances in the understanding of innate immunity have begun to provide insights into the immunological mechanisms of adjuvant action. Many of the immunostimulatory adjuvants are recognized by various members of the toll-like receptor (TLR) family, a subclass of pathogen-recognition receptors, while other adjuvants may target other families of pathogen-recognition receptors that could prove to be important in shaping the adaptive immune response. Furthermore, there are complex regulatory interactions between the many families of innate receptors and other signalling pathways. Within this framework, the activities exerted by adjuvants include, but are not limited to, the facilitation of: (a) mobilization of antigen-presenting and/or polymorphonuclear cells; (b) antigen uptake and presentation of the antigen(s) in the vaccine by antigen-presenting cells; (c) secretion of proteins by antigen-presenting cells; (d) recruitment, targeting and activation of antigen-specific cells; (e) modulation of activities that regulate the ensuing immune responses; and/or (f) protection of the antigen from degradation and elimination.

The scientific rationale supporting the benefit of adding the adjuvant and the choice of specific adjuvant(s) should be provided by the adjuvanted vaccine manufacturer. Before evaluating a particular adjuvant in combination with an antigen in a clinical trial, it is recommended that data from in vitro and/or in vivo studies be generated to support the rationale for including the specific adjuvant in the vaccine formulation and for selecting the dose range of adjuvant to be tested. In the ideal case, the mode of action of the selected adjuvant as well as the mechanism of the enhanced immune response would be well understood prior to the initiation of later-stage clinical development. When the mode of adjuvant action is not well defined, supplemental in vivo or in vitro data (as discussed in sections B.1 and B.2, respectively) may be provided in addition to the pivotal toxicity study to support the added benefit of the adjuvant to the immune response induced by the adjuvanted vaccine as well as the safety of the adjuvanted vaccine.

B.1 In vivo proof-of-concept studies

Data from proof-of-concept studies, including data from early studies conducted to evaluate optimal antigen/adjuvant formulations, can provide important information with regard to the characteristics of the adjuvanted vaccine. These data include evidence for the need for the adjuvant, the type and magnitude of the immune responses induced (i.e. innate immunity, or humoral and cellular immunity), and the functional capacity of the immune response to either protect against disease (i.e. prophylactic vaccine) or ameliorate an existing infectious disease (i.e. therapeutic vaccine) when a relevant nonclinical disease model

is available. These pilot or exploratory studies designed to identify and screen adjuvanted vaccine formulations may be non-GLP-compliant; however, they may identify unknown or potential adverse effects, and provide crucial information for the design of GLP-compliant toxicity studies. In addition, in vivo proof-of-concept studies may provide the scientific justification for manufacturing changes and for optimization of adjuvanted vaccine formulation, dose and route of administration during the clinical development of the adjuvanted vaccine product.

It is recommended that proof-of-concept studies to support the use of an adjuvant be carried out to evaluate vaccine formulations with and without the adjuvant. Depending on the specific antigen and/or adjuvant being considered, possible examples of these types of studies include:

- evaluation of humoral immune responses with regard to magnitude (e.g. mean titre or concentration), quality (e.g. affinity or avidity), and functional activity (e.g. neutralizing activity);
- evaluation of cellular immune responses including assessment of the induction of specific types of cellular responses (e.g. examining Th1 or Th2 cytokine profiles, or testing for the induction of cytotoxic T cells);
- evaluation of protective or therapeutic responses against the relevant pathogen using appropriate animal or in vitro disease models and/or evaluation of functional immune responses (e.g. neutralizing activity, serum bactericidal or opsonophagocytic antibody titres);
- evaluation of duration of (*24*) and extent of cross-protection provided by the induced immune response (*25*, *26*).

These studies will contribute to the elucidation of the adjuvant mode of action and may provide indication of the adjuvant-specific immune modulatory effects. In addition, these studies may assist in the interpretation of nonclinical safety studies and the identification of potential adverse effects to be monitored during clinical development. The development of in vitro model systems, particularly those using human cells, is recommended when possible, as they may provide additional relevant information to elucidate the mechanism of action of the adjuvant (see section B.2).

B.2 In vitro supporting studies

Functional in vitro bioassays may also provide helpful insight in understanding the mode of action of a particular adjuvant, and may provide valuable supplemental and complementary data to animal studies. This is particularly important when there are limitations to the animal models, such as species-specific differences (e.g. in TLRs). Antigen-presenting cells or other immune cells are widely used to assess and monitor the direct or indirect effects of adjuvants by measuring activation parameters (such as changes in the expression of cell

surface molecules and the pattern of cytokine secretion), and more recently such human cells have been used to develop in vitro assays that may be predictive of adjuvant safety in vivo (*27*). More complex tissue culture systems, containing a mixture of human immune cells mimicking lymphoid tissue, are being explored with the aim of evaluating human immune responses in vitro (*28*).

Part C. Considerations for selection of the animal species for nonclinical evaluation of vaccine adjuvants and adjuvanted vaccines

Investigations of the properties that influence the safety and pharmacological activity of the adjuvant and the adjuvanted vaccine require the use of appropriate animal species. The animal species used for pharmacological and safety evaluations should be chosen carefully and justified. For ethical reasons, it is desirable to apply the 3Rs concept of "Replace Reduce Refine" to minimize the use of animals in research where scientifically appropriate (*29*). Both manufacturers and staff at the NRA or national control laboratory are encouraged to further develop in vitro assays and to evaluate their suitability for the control of vaccines (*30*).

C.1 Selection of animal species for nonclinical pharmacology studies

For the purpose of this document, the nonclinical pharmacological activity of an adjuvanted vaccine is defined as the ability of the adjuvanted vaccine to induce and/or modify an immune response in an animal species. Factors influencing the selection of a particular animal species include, but are not limited to, the vaccine antigen, the adjuvant chosen, the type of immunity (i.e. cell-mediated or humoral) to be induced and the route of administration. It is recommended that proof-of-concept studies be undertaken using an animal species in which: (a) an immune response to the vaccine antigen is developed; and (b) the immune response to the antigen is enhanced by the adjuvant through a mechanism similar to that expected in humans (e.g. TLRs known to be targeted by the adjuvant are present in the species, and enhanced humoral and/or cellular immunity is observed). However, it is acknowledged that species-specific differences in the immune responses induced in the animal species compared to the human are likely. Proof-of-concept studies most commonly are conducted in several animal species, including both naive and pre-exposed animals. In addition to evaluating the immune response induced by the vaccine antigen alone and in the presence of the adjuvant, the mechanism of action of the adjuvant in the absence of the vaccine antigen should also be evaluated.

If the adjuvanted vaccine is a therapeutic vaccine for an infectious disease indication, where feasible, disease animal models may need to be developed to

study the pharmacological activity of the adjuvanted vaccine and its effect on the disease. For preventive adjuvanted vaccines, the use, when available, of an animal species sensitive to the human pathogen may provide important insight into the mechanism of protection from the disease (e.g. the ferret model for human influenza).

Nonclinical pharmacology studies may be conducted under non-GLP compliant conditions. It is advisable to incorporate into the study design toxicological end-points to guide the design of GLP-compliant nonclinical safety studies. It is sufficient to conduct these studies in small animal species if it can be demonstrated that the animal species chosen is relevant and responsive to the vaccine antigen and the adjuvant when given by the intended route of administration. Nonhuman primates should be used only if no other relevant animal species is available.

C.2 Selection of animal species for nonclinical safety studies

When selecting the animal species for nonclinical safety studies, it is important to document the pharmacological activity of the vaccine in the presence and absence of adjuvant in that species. It is recommended that manufacturers conduct nonclinical safety studies in compliance with GLPs (see section D.2 and Table 2.1) and using an animal species in which an immune response to the vaccine antigen is developed and, ideally, the immune response to the antigen is enhanced by the adjuvant through a similar mechanism as expected in humans. It is not necessary, however, to conduct the nonclinical safety study in the same animal species used for proof-of-concept or nonclinical pharmacology studies (see sections B.1 and C.1). Nonhuman primates should be used only if no other relevant animal species is available. In situations where no animal species is available that is responsive to the adjuvanted vaccine, the choice of the animal species should be justified. In some circumstances, the use of in vitro model systems, particularly those using human cells, to evaluate the toxicity of the adjuvanted vaccine may provide additional supplementary information to assist in interpreting toxicity data (*27*).

It is highly recommended that the animal species chosen is one for which relevant and sufficient historical control data exist. Analysis and interpretation of data from the toxicity studies commonly includes a comparison with the inactive control (e.g. saline control) in the same study. However, historical control data from the same laboratory in which the study was conducted and for animals of comparable age and from the same species and/or strain may provide additional information. When historical control data are used, the data should be provided to the NRA.

The route of administration used in the toxicity study should correspond to that intended for use in the clinic. Also, when the adjuvanted vaccine is to be

administered in the clinic using a particular device, the same device should be used in the animal study, where feasible. For example, a small rodent species may not be an appropriate choice for nonclinical evaluation of a vaccine that is to be delivered intranasally because some of the inoculum could be delivered to the lungs. In this case, a larger animal or one with nasal surface area, anatomy and physiology similar to that of humans would be more appropriate.

Use of a single species is generally acceptable (see section D.2). This approach has commonly been accepted based primarily on pragmatic considerations – for example, the ability to predict the human immune response may be limited due to the species specificity of the response in animals to the antigen, the adjuvant or both.

C.3 Limitations of animal studies

The limitations of using animals to characterize the pharmacological and safety profile of an adjuvant or adjuvanted vaccine are acknowledged. The ability to predict the human immune response based on pharmacological studies in an animal may be limited due to the species specificity of the response to the antigen, the adjuvant, or both. Similarly, local and systemic adverse effects observed in a nonclinical safety study may not be directly translatable to the clinic. In addition, rare and/or late-onset adverse events that may occur in human subjects as a result of adjuvanted vaccine administration may not be observed in animal studies. Nevertheless, these studies offer the best currently available tools to evaluate the preclinical safety and pharmacology of adjuvanted vaccines.

D. Nonclinical safety assessment in animals

D.1 General remarks

Safety concerns for products such as vaccines include the potential inherent toxicities of the antigen and other vaccine components, as well as potential toxicities due to interactions of the components present in the final formulation. For adjuvanted vaccines, these concerns include the possibility that the immune-modulatory and/or inflammatory response induced may lead to undesired toxic side effects. Additionally, some adjuvants may elicit elevated levels of proinflammatory cytokines and other mediators of toxicity, irrespective of the immune response against the antigen.

Safety assessments in animal studies are valuable tools to help define an acceptable adjuvant/antigen ratio and a safe dose, as well as to identify unknown or potential adverse effects that should be taken into consideration for further product development or to be monitored in future clinical trials. The type of studies and the timing in relation to the clinical programme are presented in section D.2.

D.2 Toxicity studies of vaccine adjuvants and final adjuvanted vaccine formulations

The preclinical toxicity studies of the final adjuvanted vaccine formulation should be adequate to identify and characterize potential adverse effects of the vaccine in order to conclude that it is reasonably safe to proceed to first-in-human clinical investigation. As the mechanism of action of the adjuvant and/or adjuvanted vaccine formulation is often not fully understood, the toxicity studies should be designed to evaluate a broad spectrum of parameters due to the uncertainty of the in vivo effects and associated outcomes. Toxicity studies should be designed to mimic the intended route of administration in the clinic and to evaluate local reactogenicity (e.g. injection-site inflammation) and systemic toxicity (i.e. toxicity that occurs at sites distant from the site of initial administration). Pivotal toxicity studies should use the intended final formulation and dose of the adjuvanted vaccine (see section A.2) and should be conducted in compliance with GLPs.

When properly designed, conducted and interpreted, and when no major safety signals are revealed in the study results, one repeated-dose toxicity study in one relevant species should be sufficient. However, if there are significant manufacturing or formulation changes during product development, additional animal toxicity studies may be recommended to confirm that the safety profile of the product has not been changed. Also, throughout the clinical programme, additional animal toxicity studies (e.g. developmental and reproductive toxicity studies) may be necessary to investigate any adverse events observed in clinical trials or to support the use of the vaccine in a special population.

While comprehensive toxicity evaluations of the final adjuvanted vaccine formulation are considered essential, the advantages and limitations of toxicity studies with adjuvant alone have been discussed extensively in previous meetings and workshops (*7–11*). A comprehensive toxicity assessment of the adjuvant alone in animals (or of individual evaluations of its multiple components, if it is a combination adjuvant) may not be needed as a separate programme. However, to enable the interpretation of immunogenicity and safety studies of the adjuvanted vaccine, a study arm receiving adjuvant alone may be included in the repeated-dose toxicity studies (see section D.2.2) that are part of the comprehensive toxicity evaluations of the final adjuvanted vaccine formulation.

D.2.1 Safety pharmacology studies

The purpose of a safety pharmacology study is to investigate the effects of the candidate vaccine on vital functions. Although not usually required, safety pharmacology studies may be recommended by the NRA in some cases. For example, if data from nonclinical and/or human clinical studies suggest that the adjuvanted vaccine may affect physiological functions other than the immune

system (e.g. the central nervous system, respiratory or cardiovascular system, renal function or body temperature) then safety pharmacology studies should be incorporated into the safety assessment programme.

D.2.2 Repeated-dose toxicity studies

This section highlights important considerations regarding the study design for pivotal toxicity studies that should be conducted with the same vaccine formulation intended to be used in clinical trials (see section A.2). If more than one dose of an antigen or adjuvant is to be evaluated in the clinical study, the formulation containing the highest dose (i.e. the "worst case") should be included in the pivotal toxicity studies. Single-dose toxicity studies on the final formulated vaccine product, which are applicable to small-molecule chemical medicines, are usually not needed in accordance with *Guidance on nonclinical safety studies for the conduct of human clinical trials and marketing authorization for pharmaceuticals: M3(R2)* (*31*). Acute effects of administering a vaccine can also be monitored in repeated-dose toxicity studies if they are adequately designed (e.g. an evaluation is conducted after the first administration). Alternatively, acute effects can be assessed in a single-dose design as part of a local tolerance study. For a study intended to support a first-in-human clinical trial, the number of animals studied per sex, group and time interval should be sufficient to allow meaningful scientific interpretation of the data generated. The size of the treatment group will depend on the animal species chosen; i.e. the number of animals included in studies using non-rodents (e.g. miniature pigs) would be expected to be fewer than the number included in studies using rodents. For mice and rats, it is recommended that at least 10 animals of each sex per group be used for the necropsy at the end of the treatment interval, and at least 5 animals of each sex per group be used for the necropsy at the end of the recovery period. For rabbits, it is recommended that at least five animals of each sex per group for each time interval be used. In general, the approximate age for rodents should be 6–8 weeks, and for rabbits, 3–4 months, at the start of the study.

D.2.2.1 Dose, dosing regimen and controls

Dose–response evaluation for the adjuvanted vaccine is generally not required as part of the basic toxicity assessment, given that, in most cases, dose–response assessment was explored in nonclinical pharmacology studies. For adjuvanted vaccines, the toxicity study should be performed using the highest anticipated human dose (in absolute terms) of the final adjuvanted vaccine to be used in the proposed clinical trial, where feasible. Ideally this dose provides optimal exposure of the animal to the candidate vaccine and the immune response induced. However, in the case of a novel adjuvant, it may be advisable to include additional (lower and higher) doses of the adjuvanted vaccine formulation or

adjuvant alone in order to identify a safe dose that could be used in a first-in-human clinical trial.

If the dose to be administered is limited by the total volume that can be administered in a single injection, guidelines for animal welfare should be followed (*32*). In such cases, the total volume may need to be administered at multiple sites using the same route of administration; however, it should be noted that the evaluation of local reactogenicity might be less reliable in such cases.

For adjuvanted vaccines intended to be given repeatedly, the number of doses administered to the animals in repeated-dose toxicity studies should equal or exceed the number of doses proposed in humans. However, in many cases, the studies are designed to include one dose more than planned for the clinical trial to allow for the possible inclusion of an additional dose in the clinical trial. To simulate the proposed clinical usage, vaccine doses should be given as episodic doses, but the dosing interval used in the toxicity study may be reduced (e.g. to 2 weeks or 3 weeks) compared with the proposed clinical dosing interval (which usually is greater than 2 weeks to 3 weeks). The nonclinical dosing interval should be based primarily on the kinetics of the primary and secondary antibody response observed in the animal study.

In general, the study design should include a negative control group that receives an inert placebo, such as saline, to evaluate a baseline level of treatment, and an adjuvant-alone arm to aid in the interpretation of safety data from the adjuvanted vaccine. Also, the treatment groups in the study should include a sufficient number of animals for evaluation (as described in section D.2.2.3) at later time points after treatment to evaluate the reversibility of adverse effects observed during the treatment period and to detect potentially delayed adverse effects.

D.2.2.2 Route of administration

The route of administration should correspond to that intended for use in the clinical trials. When the vaccine will be administered in human clinical trials using a particular device, the same device should be used in the animal study, where feasible.

D.2.2.3 End-points in toxicity studies

The following section discusses end-points that are especially relevant and important in the evaluation of adjuvanted vaccines in repeated-dose toxicity studies using the final vaccine formulation. In general, potential adverse effects of the adjuvanted vaccine should be evaluated in repeated-dose studies with regard to target organs (see Appendix 2), dose, route(s) of exposure, duration and frequency of exposure, and potential reversibility of observed toxic effects.

D.2.2.3.1 *Parameters for monitoring of systemic toxicity*

Toxicity studies, repeated-dose toxicity studies in particular, should address the potential for systemic toxicity including, but not limited to, the systemic effects on the immune system. A broad spectrum of information should be obtained from the toxicity study, and both in-life and postmortem data should be collected. This routinely includes careful monitoring of body weight and food consumption, body temperature, histopathology, clinical chemistry, haematology, coagulation parameters and acute phase reactants. In addition, the immune response should be evaluated in a group of treated animals to confirm that the anticipated immune response occurred during the toxicity study. A detailed description of the assay(s) used should be provided with the toxicity study results.

While the standard in-life parameters routinely assessed for general pharmaceuticals (e.g. overall health, body weight and food consumption) are appropriate, it is important to note that for adjuvanted vaccines more frequent (e.g. daily) measurements of body weight and food consumption are recommended, especially during the first week after the administration of each dose as these parameters are very sensitive in detecting systemic toxicity effects. After the first week, body weights may be collected less frequently (e.g. 2–3 times each week). Body temperature should also be evaluated prior to, and 3–8 h and 24 h after each dose. If there is an increase in temperature, additional measurements should be taken every 24 h until the values return to baseline. Interim analyses of haematology and serum chemistry should be considered within approximately 1–3 days following the first and last dose administration, and at the end of the recovery period; in addition, the collection of a predosing sample is recommended. Coagulation parameters should be included routinely; in some cases, evaluation of urine samples and serum immunoglobulin classes may be of value. Additionally, it is recommended that species-appropriate acute phase reactants (e.g. C reactive protein) be measured in the toxicity study prior to immunization, at time points following the administration of the adjuvant or adjuvanted vaccine that have been demonstrated to reflect peak elevations in the acute phase reactants being evaluated (commonly 24–48 h), and after a recovery phase of 7 days. When measuring acute phase reactants, the choice of the animal species may determine which proteins can be measured as these reactants vary among species (*33*). The data discussed above should be collected not only prior to and during the treatment phase, but also following the treatment-free (recovery) phase (i.e. 2 or more weeks following the last dose) to determine persistence, exacerbation and/or reversibility of potential adverse effects.

Postmortem data, including data from gross necropsy (with tissue collection and preservation, including gross lesions and organ weights), should be collected within 3 days following the last dose and following the above-mentioned recovery period (e.g. 2 or more weeks following the last dose) (*1*). At study termination, final body weights (following overnight fasting) should be

obtained. Terminal blood collection and analysis should include serum chemistry, haematology, and coagulation parameters as well as an immune-response evaluation. Histopathological examinations should always include pivotal organs (brain, lung, heart, kidneys, liver, reproductive organs), and the site of adjuvant or adjuvanted vaccine administration. Special attention should be paid to the immune organs – i.e. lymph nodes (draining and distant to the application site), thymus, spleen, bone marrow, and Peyer's patches or bronchus-associated lymphoid tissue – as well as organs that may be primarily affected due to the particular route of administration. The extent of the list of tissues to be examined (i.e. the full tissue list as provided in Appendix 2 versus the reduced list mentioned above, which is limited to the immune system and pivotal organs) will depend on the adjuvant or adjuvanted vaccine in question, as well as on the experience and knowledge obtained through previous nonclinical and clinical testing of the vaccine's components. Additionally, any known target organs of the adjuvant or adjuvanted vaccine should be evaluated. For novel adjuvants and adjuvanted vaccines containing a novel adjuvant, it is recommended that the full tissue list be evaluated.

D.2.2.3.2 *Parameters for monitoring of local reactogenicity*

Local toxicities should be determined at the site(s) of adjuvant or adjuvanted vaccine administration and any other sites that come into contact with the adjuvant or adjuvanted vaccine components as a result of the method of administration. Local toxicity studies of intramuscularly administered vaccines should preferably be conducted in animals with sufficient muscle mass to test the full human dose of the final vaccine formulation.

Injection site reaction after inoculation should be scored using a prospectively defined system (e.g. the modified Draize test) (*34*) along with an assessment of any vesiculation, ulceration, severe eschar formation and other manifestations of significant toxicity (e.g. limb impairment).

The site of administration and any other site that comes in contact with the adjuvant or adjuvanted vaccine (e.g. eye exposure during aerosol administration, or digestive tract after oral administration) should also be evaluated histopathologically. In addition, a description of cellular infiltrates based on routine histological staining, if present, should be reported as part of the postmortem evaluation, as well as any manifestation of tissue damage at the site of injection and surrounding anatomic structures (e.g. sciatic nerves, nasal cavities or olfactory bulb).

D.2.3 Developmental and reproductive toxicity

Because vaccination programmes may include women of childbearing potential, it is important to consider the need for developmental and reproductive toxicity studies. As is the case for general toxicity, the use of a novel adjuvant may require

adding an adjuvant-alone arm to the reproductive toxicity studies. However, the study design is also dependent on the intended clinical use of the vaccine. For example, vaccination may be given early in pregnancy to protect the mother at risk, or might be given later in pregnancy to induce passive immunization to protect the infant directly from birth.

In general, the administration of one or several additional doses during organogenesis (i.e. implantation to closure of the hard palate) is recommended in order to evaluate the potential, direct embryotoxic effects of the components of the vaccine formulation, and, depending on the animal model, to allow maternal antibody to transfer to the progeny during pregnancy or the lactation period. Depending on the adjuvant, there may be concern about an adjuvant-induced systemic inflammatory response, such as fever, which may adversely affect early pregnancy (e.g. implantation or placental growth) (*35*). In these cases, it is recommended to include in the study design an additional treatment group to evaluate the effect of adjuvant on early pregnancy parameters. Rather than dosing this treatment arm prior to mating, it is recommended to dose animals post-mating and prior to implantation (e.g. post-mating day 1). Considering the short gestational period of the animal species that are most frequently used, it may be necessary to administer priming doses to the animals several days or weeks prior to mating in order to elicit a peak antibody response during the period of organogenesis.

End-points in embryo-fetal/perinatal-postnatal toxicity studies include, but are not limited to, viability, abortions, number of resorptions, fetal body weight, morphology, preweaning development and growth, as well as survival incidence and developmental landmarks. For details on such studies, please see the United States Food and Drug Administration's *Guidance for industry: considerations for developmental toxicity studies for preventive and therapeutic vaccines for infectious disease indications* (*36*) and WHO guidelines on nonclinical evaluation of vaccines (*1*).

In most cases, the developmental and reproductive toxicity studies can be performed in parallel to the clinical trials. However, some NRAs require that women of childbearing potential be excluded from large-scale late-stage clinical trials that are conducted prior to the completion of developmental and reproductive toxicity studies; other NRAs require the use of appropriate birth control methods for women of childbearing potential that are included in clinical trials. Further considerations can be found in *Guidance on nonclinical safety studies for the conduct of human clinical trials and marketing authorization for pharmaceuticals: M3(R2)* (*31*).

D.2.4 Biodistribution studies

Adjuvants are expected to exert their action locally in close connection to the antigen. However, biodistribution studies can be helpful in understanding the

distribution of the adjuvant following injection. The feasibility of and need for such biodistribution studies should be evaluated on a case-by-case basis.

D.2.5 Genotoxicity and carcinogenicity studies

Genotoxicity studies are normally not needed for the final vaccine formulation (*1*). However, a standard battery of genotoxicity studies is generally recommended for most novel adjuvants that are (or contain) new chemical entities (*31*, *37*). Based on previous experience, carcinogenicity studies are generally not needed for adjuvants or adjuvanted vaccines.

D.2.6 Toxicity studies of adjuvant alone

As noted in the introduction to section D.2, comprehensive toxicity assessment of the adjuvant alone in animals may be included as part of the study design with the adjuvanted vaccine. However, evaluation of the adjuvant alone can be important for novel adjuvants that have not been studied previously or will be used in multiple different vaccine formulations. In the case of a novel adjuvant or combination adjuvant, it may be advisable to include additional (lower and higher) doses of the adjuvant component(s) in order to identify a safe dose that could be used in a first-in-human clinical trial, as well as safety signals that should be monitored in the proposed clinical trial.

Although not usually required, safety pharmacology studies may be recommended in some cases to demonstrate that a novel adjuvant has no adverse effects on physiological functions (e.g. on the central nervous system, or the respiratory or cardiovascular system, renal function, and body temperature). If needed, such evaluations could also be included as a specific arm with the adjuvant alone in the repeated-dose toxicity study of the intended final vaccine formulation (*1*, *38*). It is expected that these studies would be conducted before initiating first-in-human clinical trials.

D.2.7 Summary of recommendations regarding timing of studies

In general, the guidance provided in this document regarding the timing of studies in relation to clinical trials is consistent with that of other guidance documents (*31*). A repeated-dose toxicology study (including safety pharmacology end-points, if needed) should be conducted before the first-in-human clinical trial. It may be important to conduct some studies with adjuvant alone (e.g. systemic toxicity and genotoxicity, when needed as discussed in sections D.2.5 and D.2.6) prior to initiation of clinical trials (*31*). Developmental toxicology studies should be performed prior to initiation of any clinical study to be conducted in pregnant women – i.e. for those vaccines specifically developed for use in pregnancy. For vaccines indicated for females of childbearing potential, subjects can be enrolled in clinical trials provided that appropriate precautions are taken to

avoid vaccination during pregnancy, such as pregnancy testing and use of birth control. For these products, developmental toxicity studies (section D.2.3) may be performed in parallel to the clinical study.

D.3 Additional considerations

Additional studies for safety assessment have been considered for the specific situation in which the target population for a vaccine containing a novel adjuvant includes very young subjects – such as neonates. At this time, however, there is insufficient knowledge about suitable animal models to evaluate whether neonates with an immature immune system would adequately respond to adjuvanted vaccines or whether the adjuvant could modify the neonatal immune system in an undesirable way. Modified immune responses to vaccination also have been observed in elderly populations; however, there also is insufficient knowledge about animal models to evaluate the response to adjuvants and adjuvanted vaccines in the ageing population. Further research to improve methods that can be used for the nonclinical evaluation of adjuvanted vaccines that are targeted for neonatal and elderly populations is encouraged.

Thus far, there is no compelling clinical evidence that adjuvants are causally related to the induction of autoimmune phenomena (or autoimmune disease) or hypersensitivity in humans (*4*). Although there has been interest in developing animal models that could be used to screen adjuvants and adjuvanted vaccines for induction of autoimmunity or hypersensitivity, such models do not currently exist. Therefore, no recommendations can be made at this time regarding specific nonclinical studies that should be conducted. These are complex and multifactorial conditions; further research is needed to identify additional biomarkers related to autoimmunity and hypersensitivity phenomena.

Part E. Considerations for first-in-human clinical trials

As with the nonclinical safety assessment considerations, the first-in-human trial considerations for new adjuvanted vaccines are similar to those for non-adjuvanted vaccines (*2*); however, some issues unique to the clinical evaluation of vaccines with novel adjuvants may need to be considered. The initial clinical trials of adjuvanted vaccines are usually intended to: (a) determine the subjects' tolerability to the range of doses of antigen and adjuvant, and the dosing regimen that may be needed for later immunogenicity and clinical end-point trials; and (b) to aid in the collection of information on the nature of the adverse reactions that can be expected. This section provides guidance on the points to consider when transitioning from nonclinical to clinical testing of adjuvanted vaccines as signals observed in nonclinical studies can aid in the design of the first-in-human clinical trials. This section is intended to supplement the information

provided in the WHO Guidelines on clinical evaluation of vaccines: regulatory expectations (*2*).

Although there are limitations in the ability of animal and in vitro studies to predict safety in humans, all of the relevant nonclinical data, including the information on the pharmacologically active dose and the full toxicological profile of the adjuvanted vaccine, should be considered when designing the first-in-human trials. These data may aid in the selection of a safe starting dose, schedule, and route of administration, and in the identification of potential adverse effects for specific monitoring in the first-in-human clinical trial. A summary of such data from the nonclinical studies with the adjuvanted vaccine, and any available clinical data from similar or related adjuvanted vaccines, should be provided to support the acceptability of the proposed first-in-human clinical trial design. If, for example, dose-limiting toxicity was observed with the adjuvanted vaccine in the animal studies and the studies were repeated with lower doses to identify a dose that was without adverse effect in animals, it would be important to point that out and to summarize the specific adverse effects observed in the nonclinical studies.

Manufacturers should provide a rationale and scientific support for the use of an adjuvant in their vaccine. This could include information supporting the "added benefit" of the adjuvant derived from nonclinical studies (e.g. in vitro assays and/or proof-of-concept studies in animal models, including relevant challenge models when available) conducted prior to the initiation of clinical trials. In addition, it is recommended that the early clinical evaluations of an adjuvanted vaccine be designed to include the evaluation of both antigen-alone and adjuvanted vaccine arms to demonstrate the added benefit of the adjuvant; such data may include, for example, evidence of enhanced immune responses or antigen sparing.

If the safety of the adjuvanted vaccine was evaluated in appropriately designed toxicology studies that were conducted in line with the recommendations outlined above, and if there were no adverse effects observed in the toxicology studies conducted, the human dose tested in the toxicology studies may be acceptable as the starting dose in the first-in-human trials. However, such clinical trials are often designed as dose-escalating studies where the antigen and/or the adjuvant are given at escalating doses. With this in mind, given the limitations of the animal studies, it may be prudent to consider using a safety factor (a safety factor of 10 has been used historically) and to divide the human dose tested in the toxicology studies by the safety factor to find the recommended starting dose, and then escalate the dose from there. While it is anticipated that the adjuvant may have an antigen-sparing effect, the first-in-human trials should be designed to attempt to establish whether the adjuvant is needed and, if so, the minimum dose of adjuvant that is necessary to achieve adequate immunogenicity.

Although an inactive control (placebo) group may not be required in the first-in-human trial of an adjuvanted vaccine, the inclusion of a group receiving an inactive control, such as inert saline placebo, in early-phase clinical trials will enhance interpretation of the initial safety data through control for placebo effects and circulating community-acquired illnesses. It is recommended that the inclusion of an adjuvant-alone arm be discussed with the relevant NRA as some regulatory authorities recommend that such arms be avoided for ethical reasons; in those cases, an antigen-alone control arm may be preferred.

As with first-in-human trials of non-adjuvanted vaccines, those for adjuvanted vaccines are usually conducted in a limited number of healthy, adult volunteers (e.g. aged 18–50 years) with safety as the primary objective. The number of subjects enrolled in these first-in-human clinical trials typically ranges from 20 to 80 subjects; however, depending on the study design, the formulation of adjuvanted vaccine to be studied, and other relevant factors, a lower or higher number of subjects may be enrolled. To aid in the overall risk/benefit evaluation of the adjuvanted vaccine, the subject population should be clearly defined by inclusion and exclusion criteria, and the subjects should be closely monitored for safety. The clinical protocol should contain a safety monitoring plan with details of active post-vaccination monitoring, and predefined toxicity criteria for assessing the severity of clinical and laboratory parameters (*39*). In addition, the plan for increasing the dose of antigen and adjuvant, with predefined stepwise criteria for doing so, should be included in the clinical protocol. Also, it is recommended, especially when a novel adjuvant is used, that safety monitoring be extended through 12 months following the last vaccination (where the last follow-up may be accomplished by a telephone call). In this regard, it is recommended that serum specimens be banked where possible for potential future assessment in the event of a serious adverse event, a new-onset medical condition, or an adverse event of special interest that develops later in the course of the first-in-human clinical trial.

Any safety data based on experience with the same adjuvant formulated with other vaccine antigens, if available, may assist in developing the safety monitoring plan for the adjuvanted vaccine. However, since the mode of action in humans for the adjuvant in the specific adjuvanted vaccine to be evaluated in the first-in-human trial is usually unknown, and adjuvants may exhibit a range of properties that induce complex immune responses, it is recommended that subjects in first-in-human trials of adjuvanted vaccines be asked about specific adverse events. This may include, for example, inquiries on local reactions (e.g. pain, redness, swelling, granuloma formation, abscess, necrosis and regional lymphadenopathy), systemic reactions (e.g. fever, nausea, diarrhoea, and malaise), immune-mediated toxicity (e.g. cytokine release, immune suppression and autoimmune disease), and teratology. Examples of

adverse events of "special interest" may include neuroinflammatory disorders (e.g. optic neuritis and transverse myelitis), musculoskeletal and connective tissue diseases (e.g. rheumatoid arthritis, systemic lupus erythematosus and Wegener granulomatosis), and gastrointestinal disorders (e.g. Crohn disease and ulcerative colitis). Additionally, targeted laboratory assessments (e.g. C reactive protein, fibrinogen, antinuclear antibody, antineutrophil cytoplasmic antibodies, and rheumatoid factor) may aid in the evaluation of adverse events and medical conditions.

Table 2.1
Points to consider for the manufacturing and quality information to be provided for pharmacology studies, toxicology studies[a] and first-in-human trials

Considerations	Comment on information needed, by type of study		
	Pharmacology	Toxicology[a]	First-in-human trials
Quality information regarding raw materials[b]	Information regarding purity and source of raw materials is important	Information regarding purity and source of raw materials is important	Information regarding purity and source of raw materials is important
Production of intermediates and adjuvanted vaccine	Production of intermediates and adjuvanted vaccine may be small scale	Production of intermediates and adjuvanted vaccine may be small scale; ideally, the lots used for the toxicology study should be the same as those that will be used in the first-in-human trials (or the lots should be comparable to the lots that will be used in the first-in-human trials in terms of the manufacturing process and the controls)	Production of intermediates and adjuvanted vaccine may be small scale, but control of manufacture is important; intermediates and adjuvanted vaccine should be manufactured in compliance with the appropriate good manufacturing practices

Table 2.1 *continued*

Considerations	Comment on information needed, by type of study		
	Pharmacology	Toxicology[a]	First-in-human trials
Presentation	Adjuvanted vaccine components (or antigen and adjuvant intermediates) often are provided in separate containers to be mixed prior to use	Adjuvanted vaccine may be provided as a premixed formulation or as two components (in separate containers) to be mixed prior to administration	Adjuvanted vaccine may be provided as a premixed formulation or as two components (in separate containers) to be mixed prior to administration
Characterization	Characterization of material may not be extensive; usually general quality information (e.g. composition, purity, potency[c, d]) is provided	Material should undergo considerable characterization to include, for example, information on purity, physicochemical characteristics and potency;[c, d] also, stability should be assessed	Material should undergo considerable characterization to include, for example, information on purity, physicochemical characteristics and potency;[c, d] also, stability should be assessed

[a] Toxicology studies should be compliant with GLPs (see "Terminology" section above).
[b] Ideally, the raw materials should be the same throughout all of the studies: pharmacology, toxicology and first-in-human trials.
[c] If a potency assay has been developed for the adjuvanted vaccine, such information should be provided. Alternatively, testing the antigen for potency, and the adjuvant for identity and content, is recommended.
[d] If the adjuvanted vaccine is provided premixed in one container, it should be tested for potency. However, in some cases, the potency assessment of the adjuvanted vaccine may require multiple types of tests (e.g. in the case of aluminium-adsorbed vaccines). In these cases, the determination of potency and amount of antigen present in the antigen intermediate preparation prior to adsorption (as well as the completeness of adsorption) may be recommended in addition to an in vivo method to assess the potency of the adjuvanted vaccine.

Authors and acknowledgements

Taking into account comments received during a WHO Consultation on the Nonclinical and Preclinical Evaluation of Adjuvanted Vaccines, held 7–8 September 2011 in Rockville, MD, USA, a first draft of these Guidelines was prepared by the following WHO Drafting Group: Dr M. Baca-Estrada, Health Canada, Canada; Dr G. Coleman, Health Canada, Canada; Dr M. Gruber, United States Food and Drug Administration Center for Biologics Evaluation

and Research, USA; Dr B. Meade, Meade Biologics, USA; Dr G. Raychaudhuri, United States Food and Drug Administration Center for Biologics Evaluation and Research, USA; Dr L. Slamet, National Agency of Drug and Food Control, Indonesia; Dr E. Sutkowski, United States Food and Drug Administration Center for Biologics Evaluation and Research, USA; Dr J.W. van der Laan, Medicines Evaluation Board, the Netherlands; Dr T.Q. Zhou, Department of Essential Medicines and Health Products, World Health Organization, Switzerland. Dr C. Wrzesinski, United States Food and Drug Administration Center for Biologics Evaluation and Research, USA and Dr C. Alfonso, Department of Essential Medicines and Health Products, World Health Organization, Switzerland provided critical review inputs.

The WHO Consultation had been attended by: Dr K. Ishii, National Institute of Biomedical Innovation, Japan; Dr B. Meade, Meade Biologics, USA; Dr M. Pallardy, Université Paris-Sud, France; Dr S. Reed, Infectious Disease Research Institute, USA; Dr J.W. van der Laan, Medicines Evaluation Board, the Netherlands; Dr M. Baca-Estrada, Health Canada, Canada; Dr E. Griffiths, Health Canada, Canada; Dr M. Gruber, United States Food and Drug Administration Center for Biologics Evaluation and Research, USA; Mr B.L. Moraes Moreira, Ministerio da Saude, Brazil; Dr G. Raychaudhuri, United States Food and Drug Administration Center for Biologics Evaluation and Research, USA; Dr H.L. Davis, Pfizer Vaccine Research, Canada; Dr N. Garçon, GlaxoSmithKline Biologicals, Belgium; Dr. D.L. Novicki, Novartis Vaccines, USA; Dr F. Verdier, Sanofi Pasteur, USA; Dr S. Gairola, Serum Institute of India, India; Dr I. Raw, Technology and Scientific Council, Brazil; Dr L. Slamet, National Agency of Drug and Food Control, Indonesia; Dr C. Conrad, Department of Immunization, Vaccines and Biologicals, World Health Organization, Switzerland; Dr C. Alfonso, Department of Immunization, Vaccines and Biologicals, World Health Organization, Switzerland; Dr M.L. Pombo, WHO Regional Office for the Americas, World Health Organization, USA; Dr D. Pfeiffer, WHO Regional Office for Europe, World Health Organization, Denmark.

Following review and consultation with involved experts a second draft was subsequently prepared by the WHO Drafting Group based on comments submitted by: Dr M. Khaitov, Federal Medical and Biological Agency of the Russian Federation, Russia; Dr Y. Sun, Paul-Ehrlich-Institut, Germany; and Dr N. Garçon, GlaxoSmithKline Biologicals, Belgium; Dr H.L. Davis, Pfizer Canada. The International Federation of Pharmaceutical Manufacturers & Associations (IFPMA) provided combined comments from: Dr N. Garçon (GlaxoSmithKline), Dr D. Novicki (Novartis Vaccines), Dr D. Clarke (Pfizer), Dr S. Gould and Dr F. Verdier (Sanofi Pasteur); Dr M. Matsumoto and Ms M. Iguchi, Pharmaceutical and Medical Devices Agency, Japan; and Dr J. Southern, Ministry of Health, South Africa. Combined comments were also received from the following contributors at the United States Food and Drug Administration Center for Biologics Evaluation

and Research: Dr M. Gruber, Dr C. Wrzesinski, Dr H. Golding, Dr M. Zaitseva, Dr B. Baldwin and Dr E. Sutkowski. The second draft was then subjected to expert review at an informal consultation held by WHO.

The third draft was prepared by the WHO Drafting Group taking into account comments received during the WHO Informal Consultation on Guidelines for the Nonclinical Evaluation of Adjuvanted Vaccines, held 27–28 November 2012, in Geneva, Switzerland. The consultation was attended by: Dr M. Baca-Estrada, Health Canada, Canada; Dr D. Carter, Infectious Disease Research Institute, USA; Dr L.G. Castanheira, National Health Surveillance Agency, Brazil; Dr G. Coleman, Health Canada, Canada; Professor I. Feavers, National Institute for Biological Standards and Control, England; Dr E. Griffiths, Consultant, England; Dr M. Gruber, United States Food and Drug Administration Center for Biologics Evaluation and Research, USA; Ms M. Iguchi, Pharmaceuticals and Medical Devices Agency, Japan; Dr K. Ishii, National Institute of Biomedical Innovation, Japan; Mrs T. Jivapaisarnpong, Ministry of Public Health, Thailand; Ms J. Dahlan, National Agency of Drug and Food Control, Indonesia; Dr M. Khaitov, Federal Medical and Biological Agency of the Russian Federation, Russia; Dr D. Masset, Agence nationale de sécurité du médicament et des produits de santé, France; Dr M. Matsumoto, Pharmaceuticals and Medical Devices Agency, Japan; Dr B. Meade, Meade Biologics, USA; Dr L. Martinez Munoz, Ministerio de Salud Pública, Cuba; Dr S.R. Pakzad, Food and Drug Control Laboratory, Islamic Republic of Iran; Dr M. Pallardy, Université Paris-Sud, France; Dr V.G. Somani, Ministry of Health and Family Welfare, India; Dr J. Southern, Ministry of Health, South Africa; Dr Y. Sun, Paul-Ehrlich-Institut, Germany; Dr E. Sutkowski, United States Food and Drug Administration Center for Biologics Evaluation and Research, USA; Dr J.W. van der Laan, Medicines Evaluation Board, the Netherlands; Dr M. Xu, National Institutes for Food and Drug Control, China; Dr M. Bonelli, European Medicines Agency, England; Dr B. Fritzell (*International Alliance for Biological Standardization representative*), France. The following IFPMA representatives also attended: Dr D. Clarke (Pfizer), Dr N. Garçon (GlaxoSmithKline), Dr S. Gould (Sanofi Pasteur), Dr D. Novicki (Novartis Vaccines), Dr R. Zahn (Crucell). Representatives from the Developing Countries Vaccine Manufacturers Network (DCVMN) included: Dr S. Gairola, (Serum Institute of India), Dr M.A. Medeiros (Biomanguinhos), Dr R.I. Modi (Cadila Pharmaceuticals), Dr J. Petre (BioNet-Asia), Dr Q. Zhao (Xiamen Innovax) and Dr M. Reers (Biological E). Another industry representative who attended was Dr S. Dewasthaly (Intercell AG). WHO Secretariat members included: Dr J. Fournier-Caruana, Department of Essential Medicines and Health Products; Dr M.H. Friede, Information, Evidence and Research; Dr U. Fruth, Department of Immunization, Vaccines and Biologicals; Dr I. Knezevic, Department of Essential Medicines and Health Products; Dr S. Nishioka, Department of Essential Medicines and Health Products; Dr D.J. Wood, Department of Essential Medicines and

Health Products; Dr T.Q. Zhou, Department of Essential Medicines and Health Products; Dr P. Zuber, Department of Essential Medicines and Health Products.

A fourth draft document was subsequently prepared by the WHO Drafting Group taking into account comments submitted by the following reviewers: Dr E. Griffiths, England; Ms M. Iguchi, Pharmaceuticals and Medical Devices Agency, Japan; Dr K. Ishii, National Institute of Biomedical Innovation, Japan; Ms J. Dahlan, National Agency of Drug and Food Control, Indonesia; Dr M. Khaitov, Federal Medical and Biological Agency of the Russian Federation, Russia; Dr M. Matsumoto, Pharmaceuticals and Medical Devices Agency, Japan; Dr L. Martinez Munoz, Ministerio de Salud Pública, Cuba; Dr J. Southern, Ministry of Health, South Africa; Dr D. Clarke, Pfizer, USA; Dr N. Garçon, GlaxoSmithKline, Belgium; Dr S. Gould, Sanofi Pasteur, France; Dr D. Novicki, Novartis Vaccines, USA; Dr S. Gairola, Serum Institute of India, India. Contributors to combined comments received from the United States Food and Drug Administration Center for Biologics Evaluation and Research included: Dr M. Gruber, Dr C. Wrzesinski, Dr H. Golding, Dr M. Zaitseva, Dr B. Baldwin and Dr E. Sutkowski. Comments were also received from Dr J. Fournier-Caruana and Dr S. Nishioka, both from the Department of Essential Medicines and Health Products, World Health Organization, Switzerland.

During a round of public consultation organized through the WHO Biologicals website in April and early May 2013 comments were received from the following reviewers, and were taken into account by the WHO Drafting Group in the preparation of the document WHO/BS/2013.2214: Ms J. Dahlan, National Agency of Drug and Food Control, Indonesia; Dr M. Matsumoto, Pharmaceutical and Medical Devices Agency, Japan; Dr S. Løkstad, Brenntag Biosector A/S, Denmark; Dr M. Satoh, University of Florida, USA; Dr L. Martinez Munoz, Ministerio de Salud Pública, Cuba; Dr S. Sontakke, BGTD/Health Canada, Canada; Dr B. Keller-Stanislawski, Paul-Ehrlich-Institut, Germany; Dr S. Oh, Ministry of Food and Drug Safety, Republic of Korea; Dr N. Jain, Panacea Biotec, India; Dr G. Waxenecker, Austrian Agency for Health and Food Safety, Austria; Dr T. Morris, United States Pharmacopeia, USA; Dr K. Abraham, VaxInnate Corporation, USA. Comments from the IFPMA were coordinated by Dr L. Bigger, Vaccines Policy.

During a second round of public consultation on document WHO/BS/2013.2214 organized through the WHO Biologicals website from July to September 2013 further comments were provided by the following experts: Dr K. Zoon and F. Kaltovich, National Institutes of Health, USA; Dr M. Matsumoto, Pharmaceutical and Medical Devices Agency, Japan; Dr F. Cano, Dr D. Garcia and Dr S. Morgeaux, Agence nationale de sécurité du médicament et des produits de santé, France; Dr T. Nakano, Kyowa Hakko Bio Co., Japan; Dr S. Jadhav, Serum Institute of India, India; Dr M. Gruber, Dr E. Sutkowski, Dr C. Wrzesinski, Dr M. Green, Dr M. Serabian, and Dr G. Price, United States Food

and Drug Administration Center for Biologics Evaluation and Research, USA; Dr W. Van Molle, Scientific Institute of Public Health, Belgium; Dr C.F. Paulsen, Statens Serum Institut, Denmark; Dr M.P. Moya, Instituto Nacional de Vigilancia de Medicamentos y Alimentos, Colombia.

References

1. WHO guidelines on nonclinical evaluation of vaccines. In: *WHO Expert Committee on Biological Standardization. Fifty-fourth report*. Geneva, World Health Organization, 2005 (WHO Technical Report Series, No. 927), Annex 1.
2. Guidelines on clinical evaluation of vaccines: regulatory expectations. In: *WHO Expert Committee on Biological Standardization. Fifty-second report*. Geneva, World Health Organization, 2004 (WHO Technical Report Series, No. 924), Annex 1.
3. Global Advisory Committee on Vaccine Safety, June 2012. *Weekly Epidemiological Record*, 2012, 87:281–287.
4. Ahmed SS et al. Assessing the safety of adjuvanted vaccines. *Science Translational Medicine*, 2011 3(93):93rv2 (doi: 10.1126/scitranslmed.3002302).
5. Committee for Medicinal Products for Human Use. *Guideline on adjuvants in vaccines for human use*. London, European Medicines Agency, 2005 (EMEA/CHMP/VEG/134716/2004) (http://www.ema.europa.eu/docs/en_GB/document_library/Scientific_guideline/2009/09/WC500003809.pdf, accessed 26 June 2013).
6. *Guideline for nonclinical studies of preventive vaccines for infectious diseases: notification of yakushokushinsahatsu No. 0527-1 May 27*. Tokyo, Japan, Ministry of Health, Labour and Welfare, 2010 (Supplemental Information).
7. Global Advisory Committee on Vaccine Safety, 10–11 June 2004. *Weekly Epidemiological Record*, 2004, 79:269–272.
8. *Workshop on: non-clinical safety evaluation of preventive vaccines: recent advances and regulatory considerations*, vol. I. Arlington, VA, Center for Biologics Research and Review, United States Food and Drug Administration, 2002 (http://www.fda.gov/downloads/biologicsbloodvaccines/newsevents/workshopsmeetingsconferences/transcriptsminutes/ucm054459.pdf, accessed 26 June 2013).
9. van der Laan JW et al. Nonclinical testing of vaccines: report from a workshop. *Drug Information Journal*, 2009, 43:97–107.
10. *Workshop on adjuvants and adjuvanted preventive and therapeutic vaccines for infectious disease indications*. Arlington, VA, Center for Biologics Research and Review, United States Food and Drug Administration, 2008 (http://www.fda.gov/downloads/biologicsbloodvaccines/newsevents/workshopsmeetingsconferences/ucm095708.pdf, accessed 26 June 2013).
11. Mastelic B et al. Mode of action of adjuvants: implications for vaccine safety and design. *Biologicals*, 2010, 38:594–601.
12. Sun Y, Gruber M, Matsumoto M. Overview of global regulatory toxicology requirements for vaccines and adjuvants. *Journal of Pharmacological and Toxicological Methods*, 2012, 65:49–57.
13. *Handbook: good laboratory practice (GLP): quality practices for regulated non-clinical research and development*, 2nd ed. Geneva, UNDP/World Bank/WHO Special Programme for Research and Training in Tropical Diseases, 2009 (http://www.who.int/tdr/publications/documents/glp-handbook.pdf, accessed 26 June 2013).

14. Good manufacturing practices for biological products. In: *WHO Expert Committee on Biological Standardization. Forty-second report*. Geneva, World Health Organization, 1992 (WHO Technical Report Series, No. 822), Annex 1.
15. Good manufacturing practices: main principles for pharmaceutical products. In: *WHO Expert Committee on Specifications for Pharmaceutical Preparations. Forty-fifth report*. Geneva, World Health Organization, 2011 (WHO Technical Report Series, No. 961), Annex 3.
16. Good manufacturing practices: supplementary guidelines for the manufacture of investigational pharmaceutical products for clinical trials in humans. In: *WHO Expert Committee on Specifications for Pharmaceutical Preparations. Thirty-fourth report*. Geneva, World Health Organization, 1996 (WHO Technical Report Series, No. 863), Annex 7.
17. *Guidance for industry: CGMP for phase 1 investigational drugs*. Rockville, MD, United States Food and Drug Administration, 2008 (http://www.fda.gov/downloads/Drugs/GuidanceComplianceRegulatoryInformation/Guidances/ucm070273.pdf, accessed 26 June 2013).
18. Cussler K. A 4R concept for the safety testing of immunobiologicals. *Developments in Biological Standardization*, 1999, 101:121–126.
19. Gupta RK. Is the test for abnormal toxicity, general safety or innocuity necessary for vaccines? *Vaccine*, 1996, 14(17–18):1718.
20. Halder M. Three Rs potential in the development and quality control of immunobiologicals. *ALTEX*, 2001, 18(Suppl. 1):S13–S47.
21. Guidelines on stability evaluation of vaccines. In: *WHO Expert Committee on Biological Standardization. Fifty-seventh report*. Geneva, World Health Organization, 2011 (WHO Technical Report Series, No. 962), Annex 3.
22. Friede M et al. WHO initiative to increase global and equitable access to influenza vaccine in the event of a pandemic: supporting developing country production capacity through technology transfer. *Vaccine*, 2011, 29(Suppl. 1):A2–A7.
23. Verdijk P, Rots NY, Bakker WA. Clinical development of a novel inactivated poliomyelitis vaccine based on attenuated Sabin poliovirus strains. *Expert Review of Vaccines*, 2011, 10:635–644.
24. Giannini SL et al. Enhanced humoral and memory B cellular immunity using HPV16/18 L1 VLP vaccine formulated with the MPL/aluminium salt combination (AS04) compared to aluminium salt only. *Vaccine*, 2006, 24:5937–5949.
25. De Vleeschauwer AR et al. Efficacy of an AS03A-adjuvanted split H5N1 influenza vaccine against an antigenically distinct low pathogenic H5N1 virus in pigs. *Vaccine*, 2012, 30:5557–5563.
26. Stephenson I et al. Cross-reactivity to highly pathogenic avian influenza H5N1 viruses after vaccination with nonadjuvanted and MF59-adjuvanted influenza A/Duck/Singapore/97 (H5N3) vaccine: a potential priming strategy. *Journal of Infectious Diseases*, 2005, 191:1210–1215.
27. Zaitseva M et al. Use of human MonoMac6 cells for development of in vitro assay predictive of adjuvant safety in vivo. *Vaccine*, 2012, 30:4859–4865.
28. Ma Y et al. Assessing the immunopotency of Toll-like receptor agonists in an in vitro tissue-engineered immunological model. *Immunology*, 2010, 130:374–387.
29. Shin J et al. International regulatory requirements for vaccine safety and potency testing: a WHO perspective. *Procedia in Vaccinology*, 2011, 5:164–170.
30. Guidelines for independent lot release of vaccines by regulatory authorities. In: *WHO Expert Committee on Biological Standardization. Sixty-first report*. Geneva, World Health Organization, 2013 (WHO Technical Report Series, No. 978), Annex 2.

31. *Guidance on nonclinical safety studies for the conduct of human clinical trials and marketing authorization for pharmaceuticals*. Tripartite Harmonised Guideline M3(R2). Geneva, International Conference on Harmonisation of Technical Requirements for Registration of Pharmaceuticals for Human Use, 2009.
32. Diehl KH et al. A good practice guide to the administration of substances and removal of blood, including routes and volumes. *Journal of Applied Toxicology*, 2001, 21:15–23.
33. Kushner I, Mackiewicz A. The acute phase response: an overview. In: Mackiewicz A, Kushner I, Baumann H, eds. *Acute phase proteins: molecular biology, biochemistry, and clinical applications*. Boca Raton: CRC Press, 1993:3–19.
34. Draize JH, Woodard G, Calvery HO. Methods for the study of irritation and toxicity of substances applied topically to the skin and mucous membranes. *Journal of Pharmacology and Experimental Therapeutics*, 1944, 82:377–390.
35. Herberts C et al. New adjuvanted vaccines in pregnancy: what is known about their safety? *Expert Review of Vaccines*, 2010, 9:1411–1422.
36. *Guidance for industry: considerations for developmental toxicity studies for preventive and therapeutic vaccines for infectious disease indications*. Center for Biologics Evaluation and Research, United States Food and Drug Administration, 2006 (http://www.fda.gov/downloads/BiologicsBloodVaccines/GuidanceComplianceRegulatoryInformation/Guidances/Vaccines/ucm092170.pdf, accessed 26 June 2013).
37. *Guidance on genotoxicity testing and data interpretation for pharmaceuticals intended for human use*. Tripartite Harmonised Guideline S2(R1). Geneva, International Conference on Harmonisation of Technical Requirements for Registration of Pharmaceuticals for Human Use, 2011.
38. *Safety pharmacology studies for human pharmaceuticals*. Tripartite Harmonised Guideline S7A. Geneva, International Conference on Harmonisation of Technical Requirements for Registration of Pharmaceuticals for Human Use, 2000.
39. *Guidance for industry: toxicity grading scale for healthy adult and adolescent volunteers enrolled in preventive vaccine clinical trials*. Center for Biologics Evaluation and Research, United States Food and Drug Administration, 2007 (http://www.fda.gov/downloads/BiologicsBloodVaccines/GuidanceComplianceRegulatoryInformation/Guidances/Vaccines/ucm091977.pdf, accessed 26 June 2013).

Appendix 1

Examples of classes of adjuvants

The following main classes of adjuvants (see section on "Scope" and section 2 above) are currently used in licensed vaccines or are being investigated. The list is an updated version of the list of adjuvants developed by the European Medicines Agency, Committee for Medicinal Products for Human Use (*1*). For each category, representative examples are provided.

Classification of adjuvants

- **Mineral salts or gels** – for example, aluminium hydroxide, aluminium phosphate gels or calcium phosphate gels.
- **Oil-in-water and water-in-oil emulsions, amphiphilic molecules and surfactant-based formulations** – for example, Novartis' MF59 (microfluidized detergent-stabilized oil-in-water emulsion); QS-21 (purified saponin, which is derived from plants); GlaxoSmithKline's AS03 adjuvant (an oil-in-water emulsion plus α-tocopherol); and SEPPIC's Montanide ISA 51 and Montanide ISA 720.
- **Particulate adjuvants** – for example, liposomes; virosomes (unilamellar liposomal vehicles incorporating influenza haemagglutinin); DC Chol (a lipoidal immunostimulator able to self-organize into liposomes); immune-stimulating complexes known as ISCOMS (structured complexes of saponins and lipids) and CSL's Iscomatrix (the iscom without the incorporated antigen); and biopolymers such as Poly(lactide-co-glycolide) (PLGA).
- **Pathogen-associated molecular patterns (natural and synthetic)** – for example, low-toxicity versions of LPS, including monophosphoryl lipid A (MPL or MPLA) and RC-529 (a synthetic acylated monosaccharide); Detox adjuvant (an oil drop emulsion of MPL plus *Mycobacterium phlei* cell-wall skeleton); OM-174 (lipid A derivative); CpG motifs (synthetic oligodeoxynucleotides containing immunostimulatory CpG motifs); bacterial flagellin genetically fused with an antigen; bacterial toxins that have been genetically modified to provide nontoxic adjuvant effects such as modified heat-labile enterotoxin (LT) and cholera toxin (CT); and synthetic dsRNA such as Poly IC, Poly ICLC (also known as Hiltonol), and poly I:poly C12U (known as Ampligen).

- **Endogenous human immunostimulators** – for example, cytokines such as human granulocyte-macrophage colony-stimulating factor (hGM-CSF) or human interleukin-12 (hIL-12) that may be administered as proteins or as plasmid preparations (DNA sequences contained in DNA vaccine vectors that promote gene expression and are capable of inducing and/or promoting an immune response against an antigen in vaccine recipients).
- **Inert vehicles** – for example, gold particles.
- **Adjuvants derived from inulin** – for example, Vaxine's delta inulin (a plant-derived polysaccharide also known as Advax).
- **Combination adjuvants or adjuvant systems** consisting of combinations of vaccine-delivery systems and immunostimulatory agents that may result in more effective delivery of the immunostimulatory adjuvant as well as the antigen – for example, AS01 (liposomes, MPL and QS-21), AS02 (an oil-in-water emulsion plus MPL and QS-21), AS03 (an oil-in-water emulsion plus α-tocopherol), AS04 (MPL and aluminium hydroxide), AS15 (liposomes, MPL, QS-21 and a CpG oligodeoxynucleotide), glucopyranosyl lipid adjuvant-stable emulsion (GLA-SE) (a synthetic acylated monosaccharide in a stable oil-in-water emulsion) and CAF01 (liposomes, a quaternary ammonium lipid and a synthetic analogue of a mycobacterial lipid).

Reference

1. Committee for Medicinal Products for Human Use. *Guideline on adjuvants in vaccines for human use*. London, European Medicines Agency, 2005 (EMEA/CHMP/VEG/134716/2004) (http://www.ema.europa.eu/docs/en_GB/document_library/Scientific_guideline/2009/09/WC500003809.pdf, accessed 26 June 2013).

Appendix 2

Tissue samples to be collected for a repeated-dose toxicity study

This is a comprehensive list of the tissues that should be evaluated for local and systemic toxicity in repeated-dose toxicity studies; some additional tissues have been included to represent those specifically targeted by adjuvanted vaccines. This is an updated version of a list developed initially by WHO for vaccines (*1*) that was broadened and harmonized by the European Medicines Agency, Committee for Medicinal Products for Human Use (*2*) and the Society of Toxicologic Pathology (*3*).

Samples should be collected from the following tissues. The type of tissue to be collected depends upon the species used for testing.

adrenal glands

aorta (thoracic)

bone (femur) with articulation

bone (sternum) with bone marrow

bone marrow smears[1]

brain

bronchi (main stem)

caecum

colon

diaphragm

duodenum

epididymides

eyes

gall bladder

Harderian glands

heart

ileum

injection site(s) (a sample should be taken from the area of injection)

jejunum

kidneys

lachrymal glands (from the main body and subconjunctival part)

larynx

liver

lungs

lymph nodes that drain the injection site

lymph nodes that do not drain the injection site (e.g. mandibular or mesenteric)

mammary gland

nasal–oropharyngeal cavity (depending on the vaccine and adjuvant)

[1] Bone marrow smears should be prepared for all animals at the time of necropsy, including from any moribund animals killed during the study. The smears should be fixed in methanol and then stained using the May-Grunwald-Giemsa method.

nasal tissue (skull/nasal cavity)
oesophagus
optic nerves
ovaries
oviducts
pancreas
parathyroid glands
Peyer's patches
pituitary gland
prostate
rectum
salivary glands (mandibular, parotid and sublingual)
sciatic nerves
seminal vesicles
skeletal muscle
skin
spinal cord (cervical, thoracic and lumbar)
spleen
stomach
testes
thymus
thyroid glands
tissues with macroscopic observations (a sample should be taken from any and all tissues with macroscopic observations)
tongue
trachea
ureters
urinary bladder
uterus (from the body, horns and cervix)
vagina

References

1. WHO guidelines on nonclinical evaluation of vaccines. In: *WHO Expert Committee on Biological Standardization. Fifty-fourth report*. Geneva, World Health Organization, 2005 (WHO Technical Report Series, No. 927), Annex 1.
2. Committee for Medicinal Products for Human Use. *Guideline on repeated dose toxicity*. London, European Medicines Agency, 2010 (EMEA/CHMP/SWP/1042/99 Rev. 1 Corr.) (http://www.ema.europa.eu/docs/en_GB/document_library/Scientific_guideline/2010/03/WC500079536.pdf, accessed 26 June 2013).
3. Bregman CL et al. Recommended tissue list for histopathologic examination in repeat-dose toxicity and carcinogenicity studies: a proposal of the Society of Toxicologic Pathology (STP). *Toxicologic Pathology*, 2003, March–April, 31(2):252–253 (http://www.ncbi.nlm.nih.gov/pubmed/12696587, accessed 22 February 2014).

CORONAVIRUS

Cryo-EM structure of the 2019-nCoV spike in the prefusion conformation

Daniel Wrapp[1]*, Nianshuang Wang[1]*, Kizzmekia S. Corbett[2], Jory A. Goldsmith[1], Ching-Lin Hsieh[1], Olubukola Abiona[2], Barney S. Graham[2], Jason S. McLellan[1]†

The outbreak of a novel coronavirus (2019-nCoV) represents a pandemic threat that has been declared a public health emergency of international concern. The CoV spike (S) glycoprotein is a key target for vaccines, therapeutic antibodies, and diagnostics. To facilitate medical countermeasure development, we determined a 3.5-angstrom-resolution cryo–electron microscopy structure of the 2019-nCoV S trimer in the prefusion conformation. The predominant state of the trimer has one of the three receptor-binding domains (RBDs) rotated up in a receptor-accessible conformation. We also provide biophysical and structural evidence that the 2019-nCoV S protein binds angiotensin-converting enzyme 2 (ACE2) with higher affinity than does severe acute respiratory syndrome (SARS)-CoV S. Additionally, we tested several published SARS-CoV RBD-specific monoclonal antibodies and found that they do not have appreciable binding to 2019-nCoV S, suggesting that antibody cross-reactivity may be limited between the two RBDs. The structure of 2019-nCoV S should enable the rapid development and evaluation of medical countermeasures to address the ongoing public health crisis.

The novel coronavirus 2019-nCoV has recently emerged as a human pathogen in the city of Wuhan in China's Hubei province, causing fever, severe respiratory illness, and pneumonia—a disease recently named COVID-19 (*1*, *2*). According to the World Health Organization (WHO), as of 16 February 2020, there had been >51,000 confirmed cases globally, leading to at least 1600 deaths. The emerging pathogen was rapidly characterized as a new member of the betacoronavirus genus, closely related to several bat coronaviruses and to severe acute respiratory syndrome coronavirus (SARS-CoV) (*3*, *4*). Compared with SARS-CoV, 2019-nCoV appears to be more readily transmitted from human to human, spreading to multiple continents and leading to the WHO's declaration of a Public Health Emergency of International Concern (PHEIC) on 30 January 2020 (*1*, *5*, *6*).

2019-nCoV makes use of a densely glycosylated spike (S) protein to gain entry into host cells. The S protein is a trimeric class I fusion protein that exists in a metastable prefusion conformation that undergoes a substantial structural rearrangement to fuse the viral membrane with the host cell membrane (*7*, *8*). This process is triggered when the S1 subunit binds to a host cell receptor. Receptor binding destabilizes the prefusion trimer, resulting in shedding of the S1 subunit and transition of the S2 subunit to a stable postfusion conformation (*9*). To engage a host cell receptor, the receptor-binding domain (RBD) of S1 undergoes hinge-like conformational movements that transiently hide or expose the determinants of receptor binding. These two states are referred to as the "down" conformation and the "up" conformation, where down corresponds to the receptor-inaccessible state and up corresponds to the receptor-accessible state, which is thought to be less stable (*10*–*13*). Because of the indispensable function of the S protein, it represents a target for antibody-mediated neutralization, and characterization of the prefusion S structure would provide atomic-level information to guide vaccine design and development.

Based on the first reported genome sequence of 2019-nCoV (*4*), we expressed ectodomain residues 1 to 1208 of 2019-nCoV S, adding two stabilizing proline mutations in the C-terminal S2 fusion machinery using a previous stabilization strategy that proved effective for other betacoronavirus S proteins (*11*, *14*). Figure 1A shows the domain organization of the expression construct, and figure S1 shows the purification process. We obtained ~0.5 mg/liter of the recombinant prefusion-stabilized S ectodomain from FreeStyle 293 cells and purified the protein to homogeneity by affinity chromatography and size-exclusion chromatography (fig. S1). Cryo–electron microscopy (cryo-EM) grids were prepared using this purified, fully glycosylated S protein, and preliminary screening revealed a high particle density with little aggregation near the edges of the holes.

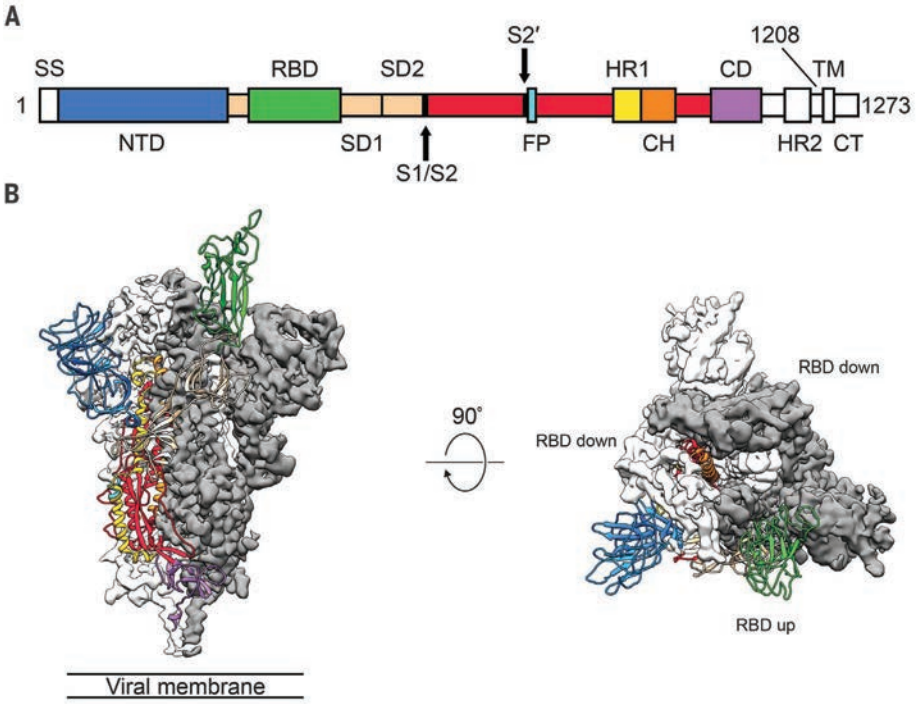

Fig. 1. Structure of 2019-nCoV S in the prefusion conformation. (**A**) Schematic of 2019-nCoV S primary structure colored by domain. Domains that were excluded from the ectodomain expression construct or could not be visualized in the final map are colored white. SS, signal sequence; S2′, S2′ protease cleavage site; FP, fusion peptide; HR1, heptad repeat 1; CH, central helix; CD, connector domain; HR2, heptad repeat 2; TM, transmembrane domain; CT, cytoplasmic tail. Arrows denote protease cleavage sites. (**B**) Side and top views of the prefusion structure of the 2019-nCoV S protein with a single RBD in the up conformation. The two RBD down protomers are shown as cryo-EM density in either white or gray and the RBD up protomer is shown in ribbons colored corresponding to the schematic in (A).

[1]Department of Molecular Biosciences, The University of Texas at Austin, Austin, TX 78712, USA. [2]Vaccine Research Center, National Institute of Allergy and Infectious Diseases, National Institutes of Health, Bethesda, MD 20892, USA.
*These authors contributed equally to this work.
†Corresponding author. Email: jmclellan@austin.utexas.edu

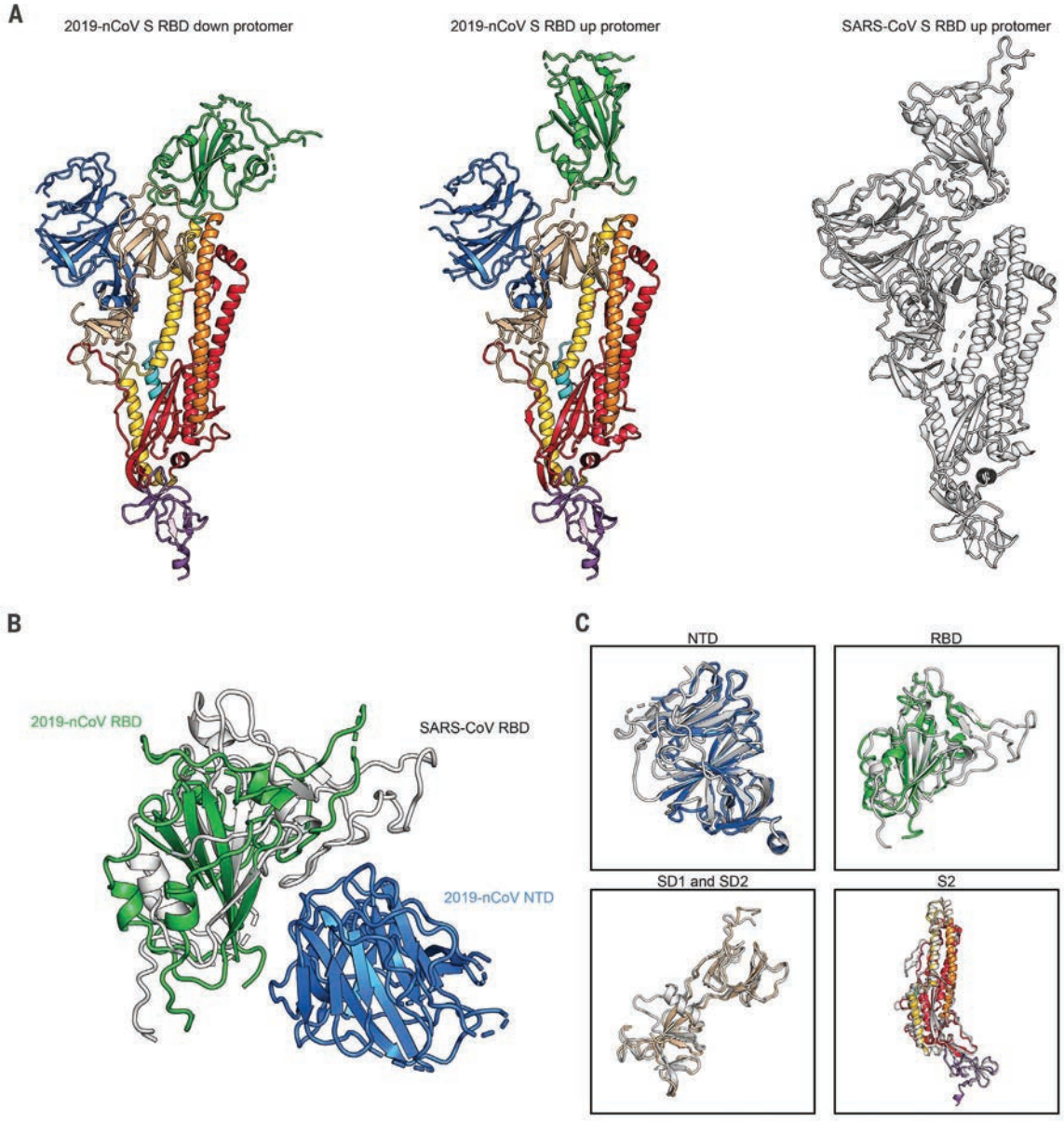

Fig. 2. Structural comparison between 2019-nCoV S and SARS-CoV S. (**A**) Single protomer of 2019-nCoV S with the RBD in the down conformation (left) is shown in ribbons colored according to Fig. 1. A protomer of 2019-nCoV S in the RBD up conformation is shown (center) next to a protomer of SARS-CoV S in the RBD up conformation (right), displayed as ribbons and colored white (PDB ID: 6CRZ). (**B**) RBDs of 2019-nCoV and SARS-CoV aligned based on the position of the adjacent NTD from the neighboring protomer. The 2019-nCoV RBD is colored green and the SARS-CoV RBD is colored white. The 2019-nCoV NTD is colored blue. (**C**) Structural domains from 2019-nCoV S have been aligned to their counterparts from SARS-CoV S as follows: NTD (top left), RBD (top right), SD1 and SD2 (bottom left), and S2 (bottom right).

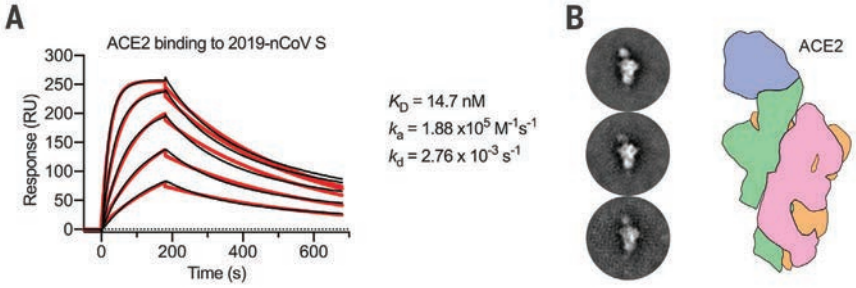

Fig. 3. 2019-nCoV S binds human ACE2 with high affinity. (**A**) Surface plasmon resonance sensorgram showing the binding kinetics for human ACE2 and immobilized 2019-nCoV S. Data are shown as black lines, and the best fit of the data to a 1:1 binding model is shown in red. (**B**) Negative-stain EM 2D class averages of 2019-nCoV S bound by ACE2. Averages have been rotated so that ACE2 is positioned above the 2019-nCoV S protein with respect to the viral membrane. A diagram depicting the ACE2-bound 2019-nCoV S protein is shown (right) with ACE2 in blue and S protein protomers colored tan, pink, and green.

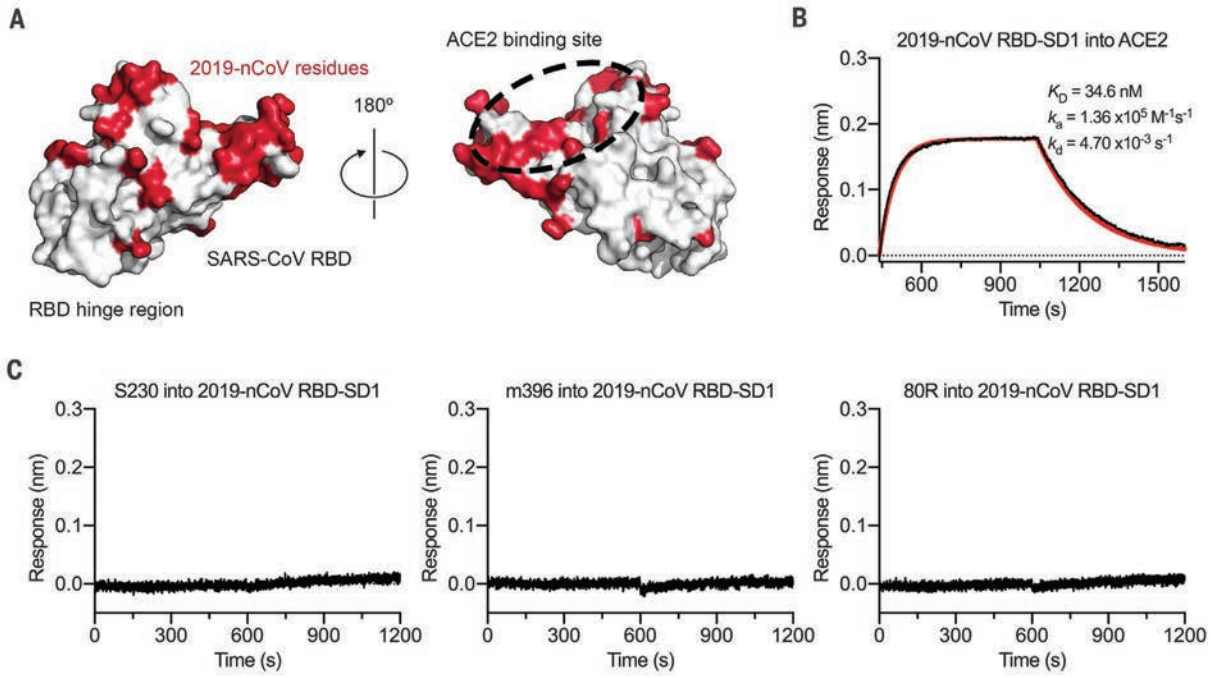

Fig. 4. Antigenicity of the 2019-nCoV RBD. (**A**) SARS-CoV RBD shown as a white molecular surface (PDB ID: 2AJF), with residues that vary in the 2019-nCoV RBD colored red. The ACE2-binding site is outlined with a black dashed line. (**B**) Biolayer interferometry sensorgram showing binding to ACE2 by the 2019-nCoV RBD-SD1. Binding data are shown as a black line, and the best fit of the data to a 1:1 binding model is shown in red. (**C**) Biolayer interferometry to measure cross-reactivity of the SARS-CoV RBD-directed antibodies S230, m396, and 80R. Sensor tips with immobilized antibodies were dipped into wells containing 2019-nCoV RBD-SD1, and the resulting data are shown as a black line.

After collecting and processing 3207 micrograph movies, we obtained a 3.5-Å-resolution three-dimensional (3D) reconstruction of an asymmetrical trimer in which a single RBD was observed in the up conformation. (Fig. 1B, fig. S2, and table S1). Because of the small size of the RBD (~21 kDa), the asymmetry of this conformation was not readily apparent until ab initio 3D reconstruction and classification were performed (Fig. 1B and fig. S3). By using the 3D variability feature in cryoSPARC v2 (*15*), we observed breathing of the S1 subunits as the RBD underwent a hinge-like movement, which likely contributed to the relatively poor local resolution of S1 compared with the more stable S2 subunit (movies S1 and S2). This seemingly stochastic RBD movement has been captured during structural characterization of the closely related betacoronaviruses SARS-CoV and MERS-CoV, as well as the more distantly related alphacoronavirus porcine epidemic diarrhea virus (PEDV) (*10*, *11*, *13*, *16*). The observation of this phenomenon in 2019-nCoV S suggests that it shares the same mechanism of triggering that is thought to be conserved among the Coronaviridae, wherein receptor binding to exposed RBDs leads to an unstable three-RBD up conformation that results in shedding of S1 and refolding of S2 (*11*, *12*).

Because the S2 subunit appeared to be a symmetric trimer, we performed a 3D refinement imposing C3 symmetry, resulting in a 3.2-Å-resolution map with excellent density for the S2 subunit. Using both maps, we built most of the 2019-nCoV S ectodomain, including glycans at 44 of the 66 *N*-linked glycosylation sites per trimer (fig. S4). Our final model spans S residues 27 to 1146, with several flexible loops omitted. Like all previously reported coronavirus S ectodomain structures, the density for 2019-nCoV S begins to fade after the connector domain, reflecting the flexibility of the heptad repeat 2 domain in the prefusion conformation (fig. S4A) (*13*, *16*–*18*).

The overall structure of 2019-nCoV S resembles that of SARS-CoV S, with a root mean square deviation (RMSD) of 3.8 Å over 959 Cα atoms (Fig. 2A). One of the larger differences between these two structures (although still relatively minor) is the position of the RBDs in their respective down conformations. Whereas the SARS-CoV RBD in the down conformation packs tightly against the N-terminal domain (NTD) of the neighboring protomer, the 2019-nCoV RBD in the down conformation is angled closer to the central cavity of the trimer (Fig. 2B). Despite this observed conformational difference, when the individual structural domains of 2019-nCoV S are aligned to their counterparts from SARS-CoV S, they reflect the high degree of structural homology between the two proteins, with the NTDs, RBDs, subdomains 1 and 2 (SD1 and SD2), and S2 subunits yielding individual RMSD values of 2.6 Å, 3.0 Å, 2.7 Å, and 2.0 Å, respectively (Fig. 2C).

2019-nCoV S shares 98% sequence identity with the S protein from the bat coronavirus RaTG13, with the most notable variation arising from an insertion in the S1/S2 protease cleavage site that results in an "RRAR" furin recognition site in 2019-nCoV (*19*) rather than the single arginine in SARS-CoV (fig. S5) (*20*–*23*). Notably, amino acid insertions that create a polybasic furin site in a related position in hemagglutinin proteins are often found in highly virulent avian and human influenza viruses (*24*). In the structure reported here, the S1/S2 junction is in a disordered, solvent-exposed loop. In addition to this insertion of residues in the S1/S2 junction, 29 variant residues exist between 2019-nCoV S and RaTG13 S, with 17 of these positions mapping to the RBD (figs. S5 and S6). We also analyzed the 61 available 2019-nCoV S sequences in the Global Initiative on Sharing All Influenza Data database (https://www.gisaid.org/) and found that there were only nine amino acid substitutions among all deposited sequences. Most of these substitutions are relatively conservative and are not expected to have a substantial effect on the structure or function of the 2019-nCoV S protein (fig. S6).

Recent reports demonstrating that 2019-nCoV S and SARS-CoV S share the same functional host

cell receptor, angiotensin-converting enzyme 2 (ACE2) (*22*, *25*–*27*), prompted us to quantify the kinetics of this interaction by surface plasmon resonance. ACE2 bound to the 2019-nCoV S ectodomain with ~15 nM affinity, which is ~10- to 20-fold higher than ACE2 binding to SARS-CoV S (Fig. 3A and fig. S7) (*14*). We also formed a complex of ACE2 bound to the 2019-nCoV S ectodomain and observed it by negative-stain EM, which showed that it strongly resembled the complex formed between SARS-CoV S and ACE2 that has been observed at high resolution by cryo-EM (Fig. 3B) (*14*, *28*). The high affinity of 2019-nCoV S for human ACE2 may contribute to the apparent ease with which 2019-nCoV can spread from human to human (*1*); however, additional studies are needed to investigate this possibility.

The overall structural homology and shared receptor usage between SARS-CoV S and 2019-nCoV S prompted us to test published SARS-CoV RBD-directed monoclonal antibodies (mAbs) for cross-reactivity to the 2019-nCoV RBD (Fig. 4A). A 2019-nCoV RBD-SD1 fragment (S residues 319 to 591) was recombinantly expressed, and appropriate folding of this construct was validated by measuring ACE2 binding using biolayer interferometry (BLI) (Fig. 4B). Cross-reactivity of the SARS-CoV RBD-directed mAbs S230, m396, and 80R was then evaluated by BLI (*12*, *29*–*31*). Despite the relatively high degree of structural homology between the 2019-nCoV RBD and the SARS-CoV RBD, no binding to the 2019-nCoV RBD could be detected for any of the three mAbs at the concentration tested (1 μM) (Fig. 4C), in contrast to the strong binding that we observed to the SARS-CoV RBD (fig. S8). Although the epitopes of these three antibodies represent a relatively small percentage of the surface area of the 2019-nCoV RBD, the lack of observed binding suggests that SARS-directed mAbs will not necessarily be cross-reactive and that future antibody isolation and therapeutic design efforts will benefit from using 2019-nCoV S proteins as probes.

The rapid global spread of 2019-nCoV, which prompted the PHEIC declaration by WHO, signals the urgent need for coronavirus vaccines and therapeutics. Knowing the atomic-level structure of the 2019-nCoV spike will allow for additional protein-engineering efforts that could improve antigenicity and protein expression for vaccine development. The structural data will also facilitate the evaluation of 2019-nCoV spike mutations that will occur as the virus undergoes genetic drift and help to define whether those residues have surface exposure and map to sites of known antibody epitopes for other coronavirus spike proteins. In addition, the structure provides assurance that the protein produced by this construct is homogeneous and in the prefusion conformation, which should maintain the most neutralization-sensitive epitopes when used as candidate vaccine antigens or B cell probes for isolating neutralizing human mAbs. Furthermore, the atomic-level detail will enable the design and screening of small molecules with fusion-inhibiting potential. This information will support precision vaccine design and the discovery of antiviral therapeutics, accelerating medical countermeasure development.

REFERENCES AND NOTES

1. J. F. Chan *et al*., *Lancet* **395**, 514–523 (2020).
2. C. Huang *et al*., *Lancet* **395**, 497–506 (2020).
3. R. Lu *et al*., *Lancet* S0140-6736(20)30251-8 (2020).
4. F. Wu *et al*., *Nature* (2020).
5. N. Chen *et al*., *Lancet* **395**, 507–513 (2020).
6. Q. Li *et al*., *N. Engl. J. Med.* NEJMoa2001316 (2020).
7. F. Li, *Annu. Rev. Virol.* **3**, 237–261 (2016).
8. B. J. Bosch, R. van der Zee, C. A. de Haan, P. J. Rottier, *J. Virol.* **77**, 8801–8811 (2003).
9. A. C. Walls *et al*., *Proc. Natl. Acad. Sci. U.S.A.* **114**, 11157–11162 (2017).
10. M. Gui *et al*., *Cell Res.* **27**, 119–129 (2017).
11. J. Pallesen *et al*., *Proc. Natl. Acad. Sci. U.S.A.* **114**, E7348–E7357 (2017).
12. A. C. Walls *et al*., *Cell* **176**, 1026–1039.e15 (2019).
13. Y. Yuan *et al*., *Nat. Commun.* **8**, 15092 (2017).
14. R. N. Kirchdoerfer *et al*., *Sci. Rep.* **8**, 15701 (2018).
15. A. Punjani, J. L. Rubinstein, D. J. Fleet, M. A. Brubaker, *Nat. Methods* **14**, 290–296 (2017).
16. D. Wrapp, J. S. McLellan, *J. Virol.* **93**, e00923-19 (2019).
17. A. C. Walls *et al*., *Nat. Struct. Mol. Biol.* **23**, 899–905 (2016).
18. R. N. Kirchdoerfer *et al*., *Nature* **531**, 118–121 (2016).
19. B. Coutard *et al*., *Antiviral Res.* **176**, 104742 (2020).
20. B. J. Bosch, W. Bartelink, P. J. Rottier, *J. Virol.* **82**, 8887–8890 (2008).
21. I. Glowacka *et al*., *J. Virol.* **85**, 4122–4134 (2011).
22. W. Li *et al*., *Nature* **426**, 450–454 (2003).
23. S. Belouzard, V. C. Chu, G. R. Whittaker, *Proc. Natl. Acad. Sci. U.S.A.* **106**, 5871–5876 (2009).
24. J. Chen *et al*., *Cell* **95**, 409–417 (1998).
25. M. Hoffmann *et al*., The novel coronavirus 2019 (2019-nCoV) uses the SARS-coronavirus receptor ACE2 and the cellular protease TMPRSS2 for entry into target cells. bioRxiv 929042 [Preprint]. 31 January 2020. https://doi.org/10.1101/2020.01.31.929042.
26. Y. Wan, J. Shang, R. Graham, R. S. Baric, F. Li, *J. Virol.* JVI.00127-20 (2020).
27. P. Zhou *et al*., *Nature* (2020).
28. W. Song, M. Gui, X. Wang, Y. Xiang, *PLOS Pathog.* **14**, e1007236 (2018).
29. W. C. Hwang *et al*., *J. Biol. Chem.* **281**, 34610–34616 (2006).
30. P. Prabakaran *et al*., *J. Biol. Chem.* **281**, 15829–15836 (2006).
31. X. Tian *et al*., *bioRxiv* **9**, 382–385 (2020).

ACKNOWLEDGMENTS

We thank J. Ludes-Meyers for assistance with cell transfection, members of the McLellan laboratory for critical reading of the manuscript, and A. Dai from the Sauer Structural Biology Laboratory at the University of Texas at Austin for assistance with microscope alignment. **Funding:** This work was supported in part by a National Institutes of Health (NIH)/National Institute of Allergy and Infectious Diseases (NIAID) grant awarded to J.S.M. (R01-AI127521) and by intramural funding from NIAID to B.S.G. The Sauer Structural Biology Laboratory is supported by the University of Texas College of Natural Sciences and by award RR160023 from the Cancer Prevention and Research Institute of Texas (CPRIT). **Author contributions:** D.W. collected and processed cryo-EM data. D.W., N.W., and J.S.M. built and refined the atomic model. N.W. designed and cloned all constructs. D.W., N.W., K.S.C., J.A.G., and O.A. expressed and purified proteins. D.W., J.A.G., and C.-L.H. performed binding studies. B.S.G. and J.S.M. supervised experiments. D.W., B.S.G., and J.S.M. wrote the manuscript with input from all authors. **Competing interests:** N.W., K.S.C., B.S.G., and J.S.M. are inventors on U.S. patent application no. 62/412,703 ("Prefusion Coronavirus Spike Proteins and Their Use"), and D.W., N.W., K.S.C., O.A., B.S.G., and J.S.M. are inventors on U.S. patent application no. 62/972,886 ("2019-nCoV Vaccine"). **Data and materials availability:** Atomic coordinates and cryo-EM maps of the reported structure have been deposited in the Protein Data Bank under accession code 6VSB and in the Electron Microscopy Data Bank under accession codes EMD-21374 and EMD-21375. Plasmids are available from B.S.G. under a material transfer agreement with the NIH or from J.S.M. under a material transfer agreement with The University of Texas at Austin.

SUPPLEMENTARY MATERIAL

science.sciencemag.org/content/367/6483/1260/suppl/DC1
Materials and Methods
Figs S1 to S8
Table S1
Movies S1 and S2
References (*32*–*41*)
MDAR Reproducibility Checklist

View/request a protocol for this paper from *Bio-protocol*.

10 February 2020; accepted 17 February 2020
Published online 19 February 2020
10.1126/science.abb2507

CORONAVIRUS

A noncompeting pair of human neutralizing antibodies block COVID-19 virus binding to its receptor ACE2

Yan Wu[1,2]*†, Feiran Wang[3,4]*, Chenguang Shen[3,5]*, Weiyu Peng[3,6]*, Delin Li[3,5,7]*, Cheng Zhao[3,8], Zhaohui Li[3,9], Shihua Li[3], Yuhai Bi[3,10], Yang Yang[5], Yuhuan Gong[3,10], Haixia Xiao[7], Zheng Fan[3], Shuguang Tan[3], Guizhen Wu[11], Wenjie Tan[11], Xuancheng Lu[12], Changfa Fan[13], Qihui Wang[3], Yingxia Liu[5], Chen Zhang[1], Jianxun Qi[3], George Fu Gao[3]†, Feng Gao[7]†, Lei Liu[5]†

Neutralizing antibodies could potentially be used as antivirals against the coronavirus disease 2019 (COVID-19) pandemic. Here, we report isolation of four human-origin monoclonal antibodies from a convalescent patient, all of which display neutralization abilities. The antibodies B38 and H4 block binding between the spike glycoprotein receptor binding domain (RBD) of the virus and the cellular receptor angiotensin-converting enzyme 2 (ACE2). A competition assay indicated different epitopes on the RBD for these two antibodies, making them a potentially promising virus-targeting monoclonal antibody pair for avoiding immune escape in future clinical applications. Moreover, a therapeutic study in a mouse model validated that these antibodies can reduce virus titers in infected lungs. The RBD-B38 complex structure revealed that most residues on the epitope overlap with the RBD-ACE2 binding interface, explaining the blocking effect and neutralizing capacity. Our results highlight the promise of antibody-based therapeutics and provide a structural basis for rational vaccine design.

Coronavirus disease 2019 (COVID-19) caused by the novel COVID-19 virus has become a pandemic. The virus has spread worldwide, causing fever, severe respiratory illness, and pneumonia (*1*, *2*). Phylogenetic analysis indicates that the virus is closely related to severe acute respiratory syndrome coronavirus (SARS-CoV) (*3*–*5*), but it appears to be more easily transmitted from person to person than SARS-CoV (*6*). To date, no specific drugs or vaccines are available for COVID-19.

The COVID-19 virus belongs to the betacoronavirus genus, which includes five pathogens that infect humans (*7*, *8*). Among them, SARS-CoV and Middle East respiratory syndrome coronavirus (MERS-CoV) are two highly pathogenic viruses. As with other coronaviruses, the spike (S) glycoprotein homotrimer on the COVID-19 virus surface plays an essential role in receptor binding and virus entry. The S protein is a class I fusion protein—each S protomer consists of S1 and S2 domains (*9*), with the receptor binding domain (RBD) located within the S1 domain (*8*). Previous studies have revealed that the COVID-19 virus, similarly to SARS-CoV, uses the angiotensin-converting enzyme 2 (ACE2) receptor for cell entry (*3*, *10*–*13*). Numerous neutralizing antibodies have been found to target the RBDs of SARS-CoV or MERS-CoV (*14*–*16*). Therefore, screening for neutralizing antibodies that target the COVID-19 virus RBD is a priority.

We expressed COVID-19 virus RBD protein as bait to isolate specific single memory B cells from COVID-19 patient peripheral blood mononuclear cells (PBMCs). The variable regions encoding the heavy and light chains were each amplified from separate single B cells and then cloned into a pCAGGS vector with the constant region to produce immunoglobulin G1 (IgG1) antibodies, as described previously (*17*). Seventeen paired B cell clones were amplified, three of which were identical (B5, B59, and H1). To identify the antibody binding abilities, the plasmids containing the paired heavy and light chains were cotransfected into human embryonic kidney–293T (HEK 293T) cells for monoclonal antibody (mAb) production. The supernatants were then screened for binding to the RBD by biolayer interferometry (BLI). An irrelevant anti–severe fever with thrombocytopenia syndrome virus Gn antibody and a SARS-specific antibody were used as controls (*18*). The supernatants from four different antibodies (B5, B38, H2, and H4) bound to COVID-19 virus RBD but not to SARS-CoV RBD (fig. S1), suggesting that the epitopes of the two RBDs are immunologically distinct. The usage of heavy chain (V_H) and light chain (V_L) variable genes in these four antibodies is listed in table S1.

The dissociation constants (K_d) for the four antibodies binding to COVID-19 virus RBD, measured using surface plasmon resonance (SPR), ranged from 10^{-7} to 10^{-9} M (Fig. 1, A to D). We next studied the neutralizing activities of these four antibodies against COVID-19 virus (the BetaCoV/Shenzhen/SZTH-003/2020 strain). All four antibodies exhibited neutralizing activities, with median inhibitory concentration (IC_{50}) values ranging from 0.177 to 1.375 μg/ml (Fig. 2, A to D). A cocktail of B38 and H4 exhibited synergetic neutralizing ability, even in the presence of a higher virus titer (Fig. 2E).

To evaluate the ability of each antibody to inhibit binding between RBD and ACE2, we performed a competition assay using BLI and a blocking assay using fluorescence-activated cell sorting (FACS). For the BLI assay, streptavidin biosensors labeled with biotinylated RBD were saturated with antibodies, and then the test antibodies were flowed through in the presence of soluble ACE2. B38 and H4 showed complete competition with ACE2 for binding to RBD. In contrast, B5 displayed partial competition, whereas H2 did not compete with ACE2 for RBD binding (Fig. 1, E to H). The blocking assay by FACS presented the same result (Fig. 1I). To determine whether B38 and H4 target the same epitope, we performed an epitope competition assay by BLI. The nickel–nitrilotriacetic acid sensor labeled with the RBD was saturated with B38 IgG, and H4 IgG was flowed through, or the reverse (sensor saturated with H4 IgG, and B38 IgG flowed through). Although RBD was saturated with the first antibody, the second antibody could still bind to RBD, but with some inhibition. This suggests that B38 and H4 recognize different epitopes on RBD with partial overlap (Fig. 1, J and K).

To explore the protection efficacy of B38 and H4 against challenge with COVID-19 virus in vivo, hACE2 transgenic mice were administered a single 25 mg/kg dose of B38 or H4 12 hours after viral challenge. The body weight of the B38 group decreased slowly and recovered at 3 days postinfection (dpi) compared with the phosphate-buffered saline (PBS) control group and the H4 group (Fig. 3A). The number of viral RNA copies in the lung were also measured at 3 dpi. The RNA copies of both the B38 group and the H4 group were significantly lower than those of the PBS group, with a reduction of 3.347 and 2.655 logs, respectively (Fig. 3B). These results show the same trends as the neutralization abilities. Histopathological examination indicated that severe bronchopneumonia and interstitial pneumonia could be observed in

[1]Department of Pathogen Microbiology, School of Basic Medical Sciences, Capital Medical University, Beijing, China. [2]Research Network of Immunity and Health (RNIH), Beijing Institutes of Life Science, Chinese Academy of Sciences, Beijing, China. [3]CAS Key Laboratory of Pathogenic Microbiology and Immunology, Institute of Microbiology, Chinese Academy of Sciences (CAS), Beijing, China. [4]School of Life Sciences, University of Science and Technology of China, Hefei, Anhui, China. [5]Shenzhen Key Laboratory of Pathogen and Immunity, Shenzhen Third People's Hospital, Shenzhen, China. [6]College of Veterinary Medicine, China Agricultural University, Beijing, China. [7]Laboratory of Protein Engineering and Vaccines, Tianjin Institute of Industrial Biotechnology, Chinese Academy of Sciences (CAS), Tianjin, China. [8]Shanxi Academy of Advanced Research and Innovation, Taiyuan, China. [9]University of Chinese Academy of Sciences, Beijing, China. [10]Center for Influenza Research and Early Warning, Chinese Academy of Sciences (CASCIRE), Beijing, China. [11]NHC Key Laboratory of Biosafety, National Institute for Viral Disease Control and Prevention, Chinese Center for Disease Control and Prevention, Beijing, China. [12]Laboratory Animal Center, Chinese Center for Disease Control and Prevention, Beijing, China. [13]Division of Animal Model Research, Institute for Laboratory Animal Resources, National Institutes for Food and Drug Control, Beijing, China.
*These authors contributed equally to this work.
†Corresponding author. Email: wuy@biols.ac.cn (Y.W.); gaofeng@tib.cas.cn (F.G.); gaof@im.ac.cn (G.F.G.); liulei3322@aliyun.com (L.L.)

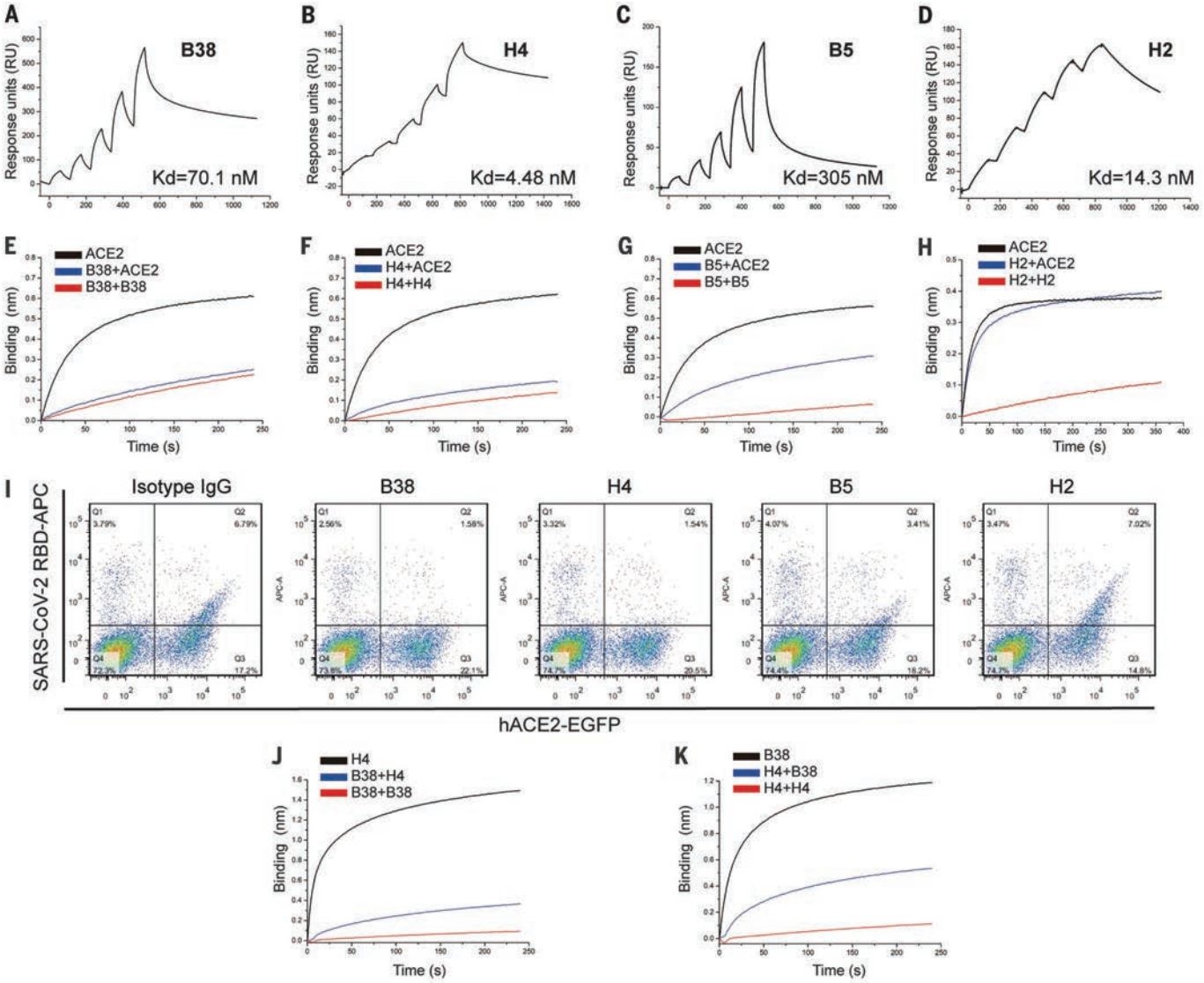

Fig. 1. Characterization of COVID-19 virus–specific neutralizing antibodies. (**A** to **D**) The binding kinetics between four antibodies (B38, H4, B5, and H2) and COVID-19 virus RBD were measured using a single-cycle Biacore 8K system. (**E** to **H**) Competition binding to the COVID-19 virus RBD between antibodies and ACE2 was measured by BLI. Immobilized biotinylated COVID-19 virus RBD (10 μg/ml) was saturated with antibodies and then flowed with corresponding antibody in the presence of 300 nM soluble ACE2 (blue) or without ACE2 (red). As a control, the immobilized biotinylated RBD was flowed with buffer and then flowed with the equal molar concentration of ACE2 (black). The graphs show binding patterns after antibody saturation. (**I**) hACE2–enhanced green fluorescent protein (EGFP) was expressed on the HEK293T cell surface, and the cells were stained with 200 ng/ml COVID-19 virus RBD his-tag proteins preincubated with isotype IgG, B38, H4, B5, or H2. The percentages of anti-his-tag APC^+ (allophycocyanin) cells and $EGFP^+$ cells were calculated. (**J** and **K**) Competition binding to COVID-19 virus RBD between B38 and H4 was measured by BLI. Immobilized COVID-19 virus RBD (10 μg/ml) was saturated with 300 nM of the first antibody and then flowed with equal molar concentration of the first antibody in the presence of (blue) or without (red) the second antibody. Equal molar concentration of the second antibody was flowed on the immobilized RBD as a control (black). The graphs show binding patterns after saturation of the first antibody.

the mice of the PBS control group, with edema and bronchial epithelial cell desquamation and infiltration of lymphocytes within alveolar spaces (Fig. 3, C and F). Mild bronchopneumonia was observed in the H4 group (Fig. 3, E and H), whereas no lesions were observed in the B38 group (Fig. 3, D and G).

As is consistent with the binding affinity between RBD and B38 or H4, stable complexes were obtained in both RBD-B38 and RBD-H4 mixtures (fig. S2). The complex crystal structure of RBD-B38 Fab was solved at 1.9-Å resolution (table S2). Three complementarity-determining regions (CDRs) on the heavy chain and two CDRs on the light chain are involved in interaction with RBD (Fig. 4, A, B, and G to K). The buried surface area of heavy and light chains on the epitope is 713.9 and 497.7 Å, respectively. There are 36 residues in the RBD involved in the interaction with B38, in which 21 residues and 15 residues interact with heavy and light chains, respectively (table S3 and Fig. 4B). Sequence alignment indicates that only 15 of the 36 residues in the epitope (defined as residues buried by B38) are conserved between COVID-19 virus and SARS-CoV (Fig. 4, D to F, and fig. S3). Notably, most contacts in the interface between B38 and RBD are hydrophilic interactions (table S4). Water molecules play an important role in the binding between COVID-19

RBD and B38 (Fig. 4, G and I to K). These differences explain the B38-specific binding to the COVID-19 virus rather than SARS-CoV.

To explore the structural basis for B38 blocking the interaction between COVID-19 virus RBD and ACE2, the complex structures of RBD–B38-Fab and RBD-hACE2 were superimposed. Both the V_H and V_L of B38 would sterically hinder ACE2 binding (Fig. 4C). Notably, the RBDs in B38-bound form and hACE2-bound form have no notable conformational differences, with a Cα root mean square deviation of 0.489 Å (for 194 atoms). Further analysis indicated that 18 of the 21 amino acids on the RBD are involved in binding both B38 and

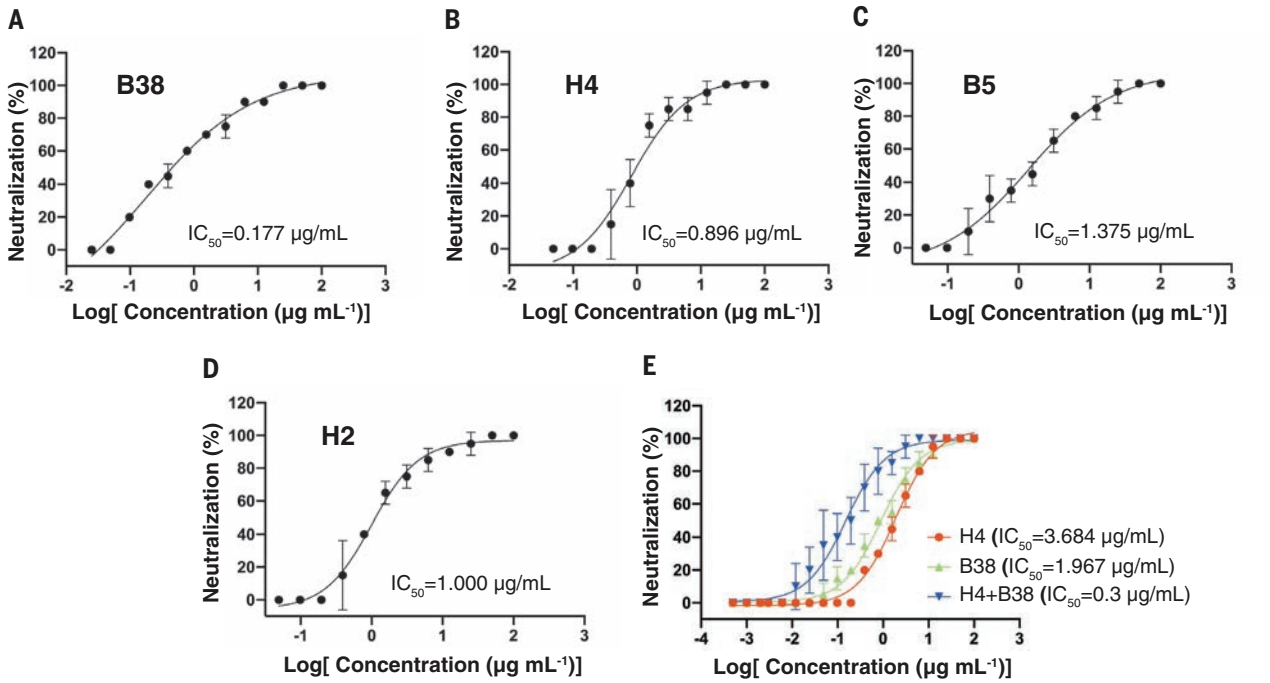

Fig. 2. Four antibodies can effectively neutralize COVID-19 virus, and two of them exhibit additive inhibition effect. The mixtures of COVID-19 virus and serially diluted antibodies were added to Vero E6 cells. After 5 days of incubation, IC_{50} values were calculated by fitting the cytopathic effect from serially diluted antibody to a sigmoidal dose-response curve. Medium containing 100 and 200 times the median tissue culture infectious dose of COVID-19 virus was used for testing the neutralizing abilities of individual antibody (**A** to **D**) and cocktail antibodies (**E**), respectively.

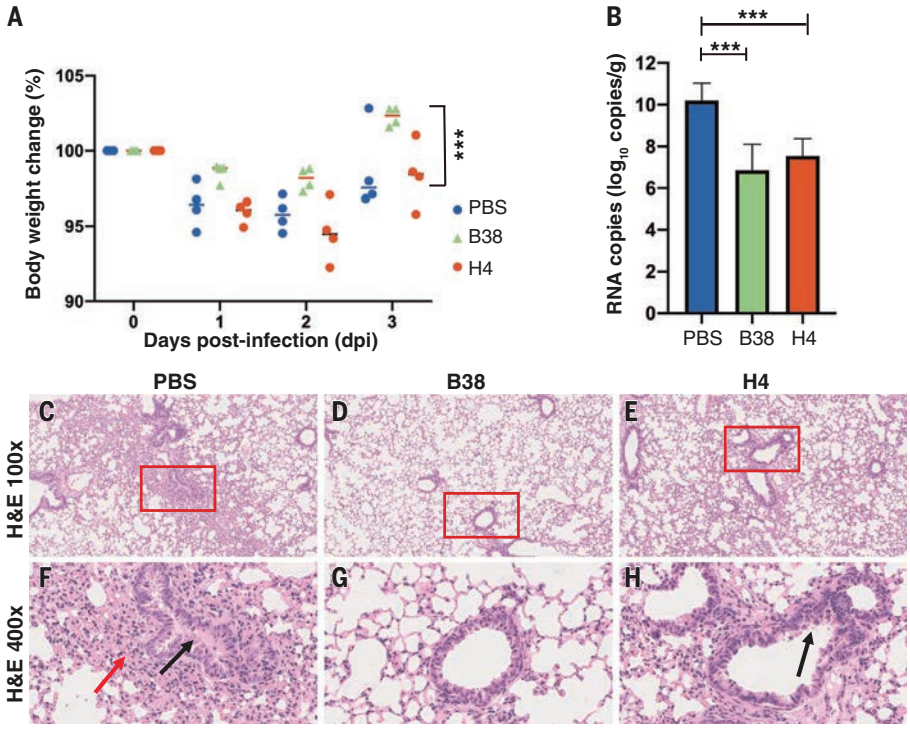

Fig. 3. The protection efficiency of mAbs in hACE2 mice model after infection with COVID-19 virus. (**A**) Body weight loss was recorded for PBS, B38 treatment, and H4 treatment groups (for all groups, $n = 4$ mice). All the mice were challenged intranasally with COVID-19 virus, and a 25 mg/kg dose of antibodies was injected (intraperitoneally) 12 hours after infection. Equal volume of PBS was used as a control. The weight loss was recorded over 3 days, and a significant difference could be observed between the B38 group and the PBS group (unpaired *t* test, $^{***}P < 0.001$). (**B**) The virus titer in lungs of three groups was determined at 3 dpi by real-time quantitative reverse transcription polymerase chain reaction (qRT-PCR). The mAb treatment group reduced the viral load in the lungs of mice (unpaired *t* test, $^{***}P < 0.001$). (**C** to **H**) Representative histopathology of the lungs in COVID-19 virus–infected hACE2 mice (3 dpi). Severe bronchopneumonia and interstitial pneumonia was observed in the PBS group [(C) and (F)], with edema and bronchial epithelial cell desquamation (black arrow) and infiltration of lymphocytes within alveolar spaces (red arrow). Mild bronchopneumonia was observed in the H4 group [(E) and (H)], whereas no lesions were observed in the B38 group [(D) and (G)]. The images and areas of interest (red boxes) are magnified 100× and 400×, respectively.

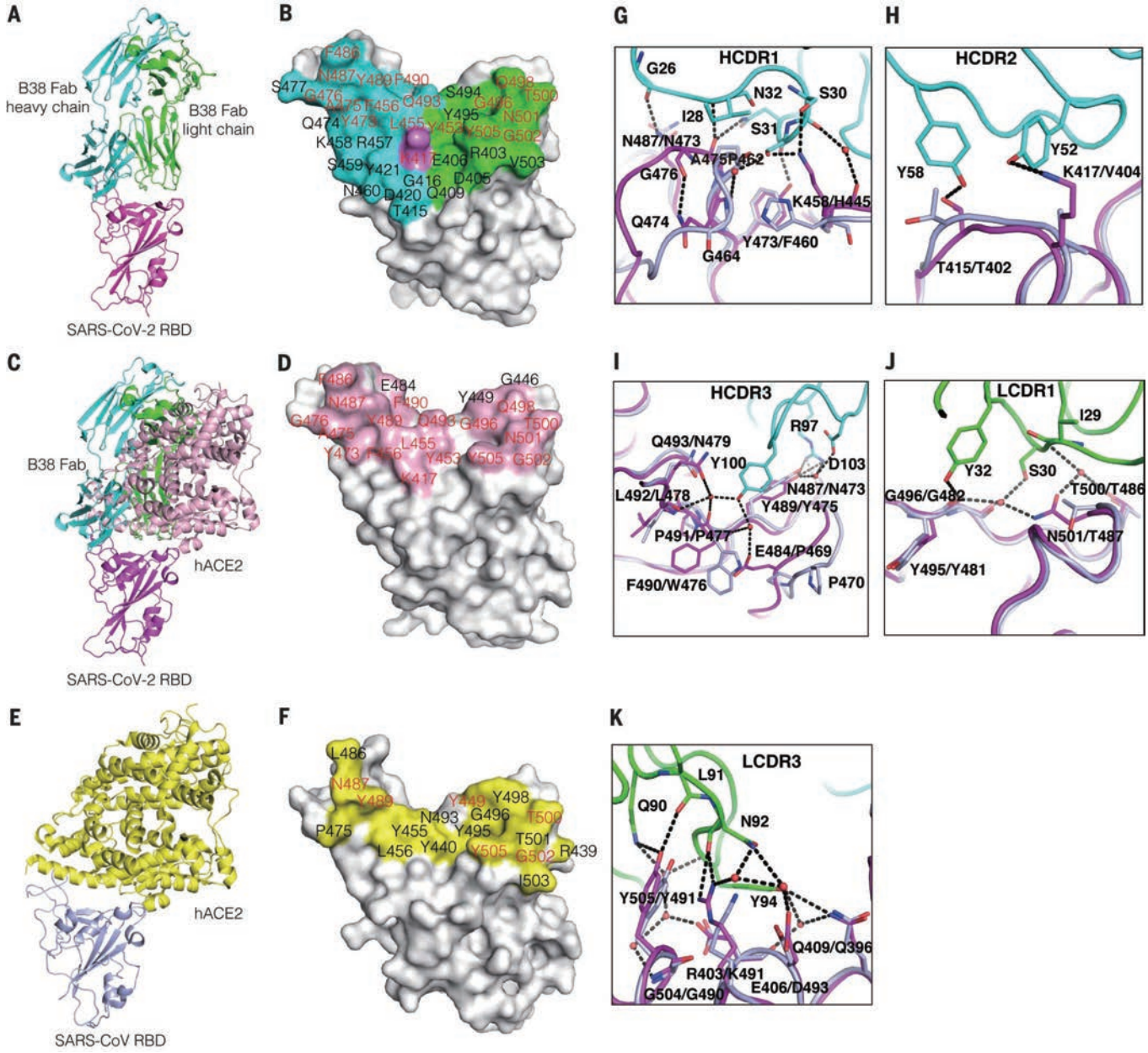

Fig. 4. Structural analysis of B38 and COVID-19 virus RBD complex and the epitope comparison between B38 and hACE2. (**A**) The overall structure of B38 Fab and COVID-19 virus RBD. The B38 heavy chain (cyan), light chain (green), and COVID-19 virus RBD (magenta) are shown in cartoon representation. (**B**) The epitope of B38 is shown in surface representation. The contact residues by heavy chain, light chain, or both are colored in cyan, green, and magenta, respectively. The residues on RBD involved in both B38 and hACE2 binding are labeled in red. (**C**) Superimposition of RBD-B38 and RBD-hACE2 [Protein Data Bank (PDB) ID 6LZG]. All molecules are shown in cartoon representation, with the same colors as in (A). hACE2 is colored in light pink. (**D**) The residues involved in hACE2-RBD binding are highlighted in light pink. The residues on RBD involved in both B38 and hACE2 binding are labeled in red. (**E**) The complex structure of SARS-CoV RBD (light blue) and hACE2 (yellow) (PDB ID 2AJF). (**F**) The residues in contact with hACE2 are colored in yellow. The residues are numbered according to SARS-CoV RBD. The residues involved in hACE2 binding of two RBDs are labeled in red. (**G** to **I**) The detailed interactions between COVID-19 virus RBD and CDR loops of the heavy chain. (**J** and **K**) The detailed interactions between COVID-19 virus RBD and CDR loops of the light chain. The residues are shown in stick representation, with the same colors as in (C). The water molecules are shown as red spheres. Single-letter abbreviations for the amino acid residues are as follows: A, Ala; D, Asp; E, Glu; F, Phe; G, Gly; I, Ile; K, Lys; L, Leu; N, Asn; P, Pro; Q, Gln; R, Arg; S, Ser; T, Thr; V, Val; W, Trp; and Y, Tyr.

ACE2 (Fig. 4D), which explains why B38 abolishes the binding between COVID-19 virus RBD and the receptor.

As the COVID-19 outbreak continues to spread, characterization of the epitopes on the COVID-19 virus RBD will provide valuable information for vaccine development. Furthermore, the molecular features of the neutralizing antibody targeting epitopes are helpful for the development of small-molecule or peptide drugs and inhibitors. The neutralizing antibodies themselves are also promising candidates for prophylactic and therapeutic treatment against the COVID-19 virus.

REFERENCES AND NOTES

1. N. Zhu *et al.*, *N. Engl. J. Med.* **382**, 727–733 (2020).
2. C. Wang, P. W. Horby, F. G. Hayden, G. F. Gao, *Lancet* **395**, 470–473 (2020).

3. P. Zhou *et al*., *Nature* **579**, 270–273 (2020).
4. W. Tan *et al*., *China CDC Weekly* **2**, 61–62 (2020).
5. R. Lu *et al*., *Lancet* **395**, 565–574 (2020).
6. J. F. Chan *et al*., *Lancet* **395**, 514–523 (2020).
7. F. Wu *et al*., *Nature* **579**, 265–269 (2020).
8. G. Lu, Q. Wang, G. F. Gao, *Trends Microbiol.* **23**, 468–478 (2015).
9. D. M. Knipe, P. M. Howley, Eds., *Fields Virology* (Lippincott Williams & Wilkins, ed. 6, 2013).
10. A. C. Walls *et al*., *Cell* **181**, 281–292.e6 (2020).
11. M. Hoffmann *et al*., *Cell* **181**, 271–280.e8 (2020).
12. Q. Wang *et al*., *Cell* **181**, 894–904.e9 (2020).
13. D. Wrapp *et al*., *Science* **367**, 1260–1263 (2020).
14. Y. Zhou, Y. Yang, J. Huang, S. Jiang, L. Du, *Viruses* **11**, 60 (2019).
15. L. Du *et al*., *Expert Opin. Ther. Targets* **21**, 131–143 (2017).
16. L. Du *et al*., *Nat. Rev. Microbiol.* **7**, 226–236 (2009).
17. Q. Wang *et al*., *Nat. Microbiol.* **4**, 1231–1241 (2019).
18. Y. Wu *et al*., *Proc. Natl. Acad. Sci. U.S.A.* **114**, E7564–E7573 (2017).

ACKNOWLEDGMENTS

We thank the staff of the BL17U1 beamline at the Shanghai Synchrotron Radiation Facility (SSRF) for data collection. We thank H. Sun for discussion of the histopathology experiment.

Funding: This work was supported by the Zhejiang University special scientific research fund for COVID-19 prevention and control (2020XGZX019), the National Science and Technology Major Project (2018ZX10733403), the National Key R&D Program of China (2018YFC1200603), the National Key Plan for Scientific Research and Development of China (2016YFD0500304), National Natural Science Foundation of China (31872745, 81902058, and 32041010), and the National Science and Technology Major Projects of Infectious Disease Funds (2017ZX10304402). **Author contributions:** Y.W., F.G., G.F.G., and L.L. initiated and coordinated the project. Y.W., F.G., and G.F.G. designed the experiments. Y.L. and L.L. provided the convalescent PBMCs. Y.W. and C.S. performed the cell sorting. W.P., C. Zhao, Z.L., and C.S. sequenced and constructed the antibodies. Y.W. conducted the SPR and Octet analysis with the help of Z.F., F.W., Z.L., and Q.W. C.S. and Y.Y. evaluated the neutralizing potency. S.L. and Y.B. conducted the animal experiments with the help from G.W., W.T., X.L., C.F., C. Zhang and H.X. qRT-PCR was conducted by Y.G. F.W., W.P., D.L., C. Zhao, and Z.L. expressed and purified proteins. J.Q. and F.G. collected the diffraction data and determined the complex structure. Y.W., F.G., and G.F.G. analyzed the data and wrote the manuscript. S.T. revised the manuscript. **Competing interests:** Y.W., F.W., C.S., D.L., S.T., Y.L., G.F.G., and L.L. are listed as inventors on pending patent applications for mAb B38 and H4. The other authors declare that they have no competing interests. **Data and materials availability:** The atomic coordinate for the complex of the COVID-19 virus RBD and B38 has been deposited in the Protein Data Bank (www.rcsb.org). The PDB ID is 7BZ5. Antibody sequences beyond those in the supplementary materials are available under an MTA.

SUPPLEMENTARY MATERIALS

science.sciencemag.org/content/368/6496/1274/suppl/DC1
Materials and Methods
Figs. S1 to S3
Tables S1 to S4
References (*19*–*22*)
MDAR Reproducibility Checklist

View/request a protocol for this paper from *Bio-protocol*.

13 April 2020; accepted 5 May 2020
Published online 13 May 2020
10.1126/science.abc2241

Resource

Cell Host & Microbe

An Infectious cDNA Clone of SARS-CoV-2

Graphical Abstract

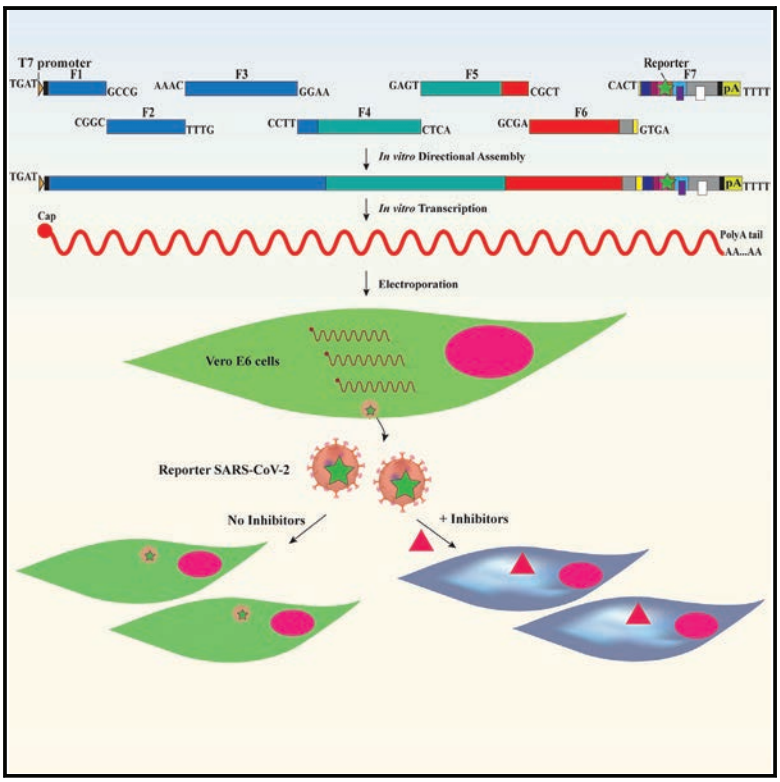

Highlights

- A reverse genetic system has been established for SARS-CoV-2
- Recombinant SARS-CoV-2 replicates as efficiently as the original clinical isolate
- A stable mNeonGreen reporter SARS-CoV-2 has been developed
- The mNeonGreen SARS-CoV-2 can be used to screen antiviral inhibitors

Authors

Xuping Xie, Antonio Muruato, Kumari G. Lokugamage, ..., James W. LeDuc, Vineet D. Menachery, Pei-Yong Shi

Correspondence

xuxie@UTMB.edu (X.X.), vimenach@UTMB.edu (V.D.M.), peshi@UTMB.edu (P.-Y.S.)

In Brief

Severe acute respiratory syndrome coronavirus 2 (SARS-CoV-2) has caused a devastating global pandemic. Xie et al. generated an infectious cDNA clone of SARS-CoV-2 and a mNeonGreen reporter virus. Recombinant SARS-CoV-2 and reporter virus replicate as efficiently as the original clinical isolate.

Xie et al., 2020, Cell Host & Microbe *27*, 841–848
May 13, 2020 © 2020 Elsevier Inc.
https://doi.org/10.1016/j.chom.2020.04.004

Cell Host & Microbe

CellPress

Resource

An Infectious cDNA Clone of SARS-CoV-2

Xuping Xie,[1,*] Antonio Muruato,[1,2] Kumari G. Lokugamage,[2] Krishna Narayanan,[2] Xianwen Zhang,[1] Jing Zou,[1] Jianying Liu,[2] Craig Schindewolf,[2] Nathen E. Bopp,[3] Patricia V. Aguilar,[3,4,5] Kenneth S. Plante,[2,4] Scott C. Weaver,[2,4,5,6,7,8] Shinji Makino,[2,5,10] James W. LeDuc,[2,9] Vineet D. Menachery,[2,5,7,*] and Pei-Yong Shi[1,5,8,10,11,12,*]

[1]Department of Biochemistry and Molecular Biology, University of Texas Medical Branch, Galveston, TX, USA
[2]Department of Microbiology and Immunology, University of Texas Medical Branch, Galveston, TX, USA
[3]Department of Pathology, University of Texas Medical Branch, Galveston, TX, USA
[4]World Reference Center for Emerging Viruses and Arboviruses, University of Texas Medical Branch, Galveston, TX, USA
[5]Institute for Human Infection and Immunity, University of Texas Medical Branch, Galveston, TX, USA
[6]Institute for Translational Sciences, University of Texas Medical Branch, Galveston, TX, USA
[7]Department of Pathology and Center for Biodefense & Emerging Infectious Diseases, University of Texas Medical Branch, Galveston, TX, USA
[8]Sealy Institute for Vaccine Sciences, University of Texas Medical Branch, Galveston, TX, USA
[9]Galveston National Laboratory, University of Texas Medical Branch, Galveston, TX, USA
[10]Sealy Center for Structural Biology & Molecular Biophysics, University of Texas Medical Branch, Galveston, TX, USA
[11]Department of Pharmacology & Toxicology, University of Texas Medical Branch, Galveston, TX, USA
[12]Lead Contact
*Correspondence: xuxie@UTMB.edu (X.X.), vimenach@UTMB.edu (V.D.M.), peshi@UTMB.edu (P.-Y.S.)
https://doi.org/10.1016/j.chom.2020.04.004

SUMMARY

The ongoing pandemic of COVID-19, caused by severe acute respiratory syndrome coronavirus 2 (SARS-CoV-2), underscores the urgency to develop experimental systems for studying this virus and identifying countermeasures. We report a reverse genetic system for SARS-CoV-2. Seven complimentary DNA (cDNA) fragments spanning the SARS-CoV-2 genome were assembled into a full-genome cDNA. RNA transcribed from the full-genome cDNA was highly infectious after electroporation into cells, producing 2.9×10^6 plaque-forming unit (PFU)/mL of virus. Compared with a clinical isolate, the infectious-clone-derived SARS-CoV-2 (icSARS-CoV-2) exhibited similar plaque morphology, viral RNA profile, and replication kinetics. Additionally, icSARS-CoV-2 retained engineered molecular markers and did not acquire other mutations. We generated a stable mNeonGreen SARS-CoV-2 (icSARS-CoV-2-mNG) by introducing this reporter gene into ORF7 of the viral genome. icSARS-CoV-2-mNG was successfully used to evaluate the antiviral activities of interferon (IFN). Collectively, the reverse genetic system and reporter virus provide key reagents to study SARS-CoV-2 and develop countermeasures.

INTRODUCTION

Severe acute respiratory syndrome coronavirus 2 (SARS-CoV-2) emerged in early 2020 with human cases in Wuhan, China (Zhou et al., 2020; Zhu et al., 2020). It has rapidly rampaged worldwide, causing a pandemic of coronavirus disease (COVID-19) that ranges from fever and breathing difficulty to acute respiratory distress and death (Huang et al., 2020; Zhu et al., 2020). With over 300,000 people infected in less than 3 months, SARS-CoV-2 causes the most severe disease in older patients and people with co-morbidities, including heart disease, diabetes, and other health conditions (Wu and McGoogan, 2020). Before 2019, six α- and β-coronaviruses were known to cause respiratory diseases of different severity, including four common cold coronaviruses (229E, NL63, OC43, and HKU1) and two highly pathogenic coronaviruses (severe acute respiratory syndrome [SARS-CoV] and Middle East respiratory syndrome [MERS-CoV], which emerged in 2003 and since 2012, respectively) (Assiri et al., 2013; Huang et al., 2020). Importantly, with massive hospitalization rates and high mortality, SARS-CoV-2 remains a major threat to humankind and intervention strategies are being rapidly pursued.

A key tool in responding to emergent viruses is the generation of reverse genetic systems to explore and characterize new pathogens. Classically, reverse genetic systems for coronaviruses have been complicated by their large genome size (~30,000 nucleotides) and the existence of bacteriotoxic elements in their genome that make them difficult to propagate (Almazán et al., 2014). Several approaches have been devised to overcome this barrier, such as multiple plasmid systems to disrupt toxic elements and to reduce deletions and mutations (Yount et al., 2002). Using this approach, researchers have developed infectious clones for several coronaviruses, including SARS-CoV, MERS-CoV, and others (Menachery et al., 2015; Menachery et al., 2016; Scobey et al., 2013; Yount et al., 2003). Thao et al., (2020) recently reported a yeast-based synthetic genomics platform for rapid construction of infectious clones for murine hepatitis coronavirus (MHV-CoV), MERS-CoV, and SARS-CoV-2. However, the yeast-platform-produced SARS-CoV-2 has not been fully characterized for its biological

properties (e.g., replication kinetics) in comparison with its original clinical isolate. Such characterization is essential for ensuring the quality of the genetic system to rescue recombinant viruses that recapitulate the biological features of their corresponding clinical isolates. Once validated, the reverse genetic systems allow rapid characterization of novel viruses, development of reporter viruses, and generation of live-attenuated vaccine candidates to respond to emerging infections. Together with animal pathogenesis models, reverse genetic systems offer powerful tools needed to characterize, understand, and respond to emerging virus outbreaks.

In response to the ongoing pandemic of SARS-CoV-2, we have developed a robust reverse genetic system for SARS-CoV-2 and a mNeonGreen reporter virus. Recombinant virus derived from the system recapitulates the replication kinetics of the original clinical isolates. In addition, the mNeonGreen reporter remains stable for at least five passages, allowing its use in long-term studies. Using type I interferon (IFN), we demonstrated that the mNeonGreen virus could be reliably used to study viral replication and pathogenesis as well as to develop vaccines and antiviral drugs.

RESULTS

Design of a SARS-CoV-2 Full-Length cDNA

We designed an *in vitro* ligation approach, similar to that used for constructing the infectious clones of SARS-CoV and MERS-CoV (Scobey et al., 2013; Yount et al., 2003), to directionally assemble the full-length complimentary DNA (cDNA) of the SARS-CoV-2 genome (Figure 1A). Our reverse genetic system was based on the virus strain (2019-nCoV/USA_WA1/2020) isolated from the first reported SARS-CoV-2 case in the US (Harcourt et al., 2020; Holshue et al., 2020). Viral RNA, extracted from the passage 4 virus from Vero E6 cells, was used as a template for RT-PCR to produce cDNA fragments. Seven contiguous cDNA fragments were constructed to cover the entire viral genome (Figure 1B). Some of the seven cDNA fragments were prepared through RT-PCR, whereas others were generated by chemical synthesis (see Method Details). All cDNA fragments were individually cloned into plasmid vectors. For facilitating directional assembly of genome-length cDNA, each cDNA fragment was flanked by a class IIS restriction endonuclease site (BsaI or Esp3I). The class IIS endonucleases recognize asymmetric DNA sequences, cleave outside their recognition sequences, and generate unique cohesive overhangs (Figure 1C). After digestion with BsaI or Esp3I, the seven fragments were directionally ligated to assemble the genome-length cDNA. The unique cohesive ends of each fragment ensured one directional, seamless assembly of the seven fragments with the concomitant loss of the restriction enzyme sites. Figure 1C depicts the details of the seven fragments: F1 (T7 promoter sequence plus nucleotides 1–3,618), F2 (nucleotides 3,619–7,504), F3 (nucleotides 7,505–11,984), F4 (nucleotides 11,985–17,591), F5 (nucleotides 17,592–22,048), F6 (nucleotides 22,049–26,332), and F7 (nucleotides 26,333–29,870 plus a poly(A)$_{29}$ sequence). We engineered a T7 promoter and a poly(A)$_{29}$ tail at the upstream end of F1 and the downstream end of F7, respectively. *In vitro* transcription of the ligated F1–F7 DNA was expected to produce a 5′ capped (because cap analog was included in the *in vitro* transcription reaction) and 3′ polyadenylated genome-length RNA. To differentiate the infectious clone-derived virus from the parental clinical isolate, we engineered three synonymous nucleotide mutations as markers.

Assembly of a SARS-CoV-2 Full-Length cDNA

We cloned each of the seven cDNA fragments into a plasmid and sequenced them to ensure no undesired mutations. For assembly of full-length cDNA, the seven cDNA plasmids were digested with BsaI or Esp3I. The resulting cDNA fragments were gel-purified (Figure 1D) then *in vitro* ligated to assemble the genome-length cDNA in three steps: (1) ligation of F1, F2, F3, and F4 to produce F1–4 cDNA; (2) ligation of F5, F6, and F7 to produce F5–7 cDNA; and (3) ligation of F1–4 and F5–7 to produce the full-length F1–7 cDNA. Agarose gel analysis of the ligation (3) reaction showed a major DNA product representing the size of genome-length cDNA (~29.87 kb, indicated by an arrow in Figure 1E) in addition to several smaller intermediate cDNA products (indicated by circles). *In vitro* transcription using the cDNA template (directly from ligation (3) without gel purification) generated multiple RNA bands, among which a faint high molecular band might represent the genome-length RNA (indicated by an arrow in Figure 1F) together with several smaller RNA transcripts (indicated by circles).

Recovery of Recombinant SARS-CoV-2

To recover recombinant SARS-CoV-2 from the infectious cDNA clone (icSARS-CoV-2), we electroporated *in-vitro*-transcribed genome-length RNA into Vero E6 cells. We directly electroporated the RNA transcription mixture from Figure 1F into cells without purification. Given that N protein was reported to enhance the infectivity of coronavirus RNA transcripts (Curtis et al., 2002; Yount et al., 2003; Yount et al., 2002), we co-electroporated an mRNA encoding the SARS-CoV-2 N protein with the full-length RNA. The transfected cells developed cytopathic effects (CPEs) on day 4 after transfection and produced infectious virus (denoted as passage 0 (P0) virus) with a titer of 2.9×10^6 plaque-forming units (PFU)/mL (Figure 2A). It is worth emphasizing that such a high titer of recombinant virus was produced directly from the electroporated cells without additional rounds of cell culture passaging, indicating the robustness of the system and also suggesting a lack of any errors. Next, we compared the replication properties between the recombinant virus and the original clinical isolate. The wild-type icSARS-CoV-2 (icSARS-CoV-2-WT) developed plaques similar to the original clinical isolate (Figure 2B) and exhibited equivalent replication kinetics on Vero E6 cells (Figure 2C). We did not extend the time points of replication beyond 48 h because CPEs were observed at 40–48 h after infection. Northern blot analysis showed that viral messenger RNA (mRNA) species from the clinical-isolate-infected cells and the icSARS-CoV-2-infected cells were identical to the predicted set of genome-length RNA and eight subgenomic RNAs (Figure 2D). Full-genome sequencing showed that the recombinant virus retained the three engineered synonymous mutations with no other sequence changes, demonstrating the rescued virus did not result from contamination by the parental virus isolate (Figure 2E). Furthermore, the DNA sequencing chromatogram did not show any partial reversion of the three engineered molecular markers (Figure 2F). Collectively, the results demonstrate that (1) the *in-vitro*-transcribed full-length RNA is highly infectious upon electroporation into

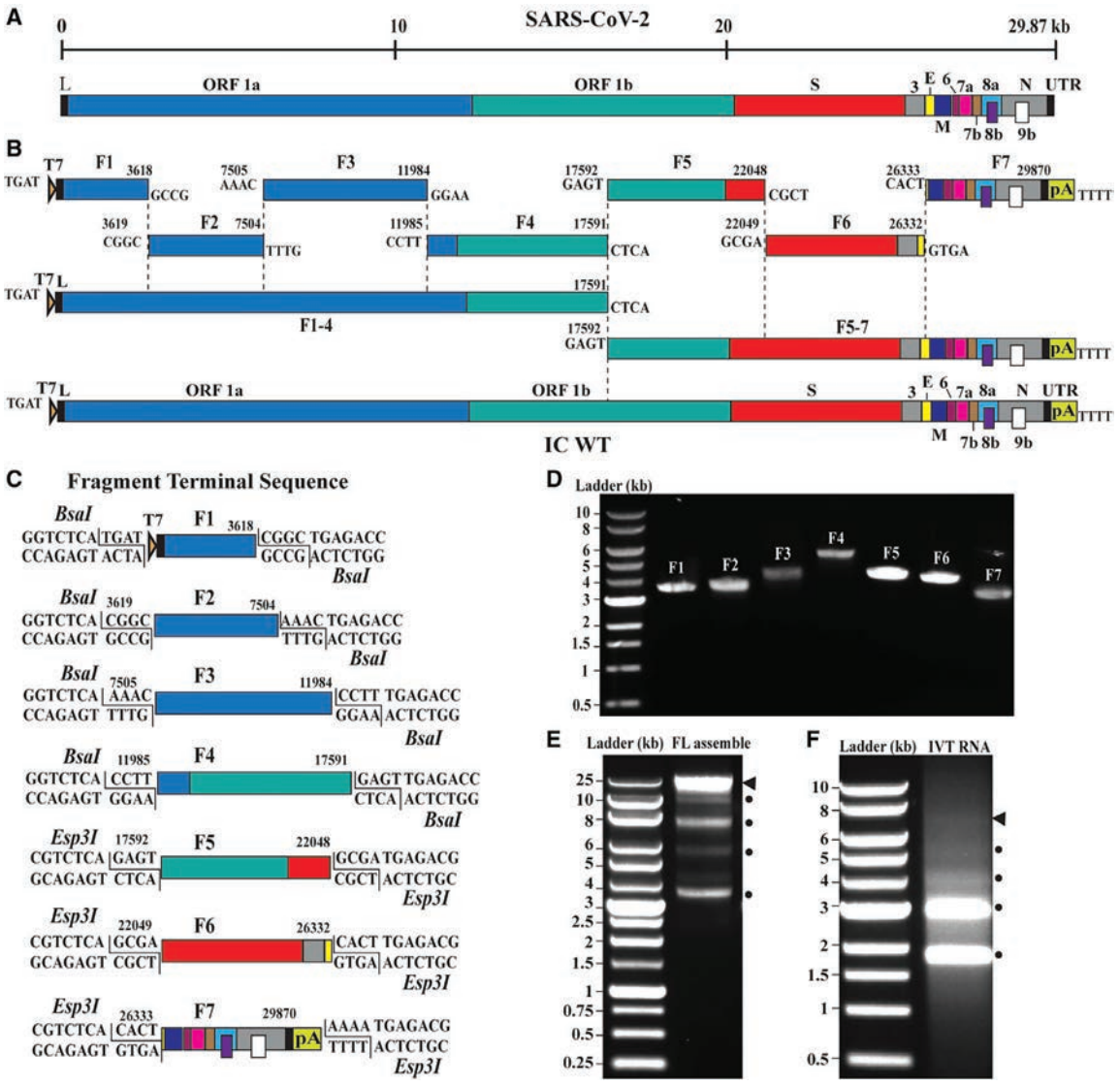

Figure 1. Assembly of a Full-Length SARS-CoV-2 Infection cDNA Clone

(A) Genome structure SARS-CoV-2. The open reading frames (ORFs) from the full genome are indicated.

(B) Strategy for *in vitro* assembly of an infectious cDNA clone of SARS-CoV-2. The nucleotide sequences and genome locations of the cohesive overhangs are indicated. The WT full-length (FL) cDNA of SARS-CoV-2 (IC WT) was directionally assembled using *in vitro* ligation.

(C) Diagram of the terminal sequences of each cDNA fragment recognized by BsaI and Esp3I.

(D) Gel analysis of the seven purified cDNA fragments. Individual fragments (F1–F7) were digested from corresponding plasmid clones and gel purified. Seven purified cDNA fragments (50–100 ng) were analyzed on a 0.6% native agarose gel. The 1-kb DNA ladders are indicated.

(E) Gel analysis of cDNA ligation products. About 400 ng of purified ligation product was analyzed on a 0.6% native agarose gel. Triangle indicates the FL cDNA product. Circles indicate the intermediate cDNA products.

(F) Gel analysis of RNA transcripts. About 1 μg of *in-vitro*-transcribed (IVT) RNAs were analyzed on a 0.6% native agarose gel. DNA ladders are indicated. Because this is a native agarose gel, the DNA size is not directly corelated to the RNA size. Triangle indicates the genome-length RNA transcript. Circles show the shorter RNA transcripts.

cells, and (2) the recombinant virus recapitulates the replication properties of the original clinical isolate on Vero E6 cells.

Development and Characterization of mNeonGreen SARS-CoV-2

Reporter viruses are useful tools to study viral replication and pathogenesis and to develop countermeasures. To establish a reporter SARS-CoV-2 infectious clone, we engineered an mNeonGreen (mNG) gene into the ORF7 of viral genome (Figure 3A), similar to the SARS-CoV reporter (Sims et al., 2005). The same *in vitro* ligation and transcription protocols (described above) were used to prepare the mNG full-length RNA. After electroporation, we recovered icSARS-CoV-2-mNG (6.9×10^6 PFU/mL). To examine whether the reporter gene attenuates viral replication, we compared the replication properties between the WT and reporter viruses on Vero E6 cells. The icSARS-CoV-2-mNG produced plaques similar to

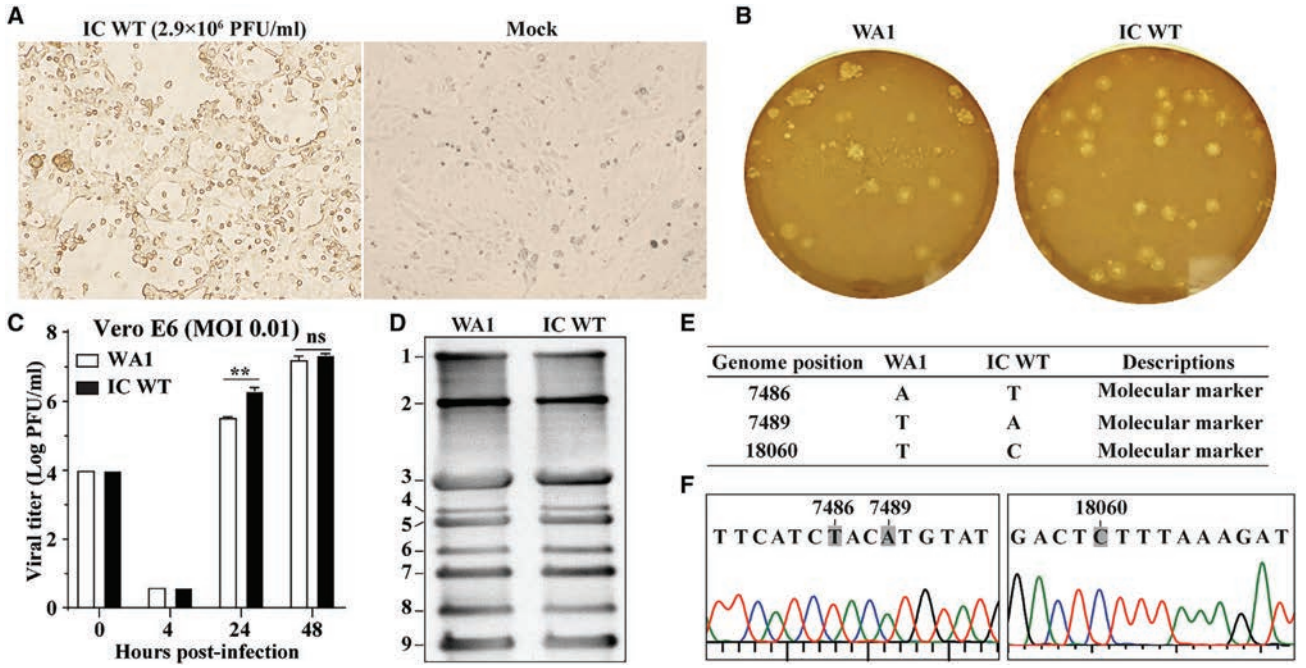

Figure 2. Characterization of the IC WT

(A) Bright-field images of the Vero E6 cells electroporated with RNA transcripts. CPEs appeared in the IC-WT-RNA-transfected cells on day 4 after transfection. The titer of the P0 virus (directly from the transfected cells) is shown in PFUs per ml.

(B) Plaque morphology of the original clinical isolate (WA1 = 2019-nCoV/USA_WA1/2020) and the recombinant P1 IC WT virus. Plaques were developed in Vero E6 cells on day 2 after infection.

(C) Replication kinetics. Vero E6 cells were infected with the clinical isolate or recombinant P1 IC WT virus at MOI 0.01. Viruses in culture fluids were quantified by plaque assay. Results from triplicate experiments were presented with error bars indicating standard deviations.

(D) Northern blot analysis of FL and subgenomic RNAs. Numbers indicated the FL (band 1) and eight subgenomic RNAs (bands 2–9).

(E) Sequence differences between the original clinical isolate WA1 and the recombinant P1 IC WT. The three silent nucleotide changes were engineered as molecular markers.

(F) Chromatograms of Sanger sequencing results. The engineered molecular maker mutations are indicated.

those of the icSARS-CoV-WT (compare Figure 3B with 2B). Indistinguishable replication kinetics were observed for the icSARS-CoV-2-mNG and icSARS-CoV-WT (Figure 3C). Infection with icSARS-CoV-2-mNG developed increasing numbers of mNG-positive cells over time (Figure 3D). Concurrently, the fluorescent signals increased from 12 to 48 h after infection (Figure 3E). At 12–36 h after infection, the level of fluorescent signal correlated with the initial multiplicities of infection (MOIs), whereas a reverse trend was observed at 48 h after infection, most likely due to earlier CPEs caused by the higher MOI. Full-genome sequencing showed that icSARS-CoV-2-mNG retained the three engineered markers with no additional mutations (Figure 3F). These results indicate that icSARS-CoV-2-mNG is initially stable, maintains the WT replication, and expresses robust mNG in Vero E6 cells.

Stability of icSARS-CoV-2-mNG

To examine the longer-term stability of icSARS-CoV-2-mNG, we serially passaged the reporter virus on Vero cells for 5 rounds (1–2 days per round). Cells infected with equal PFU of passage 1 (P1) or passage 5 (P5) viruses produced comparable numbers of mNG-positive cells (Figure 4A). Next, RT-PCR was performed to verify the retention of mNG in the P1 and P5 viral genomes by using two primers targeting the insertion junctions (corresponding to nucleotides 25,068–28,099 of the viral genome). As expected, the RT-PCR products derived from both P1 and P5 mNG viruses were larger than those from the WT icSARS-CoV-2 (Figure 4B, lanes 1–3). Digestion of the RT-PCR products with BsrGI (located upstream of the mNG insertion site) and StuI (in the mNG gene) developed distinct cleavage patterns between the reporter and WT viruses, whereas P1 and P5 viruses produced an identical digestion pattern (Figure 4B, lanes 4–6). Finally, sequencing the P1 and P5 RT-PCR products confirmed the retention of the mNG gene (data not shown). Altogether, the results demonstrate the stability of icSARS-CoV-2-mNG after five rounds of passaging on Vero E6 cells. Given that Vero E6 cells are defective in type 1 IFN production, it remains to be tested whether the reporter virus is stable when passaged on interferon-competent cell lines.

Application of icSARS-CoV-2-mNG

To explore the utility of icSARS-CoV-2-mNG, we used the reporter virus to rapidly screen the antiviral activity of a known inhibitor of coronaviruses. We previously showed that pre-treatment of Vero cells with type 1 IFN inhibits SARS-CoV-2 replication (Lokugamage et al., 2020). Here, we explored the dose-responsive effect of IFN-α pre-treatment on icSARS-CoV-mNG replication (Figure 4C). No mNG expression was visually observed when the infected cells were pre-treated with the highest dose of IFN-α (1,000 u/mL), whereas a dose-dependent

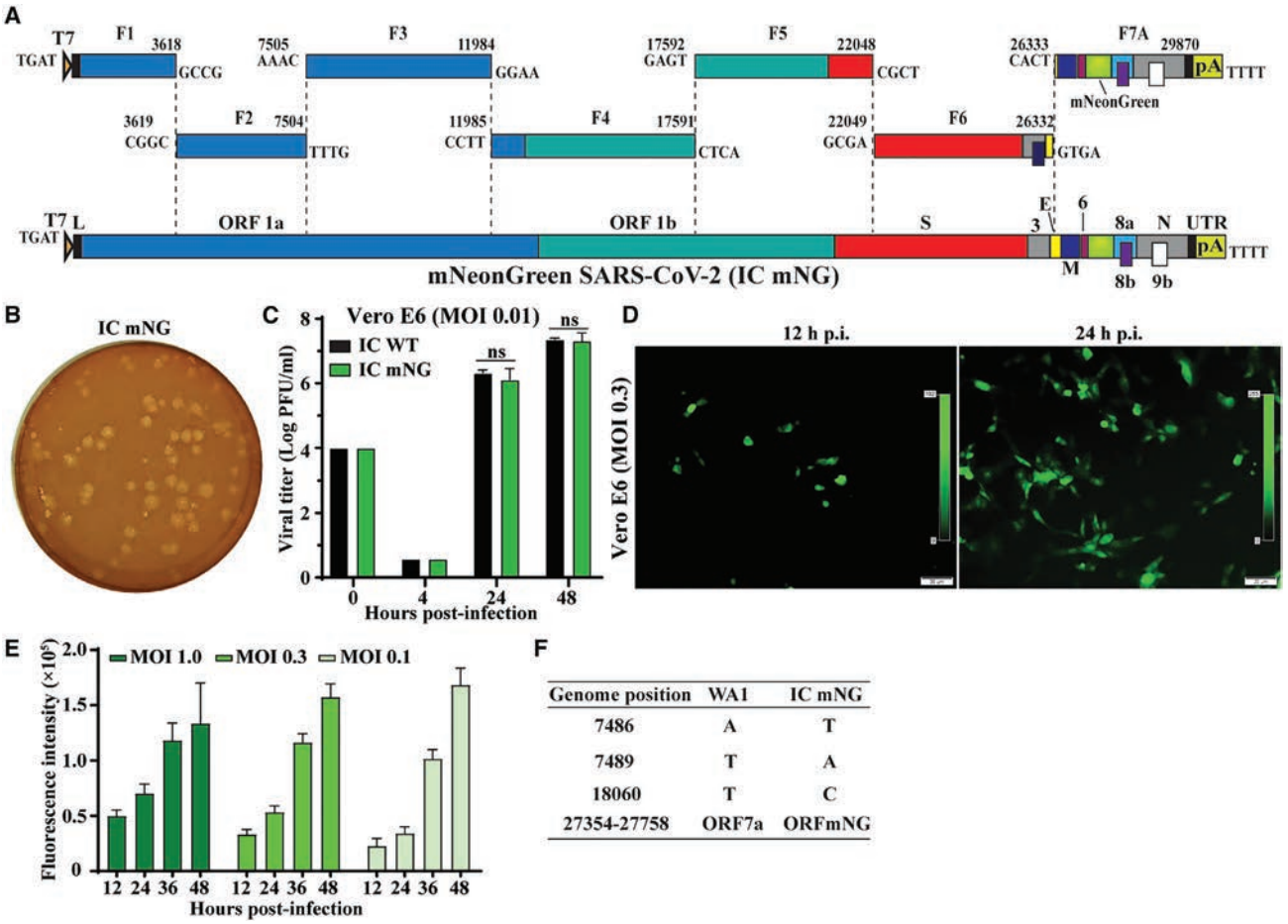

Figure 3. Generation of a mNeonGreen SARS-CoV-2

(A) Assembly of the FL mNG SARS-CoV-2 cDNA. The mNG gene was placed downstream of the regulatory sequence of ORF7 to replace the ORF7 sequence (Sims et al., 2005) in the subclone F7.

(B) Plaque morphology of the P1 IC mNG virus. Plaques were developed in Vero E6 cells on day 2 after infection.

(C) Replication kinetics. Vero E6 cells were infected with the IC WT or reporter icSARS-CoV-2-mNG (IC mNG) at MOI of 0.01. Viruses in culture medium were quantified by plaque assay.

(D) Fluorescence microscopy analysis of P1-mNG-virus-infected cells. Vero E6 cells were infected with P1 mNG viruses at MOI of 0.3. Representative mNG-positive (green) images are shown.

(E) Kinetics of fluorescence intensity. Vero E6 cells were infected with MOIs of 1.0, 0.3, or 0.1. After background signal subtraction, the fluorescence intensities from 12 to 48 h after infection are shown. Results from triplicate experiments were presented with bars representing standard deviations.

(F) Summary of full-genome sequence of mNG virus (P1 IC mNG). Nucleotides different from the original clinical isolate (WA1) are indicated.

reduction of mNG signal was detected at an intermediate dose (111 u/mL) (Figure 4D). Quantification of the fluorescent readouts estimated a concentration inhibiting 50% of viral replication (EC_{50}) of 101 u/mL, confirming the inhibition of SARS-CoV-2 by IFN-α (Figure 4E). This result is consistent with previous findings that SARS-CoV-2 is sensitive to type 1 IFN inhibition. The reporter virus assay required fewer days and less labor than with the conventional plaque-reduction assay. Collectively, the results indicate that icSARS-CoV-2-mNG could be reliably used to study SARS-CoV-2 replication and to screen antiviral inhibitors.

DISCUSSION

We report the development of a full-length infectious clone and a reporter virus for SARS-CoV-2. One of the key utilities for the reverse genetic system is to facilitate antiviral testing and therapeutic development. The icSARS-CoV-2-mNG reporter virus allows the use of fluorescence as a surrogate readout for viral replication. Compared with a standard plaque assay or median tissue culture infectious dose ($TCID_{50}$) quantification, the fluorescent readout shortens the assay turnaround time by several days. In addition, the fluorescent readout offers a quantitative measure that is less labor-intensive than the traditional means of viral titer reduction. Furthermore, the mNG-virus-based assay could be automated in a high-throughput format to screen compounds against viral replication. As a proof-of-concept, we demonstrated that, after treatments with type 1 IFN, the reporter virus reliably revealed efficacy in a rapid and efficient manner. In addition, the stability of the mNG reporter virus allows it to be used for longer-term studies and *in vivo* without fear of losing

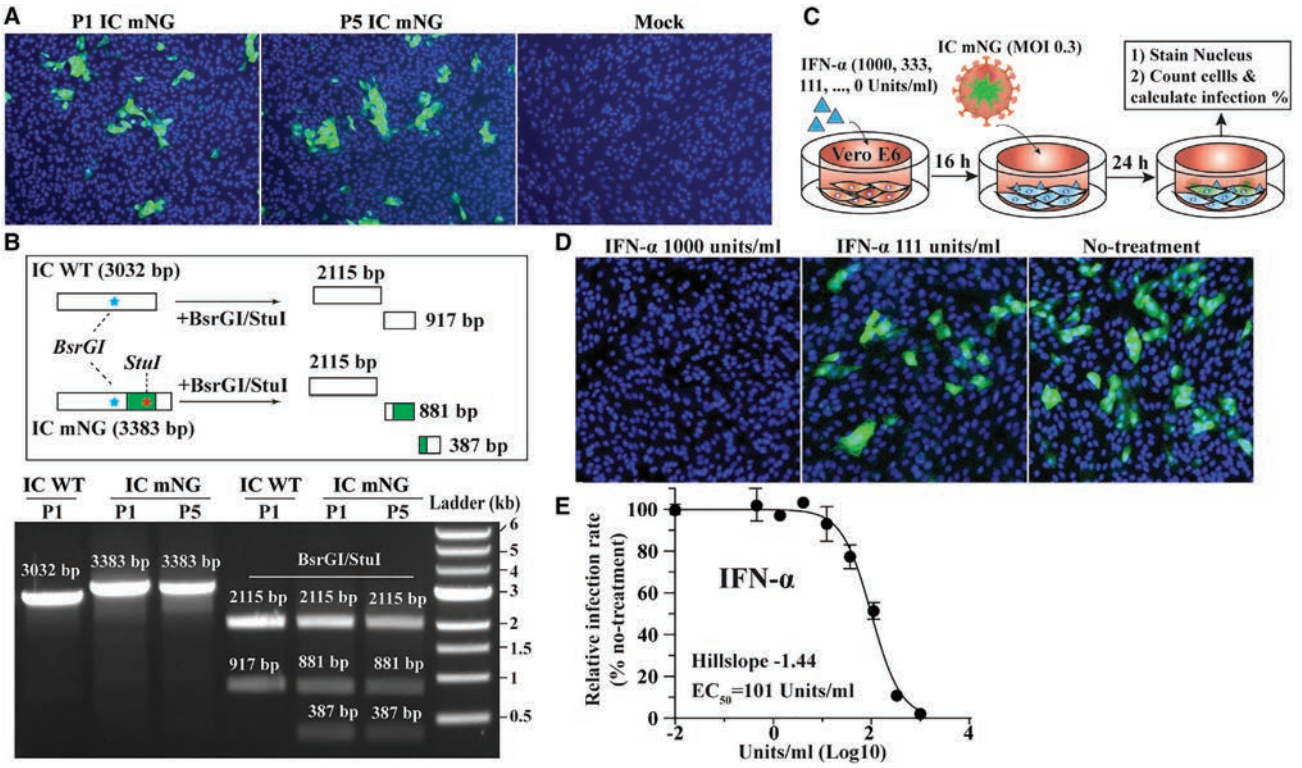

Figure 4. Stability and Application of mNeonGreen Virus

The stability of mNG virus was analyzed by comparing the fluorescent signals between the cells infected with P1 and P5 reporter viruses. The presence of mNG gene in the P1 and P5 reporter viruses was also verified using RT-PCR. The application of mNG virus was examined by testing the antiviral activity of IFN-α treatment.

(A) Fluorescence microscopy analysis of the P1- and P5-mNG-virus-infected cells. Vero E6 cells were infected with P1 or P5 virus at an MOI of 0.3. The cells were monitored for mNG-positive signals at 24 h after infection. Color representations are as follows: green, mNG; blue, nucleus.

(B) Gel analysis of mNG virus stability. The top graphic depicts the theoretical results of RT-PCR followed by restriction enzyme digestion. The bottom graphic shows the gel analysis of the RT-PCR products before (lanes 1–3) and after BsrGI/StuI digestion (lanes 4–6). About 100 ng DNA samples were analyzed on a 0.6% agarose gel. The DNA sizes are indicated.

(C) Schematic diagram of IFN-α treatment.

(D) Representative fluorescence images of reporter-virus-infected cells after IFN-α treatment. The doses of IFN-α treatment are indicated.

(E) Dose response curve of mNG signal inhibited by IFN-α. The Hillslope and EC_{50} values are indicated. Results from triplicate experiments were presented with bars representing standard deviations.

its fluorescent marker. Thus, this reporter virus offers a huge advantage for the research community and pharmaceutical companies to develop therapeutics for COVID-19.

Our reverse genetic system represents a major reagent in the pursuit of understanding SARS-CoV-2 and COVID-19. Compared with the clinical isolate, the recombinant WT SARS-CoV-2 has no deficit in terms of viral RNA species produced, plaque morphology, or replication kinetics. Therefore, it might be used as an equivalent to the clinical strain, and mutant viruses can be generated to characterize mutational effect on viral infection. This approach has allowed researchers to identify key viral antagonists of innate immunity for SARS-CoV and MERS-CoV (Menachery et al., 2015; Totura and Baric, 2012). Several of these mutant viruses have subsequently been employed as live-attenuated vaccine candidates for SARS-CoV and MERS-CoV (de Wit et al., 2016; Schindewolf and Menachery, 2019). Using our system, this knowledge might now be applied to the current SARS-CoV-2. Characterizing these mutations might provide insight into SARS-CoV-2 pathogenesis.

Our reverse genetic system also allows exploration of research questions fundamental to understanding the SARS-CoV-2 pandemic. As additional genomic sequences become available, evolutionary mutations can be interrogated for their effect on viral transmission and disease outcome. For example, a 382-nucleotide deletion covering almost the entire ORF8 of SARS-CoV-2 was observed in eight hospitalized patients in Singapore; virus isolation of the deletion strains has not been reported in the study (Su et al., 2020). A four-amino-acid insertion (conferring a possible furin cleavage site) was reported in the spike (S) protein of SARS-CoV-2 but is absent in the S protein of SARS-CoV and other group-2B CoVs (Coutard et al., 2020). Using the infectious clone, we can now evaluate the effect of these genetic changes by removing the reported sequences from SARS-CoV-2 and examining their effect on virus replication and S protein processing. In addition, mouse models for SARS-CoV-2 have been limited by the absence of viruses capable of binding to mouse angiotensin-converting enzyme 2 (ACE2) (Zhu et al., 2020). Point mutations in the receptor binding domain

of the SARS-CoV-2 S protein might facilitate mouse adaptation and development of a model that recapitulates human diseases in a standard mouse strain. Altogether, the above questions are a few examples of how our infectious clone can be used to advance SARS-CoV-2 research.

In summary, we have developed a robust reverse genetic system for SARS-CoV-2 that can be used to study viral replication and pathogenesis. We have also established an mNG reporter SARS-CoV-2 that is a reliable surrogate for high-throughput drug discovery. The reverse genetic system represents a major tool for the research community and significantly advances opportunities for countermeasure development for COVID-19.

STAR★METHODS

Detailed methods are provided in the online version of this paper and include the following:

- KEY RESOURCES TABLE
- LEAD CONTACT AND MATERIALS AVAILABILITY
- EXPERIMENTAL MODEL AND SUBJECT DETAILS
  - Virus and Cell Lines
- METHOD DETAILS
  - Cloning the SARS-CoV-2 cDNAs
  - Assembly of a Full-Length SARS-CoV-2 cDNA
  - RNA Transcription, Electroporation, Virus Production and Quantification
  - Interferon Treatment
  - RNA Extraction, RT-PCR and Sanger Sequencing
  - Northern Blot
- QUANTIFICATION AND STATISTICAL ANALYSIS
- DATA AND CODE AVAILABILITY

ACKNOWLEDGMENTS

We thank Natalie Thornburg and other colleagues from the Centers for Disease Control and Prevention for providing the clinical virus isolate. We also thank colleagues at University of Texas Medical Branch (UTMB) for support and discussions. Research was supported by grants from NIA and NIAID of the NIH (U19AI100625 and R00AG049092 to V.D.M.; R24AI120942 (WRCEVA) to S.C.W.; AI114657 and AI146081 to S.M.; and 5UC7AI094660 to J.W.L.). Research was also supported by a STARs Award provided by the University of Texas System to V.D.M., trainee funding provided by the McLaughlin Fellowship Fund at UTMB, and an IHII Pilot grant to S.M. P.-Y.S. was supported by NIH grants AI142759, AI145617, AI127744, AI136126, AI134907 and UL1TR001439 and by awards from the Kleberg Foundation, the John S. Dunn Foundation, the Amon G. Carter Foundation, the Gilson Longenbaugh Foundation, and the Summerfield Robert Foundation. A.M. is supported by a Clinical and Translational Science Award NRSA (TL1) Training Core (TL1TR001440) from the NIH.

AUTHOR CONTRIBUTIONS

Conceptualization, X.X., V.D.M., and P.-Y.S.; Methodology, X.X., A.M., K.G.L., K.N., X.Z., J.Z., J.L., C.S., N.B., P.A., K.S.P., S.W, S.M., J.W.L., V.D.M, and P.-Y.S.; Investigation, X.X., A.M., K.G.L., K.N., X.Z., J.Z., J.L., C.S., N.B., and P.A.; Resources, K.S.P., S.W., and C.-T.K.T.; Data Curation, X.X., A.M., K.G.L., K.N., J.L., and N.B.; Writing-Original Draft, X.X., K.N., V.D.M., and P.-Y.S.; Writing-Review & Editing, X.X., V.D.M., and P.-Y.S.; Visualization, X.X., A.M., K.G.L., N.B., and P.-Y.S.; Supervision, X.X., V.D.M., and P.-Y.S.; Funding Acquisition, P.A., S.W., S.J., J.W.L., V.D.M., and P.-Y.S.

DECLARATION OF INTERESTS

X.X., V.D.M, and P.-Y.S. have filed a provisional patent on the reverse genetic system of SARS-CoV-2. Other authors have no conflicts of interest to declare.

Received: March 22, 2020
Revised: March 30, 2020
Accepted: April 1, 2020
Published: April 13, 2020

REFERENCES

Almazán, F., Sola, I., Zuñiga, S., Marquez-Jurado, S., Morales, L., Becares, M., and Enjuanes, L. (2014). Coronavirus reverse genetic systems: infectious clones and replicons. Virus Res. *189*, 262–270.

Assiri, A., Al-Tawfiq, J.A., Al-Rabeeah, A.A., Al-Rabiah, F.A., Al-Hajjar, S., Al-Barrak, A., Flemban, H., Al-Nassir, W.N., Balkhy, H.H., Al-Hakeem, R.F., et al. (2013). Epidemiological, demographic, and clinical characteristics of 47 cases of Middle East respiratory syndrome coronavirus disease from Saudi Arabia: a descriptive study. Lancet Infect. Dis. *13*, 752–761.

Coutard, B., Valle, C., de Lamballerie, X., Canard, B., Seidah, N.G., and Decroly, E. (2020). The spike glycoprotein of the new coronavirus 2019-nCoV contains a furin-like cleavage site absent in CoV of the same clade. Antiviral Res. *176*, 104742.

Curtis, K.M., Yount, B., and Baric, R.S. (2002). Heterologous gene expression from transmissible gastroenteritis virus replicon particles. J. Virol. *76*, 1422–1434.

de Wit, E., van Doremalen, N., Falzarano, D., and Munster, V.J. (2016). SARS and MERS: recent insights into emerging coronaviruses. Nat. Rev. Microbiol. *14*, 523–534.

Harcourt, J., Tamin, A., Lu, X., Kamili, S., Sakthivel, S.K., Murray, J., Queen, K., Tao, Y., Paden, C.R., Zhang, J., et al. (2020). Severe Acute Respiratory Syndrome Coronavirus 2 from Patient with 2019 Novel Coronavirus Disease, United States. Emerg. Infect. Dis. https://doi.org/10.3201/eid2606.200516.

Holshue, M.L., DeBolt, C., Lindquist, S., Lofy, K.H., Wiesman, J., Bruce, H., Spitters, C., Ericson, K., Wilkerson, S., Tural, A., et al.; Washington State 2019-nCoV Case Investigation Team (2020). First Case of 2019 Novel Coronavirus in the United States. N. Engl. J. Med. *382*, 929–936.

Huang, C., Wang, Y., Li, X., Ren, L., Zhao, J., Hu, Y., Zhang, L., Fan, G., Xu, J., Gu, X., et al. (2020). Clinical features of patients infected with 2019 novel coronavirus in Wuhan, China. Lancet *395*, 497–506.

Lokugamage, K.G., Hage, A., Schindewolf, C., Rajsbaum, R., and Menachery, V.D. (2020). SARS-CoV-2 sensitive to type I interferon pretreatment. bioRxiv. https://doi.org/10.1101/2020.03.07.982264.

Menachery, V.D., Yount, B.L., Jr., Debbink, K., Agnihothram, S., Gralinski, L.E., Plante, J.A., Graham, R.L., Scobey, T., Ge, X.Y., Donaldson, E.F., et al. (2015). A SARS-like cluster of circulating bat coronaviruses shows potential for human emergence. Nat. Med. *21*, 1508–1513.

Menachery, V.D., Yount, B.L., Jr., Sims, A.C., Debbink, K., Agnihothram, S.S., Gralinski, L.E., Graham, R.L., Scobey, T., Plante, J.A., Royal, S.R., et al. (2016). SARS-like WIV1-CoV poised for human emergence. Proc. Natl. Acad. Sci. USA *113*, 3048–3053.

Narayanan, K., Huang, C., Lokugamage, K., Kamitani, W., Ikegami, T., Tseng, C.T., and Makino, S. (2008). Severe acute respiratory syndrome coronavirus nsp1 suppresses host gene expression, including that of type I interferon, in infected cells. J. Virol. *82*, 4471–4479.

Schindewolf, C., and Menachery, V.D. (2019). Middle East Respiratory Syndrome Vaccine Candidates: Cautious Optimism. Viruses *11*, E74.

Scobey, T., Yount, B.L., Sims, A.C., Donaldson, E.F., Agnihothram, S.S., Menachery, V.D., Graham, R.L., Swanstrom, J., Bove, P.F., Kim, J.D., et al. (2013). Reverse genetics with a full-length infectious cDNA of the Middle East respiratory syndrome coronavirus. Proc. Natl. Acad. Sci. USA *110*, 16157–16162.

Shan, C., Xie, X., Muruato, A.E., Rossi, S.L., Roundy, C.M., Azar, S.R., Yang, Y., Tesh, R.B., Bourne, N., Barrett, A.D., et al. (2016). An Infectious cDNA

Clone of Zika Virus to Study Viral Virulence, Mosquito Transmission, and Antiviral Inhibitors. Cell Host Microbe *19*, 891–900.

Shaner, N.C., Lambert, G.G., Chammas, A., Ni, Y., Cranfill, P.J., Baird, M.A., Sell, B.R., Allen, J.R., Day, R.N., Israelsson, M., et al. (2013). A bright monomeric green fluorescent protein derived from Branchiostoma lanceolatum. Nat. Methods *10*, 407–409.

Sims, A.C., Baric, R.S., Yount, B., Burkett, S.E., Collins, P.L., and Pickles, R.J. (2005). Severe acute respiratory syndrome coronavirus infection of human ciliated airway epithelia: role of ciliated cells in viral spread in the conducting airways of the lungs. J. Virol. *79*, 15511–15524.

Su, Y.C.F., Anderson, D.E., Young, B.E., Zhu, F., Linster, M., Kalimuddin, S., Low, J.G.H., Yan, Z., Jayakumar, J., Sun, L., et al. (2020). Discovery of a 382-nt deletion during the early evolution of SARS-CoV-2. bioRxiv. https://doi.org/10.1101/2020.03.11.987222.

Thao, T.T.N., Labroussaa, F., Ebert, N., V'kovski, P., Stalder, H., Portmann, J., Kelly, J., Steiner, S., Holwerda, M., Kratzel, A., et al. (2020). Rapid reconstruction of SARS-CoV-2 using a synthetic genomics platform. bioRxiv. https://doi.org/10.1101/2020.02.21.959817.

Totura, A.L., and Baric, R.S. (2012). SARS coronavirus pathogenesis: host innate immune responses and viral antagonism of interferon. Curr. Opin. Virol. *2*, 264–275.

Wu, Z., and McGoogan, J.M. (2020). Characteristics of and Important Lessons From the Coronavirus Disease 2019 (COVID-19) Outbreak in China: Summary of a Report of 72314 Cases From the Chinese Center for Disease Control and Prevention. JAMA. https://doi.org/10.1001/jama.2020.2648.

Yount, B., Denison, M.R., Weiss, S.R., and Baric, R.S. (2002). Systematic assembly of a full-length infectious cDNA of mouse hepatitis virus strain A59. J. Virol. *76*, 11065–11078.

Yount, B., Curtis, K.M., Fritz, E.A., Hensley, L.E., Jahrling, P.B., Prentice, E., Denison, M.R., Geisbert, T.W., and Baric, R.S. (2003). Reverse genetics with a full-length infectious cDNA of severe acute respiratory syndrome coronavirus. Proc. Natl. Acad. Sci. USA *100*, 12995–13000.

Zhou, P., Yang, X.L., Wang, X.G., Hu, B., Zhang, L., Zhang, W., Si, H.R., Zhu, Y., Li, B., Huang, C.L., et al. (2020). A pneumonia outbreak associated with a new coronavirus of probable bat origin. Nature *579*, 270–273.

Zhu, N., Zhang, D., Wang, W., Li, X., Yang, B., Song, J., Zhao, X., Huang, B., Shi, W., Lu, R., et al.; China Novel Coronavirus Investigating and Research Team (2020). A Novel Coronavirus from Patients with Pneumonia in China, 2019. N. Engl. J. Med. *382*, 727–733.

STAR★METHODS

KEY RESOURCES TABLE

REAGENT or RESOURCE	SOURCE	IDENTIFIER
Bacterial and Virus Strains		
E. coli strain Top10	ThermoFisher Scientific	Cat#C404006
TransforMax™ EPI300™ Chemically Competent *E. coli*	Lucigen Corporation, Middleton, WI 53562	Cat#C300C105
SARS-CoV strain 2019-nCoV/USA_WA1/2020 (WA1)	World Reference Center of Emerging Viruses and Arboviruses (WRCEVA) at the University of Texas Medical Branch	N/A
Chemicals, Peptides, and Recombinant Proteins		
IFN-α A Protein, Recombinant human	Millipore Sigma	Cat#IF007
Critical Commercial Assays		
T7 mMessage mMachine kit	Thermo Fisher Scientific	Cat#AM1344
Ingenio® Electroporation solution	Mirus Bio LLC	Cat#MIR 50117
SuperScript™ IV First-Strand Synthesis System	Thermo Fisher Scientific	Cat#18091300
Platinum™ SuperFi II DNA Polymerase	Thermo Fisher Scientific	Cat#12361010
Experimental Models: Cell Lines		
Vero E6 cells	ATCC	Cat# CRL-1586; RRID: CVCL_0574
Oligonucleotides		
primer Cov-T7-N-F (TACTGTAATACGA CTCAC TATAGGATGTCTGATAATGGACCCCAAAATC)	Integrated DNA Technologies (Skokie, Illinois)	N/A
primer polyT-N-R (TTTTTTTTTTTTTTT TTT TTTT TTTTTTTTTTTTTTAGGCCT GAGTTGAGTCAGCAC)	Integrated DNA Technologies (Skokie, Illinois)	N/A
Recombinant DNA		
pUC57-CoV2-F1	This paper	N/A
pCC1-CoV2-F2	This paper	N/A
pCC1-CoV2-F3	This paper	N/A
pUC57-CoV2-F4	This paper	N/A
pUC57-CoV2-F5	This paper	N/A
pUC57-CoV2-F6	This paper	N/A
pCC1-CoV2-F7	This paper	N/A
pCC1-CoV2-F7-mNG	This paper	N/A
Synthesized mNeonGreen gene (sequence-optimized)	This paper and Shaner et al., 2013	N/A
Software and Algorithms		
ImageJ	NIH	N/A
Prism 8.0 software	GraphPad	N/A
Illustrator CC	Adobe	N/A

LEAD CONTACT AND MATERIALS AVAILABILITY

Further information and requests for resources and reagents should be directed to and will be fulfilled by the Lead Contact, Pei-Yong Shi (peshi@utmb.edu). Plasmids and virus generated in this study will be made available on request, but we might require a payment and/or a completed Materials Transfer Agreement if there is potential for commercial application.

EXPERIMENTAL MODEL AND SUBJECT DETAILS

Virus and Cell Lines

The stock of SARS-CoV-2 strain 2019-nCoV/USA_WA1/2020 was derived from the first patient diagnosed in the US. The virus isolate was originally provided by Dr. Natalie Thornburg from the Centers for Disease Control and Prevention in Atlanta, GA as described

previously (Holshue et al., 2020), and amplified on Vero E6 cells at the World Reference Center for Emerging Viruses and Arboviruses (WRCEVA) at the University of Texas Medical Branch at Galveston (UTMB). The P5 passage was used in this study.

African green monkey kidney epithelial cells (Vero E6; CRL-1586) were purchased from the American Type Culture Collection (ATCC, Bethesda, MD) and maintained in a high-glucose Dulbecco's modified Eagle's medium (DMEM) supplemented with 10% fetal bovine serum (FBS; HyClone Laboratories, South Logan, UT) and 1% penicillin/streptomycin (P/S). Cells were grown at 37°C with 5% CO_2. All culture media and antibiotics were purchased from ThermoFisher Scientific (Waltham, MA). All cell lines were tested negative for mycoplasma.

METHOD DETAILS

Cloning the SARS-CoV-2 cDNAs

Two approaches were taken to rapidly obtain stable cDNAs of SARS-CoV-2. First, the cDNAs of fragments F1, F4, F5, and F6 were successfully synthesized from the GenScript company (Piscataway, NJ) and cloned into a high-copy plasmid pUC57. The F1 contains a T7 promoter sequence at the upstream of the 5′ end of the SARS-CoV-2 sequence. Other cDNA fragments were also synthesized but found unstable after cloning into plasmid pUC57. For overcoming this hurdle, the cDNAs of fragments F2, F3, and F7 were obtained by reverse transcription and PCR (RT-PCR). RT was performed by using the SuperScript IV First-Strand Synthesis System (ThermoFisher Scientific) with random hexamer primers and extracellular viral RNA (extracted from the supernatants of SARS-CoV-2-infected Vero E6 cells). The cDNA was used as a template to amplify the fragments F2, F3, and F7 by high fidelity PCR with the Platinum SuperFi II DNA Polymerase (ThermoFisher Scientific) according to the manufacturer's instructions. A poly$(T)_{29}$ sequence was introduced by PCR to the 3′ end of the untranslated region of viral genome. The amplicons were cloned into a single-copy vector pCC1BAC (Epicenter) to increase the stability of the cDNA plasmids when propagated in *E. coli*. To ensure a seamless assembly of the full-length cDNA, we introduced two cleavage sites of class IIS restriction enzymes (BsaI and Esp3I) at both ends of each sibling cDNA during PCR or gene synthesis. To differentiate the infectious clone-derived virus from the parental clinical isolate 2019-nCoV/USA_WA1/2020, we engineered three silent mutations at nucleotide positions 7,486 (A-to-T change), 7,489 (T-to-A change), and 18,058 (T-to-C change). For constructing the pCC1-F7-mNG, the gene of mNeonGreen (sequence-optimized) was synthesized and inserted at the downstream of the regulatory sequence of ORF7a to replace the entire ORF7a, according to the study as described previously (Sims et al., 2005). All subclones were finally validated by Sanger sequencing.

Assembly of a Full-Length SARS-CoV-2 cDNA

To assemble the full-length cDNA, we digested individual cDNA plasmids and purified each cDNA fragment. Specifically, F1, F2, F3 and F4 cDNA fragments were obtained by digesting the corresponding plasmids with enzyme BsaI. F5 and F6 fragments were obtained by digesting the plasmids with enzymes Esp3I and PvuI. F7 and F7-mNG cDNA fragments were obtained by digesting the corresponding plasmids by Esp3I and SnaBI. PvuI and SnaBI were included in the digestion to eliminate undesired DNA bands that co-migrated with the targeted fragments on agarose gels. All fragments after restriction enzyme digestion were separated on 0.6% agarose gels, visualized under a darkreader lightbox (Clare Chemical Research, Dolores, CO), excised, and purified using the QIAquick Gel Extraction Kit (QIAGEN, Germantown, MD). To assemble the full-length cDNA, we ligated the seven cDNA fragments in a three-step manner. First, equimolar amounts of F1 (0.61 μg), F2 (0.65 μg), F3 (0.75 μg), and F4 (0.94 μg) were ligated in a PCR tube using T4 DNA ligase in a 40 μl-reaction at 4°C for 18 h, resulting in F1-4 DNA. Second, equimolar amounts of fragments F5 (0.75 μg), F6 (0.72 μg), and F7 (0.60 μg) were ligated in a separate PCR tube to produce F5-7 DNA using the same ligation conditions. Third, without any DNA purification, the two reactions (containing F1-4 and F5-7) were combined (total 80 μl) and topped with additional T4 ligase (2 μl), buffer (2 μl) and nuclease-free water (16 μl) to a 100 μL reaction. The final reaction was incubated at 4°C for 18 h to produce the full-length F1-7 DNA. Afterward, the full-length cDNA was phenol/chloroform extracted, isopropanol precipitated, and resuspended in 10 μL nuclease-free water.

RNA Transcription, Electroporation, Virus Production and Quantification

RNA transcript was *in vitro* synthesized by the mMESSAGE mMACHINE T7 Transcription Kit (ThermoFisher Scientific) according to the manufacturer's instruction with some modifications. A 50 μL reaction was set up by adding 1 μg DNA template and 7.5 μL GTP (cap analog-to-GTP ratio of 1:1). The reaction was incubated at 32°C for 5 h. After removing the template DNA by nuclease per manufacturer's protocol, the RNA was phenol/chloroform extracted and isopropanol precipitated. A SARS-CoV-2 N gene transcript was *in vitro* transcribed from a DNA template using the mMESSAGE mMACHINE T7 Transcription Kit with a 2:1 ratio of cap analog to GTP. The N gene DNA template was prepared by PCR using primer Cov-T7-N-F (tactgTAATACGACTCACTATAGGatgtctgataatggaccc-caaaatc; the uppercase sequence represents T7 promoter; the underlined sequence represents the 5′ end of N gene) and primer polyT-N-R [$(t)_{37}$aggcctgagttgagtcagcac].

RNA transcripts were electroporated into Vero E6 cells using a protocol as previously described (Shan et al., 2016) with some modifications. Twenty micrograms of total RNA transcripts (containing both full-length RNA and short RNAs) and 20 μg N gene transcript were mixed and added to a 4-mm cuvette containing 0.8 mL of Vero E6 cells (8×10^6) in Ingenio® Electroporation Solution (Mirus). Single electrical pulse was given with a GenePulser apparatus (Bio-Rad) with setting of 270V at 950 μF. After 5 min recovery at room temperature, the electroporated cells were seeded into a T-75 flask and incubated at 37°C with 5% CO_2. On the next day, the culture fluid was replaced with 2% FBS DMEM medium. The cells were monitored daily for virus-mediated cytopathic effect (CPE). One

milliliter of the P0 virus was inoculated to a T-175 flask containing 80% confluence Vero E6 cells. The infected cells were incubated at 37°C with 5% CO_2 for 2-3 days. Culture supernatants (P1) were harvested when CPE occurred. The amount of infectious virus was determined by a standard plaque assay on Vero E6 cells. All virus cultures were performed in a biosafety level 3 (BSL-3) laboratory with redundant fans in the biosafety cabinets. All personnel wore powered air purifying respirators (Breathe Easy, 3M) with Tyvek suits, aprons, booties, and double gloves.

Interferon Treatment

Vero E6 cells were plated as 1.5×10^4 cells/well in a black 96-well plate (Greiner). For interferon treatment, at 6 h post-seeding, cells were treated with various doses of IFN-α (Millipore Sigma). After 14 h of treatment, the culture fluids were replaced with 2% FBS medium, and P1 IC mNG viruses were added to the cells at MOI 0.3 with additional IFN-α at corresponding concentrations. At 24 h post-infection, Hoechst 33342 (ThermoFisher Scientific) was added to a final concentration of 0.1% to counterstain the nucleus. The green fluorescence signals were detected by Cytation 5 (BioTek) and the infection rate was calculated according to the manufacturer's instructions.

RNA Extraction, RT-PCR and Sanger Sequencing

250 μL of culture fluids were mixed with three volumes of TRIzol LS Reagent (Thermo Fisher Scientific). Viral RNAs were extracted per manufacturer's instructions. The final RNAs were dissolved in 30 μL nuclease-free water. 11 μL of RNA sample was used for reverse transcription by using the SuperScript IV First-Strand Synthesis System (ThermoFisher Scientific) with random hexamer primers. Nine DNA fragments covering the entire viral genome were amplified by PCR with specific primers. The resulting DNAs were cleaned up by the QIAquick PCR Purification Kit and Sanger sequencing was performed by GENEWIZ (South Plainfield, NJ).

Northern Blot

Vero E6 cells were infected with clinical isolate WA1 or the infectious clone-derived SARS-CoV-2 (IC WT) at MOI 0.01. At 48 h post-infection, total intracellular RNAs were isolated using TRIzol reagent (Invitrogen). Northern blot analysis was performed using total intracellular RNAs as described previously (Narayanan et al., 2008). A digoxigenin (DIG)-labeled random-primed probe, corresponding to nucleotides 28,999 to 29,573 of the SARS-CoV-2 genome, was used to detect SARS-CoV-2 mRNAs and visualized by DIG luminescent detection kit (Roche, Indianapolis, IN) according to the manufacturer's protocol.

QUANTIFICATION AND STATISTICAL ANALYSIS

All numerical data are presented as the mean ± SD (standard deviations). Group comparisons of viral growth kinetics in Figures 2 and 3 were performed using multiple t test with Bonferroni-Dunn correction in software Prism 8.0 (GraphPad). *$p < 0.05$, significant; **$p < 0.01$, significant; $p > 0.05$, ns (not significant). The 50% effective concentration (EC_{50}) in Figure 4 was estimated by using a four-parameter logistic regression model from the GraphPad Prism 8 software (GraphPad Software Inc., San Diego CA). Minimal adjustment was made in the software ImageJ to enhance the contrast for bright-field images in Figures 1, 2, and 3. Blue- and green-fluorescence images were merged in ImageJ. Figures were finally assembled using the software Adobe illustrator CC.

DATA AND CODE AVAILABILITY

All data are present in this study.

frontiers in Microbiology

REVIEW
published: 02 August 2019
doi: 10.3389/fmicb.2019.01781

Recent Advances in the Vaccine Development Against Middle East Respiratory Syndrome-Coronavirus

*Chean Yeah Yong[1,2], Hui Kian Ong[3], Swee Keong Yeap[4], Kok Lian Ho[3] and Wen Siang Tan[1,2]**

[1] Department of Microbiology, Faculty of Biotechnology and Biomolecular Sciences, Universiti Putra Malaysia, Serdang, Malaysia, [2] Laboratory of Vaccines and Immunotherapeutics, Institute of Bioscience, Universiti Putra Malaysia, Serdang, Malaysia, [3] Department of Pathology, Faculty of Medicine and Health Sciences, Universiti Putra Malaysia, Serdang, Malaysia, [4] China ASEAN College of Marine Sciences, Xiamen University Malaysia, Sepang, Malaysia

Middle East respiratory syndrome (MERS) is a deadly viral respiratory disease caused by MERS-coronavirus (MERS-CoV) infection. To date, there is no specific treatment proven effective against this viral disease. In addition, no vaccine has been licensed to prevent MERS-CoV infection thus far. Therefore, our current review focuses on the most recent studies in search of an effective MERS vaccine. Overall, vaccine candidates against MERS-CoV are mainly based upon the viral spike (S) protein, due to its vital role in the viral infectivity, although several studies focused on other viral proteins such as the nucleocapsid (N) protein, envelope (E) protein, and non-structural protein 16 (NSP16) have also been reported. In general, the potential vaccine candidates can be classified into six types: viral vector-based vaccine, DNA vaccine, subunit vaccine, nanoparticle-based vaccine, inactivated-whole virus vaccine and live-attenuated vaccine, which are discussed in detail. Besides, the immune responses and potential antibody dependent enhancement of MERS-CoV infection are extensively reviewed. In addition, animal models used to study MERS-CoV and evaluate the vaccine candidates are discussed intensively.

Keywords: Middle East respiratory syndrome, coronavirus, animal model, vaccine, antibody dependent enhancement

OPEN ACCESS

Edited by:
Lu Lu,
Fudan University, China

Reviewed by:
Jincun Zhao,
Guangzhou Medical University, China
Vincent Munster,
National Institutes of Health (NIH), United States
Jasper Fuk Woo Chan,
The University of Hong Kong, Hong Kong

***Correspondence:**
Wen Siang Tan
wstan@upm.edu.my

Specialty section:
This article was submitted to Virology, a section of the journal Frontiers in Microbiology

Received: *10 May 2019*
Accepted: *18 July 2019*
Published: *02 August 2019*

Citation:
Yong CY, Ong HK, Yeap SK, Ho KL and Tan WS (2019) Recent Advances in the Vaccine Development Against Middle East Respiratory Syndrome-Coronavirus. Front. Microbiol. 10:1781. doi: 10.3389/fmicb.2019.01781

INTRODUCTION

Camel flu, or more commonly known as the Middle East respiratory syndrome (MERS), is a respiratory disease caused by MERS-coronavirus (MERS-CoV). MERS-CoV was first identified in Saudi Arabia in 2012 (Zaki et al., 2012). As of February 2019, 27 countries worldwide have reported cases of MERS-CoV infection, with 2,374 reported viral infection and 823 associated deaths, which corresponds to ~35% fatality in identified cases (World Health Organization [WHO], 2019b), although the actual fatality rate of the viral infection is most likely below 35% due to some unidentified, mild, or asymptomatic cases. Majority of these cases occurred in Saudi Arabia, amounting to 1,983 of reported cases, with 745 associated deaths or ~37.5% fatality (World Health Organization [WHO], 2019a).

Majority of the identified MERS-CoV cases are nosocomially acquired via direct close contact with infected patients (Chowell et al., 2015; Cauchemez et al., 2016), whereas cases of zoonotic transmission from dromedary camels to humans were reported primarily in Saudi Arabia, where

human-camel interaction is frequent (Gossner et al., 2016). Hitherto, no specific treatments and vaccines are available for MERS-CoV infections. Although MERS-CoV is currently not listed as a potential pandemic threat, a recent outbreak in South Korea which demonstrated virus emergence in second and third generation contacts, has immediately raised concern that multiple mutations of MERS-CoV might cause enhanced human-to-human transmission (Wang et al., 2015b; Oh et al., 2018). Recently, MERS-CoV was added to the NIAID's pathogen priority list as Category C Priority Pathogens due to its potential applications in biological warfare (Du et al., 2016b). Preventive measures against MERS-CoV infection, particularly vaccine development, are crucial to avoid deadly and unexpected future pandemics.

Middle East respiratory syndrome-coronavirus, the causative agent of MERS, is a positive sense, single-stranded RNA *Betacoronavirus* which belongs to the family of *Coronaviridae*. Its viral genome is about 30 kb in length, flanked by a 5'-terminal cap and 3'-poly(A) tail (van Boheemen et al., 2012; Scobey et al., 2013). MERS-CoV genome contains at least 10 open reading frames (ORFs), which encodes for 4 structural proteins: spike (S) protein, envelope (E) protein, membrane (M) protein, nucleocapsid (N) protein, 16 non-structural proteins (NSP1-NSP16), and 5 accessory proteins (ORF3, ORF4a, ORF4b, ORF5, and ORF8b) (van Boheemen et al., 2012; Du et al., 2017). Of all these viral proteins, S and N proteins are of particular interest in the development of vaccines against MERS-CoV, although other proteins such as E protein and NSP16 are potential immunogens as live attenuated vaccines (Almazan et al., 2013; Menachery et al., 2017).

CRITERIA FOR AN EFFECTIVE MERS-CoV VACCINE

Two viral proteins of MERS-CoV, S and N proteins, were demonstrated to be highly immunogenic and capable of eliciting T-cell responses. However, only S protein was shown to induce neutralizing antibodies, the critical effectors against MERS-CoV (Agnihothram et al., 2014). Notably, N protein had also been proposed to be a potential protective immunogen for both neutralizing antibodies and T-cell immune responses through *in silico* approaches (Shi et al., 2015). Despite the prediction, no biological data have been presented thus far. Another potential B cell epitope of the MERS-CoV E protein was identified recently using *in silico* methods, yet similarly, no biological data were presented (Xie et al., 2018). Therefore, most of the MERS-CoV vaccine candidates are still based on the full length or part of the S protein.

Ideally, an effective MERS-CoV vaccine is required to induce both robust humoral and cell-mediated immunities, particularly antibody responses are crucial for the survival of the vaccinated hosts (Du et al., 2016b). Previous studies indicated that the level of serum neutralizing antibodies correlated positively with the reduction of lung pathogenesis, which increased the survival of animals challenged with MERS-CoV (Zhao et al., 2015; Zhang et al., 2016). In general, most of the potential MERS-CoV vaccine candidates were able to elicit systemic antibody responses, producing high titer of serum IgG upon immunization, but many failed to generate sufficient mucosal immunity unless the vaccines were administered via a mucosal or intranasal route. Activation of mucosal immunity is heavily dependent on the route of immunization, and this is a common challenge in vaccine development for many respiratory pathogens (Ma et al., 2014a; Guo et al., 2015). Pre-existing neutralizing mucosal antibodies are important as a first line of defenses against MERS-CoV infection (Guo et al., 2015). All neutralizing antibodies elicited by vaccines based on S protein could bind to the receptor binding domain (RBD) of the protein thereby inhibiting viral internalization and membrane fusion (Du et al., 2017). Little is known about the memory B-cell responses against MERS-CoV, apart from a recent study which demonstrated the persistence of anti-MERS-CoV antibodies in MERS survivors up to 34 months (Payne et al., 2016). On the other hand, antibody responses against another closely related coronavirus, SARS-CoV, were not persistent, whereby a 6-year follow-up study did not detect memory B-cell responses in SARS survivors (Tang et al., 2011). It is likely that some of the B-cells differentiate into MERS-CoV-specific memory B-cells following infection or vaccination, but the longevity and protective efficacy of these memory B-cells against MERS-CoV infection or re-challenge remain unresolved questions (Du et al., 2016b; Perlman and Vijay, 2016).

T-cell responses elicited by MERS-CoV vaccines also play important roles in protection against MERS. This is supported by the fact that viral clearance was impossible in T-cell deficient mice, but was possible in mice lacking B-cells (Zhao et al., 2014). Although T-cells are demonstrated to be a critical effector in acute viral clearance, protection for subsequent MERS-CoV infection is largely mediated by humoral immunity (Zhao et al., 2014). Several animal studies also demonstrated activation of T-cell responses following immunization with a MERS-CoV vaccine candidate, resulting in the elevated secretion of Th1 and Th2 cytokines (Lan et al., 2014; Ma et al., 2014a; Malczyk et al., 2015; Muthumani et al., 2015). It is also noteworthy to mention that adjuvants could be co-administered with MERS-CoV vaccines to tailor and possibly enhance the immune responses elicited by the vaccines. One study has indicated that co-administration of the MERS-CoV vaccine based on the S protein with Alum in mice resulted in a Th2 biased immunity, whereas a more robust Th1 and Th2 mixed immune response was produced when an additional adjuvant, cysteine-phosphate-guanine (CpG) oligodeoxynucleotides (ODN) was included in the formulation (Lan et al., 2014). To date, no detail investigation on MERS-CoV vaccine-induced memory T-cell responses is reported. However, MERS-CoV infection was shown to induce memory CD4+ and CD8+ T-cells responses in MERS survivors, at least up to 24 months (Zhao et al., 2017). There is little understanding about the biological function of memory CD4+ T-cells but they are likely to contribute to direct virus inhibition via cytokine production, particularly IFN-γ, and enhance the effector functions of CD8+ T-cells and B-cells (MacLeod et al., 2010). Although subsequent MERS-CoV infection is generally antibody mediated, memory CD8+ T cells are believed to facilitate virus clearance by eliminating

infected cells (Kaech and Ahmed, 2001; Zhao et al., 2017). MERS survivors who later demonstrated strong virus-specific memory CD8+ T-cell responses were also shown to experience mitigated morbidity during the hospitalization period (Zhao et al., 2017). Similarly, the importance of T-cell responses against SARS-CoV was also highlighted in many studies (Channappanavar et al., 2014; Chu H. et al., 2014; Zhao et al., 2016). Interestingly, unlike SARS-CoV, MERS-CoV can infect both the CD4+ and CD8+ T cells in human, resulting in the downregulation of hDPP4, and induced intrinsic and extrinsic caspase-dependent apoptosis in T cells, which may lead to severe immunopathology (Chu et al., 2016). In addition, Chu et al. (2016) demonstrated the capability of MERS-CoV in infecting the T cells of common marmosets.

It is critical for a potential MERS-CoV vaccine to induce robust humoral and cell-mediated immunities. Although the protection against MERS-CoV is mainly mediated by humoral immunity, T-cell responses are crucial for acute viral clearance. Mucosal route is recommended for MERS-CoV vaccine delivery to induce the mucosal immunity in addition to the systemic responses. Persistence of the virus-specific antibodies induced by MERS-CoV vaccine is not thoroughly studied but represents a major challenge. An effective MERS-CoV vaccine is also required to induce immunological memory to provide a long-lived protection which in turn reduces the need of boosters, and in the long run will bring down the cost of vaccinations. Lastly, different adjuvants may also be used to improve the immunogenicity of MERS-CoV vaccines but would require detail studies on the interactions between them to ensure optimal vaccine efficacy and safety. So far, three potential MERS-CoV vaccines: a DNA vaccine and two viral vector-based vaccines have advanced into clinical trials (National Institutes of Health [NIH], 2016, 2018b,c).

POTENTIAL ANTIBODY DEPENDENT ENHANCEMENT (ADE) OF MERS-CoV INFECTION

Antibody dependent enhancement (ADE) is a condition whereby non-neutralizing antibodies are produced following an infection or a vaccination, which enhance the infectivity of the subsequent infection (Kuzmina et al., 2018). ADE of viral infections have been reported for dengue virus, human immunodeficiency virus, influenza virus, other alpha and flaviviruses, SARS-CoV, and Ebola virus (Dutry et al., 2011; Kuzmina et al., 2018). Thus, ADE is a critical issue that should be considered seriously in designing a MERS-CoV vaccine.

Attributed to the taxonomic and structural similarities between SARS-CoV and MERS-CoV, the processes involved in development of new vaccines against these two viruses, to a large extent, are similar. Vaccine candidates against SARS-CoV were initially developed based on the full-length S protein. However, these vaccines were later demonstrated to induce non-neutralizing antibodies which did not prevent MERS-CoV infection, and the immunized animals were not protected from the viral challenge instead they experienced adverse effects like enhanced hepatitis, increased morbidity, and stronger inflammatory responses (Weingartl et al., 2004; Czub et al., 2005). Many potential vaccines against MERS-CoV were also mainly focused on the same full-length S protein, raising a safety concern on the practical application of these vaccines (Du et al., 2016b).

To date, no ADE has been observed in MERS-CoV. Indeed, the ADE of SARS-CoV infection in human cells was only discovered 8 years after the virus was first identified in 2003 (Yip et al., 2011). Jaume et al. (2012) demonstrated that non-neutralizing antibodies induced by the full-length S protein of SARS-CoV facilitated the viral entry into host cells via a FcγR-dependent pathway. Our understanding about MERS-CoV is relatively lesser compared to SARS-CoV, mainly due to the fact that the former was discovered less than 7 years, thus it is unsurprising that the ADE of MERS-CoV has yet to be reported (Du et al., 2016b). Nevertheless, by employing appropriate strategies and methods, the ADE of MERS-CoV infection could be revealed in the future.

Two approaches have been suggested to mitigate the adverse effects of ADE. The first approach involves shielding the non-neutralizing epitopes of the S proteins by glycosylation, whereas the second approach, namely immunofocusing, aims to direct the adaptive immune responses to target only the critical neutralizing epitope to elicit a more robust protective immunity (Du et al., 2016a; Okba et al., 2017). A supporting evidence for the latter is that a MERS-CoV vaccine candidate based on a shorter S1 domain induced slightly stronger neutralizing activity than that based on the full-length S protein. In addition, a vaccine candidate based on the even shorter RBD induced the highest neutralizing immune responses (Okba et al., 2017).

CURRENT ANIMAL MODELS EMPLOYED FOR EVALUATION OF MERS-CoV VACCINES

Animal models available for evaluation of MERS-CoV vaccines are highly limited, thus representing a huge challenge for vaccine development. MERS-CoV infects the human (Zaki et al., 2012), non-human primates-rhesus macaques (de Wit et al., 2013; Munster et al., 2013) and marmosets (Falzarano et al., 2014), and dromedary camels (Alagaili et al., 2014; Chu D.K. et al., 2014; Memish et al., 2014). The first animal model adopted for the development of MERS-CoV vaccine was rhesus macaques (de Wit et al., 2013; Munster et al., 2013). They demonstrated clinical symptoms of MERS-CoV infection including an increase in respiratory rate and body temperature, hunched posture, piloerection, cough, and reduced food intake. Radiographic imaging analysis also revealed varying degree of pulmonary diseases following infection. Although the viral RNA of MERS-CoV was detected in most of the respiratory tissues, but viral tropism was restricted primarily to the lower respiratory tract. Rhesus macaques infected with MERS-CoV experienced transient, mild to moderate disease severity (van Doremalen and Munster, 2015; Du et al., 2016b). It is noteworthy that the pathological changes induced in rhesus macaques infected by MERS-CoV were

the results of the host inflammatory responses triggered by the virus instead of the direct viral cytolytic activity (Prescott et al., 2018).

The common marmoset is another frequently used animal model to evaluate MERS-CoV vaccines (Falzarano et al., 2014). Similar to rhesus macaques, humoral and cell-mediated immunities could be detected in these animals following MERS-CoV vaccination. The common marmosets infected with MERS-CoV developed moderate to severe acute pneumonia and increased viral load in the respiratory tract in addition to other clinical symptoms experienced by rhesus macaques (van Doremalen and Munster, 2015; Yu et al., 2017). Intriguingly, the common marmoset also demonstrated signs of renal damage as in human cases following MERS-CoV infection, and the viral RNA could be detected in other non-respiratory organs contrary to rhesus macaques (van Doremalen and Munster, 2015; Yeung et al., 2016). Falzarano et al. (2014) also reported that the common marmoset could serve as a partially lethal animal model. Similarly, Chan et al. (2015) demonstrated that marmosets challenged with MERS-CoV developed severe diseases, leading to fatality. Thereafter, marmosets have been successfully used as a moderate and severe model to study MERS-CoV (Baseler et al., 2016; Yeung et al., 2016; Chen et al., 2017; van Doremalen et al., 2017; Yu et al., 2017; de Wit et al., 2019).

The dromedary camels serve as a natural reservoir for MERS-CoV, and are responsible for zoonotic transmission of the virus to humans. Mild clinical symptoms such as increase in body temperature and rhinorrhea were observed in the dromedary camels infected with MERS-CoV (Adney et al., 2014). Interesting, MERS-CoV tropism in dromedary camels is limited to the upper respiratory tract, and is less apparent in the lower respiratory tract, contrary to rhesus macaques (Adney et al., 2014). The viral RNAs of MERS-CoV are detectable in the respiratory tract, lymph node and the excreted breath of the infected dromedary camels. Viral shedding from the upper respiratory tract of the dromedary camels may explain the efficiency of virus transmission among the camels, and from camels to humans (Adney et al., 2014). The dromedary camels immunized with MERSV-CoV vaccines were also shown to activate both the B-cell and T-cell responses (Muthumani et al., 2015; Haagmans et al., 2016; Adney et al., 2019).

Although camels are the natural reservoirs of MERS-CoV, whilst macaques and marmosets are closely related to the human, the handling of these large mammals is laborious and costly. The lack of small animal models for the initial screening of potential vaccine candidates greatly hampers the development of MERS-CoV vaccines. Unlike SARS-CoV, MERS-CoV does not readily infect smaller rodents such as mice or hamsters due to the substantial differences in the viral binding receptors, dipeptidyl peptidase 4 (DPP4) (Goldstein and Weiss, 2017). Nevertheless, considerable amount of efforts have been devoted to produce MERS-CoV-permissive small rodents for evaluation of MERS-CoV vaccines. Mice transduced by a viral vector to express human DPP4 (hDPP4) were shown to be susceptible to MERS-CoV infection, manifested by the development of pneumonia and histopathological changes in the lungs. However, viral clearance in these infected mice was observed at day-8 post-infection, failing to recapitulate severe human diseases (Zhao et al., 2014). Later, a more established transgenic mouse model expressing hDPP4 globally was developed, and it was the first lethal animal model available to evaluate MERS-CoV vaccines. Mortality was noted in these mice within days post-infection, and virus dissemination to other organs was observed with exceptionally high titer detected in the lung and brain (Agrawal et al., 2015). Recently, a transgenic mouse model was produced by replacing the full-length mouse *DPP4* gene with the human equivalent. However, these transgenic mice did not demonstrate any sign of diseases following the MERS-CoV infection, and no virus dissemination to other organs was observed (Pascal et al., 2015). CRISPR/Cas9 was also previously employed to sensitize the mice to MERS-CoV infection by substituting two amino acids at positions 288 and 230 of the mouse DPP4. Although these genetically engineered mice allowed viral replication in the lungs, they did not experience apparent morbidity following infection by the wild-type MERS-CoV. Severe diseases were observed only when the mice were infected by mouse-adapted MERS-CoV generated via 15 serial lung passages (Cockrell et al., 2016). As mouse DPP4 is vital to normal glucose homeostasis and immunity, altering the mouse DPP4 could have unforeseen complications to the mouse model (Fan et al., 2018). Therefore, another transgenic mouse model has been introduced, in which the *hDPP4* gene was inserted into the genome of C57BL/6-mouse at Rosa26 locus using the CRISPR/Cas9 technology. This mouse model, namely R26-hDPP4, when infected by MERS-CoV at low dose, developed severe lung diseases related to acute respiratory symptoms (ARDS) and central nervous system (CNS). In addition, the R26-hDPP4 is also susceptible to infection by a MERS-CoV pseudovirus, serving as an alternative to test MERS-CoV vaccines in the absence of BSL-3 facility (Fan et al., 2018). All of the animal models described above are summarized in **Table 1**.

Apart from the mouse model, rabbits were also reported to be asymptomatically infected by MERS-CoV. By extensive research, these animals could represent another potential animal model to evaluate MERS-CoV vaccines (Haagmans et al., 2015). Smaller animal models are more economically available to vaccine evaluations in addition to the ease of animal manipulation and readily available methods in testing vaccine efficacy.

CURRENT MERS-CoV VACCINE PLATFORMS

As of now, SARS-CoV and MERS-CoV are the only coronaviruses known to cause severe diseases in human. Development of SARS vaccines was mainly focused on the S protein of SARS-CoV (Bukreyev et al., 2004; Weingartl et al., 2004; Yang et al., 2004; Czub et al., 2005; Kam et al., 2007; Lin et al., 2007; Fett et al., 2013). To date, no vaccine has been licensed to prevent MERS-CoV infection. Although several vaccine candidates are currently in clinical trials, many still remained in the pre-clinical stage. Current approaches for the

TABLE 1 | Animal models used for vaccine development against Middle East respiratory syndrome-coronavirus.

Animal models	Results	Advantages/Limitations	References
Rhesus macaques	The animals manifested clinical signs within 24 h following infection, including increase in respiratory rate and body temperature, hunched posture, piloerection, cough, reduced food intake and varying degree of pneumonia. No mortality was observed in the infected animals throughout the study. The increase in white blood cell counts was early and transient, and viral-load was reported to be higher in lower respiratory tract and decreased overtime.		Munster et al., 2013
Rhesus macaques	The animals experienced early increase in neutrophil at day-1 post-infection (P.I.), and restored at day-3 P.I. Development of pneumonia in the animals was rapid after the infection but short-lived. No mortality or virus dissemination to other non-respiratory tissue was observed in the infected animals. Infection is restricted primarily at lower respiratory tract.	– Genetically closer to human – Do not recapitulate severe diseases in human – Expensive model due to high husbandry requirement	de Wit et al., 2013
Rhesus macaques	The rectal temperature of the animals increased at 1 to 2 days P.I. and restored thereafter. Extensive lung lesions and varying degree of inflammation were observed in the lungs of the animals collected at day-3 P.I. Other pathological changes of the infected lungs include interstitial pneumonia, pulmonary edema, hemorrhaging, degeneration and necrosis of pneumocytes and bronchial epithelial cells. No sign of damage in other non-respiratory organs was observed.		Yu et al., 2017
Immunosuppressed rhesus macaques	The immunosuppressed animals developed rapid pneumonia but less severe than the non-immunosuppressed monkey. Higher viral load, viral shedding, and virus dissemination to other non-respiratory organs were observed in the immunosuppressed animals following infection.	– Potential model for mimicking MERS-CoV infection in immunocompromised patients – Expensive model due to high husbandry requirement – Additional treatment is required to produce immunosuppressed animals	Prescott et al., 2018
Common marmosets	Most of the infected animals developed progressive severe pneumonia characterized by interstitial infiltration. Some animals were euthanized because of diseases severity. Extensive lung lesions were observed in all the infected animals at different necropsies time points. Viral RNA could be detected in blood, respiratory organs and other non-respiratory organs including kidney, suggesting virus dissemination.	– Severe, partially lethal animal model – Able to manifest renal damage – Expensive model due to high husbandry requirement	Falzarano et al., 2014
Common marmosets	Infected animals developed severe pneumonia at day-3 P.I. characterized by exudative pathological changes with widespread pulmonary edema, hemorrhaging, and huge number of inflammatory cells.		Yu et al., 2017
Common marmosets	*In vitro* analysis using lung and kidney cells showed that hyperexpression of Smad7 or FGF2 induced by MERS-CoV led to an immense apoptotic response. Common marmosets infected with MERS-CoV demonstrated acute respiratory distress and disseminated infection in kidneys and other organs.		Yeung et al., 2016
Dromedary camels	The animals infected experimentally with MERS-CoV developed mild symptoms such as increase in body temperature and rhinorrhea. Symptoms of the infected animals lasted less than 2 weeks. Shedding of infectious virus was detected in less than 7 days P.I. but viral RNA remained detectable up to 35 days P.I. in the nasal swabs. Viral RNA, but not infectious virus, was detected in the exhaled breath of the infected animals at day-3 and -5 P.I. The Infection was restricted to upper-respiratory tract.	– Potential model for pathogenesis studies of MERS-CoV and transmission to human – Do not recapitulate severe diseases in human – Expensive model due to high husbandry requirement	Adney et al., 2014
hDPP4-transduced mice	Mice transduced with adenoviral vector to express hDPP4 in lungs were susceptible to MERS-CoV infection. Following the infection, mice developed interstitial pneumonia in addition to reduced weight gain in young mice and weight loss in aged mice. No mortality was observed in all infected animals, and virus clearance was detected at day-6 to -8 P.I. Expression of hDPP4 in the animals' lungs lasted for 17 to 22 days after transduction.	– Ease of manipulation – Low husbandry requirement – Readily available methods in testing vaccine efficacy – Do not recapitulate severe diseases in human	Zhao et al., 2014

(Continued)

TABLE 1 | Continued

Animal models	Results	Advantages/Limitations	References
Transgenic mice expressing hDPP4 globally	Following the infection, the transgenic animals developed severe pneumonia, and 100% mortality was detected at day-6 P.I. Virus dissemination to other non-respiratory organs was detected with significantly high viral RNA in the brains and lungs. No viral RNA could be detected in the kidney or the liver of the infected mice.	– Lethal animal model – Ease of manipulation – Low husbandry requirement – Readily available methods in testing vaccine efficacy – Lack physiological expression pattern because all mouse cells express hDPP4	Agrawal et al., 2015
hDPP4-humanized transgenic mice	Humanized mice can be infected with MERS-CoV but do not demonstrate clinical sign of diseases. Pathological changes including peri-bronchiolar inflammation, interstitial infiltration, and minimal peri-vascular inflammation were observed at 2 to 4 days P.I. Viral RNA was detected in the lungs, and no virus dissemination to other organs was observed	– Ease of manipulation – Low husbandry requirement – Readily available methods in testing vaccine efficacy – Correct physiological expression pattern – Little to no clinical sign	Pascal et al., 2015
CRISPR/Cas9-engineered mice	Mice genome was modified to incorporate human codons at amino acid positions 288 and 330 in the mouse *DPP4* gene causing them to become susceptible to MERS-CoV infection. The infected mice did not demonstrate any sign of diseases but supported viral replication in the lungs. Inflammation of the infected lungs was moderate. Severe disease could be induced in these mice by infecting them with mouse-adapted MERS-CoV.	– Severe, partially lethal animal model (challenged with mouse-adapted MERS-CoV only) – Ease of manipulation – Low husbandry requirement – Readily available methods in testing vaccine efficacy	Cockrell et al., 2016
hDPP4-knockin mice using CRISPR/Cas9	hDPP4-knockin mice were susceptible to MERS-CoV infection. The mice experienced drastic weight loss above the typical euthanization endpoint (20%) by day-5 P.I. Lesions and virus load were detected in the brains and the lungs of the mice but not in the kidneys or livers.	– Lethal animal model – Ease of manipulation – Low husbandry requirement – Readily available methods in testing vaccine efficacy – Lack physiological expression pattern because all mouse cells express hDPP4	Fan et al., 2018

MERS-CoV, Middle East respiratory syndrome-coronavirus; DPP4, dipeptidyl peptidase 4; hDPP4, human dipeptidyl peptidase 4; P.I., post-infection.

development of MERS-CoV vaccines are mostly referred to the methods used for the development of SARS-CoV vaccines during the past two decades, which include: viral vector-based vaccine, DNA vaccine, subunit vaccine, virus-like particles (VLPs)-based vaccine, inactivated whole-virus (IWV) vaccine and live attenuated vaccine.

In general, IWV vaccine is the most rapid approach for vaccine production following a new outbreak. However, the use of IWV as a vaccine in MERS was reported to be associated with hypersensitivity-type lung immunopathologic reaction in the mouse model (Agrawal et al., 2015), thereby limiting its potential. Subunit vaccine is by far the most popular method in the development of MERS vaccine, mostly focusing on the recombinant RBD of the S protein produced in heterologous expression systems. Subunit vaccines, however, are often administered along with adjuvants to boost the immunogenicity of the recombinant antigens. Nanoparticles such as VLPs-based vaccines are similar to subunit vaccines, in which only specific viral proteins are expressed. Unlike subunit vaccines, VLPs-based vaccines are comprised of recombinant viral proteins capable of self-assembling into larger particles resembling viruses. Although the immunogenicity of VLPs-based vaccines could be enhanced by adjuvants, the VLPs themselves can serve as adjuvants which increase the immunogenicity of displayed epitopes, particularly those of smaller ones (Murata et al., 2003; Quan et al., 2008). Live attenuated vaccines are composed of live viruses, which have been modified to remove or reduce their virulence. This type of vaccine is often very immunogenic, whereby a single administration without an adjuvant is sufficient to induce protective immunity. However, the risk of reversion to a virulent virus has limited its usage as MERS vaccine. Viral vector-based vaccine is one of the most popular approaches in developing MERS vaccines. Two out of the three candidate vaccines which have entered the clinical phase are viral vector vaccines. This approach utilizes well-studied virus replication system to display MERS-CoV antigen, thereby inducing protective immunity against MERS-CoV. Another candidate vaccine currently in phase I/II clinical trial is a DNA vaccine. Unlike other types of vaccines, DNA vaccine production does not involve virus replication, protein expression and purification, therefore reduce the cost of production. However, administration of DNA vaccines often requires an external device such as electroporator or gene gun, which eventually increases the cost of immunization. **Table 2** summarizes the vaccine candidates against MERS-CoV infection, which are further discussed intensively in the following sections.

TABLE 2 | Potential vaccine candidates against Middle East respiratory syndrome-coronavirus.

Vaccine type	Vector and antigen	Administration route	Results	References
Viral-vector	rAd5 encoding S1 protein	IM	Immunization with rAd5 constructs expressing CD40-targeted S1 fusion protein (rAd5-S1/F/CD40L) offered complete protection to hDPP4 transgenic mice against MERS-CoV challenge and prevented pulmonary perivascular hemorrhage.	Hashem et al., 2019
	rAd5 or rAd41 encoding S protein	IM or IG	IG administration of rAd5-S or rAd41-S elicited antigen-specific IgG and neutralizing antibody in serum, but T-cell responses were not detected. A single IM injection of Ad5-S or Ad41-S induced systemic humoral response in addition to the functional antigen-specific T-cell responses in the spleen and pulmonary lymphocytes of the mice, which persisted for several months.	Guo et al., 2015
	rAd5 encoding S protein or S1	IM and later boosted with IN	Immunized mice demonstrated antibody responses against spike protein, which neutralized MERS-CoV *in vitro*. Stronger neutralizing antibody responses were observed in the mice vaccinated with the vector encoding the shorter S1 protein than the full-length S protein.	Kim et al., 2014
	ChAdOx1 encoding S protein*	IM or IN	Single dose intranasal or intramuscular immunization protected transgenic BALB/c mice against lethal virus challenge. Immunogenicity and efficacy were comparable between immunization routes.	Munster et al., 2017
	ChAdOx1 encoding S protein*	IM	Single dose immunization with ChAdOx1 MERS vaccine with tPA induced 5 logs of neutralizing antibodies in BALB/c mice.	Alharbi et al., 2017
	MVA encoding S protein	IM	Immunization with MVA MERS vaccine containing tPA regulated by F11 promoter induced 4.7 logs of neutralizing antibodies in BALB/c mice.	Alharbi et al., 2017
	MVA encoding S protein**	IM or SC	Both immunization routes induced neutralizing antibodies and CD8+ T-cell responses in mice. Vaccinated mice were protected against MERS-CoV challenge infection after transduction with the hDPP4 receptor.	Volz et al., 2015
	MVA encoding S protein**	IM	Neutralizing antibody responses were induced in immunized mice.	Song et al., 2013
	MVA encoding the N-protein	IM or IP	CD8+ T-cell response was elicited in the immunized mice in both immunization routes.	Veit et al., 2018
	NDV encoding S protein	IM	Recombinant NDV expressing MERS-CoV S protein induced neutralizing antibodies in BALB/c mice and Bactrian camels.	Liu et al., 2017
Viral-vector and nanoparticle	rAd5 and MERS-CoV S nanoparticle	IM	Heterologous prime-boost vaccination with rAd5-S protein and alum-adjuvanted recombinant S protein induced both Th1 and Th2 immune responses in SPF BALB/c mice.	Jung et al., 2018
DNA	DNA encoding S protein***	IM followed by EP	The DNA vaccine was immunogenic in mice, camels and rhesus macaques. When the immunized macaques were challenged with MERS-CoV, characteristic clinical symptoms including pneumonia were reduced.	Muthumani et al., 2015
	DNA encoding S or S1 protein	IM	DNA encoding S1 protein elicited stronger antibody and cellular immune responses in mice than that encoding the S protein. Both DNAs encoding S1 and S proteins induced neutralizing antibodies that cross-reacted with MERS-CoV strains of human and camel origins.	Al-Amri et al., 2017
	DNA encoding S1 protein	IM	Immunization with DNA encoding S1 protein and passive transfer of immune sera from the vaccinated mice protected hDPP4-transduced-mice from MERS-CoV infection.	Chi et al., 2017

(Continued)

TABLE 2 | Continued

Vaccine type	Vector and antigen	Administration route	Results	References
Subunit	MERS-CoV S1 protein	SC	Adjuvanted (MF59) MERS-CoV S1 protein protected hDPP4 transgenic mice against lethal MERS-CoV challenge, where the protection correlated well with the neutralizing antibody titer.	Wang et al., 2017c
	MERS-CoV S1 protein	IM	Immunization with adjuvanated (Advax HCXL adjuvant and Sigma Adjuvant System) S1 protein reduced and delayed virus shedding in the upper respiratory tract of dromedary camels and provided complete protection in alpaca against MERS-CoV challenge.	Adney et al., 2019
	MERS-CoV S protein trimer on Fd	IM	Recombinant prefusion trimeric MERS-CoV S protein induced high titer of neutralizing antibodies in BALB/cJ mice.	Pallesen et al., 2017
	RBD trimer on Fd	SC or IM	Adjuvanted (alum) RBD-Fd induced neutralizing antibodies in BALB/c mice and protected (83%) hDPP4 transgenic mice against lethal MERS-CoV challenge.	Tai et al., 2016
	RBD fused to Fc	SC	Adjuvanted RBD-Fc induced high titer of neutralizing antibodies in BALB/c mice and New Zealand white rabbits.	Ma et al., 2014b
	RBD fused to Fc	SC	Mice immunized with the vaccine and Montanide ISA 51 adjuvant produced neutralizing antibodies which inhibited binding of the RBD to DPP4 receptor, neutralizing MERS-CoV infection.	Du et al., 2013
	RBD fused to Fc	IN or SC	Mice vaccinated with both immunization routes in the presence of adjuvants (Montanide ISA 51 adjuvant for SC and Poly(I:C) for IN) elicited systemic humoral immune responses. Stronger systemic cellular immune responses and local mucosal immune responses were observed in mice immunized via IN route.	Ma et al., 2014a
	RBD fused to Fc	IM	hCD26/DPP4 transgenic mice immunized with the vaccine in the presence of adjuvant, AddaVax elicited neutralizing antibodies and were protected against MERS-CoV infection.	Nyon et al., 2018
	RBD fused to Fc	SC	Mice immunized with the vaccine alone produced detectable neutralizing antibodies and cellular immune responses. Immunogenicity of the vaccine improved when the adjuvants such as Freund's adjuvant, alum, monophosphoryl lipid A, Montanide ISA51 or MF59 was included in the formulation. MF59 was demonstrated to be superior in enhancing the vaccine immunogenicity and protection against viral challenge.	Zhang et al., 2016
	Recombinant RBD	IM or SC	When the subunit vaccine was administered together with combination of alum and CpG ODN, optimized RBD-specific humoral and cellular immunity were elicted. Robust RBD-specific antibody and T-cell responses were induced in mice immunized with the vaccine in combination with IFA and CpG ODN, but low level of neutralizing antibodies were induced.	Lan et al., 2014
	Recombinant RBD	IM	Rhesus macaques immunized with the subunit vaccine and alum adjuvant produced neutralizing antibodies and experienced mitigated clinical symptoms when challenged with MERS-CoV.	Lan et al., 2015
	rNTD of S protein	IM	Immunization with rNTD of MERS-CoV S protein adjuvanted with alum induced neutralizing antibodies and reduced the respiratory tract pathology of BALB/c mice challenged with MERS-CoV.	Jiaming et al., 2017

(Continued)

TABLE 2 | Continued

Vaccine type	Vector and antigen	Administration route	Results	References
VLPs	MERS-CoV VLPs	IM	Co-administration of the VLPs-based vaccine and alum activated RBD specific humoral and cellular immune responses in rhesus macaques.	Wang et al., 2017b
	S protein nanoparticles	IM	S protein produced in the baculovirus insect cells expression system assembled into nanoparticles of approximately 25 nm. Mice immunized with these nanoparticles in the presence of alum produced high titer of neutralizing antibody.	Coleman et al., 2014
	S protein nanoparticles	IM	The vaccine together with Matrix M1 adjuvant activated S protein specific humoral immune responses, and protected hDPP4 transduced mice against viral challenge.	Coleman et al., 2017
	CPV VLP displaying RBD	IM	Immunization of the mice with the chimeric VLPs displaying RBD in the presence of adjuvants [alum or Poly(I:C)] elicited neutralizing antibody responses as well as cellular immune responses.	Wang et al., 2017a
	Influenza A VLP displaying S protein	IM	Immunization of the mice with the chimeric VLPs displaying RBD in the presence of a combination of adjuvants (alum and CpG ODN) elicited neutralizing antibody responses.	Lan et al., 2018
Nanoparticle	Ferritin displaying RBD	IM	Immunization with chaperna-mediated ferritin nanoparticle displaying MERS-CoV RBD adjuvanted with MF59 induced RBD-specific antibodies in BALB/c mice which inhibited RBD binding to hDPP4 receptor protein.	Kim et al., 2018
Inactivated whole -virus	MERS-CoV	IM	Mice immunized with the inactivated vaccine in the presence of a combination of adjuvants (alum and CpG ODN) elicited neutralizing activity but not cell-mediated immunity. This vaccine also protected hDPP4 transduced mice against MERS-CoV challenge.	Deng et al., 2018
	MERS-CoV	IM	Gamma radiation-inactivated MERS-CoV induced neutralizing antibodies and reduced viral load in hDPP4 transgenic mice but may cause hypersensitivity-type lung immunopathologic reaction upon MERS-CoV challenge.	Agrawal et al., 2016
	Chimeric RABV displaying S1 protein	IM	The inactivated vaccine induced high titer of neutralizing antibodies in mice, and protected hDPP4-transduced-mice against MERS-CoV infection.	Wirblich et al., 2017
Live-attenuated	MERS-CoV mutant	-	The mutant was produced by deleting the *E* gene of the MERS-CoV. This mutant lacked infectivity but was single-cycle replicative.	Almazan et al., 2013
	MERS-CoV mutant	IN	Attenuated MERS-CoV through mutation of NSP16 (D130A) protected CRISPR-Cas9-targeted 288–330$^{+/+}$ C57BL/6 mice from mouse-adapted MERS-CoV challenge.	Menachery et al., 2017
	MV expressing full-length or truncated, soluble variant of S protein	IP	The recombinant MV was replication competent. Immunization of the type I interferon receptor-deficient (IFNAR$^{-/-}$) CD46Ge mice with the recombinant MV induced both MV and S protein specific neutralizing antibodies as well as cellular immune responses. The recombinant MV protected hDPP4-transduced-mice against viral challenge.	Malczyk et al., 2015
	MV expressing N protein	IP	Recombinant MV expressing MERS-CoV N protein induced N-specific T cell responses in IFNAR$^{-/-}$-CD46Ge mice.	Bodmer et al., 2018

(Continued)

TABLE 2 | Continued

Vaccine type	Vector and antigen	Administration route	Results	Reference
	Recombinant VSV expressing S protein	IN or IM	Recombinant VSV was produced by replacing the glycoprotein of VSV with the S protein of MERS-CoV. The recombinant virus induced neutralizing antibodies and T cell responses in rhesus macaques after a single intramuscular or intranasal immunization dose.	Liu et al., 2018

MERS-CoV, Middle East respiratory syndrome-coronavirus; rAd5, recombinant human adenovirus type-5; rAd41, recombinant human adenovirus type-41; MVA, modified vaccinia virus Ankara; ChAdOx1, chimpanzee adenovirus, Oxford University #1; NDV, Newcastle disease virus; MV, measles virus; CPV, canine parvovirus; RABV, rabies virus; VLP, virus-like particle; NSP, non-structural protein; S protein, spike protein; S1 protein, spike protein receptor binding subunit; RBD, receptor-binding domain in S1; N protein, nucleocapsid protein; rNTD, recombinant N-terminal domain; Fd, foldon trimerization motif; Fc, Fc region of human IgG; tPA, leader sequence of the human tissue plasminogen activator gene; IFNAR$^{-/-}$-CD46Ge mice, genetically modified mice deficient of type I IFN receptor and transgenically expressing human CD46; SPF, specific-pathogen-free; IM, intramuscular; IN, intranasal; IP, intraperitoneal; SC, subcutaneous; IG, intragastric; EP, electroporation. Vectors and antigens marked with "" have entered phase I clinical trial (*MERS001; **MVA-MERS-S; ***GLS-5300).*

VIRAL VECTOR-BASED VACCINE

The first viral vector-based vaccine was reported by Moss et al. (1984) who developed a potential hepatitis B vaccine using the vaccinia viral vector. Unlike subunit or inactivated vaccines, which generally function as extracellular antigens, a viral vector works by carrying a DNA encoding immunogenic components into host cells, followed by intracellular antigen expression, thereby activating a broad spectrum cell-mediated immunity in addition to the humoral immune responses. Majority of the viral-vector based vaccines do not require adjuvant for optimum efficacy (Ura et al., 2014). Adenovirus and modified vaccinia virus Ankara (MVA) are the two most common viral vectors used in the development of MERS-CoV vaccines.

Mice immunized intramuscularly with the recombinant human adenoviral (type 5 or 41) vector encoding the full-length S protein were shown to induce systemic neutralizing antibodies and mucosal T-cells immunity. Intriguingly, no mucosal T-cell response was detected when the vaccine was administered via an intragastric route, contrary to previous findings which suggested the importance of mucosal vaccination in activating the mucosal immunity (Guo et al., 2015). A recombinant human adenovirus type 5 (rAd5) vector encoding the shorter S1 extracellular domain of the S protein was reported to elicit slightly stronger neutralizing antibody responses than that encoding the full-length, suggesting the effect of immunofocusing (Kim et al., 2014). A recent study by Hashem et al. (2019) demonstrated that rAd5 constructs expressing CD40-targeted S1 fusion protein (rAd5-S1/F/CD40L) offered a complete protection to hDPP4 transgenic mice against MERS-CoV challenge, and prevented pulmonary perivascular hemorrhage. Additionally, Jung et al. (2018) showed that heterologous prime-boost vaccination with rAd5-S protein and alum-adjuvanted recombinant S protein nanoparticle successfully induced both the Th1 and Th2 immune responses in specific-pathogen-free BALB/c mice.

Pre-existing immunity against human adenovirus in human population is widespread, hampering its clinical application as a vector for vaccine development (Fausther-Bovendo and Kobinger, 2014). Recent developments of new adenovirus vectors for vaccine antigen delivery focus on the serotype to which human population is less exposed. Chimpanzee adenovirus (ChAdOx1) represents an attractive alternative to the human adenoviral vector due to its good safety profile and lack of pre-existing immunity in human population (Dicks et al., 2012), and has since been employed in the vaccine development against MERS-CoV infection. The recombinant ChAdOx1 encoding full-length S protein (ChAdOx1 MERS) was shown to be immunogenic in mice, and lethal virus challenge using hDPP4 transgenic mouse model further demonstrated its high protective efficacy against MERS-CoV (Alharbi et al., 2017; Munster et al., 2017). It is noteworthy that the immunogenicity of S protein could be improved by insertion of a gene encoding the signal peptide of human tissue plasminogen activator (tPA) upstream of the *S* gene of MERS-CoV, in both ChAdOx1 and MVA vectors (Alharbi et al., 2017). Currently, a candidate MERS-CoV vaccine known as MERS001, which contains the ChAdOx1 encoding the S protein of MERS-CoV is at phase I clinical trial. The trial is estimated to be completed by December 2019, in which the safety and immunogenicity of MERS001 at different dosage are being studied in healthy adult volunteers recruited and sponsored by the University of Oxford, United Kingdom (National Institutes of Health [NIH], 2018b).

Recombinant MVA encoding the full-length S protein represents another potential MERS-CoV vaccine candidate due to its good safety profile, decent immunogenicity, and high protective efficacy against MERS-CoV (Song et al., 2013; Volz et al., 2015; Alharbi et al., 2017). Another candidate vaccine currently in phase I clinical trial is MVA-MERS-S. The trial is being performed by the University Medical Center Hamburg-Eppendorf, Germany, in which the safety and immunogenicity of MVA-MERS-S in healthy adult volunteers are being assessed (National Institutes of Health [NIH], 2018c). Apart from the S protein, the highly conserved N protein of MERS-CoV was inserted into MVA, and inoculated into mice. Although the recombinant MVA encoding the N-protein elicited CD8+ T-cell response in the immunized mice, its protective efficacy was not investigated (Veit et al., 2018).

Apart from adenovirus and MVA, Newcastle disease virus (NDV) was also used as a viral-vector for displaying MERS-CoV S protein. The NDV-based vaccine candidate induced neutralizing antibodies in BALB/c mice and Bactrian camels (Liu et al., 2017). Although viral vector-based vaccines are able

to induce robust immune responses, they are not free from drawbacks, which include pre-existing immunity against viral vector, risk of pathogenesis, low viral titer production, and potential tumorigenesis (Ura et al., 2014).

DNA VACCINE

DNA vaccine is composed of a recombinant plasmid encoding immunogens. This vaccine is typically delivered via direct injection, gene gun, or electroporation into host cells, where the immunogens can be expressed and prime the immune system (Ferraro et al., 2011). DNA vaccine offers two distinct advantages over the subunit or protein-based vaccine: the ease of DNA manipulation and low cost of production (Leitner et al., 1999).

Similarly, all DNA vaccines developed against MERS-CoV target the S protein or the shorter S1 domain of MERS-CoV. DNA encoding the full-length S protein was shown to induce neutralizing antibodies and robust cell-mediated immunity in mice, macaques, and camels. When the immunized macaques were challenged with MERS-CoV, characteristic clinical symptoms including pneumonia were mitigated (Muthumani et al., 2015). GLS-5300 is one of the three candidate vaccines currently in a clinical trial. Sponsored by the GeneOne Life Science, Inc., Korea, a phase I clinical trial to test the vaccine's safety profile in human volunteers was completed in the Walter Reed Army Institute of Research, United States (National Institutes of Health [NIH], 2016). Currently, the phase I and phase II clinical trials are being performed in the International Vaccine Institute, Korea, to further evaluate the safety and immunogenicity of GLS-5300, as well as a device for electroporation (CELLECTRA® 2000 Electroporation) (National Institutes of Health [NIH], 2018a).

To avoid the possible adverse effects induced by the full-length S protein, other researchers revealed that immunization with a DNA encoding the S1 domain, and passive transfer of immune sera from the vaccinated mice protected hDPP4-transduced-mice from MERS-CoV infection (Chi et al., 2017). The DNA encoding the S1 domain was also demonstrated to be more superior than that encoding the full-length S protein in eliciting antibody and cellular responses. Both DNAs encoding the S1 and S proteins were shown to induce neutralizing antibodies that cross-reacted with MERS-CoV strains of human and camel origins (Al-Amri et al., 2017). Despite the effectiveness of DNA vaccines, spontaneous plasmid integration into host genomes represents a potential risk, but the probability is extremely low (Ledwith et al., 2000).

SUBUNIT VACCINE

In general, subunit vaccines have the highest safety profile among all current vaccines despite their low immunogenicities (Du et al., 2016b). Precautions should be taken during the development of MERS-CoV vaccines based on the S protein to avoid induction of non-neutralizing antibodies. Unlike the full-length S protein, RBD of MERS-CoV comprises the critical neutralizing domains but lacking the non-neutralizing immunodominant region. Therefore, upon immunization, the RBD-based vaccines are restricted to produce RBD-specific neutralizing immune responses, thus are incapable of inducing non-neutralizing antibodies that may potentially contribute to harmful pathological effects (Du and Jiang, 2015; Wang et al., 2015a). From the safety and effectiveness perspectives, the RBD is a more promising candidate in the development of MERS-CoV vaccines over the full-length S protein.

The RBD of MERS-CoV was reported to induce neutralizing antibodies against multiple strains of MERS-CoV due to the presence of several conformational neutralizing epitopes (Du et al., 2016b). Any MERS-CoV strains with a single mutation in an epitope may not suffice to escape the RBD-specific neutralizing antibodies. Wang et al. (2015a) demonstrated that an amino acid mutation at position 509 (aspartic acid to glycine substitution) in RBD rendered the mutated strain resisted to neutralization by a RBD-specific monoclonal antibody, F11, but susceptible to another RBD-specific monoclonal antibody, D12. Both of these antibodies could bind to different regions of the RBD of MERS-CoV. Similarly, the RBD of SARS-CoV also consists of multiple neutralizing domains that are capable of inducing broad neutralizing immune responses against many SARS-CoV strains (He et al., 2006). Development of antibody escape mutants may require a mutation in two or more epitopes in the RBD of MERS-CoV, which is less likely to take place, and if developed, may exhibit reduced viral fitness (Tang et al., 2014; Tai et al., 2017).

It was demonstrated that the MERS-CoV S1 protein with MF59 adjuvant protected hDPP4 transgenic mice against lethal MERS-CoV challenge, where the protection correlated well with the neutralizing antibody titer (Wang et al., 2017c). In addition, adjuvanted recombinant S1 proteins (Advax HCXL adjuvant and Sigman Adjuvant System) reduced and delayed virus shedding in the upper respiratory tract of dromedary camels (MERS-CoV animal reservoir), and provided complete protection in alpaca (a surrogate infection model) against MERS-CoV challenge (Adney et al., 2019).

In general, MERS-CoV subunit vaccines based on the S1 domain require the use of adjuvant or fusion with an immune enhancer to heighten immunogenicity. Several studies have indicated that RBD fused with Fc fragment of human IgG (RBD-Fc) elicited strong systemic neutralizing antibody and cellular immune responses in vaccinated mice (Du et al., 2013; Ma et al., 2014a; Tang et al., 2015; Nyon et al., 2018) and New Zealand white rabbits (Ma et al., 2014b). hDPP4-transduced-mice immunized with RBD-Fc were also protected from viral challenge (Ma et al., 2014a). Other adjuvants such as Freund's adjuvant, alum, monophosphoryl lipid A, Montanide ISA51 and MF59 were also reported to further improve the immunogenicity and protection of RBD-Fc in mice, particularly MF59 is superior among these adjuvants (Zhang et al., 2016). In addition, co-administration of multiple adjuvants together with RBD antigen could synergistically improve the immunogenicity of the RBD-based subunit vaccine. Mice immunized with RBD antigen together with alum and CpG ODN produced stronger humoral and cellular immune responses than those immunized with RBD

antigen and alum or CPG ODN alone (Lan et al., 2014). RBD-based subunit vaccine was also previously tested in the rhesus macaque model in the presence of alum. This vaccine formulation was shown to induce robust and sustained humoral and cellular immunities, and partially protected rhesus macaques from viral challenge (Lan et al., 2015).

As native spikes of MERS-CoV exist in the form of trimers, vaccine designs mimicking the native viral S proteins have also been reported (Tai et al., 2016; Pallesen et al., 2017). Through the use of foldon (Fd), a T4 fibritin trimerization domain, Pallesen et al. (2017) synthesized a recombinant prefusion trimeric MERS-CoV S protein, which induced high titer of neutralizing antibodies in BALB/cJ mice. Similarly, Tai et al. (2016) expressed RBD trimers on Fd, and demonstrated the vaccine's protective efficacy (83% survival) in hDPP4 transgenic mice against lethal MERS-CoV challenge.

Although most of the subunit vaccine studies focused on the RBD of the S protein, a recent study by Jiaming et al. (2017) proposed the use of recombinant N-terminal domain (rNTD) of the S protein as another potential vaccine candidate. The rNTD, when used to immunize BALB/c mice, induced neutralizing antibodies and reduced the respiratory tract pathology of mice in a non-lethal MERS-CoV challenge.

Apart from focusing on the S protein, multivalent vaccines designed using *in silico* methods which contain the B cell and T cell epitopes of S, E, M, N and NSPs have been proposed (Srivastava et al., 2018). However, until now, no biological data have been presented for these multivalent vaccines. In addition, the N protein and S2 domain of S protein are more conserved among coronaviruses, representing other attractive targets in the development of a broad-spectrum coronavirus vaccine (Schindewolf and Menachery, 2019). Nevertheless, it is crucial to ensure that these proteins do not contribute to the ADE of MERS-CoV infection.

VIRUS-LIKE PARTICLES (VLPs)-BASED VACCINE

Virus-like particles are nanoscale particles similar to the native viral particles but devoid of infectious genetic materials. They are composed of repetitive viral structural proteins with inherent self-assembly properties. VLPs are non-replicative and non-infectious. VLPs can be produced by expressing the viral structural proteins in a suitable expression system (Yong et al., 2015a,b; Ong et al., 2017). In general, VLPs-based vaccine is similar to the whole inactivated virus vaccine, but it does not require the viral inactivation step which may alter the antigenicity and immunogenicity of a viral protein. Because no live virus is involved in the manufacturing process, VLPs can be easily generated in a low-containment manufacturing environment (DeZure et al., 2016).

Virus-like particles of MERS-CoV were previously produced in baculoviral expression system by co-expressing the S, E and M proteins of MERS-CoV. The VLPs generated were indistinguishable from the authentic viral particle when observed under an electron microscope. These VLPs, when administered with alum induced neutralizing antibodies and a Th1-biased immunity in rhesus macaques (Wang et al., 2017b). Intriguingly, when the S protein of MERS-CoV was expressed alone, it self-assembles into nanoparticles of approximately 25 nm, about a quarter of the diameter of the authentic viral particle. Immunogenicity studies in mice demonstrated that these nanoparticles elicited antibody responses in the presence of alum, and when the adjuvant was replaced with Matrix M1 adjuvant, they induced a significantly higher titer of neutralizing antibodies (Coleman et al., 2014). Viral challenge in hDPP4-transduced-mice which had been immunized with Matrix M1 and S protein nanoparticles further proven the protective efficacy of this vaccine formulation against MERS-CoV (Coleman et al., 2017). As mentioned earlier under the viral vector-based vaccine, adjuvanted S protein nanoparticles as boosters in mice primed with rAd-5 S have also yielded promising Th1 and Th2 immune responses (Jung et al., 2018).

Advancement in genetic engineering enables VLPs to display different epitopes of viruses, producing chimeric VLPs (cVLPs) (Ong et al., 2017). Expression of the RBD of MERS-CoV fused to the VP2 structural protein of canine parvovirus (CPV) produced cVLPs displaying the RBD of MERS-CoV. These cVLPs were morphologically similar to native CPV and elicited both RBD-specific humoral and cell-mediated immunities in mice (Wang et al., 2017a). The cVLPs displaying the S protein of MERS-CoV and matrix 1 protein of influenza A virus were also developed, and shown to be immunogenic in mouse models. However, the actual protective efficacy of these cVLPs against MERS-CoV has yet to be investigated *in vivo* (Lan et al., 2018).

In addition to vaccines based on VLPs, non-viral nanoparticle such as ferritin has also been reported as a potential carrier for MERS-CoV antigen (Kim et al., 2018). Kim et al. (2018) utilized a chaperna-mediated ferritin nanoparticle to display MERS-CoV RBD. When adjuvanted with MF59, the ferritin-based nanoparticle induced RBD-specific antibodies in BALB/c mice, which inhibited RBD binding to hDPP4 receptor protein, suggesting its potential use as MERS-CoV antigen carrier (Kim et al., 2018).

INACTIVATED WHOLE-VIRUS VACCINE

Inactivated whole-virus comprises the entire disease causing virion which is inactivated physically (heat) or chemically. IWV offers several advantages, including relatively low cost of production, good safety profile, and does not involve laborious genetic manipulation (DeZure et al., 2016). Nevertheless, production of IWV requires the live virus to be grown under a high-level containment, and the antigenicity of the immunogen could be altered in the viral inactivation step (DeZure et al., 2016).

Formaldehyde-inactivated-MERS-CoV induced neutralizing antibodies in mice, but not T-cell response. Supplementing this IWV with a combined adjuvant (alum and CpG ODN) was reported to enhance its protective immunity against MERS-CoV in mice transduced with hDPP4 (Deng et al., 2018). On the other hand, an inactivated bivalent whole virus vaccine

that targets rabies virus (RABV) and MERS-CoV was recently developed using a recombinant vector encoding a fusion protein comprising the MERS-CoV S1 domain fused to the C-terminus of RABV G protein. Following expression, the S1 domain was incorporated into RABV particles (BNSP333-S1). When the mice were immunized with the chemically inactivated BNSP333-S1, robust neutralizing antibody responses against S1 and G proteins were detected. Inactivated BNSP333-S1 also protected hDPP4-transduced-mice against MERS-CoV challenge (Wirblich et al., 2017). Despite the benefits associated with IWV-based vaccines, inactivated MERS-CoV vaccine was reported to potentially cause a hypersensitivity-type lung immunopathologic reaction upon MERS-CoV challenge, even though it induced neutralizing antibodies and reduced the viral load in hDPP4 transgenic mice, similar to those observed in SARS-CoV (Agrawal et al., 2016).

LIVE ATTENUATED VACCINE

Live attenuated vaccine is one of the most effective vaccines due to its capability to induce immunity similar to the natural infection. This vaccine contains viable but attenuated virus. Common approaches to develop a live attenuated vaccine include deletion of the viral genes that confer virulence, and via reverse genetic. In general, live attenuated vaccines are highly immunogenic, thus do not require adjuvant for optimal efficacy, and single immunization is usually sufficient to induce protective immunity. Nevertheless, live attenuated vaccines come with some unwanted limitations, particularly the risk of reversion to a virulent strain, and the absolute need for vaccine cold chain. Live attenuated vaccine is also not suitable for infants, immunocompromised individuals, and elderly people (Lauring et al., 2010).

A live attenuated vaccine against MERS-CoV was previously developed by deleting the *E* gene of MERS-CoV (rMERS-CoV-ΔE). This engineered virus lacked infectivity and replicated in a single cycle. Vaccines based on the live attenuated viruses could pose biosafety problems associated with the risk of virulence reversion, whereas rMERS-CoV-ΔE is propagation defective in the absence of E protein, preventing a straightforward reversion to virulence, thus providing a safer alternative (Almazan et al., 2013). More recently, a live attenuated MERS-CoV was generated through mutation of NSP16 (D130A), where the attenuated virus protected CRISPR-Cas9-targeted 288–330$^{+/+}$ C57BL/6 mice from a mouse-adapted MERS-CoV challenge (Menachery et al., 2017).

Other than MERS-CoV, a replication competent recombinant measles virus (MV) was used as a platform for the development of live attenuated MERS-CoV vaccine. The recombinant MV was engineered to express the full-length S protein (MV_{vac2}-CoV-S) or its truncated version (MV_{vac2}-CoV-solS). Both MV_{vac2}-CoV-S and MV_{vac2}-CoV-solS were shown to induce neutralizing antibodies and cell-mediated immune responses against MV and MERS-CoV, and protected hDPP4-transduced-mice from MERS-CoV challenge (Malczyk et al., 2015). Three years later, Bodmer et al. (2018) compared the MV_{vac2}-CoV-S with its UV-inactivated derivative, and showed that the inactivated version did not induce any specific immune response against both the MV and MERS-CoV. Concurrently, Bodmer et al. (2018) constructed a live attenuated recombinant MV expressing MERS-CoV N protein (MV_{vac2}-MERS-N), and its administration into IFNAR$^{-/-}$-CD46Ge mice (genetically modified mice deficient of type I IFN receptor and transgenically expressing human CD46) induced N-specific T cell responses, although not as strong as those of MV_{vac2}-CoV-S. Similarly, in another study, a viable recombinant vesicular stomatitis virus (VSV) with its G protein replaced with the S protein of MERS-CoV also elicited both humoral and cell-mediated immunities in rhesus macaques (Liu et al., 2018).

OBSTACLES IN BRINGING MERS VACCINES TO THE MARKET

Development of MERS vaccines started immediately following the discovery of MERS-CoV in 2012. Pre-clinical trials on animal models capable of recapitulating the clinical signs and symptoms in the human are a must prior to clinical trials and licensing of a vaccine (Gerdts et al., 2007). The choice of an animal model is generally preferable to be as phylogenetically closer as possible to the human (Swearengen, 2018). Therefore, majority of the vaccine candidates will be evaluated in non-human primates such as chimpanzees, rhesus macaques (Sibal and Samson, 2001) or marmosets (Carrion and Patterson, 2012). Employing these animal models in experiments, however, is extremely costly (Gerdts et al., 2015). Before involving non-human primates in a vaccine evaluation, strong justification or supporting evidence from *in vitro* analysis, or more preferable from animal studies such as small rodents are often required (Gerdts et al., 2015). However, MERS-CoV cannot infect smaller rodents naturally, representing a huge challenge in initial vaccine developments (Goldstein and Weiss, 2017). Although transgenic mouse models for evaluation of MERS-CoV vaccines have been successfully developed, the costs of these transgenic animals are not affordable by many research groups, especially those from the less affluent parts of the world. This issue consequently delayed the development of an effective vaccine, and its advancement into clinical trial.

Funding is the primary drivers in any vaccine developments. Many vaccines demonstrating promising results at the pre-clinical stage require additional investments from the government or the private industry to advance into clinical trials (Hakoum et al., 2017). However, government funding for clinical trials is rather restricted, whereas private industry is generally profit oriented, of which the market size and potential profits are of priority (Smith, 2000). Unlike other widespread diseases such as hepatitis and influenza, MERS cases are primarily reported in Saudi Arabia apart from the Korea outbreak (Gossner et al., 2016). Its relatively low occurrence is likely to limit the market size of MERS vaccines, leading to lower interest by the private funding bodies. Although three potential MERS vaccine candidates have advanced into clinical trials, they are currently

in phase I/II. As completing the entire trials often take 10 years and above, they are unlikely to be commercially available in the coming 3–5 years.

CONCLUSION

Despite having a low occurrence of recorded human-to-human transmission, the recent MERS outbreak in South Korea which demonstrated virus emergence in second and third generation contacts has reignited public awareness regarding the danger of MERS-CoV. As no effective treatment against MERS is currently available, therefore the best solution is to develop a functional MERS vaccine to prevent MERS-CoV infection. Amongst the six types of vaccines discussed above, more studies are focused on the viral vector-based and subunit vaccines. Even though many promising vaccine candidates have been proposed and reported, as of now, only three potential MERS-CoV vaccine candidates have progressed to phase I clinical trials: a DNA vaccine (GLS-5300) and two viral vector-based vaccines (MVA-MERS-S and MERS001. It is still very likely that no MERS vaccine will be available in the market for human in the near future. Therefore, considerable efforts should be given to minimize delays in executing clinical trials, such as better understanding and coordination between sponsors, primary investigators, investigators, participants and stakeholders.

AUTHOR CONTRIBUTIONS

CY and HO wrote the manuscript. SY, KH, and WT reviewed, edited, and approved its final version.

FUNDING

This work was supported by the Universiti Putra Malaysia (Grant No: GP-IPS/2018/9602500).

REFERENCES

Adney, D. R., van Doremalen, N., Brown, V. R., Bushmaker, T., Scott, D., de Wit, E., et al. (2014). Replication and shedding of MERS-CoV in upper respiratory tract of inoculated dromedary camels. *Emerg. Infect. Dis.* 20, 1999–2005. doi: 10.3201/eid2012.141280

Adney, D. R., Wang, L., van Doremalen, N., Shi, W., Zhang, Y., Kong, W. P., et al. (2019). Efficacy of an adjuvanted middle east respiratory syndrome coronavirus spike protein vaccine in dromedary camels and alpacas. *Viruses*11:E212. doi: 10.3390/v11030212

Agnihothram, S., Gopal, R., Yount, B. L., Jr., Donaldson, E. F., Menachery, V. D., Graham, R. L. (2014). Evaluation of serologic and antigenic relationships between middle eastern respiratory syndrome coronavirus and other coronaviruses to develop vaccine platforms for the rapid response to emerging coronaviruses. *J. Infect Dis.* 209, 995–1006. doi: 10.1093/infdis/jit609

Agrawal, A. S., Garron, T., Tao, X., Peng, B. H., Wakamiya, M., Chan, T. S., et al. (2015). Generation of a transgenic mouse model of middle east respiratory syndrome coronavirus infection and disease. *J. Virol.* 89, 3659–3670. doi: 10.1128/JVI.03427-3414

Agrawal, A. S., Tao, X., Algaissi, A., Garron, T., Narayanan, K., Peng, B. H., et al. (2016). Immunization with inactivated middle east respiratory syndrome coronavirus vaccine leads to lung immunopathology on challenge with live virus. *Hum. Vaccin. Immunother.* 12, 2351–2356. doi: 10.1080/21645515.2016.1177688

Al-Amri, S. S., Abbas, A. T., Siddiq, L. A., Alghamdi, A., Sanki, M. A., Al-Muhanna, M. K., et al. (2017). Immunogenicity of candidate MERS-CoV DNA vaccines based on the spike protein. *Sci. Rep.* 7:44875. doi: 10.1038/srep44875

Alagaili, A. N., Briese, T., Mishra, N., Kapoor, V., Sameroff, S. C., Burbelo, P. D., et al. (2014). Middle east respiratory syndrome coronavirus infection in dromedary camels in Saudi Arabia. *MBio* 5:e00884-e14. doi: 10.1128/mBio.00884-14

Alharbi, N. K., Padron-Regalado, E., Thompson, C. P., Kupke, A., Wells, D., Sloan, M. A., et al. (2017). ChAdOx1 and MVA based vaccine candidates against MERS-CoV elicit neutralising antibodies and cellular immune responses in mice. *Vaccine* 35, 3780–3788. doi: 10.1016/j.vaccine.2017.05.032

Almazan, F., DeDiego, M. L., Sola, I., Zuniga, S., Nieto-Torres, J. L., Marquez-Jurado, S., et al. (2013). Engineering a replication-competent, propagation-defective middle east respiratory syndrome coronavirus as a vaccine candidate. *MBio* 4:e00650-13. doi: 10.1128/mBio.00650-13

Baseler, L. J., Falzarano, D., Scott, D. P., Rosenke, R., Thomas, T., Munster, V. J., et al. (2016). An acute immune response to middle east respiratory syndrome coronavirus replication contributes to viral pathogenicity. *Am. J. Pathol.* 186, 630–638. doi: 10.1016/j.ajpath.2015.10.025

Bodmer, B. S., Fiedler, A. H., Hanauer, J. R. H., Prufer, S., and Muhlebach, M. D. (2018). Live-attenuated bivalent measles virus-derived vaccines targeting middle east respiratory syndrome coronavirus induce robust and multifunctional T cell responses against both viruses in an appropriate mouse model. *Virol* 521, 99–107. doi: 10.1016/j.virol.2018.05.028

Bukreyev, A., Lamirande, E. W., Buchholz, U. J., Vogel, L. N., Elkins, W. R., St Claire, M., et al. (2004). Mucosal immunisation of African green monkeys (*Cercopithecus aethiops*) with an attenuated parainfluenza virus expressing the SARS coronavirus spike protein for the prevention of SARS. *Lancet* 363, 2122–2127. doi: 10.1016/s0140-6736(04)16501-x

Carrion, R., Jr., and Patterson, J. L. (2012). An animal model that reflects human disease: the common marmoset (*Callithrix jacchus*). *Curr. Opi. Virol.* 2, 357–362. doi: 10.1016/j.coviro.2012.02.007

Cauchemez, S., Nouvellet, P., Cori, A., Jombart, T., Garske, T., Clapham, H., et al. (2016). Unraveling the drivers of MERS-CoV transmission. *Proc. Natl. Acad. Sci. U.S.A.* 113, 9081–9086. doi: 10.1073/pnas.1519235113

Chan, J. F., Yao, Y., Yeung, M. L., Deng, W., Bao, L., Jia, L., et al. (2015). Treatment with lopinavir/ritonavir or interferon-beta1b improves outcome of MERS-CoV infection in a nonhuman primate model of common marmoset. *J. Infect. Dis.* 212, 1904–1913. doi: 10.1093/infdis/jiv392

Channappanavar, R., Zhao, J., and Perlman, S. (2014). T cell-mediated immune response to respiratory coronaviruses. *Immunol. Res.* 59, 118–128. doi: 10.1007/s12026-014-8534-z

Chen, Z., Bao, L., Chen, C., Zou, T., Xue, Y., Li, F., et al. (2017). Human neutralizing monoclonal antibody inhibition of middle east respiratory syndrome coronavirus replication in the common marmoset. *J. Infect. Dis.* 215, 1807–1815. doi: 10.1093/infdis/jix209

Chi, H., Zheng, X., Wang, X., Wang, C., Wang, H., Gai, W., et al. (2017). DNA vaccine encoding middle east respiratory syndrome coronavirus S1 protein induces protective immune responses in mice. *Vaccine* 35, 2069–2075. doi: 10.1016/j.vaccine.2017.02.063

Chowell, G., Abdirizak, F., Lee, S., Lee, J., Jung, E., Nishiura, H., et al. (2015). Transmission characteristics of MERS and SARS in the healthcare setting: a comparative study. *BMC Med.* 13:210. doi: 10.1186/s12916-015-0450-450

Chu, D. K., Poon, L. L., Gomaa, M. M., Shehata, M. M., Perera, R. A., Abu Zeid, D., et al. (2014). MERS coronaviruses in dromedary camels, Egypt. *Emerg. Infect. Dis.* 20, 1049–1053. doi: 10.3201/eid2006.140299

Chu, H., Zhou, J., Wong, B. H., Li, C., Chan, J. F., Cheng, Z. S., et al. (2016). Middle east respiratory syndrome coronavirus rfficiently infects human primary T lymphocytes and activates the extrinsic and intrinsic apoptosis pathways. *J. Infect. Dis.* 213, 904–914. doi: 10.1093/infdis/jiv380

Chu, H., Zhou, J., Wong, B. H., Li, C., Cheng, Z. S., Lin, X., et al. (2014). Productive replication of middle east respiratory syndrome coronavirus

in monocyte-derived dendritic cells modulates innate immune response. *Virol* 454-455, 197–205. doi: 10.1016/j.virol.2014.02.018

Cockrell, A. S., Yount, B. L., Scobey, T., Jensen, K., Douglas, M., Beall, A., et al. (2016). A mouse model for MERS coronavirus-induced acute respiratory distress syndrome. *Nat. Microbiol.* 2:16226. doi: 10.1038/nmicrobiol.2016.226

Coleman, C. M., Liu, Y. V., Mu, H., Taylor, J. K., Massare, M., Flyer, D. C., et al. (2014). Purified coronavirus spike protein nanoparticles induce coronavirus neutralizing antibodies in mice. *Vaccine* 32, 3169–3174. doi: 10.1016/j.vaccine.2014.04.016

Coleman, C. M., Venkataraman, T., Liu, Y. V., Glenn, G. M., Smith, G. E., Flyer, D. C., et al. (2017). MERS-CoV spike nanoparticles protect mice from MERS-CoV infection. *Vaccine* 35, 1586–1589. doi: 10.1016/j.vaccine.2017.02.012

Czub, M., Weingartl, H., Czub, S., He, R., and Cao, J. (2005). Evaluation of modified vaccinia virus ankara based recombinant SARS vaccine in ferrets. *Vaccine* 23, 2273–2279. doi: 10.1016/j.vaccine.2005.01.033

de Wit, E., Feldmann, F., Horne, E., Okumura, A., Cameroni, E., Haddock, E., et al. (2019). Prophylactic efficacy of a human monoclonal antibody against MERS-CoV in the common marmoset. *Antiviral. Res.* 163, 70–74. doi: 10.1016/j.antiviral.2019.01.016

de Wit, E., Rasmussen, A. L., Falzarano, D., Bushmaker, T., Feldmann, F., Brining, D. L., et al. (2013). Middle east respiratory syndrome coronavirus (MERS-CoV) causes transient lower respiratory tract infection in rhesus macaques. *Proc. Natl. Acad. Sci. U.S.A.* 110, 16598–16603. doi: 10.1073/pnas.1310744110

Deng, Y., Lan, J., Bao, L., Huang, B., Ye, F., Chen, Y., et al. (2018). Enhanced protection in mice induced by immunization with inactivated whole viruses compare to spike protein of middle east respiratory syndrome coronavirus. *Emerg. Microbes. Infect.* 7:60. doi: 10.1038/s41426-018-0056-57

DeZure, A. D., Berkowitz, N. M., Graham, B. S., and Ledgerwood, J. E. (2016). Whole-Inactivated and virus-like particle vaccine strategies for chikungunya virus. *J. Infect. Dis.* 214(suppl. 5), S497–S499. doi: 10.1093/infdis/jiw352

Dicks, M. D. J., Spencer, A. J., Edwards, N. J., Wadell, G., Bojang, K., Gilbert, S. C., et al. (2012). A novel chimpanzee adenovirus vector with low human seroprevalence: improved systems for vector derivation and comparative immunogenicity. *PLoS One* 7:e40385. doi: 10.1371/journal.pone.0040385

Du, L., and Jiang, S. (2015). Middle east respiratory syndrome: current status and future prospects for vaccine development. *Exp. Opin. Biol. Ther.* 15, 1647–1651. doi: 10.1517/14712598.2015.1092518

Du, L., Kou, Z., Ma, C., Tao, X., Wang, L., Zhao, G., et al. (2013). A truncated receptor-binding domain of MERS-CoV spike protein potently inhibits MERS-CoV infection and induces strong neutralizing antibody responses: implication for developing therapeutics and vaccines. *PLoS One* 8:e81587. doi: 10.1371/journal.pone.0081587

Du, L., Tai, W., Yang, Y., Zhao, G., Zhu, Q., Sun, S., et al. (2016a). Introduction of neutralizing immunogenicity index to the rational design of MERS coronavirus subunit vaccines. *Nat. Commun.* 7:13473. doi: 10.1038/ncomms13473

Du, L., Tai, W., Zhou, Y., and Jiang, S. (2016b). Vaccines for the prevention against the threat of MERS-CoV. *Expert. Rev. Vaccines* 15, 1123–1134. doi: 10.1586/14760584.2016.1167603

Du, L., Yang, Y., Zhou, Y., Lu, L., Li, F., and Jiang, S. (2017). MERS-CoV spike protein: a key target for antivirals. *Expert. Opin. Ther. Targets* 21, 131–143. doi: 10.1080/14728222.2017.1271415

Dutry, I., Yen, H. L. Lee, H., Peiris, M., and Jaume, M. (2011). Antibody-dependent enhancement (ADE) of infection and its possible role in the pathogenesis of influenza. *BMC Proc.* 5(Suppl. 1):P62. doi: 10.1186/1753-6561-5-S1-P62

Falzarano, D., de Wit, E., Feldmann, F., Rasmussen, A. L., Okumura, A., Peng, X., et al. (2014). Infection with MERS-CoV causes lethal pneumonia in the common marmoset. *PLoS Pathog.* 10:e1004250. doi: 10.1371/journal.ppat.1004250

Fan, C., Wu, X., Liu, Q., Li, Q., Liu, S., Lu, J., et al. (2018). A human DPP4-knockin mouse's susceptibility to infection by authentic and pseudotyped MERS-CoV. *Viruses* 10:E448. doi: 10.3390/v10090448

Fausther-Bovendo, H., and Kobinger, G. P. (2014). Pre-existing immunity against Ad vectors: humoral, cellular, and innate response, what's important? *Hum. Vaccines Immunother.* 10, 2875–2884. doi: 10.4161/hv.29594

Ferraro, B., Morrow, M. P., Hutnick, N. A., Shin, T. H., Lucke, C. E., and Weiner, D. B. (2011). Clinical applications of DNA vaccines: current progress. *Clin. Infect. Dis.* 53, 296–302. doi: 10.1093/cid/cir334

Fett, C., DeDiego, M. L., Regla-Nava, J. A., Enjuanes, L., and Perlman, S. (2013). Complete protection against severe acute respiratory syndrome coronavirus-mediated lethal respiratory disease in aged mice by immunization with a mouse-adapted virus lacking E protein. *J. Virol.* 87, 6551–6559. doi: 10.1128/jvi.00087-13

Gerdts, V., Littel-van den Hurk, S. V. D., Griebel, P. J., and Babiuk, L. A. (2007). Use of animal models in the development of human vaccines. *Future Microbio.* 2, 667–675. doi: 10.2217/17460913.2.6.667

Gerdts, V., Wilson, H. L., Meurens, F., van Drunen Littel-van den Hurk, S., Wilson, D., Walker, S., et al. (2015). Large animal models for vaccine development and testing. *ILAR J.* 56, 53–62. doi: 10.1093/ilar/ilv009

Goldstein, S. A., and Weiss, S. R. (2017). Origins and pathogenesis of middle east respiratory syndrome-associated coronavirus: recent advances. *F1000Res* 6:1628. doi: 10.12688/f1000research.11827.1

Gossner, C., Danielson, N., Gervelmeyer, A., Berthe, F., Faye, B., Kaasik Aaslav, K., et al. (2016). Human-dromedary camel interactions and the risk of acquiring zoonotic middle east respiratory syndrome coronavirus infection. *Zoonoses Public Health* 63, 1–9. doi: 10.1111/zph.12171

Guo, X., Deng, Y., Chen, H., Lan, J., Wang, W., Zou, X., et al. (2015). Systemic and mucosal immunity in mice elicited by a single immunization with human adenovirus type 5 or 41 vector-based vaccines carrying the spike protein of Middle East respiratory syndrome coronavirus. *Immunology* 145, 476–484. doi: 10.1111/imm.12462

Haagmans, B. L., van den Brand, J. M., Provacia, L. B., Raj, V. S., Stittelaar, K. J., Getu, S., et al. (2015). Asymptomatic middle east respiratory syndrome coronavirus infection in rabbits. *J. Virol.* 89, 6131–6135. doi: 10.1128/JVI.00661-615

Haagmans, B. L., van den Brand, J. M., Raj, V. S., Volz, A., Wohlsein, P., Smits, S. L., et al. (2016). An orthopoxvirus-based vaccine reduces virus excretion after MERS-CoV infection in dromedary camels. *Science* 351, 77–81. doi: 10.1126/science.aad1283

Hakoum, M. B., Jouni, N., Abou-Jaoude, E. A., Hasbani, D. J., Abou-Jaoude, E. A., Lopes, L. C., et al. (2017). Characteristics of funding of clinical trials: cross-sectional survey and proposed guidance. *BMJ Open* 7:e015997. doi: 10.1136/bmjopen-2017-015997

Hashem, A. M., Algaissi, A., Agrawal, A., Al-Amri, S. S., Alhabbab, R. Y., Sohrab, S. S., et al. (2019). A highly immunogenic, protective and safe adenovirus-based vaccine expressing MERS-CoV S1-CD40L fusion protein in transgenic human DPP4 mouse model. *J. Infect. Dis.* 26:jiz137. doi: 10.1093/infdis/jiz137

He, Y., Li, J., Li, W., Lustigman, S., Farzan, M., and Jiang, S. (2006). Cross-neutralization of human and palm civet severe acute respiratory syndrome coronaviruses by antibodies targeting the receptor-binding domain of spike protein. *J. Immunol.* 176, 6085–6092. doi: 10.4049/jimmunol.176.10.6085

Jaume, M., Yip, M. S., Kam, Y. W., Cheung, C. Y., Kien, F., Roberts, A., et al. (2012). SARS CoV subunit vaccine: antibody-mediated neutralisation and enhancement. *Hong Kong Med. J.* 18 (Suppl. 2), 31–36.

Jiaming, L., Yanfeng, Y., Yao, D., Yawei, H., Linlin, B., Baoying, H., et al. (2017). The recombinant N-terminal domain of spike proteins is a potential vaccine against Middle East respiratory syndrome coronavirus (MERS-CoV) infection. *Vaccine* 35, 10–18. doi: 10.1016/j.vaccine.2016.11.064

Jung, S. Y., Kang, K. W., Lee, E. Y., Seo, D. W., Kim, H. L., Kim, H., et al. (2018). Heterologous prime-boost vaccination with adenoviral vector and protein nanoparticles induces both Th1 and Th2 responses against middle east respiratory syndrome coronavirus. *Vaccine* 36, 3468–3476. doi: 10.1016/j.vaccine.2018.04.082

Kaech, S. M., and Ahmed, R. (2001). Memory CD8+ T cell differentiation: initial antigen encounter triggers a developmental program in naïve cells. *Nat. Immunol.* 2, 415–422. doi: 10.1038/87720

Kam, Y. W., Kien, F., Roberts, A., Cheung, Y. C., Lamirande, E. W., Vogel, L., et al. (2007). Antibodies against trimeric S glycoprotein protect hamsters against SARS-CoV challenge despite their capacity to mediate FcgammaRII-dependent entry into B cells *in vitro*. *Vaccine* 25, 729–740. doi: 10.1016/j.vaccine.2006.08.011

Kim, E., Okada, K., Kenniston, T., Raj, V. S., AlHajri, M. M., Farag, E. A., et al. (2014). Immunogenicity of an adenoviral-based middle east respiratory Syndrome coronavirus vaccine in BALB/c mice. *Vaccine* 32, 5975–5982. doi: 10.1016/j.vaccine.2014.08.058

Kim, Y. S., Son, A., Kim, J., Kwon, S. B., Kim, M. H., Kim, P., et al. (2018). Chaperna-mediated assembly of ferritin-based middle east respiratory syndrome-coronavirus nanoparticles. *Front. Immunol.* 9:1093. doi: 10.3389/fimmu.2018.01093

Kuzmina, N. A., Younan, P., Gilchuk, P., Santos, R. I., Flyak, A. I., Ilinykh, P. A., et al. (2018). Antibody-dependent enhancement of ebola virus infection by human antibodies isolated from survivors. *Cell Rep.* 24, 1802.e5–1815.e5. doi: 10.1016/j.celrep.2018.07.035

Lan, J., Deng, Y., Chen, H., Lu, G., Wang, W., Guo, X., et al. (2014). Tailoring subunit vaccine immunity with adjuvant combinations and delivery routes using the middle east respiratory coronavirus (MERS-CoV) receptor-binding domain as an antigen. *PLoS One* 9:e112602. doi: 10.1371/journal.pone.0112602

Lan, J., Deng, Y., Song, J., Huang, B., Wang, W., and Tan, W. (2018). Significant spike-specific IgG and neutralizing antibodies in mice induced by a novel chimeric virus-iike particle vaccine candidate for middle east respiratory syndrome coronavirus. *Virol. Sin.* 33, 453–455. doi: 10.1007/s12250-018-0064-68

Lan, J., Yao, Y., Deng, Y., Chen, H., Lu, G., Wang, W., et al. (2015). Recombinant receptor binding domain protein induces partial protective immunity in rhesus macaques against middle east respiratory syndrome coronavirus challenge. *EBioMedicine* 2, 1438–1446. doi: 10.1016/j.ebiom.2015.08.031

Lauring, A. S., Jones, J. O., and Andino, R. (2010). Rationalizing the development of live attenuated virus vaccines. *Nat. Biotechnol.* 28, 573–579. doi: 10.1038/nbt.1635

Ledwith, B. J., Manam, S., Troilo, P. J., Barnum, A. B., Pauley, C. J., Griffiths, T. G., et al. (2000). Plasmid DNA vaccines: assay for integration into host genomic DNA. *Dev. Biol.* 104, 33–43.

Leitner, W. W., Ying, H., and Restifo, N. P. (1999). DNA and RNA-based vaccines: principles, progress and prospects. *Vaccine* 18, 765–777. doi: 10.1016/s0264-410x(99)00271-6

Lin, J. T., Zhang, J. S., Su, N., Xu, J. G., Wang, N., Chen, J. T., et al. (2007). Safety and immunogenicity from a phase I trial of inactivated severe acute respiratory syndrome coronavirus vaccine. *Antivir. Ther.* 12, 1107–1113.

Liu, R. Q., Ge, J. Y., Wang, J. L., Shao, Y., Zhang, H. L., Wang, J. L., et al. (2017). Newcastle disease virus-based MERS-CoV candidate vaccine elicits high-level and lasting neutralizing antibodies in Bactrian camels. *J. Integrat. Agri.* 16, 2264–2273. doi: 10.1016/S2095-3119(17)6166061665

Liu, R., Wang, J., Shao, Y., Wang, X., Zhang, H., Shuai, L., et al. (2018). A recombinant VSV-vectored MERS-CoV vaccine induces neutralizing antibody and T cell responses in rhesus monkeys after single dose immunization. *Antiviral. Res.* 150, 30–38. doi: 10.1016/j.antiviral.2017.12.007

Ma, C., Li, Y., Wang, L., Zhao, G., Tao, X., Tseng, C. T. K., et al. (2014a). Intranasal vaccination with recombinant receptor-binding domain of MERS-CoV spike protein induces much stronger local mucosal immune responses than subcutaneous immunization: implication for designing novel mucosal MERS vaccines. *Vaccine* 32, 2100–2108. doi: 10.1016/j.vaccine.2014.02.004

Ma, C., Wang, L., Tao, X., Zhang, N., Yang, Y., Tseng, C. K., et al. (2014b). Searching for an ideal vaccine candidate among different MERS coronavirus receptor-binding fragments–the importance of immunofocusing in subunit vaccine design. *Vaccine* 32, 6170–6176. doi: 10.1016/j.vaccine.2014.08.086

MacLeod, M. K. L., Kappler, J. W., and Marrack, P. (2010). Memory CD4 T cells: generation, reactivation and re-assignment. *Immunology* 130, 10–15. doi: 10.1111/j.1365-2567.2010.03260.x

Malczyk, A. H., Kupke, A., Prufer, S., Scheuplein, V. A., Hutzler, S., Kreuz, D., et al. (2015). A highly immunogenic and protective middle east respiratory syndrome coronavirus vaccine based on a recombinant measles virus vaccine platform. *J. Virol.* 89, 11654–11667. doi: 10.1128/JVI.01815-1815

Memish, Z. A., Cotten, M., Meyer, B., Watson, S. J., Alsahafi, A. J., Al Rabeeah, A. A., et al. (2014). Human infection with MERS coronavirus after exposure to infected camels, Saudi Arabia, 2013. *Emerg. Infect. Dis.* 20, 1012–1015. doi: 10.3201/eid2006.140402

Menachery, V. D., Gralinski, L. E., Mitchell, H. D., Dinnon, K. H., 3rd, Leist, S. R., Yount, B. L., et al. (2017). Middle east respiratory syndrome coronavirus nonstructural protein 16 Is necessary for interferon resistance and viral pathogenesis. *mSphere* 2:e00346-17.

Moss, B., Smith, G. L., Gerin, J. L., and Purcell, R. H. (1984). Live recombinant vaccinia virus protects chimpanzees against hepatitis B. *Nature* 311, 67–69. doi: 10.1038/311067a0

Munster, V. J., de Wit, E., and Feldmann, H. (2013). Pneumonia from human coronavirus in a macaque model. *N. Engl. J. Med.* 368, 1560–1562. doi: 10.1056/NEJMc1215691

Munster, V. J., Wells, D., Lambe, T., Wright, D., Fischer, R. J., Bushmaker, T., et al. (2017). Protective efficacy of a novel simian adenovirus vaccine against lethal MERS-CoV challenge in a transgenic human DPP4 mouse model. *NPJ Vaccines* 2:28. doi: 10.1038/s41541-017-0029-21

Murata, K., Lechmann, M., Qiao, M., Gunji, T., Alter, H. J., and Liang, T. J. (2003). Immunization with hepatitis C virus-like particles protects mice from recombinant hepatitis C virus-vaccinia infection. *Proc. Natl. Acad. Sci. U.S.A.* 100, 6753–6758. doi: 10.1073/pnas.1131929100

Muthumani, K., Falzarano, D., Reuschel, E.L., Tingey, C., Flingai, S., Villarreal, D.O., et al. (2015). A synthetic consensus anti-spike protein DNA vaccine induces protective immunity against middle east respiratory syndrome coronavirus in nonhuman primates. *Sci. Trans. Med.* 7:301ra132. doi: 10.1126/scitranslmed.aac7462

National Institutes of Health [NIH] (2016). *Phase I, Open Label Dose Ranging Safety Study of GLS-5300 in Healthy Volunteers*. Available at: https://clinicaltrials.gov/ct2/show/NCT02670187?term=GLS-5300 (accessed February 25, 2019).

National Institutes of Health [NIH] (2018a). *Evaluate the Safety, Tolerability and Immunogenicity Study of GLS-5300 in Healthy Volunteers.* Available at: https://clinicaltrials.gov/ct2/show/NCT03721718 (accessed June 2019).

National Institutes of Health [NIH] (2018b). *Safety and Immunogenicity of a Candidate MERS-CoV Vaccine (MERS001)*. Available at: https://clinicaltrials.gov/ct2/show/study/NCT03399578 (accessed February 25, 2019).

National Institutes of Health [NIH] (2018c). *Safety, Tolerability and Immunogenicity of Vaccine Candidate MVA-MERS-S.* Available at: https://clinicaltrials.gov/ct2/show/NCT03615911#outcomemeasures (accessed February 25, 2019).

Nyon, M. P., Du, L., Tseng, C. K., Seid, C. A., Pollet, J., Naceanceno, K. S., et al. (2018). Engineering a stable CHO cell line for the expression of a MERS-coronavirus vaccine antigen. *Vaccine* 36, 1853–1862. doi: 10.1016/j.vaccine.2018.02.065

Oh, M. -D., Park, W. B., Park, S. -W., Choe, P. G., Bang, J. H., Song, K. -H., et al. (2018). Middle east respiratory syndrome: what we learned from the 2015 outbreak in the Republic of Korea. *Korean J. Int. Med.* 33, 233–246. doi: 10.3904/kjim.2018.031

Okba, N. M., Raj, V. S., and Haagmans, B. L. (2017). Middle east respiratory syndrome coronavirus vaccines: current status and novel approaches. *Curr. Opin. Virol.* 23, 49-58. doi: 10.1016/j.coviro.2017.03.007

Ong, H. K., Tan, W. S., and Ho, K. L. (2017). Virus like particles as a platform for cancer vaccine development. *PeerJ* 5:e4053. doi: 10.7717/peerj.4053

Pallesen, J., Wang, N., Corbett, K. S., Wrapp, D., Kirchdoerfer, R. N., Turner, H. L., et al. (2017). Immunogenicity and structures of a rationally designed prefusion MERS-CoV spike antigen. *Proc. Natl. Acad. Sci. U.S.A.* 114, E7348–E7357. doi: 10.1073/pnas.1707304114

Pascal, K. E., Coleman, C. M., Mujica, A. O., Kamat, V., Badithe, A., Fairhurst, J., et al. (2015). Pre- and postexposure efficacy of fully human antibodies against spike protein in a novel humanized mouse model of MERS-CoV infection. *Proc. Natl. Acad. Sci. U.S.A.* 112, 8738–8743. doi: 10.1073/pnas.1510830112

Payne, D. C., Iblan, I., Rha, B., Alqasrawi, S., Haddadin, A., Al Nsour, M., et al. (2016). Persistence of antibodies against middle east respiratory syndrome coronavirus. *Emerg. Infect. Dis.* 22, 1824–1826. doi: 10.3201/eid2210.160706

Perlman, S., and Vijay, R. (2016). Middle east respiratory syndrome vaccines. *Int. J. Infect. Dis.* 47, 23–28. doi: 10.1016/j.ijid.2016.04.008

Prescott, J., Falzarano, D., de Wit, E., Hardcastle, K., Feldmann, F., Haddock, E., et al. (2018). Pathogenicity and viral shedding of MERS-CoV in immunocompromised rhesus macaques. *Front. Immunol.* 9:205. doi: 10.3389/fimmu.2018.00205

Quan, F. S., Compans, R. W., Nguyen, H. H., and Kang, S. M. (2008). Induction of heterosubtypic immunity to influenza virus by intranasal immunization. *J. Virol.* 82, 1350–1359. doi: 10.1128/jvi.01615-1617

Schindewolf, C., and Menachery, V. D. (2019). Middle east respiratory syndrome vaccine candidates: cautious optimism. *Viruses* 11:E74. doi: 10.3390/v11010074

Scobey, T., Yount, B. L., Sims, A. C., Donaldson, E. F., Agnihothram, S. S., Menachery, V. D., et al. (2013). Reverse genetics with a full-length infectious cDNA of the middle east respiratory syndrome coronavirus. *Proc. Natl. Acad. Sci. U.S.A.* 110, 16157–16162. doi: 10.1073/pnas.1311542110

Shi, J., Zhang, J., Li, S., Sun, J., Teng, Y., Wu, M., et al. (2015). Epitope-based vaccine target screening against highly pathogenic MERS-CoV: an *in silico* approach applied to emerging infectious diseases. *PLoS One* 10:e0144475. doi: 10.1371/journal.pone.0144475

Sibal, L. R., and Samson, K. J. (2001). Nonhuman primates: a critical role in current disease research. *ILAR J.* 42, 74–84. doi: 10.1093/ilar.42.2.74.

Smith, R. (2000). Vaccines and medicines for the world's poorest. Public-private partnerships seem to be essential. *BMJ* 320, 952–953. doi: 10.1136/bmj.320.7240.952

Song, F., Fux, R., Provacia, L. B., Volz, A., Eickmann, M., Becker, S., et al. (2013). Middle east respiratory syndrome coronavirus spike protein delivered by modified vaccinia virus Ankara efficiently induces virus-neutralizing antibodies. *J. Virol.* 87, 11950–11954. doi: 10.1128/JVI.01672-1613

Srivastava, S., Kamthania, M., Singh, S., Saxena, A. K., and Sharma, N. (2018). Structural basis of development of multi-epitope vaccine against middle east respiratory syndrome using *in silico* approach. *Infect. Drug Resist.* 11, 2377–2391. doi: 10.2147/idr.s175114

Swearengen, J. R. (2018). Choosing the right animal model for infectious disease research. *Animal Model Exp. Med.* 1, 100–108. doi: 10.1002/ame2.12020

Tai, W., Wang, Y., Fett, C. A., Zhao, G., Li, F., Perlman, S., et al. (2017). Recombinant receptor-binding domains of multiple middle east respiratory syndrome coronaviruses (MERS-CoVs) induce cross-neutralizing antibodies against divergent human and camel MERS-CoVs and antibody escape mutants. *J. Virol.* 91:e01651-16. doi: 10.1128/JVI.01651-1616

Tai, W., Zhao, G., Sun, S., Guo, Y., Wang, Y., Tao, X., et al. (2016). A recombinant receptor-binding domain of MERS-CoV in trimeric form protects human dipeptidyl peptidase 4 (hDPP4) transgenic mice from MERS-CoV infection. *Virol* 499, 375–382. doi: 10.1016/j.virol.2016.10.005

Tang, F., Quan, Y., Xin, Z. T., Wrammert, J., Ma, M. J., Lv, H., et al. (2011). Lack of peripheral memory B cell responses in recovered patients with severe acute respiratory syndrome: a six-year follow-up study. *J. Immunol.* 186, 7264–7268. doi: 10.4049/jimmunol.0903490

Tang, J., Zhang, N., Tao, X., Zhao, G., Guo, Y., Tseng, C. T., et al. (2015). Optimization of antigen dose for a receptor-binding domain-based subunit vaccine against MERS coronavirus. *Hum. Vaccin. Immunother.* 11, 1244–1250. doi: 10.1080/21645515.2015.1021527

Tang, X. -C., Agnihothram, S. S., Jiao, Y., Stanhope, J., Graham, R. L., Peterson, E. C., et al. (2014). Identification of human neutralizing antibodies against MERS-CoV and their role in virus adaptive evolution. *Proc. Natl. Acad. Sci. U.S.A.* 111:E2018. doi: 10.1073/pnas.1402074111

Ura, T., Okuda, K., and Shimada, M. (2014). Developments in viral vector-based vaccines. *Vaccines* 2, 624–641. doi: 10.3390/vaccines2030624

van Boheemen, S., de Graaf, M., Lauber, C., Bestebroer, T. M., Raj, V. S., Zaki, A. M., et al. (2012). Genomic characterization of a newly discovered coronavirus associated with acute respiratory distress syndrome in humans. *MBio* 3:e00473-12. doi: 10.1128/mBio.00473-412

van Doremalen, N., Falzarano, D., Ying, T., de Wit, E., Bushmaker, T., Feldmann, F., et al. (2017). Efficacy of antibody-based therapies against middle east respiratory syndrome coronavirus (MERS-CoV) in common marmosets. *Antiviral Res.* 143, 30–37. doi: 10.1016/j.antiviral.2017.03.025

van Doremalen, N., and Munster, V. J. (2015). Animal models of middle east respiratory syndrome coronavirus infection. *Antiviral Res.* 122, 28–38. doi: 10.1016/j.antiviral.2015.07.005

Veit, S., Jany, S., Fux, R., Sutter, G., and Volz, A. (2018). CD8+ T cells responding to the middle east respiratory syndrome coronavirus nucleocapsid protein delivered by vaccinia virus MVA in mice. *Viruses* 10:718. doi: 10.3390/v10120718

Volz, A., Kupke, A., Song, F., Jany, S., Fux, R., Shams-Eldin, H., et al. (2015). Protective efficacy of recombinant modified vaccinia virus ankara delivering middle east respiratory syndrome coronavirus spike glycoprotein. *J. Virol.* 89, 8651–8656. doi: 10.1128/JVI.00614-615

Wang, C., Zheng, X., Gai, W., Wong, G., Wang, H., Jin, H., et al. (2017a). Novel chimeric virus-like particles vaccine displaying MERS-CoV receptor-binding domain induce specific humoral and cellular immune response in mice. *Antiviral Res.* 140, 55–61. doi: 10.1016/j.antiviral.2016.12.019

Wang, C., Zheng, X., Gai, W., Zhao, Y., Wang, H., Wang, H., et al. (2017b). MERS-CoV virus-like particles produced in insect cells induce specific humoural and cellular imminity in rhesus macaques. *Oncotarget* 8, 12686–12694.

Wang, L., Shi, W., Joyce, M. G., Modjarrad, K., Zhang, Y., Leung, K., et al. (2015a). Evaluation of candidate vaccine approaches for MERS-CoV. *Nat. Commun.* 6:7712. doi: 10.1038/ncomms8712

Wang, Y., Liu, D., Shi, W., Lu, R., Wang, W., Zhao, Y., et al. (2015b). Origin and possible genetic recombination of the middle east respiratory syndrome coronavirus from the rirst imported case in China: phylogenetics and coalescence analysis. *MBio* 6, e1280-15. doi: 10.1128/mBio.01280-1215

Wang, Y., Tai, W., Yang, J., Zhao, G., Sun, S., Tseng, C. K., et al. (2017c). Receptor-binding domain of MERS-CoV with optimal immunogen dosage and immunization interval protects human transgenic mice from MERS-CoV infection. *Hum. Vaccin. Immunother.* 13, 1615–1624. doi: 10.1080/21645515.2017.1296994

Weingartl, H., Czub, M., Czub, S., Neufeld, J., Marszal, P., Gren, J., et al. (2004). Immunization with modified vaccinia virus ankara-based recombinant vaccine against severe acute respiratory syndrome is associated with enhanced hepatitis in ferrets. *J. Virol.* 78:12672. doi: 10.1128/JVI.78.22.12672-12676.2004

World Health Organization [WHO] (2019a). *MERS Situation Update*. Available at: http://applications.emro.who.int/docs/EMROPub_2019_EN_22346.pdf?ua=1&ua=1 (accessed May 2019).

World Health Organization [WHO] (2019b). *Middle East Respiratory Syndrome Coronavirus (MERS-CoV)*. Available at: https://www.who.int/emergencies/mers-cov/en/ (accessed May 2019).

Wirblich, C., Coleman, C. M., Kurup, D., Abraham, T. S., Bernbaum, J. G., Jahrling, P. B., et al. (2017). One-Health: a safe, efficient, dual-use vaccine for humans and animals against middle east respiratory syndrome coronavirus and rabies Virus. *J. Virol.* 91, e02040-16

Xie, Q., He, X., Yang, F., Liu, X., Li, Y., Liu, Y., et al. (2018). Analysis of the genome sequence and prediction of B-Cell epitopes of the envelope protein of middle east respiratory syndrome-coronavirus. *IEEE/ACM Trans. Comput. Biol. Bioinf.* 15, 1344–1350. doi: 10.1109/tcbb.2017.2702588

Yang, Z. -Y., Kong, W. -P., Huang, Y., Roberts, A., Murphy, B. R., Subbarao, K., et al. (2004). A DNA vaccine induces SARS coronavirus neutralization and protective immunity in mice. *Nature* 428, 561–564. doi: 10.1038/nature02463

Yeung, M. L., Yao, Y., Jia, L., Chan, J. F., Chan, K. H., Cheung, K. F., et al. (2016). MERS coronavirus induces apoptosis in kidney and lung by upregulating Smad7 and FGF2. *Nat. Microbiol.* 1:16004. doi: 10.1038/nmicrobiol.2016.4

Yip, M. S., Cheung, C. Y., Li, P. H., Bruzzone, R., Peiris, J. S. M., and Jaume, M. (2011). Investigation of antibody-dependent enhancement (ADE) of SARS coronavirus infection and its role in pathogenesis of SARS. *BMC Proc.* 5(Suppl. 1):P80.

Yong, C. Y., Yeap, S. K., Goh, Z. H., Ho, K. L., Omar, A. R., and Tan, W. S. (2015a). Induction of humoral and cell-mediated immune responses by hepatitis B virus epitope displayed on the virus-Like particles of prawn nodavirus. *Appl. Environ. Microbiol.* 81, 882–889. doi: 10.1128/AEM.03695-3614

Yong, C. Y., Yeap, S. K., Ho, K. L., Omar, A. R., and Tan, W. S. (2015b). Potential recombinant vaccine against influenza A virus based on M2e displayed on nodaviral capsid nanoparticles. *Int. J. Nanomed.* 10, 2751–2763. doi: 10.2147/IJN.S77405

Yu, P., Xu, Y., Deng, W., Bao, L., Huang, L., Xu, Y., et al. (2017). Comparative pathology of rhesus macaque and common marmoset animal models with middle east respiratory syndrome coronavirus. *PLoS One* 12:e0172093. doi: 10.1371/journal.pone.0172093

Zaki, A. M., Van Boheemen, S., Bestebroer, T. M., Osterhaus, A. D., and Fouchier, R. A. (2012). Isolation of a novel coronavirus from a man with pneumonia in Saudi Arabia. *N. Engl. J. Med.* 367, 1814–1820. doi: 10.1056/NEJMoa1211172

Zhang, N., Channappanavar, R., Ma, C., Wang, L., Tang, J., Garron, T., et al. (2016). Identification of an ideal adjuvant for receptor-binding domain-based subunit vaccines against middle east respiratory syndrome coronavirus. *Cell Mol. Immunol.* 13, 180–190. doi: 10.1038/cmi.2015.03

Zhao, J., Alshukairi, A. N., Baharoon, S. A., Ahmed, W. A., Bokhari, A. A., Nehdi, A. M., et al. (2017). Recovery from the middle east respiratory syndrome is associated with antibody and T-cell responses. *Sci. Immunol.* 2:eaan5393. doi: 10.1126/sciimmunol.aan5393

Zhao, J., Li, K., Wohlford-Lenane, C., Agnihothram, S. S., Fett, C., Zhao, J., et al. (2014). Rapid generation of a mouse model for middle east respiratory

syndrome. *Proc. Natl. Acad. Sci. U.S.A.* 111, 4970–4975. doi: 10.1073/pnas.1323279111

Zhao, J., Perera, R. A., Kayali, G., Meyerholz, D., Perlman, S., and Peiris, M. (2015). Passive immunotherapy with dromedary immune serum in an experimental animal model for middle east respiratory syndrome coronavirus infection. *J. Virol.* 89, 6117–6120. doi: 10.1128/JVI.00446-415

Zhao, J., Zhao, J., Mangalam, A. K., Channappanavar, R., Fett, C., Meyerholz, D. K., et al. (2016). Airway Memory CD4(+) T cells mediate protective immunity against emerging respiratory coronaviruses. *Immunity* 44, 1379–1391. doi: 10.1016/j.immuni.2016.05.006

Conflict of Interest Statement: The authors declare that the research was conducted in the absence of any commercial or financial relationships that could be construed as a potential conflict of interest.

CORONAVIRUS

A highly conserved cryptic epitope in the receptor binding domains of SARS-CoV-2 and SARS-CoV

Meng Yuan[1]*, Nicholas C. Wu[1]*, Xueyong Zhu[1], Chang-Chun D. Lee[1], Ray T. Y. So[2], Huibin Lv[2], Chris K. P. Mok[2]†, Ian A. Wilson[1,3]†

The outbreak of coronavirus disease 2019 (COVID-19) caused by severe acute respiratory syndrome–coronavirus 2 (SARS-CoV-2) has now become a pandemic, but there is currently very little understanding of the antigenicity of the virus. We therefore determined the crystal structure of CR3022, a neutralizing antibody previously isolated from a convalescent SARS patient, in complex with the receptor binding domain (RBD) of the SARS-CoV-2 spike (S) protein at 3.1-angstrom resolution. CR3022 targets a highly conserved epitope, distal from the receptor binding site, that enables cross-reactive binding between SARS-CoV-2 and SARS-CoV. Structural modeling further demonstrates that the binding epitope can only be accessed by CR3022 when at least two RBDs on the trimeric S protein are in the "up" conformation and slightly rotated. These results provide molecular insights into antibody recognition of SARS-CoV-2.

The ongoing outbreak of coronavirus disease 2019 (COVID-19) originated in China in December 2019 (*1*) and became a global pandemic by March 2020. COVID-19 is caused by a novel coronavirus, severe acute respiratory syndrome–coronavirus 2 (SARS-CoV-2) (*2*). Two other coronaviruses have caused worldwide outbreaks in the past two decades, namely SARS-CoV (2002–2003) and Middle East respiratory syndrome coronavirus (MERS-CoV) (2012–present). The surface spike (S) glycoprotein, which is critical for virus entry through engaging the host receptor and mediating virus-host membrane fusion, is the major antigen of coronaviruses. The S proteins of SARS-CoV-2 and SARS-CoV, which are phylogenetically closely related, have an amino acid sequence identity of ~77% (*3*). Such a high degree of sequence similarity raises the possibility that cross-reactive epitopes may exist.

CR3022, which was previously isolated from a convalescent SARS patient, is a neutralizing antibody that targets the receptor binding domain (RBD) of SARS-CoV (*4*). The immunoglobulin heavy chain variable, diversity, and joining (IGHV, IGHD, and IGHJ) regions are encoded by germline genes IGHV5-51, IGHD3-10, and IGHJ6, and the light chain variable and joining regions (IGKV and IGKJ) are encoded by IGKV4-1 and IGKJ2 (*4*). IgBlast analysis (*5*) indicates that the IGHV of CR3022 is 3.1% somatically mutated at the nucleotide sequence level, which results in eight amino acid changes from the germline sequence, whereas IGKV of CR3022 is 1.3% somatically mutated, resulting in three amino acid changes from the germline sequence (fig. S1). A recent study has shown that CR3022 can also bind to the RBD of SARS-CoV-2 (*6*). This finding provides an opportunity to uncover a cross-reactive epitope. We therefore determined the crystal structure of CR3022 with the SARS-CoV-2 RBD (Fig. 1A) at 3.1-Å resolution (table S1 and fig. S2, A and B) (*7*). CR3022 uses both heavy and light chains (Fig. 1B) as well as all six complementarity-determining region (CDR) loops (Fig. 1C) for interaction with the RBD. The buried surface area on the epitope is 917 Å^2, and SARS-CoV-2 recognition by CR3022 is largely driven by hydrophobic interactions (Fig. 1E). Five out of 11 somatic mutations are found in the paratope region (defined as residues on the antibody buried by RBD) (fig. S2C), implying their likely importance in the affinity maturation process.

Out of 28 residues in the epitope (defined as residues buried by CR3022), 24 (86%) are conserved between SARS-CoV-2 and SARS-CoV (Figs. 1D and 2A). This high sequence conservation explains the cross-reactivity of CR3022. Nonetheless, despite having a high conservation of the epitope residues, CR3022 Fab binds to SARS-CoV RBD [dissociation constant (K_d) = 1 nM] with a much higher affinity than it does to SARS-CoV-2 RBD (K_d = 115 nM) (Table 1 and fig. S3). The difference in binding affinity of CR3022 to SARS-CoV-2 and SARS-CoV RBDs is likely due to the nonconserved residues in the epitope (Fig. 2). The most drastic difference is an additional N-glycosylation site at N370 on SARS-CoV (N357 in SARS-CoV numbering). The N-glycan sequon (N-X-S/T, where X is any amino acid but proline) arises from an amino acid difference at residue 372, where SARS-CoV has a Thr compared with Ala in SARS-CoV-2 (Fig. 2B). Mass spectrometry analysis shows that a complex glycan is indeed present at this N-glycosylation site in SARS-CoV (*8*). An N-glycan at N370 would fit into a groove formed between heavy and light chains (Fig. 2C), which could increase contact and thus binding affinity to CR3022. This result also suggests that the difference in antigenicity between the RBDs of SARS-CoV-2 and SARS-CoV can be at least partially attributed to the N-glycosylation site at residue 370. We tested whether CR3022 was able to neutralize SARS-CoV-2 and SARS-CoV in an in vitro microneutralization assay (*7*). Although CR3022 could neutralize SARS-CoV, it did not neutralize SARS-CoV-2 at the highest concentration tested (400 μg/ml) (fig. S4). This in vitro neutralization result is consistent with lower affinity binding of CR3022 for SARS-CoV-2, although other explanations are also possible, as outlined below.

SARS-CoV-2 uses the same host receptor, angiotensin I–converting enzyme 2 (ACE2), as SARS-CoV (*3*, *9*–*11*). The epitope of CR3022 does not overlap with the ACE2-binding site (Fig. 3A). Structural alignment of the CR3022–SARS-CoV-2 RBD complex with the ACE2–SARS-CoV-2 RBD complex (*11*) further indicates that binding of CR3022 would not clash with ACE2 (*12*). This analysis implies that the neutralization mechanism of CR3022 for SARS-CoV does not depend on direct blocking of receptor binding, which is consistent with the observation that CR3022 does not compete with ACE2 for binding to the RBD (*6*). Unlike CR3022, most known SARS RBD-targeted antibodies compete with ACE2 for binding to RBD (*4*, *13*–*16*). The epitopes of these antibodies are very different from that of CR3022 (Fig. 3B). It has been shown that CR3022 can synergize with other RBD-targeted antibodies to neutralize SARS-CoV (*4*). Although CR3022 itself cannot neutralize SARS-CoV-2 in this in vitro assay, whether CR3022 can synergize with other SARS-CoV-2 RBD-targeted monoclonal antibodies for neutralization remains to be investigated.

Table 1. Binding affinity of CR3022 to recombinant RBD and S protein. Binding affinity is expressed as the nanomolar dissociation constant (K_d).

Target	CR3022 IgG binding affinity (K_d)	CR3022 Fab binding affinity (K_d)
SARS-CoV-2 RBD	<0.1	115 ± 3
SARS-CoV RBD	<0.1	1.0 ± 0.1

[1]Department of Integrative Structural and Computational Biology, The Scripps Research Institute, La Jolla, CA 92037, USA. [2]HKU-Pasteur Research Pole, School of Public Health, Li Ka Shing Faculty of Medicine, The University of Hong Kong, Hong Kong SAR, China. [3]The Skaggs Institute for Chemical Biology, The Scripps Research Institute, La Jolla, CA, 92037, USA.
*These authors contributed equally to this work.
†Corresponding author. Email: ch02mkp@hku.hk (C.K.P.M.); wilson@scripps.edu (I.A.W.)

The recent cryo–electron microscopy (cryo-EM) structures of the homotrimeric SARS-CoV-2 S protein (*17*, *18*) demonstrated that the RBD, as in other coronaviruses (*19*, *20*), can undergo a hinge-like movement to transition between "up" and "down" conformations (Fig. 4A). ACE2 host receptor can only interact with the RBD when it is in the up conformation—the down conformation is inaccessible to ACE2. The epitope of CR3022 is also only accessible when the RBD is in the up conformation (Fig. 4, B and C). However, even when one RBD in the SARS-CoV-2 S protein is in the up conformation, the binding of CR3022 to RBD can still be sterically hindered. Structural alignment of the CR3022–SARS-CoV-2 RBD complex with the SARS-CoV-2 S protein (*17*, *18*) indicates that the CR3022 variable region would clash with the RBD on the adjacent protomer if the latter adopted a down conformation. In addition, the CR3022 variable domain would clash with the S2 domain underneath the RBD, and the CR3022 constant region would clash with the N-terminal domain (Fig. 4D). Although,

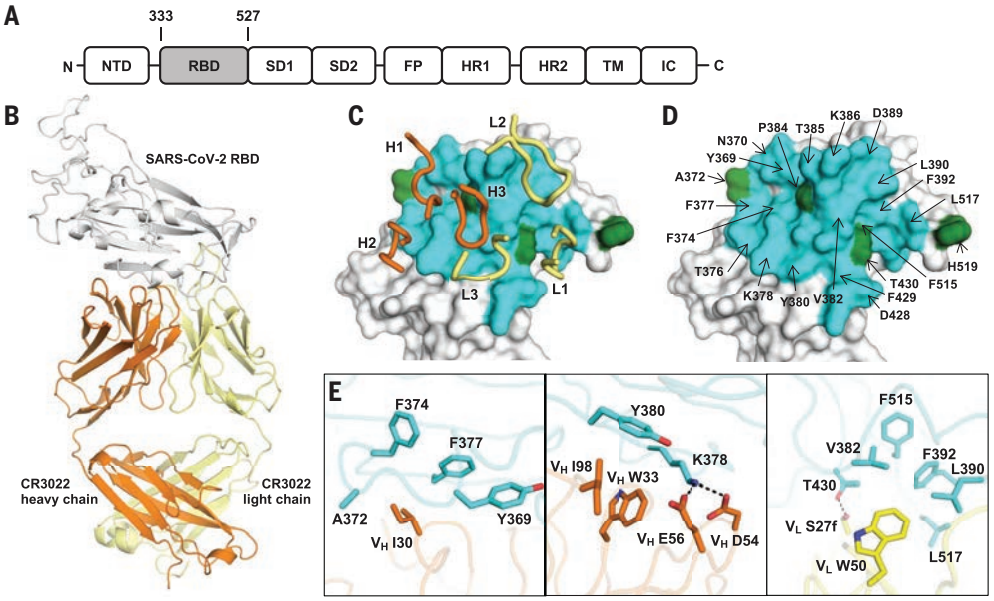

Fig. 1. Crystal structure of CR3022 in complex with SARS-CoV-2 RBD. (**A**) Overall topology of the SARS-CoV-2 spike glycoprotein. NTD, N-terminal domain; RBD, receptor binding domain; SD1, subdomain 1; SD2, subdomain 2; FP, fusion peptide; HR1, heptad repeat 1; HR2, heptad repeat 2; TM, transmembrane region; IC, intracellular domain; N, N terminus; C, C terminus. (**B**) Structure of CR3022 Fab in complex with SARS-CoV-2 RBD. CR3022 heavy chain is orange, CR3022 light chain is yellow, and SARS-CoV-2 RBD is light gray. (**C** and **D**) Epitope residues on SARS-CoV-2 are shown. CDR loops are labeled. Epitope residues that are conserved between SARS-CoV-2 and SARS-CoV are shown in cyan, and those that are not conserved are shown in green. (D) Epitope residues that are important for binding to CR3022 are labeled. Epitope residues are defined here as residues in SARS-CoV-2 RBD with buried surface area > 0 Å^2 after Fab CR3022 binding, as calculated with Proteins, Interfaces, Structures and Assemblies (PISA) (*34*). Single-letter abbreviations for the amino acid residues are as follows: A, Ala; D, Asp; E, Glu; F, Phe; H, His; I, Ile; K, Lys; L, Leu; M, Met; N, Asn; P, Pro; S, Ser; T, Thr; V, Val; W, Trp; and Y, Tyr. (**E**) Several key interactions between CR3022 and SARS-CoV-2 RBD are highlighted. CR3022 heavy chain is orange, CR3022 light chain is yellow, and SARS-CoV-2 RBD is cyan. Hydrogen bonds are represented by dashed lines.

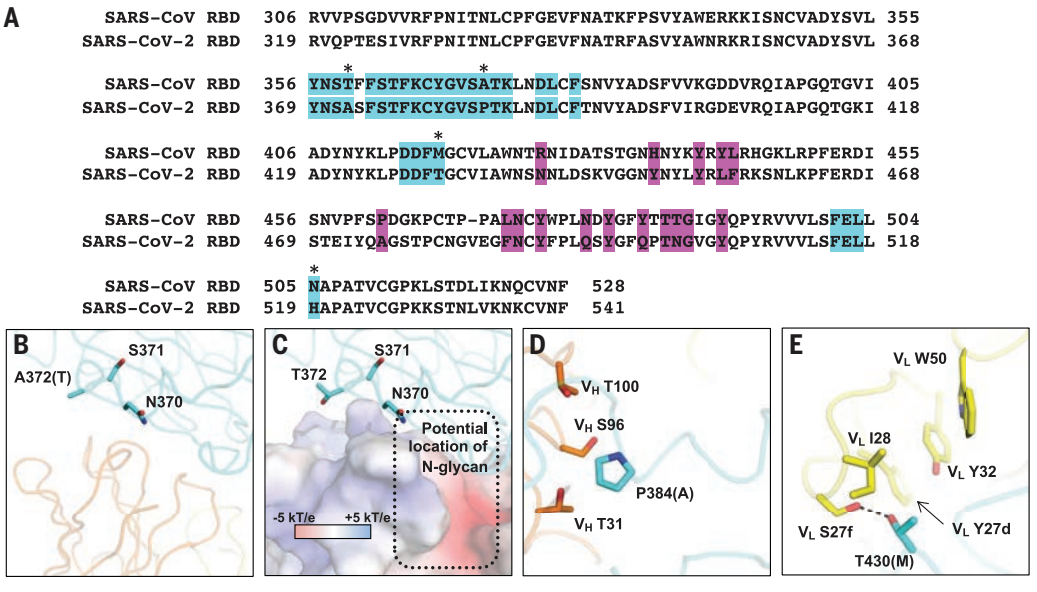

Fig. 2. Conservation of epitope residues. (**A**) Sequence alignment of SARS-CoV-2 RBD and SARS-CoV RBD. CR3022 epitope residues are highlighted in cyan. ACE2-binding residues are highlighted in magenta. Nonconserved epitope residues are marked with asterisks. (**B** to **E**) Interactions between the nonconserved epitope residues and CR3022 are shown. Amino acid variants observed in SARS-CoV are in parentheses. SARS-CoV-2 RBD is cyan, CR3022 heavy chain is orange, and CR3022 light chain is yellow. Residues are numbered according to their positions on the SARS-CoV-2 S protein sequence. (B) Whereas SARS-CoV-2 has an Ala at residue 372, SARS-CoV has Thr, which introduces an N-glycosylation site at residue N370. (C) The potential location of N370 glycan in SARS-CoV RBD is indicated by the dotted box. CR3022 is shown as an electrostatic potential surface presentation with units of kT/e, where e is the charge of an electron, k is the Boltzmann constant, and T is temperature in kelvin. (D) P384 interacts with T31, S96, and T100 of CR3022 heavy chain. Ala at this position in SARS-CoV would allow the backbone to adopt a different conformation when binding to CR3022. (E) T430 forms a hydrogen bond (dashed line) with S27f of CR3022 light chain. Met at this position in SARS-CoV would instead likely insert its side chain into the hydrophobic pocket formed by Y27d, I28, Y32, and W50 of CR3022 light chain.

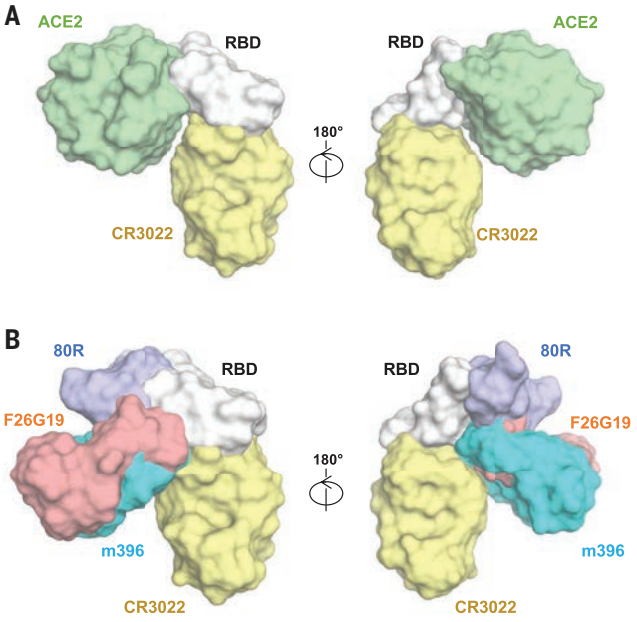

Fig. 3. The relative binding location of CR3022 with respect to receptor ACE2 and other SARS-CoV RBD monoclonal antibodies. (**A**) Structures of CR3022–SARS-CoV-2 RBD complex and ACE2–SARS-CoV-2 RBD complex (*11*) are aligned on the basis of the SARS-CoV-2 RBD. ACE2 is green, RBD is light gray, and CR3022 is yellow. (**B**) Structural superposition of CR3022–SARS-CoV-2 RBD complex, F26G19–SARS-CoV RBD complex [Protein Data Bank (PDB) ID 3BGF] (*35*), 80R–SARS-CoV RBD complex (PDB ID 2GHW) (*36*), and m396–SARS-CoV RBD complex (PDB ID 2DD8) (*16*).

as compared with SARS-CoV-2, the up conformation of the RBD in SARS-CoV has a larger dihedral angle to the horizontal plane of the S protein (fig. S5), the clashes described above would also exist in the SARS-CoV S protein (fig. S6).

For CR3022 to bind to the S protein, the previously described clashes need to be resolved. The clash with the CR3022 variable domain can be partially relieved when the targeted RBD on one protomer of the trimer and the RBD on the adjacent protomer are both in the up conformation (Fig. 4E). SARS-CoV S protein with two RBDs in the up conformation has been observed in cryo-EM studies (*19*, *21*, *22*). Nevertheless, clashes with the N-terminal domain (NTD) and S2 domain would still exist in the "two-up" conformation. Further structural modeling shows that all clashes can be avoided with a slight rotation of the targeted RBD in the "double-up" conformation (Fig. 4F). This conformational change is likely to be physiologically relevant because CR3022 can neutralize SARS-CoV. In addition, our enzyme-linked immunosorbent assay (ELISA)

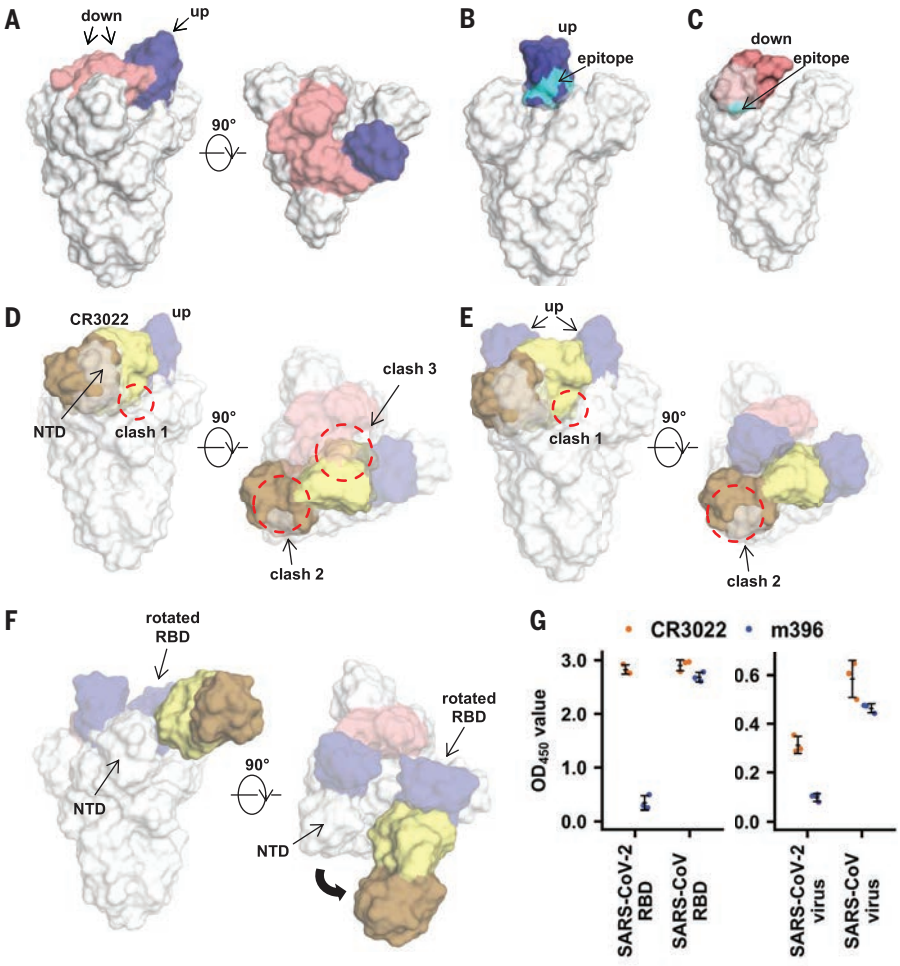

Fig. 4. Model of the binding of CR3022 to the homotrimeric S protein. (**A**) RBD in the S proteins of SARS-CoV-2 and SARS-CoV can adopt either an up conformation (blue) or a down conformation (red). PDB ID 6VSB (cryo-EM structure of SARS-CoV-2 S protein) (*17*) is shown. (**B** and **C**) CR3022 epitope (cyan) on the RBD is exposed in (B) the up conformation but not in (C) the down conformation. (**D**) Binding of CR3022 to single-up conformation would clash (indicated by the red dashed circles) with the S protein. Clash 1: CR3022 variable region (yellow) clashes with the S2 domain. Clash 2: CR3022 constant region (brown) clashes with NTD. Clash 3: CR3022 variable region clashes with the neighboring RBD that is in the down conformation. (**E**) Clash 3 is resolved when the neighboring RBD is in the up conformation (i.e., S protein in double-up conformation). (**F**) All clashes are resolved if the targeted RBD is slightly rotated in the double-up conformation. The curved arrow indicates the change in CR3022 orientation due to the slight rotation of the RBD. Of note, given that the elbow angle between the constant and variable domains of CR3022 is the same as observed in our crystal structure, our model shows that a maximum rotation angle of ~45° for the RBD would avoid all clashes. However, the elbow region of an antibody is known to be highly flexible. Therefore, the rotation angle of the RBD could be much smaller when the spike trimer is bound to CR3022. (**G**) Binding of CR3022 immunoglobulin G (IgG) and m396 IgG to recombinant RBD proteins from SARS-CoV-2 and SARS-CoV (left panel) and to SARS-CoV-2 and SARS-CoV viruses (right panel). Black lines indicate mean ± standard deviation of three technical replicates. OD_{450}, optical density at 450-nm wavelength.

experiment demonstrated that CR3022 is able to interact with the SARS-CoV-2 virus. Although the binding signals of CR3022 and m396, which is a SARS-CoV–specific antibody (*6*, *17*), to SARS-CoV were comparable in ELISA ($P > 0.05$, two-tailed t test) (Fig. 4G, left panel), CR3022 had a significantly higher binding signal to SARS-CoV-2 than did m396 ($P = 0.003$, two-tailed t test) (Fig. 4G, left panel), but not higher than its own binding signal to SARS-CoV, which is consistent with their relative binding to the RBD (Table 1 and fig. S3).

Our study provides insight into how SARS-CoV-2 can be targeted by the humoral immune response, and it reveals a conserved, but cryptic, epitope shared between SARS-CoV-2 and SARS-CoV. Recently, our group and others have identified a conserved epitope on influenza A virus hemagglutinin (HA) that is located in the trimeric interface and is only exposed through protein "breathing" (*23*–*25*), which is somewhat analogous to the epitope of CR3022. Antibodies to this influenza HA trimeric interface epitope do not exhibit in vitro neutralization activity but can confer in vivo protection. Similarly, antibodies to another conserved epitope that partially overlaps with the influenza HA trimeric interface are also non-neutralizing in vitro but protective in vivo (*26*). Examples of antibodies that do not have in vitro neutralization activity but confer in vivo protection have also been reported for influenza virus (*27*), herpesvirus (*28*), cytomegalovirus (*29*), alphavirus (*30*), and dengue virus (*31*). Therefore, although CR3022 does not neutralize SARS-CoV-2 in vitro, it is possible that this epitope can confer in vivo protection. Further study will require suitable animal models, which have yet to be established.

This coronavirus outbreak continues to pose an enormous global risk (*32*, *33*), and the availability of conserved epitopes may allow structure-based design not only of a SARS-CoV-2 vaccine but also of cross-protective antibody responses against future coronavirus epidemics and pandemics. Although a more universal coronavirus vaccine is not the most urgent goal at present, it is certainly worth future consideration, especially as cross-protective epitopes are identified, so that we can be better prepared for the next novel coronavirus outbreak.

REFERENCES AND NOTES

1. C. Huang *et al.*, *Lancet* **395**, 497–506 (2020).
2. Coronaviridae Study Group of the International Committee on Taxonomy of Viruses, *Nat. Microbiol.* **5**, 536–544 (2020).
3. P. Zhou *et al.*, *Nature* **579**, 270–273 (2020).
4. J. ter Meulen *et al.*, *PLOS Med.* **3**, e237 (2006).
5. J. Ye, N. Ma, T. L. Madden, J. M. Ostell, *Nucleic Acids Res.* **41**, W34–W40 (2013).
6. X. Tian *et al.*, *Emerg. Microbes Infect.* **9**, 382–385 (2020).
7. See supplementary materials.
8. Y. Watanabe *et al.*, bioRxiv 2020.02.20.957472 [Preprint]. 21 February 2020; https://doi.org/10.1101/2020.02.20.957472.
9. M. Letko, A. Marzi, V. Munster, *Nat. Microbiol.* **5**, 562–569 (2020).
10. R. Yan *et al.*, *Science* **367**, 1444–1448 (2020).
11. J. Lan *et al.*, bioRxiv 2020.02.19.956235 [Preprint]. 20 February 2020; https://doi.org/10.1101/2020.02.19.956235.
12. ACE2 also forms a dimer when it associates with the amino acid transporter B^0AT1 (*10*). We modeled a CR3022 IgG onto this dimer structure and found no clashes of CR3022 with ACE2 in its dimeric form, where the RBDs would likely come from adjacent trimers on the virus (*10*).
13. J. Sui *et al.*, *Proc. Natl. Acad. Sci. U.S.A.* **101**, 2536–2541 (2004).
14. E. N. van den Brink *et al.*, *J. Virol.* **79**, 1635–1644 (2005).
15. J. D. Berry *et al.*, *J. Virol. Methods* **120**, 87–96 (2004).
16. P. Prabakaran *et al.*, *J. Biol. Chem.* **281**, 15829–15836 (2006).
17. D. Wrapp *et al.*, *Science* **367**, 1260–1263 (2020).
18. A. C. Walls *et al.*, *Cell* **181**, 281–292.e6 (2020).
19. Y. Yuan *et al.*, *Nat. Commun.* **8**, 15092 (2017).
20. M. Gui *et al.*, *Cell Res.* **27**, 119–129 (2017).
21. R. N. Kirchdoerfer *et al.*, *Sci. Rep.* **8**, 15701 (2018).
22. Yuan *et al.* (*19*) observed 56% of the wild-type recombinant SARS-CoV S protein particle in "none-up" conformation and 44% in "single-up" conformation, whereas Kirchdoerfer *et al.* (*21*) found that recombinant SARS-CoV S protein, with Lys^{968}→Pro and Val^{969}→Pro mutations in the S2 domain to stabilize the prefusion conformation, has 58% in single-up, 39% in double-up, and 3% in triple-up conformations. However, it is not known whether the distribution of different conformations of S proteins on virus surface is the same as that of recombinant S protein.
23. S. Bangaru *et al.*, *Cell* **177**, 1136–1152.e18 (2019).
24. A. Watanabe *et al.*, *Cell* **177**, 1124–1135.e16 (2019).
25. G. Bajic *et al.*, *Cell Host Microbe* **25**, 827–835.e6 (2019).
26. J. Lee *et al.*, *Nat. Med.* **22**, 1456–1464 (2016).
27. C. Dreyfus *et al.*, *Science* **337**, 1343–1348 (2012).
28. C. Petro *et al.*, *eLife* **4**, e06054 (2015).
29. A. Bootz *et al.*, *PLOS Pathog.* **13**, e1006601 (2017).
30. C. W. Burke *et al.*, *Viruses* **10**, 147 (2018).
31. E. A. Henchal, L. S. Henchal, J. J. Schlesinger, *J. Gen. Virol.* **69**, 2101–2107 (1988).
32. V. D. Menachery *et al.*, *Nat. Med.* **21**, 1508–1513 (2015).
33. V. D. Menachery *et al.*, *Proc. Natl. Acad. Sci. U.S.A.* **113**, 3048–3053 (2016).
34. E. Krissinel, K. Henrick, *J. Mol. Biol.* **372**, 774–797 (2007).
35. J. E. Pak *et al.*, *J. Mol. Biol.* **388**, 815–823 (2009).
36. W. C. Hwang *et al.*, *J. Biol. Chem.* **281**, 34610–34616 (2006).

ACKNOWLEDGMENTS

We thank H. Tien for technical support with the crystallization robot, J. Matteson for contribution to mammalian cell culture, W. Yu for contribution to insect cell culture, R. Stanfield for assistance with data collection, and A. Ward for discussion. **Funding:** This work was supported by National Institutes of Health grant K99 AI139445 (N.C.W.); a Calmette and Yersin scholarship from the Pasteur International Network Association (H.L.); Bill and Melinda Gates Foundation grant OPP1170236 (I.A.W.); Guangzhou Medical University High-level University Innovation Team Training Program (Guangzhou Medical University released [2017] no. 159) (C.K.P.M.); and National Natural Science Foundation of China (NSFC)/ Research Grants Council (RGC) Joint Research Scheme (N_HKU737/18) (C.K.P.M.). General Medical Sciences and Cancer Institutes Structural Biology Facility at the Advanced Photon Source (APS) has been funded by federal funds from the National Cancer Institute (ACB-12002) and the National Institute of General Medical Sciences (AGM-12006). This research used resources of the APS, a U.S. Department of Energy (DOE) Office of Science User Facility operated for the DOE Office of Science by Argonne National Laboratory under contract DE-AC02-06CH11357. **Author contributions:** M.Y., N.C.W., X.Z., C.K.P.M., and I.A.W. conceived of and designed the study. M.Y., N.C.W., and C.-C.D.L. expressed and purified the proteins. M.Y. and N.C.W. performed biolayer interferometry binding assays. R.T.Y.S., H.L., and C.K.P.M. performed the neutralization and virus-binding experiments. M.Y., N.C.W., and X.Z. collected the x-ray data and determined and refined the x-ray structures. M.Y., N.C.W., and C.K.P.M. analyzed the data. M.Y., N.C.W., and I.A.W. wrote the paper, and all authors reviewed and edited the paper. **Competing interests:** The authors declare no competing interests. **Data and materials availability:** X-ray coordinates and structure factors are deposited in the RCSB Protein Data Bank under ID 6W41. This work is licensed under a Creative Commons Attribution 4.0 International (CC BY 4.0) license, which permits unrestricted use, distribution, and reproduction in any medium, provided the original work is properly cited. To view a copy of this license, visit https://creativecommons.org/licenses/by/4.0/. This license does not apply to figures/photos/artwork or other content included in the article that is credited to a third party; obtain authorization from the rights holder before using such material.

SUPPLEMENTARY MATERIALS

science.sciencemag.org/content/368/6491/630/suppl/DC1
Materials and Methods
Figs. S1 to S6
Tables S1 to S3
References (*37*–*46*)
MDAR Reproducibility Checklist

View/request a protocol for this paper from *Bio-protocol*.

14 March 2020; accepted 1 April 2020
Published online 3 April 2020
10.1126/science.abb7269

Available online at www.sciencedirect.com
ScienceDirect
Vaccine 25 (2007) 136–143
Vaccine
www.elsevier.com/locate/vaccine

Immunogenicity of a receptor-binding domain of SARS coronavirus spike protein in mice: Implications for a subunit vaccine

Alexander N. Zakhartchouk [a,*], Chetna Sharon [b,e], Malathy Satkunarajah [b,e], Thierry Auperin [b,e,1], Sathiyanarayanan Viswanathan [a], George Mutwiri [a], Martin Petric [c], Raymond H. See [c], Robert C. Brunham [c], B. Brett Finlay [d], Cheryl Cameron [f], David J. Kelvin [f], Alan Cochrane [b], James M. Rini [b,e], Lorne A. Babiuk [a]

[a] *Vaccine and Infectious Disease Organization (VIDO), University of Saskatchewan, 120 Veterinary Road, Saskatoon, Sask., Canada S7N 5E3*
[b] *Departments of Molecular and Medical Genetics and Microbiology, University of Toronto, Ont., Canada M5S 1A8*
[c] *University of British Columbia Centre for Disease Control, Vancouver, BC, Canada V5Z 4R4*
[d] *Michael Smith Laboratories and Departments of Biochemistry and Molecular Biology and Microbiology and Immunology, University of British Columbia, Vancouver, BC, Canada V6T 1Z3*
[e] *Department of Biochemistry, University of Toronto, Ont., Canada M5S 1A8*
[f] *Division of Experimental Therapeutics, University Health Network, Toronto General Research Institute, Toronto, Ont., Canada*

Received 20 March 2006; received in revised form 5 June 2006; accepted 20 June 2006
Available online 2 August 2006

Abstract

We studied the immunogenicity of an anti-SARS subunit vaccine comprised of the fragment of the SARS coronavirus (SARS-CoV) spike protein amino acids 318–510 (S318–510) containing the receptor-binding domain. The S protein fragment was purified from the culture supernatant of stably transformed HEK293T cells secreting a tagged version of the protein. The vaccine was given subcutaneously to 129S6/SvEv mice in saline, with alum adjuvant or with alum plus CpG oligodeoxynucleotides (ODN). Mice immunized with the adjuvanted antigen elicited strong antibody and cellular immune responses; furthermore, adding the CpG ODN to the alum resulted in increased IgG2a antibody titers and a higher number of INF-γ-secreting murine splenocytes. Mice vaccinated with S318–510 deglycosylated by PNGase F (dgS318–510) showed a lower neutralizing antibody response but had similar numbers of INF-γ-producing cells in the spleen. This finding suggests that carbohydrate is important for the immunogenicity of the S318–510 protein fragment and provide useful information for designing an effective and safe SARS subunit vaccine.

Keywords: SARS coronavirus; Subunit vaccine; Spike protein; Receptor binding domain

1. Introduction

Severe acute respiratory syndrome (SARS) first appeared in Guangdong Province, Southern China in November 2002. This newly emerging infectious disease quickly spread to 29 countries on five continents along international air travel routes, causing large-scale outbreaks in Hong Kong, Singapore and Toronto in early 2003. The World Health Organization (WHO) issued a global alert for SARS on 12 March 2003. With the support of the WHO, authorities in affected regions implemented epidemiologic surveillance and adherence to infection-control procedures, which helped contain the SARS outbreak by mid-July 2003. However, a total of 8096 SARS cases and 774 associated deaths were reported in the interim [1].

* Corresponding author. Tel.: +1 306 966 1570; fax: +1 306 966 7478.
E-mail address: zakhartchouk@sask.usask.ca (A.N. Zakhartchouk).
[1] Current address: Columbia University, Fairchild Center, MC2452, 1212 Amsterdam Avenue, New York, NY 10027, USA.

0264-410X/$ – see front matter © 2006 Elsevier Ltd. All rights reserved.
doi:10.1016/j.vaccine.2006.06.084

Within a month of the WHO-issued global threat alert for SARS, a novel coronavirus (SARS-CoV) was identified as its etiological agent and its genome was sequenced [2,3]. Like all coronaviruses, the SARS-CoV genome is a single-stranded plus-sense RNA genome of about 30,000 nucleotides. All predicted open reading frames (ORFs) are divided into two groups: (i) those with a clear homology to other coronaviruses and for which viral functions are proposed (such ORFs include the replicase and the structural genes) and (ii) those with no clear homology to any known genes and often referred to as group-specific genes [4].

The coronavirus spike (S) protein is a large, type I membrane glycoprotein that has long been known to play a major role in viral entry and pathogenesis [5]. This protein is responsible for binding to receptors on host cells and plays an important role in membrane fusion [6]. The main receptor for SARS-CoV is angiotensin-converting enzyme 2 (ACE2) [7], and it has been shown that amino acids 318–510 of the SARS-CoV S protein are sufficient to bind to ACE2 [8,9]. The S protein is an attractive target for both therapeutics and vaccine development because monoclonal antibodies to the S protein can neutralize SARS-CoV infection [10,11]. Moreover, the S protein has been shown to induce serum neutralizing antibodies and confer protective immunity against SARS-CoV challenge [12–14].

Although SARS human-to-human transmission stopped in 2003, the development of a SARS vaccine remains a public health priority given the possibility of reemergence. Several potential strategies can be considered for vaccination against SARS-CoV, including a whole-killed virus vaccine, a viral vectored vaccine, a recombinant subunit vaccine and DNA-based vaccines [15,16]. We have previously reported on the development of two SARS vaccine candidates, a whole-killed virus and two adenovirus-based vectors consisting of the SARS-CoV S and N proteins that induce serum neutralizing antibodies and inhibit pulmonary SARS-CoV replication [17]. In this report, we describe a third candidate a SARS-CoV subunit vaccine comprised of residues 318–510 of the S protein (S318–510) produced in a bioreactor-based mammalian cell expression system. The protein was formulated with different adjuvants and evaluated for its immunogenicity in a murine model, in both its fully glycosylated form and after deglycosylation (dgS318–510) by PNGase F.

2. Materials and methods

2.1. Production of S318–510 in a bioreactor-based mammalian cell expression system

An expression vector incorporating a codon-optimized version of the SARS-CoV S318–510 fragment, the mammalian transin secretion signal and *N*-terminal Protein-A (PrA) purification tag [18] and a tobacco etch virus (TEV) protease cleavage site was generated using plasmid, pIRES-Spuro3 (Clontech). HEK293T cells were transfected by the calcium phosphate method and a bulk culture resistant to puromycin (5 μg/ml) was expanded and the media assayed for secreted protein levels by Western blot analysis using an anti PrA antibody (Sigma). Production of the PrA-S318–510 fusion protein was scaled-up from these adherent cells in a 2.2 l New Brunswick Celligen bioreactor using 25 g of Fibra-Cel disks (New Brunswick Scientific). The bioreactor was run in perfusion mode using CHO-S-SFM II media (Gibco) supplemented with 3% fetal bovine serum (FBS), 2.25 g/l glucose, 1× non essential amino acids (Gibco), 1 mg/l aprotinin (Bioshop, Burlington, Ontario), 5 mg/l puromycin (Bioshop, Burlington, Ontario) and 1× penicillin-streptomycin (Gibco) at a flow rate of about 3 l/day. The harvested media was concentrated 10-fold and the fusion protein was purified by IgG-Sepharose (Amersham Biosciences) affinity chromatography. The PrA-S318–510 fusion protein was then digested by TEV protease at a ratio of 6:1 (w/w) at 4 °C for 18 h to remove the *N*-terminal PrA fusion tag. As a result of the cloning strategy and TEV protease cleavage the resulting protein fragment contains four additional amino acids (GGRP) at the *N*-terminus of the S318–510 fragment. S318–510 was further purified by HiTrap phenyl hydrophobic interaction chromatography, HiTrap Q anion exchange chromatography and Superdex 200 gel filtration chromatography (Amersham Biosciences). A portion of the purified S318–510 was deglycosylated by PNGase F digestion at a ratio of 10:1 (w/w) at 37 °C for 21 h and again purified by Superdex 200 gel filtration chromatography. Following gel filtration both the naturally glycosylated (S318–510) and the PNGase F deglycosylated (dgS318–510) samples were dialyzed against phosphate buffer saline (PBS) without $CaCl_2$ and $MgCl_2$ and concentrated to 0.5–1.0 mg/ml for injections.

2.2. Mouse immunizations

Six to eight-week-old female 129S6/SvEv mice were purchased from Taconic Farms (Germantown, NY). Four groups of five mice were immunized subcutaneously twice at a 4-week interval, with one of the following formulations: (1) 8 μg S318–510 protein in saline; (2) 8 μg S318–510 protein with alum (Alhydrogel 2%, Superfos Biosector; 2.5 μl/μg of the protein to give 25 mg Al^{3+}/mg); (3) 8 μg S318–510 protein with alum and CpG oligodeoxynucleotide (ODN) 1826 (Qiagen) at a dose of 10 μg/mouse; (4) 8 μg dgS318–510 protein with alum and CpG ODN 1826. A fifth group of mice was immunized with saline. Sera were collected on days 28 and 49, and the mice were sacrificed on day 49.

2.3. Virus neutralization assay

Sera were tested in a standard virus neutralization assay as previously described [19]. Briefly, each serum sample was heated at 56 °C for 30 min and duplicate serial two-fold dilutions were incubated with 100 p.f.u. of SARS-CoV (strain Tor-2) for 2 h, then added to monolayers of Vero-E6 cells.

Cultures were examined after 72 h for characteristic viral CPE.

2.4. Interferon-gamma (IFN-γ) ELISPOT assay

Cellular immune responses to SARS-CoV were assessed by an IFN-γ ELISPOT assay using murine splenocytes. Unifilter 96-well plates coated overnight with 0.1 ml/well of 1.25 μg/ml rat anti-mouse IFN-γ (BD PharMingen) were washed once with RPMI 1640 (Life Technologies) containing 10% FBS, and incubated in triplicate with 5×10^5 splenocytes/well in a 0.1 ml RPMI 1640 media with 10% FBS containing 10 μg/ml of the S318–510 protein fragment. After 48 h of incubation at 37 °C in a CO_2 incubator, the plates were washed five times in PBS (0.1 M, pH 7.3) containing 0.05% Tween 20, and incubated overnight at 4 °C with biotinylated rat anti-mouse INF-γ antibody (BD PharMingen, 0.1 ml/well, 1.25 μg/ml). After washing with PBS containing 0.05% Tween 20, the plates were incubated for 1.5 h with a 1/500 dilution of streptavidin-alkaline phosphatase (Jackson ImmunoResearch). After eight washes with water, the plates were developed with SIGMA FAST 5-bromo-4-chloro-3-indolyl phosphate/nitro blue tetrazolium. Development was stopped by washing with tap water, and plates were air-dried and the number of spots counted under a light microscope.

2.5. Western blot analysis

Ten microgram of SARS-CoV infected Vero-E6 cell lysate in sample buffer was run on 10% SDS-PAGE and transferred to a nitrocellulose membrane. Non-specific binding sites on the membrane were blocked with 5% non-fat dry milk (BioRad). S protein was detected by exposing the membrane to pooled mouse sera in 1:100 dilution followed by anti-mouse IgG conjugated to alkaline phosphatase. The blot was developed using an AP conjugate substrate kit (BioRad).

2.6. SARS-CoV-specific ELISA

Total SARS-CoV-specific IgG and IgG isotype titers in sera from immunized mice were measured by an ELISA as described previously [19]. Briefly, 96-well plates were coated overnight with 0.1 ml per well of 1 μg/ml antigen (purified inactivated SARS-CoV, S318–510 or dgS318–510 protein). The washing of plates, addition of sera and color development were performed as previously described [19].

2.7. Statistical analyses

Statistical significance was assessed using a one-way ANOVA followed by the Tukey-test. Differences between mean values for the vaccine groups were considered significant if the P-value was <0.05.

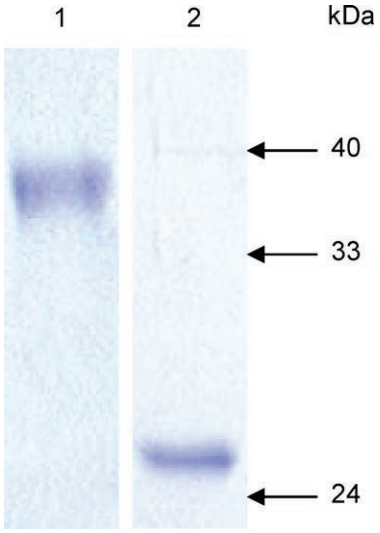

Fig. 1. Antigen characterization. Gel electrophoresis (12% SDS-PAGE, reducing conditions) of the S318–510 protein stained by Coomassie blue. Lane 1 is a sample before PNGase F treatment and lane 2 after the treatment.

3. Results

3.1. Characterization of the subunit vaccine

Recent studies indicate that immune responses to the *N*-terminal segment of the SARS-CoV S protein confer protection against SARS-CoV infection [20]. Therefore, we used a human cell culture system to express a protein-A tagged fragment of the S protein (amino acids 318–510) as a secreted glycosylated protein that could be readily purified under native conditions. After cleavage of the tag, the protein was further purified and an aliquot was analyzed by SDS-PAGE. The purified S318–510 protein migrated as a 38 kDa band (Fig. 1, lane 1), while deglycosylation of the protein with PNGase F led to the appearance of a 25 kDa band (Fig. 1, lane 2). The yield of the recombinant purified protein was 2–4 mg/l of culture medium.

3.2. SARS-CoV-specific antibody immune responses in vaccinated mice

To determine whether the S318–510 protein fragment was immunogenic, the antigen was formulated in the following manner prior to subcutaneous injection into 129S6/SvEv mice on days 0 and 28: (i) with saline alone, (ii) with alum or (iii) with alum plus CpG ODN 1826. Control mice were immunized with PBS alone. Following immunization, the humoral SARS-CoV specific immune responses were assessed in sera. Total SARS-CoV specific IgG titers on days 28 and 49 were determined by an ELISA using inactivated SARS-CoV as the capture antigen. In contrast to the PBS control and the antigen in saline alone group, mice immunized with the S318–510 protein formulated in adjuvants showed detectable SARS-CoV specific IgG titers on day 28 and after

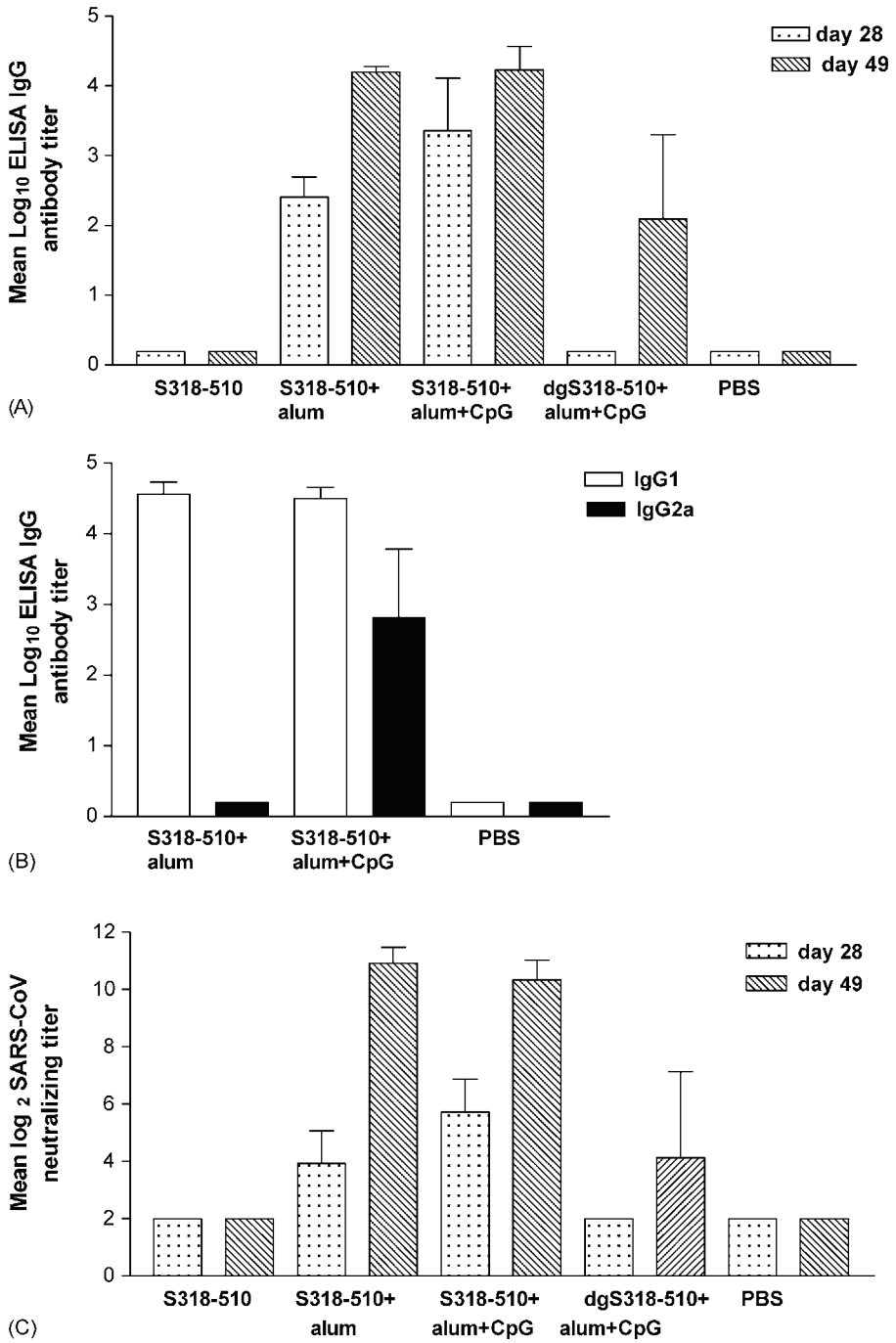

Fig. 2. Humoral immune responses in mice following immunization. (A) SARS-CoV-specific total IgG titers in sera. (B) SARS-CoV-specific IgG1 and IgG2a titers in day 49 sera. Purified inactivated SARS-CoV was used in ELISA as the capture antigen. (C) SARS-CoV neutralizing antibody titers in sera. Error bars represent the S.D. of the mean of five mice per group.

the second injection, the titers had significantly increased by day 49 ($P < 0.05$, Fig. 2A). Mice immunized with the antigen adjuvanted with alum plus CpG ODN elicited higher antibody titers ($P < 0.05$) than mice vaccinated with antigen plus alum on day 28. However, after the second injection, the total SARS-CoV specific serum IgG titers were similar in all mouse groups vaccinated with the adjuvanted antigen (Fig. 2A).

The SARS-CoV-specific IgG subclass titers were determined on day 49 sera by ELISA. As evident in Fig. 2B, mice immunized with antigen plus alum elicited predominantly SARS-CoV-specific IgG1 titers, whereas the combination of alum and CpG ODN stimulated both IgG1 and IgG2a antibody production.

In line with the ELISA data, the SARS-CoV-specific serum neutralizing titers were significantly higher ($P < 0.05$)

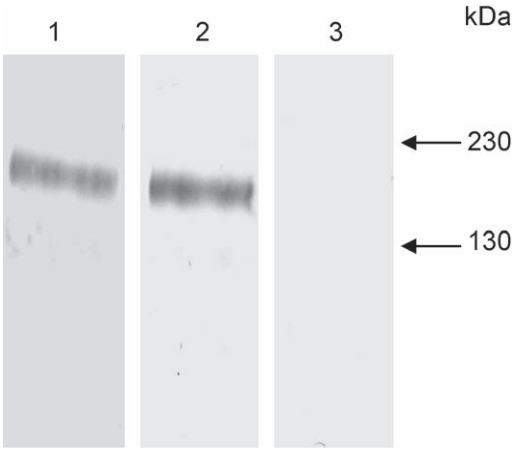

Fig. 3. Western blot analysis of day 49 sera from mice vaccinated with S318–510 with alum (lane 1), S318–510 with alum plus CpG ODN (lane 2) or with saline (lane 3). The sera were probed against SARS-CoV infected Vero-E6 cell lysate.

on day 28 in the vaccinated group receiving the alum plus CpG ODN combination compared to the vaccinated group receiving the antigen with only alum (Fig. 2C). After the second injection, the titers had increased by day 49, and the difference between the two vaccinated groups was not significant (Fig. 2C). PBS-vaccinated mice and mice vaccinated with the S318–510 antigen in saline did not show any specific serum neutralization of SARS-CoV.

To determine if the spike protein of SARS-CoV could be recognized by the sera of vaccinated mice, western blot analysis was performed on day 49 sera using the SARS-CoV infected cells as an antigen. The sera recognized a 200 kDa band corresponding to the full-length spike protein (Fig. 3).

3.3. SARS-CoV-specific cellular immune responses

An effective SARS vaccine should not only induce neutralizing antibodies to prevent SARS-CoV replication in mice [14], but it should induce cellular immunity as well. To evaluate S protein specific cellular immune responses, splenocytes were isolated from vaccinated and control mice and antigen-specific responses were measured by INF-γ ELISPOT assay. As indicated in Fig. 4, vaccination of mice with S318–510 formulated with alum plus CpG ODN resulted in nearly a three-fold increase in the number of IFN-γ spots compared to the splenocytes of mice immunized with spike protein formulated with alum. The S protein specific IL-4 response in splenocytes was also evaluated by ELISPOT assay, but IL-4 spots were not observed (data not shown).

3.4. Role of carbohydrate in immunogenicity of S318–510 protein

The SARS-CoV spike protein is heavily glycosylated with three of these sites found within the S318–510 amino acid fragment [21]. To determine whether carbohydrates play a

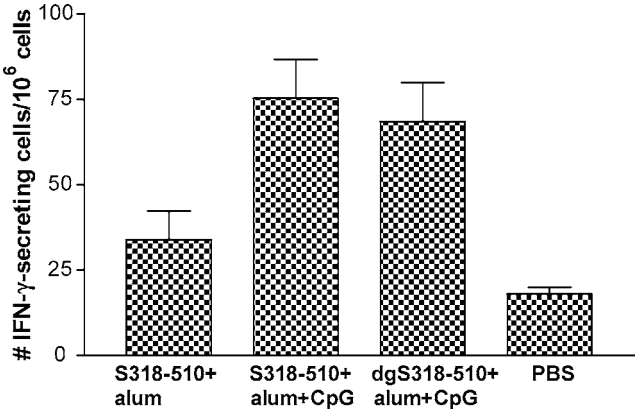

Fig. 4. Cellular immune response to SARS vaccine. Shown is the number of INF-γ secreted cells in spleen of mice harvested on day 49 and stimulated *in vitro* with the S318–510 recombinant protein. The results represent the average of triplicate wells and are expressed as the means and S.E.

role in the immunogenicity of the S318–510 protein fragment, we used PNGase F to generate dgS318–510 for mouse immunizations. As shown in Fig. 1, the protein was completely deglycosylated under native conditions by this procedure. Sera from mice vaccinated with the dgS318–510 did not show any SARS-CoV-specific IgG titers or virus neutralizing activity on day 28, but on day 49 the dgS318–510-vaccinated mice showed both detectable SARS-CoV-specific total IgG ELISA titers and SARS-CoV neutralizing antibodies (Fig. 2A and C). However, these serum titers were significantly lower ($P < 0.05$) than those of mice immunized with S318–510 protein formulated with the same adjuvants. In contrast, cellular S protein specific immune responses as measured by the number of INF-γ-secreting cells were similar in mice vaccinated with either the glycosylated or deglycosylated form of the S318–510 protein fragment (Fig. 4).

To further investigate antibody immune responses, we analyzed day 49 sera from two groups of vaccinated mice using S318–510 or dgS318–510 protein as capture antigens for the ELISA. As shown in Fig. 5, both mouse

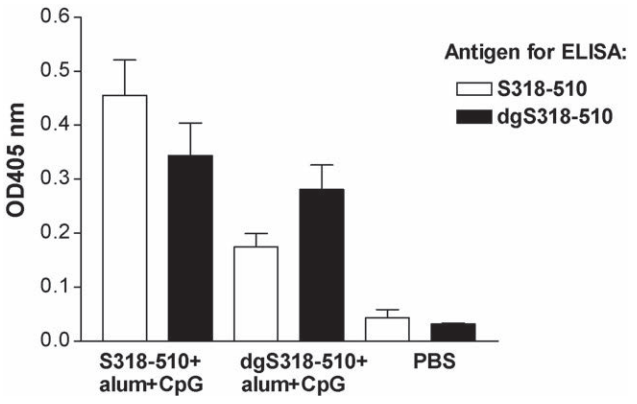

Fig. 5. IgG antibody levels in day 49 sera as determined by an ELISA using S318–510 or dgS318–510 as the capture antigen. Each sample was 1:6400 diluted. Error bars represent the S.D. of the mean of the absorbance at 405 nm ($n = 5$).

groups (S318–510-vaccinated and dgS318–510-vaccinated adjuvanted with alum plus CpG ODN) showed similar IgG antibody levels against dgS318–510 antigen. In addition, the S318–510 vaccinated mice elicited similar IgG antibody immune response to both S318–510 and dgS318–510 antigens. In contrast, the dgS318–510 vaccinated mice elicited a higher ($P < 0.05$) IgG antibody response against dgS318–510 protein compared to S318–510.

4. Discussion

The S protein of SARS-CoV has been shown to be important for inducing host responses and virus neutralization activity mediated by antibodies. Consequently, much attention has been focused on the S protein for the development of a SARS vaccine. Compared to the inactivated SARS-CoV or vector-based SARS vaccines that we have previously reported [17], the development of a recombinant subunit vaccine eliminates the safety risks encountered during vaccine manufacturing and administration. However, the disadvantages of recombinant subunit vaccines are their low immunogenicity and their poor ability to generate cellular responses.

In the present study, we used two adjuvants: aluminum hydroxide, commonly known as alum, and CpG ODN 1826. Alum is the most extensively used adjuvant in commercial vaccines and acts mainly by stimulating Th2-type immune responses [22]. The mechanisms by which alum produces its adjuvant effect include formation of an antigen depot and activation of antigen-presenting cells [23]. In contrast, CpG ODNs bind to the TLR9 receptor and preferentially induce Th1-biased immune responses [24,25]. Several reports have shown that co-administration of alum with CpG ODN and antigen enhanced the effect of CpG ODN and stimulated both Th1- and Th2-type immune responses [26,27]. The mechanism for this effect has not been investigated. Our data indicate that CpG ODN 1826 stimulates a Th1-type immune response as evidenced by the increased serum IgG2a titers (Fig. 2B) and INF-γ secretion (Fig. 4). As for the magnitude of the antibody response, we detected increased total serum SARS-CoV IgG titers after the first injection with CpG ODN, compared to alum adjuvant alone; however, after the second injection the titers were similar (Fig. 2A and C). These results suggest that CpG ODN 1826 may only enhance the primary antibody response against the S318–510 antigen or that the level of immunity had reached maximal levels such that further boosting was not possible.

Previously, we have evaluated two other SARS vaccine candidates in the same mouse strain used in this study [17]. Comparison with the results reported here show that mice vaccinated with the adjuvanted (alum plus CpG ODN) subunit vaccine show higher serum neutralizing antibody titers than mice immunized with recombinant adenoviruses expressing the S and nucleocapsid protein and comparable virus neutralizing titers to mice immunized with the whole-killed SARS-CoV vaccine. Overall, geometrical titers mean (1:640) induced by our subunit vaccine was much higher than those reported for convalescent sera (1:54) [28]. These results support the suggestion that we had reached maximal titers after immunization and boosting with the subunit vaccine.

The *N*-terminal portion of the SARS-CoV S protein is an attractive target for vaccine development because it contains the ACE2 receptor-binding domain and virus-neutralizing epitopes [29–31]. As previously suggested [32], we propose that S318–510 would be an effective and safe subunit vaccine for SARS prevention. In contrast to the study by He et al. [32] in which vaccine formulated in different adjuvant was tested in rabbits, our subunit vaccine was evaluated in a murine model previously demonstrated to support SARS-CoV replication [33]. Furthermore, the S protein fragment developed by He et al. [32] was fused to a human IgG1 Fc fragment, whereas the S318–510 protein used in our study contained only four additional amino acids at the *N*-terminus. In other studies [20,34] a longer polypeptide was produced in insect cells by a recombinant baculovirus, which contrasts with our recombinant protein that was produced in bioreactor-based human cell culture system. A technology based on a human cell line is ideal for large-scale vaccine manufacturing; the strength of the cell line based technology is its safety, scalability and productivity. In addition, protein produced in human cells most closely resembles the natural viral protein, particularly in terms of post-translational modifications.

Our data clearly show that both S318–510 and dgS318–510 elicited S specific INF-γ and antibody immune responses. However, the SARS-CoV specific total IgG ELISA titers and the virus neutralizing titers were both lower in the sera of dgS318–510 vaccinated mice (Fig. 2A and C). We have also found that the S318–510 vaccinated and dgS318–510 vaccinated (adjuvanted with alum plus CpG ODN) mice showed similar serum IgG antibody levels against the dgS318–510 antigen (Fig. 5). This suggests that a similar immune response was reached in the case of both vaccine candidates. In addition, the S318–510 vaccinated mice elicited similar IgG antibody levels to both the S318–510 and dgS318–510 antigens. This result suggests that common epitopes are present in both S318–510 and dgS318–510 antigens. In contrast, the dgS318–510 vaccinated mice showed higher IgG antibody levels against dgS318–510 than against S318–510. This result suggests that dgS318–510 contains epitopes that are blocked or shielded by carbohydrate in S318–510. Since we observed a decrease in the serum neutralizing titers in the dgS318–510 vaccinated mice, these epitopes presumably do not lead to a neutralizing antibody response. This suggestion is in agreement with the X-ray crystal structure of S318–510 complexed with ACE2, which shows that the three *N*-linked oligosaccharides are positioned on one face of the S318–510 molecular opposite to that of the ACE2 interaction face [35]. In summary, our data suggest that glycosylation of S318–510 protein is important for vaccination, because it helps to increase the amount of antibodies directed to the virus neutralizing epitopes by shielding the non-neutralizing epitopes.

Disease enhancement after immunization is a concern in development of any vaccine. This is particularly true for a SARS vaccine since increased disease severity has been observed for a vaccine against feline infectious peritonitis virus (coronavirus) [36]. In addition, synthetic versions of S variants were tested for their sensitivity to antibody neutralization with pseudotyped lentiviruses. In these experiments, antibodies that neutralized most human isolates-derived S proteins enhanced entry mediated by the civet virus S protein [37]. Furthermore, liver inflammation was found in MVA-S vaccinated ferrets after challenge with SARS-CoV [38]; however, there were no reports of adverse effects from other laboratories working with ferrets or other animals (rodents and monkeys). Since the mouse is not an ideal model for SARS, we did not assess the effect of immunization with the S318–510 protein fragment on disease enhancement. However, the issue of disease enhancement will have to be carefully studied if and when an appropriate animal model becomes available.

Finally, we have demonstrated that the S318–510 protein fragment formulated with clinically useful adjuvants (alum and CpG ODN) elicited strong immune responses in mice. We are planning to conduct SARS-CoV challenge experiments in mice and ferrets to study whether our vaccine can protect against SARS-CoV infection.

Acknowledgements

We would like to thank all members of the SARS Accelerated Vaccine Initiative (SAVI) for their dedication and commitment towards this rapid response initiative. We thank the Province of British Columbia, Canada, the Michael Smith Foundation for Health Research and the Protein Engineering Network of Centres of Excellence for funding this project. In addition, we thank the Canadian Institutes of Health Research Strategic Training Program for fellowships to T.A. and C.S. We would like to thank Mr. Barry Carroll and Dr. Igor Moshynskyy for help in work with animals and Mr. Ponn Benjamin for help in setting up the immunological assays. Dr. L.A. Babiuk is a holder of a Canada Research Chair in Vaccinology and Biotechnology. Published as Vaccine and Infectious Disease Organization Series no. 439.

References

[1] Skowronski DM, Astell C, Brunham RC, Low DE, Petric M, Roper RL, et al. Severe acute respiratory syndrome (SARS): a year in review. Annu Rev Med 2005;56:357–81.
[2] Marra MA, Jones SJ, Astell CR, Holt RA, Brooks-Wilson A, Butterfield YS, et al. The genome sequence of the SARS-associated coronavirus. Science 2003;300:1399–404.
[3] Rota PA, Oberste MS, Monroe SS, Nix WA, Campagnoli R, Icenogle JP, et al. Characterization of a novel coronavirus associated with severe acute respiratory syndrome. Science 2003;300:1394–9.
[4] Weiss SR, Navas-Martin S. Coronavirus pathogenesis and the emerging pathogen severe acute respiratory syndrome coronavirus. Microbiol Mol Biol Rev 2005;69(4):635–64.
[5] Gallagher TM, Buchmeier MJ. Coronavirus spike proteins in viral entry and pathogenesis. Virology 2001;279(2):371–4.
[6] Godet M, Grosclaude J, Delmas B, Laude H. Major receptor-binding and neutralization determinants are located within the same domain of the transmissible gastroenteritis virus (coronavirus) spike protein. J Virol 1994;68(12):8008–16.
[7] Li W, Moore MJ, Vasilieva N, Sui J, Wong SK, Berne MA, et al. Angiotensin-converting enzyme 2 is a functional receptor for the SARS coronavirus. Nature 2003;426(6965):450–4.
[8] Babcock GJ, Esshaki DJ, Thomas Jr WD, Ambrosino DM. Amino acids 270 to 510 of the severe acute respiratory syndrome coronavirus spike protein are required for interaction with receptor. J Virol 2004;78(9):4552–60.
[9] Wong SK, Li W, Moore MJ, Choe H, Farzan M. A 193-amino acid fragment of the SARS coronavirus S protein efficiently binds angiotensin-converting enzyme 2. J Biol Chem 2004;279(5):3197–201.
[10] ter Meulen J, Bakker AB, van den Brink EN, Weverling GJ, Martina BE, Haagmans BL, et al. Human monoclonal antibody as prophylaxis for SARS coronavirus infection in ferrets. Lancet 2004;363(9427):2139–41.
[11] Greenough TC, Babcock GJ, Roberts A, Hernandez HJ, Thomas Jr WD, Coccia JA, et al. Development and characterization of a severe acute respiratory syndrome-associated coronavirus-neutralizing human monoclonal antibody that provides effective immunoprophylaxis in mice. J Infect Dis 2005;91(4):507–14.
[12] Bisht H, Roberts A, Vogel L, Bukreyev A, Collins PL, Murphy BR, et al. Severe acute respiratory syndrome coronavirus spike protein expressed by attenuated vaccinia virus protectively immunizes mice. Proc Natl Acad Sci USA 2004;101(17):6641–6.
[13] Bukreyev A, Lamirande EW, Buchholz UJ, Vogel LN, Elkins WR, St Claire M, et al. Mucosal immunisation of African green monkeys (*Cercopithecus aethiops*) with an attenuated parainfluenza virus expressing the SARS coronavirus spike protein for the prevention of SARS. Lancet 2004;363(9427):2122–7.
[14] Yang ZY, Kong WP, Huang Y, Roberts A, Murphy BR, Subbarao K, et al. A DNA vaccine induces SARS coronavirus neutralization and protective immunity in mice. Nature 2004;428(6982):561–4.
[15] Taylor DR. Obstacles and advances in SARS vaccine development. Vaccine 2006;24(7):863–71.
[16] Stark CJ, Atreya CD. Molecular advances in the cell biology of SARS-CoV and current disease prevention strategies. Virol J 2005; 2:35.
[17] See RH, Zakhartchouk AN, Petric M, Lawrence DJ, Mok CPY, Hogan RJ, et al. Comparative evaluation of two severe acute respiratory syndrome (SARS) vaccine candidates in mice challenged with SARS coronavirus. J Gen Virol 2006;87:641–50.
[18] Sanchez-Lopez R, Nicholson R, Gesnel MC, Matrisian LM, Breathnach R. Structure-function relationships in the collagenase family member transin. J Biol Chem 1988;263(24):11892–9.
[19] Zakhartchouk AN, Liu Q, Petric M, Babiuk LA. Augmentation of immune responses to SARS coronavirus by a combination of DNA and whole killed virus vaccines. Vaccine 2005;23(35):4385–91.
[20] Bisht H, Roberts A, Vogel L, Subbarao K, Moss B. Neutralizing antibody and protective immunity to SARS coronavirus infection of mice induced by a soluble recombinant polypeptide containing an *N*-terminal segment of the spike glycoprotein. Virology 2005;334(2): 160–5.
[21] Chakraborti S, Prabakaran P, Xiao X, Dimitrov DS. The SARS coronavirus S glycoprotein receptor binding domain: fine mapping and functional characterization. Virol J 2005;2:73.
[22] Comoy EE, Capron A, Thyphronitis G. In vivo induction of type 1 and 2 immune responses against protein antigens. Int Immunol 1997;9(4):523–31.

[23] HogenEsch H. Mechanisms of stimulation of the immune response by aluminum adjuvants. Vaccine 2002;20(Suppl. 3):S34–9.
[24] Harandi AM, Eriksson K, Holmgren J. A protective role of locally administered immunostimulatory CpG oligodeoxynucleotide in a mouse model of genital herpes infection. J Virol 2003;77(2):953–62.
[25] Rao M, Matyas GR, Vancott TC, Birx DL, Alving CR. Immunostimulatory CpG motifs induce CTL responses to HIV type I oligomeric gp140 envelope protein. Immunol Cell Biol 2004;82(5):523–30.
[26] Rankin R, Pontarollo R, Gomis S, Karvonen B, Willson P, Loehr BI, et al. CpG-containing oligodeoxynucleotides augment and switch the immune responses of cattle to bovine herpesvirus-1 glycoprotein D. Vaccine 2002;20(23–24):3014–22.
[27] Weeratna R, Comanita L, Davis HL. CPG ODN allows lower dose of antigen against hepatitis B surface antigen in BALB/c mice. Immunol Cell Biol 2003;81(1):59–62.
[28] Zhang J, Liu Y, Hu L, Gao Q, Zhang Z, Zhang X, et al. Preparation and characterization of SARS in-house reference antiserum. Vaccine 2005;23(48–49):5666–9.
[29] Sui J, Li W, Murakami A, Tamin A, Matthews LJ, Wong SK, et al. Potent neutralization of severe acute respiratory syndrome (SARS) coronavirus by a human mAb to S1 protein that blocks receptor association. Proc Natl Acad Sci USA 2004;101(8):2536–41.
[30] van den Brink EN, Ter Meulen J, Cox F, Jongeneelen MA, Thijsse A, Throsby M, et al. Molecular and biological characterization of human monoclonal antibodies binding to the spike and nucleocapsid proteins of severe acute respiratory syndrome coronavirus. J Virol 2005;79(3):1635–44.
[31] He Y, Lu H, Siddiqui P, Zhou Y, Jiang S. Receptor-binding domain of severe acute respiratory syndrome coronavirus spike protein contains multiple conformation-dependent epitopes that induce highly potent neutralizing antibodies. J Immunol 2005;174(8):4908–15.
[32] He Y, Zhou Y, Liu S, Kou Z, Li W, Farzan M, et al. Receptor-binding domain of SARS-CoV spike protein induces highly potent neutralizing antibodies: implication for developing subunit vaccine. Biochem Biophys Res Commun 2004;324(2):773–81.
[33] Hogan RJ, Gao G, Rowe T, Bell P, Flieder D, Paragas J, et al. Resolution of primary severe acute respiratory syndrome-associated coronavirus infection requires stat1. J Virol 2004;78: 11416–21.
[34] Zhou Z, Post P, Chubet R, Holtz K, McPherson C, Petric M, et al. A recombinant baculovirus-expressed S glycoprotein vaccine elicits high titers of SARS-associated coronavirus (SARS-CoV) neutralizing antibodies in mice. Vaccine 2006;24:3624–31.
[35] Li F, Li W, Farzan M, Harrison SC. Structure of SARS coronavirus spike receptor-binding domain complexed with receptor. Science 2005;309(5742):1864–8.
[36] Vennema H, de Groot RJ, Harbour DA, Dalderup M, Gruffydd-Jones T, Horzinek MC, et al. Early death after feline infectious peritonitis virus challenge due to recombinant vaccinia virus immunization. J Virol 1990;64(3):1407–9.
[37] Yang ZY, Werner HC, Kong WP, Leung K, Traggiai E, Lanzavecchia A, et al. Evasion of antibody neutralization in emerging severe acute respiratory syndrome coronaviruses. Proc Natl Acad Sci USA 2005;102(3):797–801.
[38] Weingartl H, Czub M, Czub S, Neufeld J, Marszal P, Gren J, et al. Immunization with modified vaccinia virus Ankara-based recombinant vaccine against severe acute respiratory syndrome is associated with enhanced hepatitis in ferrets. J Virol 2004;78:12672–6.

Front. Med.
https://doi.org/10.1007/s11684-020-0767-8

REVIEW

Coronavirus disease 2019 (COVID-19): a clinical update

Min Zhou[1,2,3], Xinxin Zhang[1,4], Jieming Qu (✉)[1,2,3]

[1]National Research Center for Translational Medicine, Ruijin Hospital Affiliated to Shanghai Jiao Tong University School of Medicine, Shanghai 200025, China; [2]Department of Respiratory and Critical Care Medicine, Ruijin Hospital Affiliated to Shanghai Jiao Tong University School of Medicine, Shanghai 200025, China; [3]Institute of Respiratory Diseases, Shanghai Jiao Tong University School of Medicine, Shanghai 200025, China; [4]Research Laboratory of Clinical Virology, Ruijin Hospital and Ruijin Hospital North Affiliated to Shanghai Jiao Tong University School of Medicine, Shanghai 200025, China

Abstract **Coronavirus disease 2019 (COVID-19) caused by severe acute respiratory syndrome coronavirus-2 (SARS-CoV-2) has posed a significant threat to global health. It caused a total of 80 868 confirmed cases and 3101 deaths in Chinese mainland until March 8, 2020. This novel virus spread mainly through respiratory droplets and close contact. As disease progressed, a series of complications tend to develop, especially in critically ill patients. Pathological findings showed representative features of acute respiratory distress syndrome and involvement of multiple organs. Apart from supportive care, no specific treatment has been established for COVID-19. The efficacy of some promising antivirals, convalescent plasma transfusion, and tocilizumab needs to be investigated by ongoing clinical trials.**

Keywords coronavirus disease 2019; epidemiology; pathology; radiology; clinical characteristics; treatment

Introduction

Currently, coronavirus disease 2019 (COVID-19) poses a significant threat to global health. World Health Organization (WHO) has declared this outbreak as a "public health emergency of international concern" on January 31, 2020. Within the first two months of the outbreak, the epidemic spread rapidly around the country and the world. As of March 8, 2020, a total of 80 868 confirmed cases and 3101 deaths had been reported in Chinese mainland by National Health Commission of China, and 90 other countries are affected. COVID-19 as an emerging disease, has unique biological characteristics, clinical symptoms, and imaging manifestations, though considerable progress has been made on the clinical management. This article will summarize the epidemiological, etiological, clinical, pathological, and radiological characteristics of COVID-19 and review the latest advancements in the treatment.

Received March 9, 2020; accepted March 11, 2020
Correspondence: Jieming Qu, jmqu0906@163.com

The epidemiology of COVID-19

Epidemic curves reflect that this epidemic may be a mixed outbreak pattern, with early cases suggestive of a continuous common source, potentially at Huanan Seafood Wholesale Market (HSWM), and later cases suggestive of a propagated source as the virus began to be transmitted from person to person [1]. A retrospective analysis on the first 425 patients with confirmed COVID-19 showed that during the early stages of this outbreak, the basic reproduction number R_0 was estimated to be 2.2 [2]. Another modeling study estimated that the R_0 for COVID-19 was 2.68 [3]. Considering the strict prevention and control measures implemented by the Chinese government, a phase-adjusted estimation of epidemic dynamics assumed that the effective reproduction number R_0 was 3.1 at the early phase of the epidemic, and could be gradually decreased [4].

Of the first 99 laboratory-confirmed patients, 49 (49%) had been exposed to HSWM, which was reported to be the possible initial source of severe acute respiratory syndrome coronavirus-2 (SARS-CoV-2) [5]. A Shenzhen family cluster without exposure history to Wuhan markets or wild animals also proved the possibility of person-to-person transmission [6]. Another family cluster of patients provided evidence that asymptomatic carriers may also

be potential sources of SARS-CoV-2 infection [7]. Evidence has recently been obtained to suggest transmission along a chain of 4 generations [8].

SARS-CoV-2 spread mainly through respiratory droplets or close contact. While in the later stage of infection, the virus is also detectable in anal swabs, suggesting the possibility of oral-fecal route transmission [9]. Significant environmental contamination by patients carrying SARS-CoV-2 through respiratory droplets and fecal shedding suggests that the environment serves as a potential medium of transmission and supports the requirement for strict adherence to environmental and hand hygiene [10]. Currently, there is no clear evidence of infection caused by vertical transmission or aerosol transmission.

Virological characteristics of SARS-CoV-2

SARS-CoV-2 is the causative pathogen of COVID-19, identified as the seventh type of coronavirus to infect humans [11]. Six other kinds of coronaviruses are known to cause human disease, including severe acute respiratory syndrome coronavirus (SARS-CoV) and Middle East respiratory syndrome coronavirus (MERS-CoV) with high mortality rate [12]. According to the genome characteristics, coronavirus is separated into four genera: α-CoV, β-CoV, γ-CoV, and δ-CoV [12]. Deep sequencing revealed that this novel coronavirus isolated from lower respiratory tract samples of patient with COVID-19 belongs to β-CoV [11].

Coronavirus has the appearance of crown under electron microscopy. They are enveloped viruses with a single-strand, positive-sense RNA genome, which is the largest known genome for an RNA virus [13]. All coronaviruses share the same genome organization and expression pattern, with two large overlapping reading frames (ORF1a/b) which encode 16 nonstructural proteins, followed by ORFS for four major structural proteins: spike (S), envelope (E), membrane (M), and nucleocapsid (N) [13]. The SARS-CoV-2 protein also contains eight accessory proteins [14]. Spike protein plays an essential role in binding to receptors and is critical for determining host tropism and transmission capacity. It is functionally divided into S1 domain and S2 domain, responsible for receptor binding and cell membrane fusion respectively. The receptor binding domain (RBD) of β-CoV is commonly located in the C-terminal domain of S1 [15]. A team analyzed the cryogenic electron microscopy (Cryo-EM) structure of the SARS-CoV-2 spike protein and found that it has 10 to 20-fold higher binding affinity to human angiotensin-converting enzyme 2 (ACE2) than SARS-CoV does [16].

Phylogenetic analysis of the evolution history showed that SARS-CoV-2 shared a closer sequence homology toward the genomes of SARS-CoV than to that of MERS-CoV [17]. SARS-CoV-2 is highly similar to a bat coronavirus RaTG13, with an overall genome sequence identity of 96.2% [18], indicating that bat, which was discovered to be the natural reservoir host of various SARS-related coronaviruses [19], may also be the original host of SARS-CoV-2. The intermediate host in the process of transmission remains uncertain.

Clinical characteristics

Clinical manifestation

COVID-19 has an incubation period of 1–14 days, mostly ranging from 3 to 7 days [20]. The most common symptoms in mild to moderate patients are fever, fatigue, and dry cough, followed by other symptoms including headache, nasal congestion, sore throat, myalgia, and arthralgia [5,21–23]. A minority of patients had gastrointestinal symptoms, such as nausea, vomiting, and diarrhea, especially in children. In the study of 1099 COVID-19 patients, 43.8% cases presented fever at onset of illness and the percentage further increased to 88.7% during following hospitalization [24]. Notably, fever may occasionally be absent from elderly persons or immunocompromised ones.

A part of patients may progress to shortness of breath, usually in the second week of the illness, and might be accompanied by or progress to hypoxemia [25,26]. For patients presenting tachypnea, chest indrawing, or inability to feed or drink, severe pneumonia should be considered. In 10% to 20% of severe patients, the respiratory injury will inevitably develop into acute respiratory distress syndrome (ARDS) during 8–14 days of the illness, defined as partial pressure of oxygen (PaO_2) to fraction of inspired oxygen (FiO_2) ratio lower than 300 mmHg, as well as resultant non-cardiogenic pulmonary edema and mechanical ventilation [24,25,27]. ARDS, as the main cause of respiratory failure, is associated with high morbidity and mortality. Risk factors for developing into severe to critical cases include advanced age, underlying comorbidities such as hypertension, diabetes, cardiovascular disease, and cerebrovascular disease [23,25,26].

As disease progresses, a series of complications tend to occur, especially in critically ill patients admitted to ICU, including shock, sepsis, acute cardiac injury, acute kidney injury, and even multi-organ dysfunction [23,24,26]. Patients may manifest altered mental status, low oxygen saturation, reduced urine output, weak pulse, cold extremities, low blood pressure, and mottled skin. Besides, patients with acute cardiac injury would present tachycardia or bradycardia. Critically ill ones may also suffer acidosis and increased lactate [23–25]. Current studies reported the peak value of temperature in non-survivors of COVID-19 was significantly higher than that in survivals

during hospitalization [23,24]. Thus, patients presenting hyperthermia and chill should exclude the possibilities of co-infection with bacteria or other pathogens. Attentions should be paid to prevent hospital-acquired pneumonia (HAP) in critical cases and ventilator-associated pneumonia (VAP) in those receiving mechanical ventilation. Coagulopathy and thrombocytopenia are also common complications for COVID-19 infection, which increase the risk of hemorrhage and thrombosis. Mottled skin, petechial or purpuric rash, appearance of black stool or hematuresis could be found in some cases. Patients with the syndrome of persistent hypoxemia, chest pain, pre-syncope or syncope, and hemoptysis should be suspected of having pulmonary thromboembolism (PTE) [28]. The manifestation of limb pain, swelling, erythema, and dilated superficial veins should be suspected of deep vein thrombosis (DVT). Nearly 20% of patients had abnormal coagulation function, and most of severe and critical patients presented coagulation disorders and had the tendency to develop into disseminated intravascular coagulation (DIC) [5,25,26].

Radiological and pathological features

In the early stage of infection, the involved lung lobe presented obvious alveolar edema, proteinaceous exudates, and reactive pneumocyte hyperplasia, accompanied by mild inflammatory infiltration [29]. On gross examination, the whole lung showed bronzing surface and diffuse congestive appearance, with partly hemorrhagic necrosis, as same as the cut surfaces. On histological examination, the typical manifestations were extensive proteinaceous and serous exudation in the alveolar, hyaline membrane formation, and inflammatory infiltration with multinucleated syncytial cells. Type II alveolar epithelial cells showed extensive hyperplasia, and some presented necrosis and desquamation. Viral inclusions could be identified in epithelium and macrophage. Besides, alveolar septal vessels manifested congestion with alveolar edema. The infiltration of monocytes and lymphocytes in alveolar cavity and microthrombosis were prominent. Some parts showed alveolar exudate organization and pulmonary interstitial fibrosis. With a fraction of desquamation of mucosal epithelium, bronchi were covered by mucus even mucus plug [20,30,31].

In addition, other organs also suffered pathological damage to some extent [20]. The atrophic spleen showed significantly reduced lymphocytes, focal hemorrhage and necrosis, and macrophage hyperplasia. With degeneration and necrosis of cardiomyocytes, a small number of monocytes, lymphocytes, and/or neutrophils were infiltrated in the myocardial interstitium. Protein exudation was seen in renal glomerulus and within hyaline cast, and renal tubular epithelium degenerated and desquamated. Besides, hepatocytes degeneration, necrosis, and inflammatory infiltration also occurred. The brain presented congestion, edema, and degeneration of some neurons. Meanwhile, microthrombosis could be found in multiple organs.

Radiological images play an important role in the diagnosis and providing guidance for treatment. Guan *et al.* found that 86.2% of patients manifested abnormalities in chest CT images, of whom more than 75% had bilateral lung involvement, mainly with peripheral and diffused distribution [24]. Patients of different severity presented significant different lesions on chest CT (Fig. 1). Mild patients manifested unilateral and focal ground-glass opacity (GGO) which gradually develops to bilateral or multilobular lesions. As the disease progressed further, GGOs evolved to consolidation lesions, presenting mix-pattern or pure consolidation, with the latter being more common in critically ill patients admitted to ICU [5,25,32]. Consistent with the interstitial involvement in viral pneumonia, Zhao *et al.* suggested that 48.5% of CT images manifested reticular patterns, and 28.7% presented interlobular septal thickening [33]. Unlike influenza pneumonia, which usually exhibited unilateral GGO and significant solid nodules, only 6% of COVID-19 patients had solid nodules [32,34,35]. Moreover, other lesions included adjacent pleura thickening, vascular enlargement, bronchial wall thickening, traction bronchiectasis, air bronchogram, pericardial effusion, etc. [32,33,36].

Follow-up of CT scan could help to monitor disease changes and evaluate therapeutic effects [32]. Some dynamic images fluctuate repeatedly, and showed coexistence of absorption of primary lesions and emergence of new ones. During disease deterioration, increased number of or enlarged lesions could be observed in radiological imaging, and part of them even developed into a "white lung" with diffusely involved lung [37].

Laboratory examinations

A majority of COVID-19 patients showed normal leucocyte count, and nearly one third had leucopenia [21,24]. Lymphocytopenia, as one of the most typical laboratory abnormalities, was present in 83.2% of patients, with an even higher proportion in severe ones [24,26]. In addition, previous studies also revealed that increased D-dimer level and prolonged prothrombin time were also common features of COVID-19, especially for severe patients [24–26]. Meanwhile, SARS-CoV-2 might damage liver and myocardium to some extent, showing elevated levels of aminotransferase, creatine kinase, and myoglobin with diverse degrees, as well as increased troponin in critical patients [5,23,25]. A few patients had renal dysfunction, presenting increased serum creatinine or blood urea nitrogen [5].

As for infection-related serum biomarkers, our studies have reported that most of patients had increased concentration of C-reactive protein, interleukin-6 (IL-6), and erythrocyte sedimentation rate [5]. Likewise, Huang

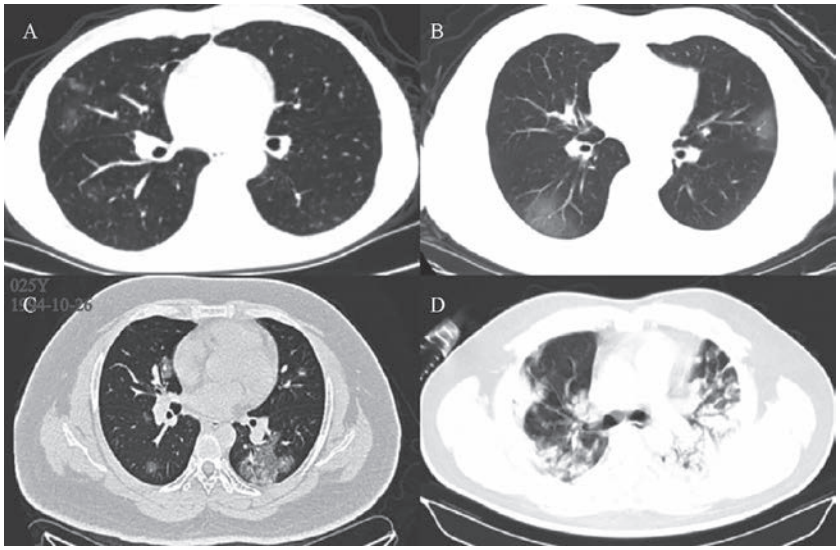

Fig. 1 Chest CT of COVID-19 patients with different severity. (A) A 57-year-old man with mild COVID-19 showed unilateral and slight GGO. (B) A 52-year-old male patient classified into moderate type exhibited multifocal and bilateral GGO with sub-pleural distribution. (C) In a 26-year-old man with severe COVID-19, bilateral and multifocal lesions were observed with a combination of pure GGO, mixed GGO, and consolidation. (D) In a 50-year-old critically ill women, chest CT showed bilateral massive shadows of high density and GGO, accompanied by air bronchogram sign.

et al. observed similar phenomenon and proposed that ICU patients might suffer severe cytokine storms, with a overproduction of IL-7, IL-10, GCSF, IP10, MCP1, MIP1A, and TNF-α, etc. [25]. Multi-drug resistant *Acinetobacter baumannii* and *Klebsiella pneumoniae* have been isolated in COVID-19 patients [5,23]. Other identified microorganisms included *Pseudomonas aeruginosa*, *Aspergillus flavus*, *Aspergillus fumigatus*, *Candida albicans,* and *Candida glabrata* [5,23].

Diagnostic testing for COVID-19

Laboratory confirmed COVID-19 patients had positive results on real-time reverse transcriptase polymerase chain reaction (RT-PCR) of nasal and pharyngeal swab, sputum, blood, faeces, and urine specimens [25]. The collected clinical specimens need to be transported to designated laboratories promptly, and extracted for RNA correctly, followed by RT-PCR detection with primers and probes of appropriate sequences [25]. The value of cycle threshold (Ct) was the criterion to determine the detection result, with less than 37 being defined as negative, above 40 as positive and a medium load (37–40) calling for confirmation by retesting [2].

The detection of SARS-CoV-2 specific IgM and IgG antibodies can also be used for diagnosis [20]. COVID-19 infection could be determined with one of the following criteria: positive specific IgM, the transformation of specific IgG from negative to positive, a 4-fold increase in IgG titer during recovery period compared with the result of acute phase. Although antibody detection was simple, rapid, and inexpensive, it is still not widely used due to inherent limitations, for example, false-negativity resulted from the existence of window period, non-comparable sensitivity and specificity with PT-PCR, absence of exclusion criteria making it a diagnosis tool only.

Treatment

Antiviral agents

These is no specific antiviral treatment which has been proven to be effective for COVID-19. Combinations of over three antivirals are not suggested. Current treatment options are mainly based on previous experience showing clinical benefits in treating influenza, Ebola, MERS, SARS, and other viral infections. It is reported that most of COVID-19 patients received antiviral therapy in China [5,21,25], and here we will introduce some commonly used drugs.

Ribavirin is representative of nucleoside analogs. The combination of ribavirin and recombinant interferon, a broad spectrum antiviral agent, showed augmentation effect in inhibiting MERS-CoV replication and reduced doses of both ribavirin and interferon [38]. However, most of clinical experiences in MERS patients come from limited case reports and observational studies, making the quality of evidence for ribavirin and interferon treatment

efficacy very low [39]. It is recommended to administer ribavirin by intravenous infusion in combination with inhaled interferon-α or oral lopinavir/ritonavir in the 5th version guideline on COVID-19 diagnosis and treatment issued by Chinese National Health Commission [20]. Notably, ribavirin is not suggested by military medical team coming to Hubei [40] and interferon-α inhalation is worried to increase the risk of virus-containing aerosol production and airway stimulation.

Lopinavir/ritonavir is a combination of a protease inhibitor and a booster used for the treatment of human immunodeficiency virus (HIV) infection. Currently, randomized controlled trials for the efficacy of a combination of lopinavir/ritonavir with interferon-α in mild to moderate patients (ChiCTR2000029387) and severe to critical patients with COVID-19 (ChiCTR2000029308) are in progress.

Remdesivir, a novel nucleotide analog RNA polymerase inhibitor, is considered as the most promising antiviral drug for the treatment of COVID-19. It showed broad spectrum antiviral activities, from inhibition of human and zoonotic coronavirus (including SARS-CoV-2 [41] as well Ebola virus) *in vitro*, to prophylactic and therapeutic effects in animal model of MERS-CoV and SARS-CoV infection [42,43]. The first COVID-19 patient identified in the United States was given remdesivir without obvious adverse reactions. Two trials on efficacy of remdesivir have been launched in China among mild to moderate patients (NCT04252664) and severe to critical patients (NCT04257656) infected with SARS-CoV-2.

Neuraminidase inhibitors (NAIs), such as oral oseltamivir and intravenous peramivir, showed substantial clinical improvement in treating influenza patients [44]. Oseltamivir was widely used for suspected and confirmed COVID-19 patients in China [26], however, there is no exact evidence that supports its application.

A research team from Zhejiang University reported that abidol has the potential to inhibit SARS-CoV-2, which was previously used for influenza. There is a multicenter, randomized, and controlled trial (ChiCTR2000029573) to evaluate the efficacy of abidol and lopinavir/litonavir, either alone or in combination with a new type of interferon, Novaferon.

Corticosteroids

According to current WHO interim guidance on COVID-19 management [27], corticosteroids were not recommended as routine therapy unless indicated for another reason, because possible harms and higher risk of mortality attributed to corticosteroids therapy have been identified by studies on other coronaviruses and influenza.

An epidemiological study conducted in Wuhan observed a larger percentage of patients receiving corticosteroids in ICU groups when compared with non-ICU groups (6 (46%) vs. 3 (11%); $P = 0.013$), while we still cannot determine the effects of corticosteroids due to the limited sample size [25]. According to the latest guidelines issued by National Health Commission of China (version 7) [20] and the interim guidance of WHO [27], when SARS-CoV-2 infection is suspected, corticosteroids should be recommended to use with caution. New Coronavirus Infection Diagnosis and Treatment Scheme (Trial Version) published by Military Support Hubei Medical Team also put forward that for mild to moderate COVID-19 patients, corticosteroids should not be given principally and high-dose corticosteroid pulse therapy was not recommended. Only patients presenting ongoing deterioration in oxygenation index, or rapid progression of radiological findings, or excessive activation of immune responses, will be considered to use short-term corticosteroid therapy within 10 days of illness onset. Seven designated hospitals in Zhejiang Province gave patients corticosteroids when they showed increased resting respiratory rate ($>$ 30 breaths/minute), drop in oxygen saturation ($<$ 93%) on room air, or multi-lobular progression ($>$ 50%) on imaging within 48 h [21]. Timely and appropriate use of corticosteroids combined with ventilator support should be considered for severe patients to prevent progression to ARDS [30].

The pharmacologic use of corticosteroids in COVID-19 treatment should vary with severity [20,40]. For severe cases, it is suggested to start at a dose of 40 to 80 mg/day methylprednisolone and slowly taper over 7 to 10 days, and some suggested for a shorter period of 3 to 5 days. For critically ill cases, a starting dose of 80 to 160 mg/day methylprednisolone, following a slow withdrawal within 7 to 10 days is considered.

Antimicrobial therapy

It is widely recognized that many patients, especially critically ill patients were susceptible to secondary infections. Patients receiving corticosteroids had increased risks of developing HAP due to the immunosuppression effects, and those who received mechanical ventilation were susceptible to VAP. The latest guidelines issued by National Health Commission of China for the diagnosis and treatment of COVID-19 infection (version 7) [20] advise against inappropriate and unnecessary use of antimicrobial therapy, especially combination of broad-spectrum antibiotics. If the sputum or blood specimens showed a clear evidence of etiology or the PCT levels increased, administration of antimicrobial agents should be considered.

As shown in a study of 99 patients with COVID-19, *Acinetobacter baumannii*, *Klebsiella pneumoniae,* and *Aspergillus flavus* were simultaneously cultured in one patient. Meanwhile, one case of fungal infection was

attributed to *Candida glabrata* and three cases of fungal infection were caused by *Candida albicans* [5].

When selecting antimicrobial agents for initial empiric treatment, in addition to the local epidemiological data of HAP/VAP pathogens, imaging features of pulmonary lesions should also be taken into account [45].

As for fungal infections, voriconazole is recommended for the treatment of *Aspergillus* infections, while fluconazole is more suitable for *Candida* spp. infections. When patients are suspected with *Pneumocystis* pneumonia, sulfamethoxazole and caspofungin should be promptly administrated [45].

Anticoagulant

In clinical practice, nearly 20% of patients with COVID-19 are found to have abnormal coagulation function, and almost all severely and critically ill patients presented coagulation disorders [5,25,26]. In view of no relevant experience for reference, anticoagulation should be given with great caution in patients with DIC though microthrombosis was observed in lung, liver, and other organs by autopsy. When patients exhibit a bleeding tendency or when surgical treatment is needed, platelet transfusion or administration of fresh-frozen plasma is recommended to correct coagulopathies analogs [46].

Low molecular weight heparin (LMWH) can be used for drug prevention. As for subjects with clinical manifestations, clinicians need to be alert to the occurrence of PTE, initiate the diagnostic procedures, and develop corresponding treatment strategies based on risk stratification. Considering the risk of disease transmission and the false positive results caused by the presence of lung lesions, the diagnosis of PTE by pulmonary ventilation-perfusion imaging is not recommended.

If the critically ill patients cannot take examination due to specific conditions and the infectivity of COVID-19, it is recommended to perform anticoagulant therapy for patients without contraindications. If the condition is life-threatening and bedside echocardiography indicates new onset of right ventricular volume overload or pulmonary hypertension, thrombolytic therapy or other cardiopulmonary support treatments, such as extracorporeal membrane oxygenation (ECMO) can be initiated with the patient's full informed consent.

Oxygen therapy

For mild to moderate patients with hypoxemia, nasal catheters and masks and even high-flow nasal cannula oxygen therapy (HFNC) are advised. While for severe and critical patients with respiratory distress, HFNC, non-invasive mechanical ventilation (NIV) or invasive mechanical ventilation, and even ECMO should be considered.

HFNC

HFNC can provide accurate oxygen concentration and a certain positive airway pressure to promote alveolar expansion to improve oxygenation and respiratory distress [47]. However, according to expert consensus on the use of HFNC for COVID-19, patients with cardiac arrest, weak spontaneous breathing, $PaO_2/FiO_2 < 100$ mmHg, $PaCO_2 > 45$ mmHg and pH < 7.25 and upper airway obstruction are contraindicated.

NIV or invasive mechanical ventilation

For severe patients with respiratory distress or hypoxemia that cannot be alleviated after standard oxygen therapy, NIV can also be considered with close surveillance [24,26]. Dangers *et al*. considered that changes in dyspnea could be used as a variable to predict the failure of non-invasive ventilation [48]. If the patient continuously deteriorates or the respiratory rate cannot be improved after a short time (about 1–2 h), timely tracheal intubation and invasive ventilation are required [49]. Notably, patients with hemodynamic instability, multiple organ failure or abnormal mental status should not receive non-invasive ventilation.

Lung protection ventilation strategies (small tidal volume, limited plateau pressure, and permissive hypercapnia) are suggested to be adopted in invasive mechanical ventilation to reduce ventilator-related lung injury [50]. Compared with NIV, invasive mechanical ventilation can more effectively improve the pulmonary ventilation function and respiratory mechanics of patients with acute respiratory failure. It can effectively increase the SaO_2 level and is more conducive to lower the plasma BNP level [51]. However, invasive mechanical ventilation requires tracheotomy, or oral/nasal tracheal intubation to establish an artificial airway, which is very likely to cause damage to patients, such as mediastinal emphysema, ventilator-related lung injury, and other related complications, such as reduced swallowing function, gastresophageal reflux, infections, etc. What's more, invasive mechanical ventilation also increases the risk of secondary infections transmitted by aerosol particles [52].

Continuous renal replacement therapy (CRRT)

For critical patients, CRRT can support organ function, reduce cytokine storms and maintain internal environment stability [53]. Three clinical studies showed that the incidence of AKI in patients with COVID-19 was 3% to 7%, and 7% to 9.0% were treated with CRRT. In ICU, the rate of CRRT application was 5.6% to 23.0% and reached as high as 66.7% to 100% in patients with AKI [5,26,54]. CRRT is recommended for patients who exhibit AKI

indications (hyperkalemia, acidosis, pulmonary edema, severe sodium ion disorders) or patients with CKD who have not undergone hemodialysis. During septic shock, CRRT can effectively remove inflammatory mediators and significantly improve hemodynamics. When ARDS appears in combination with multiple organ dysfunction syndrome (MODS), early CRRT is recommended [55]. CRRT combined with the treatment of ECMO may remove cytokines, reduce the activity of macrophages and monocytes, and better preserve lung parenchyma.

Convalescent plasma therapy for COVID-19

Some studies reported that early convalescent plasma treatment for influenza and SARS-CoV infection is associated with decreased viral load and reduction in mortality [56], however, the studies were heterogeneous and of low quality. The WHO deemed convalescent plasma transfusion as the most promising therapy for MERS-CoV infection, while the efficacy remained inconclusive, with a lack of adequate clinical trials [56–58]. Since the virological and clinical characteristics among SARS, MERS, and COVID-19 were comparable [59], convalescent plasma could have immunotherapeutic potential in COVID-19 treatment and further investigations are needed to prove its safety and efficacy.

One possible explanation for the efficacy of convalescent plasma therapy is that the neutralizing antibodies from convalescent plasma might suppress viremia [60], so understanding the antibody response during the course of SARS-CoV-2 infection could provide strong empirical support for the application of convalescent plasma therapy. A study reported that on day 5 after treatment, an increase of viral antibodies can be seen in nearly all patients, IgM positive rate increased to 81%, whereas IgG positive rate increased to 100%, which was considered as a transition from earlier to later period of infection [9]. Preliminary study has showed that patients who have recovered from COVID-19 with a high neutralizing antibody titer and could provide a valuable source of the convalescent plasma.

Plasma transfusion may cause adverse effects, so convalescent plasma therapy is recommended as a last resort to improve the survival rate of severe patients with COVID-19. The optimal dose and treatment time point, as well as the therapeutic indications of convalescent blood products in COVID-19 remain uncertain, which need to be further investigated in randomized clinical studies.

Tocilizumab

Tocilizumab is a humanized IgG1κ monoclonal antibody which can specifically bind soluble or membrane-type IL-6 receptors (Sil-6R and Mil-6R), and has been widely used in the treatment of autoimmune diseases such as rheumatoid arthritis [61], adult-onset Still's disease [62], and large vessel vasculitis [63]. For COVID-19 infection, clinical studies have shown that serum levels of inflammatory mediators in severe patients are significantly higher than those in common patients [25]. Excessive immune responses can trigger cytokine storms and cause damage to multiple target organs. Recent guidelines also point that a progressive rise in IL-6 may be a clinical warning indicator for the deterioration of COVID-19. A domestic research team found that tocilizumab can block the signaling pathways of two key inflammatory factors, IL-6 and GM-CSF, and reduce the inflammatory response. A multicenter, randomized, controlled clinical study has been coducted to evaluate the efficacy and safety of tocilizumab in the treatment of moderate patients at high risk to develop into severe and critical patients (registration number: ChiCTR2000029765). For patients with elevated IL-6 levels, the efficacy of tocilizumab can be expected.

Conclusions

In this review, we gave an overview of epidemiological, etiological, clinical, pathological, and imaging characteristics of COVID-19 and introduced the latest advancements in the treatment. This novel virus spread mainly through respiratory droplets and close personal contact. A series of complications tend to develop during disease progression, especially in critically ill patients. Pathological studies of autopsy showed typical presentations of acute respiratory distress syndrome and involvement of multiple organs. Apart from supportive care, no specific treatment has been established for COVID-19. The efficacy of some promising antivirals, convalescent plasma transfusion, and tocilizumab needs to be further validated by ongoing clinical trials.

Acknowledgements

This work was funded in part by a grant from innovative research team of high-level local universities in Shanghai.

Compliance with ethic guidelines

Min Zhou, Xinxin Zhang, and Jieming Qu declare that they have no conflict of interest. This manuscript is a review article that does not involve a research protocol requiring approval by the relevant institutional review board or ethics committee.

References

1. Wu Z, McGoogan JM. Characteristics of and important lessons from the coronavirus disease 2019 (COVID-19) outbreak in China: summary of a report of 72 314 cases from the Chinese Center for Disease Control and Prevention. JAMA 2020 Feb 24. [Epub ahead

of print] doi: 10.1001/jama.2020.2648
2. Li Q, Guan X, Wu P, Wang X, Zhou L, Tong Y, Ren R, Leung KSM, Lau EHY, Wong JY, Xing X, Xiang N, Wu Y, Li C, Chen Q, Li D, Liu T, Zhao J, Liu M, Tu W, Chen C, Jin L, Yang R, Wang Q, Zhou S, Wang R, Liu H, Luo Y, Liu Y, Shao G, Li H, Tao Z, Yang Y, Deng Z, Liu B, Ma Z, Zhang Y, Shi G, Lam TTY, Wu JTK, Gao GF, Cowling BJ, Yang B, Leung GM, Feng Z. Early transmission dynamics in Wuhan, China, of novel coronavirus-infected pneumonia. N Engl J Med 2020 Jan 29. [Epub ahead of print] doi: 10.1056/NEJMoa2001316
3. Wu JT, Leung K, Leung GM. Nowcasting and forecasting the potential domestic and international spread of the 2019-nCoV outbreak originating in Wuhan, China: a modelling study. Lancet 2020; 395(10225): 689–697
4. Wang H, Wang Z, Dong Y, Chang R, Xu C, Yu X, Zhang S, Tsamlag L, Shang M, Huang J, Wang Y, Xu G, Shen T, Zhang X, Cai Y. Phase-adjusted estimation of the number of coronavirus disease 2019 cases in Wuhan, China. Cell Discov 2020; 6(1): 10
5. Chen N, Zhou M, Dong X, Qu J, Gong F, Han Y, Qiu Y, Wang J, Liu Y, Wei Y, Xia J, Yu T, Zhang X, Zhang L. Epidemiological and clinical characteristics of 99 cases of 2019 novel coronavirus pneumonia in Wuhan, China: a descriptive study. Lancet 2020; 395 (10223): 507–513
6. Chan JF, Yuan S, Kok KH, To KK, Chu H, Yang J, Xing F, Liu J, Yip CC, Poon RW, Tsoi HW, Lo SK, Chan KH, Poon VK, Chan WM, Ip JD, Cai JP, Cheng VC, Chen H, Hui CK, Yuen KY. A familial cluster of pneumonia associated with the 2019 novel coronavirus indicating person-to-person transmission: a study of a family cluster. Lancet 2020; 395(10223): 514–523
7. Huang R, Xia J, Chen Y, Shan C, Wu C. A family cluster of SARS-CoV-2 infection involving 11 patients in Nanjing, China. Lancet Infect Dis 2020 Feb 28. [Epub ahead of print] doi: 10.1016/S1473-3099(20)30147-X
8. Phelan AL, Katz R, Gostin LO. The novel coronavirus originating in Wuhan, China: challenges for global health governance. JAMA 2020; 323(8): 709
9. Zhang W, Du RH, Li B, Zheng XS, Yang XL, Hu B, Wang YY, Xiao GF, Yan B, Shi ZL, Zhou P. Molecular and serological investigation of 2019-nCoV infected patients: implication of multiple shedding routes. Emerg Microbes Infect 2020; 9(1): 386–389
10. Ong SWX, Tan YK, Chia PY, Lee TH, Ng OT, Wong MSY, Marimuthu K. Air, surface environmental, and personal protective equipment contamination by severe acute respiratory syndrome coronavirus 2 (SARS-CoV-2) from a symptomatic patient. JAMA 2020 Mar 4. [Epub ahead of print] doi: 10.1001/jama.2020.3227
11. Zhu N, Zhang D, Wang W, Li X, Yang B, Song J, Zhao X, Huang B, Shi W, Lu R, Niu P, Zhan F, Ma X, Wang D, Xu W, Wu G, Gao GF, Tan W; China Novel Coronavirus Investigating and Research Team. A novel coronavirus from patients with pneumonia in China, 2019. N Engl J Med 2020; 382(8): 727–733
12. Su S, Wong G, Shi W, Liu J, Lai ACK, Zhou J, Liu W, Bi Y, Gao GF. Epidemiology, genetic recombination, and pathogenesis of coronaviruses. Trends Microbiol 2016; 24(6): 490–502
13. Forni D, Cagliani R, Clerici M, Sironi M. Molecular evolution of human coronavirus genomes. Trends Microbiol 2017; 25(1): 35–48
14. Wu A, Peng Y, Huang B, Ding X, Wang X, Niu P, Meng J, Zhu Z, Zhang Z, Wang J, Sheng J, Quan L, Xia Z, Tan W, Cheng G, Jiang T. Genome composition and divergence of the novel coronavirus (2019-nCoV) originating in China. Cell Host Microbe 2020 Feb 7. [Epub ahead of print] doi: 10.1016/j.chom.2020.02.001
15. Lu R, Zhao X, Li J, Niu P, Yang B, Wu H, Wang W, Song H, Huang B, Zhu N, Bi Y, Ma X, Zhan F, Wang L, Hu T, Zhou H, Hu Z, Zhou W, Zhao L, Chen J, Meng Y, Wang J, Lin Y, Yuan J, Xie Z, Ma J, Liu WJ, Wang D, Xu W, Holmes EC, Gao GF, Wu G, Chen W, Shi W, Tan W. Genomic characterisation and epidemiology of 2019 novel coronavirus: implications for virus origins and receptor binding. Lancet 2020; 395(10224): 565–574
16. Wrapp D, Wang N, Corbett KS, Goldsmith JA, Hsieh CL, Abiona O, Graham BS, McLellan JS. Cryo-EM structure of the 2019-nCoV spike in the prefusion conformation. Science 2020 Feb 19. [Epub ahead of print] doi: 10.1126/science.abb2507
17. Xu X, Chen P, Wang J, Feng J, Zhou H, Li X, Zhong W, Hao P. Evolution of the novel coronavirus from the ongoing Wuhan outbreak and modeling of its spike protein for risk of human transmission. Sci China Life Sci 2020; 63(3): 457–460
18. Zhou P, Yang XL, Wang XG, Hu B, Zhang L, Zhang W, Si HR, Zhu Y, Li B, Huang CL, Chen HD, Chen J, Luo Y, Guo H, Jiang RD, Liu MQ, Chen Y, Shen XR, Wang X, Zheng XS, Zhao K, Chen QJ, Deng F, Liu LL, Yan B, Zhan FX, Wang YY, Xiao GF, Shi ZL. A pneumonia outbreak associated with a new coronavirus of probable bat origin. Nature 2020; 579(7798): 270–273
19. de Wit E, van Doremalen N, Falzarano D, Munster VJ. SARS and MERS: recent insights into emerging coronaviruses. Nat Rev Microbiol 2016; 14(8): 523–534
20. National Health Commission of the People's Republic of China. Guideline for the diagnosis and treatment of COVID-19 infections (version 1–7). 2020. http://www.nhc.gov.cn/yzygj/zcwj2/new_zcwj.shtml (accessed March 9, 2020)
21. Xu XW, Wu XX, Jiang XG, Xu KJ, Ying LJ, Ma CL, Li SB, Wang HY, Zhang S, Gao HN, Sheng JF, Cai HL, Qiu YQ, Li LJ. Clinical findings in a group of patients infected with the 2019 novel coronavirus (SARS-Cov-2) outside of Wuhan, China: retrospective case series. BMJ 2020; 368: m606
22. Zhang JJ, Dong X, Cao YY, Yuan YD, Yang YB, Yan YQ, Akdis CA, Gao YD. Clinical characteristics of 140 patients infected with SARS-CoV-2 in Wuhan, China. Allergy 2020 Feb 19. [Epub ahead of print] doi: 10.1111/all.14238
23. Yang X, Yu Y, Xu J, Shu H, Xia J, Liu H, Wu Y, Zhang L, Yu Z, Fang M, Yu T, Wang Y, Pan S, Zou X, Yuan S, Shang Y. Clinical course and outcomes of critically ill patients with SARS-CoV-2 pneumonia in Wuhan, China: a single-centered, retrospective, observational study. Lancet Respir Med 2020 Feb 24. [Epub ahead of print] doi: 10.1016/S2213-2600(20)30079-5
24. Guan WJ, Ni ZY, Hu Y, Liang WH, Ou CQ, He JX, Liu L, Shan H, Lei CL, Hui DSC, Du B, Li LJ, Zeng G, Yuen KY, Chen RC, Tang CL, Wang T, Chen PY, Xiang J, Li SY, Wang JL, Liang ZJ, Peng YX, Wei L, Liu Y, Hu YH, Peng P, Wang JM, Liu JY, Chen Z, Li G, Zheng ZJ, Qiu SQ, Luo J, Ye CJ, Zhu SY, Zhong NS; China Medical Treatment Expert Group for COVID-19. Clinical characteristics of coronavirus disease 2019 in China. N Engl J Med 2020 Feb 28. [Epub ahead of print] doi: 10.1056/NEJMoa2002032
25. Huang C, Wang Y, Li X, Ren L, Zhao J, Hu Y, Zhang L, Fan G, Xu

J, Gu X, Cheng Z, Yu T, Xia J, Wei Y, Wu W, Xie X, Yin W, Li H, Liu M, Xiao Y, Gao H, Guo L, Xie J, Wang G, Jiang R, Gao Z, Jin Q, Wang J, Cao B. Clinical features of patients infected with 2019 novel coronavirus in Wuhan, China. Lancet 2020; 395(10223): 497–506

26. Wang D, Hu B, Hu C, Zhu F, Liu X, Zhang J, Wang B, Xiang H, Cheng Z, Xiong Y, Zhao Y, Li Y, Wang X, Peng Z. Clinical characteristics of 138 hospitalized patients with 2019 novel coronavirus-infected pneumonia in Wuhan, China. JAMA 2020 Feb 7. [Epub ahead of print] doi: 10.1001/jama.2020.1585
27. WHO. Clinical management of severe acute respiratory infection when novel coronavirus (nCoV) infection is suspected: interim guidance. 2020. https://www.who.int/publications-detail/clinical-management-of-severe-acute-respiratory-infection-when-novel-coronavirus-(ncov)-infection-is-suspected (accessed March 9, 2020)
28. Konstantinides SV, Meyer G, Becattini C, Bueno H, Geersing GJ, Harjola VP, Huisman MV, Humbert M, Jennings CS, Jiménez D, Kucher N, Lang IM, Lankeit M, Lorusso R, Mazzolai L, Meneveau N, Ní Áinle F, Prandoni P, Pruszczyk P, Righini M, Torbicki A, Van Belle E, Zamorano JL; ESC Scientific Document Group. 2019 ESC Guidelines for the diagnosis and management of acute pulmonary embolism developed in collaboration with the European Respiratory Society (ERS). Eur Heart J 2020; 41(4): 543–603
29. Tian S, Hu W, Niu L, Liu H, Xu H, Xiao SY. Pulmonary pathology of early phase 2019 novel coronavirus (COVID-19) pneumonia in two patients with lung cancer. J Thorac Oncol 2020 Feb 27. [Epub ahead of print] doi: 10.1016/j.jtho.2020.02.010
30. Xu Z, Shi L, Wang Y, Zhang J, Huang L, Zhang C, Liu S, Zhao P, Liu H, Zhu L, Tai Y, Bai C, Gao T, Song J, Xia P, Dong J, Zhao J, Wang FS. Pathological findings of COVID-19 associated with acute respiratory distress syndrome. Lancet Respir Med 2020 Feb 18. [Epub ahead of print] doi: 10.1016/S2213-2600(20)30076-X
31. Luo W,Yu H,Gou J,Li X,Sun Y,Li J,Liu L.Clinical pathology of critical patient with novel coronavirus pneumonia (COVID-19). Preprints 2020; 2020020407 https://www.preprints.org/manuscript/202002.0407/v4
32. Shi H, Han X, Jiang N, Cao Y, Alwalid O, Gu J, Fan Y, Zheng C. Radiological findings from 81 patients with COVID-19 pneumonia in Wuhan, China: a descriptive study. Lancet Infect Dis 2020 Feb 24. [Epub ahead of print] doi: 10.1016/S1473-3099(20)30086-4
33. Zhao W, Zhong Z, Xie X, Yu Q, Liu J. Relation between chest CT findings and clinical conditions of coronavirus disease (COVID-19) pneumonia: a multicenter study. AJR Am J Roentgenol 2020 Mar 3. [Epub ahead of print] doi: 10.2214/AJR.20.22976
34. Koo HJ, Lim S, Choe J, Choi SH, Sung H, Do KH. Radiographic and CT features of viral pneumonia. Radiographics 2018; 38(3): 719–739
35. Franquet T, Müller NL, Giménez A, Martínez S, Madrid M, Domingo P. Infectious pulmonary nodules in immunocompromised patients: usefulness of computed tomography in predicting their etiology. J Comput Assist Tomogr 2003; 27(4): 461–468
36. Xu X, Yu C, Qu J, Zhang L, Jiang S, Huang D, Chen B, Zhang Z, Guan W, Ling Z, Jiang R, Hu T, Ding Y, Lin L, Gan Q, Luo L, Tang X, Liu J. Imaging and clinical features of patients with 2019 novel coronavirus SARS-CoV-2. Eur J Nucl Med Mol Imaging 2020 Feb 28. [Epub ahead of print] doi: 10.1007/s00259-020-04735-9
37. Wu J, Feng CL, Xian XY, Qiang J, Zhang J, Mao QX, Kong SF, Chen YC, Pan JP. Novel coronavirus pneumonia (COVID-19) CT distribution and sign features. Chin J Tuberc Respir Dis (Zhonghua Jie He He Hu Xi Za Zhi) 2020 Mar 3. [Epub ahead of print] (in Chinese) doi: 10.3760/cma.j.cn112147-20200217-00106
38. Falzarano D, de Wit E, Martellaro C, Callison J, Munster VJ, Feldmann H. Inhibition of novel β coronavirus replication by a combination of interferon-α2b and ribavirin. Sci Rep 2013; 3(1): 1686
39. Momattin H, Al-Ali AY, Al-Tawfiq JA. A Systematic review of therapeutic agents for the treatment of the Middle East respiratory syndrome coronavirus (MERS-CoV). Travel Med Infect Dis 2019; 30: 9–18
40. Shi Y. What are the highlights of "Diagnosis and treatment of Disease 2019 novel coronavirus infection suitable for Military support Hubei medical team". Chin J Tuberc Respir Dis (Zhonghua Jie He He Hu Xi Za Zhi) 2020 Feb 26. [Epub ahead of print] (in Chinese) doi: 10.3760/cma.j.cn112147-20200225-00183
41. Wang M, Cao R, Zhang L, Yang X, Liu J, Xu M, Shi Z, Hu Z, Zhong W, Xiao G. Remdesivir and chloroquine effectively inhibit the recently emerged novel coronavirus (2019-nCoV) *in vitro*. Cell Res 2020; 30(3): 269–271
42. Sheahan TP, Sims AC, Graham RL, Menachery VD, Gralinski LE, Case JB, Leist SR, Pyrc K, Feng JY, Trantcheva I, Bannister R, Park Y, Babusis D, Clarke MO, Mackman RL, Spahn JE, Palmiotti CA, Siegel D, Ray AS, Cihlar T, Jordan R, Denison MR, Baric RS. Broad-spectrum antiviral GS-5734 inhibits both epidemic and zoonotic coronaviruses. Sci Transl Med 2017; 9(396): eaal3653
43. de Wit E, Feldmann F, Cronin J, Jordan R, Okumura A, Thomas T, Scott D, Cihlar T, Feldmann H. Prophylactic and therapeutic remdesivir (GS-5734) treatment in the rhesus macaque model of MERS-CoV infection. Proc Natl Acad Sci USA 2020 Feb 13. [Epub ahead of print] doi: 10.1073/pnas.1922083117
44. Chow EJ, Doyle JD, Uyeki TM. Influenza virus-related critical illness: prevention, diagnosis, treatment. Crit Care 2019; 23(1): 214
45. Shi Y, Huang Y, Zhang TT, Cao B, Wang H, Zhuo C, Ye F, Su X, Fan H, Xu JF, Zhang J, Lai GX, She DY, Zhang XY, He B, He LX, Liu YN, Qu JM. Chinese guidelines for the diagnosis and treatment of hospital-acquired pneumonia and ventilator-associated pneumonia in adults (2018 Edition). J Thorac Dis 2019; 11(6): 2581–2616
46. Nishida O, Ogura H, Egi M, Fujishima S, Hayashi Y, Iba T, Imaizumi H, Inoue S, Kakihana Y, Kotani J, Kushimoto S, Masuda Y, Matsuda N, Matsushima A, Nakada TA, Nakagawa S, Nunomiya S, Sadahiro T, Shime N, Yatabe T, Hara Y, Hayashida K, Kondo Y, Sumi Y, Yasuda H, Aoyama K, Azuhata T, Doi K, Doi M, Fujimura N, Fuke R, Fukuda T, Goto K, Hasegawa R, Hashimoto S, Hatakeyama J, Hayakawa M, Hifumi T, Higashibeppu N, Hirai K, Hirose T, Ide K, Kaizuka Y, Kan'o T, Kawasaki T, Kuroda H, Matsuda A, Matsumoto S, Nagae M, Onodera M, Ohnuma T, Oshima K, Saito N, Sakamoto S, Sakuraya M, Sasano M, Sato N, Sawamura A, Shimizu K, Shirai K, Takei T, Takeuchi M, Takimoto K, Taniguchi T, Tatsumi H, Tsuruta R, Yama N, Yamakawa K, Yamashita C, Yamashita K, Yoshida T, Tanaka H, Oda S. The Japanese Clinical Practice Guidelines for Management of Sepsis and Septic Shock 2016 (J-SSCG 2016). Acute Med Surg 2018; 5(1): 3–89
47. Lee HY, Rhee CK, Lee JW. Feasibility of high-flow nasal cannula oxygen therapy for acute respiratory failure in patients with hematologic malignancies: a retrospective single-center study. J Crit Care 2015; 30(4): 773–777

48. Dangers L, Montlahuc C, Kouatchet A, Jaber S, Meziani F, Perbet S, Similowski T, Resche-Rigon M, Azoulay E, Demoule A; REVA Network (Research Network in Mechanical Ventilation) and the Groupe de Recherche en Réanimation Respiratoire en Onco-Hématologie (GrrrOH); List of contributors who included study patients: Angers University Hospital, Angers, France. Dyspnoea in patients receiving noninvasive ventilation for acute respiratory failure: prevalence, risk factors and prognostic impact: a prospective observational study. Eur Respir J 2018; 52(2): 1702637
49. Fan E, Del Sorbo L, Goligher EC, Hodgson CL, Munshi L, Walkey AJ, Adhikari NKJ, Amato MBP, Branson R, Brower RG, Ferguson ND, Gajic O, Gattinoni L, Hess D, Mancebo J, Meade MO, McAuley DF, Pesenti A, Ranieri VM, Rubenfeld GD, Rubin E, Seckel M, Slutsky AS, Talmor D, Thompson BT, Wunsch H, Uleryk E, Brozek J, Brochard LJ; American Thoracic Society, European Society of Intensive Care Medicine, and Society of Critical Care Medicine. An Official American Thoracic Society/European Society of Intensive Care Medicine/Society of Critical Care Medicine Clinical Practice Guideline: Mechanical Ventilation in Adult Patients with Acute Respiratory Distress Syndrome. Am J Respir Crit Care Med 2017; 195(9): 1253–1263
50. Fan E, Brodie D, Slutsky AS. Diagnosis and treatment in acute respiratory distress syndrome-reply. JAMA 2018; 320(3): 306
51. Yang HH, Zhou Y. Effect of invasive and non-invasive positive pressure ventilation on plasma brain natriuretic peptide in patients with chronic obstructive pulmonary disease and severe respiratory failure. J South Med Univ (Nan Fang Yi Ke Da Xue Xue Bao) 2010; 30(10): 2377–2379 (in Chinese)
52. Hui DS. Severe acute respiratory syndrome (SARS): lessons learnt in Hong Kong. J Thorac Dis 2013; 5(Suppl 2): S122–S126
53. Ronco C, Navalesi P, Vincent JL. Coronavirus epidemic: preparing for extracorporeal organ support in intensive care. Lancet Respir Med 2020; 8(3): 240–241
54. Cheng Y, Luo R, Wang K, Zhang M, Wang Z, Dong L, Li J, Yao Y, Ge S, Xu G. Kidney impairment is associated with in-hospital death of COVID-19 patients. Medrxiv 2020; doi: 10.1101/2020.02.18.20023242
55. Träger K, Schütz C, Fischer G, Schröder J, Skrabal C, Liebold A, Reinelt H. Cytokine reduction in the setting of an ARDS-associated inflammatory response with multiple organ failure. Case Rep Crit Care 2016; 2016: 9852073
56. Mair-Jenkins J, Saavedra-Campos M, Baillie JK, Cleary P, Khaw FM, Lim WS, Makki S, Rooney KD, Nguyen-Van-Tam JS, Beck CR; Convalescent Plasma Study Group. The effectiveness of convalescent plasma and hyperimmune immunoglobulin for the treatment of severe acute respiratory infections of viral etiology: a systematic review and exploratory meta-analysis. J Infect Dis 2015; 211(1): 80–90
57. Stockman LJ, Bellamy R, Garner P. SARS: systematic review of treatment effects. PLoS Med 2006; 3(9): e343
58. Mustafa S, Balkhy H, Gabere MN. Current treatment options and the role of peptides as potential therapeutic components for Middle East respiratory syndrome (MERS): a review. J Infect Public Health 2018; 11(1): 9–17
59. Lee PI, Hsueh PR. Emerging threats from zoonotic coronaviruses-from SARS and MERS to 2019-nCoV. J Microbiol Immunol Infect 2020 Feb 4. [Epub ahead of print] doi: 10.1016/j.jmii.2020.02.001
60. Chen L, Xiong J, Bao L, Shi Y. Convalescent plasma as a potential therapy for COVID-19. Lancet Infect Dis 2020 Feb 27. [Epub ahead of print] doi: 10.1016/S1473-3099(20)30141-9
61. Kaneko Y, Kato M, Tanaka Y, Inoo M, Kobayashi-Haraoka H, Amano K, Miyata M, Murakawa Y, Yasuoka H, Hirata S, Tanaka E, Miyasaka N, Yamanaka H, Yamamoto K, Takeuchi T; SURPRISE study group. Tocilizumab discontinuation after attaining remission in patients with rheumatoid arthritis who were treated with tocilizumab alone or in combination with methotrexate: results from a prospective randomised controlled study (the second year of the SURPRISE study). Ann Rheum Dis 2018; 77(9): 1268–1275
62. Kaneko Y, Kameda H, Ikeda K, Ishii T, Murakami K, Takamatsu H, Tanaka Y, Abe T, Takeuchi T. Tocilizumab in patients with adult-onset still's disease refractory to glucocorticoid treatment: a randomised, double-blind, placebo-controlled phase III trial. Ann Rheum Dis 2018; 77(12): 1720–1729
63. Stone JH, Tuckwell K, Dimonaco S, Klearman M, Aringer M, Blockmans D, Brouwer E, Cid MC, Dasgupta B, Rech J, Salvarani C, Schett G, Schulze-Koops H, Spiera R, Unizony SH, Collinson N. Trial of tocilizumab in giant-cell arteritis. N Engl J Med 2017; 377 (4): 317–328

LETTERS
https://doi.org/10.1038/s41591-020-0998-x

nature medicine

Rapid isolation and profiling of a diverse panel of human monoclonal antibodies targeting the SARS-CoV-2 spike protein

Seth J. Zost[1,14], Pavlo Gilchuk[1,14], Rita E. Chen[2,3], James Brett Case[3], Joseph X. Reidy[1], Andrew Trivette[1], Rachel S. Nargi[1], Rachel E. Sutton[1], Naveenchandra Suryadevara[1], Elaine C. Chen[4], Elad Binshtein[1], Swathi Shrihari[3], Mario Ostrowski[5], Helen Y. Chu[6], Jonathan E. Didier[7], Keith W. MacRenaris[7], Taylor Jones[1], Samuel Day[1], Luke Myers[1], F. Eun-Hyung Lee[8], Doan C. Nguyen[8], Ignacio Sanz[8], David R. Martinez[9], Paul W. Rothlauf[10,11], Louis-Marie Bloyet[11], Sean P. J. Whelan[10,11], Ralph S. Baric[9], Larissa B. Thackray[3], Michael S. Diamond[2,3,11,12], Robert H. Carnahan[1,13] ✉ and James E. Crowe Jr.[1,4,13] ✉

Antibodies are a principal determinant of immunity for most RNA viruses and have promise to reduce infection or disease during major epidemics. The novel coronavirus SARS-CoV-2 has caused a global pandemic with millions of infections and hundreds of thousands of deaths to date[1,2]. In response, we used a rapid antibody discovery platform to isolate hundreds of human monoclonal antibodies (mAbs) against the SARS-CoV-2 spike (S) protein. We stratify these mAbs into five major classes on the basis of their reactivity to subdomains of S protein as well as their cross-reactivity to SARS-CoV. Many of these mAbs inhibit infection of authentic SARS-CoV-2 virus, with most neutralizing mAbs recognizing the receptor-binding domain (RBD) of S. This work defines sites of vulnerability on SARS-CoV-2 S and demonstrates the speed and robustness of advanced antibody discovery platforms.

Human mAbs against the S glycoprotein on the viral surface mediate immunity to other betacoronaviruses including SARS-CoV[3–7] and Middle East respiratory syndrome coronavirus (MERS-CoV)[8–17]. Because of this, we and others have hypothesized that human mAbs may have promise for use in prophylaxis, post-exposure prophylaxis or treatment of SARS-CoV-2 infection[18]. MAbs can neutralize betacoronaviruses by several mechanisms, including blocking attachment of the S protein receptor-binding domain (RBD) to a receptor on host cells (which, for SARS-CoV and SARS-CoV-2 (ref. [1]), is angiotensin-converting enzyme 2 (ACE2))[12]. We hypothesized that the SARS-CoV-2 S protein would induce diverse human neutralizing antibodies following natural infection. While antibody discovery and therapeutic candidate development usually takes months to years, there is an urgent need to both characterize the human immune response to SARS-CoV-2 infection and to develop potential medical countermeasures. Using Zika virus as a simulated pandemic pathogen and leveraging recent technological advances in synthetic genomics and single-cell sequencing, we recently isolated hundreds of human mAbs from a single-B-cell suspension and tested them in vitro for neutralization and for protection in small animals and non-human primates, all within 78 d[19]. Using similar methodologies and further efficiency improvements, we sought to obtain human mAbs rapidly for SARS-CoV-2 from the B cells of some of the first humans identified with the infection in North America. We used an approach similar to that in our previous technical demonstration with Zika; however, for the SARS-CoV-2 discovery effort we report here, we used several different workflows in parallel (Fig. 1 and Supplementary Table 1), which we completed in an expedited time frame (Fig. 1).

We first developed or obtained antigens and recombinant proteins necessary for identifying and isolating antigen-reactive B cells. We synthesized a complementary-DNA encoding a stabilized trimeric prefusion ectodomain of S protein ($S2P_{ecto}$)[20], expressed the protein in 293-F cells, and verified the presence of the prefusion conformation by electron microscopy (Extended Data Fig. 1 and Supplementary Table 2). We also synthesized and expressed the S protein RBD (S_{RBD}) and obtained recombinant S protein amino-terminal domain (S_{NTD}) that had been prepared by academic or commercial sources. Using these tools, we designed a mAb discovery approach focused on identifying naturally occurring human mAbs specific for S.

We obtained informed consent and collected blood samples from four patients infected in China who were among the earliest identified patients with SARS-CoV-2 infection in North America,

[1]Vanderbilt Vaccine Center, Vanderbilt University Medical Center, Nashville, TN, USA. [2]Department of Pathology & Immunology, Washington University School of Medicine, St. Louis, MO, USA. [3]Department of Medicine, Washington University School of Medicine, St. Louis, MO, USA. [4]Department of Pathology, Microbiology, and Immunology, Vanderbilt University Medical Center, Nashville, TN, USA. [5]Department of Medicine, University of Toronto, Toronto, Ontario, Canada. [6]Division of Allergy and Infectious Diseases, University of Washington, Seattle, WA, USA. [7]Berkeley Lights, Inc., Emeryville, CA, USA. [8]Department of Medicine, Emory University, Atlanta, GA, USA. [9]Department of Epidemiology, University of North Carolina at Chapel Hill, Chapel Hill, NC, USA. [10]Program in Virology, Harvard Medical School, Boston, MA, USA. [11]Department of Molecular Microbiology, Washington University School of Medicine, St. Louis, MO, USA. [12]Andrew M. and Jane M. Bursky Center for Human Immunology and Immunotherapy Programs, Washington University School of Medicine, St. Louis, MO, USA. [13]Department of Pediatrics, Vanderbilt University Medical Center, Nashville, TN, USA. [14]These authors contributed equally: Seth J. Zost, Pavlo Gilchuk. ✉e-mail: robert.carnahan@vumc.org; james.crowe@vumc.org

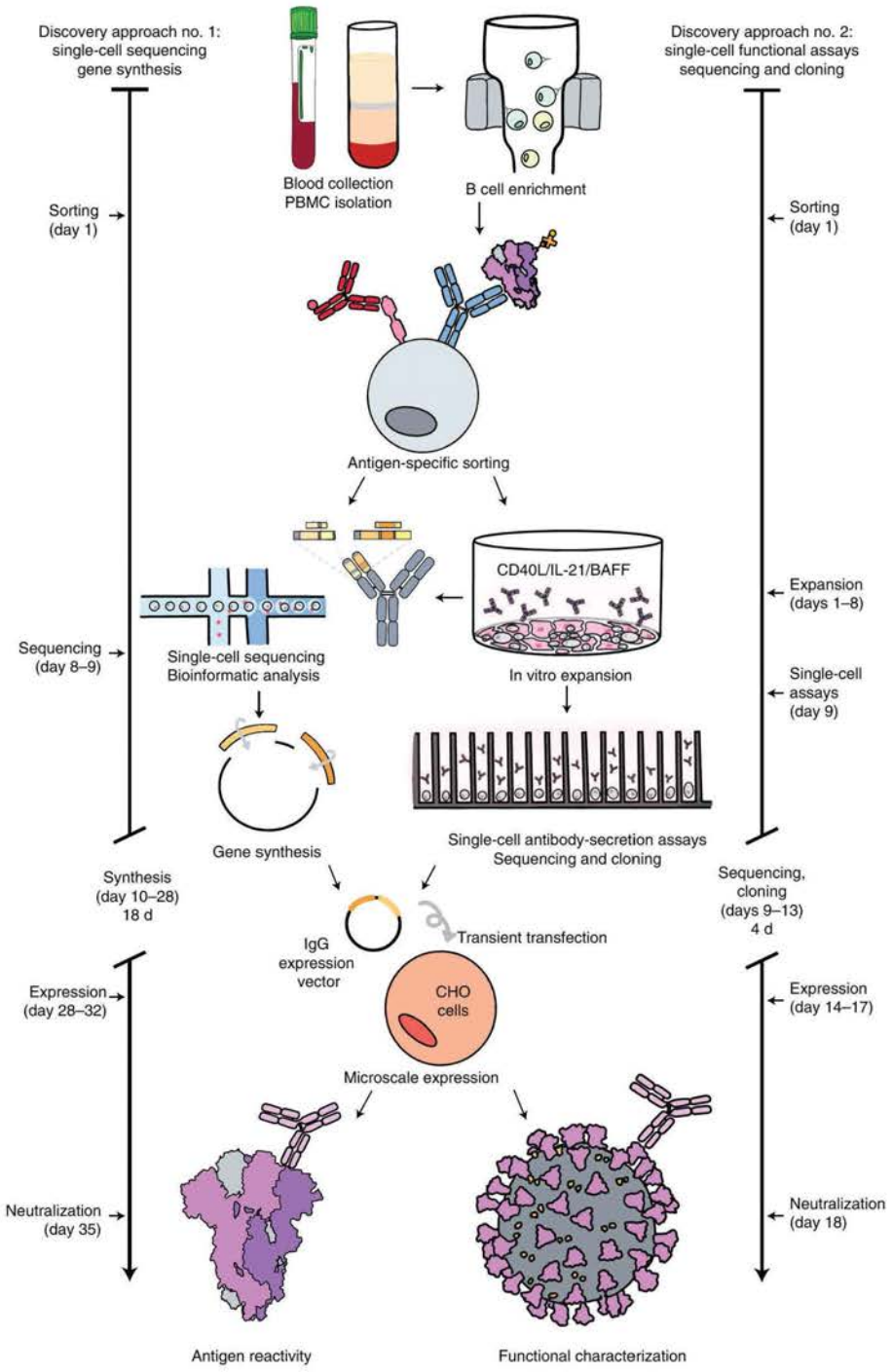

Fig. 1 | Workflows and timelines. a, Overview of rapid mAb discovery workflows. The overall scheme is shown, representing the several specific workflows conducted in parallel (specified in Supplementary Table 1). Blood was collected and white blood cells were separated, B cells were enriched from PBMCs by negative selection using magnetic beads and antigen-specific cells were isolated by flow-cytometric sorting and then were processed for direct B cell selection and sequencing or in vitro expansion/activation. Cultured B cells were loaded on a Beacon instrument (Berkeley Lights) for functional screening (Extended Data Fig. 3 and Supplementary Video 1) or in a Chromium device (10X Genomics) followed by reverse transcription with PCR, sequence analysis, cDNA gene synthesis and cloning into an expression vector and microscale IgG expression in Chinese hamster ovary (CHO) cells by transient transfection. Recombinant IgG was tested by ELISA for binding to determine antigen reactivity and by a high-throughput neutralization screening assay (xCelligence; ACEA) (Extended Data Fig. 4) with authentic virus in a biosafety-level-3 (BSL-3) laboratory for functional characterization.

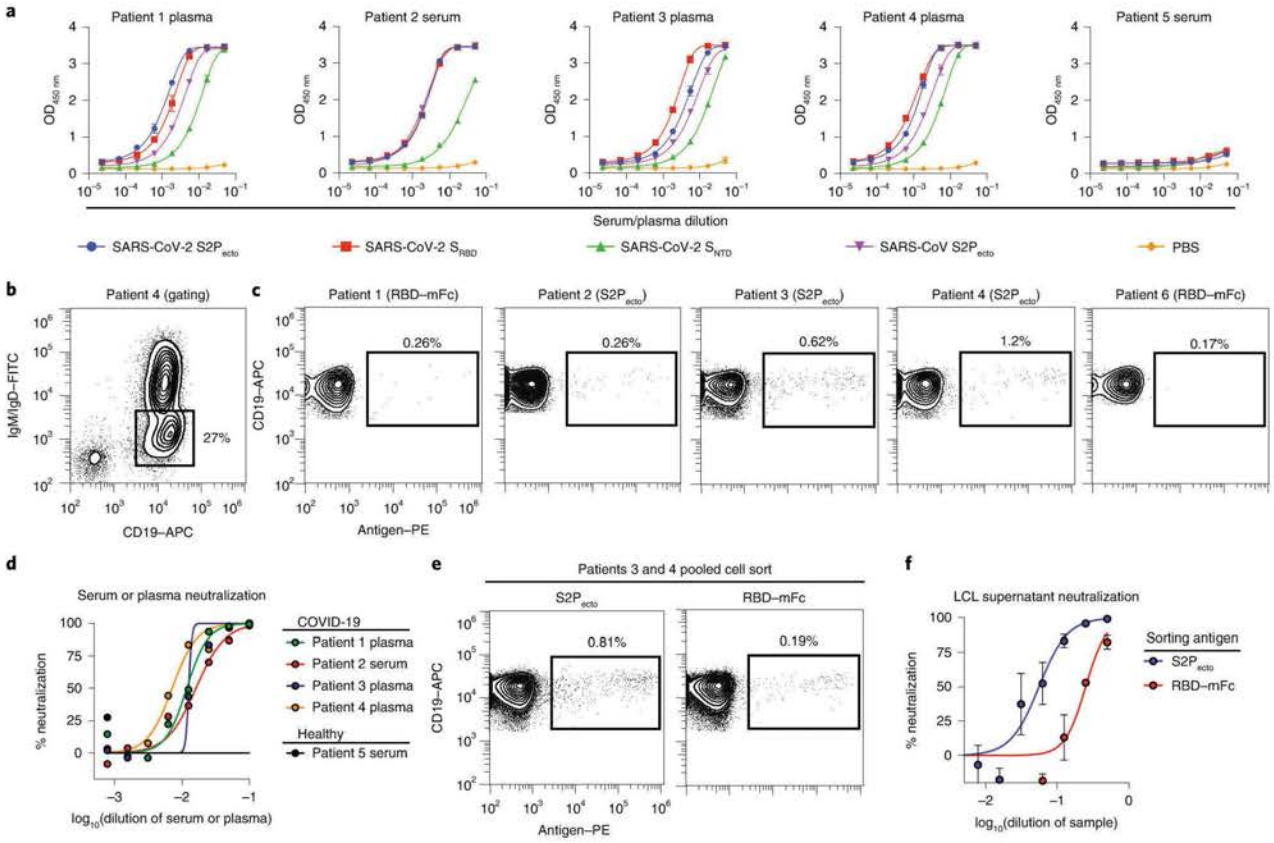

Fig. 2 | Characterization of SARS-CoV-2 immune donor samples. a, Serum or plasma antibody reactivity for the four SARS-CoV-2 exposed patients and one non-immune healthy control, assessed by ELISA using SARS-CoV-2 $S2P_{ecto}$, S_{RBD}, S_{NTD}, SARS-CoV $S2P_{ecto}$ or PBS. OD_{450}, optical density measurement using a microplate reader with a 450-nm filter. **b**, Gating for memory B cells in total B cells enriched by negative selection using magnetic beads for patient 4; cells were stained with anti-CD19 antibody conjugated to allophycocyanin (APC) and anti-IgM and anti-IgD antibodies conjugated to fluorescein isothiocyanate (FITC). **c**, Analytical flow cytometric analysis of B cells for patients 1 to 4, compared with that of a healthy individual (patient 6). Plots show $CD19^+IgD^-IgM^-$ population using the gating strategy that was used in **b**. Cells labeled with biotinylated $S2P_{ecto}$ or RBD–mFc antigens were detected using phycoerythrin (PE)-conjugated streptavidin. **d**, Plasma or serum neutralizing activity against the WA1/2020 strain SARS-CoV-2 for patients 1 to 4 or a healthy donor (patients 6). The percentage neutralization is reported. **e**, FACS isolation of $S2P_{ecto}$ or RBD–mFc-reactive B cells from pooled B cells of patients 3 and 4. Plots show $CD19^+IgD^-IgM^-$ population using gating strategy as in **b**, and antigen-reactive B cells were identified as in **c**. **f**, Lymphoblastoid cell line (LCL) supernatant neutralization. Neutralization of the WA1/2020 strain SARS-CoV-2 by supernatant collected from cell cultures of $S2P_{ecto}$- or RBD–mFc-sorted memory B cells that had been stimulated in bulk in vitro on feeder layers expressing CD40L and secreting IL-21 and BAFF. The supernatants were tested in a ten-point dilution series in the FRNT, and percentage neutralization is reported. Values shown are the mean ± s.d. of technical duplicates.

as well as one healthy donor who served as a negative control (Supplementary Table 3). These patients had a history of recent laboratory-confirmed SARS-CoV-2 infection acquired in Wuhan or Beijing, China. The samples were obtained 35 d (patient 1; the case identified in the United States[21]), 36 d (patient 2) or 50 d (patients 3 and 4) after the onset of symptoms. We tested plasma or serum specimens from the four patients infected with SARS-CoV-2, or from a healthy donor (patient 5) as control. Serum/plasma antibody ELISA binding assays using $S2P_{ecto}$, S_{RBD} or S_{NTD} protein from SARS-CoV-2 or $S2P_{ecto}$ protein from SARS-CoV revealed that the previously infected patients had circulating antibodies that recognized each of the proteins tested, with the highest reactivity against the SARS-CoV-2 $S2P_{ecto}$ and S_{RBD} proteins (Fig. 2a). Each of the previously infected patients also had circulating antibodies that bound to SARS-CoV $S2P_{ecto}$. The serum antibodies from the healthy donor did not react with any of the antigens. B cells were enriched from peripheral blood mononuclear cells (PBMCs) by negative selection using antibody-coated magnetic beads and were stained with phenotyping antibodies specific for CD19, IgD and IgM. Analytical flow cytometry was performed to assess the frequency of antigen-specific memory B cells for each donor. We identified class-switched memory B cells by gating for an $IgD^-IgM^-CD19^+$ population (Fig. 2b, and Extended Data Fig. 2). From this memory B cell population, we identified antigen-reactive cells using biotinylated recombinant $S2P_{ecto}$ protein or biotinylated RBD fused to mouse Fc (RBD–mFc). Patients 1 and 2 had very low frequencies of antigen-specific memory B cells that were not greater than twofold above the background staining frequency in a non-immune sample (from patient 6) (Fig. 2c). In contrast to patients 1 and 2, convalescence in patients 3 and 4 was 2 weeks later, and they exhibited 0.62% or 1.22% of class-switched B cells that reacted with antigen (Fig. 2c). Patients 3 and 4 also exhibited high titers in a serum-antibody focus reduction neutralization test (FRNT) with an authentic SARS-CoV-2 strain (WA/1/2020) (Fig. 2d). Therefore, we focused subsequent efforts on sorting B cells from the specimens of patients 3 and 4, which were pooled for efficiency.

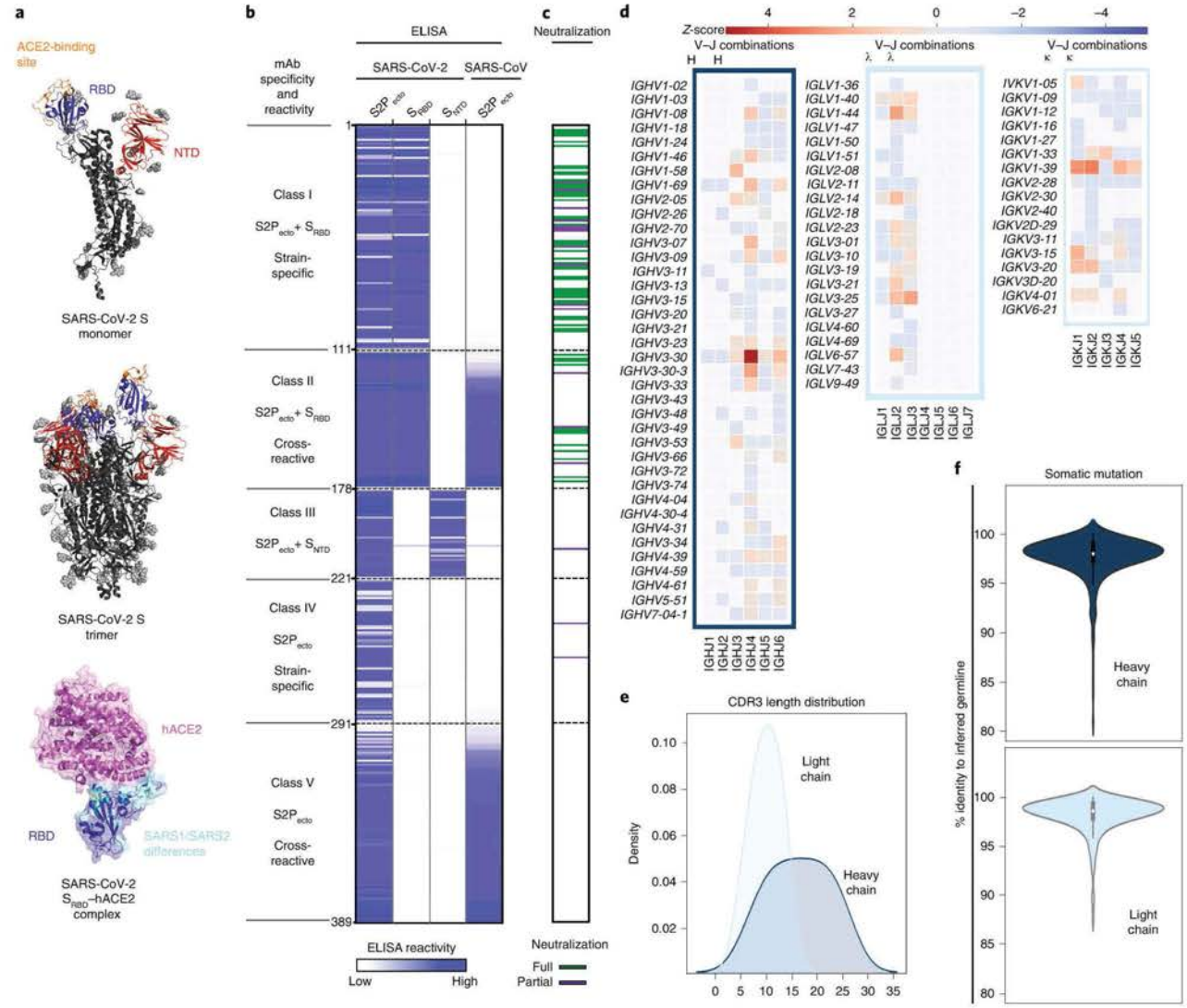

Fig. 3 | Reactivity and functional activity of 389 human mAbs. a, Structures of SARS-CoV-2 S antigen. Top, S protein monomer of SARS-CoV-2 highlighting RBD (blue) and NTD (red) subdomains that were expressed as recombinant proteins. The ACE2-binding site on RBD is shown in orange. Known glycans are shown as light gray spheres (PDB 6VYB)[37]. Middle, The structure of trimeric SARS-CoV-2 spike with one RBD in the 'head up' conformation. Bottom, Structure (PDB 6M0J)[38] of SARS-CoV-2 RBD (blue) and hACE2 (pink), highlighting differences between RBDs of SARS-CoV-2 and SARS-CoV (cyan). **b**, mAbs binding to each of four S proteins or subdomains. The figure shows a heatmap for binding of 389 mAbs expressed recombinantly, representing OD values collected at 450 nm for each antigen (range, 0.035–4.5). White indicates a lack of detectable binding, while blue indicates binding and darker blue indicates higher OD values. **c**, Screening test for neutralizing activity. Each mAb was tested by RTCA neutralization test (Extended Data Figs. 4 and 5) that was based on measurement of rapid cytopathic effect in Vero-furin cells caused by an authentic SARS-CoV-2 (strain WA1/2020) in a BSL-3 laboratory. Green indicates full protection of cells (full neutralization), purple indicates partial protection of cells (partial neutralization) and white indicates that neutralizing activity was not detected. On the basis of both binding and neutralization, we grouped the mAbs into classes. Class I mAbs bind to both $S2P_{ecto}$ and S_{RBD} proteins and are SARS-CoV-2-specific. Class II mAbs also bind to both $S2P_{ecto}$ and S_{RBD} proteins and cross-react with SARS-CoV. Class III mAbs bind to both $S2P_{ecto}$ and S_{NTD} proteins and are mostly SARS-CoV-2-specific. Class IV mAbs bind only to $S2P_{ecto}$ protein and are SARS-CoV-2-specific. Class V mAbs bind only to $S2P_{ecto}$ protein and cross-react with SARS-CoV. **d**, Heatmap showing usage of antibody variable-gene segments for variable (*V*) and joining (*J*) genes. Of the 389 antibodies tested in **b** and **c**, 324 were found to have unique sequences, and those unique sequences were analyzed for genetic features. The frequency counts are derived from the total number of unique sequences with the corresponding *V* and *J* genes. The *V*/*J* frequency counts then were transformed into a *Z*-score by first subtracting the average frequency, then normalizing by the s.d. of the set of antigen-reactive mAbs. Red denotes more common gene usage, and blue denotes less common gene usage. **e**, CDR3 amino acid length distribution. The CDR3 of each sequence was determined using PyIR software. The amino acid length of each CDR3 was counted. The distribution of CDR3 amino acid lengths for heavy or light chains then was plotted as a histogram and fitted using kernel density estimation for the curves. **f**, Divergence from inferred germline gene sequences. The number of mutations of each mAb relative to the inferred germline variable gene was counted for each clone. These numbers then were transformed into percent values and plotted as violin plots. For the heavy chain, values range from 81 to 100, with a median of 98, a 25th quartile of 97.3 and a 75th quartile of 99. For the light chain, values range from 87.5 to 100, with a median of 98.6, a 25th quartile of 97.9 and a 75th quartile of 99.3.

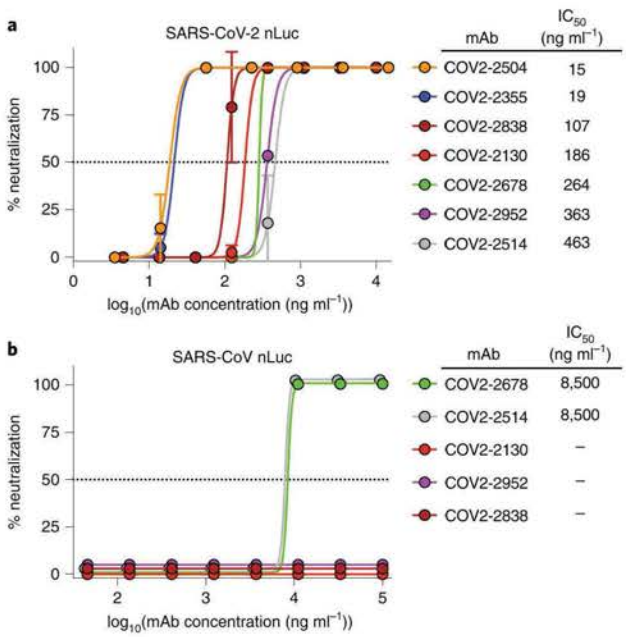

Fig. 4 | Neutralizing activity of potent mAbs against SARS-CoV-2 and SARS-CoV. a, Dose–response neutralization of SARS-CoV-2 luciferase reporter virus by representative potently neutralizing mAbs that were identified by rapid RTCA screening assay. IC_{50} values are indicated for each mAb. Data shown are the mean of two technical replicates from one of two independent experiments, and error bars denote the s.d. for each point. **b**, Neutralization of SARS-CoV luciferase reporter virus by cross-reactive mAbs COV2-2678 and COV2-2514. IC_{50} values are indicated for each mAb, with the '–' symbol indicating that mAbs that did not neutralize SARS-CoV. Data shown are the mean ± s.d. of two technical replicates from one of two independent experiments.

The pooled memory B cell suspension had frequencies for $S2P_{ecto}$ and RBD–mFc that were 0.81% and 0.19% of the $IgD^-IgM^-CD19^+$ population, respectively (Fig. 2e). The bulk sorted $S2P_{ecto}$- or RBD–mFc-specific B cells were stimulated on a feeder layer with CD40L, interleukin-21 (IL-21) and B cell activating factor (BAFF)[22], and the secreted antibodies in the resulting cell-culture supernatants exhibited neutralizing activity against the WA1/2020 strain (Fig. 2f). After 7 d in culture, these activated B cells were removed from the feeder layers. Roughly half of these B cells were single-cell sequenced using a 10x Chromium single-cell encapsulation automated system, and antibody genes were synthesized as previously described[19]. The remaining cells were loaded onto a Berkeley Lights Beacon optofluidic instrument in a novel medium promoting plasma-cell survival, and antigen reactivity of secreted antibodies from individual B cells was measured for thousands of cells (Extended Data Fig. 3). This single-cell analysis showed that ~55% of cultured B cells secreted $SP2_{ecto}$-reactive IgG (Supplementary Video 1). Using the Beacon instrument, we also screened a subset of expanded B cells for the ability to block human ACE2 (hACE2) receptor binding to the RBD–mFc construct and identified several clones secreting mAbs that inhibited RBD–hACE2 interaction (Extended Data Fig. 3d). Antigen-reactive B cells were exported from the instrument, and the heavy- and light-chain genes from single B cells were sequenced and cloned into immunoglobulin expression vectors. From 288 total exported cells, we succeeded in cloning 78 antigen-reactive mAbs (Supplementary Table 1), including two closely related mAbs that blocked hACE2 binding to the RBD.

Using the parallel workflows, we isolated 389 recombinant SARS-CoV-2-reactive human mAbs that expressed sufficiently well as recombinant IgG to characterize the activity of the mAb. The recombinant mAbs were tested for binding in ELISA to recombinant monomeric S_{RBD} or S_{NTD} of SARS-CoV-2 or trimeric $S2P_{ecto}$ proteins of SARS-CoV-2 or SARS-CoV (Fig. 3a). Neutralizing activity of mAbs was assessed using an automated real-time cell analysis (RTCA) rapid screening assay[19] that allows quantitation of cytopathic effect (CPE) with WA1/2020 strain SARS-CoV-2 in Vero-furin cells (Extended Data Fig. 4). The ELISA and neutralization screening assays revealed that the antibodies could be grouped into five binding patterns on the basis of domain recognition and cross-reactivity (Fig. 3b). There were 178 that mAbs recognized the RBD domain and 43 that recognized the NTD domain. Comparison of binding patterns with full or partial neutralizing activity measured by RTCA with SARS-CoV-2 (Fig. 3c) clearly showed that most of the neutralizing antibodies (67/70) mapped to the RBD, revealing the RBD to be the principal site of vulnerability for SARS-CoV-2 neutralization in these patients. Overall, 49% of the SARS-CoV-2-specific RBD mAbs were neutralizing, and 19% of the SARS-CoV cross-reactive mAbs were neutralizing. We then used the RTCA assay to rank mAbs by their neutralizing potency (Extended Data Fig. 5) and identified several mAbs with half-maximal inhibitory concentration (IC_{50}) values below 100 ng ml^{-1}. We examined the sequences for the 389 antibodies to assess the diversity of antigen-specific B cell clonotypes discovered. The analysis showed that among the 389 mAbs, 321 unique amino acid sequences were present and 313 unique V_H–J_H–CDRH3–V_L–J_L–CDRL3 clonotypes were represented, with diverse usage of antibody variable genes (Fig. 3d and Supplementary Table 4). The length distributions of CDR3 amino acids in the heavy and light chains were typical of human repertoires (Fig. 3e)[23]. The high relatedness of sequences to the inferred germline variable genes observed for this panel of antibodies (Fig. 3f) contrasts with the much higher levels of somatic mutation seen in B cell recall responses against common human pathogens such as influenza[24]. These data suggest that the SARS-CoV-2 antibodies were likely induced during the primary response to SARS-CoV-2 infection and not by a recall response to a distantly related seasonal coronavirus. We next performed neutralization assays with a recombinant vesicular stomatitis virus (VSV) expressing SARS-CoV-2 S (VSV-SARS-CoV-2)[25] that confirmed neutralizing activity of 49 mAbs identified as neutralizing by the rapid RTCA screening assay (Extended Data Fig. 6). We also confirmed high neutralizing potency for representative potent mAbs in a quantitative conventional neutralization assay using a SARS-CoV-2 luciferase reporter virus (Fig. 4a). In addition, we tested SARS-CoV $S2P_{ecto}$ cross-reactive mAbs for cross-neutralization of a SARS-CoV luciferase reporter virus (Fig. 4b), which revealed relatively weak neutralization of heterologous SARS-CoV. Together, these results confirmed that mAbs recognizing multiple epitopes on S were able to neutralize SARS-CoV-2 and cross-react with SARS-CoV, with most neutralizing mAbs specific for the RBD of S.

Since the emergence of SARS-CoV-2, several groups have reported the isolation of neutralizing antibodies from survivors that target the S protein[26–33]. There are similarities between our approaches and those of others, for example employing antigen-specific enrichment with both RBD[26,27,29,30,32] and full-length S trimer[26,28,33] as well as the use of single-cell sequencing and gene synthesis[29]. A common finding across these studies is that the SARS-CoV-2 RBD is the target of potent neutralizing antibodies. In this work, we coupled single-B-cell antibody gene sequencing with high-throughput IgG isolation and screening assays to isolate and profile a large number of neutralizing mAbs in a period of only weeks after sample acquisition. The technological advances of our workflow included rapid antigen binding and functional (hACE2 blocking) screens at the single-B-cell level as well as high-throughput (hundreds

to thousands) screening of mAbs for neutralization of authentic SARS-CoV-2 virus to rapidly identify the leads. In our particular example, sequences of confirmed neutralizing antibodies were transferred to downstream manufacturing partners only 18 d after antigen-specific cell sorting. However, given the need for affinity maturation and the development of a mature B cell response, there are limits on the timeline from infection to isolation of potent neutralizing antibodies with therapeutic promise. It has been previously shown for Ebola virus infection that potently neutralizing antibodies are not easily isolated from memory B cells until later timepoints in the first year after infection[34,35]. It is possible that our success in identifying antigen-specific B cells from patients 3 and 4 here at 50 d after onset, but not from patients 1 and 2 at 35 or 36 d after onset, reflected additional maturation of the memory B cell response that occurred in the additional 2 weeks of convalescence, although we note that others have isolated neutralizing mAbs from individuals approximately 30 d after infection[27]. Overall, our work illustrates the promise of integrating recent technological advances for antibody discovery and helps to define the RBD of SARS-CoV-2 S as a major site of vulnerability for vaccine design and therapeutic-antibody development. The most potent neutralizing human mAbs isolated here also could serve as candidate biologics to prevent or treat SARS-CoV-2 infection[36].

Online content

Any methods, additional references, Nature Research reporting summaries, source data, extended data, supplementary information, acknowledgements, peer review information; details of author contributions and competing interests; and statements of data and code availability are available at https://doi.org/10.1038/s41591-020-0998-x.

Received: 12 May 2020; Accepted: 26 June 2020;
Published online: 10 July 2020

References

1. Zhou, P. et al. A pneumonia outbreak associated with a new coronavirus of probable bat origin. *Nature* **579**, 270–273 (2020).
2. Zhu, N. et al. A novel coronavirus from patients with pneumonia in China, 2019. *N. Engl. J. Med.* **382**, 727–733 (2020).
3. Sui, J. et al. Potent neutralization of severe acute respiratory syndrome (SARS) coronavirus by a human mAb to S1 protein that blocks receptor association. *Proc. Natl Acad. Sci. USA* **101**, 2536–2541 (2004).
4. ter Meulen, J. et al. Human monoclonal antibody as prophylaxis for SARS coronavirus infection in ferrets. *Lancet* **363**, 2139–2141 (2004).
5. ter Meulen, J. et al. Human monoclonal antibody combination against SARS coronavirus: synergy and coverage of escape mutants. *PLoS Med.* **3**, e237 (2006).
6. Zhu, Z. et al. Potent cross-reactive neutralization of SARS coronavirus isolates by human monoclonal antibodies. *Proc. Natl Acad. Sci. USA* **104**, 12123–12128 (2007).
7. Rockx, B. et al. Structural basis for potent cross-neutralizing human monoclonal antibody protection against lethal human and zoonotic severe acute respiratory syndrome coronavirus challenge. *J. Virol.* **82**, 3220–3235 (2008).
8. Chen, Z. et al. Human neutralizing monoclonal antibody inhibition of Middle East respiratory syndrome coronavirus replication in the common marmoset. *J. Infect. Dis.* **215**, 1807–1815 (2017).
9. Choi, J. H. et al. Characterization of a human monoclonal antibody generated from a B-cell specific for a prefusion-stabilized spike protein of Middle East respiratory syndrome coronavirus. *PLoS ONE* **15**, e0232757 (2020).
10. Niu, P. et al. Ultrapotent human neutralizing antibody repertoires against Middle East respiratory syndrome coronavirus from a recovered patient. *J. Infect. Dis.* **218**, 1249–1260 (2018).
11. Wang, L., et al. Importance of neutralizing monoclonal antibodies targeting multiple antigenic sites on the Middle East respiratory syndrome coronavirus spike glycoprotein to avoid neutralization escape. *J. Virol.* **92**, e02002-17 (2018).
12. Wang, N. et al. Structural definition of a neutralization-sensitive epitope on the MERS-CoV S1-NTD. *Cell Rep.* **28**, e3396 (2019).
13. Zhang, S. et al. Structural definition of a unique neutralization epitope on the receptor-binding domain of MERS-CoV spike glycoprotein. *Cell Rep.* **24**, 441–452 (2018).
14. Corti, D. et al. Prophylactic and postexposure efficacy of a potent human monoclonal antibody against MERS coronavirus. *Proc. Natl Acad. Sci. USA* **112**, 10473–10478 (2015).
15. Jiang, L. et al. Potent neutralization of MERS-CoV by human neutralizing monoclonal antibodies to the viral spike glycoprotein. *Sci. Transl. Med.* **6**, 234ra259 (2014).
16. Tang, X. C. et al. Identification of human neutralizing antibodies against MERS-CoV and their role in virus adaptive evolution. *Proc. Natl Acad. Sci. USA* **111**, E2018–E2026 (2014).
17. Ying, T. et al. Exceptionally potent neutralization of Middle East respiratory syndrome coronavirus by human monoclonal antibodies. *J. Virol.* **88**, 7796–7805 (2014).
18. Jiang, S., Hillyer, C. & Du, L. Neutralizing antibodies against SARS-CoV-2 and other human coronaviruses. *Trends Immunol.* **41**, 355–359 (2020).
19. Gilchuk, P. et al. Integrated technology platform for accelerated discovery of antiviral antibody therapeutics. *Nat. Biomed. Eng.* (in the press).
20. Wrapp, D. et al. Cryo-EM structure of the 2019-nCoV spike in the prefusion conformation. *Science* **367**, 1260–1263 (2020).
21. Holshue, M. L. et al. First case of 2019 novel coronavirus in the United States. *N. Engl. J. Med.* **382**, 929–936 (2020).
22. Gilchuk, P. et al. Analysis of a therapeutic antibody cocktail reveals determinants for cooperative and broad ebolavirus meutralization. *Immunity* **52**, e312 (2020).
23. Soto, C. et al. High frequency of shared clonotypes in human B cell receptor repertoires. *Nature* **566**, 398–402 (2019).
24. Wrammert, J. et al. Broadly cross-reactive antibodies dominate the human B cell response against 2009 pandemic H1N1 influenza virus infection. *J. Exp. Med.* **208**, 181–193 (2011).
25. Case, J. B. et al. Neutralizing antibody and soluble ACE2 inhibition of a replication-competent VSV-SARS-CoV-2 and a clinical isolate of SARS-CoV-2. *Cell Host Microbe* https://doi.org/10.1016/j.chom.2020.06.021 (2020).
26. Rogers, T. F. et al. Rapid isolation of potent SARS-CoV-2 neutralizing antibodies and protection in a small animal model. *Science* https://doi.org/10.1126/science.abc7520 (2020).
27. Robbiani, D. F. et al. Convergent antibody responses to SARS-CoV-2 infection in convalescent individuals. *Nature* https://doi.org/10.1038/s41586-020-2456-9 (2020).
28. Brouwer, P. J. M. et al. Potent neutralizing antibodies from COVID-19 patients define multiple targets of vulnerability. *Science* eabc5902 (2020).
29. Cao, Y. et al. Potent neutralizing antibodies against SARS-CoV-2 identified by high-throughput single-cell sequencing of convalescent patients' B cells. *Cell* https://doi.org/10.1016/j.cell.2020.05.025 (2020).
30. Shi, R. et al. A human neutralizing antibody targets the receptor binding site of SARS-CoV-2. *Nature* https://doi.org/10.1038/s41586-020-2381-y (2020).
31. Wu, Y. et al. A noncompeting pair of human neutralizing antibodies block COVID-19 virus binding to its receptor ACE2. *Science* **368**, 1274–1278 (2020).
32. Ju, B. et al. Human neutralizing antibodies elicited by SARS-CoV-2 infection. *Nature* https://doi.org/10.1038/s41586-020-2380-z (2020).
33. Wec, A. Z. et al. Broad neutralization of SARS-related viruses by human monoclonal antibodies. *Science* https://doi.org/10.1126/science.abc7424 (2020).
34. Williamson, L. E. et al. Early human B cell response to Ebola virus in four U.S. survivors of infection. *J. Virol.* **93**, e01439-18 (2019).
35. Davis, C. W. et al. Longitudinal analysis of the human B cell response to Ebola virus infection. *Cell* **177**, e1517 (2019).
36. Zost, S. J. et al. Potently neutralizing human antibodies that block SARS-CoV-2 receptor binding and protect animals. *Nature* (in the press).
37. Walls, A. C. et al. Structure, function, and antigenicity of the SARS-CoV-2 spike glycoprotein. *Cell* **181**, e286 (2020).
38. Lan, J. et al. Structure of the SARS-CoV-2 spike receptor-binding domain bound to the ACE2 receptor. *Nature* **581**, 215–220 (2020).

Methods

Research participants. We studied four patients in North America with recent laboratory-confirmed symptomatic SARS-CoV-2 infections that were acquired in China (Supplementary Table 3). The studies were approved by the Institutional Review Board of Vanderbilt University Medical Center, and subsite studies were approved by the Institutional Review Board of the University of Washington or the Research Ethics Board of the University of Toronto. Samples were obtained after written informed consent. Patient 1 (35-year-old male) was the earliest reported case of SARS-CoV-2 infection in the United States, who presented with disease in Seattle, Washington, on 19 January 2020 (ref. [21]), a blood sample was obtained for study on 19 February 2020. Patient 2 (52-year-old female) was infected following close exposure in Beijing, China, to an infected person from Wuhan, China, during the period between 23 January 2020 to 29 January 2020. She presented with mild respiratory disease symptoms from 1 February 2020 to 4 February 2020 that occurred after travel to Madison, Wisconsin. She obtained a diagnosis of infection by testing at the US Centers for Disease Control on 5 February 2020. Blood samples were obtained for study on 7 March 2020 and 8 March 2020. Patient 3 (a 56-year-old male) and patient 4 (a 56-year-old female) are a married couple and residents of Wuhan, China, who traveled to Toronto, Canada, on 22 January 2020. Patient 3 first developed a cough without fever on 20 January 2020 in the city of Wuhan, where he had a normal chest X-ray on that day. He flew to Canada with persisting cough and arrived in Canada on 22 January 2020, where he became febrile. He presented to a hospital in Toronto, 23 January 2020 complaining of fever, cough and shortness of breath; a nasopharyngeal swab was positive by PCR testing for SARS-CoV-2. His chest X-ray at that time was abnormal, and he was admitted for non-intensive-care-unit impatient care. He improved gradually with supportive care, was discharged 30 January 2020 and rapidly became asymptomatic except for a residual dry cough that persisted for a month. He had a negative nasopharyngeal swab PCR test on 19 February 2020. Patient 4 is the wife of patient 3 who traveled with her husband from Wuhan. She was never symptomatic with respiratory symptoms or fever but was tested because of her exposure. Her nasopharyngeal swab was positive for SARS-CoV-2 by PCR, on 24 January 2020; repeat testing in follow-up on 21 February 2020 was negative. PBMCs were obtained by leukapheresis from patients 3 and 4 on 10 March 2020, which was 50 d since symptom onset of patient 3. Samples were transferred to Vanderbilt University Medical Center in Nashville, Tennessee, on 14 March 2020.

Cell culture. Vero E6 (CRL-1586, American Type Culture (ATCC)), Vero CCL81 (CCL-81, ATCC) and HEK293T (CRL-3216 ATCC) were maintained at 37 °C in 5% CO_2 in DMEM containing 10% (vol/vol) heat-inactivated FBS, 10 mM HEPES pH 7.3, 1 mM sodium pyruvate, 1× non-essential amino acids, and 100 U ml^{-1} of penicillin–streptomycin. Vero-furin cells were obtained from T. Pierson (NIH) and have been described previously[20]. Expi293F cells (Thermo Fisher Scientific, A1452) were maintained at 37 °C in 8% CO_2 in Expi293F Expression Medium (Thermo Fisher Scientific, A1435102). ExpiCHO cells (Thermo Fisher Scientific, A29127) were maintained at 37 °C in 8% CO_2 in ExpiCHO Expression Medium (Thermo Fisher Scientific, A2910002). Mycoplasma testing of Expi293F and ExpiCHO cultures was performed on a monthly basis using a PCR-based mycoplasma detection kit (ATCC, 30-1012K).

Viruses. SARS-CoV-2 strain 2019 n-CoV/USA_WA1/2020 was obtained from the Centers for Disease Control and Prevention (a gift from N. Thornburg). Virus was passaged in Vero CCL81 cells and titrated by plaque assay on Vero E6 cells. All work with infectious SARS-CoV-2 was approved by the Washington University School of Medicine or UNC-Chapel Hill Institutional Biosafety Committees and conducted in approved BSL-3 facilities using appropriate powered air-purifying respirators and personal protective equipment.

Recombinant antigens and proteins. A gene encoding the ectodomain of a prefusion conformation-stabilized SARS-CoV-2 S ($S2P_{ecto}$) protein was synthesized and cloned into a DNA plasmid expression vector for mammalian cells. A similarly designed S protein antigen with two prolines and removal of the furin cleavage site for stabilization of the prefusion form of S was reported previously[20]. Briefly, this gene includes the ectodomain of SARS-CoV-2 (to residue 1,208), a T4 fibritin trimerization domain, an AviTag site-specific biotinylation sequence, and a carboxy-terminal 8×-histidine tag. To stabilize the construct in the prefusion conformation, we included substitutions K986P and V987P and mutated the furin cleavage site at residues 682–685 from RRAR to ASVG. This recombinant spike 2P-stabilized protein (designated here as $S2P_{ecto}$) was isolated by metal affinity chromatography on HisTrap Excel columns (GE Healthcare), and protein preparations were purified further by size-exclusion chromatography on a Superose 6 Increase 10/300 column (GE Healthcare). The presence of trimeric, prefusion conformation S protein was verified by negative-stain electron microscopy (Extended Data Fig. 1 and Supplementary Table 2). To express the S_{RBD} subdomain of SARS-CoV-2 S protein, residues 319–541 were cloned into a mammalian expression vector downstream of an IL-2 signal peptide and upstream of a thrombin cleavage site, an AviTag, and a 6×-His tag. RBD–mFc was purchased from Sino Biological (40592-V05H). For B cell labeling and sorting, RBD–mFc and $S2P_{ecto}$ proteins were biotinylated using the EZ-Link Sulfo-NHS-LC-Biotinylation Kit and vendor's protocol (Thermo Fisher Scientific, 21435).

Electron microscopy stain grid preparation and imaging of SARS-CoV-2 $S2P_{ecto}$ protein. For screening and imaging of negatively stained SARS-CoV-2 $S2P_{ecto}$ protein, approximately 3 µL of the sample at concentrations of about 10 to 15 µg/mL was applied to a glow discharged grid with continuous carbon film on 400 square mesh copper EM grids (Electron Microscopy Sciences). The grids were stained with 0.75% uranyl formate (UF)[40]. Images were recorded on a Gatan US4000 4k × 4k CCD camera using an FEI TF20 (TFS) transmission electron microscope operated at 200 keV and control with SerialEM[41]. All images were taken at ×50,000 magnification with a pixel size of 2.18 Å pix^{-1} in low-dose mode at a defocus of 1.5–1.8 µm. The total dose for the micrographs was ~25 e^- per $Å^2$. Image processing was performed using the cryoSPARC software package[42]. Images were imported, and CTF estimation was done for the particles. The images then were denoised and picked with Topaz[43]. The particles were extracted with a box size of 256 pixels and binned to 128 pixels. Two-dimensional class averages were performed (see Supplementary Table 2 for details).

Patient selection and target-specific memory B cells isolation. B cell responses to SARS-CoV-2 in PBMCs from a cohort of four patients with documented previous infection with the virus were analyzed for antigen specificity, and PBMCs were used for SARS-CoV-2-specific B cell enrichment. The frequency of SARS-CoV-2 S protein-specific B cells was identified by antigen-specific staining with either biotinylated $S2P_{ecto}$ or RBD–mFc protein. Briefly, B cells were purified magnetically (STEMCELL Technologies) and stained with anti-CD19–APC (BioLegend clone HIB19 cat. no. 982406, lot B270238, 1:10 dilution), anti-IgD–FITC (BioLegend clone IA6–2, cat. no. 348206, lot B258195, 1:20 dilution), and anti-IgM–FITC (BioLegend clone MHM-88, cat. no. 314506, lot B218736, 1:20 dilution) phenotyping antibodies and biotinylated antigen. A DAPI stain was used as a viability dye to distinguish dead cells. Antigen-labeled class-switched memory B cell–antigen complexes ($CD19^+IgM^-IgD^-Ag^+DAPI^-$) were detected with a R-PE-labeled streptavidin conjugate (Thermo Fisher Scientific, S866, 1:500 dilution). After identification of the two patients with the highest B cell response against SARS-CoV-2 (patients 3 and 4), target-specific memory B cells were isolated by flow-cytometric sorting using an SH800 cell sorter (Sony) from pooled PBMCs of these two patients, after labeling of B cells with either biotinylated $S2P_{ecto}$ or RBD–mFc proteins. Flow-cytometric data were analyzed with the SH800 software and FlowJo version 10 (Tree Star).

Overall, from >4 ×10^8 PBMCs, 2,126 RBD–mFc-reactive and 5,544 $S2P_{ecto}$-reactive B cells were sorted and subjected to further analysis. Several methods were implemented for the preparation of sorted B cells for sequencing. Approximately 4,500 sorted cells were subjected to direct sequencing immediately after flow cytometric sorting. The remaining cells were expanded in culture for 8 d in the presence of irradiated 3T3 feeder cells that were engineered to express human CD40L, IL-21 and BAFF, as described previously[22]. The expanded lymphoblastoid cell lines (LCLs) secreted high levels of S-protein-specific antibodies, as confirmed by ELISA, to detect antigen-specific human antibodies in culture supernatants. Approximately 40,000 expanded LCLs were sequenced using the Chromium sequencing method (10x Genomics).

Microfluidic device selection of single antigen-specific B cells. Activated memory B cells were screened using Berkeley Lights' Beacon optofluidic system. Purified B cell samples were imported automatically onto OptoSelect 11k chips in a novel plasmablast survival medium that promotes antibody secretion and preserves cell viability[44]. Single-cell penning was then performed using OEP technology, in which light is used to transfer B cells into individual nanoliter-volume chambers (NanoPens). Using this light-based manipulation, thousands of LCLs were transferred into pens across multiple chips in each workflow. We performed an on-chip, fluorescence-based assay to identify antibodies that bound SARS-CoV-2 $S2P_{ecto}$ or RBD–mFc protein. We prepared 6- to 8-µm and 10- to 14-µm RBD–mFc-conjugated beads by coupling biotinylated RBD–mFc protein to streptavidin-coated polystyrene particles (Spherotech). We prepared 6- to 8-µm $S2P_{ecto}$ protein-conjugated beads by coupling full-length $S2P_{ecto}$ protein to streptavidin-coated polystyrene particles. Assays consisted of mixing beads conjugated with the RBD–mFc or $S2P_{ecto}$ proteins with Alexa Fluor (AF)-labeled anti-human secondary antibodies (Thermo Fisher Scientific cat. no. A-21090) at a 1:100 dilution and importing this assay mixture into OptoSelect 11k chips. Antigen-specific antibodies bound the antigen-conjugated beads, which then sequestered the fluorescent secondary antibody. Cells secreting antigen-specific antibodies were identified by locating the NanoPens immediately adjacent to the fluorescent beads. We also performed an on-chip assay to select antibodies that blocked the interaction of hACE2 and the RBD of SARS-CoV-2. The blocking assay was performed by first co-incubating LCLs and 10- to 14-µm RBD–mFc-conjugated streptavidin-coated beads (Spherotech) in the NanoPen chambers to allow for secreted antibodies to saturate the antigen. Then, a mixture of recombinant hACE2 with a FLAG tag (Sigma-Aldrich cat. no. SAE0064), a rat anti-FLAG AF 647 antibody at a 1:50 dilution (BioLegend clone L5, cat. no. 637315, Lot B265929) and an anti-human IgG AF 568 antibody at a 1:100 dilution (Thermo

Fisher Scientific cat. no. A-21090) was perfused through the OptoSelect 11k chip and allowed to diffuse into the NanoPen chambers. RBD-binding antibodies were identified by locating pens with RBD–mFc-conjugated beads that were fluorescent when imaged using the Beacon TRED filter cube. Simultaneously, hACE2 binding to the RBD-coated beads was detected using a Cy5 filter cube. NanoPen chambers containing RBD–mFc-conjugated beads with fluorescence in both filter cubes were classified as containing B cells secreting anti-SARS-CoV-2 antibodies that bound RBD but that did not demonstrate hACE2-blocking activity. NanoPen chambers that contained RBD–mFc-conjugated beads that were fluorescent in the TRED channel but non-fluorescent in the Cy5 channel contained secreted antibodies that had both bound RBD and blocked hACE2–RBD interaction. Antigen-specific cells of interest were exported from specific NanoPen chambers to individual wells of 96-well reverse transcription–PCR plates containing lysis buffer.

Sequencing and cloning of single antigen-specific B cells. After export from the Beacon instrument, antibody heavy- and light-chain sequences for B cells secreting RBD–mFc- or $S2P_{ecto}$-binding antibodies were amplified and recovered using components of the Opto Plasma B Discovery cDNA Synthesis Kit (Berkeley Lights). Antibody heavy- and light-chain sequences were amplified through a 5′ RACE approach using the kit's included 'BCR Primer 2' forward primer and isotype-specific reverse primers. The 5′-RACE-amplified cDNA was sequenced using the Pacific Biosciences Sequel platform using the SMRTbell Barcoded Adapt Complete Prep-96 kit (Pacific Biosciences) and a 6-h movie time. In a redundant sequencing approach, heavy- and light-chain sequences were amplified using a cocktail of custom V- and J-gene-specific primers (similar to previously described human Ig gene-specific primers[45]) from the original 5′-RACE-amplified cDNA while the products of the gene-specific amplification were sent for Sanger sequencing (GENEWIZ). The sequences generated by these two approaches were analyzed using our Python-based antibody variable-gene analysis tool (PyIR; https://github.com/crowelab/PyIR)[46] to identify which *V* and *J* genes most closely matched the nucleotide sequence. Heavy- and light-chain sequences were then amplified from the original cDNA using cherry-picked *V*- and *J*-gene-specific primers most closely corresponding to the *V* and *J* gene calls made by PyIR. These primers include adapter sequences which allow Gibson-based cloning into a monocistronic IgG1 expression vector (pMCis_G1). Similar to a vector described below, this vector contains an enhanced 2A sequence and GSG linker that allows simultaneous expression of mAb heavy and light chain genes from a single construct upon transfection[47]. The pMCis_G1 vector was digested using the New England BioLabs restriction enzyme FspI, and the amplified paired heavy- and light-chain sequences were cloned through Gibson assembly using NEBuilder HiFi DNA Assembly Master Mix. After recovered sequences were cloned into pMCis_G1 expression constructs, recombinant antibodies were expressed in CHO cells and were purified by affinity chromatography as detailed below. Antigen-binding activity was confirmed using plate-based ELISA.

Generation of antibody variable-gene libraries from single B cells. As an alternative approach, we also used a second major approach for isolation of SARS-CoV-2-reactive antibodies. In some experiments, the Chromium Single Cell V(D)J workflow with B-cell-only enrichment option was used for generating linked heavy-chain and light-chain antibody profiling libraries. Approximately 2,866 directly sorted $S2P_{ecto}$ or 1,626 RBD–mFc protein-specific B cells were split evenly into 2 replicates each and separately added to 50 µl of RT Reagent Mix, 5.9 µl of Poly-dt RT Primer, 2.4 µl of Additive A and 10 µl of RT Enzyme Mix B to complete the Reaction Mix as per the vendor's protocol, which then was loaded directly onto a Chromium chip (10x Genomics). Similarly, for the remaining sorted cells that were expanded in bulk, approximately 40,000 cells from 2 separate sorting approaches were split evenly across 4 reactions and processed separately as described above, before loading onto a Chromium chip. The libraries were prepared following the User Guide for Chromium Single Cell V(D)J Reagents kits (CG000086_REV K).

Next-generation DNA sequence analysis of antibody variable genes. Chromium Single Cell V(D)J B-Cell-enriched libraries were quantified, normalized and sequenced according to the User Guide for Chromium Single Cell V(D)J Reagents kits (CG000086_REV C). The two enriched libraries from direct flow cytometric cell sorting were sequenced on a NovaSeq sequencer (Illumina) with a NovaSeq 6000 S1 Reagent Kit (300 cycles) (Illumina). The four enriched libraries from bulk expansion were sequenced on a NovaSeq sequencer with a NovaSeq 6000 S4 Reagent Kit (300 cycles) (Illumina). All enriched V(D)J libraries were targeted for sequencing depth of at least 5,000 raw read pairs per cell.

Bioinformatics analysis of single-cell sequencing data. Following sequencing, all samples were demultiplexed and processed through the 10x Genomics Cell Ranger software (version 2.1.1). The down-selection to identify lead candidates for expression was carried out in two phases. In the first phase, all paired antibody heavy- and light-chain variable-gene cDNA nucleotide sequences obtained that contained a single heavy- and light-chain sequence were processed using PyIR. We considered heavy- and light-chain-encoding gene pairs productive and retained them for additional downstream processing if they met the following criteria: (1) did not contain a stop codon, (2) encoded an intact CDR3 and (3) contained an in-frame junctional region. The second phase of processing eliminated redundant sequences (those with identical amino acid sequences). Any antibody variant that was designated as an IgM isotype (based on the sequence and assignment using the 10x Genomics Cell Ranger V(D)J software, version 2.1.1) was removed from consideration (while IgG and IgA isotype antibodies were retained). The identities of antibody variable-gene segments, CDRs and mutations from inferred germline gene segments were determined by using PyIR.

Antibody gene synthesis. Sequences of selected mAbs were synthesized using a rapid high-throughput cDNA synthesis platform (Twist Bioscience) and subsequently cloned into an IgG1 monocistronic expression vector (designated as pTwist-mCis_G1) for mammalian cell culture mAb secretion. This vector contains an enhanced 2A sequence and GSG linker that allows simultaneous expression of mAb heavy- and light-chain genes from a single construct upon transfection[47].

MAb production and purification. For high-throughput production of recombinant mAbs, we adopted approaches designated as 'micro-scale' or 'midi-scale'. For 'micro-scale' mAbs expression, we performed micro-scale transfection (~1 ml per antibody) of CHO cell cultures using the Gibco ExpiCHO Expression System and a protocol for deep 96-well blocks (Thermo Fisher Scientific), as previously described[19]. Briefly, synthesized antibody-encoding lyophilized DNA was reconstituted in OptiPro serum-free medium (OptiPro SFM) and used for transfection of ExpiCHO cell cultures into 96-deep-well blocks. For high-throughput micro-scale mAb purification, clarified culture supernatants were incubated with MabSelect SuRe resin (Cytiva), washed with PBS, eluted, buffer-exchanged into PBS using Zeba Spin Desalting Plates (Thermo Fisher Scientific) and stored at 4 °C until use. For 'midi-scale' mAbs expression, we performed transfection (~15 ml per antibody) of CHO cell cultures using the Gibco ExpiCHO Expression System and protocol for 50 ml mini bioreactor tubes (Corning), as described by the vendor. For high-throughput midi-scale mAb purification, culture supernatants were purified using HiTrap MabSelect SuRe (Cytiva) on a 24-column parallel protein chromatography system (Protein BioSolutions). Purified mAbs were buffer-exchanged into PBS, concentrated using Amicon Ultra-4 50 KDa Centrifugal Filter Units (Millipore Sigma) and stored at 4 °C until use.

ELISA binding screening assays. Wells of 96-well microtiter plates were coated with purified recombinant SARS-CoV-2 S protein, SARS-CoV-2 S_{RBD} protein, SARS-CoV-2 S_{NTD} (kindly provided by P. McTamney, K. Ren and A. Barnes, Astra Zeneca) or SARS-CoV S protein (kindly provided by S. Bangaru and A. Ward, Scripps Research Institute) at 4 °C overnight. Plates were blocked with 2% non-fat dry milk and 2% normal goat serum in DPBS containing 0.05% Tween-20 (DPBS-T) for 1 h. For mAb screening assays, Supernatants from CHO cell culture or purified mAbs were diluted 1:20 in blocking buffer, added to the wells and incubated for 1 h at ambient temperature. The bound antibodies were detected using goat anti-human IgG conjugated with horseradish peroxidase (Southern Biotech) and TMB substrate (Thermo Fisher Scientific). Color development was monitored, 1N hydrochloric acid was added to stop the reaction and the absorbance was measured at 450 nm using a spectrophotometer (Biotek).

RTCA. To screen for neutralizing activity in the panel of recombinantly expressed mAbs, we used a high-throughput and quantitative RTCA assay and xCelligence RTCA HT Analyzer (ACEA Biosciences) that assesses kinetic changes in cell physiology, including virus-induced cytopathic effect (CPE). Twenty µl of cell culture medium (DMEM supplemented with 2% FBS) was added to each well of a 384-well E-plate using a ViaFlo384 liquid handler (Integra Biosciences) to obtain background reading. Six thousand (6,000) Vero-furin cells in 20 µl of cell culture medium were seeded per well, and the plate was placed on the analyzer. Sensograms were visualized using RTCA HT software version 1.0.1 (ACEA Biosciences). For a screening neutralization assay, equal amounts of virus were mixed with micro-scale purified antibodies in a total volume of 40 µ using DMEM supplemented with 2% FBS as a diluent and incubated for 1 h at 37 °C in 5% CO_2. At ~17–20 h after seeding the cells, the virus–mAb mixtures were added to the cells in 384-well E-plates. Wells containing virus only (in the absence of mAb) and wells containing only Vero cells in medium were included as controls. Plates were measured every 8–12 h for 48–72 h to assess virus neutralization. Micro-scale antibodies were assessed in four 5-fold dilutions (starting from a 1:20 sample dilution), and their concentrations were not normalized. In some experiments, mAbs were tested in triplicate using a single (1:20) dilution. Neutralization was calculated as the percent of maximal cell index in control wells without virus minus cell index in control (virus-only) wells that exhibited maximal CPE at 40–48 h after applying virus–antibody mixture to the cells. A mAb was classified as fully neutralizing if it completely inhibited SARS-CoV-2-induced CPE at the highest tested concentration, while a mAb was classified as partially neutralizing if it delayed but did not fully prevent CPE at the highest tested concentration. Representative sensograms for fully neutralizing and partially neutralizing mAbs are shown in Extended Data Fig. 4. For mAb potency ranking experiments, individual mAbs identified as fully neutralizing from the screening study were assessed by FRNT.

Sequence analysis of antigen-reactive mAb sequences. Sequences of the 389 mAbs isolated by different approaches were combined and run through PyIR to identity the V genes, J genes, CDR3 lengths and percent identity to germline, and sequence within the FR1–FR4 region for both heavy and light chains. Sequences were then deduplicated on the nucleotide sequences identified in the FR1–FR4 region. Among the 389 mAbs, there were 324 unique nucleotide sequences (321 unique amino acid sequences) that were analyzed for *V*/*D*/*J* gene usage, CDR3 length and somatic mutation. First, the number of sequences with corresponding *V* and *J* genes were counted. The *V*/*J* frequency counts were then transformed into a *Z*-score by first subtracting away the average frequency then normalizing by the s.d. of the total set of antigen-reactive mAbs. The *Z*-score was then plotted as a heatmap using python seaborn library. The amino acid length of each CDR3 was counted. The distribution of CDR3 amino acid lengths were then plotted as histograms and fitted using kernel density estimation for the curves using python seaborn library. The number of mutations for each mAb relative to the inferred germline variable-gene sequence was counted for each chain. This number was then transformed into a percentage value. These values were then plotted as a categorical distribution plot as a violin plot using the python seaborn. catplot library.

FRNT. Serial dilutions of serum or plasma were incubated with 10^2 FFU of SARS-CoV-2 for 1 h at 37 °C. The serum–virus or plasma–virus mixtures were then added to Vero E6 cell monolayers in 96-well plates for 1 h at 37 °C. Subsequently, cells were overlaid with 1% (wt/vol) methylcellulose in Minimum Essential Medium (MEM) supplemented to contain 2% heat-inactivated FBS. Plates were fixed 30 h later by removing overlays and were fixed with 4% PFA in PBS for 20 min at room temperature. The plates were incubated sequentially with 1 μg ml^{-1} rCR3022 anti-S antibody[5] and a goat anti-human IgG (γ-chain specific)-peroxidase antibody (Sigma-Aldrich, cat. no. A6029) in PBS supplemented with 0.1% (wt/vol) saponin (Sigma) and 0.1% BSA. SARS-CoV-2-infected cell foci were visualized using TrueBlue peroxidase substrate (KPL) and quantitated on an ImmunoSpot 5.0.37 Macro Analyzer (Cellular Technologies).

SARS-CoV or SARS-CoV-2 neutralization assays using SARS-CoV or SARS-CoV-2 luciferase reporter viruses. Full-length viruses expressing luciferase were designed and recovered via reverse genetics as described previously[48,49]. Viruses were titered in Vero E6 cell culture monolayers to obtain a relative light units (RLU) signal of at least 20× the cell-only control background. Vero E6 cells were plated at 20,000 cells per well the day prior in clear-bottom black-walled 96-well plates (Corning no. 3904). Neutralizing antibodies were diluted serially by fourfold for up to eight dilutions. SARS-Urbani NanoLuc or SARS-CoV-2 NanoLuc virus were mixed with serially diluted antibodies. Antibody–virus complexes were incubated at 37 °C in 5% CO_2 for 1 h. Following incubation, growth medium was removed, and virus–antibody dilution complexes were added to the cells in duplicate. Virus-only and cell-only controls were included in each neutralization-assay plate. Following infection, plates were incubated at 37 °C in 5% CO_2 for 48 h. After the 48-h incubation, cells were lysed and luciferase activity was measured using the Nano-Glo Luciferase Assay System (Promega), according to the manufacturer's specifications.

Neutralization assays using a recombinant VSV-SARS-CoV-2 virus. Neutralization assays using replication-competent VSV expressing enhanced green fluorescent protein (eGFP) and the SARS-CoV-2 S protein with a C-terminal deletion were performed, as previously described[25]. Briefly, indicated dilutions of mAbs were incubated with VSV-SARS-CoV-2 for 1 h at 37 °C. Antibody–virus complexes then were added to Vero E6 cells in 96-well plates and incubated at 37 °C for 7.5 h. Cells were fixed at room temperature in 2% formaldehyde containing 10 μg ml^{-1} Hoechst 33342 nuclear stain for 45 min. Fixative was replaced with PBS prior to imaging. Images were acquired using an InCell 2000 Analyzer automated microscope (GE Healthcare) in both the DAPI and FITC channels to visualize nuclei and infected cells (×4 objective, 4 fields per well). Images were analyzed using the Multi Target Analysis Module of the InCell Analyzer 1000 Workstation Software (GE Healthcare). GFP-positive cells were identified using the top hat segmentation method and counted within the InCell Workstation software. Neutralization assay data are summarized in Extended Data Fig. 6.

High-throughput mAb quantification. High-throughput quantification of micro-scale-produced mAbs was performed from CHO culture supernatants or micro-scale purified mAbs in a 96-well plate format using the Cy-Clone Plus Kit and an iQue Plus Screener flow cytometer (IntelliCyt Corp), according to the vendor's protocol. Purified mAbs were assessed at a single dilution (1:10 final, using 2 μl of purified mAb per reaction), and a control human IgG solution with known concentration was used to generate a calibration curve. Data were analyzed using ForeCyt software version 6.2 (IntelliCyt Corp).

Quantification and statistical analysis. The descriptive statistics mean ± SEM or mean ± SD were determined for continuous variables as noted. Technical and biological replicates are described in the figure legends. Statistical analyses were performed using Prism v8.0 (GraphPad).

Reporting Summary. Further information on research design is available in the Nature Research Reporting Summary linked to this article.

Data availability

The main data supporting the results in this study are available within the paper and Supplementary Information. The ImMunoGeneTics database is available from http://www.imgt.org/. The analysis pipeline PyIR (https://github.com/crowelab/PyIR) and the specific scripts used for sequence analysis (https://github.com/crowelab/cov2-panel-scripts) are available. Structures deposited by other groups for the full-length spike trimer (6VYB) and the RBD–hACE2 complex (6M0J) that were used for visualization in this paper are publicly available (www.rcsb.org). Sequences for mAbs described in this study have been deposited at GenBank and are available under the following accession codes: MT665032–MT665070, MT665419–MT665457, MT665071–MT665418 and MT665458–MT665805. Datasets are available from the corresponding authors upon reasonable request.

References

39. Mukherjee, S. et al. Enhancing dengue virus maturation using a stable furin over-expressing cell line. *Virology* **497**, 33–40 (2016).
40. Ohi, M., Li, Y., Cheng, Y. & Walz, T. Negative staining and image classification—powerful tools in modern electron microscopy. *Biol. Proced. Online* **6**, 23–34 (2004).
41. Mastronarde, D. N. Automated electron microscope tomography using robust prediction of specimen movements. *J. Struct. Biol.* **152**, 36–51 (2005).
42. Punjani, A., Rubinstein, J. L., Fleet, D. J. & Brubaker, M. A. cryoSPARC: algorithms for rapid unsupervised cryo-EM structure determination. *Nat. Methods* **14**, 290–296 (2017).
43. Bepler, T., Noble, A. J. & Berger, B. Topaz-Denoise: general deep denoising models for cryoEM. Preprint at https://doi.org/10.1101/838920 (2019).
44. Nguyen, D. C. et al. Factors of the bone marrow microniche that support human plasma cell survival and immunoglobulin secretion. *Nat. Commun.* **9**, 3698 (2018).
45. Guthmiller, J. J., Dugan, H. L., Neu, K. E., Lan, L. Y. & Wilson, P. C. An efficient method to generate monoclonal antibodies from human B cells. *Methods Mol. Biol.* **1904**, 109–145 (2019).
46. Soto C. F. J. et al. PyIR: A scalable wrapper for processing billions of immunoglobulin and T cell receptor sequences using IgBLAST. *BMC Bioinformatics* (in the press).
47. Chng, J. et al. Cleavage efficient 2A peptides for high level monoclonal antibody expression in CHO cells. *MAbs* **7**, 403–412 (2015).
48. Scobey, T. et al. Reverse genetics with a full-length infectious cDNA of the Middle East respiratory syndrome coronavirus. *Proc. Natl Acad. Sci. USA* **110**, 16157–16162 (2013).
49. Yount, B. et al. Reverse genetics with a full-length infectious cDNA of severe acute respiratory syndrome coronavirus. *Proc. Natl Acad. Sci. USA* **100**, 12995–13000 (2003).

Acknowledgements

We thank M. Mayo and N. S. Galeano for coordination of human studies, D. O'Connor, N. Safdar, G. Baird, J. Shendure and S. Mubareka for helpful advice on human patients, A. Jones and the staff of the Vanderbilt VANTAGE core laboratory for expedited sequencing, R. Trosseth for assistance with data management and analysis, R. Bombardi and C. Soto for technical consultation on genomics approaches, A. Kim for production of a recombinant form of the mAb CR3022, C. Swearingen and the staff of Fedex Express Specialty Services for expedited transport services, V. Pai and K. Breinlinger of Berkeley Lights, and K. Louder and scientists at Twist Bioscience, B. Fritz at 10x Genomics and representatives at ACEA Biosciences for providing resources, outstanding expedited services and expert applications support. We thank A. Ward, S. Bangaru, P. McTamney, K. Ren and A. Barnes for protein reagents. This study was supported by Defense Advanced Research Projects Agency (DARPA) grant HR0011-18-2-0001, NIH contracts 75N93019C00074 and 75N93019C00062 and the Dolly Parton COVID-19 Research Fund at Vanderbilt. This work was supported by NIH grant 1S10RR028106-01A1 for the Next Generation Nucleic Acid Sequencer, housed in Vanderbilt Technologies for Advanced Genomics (VANTAGE) and supported by the National Center for Research Resources, grant UL1 RR024975-01, and is now at the National Center for Advancing Translational Sciences, grant 2 UL1 TR000445-06. S.J.Z. was supported by NIH T32 AI095202. J.B.C. is supported by a Helen Hay Whitney Foundation postdoctoral fellowship. D.R.M. was supported by NIH T32 AI007151 and a Burroughs Wellcome Fund Postdoctoral Enrichment Program Award. J.E.C. is the recipient of the 2019 Future Insight Prize from Merck KGaA, which supported this research with a research grant. The content is solely the responsibility of the authors and does not necessarily represent the official views of the US government or the other sponsors.

Author contributions

Conceived of the project: S.J.Z., P.G., R.H.C., L.B.T., M.S.D., J.E.C.; Obtained funding: J.E.C. and M.S.D. Obtained human samples: M.O., H.Y.C., J.E.C.; Performed laboratory experiments: S.J.Z., P.G., R.E.C., J.B.C., J.X.R., A.T., R.S.N., R.E.S., N.S., E.B., J.E.D.,

K.W.M., S.S., D.R.M, P.W.R., L.-M.B.; Performed computational work: E.C.C., T.J., S.D., L.M.; Supervised research: S.P.J.W. M.S.D., L.B.T., R.S.B., R.H.C., J.E.C.; Provided critical reagents: J.E.D., K.W.M., F.E.-H.L., D.C.N., I.S., R.S.B.; Wrote the first draft of the paper: S.J.Z., P.G., R.H.C., J.E.C. All authors reviewed and approved the final manuscript.

Competing interests

R.S.B. has served as a consultant for Takeda and Sanofi Pasteur on issues related to vaccines. M.S.D. is a consultant for Inbios, Vir Biotechnology, NGM Biopharmaceuticals and Eli Lilly, is on the scientific advisory board of Moderna and is a recipient of unrelated research grants from Moderna and Emergent BioSolutions. H.Y.C. has served as a consultant for Merck and GlaxoSmithKline and has received research funding from Sanofi Pasteur and research support from Cepheid, Genentech and Ellume. J.E.C. has served as a consultant for Sanofi and is on the scientific advisory boards of CompuVax and Meissa Vaccines, is a recipient of previous unrelated research grants from Moderna and Sanofi and is founder of IDBiologics. Vanderbilt University has applied for patents concerning SARS-CoV-2 antibodies that are related to this work. Emory University has applied for a patent concerning the plasmablast survival medium. S.P.J.W. and P.W.R. have filed a disclosure with Washington University for the recombinant VSV. J.E.D. and K.W.M. are employees of Berkeley Lights. All other authors declared no competing interests.

Additional information

Extended data is available for this paper at https://doi.org/10.1038/s41591-020-0998-x.

Supplementary information is available for this paper at https://doi.org/10.1038/s41591-020-0998-x.

Correspondence and requests for materials should be addressed to R.H.C. or J.E.C.

Peer review information Joao Monteiro was the primary editor on this article and managed its editorial process and peer review in collaboration with the rest of the editorial team.

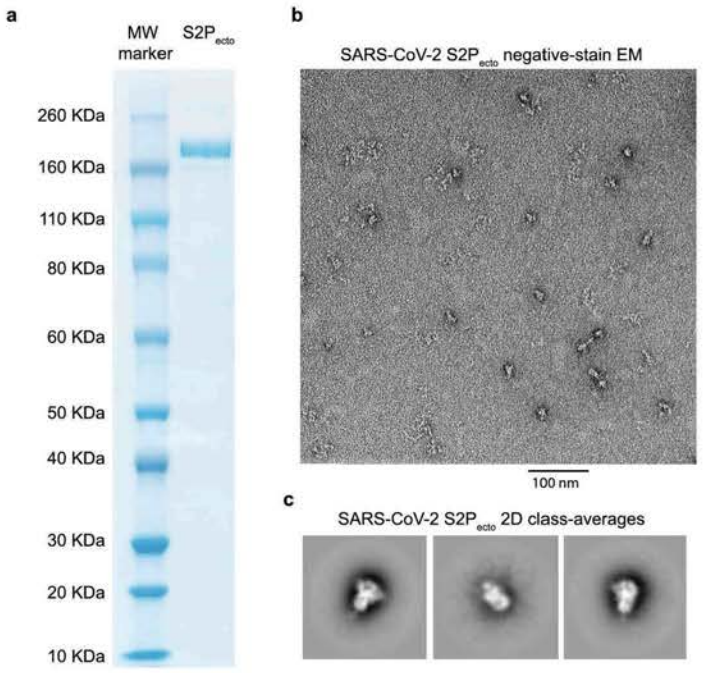

Extended Data Fig. 1 | Expression and validation of prefusion-stabilized SARS-CoV-2 S2P$_{ecto}$ protein. a. Reducing SDS-PAGE gel indicating S2P$_{ecto}$ protein migrating at approximately 180 KDa. One representative protein preparation is shown. **b**. Representative micrograph of negative-stain electron microscopy with S2Pecto protein preparation. Scale bar denotes 100 nm. **c**. 2D class-averages of S2P$_{ecto}$ protein in the prefusion conformation. The size for each box is 128 pixels. Detailed information on image collection is available in Supplementary Table 2.

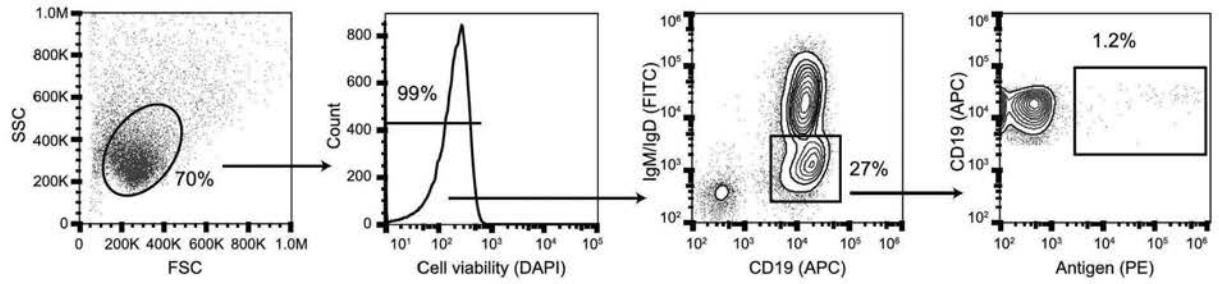

Extended Data Fig. 2 | Representative gating strategy for antigen-specific cell sorting. Representative gating strategy for profiling of antigen-specific B cell frequency for donors. Subject 4 is shown, and phenotypic markers are shown on plot axes. Arrows indicate cell populations derived from gates.

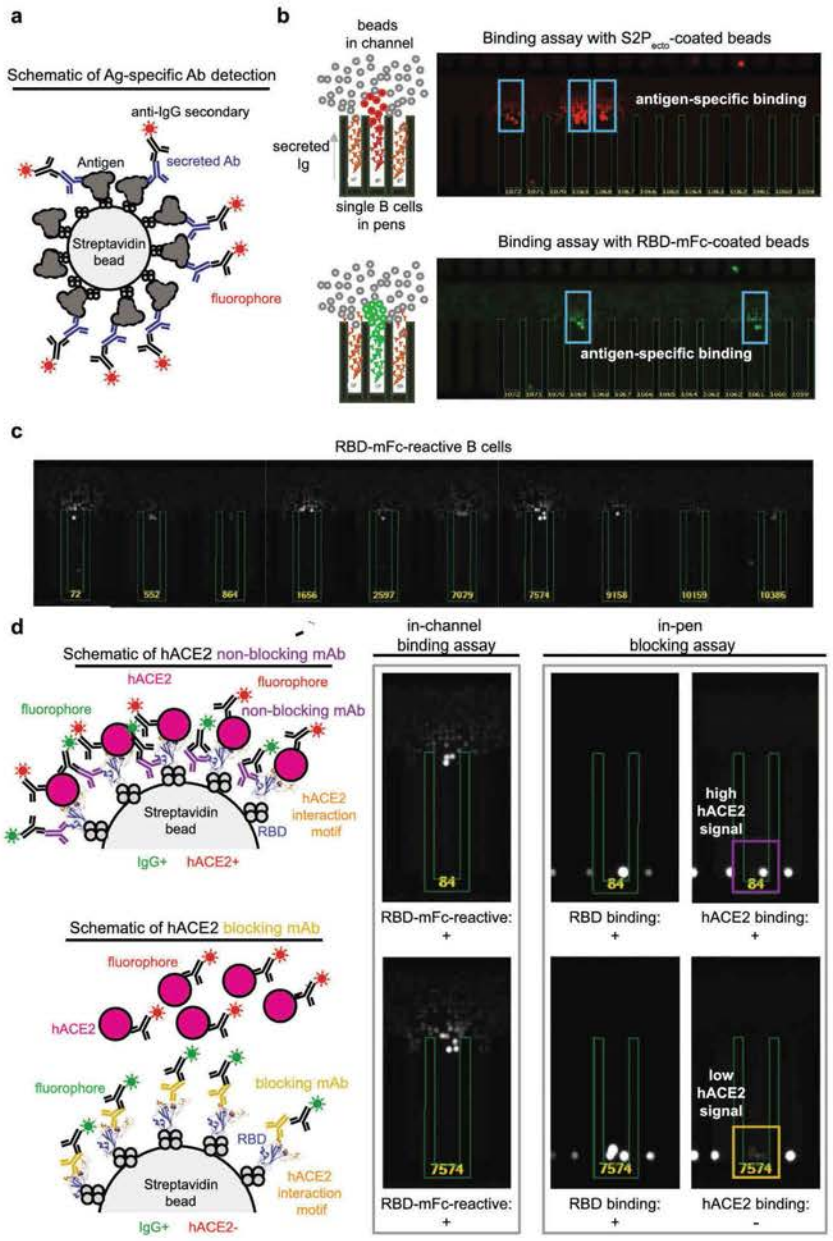

Extended Data Fig. 3 | Functional assays from single antigen-reactive B cells. a. Biotinylated antigen (dark grey) was coupled to a streptavidin-conjugated polystyrene bead (light grey). Antibodies (blue) are secreted by single B cells loaded into individual NanoPens on the Berkeley Lights Beacon optofluidic device. Antibody binding to antigen was detected with a fluorescent anti-human IgG secondary Ab (black). **b**. Left: Schematic of fluorescing beads in the channel above a pen containing an individual B cell indicates antigen-specific reactivity. Top right: False-color still image of positive wells with B cells secreting S2P$_{ecto}$-reactive antibodies. Reactive antibody diffusing out of a pen is visualized as a plume of fluorescence. Bottom right: False-color still image of positive wells with B cells secreting RBD-mFc-reactive antibodies. **c**. Representative images of RBD-mFc reactive B cells from a single-B-cell secretion assay. **d**. Identification of mAbs with hACE2-blocking activity using single-cell functional screening. Left: Schematic illustrating detection of secreted Ab and hACE2 binding on an RBD-mFc-coated streptavidin bead. Ab binding was detected in one fluorescent channel, while hACE2 binding was detected in another fluorescent channel. The top panel illustrates an RBD-binding, non-blocking mAb, where the bead is positive for both Ab and hACE2 signals, while the bottom panel illustrates an RBD-binding mAb that competes with hACE2 for binding, where the bead is positive for only Ab signal. Right: Representative images of a B cell secreting non-blocking Abs (top) and a B cell secreting hACE2-blocking mAbs (bottom). Streptavidin beads are loaded into the same pens as B cells. The fluorescence of the streptavidin beads in the same pen as the B cell secreting hACE2-blocking Abs is reduced relative to adjacent wells, indicating hACE2-blocking activity.

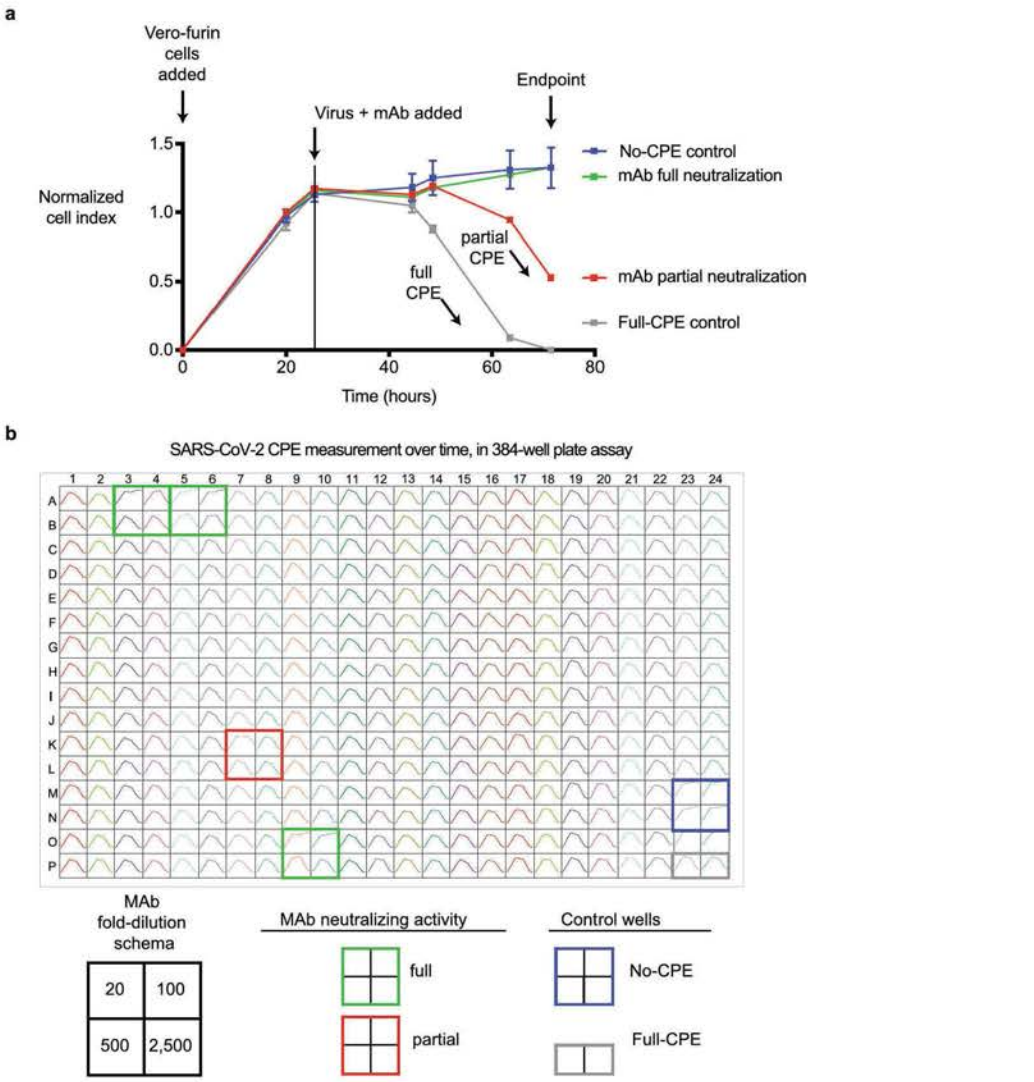

Extended Data Fig. 4 | Real-time cell analysis assay to screen for neutralization activity. a. Curves for fully neutralizing mAb (green) and partially neutralizing mAb (red) by monitoring of CPE in Vero-furin cells that were inoculated with SARS-CoV-2 and pre-incubated with the respective mAb. Uninfected cells (blue) and infected cells without antibody addition (grey) served as controls for intact monolayer and full CPE, respectively. Data represent a single well measurement for each mAb at the highest tested concentration, mean ± SD values of technical duplicates for the positive CPE control, and mean ± SD values of technical quadruplicates for the no-CPE controls. **b**. Example sensograms from individual wells of 384-well E-plate analysis showing rapid identification of SARS-CoV-2 neutralizing mAbs. Neutralization was assessed using micro-scale purified mAbs and each mAb was tested in four 5-fold dilutions as indicated. Plates were measured every 8-12 hrs for a total of 72 hrs as in (a).

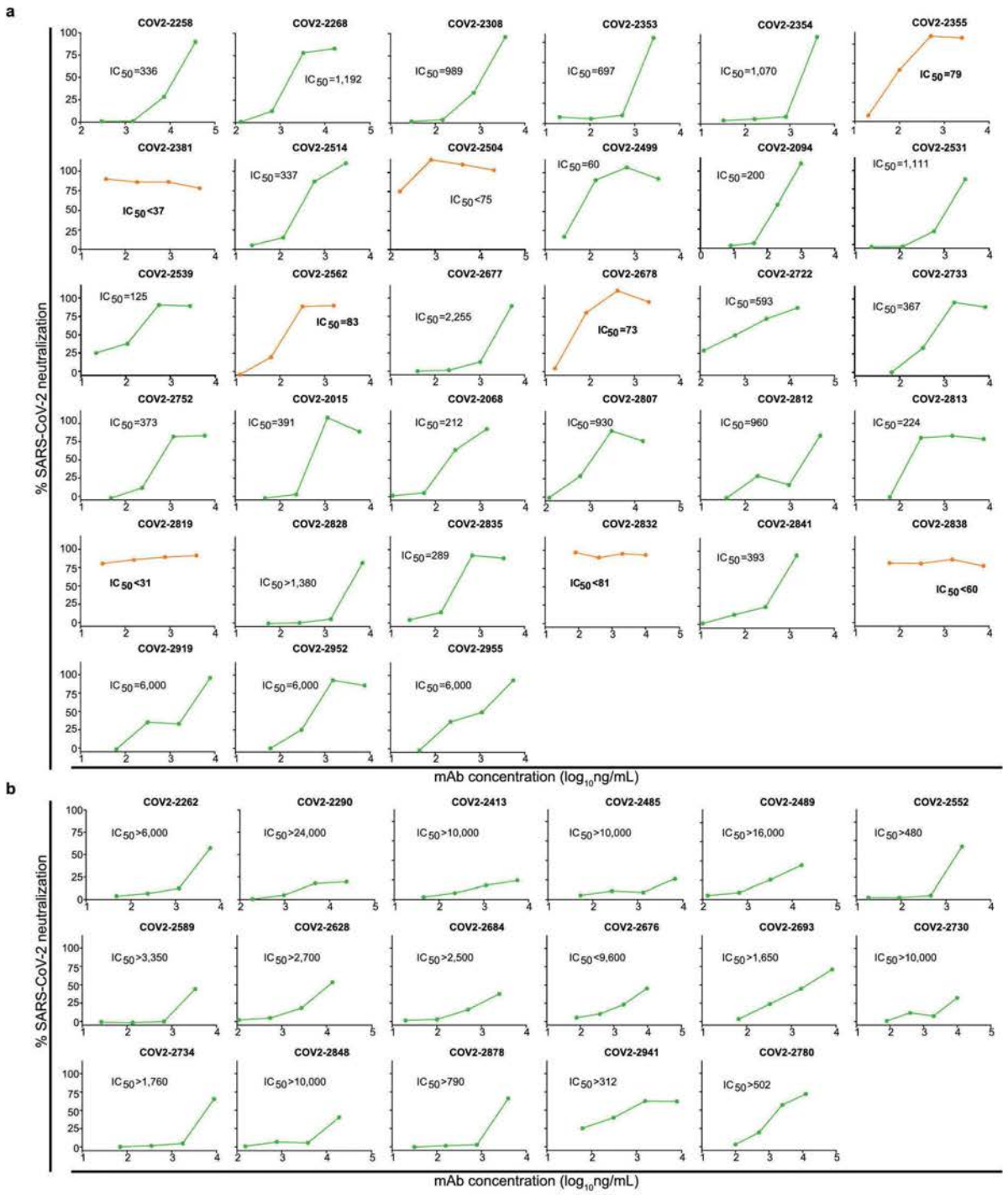

Extended Data Fig. 5 | Real-time cell analysis assay to quantify neutralization potency. Dose-response curves showing activity of neutralizing mAbs that were identified by rapid screening using the RTCA assay, as in Extended Data Fig. 4. Each mAb was tested in four sequential five-fold dilutions from micro-scale purified samples in which mAbs concentrations were not normalized but quantified. Neutralization was calculated as the percent of maximal cell index in control wells without virus minus cell index in control (virus-only) wells that exhibited maximal CPE at 40 to 48 hrs after applying virus-antibody mixture to the cells. **a**. Representative neutralizing mAbs that fully prevented CPE at the lowest tested dilution (corresponding to the highest tested mAb concentration) are shown. IC50 values estimated from each curve are indicated. Curves for potently neutralizing mAbs (IC50 < 100 ng/mL) are shown in orange, from which mAbs COV2-2355 and COV2-2381 are genetically related. **b**. Representative neutralizing mAbs that partially prevented CPE at the lowest tested dilution (corresponding to the highest tested mAb concentration) are shown.

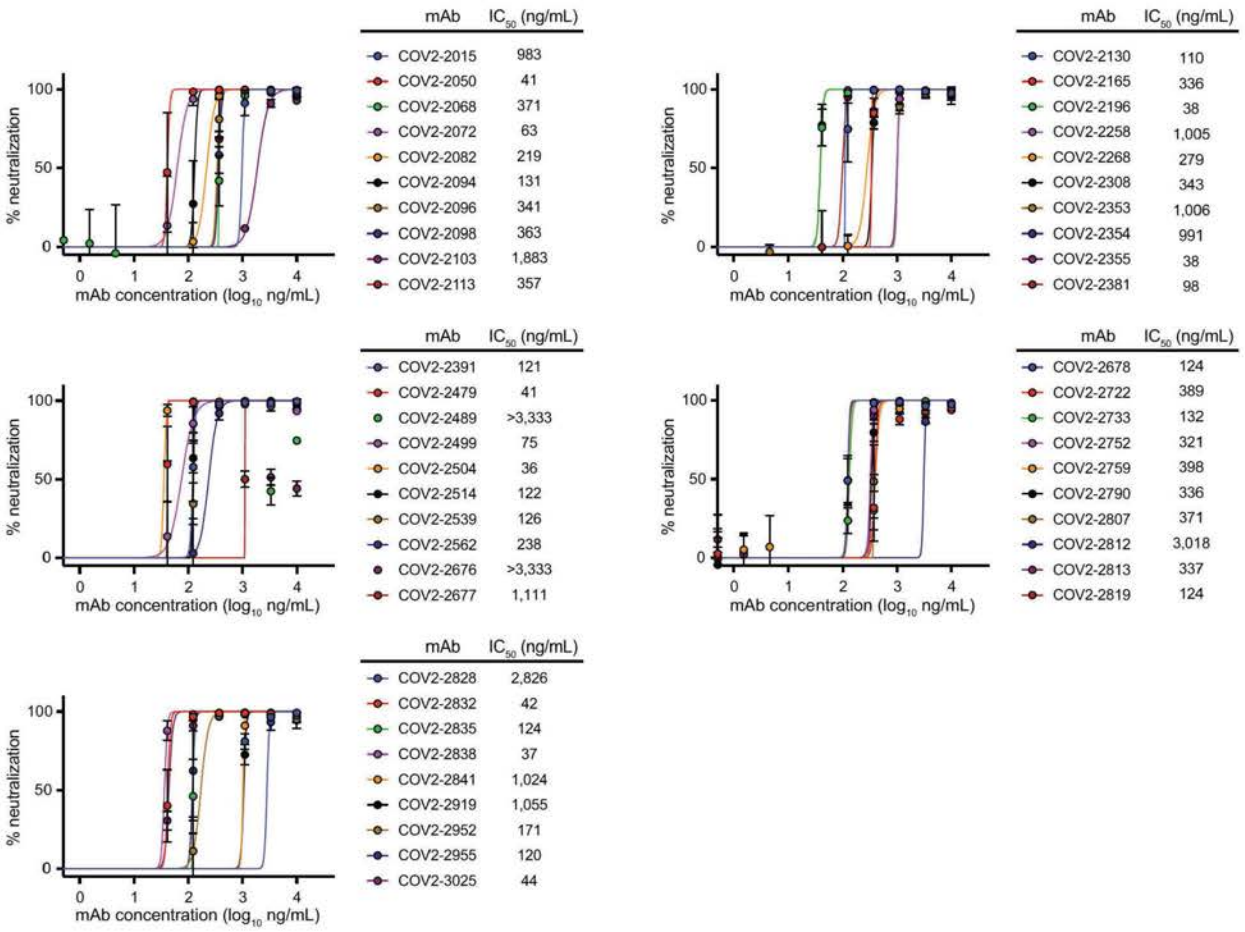

Extended Data Fig. 6 | Quantitative neutralization assays of VSV-SARS-CoV-2. Dose-response neutralization of VSV-SARS-CoV-2 by neutralizing mAbs. IC50 values are indicated for each mAb. Data shown are the mean of two technical replicates from a single experiment, and error bars denote the standard deviation for each point.

nature research

Corresponding author(s): Robert Carnahan and James Crowe

Last updated by author(s): 7/07/2020

Reporting Summary

Nature Research wishes to improve the reproducibility of the work that we publish. This form provides structure for consistency and transparency in reporting. For further information on Nature Research policies, see Authors & Referees and the Editorial Policy Checklist.

Statistics

For all statistical analyses, confirm that the following items are present in the figure legend, table legend, main text, or Methods section.

n/a	Confirmed
☐	☒ The exact sample size (*n*) for each experimental group/condition, given as a discrete number and unit of measurement
☐	☒ A statement on whether measurements were taken from distinct samples or whether the same sample was measured repeatedly
☒	☐ The statistical test(s) used AND whether they are one- or two-sided *Only common tests should be described solely by name; describe more complex techniques in the Methods section.*
☒	☐ A description of all covariates tested
☒	☐ A description of any assumptions or corrections, such as tests of normality and adjustment for multiple comparisons
☐	☒ A full description of the statistical parameters including central tendency (e.g. means) or other basic estimates (e.g. regression coefficient) AND variation (e.g. standard deviation) or associated estimates of uncertainty (e.g. confidence intervals)
☒	☐ For null hypothesis testing, the test statistic (e.g. *F*, *t*, *r*) with confidence intervals, effect sizes, degrees of freedom and *P* value noted *Give P values as exact values whenever suitable.*
☒	☐ For Bayesian analysis, information on the choice of priors and Markov chain Monte Carlo settings
☒	☐ For hierarchical and complex designs, identification of the appropriate level for tests and full reporting of outcomes
☒	☐ Estimates of effect sizes (e.g. Cohen's *d*, Pearson's *r*), indicating how they were calculated

Our web collection on statistics for biologists contains articles on many of the points above.

Software and code

Policy information about availability of computer code

Data collection	We used the 10X Genomics cellranger (version 2.1.1) [https://support.10xgenomics.com/single-cell-gene-expression/software/overview/welcome] bioinformatics processing pipeline. We began by first running the cellranger mkfastq program to generate FASTQ files that were then fed into the cellranger vdj program to generate CSV and JSON files containing processed data. All processed heavy and light chain sequences were then reprocessed using our PyIR (version 1.0) [https://github.com/crowelab/PyIR] processing pipeline. PyIR is a Python wrapper that parses out VDJ assignment from IgBLAST [PMID: 23671333].
Data analysis	We used a customized Python script, 10x-filter.py, for downstream selection of heavy-light pairs for expression and testing. The script begins by filtering out all ambiguous heavy and light chain pairings. It then bins all unique heavy chain somatic variants with the same V3J clonotype (i.e., V germline gene, J germline gene and CDR3 amino acid sequence). The heavy chain somatic variants are then rank-ordered within each V3J clonotype bin from most to least mutated. The user has the option to output only the most mutated sequence or least mutated sequence from each V3J clonotype bin for downstream expression and characterization. Code used for sequence processing for selecting sequences for synthesis and for analyses that appear in the paper is available at https://github.com/crowelab/cov2-panel-scripts. For ELISAs binding data and neutralization assays, analyses of data were performed using Prism 8.0 (GraphPad Inc). For generation of structural schematics for Figure 3, PyMOL (Schrödinger) was used to visualize previously deposited cryo EM and crystal structures. For IgG quantification, data were analyzed using ForeCyt software version 6.2 (IntelliCyt Corp). For RTCA neutralization assays, sensograms were visualized and analyzed using RTCA HT software version 1.0.1 (ACEA Biosciences Inc). For VSV-SARS-CoV-2 neutralization assays, images were analyzed using the Multi Target Analysis Module of the InCell Analyzer 1000 Workstation Software (GE Healthcare). GFP-positive cells were identified using the top hat segmentation method and counted within the

InCell Workstation software.

For negative-stain electron microscopy analysis, image processing was performed using the cryoSPARC software package.

For manuscripts utilizing custom algorithms or software that are central to the research but not yet described in published literature, software must be made available to editors/reviewers. We strongly encourage code deposition in a community repository (e.g. GitHub). See the Nature Research guidelines for submitting code & software for further information.

Data

Policy information about availability of data

All manuscripts must include a data availability statement. This statement should provide the following information, where applicable:

- Accession codes, unique identifiers, or web links for publicly available datasets
- A list of figures that have associated raw data
- A description of any restrictions on data availability

The main data supporting the results in this study are available within the paper and Supplementary Information. The ImMunoGeneTics database is available from http://www.imgt.org/. The analysis pipeline PyIR (https://github.com/crowelab/PyIR) and the specific scripts used for sequence analysis (https://github.com/crowelab/cov2-panel-scripts) are available. Structures deposited by other groups for the full-length spike trimer (6VYB) and the RBD–hACE2 complex (6M0J) that were used for visualization in this paper are publicly available (www.rcsb.org). Sequences for mAbs described in this study have been deposited at GenBank and are available under the following accession codes: MT665032 - MT665070, MT665419 - MT665457, MT665071 - MT665418, and MT665458 - MT665805. Datasets are available from the corresponding authors upon reasonable request.

Field-specific reporting

Please select the one below that is the best fit for your research. If you are not sure, read the appropriate sections before making your selection.

☒ Life sciences ☐ Behavioural & social sciences ☐ Ecological, evolutionary & environmental sciences

For a reference copy of the document with all sections, see nature.com/documents/nr-reporting-summary-flat.pdf

Life sciences study design

All studies must disclose on these points even when the disclosure is negative.

Sample size	No sample-size calculations were performed. For mAb isolation, a large number of antibodies cloned and synthesized yielded mAbs targeting multiple epitopes on the spike glycoprotein, suggesting that the pandel described here represents a diverse repertoire from these donors. Details about research subjects groups are provided in Supplementary information.
Data exclusions	No data were excluded from the analysis
Replication	Key experimental findings that include identification of SARS-CoV2-reactive and neutralizing human monoclonal antibodies were confirmed in two or more independent experiments. Initial neutralization screening results by the RTCA assay were confirmed using a VSV-SARS-CoV-2 virus neutralization assay, and the neutralization activity of several of these mAbs was confirmed using a SARS-CoV-2 luciferase reporter virus in a BSL-3 neutralization assay. All mAbs that neutralized in the cell impedance assay showed neutralizing activity in subsequent neutralization assays. For antigen-specific staining of PBMCs from the human subjects studied, analytical flow cytometry was performed prior to initiating processing of the larger sample. The antigen specific frequencies we observed for a given donor sample were similar across multiple days and independent staining reactions. Following sorting, a small fraction of sorted cells was analyzed by analytical flow cytometry to verify the purity of the sorted population prior to initiating single cell sequencing or B cell stimulation or expansion.
Randomization	Antibody sequences were randomly allocated to different 96 well plates for DNA synthesis and for the initial antibody expression and screening assays, with the end result that antibodies with highly similar sequences and phenotypes were present across plates and experimental replicates.
Blinding	The initial antibody expression and screening for antigen reactivity and neutralization activity was done in a blinded fashion, as a given antibody sequence was not known to the investigator at time of analysis. Importantly, multiple mAbs discovered by independent workflows were closely related and some had identical amino acid sequences and exhibited similar phenotypes in both antigen binding and neutralization assays. For the mAb validation experiments, investigators were not blinded to the study groups. Quantitative data analysis and validation controls were used, minimizing the risk of introducing bias through the absence of blinding.

Reporting for specific materials, systems and methods

We require information from authors about some types of materials, experimental systems and methods used in many studies. Here, indicate whether each material, system or method listed is relevant to your study. If you are not sure if a list item applies to your research, read the appropriate section before selecting a response.

Materials & experimental systems

n/a	Involved in the study
☐	☒ Antibodies
☐	☒ Eukaryotic cell lines
☒	☐ Palaeontology
☒	☐ Animals and other organisms
☐	☒ Human research participants
☒	☐ Clinical data

Methods

n/a	Involved in the study
☒	☐ ChIP-seq
☐	☒ Flow cytometry
☒	☐ MRI-based neuroimaging

Antibodies

Antibodies used

B cell phenotyping flow cytometry antibodies included APC mouse anti-human CD19 (BioLegend clone HIB19 Cat# 982406, Lot B270238), FITC anti-human IgM (BioLegend clone MHM-88, Cat# 314506, Lot B218736), and FITC anti-human IgD (BioLegend clone IA6-2, Cat# 348206, lot B258195).
Polyclonal goat anti-human IgG-HRP antibody (Southern Biotech Cat 2040-05, Lot B3919-XD29) was used for antigen binding ELISA assays.
For FRNT assay, a previously described anti-SARS S-protein human antibody CR3022 (PMID: 32245784) was used as a primary antibody and the detection was performed using a goat anti-human IgG (γ-chain specific)-peroxidase antibody (Sigma-Aldrich, Cat# A6029).
For antigen binding and hACE2 blocking screening assays on Berkeley Lights' Beacon instrument, goat anti-human IgG (H+L) cross-adsorbed secondary antibody, Alexa Fluor 568 (ThermoFisher Scientific Cat# A-21090), and rat anti-FLAG Alexa Fluor 647 antibody (BioLegend clone L5, Cat #637315, Lot B265929) were used.

Validation

All antibodies used in this study except anti-S human antibody CR3022 (PMID: 32245784) are commercially available. Antibodies used in a specific species or application have been appropriately validated by manufacturers and this information is provided on their website and information datasheets as follows:
APC mouse anti-human CD19 (https://www.biolegend.com/en-us/products/apc-anti-human-cd19-antibody-14024);
FITC anti-human IgM (https://www.biolegend.com/en-us/products/fitc-anti-human-igm-antibody-2880);
FITC anti-human IgD (https://www.biolegend.com/en-gb/products/fitc-anti-human-igd-antibody-6683);
Goat anti-human IgG-HRP (https://www.southernbiotech.com/?catno=2040-05&type=Polyclonal#&panel1-1&panel2-1);
Goat anti-human IgG (γ-chain specific)-peroxidase antibody (https://www.sigmaaldrich.com/catalog/product/sigma/a6029?lang=en&region=US).
Goat anti-human IgG (H+L) cross-adsorbed secondary antibody, Alexa Fluor 568 (https://www.thermofisher.com/order/genome-database/dataSheetPdf?producttype=antibody&productsubtype=antibody_secondary&productId=A-21090&version=105)
Rat anti-FLAG Alexa Fluor 647 (https://www.biolegend.com/fr-ch/global-elements/pdf-popup/alexa-fluor-647-anti-dykddddk-tag-14979?filename=Alexa%20Fluorreg%20647%20anti-DYKDDDDK%20Tag%20Antibody.pdf&pdfgen=true)
Activity of newly discovered SARS-CoV-2-specific monoclonal antibodies are validated via multiple assays described in this paper.

Eukaryotic cell lines

Policy information about cell lines

Cell line source(s)

Vero E6 (CRL-1586, (American Type Culture Collection [ATCC])
Vero CCL81 (CCL-81, ATCC)
HEK293T (CRL-3216 ATCC)
Vero-furin cells were obtained from T. Pierson (NIH) and have been described previously (reference 2, Online Methods).
Expi293F (ThermoFisher Scientific, A1452)
ExpiCHO (ThermoFisher Scientific, A29127)

Authentication

None of the cell lines used were authenticated

Mycoplasma contamination

All cell lines were tested and confirmed negative for Mycoplasma contamination

Commonly misidentified lines
(See ICLAC register)

None

Human research participants

Policy information about studies involving human research participants

Population characteristics

We studied five subjects in the United States, four with SARS-CoV2 exposure history and one healthy subject. Research subject demographics and SARS-CoV-2 exposure history are found in Supplemental Table 3.
SARS-CoV-2-infected subjects:
Subject 1: Male, 35 years old
Subject 2: Female, 52 years old
Subject 3: Male, 56 years old

	Subject 4: Female, 56 years old Healthy control subject: Subject 5, Male, 58 years old
Recruitment	Samples were obtained after written informed consent was obtained by the Vanderbilt Clinical Trials Center. Participants were selected for inclusion in the study based on PCR-confirmed diagnosis with SARS-CoV-2 infection and having convalesced. There was no potential self-selection bias in recruiting patients.
Ethics oversight	The studies were approved by the Institutional Review Board of Vanderbilt University Medical Center

Note that full information on the approval of the study protocol must also be provided in the manuscript.

Flow Cytometry

Plots

Confirm that:

☒ The axis labels state the marker and fluorochrome used (e.g. CD4-FITC).

☒ The axis scales are clearly visible. Include numbers along axes only for bottom left plot of group (a 'group' is an analysis of identical markers).

☒ All plots are contour plots with outliers or pseudocolor plots.

☒ A numerical value for number of cells or percentage (with statistics) is provided.

Methodology

Sample preparation	The frequency of SARS-CoV-2 spike antigen-specific B cells was enumerated from B cells pre-enriched from fresh or frozen PBMCs. B cells were labeled using a soluble recombinant S2Pecto protein produced in our laboratory and commercially available receptor-binding domain (RBD)-mouse Fc-fusion recombinant protein (Sino Biological). Functionality of antigens was validated using a conventional ACE2 binding assay. Briefly, B cells were purified magnetically (STEMCELL Technologies) and stained with anti-CD19, -IgD, -IgM, phenotyping antibodies (BD Biosciences) and biotinylated S protein. 4',6-diamidino-2- phenylindole (DAPI) was used as a viability dye to discriminate dead cells. Antigen-labeled class-switched memory B cell-S complexes (CD19+IgM-IgD-SARS-CoV2 S+DAPI-) were detected with phycoerythrin (PE)-labeled streptavidin conjugate and quantified using a SH800 cell sorter (Sony). After identification of the two subjects with the highest B cell response against S2Pecto protein, target-specific memory B cells were isolated by FACS using an SH800 cell sorter (from pooled PBMCs of these subjects, after labeling of B cells with biotinylated S protein. These details are also found in the Methods section.
Instrument	A SH800 cell sorter (Sony) was used for FACS and analytical flow cytometry studies
Software	SH800 software and FlowJo version 10 (Tree Star Inc.).
Cell population abundance	Frequency of antigen-specific B cells ranged from 0.2 to approx. 1 % of class-switched memory B cells. Antigen specificity of sorted cells was validated in functional assays after production of recombinant antibodies, which included antigen binding and virus neutralization.
Gating strategy	PBMCs were pre-enriched for B cells using magnetic negative selection with commercial (STEMCELL Technologies) kit. Extended Data Fig. 2 indicates gating strategy for sorting of antigen-labeled class switched B cells, that included staining with phenotyping anti-CD19, anti-IgM, and anti-IgD antibodies. Pre-enriched memory B cells were first gated by forward and side scatter. Dead cells were excluded using a viability dye (DAPI). Class-switched memory B cells were gated from this viable population as CD19 +,IgM-,IgD-. The gate for the antigen-specific subset was placed based on staining of B cells isolated from a non- immune healthy donor (no exposure history to SARS-CoV-2). Specificity of antigen labeling was validated in functional assays after production of recombinant antibodies, which included antigen binding and virus neutralization.

☒ Tick this box to confirm that a figure exemplifying the gating strategy is provided in the Supplementary Information.

Figure 1 (facing page). Findings from a Mouse Model of Electronic-Cigarette, or Vaping, Product Use–Associated Lung Injury (EVALI).

Panel A shows levels of vitamin E acetate (VEA) quantified by isotope-dilution mass spectrometry in bronchoalveolar-lavage (BAL) fluid harvested from mice. Values are means and standard deviations for 10 mice. Panel B shows albumin levels measured in BAL fluid from mice exposed to air, a mixture of propylene glycol and vegetable glycerin (PG–VG), or VEA. Values are means and standard deviations for 10 mice. Panel C shows the total number of CD45+ cells infiltrating the lung in mice exposed to air, PG–VG, or VEA. Values are means and standard deviations for 10 mice. The P values in Panels A, B, and C were calculated by two-way analysis of variance in Tukey's post-test comparisons among the exposure groups. Panel D shows BAL fluid from a mouse exposed to VEA, containing lipid-laden macrophages (representative examples are indicated with arrows) with cytoplasmic staining by oil red O in a vesicular pattern. The macrophages are numerous and contain variable amounts of lipid. Background pneumocytes (arrowheads) show comparatively scant cytoplasm and are present as single cells or loose sheets. Panel E shows BAL fluid from a mouse exposed to PG–VG, which contained fewer identifiable macrophages and had minimal to no specific staining by oil red O. Without lipid staining, it is more difficult to distinguish between small alveolar macrophages and pneumocytes in these preparations. Panels F and G show findings in lung sections. In mice exposed to VEA (Panel F), alveolar macrophages (arrowheads and circles) in residence among pneumocytes (P) lining the alveoli (A) contained abundant oil red O–stained lipid. In mice exposed to PG–VG, tiny oil red O–stained granules in the cytoplasm of cells lining the alveoli, including pneumocytes (arrows) and alveolar macrophages (arrowheads), were observed. B denotes bronchiole.

the generated aerosols would be required to identify such by-products. Another limitation is that we did not expose animals to aerosols that contained tetrahydrocannabinol (THC) or nicotine in a dose-dependent manner. Finally, it is possible that aerosols generated from other lipophilic solvents may produce outcomes similar to the outcome seen with vitamin E acetate in this study. Future studies are needed to address these issues. Our findings, coupled with previous research identifying vitamin E acetate in BAL fluid from patients with EVALI[1,2] and in samples of case-associated product liquids,[5] provide additional evidence for vitamin E acetate as a possible cause of EVALI.

Tariq A. Bhat, Ph.D.
Maciej L. Goniewicz, Ph.D., Pharm.D.
Yasmin M. Thanavala, Ph.D.
Roswell Park Comprehensive Cancer Center
Buffalo, NY
yasmin.thanavala@roswellpark.org

and Others

Dr. Blount is a member of the Lung Injury Response Lab Task Force; additional members are listed in the Supplementary Appendix, available with the full text of this letter at NEJM.org.

A complete list of authors is available with the full text of this letter at NEJM.org.

The views and opinions expressed in this letter are those of the authors and do not necessarily represent the official position of the Centers for Disease Control and Prevention, the National Institutes of Health, or the Food and Drug Administration.

Supported by grants from the National Heart, Lung, and Blood Institute of the National Institutes of Health (R01HL142511), the National Cancer Institute (NCI) (P30CA016056), and the NCI and the Center for Tobacco Products of the Food and Drug Administration (U54CA228110).

Disclosure forms provided by the authors are available with the full text of this letter at NEJM.org.

This letter was published on February 26, 2020, at NEJM.org.

1. Blount BC, Karwowski MP, Morel-Espinosa M, et al. Evaluation of bronchoalveolar lavage fluid from patients in an outbreak of e-cigarette, or vaping, product use–associated lung injury — 10 states, August–October 2019. MMWR Morb Mortal Wkly Rep 2019;68:1040-1.
2. Blount BC, Karwowski MP, Shields PG, et al. Vitamin E acetate in bronchoalveolar-lavage fluid associated with EVALI. N Engl J Med 2020;382:697-705.
3. Layden JE, Ghinai I, Pray I, et al. Pulmonary illness related to e-cigarette use in Illinois and Wisconsin — preliminary report. N Engl J Med. DOI: 10.1056/NEJMoa1911614.
4. Maddock SD, Cirulis MM, Callahan SJ, et al. Pulmonary lipid-laden macrophages and vaping. N Engl J Med 2019;381:1488-9.
5. Krishnasamy VP, Hallowell BD, Ko JY, et al. Update: characteristics of a nationwide outbreak of e-cigarette, or vaping, product use–associated lung injury — United States, August 2019–January 2020. MMWR Morb Mortal Wkly Rep 2020;69:90-4.

DOI: 10.1056/NEJMc2000231

SARS-CoV-2 Viral Load in Upper Respiratory Specimens of Infected Patients

TO THE EDITOR: The 2019 novel coronavirus (SARS-CoV-2) epidemic, which was first reported in December 2019 in Wuhan, China, and has been declared a public health emergency of international concern by the World Health Organization, may progress to a pandemic associated with substantial morbidity and mortality. SARS-CoV-2 is genetically related to SARS-CoV, which

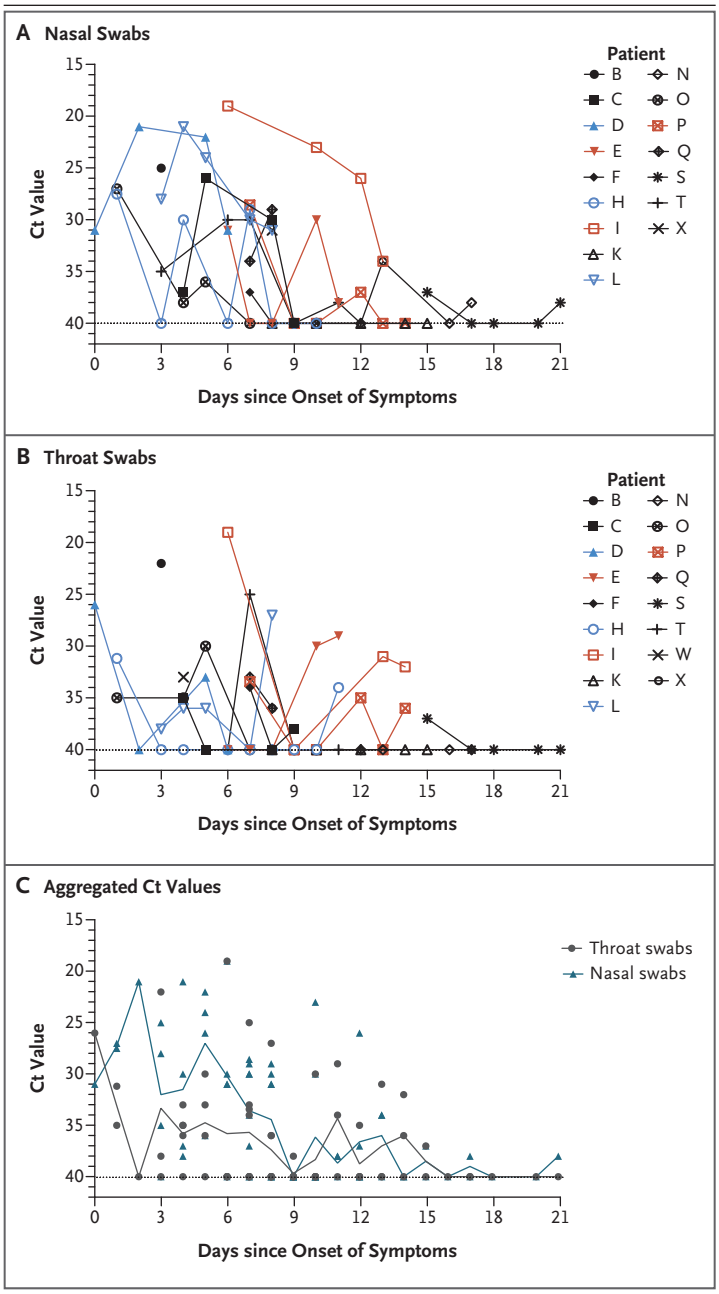

Figure 1. Viral Load Detected in Nasal and Throat Swabs Obtained from Patients Infected with SARS-CoV-2.

Panel A shows cycle threshold (Ct) values of Orf1b on reverse-transcriptase–polymerase-chain-reaction (RT-PCR) assay that were detected in nasal swabs obtained from 14 patients with imported cases and 3 patients with secondary cases, and Panel B shows the Ct values in throat swabs. Patient Z did not have clinical symptoms and is not included in the figure. Patients with imported cases who had severe illness (Patients E, I, and P) are labeled in red, patients with imported cases who had mild-to-moderate illness are labeled in black, and patients with secondary cases (Patients D, H, and L) are labeled in blue. A linear mixed-effects model was used to test the Ct values from nasal and throat swabs among severe as compared with mild-to-moderate imported cases, which allowed for within-patient correlation and a time trend of Ct change. The mean Ct values in nasal and throat swabs obtained from patients with severe cases were lower by 2.8 (95% confidence interval [CI], −2.4 to 8.0) and 2.5 (95% CI, −0.8 to 5.7), respectively, than the values in swabs obtained from patients with mild-to-moderate cases. Panel C shows the aggregated Ct values of Orf1b on RT-PCR assay in 14 patients with imported cases and 3 patients with secondary cases, according to day after symptom onset. Ct values are inversely related to viral RNA copy number, with Ct values of 30.76, 27.67, 24.56, and 21.48 corresponding to 1.5×10^4, 1.5×10^5, 1.5×10^6, and 1.5×10^7 copies per milliliter. Negative samples are denoted with a Ct of 40, which was the limit of detection.

caused a global epidemic with 8096 confirmed cases in more than 25 countries in 2002–2003.[1] The epidemic of SARS-CoV was successfully contained through public health interventions, including case detection and isolation. Transmission of SARS-CoV occurred mainly after days of illness[2] and was associated with modest viral loads in the respiratory tract early in the illness, with viral loads peaking approximately 10 days after symptom onset.[3] We monitored SARS-CoV-2 viral loads in upper respiratory specimens obtained from 18 patients (9 men and 9 women; median age, 59 years; range, 26 to 76) in Zhuhai, Guangdong, China, including 4 patients with secondary infections (1 of whom never had symptoms) within two family clusters (Table S1 in the Supplementary Appendix, available with the full text of this letter at NEJM.org). The patient who never had symptoms was a close contact of a patient with a known case and was therefore monitored. A total of 72 nasal swabs (sampled from the mid-turbinate and nasopharynx) (Fig. 1A) and 72 throat swabs (Fig. 1B) were analyzed, with 1 to 9 sequential samples obtained from each patient. Polyester flock swabs were used for all the patients.

From January 7 through January 26, 2020, a total of 14 patients who had recently returned from Wuhan and had fever (≥37.3°C) received a diagnosis of Covid-19 (the illness caused by SARS-CoV-2) by means of reverse-transcriptase–polymerase-chain-reaction assay with primers and probes targeting the N and Orf1b genes of SARS-CoV-2; the assay was developed by the Chinese Center for Disease Control and Prevention. Samples were tested at the Guangdong Provincial Center for Disease Control and Pre-

vention. Thirteen of 14 patients with imported cases had evidence of pneumonia on computed tomography (CT). None of them had visited the Huanan Seafood Wholesale Market in Wuhan within 14 days before symptom onset. Patients E, I, and P required admission to intensive care units, whereas the others had mild-to-moderate illness. Secondary infections were detected in close contacts of Patients E, I, and P. Patient E worked in Wuhan and visited his wife (Patient L), mother (Patient D), and a friend (Patient Z) in Zhuhai on January 17. Symptoms developed in Patients L and D on January 20 and January 22, respectively, with viral RNA detected in their nasal and throat swabs soon after symptom onset. Patient Z reported no clinical symptoms, but his nasal swabs (cycle threshold [Ct] values, 22 to 28) and throat swabs (Ct values, 30 to 32) tested positive on days 7, 10, and 11 after contact. A CT scan of Patient Z that was obtained on February 6 was unremarkable. Patients I and P lived in Wuhan and visited their daughter (Patient H) in Zhuhai on January 11 when their symptoms first developed. Fever developed in Patient H on January 17, with viral RNA detected in nasal and throat swabs on day 1 after symptom onset.

We analyzed the viral load in nasal and throat swabs obtained from the 17 symptomatic patients in relation to day of onset of any symptoms (Fig. 1C). Higher viral loads (inversely related to Ct value) were detected soon after symptom onset, with higher viral loads detected in the nose than in the throat. Our analysis suggests that the viral nucleic acid shedding pattern of patients infected with SARS-CoV-2 resembles that of patients with influenza[4] and appears different from that seen in patients infected with SARS-CoV.[3] The viral load that was detected in the asymptomatic patient was similar to that in the symptomatic patients, which suggests the transmission potential of asymptomatic or minimally symptomatic patients. These findings are in concordance with reports that transmission may occur early in the course of infection[5] and suggest that case detection and isolation may require strategies different from those required for the control of SARS-CoV. How SARS-CoV-2 viral load correlates with culturable virus needs to be determined. Identification of patients with few or no symptoms and with modest levels of detectable viral RNA in the oropharynx for at least 5 days suggests that we need better data to determine transmission dynamics and inform our screening practices.

Lirong Zou, M.Sc.
Guangdong Provincial Center for Disease Control and Prevention
Guangzhou, China

Feng Ruan, M.Med.
Zhuhai Center for Disease Control and Prevention
Zhuhai, China

Mingxing Huang, Ph.D.
Fifth Affiliated Hospital of Sun Yat-Sen University
Zhuhai, China

Lijun Liang, Ph.D.
Guangdong Provincial Center for Disease Control and Prevention
Guangzhou, China

Huitao Huang, B.Sc.
Zhuhai Center for Disease Control and Prevention
Zhuhai, China

Zhongsi Hong, M.D.
Fifth Affiliated Hospital of Sun Yat-Sen University
Zhuhai, China

Jianxiang Yu, B.Sc.
Min Kang, M.Sc.
Yingchao Song, B.Sc.
Guangdong Provincial Center for Disease Control and Prevention
Guangzhou, China

Jinyu Xia, M.D.
Fifth Affiliated Hospital of Sun Yat-Sen University
Zhuhai, China

Qianfang Guo, M.Sc.
Tie Song, M.Sc.
Jianfeng He, B.Sc.
Guangdong Provincial Center for Disease Control and Prevention
Guangzhou, China

Hui-Ling Yen, Ph.D.
Malik Peiris, Ph.D.
University of Hong Kong
Hong Kong, China

Jie Wu, Ph.D.
Guangdong Provincial Center for Disease Control and Prevention
Guangzhou, China
771276998@qq.com

Ms. Zou, Mr. Ruan, and Dr. Huang contributed equally to this letter.

Disclosure forms provided by the authors are available with the full text of this letter at NEJM.org.

This letter was published on February 19, 2020, and updated on February 20, 2020, at NEJM.org.

1. Summary of probable SARS cases with onset of illness from 1 November 2002 to 31 July 2003. Geneva: World Health Organization, 2004 (https://www.who.int/csr/sars/country/table2004_04_21/en/).
2. Lipsitch M, Cohen T, Cooper B, et al. Transmission dynamics and control of severe acute respiratory syndrome. Science 2003;300:1966-70.
3. Peiris JSM, Chu CM, Cheng VCC, et al. Clinical progression and viral load in a community outbreak of coronavirus-associated SARS pneumonia: a prospective study. Lancet 2003;361:1767-72.
4. Tsang TK, Cowling BJ, Fang VJ, et al. Influenza A virus shedding and infectivity in households. J Infect Dis 2015;212:1420-8.
5. Rothe C, Schunk M, Sothmann P, et al. Transmission of 2019-nCoV infection from an asymptomatic contact in Germany. N Engl J Med 2020;382:970-1.

DOI: 10.1056/NEJMc2001737